ONE-DIMENSIONAL ANALYSES: SHOCK WAVE PROPAGATION FROM UNDERWATER CRATERING DETONATIONS

Charles M. Snell

Army Engineer Waterways Experiment Station

Prepared for:

Army Research Office

January 1975

MISCELLANEOUS PAPER E-75-1

ONE-DIMENSIONAL ANALYSES: SHOCK WAVE PROPAGATION FROM UNDERWATER CRATERING DETONATIONS

Charles M. Snell

January 1975

U.S. Army Engineer Waterways Experiment Station
Explosive Excavation Research Laboratory
Livermore, California

UNCLASSIFIED

SECURITY CLASSIFICATION OF THIS PAGE (When Data Entered)

REPORT DOCUMENTATION PAGE		READ INSTRUCTIONS BEFORE COMPLETING FORM
1. REPORT NUMBER WES-MP-E-75-1	2. GOVT ACCESSION NO.	3. RECIPIENT'S CATALOG NUMBER
4. TITLE (and Subtitle) ONE-DIMENSIONAL ANALYSES: SHOCK WAVE PROPAGATION FROM UNDERWATER CRATERING DETONATIONS		5. TYPE OF REPORT & PERIOD COVERED Final 6. PERFORMING ORG. REPORT NUMBER
7. AUTHOR(s) Charles M. Snell Lawrence Livermore Laboratory, Livermore, CA		8. CONTRACT OR GRANT NUMBER(s) 20061102B 33G
9. PERFORMING ORGANIZATION NAME AND ADDRESS U.S. Army Engineer Waterways Experiment Station Explosive Excavation Research Laboratory Livermore, CA 94550		10. PROGRAM ELEMENT, PROJECT, TASK AREA & WORK UNIT NUMBERS
11. CONTROLLING OFFICE NAME AND ADDRESS U.S. Army Research Office Box CM, Duke Station Durham, North Carolina 27706		12. REPORT DATE January 1975 13. NUMBER OF PAGES 366
14. MONITORING AGENCY NAME & ADDRESS(if different from Controlling Office) U.S. Army Research Office Box CM, Duke Station Durham, North Carolina 27706		15. SECURITY CLASS. (of this report) Unclassified 15a. DECLASSIFICATION/DOWNGRADING SCHEDULE

16. DISTRIBUTION STATEMENT (of this Report)

Approved for public release; distribution unlimited.

17. DISTRIBUTION STATEMENT (of the abstract entered in Block 20, if different from Report)

18. SUPPLEMENTARY NOTES

19. KEY WORDS (Continue on reverse side if necessary and identify by block number)

Cratering	Underwater explosions
Explosive excavation	Airblast
High-explosive cratering	Spall velocities
Hydrodynamic calculations	Multilayer shock propagation
Underwater excavation	

20. ABSTRACT (Continue on reverse side if necessary and identify by block number)

Research has recently been conducted on the use of large buried chemical explosive charges for engineering excavation. Investigations in this area were initially concerned with crater formation in relatively homogeneous rock media, a process which is now well understood. However, it has become apparent that the greatest cost and operational advantages may be realized by applying the technique to rock excavation in an underwater environment. Cratering dynamics in an underwater (two-layer) configuration have not been well understood. Small-scale modeling tests and large-scale excavation projects have revealed two new

DD FORM 1 JAN 73 1473 EDITION OF 1 NOV 65 IS OBSOLETE

PRICES SUBJECT TO CHANGE

UNCLASSIFIED

SECURITY CLASSIFICATION OF THIS PAGE (When Data Entered)

20. Abstract (continued)

factors which significantly influence underwater cratering processes: (1) early-time dynamic effects caused by the presence of the rock-water interface and water layer; and (2) very late-time water washback and slope failure effects in the crater vicinity. This report addresses the first of these two effects by means of hydrodynamic computer calculations. The one-dimensional spherically-symmetric "SOC" computer program has been used to calculate the dynamic effects of a spherical explosive charge emplaced in rock media and in rock with overlying water layers of various depths. Calculations have been conducted for three different rock types: coral, weak basalt, and granite. Significant correlations of dynamic behavior with medium properties and layer depths have been established. Some comparisons with experimental data have also been accomplished. The results indicate that computer design calculations for future underwater events are quite feasible.

MISCELLANEOUS PAPER E-75-1

ONE-DIMENSIONAL ANALYSES: SHOCK WAVE PROPAGATION FROM UNDERWATER CRATERING DETONATIONS

Charles M. Snell*

U. S. ARMY ENGINEER WATERWAYS EXPERIMENT STATION
EXPLOSIVE EXCAVATION RESEARCH LABORATORY
Livermore, California

MS. date: May 1974

*Earth Sciences (K) Division, Lawrence Livermore Laboratory, Livermore, CA

FOREWORD

Within the past five years, several major engineering excavation projects have been accomplished with the use of large buried explosive charges. The U.S. Army Corps of Engineers Waterways Experiment Station Explosive Excavation Research Laboratory (EERL) has been intimately involved in the development and application of this technology. The use of large explosive cratering charges on dry land is now relatively well understood and detailed design procedures are available. However, a number of potential applications involve excavation in submerged environments. Underwater cratering dynamics are not well understood. Accordingly, it was decided to initiate a program of numerical hydrodynamic calculations to model the effects of buried underwater explosions and achieve a better understanding of the dynamic mechanisms involved. This program was implemented under the direction of EERL, and calculations were performed by the Earth Sciences (K) Division of the Lawrence Livermore Laboratory (LLL).

This report summarizes the results of 18 one-dimensional hydrodynamic calculations plus several subsidiary comparison calculations and acoustic wave calculations for high-explosive detonations in saturated media and in saturated media overlain by a layer of water. The hydrodynamic calculations provide an early-time description of close-range shock wave transmission within the rock medium, including time histories of pressure, stress, and particle velocity, shock interactions at the interfaces, spall velocities, shear stress and failure effects, etc. Safety-related phenomena may likewise be estimated from this information. These calculational results form a basis for future two-dimensional multilayer cratering calculations which may be used to design underwater excavation events, both nuclear and conventional.

The investigation described herein was sponsored by U.S. Army Research Office grant ARO-D No. I-479-E under R & D Project No. 20061102B33G. In accordance with ARO-D program requirements, this report documents results of the one-dimensional underwater calculations and related studies to date.

ONE-DIMENSIONAL ANALYSES: SHOCK WAVE PROPAGATION FROM UNDERWATER CRATERING DETONATIONS

SUMMARY

Research has recently been conducted on the use of large buried chemical explosive charges for engineering excavation. Investigations in this area were initially concerned with crater formation in relatively homogeneous rock media, a process which is now well understood. However, it has become apparent that the greatest cost and operational advantages may be realized by applying the technique to rock excavation in an underwater environment. Cratering dynamics in an underwater (two-layer) configuration have not been well understood. Small-scale modeling tests and large-scale excavation projects have revealed two new factors which significantly influence underwater cratering processes: (1) Early-time dynamic effects caused by the presence of the rock-water interface and water layer; and (2) very late-time water washback and slope failure effects in the crater vicinity. This report addresses the first of these two effects by means of hydrodynamic computer calculations. The one-dimensional spherically-symmetric "SOC" computer program has been used to calculate the dynamic effects of a spherical explosive charge emplaced in rock media and in rock with overlying water layers of various depths. Calculations have been conducted for three different rock types, coral, weak basalt, and granite. Significant correlations of dynamic behavior with medium properties and layer depths have been established. Some comparisons with experimental data have also been accomplished. The results indicate that computer design calculations for future underwater events are quite feasible.

ACKNOWLEDGMENTS

The author wishes to acknowledge the invaluable assistance of the Lawrence Livermore Laboratory's K-Division, Rock Mechanics and Containment Groups. In particular, useful suggestions were provided by D. E. Burton, J. B. Bryan, B. K. Crowley, and T. R. Butkovich. Programmers J. G. Shaw, H. O. Brovont, and F. L. Petersen aided in the use of the computer codes. Material properties and static compressibility data were provided by P. L. Turner, D. R. Stephens, and H. C. Heard. Appreciation is also expressed to J. Lattery and other staff members of the Explosive Excavation Research Laboratory for helpful discussions and unpublished information on past experiments.

I would particularly like to thank Division secretaries Diane Taasevigen and Lydia Burrow for faithful work and stoic courage during repeated revisions of this manuscript.

TABLE OF CONTENTS

LIST OF FIGURES

LIST OF FIGURES (cont.)

LIST OF FIGURES (cont.)

LIST OF FIGURES (cont.)

LIST OF FIGURES (cont.)

LIST OF FIGURES (cont.)

LIST OF FIGURES (cont.)

LIST OF FIGURES (cont.)

LIST OF TABLES

List of Tables (continued)

CONVERSION FACTORS

Units of measurement used in this report may be converted to metric units as follows:

MULTIPLY	BY	TO OBTAIN
inches	2.54	centimeters
feet	0.3048	meters
cubic feet	0.02832	cubic meters
cubic yards	0.764555	cubic meters
pounds	0.4535924	kilograms
foot-pounds	0.138255	meter-kilograms
pounds per cubic foot	16.02	kilograms per cubic meter
Fahrenheit degrees	5/9	Celsius or Kelvin degrees*
pounds per square inch	0.00689476	meganewtons per sq. meter
pounds per square inch	0.0689476	bars
atmospheres	1.0133	bars
megabars (Mbars)	10^{12}	dynes/cm^2
tons (explosive energy release)	4.186×10^{16}	ergs
tons (explosive energy release)	10^9	g-cal
tons (explosive energy release)	10^{-3}	kilotons
tons (explosive energy release)	4.186×10^4	Mbar-cm^3
psi-sec/ft (impedance)	4.42×10^{-4}	g/cm^2-sec

* To obtain Celsius (C) temperature readings from Fahrenheit (F) readings, use the following formula: C = (5/9)(F-32). To obtain Kelvin (K) readings, use: K = (5/9)(F-32)+273.15.

NOMENCLATURE AND MATERIAL PARAMETERS

Nomenclature

C_{sonic}	=	Sonic wave transmission velocity
P	=	pressure (kbar or Mbar)
σ_r	=	Radial stress (kbar or Mbar)
σ_T	=	Tangential stress (kbar or Mbar)
K	=	Elastic bulk modulus (kbar or Mbar)
G	=	Elastic shear modulus (kbar or Mbar)
σ	=	Poisson's ratio (dimensionless)
V or V_p	=	Material particle velocity (may be either peak or time-dependent velocity)
R	=	Range from center of problem (dynamic calculations); or horizontal range from surface ground zero (airblast calculations)
T_{p90}	=	Acoustic pressure transmission factor in the normal direction at an interface.
R_{p90}	=	Acoustic pressure reflection factor in the normal direction at an interface.
$V_o=V_{sp}$	=	Vertical spall velocity at an interface.
$\sigma_1,\sigma_2,\sigma_3$	=	Three normal components of stress in the principal coordinate system.
$P_{bar}=\bar{P}$	=	Mean pressure: $-1/3\ (\sigma_1+\sigma_2+\sigma_3)$
k	=	Shear strength of material = $(\sigma_1-\sigma_3)/2$ at failure surface.
KE	=	Kinetic energy contained in a given material or problem region (Mbar-cm^3)
IE	=	Internal energy contained in a given material or problem region (Mbar-cm^3)
D_r	=	Depth of rock layer (including explosive radius) in a vertical problem (equal to the total depth of burial "DOB" for an event with no water layer).
D_w	=	Depth of overlying water layer in a vertical problem.
P_{cav}	=	Volume-weighted pressure of explosive cavity gases (Mbar or kbar)

Nomenclature (continued)

DOB	=	Total depth of burial, measured from explosive center to free surface = $D_r + D_w$.
ΔP_o	=	Peak airblast overpressure immediately above surface ground zero (psi; 1 psi = 6.89×10^{-8} Mbar
ΔP	=	Peak airblast overpressure (at ground level) beyond the immediate detonation vicinity (psi).
α	=	Constant in equation for peak airblast overpressure.
ρC	=	Acoustic impedance of a medium (psi-sec/ft).
ν	=	Artificial viscosity; numerical factor ≈ 0.1 to 0.2, used to damp high-frequency noise in the code calculations.

Abbreviations:

cm	=	centimeter
m	=	meter
ft	=	foot
g	=	gram
sec	=	second
Mbar	=	megabar
kbar	=	kilobar
psi	=	pounds per square inch
kt	=	kiloton (energy)
cal	=	calorie
cm^3	=	cubic centimeter
dy	=	dyne

Subscripts:

w	=	water	
r	=	rock	
a	=	air	
cav	=	cavity	
r	=	radial	stress-related parameters
T	=	tangential	stress-related parameters

Material Parameters

ρ_o = Initial bulk density of material (mass/volume; g/cm^3)

V_o = Initial specific volume = $\frac{1}{\rho_o}$ (volume/mass; cm^3/g)

ρ = Density as a function of pressure (mass/volume; g/cm^3)

μ = $\rho/\rho_o - 1$ = volumetric compression (dimensionless)

ρ_{grain} = Grain density of a rock material (mass of solids/volume of solids; g/cm^3)

ρ_W = Water density ($\approx$ 1.0 g/cm^3 assumed)

Z = Water content by weight (weight water/total weight of sample)

ρ_{dry} = Dry density (weight of solids/total volume; g/cm^3)

ϕ = Total porosity (1.0 - volume of solids/total volume)

ψ = Gas-filled porosity (volume of gas-filled voids/total volume)

S = Saturation (volume of water-filled voids/total volume of voids)

The following formulae may be used to calculate relationships between material parameters[1]:

$$\rho_{dry} = \rho_o (1 - Z) = \rho_{grain} (1 - \phi)$$

$$\rho_o = 1/V_o$$

$$\rho_o = \rho_{grain} [(1-\phi)/(1-Z)]$$

$$\phi = 1 - \left[\frac{\rho_o(1-Z)}{\rho_{grain}}\right]$$

$$\psi = 1 - \frac{\rho_o}{\rho_{grain}} (1-Z) - Z\rho_o = \phi - Z\rho_o$$

$$S = 1 - \frac{\psi}{\phi} = [\rho_o Z]/[1 - \frac{\rho_o}{\rho grain} (1-Z)] = \rho_o Z/\phi$$

Z (for 100% saturation) = $(\rho grain - \rho_o)/(\rho_o \rho grain - \rho_o)$

RELATIONSHIPS AMONG ELASTIC CONSTANTS [1,2,3]

K = bulk modulus (dy/cm^2)
G = shear modulus (dy/cm^2)
σ = Poisson's ratio
v_c = Compressional wave elastic velocity (cm/sec)
E = Young's modulus (dy/cm^2)
λ = Lamé's constant (dy/cm^2)
$\rho = \rho_o$ = Bulk density (g/cm^3)
v_s = Shear wave elastic velocity (cm/sec)

VARIABLES: Indep. \ Dependent		σ	K	λ	$G = \rho v_s^2$	E	ρv_c^2
σ	K	σ	K	$\frac{3K\sigma}{1+\sigma}$	$\frac{3K}{2}\frac{1-2\sigma}{1+\sigma}$	$3K(1-2\sigma)$	$3K\frac{1-\sigma}{1+\sigma}$
	λ	σ	$\frac{\lambda(1+\sigma)}{3\sigma}$	λ	$\frac{\lambda}{2\sigma}(1-2\sigma)$	$\frac{\lambda}{\sigma}(1+\sigma)(1-2\sigma)$	$\frac{\lambda}{\sigma}(1-\sigma)$
	G	σ	$\frac{2G}{3}\frac{1+\sigma}{1-2\sigma}$	$\frac{2G\sigma}{1-2\sigma}$	G	$2G(1+\sigma)$	$2G\frac{1-\sigma}{1-2\sigma}$
	E	σ	$\frac{E}{3(1-2\sigma)}$	$\frac{E\sigma}{(1+\sigma)(1-2\sigma)}$	$\frac{E}{2(1+\sigma)}$	E	$\frac{E(1-\sigma)}{(1+\sigma)(1-2\sigma)}$
K	λ	$\frac{\lambda}{3K-\lambda}$	K	λ	$\frac{3}{2}(K-\lambda)$	$\frac{9K(K-\lambda)}{3K-\lambda}$	$3K-2\lambda$
	G	$\frac{3K-2G}{2(3K+G)}$	K	$K-\frac{2G}{3}$	G	$\frac{9KG}{3K+G}$	$K+\frac{4G}{3}$
	E	$\frac{3K-E}{6K}$	K	$3K\frac{3K-E}{9K-E}$	$\frac{3KE}{9K-E}$	E	$3K\frac{3K+E}{9K-E}$
λ	G	$\frac{\lambda}{2(\lambda+G)}$	$\lambda+\frac{2G}{3}$	λ	G	$G\frac{3\lambda+2G}{G+\lambda}$	$\lambda+2G$
G	E	$\frac{E-2G}{2G}$	$\frac{GE}{3(3G-E)}$	$G\frac{E-2G}{3G-E}$	G	E	$G\frac{4G-E}{3G-E}$
v_c	v_s and $G=\rho v_s^2$	$\frac{(v_c/v_s)^2-2}{2((v_c/v_s)^2-1)}$	$G((v_c/v_s)^2-\frac{4}{3})$	$G((v_c/v_s)^2-2)$	ρv_s^2	$G\frac{3(v_c/v_s)^2-4}{(v_c/v_s)^2-1}$	ρv_c^2
		$\frac{\rho v_c^2-2G}{2(\rho v_c^2-G)}$	$\rho v_c^2-\frac{4}{3}G$	ρv_c^2-2G	$\frac{3}{4}(\rho v_c^2-K)$	$\frac{3\rho v_c^2-4G}{(\rho v_c^2/G)-1}$	--

ONE DIMENSIONAL ANALYSES: SHOCK WAVE PROPAGATION FROM UNDERWATER CRATERING DETONATIONS

Charles M. Snell

I. INTRODUCTION

Widespread interest in underwater excavation with large explosive charges was first manifested during the early stages of the Plowshare program for peaceful uses of nuclear explosives.[4] This interest was primarily a result of three factors: (1) The enormous commercial value of deep-draft harbors and navigation facilities; (2) The difficulty and expense of underwater excavation in rock with conventional techniques; and (3) The apparent potential of nuclear explosives for rapid, efficient large-scale excavation. A variety of possible sites and applications were considered, including some projects which could not be economically accomplished with conventional construction techniques. An experimental harbor excavation model, Project Chariot, was planned for a remote section of the Alaskan coast, but was never implemented.[4] Other conceptual designs included the excavation of navigation channels, widening and deepening extant channels, removal of submerged obstacles, creation or improvement of harbor entranceways, etc.

During the same period, extensive investigations of dry-land cratering with nuclear explosives were carried out. Both theoretical and experimental studies were performed, culminating in the series of Plowshare cratering events at the Nevada Test Site. A physical model was developed to describe the phenomena of crater formation. Hydrodynamic computer programs were written to predict effects of buried detonations. It soon became apparent that computer techniques offered a

means of analyzing the results of past experiments and of predicting both crater dimensions and other physical effects of future events. Thus, the design uncertainties and the need for extensive field experiments could be greatly reduced. Successful calculations were performed for the Plowshare events and for high-explosive cratering tests in various media. Certain of the calculations made during the Trans-Isthmian Canal Studies involved wet or fully saturated rock, similar to the media which might be encountered in underwater excavation projects. However, no studies were performed for submerged configurations.

After conclusion of the Plowshare test series, interest in nuclear cratering applications waned. Nonetheless, some of the modeling tests associated with the Plowshare program demonstrated that high-explosive cratering charges present certain benefits for smaller excavation tasks. Within the past five years, several major engineering projects have been performed with large conventional explosive emplacements.[5,6] Two of these projects involved excavation in an underwater environment.[7,8,9] Due to the high cost of excavation in submerged rock, this area is perhaps the most promising for future use of large-charge blasting. In addition to the cost advantage, explosive excavation may also provide environmental benefits over other methods, greater speed and efficiency of construction, applicability to emergency situations, and the ability to carry out projects which would be extremely difficult or dangerous to accomplish with standard techniques. The major problem associated with underwater designs is the lack of experience and empirical data on underwater cratering. The earliest submerged high-explosive cratering tests were intended to model weapons effects; the charges were located at the water-medium interface[10], or were buried at very shallow depths in the medium (too shallow to be of interest for excavation design).[11] More recent excavation shots were emplaced in saturated sand[8] or in weak low-density coral[9], with no large-scale tests in submerged rock or other media. The ability to accurately predict dry-land crater dimensions in a variety of media is dependent on the combination of a broad data base and a fundamental

understanding of the crater formation process. Indeed, no major surprises have been encountered during any recent experiments. The opposite situation prevails for underwater cratering: Dimensions, crater shape, and collateral effects cannot be reliably predicted before the shot. In the past, it has been necessary to conduct expensive single-charge calibration events at the project site, or to utilize an untested design which may not precisely achieve project requirements.

Most underwater cratering emplacements consist essentially of a two-layer configuration, dense saturated solid material overlain by a much less dense layer of water. The considerable differences between dry land and submerged craters are thus attributable to two factors: (1) Water washback or liquefied flow of the fallback material; washback effects occur at very late times, after the ejecta mound has collapsed. And, (2) the influence of the water layer on shock propagation and material dynamics at early times, as the shock wave travels outward and is reflected at the rock interface and the water surface. The subsidiary effects of saturation may also reduce the strength of the rock and increase the efficiency of shock propagation (most submerged events are expected to occur in fully-saturated material).

Water washback effects are known to be most critical in fine-grained cohesionless media such as sand or crushed coral. For small-scale ($\approx$ one pound) cratering tests in saturated sand, it has been observed that crater dimensions and shapes change dramatically at relatively shallow water layer depths between 0.05 and 0.2 times the charge burial depth in the solid ($D_w/D_r \approx 0.05\text{-}0.2$). Craters in this depth range are modified from typical "dry-land" contours into broad, shallow, saucer-shaped depressions with little or no elevated lip material. Appearances indicate that the normal lip material is overtopped by water washback; slope failure occurs and ejected material flows into the crater, producing the flattened shape. The crater radius actually increases sharply at $D_w/D_r \approx 0.1$, while the crater depth and lip height decrease abruptly. For deeper water layers, $D_w/D_r \gtrapprox 0.3\text{-}0.4$, the crater radius begins to decrease gradually, returning to approximately the "dry-land" value at

$D_w/D_r \approx 1$, while the crater depth also continues to decrease slowly. Small lips tend to reappear for deeper water layers, but the shallow crater depths and flattened contours are maintained.[12] Current evidence indicates that shallow flat-bottomed craters are also formed by large-scale (≈ one-ton) events in a submerged sand environment ($D_w/D_r < 0.6$).[8] Finally, somewhat similar craters are produced by large charges (1-10 tons) in weak submerged coral, with the added modification that collapse and compaction of the porous coral matrix cause very large crater radii and very large volumes. The flattened shape and shallow crater depth are again apparent. The cratering process in coral is interpreted as one of shock crushing and liquefaction of the weak matrix to great ranges, beyond the distance at which the lip-forming material would normally come to rest. The lip fallback and its liquefied nonsupporting base thus fail radially and flow into the crater with the water washback. The net volume of the coral material is reduced by fracturing, compaction, and later settlement of the finely-crushed fallback, accounting for the relatively large volumes and radii of the coral craters. It is expected that flat-bottomed lipless craters will occur in coral except possibly when the ratio of water depth to burial depth is extremely small.[7,5]

Very weak or fine-grained materials are the exception rather than the rule in most underwater blasting situations. Indeed, the greatest advantages of explosive excavation methods may be attained for the more difficult tasks of excavating intermediate or high-strength rock. Unfortunately, little information is available on underwater cratering in media of this type. Small-scale tests (≈ one pound) have been conducted in rather weak saturated concrete with no overlying water and with water depths $D_w/D_r \approx 0.3$-2.1. This material fractures into large chunks, similar to rock ejecta. The limited data indicate that crater dimensions are not sensitive to the presence of water overburden, although the crater depths may be slightly reduced at all water layer depths.[13,7] It appears probable that dense media which break into large granular sizes when cratered are not subject to water washback and slope failure effects, at least for shallow to intermediate depth water layers. The conditions under which slope failure begins will depend on particle size (or size gradation), particle

density, water depth, and the exact configuration of the experiment. The relative importance of these factors has not been investigated. However, for typical high-explosive cratering configurations, washback effects are likely to be predominant in cohesionless or finely-crushed materials (particle sizes $\lesssim$ a few inches), and much less important or negligible in most rock media (particle sizes $\gtrsim$ several inches to several feet, densities > 2 g/cm^3).

Since engineering experience is not currently adequate to enable confident design of submerged events, it is appropriate to ask if the computational methods evolved during the earlier Plowshare studies may be applied to this area. In order to answer this question, it is necessary to examine briefly the characteristics of the available techniques. Several versions of Lagrangian hydrodynamic computer codes are used to calculate the effects of buried detonations. These codes utilize finite difference schemes to numerically model adiabatic shock wave propagation through media for which constitutive relations are known. Elastic, plastic, inelastic, fluid, and gaseous behavior of a material may be taken into account. The available codes include SOC[14,15] (one-dimensional, spherically symmetric shock propagation) and TENSOR[16,17] (two-dimensional, cylindrically-symmetric shock propagation). Both codes carry up to 26 variables which describe the state of the material at each point in the Lagrangian grid. The basic variables include displacements, velocities, internal energies, pressures, stress tensor normal components, local compression, etc. The one-dimensional code may be used to calculate free-field shock propagation at a constant depth in a nearly-infinite medium ("horizontal problem"); alternatively, vertical shock propagation in a constant gravitational field may be modeled, and a free surface or a rigid wall may be introduced at any desired range to reflect the shock wave back toward the center of the problem ("vertical problem"). The two-dimensional code is normally used to determine the effects of a single explosive source in a cylindrically-symmetric configuration. For example, a spherical source emplaced below a horizontal free-surface may be used to model the formation of a single-charge crater. Both codes have provision for regions of various materials with different properties.

Certain limitations inherent in the Lagrangian calculations must be considered. The codes use material zones of finite size which limit calculational resolution of "discontinuous" phenomena such as a steep-fronted shock. Resolution may be improved by finer zoning, at the cost of increased calculation time. Likewise, a numerical technique known as linear artificial viscosity, used to damp nonphysical numerical noise in the problem, may sometimes cause other nonphysical effects in the solution. The influence of zone size and viscosity parameters may sometimes be analyzed and taken into account by simple one-dimensional parameter studies. Another limitation of the hydrodynamic calculations is related to the time-scale of the problem. The codes are most efficient and accurate when used to calculate strong shock interactions, over time scales on the order of one to several shock transit times throughout the problem region. They are not suited to the analysis of very late-time "non-hydrodynamic" phenomena, after shock interactions are essentially completed. In some cases, the results of Lagrangian calculations may be combined with simpler methods to simulate material dynamics at late times.

The successful application of hydrodynamic codes hinges on a detailed knowledge of the constitutive relations of all materials in the problem, throughout the expected range of pressures and densities. The density, detonation velocity, energy release, and pressure-volume adiabat of the explosive source region must be determined. Similarly, for solid media, it is necessary to define hydrostatic compressibility curves, the high-pressure Hugoniot relation, the elastic moduli of the bulk material, and shear strength at failure as a function of confining pressure. The codes are therefore most conveniently applied to media with already-established constitutive relations. Extensive materials testing may be required to derive this information for a new explosive or geologic medium. However, the cost of testing may be more than offset by the reduced need for expensive site-calibration experiments, and by the decreased likelihood of design failure or unexpected results.

In summary, hydrodynamic codes are well-suited to the simulation of shock propagation and early-time dynamics in multiple-layer material problems. The effects of relevant medium parameters, such as degree of saturation and failure strength in shear, may be taken into account. Late-time interactions

which occur after the phase of ballistic material ejection cannot be examined with this approach. Lagrangian codes are thus directly applicable to the calculation of shock transmission and material ejection from underwater cratering events. In addition, two-dimensional codes may be used to determine final crater dimensions for most events in rock media (ballistic ejecta deposition not greatly modified by late-time effects). Crater formation in fine-grained cohesionless materials is influenced by washback, slope failure, and settlement effects which occur during or after deposition of the fallback. For this reason, the final crater contours cannot be accurately predicted, although an idealized initial or "ballistic" fallback distribution can be calculated. It is suggested that the results of Lagrangian and ballistic ejecta calculations might be combined with a late-time slope stability and washback analysis in order to determine final crater dimensions. This approach has not yet been attempted, but might be justified for the design of a large-scale excavation project in a weak medium.

The hydrodynamic codes obviously offer considerable benefits within the field of explosive excavation design. This is particularly true of underwater applications, for which empirical data are not available and the crater formation process is poorly understood. Perhaps the greatest long-range advantage to be derived from numerical modeling is the improved understanding of cratering mechanisms which can be gained by studying the stress and velocity fields in the excavated material. Detailed information about these fields cannot be obtained from experimental measurement programs at any cost.[18]

In view of the continuing interest in underwater explosive excavation and the need for more quantitative design procedures, it was decided to conduct a calculational study of submerged blasting. The initial phase of this study involved a suite of one-dimensional (spherically symmetric) calculations using a modified version of the SOC code which contains a high-explosive "burn" option. Both horizontal and vertical calculations were performed for a 10-ton high-explosive energy source emplaced in three different fully-saturated media. The vertical calculations included rock "free-surface" configurations (no overlying water layer), and configurations at the same burial depth in rock

with overlying water layers of varying thickness. The three media were selected on the basis of the following criteria: (1) Availability of material properties data and known or calculable compressibility curve; (2) Applicability to typical high-explosive excavation projects; (3) Existence of past experimental data; and (4) Moduli representative of a range of geologic media likely to be encountered in field work. Detailed discussion of the material properties is given in Chapter V.

The primary goals of the calculation series were fourfold: (1) To demonstrate the feasibility of hydrodynamic code application to multiple layer cratering configurations; (2) To investigate the properties of typical saturated media for underwater blasting calculations; (3) To achieve a basic understanding of the submerged cratering process (within the limitations of the one-dimensional code); and (4) To develop some of the knowledge required to implement two-dimensional design calculations for future engineering projects. This report presents a summary of the one-dimensional study and related underwater shock investigations to date. Peak pressures, stresses, and velocities for all configurations are given. Proper interpretation of multiple layer dynamic interactions requires a knowledge of the waveforms as well as peak values. For this reason, a data abstract of the calculated waveforms is included. This information should also be very useful in developing and verifying future two-dimensional calculations. Since the calculational suite was limited to three typical media, the analysis is concerned primarily with shock interactions, early-time dynamics, and water layer effects for these materials. The fundamental dynamic parameters may vary dramatically with medium properties and with layer depths. Thus, caution should be exercised in extrapolating from or generalizing these results; actual crater design will require two-dimensional calculations for a specific medium and depth configuration.

II. CRATER FORMATION MECHANISMS

The dynamics of explosive crater formation in "single-layer" media have previously been examined in some detail.[17,18,19] Detonation of a chemical explosive charge is completed in a time on the order of a millisecond, the exact value depending on charge size and shape, type of explosive, and other factors. When the detonation front reaches the explosive interface, a relatively steep-fronted shock wave is transmitted into the surrounding medium.

Inelastic dissipative effects gradually diffuse the sharp peak of the outward-moving wave. Stresses and velocities decay or attenuate because of dissipative energy loss and geometric divergence of the wave. At ranges very close to a strong energy source, environmental material may be vaporized or liquefied by the shock. These effects are normally absent or unimportant for high-explosive detonations in rock, since peak pressures near the explosive are on the order of 100 kbar (energy content $\simeq$0.1 Mbar-cm^3/cm^3). At lower pressure levels, energy deposition continues by compressional crushing, cracking, or deformation of the material. Finally, as the peak stresses near the shock front drop to very low levels, major dissipative processes cease to occur. The transmitting material begins to respond elastically, and the low-amplitude shock wave propagates as a sonic pulse in the local medium.

This ideal picture of shock propagation in an infinite homogeneous medium is greatly modified by the introduction of a free surface. Boundary conditions require that pressure and velocity across an interface be continuous. In the case of a free surface, the requirement that pressure "P" = 0 applies at the interface. Ignoring density changes due to irreversible compaction, the density also remains unchanged at the boundary. Finally, the displacements experienced in typical shock waves are sufficiently small so that changes in gravitational potential are negligible compared with shock compression energy. Using these assumptions, a reflected wave must occur to restore all initial conditions except for the velocity acquired by the material near the interface. In the limiting case of normal incidence, the boundary condition P=0 is satisfied by a reflected wave of rarefaction (negative pressure) travelling back from the interface. The rarefactive or tensile wave is a mirror image of the upward-travelling compression wave, and exactly cancels the wave at the boundary. The rarefaction front propagates into material which has a local particle velocity "V_p" (induced by the compressional shock) toward the boundary. The rarefaction must change this velocity by an amount " $-V_p$" relative to its direction of advance (away from the interface), leaving the material with a local velocity "$2V_p$" toward the boundary. Thus, relative to the initial or undisturbed coordinate system, the rarefaction front has

a velocity V_s-$2V_p$ away from the boundary (downward), where "V_s" is the upward velocity of the incident shock wave; the boundary is translated upward relative to the initial coordinate system with velocity $2V_p$. Velocity doubling therefore occurs when a normally-incident wave of compression is reflected at a free surface. A similar velocity reinforcement effect may be demonstrated for plane waves at non-normal incidence. The velocity vector of the incident wave is normal to the wavefront, in the upward direction of propagation. The vector of the reflected tensile wave is normal to the wavefront, opposite the downward direction of propagation. The vertical components of the incident and reflected waves at the interface reinforce, doubling the vertical velocity. The horizontal components cancel. Thus, the vertical velocity at the interface is doubled for oblique incidence, and the material velocity is strongly redirected toward the vertical. This analysis is oversimplified, since it ignores irreversible (dissipative) effects at the shock front, the tendency of rarefaction waves to "shock down" (spread) due to shock velocity variations with pressure, and failure phenomena in solid media. Likewise, the acoustic paradox for grazing incidence at a boundary cannot be taken into account (a grazing wave produces only tangential velocity changes, and yet must restore the material to its initial pressure). In spite of these problems, the simple rarefactive scheme provides an accurate description of interactions at or near a free surface, except in the case of very high pressures or oblique angles of incidence.

Tensile reflection at a free surface gives rise to one of the two primary cratering mechanisms, material spallation. Most rock media cannot support large tensile stresses (i.e., the intact rock mass will break apart easily under tension). The tensile strength of in-situ rock is further reduced by the presence of joints or other discontinuities. Cratering detonations are buried sufficiently shallow that the peak shear and tensile stresses near the surface far exceed the rock strength. Material close to the free surface is thus broken by the reflected tensile wave, if not already shattered by the compressional shock. The momentum content of the upward-moving compression wave and the downward-travelling tensile wave is trapped in the cohesionless fractured material, which spalls upward at approximately twice the vertical peak particle velocity induced by the incident compressional shock,

This material enters a state of freefall and describes a ballistic trajectory (as modified by air resistance or collisions between neighboring particles). As the head of the tensile wave propagates downward, deeper layers of material successively undergo spallation. However, the peak particle velocity is not doubled for this material, since the tensile wave arrives on the decaying tail of the compressional shock and is attenuated by divergence and inelastic propagation effects. The deeper spall layers enter a freefall phase which may however be quickly terminated by impact against overlying layers and recompaction by underlying material. Spallation may be thus thought of as a depth-and range-dependent phenomenon whereby layers of mound material above the explosion receive a vertical velocity reinforcement from the reflected tensile pulse. If a detonation is very deeply buried, the rock near the free surface may remain unbroken. In this case, the initially-doubled velocity peak at the surface may be damped because the material does not break apart and enter freefall. Spallation parting may occur at greater depths, below the surface, and thick layers of material may be launched with somewhat reduced freefall velocity.

The second primary cratering mechanism, gas acceleration, begins when the reflected tensile wave reaches the explosive cavity. Prior to this time, cavity growth is essentially spherical (slight deviations from spherical free-field growth may occur due to depth-dependent variations in hydrostatic pressure around the cavity). As the rarefaction impinges on the roof of the cavity, local stresses in the rock are relieved, and accelerated asymmetrical growth toward the free surface begins. The signal from the cavity is transmitted upward at less than the preshot acoustic velocity because of the rarefied mound material. Indeed, the gas-acceleration signal may never reach the surface layers, which have spalled away from the underlying material. Nonetheless, gas acceleration is often an important mechanism for transferring cavity energy to the lower parts of the mound. The effect of gas acceleration is to progressively recompact high-velocity material adjacent to the cavity with overlying material; thus, the closest adjacent material is decelerated and mound velocities are compacted over a relatively narrow range. Energy

is transmitted from the immediate cavity region to the mound as a whole. In contrast with the spall phenomenon, which redirects velocity vectors toward the vertical, gas acceleration forces above the cavity are more nearly radial in direction. Gas acceleration is generally most effective for rather deeply-buried events, since the cavity signal must have time to be transmitted throughout a significant part of the mound. The intense spallation wave of a shallow event rapidly launches material into ballistic trajectories, and mound breakup occurs before the gas-acceleration "push" can become effective.

The hydrodynamic phases of the explosive cratering process are completed when the coherent material mound begins to disintegrate and the explosive cavity gases vent to the atmosphere. By or before this time, significant energy transfer and velocity changes within the mound have ceased to occur. Most of the material ejected from the crater region is essentially in ballistic freefall, and the trajectories may be calculated kinematically. This technique is used in two-dimensional hydrodynamic calculations, which are carried until the mound dynamic parameters (such as kinetic energy and mound mass) approach an asymptotic limit.[19,20] The hydrodynamic code is then linked to a ballistic throwout code, which determines the final distribution of ejecta and the crater size. This procedure may create slight errors in the calculated crater, since the deep material below the ejecta mound is still somewhat compressed at the time of linking and will later rebound to some fraction of its original volume. Note, however, that the all-important dynamic calculations for the material mound above the shot are correct and accurate. The most crucial aspects of the cratering process are thus adequately described by the hydrodynamic code model.

The above-discussed crater formation process undergoes further modifications if gradual material changes or discontinuities are present in the cratering medium. Of particular interest is the case of horizontally-stratified, impedance mismatched layers above the shot point. Even for shallowly buried explosions, layers of successively lower density and sonic velocity are often encountered between shot point and the surface. The

surface layer itself may consist of porous weathered material of low sonic velocity. Submerged cratering shots present a similar configuration, since the dense rock layer is overlain by a low velocity material of lower impedance. The chief difference lies in the fact that the upper layer is a fluid with no shear or tensile strength. In either case, partial tensile reflection of the initial shock will occur at an interface between higher- and lower-impedance layers. Vertical particle velocity at the interface will be significantly increased, but not doubled. Pressure at the interface will be decreased by the tensile wave cutoff, but will not decline to zero. A weak compressional shock wave will be transmitted into the low impedance medium. The condition that pressure and particle velocity must be continuous across the interface will be fulfilled; thus, the approximate peak pressure and velocity transmission at the interface can be calculated from the acoustic wave equations. Spallation may develop if the material below the interface is sufficiently fractured. However, velocities in the material above the interface will decline as the shock is transmitted away from the interface (unless the overlying layer is very shallow, and it too spalls almost immediately). Spall material below the interface may then impact upon the overlying material, ending the freefall phase. Layer interactions do not cease at this point; the compressional wave transmitted into the overlying material is subsequently reflected as a tension wave at the next interface, perhaps creating spallation in the upper layer. This rarefaction will then return to the higher impedance interface, where it will be partially reflected again (as a rarefaction). Upper layer tensile pressures will be increased by this re-reflection, but the upward velocity component will be decreased (the downward velocity component of the upward-moving tensile re-reflection partly cancels the upward component of the downward-moving tensile wave). Pressure and velocity at the interface are continuous, so a tensile wave with an upward velocity component will be transmitted into the lower layer, producing an increase in the vertical velocities. The details of this second shock arrival at the interface can only be determined by hydrodynamic calculations, since the pressures, densities, and velocities in both layers have been modified by earlier dynamic interactions. If the upper layer has not yet been dispersed by spallation, the re-reflected tensile wave may be transmitted upward once more, suffering yet another reflection (as a

downward-travelling compressional wave). The compression pulse in turn may be partially reflected (as a compression) at the lower interface, and a compressional wave with a downward velocity component will be transmitted into the lower layer. Similar reflections will be generated by any additional layers in the configuration. Even for simple acoustic waves, the potential complexity of multi-layer interactions is quite evident. For finite-amplitude shocks, spall dispersion within a layer may decrease or block transmission of reflections after the first tensile wave (unless the layer is recompacted when a reflection arrives). The situation is further clouded by the time-dependence of material velocities and of compression or dispersion within each layer, the effects of material strength, etc. Finally, the acoustic transmission and reflection analysis breaks down completely after the first tensile reflection returns to the cavity and the gas acceleration signal propagates into the medium. The gas acceleration pulse itself will be subject to interactions at various interfaces as it recompacts the successive layers, and subsidiary gas acceleration pulses may be generated as later tensile reflections reach the cavity. Hydrodynamic calculations are required to treat the general problem of finite-amplitude multiple-layer shock propagation in nonlinear media (material moduli change with pressure).

III. CALCULATIONAL SUITE

Due to the complex interrelationships between multilayer shock interactions and material dynamics, no generalized model can be expected to simulate the cratering process for all media and layer depths. Indeed, all dynamic interactions after the first interface reflection will be affected by medium properties and shock strength. For this reason, the sample materials and layer depths were selected to conform closely with realistic high-explosive cratering designs. Eighteen one-dimensional (spherically-symmetric) SOC calculations were performed for high-explosive detonations in three saturated media: coral, basalt, and granite. Further calculations, suggested by the results of this first series, were later added for comparison.

The energy source in all calculations was a sphere of aluminized ammonium nitrate slurry explosive (AANS) weighing approximately 10 tons. The spherical source region had a radius of 1.13 m (3.71 ft) and was divided into 30 calculational zones of equal thickness. This source was "detonated" in both horizontal and vertical configurations for each of the three media. Horizontal calculations were first performed to simulate free-field shock propagation in a semi-infinite rock medium. The problem size (100 m = 328 ft) was much larger than the region of interest for close-range effects, and the calculations were run until late time (75 msec). The horizontal calculations assumed a constant overburden pressure of 2.02 bars at all ranges (i.e., constant-depth free-field environment). This pressure is equivalent to about 36 ft of saturated coral overburden, or a somewhat lesser depth of dense rock. This small overburden pressure had little effect on close-range shock calculations. The horizontal free-field calculations are useful for defining shock propagation in the absence of a free surface, but resolution is somewhat degraded and the front is smeared by the coarse zone size required in a large problem. Vertical calculations were next conducted, with the explosive source emplaced below a rock surface with or without water overburden (the upper boundary in each case being a free surface). The depth of burial beneath the rock interface "D_r" was 36 ft or 30 ft (D_r = range from the center of the explosive to the rock interface). The 36-ft depth is near optimum depth for crater size from 10-ton charges, and also simulates the Project Tugboat underwater cratering events in coral. Water layer depths "D_w" above the rock-water interface were 0 ft (no water, rock interface is a free surface), 5 ft, 10 ft, and 36 ft. Due to time limitations, every possible combination of rock and water depth could not be calculated for each of the three media. Therefore, the D_r = 36 ft configurations were emphasized. Since the size of the vertical problems was quite small, very fine constant zone size (about 0.04 m or 0.13 ft) was used in the rock layer. This zoning achieved excellent resolution of the shock front. Vertical problems were run for about 20-28 msec to allow ample time for the initial compressive wave transmission and return of the tensile reflection. Strong dynamic interactions in the vertical direction are essentially completed by this time. Figure 1 schematically depicts the horizontal and vertical problem configurations (not to scale).

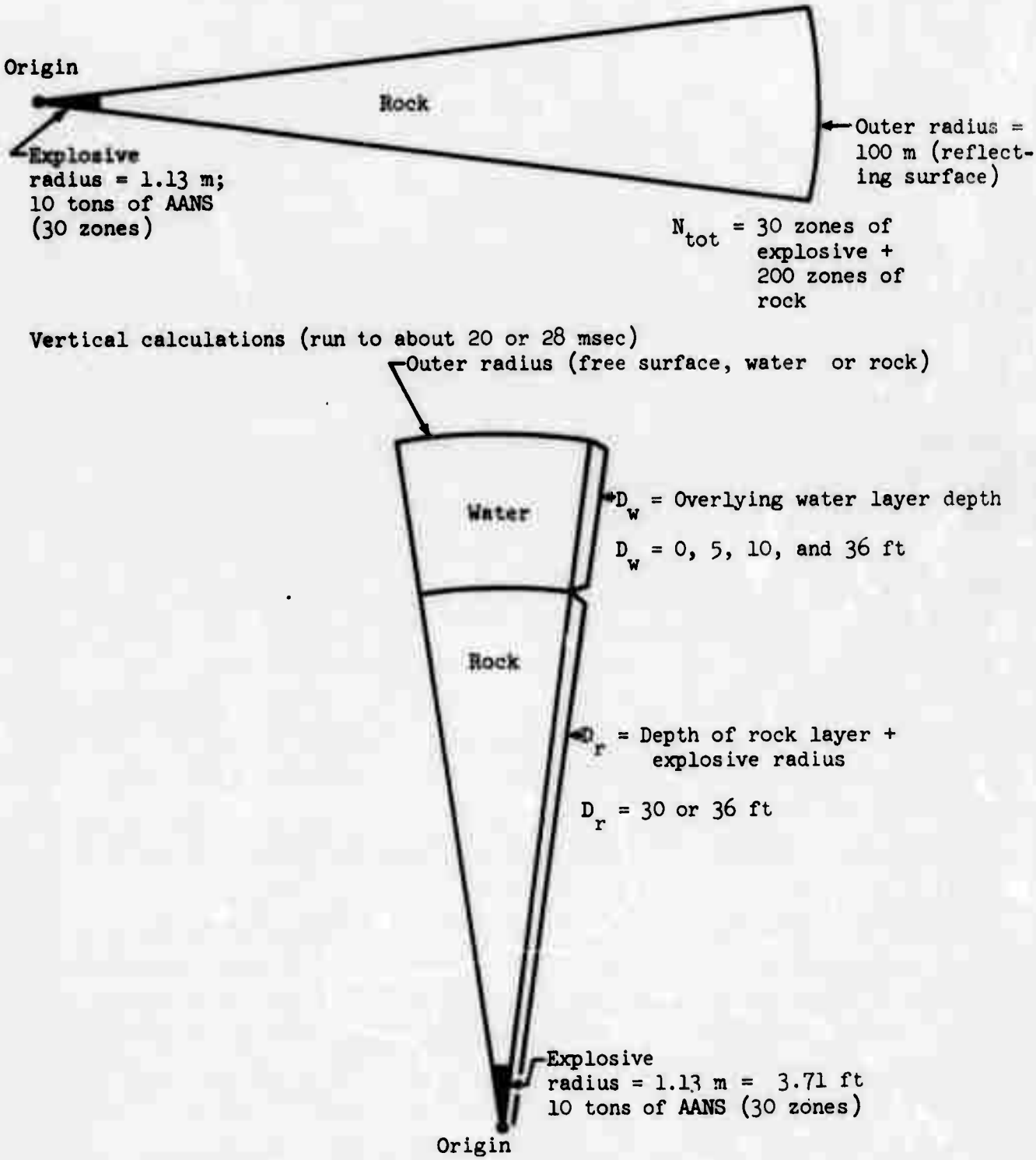

Figure 1. Horizontal and vertical problem configurations for the one-dimensional spherical (SOC) calculations.

Abbreviations have been devised for convenience in discussing the various calculations. Medium names are denoted as follows: COR (coral), BAS (basalt), and GRN (granite). The medium name is followed by the configuration, either HRZ (horizontal), or by the vertical calculation rock depth/water depth, in feet (i.e., 30/10 represents D_r = 30 ft, D_w = 10 ft). For example, the coral horizontal calculation is designated CORHRZ. The basalt calculation at a depth of 36 ft with a 36 ft overlying water layer is BAS36/36. One additional horizontal calculation in coral, using a modified constitutive relation, is denoted "PSIØHRZ". The nomenclature scheme is summarized in Table 1.

Previous studies with SOC and other hydrodynamic codes have demonstrated that generation of physically meaningless numerical noise often occurs at impedance-mismatched interfaces within a problem. Such noise usually takes the form of a "ringing" or echo effect originating at the location of a sudden change in zone size (for single-material problems) or at the interface between two different materials. Noise generation is most severe for sharply-rising incident shock fronts, and for large impedance mismatches. Difficulties of this sort may be reduced by avoiding sudden changes in zone size (within a material), and by impedance matching of adjacent zones across an interface (zone size proportional to the acoustic impedance of the medium; coarser zones in the "soft" low impedance medium).

The latter technique has been used at the rock-water discontinuity in these problems. Matching across a very-high to very-low impedance interface may degrade resolution, since much larger zones are required for the overlying material. The shock front may undergo dramatic spreading as it propagates into the low-impedance layer. For similar reasons, reflection phenomena at the interface may be inadequately resolved; the reflected shock front rapidly transits several zones of the dense material before the overlying low-impedance (low-velocity) layers become fully active. Significant errors occur when the distance travelled by the incident shock front during its rise time and the depth-scale of reflected shock interactions near the interface are smaller than

TABLE 1. Emplacement Configurations for Which Calculations were Performed; Energy Source is a Ten-ton Spherical Charge of Aluminized Ammonium Nitrate Slurry (15.9 tons equiv. energy yield).

	Calculational Suite for AANS explosive; SOC Code, High-Explosive version								
		D_r = 30 ft				D_r = 36 ft			
	Horizontal *	D_w=0	D_w=5	D_w=10	D_w=36	D_w=0	D_w=5	D_w=10	D_w=36
Tugboat Coral	PS10HRZ								
Coral, Smoothed Compressibility Curve	CORHRZ	COR30/00	COR30/05	COR30/10	COR30/36	COR36/00	COR36/05	COR36/10	COR36/36
Kaalualu Vesicular Basalt	BASHRZ					BAS36/00		BAS36/10	BAS36/36
Orinoco River High-Strength Granite	GRNHRZ					GRN36/00		GRN36/10	GRN36/36

*2.02 bars overburden, equivalent to 36 ft of coral

the zone size in the overlying material. Resolution at the interface and in the low impedance layer may be improved by using very fine zones in both materials, at the cost of increased calculation time.

During this study, it was conclusively shown that the water-transmitted shock front and the interactions at the interface could be well resolved for the smoothly-rising shock waves characteristic of coral or basalt, in spite of the coarse water zone sizes required for impedance matching. However, the very short rise times and the sharp fronts in granite gave rise to some inconsistencies. The shock wave underwent abrupt spreading, with a decrease in particle velocity upon entering the water layer. Early-time reflection phenomena in granite zones adjacent to the interface were likewise improperly calculated. These difficulties are accentuated by the fact that the impedance discontinuity is greatest for the dense granite medium, requiring coarse water zones. Accurate impedance matching is also most necessary for sharply-rising shock fronts. Finally, small granite zone sizes cannot be used due to the long calculation time required for a "stiff" high-velocity material. In order to define the errors incurred, additional granite calculations were performed with finer overlying water zones (not impedance matched). These calculations included a set with water zones half the size of the "impedance matched" zoning. It was found that the resolution factor grossly affected peak shock transmission in the water layer, but had little influence on long-term dynamics within the granite layer.

Tables 2a and 2b summarize the interface locations, rock zone sizes, and water zone sizes featured in the set of vertical calculations. Interface locations (measured from the center of the problem) and the zone sizes are given in both meters and feet. Note that the interface positions and rock zoning are identical for corresponding problems in all three media. However, the water zone sizes (Table 2b) vary because of the impedance matching requirement. In the case of granite, two different water zone sizes are listed. The first refers to the impedance-matched calculations ("coarse water zones"), while the second corresponds to half-size water zoning ("fine water zones").

TABLE 2(a). Interface Locations and Approximate Rock Zone Sizes Used in the Vertical Calculations.

Calculation*	Range from Center: Explosive-Rock Interface (m)	(ft)	Rock-Water Interface (m)	(ft)	Water Surface (m)	(ft)	Rock Zone Size* (m)	(ft)	No. Rock Zones*
30/00	1.13	3.71	9.146	30	None	None	0.04	0.131	200
30/05					10.67	35			
30/10					12.195	40			
30/36					20.12	66			
36/00	1.13	3.71	10.976	36	None	None	0.04	0.131	246
36/05					12.50	41			
36/10					14.02	46			
36/36					21.95	72			

* Identical interface locations and rock zone sizes are used for the corresponding calculations in all three media

TABLE 2(b). Approximate Water Zone Sizes Used in Vertical Calculations

Medium	Water Zone Size (m)	(ft)
Coral	0.10	0.328
Basalt	0.254	0.833
Granite (coarse water zones)	0.392	1.29
Granite (fine water zones)	0.196	0.643

Additional test calculations with somewhat modified interface locations, depths, or zone sizes were subsequently added to the study. These calculations will be discussed and compared with the "standard" configurations (Table 2) in a later chapter.

IV. ONE-DIMENSIONAL VS. TWO-DIMENSIONAL CALCULATIONS

The spherically-divergent geometry imposed in SOC calculations presents certain difficulties of interpretation when applied to cratering dynamics. Crater formation is an inherently two-dimensional process; it involves, in the simplest case, propagation of a spherically-divergent shock front, reflection at a planar interface, followed by hydrodynamic acceleration and ballistic ejection of the crushed material. Oblique reflection of the shock wave plays an important role in fracturing material near the edge of the crater and in lateral ejection. Gas acceleration effects in the lateral direction may also contribute to crater formation. Dynamics of this laterally displaced material are not directly related to the dynamics vertically above the charge; instead, they are dependent on shock attenuation, medium strength, emplacement geometry, and other factors. For these reasons, the volume of material ejected and crater dimensions cannot be accurately predicted from one-dimensional results. Likewise, the "optimum" depth of burial for a cratering charge depends upon medium properties, and is not simply related to the vertical spall velocity, residual velocity, kinetic energy, or other one-dimensional dynamic parameters. With these cautionary notes in mind, it is permissible to observe that there is, nonetheless, a considerable degree of correlation between crater formation and close-range vertical dynamics. This correlation is expressed by the relationship between the vertical spall velocity in the near-surface layers and the required depths of burial for "optimum" crater formation or for "mounding" (no apparent crater). Before the advent of two-dimensional codes, the vertical velocity was successfully used as a rough criterion for burial depth in a variety of media. Similarly, the cube-root scaling laws which describe shock front parameters (velocity, stress, spall velocity) also apply approximately to burial depth and crater dimensions in competent media at "small" length scales (i.e., typical high-explosive events) and over small ranges of yield. These simple laws are of course not valid

over great yield ranges and at large yields where gravitational scaling effects, air viscosity, and other factors become important.[21,22,23] However, given the conditions of small yield range, small variation in the size scale or depth of the experiment, and similar media, one expects that the other "non-hydrodynamic" scaling effects will be unimportant and a good correlation will exist between vertical dynamics and efficiency of material ejection.

No detailed study has been conducted to relate one-dimensional (vertical) and two-dimensional dynamic parameters for buried cratering events. Unfortunately, two-dimensional calculations are not yet available for media involved in this investigation. The nature of the difference between one- and two-dimensional calculations is illustrated in Figure 2a. This figure compares the kinetic energy content in coral (for one-dimensional calculations) with the kinetic energy content in Bearpaw clay shale (for two-dimensional calculations).[19,24] The coral results (solid curves) are shown for a horizontal (free-field) configuration and a vertical configuration at a burial depth of 36 ft (coral 36/00, no water layer). The two-dimensional clay shale kinetic energy curves (dashed) are plotted for the <u>total</u> kinetic energy in the clay shale and the kinetic energy content in the ejecta mound (material thrown above the initial ground surface level). Clay shale is a weak fully-saturated material with a compressibility curve quite similar to coral. However, certain differences should be mentioned: (1) Clay shale has a density and impedance about 17% greater than that of coral, while sonic velocities for the two media are about the same. (2) The clay shale calculations use a different explosive, nitromethane; the total energy release for the clay shale calculations is 1.23 times as great as the energy release of the AANS charge used in the coral calculations. Note that the clay shale total kinetic energy curve lies above the coral curve by a factor of approximately 1.23 at early time. (3) The clay shale calculations were at a depth of burial of 41 ft, or 1.14 times as deep as CORAL 36/00. Therefore, the shock arrives at the free surface slightly later. (4) Clay shale is a very weak, semi-fluid material with a strength on the order of the overburden pressure; therefore, cavity expansion would continue almost unhindered at late time, even for a spherical free-field calculation. Kinetic energy continues to enter the medium by a process similar to fluid-flow expansion. The ratio of kinetic energy to internal energy in the shale medium does not change dramatically with time. These contentions are borne out by free-field one-dimensional calculations (not shown), which reveal a <u>total</u> kinetic energy content similar to Figure 2a,

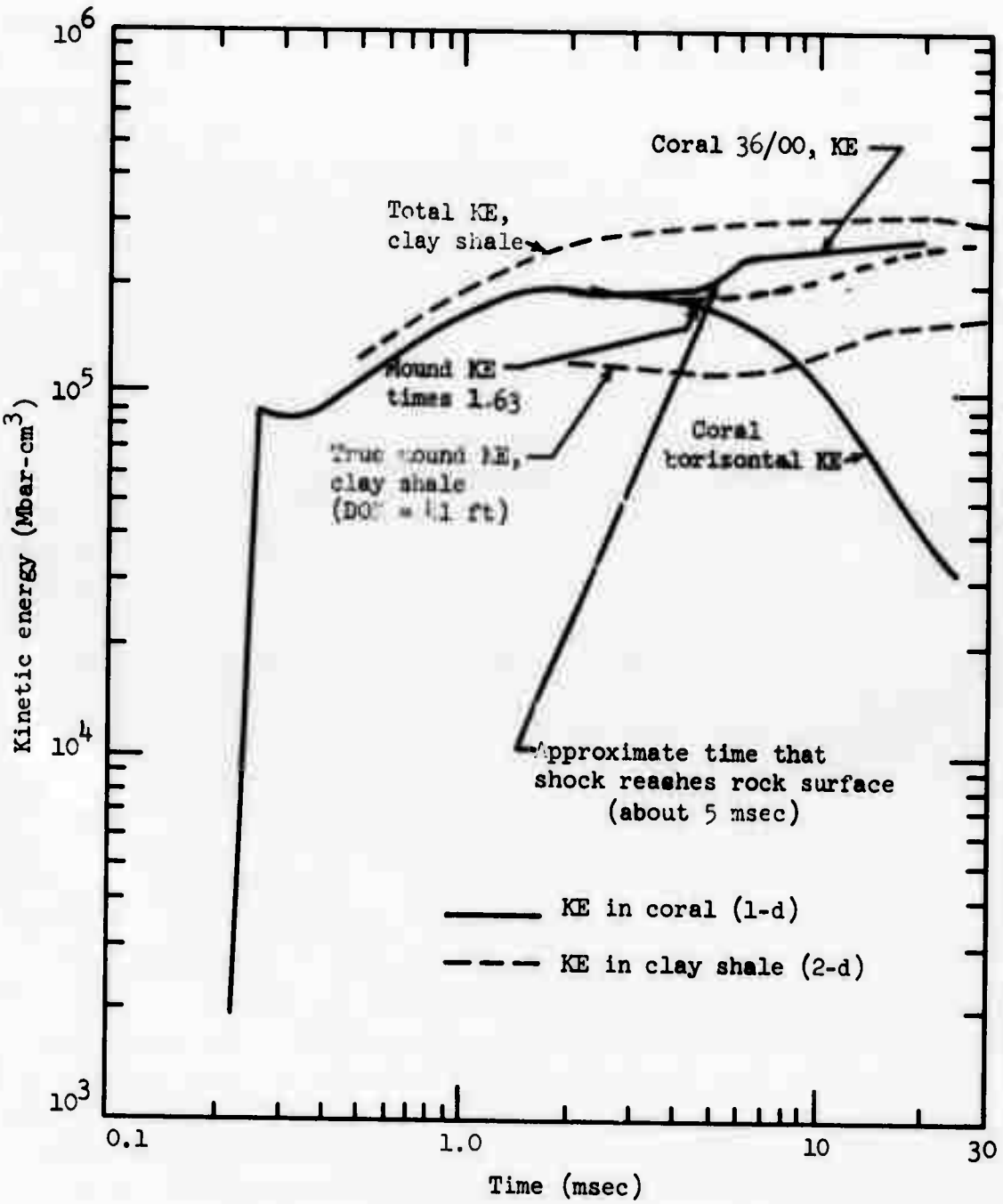

Figure 2a. Comparison of kinetic energy in coral (one-dimensional vertical calculations) and in clay shale (two-dimensional calculations).

decreasing very slightly at late times. The stronger coral material, in contrast, halts cavity expansion much sooner (see coral-horizontal), the kinetic energy content begins to decrease, and the internal energy of the medium increases correspondingly. For this reason, the total kinetic energy curve for clay shale may not be legitimately compared with coral after 2 or 3 msec. A two-dimensional coral calculation would show a large relative decrease in total kinetic energy at late times due to severe damping of expansion beneath the lower half of the cavity. However, the mound kinetic energy for clay shale may be compared with coral 36/00 at late times (after the coral is almost completely fractured and has entered freefall spallation). The clay shale curve has been multiplied by a factor of 1.63 to facilitate comparison (upper dashed curve).* Shock arrival at the free surface (≈ 4.5 to 5 msec) is indicated in the figure; spallation begins at this time. Note that the two curves show a similar percentage increase at late times, but the two-dimensional (clay shale) kinetic energy rises gradually to its maximum value between 5 and 20 msec. The coral curve ascends abruptly, and spallation is essentially complete throughout the vertical problem by 10 msec. It is evident that spall launch takes longer to propagate to long slant ranges, throughout the two-dimensional mound. However, the ultimate increase in kinetic energy during the spallation phase is encouragingly similar to the one-dimensional result. Comparing the true clay shale mound energy (lower dashed curve) with coral 36/00, it is seen that the coral kinetic energy lies above the clay shale by a factor of 1.56 to 1.68 after spallation and most dynamic interactions are complete (i.e., at times later than about 10 msec for the vertical coral 36/00, or 20 msec for the two-dimensional clay shale configuration). Correcting for the input energy differences between the two problems, this corresponds to a factor of 1.92 to 2.07 between the two-dimensional and one-dimensional (vertical) results, roughly as expected for energy division between upper and lower hemispheres. The very accurate "factor of two" difference observed here occurs fortuitously because of the very low strength properties and high shock propagation efficiency in clay shale, and also because of other slight differences between the problems. A two-dimensional coral calculation would ultimately place somewhat less than half of the corresponding one-dimensional vertical kinetic

---

* This multiplicative correction factor is used because only about half of the total energy in the two-dimensional calculation propagates into the upper hemisphere (region of mound launch). However, the total energy is 1.23 times greater. Thus, a rough compensation factor relating the two-dimensional mound launch energy to the one-dimensional vertical calculation KE is given by: $2x(1/1.23) = 1.63$.

energy into mound kinetic energy. Nonetheless, behavioral similarities shown here indicate a strong analogy between the dynamics of the one-dimensional and two-dimensional calculations. A more detailed investigation is needed to fully verify the relationship.

Other more subtle differences also complicate the interpretation of one-dimensional calculations. Chief among these is the less-than-satisfactory handling of reflected and refracted wave propagation. One-dimensional spherically-divergent calculations produce spherical convergence of reflected waves returning toward the center of the problem. This effect is not serious over time periods and distance intervals which are small compared with the propagation time and range from the problem center. The shock interactions near an interface and far removed from the center are almost planar. Thus, peak surface velocities and early time spall dynamics close to an interface may be accurately calculated. The spherical convergence effect is in one sense self-cancelling, even over larger regions of the problem. The spherically-divergent tensile reflection for a two-dimensional cratering event spreads throughout a broad region of the mound (rather than converging on the center), but still contributes to spallation and kinetic energy of the mound as a whole. Spall dynamics are thus fundamentally similar for one-dimensional and two-dimensional cases. However, significant differences in the material velocities and dynamic interactions at a given radius are likely to occur as the one-dimensional wave propagates back to the cavity and is again reflected outward. The worst "errors" (relative to a corresponding two-dimensional problem) are expected to originate within the extreme inner regions. For example, the late-time cavity gas acceleration effects in the vertical direction might be overestimated for a one-dimensional problem, since the returning tensile wave which reaches the cavity interface is convergent rather than spherically divergent. The effects will be most severe and will become apparent soonest at ranges close to the cavity. However, the inner regions of the problem account for only a small portion of the total mass. Changes in the overall material dynamics may be very small and may occur at late times. Further, if the overlying material is rarefied by spallation, reloading signals from the cavity propagate outward quite slowly and may not reach the bulk of material nearer the free surface within a time interval

relevant to crater formation. The problems considered here are relatively shallow cratering events in fully-saturated media. Previous investigations[19,25] and results of this study demonstrate that shock propagation in saturated media is a very efficient process, and that spallation is the predominant mechanism of crater formation. The upper regions of material remain in freefall long after spallation begins. Recompaction and cavity echo signals reach the outer regions only at very late times (t >> two acoustic transit times) and are extremely weak. Gas acceleration and multiple reflections from the central region exert little influence on the overall dynamics for problems of this class.

The analogy between kinetic energy in one- and two-dimensional problems has already been examined (Figure 2a). The one-dimensional coral 36/00 calculation shown in Figure 2a reveals a sudden rise in kinetic energy from 5 to 10 msec (spallation phase), followed by a very gradual increase at later times. Cavity gas acceleration and late-time recompaction effects are relatively unimportant within the scope of overall dynamics to 20 msec. The mound kinetic energy for the two-dimensional clay shale calculation presents similar behavior, although the spall wave takes longer to spread throughout the mound region. Gas acceleration effects have likewise been shown to be unimportant in the two-dimensional configuration.[19] Kinetic energy is a velocity-sensitive parameter which relates closely with material spallation and cratering dynamics. The correlation between one- and two-dimensional results thus demonstrates that spherical convergence does not adversely affect problem dynamics over times of interest (≈ 20 msec). However, the one-dimensional kinetic energy is weighted by "mass times velocity squared," de-emphasizing the low-mass inner zones. Small velocity changes near the center of the problem are not readily detected. In an effort to analyze detailed dynamic effects, the spall velocities and waveforms above shot point were examined. Due to data availability, a different set of problems was used for this examination. A vertical one-dimensional coral problem at a depth of 41.31 ft is compared with a two-dimensional clay shale event at a depth of 41 ft. The clay shale problem in this case consists of a hypothetical nuclear source and has a total kinetic energy of only 0.6 times the coral problem energy at late times. Thus,

the shock stresses and velocities far from the source are lower than for coral. However, the nuclear shock wave arrival times are slightly earlier due to the high intensity of the close-range nuclear shock when it is decoupled from the source. Figure 2b shows the velocity waveforms at a range of 9 m (29.5 ft) above the problem center. Note the earlier arrival and slightly lower amplitude of the clay shale wave. Shock interactions at spallation are similar for the one- and two-dimensional problems. In both cases, the spall wave arrives about 3.2 msec after the initial peak and causes a similar increase in velocity. The freefall phase persists until very late time (> 20 msec), and no gas acceleration arrival occurs. Approximately 62% of the total mass is located at or beyond 9 m for the one-dimensional problem. The velocity waveforms at other ranges have also been compared; Figure 2c graphs the vertical spall velocities as a function of range from the problem center. Coral spall velocities are slightly higher near the free surface due to the greater amplitude of the coral shock wave at long ranges. However, at locations very close to the source (4 to 6 m), the spall velocities are equal. This effect is caused by the slower decline in particle velocity at late times for clay shale (fluid flow effect mentioned earlier). The tail of the upward-travelling compression wave declines more slowly for clay shale than for coral, thus maintaining a slightly higher velocity when the spallation wave arrives. It is quite evident that the expected <u>increase</u> in coral spall velocity near the problem center (due to spherical convergence) is less important than this minor medium-dependent effect. This result implies that convergence has relatively little influence on spallation throughout most of the one-dimensional problem region. Late-time gas acceleration effects close to the source were examined; it was found that the coral velocity after gas acceleration was approximately 58 m/sec at a range of 6 m; the corresponding velocity for clay shale was 56 m/sec at the same range (the spall velocity before gas acceleration is 50 m/sec in both cases, Fig. 2c). This slight difference may indicate a convergence effect near the center of the one-dimensional coral calculation, but the velocity change involved is negligible and could be attributed to differences in the media and energy sources. It appears that spherical convergence has little effect on one-dimensional spall-dominated cratering calculations. This conclusion might not apply to very

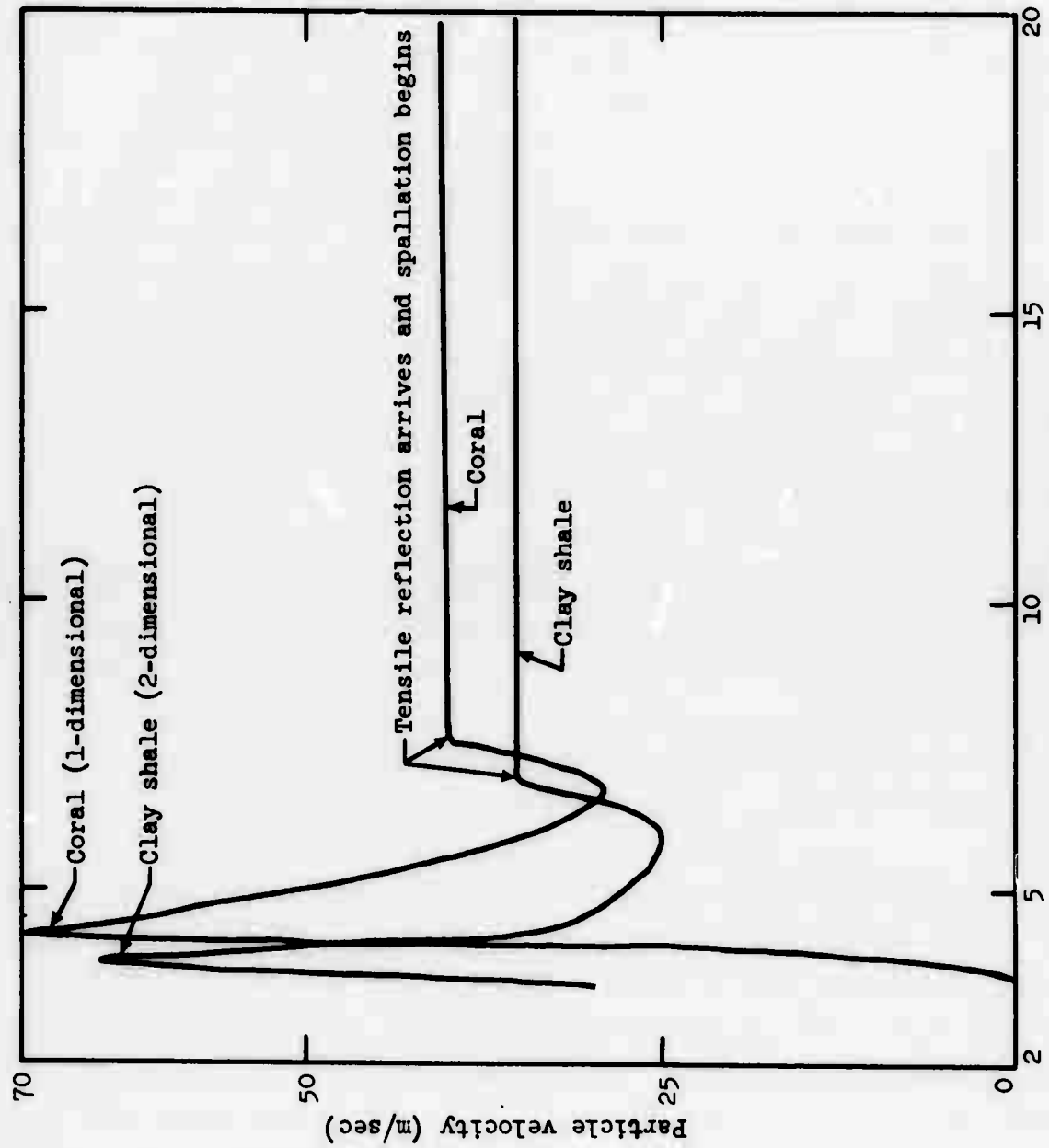

Figure 2b. Velocity waveforms above shot point as a function of time at a range of 9 m from shot point: for two-dimensional clay shale calculation (depth = 41 ft) and one-dimensional (vertical) coral calculation (depth = 41.31 ft).

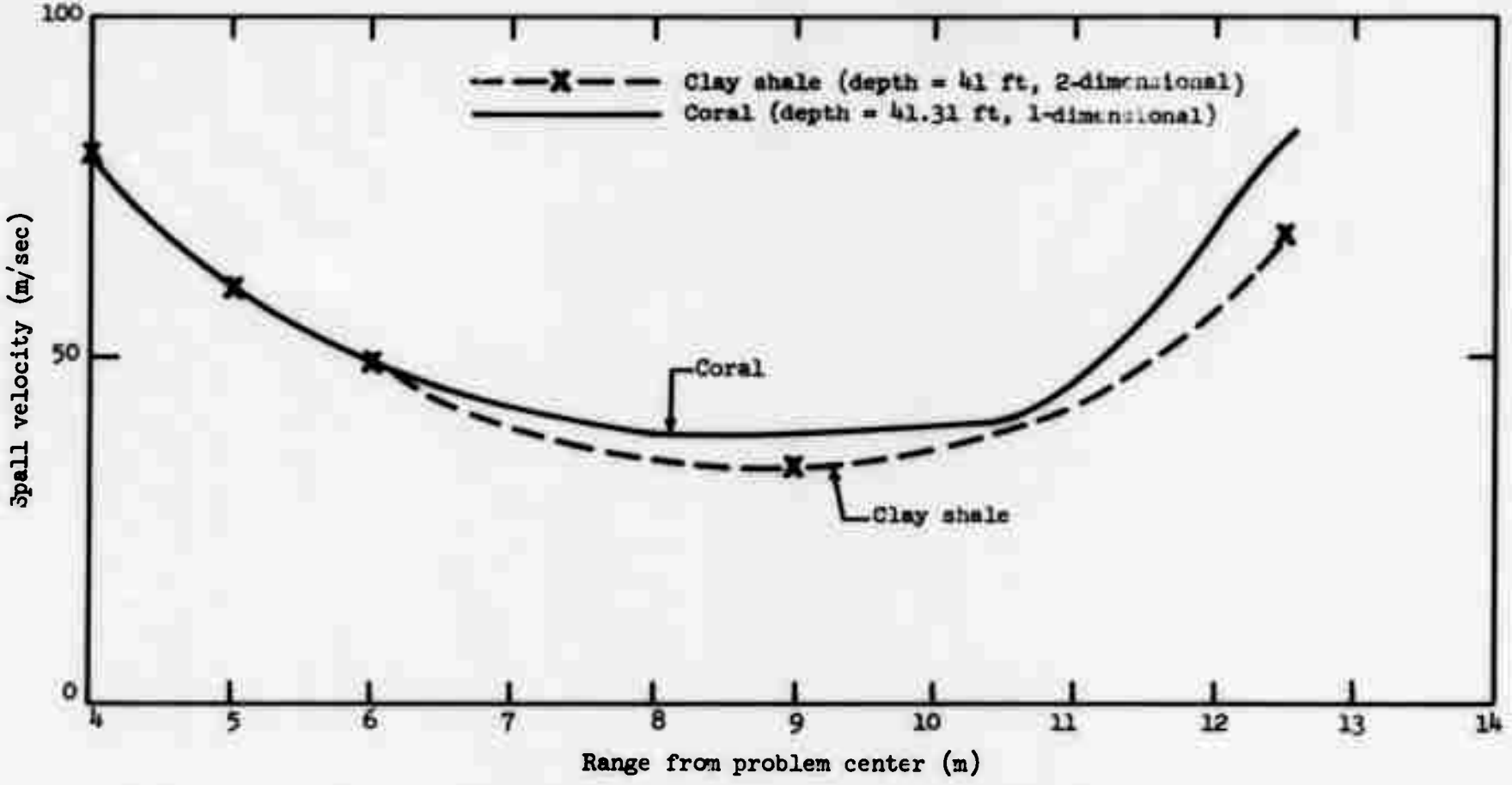

Figure 2c. Vertical spall velocities above shot point: two-dimensional clay shale calculation (depth = 41 ft) and one-dimensional (vertical) coral calculation (depth = 41.31 ft).

deeply buried events, for which the gas acceleration pulse recompacts a large portion of the mound and contributes significantly to late-time material acceleration.

The spherical geometry used in one-dimensional configurations also fails to take account of refraction at medium interfaces. The problem of reflection and transmission of a low amplitude (acoustic) wave at a discontinuous boundary and subsequent propagation of the reflected and transmitted waves is analogous to the problem of light reflection-refraction in geometric optics. General equations may be written for simple hydrodynamic compression waves (in a fluid)[26] or for compression plus shear waves.[27] The acoustic transmission and reflection conditions and geometric propagation laws apply with a high degree of accuracy to weak shock waves in fluids, and are known to be valid even for very strong shocks as long as the angle of incidence does not deviate too far from the normal.[28] Failure and hysteretic effects complicate strong shock transmission in solid media, but the acoustic and geometric laws are usually applicable to peak shock parameters across an interface. As discussed earlier, acoustic theory for a high- to low-impedance interface requires that an incident compressional shock be partially reflected as a tensile wave. The pressure at the boundary is reduced, and the vertical velocity component is increased. The transmission and reflection coefficients depend only on the characteristic impedances of the two media and the angle of incidence, approaching limiting values at normal incidence. The impedances may be sonic values "ρC_{sonic}" for an acoustic wave (C_{sonic} = sonic velocity), or finite-amplitude values "ρC_{shock}" for a discontinuous shock front (C_{shock} = shock front velocity). The "acoustic" equations apply in either case, assuming that the reversible Rankine-Hugoniot jump conditions are valid at the front. The finite difference equations used in hydrodynamic codes are not completely compatible with the discontinuous "jump" conditions at a boundary. Nonetheless, most codes will accurately treat transmission at an interface if the problem is carefully formulated. The jump conditions are sometimes used to check the accuracy of a solution.

Shock propagation within the second medium presents another unrelated problem for the calculation scheme. Refraction of the wavefront takes place at an interface. The angle of refraction is dependent on the sonic velocities (or front velocities) in the two media and the angle of incidence, according to the familiar law of geometric optics. Refraction, in turn, modifies the radius of curvature of the wavefront in two respects. The first of these is spherical aberration, caused by the shift in the wavefront's direction of propagation relative to the axis of symmetry (vertical axis perpendicular to the interface). Upon transmission at a high-velocity to low-velocity interface, the ray is refracted toward the normal direction, increasing the apparent distance to the axis of symmetry and the radius of curvature. As the radius of curvature increases, the shock attenuation rate in the second layer decreases (relative to an unrefracted spherically-divergent wavefront). The second effect is due to the change in the radius of curvature of the wavefront as measured in the radial plane. This effect likewise increases the radius of curvature at a high- to low-velocity interface. Again, the attenuation rate in the second layer will be decreased. The change in divergence of the wavefront approaches a limiting value for normal incidence, defined by the velocities in the two media.

Multilayer wave propagation thus involves two distinct phenomena: transmission at an interface, and attenuation of the transmitted wave beyond the interface. The problem of interactions at the interface for a specific ray may properly be analyzed with a one-dimensional code. However, the geometrically-conditioned problem of shock propagation into the upper layer is inherently two-dimensional. The spherical divergence condition imposed in one dimension excessively damps the shock energy and increases attenuation (if the wavefront divergence should decrease, as at a high- to low-velocity interface), or concentrates the shock energy and decreases attenuation (if divergence should increase, as at a low- to high-velocity interface). In the case of rock calculations with "low-velocity" water overburden, divergence of the shock front decreases dramatically at the interface (radius of curvature increases). The SOC code should therefore underpredict shock pressures and velocities in the upper layer.

Unlike spherical convergence, which develops only for reflected waves, this effect applies to the initial outgoing shock wave. Serious errors may occur in the first-order dynamic parameters and in safety or effects predictions for the upper layer. Initial shock front peak velocities and pressures moving into the water layer will be progressively reduced (due to excessive divergence of the outgoing shock wave beyond the interface), and the peak spall velocity at the water surface will, of course, be underpredicted. One consolation lies in the fact that tensile wave spall velocity calculations below the water surface will be improved. This improvement occurs for two reasons: (1) Spherical convergence of the water surface reflection in one-dimensional calculations causes spall velocities to be overestimated; however, divergence of the (two-dimensional) compression and reflected tension waves in the water layer is reduced by the refraction effect. The error caused by spherical convergence is thereby decreased; (2) The one-dimensional error caused by ignoring refraction decreases velocities in the outgoing compressional shock (both the peak and decaying velocities in the "tail" of the pulse). The error created by spherical convergence increases the particle velocities for the reflected tension wave below the water surface. The combined effect of these errors on the reinforced "tensile wave plus remaining compressional wave" spall velocities is partially self-cancelling near the middle of the water layer (but not at the interface or the surface).

A detailed examination has been conducted to determine the effect of refraction errors on the peak shock parameters. Water was treated as a linearly elastic medium with acoustic propagation, permissible in this case because peak pressures in the water layer are on the order of one kilobar. Refraction at the interface and transmission in the water layer were calculated using the accoustic formulae for peak pressure of a simple compressional wave.[26] Shear wave effects and shear reflection at the interface were not taken into account. It was found that the worst errors occur for large velocity mismatch at the interface and for deep water layers (long ranges from the interface). Sample results for rock and water layers of equal thickness (coral 36/36, basalt 36/36) are presented in Table 3. The SOC-calculated peak spall velocities are compared with spherically-divergent acoustic calculations (uncorrected for refraction effects on wavefront attenuation away from the interface) and corrected acoustic calculations (refraction effects included). The spherical

TABLE 3. Effect of Refraction Error on One-Dimensional (SOC) Calculated Spall Velocities.

	CORAL 36/36 *			BASALT 36/36*		
	SOC Calculation	Acoustic Spherical (Uncorrected)	Acoustic Corrected for Refraction	SOC Calculation	Acoustic Spherical (Uncorrected)	Acoustic Corrected for Refraction
Rock Interface, Spall Vel. at Shock Arrival (m/sec)	70 m/sec	71	71	52	50	50
Water Surface, Spall Vel. at Shock Arrival (m/sec)	62	65	75	43	45	67

* D_{rock} = 36 ft; D_{water} = 36 ft.

(uncorrected) acoustic velocities are similar to the SOC results. However, the corrected acoustic velocities at the water surface are higher by about 21% (for a slight velocity mismatch, coral-water), and 56% (large velocity mismatch, basalt-water). The peak velocities and pressures at the shock front are in error by a similar amount at ranges well beyond the rock-water interface. For an extreme velocity mismatch, the pressures, particle velocities, and spall velocities far from the interface may be incorrect by a factor of two or more. Results of the individual calculations are presented in a later section. The refraction error explains some discrepancies which have appeared in earlier applications of one-dimensional codes to layered configurations. This effect is particularly troublesome, since shock parameters are underpredicted for the commonly-encountered situation of decreasing sonic velocity in the shallow (near-surface) layer.

The combined influence of refraction and spherical convergence errors on multilayer calculations has not yet been fully investigated. The situation is rather complex because the dynamic effects of the compressional shock and of the rock-water interface reflection (below the rock surface) have already occurred before the water surface reflection arrives. Also, recompaction effects near the rock-water interface and the cavity gas acceleration signal (which is accentuated by the water layer recompaction of underlying material) may precede the water surface reflection in some regions. Acoustic analysis is inappropriate due to these late-time effects. In general, the same arguments applied to spherical convergence errors are appropriate here. The geometrically-caused errors may safely be ignored for small changes in distance (i.e., the shallow water-layer calculations, such as the 36/05 or 36/10 configurations). However, the shock front parameters and the dynamics of an individual zone may be greatly modified if a large change in problem geometry occurs (36/36 calculations). These changes may be rather more apparent for the refraction error, since the dynamics of the outer layers (rather than the less massive inner regions) are first affected. The overall problem dynamics are less sensitive to these errors than are the velocities at a given location. Therefore, mound kinetic energies and residual velocities throughout the mound after the shock fronts have passed provide appropriate criteria for comparing the individual calculations.

Another fortunate situation also reduces the influence of geometric errors on rock dynamics. Refraction difficulties are most significant for a large velocity mismatch at the interface (i.e., much stiffer underlying medium). However, the reflection at the interface is also strongest for these cases. In the extreme situation of a very low-impedance overlying material, the shock is almost perfectly reflected as a tensile wave. Thus, when a strong impedance mismatch exists, tensile wave spallation due to the interface reflection will be predominant in the rock layer. Likewise, the cavity gas acceleration signal and recompaction effects propagate more rapidly in high-velocity materials. These effects may have more influence on problem dynamics near or below the interface than the weak water surface reflection. In the 36/36 calculations, it was found that rock layer spallation, water layer recompaction effects, and the later gas acceleration pulse control rock dynamics near the interface. For coral 36/36 and basalt 36/36, the water surface reflection arrives at the interface immediately before the enormously larger gas acceleration pulse. Its only effect is to terminate the very slight deceleration due to water layer recompaction which is still occurring at this time. For granite 36/36, the gas acceleration pulse arrives at the interface before the water surface reflection can return, and overwhelms water tensile reflection effects. Thus, dynamics in the rock layer (and in the lower portion of the water layer) are dependent upon the initial shock wave, interface spall reflection, recompaction prior to the water surface reflection, and the cavity gas acceleration pulse. Long-range propagation and surface reflection of the water pulse influence dynamics only in the upper portion of the water layer, and are unimportant in the lower regions of the problem. The water surface effects are more significant for very shallow water layers, but geometric errors in such problems become negligible. This conclusion implies that precise modelling of the "upper layer" shock propagation is not crucial to the "lower layer" dynamics in the impedance-mismatched problems examined here. One-dimensional codes may be legitimately used for this particular class of problems. Equally important, submerged cratering dynamics at early times are controlled by the interface spall phenomenon, water layer recompaction, and the consequent enhancement of the gas acceleration pulse. For this reason, a single-layer analysis with one interface cannot adequately describe the process; multilayer calculations of the type employed here must be used.

V. MATERIAL PROPERTIES

Hydrodynamic calculations require a knowledge of the constitutive relations for all materials in the problem. Ideally, these relations should be established over the entire range of expected physical effects. Five materials are encompassed in this study: Aluminized ammonium nitrate slurry explosive, water, and the saturated rock media coral, basalt, and granite. The properties of these materials will be examined separately.

Explosive. Detonation characteristics and constitutive relations of a wide variety of high explosives have been extensively investigated. A convenient formulation, known as the Jones-Wilkins-Lee equation of state, is often used in hydrodynamic calculations.[29] The best-studied materials fall within the class of "military" or high explosives, which propagate a nearly-discontinuous detonation front at constant velocity. Energy is released immediately upon arrival of the front. The properties of commercial explosives available for civil excavation projects are somewhat less well-defined. Only one commercial explosive, an aluminized ammonium nitrate slurry, has been studied in detail.[30] A modified version of the Jones-Wilkins-Lee equation of state has been developed to describe this material. The equation of state assumes a total energy release of 0.11 Mbar-cm^3/cm^3 (1752 g-cal/g). About 23% of the explosive energy is released instantaneously upon arrival of the detonation front at a given location. The remaining part of the energy is released at a constant rate over a period of 0.025 msec after the detonation front arrival time. An explosive sphere of 1.13-m radius was used in these calculations. The properties of the energy source are as follows:

ρ_o (initial density) = 1.50 g/cm^3
Det. Velocity = 5300 m/sec
Radius = 1.13 m
Total energy input = 6.65 x 10^5 Mbar-cm^3
= 1.59 x 10^{10} g-cal
= 15.9 tons of explosive energy
Weight = 9.066 x 10^6 g $\simeq$ 10 tons.

The explosive sphere was divided into 30 zones of equal radius; calculational time step was restricted so that no more than one percent of the explosive energy could be generated per cycle. With this model, the peak of the explosive shock wave entered the surrounding medium about 0.24 msec after the beginning of the calculation.

Water. Compressibility and thermodynamic properties of water and ice are well-established over a very wide range of pressures and temperatures.[31-38] Available data have been used to produce the two water equation of state curves (pressure vs. specific volume) shown in Figures 3, 4, and 5. The upper curve in Figures 3 and 4 (larger specific volume at low pressures) is based on a measured Hugoniot centered at 20° C and one atmosphere.[31,32] This equation of state was adopted for the water layer calculations. The second curve was used by Butkovich in a model for generating equations of state of a rock-water-air matrix[39]; it was applied in determining the basalt and granite equations of state for this study (see below). The second curve has no relationship to the water layer calculations. The water equations of state do not include hydrostatic water-ice phase changes near 11 and 24 kbar; it is not known whether these transitions occur under shock loading.[3] Peak pressures in the water layer are on the order of 1 kbar for these calculations, so phase changes would not take place in the water. Shock vaporization of water was likewise ignored, since vaporization occurs only at pressures above 50 to

It is noted that the water layer compressibility curve shows a slight discontinuity at low pressure (Figure 3).[31,32] The abrupt increase and subsequent decrease in compressibility cause corresponding sudden changes in the bulk modulus and shock velocity for the water. This behavior, in turn, gives rise to a discontinuity in the hydrodynamic shock waveforms at low pressures. The equation of state has been modified to achieve constant bulk modulus at low pressures (dotted line, Figure 3). The initial bulk modulus and sonic velocity for the modified curve correspond with the expected values for water at about 20°C. Calculations were attempted using both equations of state; the constant bulk modulus eliminated low-pressure discontinuities in the water waveforms, but no significant effect on the rock layer was apparent. Results presented here are based on the constant bulk modulus calculations.

Rock Media. The three rock media were selected to typify potential underwater excavation sites and to represent a wide range of material properties. The sites which served as precise or approximate analogs for these media are listed below.

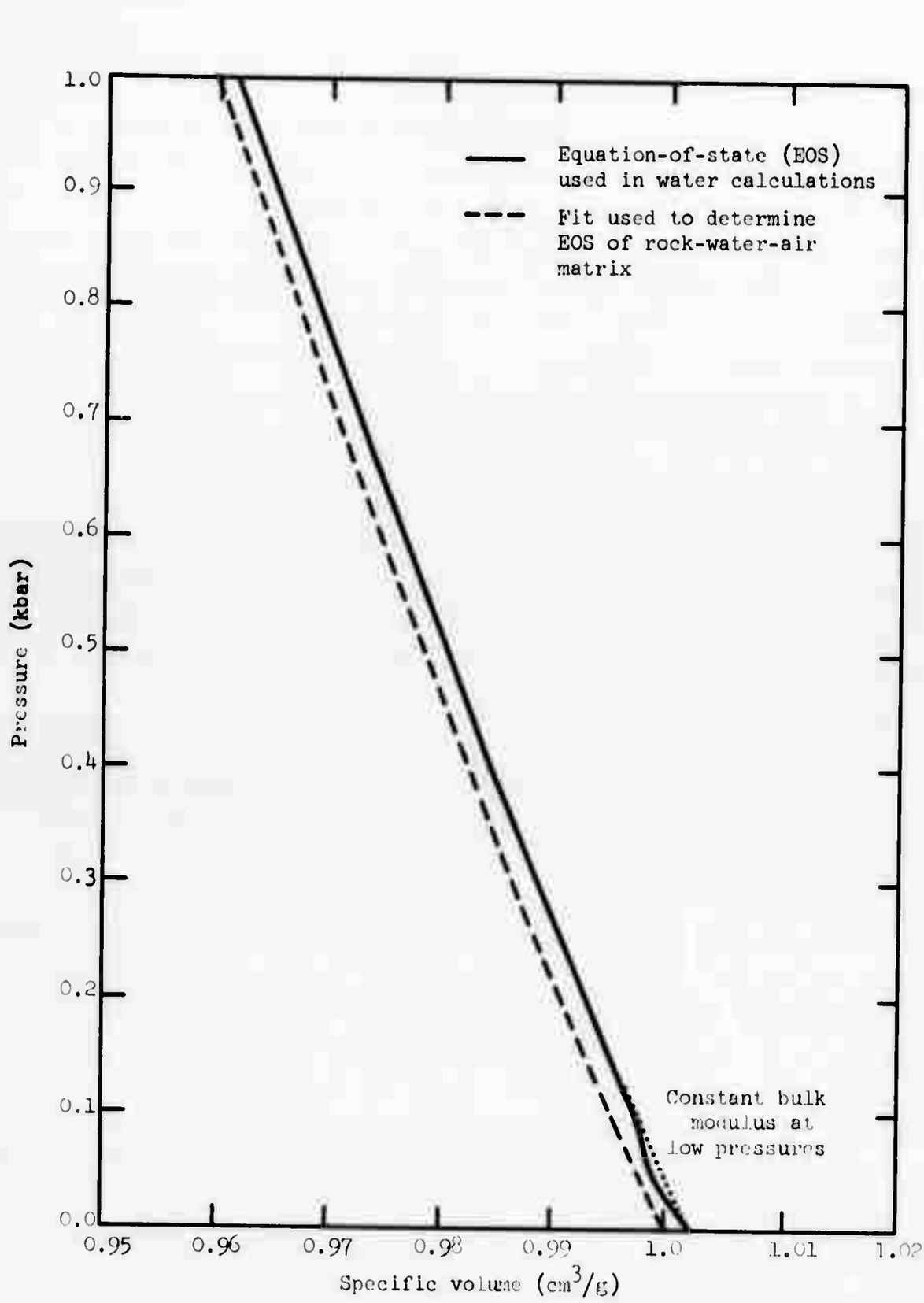

Figure 3. Equation-of-state of water, 0 to 1 kbar.

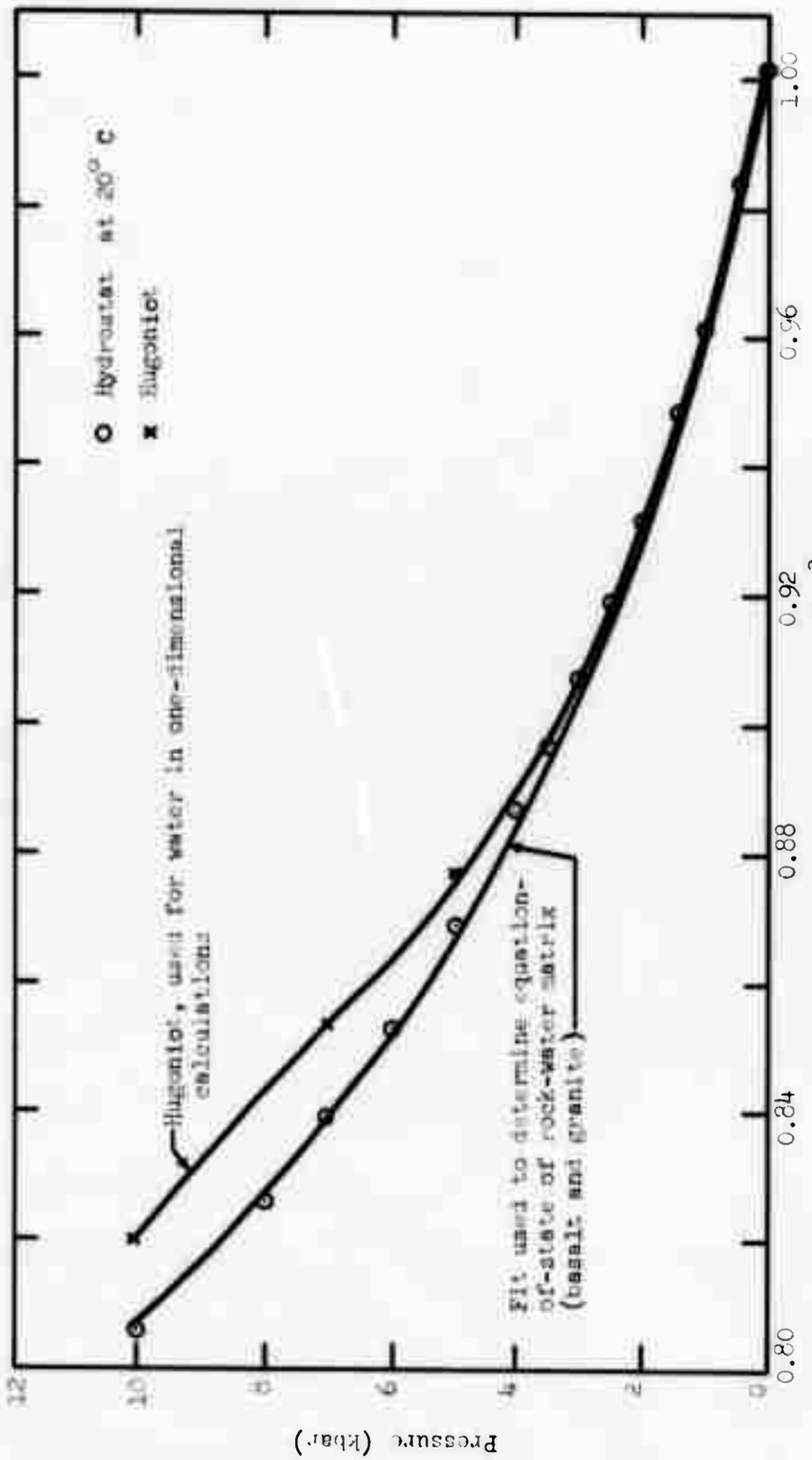

Figure 4. Equation-of-state for water, 0 to 10 kbar.

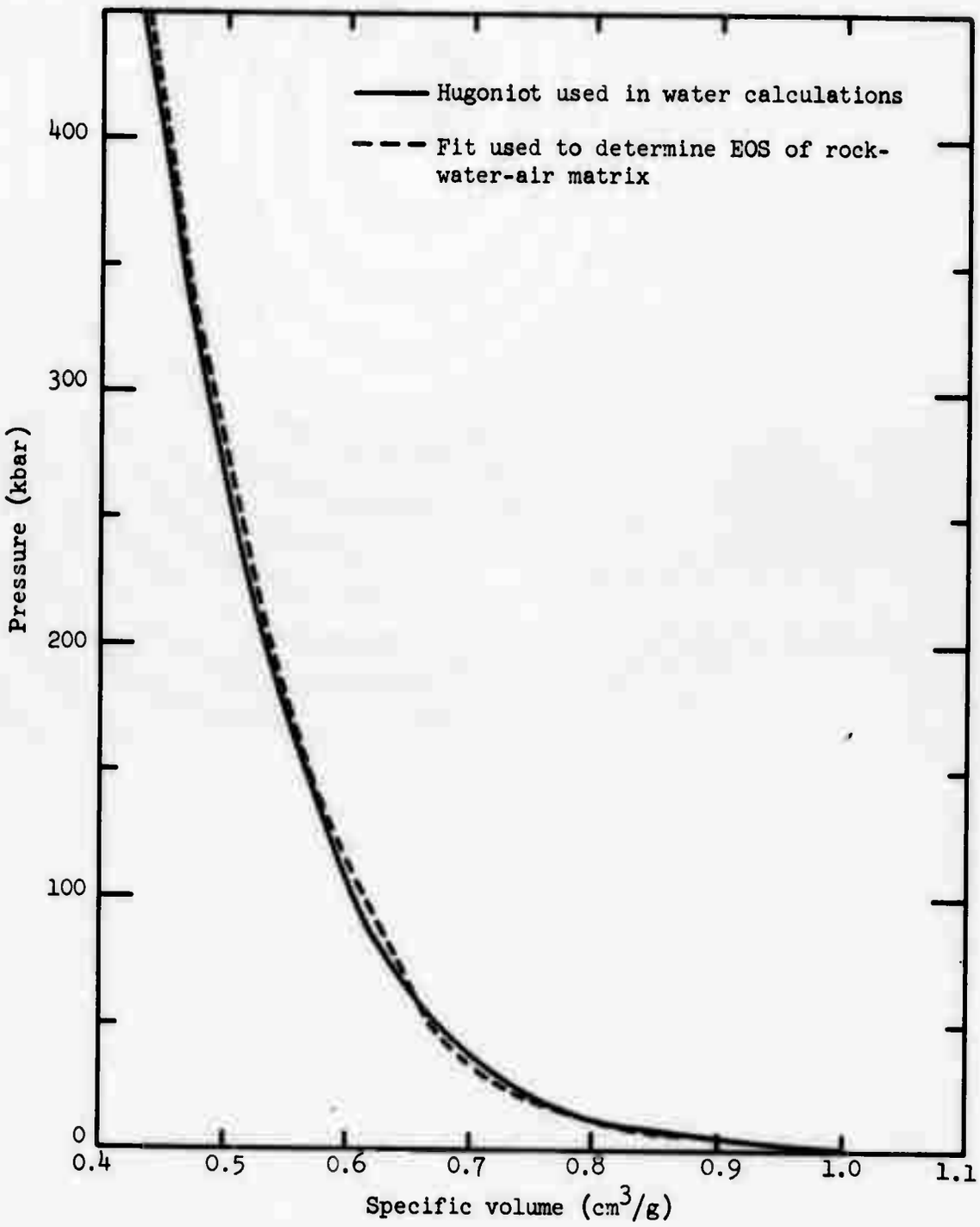

Figure 5. Equation-of-state of water, 0 to 500 kbar.

1. Coral: Tugboat coral, Kawaihae Harbor, Hawaii; site of Project Tugboat,[9] large-scale underwater explosive harbor excavation series. Material is a porous, low strength, fully-saturated aragonitic coral. Engineering properties data, pressure-volume measurements, and failure strength tests are available.[9,40] Tests were made on intact samples; the overall density of the reef is slightly lower and water content is higher due to branching of the coral. On-site measurements including seismic velocities and experimental data including airblast measurements and spall velocities from explosive events have also been obtained. [9,41,42]

2. Basalt: Kaalualu Harbor basalt, island of Hawaii; potential site of a small boat harbor. The material is a porous, low- to intermediate-strength saturated basalt representative of possible excavation sites in competent rock. Samples and engineering properties data available. No compressibility or strength tests.

3. Granite: Orinoco River high-strength granite, Orinoco River, Venezuela; site of proposed underwater excavation project. The medium is a very dense, low porosity high-strength granite. Samples and engineering properties data available. No compressibility or strength tests.

Required input data for each of these media include the pressure-volume compressibility curve or equation of state (EOS), which specifies the bulk modulus as a function of pressure. One additional modulus is required to specify material behavior. In these calculations, a constant Poisson's ratio has been used for each medium. Finally, failure envelopes are required to determine the brittle and ductile failure behavior of the material under compression, shear, and tension. Derivation of these input parameters is discussed below.

The coral medium, as previously noted, is a very low strength material subject to extensive crushing, compaction, and washback effects. Final crater sizes cannot be predicted with currently available codes. Nonetheless, coral is included in the calculation suite because of the availability of laboratory test data and limited dynamic measurements from Project Tugboat. The Tugboat excavation events utilized cylindrical charges of an ammonium nitrate slurry explosive. The emplacement configuration is compared with a schematic "SOC"

vertical problem in Figure 6. Note that the Tugboat explosive source is less dense, and therefore greater in volume, than the AANS explosive used in the calculations. The specified energy (≈ 1700 g-cal/g) and detonation velocity (≈ 5000 m/sec) of the Tugboat charges are, however, closely comparable to the calculations. The Tugboat Phase I (single-charge) events will be compared with SOC results in later sections of the paper.

Engineering properties data for numerous coral samples were derived during the course of the experiments,[9] while hydrostatic pressure-volume curves and compressional failure data were taken by Stephens.[40] Coral material parameters and elastic moduli derived from these data are listed in Table 4. Stephens' hydrostatic loading and unloading data (for loading to 30 (kbar) are presented in Table 5, and plotted in Figures 7 and 8. The loading and unloading curves coincide at low pressure, as would be expected for a saturated material (no air void porosity to be removed by compression). However, the effects of the water phase transitions are apparent from 10 to 12 kbar and 18 to 25 kbar. These transitions, which may not occur under shock loading, generate slight discontinuities in the hydrodynamic calculation waveforms. Therefore, a "smoothed" equation of state curve was drawn through loading and unloading data (Table 5 and Figure 8). Horizontal SOC calculations were performed with the measured and smoothed data (PS1OHRZ and CORHRZ, respectively). Differences between the two calculations were small and consisted primarily of noise in the waveforms close to the cavity. The smoothed curve was used in all subsequent calculations.

Stephens did not acquire loading data above 30 kbar, and no very high pressure Hugoniot measurements are available for coral. Therefore, the pressure-volume curve has been extrapolated to higher pressures (Table 5 and Figure 9). The extrapolation is partially based on measured Hugoniot data for Sabana shale (Figure 9), a very weak saturated material with a somewhat higher density and lower porosity than coral, and on data for other saturated shale media.[43-45,3] Hydrostatic and Hugoniot data are also available for dense, nonporous calcium carbonate and magnesium carbonate rocks. These data derive in part from shock experiments using marble, limestone, and other carbonate media with a composition similar to the coral matrix, but with little or no air void porosity or water content. The compressibility of a coral-water matrix may be simulated by using a calcium carbonate equation of state to describe the rock matrix and a normal water compressibility curve for the water component

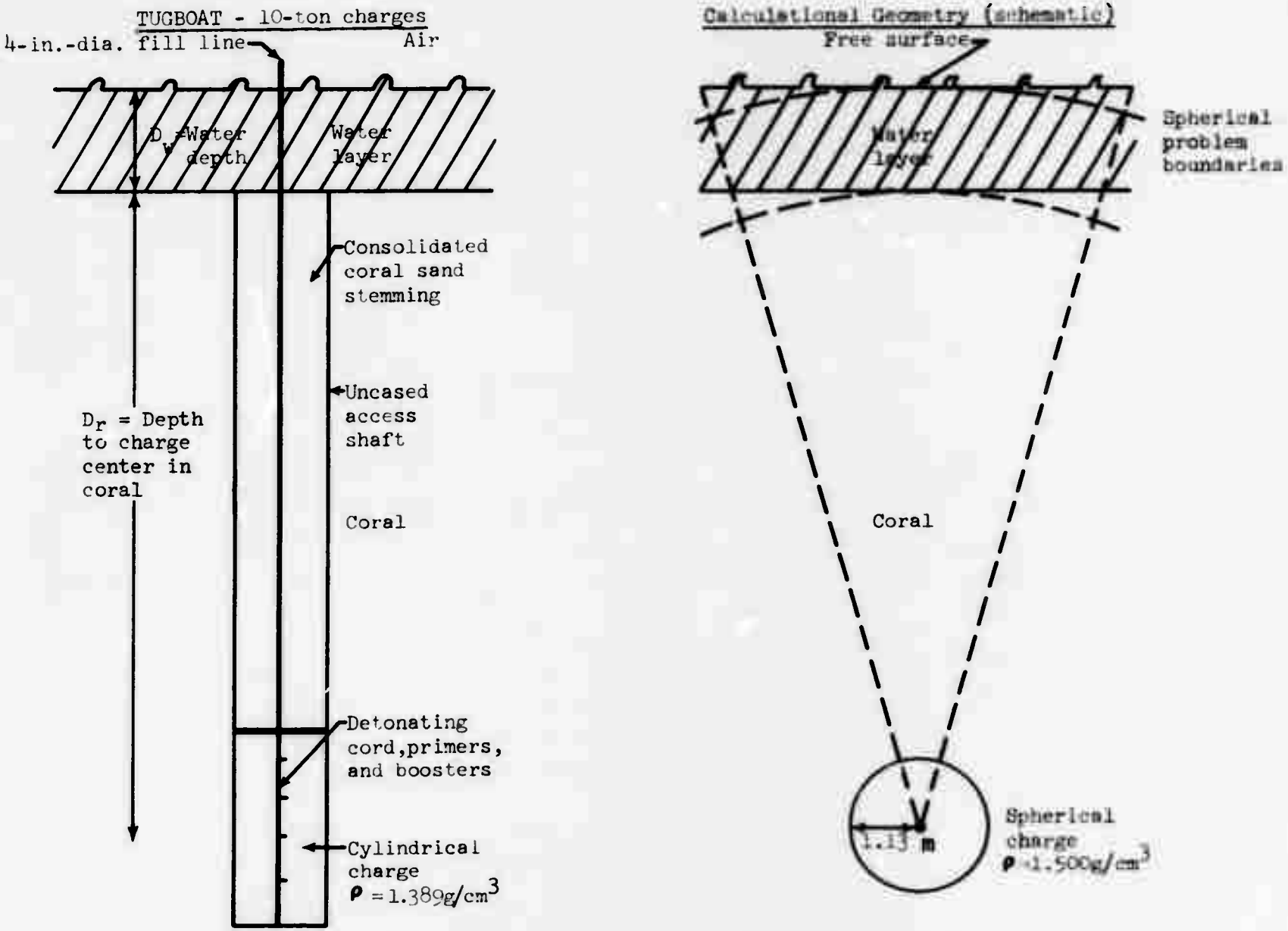

Figure 6. Emplacement configurations for 10-ton (20,000 lb) charges - TUGBOAT detonations and spherical SOC calculations.

TABLE 4. Measured and Assumed Material Parameters for Saturated Submerged Cratering Media (Saturation >99.9% in all cases

Medium	ρ_o (g/cm^3) [ρ_{dry}, gm/cc]	ρ_{grain} (g/cm^3)	Z (Water Content by weight)	ϕ Fraction Total Porosity	K Initial Bulk Modulus Mbar	V_c Compres. Sonic Velocity (m/sec)	G Initial Shear Modulus Mbar	σ Poisson's Ratio	Cohesive Strength (bars)
Vesicular basalt, Kaalualu Harbor (average values)	2.605698 [2.4285]	2.9515	0.068	0.177198	0.210*	3600*	0.095773**	0.30206**	70**
Dense Orinoco River Granite +	2.718234 [2.7080]	2.7360	0.00376489	0.010234	0.380*	5426*	0.31490*	0.17527*	300*
Tugboat Coral (Kawaihae Harbor, Hawaii)	1.880 [1.3479]	2.8806	0.283	0.5320558	0.049	1980	0.0185	0.33215	36

* Based on other measured parameters and/or on laboratory and field measurements for similar media at different sites.

** Estimated value.

\+ Assumed (nonmeasured) parameters for granite represent a relatively stiff, high-strength material of high shear modulus and low Poisson's ratio. These assumptions might be most representative of a deeply-buried or unweathered sample of low porosity.

TABLE 5. Measured, Smoothed and Extrapolated Equation of State Data for Saturated Tugboat Coral. [9,40]

Pressure P(Mbar)	Measured Loading Curve Spec. Vol. (cm^3/g)	Smoothed Loading Curve Spec. Vol. (cm^3/g)	Measured Unloading Curve Spec. Vol. (cm^3/g)
0	.531915	.531915	.531915
.001	.521277	.521277	.521277
.002	.512341	.512341	.512341
.003	.504894	.504894	.504894
.005	.492766	.492766	.492766
.007	.483245	.483245	.483245
.010	.471436	.471436	.470213
.011	.467926	.467926	.461064
.012	.458351	.4640	.458351
.015	.451755	.4550	.451755
.018	.446649	.446649	.446649
.020	.443617	.4402	---
.022	.440851	.4345	.426436
.025	.423138	.4264	.423138
.027	.420745	.4218	---
.030	.417553	.417553	---
.040		.406873*	---
.060		.387038*	---
.080		.373814*	---
.100		.361000*	---
.150		.334144**	---
.200		.315631**	---
.250		.302305**	---
.300		.291931**	---
.400		.275148**	---

* Extrapolation, 30 - 100 kbar

** Based on Hugoniot data for saturated Sabana shale, normalized to the measured specific volume of coral at 30 kbar.

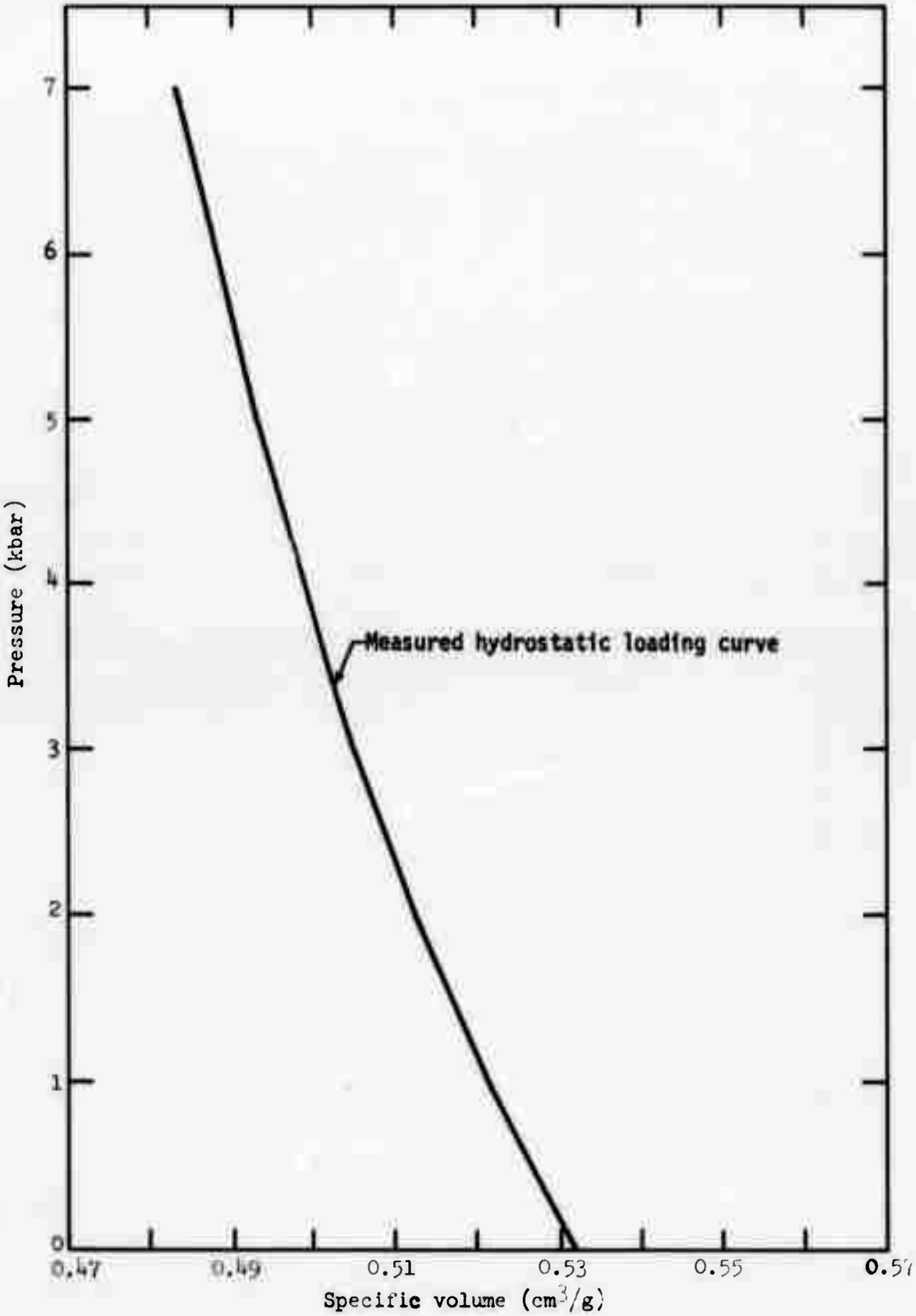

Figure 7. Hydrostatic loading curve for TUGBOAT coral, 0 to 7 kbar.

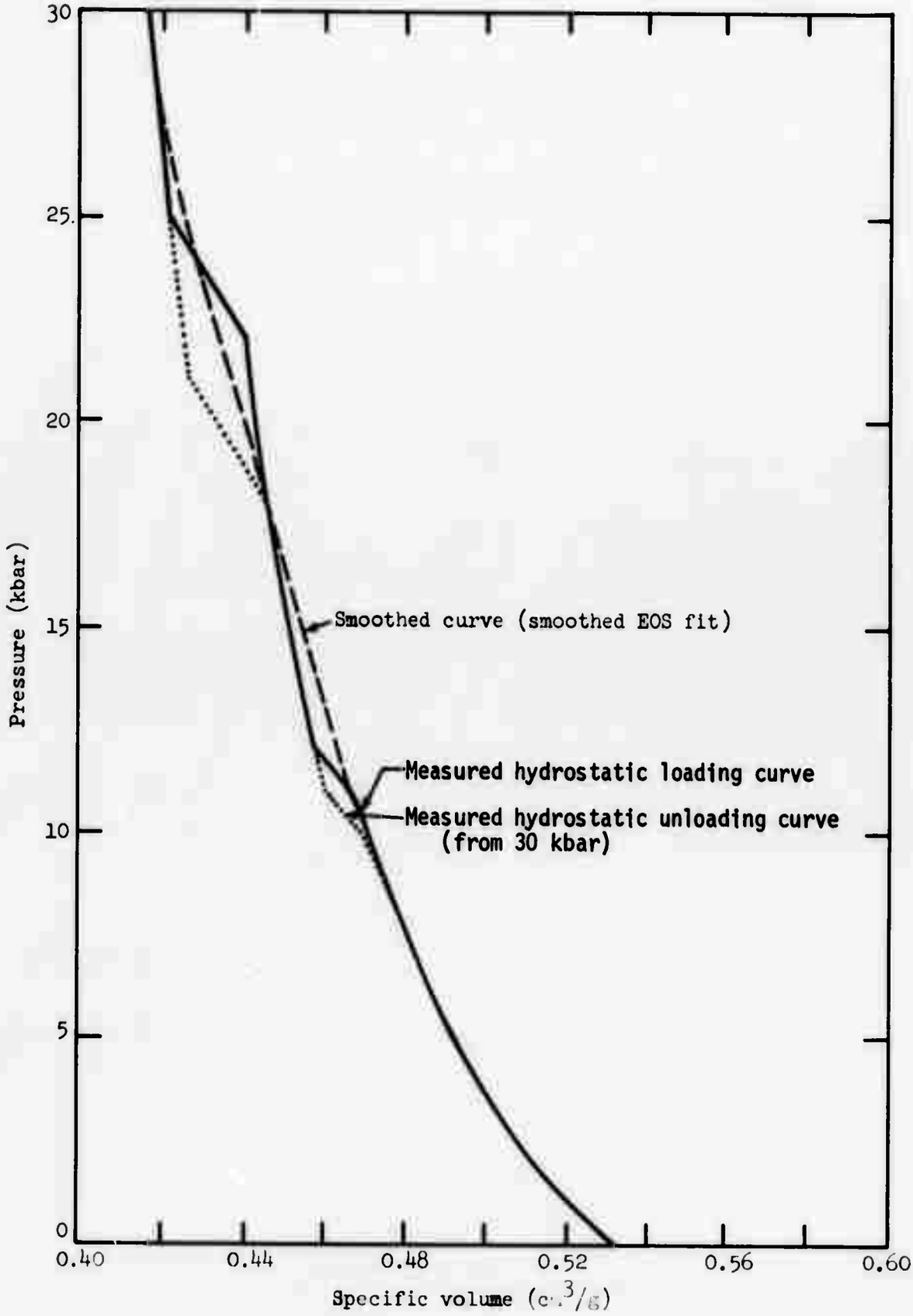

Figure 8. Hydrostatic loading and unloading curves and smoothed EOS curve for TUGBOAT coral, 0 to 30 kbar.

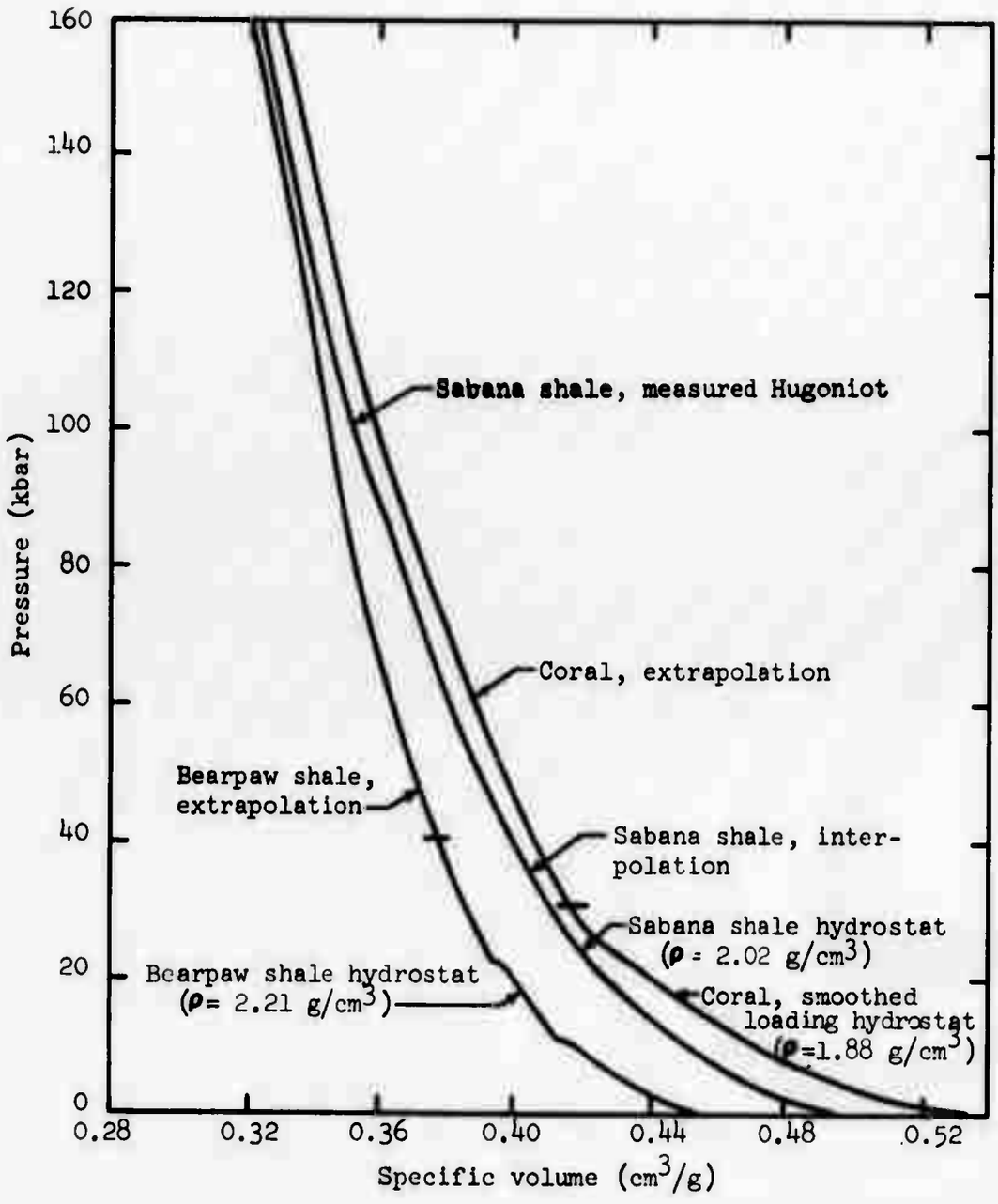

Figure 9. TUGBOAT coral: specific volume as a function of pressure, 0 to 160 kbar; extrapolation above 30 kbar is based on normalized Hugoniot data between 100 and 400 kbar for Sabana shale (a wet, weak, fully saturated material of comparable water content). Loading curves for saturated shale media are also shown for comparison.

(simple mixture volumetric compressibility model). This analysis predicts stiffer bulk moduli and lower compressibility than Figure 9 would indicate, both in the low pressure regime (measured data) and along the high pressure Hugoniot (extrapolation). Volume errors of several percent occur in the region of the hydrostatic measurements. However, the bulk modulus of coral increases significantly at the upper end of the measured pressure range (25-30 kbar). Thus, coral may be less compressible than the compromise fit in Figure 9 at high pressures. If the stiff behavior indicated by the carbonate Hugoniot is correct, the extrapolation will be increasingly inaccurate at higher pressures $\gtrsim$ 100 kbar. Since maximum pressures encountered furing high-explosive calculations are on the order of 100 kbar, the implied inaccuracies are not important here.

Strength data for the Tugboat coral material were obtained to a maximum confining pressure of 3.5 kbar by triaxial compression and Brazil tests on intact core samples.[40] Results are displayed in Figure 10. The abscissa and ordinate of the plot conform with the parameters used in the code: failure shear stress k [= $(\sigma_1-\sigma_3)/2$] and adjusted mean pressure $\bar{P}$ [=$(\sigma_1+\sigma_3)/2$]. No data were obtained for failed (crushed) material, but an estimated failure envelope has been drawn below the "intact" data (and assuming no tensile strength for failed material). The data shown in Figure 10 indicate an abrupt increase in strength to about 60 bars at very low pressures, followed by an apparent slight decrease at higher $\bar{P}$ values. This unusual behavior has been explained as a work-hardening effect involving collapse of the coral matrix.[9] The code does not accept a decreasing strength function, so a constant strength is assumed between 0.2 and 2.86 kbar (dashed) line in Figure 10). The failure surfaces have been extrapolated to a maximum shear strength of 101 bars at and beyond 5 kbar. Tests indicate that the behavior of coral is ductile except at very low confining stresses; a transition from brittle failure to ductile behavior at 0.2 kbar is assumed.

Engineering data for Kaalualu basalt and Orinoco River granite are presented in Table 4. The measurements include bulk density, rock grain density, and porosity.[46] The elastic moduli and other properties not available from measurements were estimated using data for similar media.[17,47-51] Because the elastic constants of an isotropic linearly elastic material are interrelated, the density and any two constants are sufficient to define the material (see "Relationships Among Elastic Constants", table at the beginning of this report). Such parameters as the bulk modulus, compressional velocity, shear modulus,

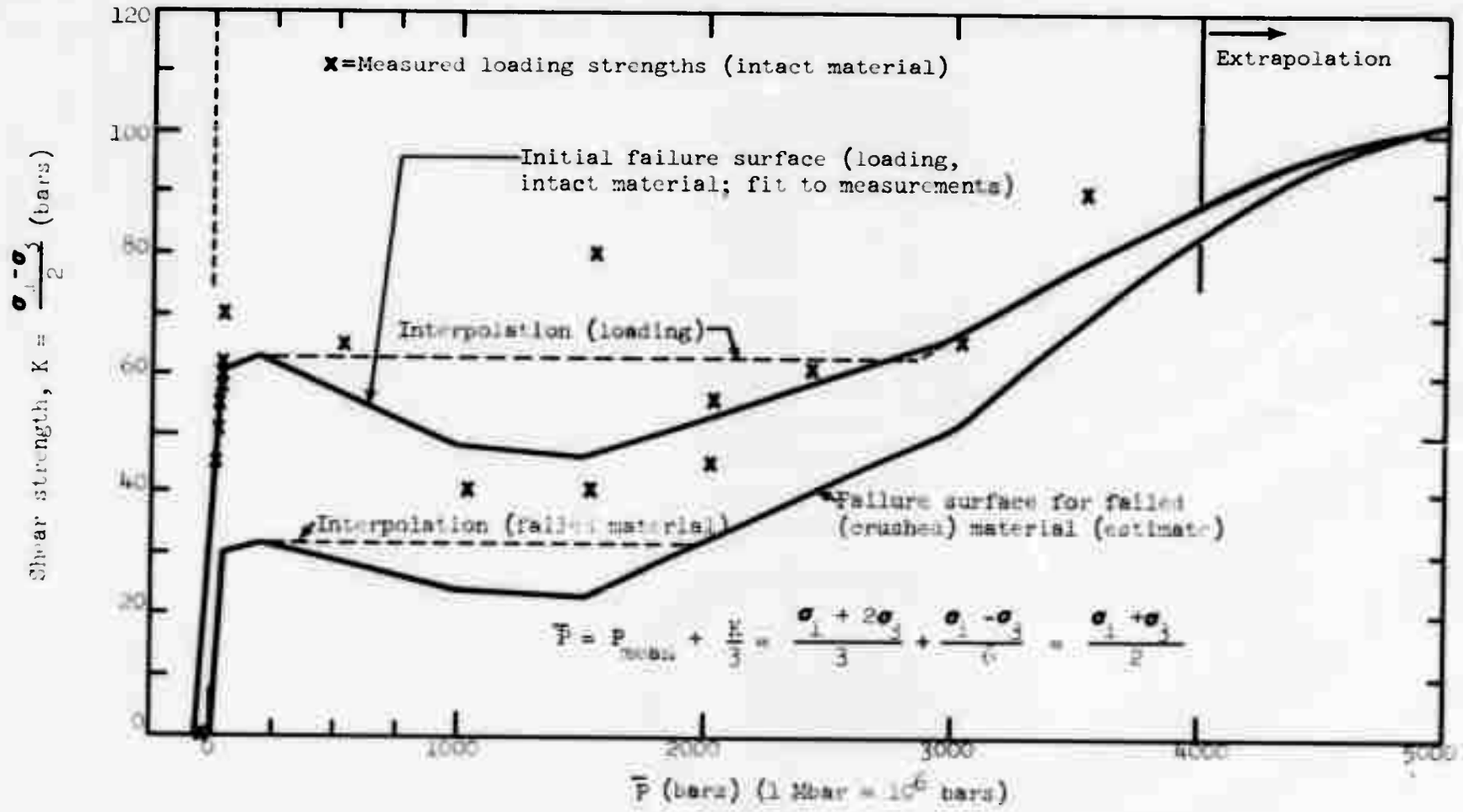

Figure 10. Failure shear strength, K, as a function of $\bar{P}$ for TUGBOAT coral (the unloading or crushed material strength curve is an estimate).

and Poisson's ratio have been determined for various basalts and granites. These measurements, in conjunction with reasonable expectations for the known sample densities, have been used to produce the values in Table 4. In particular, the bulk moduli and sonic velocities are known to be reasonable for comparable geologic materials. The shear modulus (or Poisson ratio) is less accurately fixed.* The Poisson's ratio for porous basalts does not vary dramatically, and the assumed value is probably accurate. However, a very low Poisson ratio (high shear modulus) is accepted for the granite. This is in accord with the relatively high bulk modulus and sonic velocity. Hardhat granite has been used as a model for the elastic parameters in this case.[49] The Hardhat material is a very dense high-strength rock from a deep layer (≈ 1000 ft). It has low porosity, with a high sonic velocity and shear modulus. The granite is thus being selected to represent a dense, highly competent medium at one extreme of the material properties spectrum. This choice may not be inappropriate, in view of the low porosity and probable high strength of the Orinoco rock.

Compressibility curves and failure surfaces for the basalt and granite are likewise unknown. Butkovich has recently developed a method for estimating the equation of state of silicate rocks.[39,52,53] This technique, which is based on simple mixture theory for a rock-water-air matrix, generates accurate pressure-volume relations for a variety of silicate rocks, over a broad range of porosity and water content. The equation of state for the grain density rock includes allowance for high-pressure (Hugoniot) phase transitions known to occur in silicate minerals. The water equation of state discussed previously is used for the water component. A slightly modified version of the Butkovich technique, suitable for fully-saturated materials, has been used to generate basalt and granite equations of state. Following empirical expectations and experimental evidence for saturated media,[3] the bulk modulus is assumed to be slowly and monotonically increasing at low

* The shear modulus, for example, is highly sensitive to the assumed sonic velocity. Seismically determined sonic velocities may differ from values measured for small intact rock samples, thus causing significant uncertainty if shear modulus is calculated from this parameter.

pressures ($\approx$ 0 to 2 kbar). The low-pressure curve is then smoothly connected with a rock-water matrix equation of state at higher pressures. Loading and unloading curves are assumed to be identical (no nonrecoverable air void porosity). The resultant equations of state for basalt and granite are displayed in Figures 11-12 and 13-14, respectively. In this case, pressure has been plotted against the dimensionless volumetric compression "μ" ($\mu = \frac{\rho}{\rho_o} - 1 = \frac{v_o}{v} - 1$; where ρ = density, or v = specific volume). Data for similar basalts and granites are presented for comparison. The basalt curve appears consistent with measurements of comparable porous and consolidated basalts ($\rho_o \approx 2.6$) at low pressures. It falls somewhat below (less stiff than) dense consolidated basalt, and the canal zone basalts.[17] At very high pressures ($\approx$ 300 kbar), the large water content causes the generated curve to become less stiff than the measured basalts. This region is of no interest for high-explosive calculations. The granite curve compares closely with measured data.

Failure surfaces have also been estimated on the basis of available data. The basalt medium, as indicated by extensive measurements for porous and saturated basalts,[17,31] is allowed a tensile strength of 0.1 kbar and an ultimate strength of 0.4 kbar. The granite [31,54,49] is arbitrarily assumed to have a high ultimate strength of 5 kbar, with a tensile strength of 0.38 kbar. There is some evidence that strength may decrease considerably with saturation, even in the case of a very low porosity granite.[48,14] However, the high strength is retained, in keeping with the desire for one "extreme case" calculation. Failure envelopes of the assumed ultimate strength have been smoothly fitted using an empirical hyperbolic equation.[39] The resultant failure surfaces for intact rock are shown in Figures 15-16 (basalt) and 17-18 (granite). Low-pressure failure surfaces for crushed material have been drawn at approximately one-half of the corresponding failure strengths for intact material. The condition of no tensile strength at $\bar{P}$=0 has been imposed at the lower end of these curves, as is reasonable for fully-crushed rock. The crushed failure surfaces are then smoothly connected with the intact failure envelopes at very high pressures.

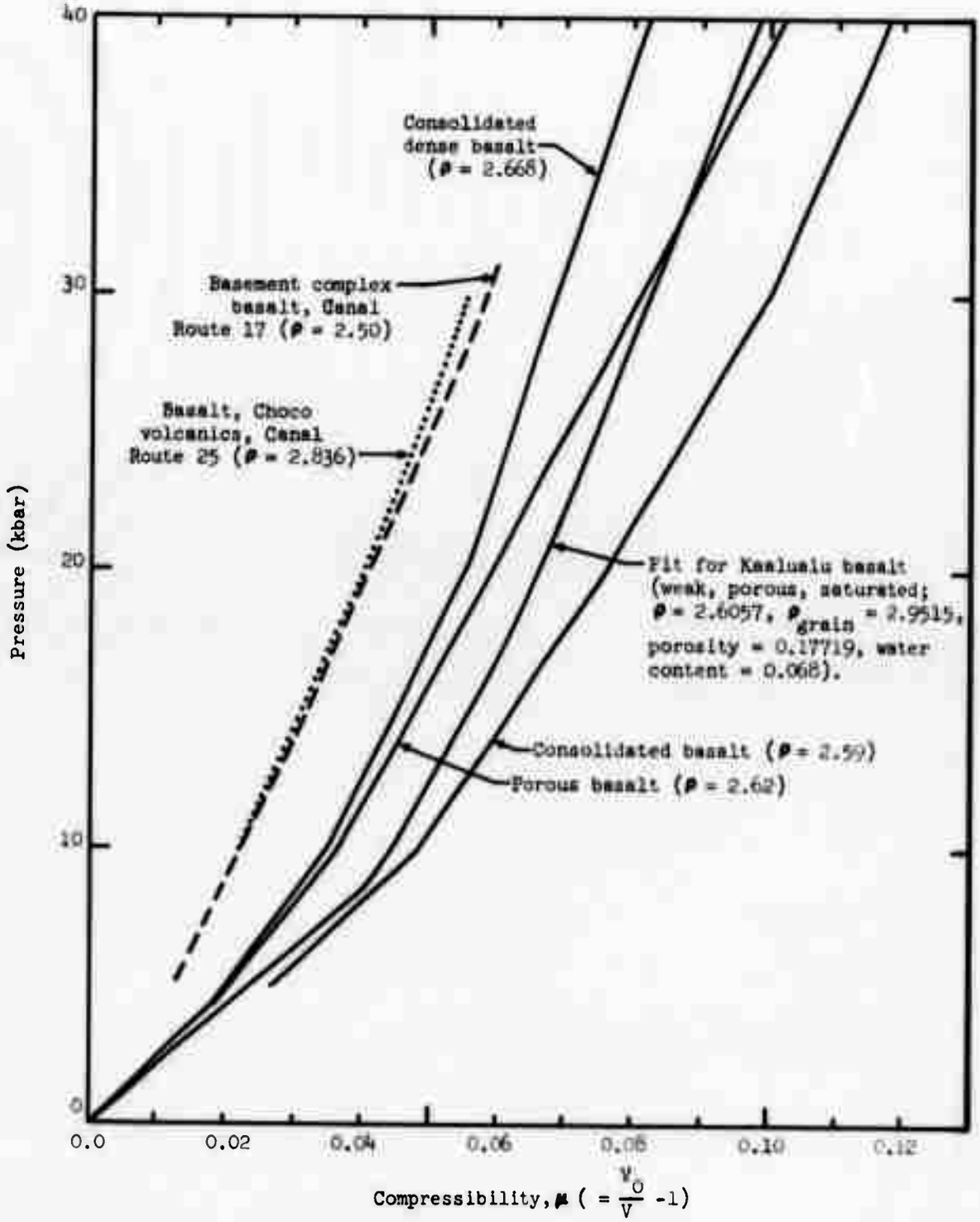

Figure 11. Pressure vs compressibility for typical basalts (hydrostat).

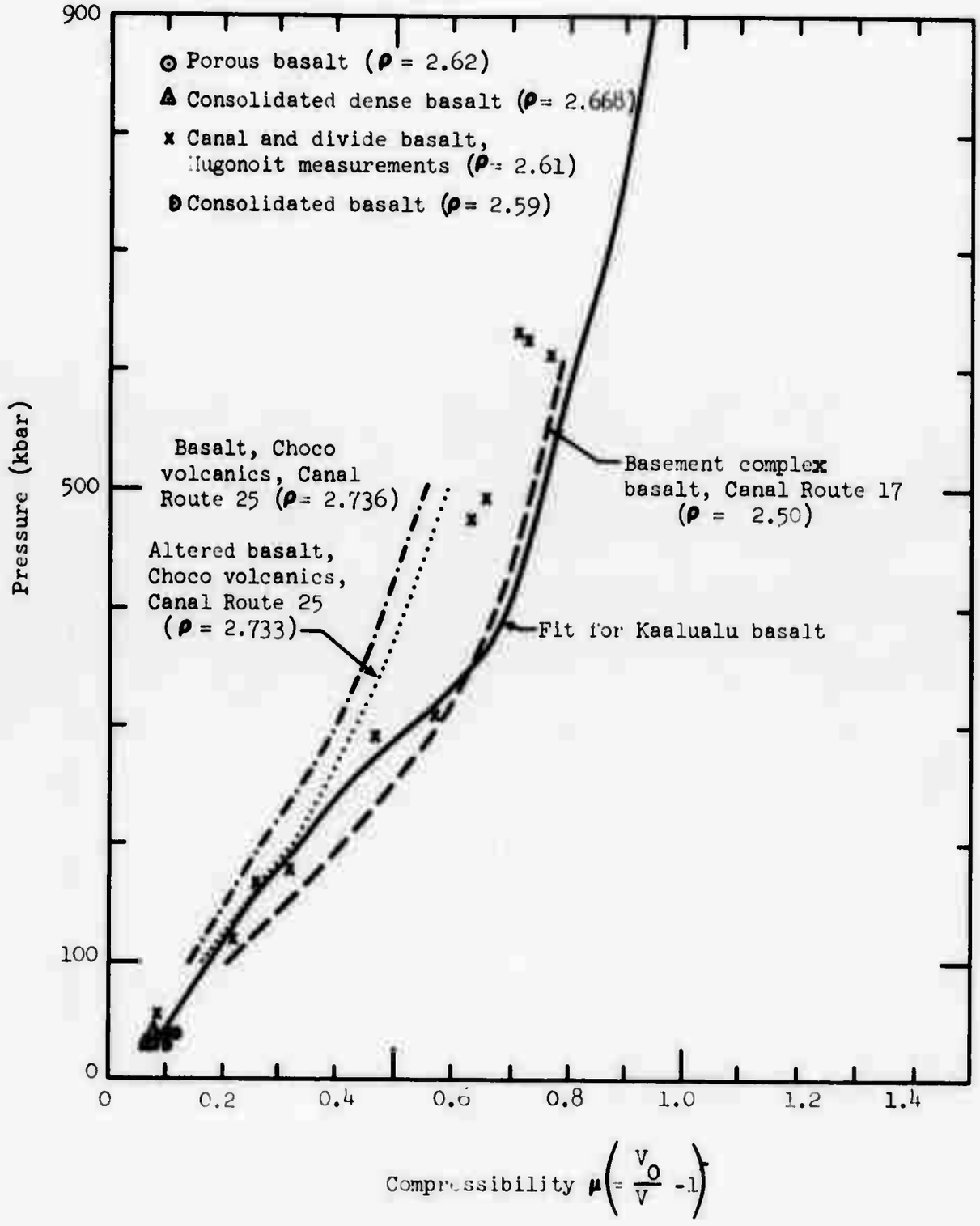

Figure 12. Pressure vs compressibility for basalts, Hugoniot (high-pressure) region.

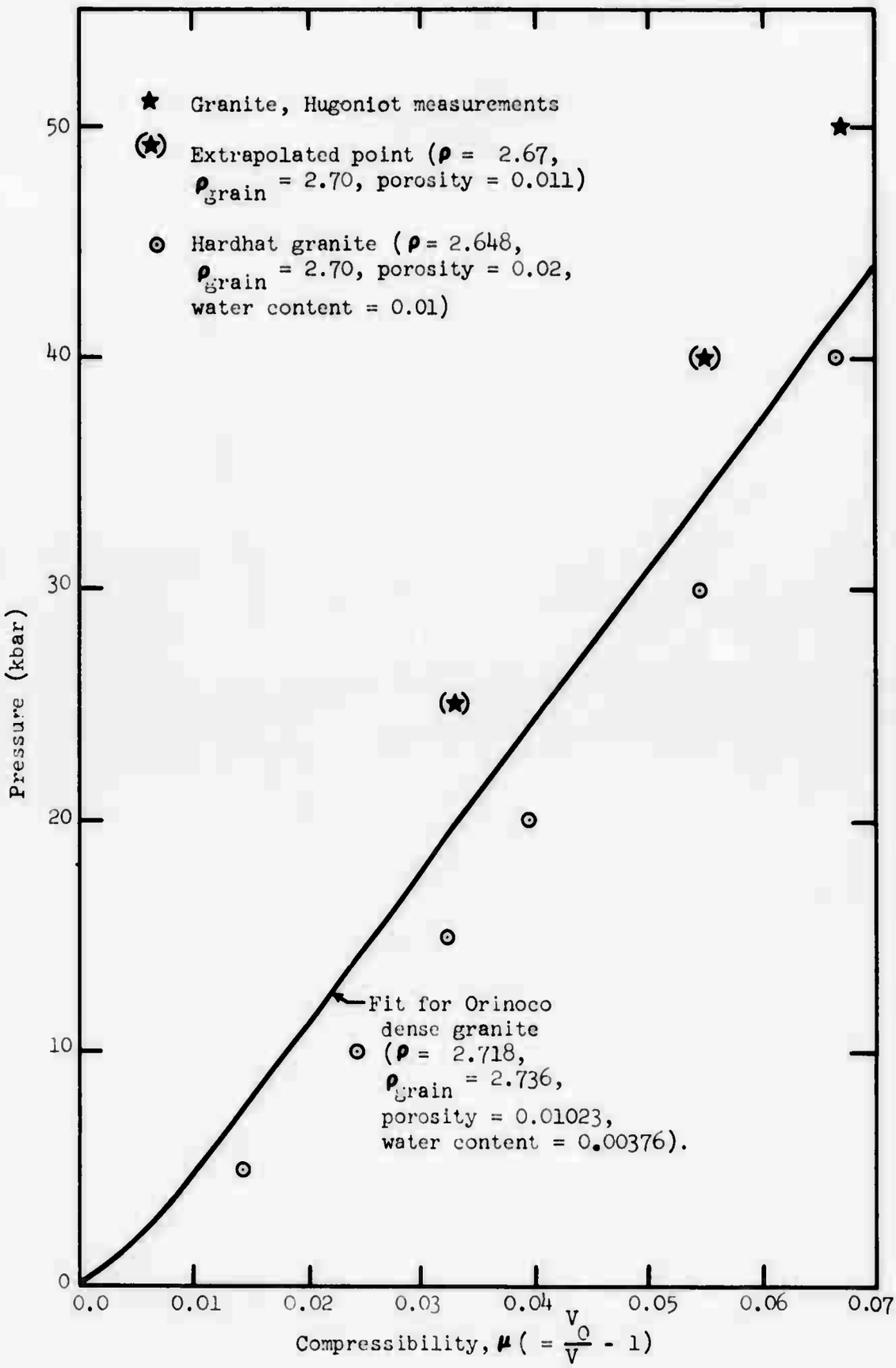

Figure 13. Pressure vs compressibility for dense granites.

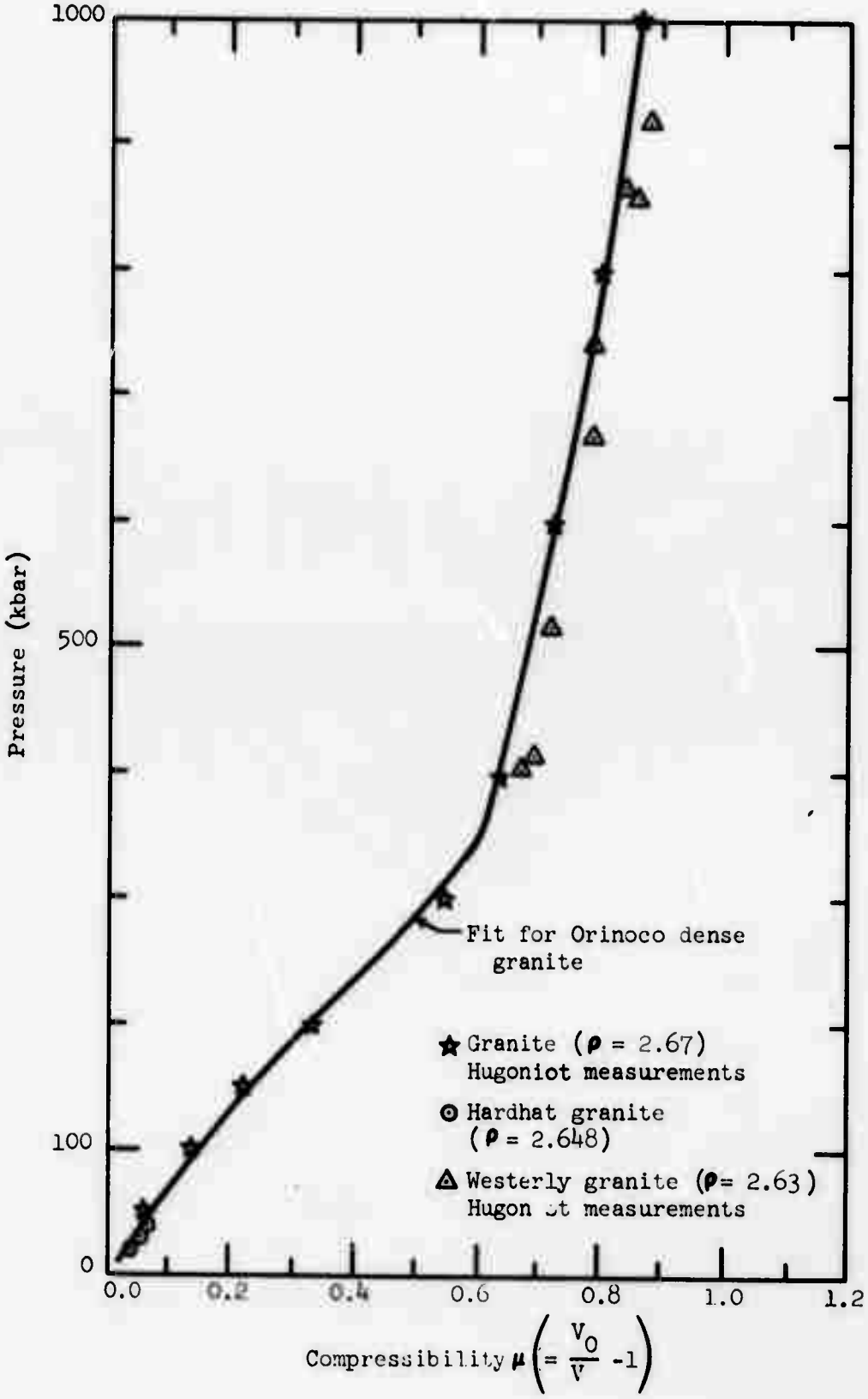

Figure 14. Pressure vs compressibility for dense granite, Hugoniot (high-pressure) region.

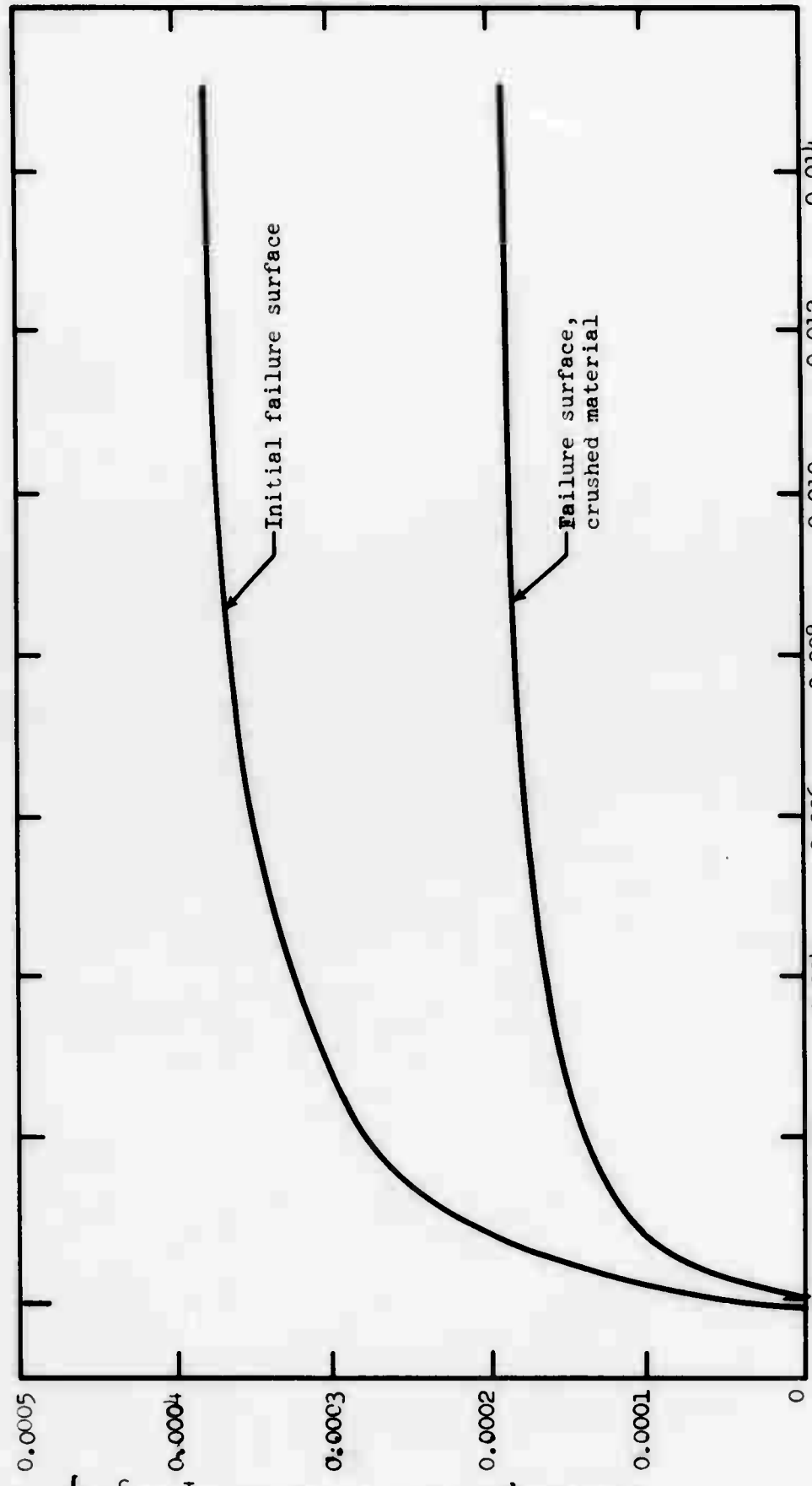

Figure 15. Failure surfaces for Kaalualu basalt - shear strength "K" vs "$\bar{P}$."

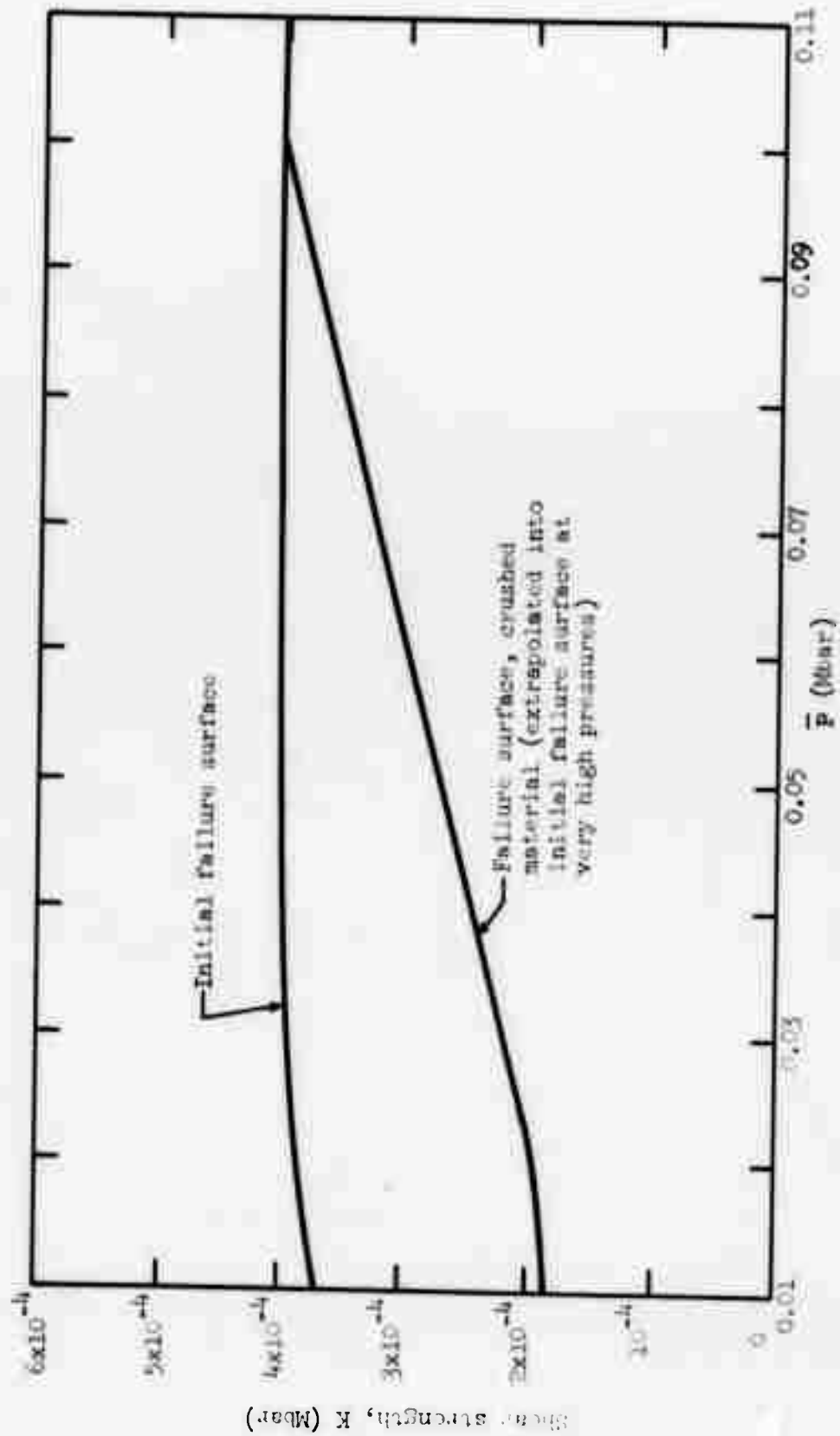

Figure 16. Failure surfaces for Kaalualu basalt - shear strength, K, vs $\bar{P}$.

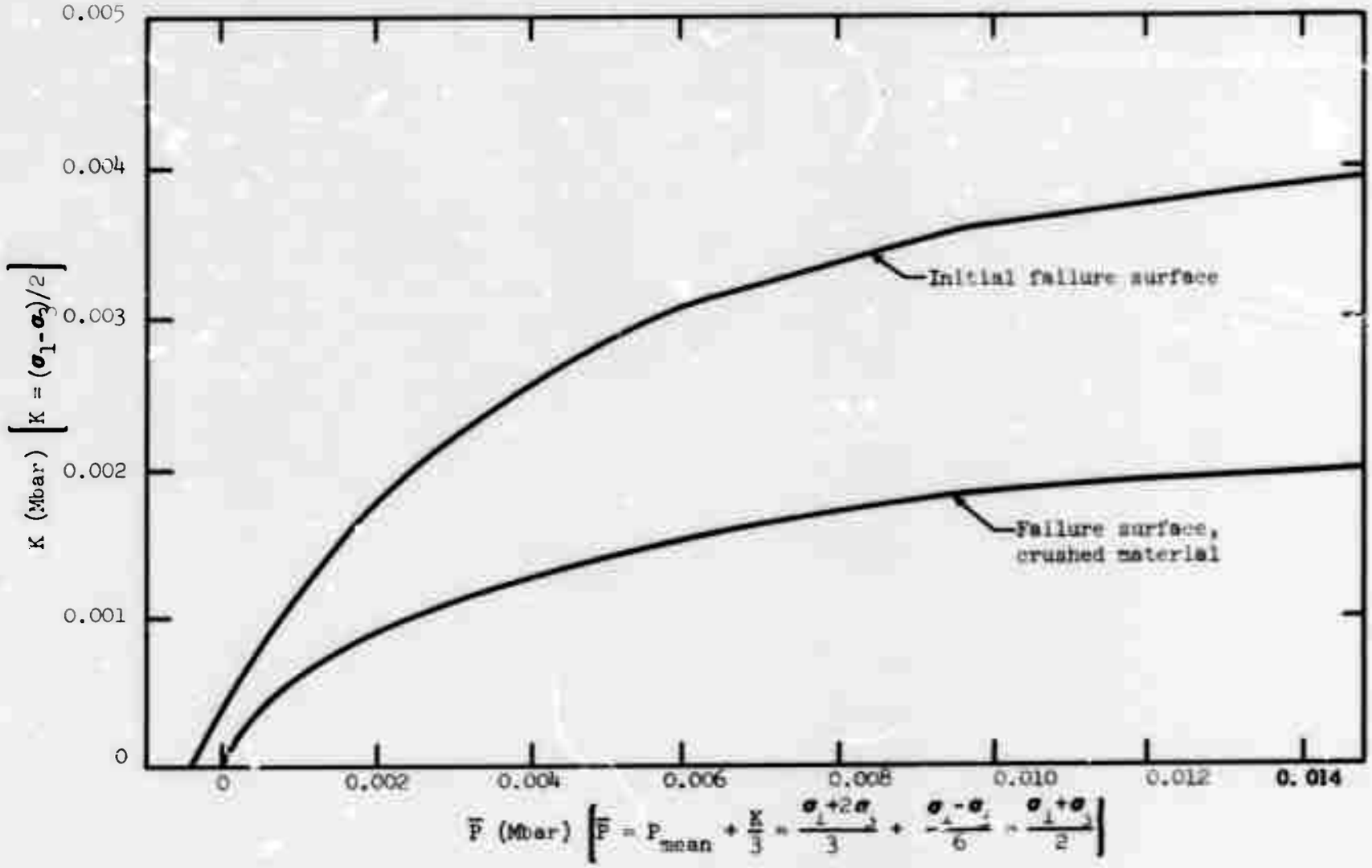

Figure 17. Failure surfaces for Orinoco high-strength granite - shear strength, K, vs $\bar{P}$.

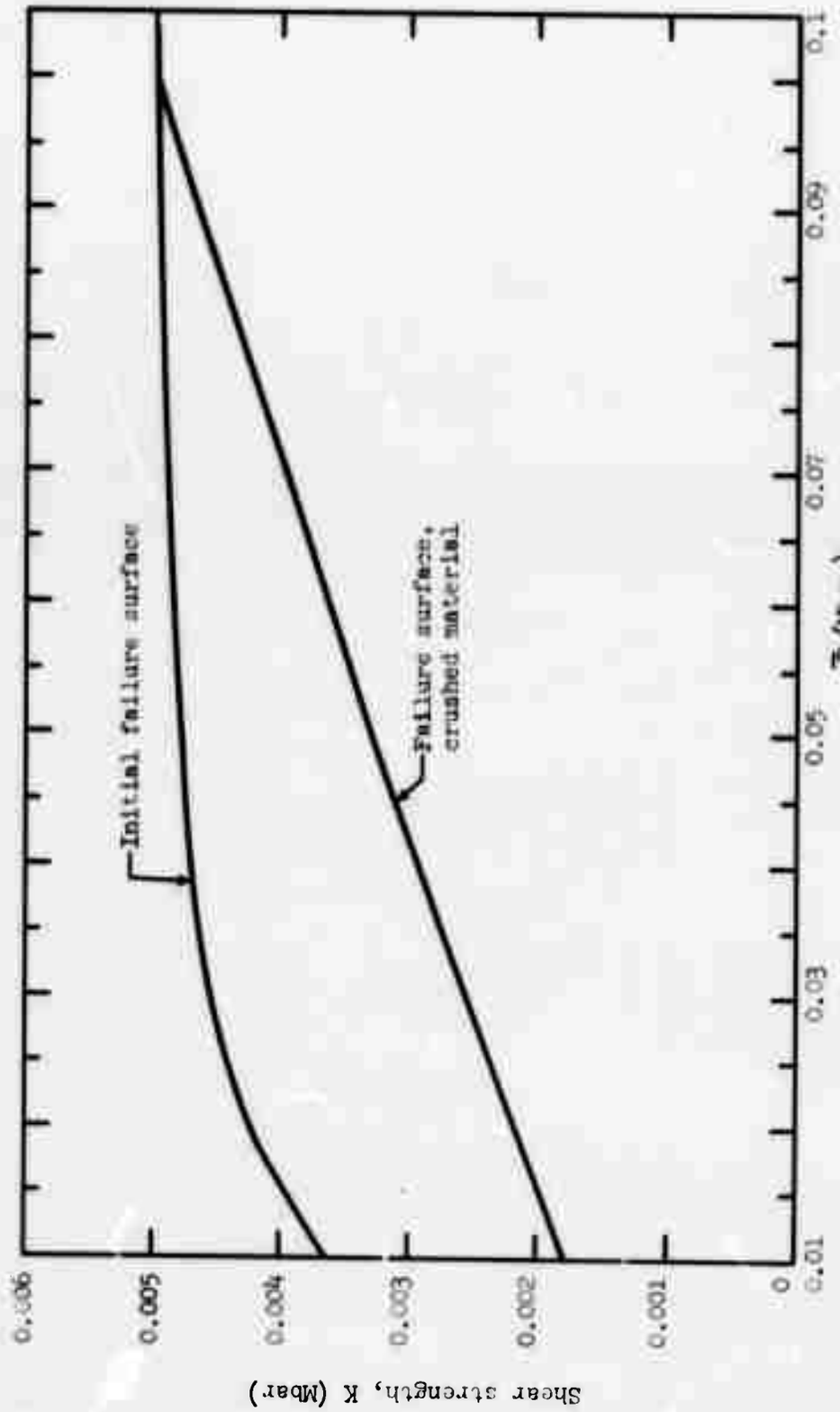

Figure 18. Failure surfaces for Orinoco high-strength granite - shear strength, K, vs F.

The parameters which control multilayer acoustic wave transmission are the impedances and sonic velocities of the layers. Acoustic parameters for the five media discussed above are summarized in Table 6. The ratio of the medium impedance to the impedance of water "$\rho_o C/\rho C_{water}$", and the pressure transmission factor normal to the medium-water interface "T_{p90}," are also given. Acoustic transmission parameters are not valid at a strong shock front. However, typical pressures near the rock-water interface are on the order of one kilobar in these calculations; the acoustic transmission analysis may be used with a high degree of accuracy.

VI. RESULTS: ARRIVAL TIMES, VELOCITIES, STRESSES, AND WAVEFORMS

This section presents detailed results of the "SOC" horizontal and vertical calculations. Since the study involved a broad-scale survey of several media and configurations, any one of which might prove applicable to a future design, it is considered worthwhile to compile a fairly extensive library of individual events. Accordingly, the peak velocities, pressures, and stresses have been plotted as a function of range for all calculations. Selected velocity and pressure time-dependent waveforms at several ranges from the center of each problem are also presented.

Before reviewing the dynamic results, it is appropriate to consider the order of effects of interest. We are examining typical cratering events of 15.9 tons energy yield, at burial depths of about 36 ft (143 ft/kt$^{1/3}$). Shock parameters at ranges in this vicinity are relevant to crater formation. For the vertical calculations, material velocities near the free surface (or rock-water interface) are a primary factor in material ejection. Thus, velocity waveform changes near the interface attributable to the water layer are significant. Peak particle velocities near the interface are typically on the order of 70 m/sec (i.e., near-optimum burial depth cratering events); peak pressures near the interface and in the water layer are $\approx$ 1 kbar. The interface region is in the range of assumed brittle failure behavior for basalt and granite, but is ductile for coral. The ultimate shear strength of 5 kbar for granite is never reached at the interface, or at ranges $\gtrsim$ 4 m from the center of the problem. The ultimate strength of basalt may or may not be exceeded in the vicinity of the interface. Finally, the

TABLE 6. Acoustic Parameters for the Media and for Aluminized Ammonium Nitrate Slurry Explosive (AANS).

Medium	K Initial Bulk Modulus (kbar)	C_{sonic} (ft/sec)	ρ_o (g/cm^3)	Impedance $\rho_o C$ ($\frac{psi\text{-}sec}{ft}$)	$\frac{\rho_o C}{\rho C(water)}$	T_{P90}* (medium-water)
Coral	49	6,500	1.880	164.53	2.4816	0.5744
Basalt	210	11,810	2.605698	414.32	6.249	0.2759
Granite	380	17,800	2.718234	651.43	9.825	0.1847
Water (fresh, Temp. ≈ 20-30°C)	22.568	4,933.4	0.9982	66.30	1.0	(1.0)
AANS explosive**	--	C_{det} =17,389	1.500	ρC_{det} =351.18	(5.2968)	(0.3176)

* T_{p90} = Pressure transmission factor for an acoustic wave propagating normal to the medium - water interface.(Reflection factor $R_{p90} = 1 - T_{p90}$; since water is of lower impedance than the other media, the transmitted wave is compressional and the reflected wave is tensile.)

** The AANS material used in these calculations is a high-energy non-ideal aluminized ammonium nitrate slurry explosive. The velocity of the propagating detonation front "C_{det}" is 17,389 ft/sec (5300 m/sec); the total energy release is assumed to be 0.11 Mbar-cm^3/cm^3. The explosive is described in greater detail in Chapter V.

ultimate strength of 0.101 kbar for coral is exceeded in virtually all zones, throughout the vertical problems. It is of interest to note that peak pressures at or near the interface lie in the relatively low pressure range, where a slowly-changing bulk modulus is assumed for saturated materials and water. Thus, nearly linear-elastic behavior for peak transmission at and beyond the interface may be expected. The peak shock parameters will be analyzed acoustically and compared with SOC runs in Chapter VIII.

Time of Arrival. Shock time of arrival measurements provide a useful means of checking code calculations. Arrival times have been obtained for only one underwater cratering event, Tugboat Phase II - IJKL (a four-charge array of 10-ton charges; $D_r \approx 36$ ft, $D_w \approx 5$ ft). Several dynamic gages were emplaced in the water layer, directly above each of the four charges.[9] Little usable information was recovered from these gages, but the initial arrival was detected in most cases. Unfortunately, the recording system used did not give accurate "real time" measurements (detonation to shock arrival), and the locations of the gages were not very precisely determined.

Vertical propagation from each charge of the Tugboat IJKL event may be compared with the almost-identical Coral 36/05 vertical calculation. Initial wavefront arrivals and peak arrival times for Coral 36/05 are shown in Figure 19. The peak arrival in the extreme upper portion of the water layer cannot be determined because the spall reflection truncates the peak. Note that the wavefront velocity in coral approaches 2000 m/sec (slope of straight line), in agreement with the assumed sonic velocity of 1980 m/sec. Tugboat IJKL measured arrivals are also plotted in Figure 19. Considerable scatter is evident, but most of the measurements lie near the calculated curve. Positions for three of the gages listed in the Tugboat report[9] lie above the water surface level, evidently an error (all gages were underwater).

Arrival times for the deep water layer calculation coral 36/36 are depicted in Figure 20. Initial and peak arrivals in the coral are identical to Figure 19. The velocity in the water layer approaches the sonic value of 1503 m/sec, indicating nearly-acoustic behavior of the wave.

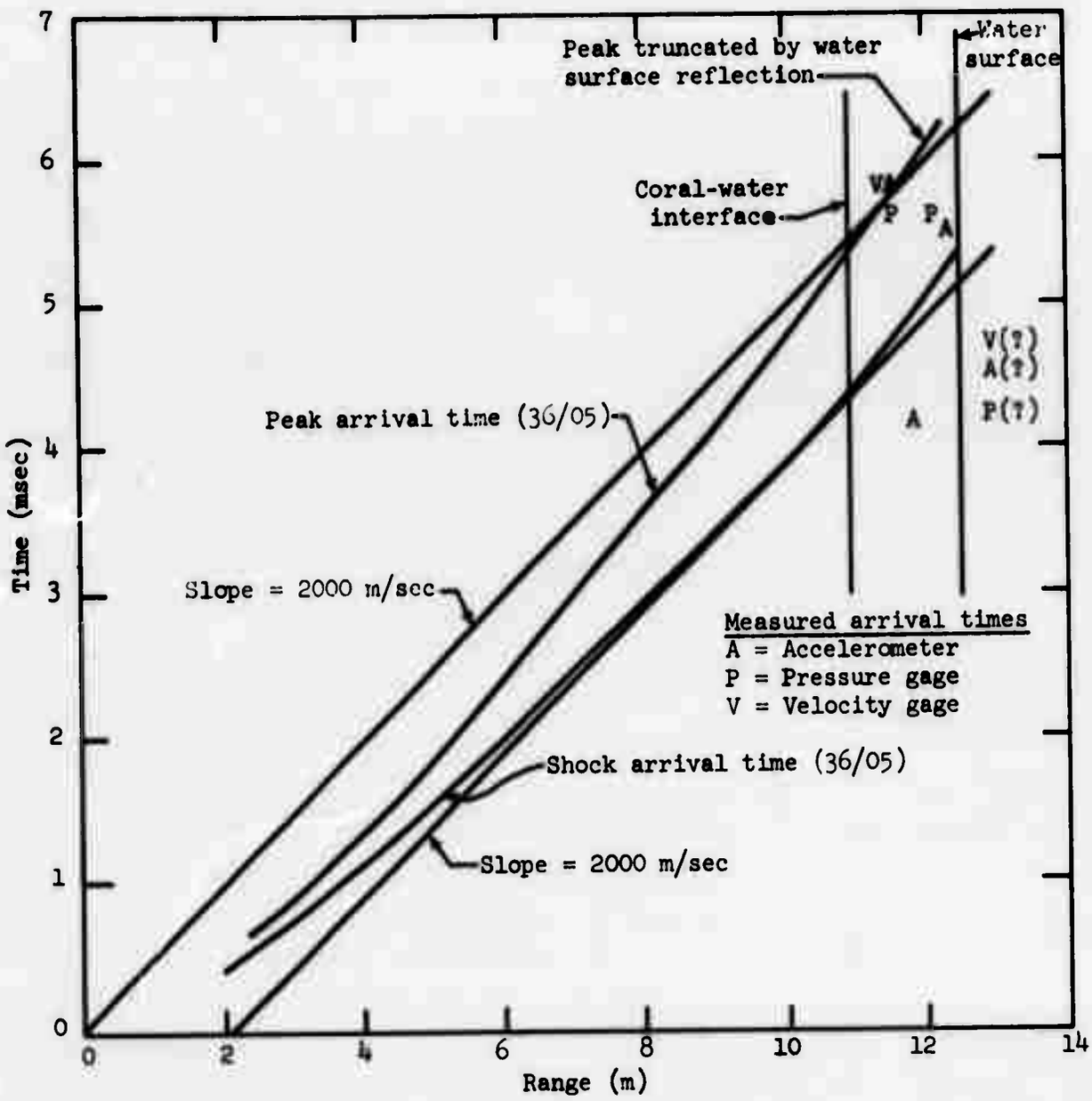

Figure 19. Pressure pulse arrival times as a function of range from problem center for coral 36/05 vertical calculation and Tugboat II-IJKL experiment.

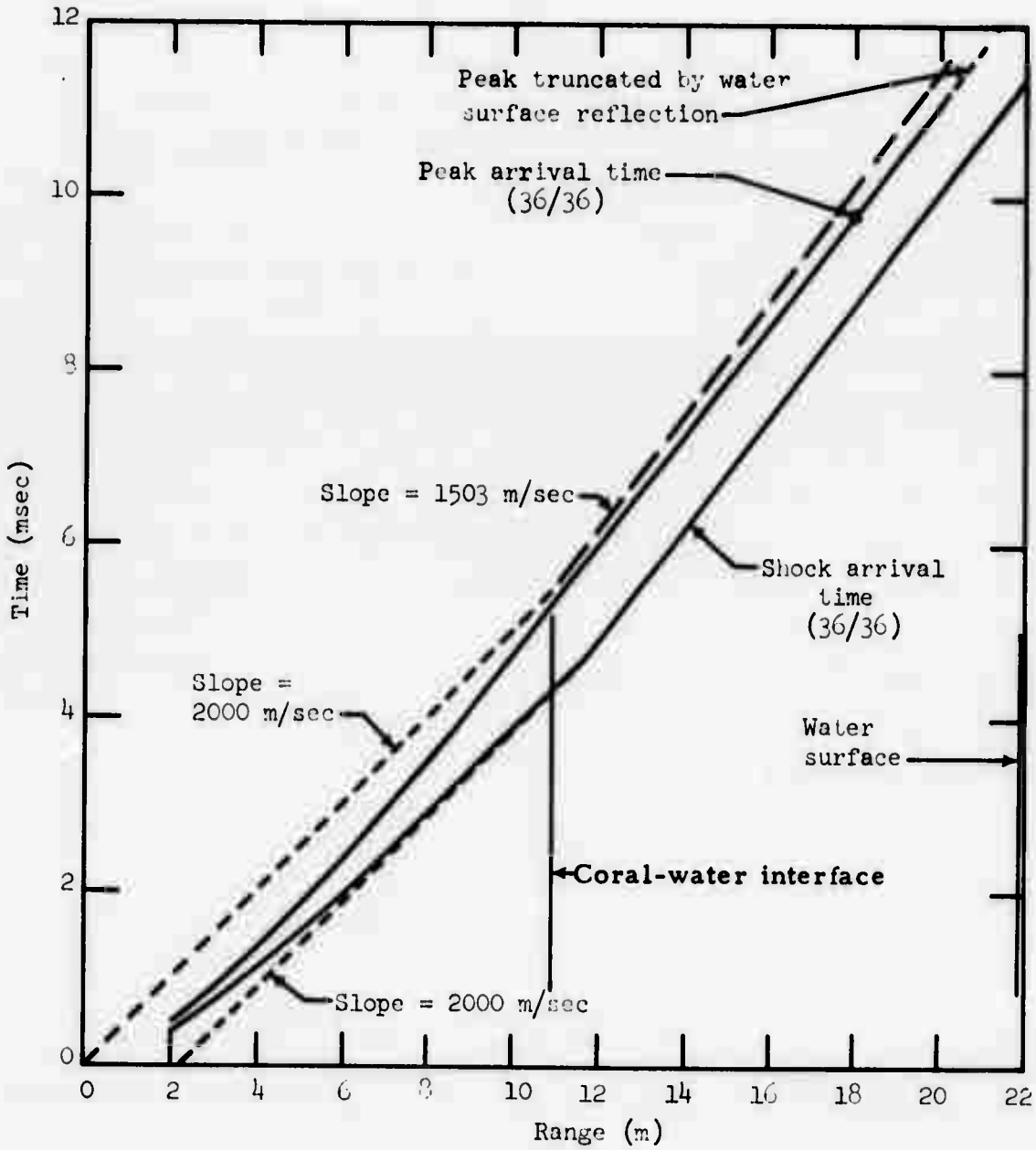

Figure 20. Pressure pulse arrival times, coral 36/36 calculation.

The SOC initial shock arrival times at the rock-water interface and at the water surface for all vertical calculations are compiled in Table 7a. These values may be used to aid in analysis of the waveforms presented later. The acoustic velocity pulse transit times from problem center to problem boundary (rock surface or water surface) are also given in Table 7b. The acoustic transit times are in all cases a fraction of a millisecond longer than the SOC-calculated arrival time at the corresponding boundary.

Peak Parameters. Appendix A presents graphs of peak particle velocities, pressures, radial stresses and tangential stresses as functions of initial range, for both horizontal and vertical calculations (Figures A1-A47). These are the maximum values of each variable which occur in a given zone during the course of the calculation. Thus, a peak velocity for a vertical calculation may represent either the peak at the shock front, or the spall velocity (if it exceeds the initial peak). Figures A1-A15 show the peak curves for the horizontal (free-field) calculations. Note that the two coral calculations CORHRZ and PS1OHRZ, for the "smoothed" and measured equations of state, are almost identical (A1-A4). Figures A5, A10, and A15 show the relationships between peak pressure, radial stress, and tangential stress for each of the rock media. Note that the three curves for each material overlap at very close ranges, where the solid shows a ductile rapidly-failing behavior, and the development of shear stress is severely limited by the ultimate strength of the material. The radial and tangential stresses are large relative to the permitted shear stress and are nearly equal. At longer ranges, the shear stress becomes appreciable (relative to the magnitudes of the radial and tangential components). Thus, the tangential stress drops below the radial value; the three curves of radial stress, pressure, and tangential stress approach the parallel behavior expected for an elastic material of constant Poisson's ratio.

Figures A16-A19 plot the peak velocities, pressures, and stresses for all three media on the same graph. The particle velocities (A16) are highest for coral, followed by basalt, then granite (coral is the lowest impedance medium, and granite is the highest). Attenuation rates of velocity and stress are distinctly higher for granite than for the other two media, particularly at ranges > 4 to 10 m. This is the expected effect, since shear strength is a dominant dissipation mechanism in these saturated (nonporous) media. The three tangential stress curves plotted in Figure A19 all show precipitous declines, but at somewhat different ranges: granite declines between 3.5 and 4.8 m, basalt between 12 m and 16 m, and coral near 25 m. At ranges within each of these respective intervals, the peak shear stresses decrease below the ultimate strength of the

TABLE 7(a). Approximate Initial Arrival Times of the Pressure Pulse at the Rock Surface (or Rock-Water Interface) and at the Water Surface.

Configuration	Initial Arrival		Configuration	Initial Arrival	
	Rock (msec)	Water (msec)		Rock (msec)	Water (msec)
Coral 30/00	3.6	-	Basalt 36/00	2.6	-
Coral 30/05	3.6	4.6	Basalt 36/10	2.6	4.4
Coral 30/10	3.6	5.4	Basalt 36/36	2.6	9.5
Coral 30/36	3.6	10.5	Granite 36/00	1.75	-
Coral 36/00	4.4	-	Granite 36/10	1.75	3.4
Coral 36/05	4.4	5.4	Granite 36/36	1.75	8.3
Coral 36/10	4.4	6.3			
Coral 36/36	4.4	11.6			

TABLE 7(b). Approximate Acoustic Transit Times From the Explosive Radius to Free-Surface (Vertical Problems). *

Configuration	Transit (msec)	Configuration	Transit (msec)
Coral 30/00	4.05	Basalt 36/00	2.7
Coral 30/05	5.1	Basalt 36/10	4.8
Coral 30/10	6.1	Basalt 36/36	10.0
Coral 30/36	11.3	Granite 36/00	1.8
Coral 36/00	4.97	Granite 36/10	3.8
Coral 36/05	6.0	Granite 36/36	9.1
Coral 36/10	7.0		
Coral 36/36	12.3		

* Material zones adjacent to the explosive radius first become significantly active about 0.22 msec, and the peak shock enters the medium at 0.24 msec. Shock front velocities somewhat exceed the acoustic velocity within the first few meters near the explosive.

material. Thus, the shear stress is no longer severely limited by material strength, and radial stresses larger than the tensile components begin to build up (i.e., the material responds in a more nearly elastic fashion). This change occurs at close range for granite because of its high strength.

Figures A20 through A27 are comparative plots of the 36/00 and 36/10 vertical problems for all three media. In the case of velocities, note the thin surface spall layer near the interface (A20); note also the tensile wave pressure "cutoff" effect below the interface (A21). For the 36/10 water overburden calculations (A24), a spall layer occurs immediately below the rock-water interface; the shock wave then enters the water layer, attenuates further, is reflected at the water surface, and creates another spall layer near the water interface. (The medium above the interface has been denoted as "air" in the diagrams; the upper boundary in the calculations is actually a free surface, with no constraint.) Comparing the media, we find that spall velocities are highest for coral, and lowest by a large margin for granite. Comparing the 36/00 and 36/10 configurations, we see that spall velocities at and near the rock interface are decreased by the presence of the water layer (A20, A24). Spall velocities in the water layer appear to be high (relative to the rock) because water is a low-impedance medium. The water layer pressures and velocities also decrease in the order: coral, basalt, granite. Finally, an abrupt decline in the water velocities very near the interface is apparent for granite 36/10 (Figure A24). The velocity continues to attenuate rapidly in the water layer and water surface spall velocity is low. Likewise, the pressure for granite does not show a "rebound" in the water layer beyond the reflection region at the rock interface (A25). This damping of the water layer pulse for granite will later be seen to be partly due to a calculational difficulty.

Figures A28 through A31 present velocities and pressures for the coral vertical configurations at D_r = 36 ft. (The coral horizontal calculations, shown for comparison, appear to lie above the "vertical" curves at very close ranges (A28, A30). This apparent discrepancy was caused by dezoning or combination of close-range zones at late times during the calculation, and by a computer plotting routine which draws a rough "averaged" fit through the remaining zones.) An interesting effect may be noted in Figures A28-A29: the rock interface spall velocities (at 10.97 m) are identical for coral 36/05, 36/10, and 36/36, but are higher for the free-surface event 36/00. It is evident that water layers of all depths exert a "constant impedance" effect on the interface spall reflection: Water layer depth causes no apparent changes in the initial spall velocity. Note that velocity behavior at the interface and attenuation in the water layer are relatively smooth for coral calculations (A28, A29). The [illegible]

spall "cutoff" layer for coral 36/05 extends almost back to the rock interface (A29). Thus, a water surface reflection might increase the rock interface peak velocity with a water layer shallower than 5 ft. A rock spall velocity due to water surface reflection which exceeds the initial spall velocity (due to the rock-water interface reflection) was not encountered for any of these calculations, and is expected to occur only for very shallow water layers.

Additional calculations were implemented to test the effect of dezoning on a vertical problem. The coral 36/05 event was run to 20 msec with and without automatic dezoning after the shock peak has passed.* Numerical results in the two cases did not differ significantly (Figures A29, A31), but the dezoned calculation required far less computer time.

Figures A32 through A35 depict peak velocities and pressures for the coral D_r = 30 ft calculations. Once more, the spall velocities at the rock interface (R = 9.146 m) are equal for 30/05, 30/10, and 30/36, but are considerably higher for 30/00 (no water). Due to the shallower depth of burial, all of the rock and water spall velocities are much higher than the corresponding values for the D_r = 36 ft series.

Figures A36 and A37 show velocity and pressure for the basalt events at D_r = 36 ft. Again, the basalt "horizontal" curve deviates because of averaging by the computer program. The basalt rock interface spall velocities are high for 36/00 (no water), lower for 36/10 and 36/36. However, the apparent difference is less than for coral (A28). This trend is expected, since the impedance mismatch is greater for basalt and tensile reflection at the rock-water interface is more efficient. The peak values in the water layer are smooth and well-behaved, with an attenuation rate similar to the coral calculations. Similar velocity and pressure plots for granite (D_r = 36 ft) are given in Figures A38 and A39. In this case, the impedance mismatch is still stronger, and the 36/00 calculation deviates only slightly from the underwater calculations at the interface. Severe attenuation effects in the water layer are evident.

*Dezoning refers to a code routine which gradually combines small adjacent zones in the inner portion of the problem far behind the shock front. This technique increases the time step and enables the calculation to run more efficiently without seriously degrading resolution.

A parameter study was carried out to test the effects of artificial viscosity in these media. Horizontal calculations in coral (smoothed equation of state) and basalt were run with artificial viscosity ν = 0.1 and 0.2. The effects on peak velocity, pressure, and stress are shown in Figures A40 through A45. Increasing viscosity reduces all of the peak shock parameters; the reduction is greatest at long ranges. Moderate changes are apparent in the coral calculation beyond 5 m. Changes in the basalt calculation are extremely small inside 11 m (i.e., within the range of interest for vertical calculations). Greater differences appear at long ranges. The coral calculation was observed to be noise-free at ν = 0.1, while a larger damping factor was required for best results in basalt. Accordingly, a viscosity of 0.1 was used for all coral calculations presented in this study, while ν = 0.2 was used for basalt and granite.

In conjunction with the artificial viscosity test, trials were conducted to determine the influence of zone size on vertical calculations. Results for typical configurations demonstrated that zone size has virtually no influence on peak shock parameters, waveforms, or late time interactions. This result holds true because of the extremely fine constant rock zone size used for the suite of vertical calculations (much finer than zoning normally used for horizontal free-field configurations[3]). Shock resolution is essentially not limited by rock zone size in the vertical calculations.

The effect of water zone size on granite-to-water shock transmission was mentioned previously. In an effort to reduce the errors encountered, granite 36/10 and 36/36 calculations were rerun with water zone sizes reduced by 50% ("fine zone" calculation; not impedance matched at granite-water interface). Results are depicted in Figures A46 and A47. The abrupt drop in water pressures and velocities immediately beyond the interface is reduced, and the water spall velocities are increased. However, rapid attenuation within the water layer persists in both calculations. The anomalous sudden damping of the shock near the interface is thus caused by zone-size-dependent resolution loss in the coarsely zoned water layer. Continuing rapid attenuation in the water is a more complex phenomenon, not entirely explained by zone-size effects. This topic will be further examined in Chapters VIII and X.

Interface spallation. Spall launch at an interface is caused by interaction of the outgoing compression wave with the reflected tension wave. At a free surface (used to represent the medium-air interface in the vertical calculations), perfect reflection occurs and the peaks of the two waves coincide. The particle velocity is doubled. As the tension wave moves downward, it interacts with the declining tail of the compression wave, producing lesser reinforcement. At some depth within the medium, dependent on attenuation and the rapidity with which the compressional wave decays, spall launch velocity will be lower than the initial peak particle velocity at the same location. Spallation is illustrated by Figure 21, which shows water layer velocity waveforms in the zones located 0.9 m and 1.6 m below the coral 30/10 water surface. The spall velocity after the tensile arrival is greater than the initial peak at 0.9 m. However, the later spall arrival at 1.6 m produces a lower velocity and fails to match the initial peak. This effect is responsible for the appearance of the peak plots (i.e., Figure A20): The spherically-divergent compression wave determines the "peak" velocity except within a narrow region near the interface. Since the peak velocity at the wavefront is a transient phenomenon, it does not control dynamics within the mound. Instead, one must examine the spall velocities and late-time residual velocities long after the peak has passed.

Spall interactions in solid media are frequently somewhat more complex due to the less regular waveforms and the failure and tensile strength effects involved. Figures 22-23 present typical pressure waveforms with their corresponding velocity waveforms near the interface for coral 36/00 and basalt 36/00. Freefall begins when the reflected tensile wave returns the pressure to zero. Due to its longer rise time, flattened peak, and slower decay, the basalt pulse produces significant spall reinforcement over a greater depth interval than coral. The basalt spall velocity exceeds the initial peak velocity at R = 9.01 m (or 1.9 m below the interface), while the coral velocity reinforcement has fallen below the initial peak at R = 9.49 m (1.5 m). By the same token, spall reinforcement within the broad basalt spall layer is somewhat less intense and well-defined than for coral (Figure A20).

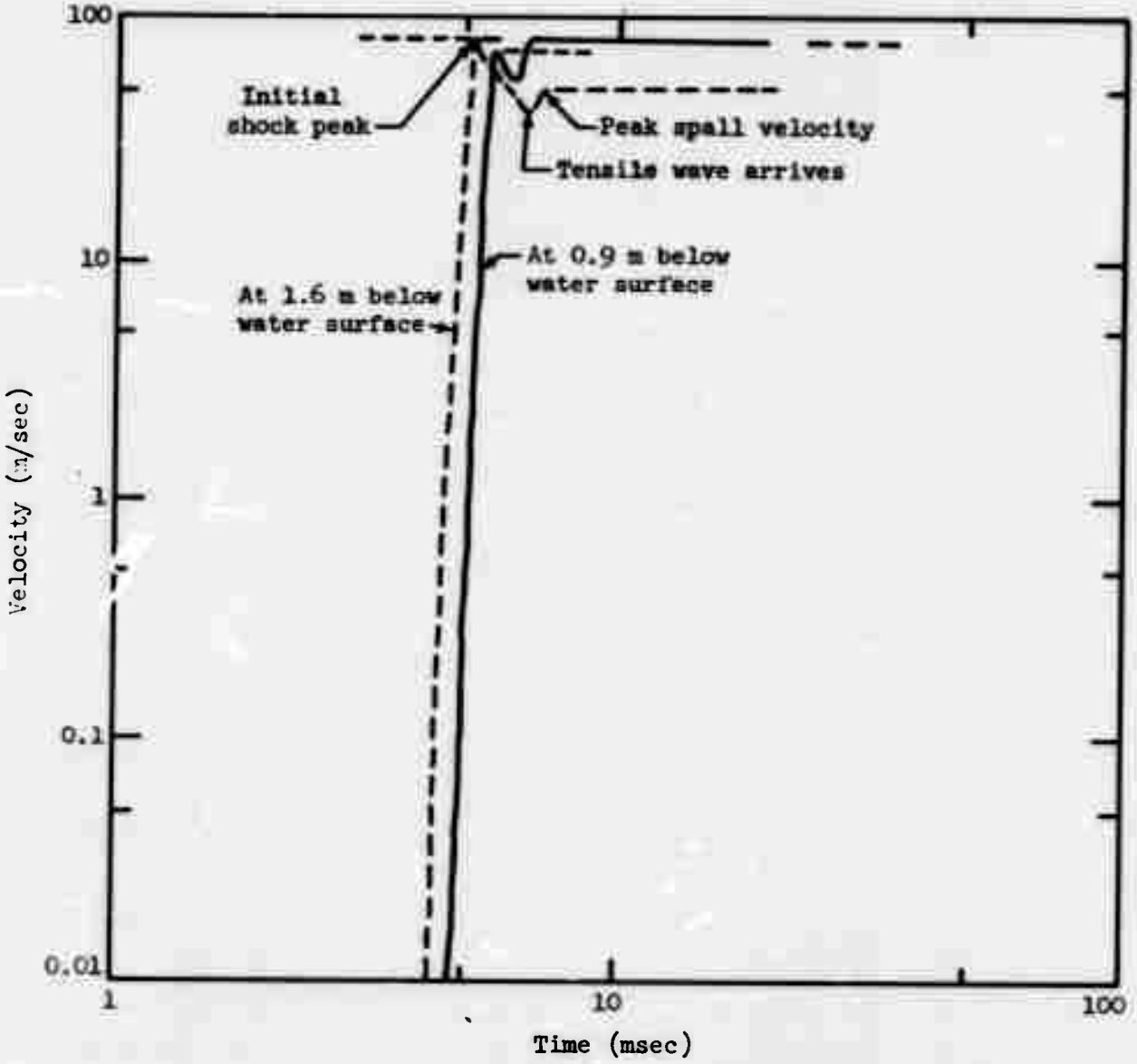

Figure 21. Peak surface spall velocities in water layer at 0.9 m and 1.6 m below surface (coral 30/10).

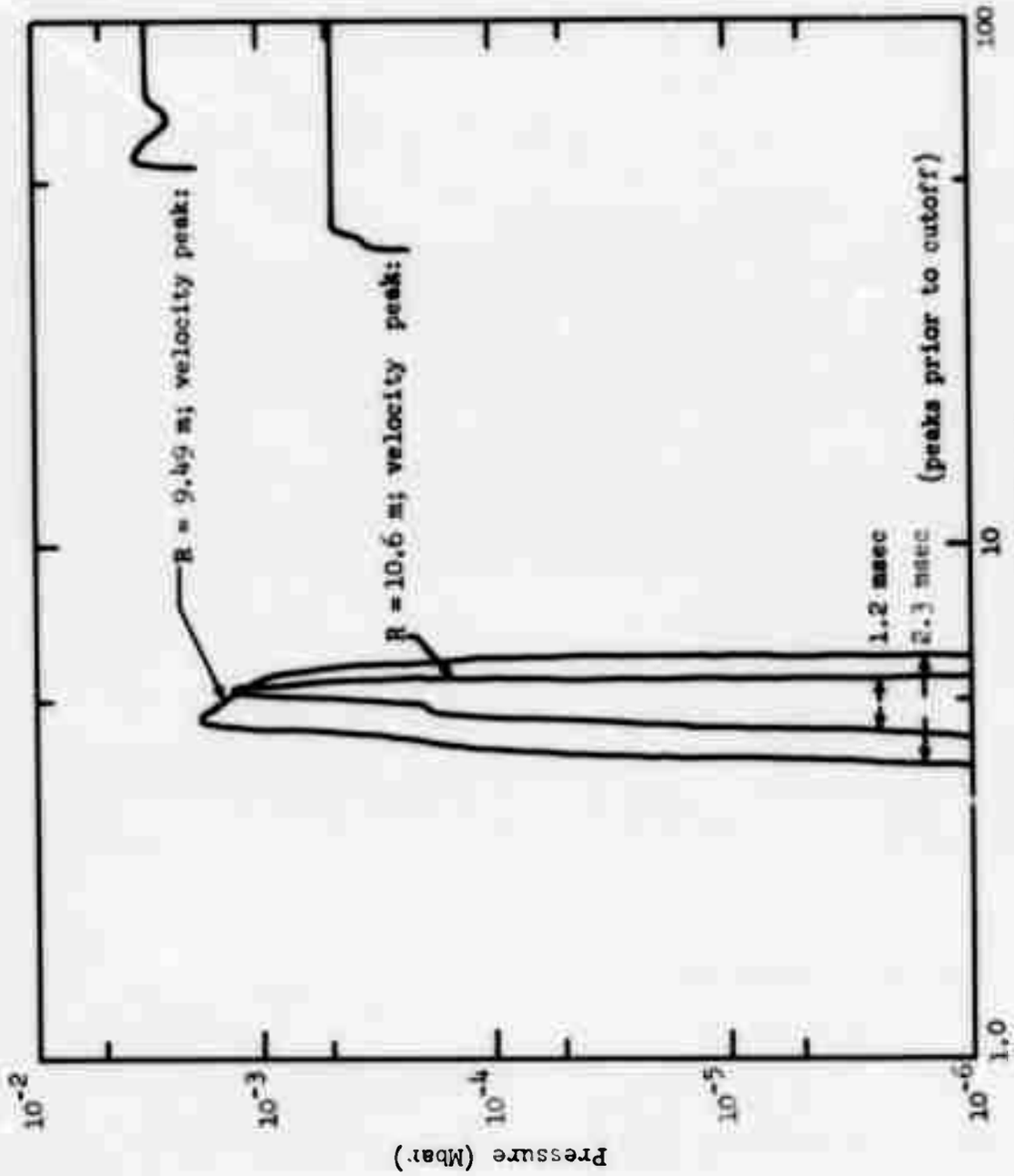

Figure 22a. Pressure waveforms and material spallation near interface (coral 36/00).

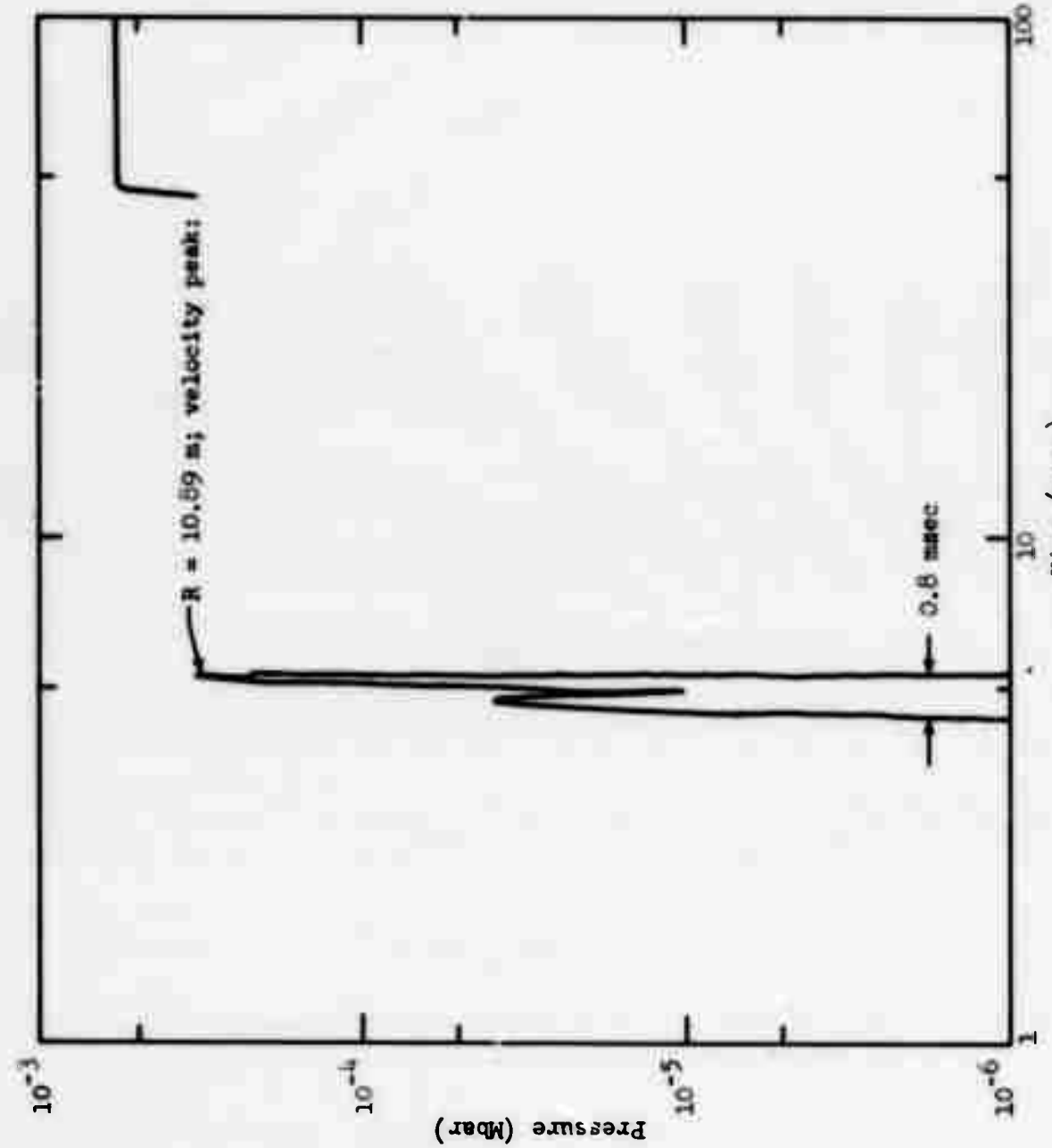

Figure 22b. Pressure waveforms and material spallation near interface (coral 36/00).

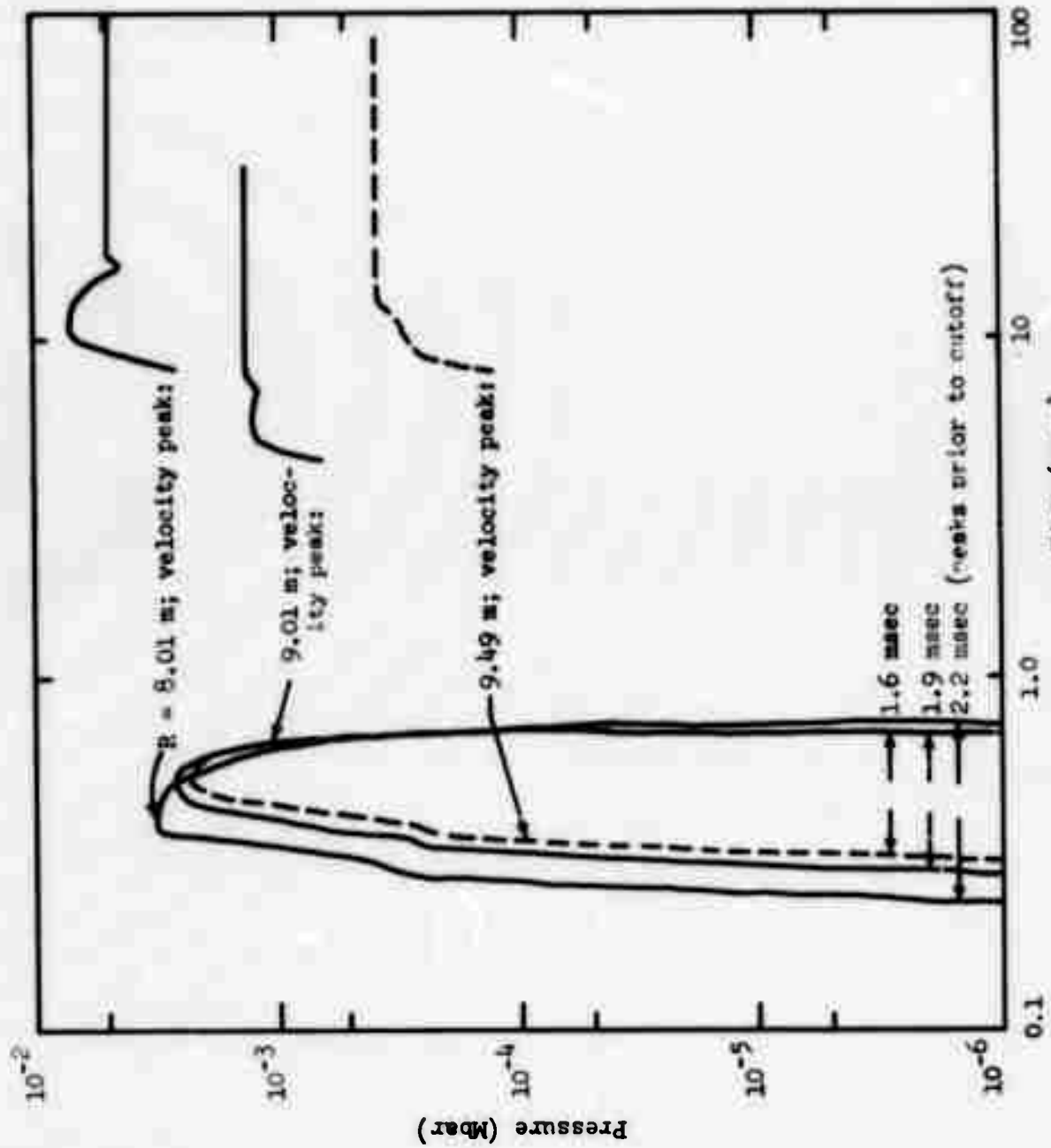

Figure 23a. Pressure waveforms and material spallation near interface (basalt 36/00).

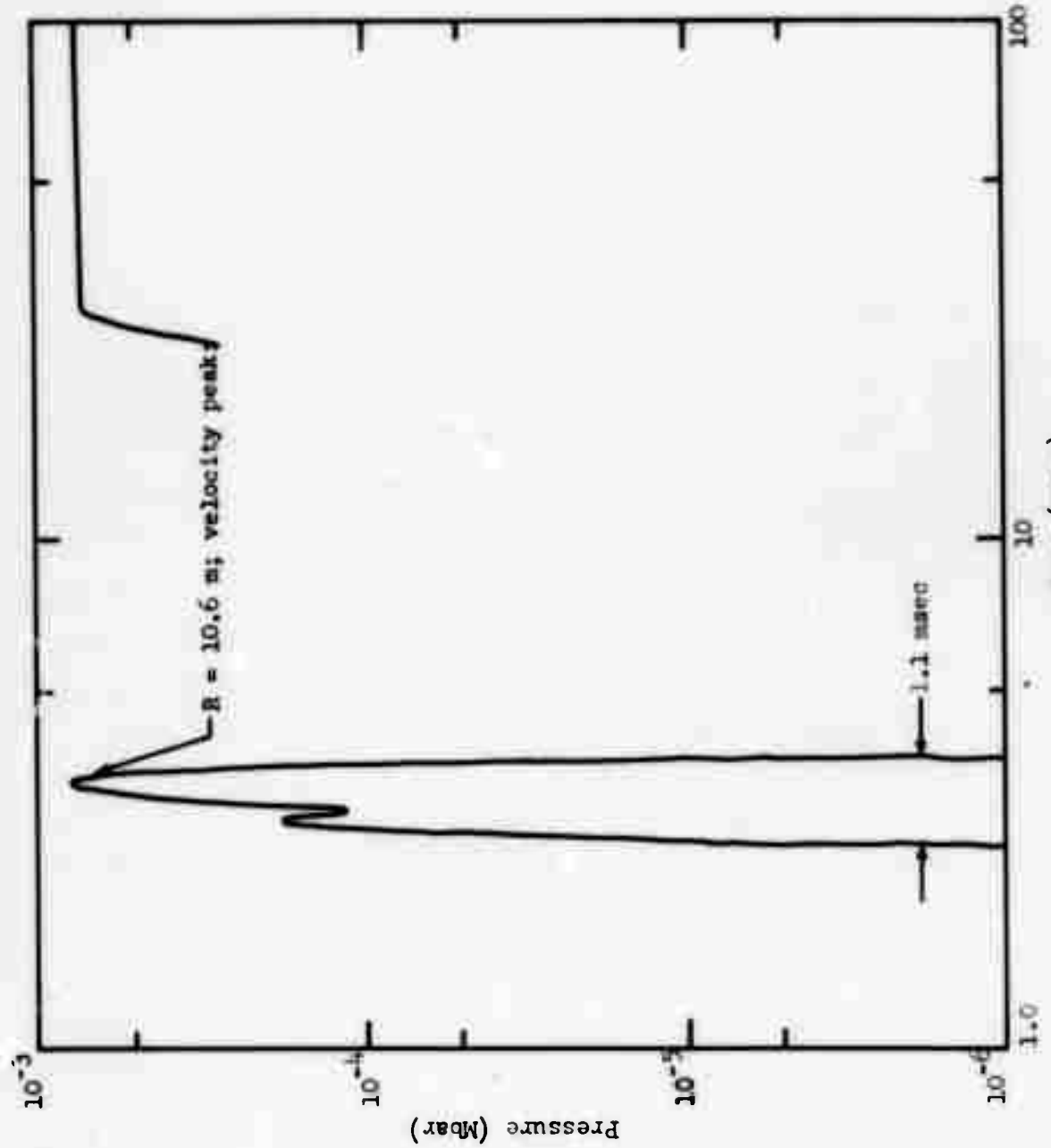

Figure 23b. Pressure waveforms and material spallation near interface (basalt 36/00).

Waveforms. Appendices B through F contain velocity and pressure waveforms at selected radii for all of the SOC calculations. A key to the nomenclature precedes Appendix B (p. 325). Results of the horizontal free-field calculations in all media are presented as Appendix B, followed by the waveforms of the vertical coral calculations (D_r = 30 and 36 ft) in Appendix C, the vertical basalt diagrams (D_r = 36 ft) in Appendix D, and the vertical granite calculations (D_r = 36 ft) in Appendix E. Finally, examples of the waveforms transmitted into the overlying water layer for vertical calculations are given in Appendix F. It should be pointed out that most of the plots are logarithmic; therefore, the apparently high noise levels appearing in some pressure waveforms are actually a factor of 50 to 100 lower than the peaks. In order to facilitate interpretation of the vertical data (Appendices C-E), important dynamic interactions have been noted on the velocity waveforms. The following abbreviations are used: R > rock surface or rock-water interface spall reflection arrival; W > water surface reflection arrival; C > cavity gas acceleration pulse arrival. In addition, certain other significant events such as freefall phases or deceleration during recompaction of overlying material have been indicated.

Horizontal waveforms at each range for the three media (Appendix B) have been plotted together. These calculations include a 2.02 bar overburden pressure (Figure B2), which, however, has little influence on the close-range results. Horizontal calculations for the two different coral equations of state (CORHRZ and PS1OHRZ) have been compared in Figures B28-30. Trivial differences are noted at ranges close to the cavity. The artificial viscosity calculations for ν = 0.1 and ν = 0.2 in coral and basalt are shown in Figures B31-B34. Small but noticeable differences occur at ranges far from the cavity; for lower viscosity, the initial arrival occurs later, pulse rise time is shorter, the peak is higher, and post-peak "noise" interactions are shifted to slightly later times.

In some instances, it is desirable to use calculational results for a comparison of cratering phenomenology in different media. Velocity waveforms for the coral, basalt, and granite calculations 36/00, 36/10, and 36/36 have

been replotted on the same scale (Figures 24-29). Locations adjacent to the rock interface were selected, since these regions are crucial to material dynamics and water layer effects show up most readily near the interface. Late-time spall velocities for the 36/00 configuration (R = 9.49 and 10.6 m) clearly show that the coral and basalt events are comparable, while the granite velocity is low by more than a factor of two (Figures 24-28). The coral velocity is slightly higher than basalt at ranges very close to the interface (10.6 m) because of the sharper shock front in coral. Underwater configurations 36/10 bear out this trend (Figures 26-27): Time-dependent dynamic interactions for the media are distinctly different, but coral and basalt ultimately attain similar velocities. Granite remains much lower. Calculations "36/36" present a similar picture, except that the late-time gas acceleration pulse reaches the rock surface somewhat sooner for dense high-velocity granite (Figures 28-29). It is interesting to note that the late-time velocities of coral and basalt near the interface for the 36/36 calculations (deep water layer) are actually greater than the corresponding granite 36/00 spall velocities (no water layer). Late-time velocities less than or on the order of 30 m/sec clearly indicate that the granite events are buried well below optimum cratering depth. It is evident that the zeal for choosing a very stiff, high-strength rock medium was carried a little too far. The parameters and calculational results may be unrepresentative of a "real-world" medium near the ground surface, where flaws, joints, and weathering reduce the effective strength of the material.

Calculated waveforms may also be used to define the detailed dynamic effects of water overburden on events in a given medium. Velocity waveforms and arrival times for all calculations in a single series are intercompared. In some cases, the free-field waveforms are very complex and must be included in the comparison as well (see, for example, Figures B7-B11, granite). A single example will serve to illustrate the technique. Let us examine water layer effects throughout the mound for coral calculations at D_r = 36 ft. Appropriate data are compiled in Appendix C (Figures C1-C54). In order to facilitate comparisons of this sort, all of the velocity waveforms have been replotted on an expanded linear scale, and corresponding waveforms for a

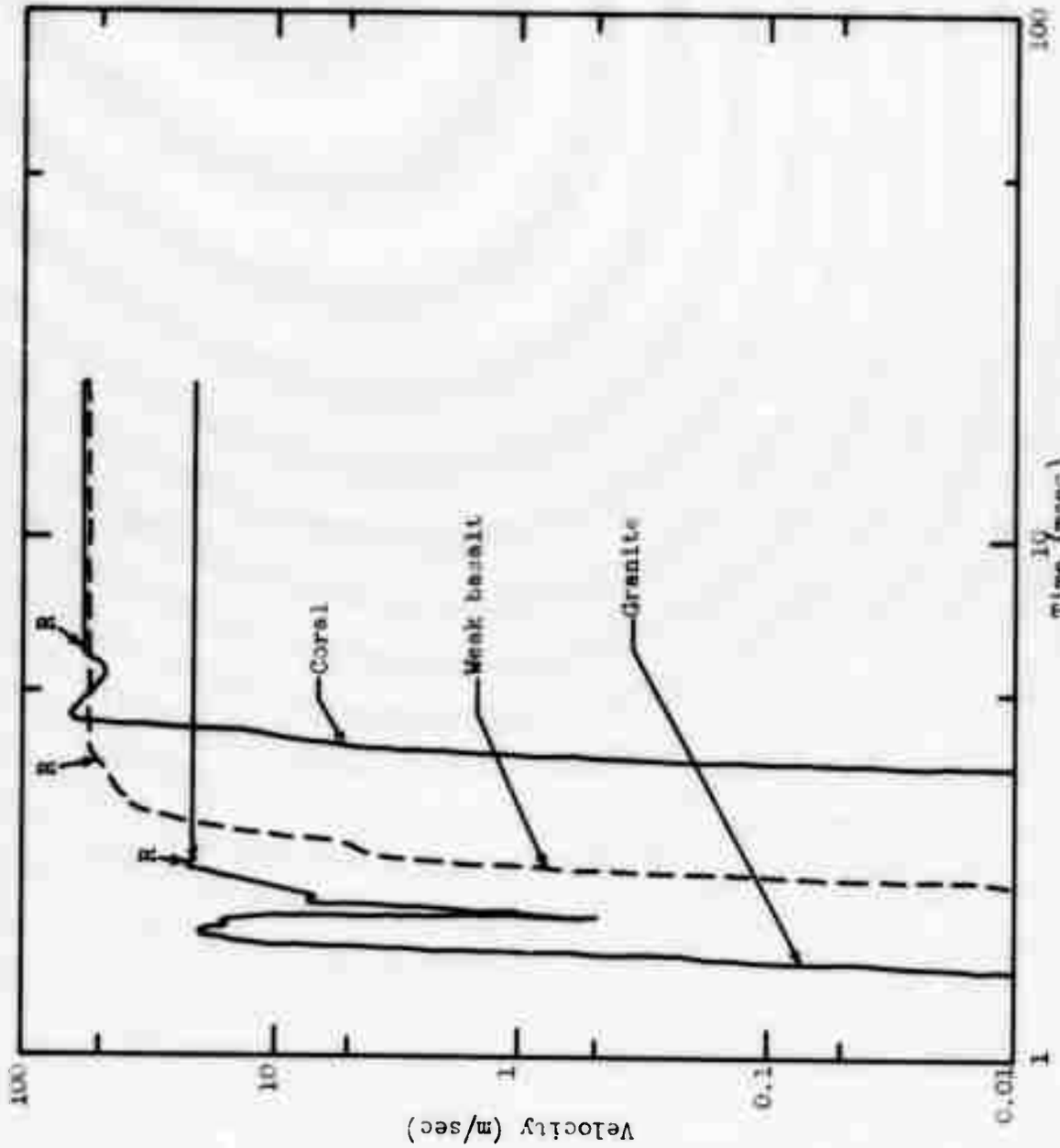

Figure 24. Velocity waveforms for 3600 calculations in coral, basalt, and granite; Range R = 1.48 m (1.48 m from medium-water interface).

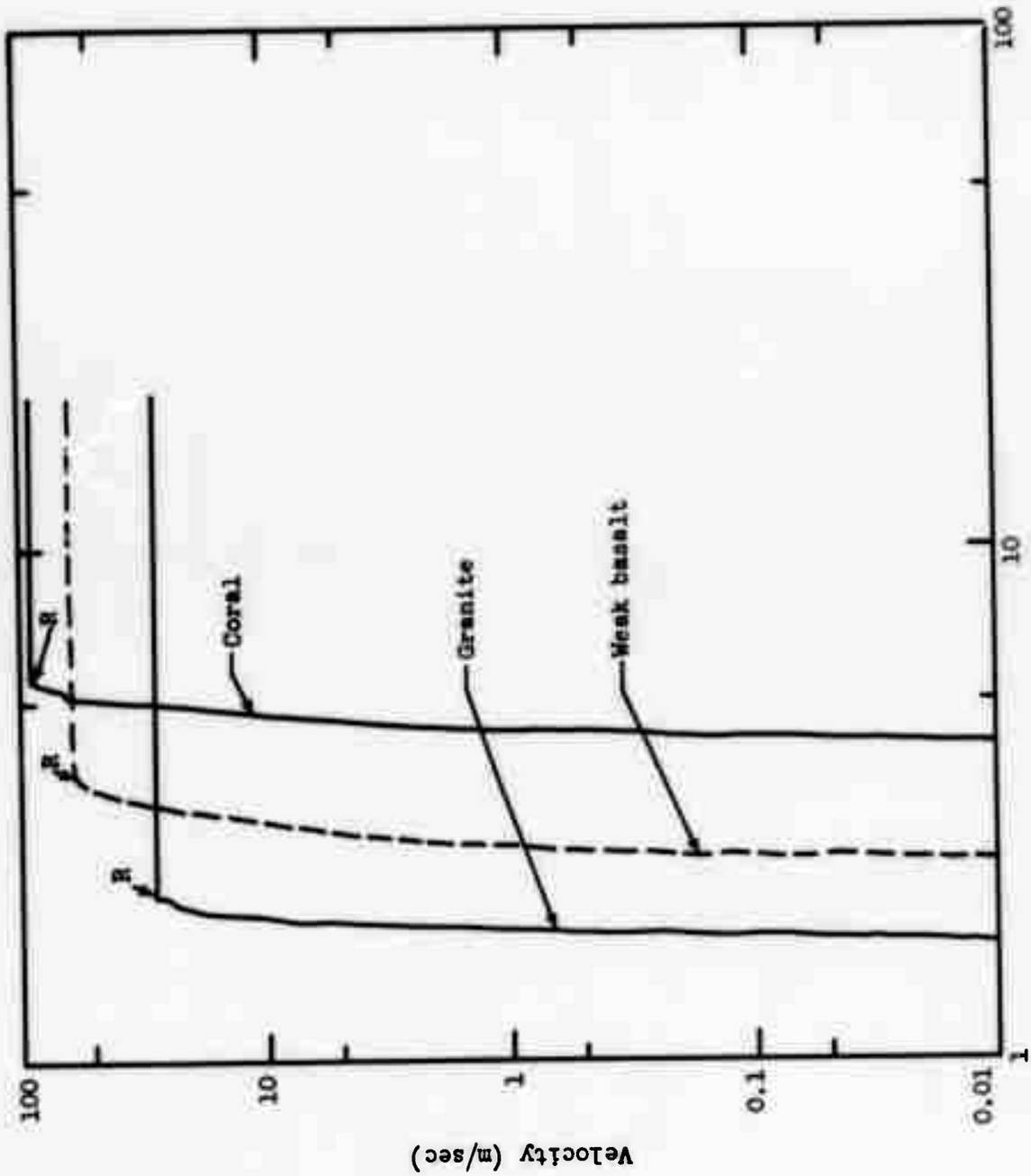

Figure 25. Velocity waveforms for 36/00 calculations, R = 10.6 m (0.37 m from medium-water interface).

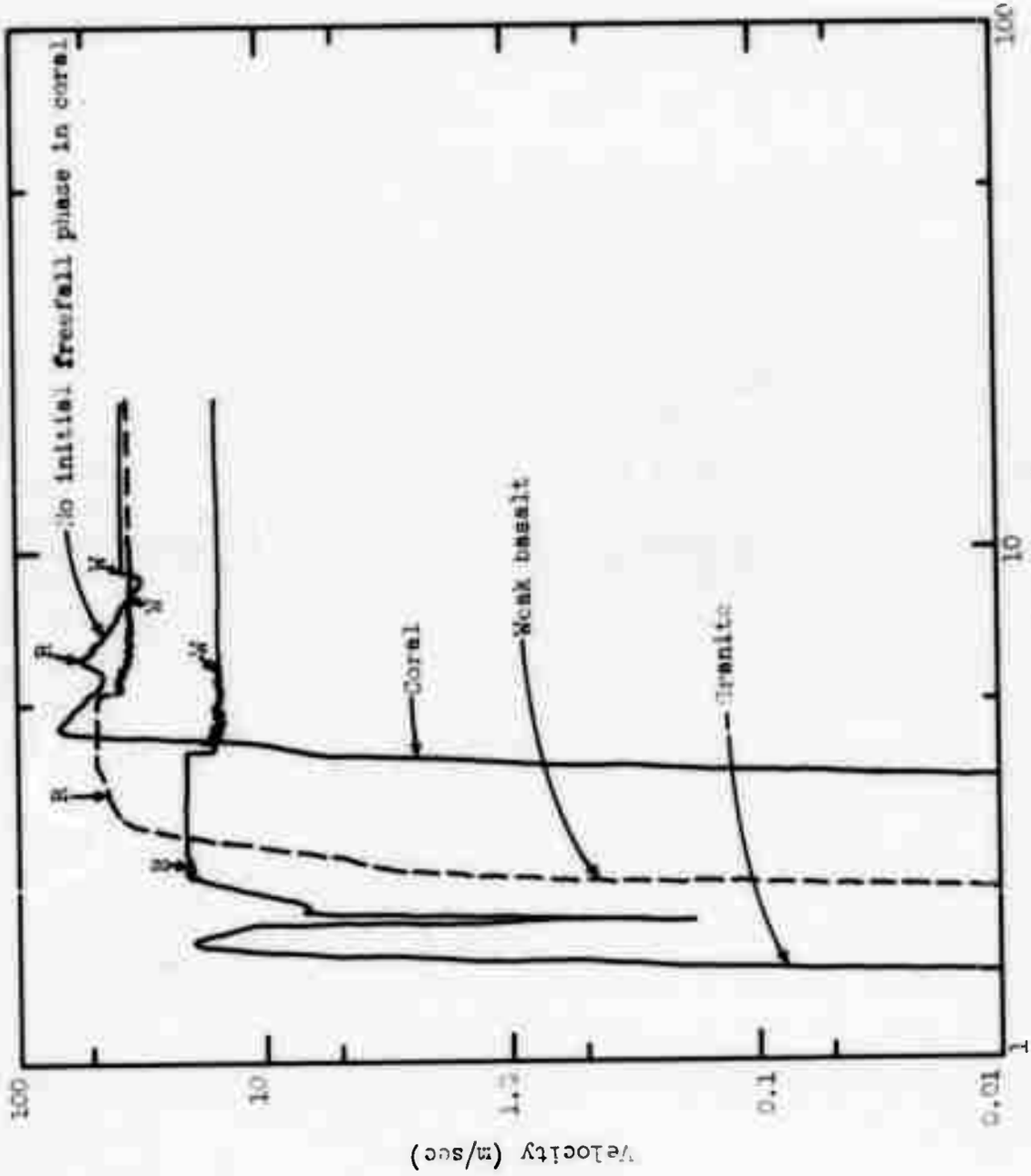

Figure 26. Velocity waveforms for 36/10 calculations, R = 9.49 m.

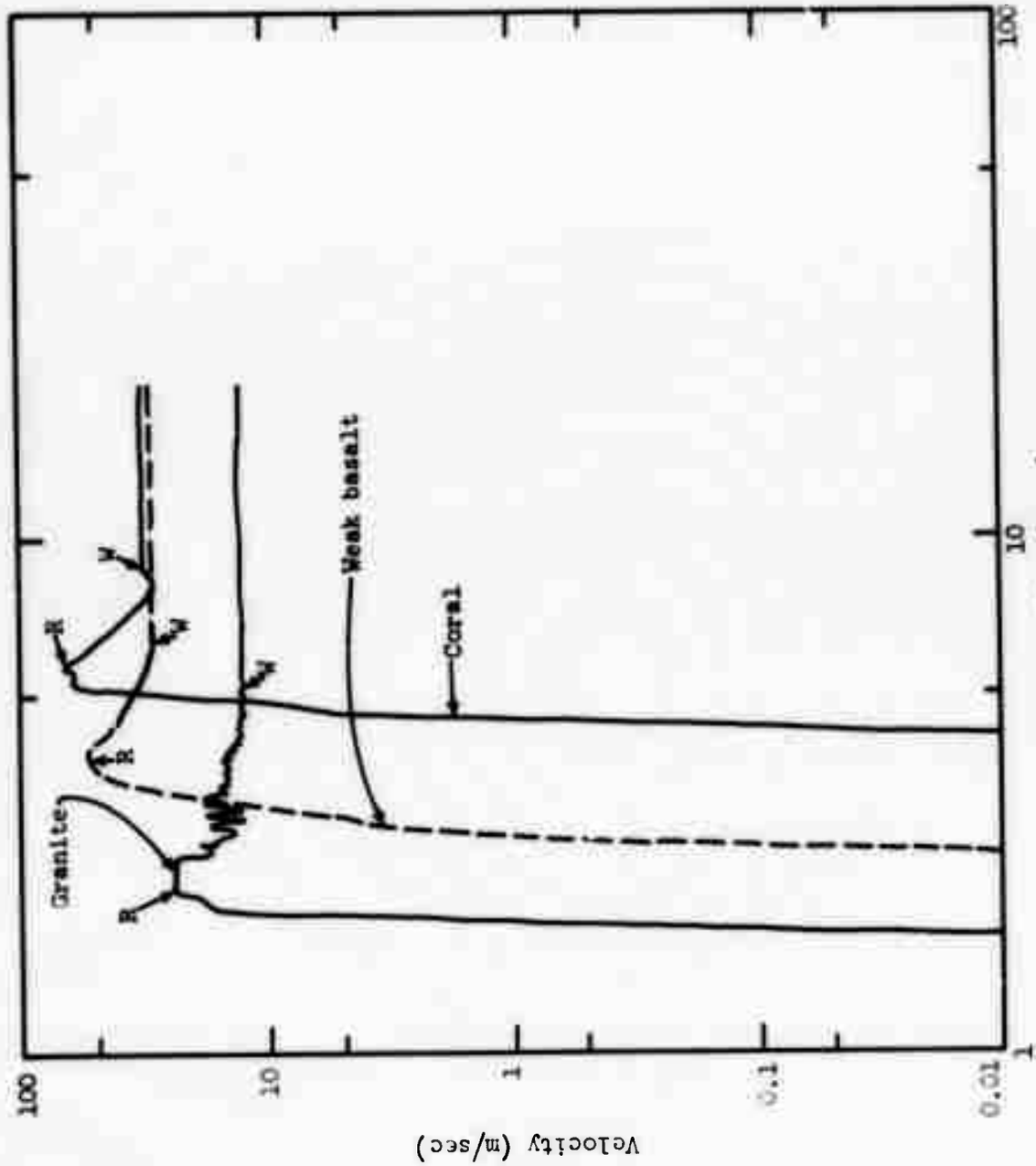

Figure 27. Velocity waveforms for 36/10 calculations, R = 10.6 m.

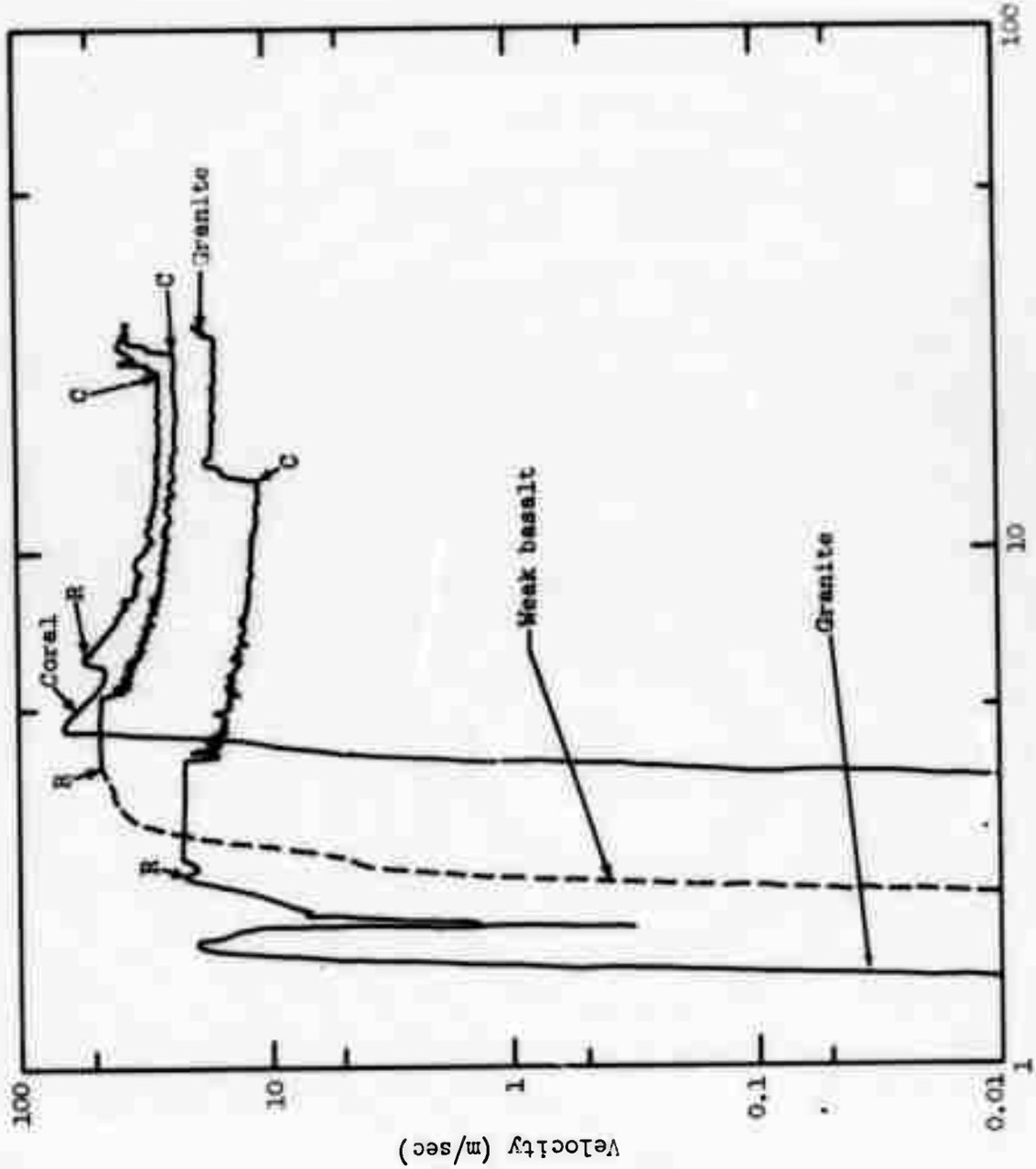

Figure 28. Velocity waveforms for 36/36 calculations, R = 9.49 m.

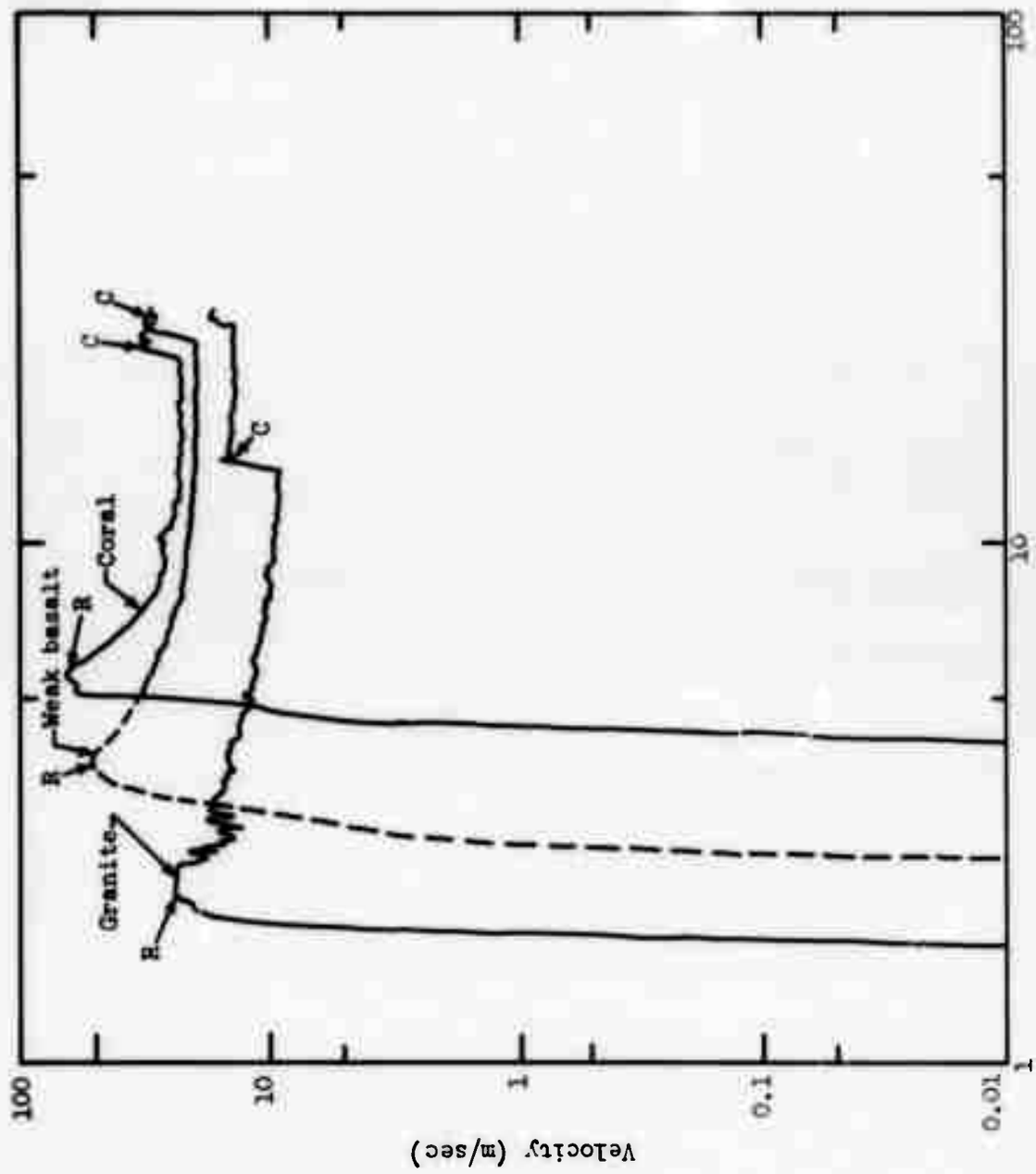

Figure 29. Velocity waveforms for 36/36 calculations, R = 10.6 m.

given medium have been placed on the same graph where possible (Figures 30-55). Thus, the velocity effects for coral 36/00 and coral underwater calculations (D_r = 36 ft) may be intercompared in Figures 30-39. Waveforms are shown for ranges between 2.01 and 10.89 m. (Coral D_r = 30 ft waveforms have also been included in Figures 30-35; the interface is located at 30 ft = 9.14 m, and no waveforms are given beyond this range.) A summary of the comparative water layer effects for D_r = 36 ft is presented below, beginning near the interface (R = 10.97 m), where water overburden effects are most evident, and moving inward.

Range = 10.89 m, near the rock-water interface or rock surface; Coral 36/00 (Figure 38a) shows the classic spall waveform very close to a free surface; the initial peak is cut off by the tensile reflection, and the velocity at the free surface is approximately doubled. Material enters the freefall phase (signified by "R") almost immediately (horizontal line of constant velocity; deceleration by gravity is very slight over the brief time interval shown). Peak velocity due to reflection at the rock-water interface for coral 36/05, 36/10 and 36/36 is somewhat lower (Figure 38b-c), about 70 m/sec instead of 100 m/sec. This decrease occurs because the rock-water interface is not a free surface (tensile reflection is not perfect). Note that all three underwater calculations have the same initial peak spall velocity independent of water depth, as expected for a constant degree of impedance mismatch. However, the overlying water layer damps motion at the interface after the initial spall reflection, and the coral material does not immediately enter freefall spallation. Subsequent velocity history depends on the water layer depth; freefall does not begin until the water surface tensile reflection ("W") returns to the rock layer and ends the damping phase. The reflection transit time and the degree of damping depend on the depth of the water layer. Figure 38b shows that the spall velocity near the interface is less than 50 m/sec for coral 36/05, and lower than 30 m/sec for coral 36/10. The water surface reflection for coral 36/36 returns to the interface at very late time (Figure 38c). Damping is almost complete, and the only apparent effect of the spall relief is to end the slight late-time noise and initiate true freefall. The damped late time velocity (or the

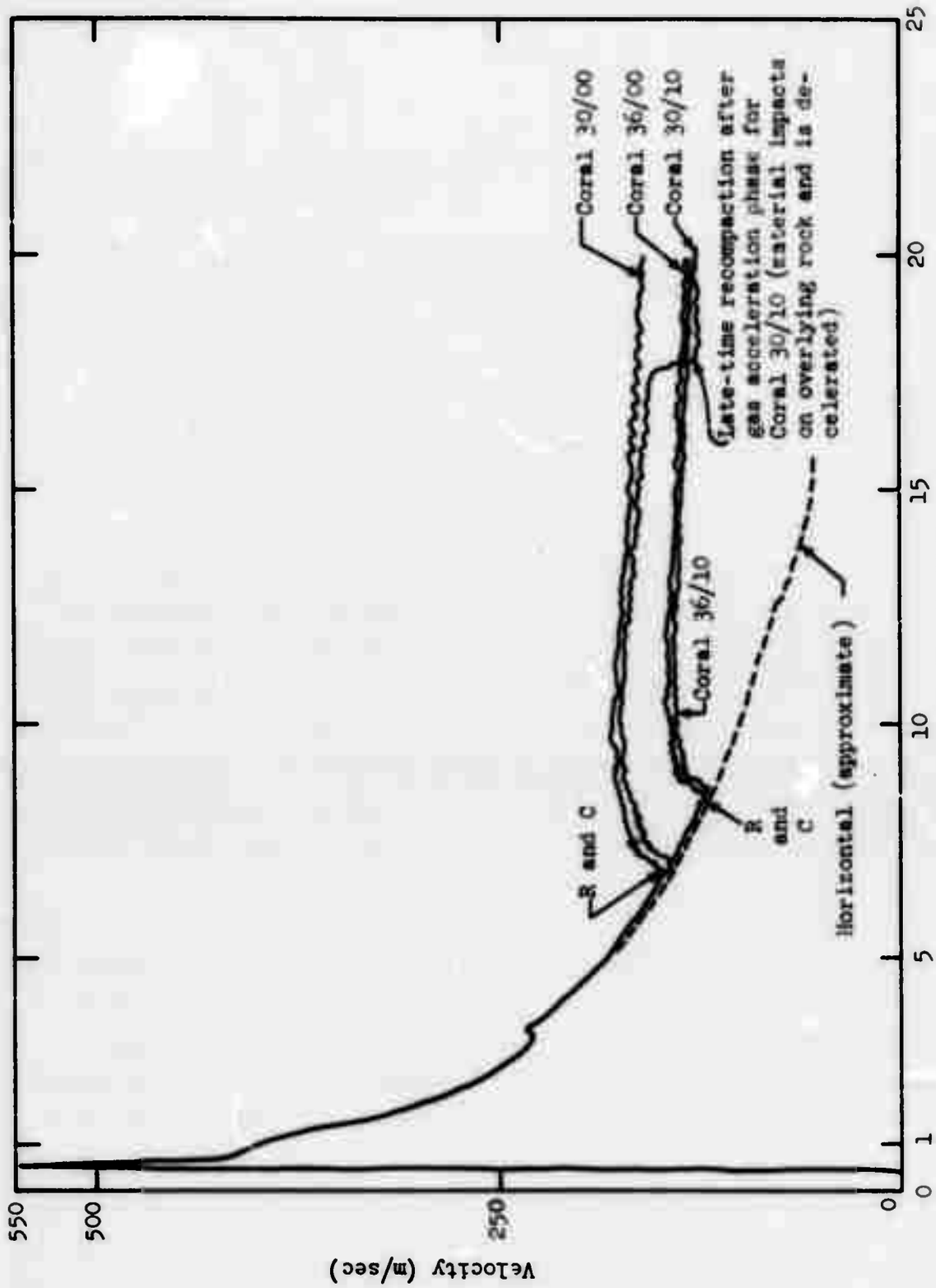

Figure 30a. Coral R = 2.01 m (sample calculations at very close range, for Coral 36/00, 36/10, 30/00, and 30/10 only).

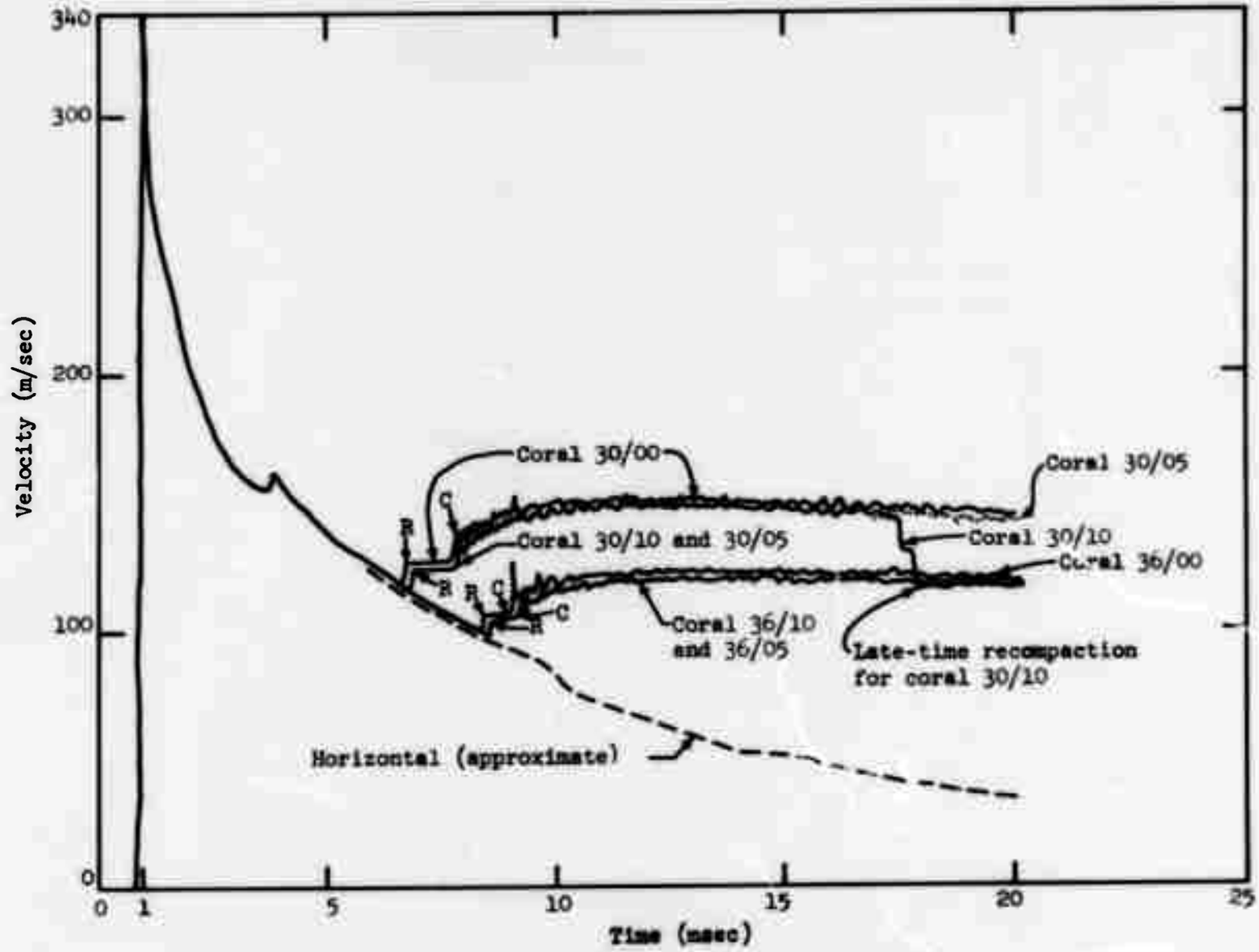

Figure 30b. Coral, range R = 3.01 m from charge center.

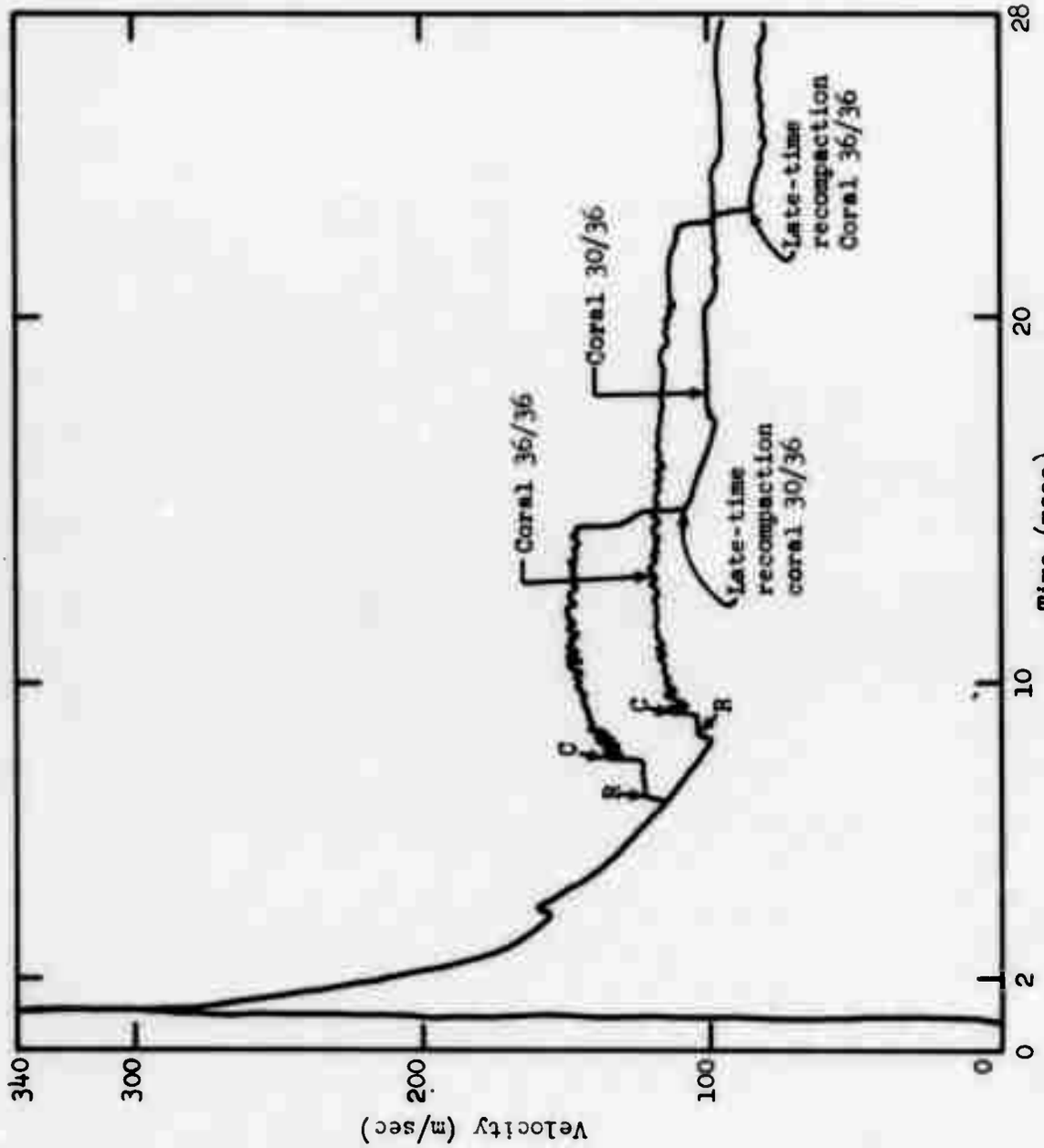

Figure 30c. Coral, R = 3.01 m.

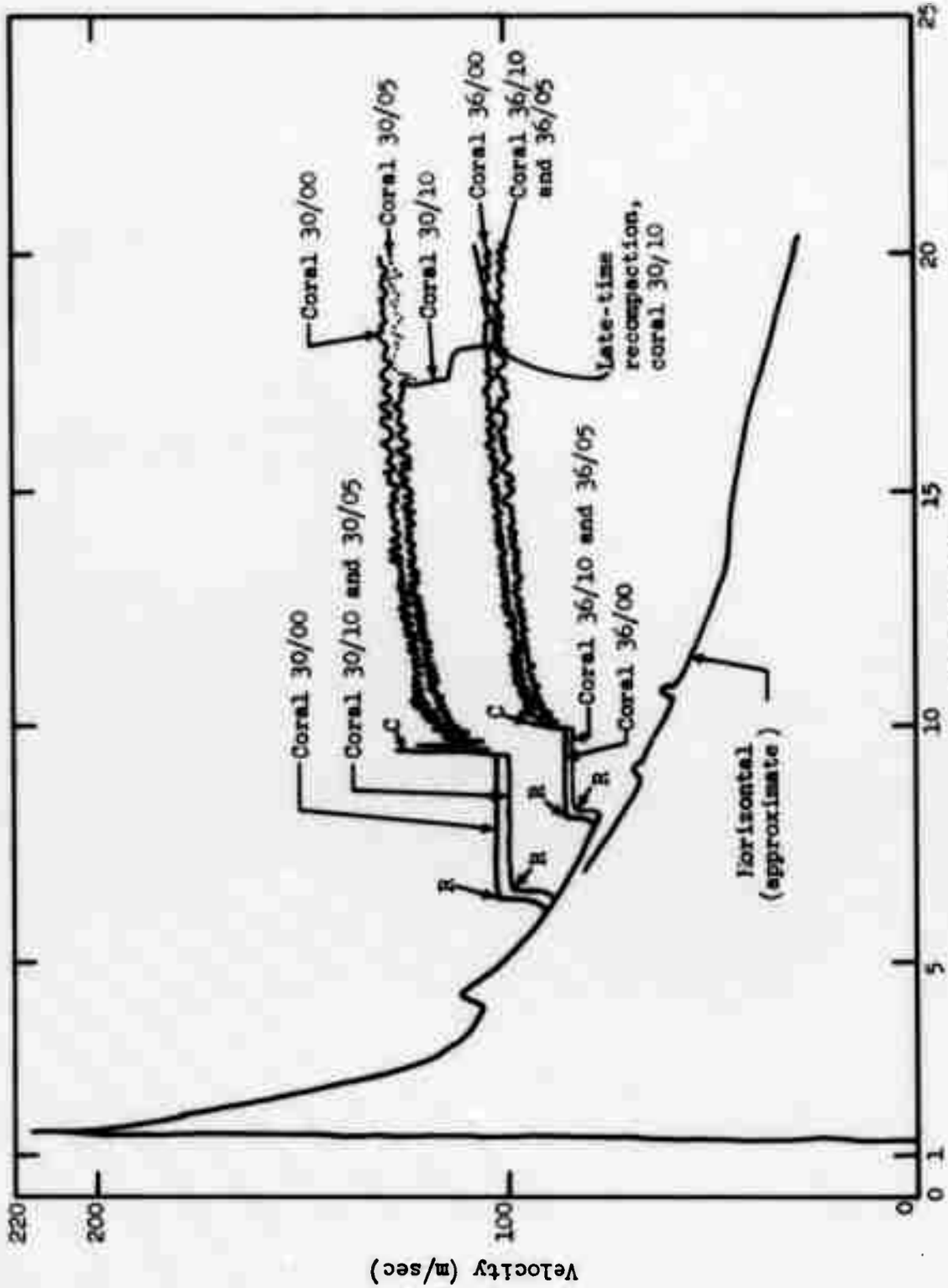

Figure 31a. Coral, R = 4.01 m.

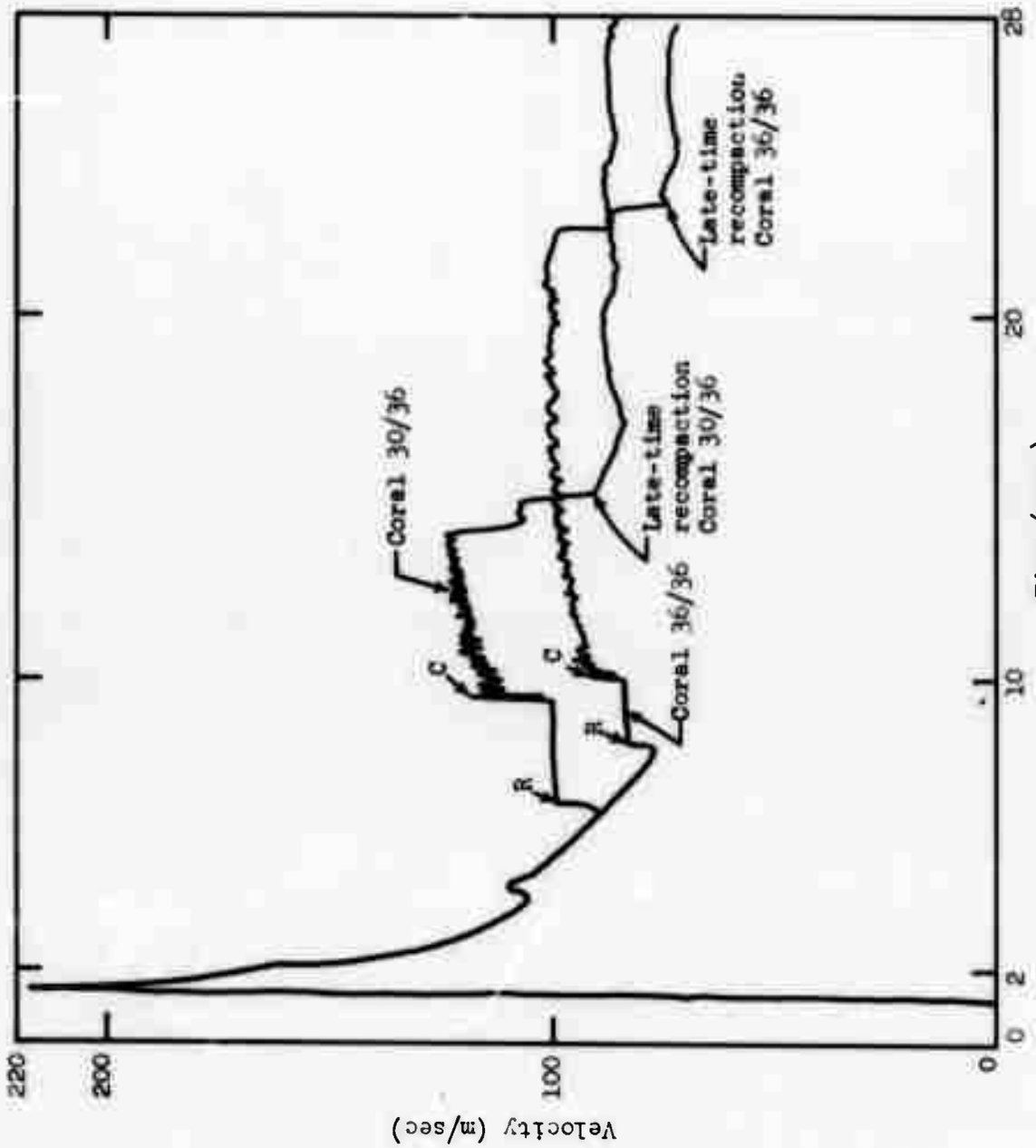

Figure 31b. Coral, R = 4.01 m.

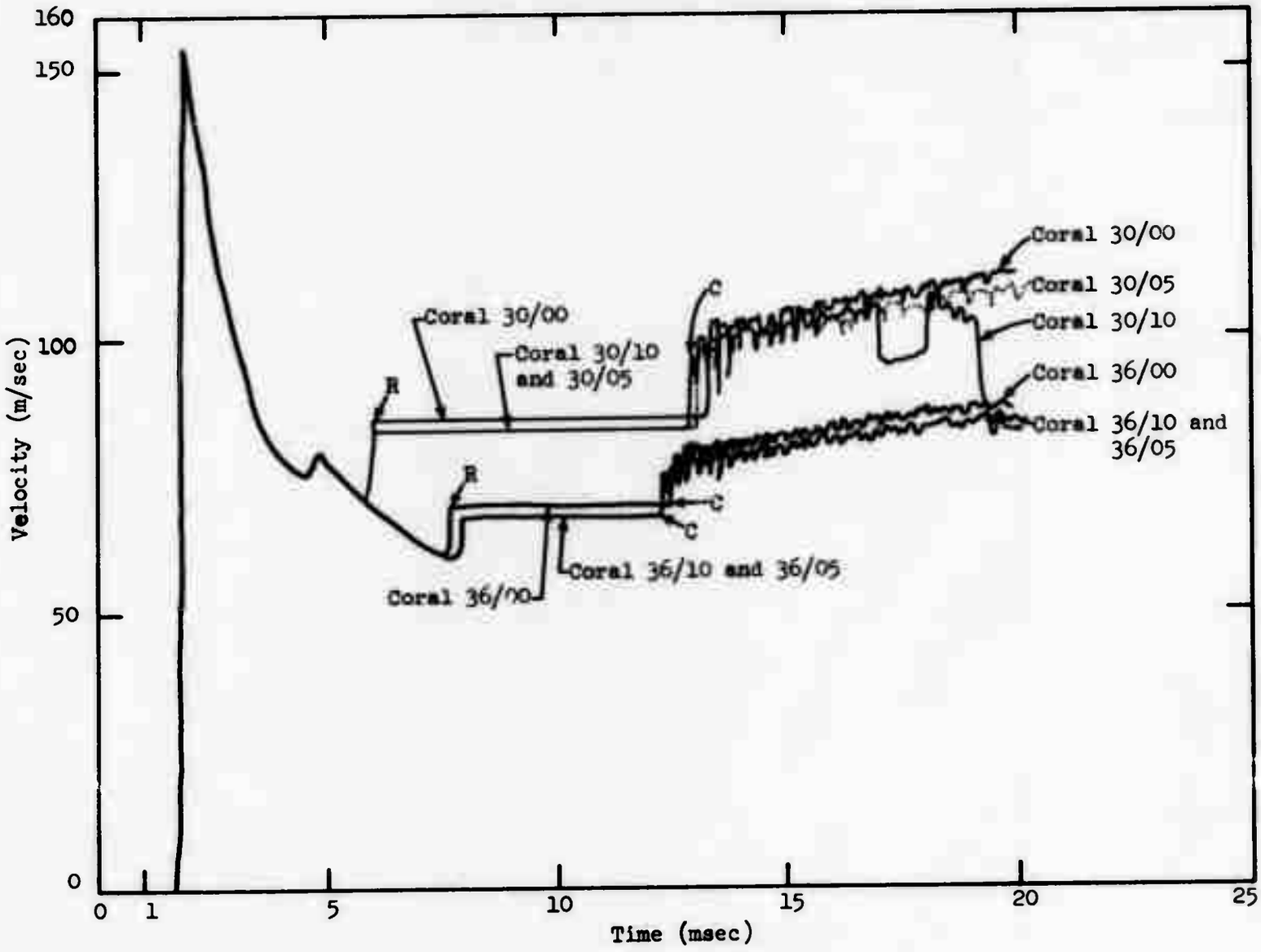

Figure 32a. Coral, R = 5.01 m.

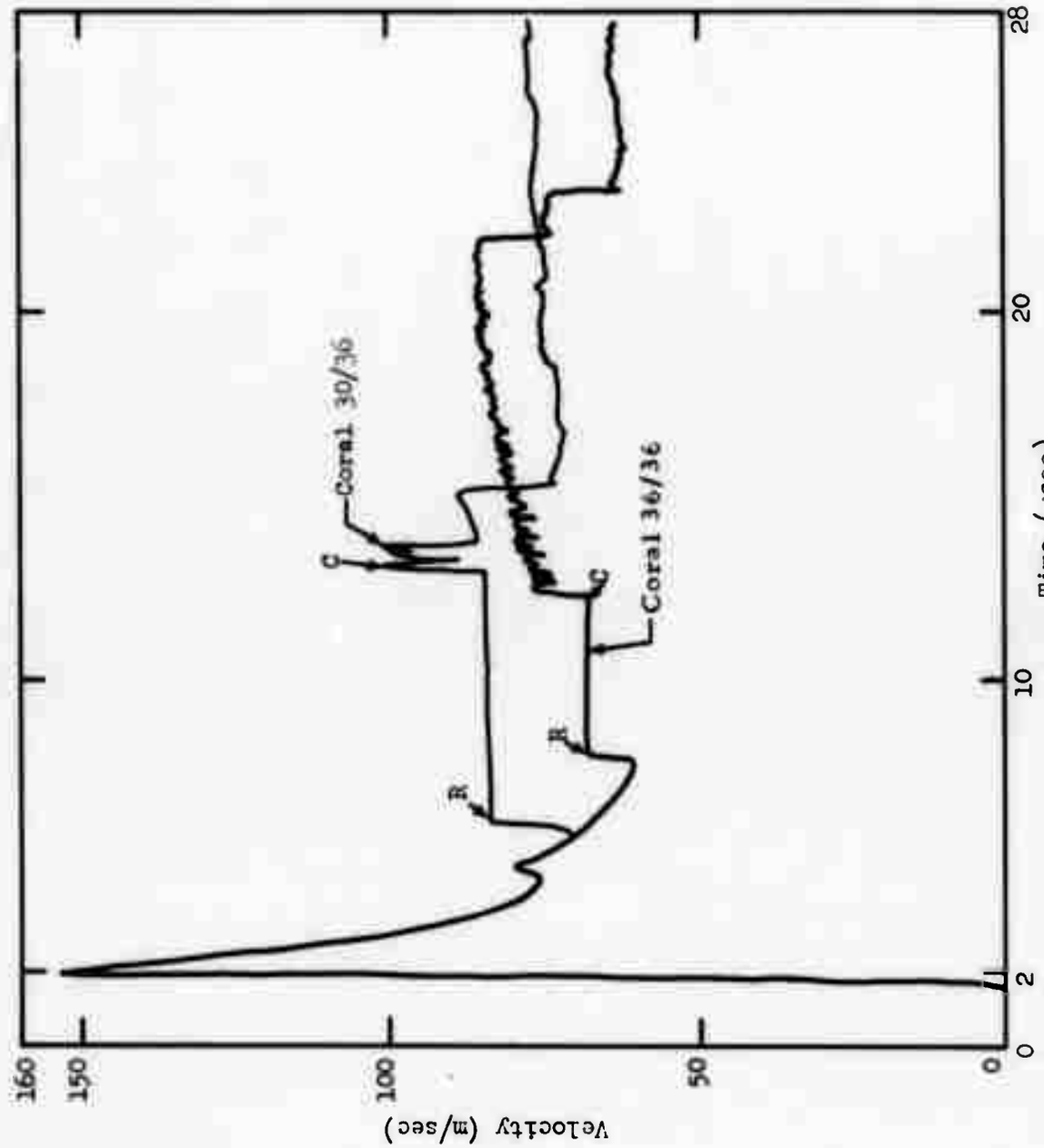

Figure 32b. Coral, R = 5.01 m.

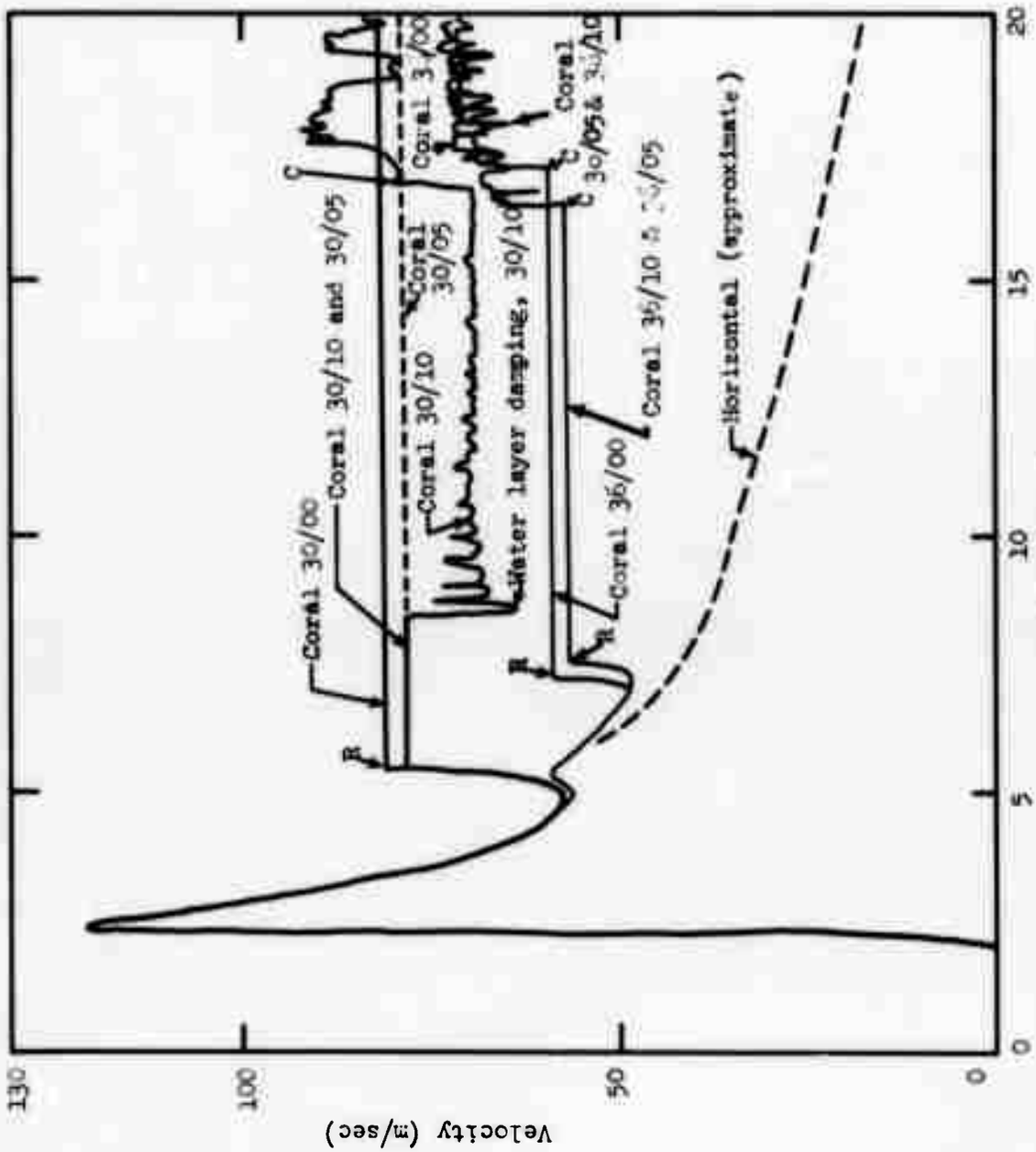

Figure 33a. Coral, R = 6.01 or 5.98 m.

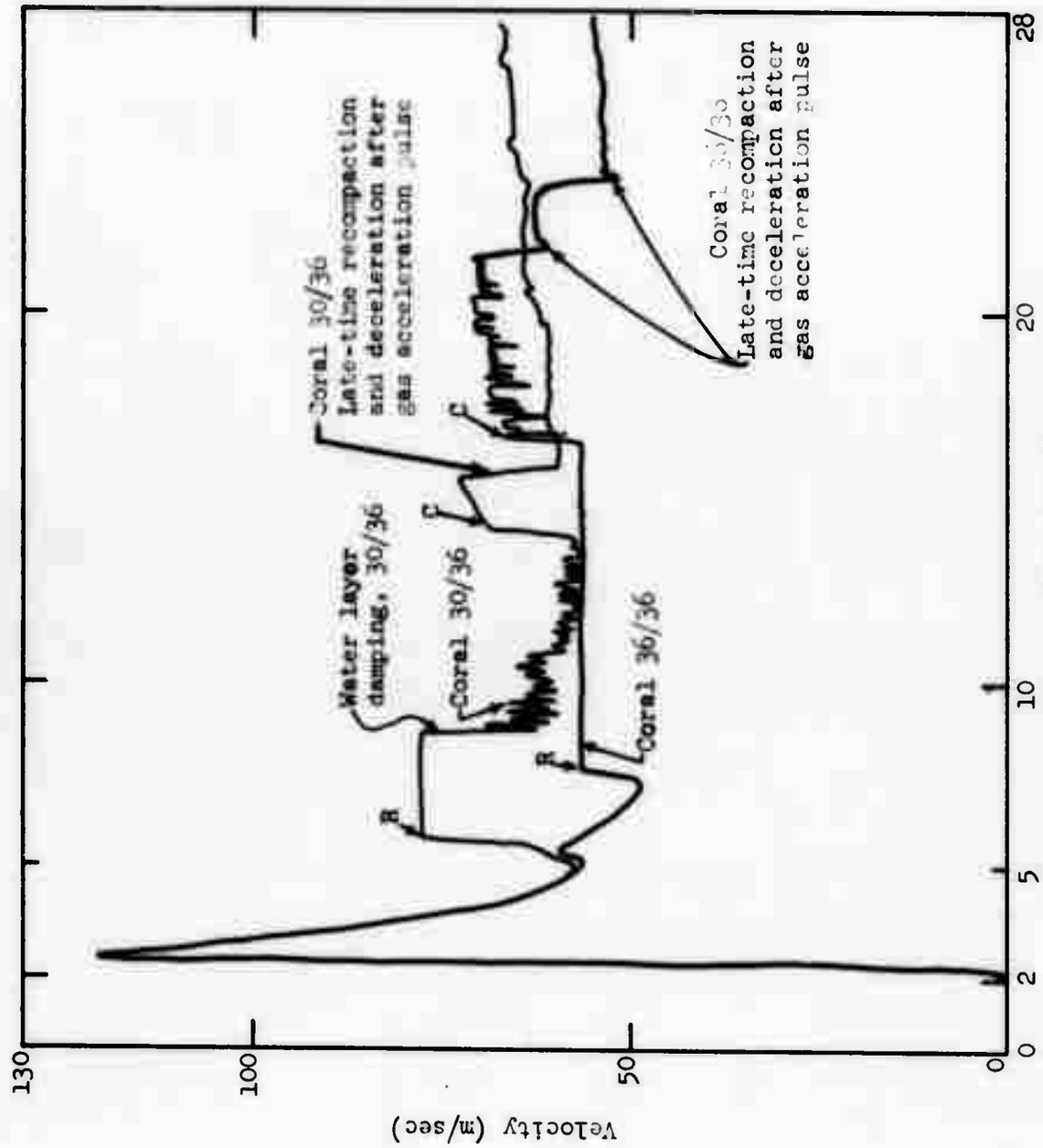

Figure 33b. Coral, R = 6.01 or 5.98 m.

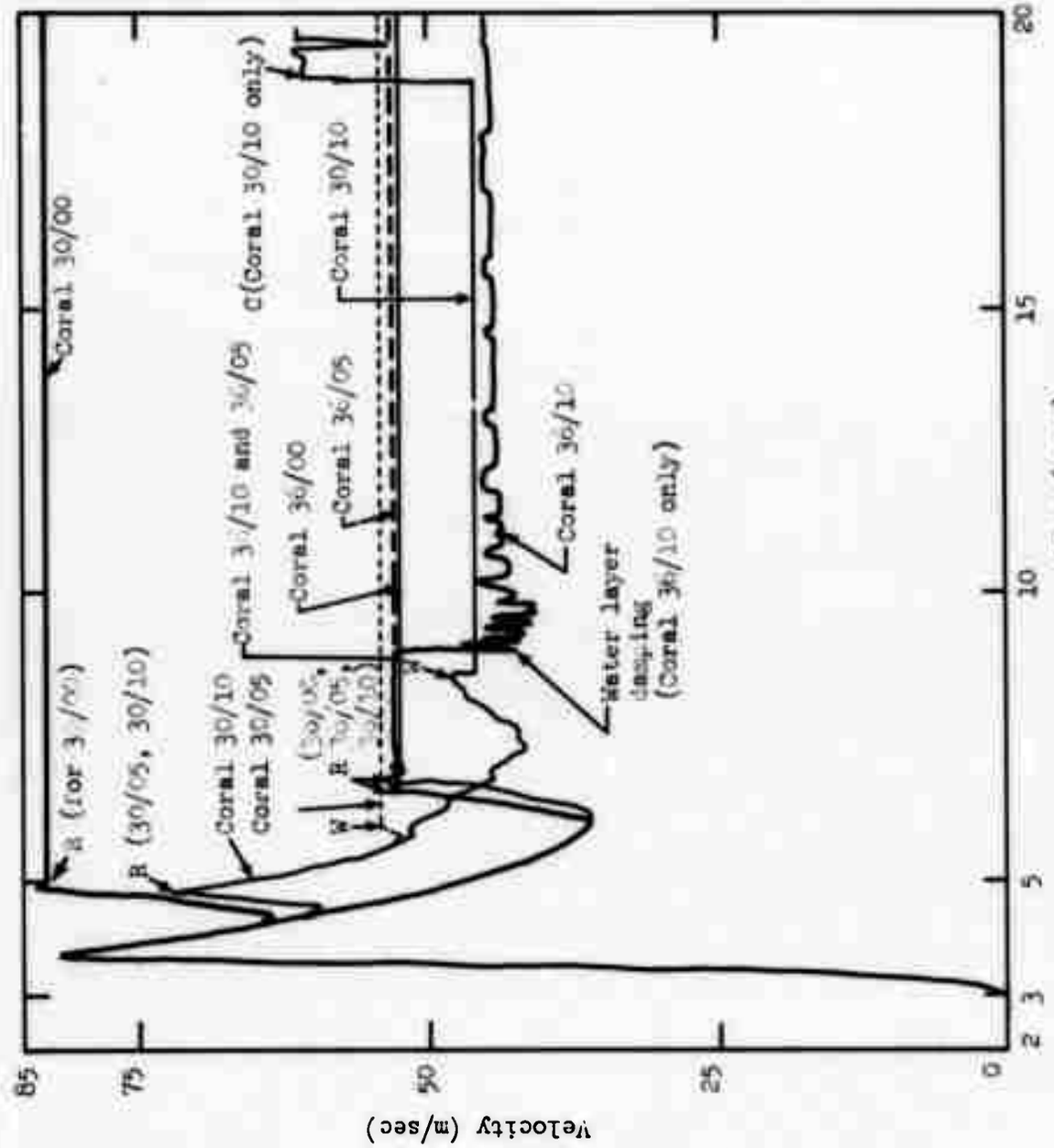

Figure 34a. Coral, R = 8.01 or 7.98 m.

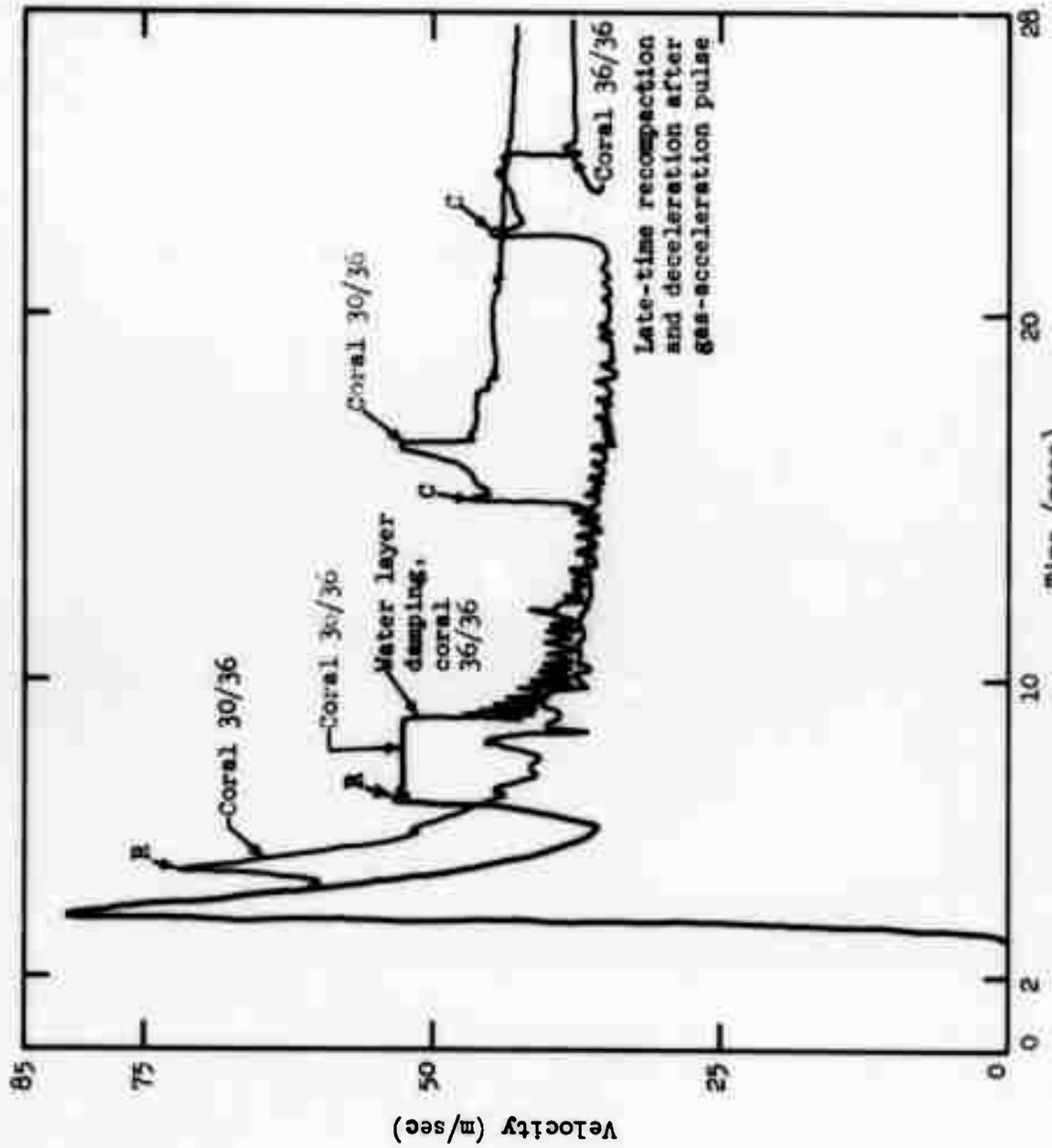

Figure 34b. Coral, R = 8.01 or 7.98 m.

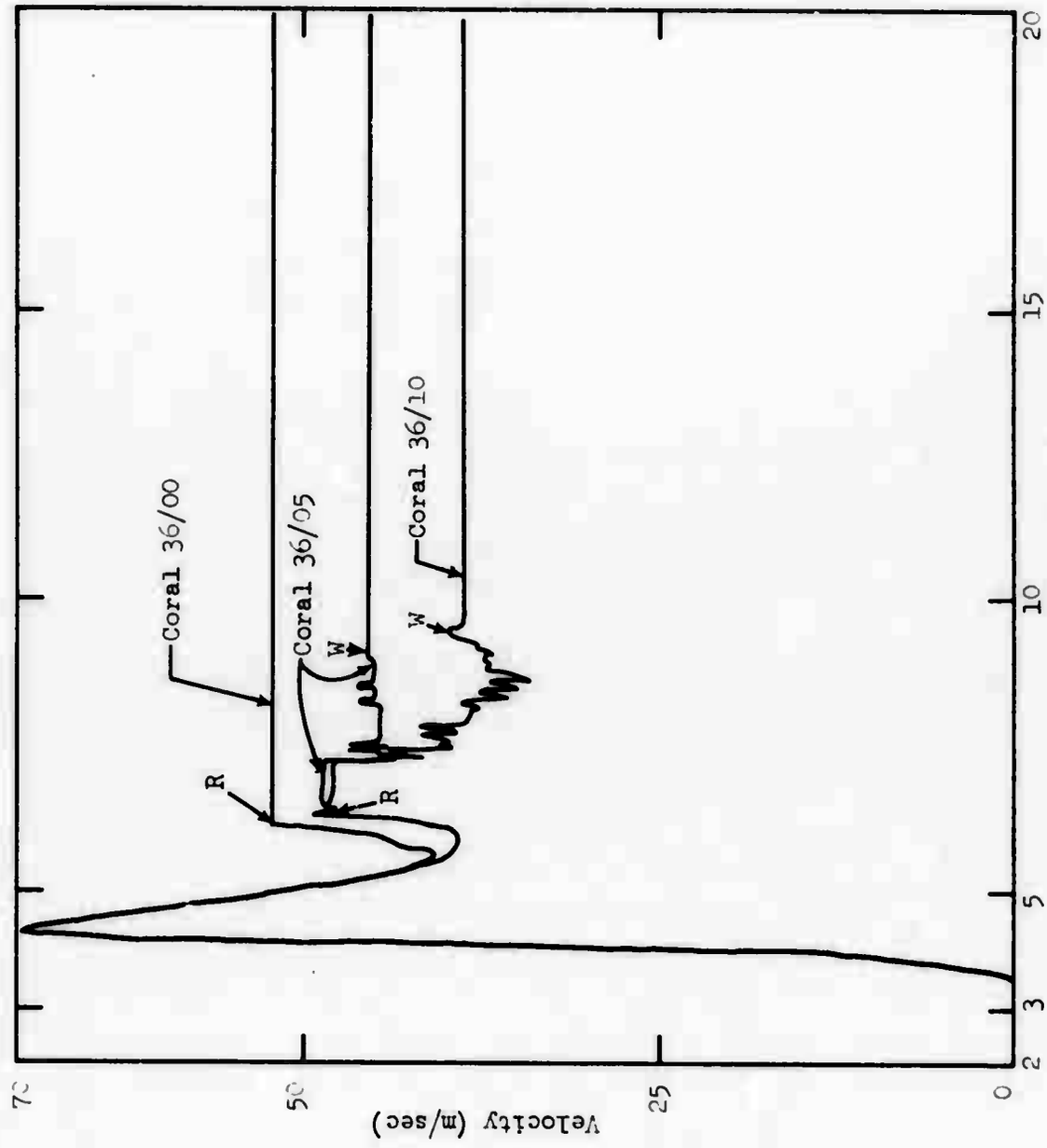

Figure 35a. Coral, R = 9.01 m.

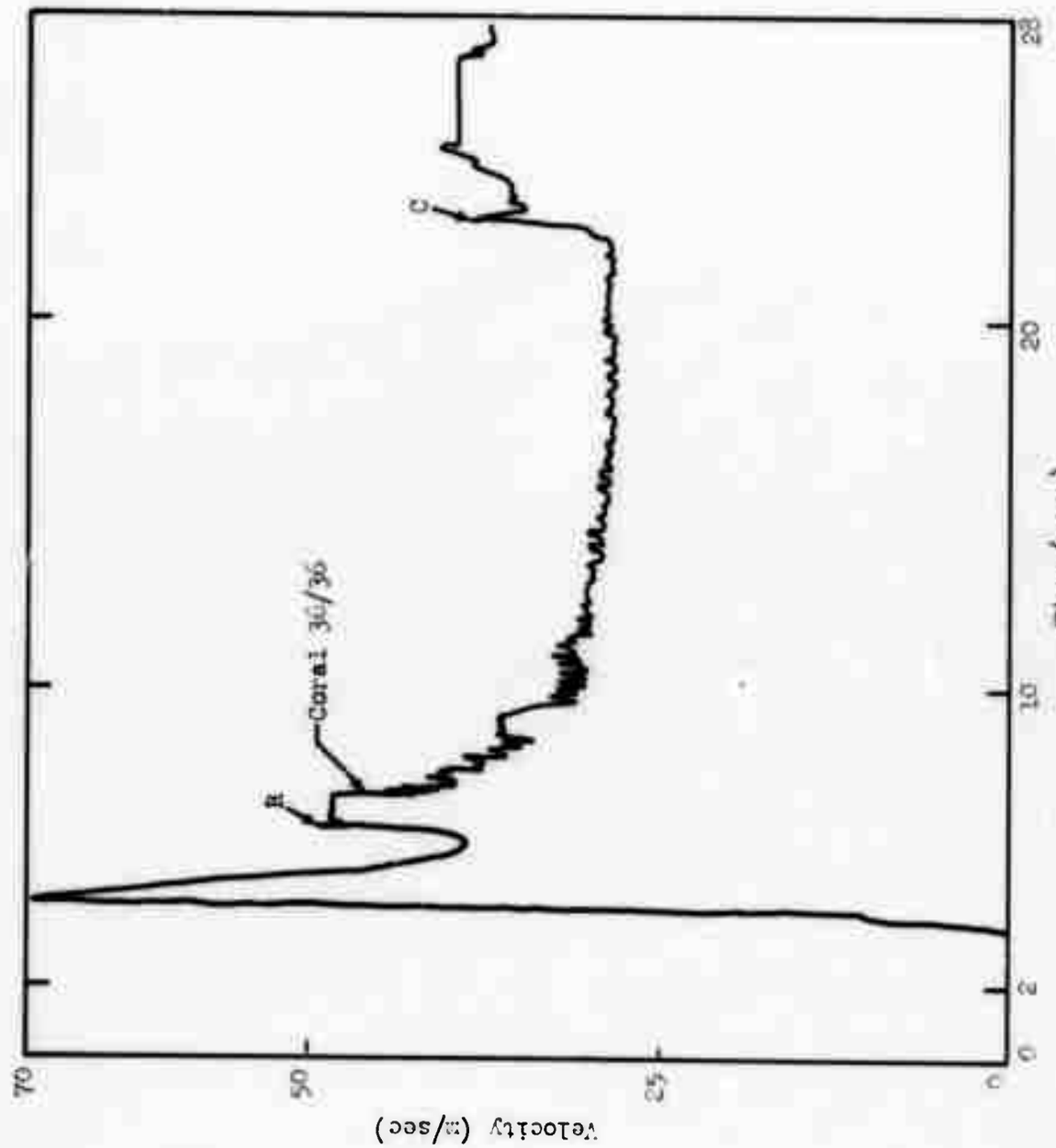

Figure 35b. Coral, R = 9.01 m (coral 36/36 only).

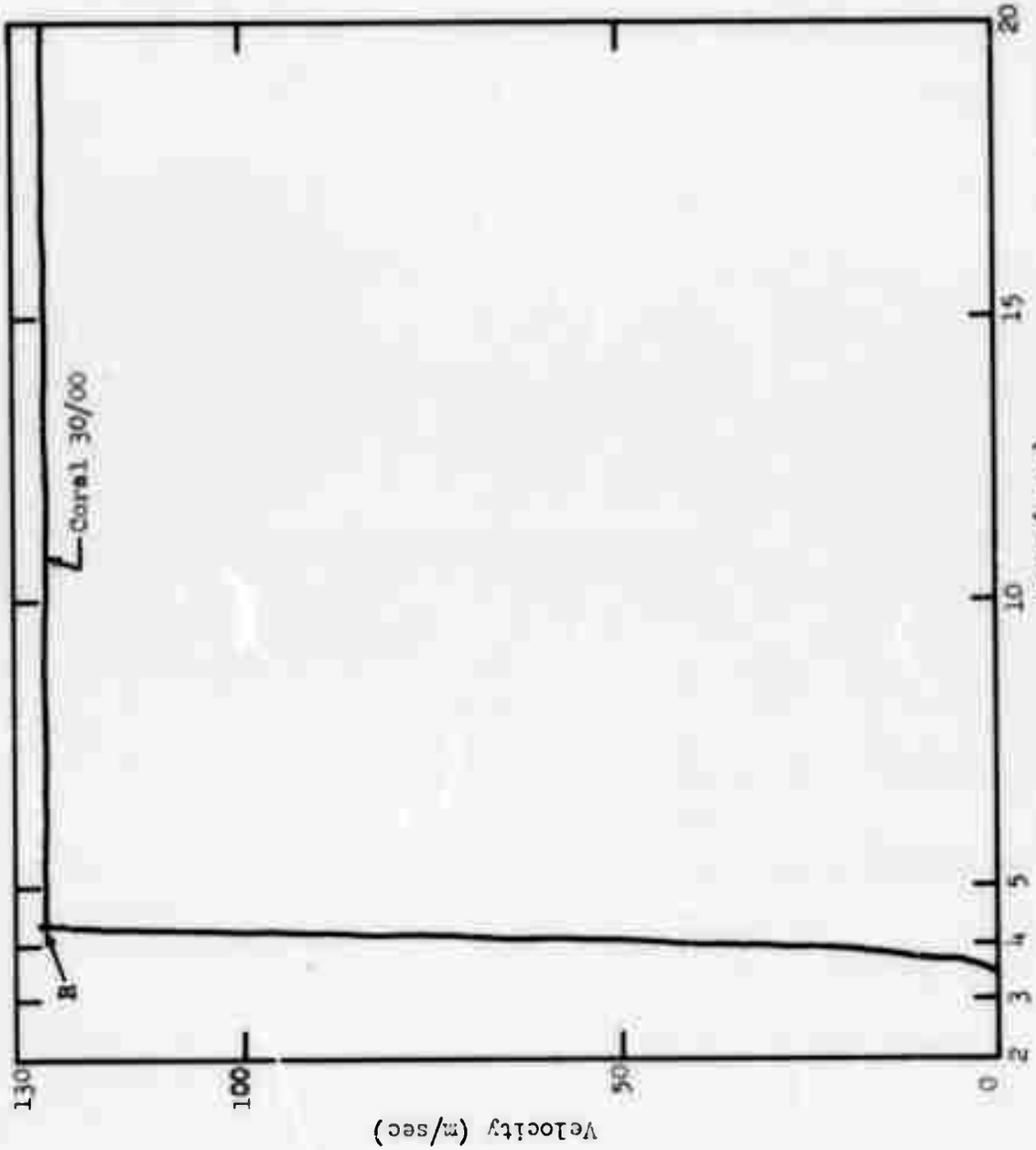

Figure 35c. Coral, R = 8.98 m.

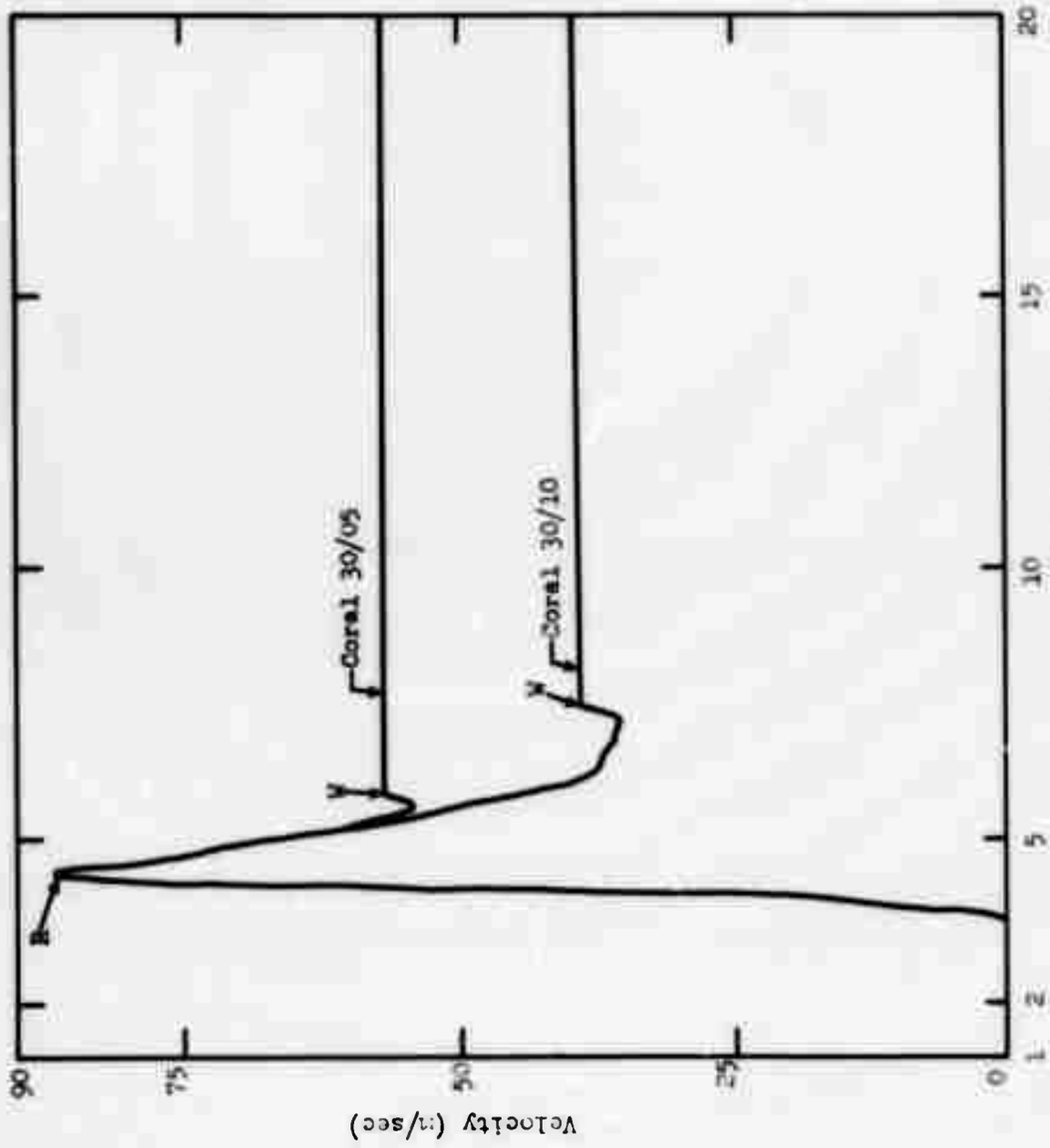

Figure 354. Coral, R = 8.98 m.

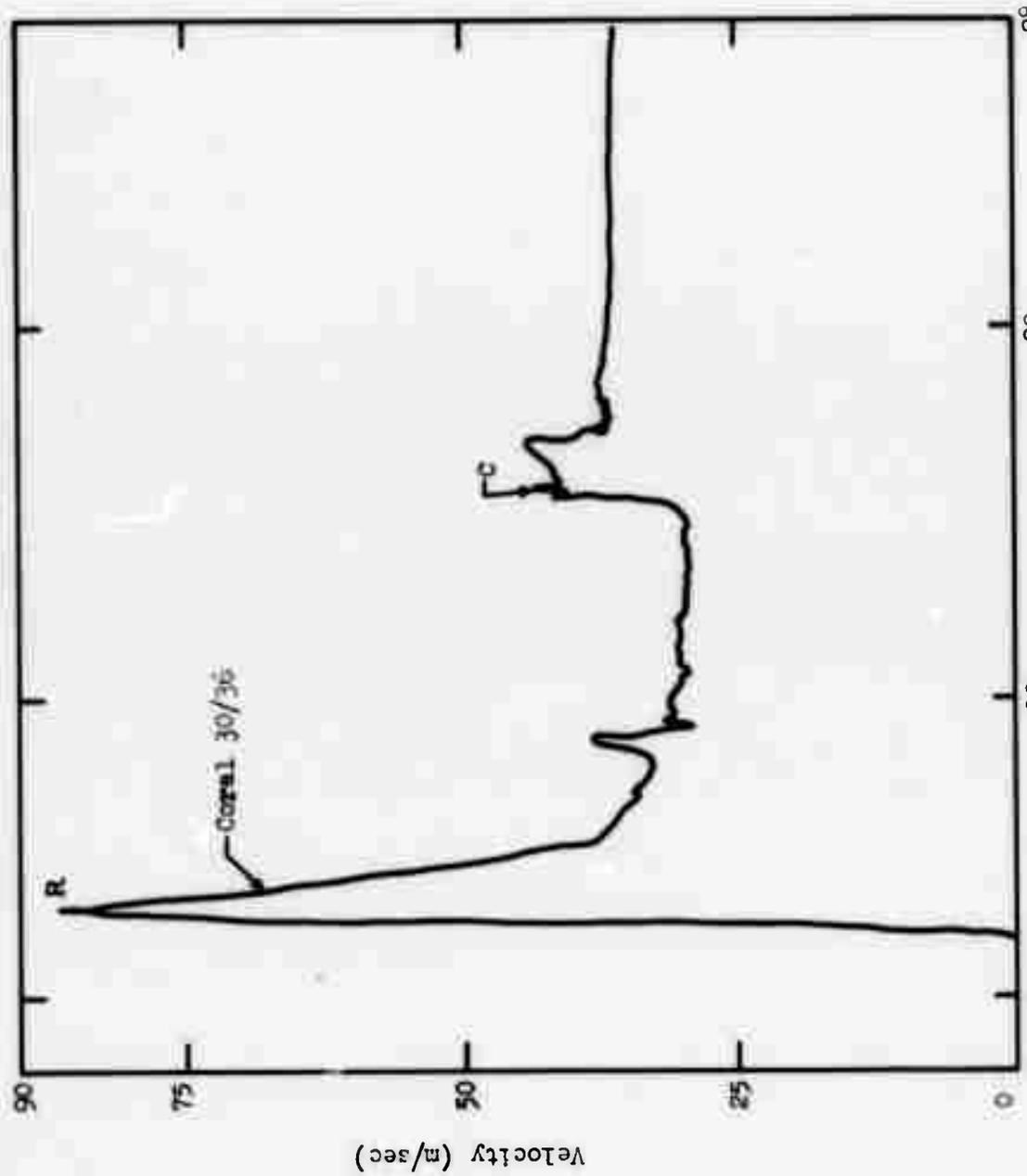

Figure 35e. Coral, R = 8.98 m, coral 30/36 only.

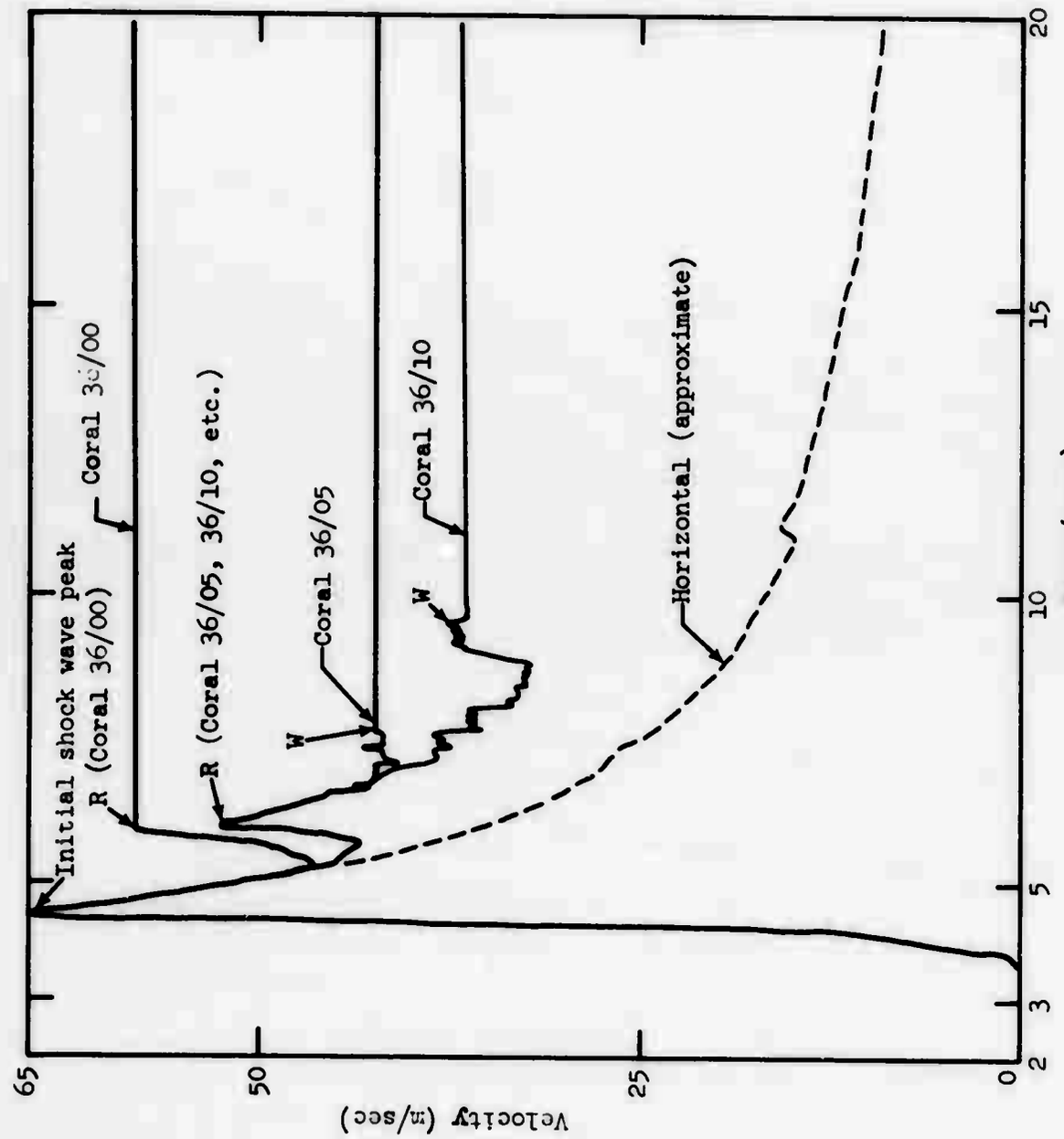

Figure 36a. Coral, R = 9.49 m (compare with 7.98 m, coral 30 ft).

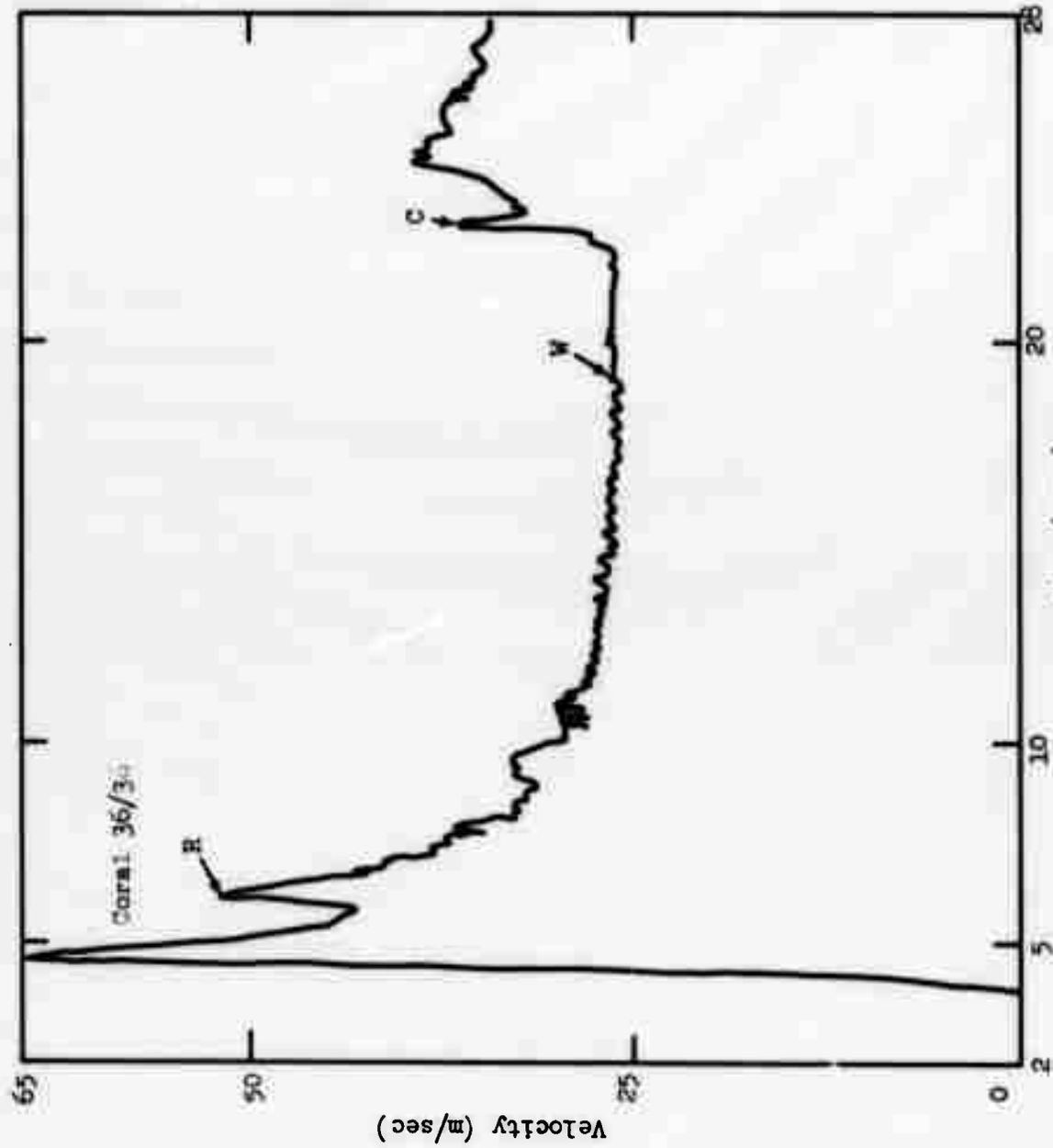

Figure 36b. Coral R = 9.49 m (compare with 7.98 m, coral 30 ft).

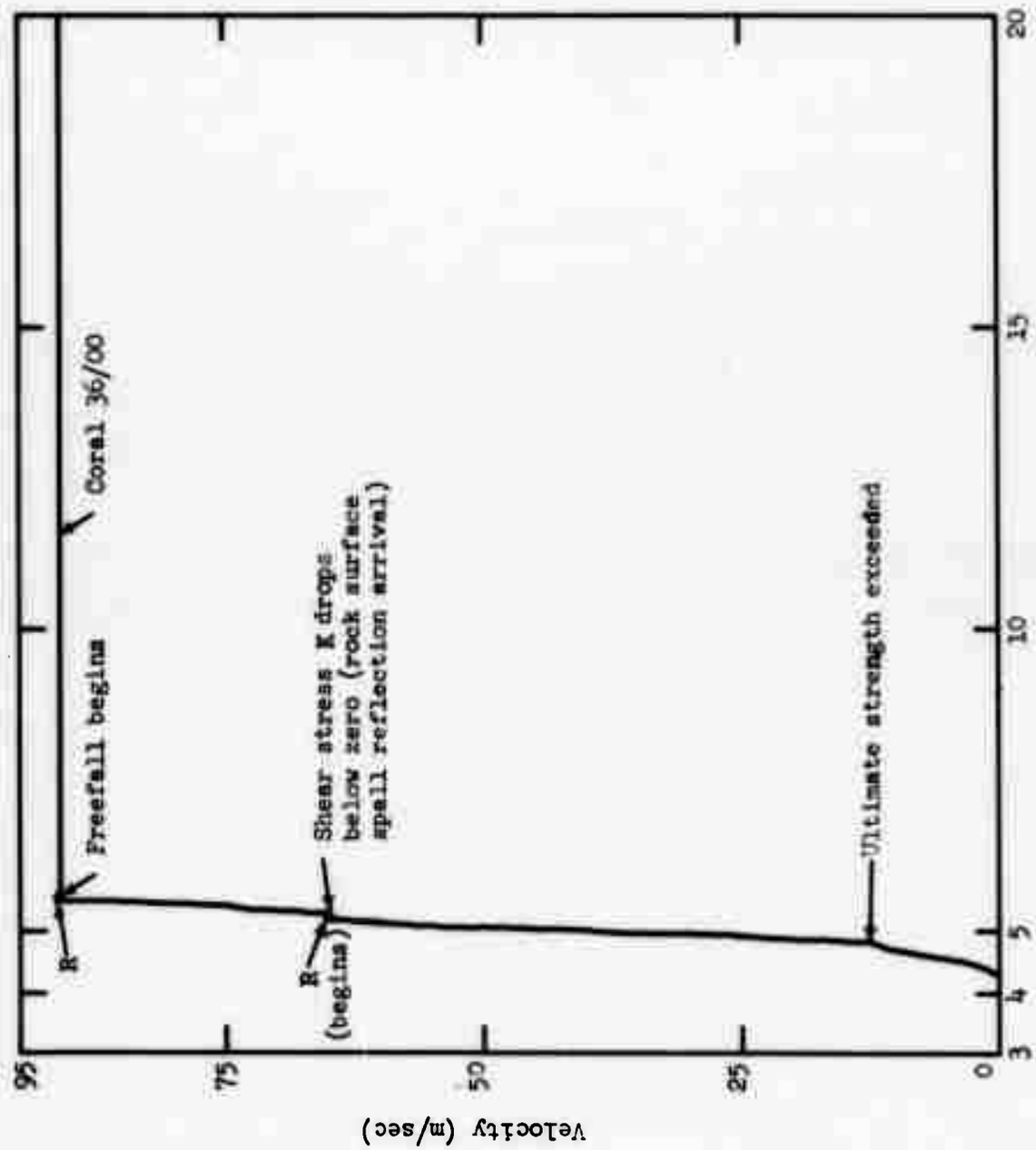

Figure 37a. Coral, R = 10.6 m (compare with 8.96 m, coral 30 ft).

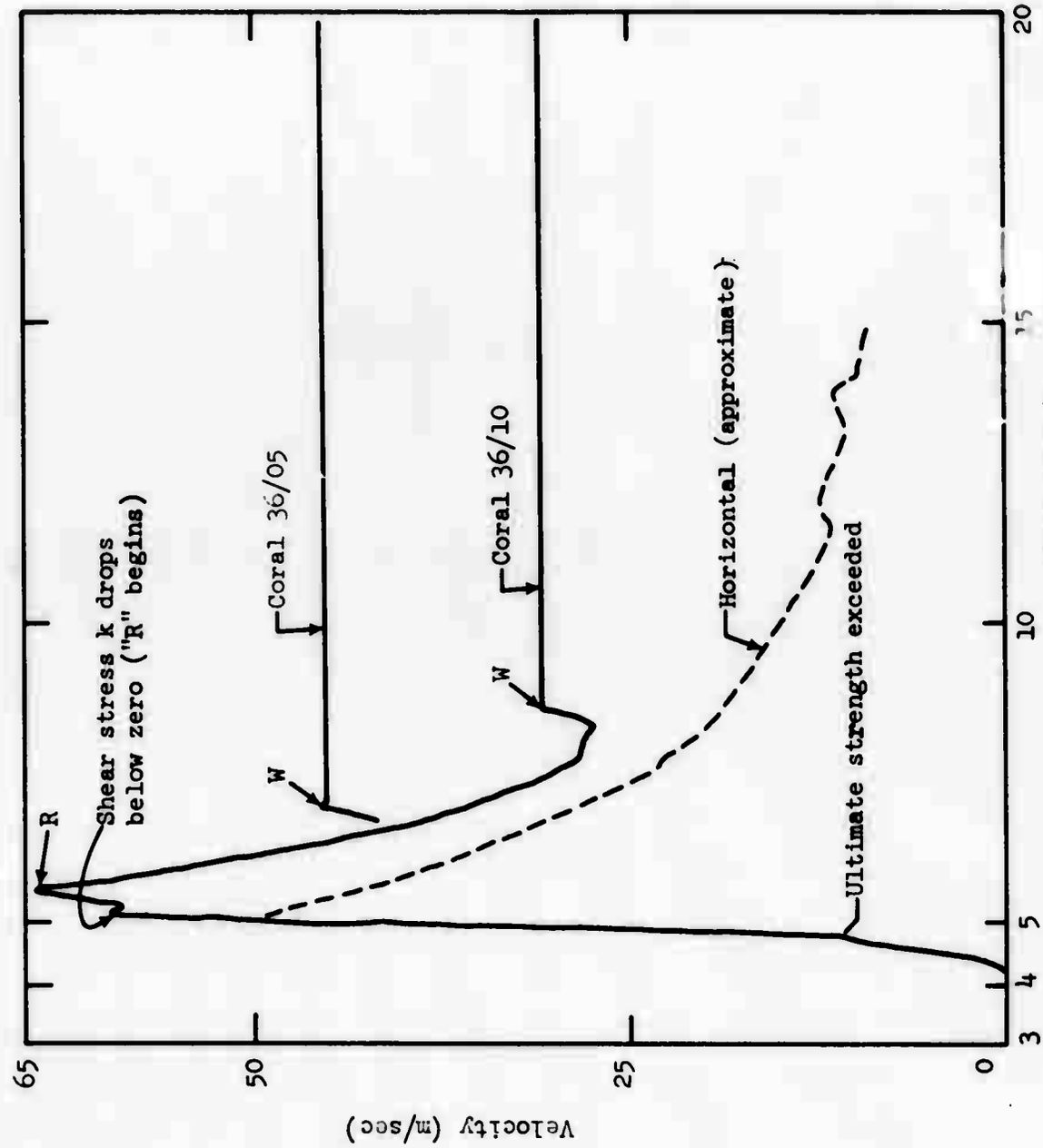

Figure 37b. Coral, R = 10.6 m (compare with 8.98 m, coral 30 ft)

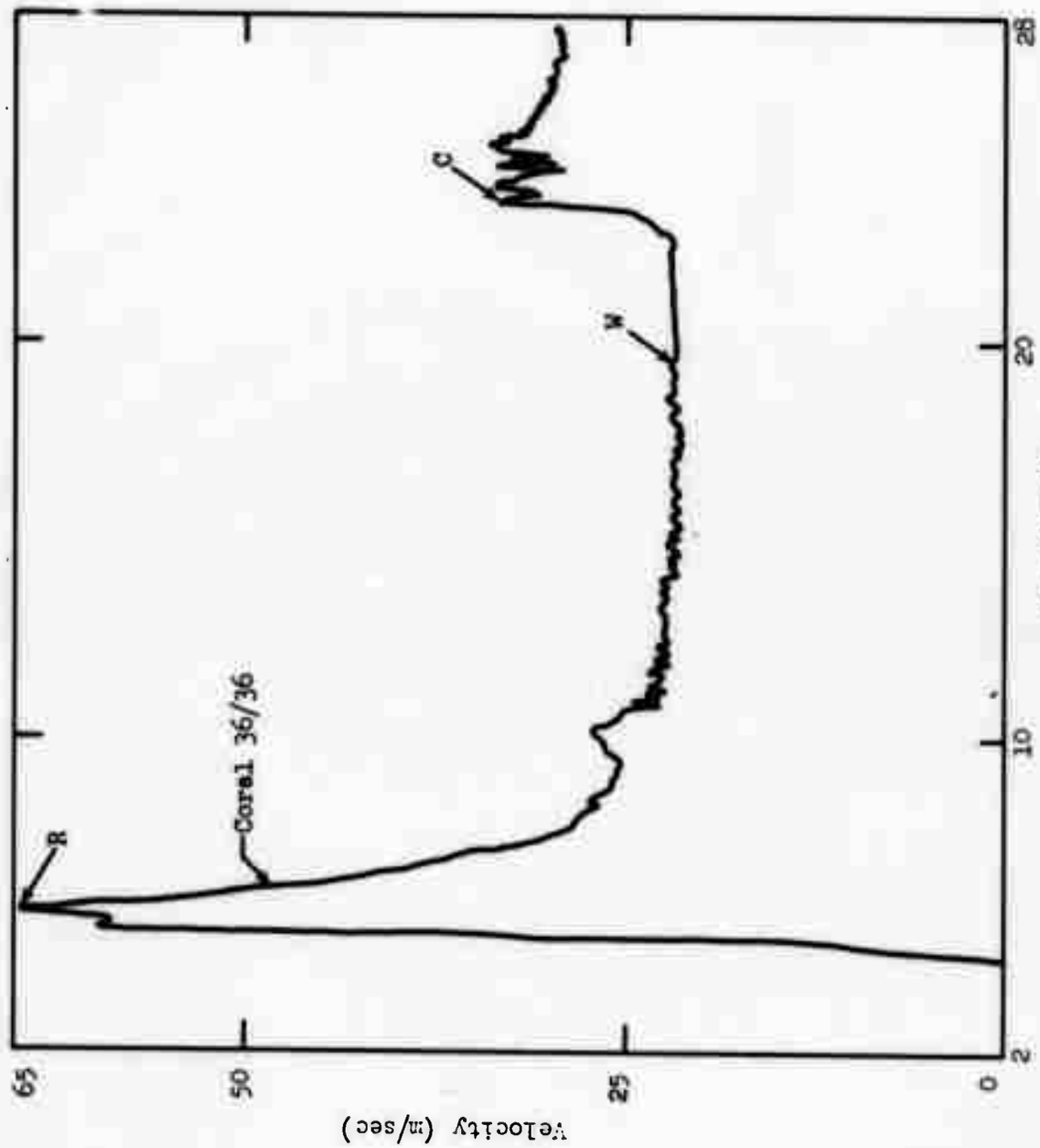

Figure 37c. Coral, R = 10.6 m (compare with 8.98 m, coral 30 ft).

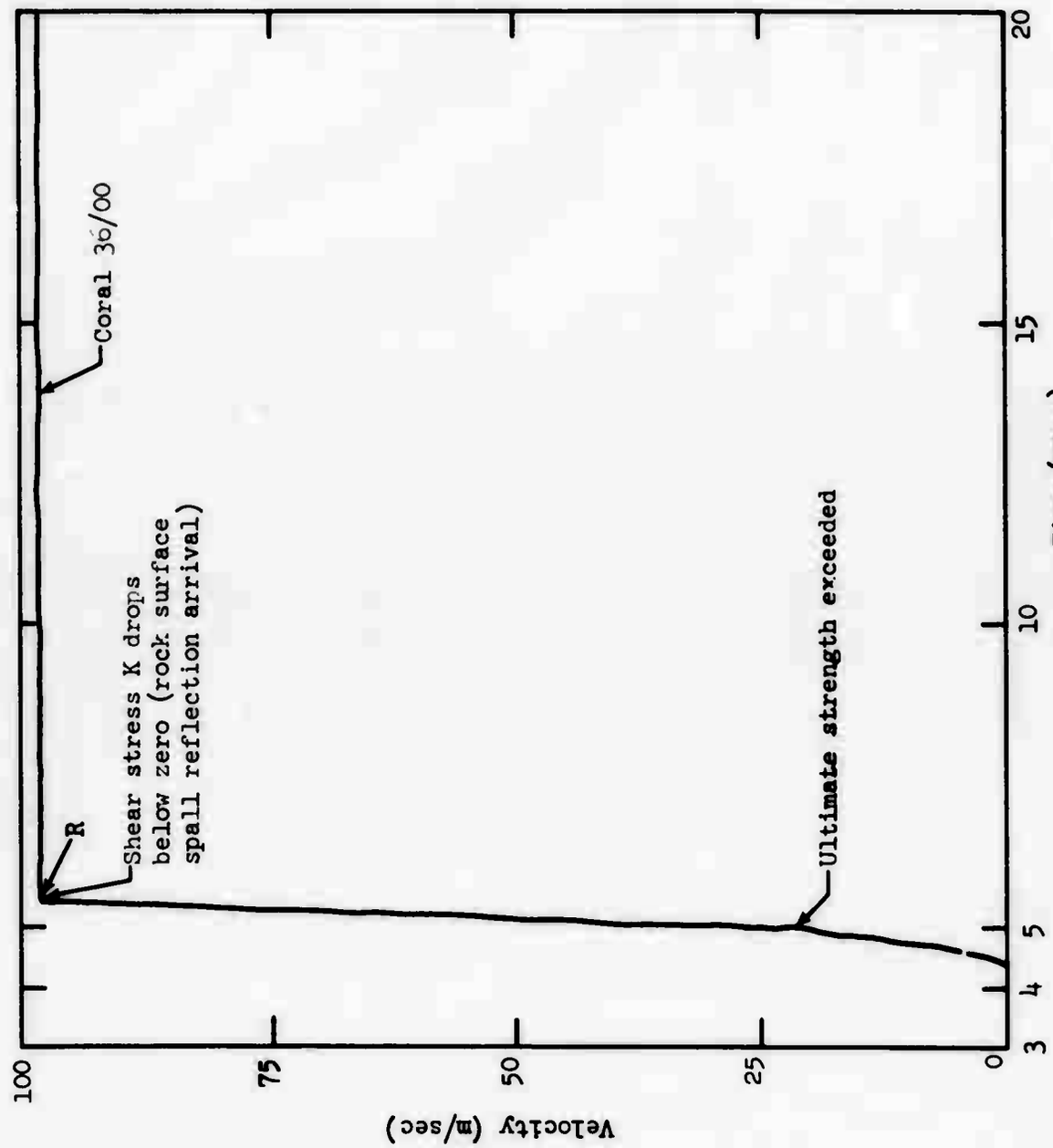

Figure 38a. Coral, R = 10.89 m (compare with 8.98 m, coral 30 ft).

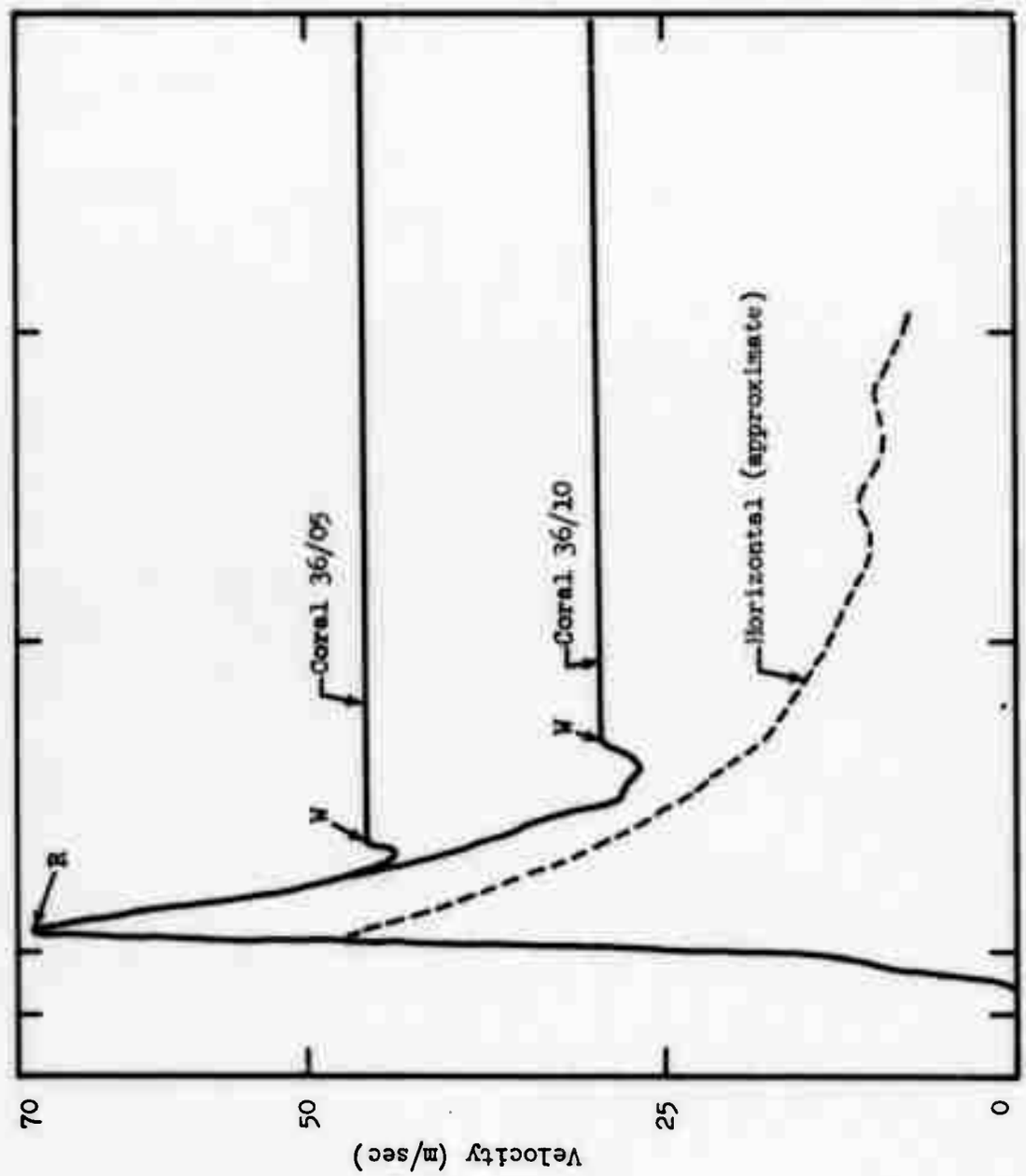

Figure 38b. Coral, R = 10.89 m (compare with 8.98 m, coral 30 ft).

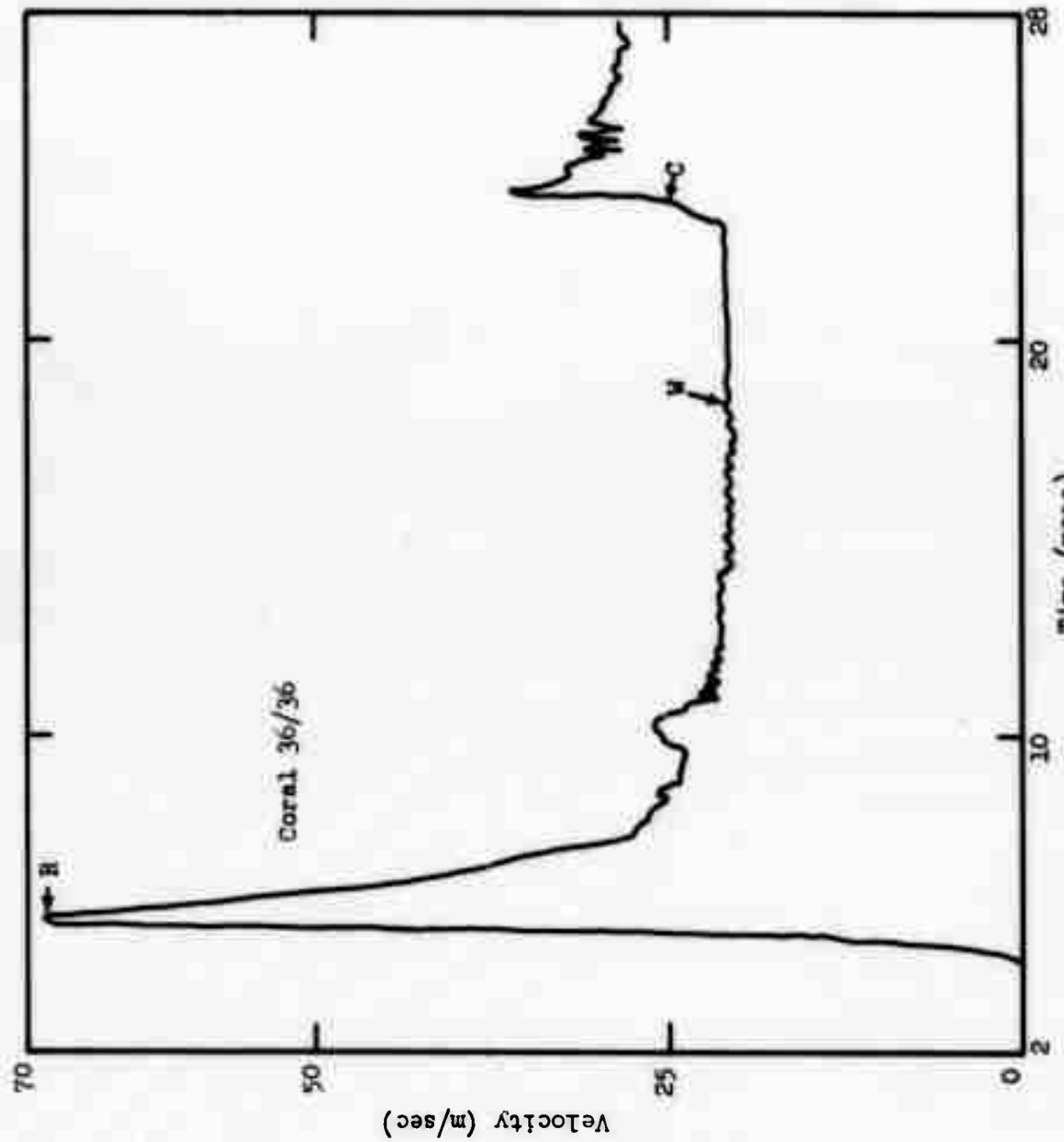

*Figure 38c. Coral, R = 10.89 m.

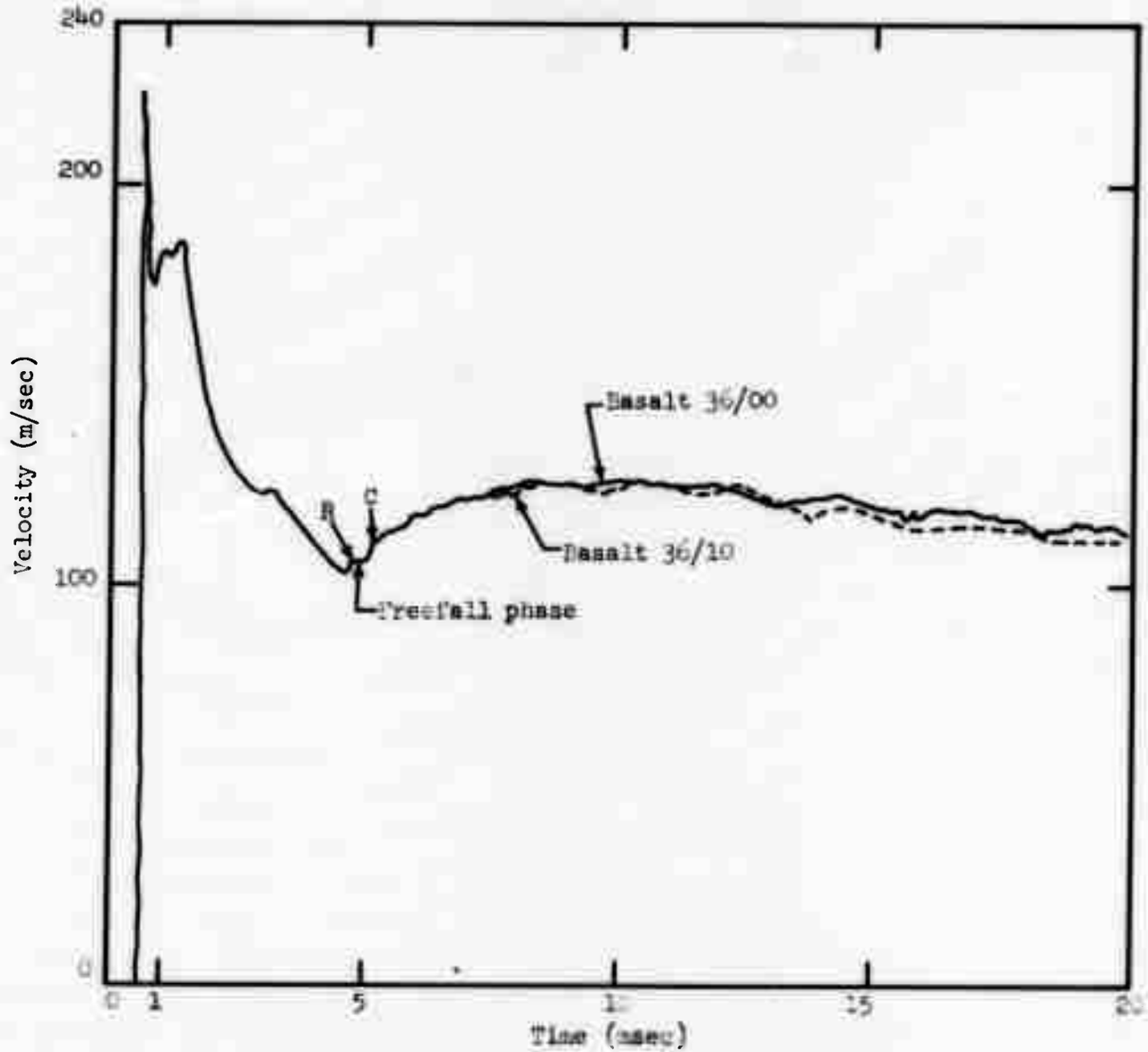

Figure 39a. Basalt, R = 3.01 m.

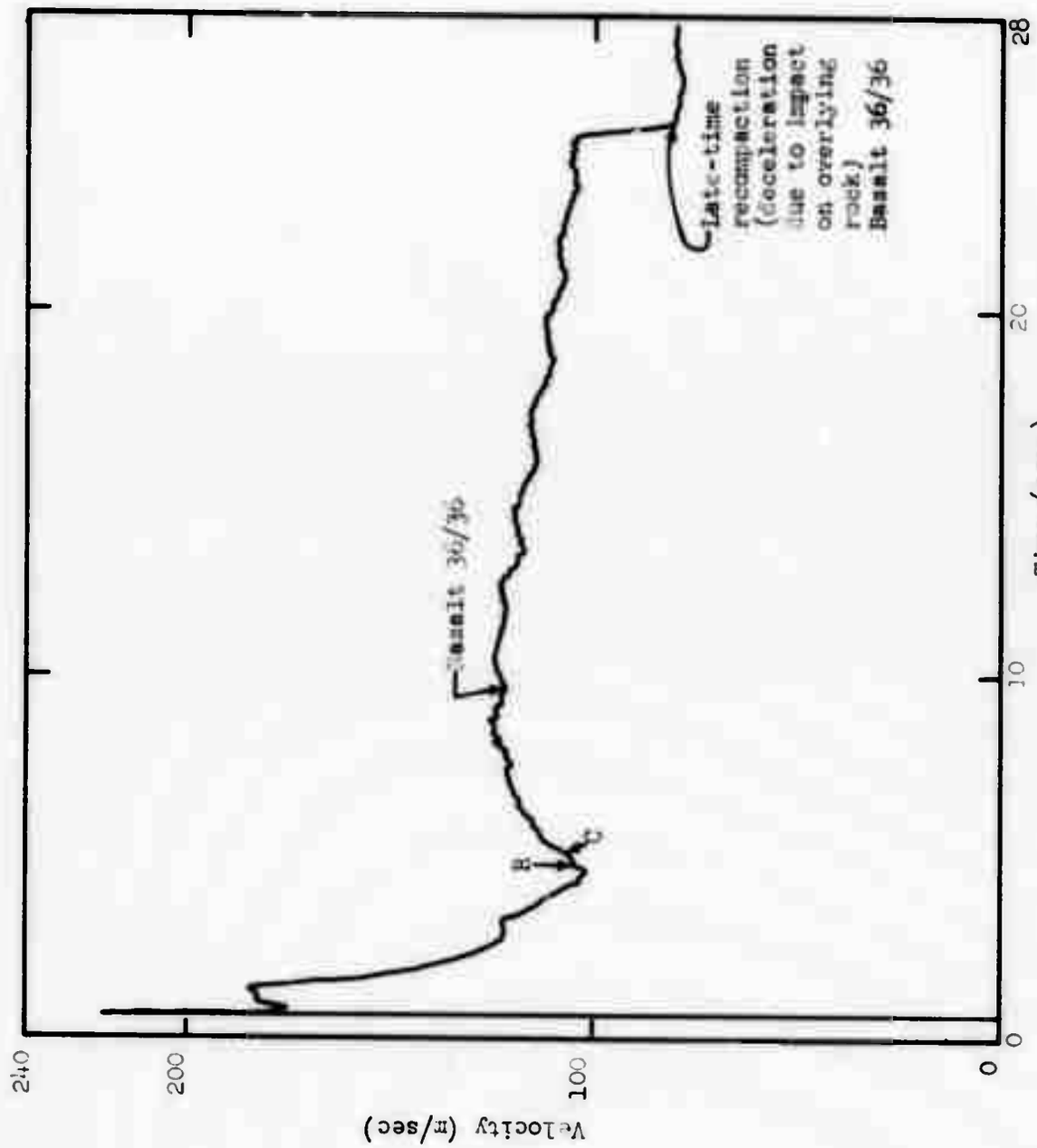

Figure 39b. Basalt, R = 3.01 m.

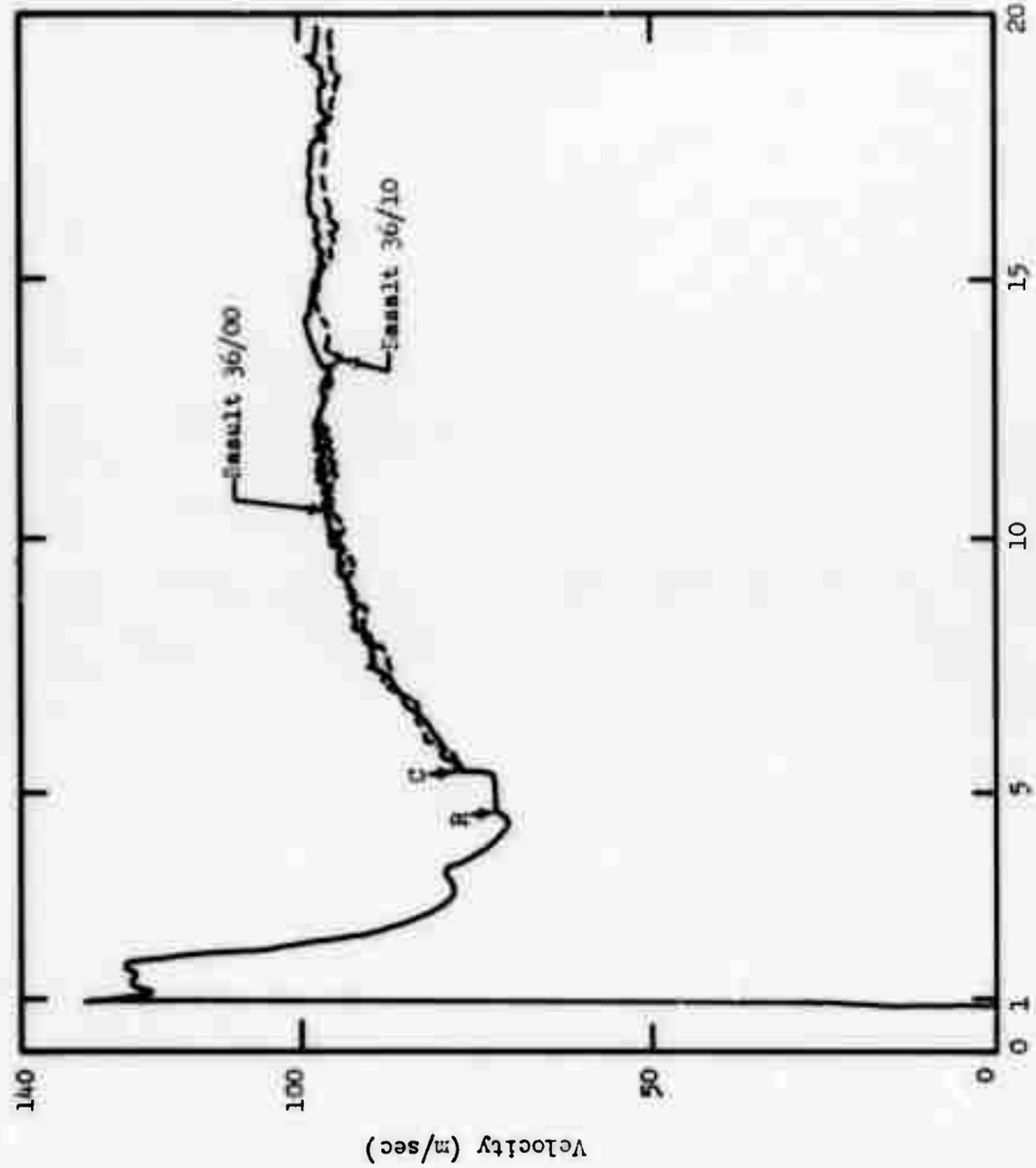

Figure 40a. Basalt, R = 4.01 m.

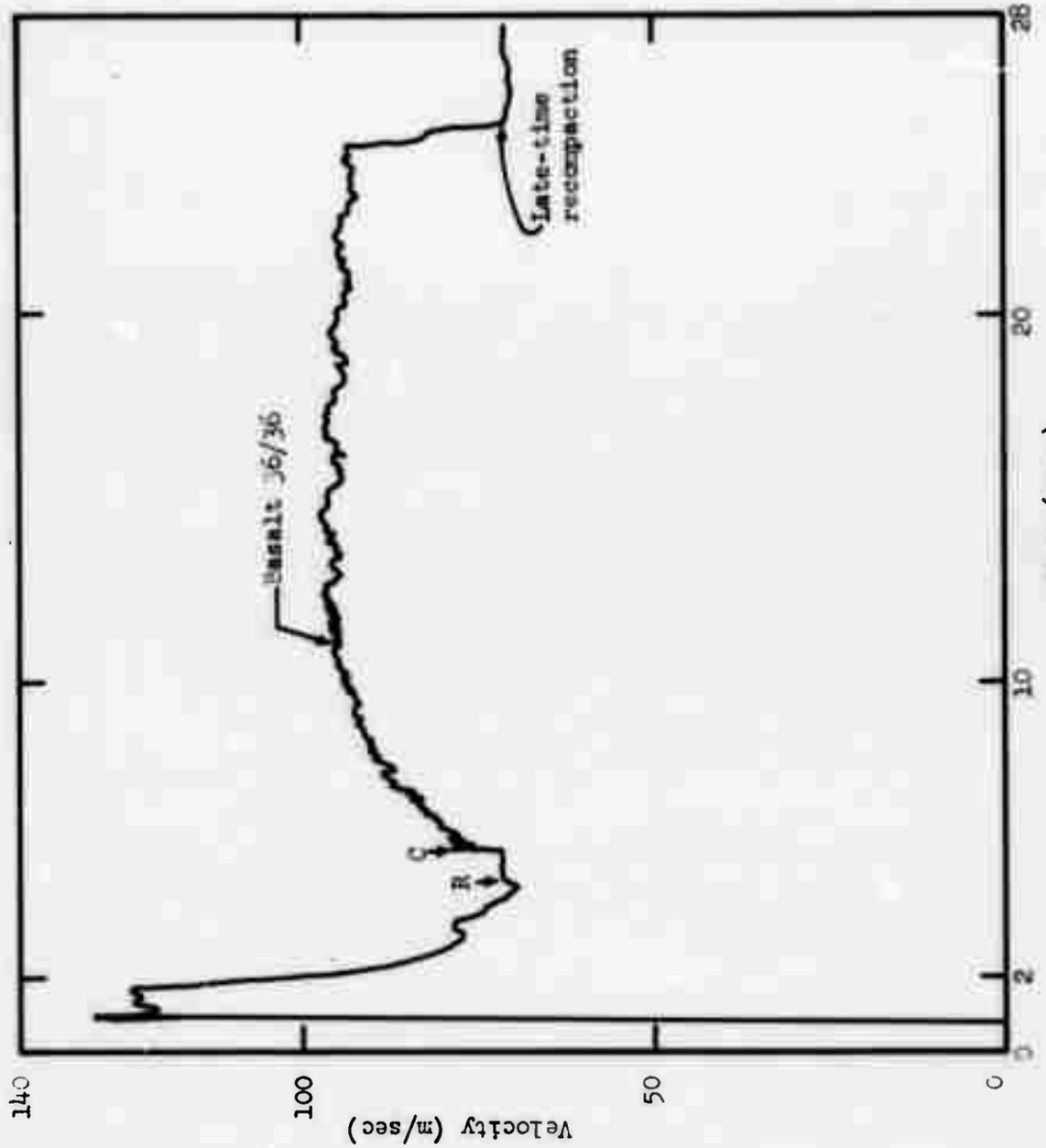

Figure 40b. Basalt, R = 4.01 m.

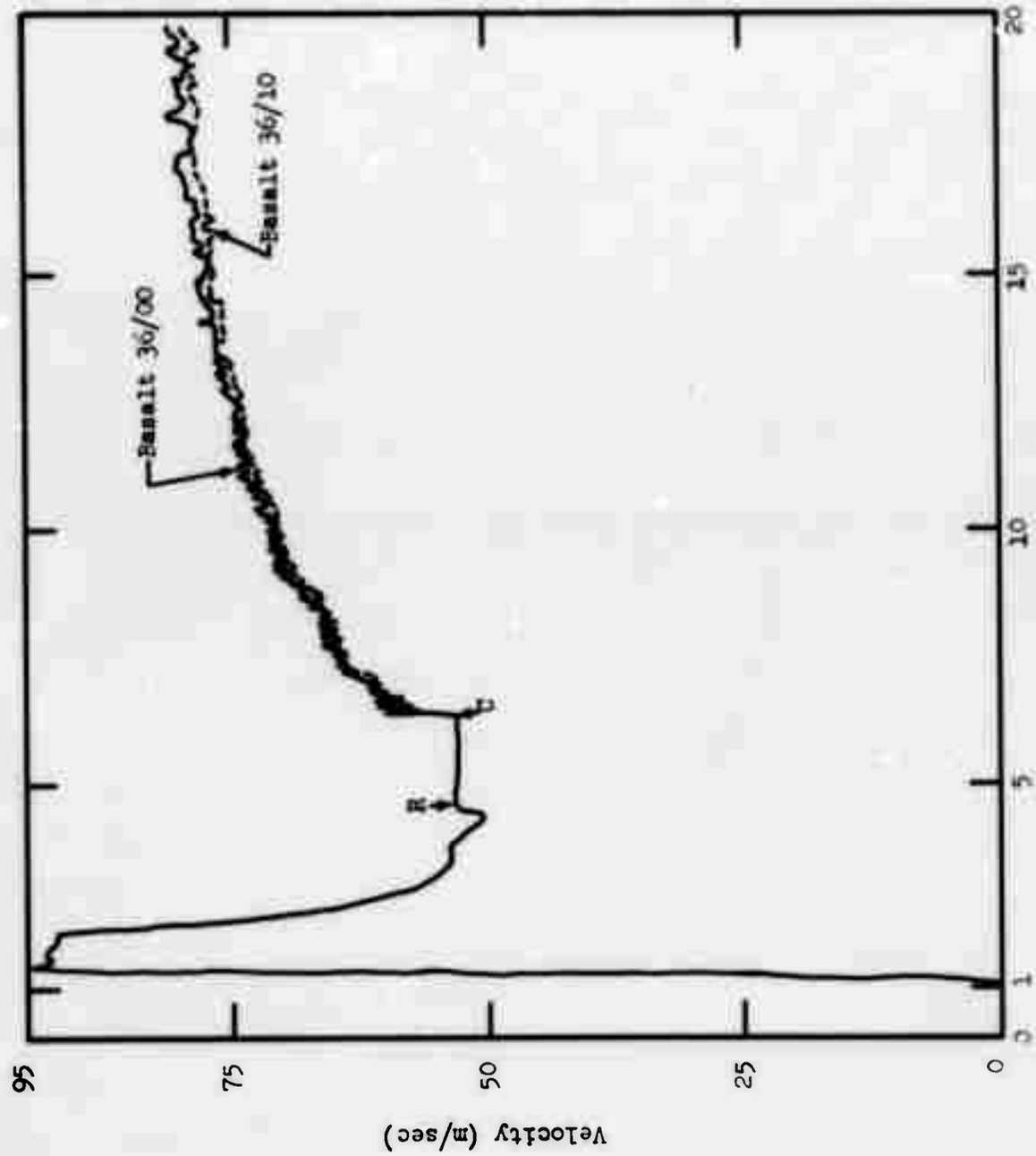

Figure 41a. Basalt, R = 5.01 m.

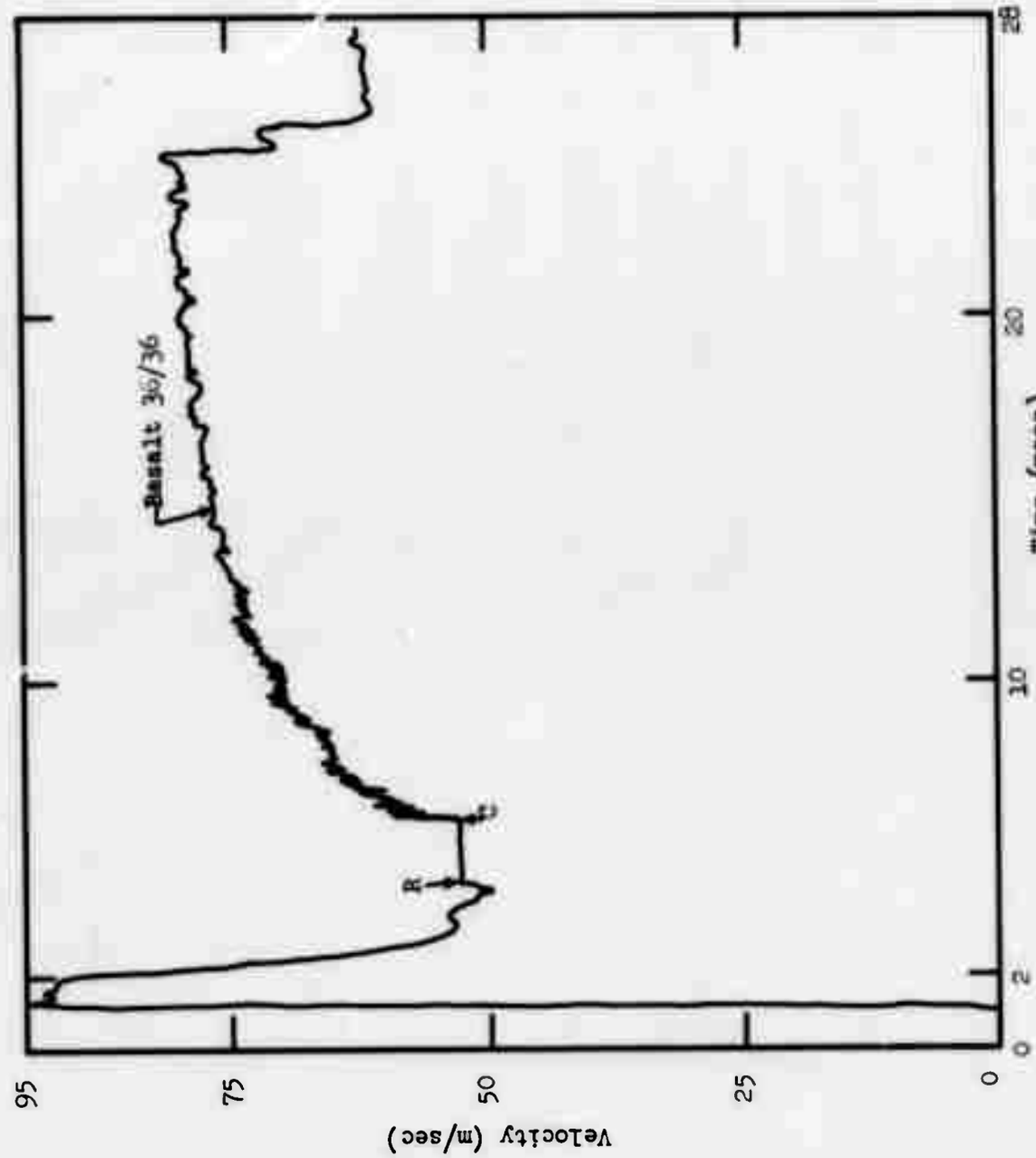

Figure 41b. Basalt, R = 5.01 m.

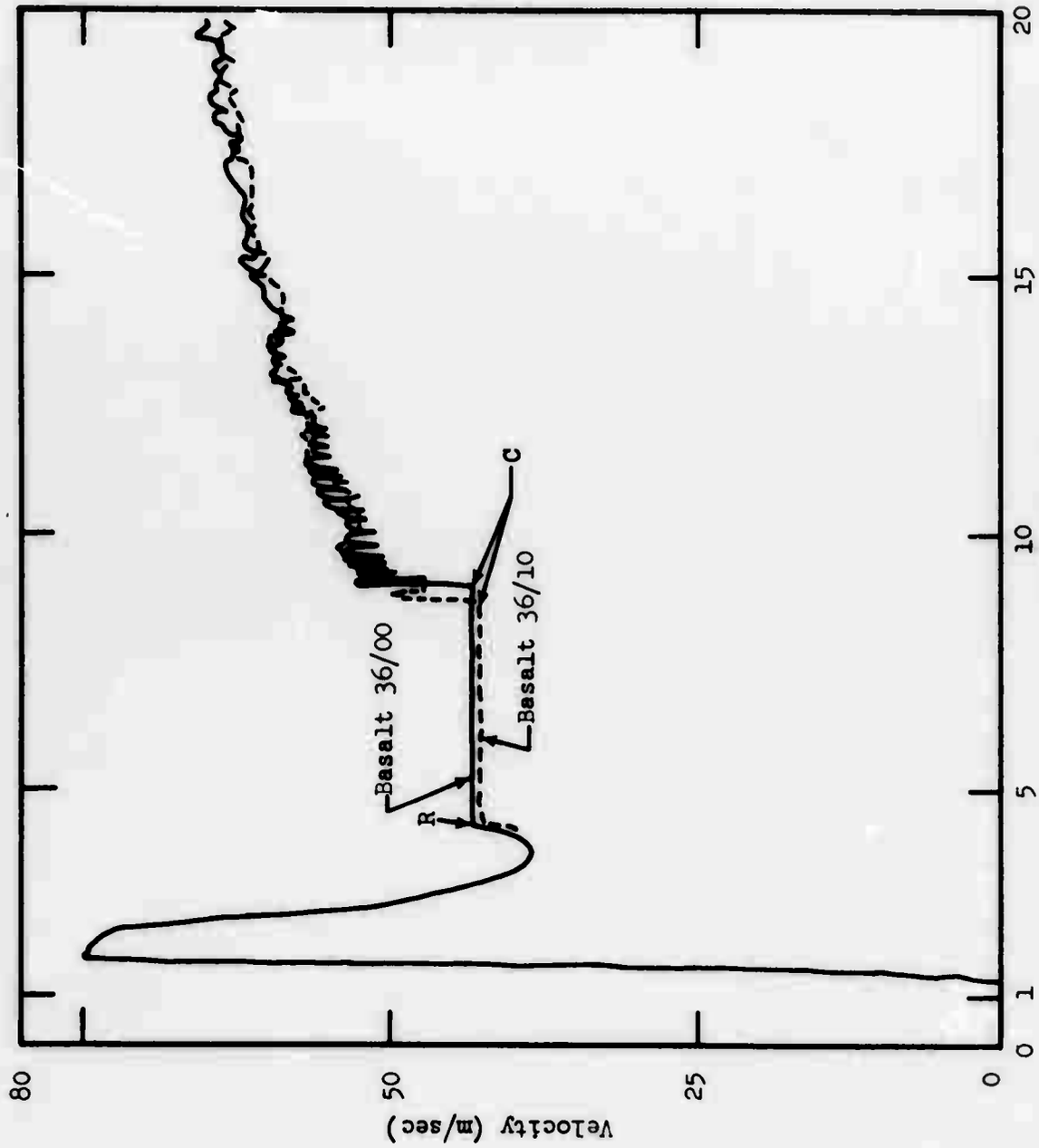

Figure 42a. Basalt, R = 6.01 m.

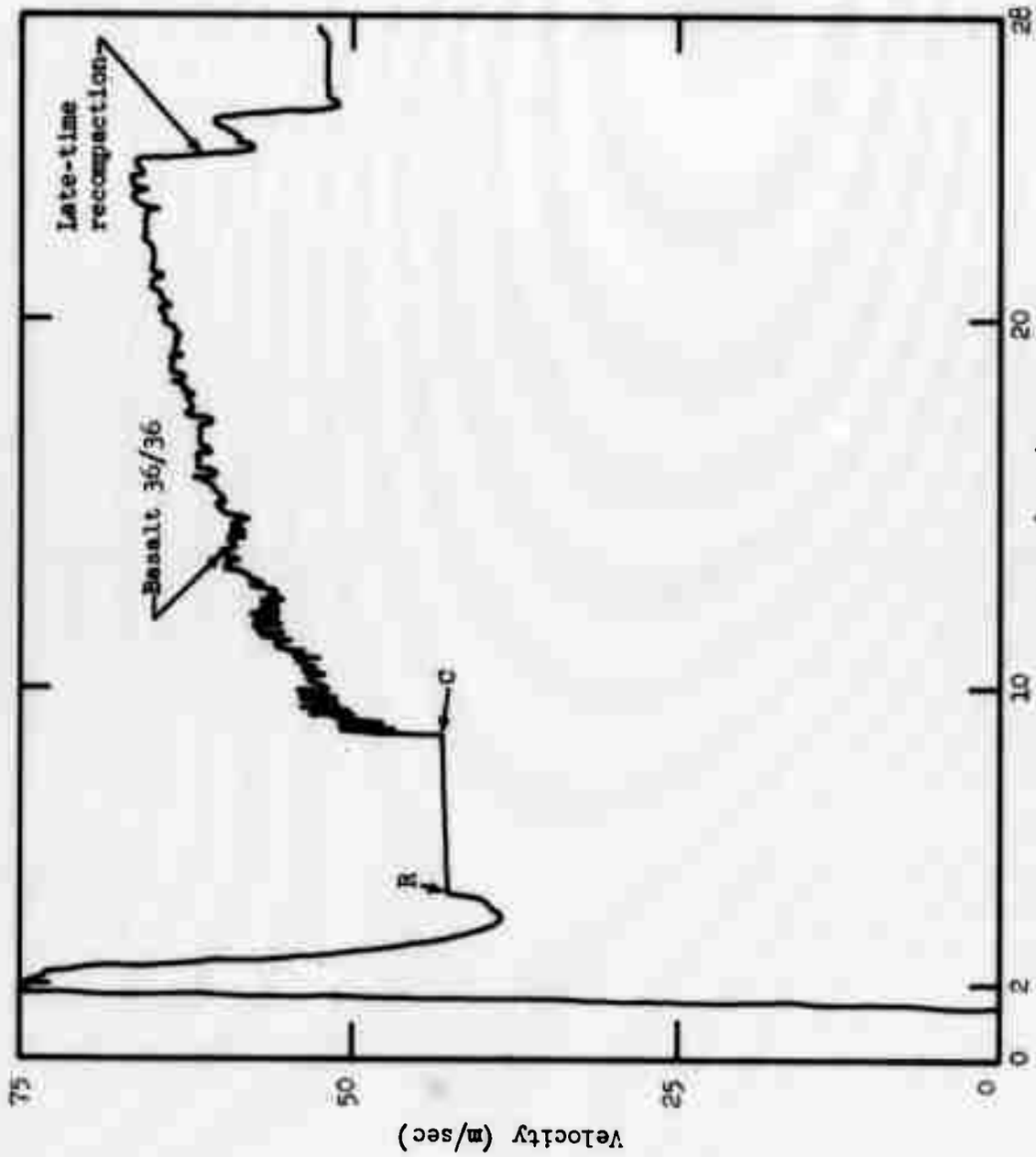

Figure 42b. Basalt, R = 6.01 m.

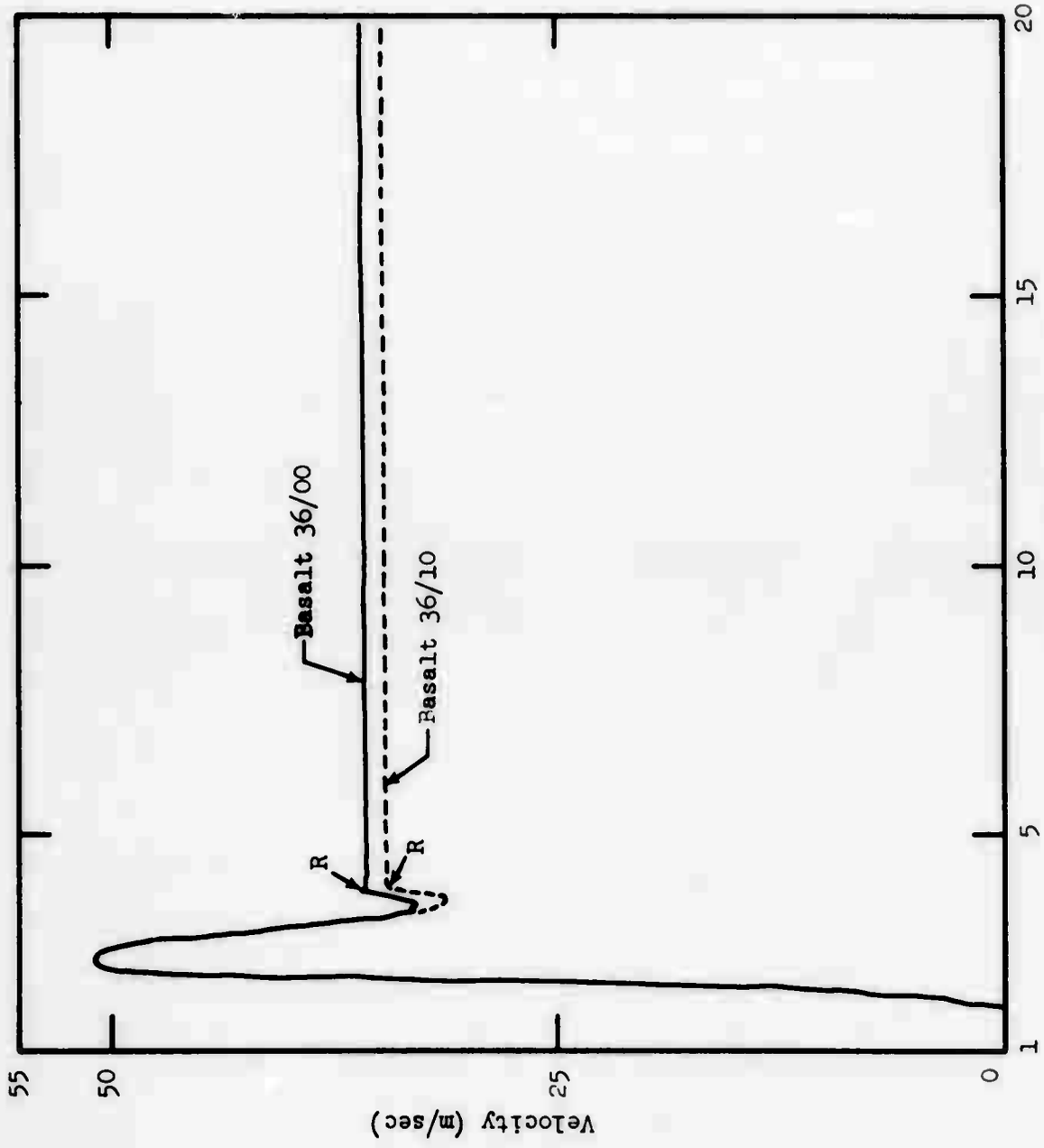

Figure 43a. Basalt, R = 8.01 m.

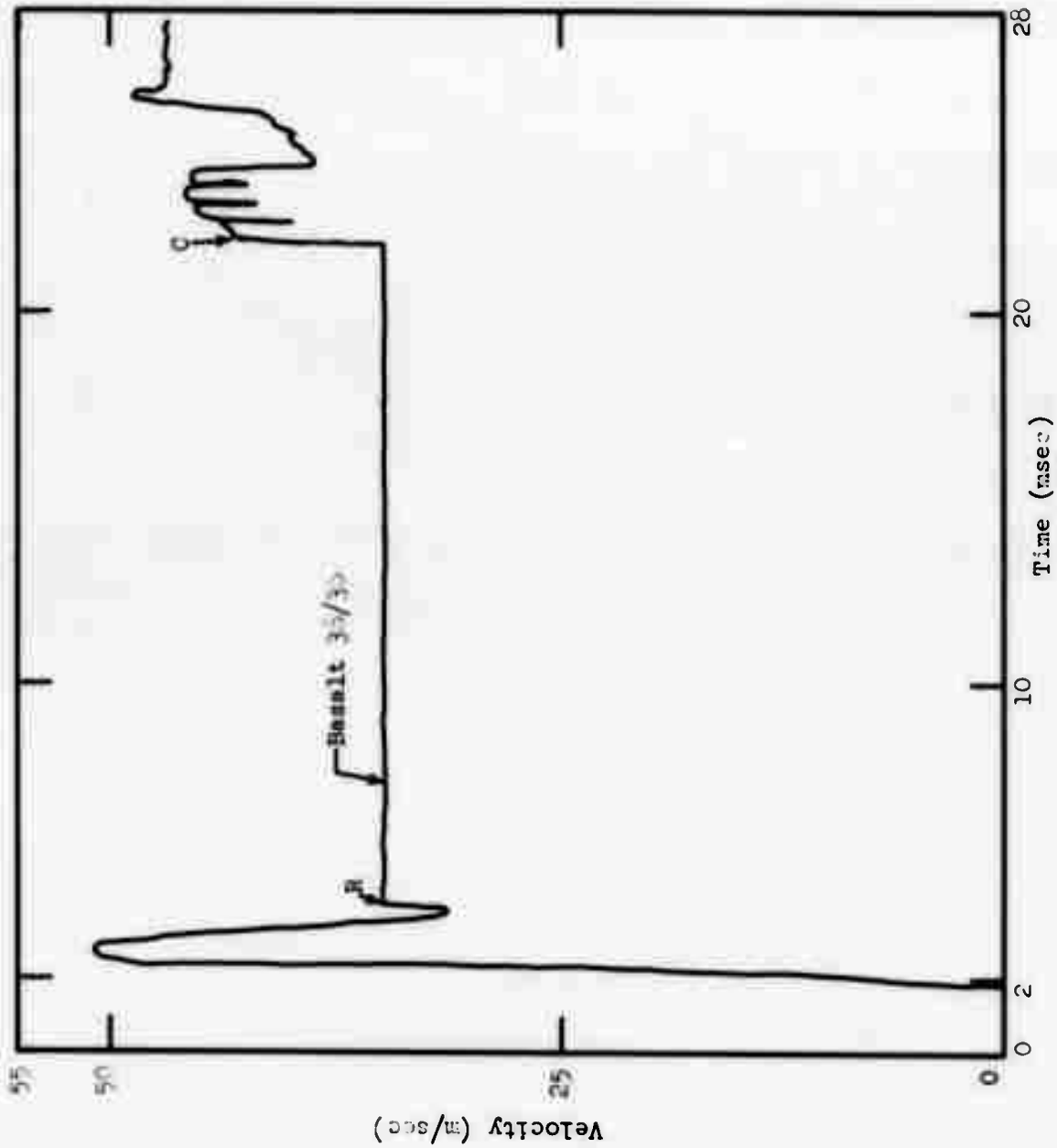

Figure 43b. Basalt, R = 8.01 m.

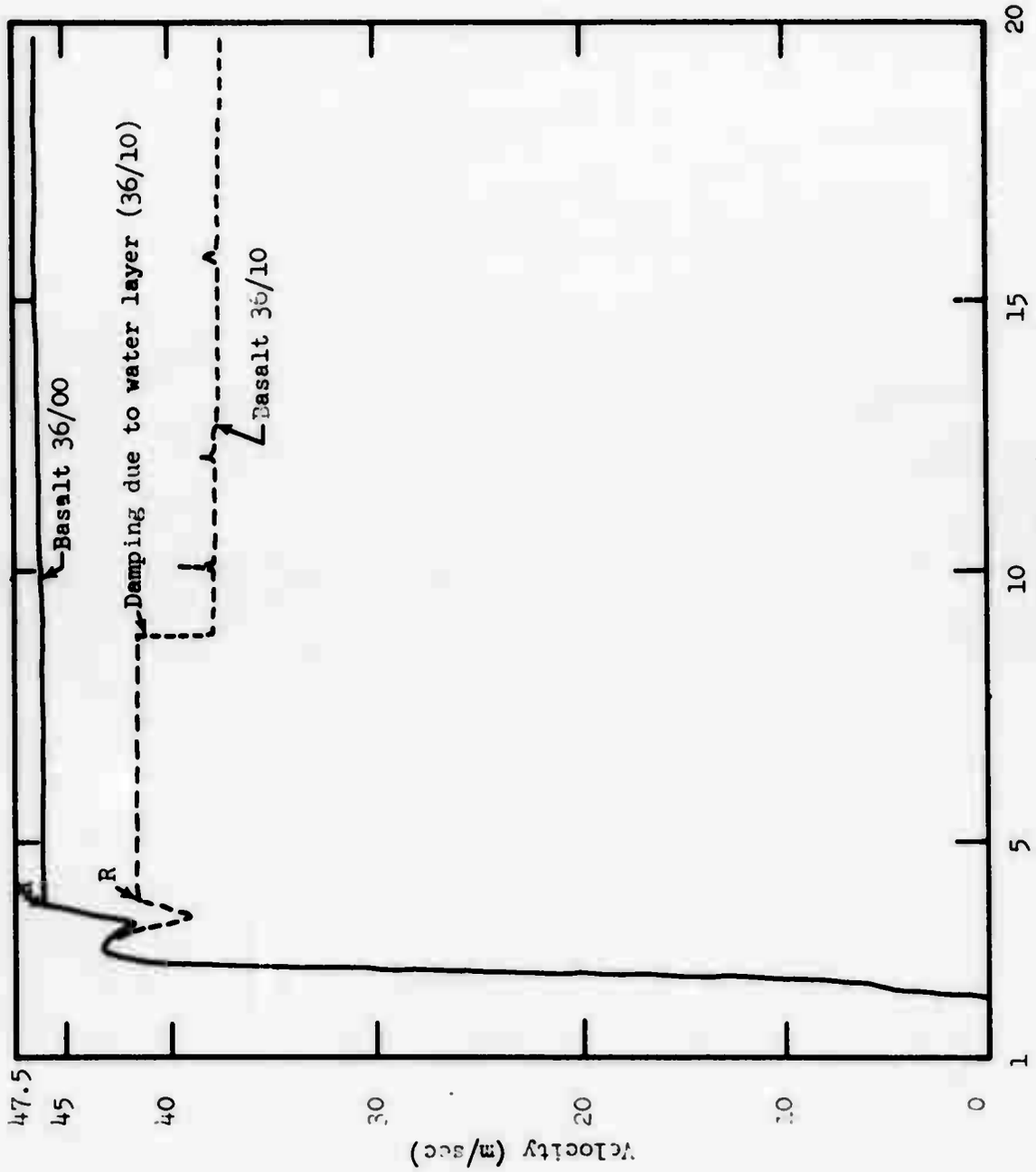

Figure 44a. Basalt, R = 9.01 m.

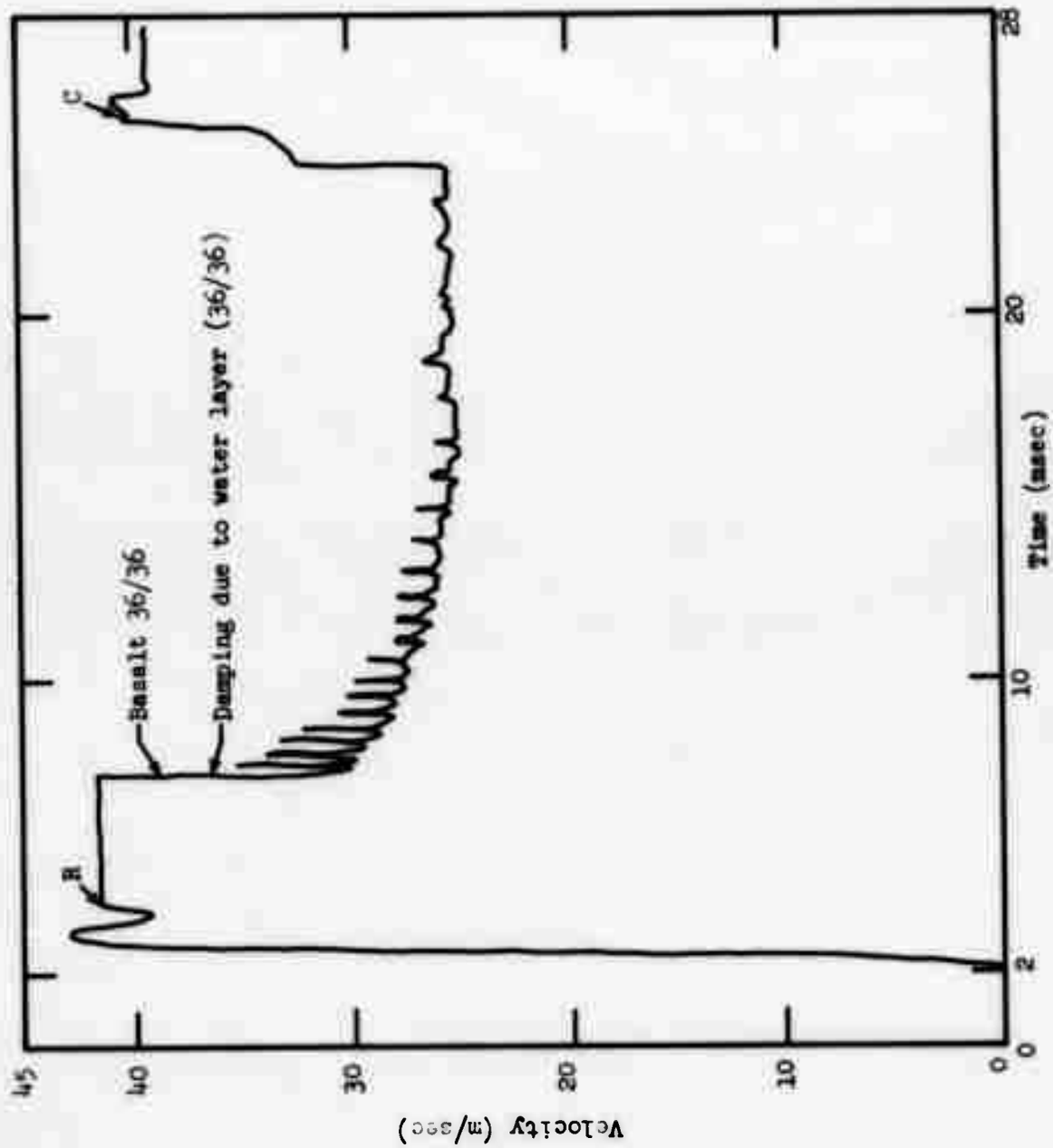

Figure 44b. Basalt, R = 9.01 m.

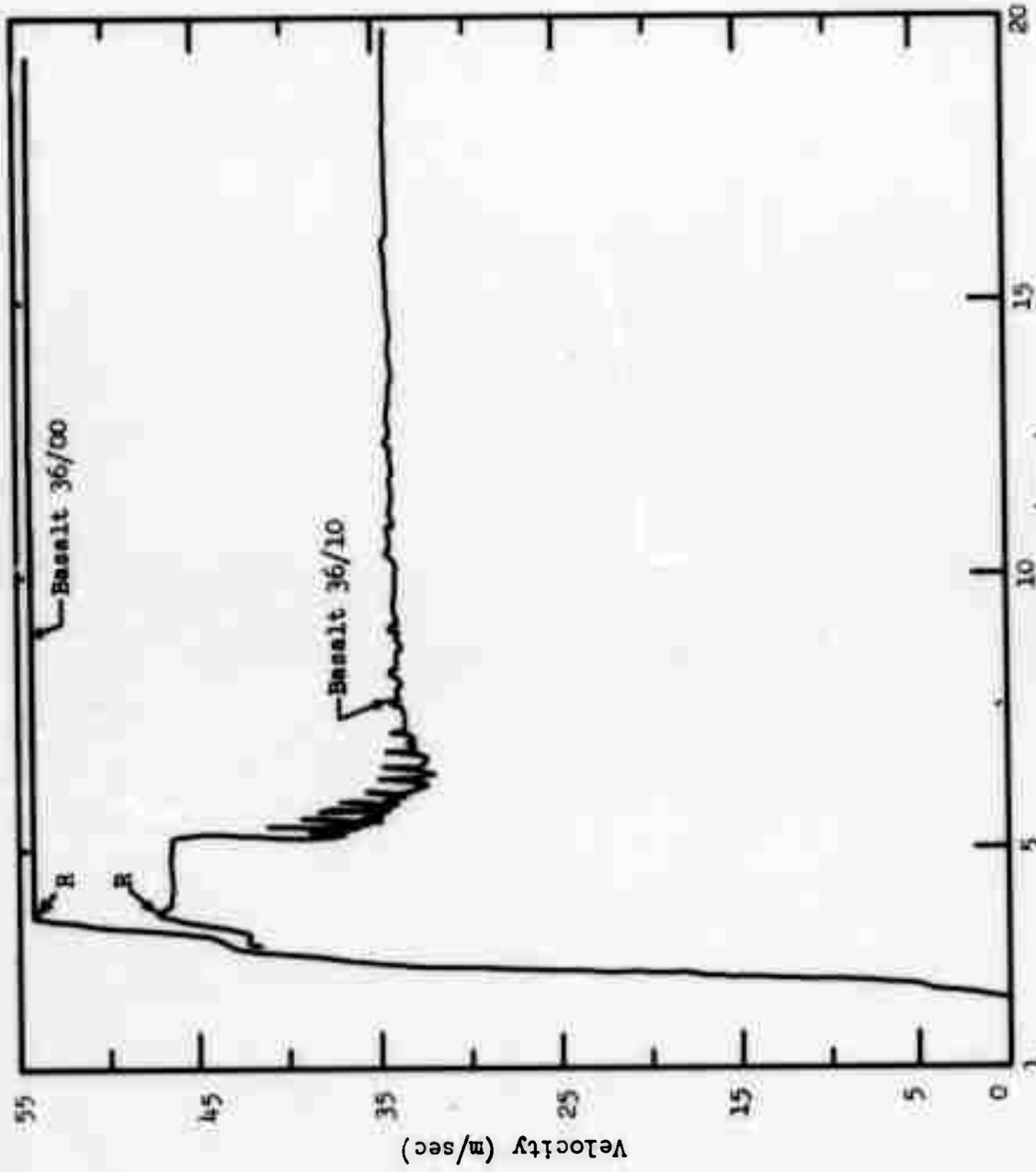

Figure 45a. Basalt, R = 5.49 m.

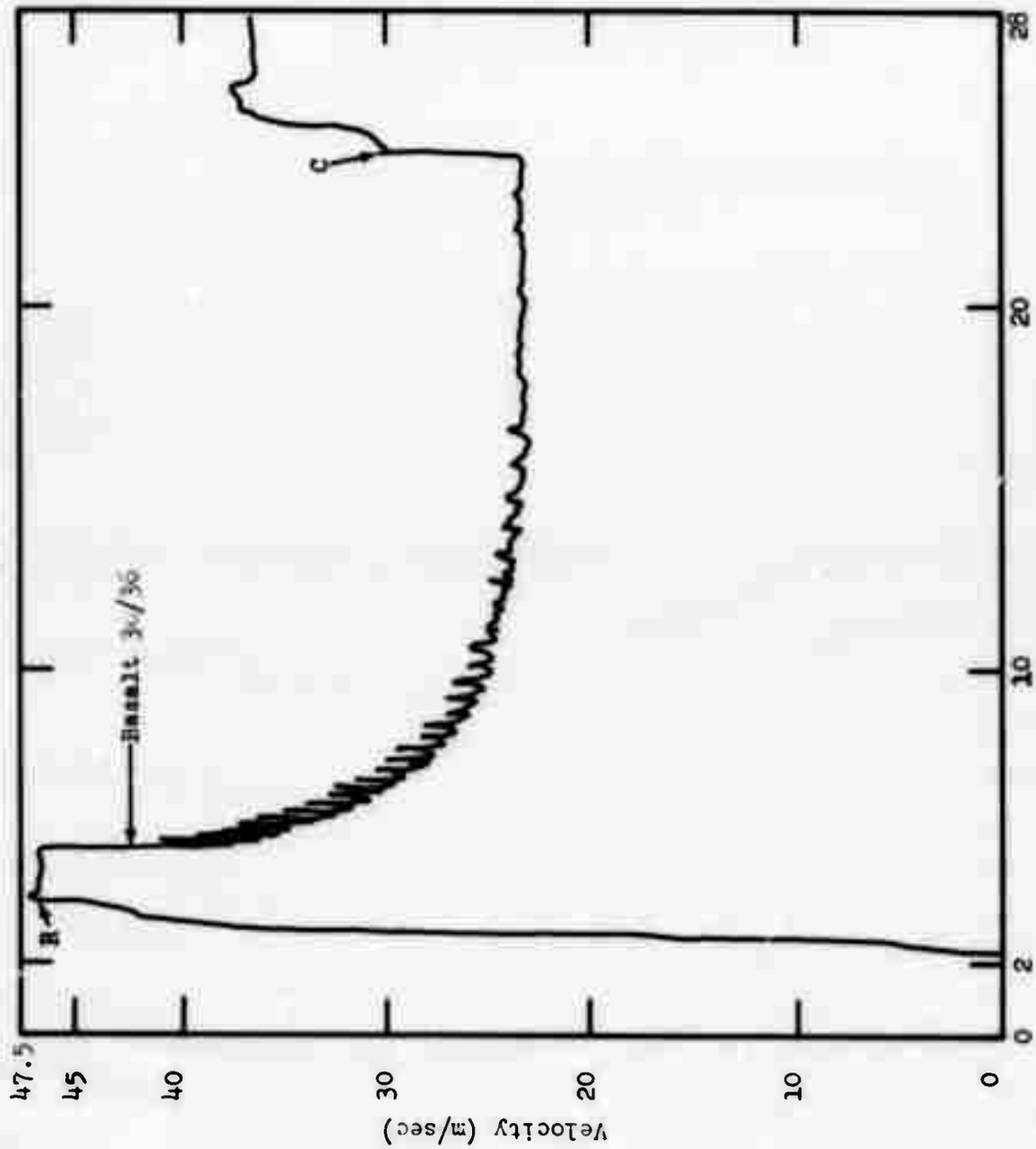

Figure 45b. Basalt, R = 9.49 m.

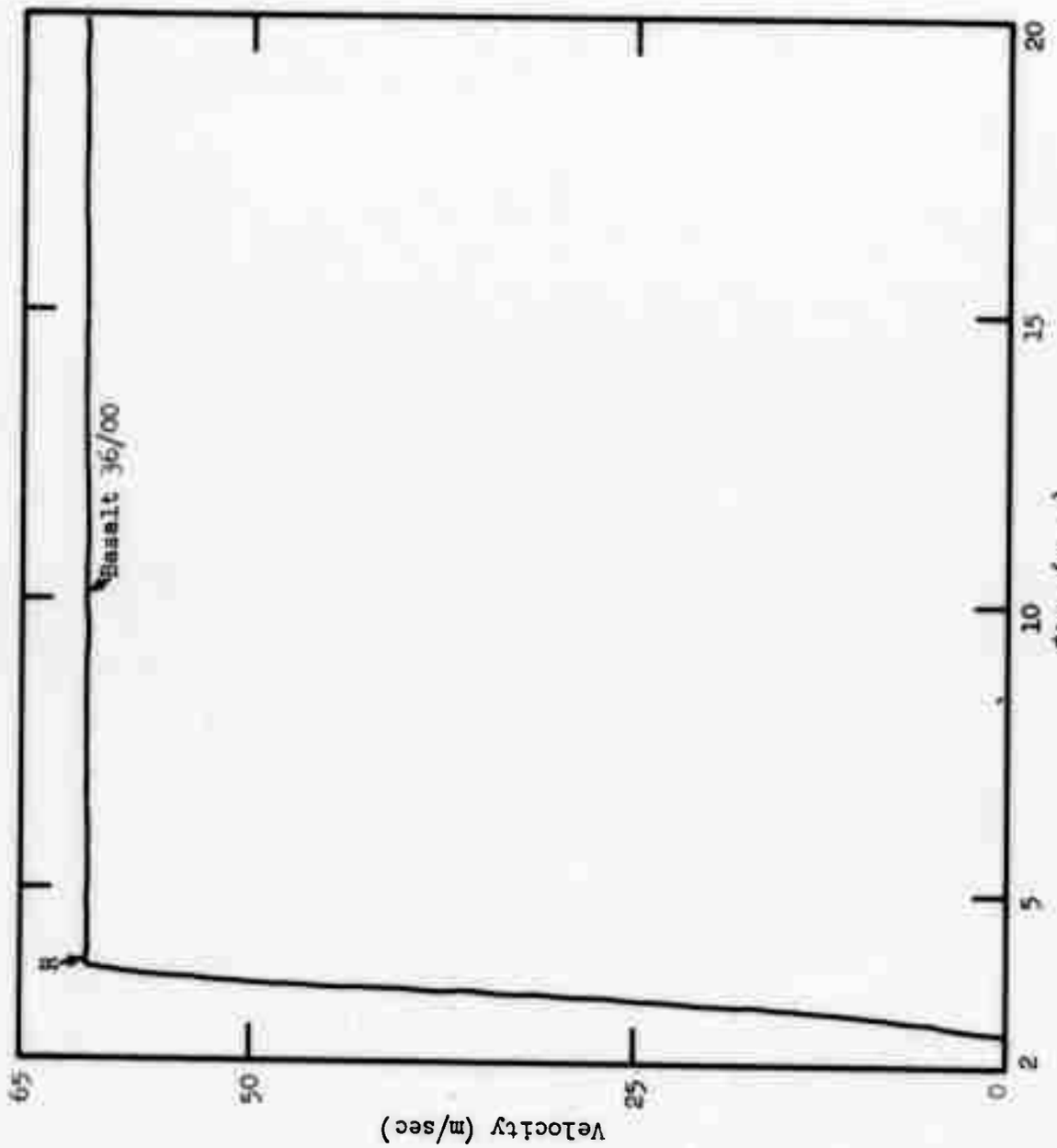

Figure 46a. Basalt, R = 10.6 m.

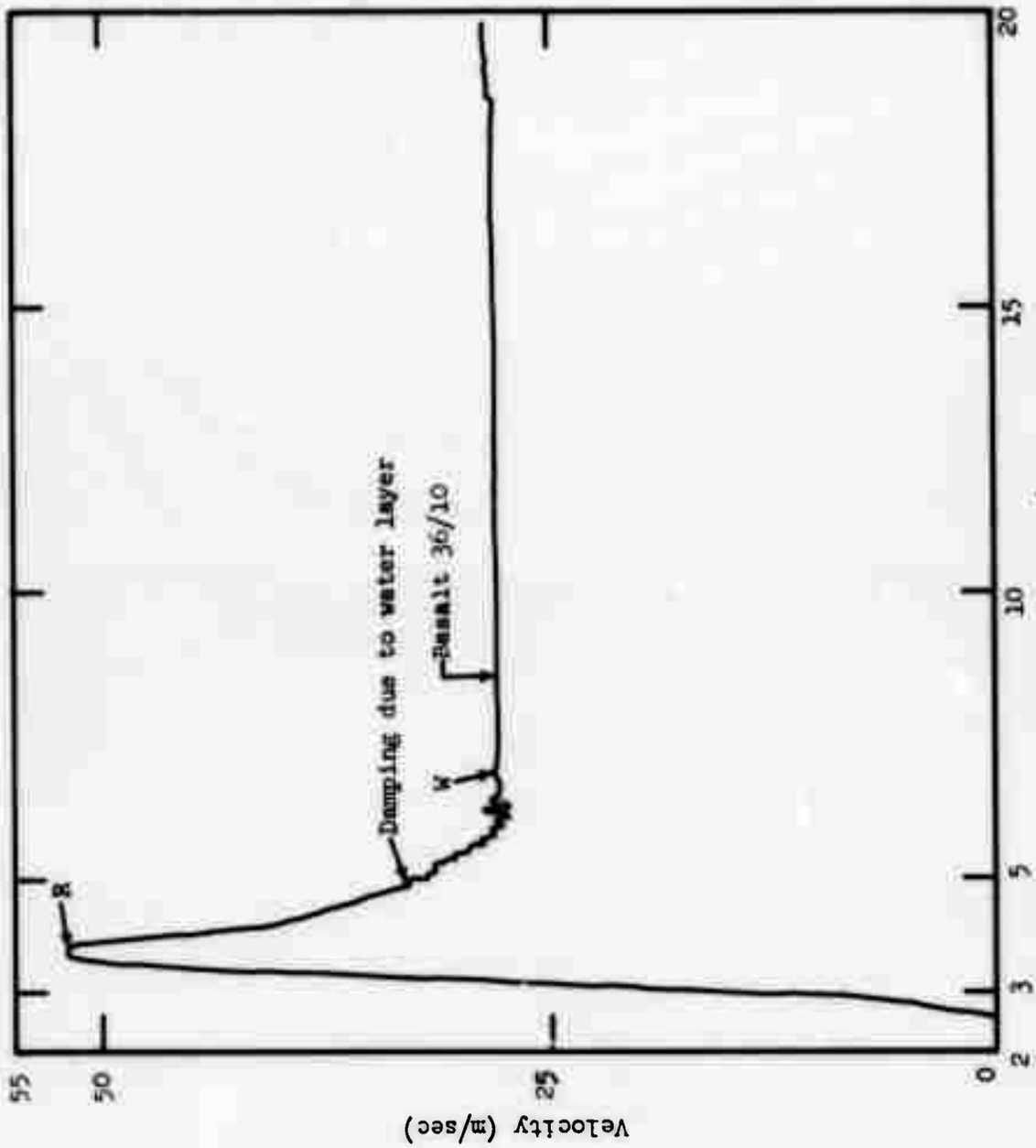

Figure 46b. Basalt, R = 10.6 m

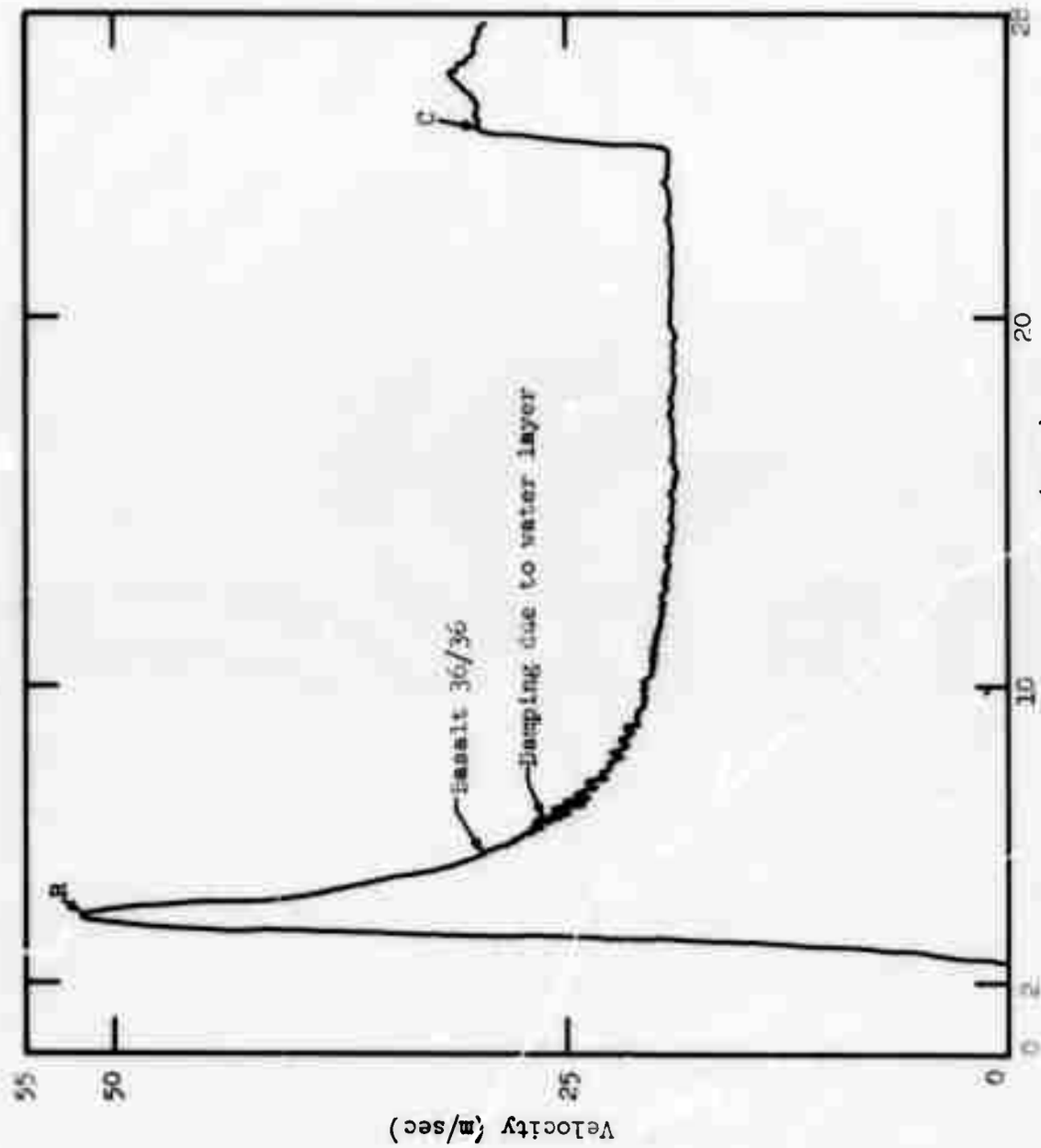

Figure 46c. Basalt, R = 10.6 m.

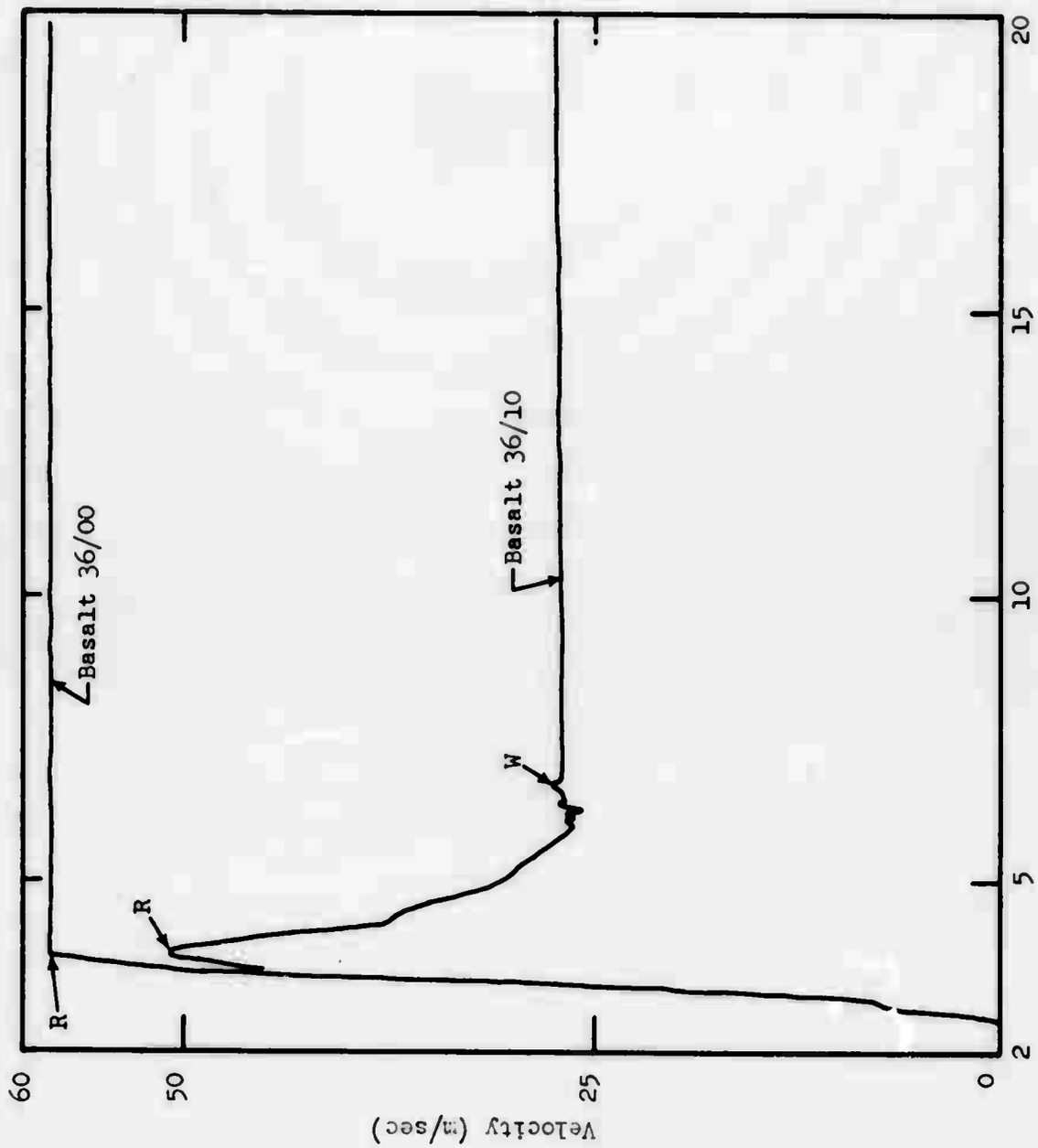

Figure 47a. Basalt, R = 10.89 m

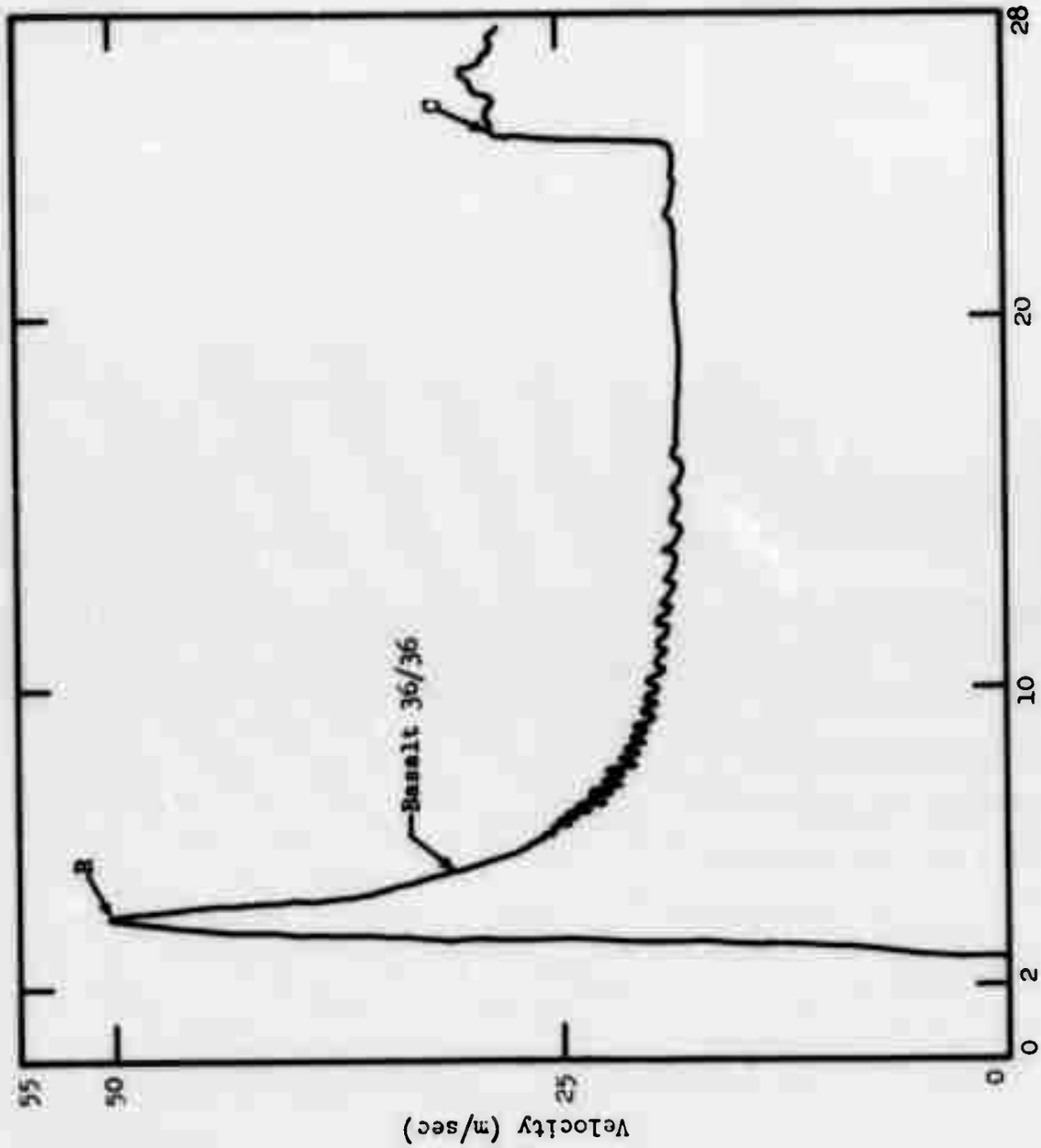

Figure 47b. Basalt, R = 10.89 m.

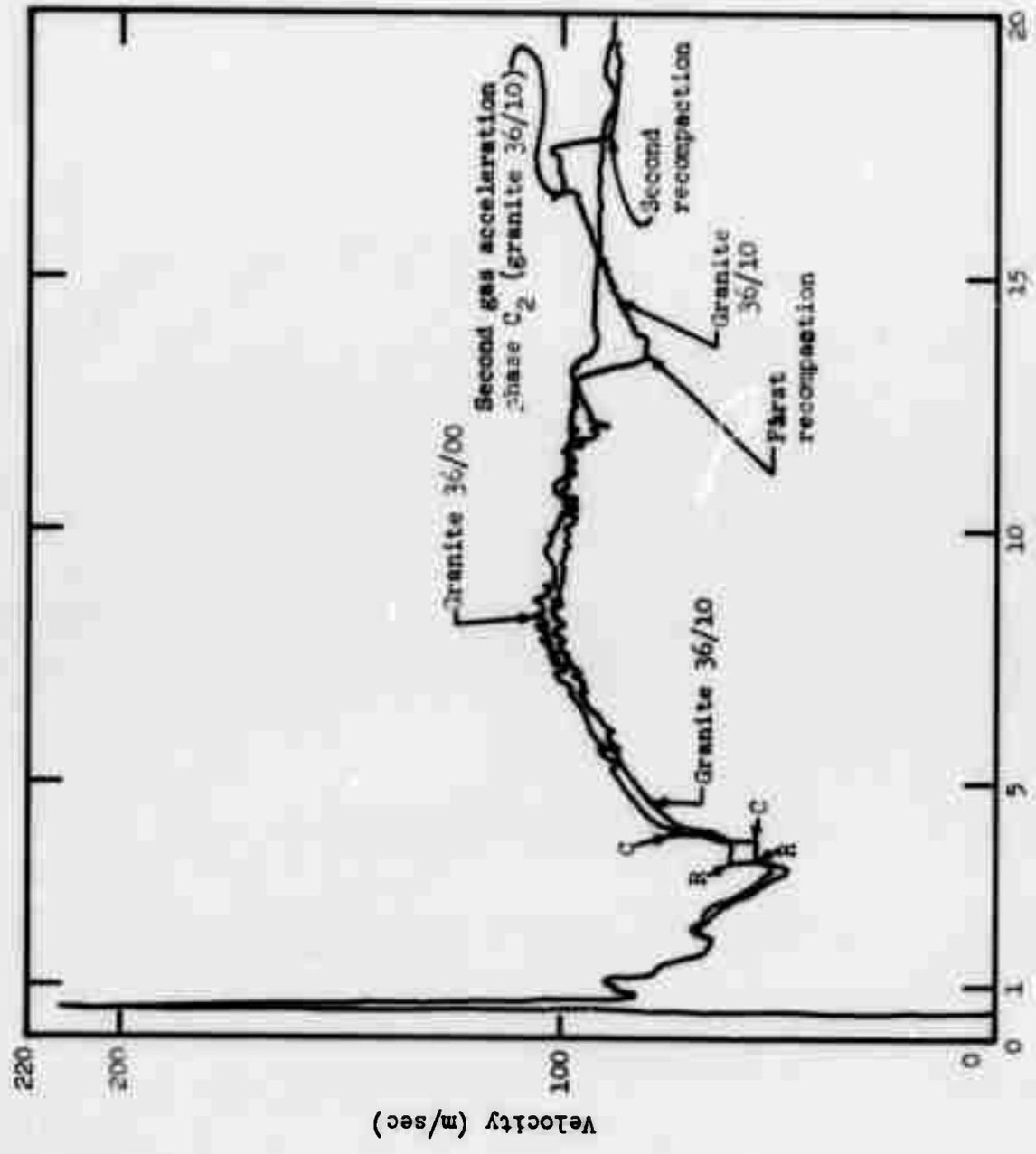

Figure 48a. Granite, R = 3.01 m.

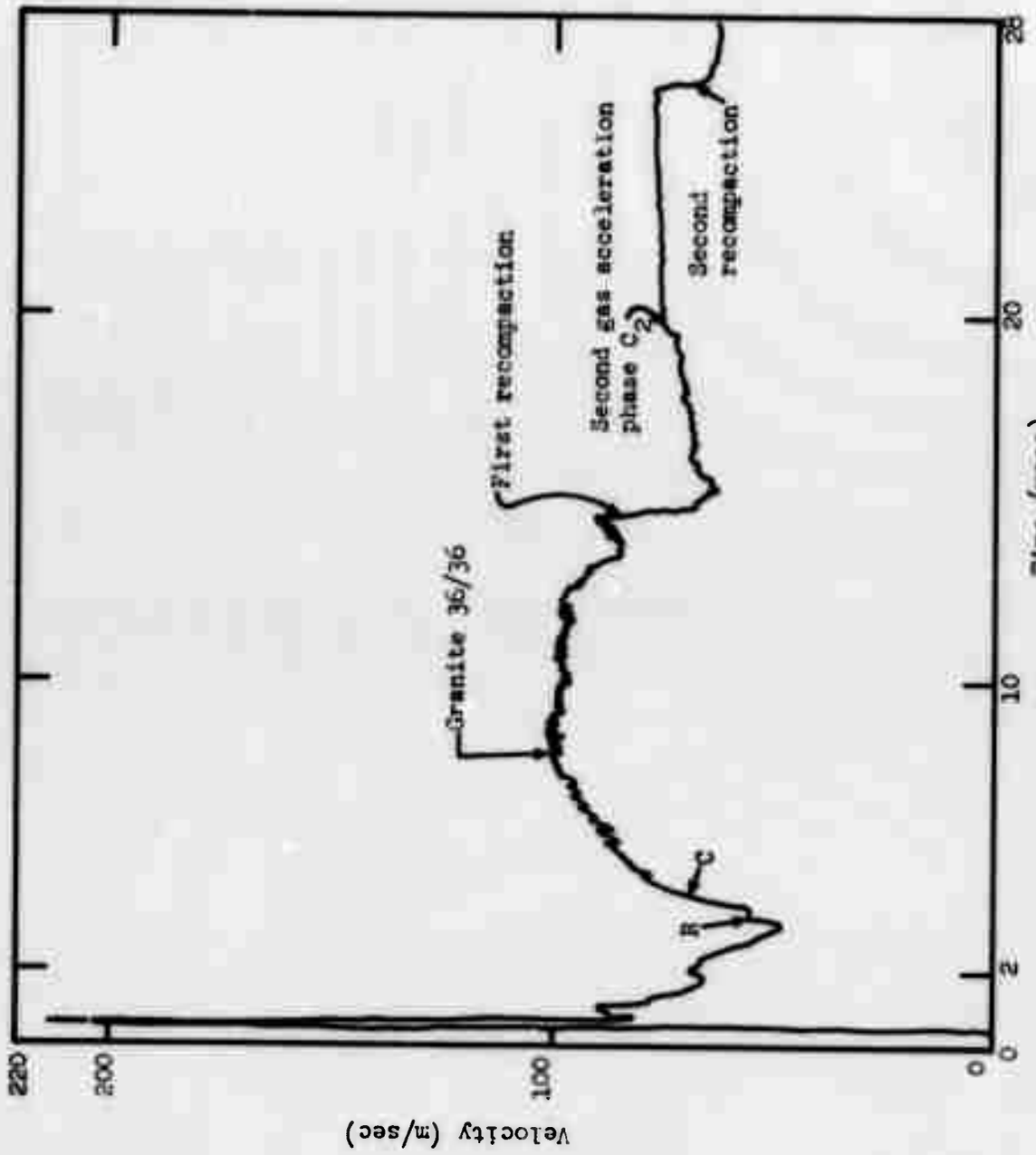

Figure 48b. Granite, R = 3.01 m.

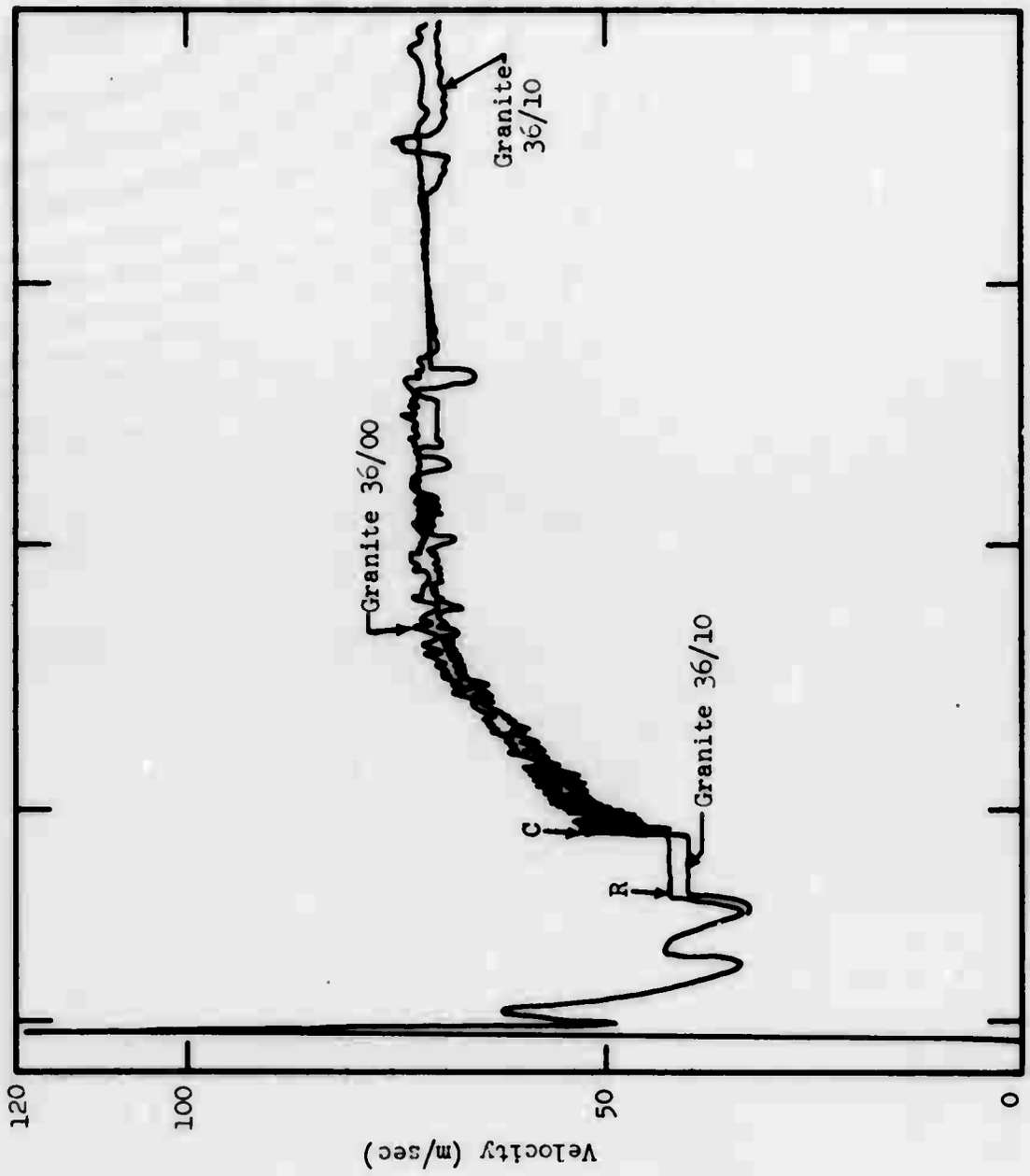

Figure 49a. Granite, R = 4.01 m.

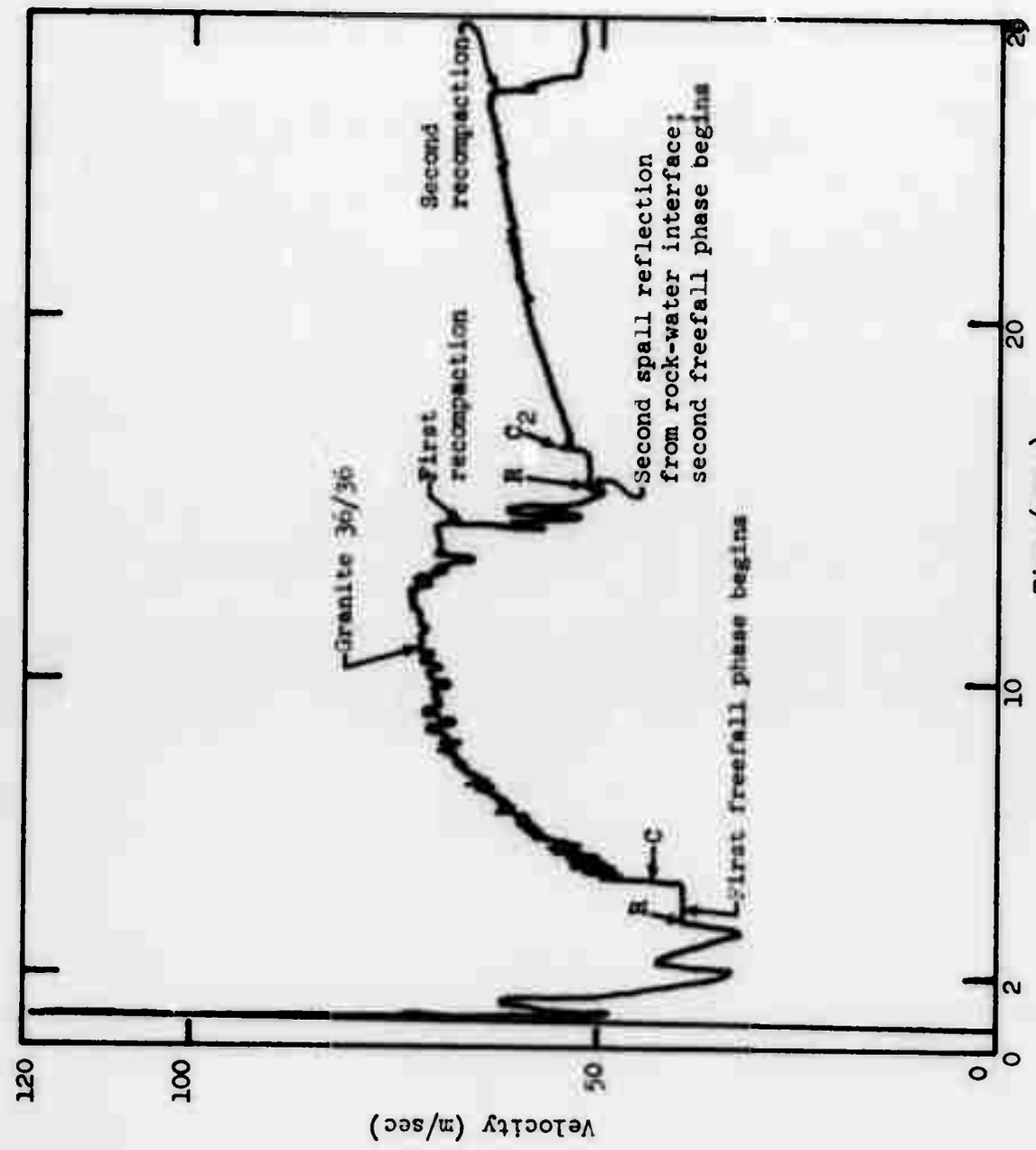

Figure 49b. Granite, R = 4.01 m.

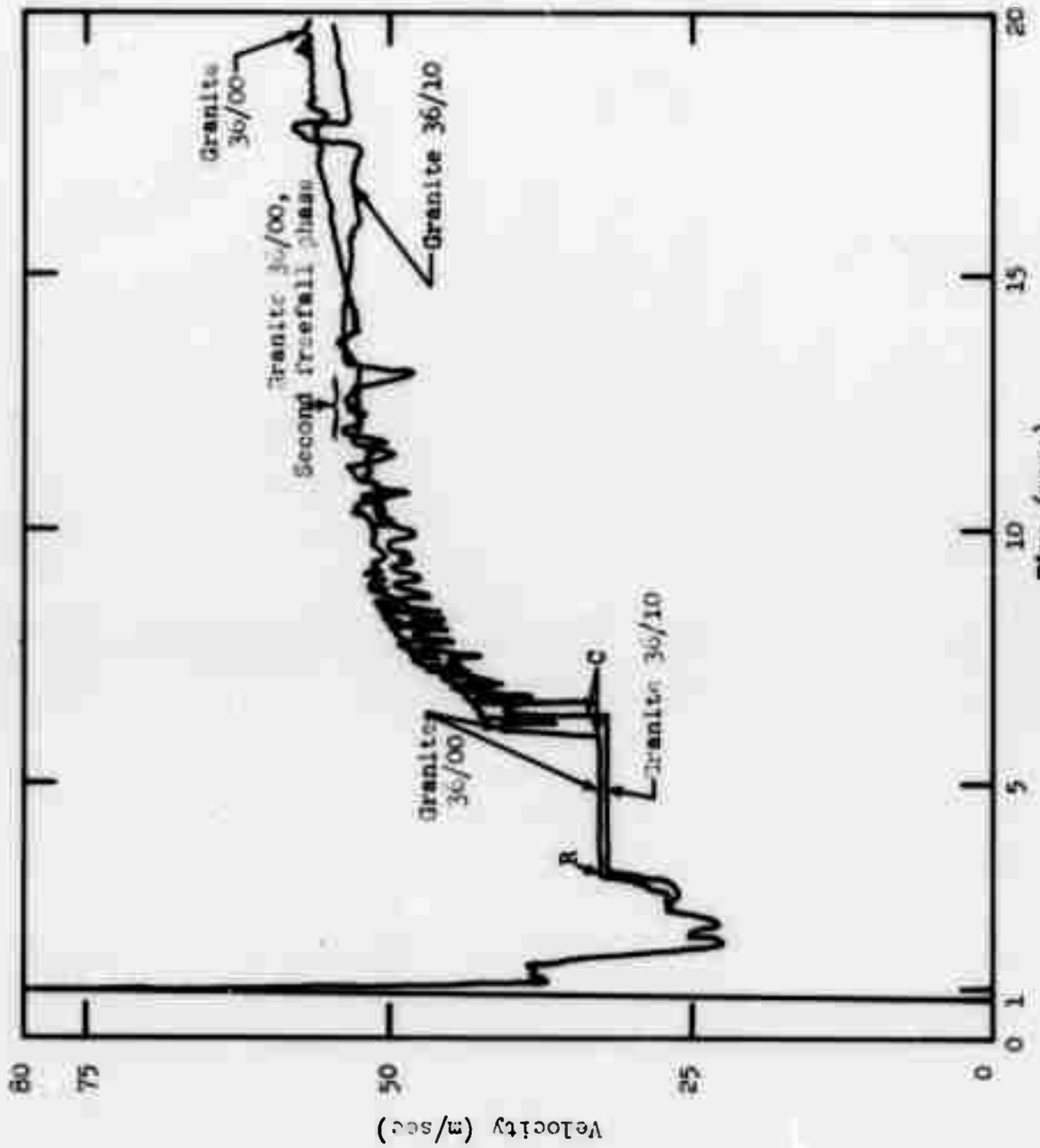

Figure 50a. Granite, R = 5.01 m.

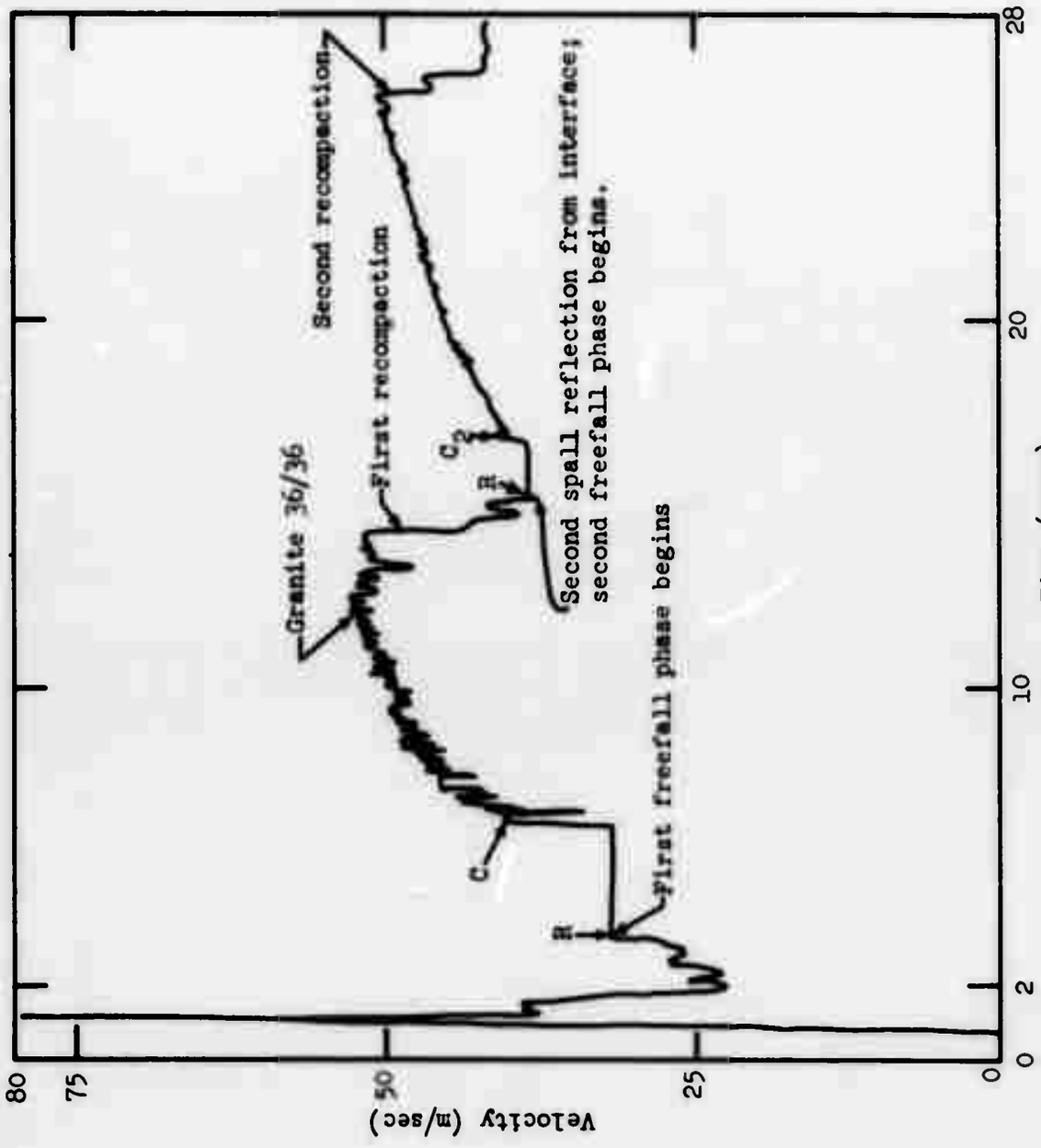

Figure 50b. Granite, R = 5.01 m.

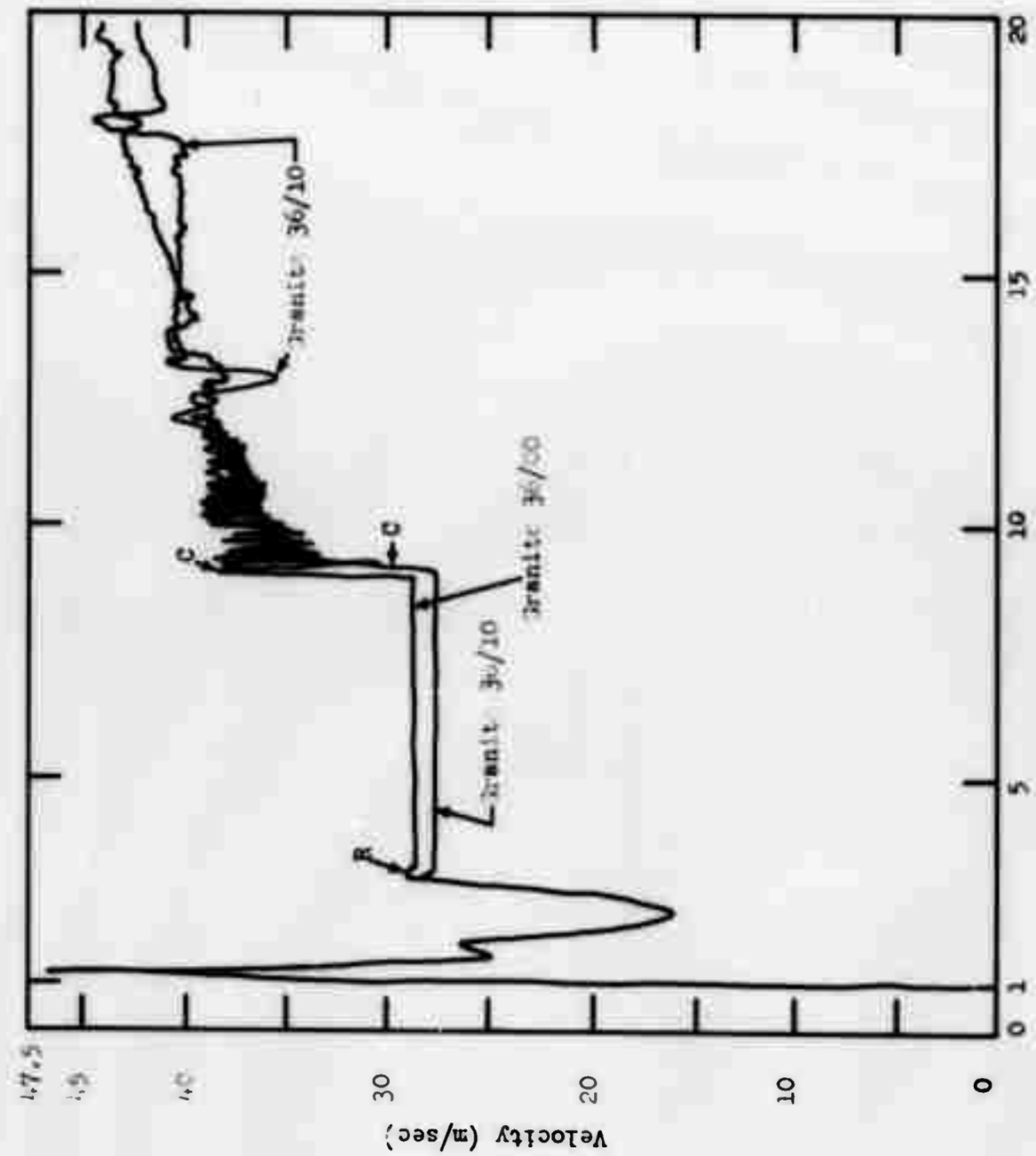

Figure 51a. Granite, R = 6.01 m.

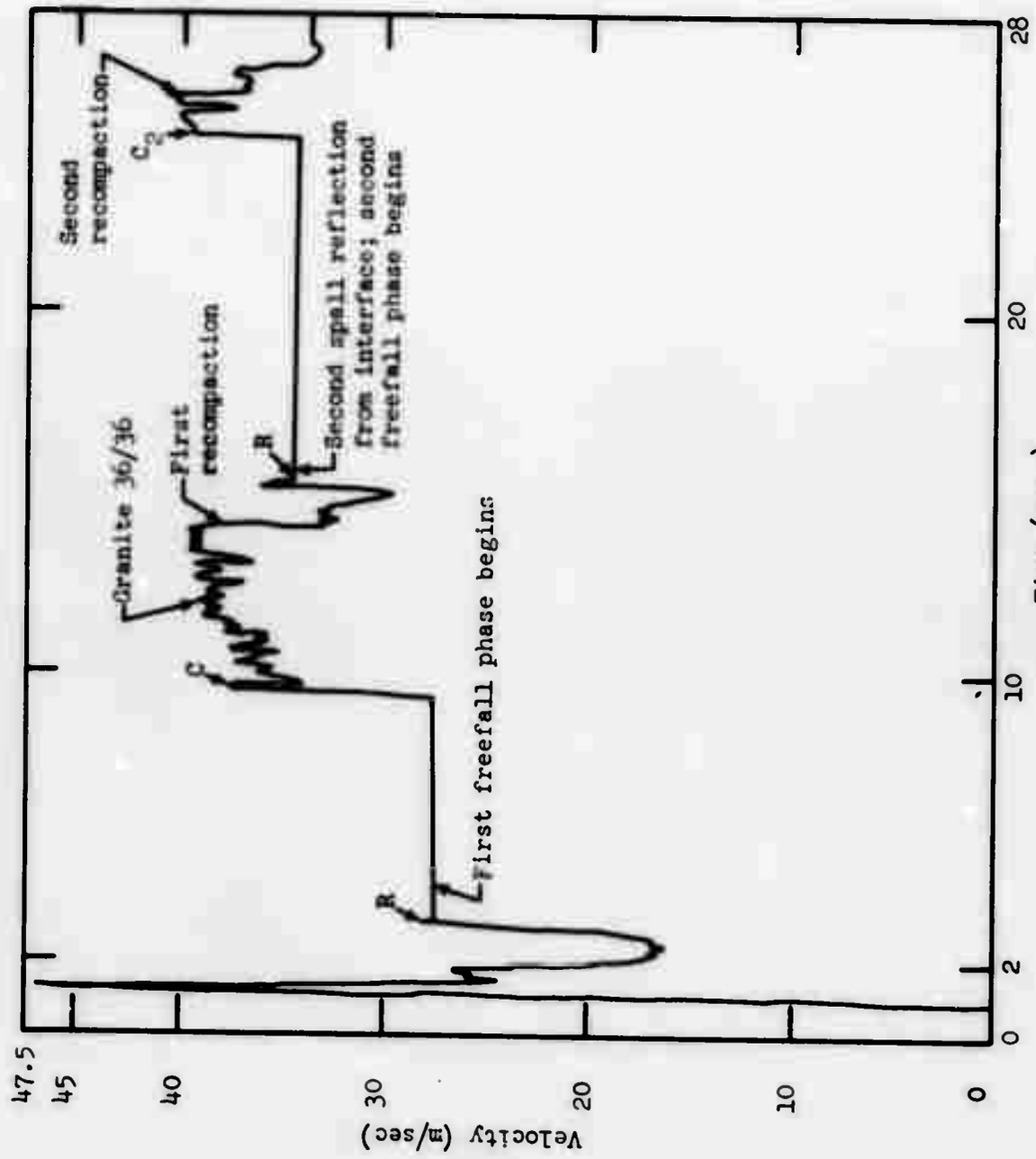

Figure 51b. Granite, R = 6.01 m.

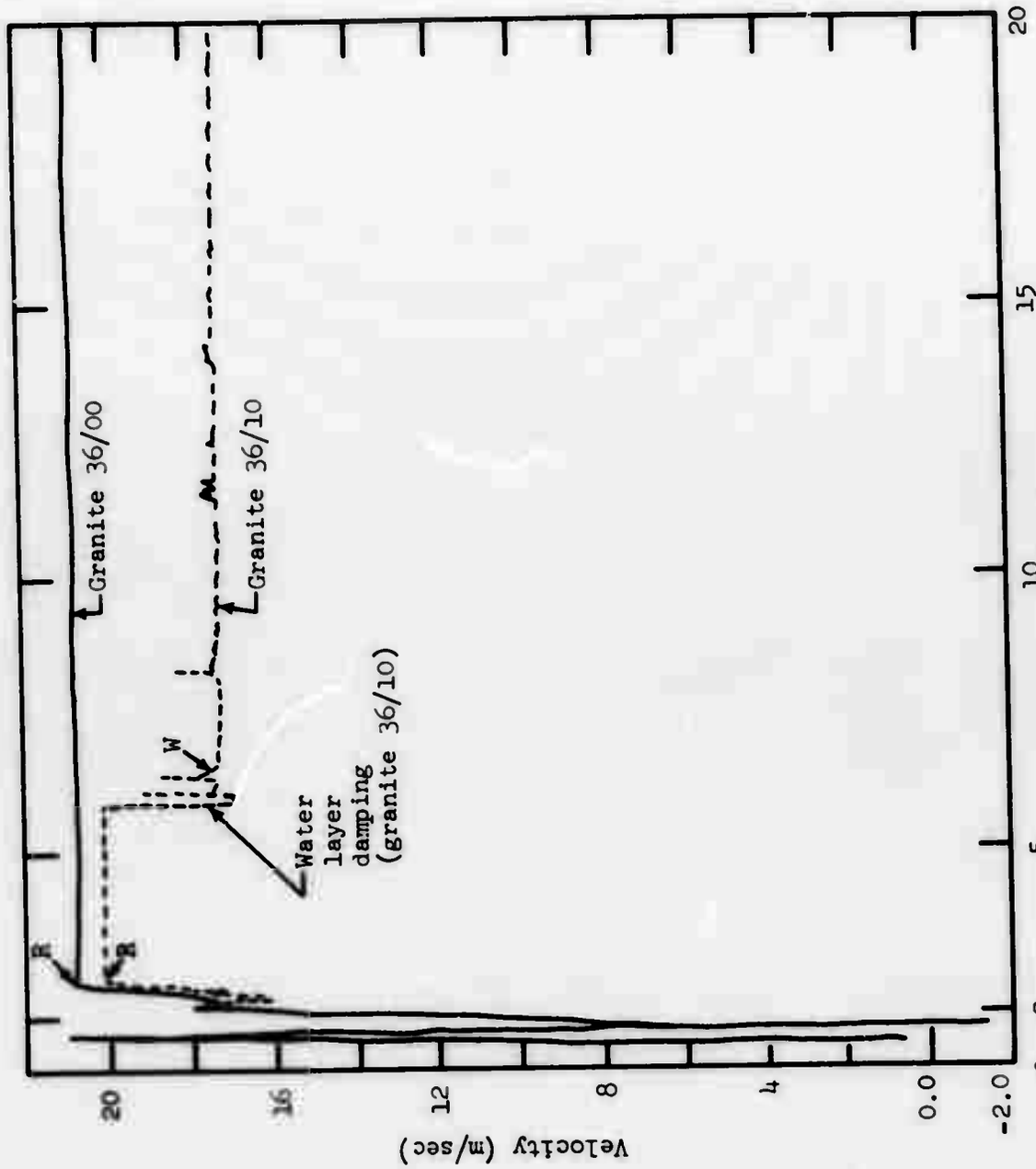

Figure 52a. Granite, R = 9.01 m.

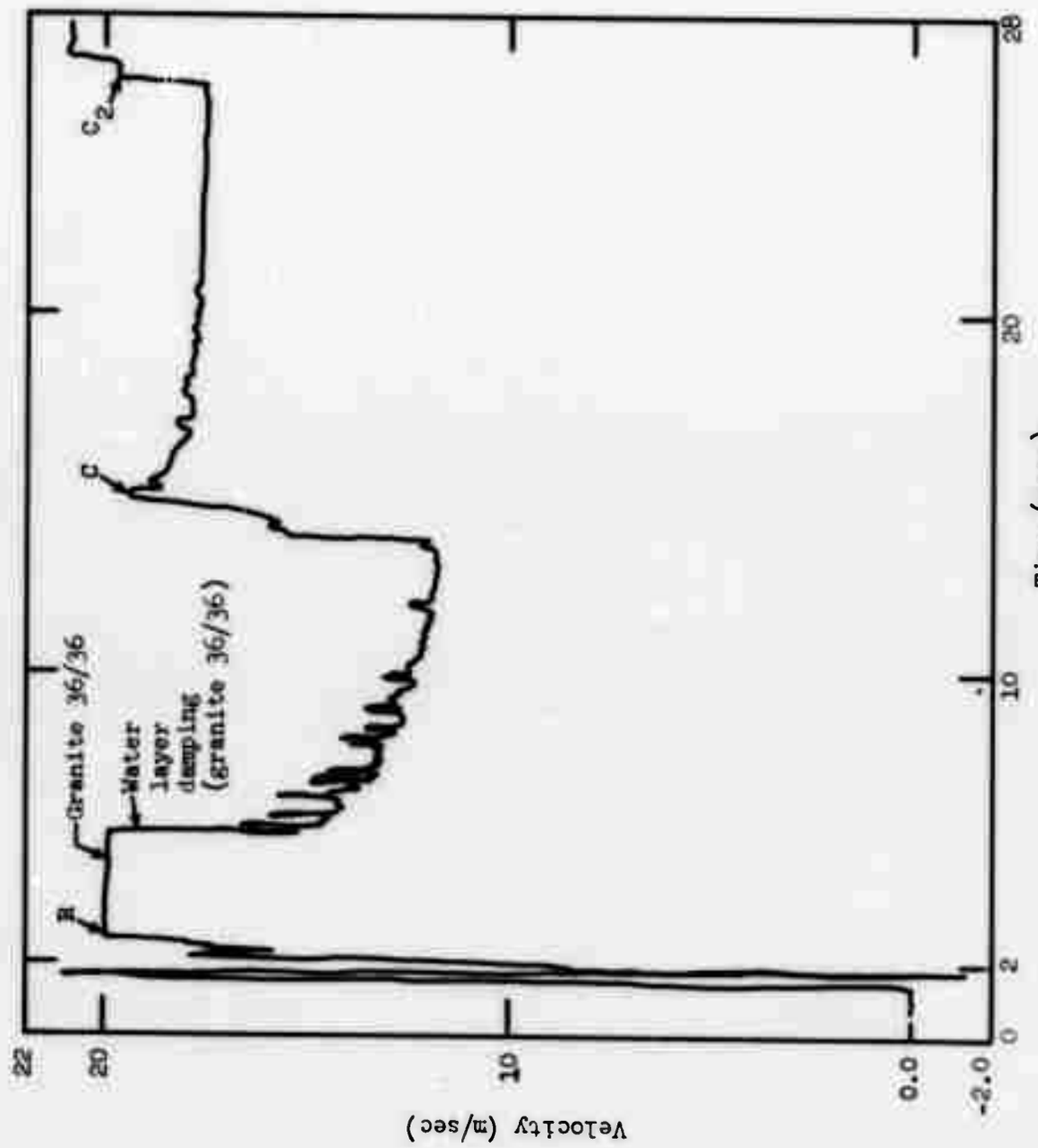

Figure 52b. Granite, R = 9.01 m.

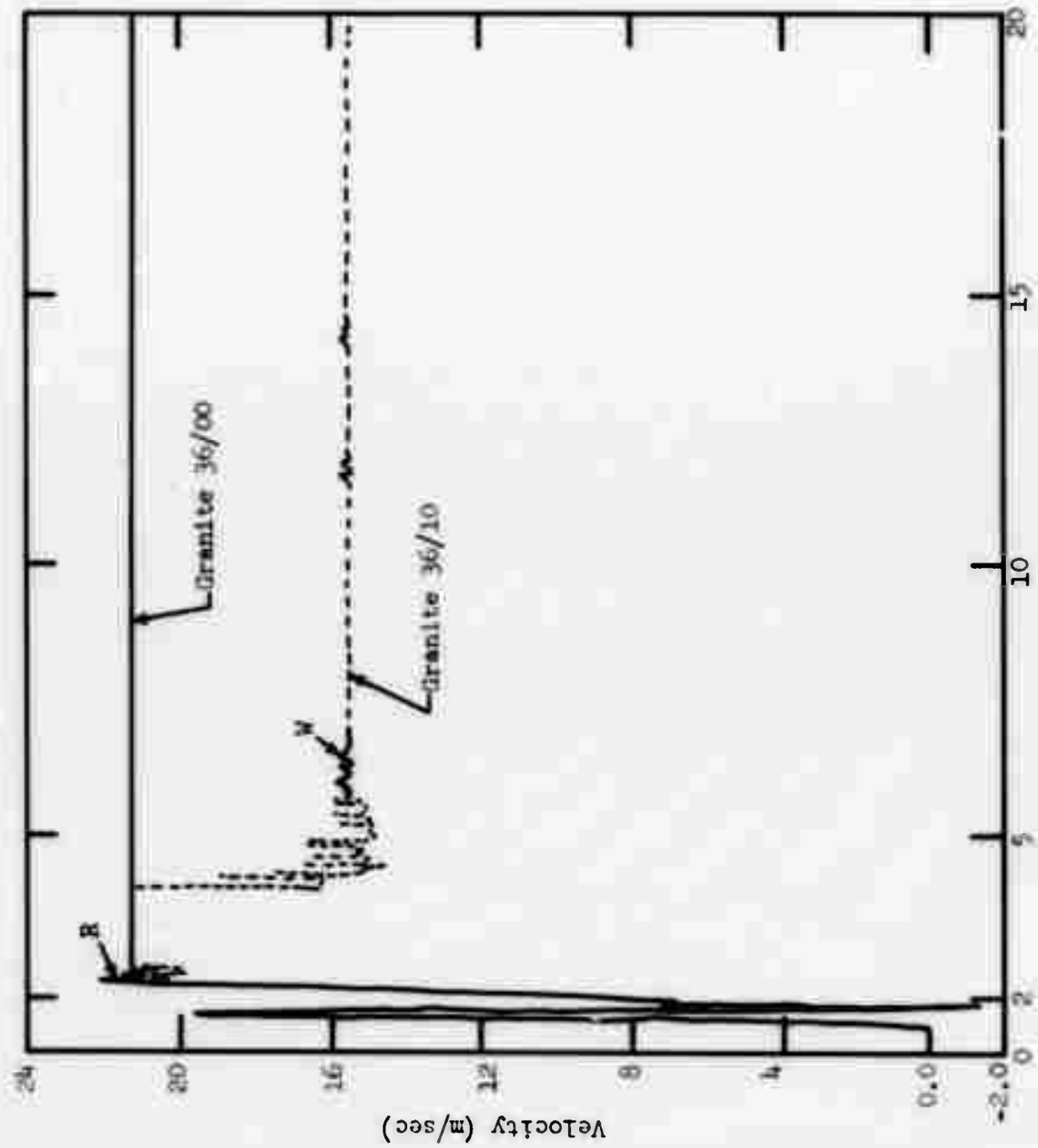

Figure 53a. Granite, R = 9.49 m.

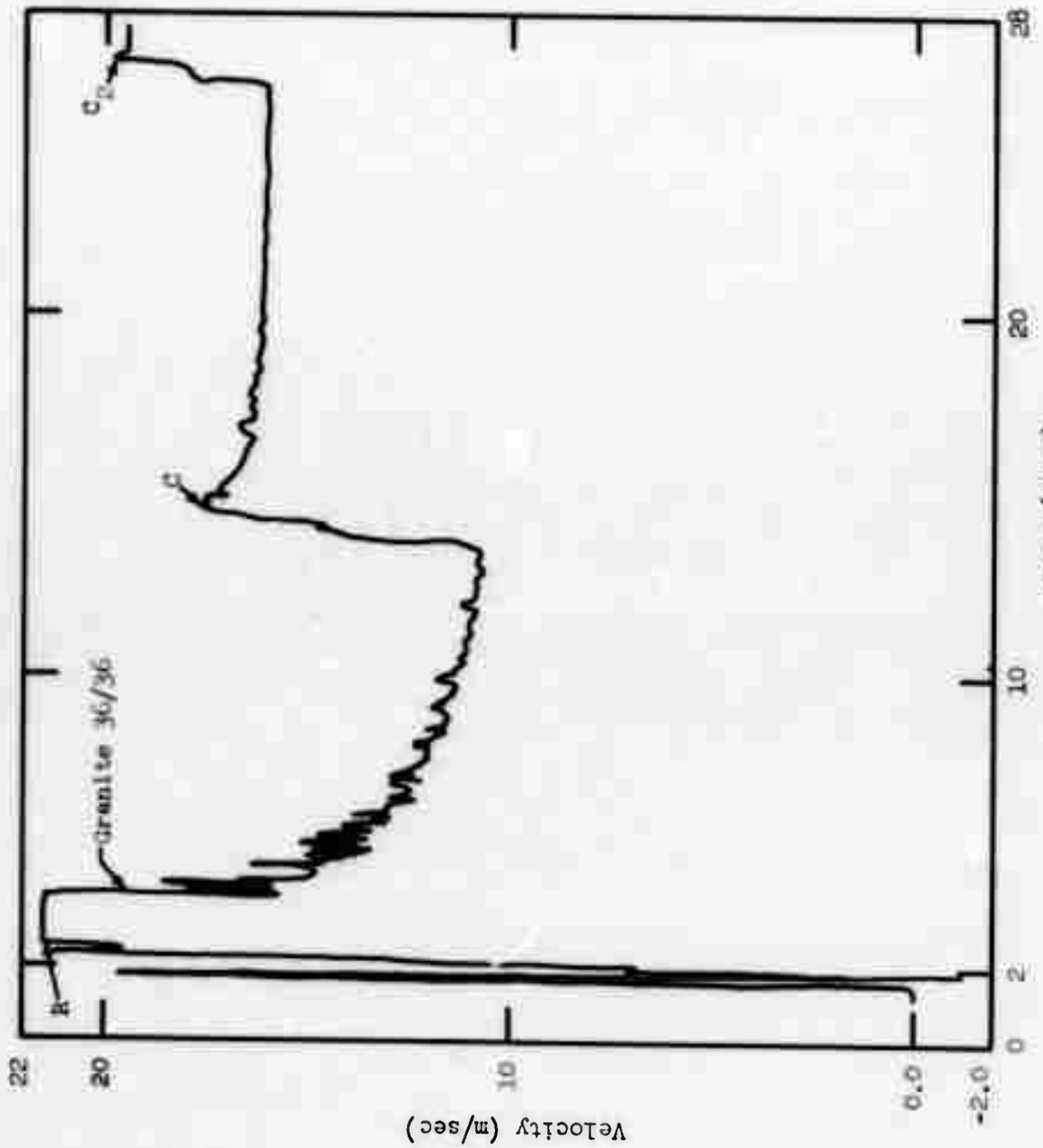

Figure 53b. Granite, R = 9.49 m.

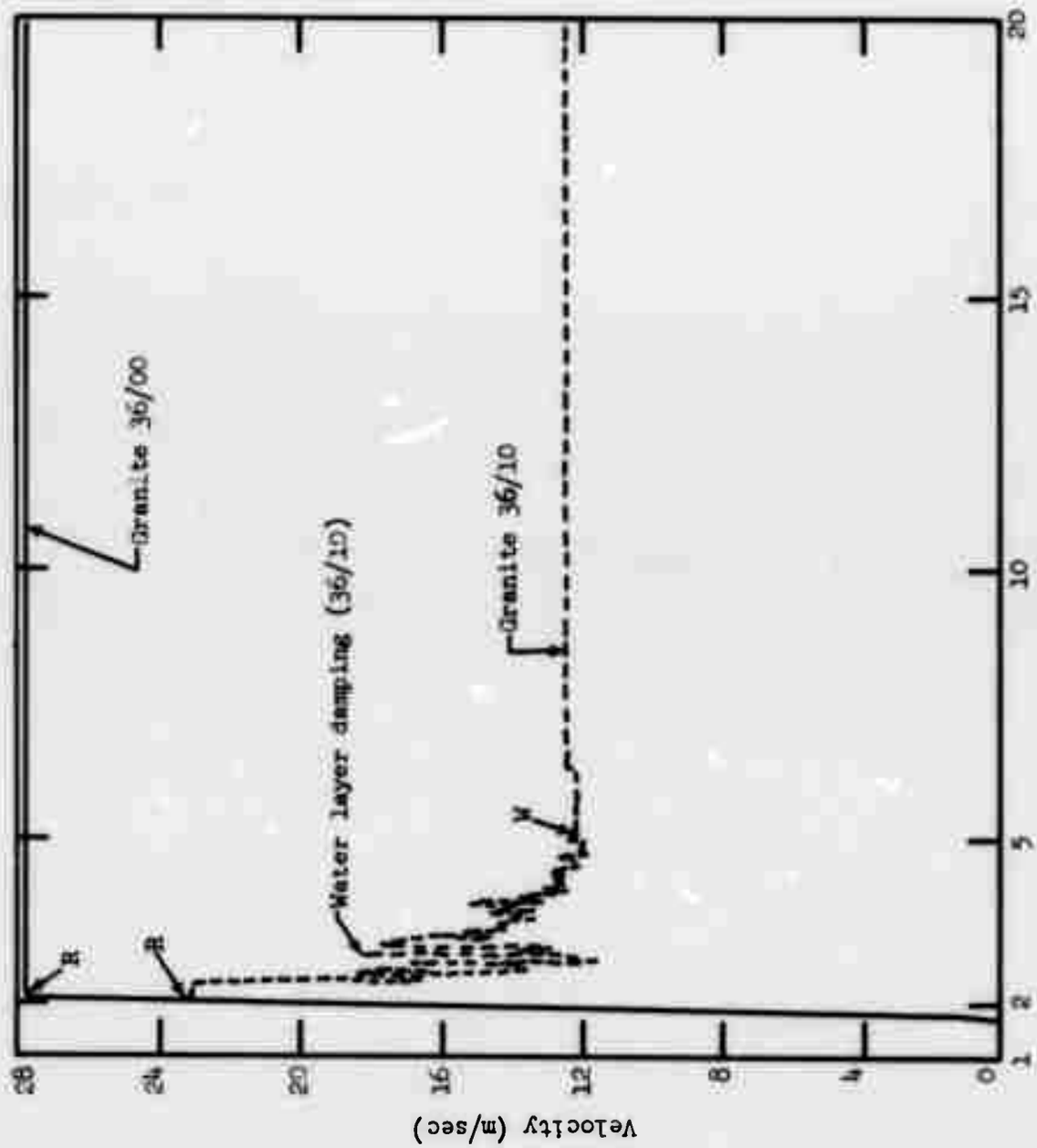

Figure 54a. Granite, R = 10.6 m.

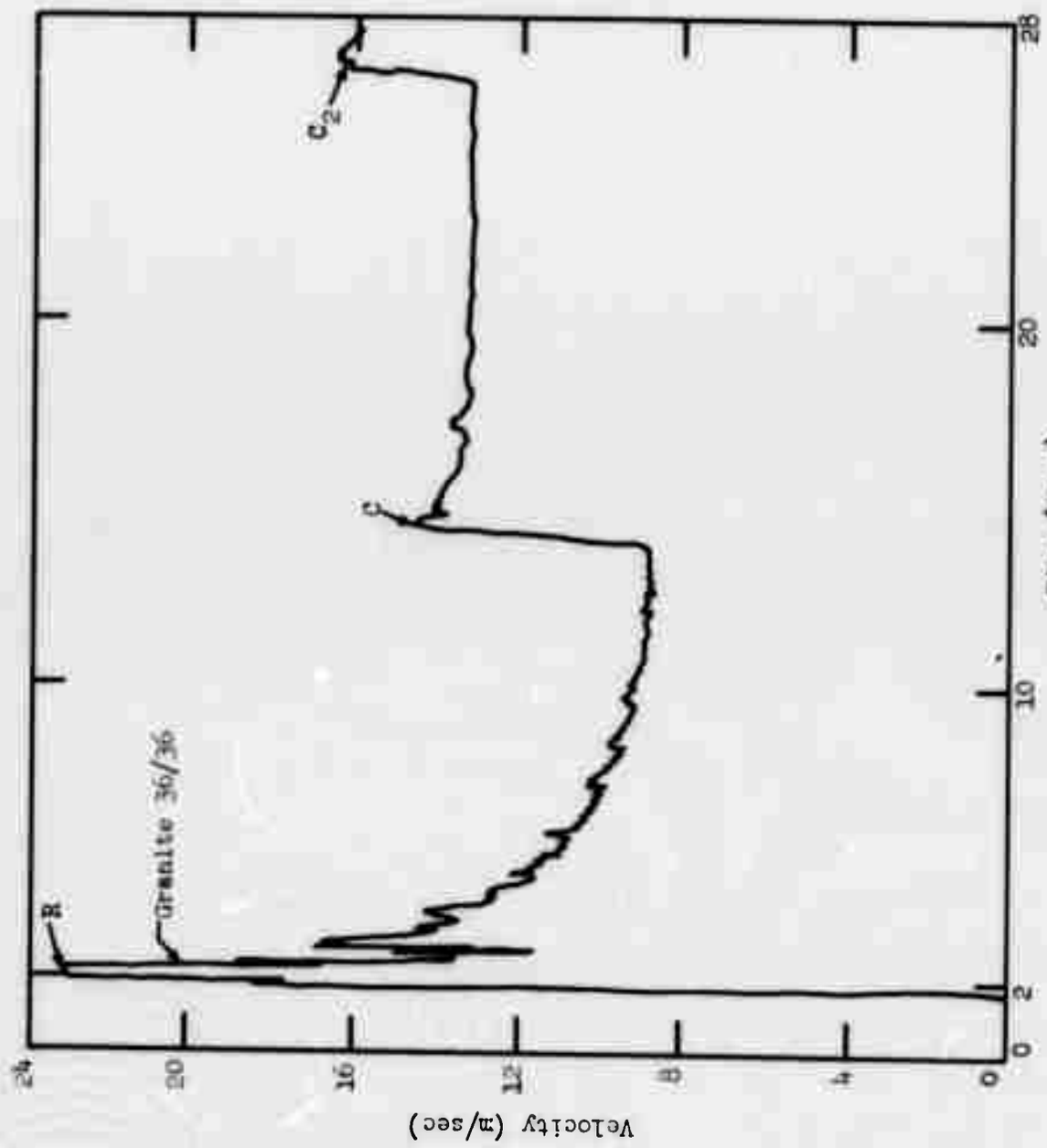

Figure 54b. Granite, R = 10.6 m.

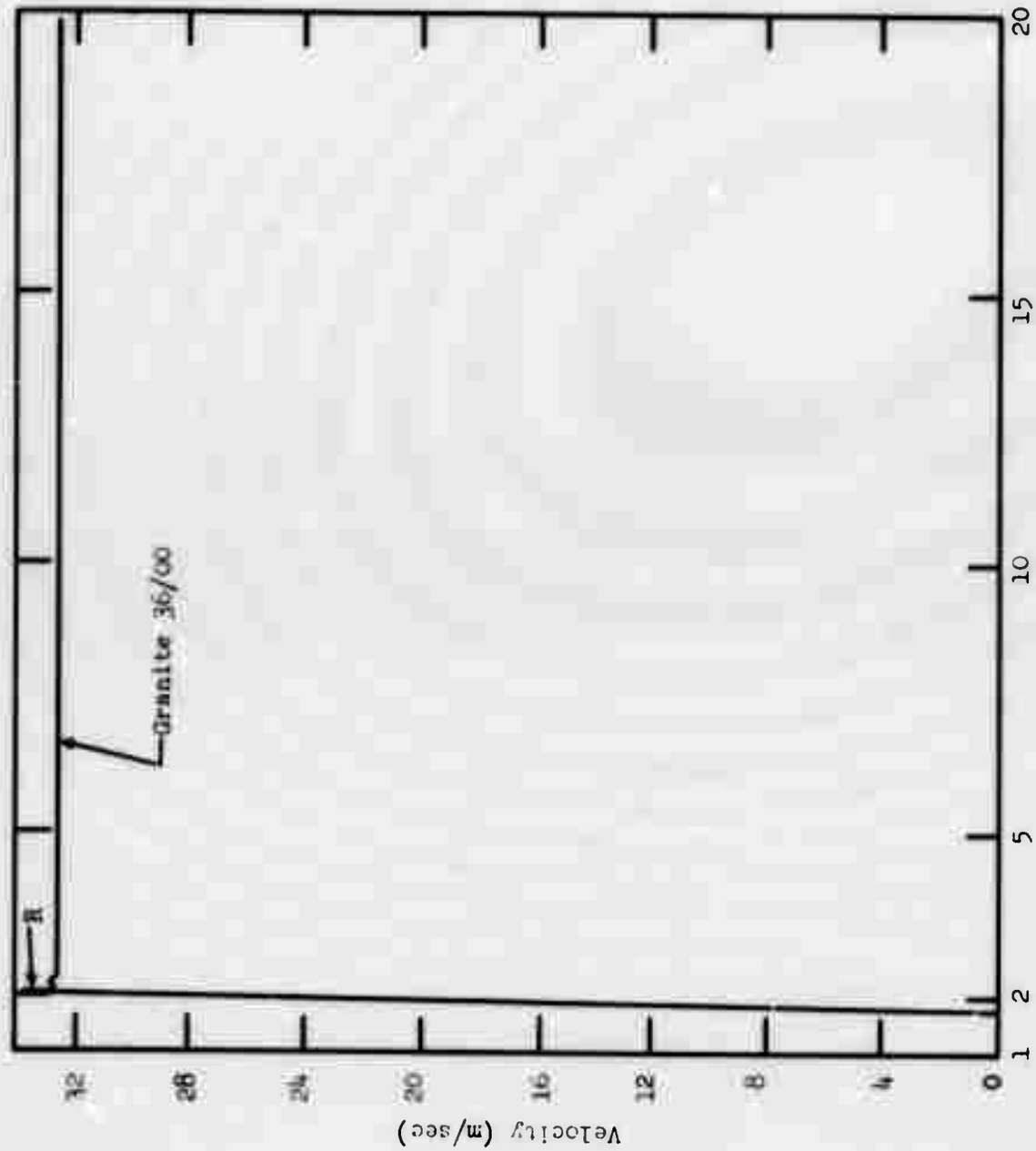

Figure 55a. Granite. R = 10.89 m.

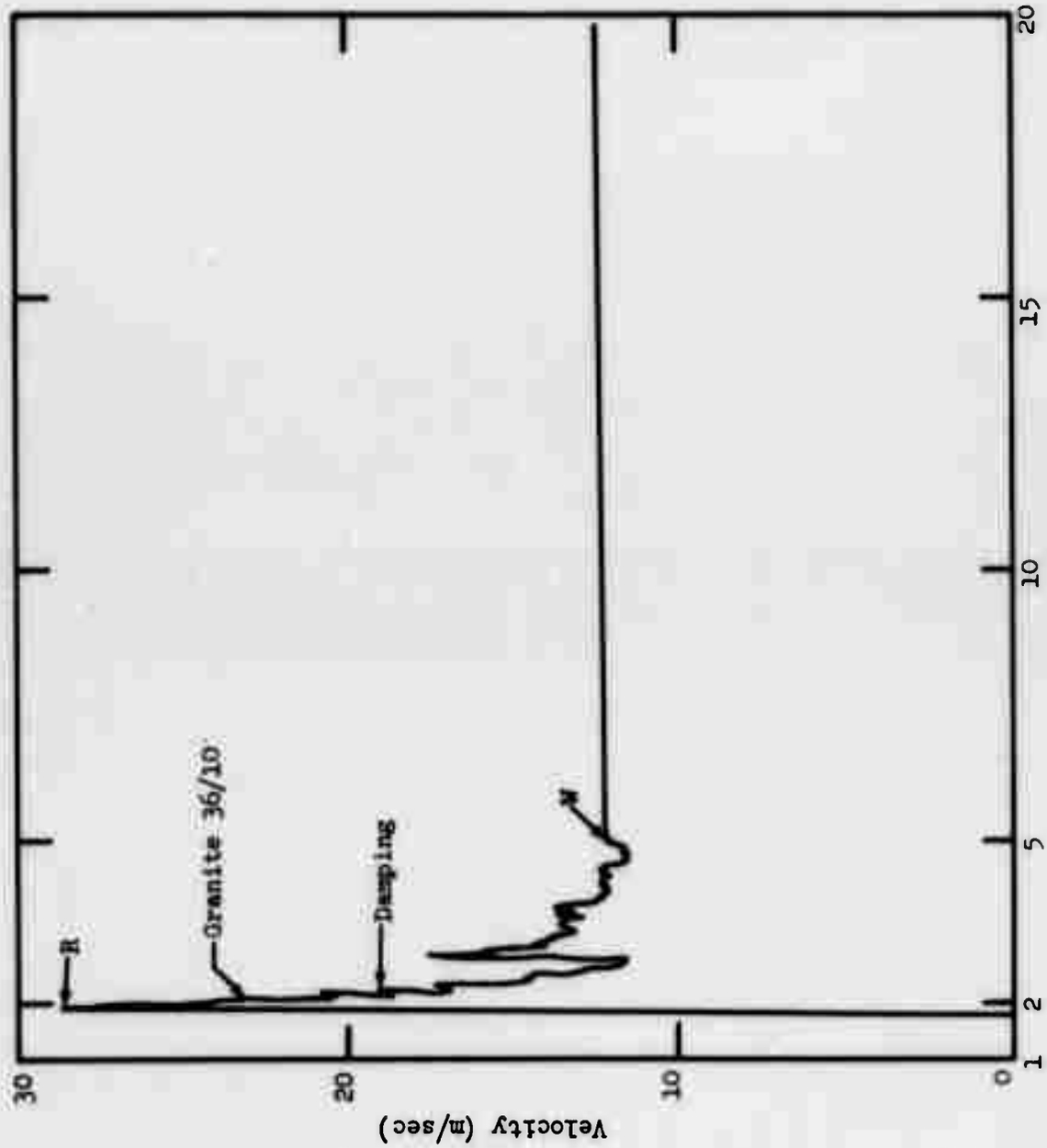

Figure 55b. Granite, R = 10.89 m.

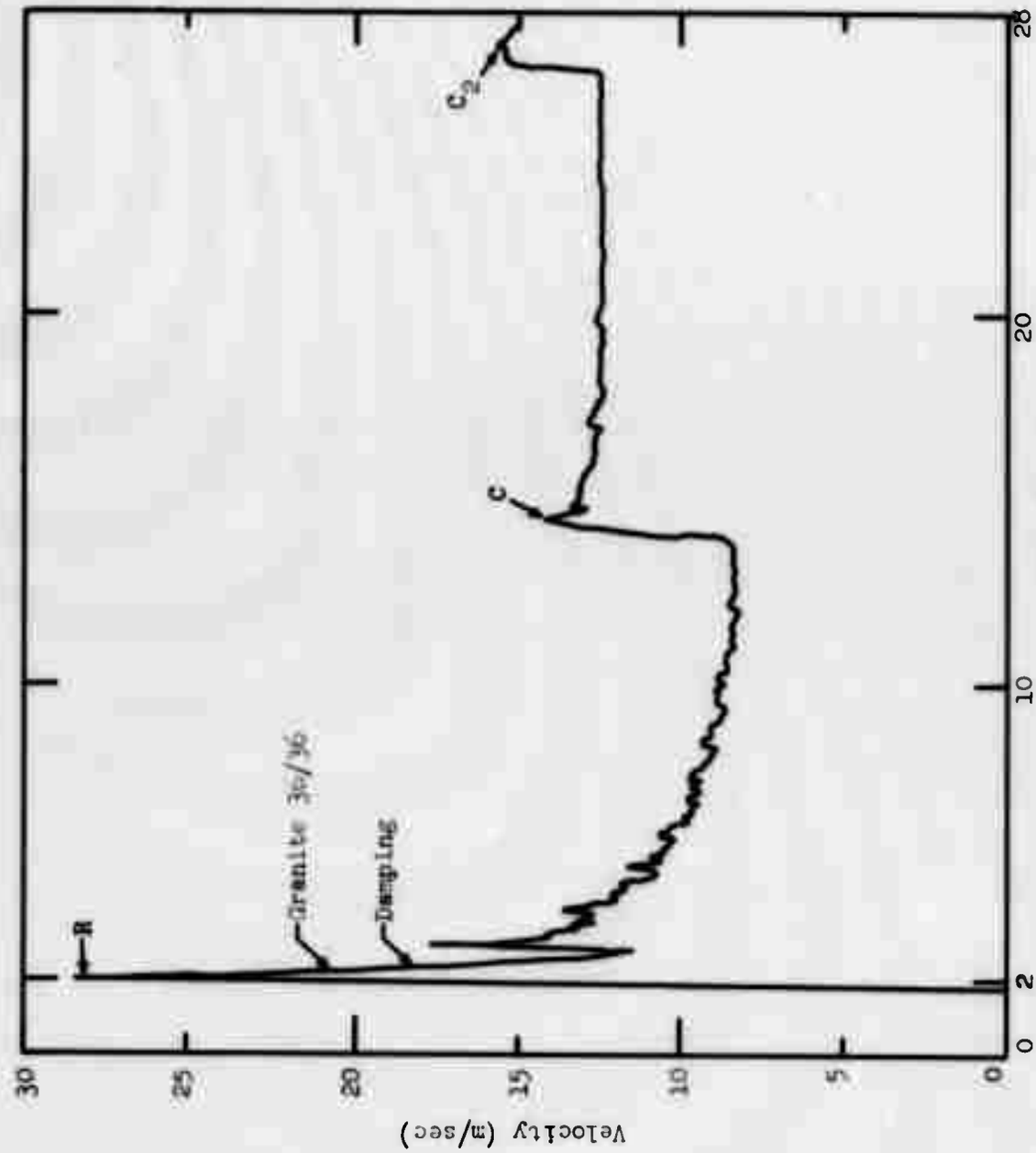

Figure 55c. Granite, R = 10.89 m.

spall velocity) for coral 36/36 is about 21 m/sec. Shortly after the 36/36 surface reflection, a powerful gas acceleration pulse "C" (moving outward from the cavity) arrives and increases the velocity to about 30 m/sec. Gas acceleration pulse transmission near the interface is accentuated for deep water layers, due to the increased velocity damping and material compaction near the interface. It is evident that the presence of water (regardless of depth) influences the initial reflection at the rock interface; the depth of the water layer greatly influences water surface reflection spall velocity and late-time history very close to the rock-water interface.

Range = 10.6 m: Motion histories shown in Figures 37a-c are similar to the trends noted above. In this case, the shock peak arrival and the spall cutoff peak are slightly separated (greater distance from the interface). Less obviously, the damping of the late-time spall velocities for the underwater events (Figures 37b-c) is less severe relative to the coral 36/00 event (Figure 37a) at this location further below the interface.

Range = 9.49 m: Figure 36a reveals that this location is beneath the narrow region of intensely reinforced spall launch near the interface; the rock interface reflection peak "R" is lower than the initial peak for both the coral 36/00 event and the underwater cases. Note that the coral 36/00 "free-surface" calculation again enters freefall upon arrival of the rock reflection, whereas the underwater events are damped until the water surface reflection arrives. However, the relative damping becomes still less outside of the "intense spall" region, and the calculations with and without water overburden are beginning to converge.

Range = 9.01 m: Figures 35a and 35b show certain changes in phenomenology well away from the interface. The "rock" spall arrival "R" remains weaker for the water-layer calculations, but a brief freefall phase occurs after this arrival (before damping due to recompaction of the overlying rock and water begins). Additional damping effects of the water layer become much less important relative to event "36/00". However, the velocity decrease for 36/36 (Figure 35b) is still quite severe until the very late-time gas acceleration pulse arrives and returns local velocities almost to the level which prevailed before the damping occurred.

Range = 8.01 m: Further modifications in relative water layer effects are visible at this range. The coral 36/00 and 36/05 waveforms (Figure 34a) are quite similar, undergoing freefall spallation after the "R" reflection arrives. No water layer damping effects act upon coral 36/05 within the time-scale of the problem. Coral 36/10 also reveals a freefall phase, which terminates with recompaction of overlying material at 9 msec. However, the velocity is decreased by only about 10 m/sec. Approximate freefall motion develops at later times, although slight noise pulses occur due to interactions with adjacent zones. Figure 34b shows a more significant damping for event 36/36 (velocity decreased from about 50 to 35 m/sec). In spite of the damping and deceleration, no water surface reflection (late-time freefall phase) is apparent in Figure 34b; the cavity gas acceleration pulse (outward-moving) actually precedes the water surface reflection (inward-moving), and completely overwhelms any further dynamic effects of the second or water surface reflection. (NOTE: Figures 34a-b and subsequent figures also contain waveforms for coral "30 ft" calculations; these are not directly comparable with coral "36 ft" at the same range, due to the difference in interface locations.)

Range = 6.01 m: At this range, water surface reflection effects are becoming negligible in all cases, but recompaction still influences material dynamics. Note that the waveforms and "rock interface" reflection spall are closely similar for coral 36/00, 36/05, 36/10, and 36/36 (Figures 33a-b). However, the cavity gas acceleration pulse arrives fractionally sooner for the underwater events, due to the slightly lower spall velocities of material moving away from the cavity. The coral 36/36 calculation (Figure 33b) reveals a significant late-time deceleration due to recompaction of overlying layers <u>after</u> the gas acceleration pulse arrives. The velocity decreases back to approximately its initial "freefall" value. Thus, the gas acceleration pulse has only a temporary influence on the waveforms and does not greatly modify overall mound dynamics for these calculations. Similar effects have been noted at intermediate or close ranges in the other media as well.

Range = 5.01 m: Here the waveforms are closely comparable for all calculations (Figures 32a-b). Again, spall velocities are a little lower and cavity gas acceleration begins slightly sooner for the underwater events.

The gas-acceleration-induced velocities are low by about the same amount as the spall velocities; this is obviously a residual effect of the "imperfect" reflection at the rock-water interface, and persists throughout the calculation. The velocity difference involved (at R = 5.01 m) is negligible. Once more, the coral 36/36 calculation, which was carried to late time, shows a recompaction and deceleration phase which roughly cancels the increase due to the gas acceleration pulse (Figure 32b).

Ranges 4.01 and 3.01 m: Interactions parallel the above description, but the freefall phase between the rock surface reflection "R" and the gas acceleration pulse "C" gets progressively shorter at ranges close to the cavity (Figures 31a-b and 30b-c). Finally, near the cavity boundary, the "R" and "C" events coincide and there is no true "spall" phase (Figure 30a, Range = 2.01 m). The gas-acceleration pulse is, of course, initiated when the first spall reflection returns to the cavity interface. The recompaction phase, which returns late-time velocities to approximately the "R" spall value, is likewise evident (Figures 31b, 30c).

Some interesting aspects of the late-time deceleration are also evident in the shallower coral "30 ft" calculations. In this case, successive interactions occur earlier due to the shallower rock layer depth, and at shorter intervals due to the higher velocities involved. The deceleration for coral 30/10 is visible in Figures 32a, 31a, and 30b; velocity returns to the "spall reflection" value. The deceleration for coral 30/36 appears in Figures 33b, 32b, 31b, and 30c. The relative velocity decrease is slightly greater than for 36/36 (higher material velocities are involved and more violent interactions can occur). The velocity decrease for 30/36 occurs relatively soon after the gas acceleration pulse arrival, almost immediately at R = 5.01-6.01 m (Figure 33b, 32b). The pulse develops a rather complex double structure involving acceleration and subsequent deceleration at successive ranges moving away from the cavity (Figure 32b, 33b, 34b, 35e). At locations near the rock-water interface, part of the energy transferred by gas acceleration remains with the material, and velocity does not decrease all the way back to the "residual" value before gas acceleration (Figures 34b, 35e; ranges of 7.98 and 8.98 m). Similar but less well-defined effects are detected near

the coral 36/36 interface (Figures 35b, 36b, 37c, etc.; ranges > 9 m). Unfortunately, the interactions occur later for coral 36/36 and the calculations were not run long enough to fully define very late time effects.

The overall dynamic interactions for coral D_r = 30 ft calculations generally parallel those for D_r = 36 ft, but are shifted closer to the cavity in the intermediate-to-long range region (interface at 9.14 m) and are compressed in time. The dynamic regimes for basalt (Figures 39-47) and granite (Figures 48-55) are likewise fundamentally similar, the chief differences being in the shock wavefront contours, which are more rounded for the basalt (deep and ill-defined surface spall layer),but sharp and "noisy" for granite (complex stress relief and spall interactions near an interface). The granite 36/36 calculations actually show two gas acceleration phases, initiated by the first tensile wave reflection from the rock-water interface and by the subsequent reflection of the first gas acceleration pulse from the rock-water interface. This interaction is apparent as two successive freefall phases near the cavity, each followed by an acceleration pulse and subsequent deceleration (Figures 49b, 50b, 51b). These signals proceed toward the outer regions of the problem as two distinct acceleration pulses separated by about 13 msec (Figures 52b, 53b). The multiple-pulse structure occurs because of the very high assumed sonic velocity in granite and the low spall velocities in these calculations (material does not become greatly rarefied by spallation; recompaction and transmission of later pulses are very efficient). Reflection effects would become less severe for an "optimum"depth calculation. Late-time velocities near the inner regions of the mound tend to return almost to the initial "R" spall level, with a slight increase (Figure 50b), in spite of the second pulse. Second or subsequent cavity pulses in a one-dimensional calculation are difficult to interpret physically because of convergence effects. Generally, multiple reflections are of little interest for shallow cratering calculations; the spall launch rarefies mound material (decreasing multiple pulse transmission), and velocity fields are already established before two or three source-to-surface transit times have elapsed. Most of the mound material enters ballistic freefall and strong "hydrodynamic" interactions cease to be important.

In summary, cratering dynamics for underwater events are controlled by the initial (rock-water interface) spall reflection, recompaction due to the water burden, first gas acceleration pulse (initiated by the "interface" spall wave), and by water surface spall reflection. The water layer effects of recompaction and particularly the water surface spall reflection are most significant near the rock-water interface, becoming less intense within the rock mound. Deceleration of the rock interface due to recompaction increases with increasing water layer depth, up to a limiting value which corresponds with late-time residual mound velocity. The limit is apparently approached in these calculations for $D_w/D_r \approx 1.0$ (i.e., 30/36 and 36/36 events). Presence of a water layer causes certain other dynamic modifications as well. The gas acceleration pulse transmits more efficiently and arrives sooner in the upper regions of the mound, due to recompaction of the mound material. This effect may partially compensate for the water layer damping in some cases. The recompaction phase near a rock-water interface ends and true freefall begins when the water surface tensile reflection arrives (except for the deep water layer events $D_w/D_r \approx 1.0$; in these cases, the material has already been decelerated to residual velocity before the reflection arrives, and the strong gas acceleration pulse may even precede the surface reflection). Water surface reflection is thus important near the interface (except for "deep layer" events); the reflection becomes progressively less important in the deeper portions of the rock mound, and does not cause an independent gas acceleration phase(i.e., gas acceleration is associated with the first interface reflection rather than the water surface reflection). Likewise, multiple reflections in the water layer and multiple gas acceleration pulses exert little influence for optimum depth cratering events with high spall velocities. This conclusion may not apply to very deeply buried low-velocity events not characterized by strong spallation.

Water-layer Waveforms. Selected velocity and pressure waveforms within the overlying water layer have been plotted in Appendix F (coral configurations, Figures F1-F3; basalt, Figures F4-F6; granite, Figures F7-F8). Waveforms within the rock layer adjacent to the interface have been included in Figures F1-F6, to demonstrate velocity and pressure continuity across the interface. The beginning of the freefall phase (water surface tensile

reflection, propagating downward through the water layer) is indicated by an arrow in the velocity waveforms. Water spall velocities are compared with detailed "acoustic" calculations and with experimental results in Chapters VIII and IX. The gas acceleration pulse arrival near the interface is also visible at late time in Figures F3, F6, and F8 (coral 36/36, basalt 36/36 and granite 36/36), but does not have time to recompact and propagate through most of the rarefied (spalled) water layer.

Water waveforms for the "coarse" and "fine" water zone granite calculations are presented in Figures F7 and F8. The "fine" calculations show later arrival times, shorter rise time, higher "peak" values, slight differences in noise behavior and late-time arrivals, and higher spall velocities. Water layer effects for granite will be analyzed in Chapter X.

VII. MOUND DYNAMICS

Peak velocities correspond with long-term spall velocities only in the narrow "cutoff" region near a free surface, where the spall arrival is higher than the initial peak and no subsequent recompaction effects occur. All other "peaks" throughout the problem history are transient values at the shock front or the temporary "undamped" values before recompaction. In order to analyze long-term mound dynamics, we should isolate the late-time residual velocity and spall velocity data from the waveforms, or, better still, determine the "averaged" dynamic parameters within appropriate problem regions (i.e., cavity pressure, overall mound momentum and kinetic energy, etc.). This section summarizes dynamic parameters for the eighteen vertical calculations. The overall mound dynamic trends may also be correlated with features appearing in the finer-resolution individual waveforms (Figures 30-55, Appendices B-E).

Residual velocities. Calculated spall velocities and late-time residual velocities within the rock mound are shown in Figures 56 (coral, D_r = 36 ft), 57 (coral, D_r = 30 ft), 58 (basalt, D_r = 36 ft), and 59 (granite, D_r = 36 ft). These velocities were arbitrarily selected at times near 20 msec. Thus, the gas acceleration phase and the very late-time recompaction

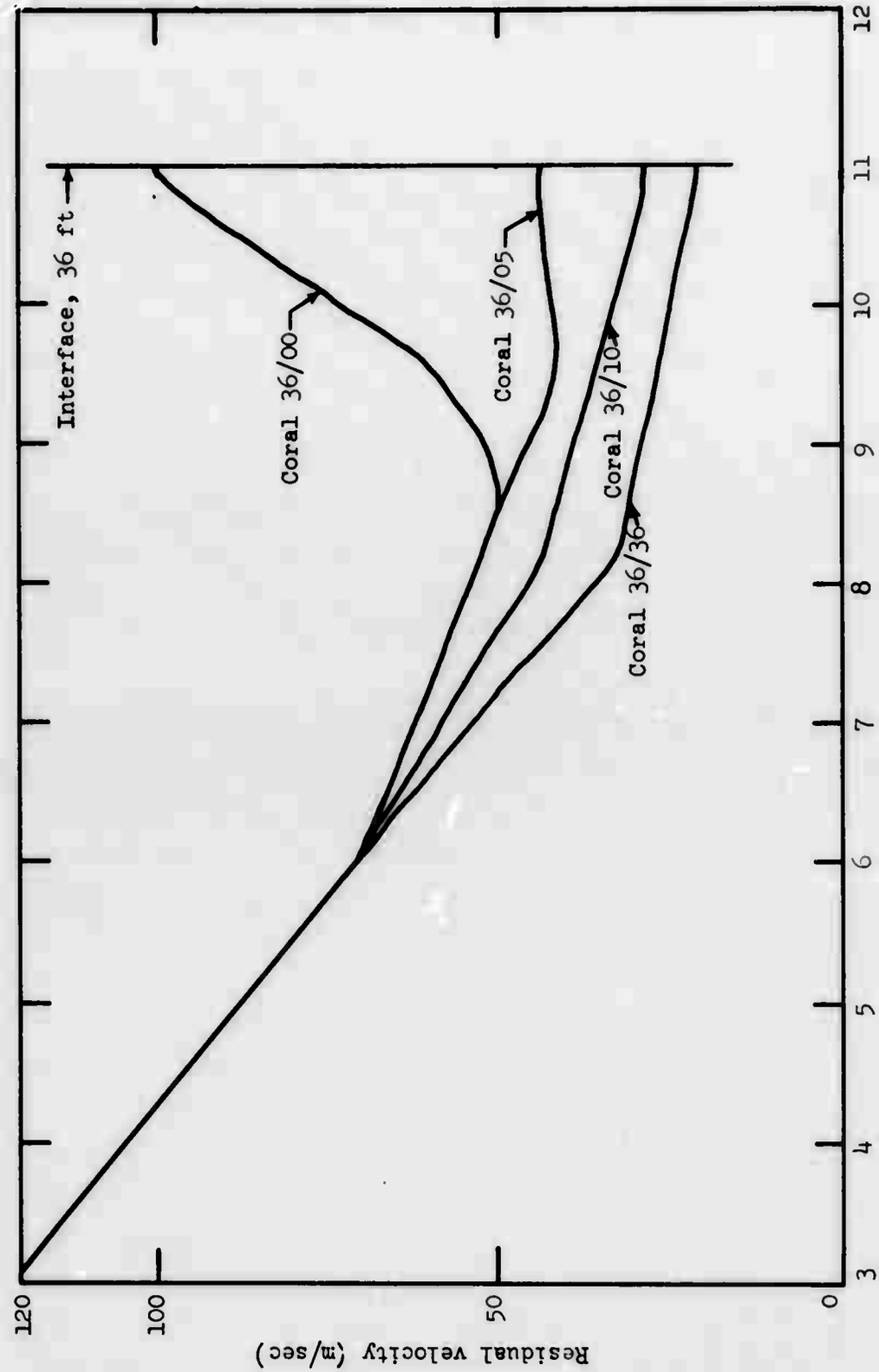

Figure 56. Residual velocities, Tugboat coral.

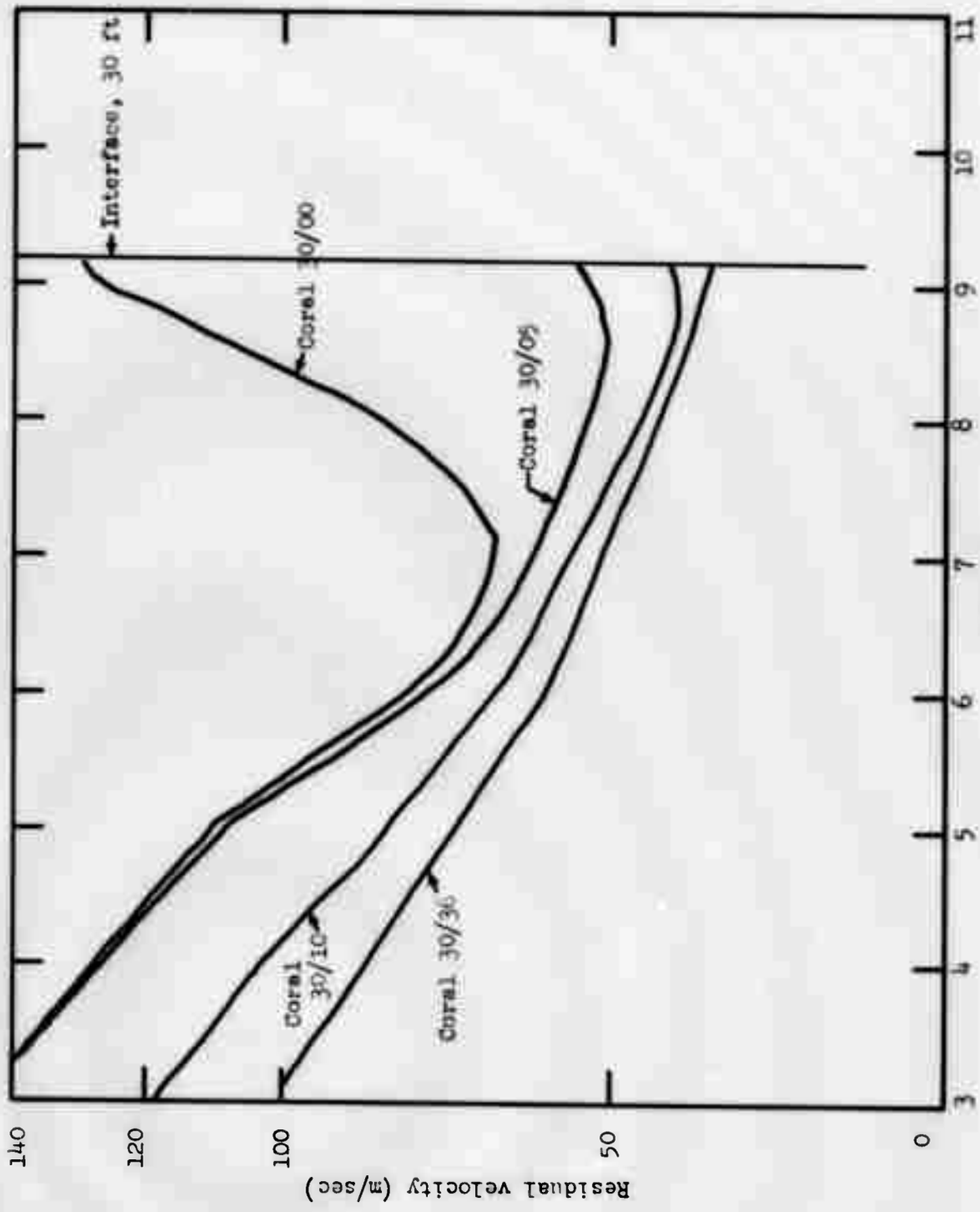

Figure 57. Residual velocities, Tugboat coral.

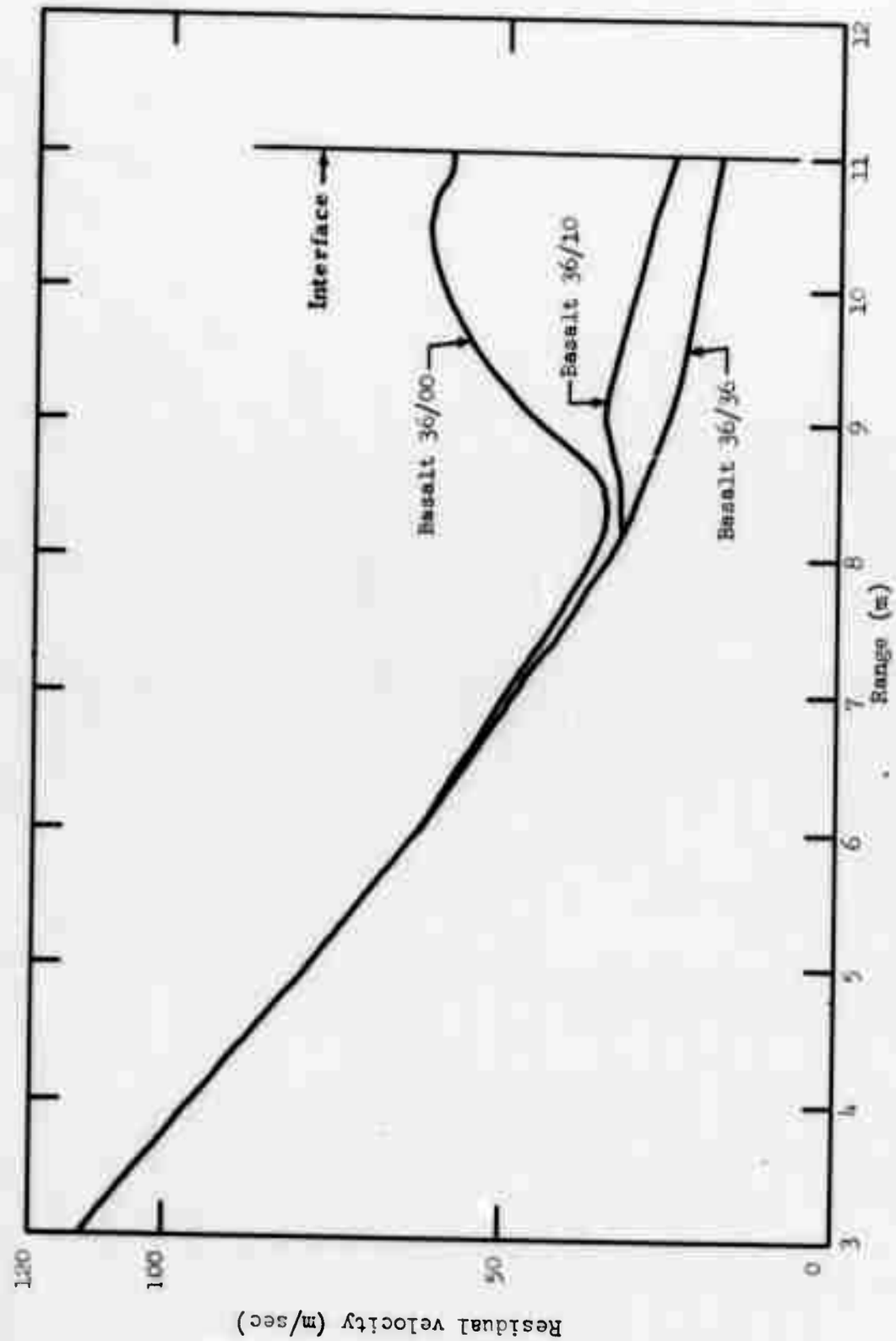

Figure 58. Residual velocities, Kaalualu weak basalt.

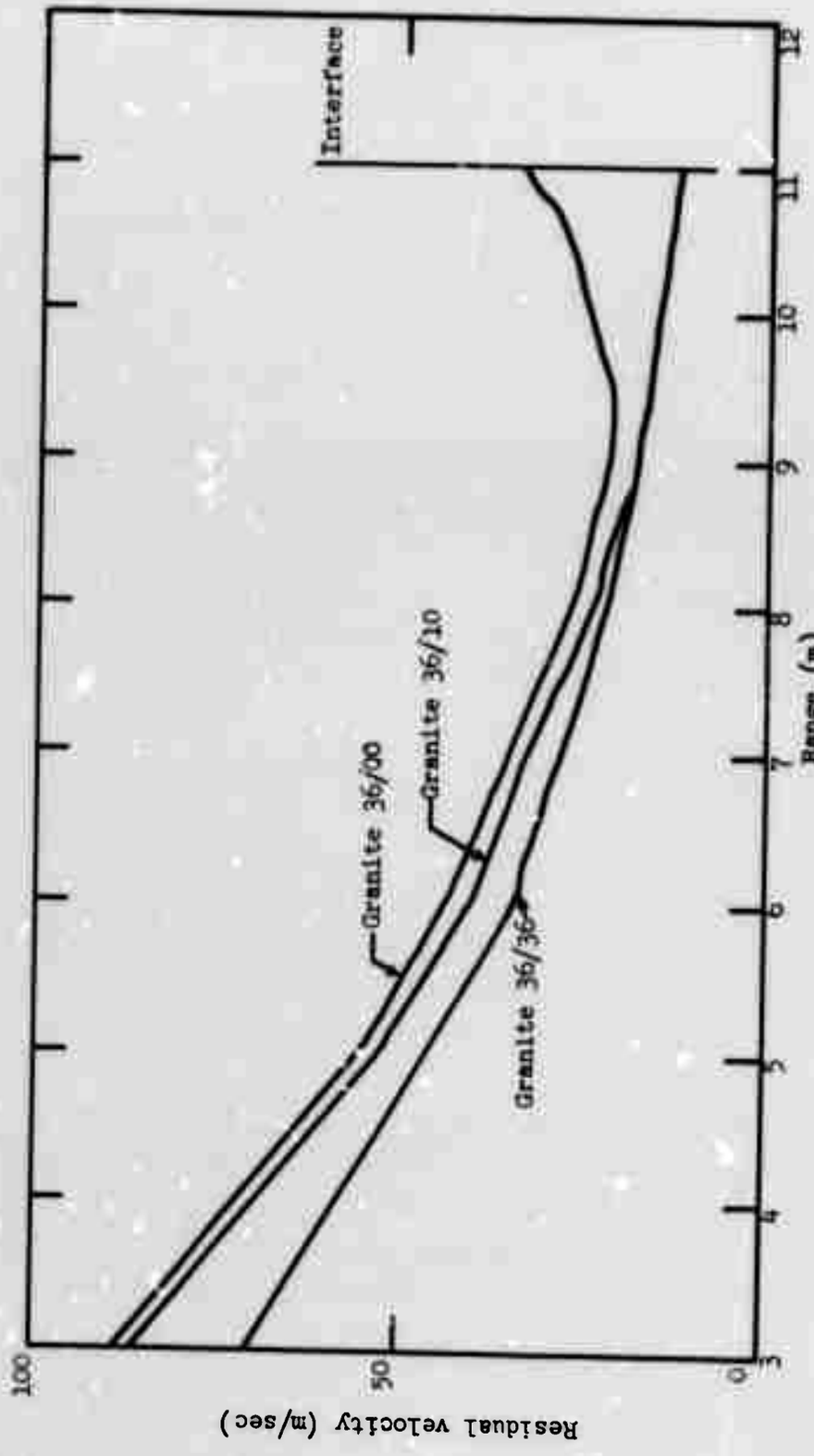

Figure 59. Residual velocities, high-strength granite.

after gas acceleration are excluded for the outer regions of some of the curves. The errors incurred are not large, since velocity changes after 20 msec are relatively minor, and, as we have seen, the gas acceleration velocity pulses are oscillatory and tend to be self-damping (i.e., the gas acceleration pulse just restores velocity lost during the previous recompaction).

The granite calculations form a special case, due to the "deeper-than-optimum" burial, low spall velocities, and high sonic velocity. The gas acceleration pulse is intense, and propagates through about 8 m of the mound (for granite 36/00 and 36/10) or all of the mound (granite 36/36) prior to 20 msec. Likewise, severe recompaction effects after the first gas acceleration phase and other late-time interactions are partially included for granite 36/36 at ranges closer than 6 m. These facts explain the somewhat peculiar behavior shown in Figure 59. Granite 36/36 residual velocities are lower than the other curves at close ranges because of the severe deceleration included immediately after the gas acceleration phase (cf. Figures 51a and 51b). Granite 36/00 and 36/10 lie close together, with 36/10 slightly lower due to imperfect spall reflection at the interface and correspondingly decreased late-time velocities. At ranges beyond about 9 m, the situation is reversed: the granite 36/00 velocities are quite high (undamped spallation near a free surface), while the granite 36/10 velocities are substantially decreased (water layer damping, relieved by the water surface reflection at later times). The gas acceleration pulse is not included in these velocities. The interactions are displayed in Figures 52a, 53a, 54a, and 55a. The granite 36/36 velocities, on the other hand, are very strongly damped by the water layer but also include a strong gas acceleration pulse (Figures 52b, 53b, 54b, and 55b). The gas acceleration pulse reaches the outer problem regions due to strong recompaction of the rock. The initial gas acceleration peak compensates for the strong water damping, and granite 36/36 residual velocities (with gas acceleration) are equal to the granite 36/10 residual velocities (no gas acceleration) beyond 9 m. This comparison may be a little misleading, since damping of the granite 36/36 gas acceleration velocities in the outer rock zones will continue at very late times. Thus, we see that very late time interactions and multiple pulse reflections may become significant for deeply buried events with very

low spall velocities. These considerations may be ignored for spall-dominated cratering events in saturated media (i.e., coral and basalt calculations with weak late-time interactions).

Discounting the minor granite difficulties, residual velocity curves in Figures 56 through 59 present a consistent picture of underwater mound dynamics. The presence of a water layer decreases the residual velocities dramatically within 2 m of the interface. Most of the decrease occurs for even the shallowest water layers (see 30/05, 36/05, and 36/10 calculations), with slight additional decreases for water depths up to 36 ft The dramatic decrease near the interface is caused primarily by imperfect spall reflection for the water layer calculations (not layer-depth dependent), and secondarily by water layer recompaction (depends on layer depth and elapsed time). As expected, the velocity decrease is most severe for coral (slight impedance mismatch, low reflection factor at the interface), less severe for basalt, and least severe for granite (strong impedance mismatch, almost perfect "free surface" reflection). Water layer effects decrease further below the interface, and the velocities for both free surface and underwater calculations tend to converge on high values (≈ 100-140 m/sec, coral and basalt). The exception to this rule occurs for the coral 30/10 and 30/36 events, Figure 57. Their close-range velocities are somewhat damped relative to coral 30/00 and 30/05 because "very late time" deceleration (after the cavity gas acceleration pulse)has already occurred at 20 msec (see Figures 32a-b, and 31a-b). Similar deceleration and recompaction of the mound for coral 30/00 and 30/05 will proceed at slightly later times. The close-range differences are largely apparent rather than real. Note that the late-time recompaction begins relatively early for D_r = 30 ft events because of the shallow scaled burial, very high spall velocities, and correspondingly rapid interactions. The deep mound velocities remain extremely high even after recompaction has begun, as expected for shallow spall-dominated cratering events. Late-time mound recompaction effects close to the cavity are not expected to modify any conclusions presented here for "optimum depth" spall cratering events.

Cavity growth and close-range interactions. The time-dependent cavity radii "R_{cav}" and cavity pressures "P_{cav}" are plotted in Figures 60-62 and Figures 63-65 (a-b), respectively. The corresponding horizontal calculation curves are included for comparison (free-field cavity growth in an infinite medium; no relief pulse reflected from an interface or free surface). Initial cavity radius is 1.13 m (= explosive radius), and growth begins about 0.3 msec. The cavity pressures are plotted beginning at 0.1 msec, while the detonation is still in progress. Pressures increase until about 0.26 msec, when the peak shock enters the surrounding medium, then drop off as the cavity expands. All pressures are average values weighted by zone volume (zone volumes are smallest hear the center of the spherical calculation; volume weighting of pressures throughout the cavity compensates for this effect). Each set of pressure curves has been plotted at compressed scale (10^{-1}-10^{-5} Mbar, Figures 53-65a), and also on an expanded scale to better reveal late-time effects (10^{-3}-10^{-5} Mbar, Figures 63-65b).

Late-time cavity expansion and cavity pressures are descriptive of the gas acceleration coupling and of dynamic effects immediately adjacent to the cavity. Cavity growth follows "free-field" expansion (infinite medium) until the spall reflection returns from the nearest free surface or interface. Growth is then accelerated toward the free surface and the gas acceleration phase begins. Deviation from free-field behavior begins soonest for a shallow event (nearby interface); the cavity expansion is also most rapid and pressure dropoff is fastest for a shallow burial depth. As burial depth increases, accelerated cavity expansion begins later and occurs more slowly. In the limit (horizontal or free-field event, no interface), cavity growth proceeds until the pressure approximately equals the lithostatic head plus restraining material strength of the adjacent rock. The cavity then begins to stabilize, although some overshoot and "ringing" effects are expected at late time. Cavity growth rates and pressures thus reveal the effects of interface reflections, overburden (including water layer depths), and material strength on gas acceleration and late-time interactions.

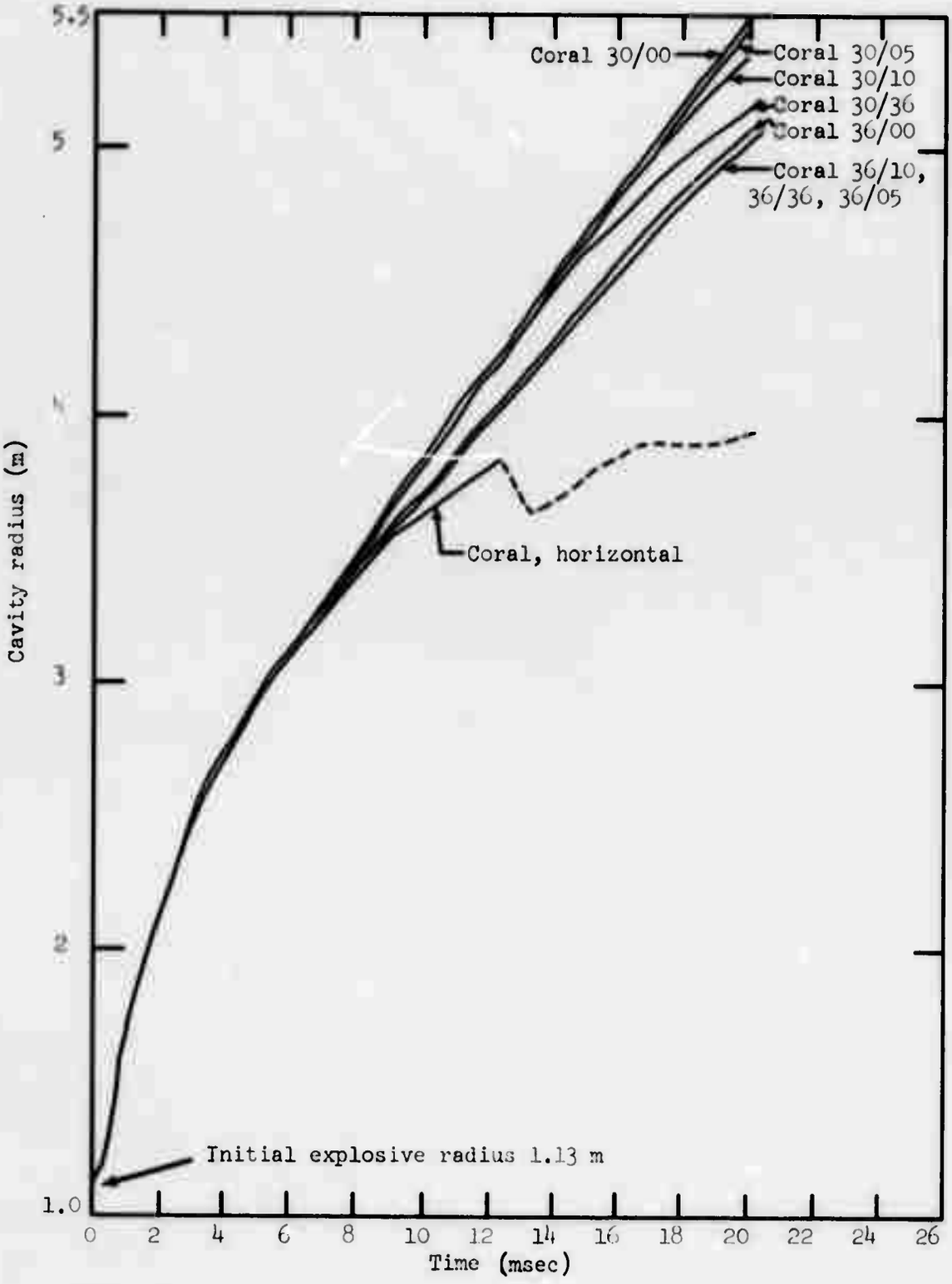

Figure 60. Cavity radius as a function of time (coral configurations).

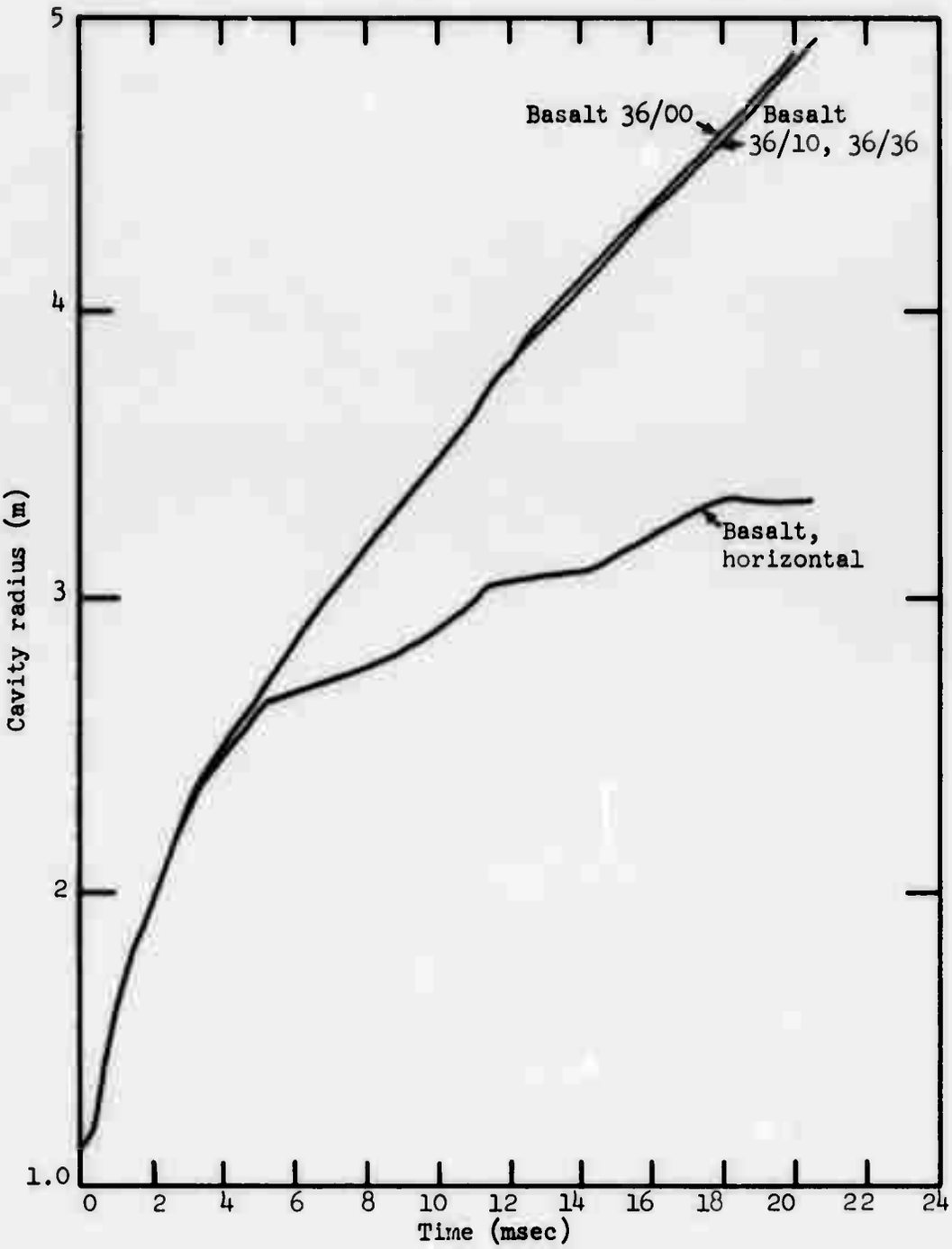

Figure 61. Cavity radius as a function of time (basalt configurations).

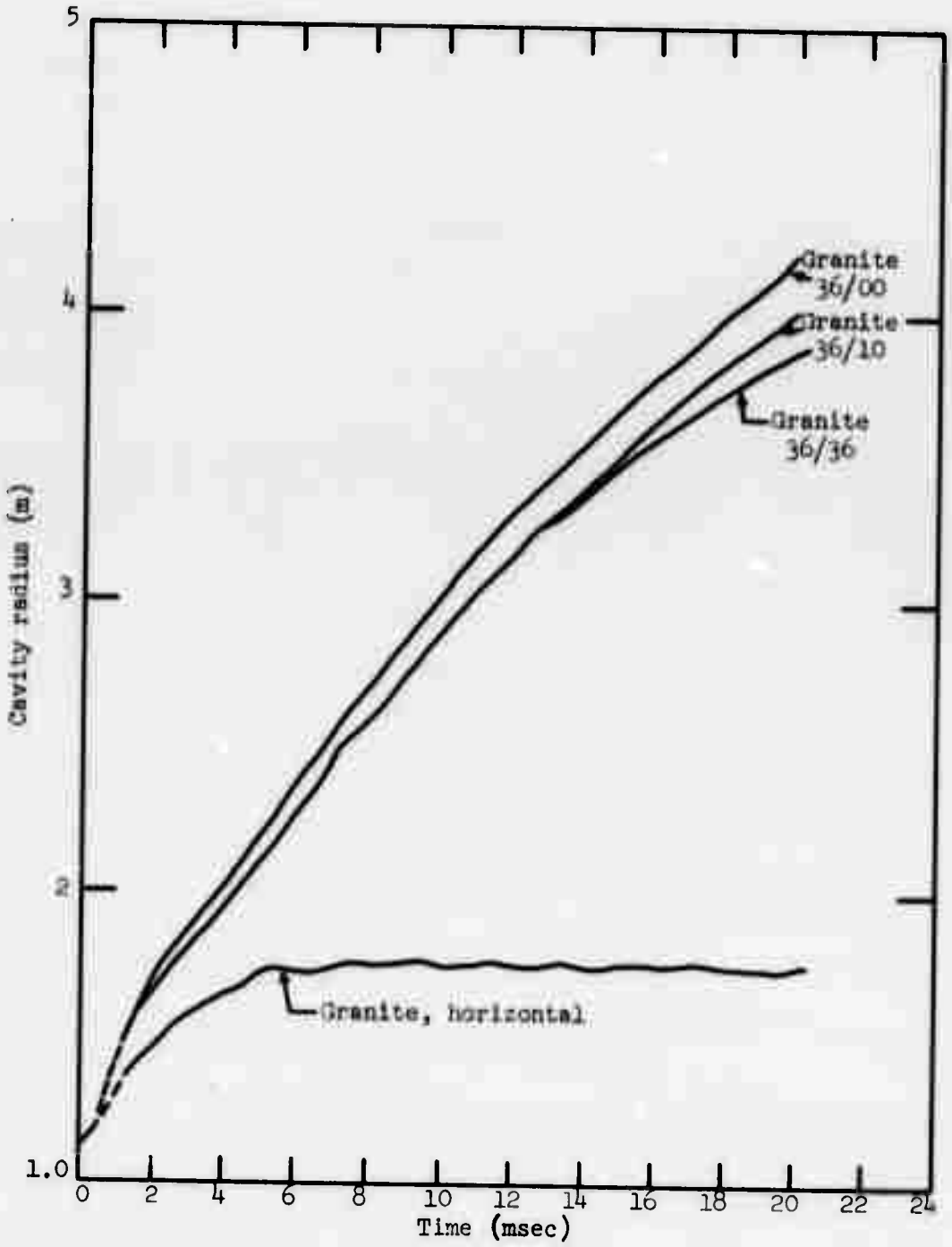

Figure 62. Cavity radius as a function of time (granite configurations).

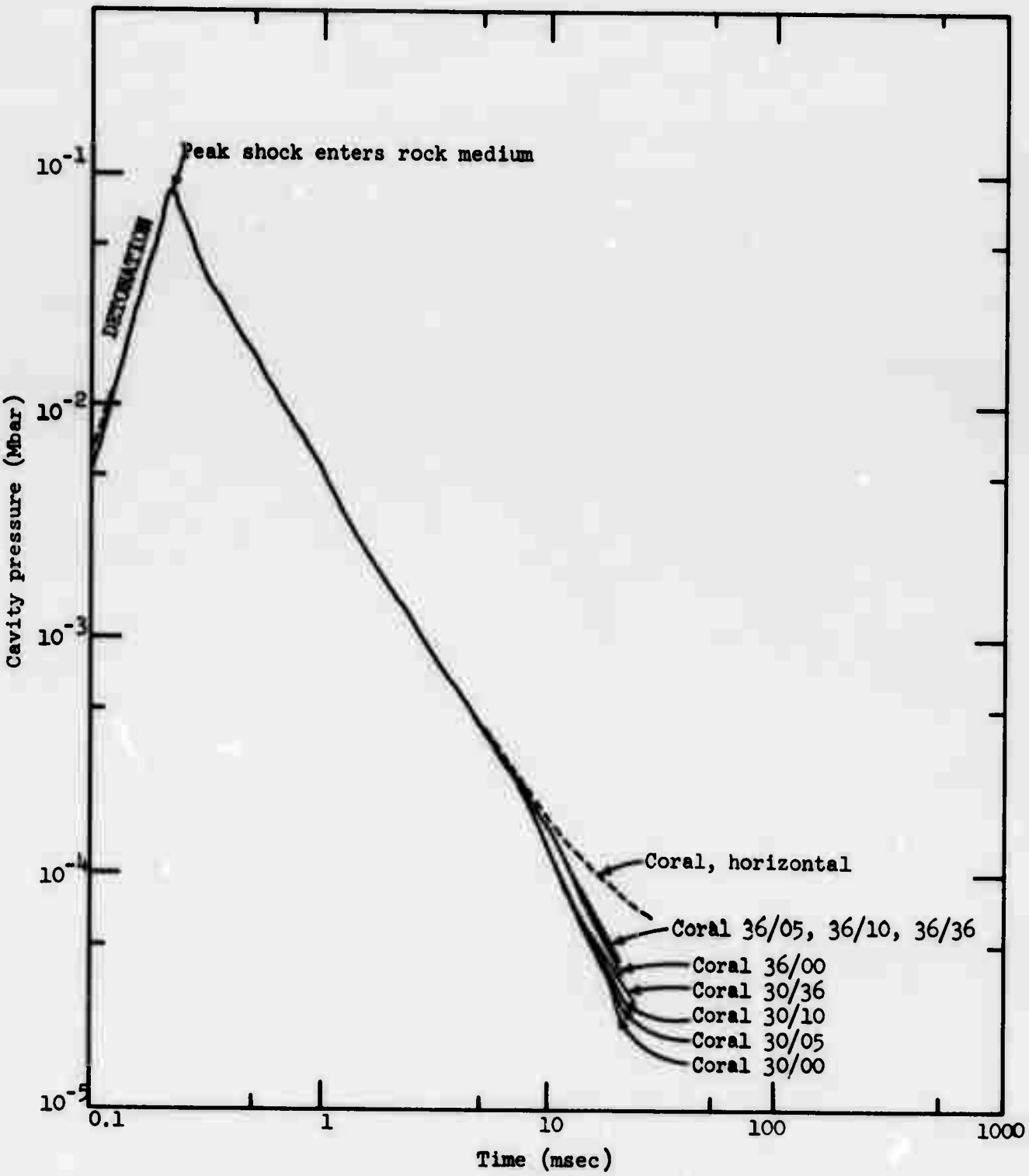

Figure 63m. Cavity pressure as a function of time (coral configurations).

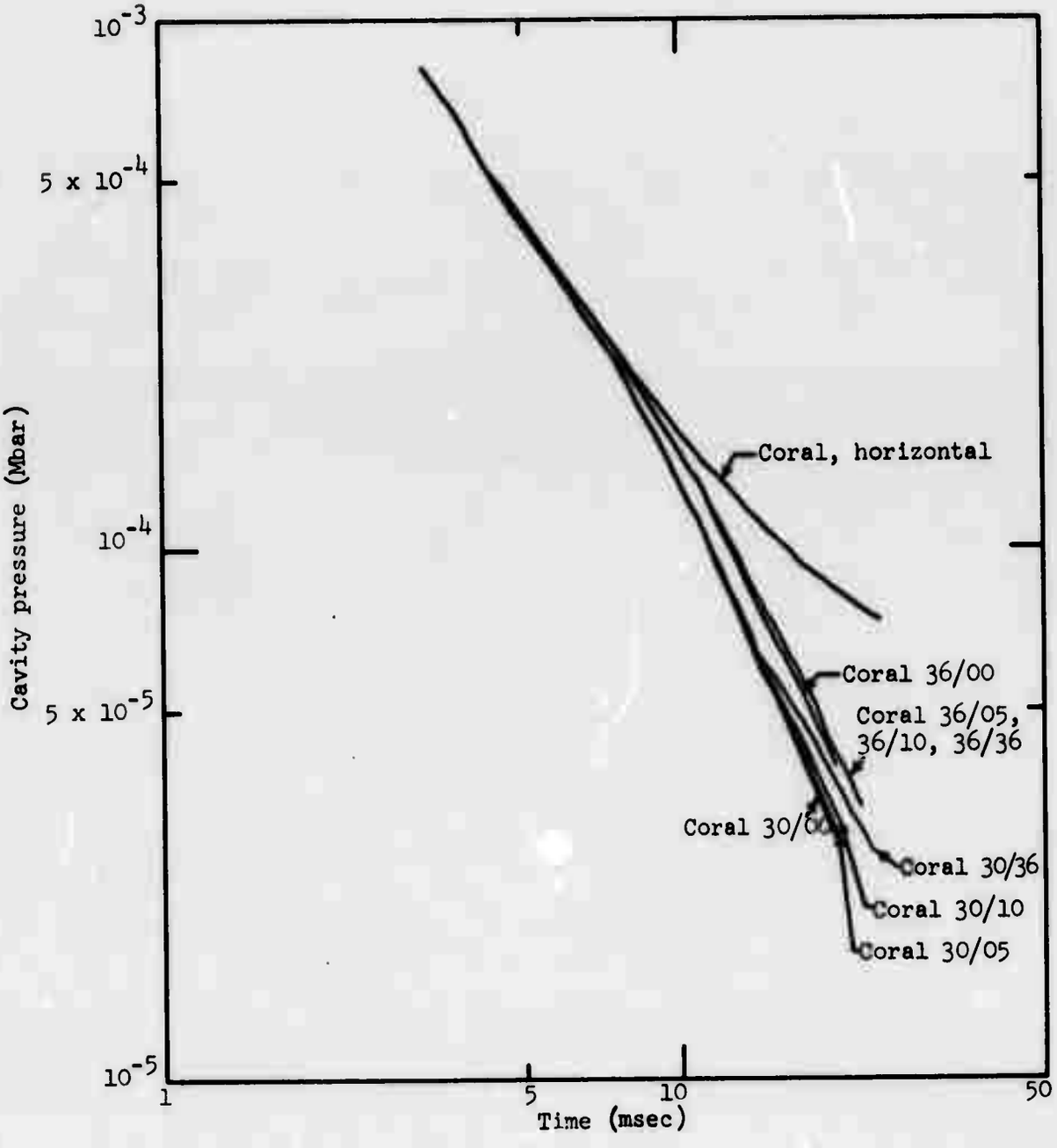

Figure 63b. Late-time cavity pressures (coral).

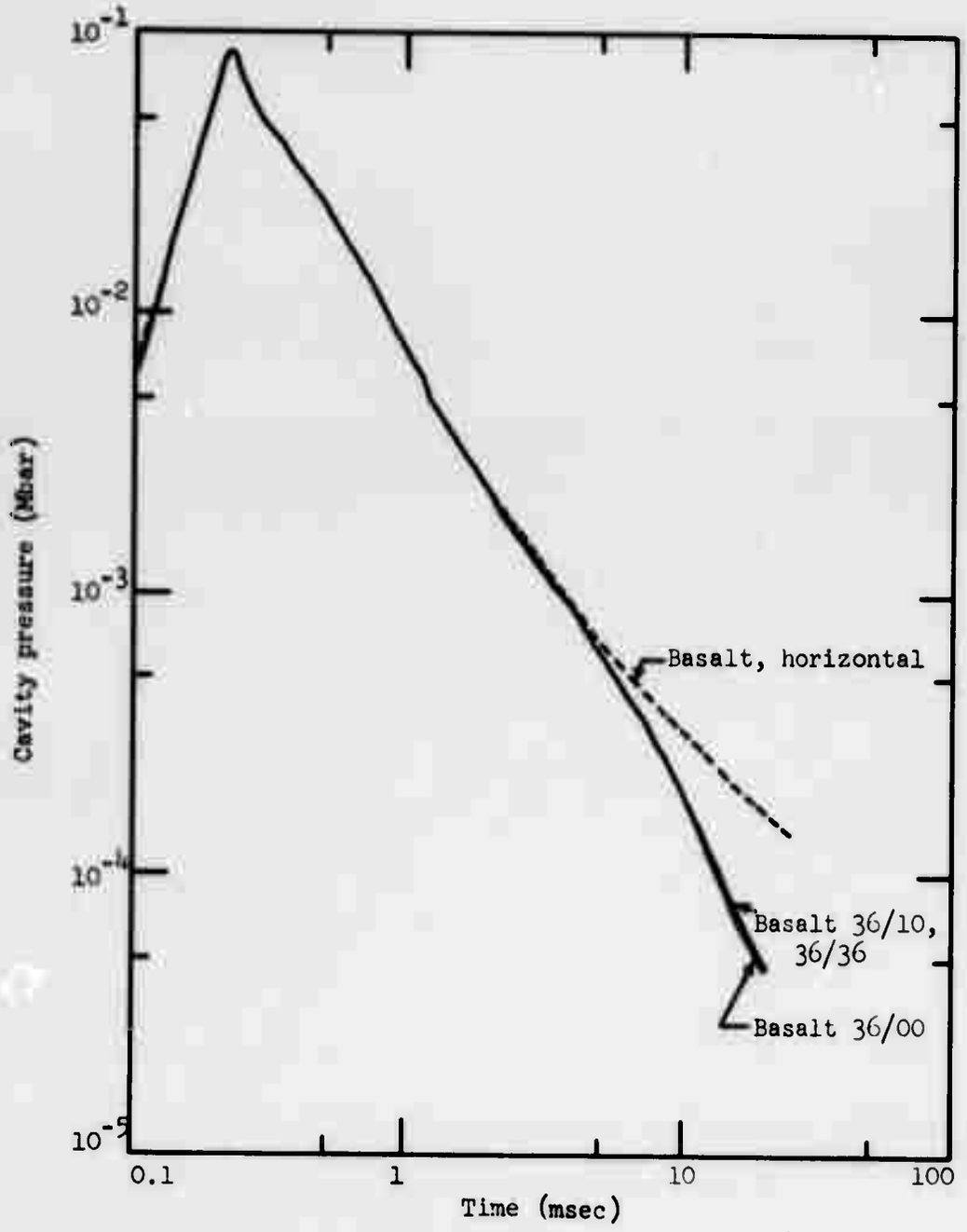

Figure 64a. Cavity pressure as a function of time (basalt configurations).

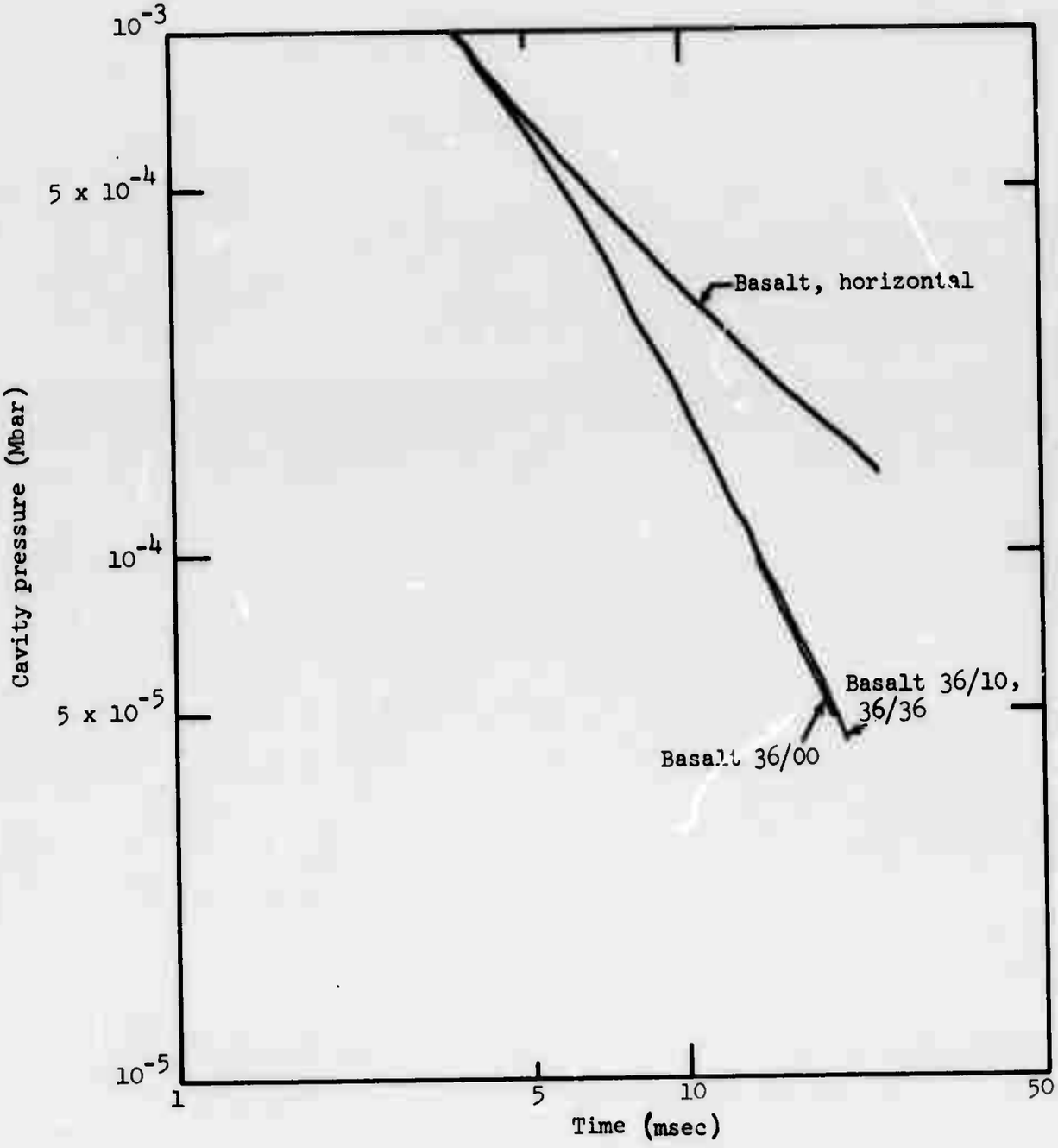

Figure 64b. Late-time cavity pressures (basalt).

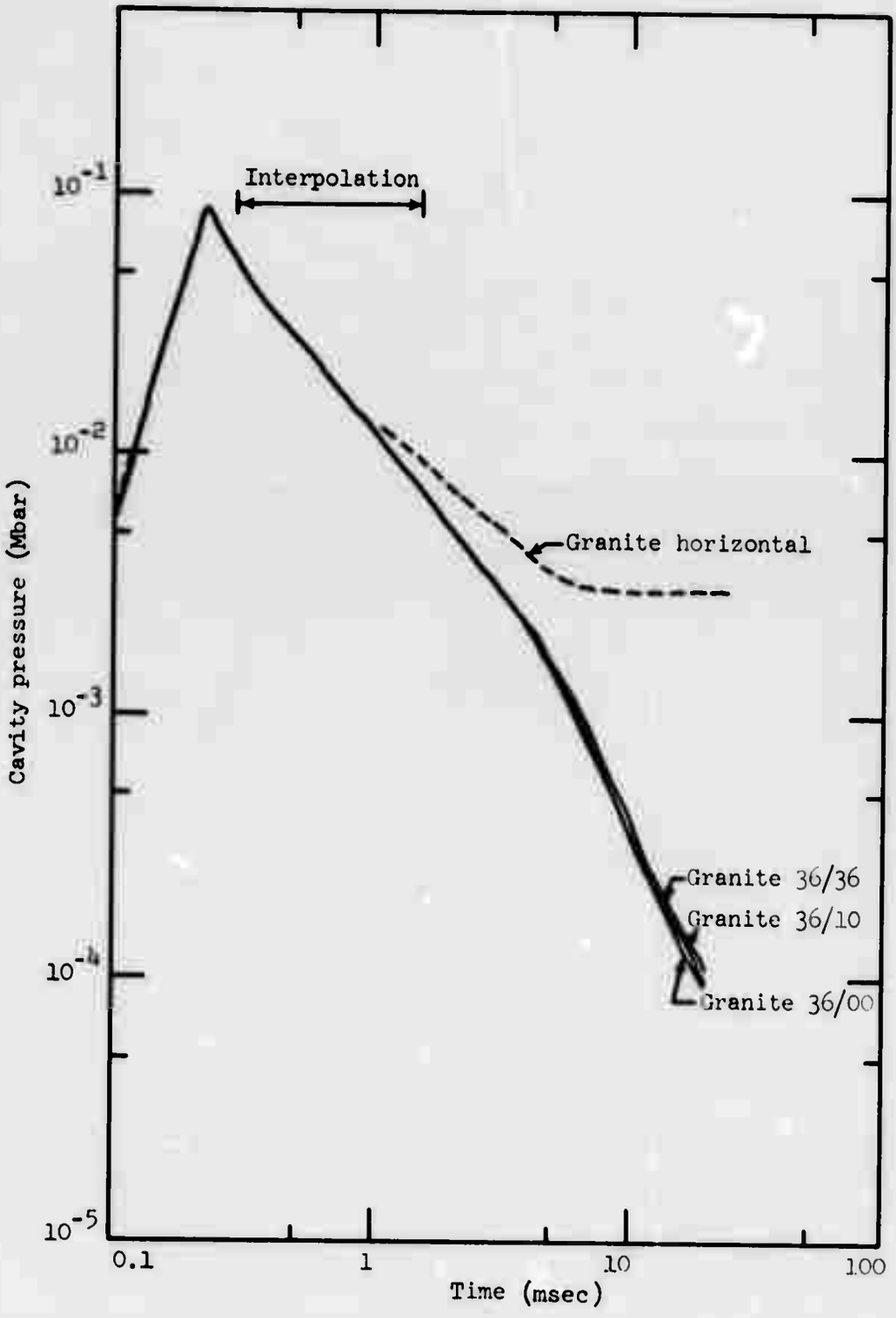

Figure 65a. Cavity pressure as a function of time (granite configurations).

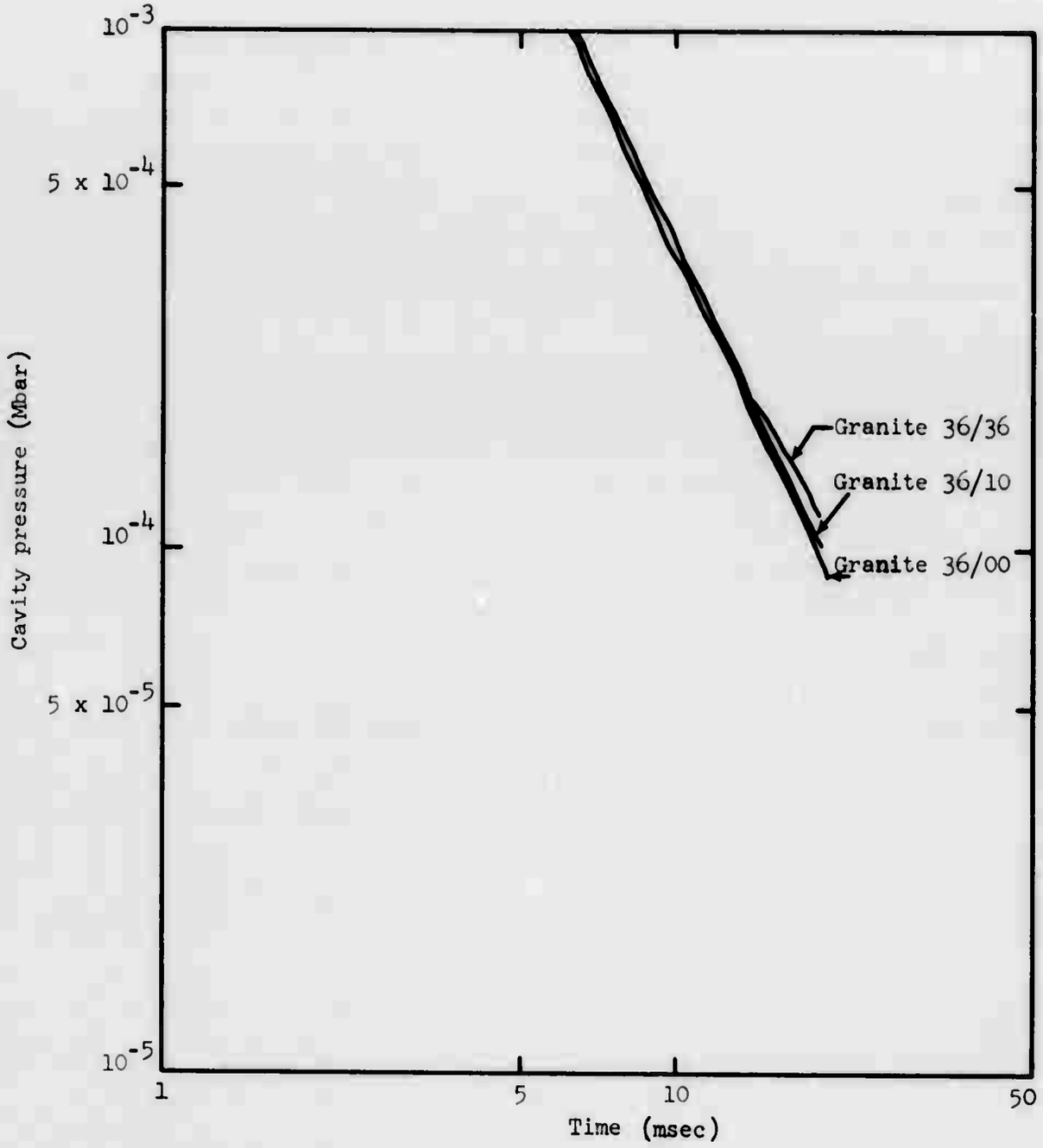

Figure 65b. Late-time cavity pressures (granite).

Cavity growth for coral is depicted in Figure 60, while the pressures are plotted in Figures 63a-b. Cavity expansion for the horizontal calculation ceases after about 12 msec (cavity pressure $\approx 10^{-5}$ Mbar or 0.1 kbar ≃ ultimate strength of coral). The vertical calculations begin to deviate after about 7 to 8 msec, when the first interface reflection impinges on the cavity for the "30 ft" configurations. (The "horizontal" curves differ very slightly before 7 msec because of the coarse zoning used.) Cavity growth and pressure decline are most rapid for the shallow "D_r = 30 ft" calculations, and are somewhat less rapid for the "D_r = 36 ft" events. Water layer effects are less important than rock burial depth "D_r". The presence of a water layer damps cavity growth and increases cavity pressure somewhat. However, at times earlier than 14 msec, the curves for coral 30/05, 30/10 and 30/36 are virtually identical, as are the curves for 36/05, 36/10, and 36/36. This fact indicates that the presence of the water layer influences early-time cavity growth and gas acceleration, but the depth of the water layer is unimportant. It is evident that imperfect spall reflection from the rock-water interface causes the decreased cavity growth rates relative to the "free-surface" events (coral 30/00 or 36/00). At times later than 14 to 17 msec, water layer depth dependence becomes apparent in the coral 30/10 and 30/36 calculations. The thick water layers damp cavity growth and increase pressure. This effect is caused by the close-range damping discussed in the previous section. Due to the shallow burial depths and high spall velocities for the "30 ft" calculations, mound recompaction occurs at relatively early times. Thus, the gas acceleration phase near the cavity is concluded and cavity growth is damped before 20 msec (termination of plotted curves). This effect is visible in Figures 30 a-b-c; recompaction and deceleration begin at about 14 msec (30/36)or 17 msec (30/10), the same times as the deviations visible in Figures 60 and 63. As noted previously, mound recompaction near the cavity will also occur (somewhat later) for the coral 30/00 and 30/05 events, thereby partly compensating for the apparent differences in cavity growth. The calculations were not carried long enough to analyze very late time cavity damping after the gas acceleration phase for coral 30/00 and 30/05. To place the "water layer" effects in

proper perspective, we note that the coral 30/36 cavity radii decline and the pressures increase almost to the levels of the 36/00 calculation at very late times. However, the coral 30/36 event actually has 37% more overburden weight than coral 36/00. In addition, the curves should separate again at later times, as cavity damping begins for the 36/00 event. Rock burial depth and rock overburden are more important than water layer overburden in determining cavity growth, and the first interface reflection is the principal factor controlling cavity interactions in these calculations.

Cavity radii and pressures for basalt are presented in Figures 61 and 64 a-b. Horizontal cavity growth decelerates at about 6 msec (P_{cav} ≈ 0.5 kbar ≃ ultimate strength). The vertical calculations 36/00, 36/10, and 36/36 are almost identical up to 20 msec, in accord with the similar close-range waveforms (Figure 29a-b). Some cavity damping would be expected for basalt 36/36 after 20 msec (Figures 39b; gas acceleration phase ends and recompaction is apparent near 25 msec), and at later times for the other events. The basalt 36/10 and 36/36 growth rates are marginally slower and pressures slightly higher than for 36/00, due to imperfect reflection at the interface.

Granite cavity expansion and pressures are shown in Figures 62 and 65a-b. Horizontal cavity growth ends abruptly at 5 msec, and the pressure is almost immediately stabilized (P_{cav} ≈ 4 kbar ≃ ultimate strength). This behavior is expected for a very high-strength rock. Cavity growth is most rapid for granite 36/00, somewhat slower for 36/10 and 36/36 (spall reflection slightly weaker). The cavity growth rate is somewhat damped and pressures are increased for granite 36/36 after 13 msec (compare with 36/10 curves). This effect is again attributed to cavity damping after the first gas acceleration phase; Figure 48b shows rather severe recompaction effects near the cavity for 36/36 during the later stages of the calculation.

To conclude, cavity growth and gas acceleration effects are dominated by the first interface reflection arrival at the cavity. Cavity growth is most rapid for a strong "free-surface" spall reflection, and is somewhat retarded for a weaker rock-water interface reflection. The relative degree of retardation is greatest for a small impedance mismatch, which causes

inefficient reflection (i.e., coral-water interface). Secondary effects of water layer depth appear only at late times, after the first gas acceleration phase is complete. Recompaction and damping of cavity growth occur earlier for deep water layers. This deceleration may be partly compensated at later times, when cavity damping must occur even for the "shallow water layer" or "free surface" events. In any case, close-range mound recompaction after the gas acceleration phase has little influence on optimum depth cratering. It is therefore expected that the presence of a water layer will exert primary control over cratering dynamics, and layer thickness will be a second-order effect. As a corollary of these conclusions, water layer depth for moderate-to-thick water layers has far less effect on cavity growth and gas acceleration than an equivalent mass of rock overburden. A rather abrupt change in dynamics is expected for shallow water layers, with much less sensitivity to increasing overburden at greater water depths. No direct parallel should be drawn between "rock overburden" and water layer thickness.

Mound kinetic energies. Cratering dynamic effects are perhaps best described by the mound kinetic energy.[19] The kinetic energy is a velocity-sensitive and, therefore, burial-depth sensitive parameter. Kinetic energy is initially transferred from the explosive to surrounding material by the detonation shock front and by subsequent spherical expansion of the cavity. After the initial shock wave is reflected at an interface or free surface, spall launch of the mound material begins. The kinetic energy then increases as spallation spreads throughout the mound. This increase occurs soonest and is greatest for shallowly-buried events. As the depth of burial is increased, spall becomes a less efficient energy transfer mechanism and the fraction of the total problem energy converted to kinetic energy decreases. Finally, for horizontal or free-field calculations, no spallation occurs. Kinetic energy achieves a maximum at early time, then declines continuously as material motion is damped in the infinite medium.

The kinetic energy content of spalled mound material in ballistic freefall is approximately constant (ignoring gravitation). Thus, if the entire mound entered ballistic freefall, one would expect the kinetic energy to rise to a peak value (during the spall phase) and remain constant thereafter.

In reality, the gas acceleration phase, beginning when the spall wave reaches the cavity, and continuing energy transfer from the cavity at late time cause the medium kinetic energy to increase gradually. The gas acceleration effects spread slowly throughout the mound, and may not reach the near-surface spall material. In addition, material interactions may change the relative energy contents of various regions of the mound. For example, mound recompaction and reassembly after the gas acceleration pulse arrival will decelerate lower parts of the mound and transfer energy to the upper sections (see the previous discussions of recompaction and cavity growth damping). Interactions of this type are of particular interest in multilayer cratering problems.

Other energy-related parameters are also useful in describing dynamic effects. The ratio of kinetic energy to total problem energy provides a measure of the efficiency of material ejection. Its behavior is, of course, similar to kinetic energy. This parameter provides a convenient means of comparing different classes of problems. The ratio of kinetic energy to internal energy (KE/IE) likewise gives an estimate of the fraction of the locally available energy (in the entire mound or a given region) which goes into material motion. The KE/IE ratio is high for shallowly buried events, and extremely high in the spall region near a free surface. Material properties also influence the ratio: other factors being equal, the internal energy content is highest (and KE/IE ratio is lowest) for stiff, high-strength, shear-supporting materials; the internal energy content decreases for weaker material and for fluids. The KE/IE ratio becomes small for deeply buried events in all media. In the horizontal problems, material motion is strongly damped at very late times and the internal energy content approaches total problem energy.

Multilayer dynamics may be examined by dividing the problem into various material regions and examining kinetic energy behavior in each region. This procedure is particularly appropriate here for three reasons: (1) Cratering material ejection for underwater events depends almost entirely on velocities and energies in the underlying rock. The dynamics of the overlying water layer (after initial shock reflection, damping, and recompaction at the interface are complete) do not influence the dynamics of the rock material and the rock

ejecta trajectories. Thus, cratering dynamics after the initial strong interaction phase may be analyzed solely in terms of the underlying rock layer. Indeed, the entire water layer for most of the shallow events in this study (D_{water} = 5 or 10 ft) enters freefall when the water surface reflection spall phase is complete, and does not interact again with the rock layer within about 20 msec (problem termination time). (2) The problem sets discussed here use a constant rock layer depth, in combination with variable water layers. Hence, the rock kinetic energies for problems in a given series may be directly compared to reveal water overburden effects. Since the kinetic energy is velocity-sensitive, damping and deceleration effects which influence rock layer motion will be readily evident. (3) Gravitational energies are negligible ($\approx 10^{-3}$ x KE) over the time and distance scales of these problems. Even for the rapidly-moving upper spalled regions, gravitational energy accounts for only one percent or so of the zone energy at late times.

Kinetic energy content in rock as a function of time for all problems is plotted in Figures 66-69 (solid lines). The kinetic energy content in the overlying water layers is also given for comparison (dashed lines). The various problem sets are displayed separately: coral (D_r = 30 ft) in Figure 66, coral (D_r = 36 ft) in Figure 67, granite (D_r = 36 ft) in Figure 68, basalt (horizontal and 36/00) in Figure 69a, and basalt (36/10 and 36/36) in Figure 69b. The basalt diagrams also show the internal energy in rock and water and the total cavity energy for all problems. Note that each figure gives the total problem input energy after detonation is complete (horizontal line at 6.65×10^5 Mbar-cm^3) and the arrows at the bottom of the figure indicate the approximate (acoustic) shock arrival times at each problem interface or boundary.*

---

* Code: 30/00Λ or 36/00Λ: Initial shock arrival at rock surface or rock-water interface.

30/05Λ or 36/05Λ: Initial shock arrival at water surface, D_w = 5 ft.

30/10Λ or 36/10Λ: Initial shock arrival at water surface, D_w = 10 ft.

30/36Λ or 36/36Λ: Initial shock arrival at water surface, D_w = 36 ft.

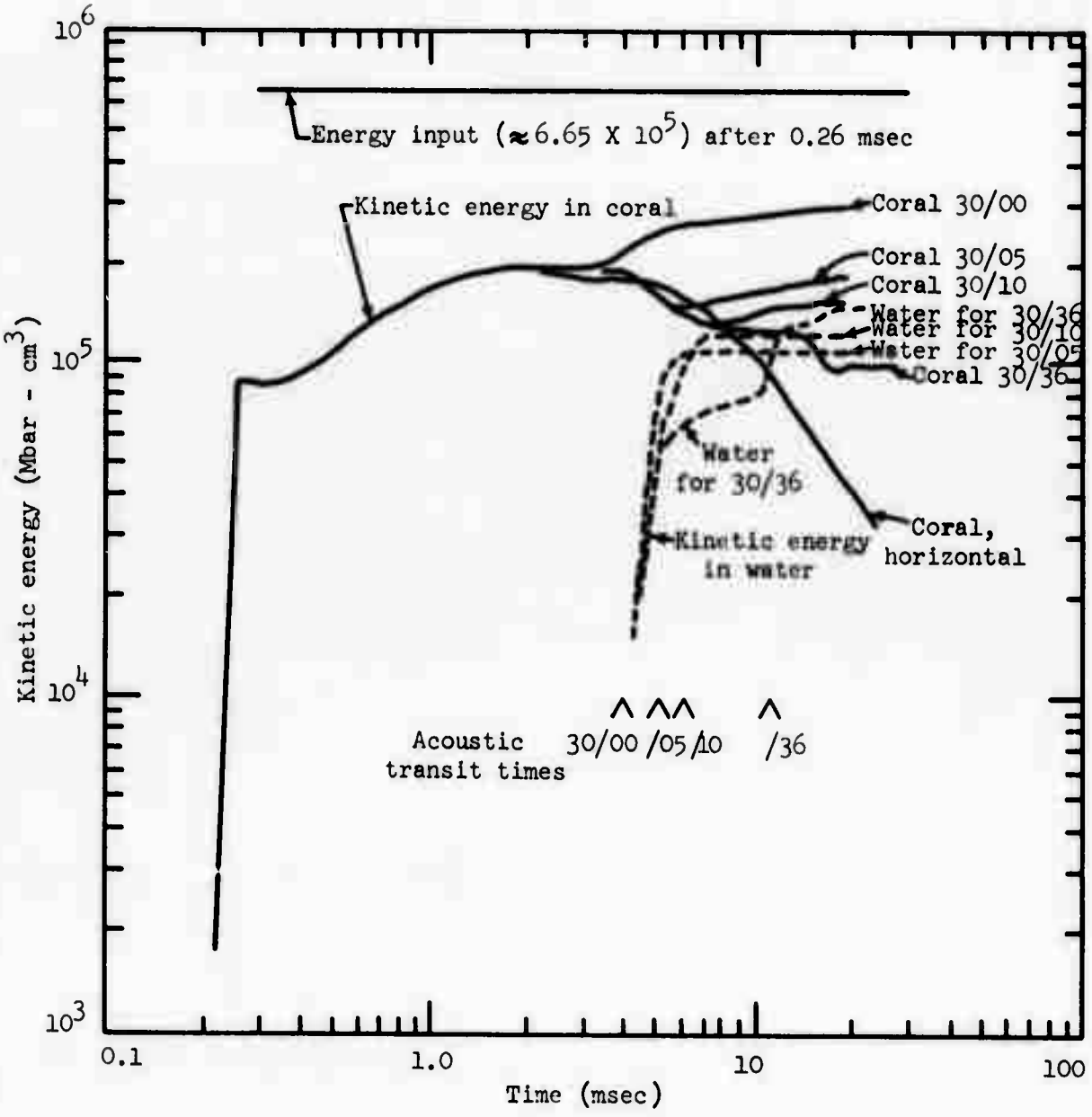

Figure 66. Kinetic energy, coral configurations, D_r = 30 ft.

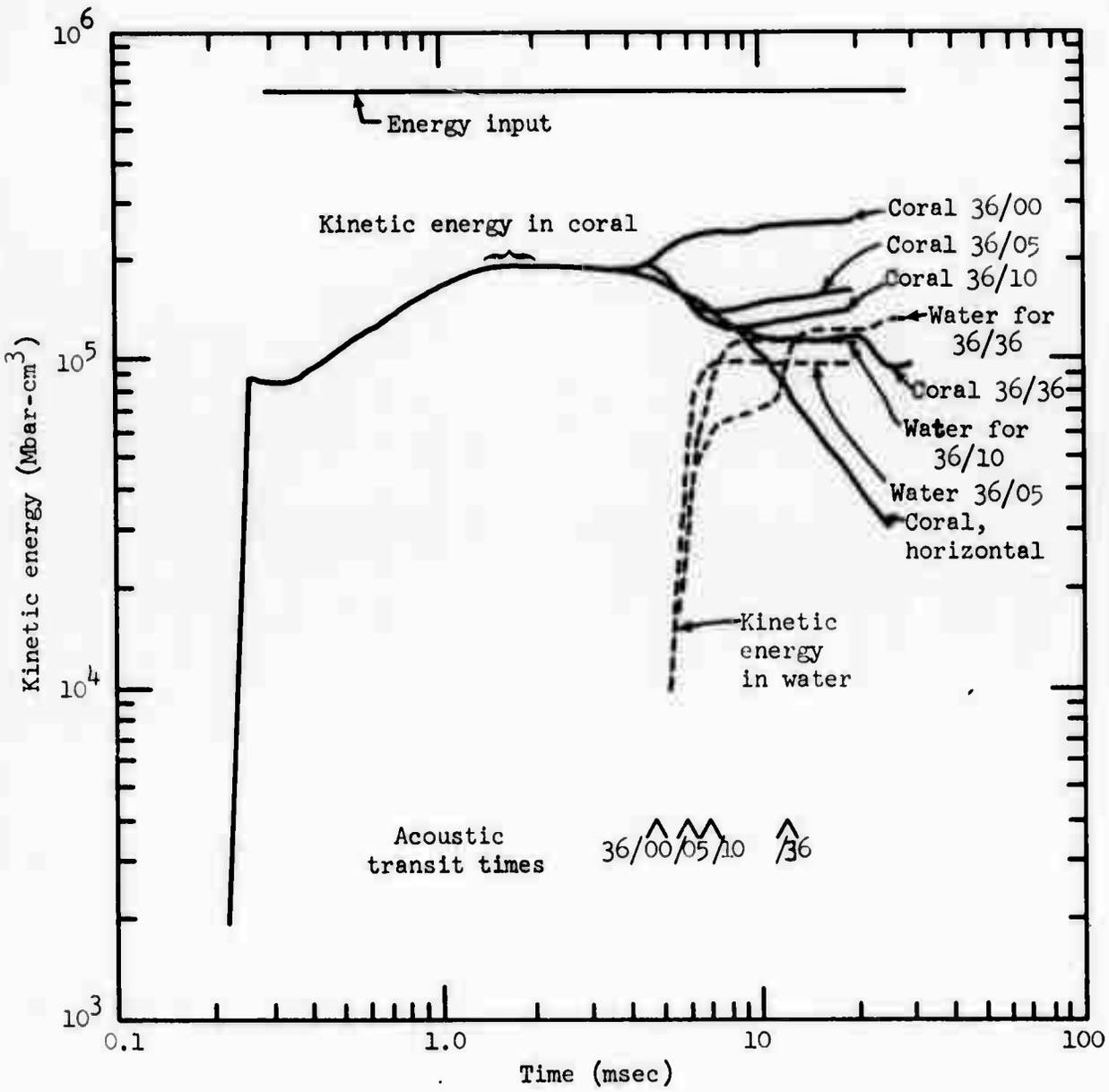

Figure 67. Kinetic energy, coral configurations, D_r = 36 ft.

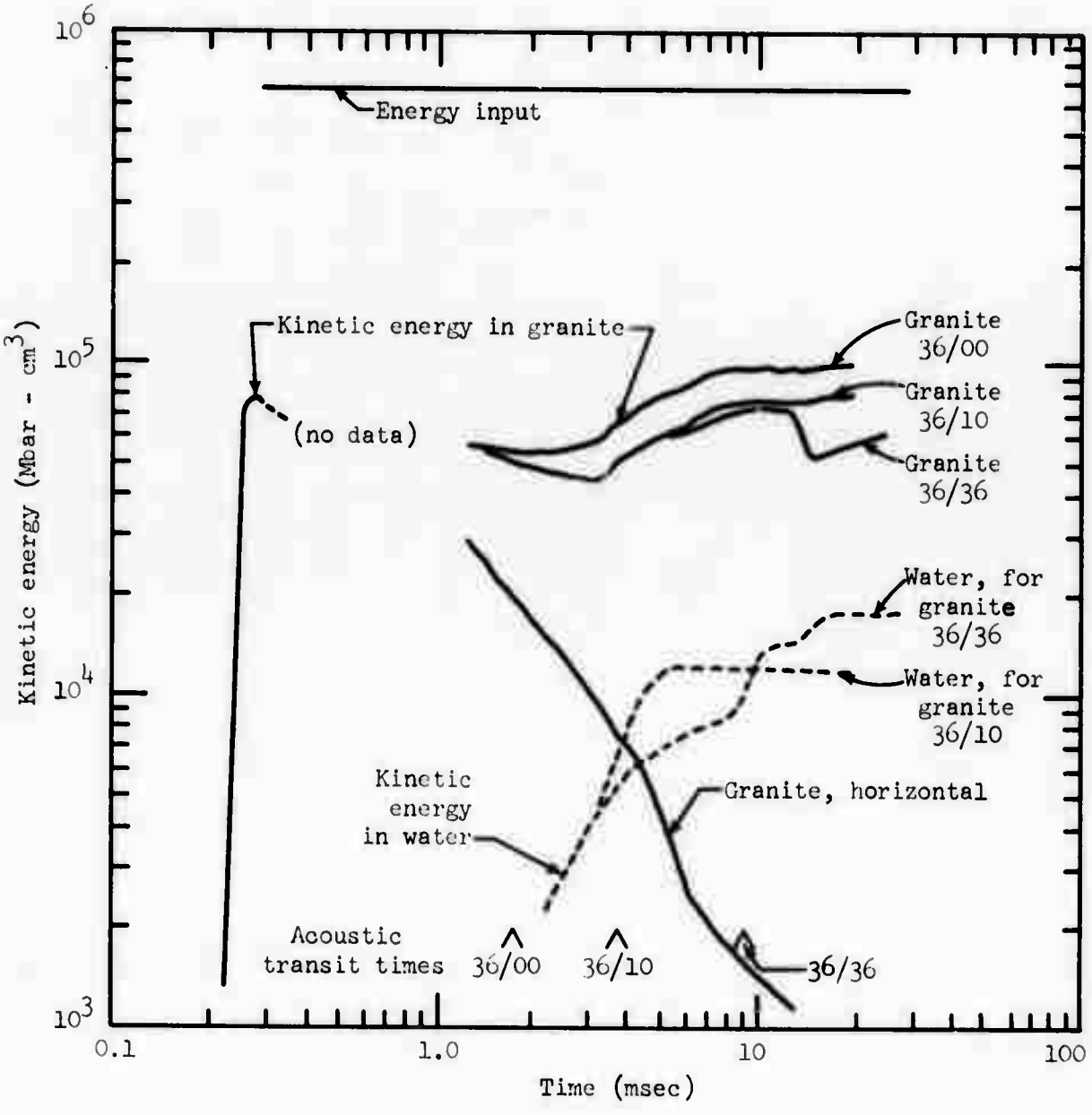

Figure 68. Kinetic energy, granite configurations (no edits of data between 0.3 and 1.3 msec).

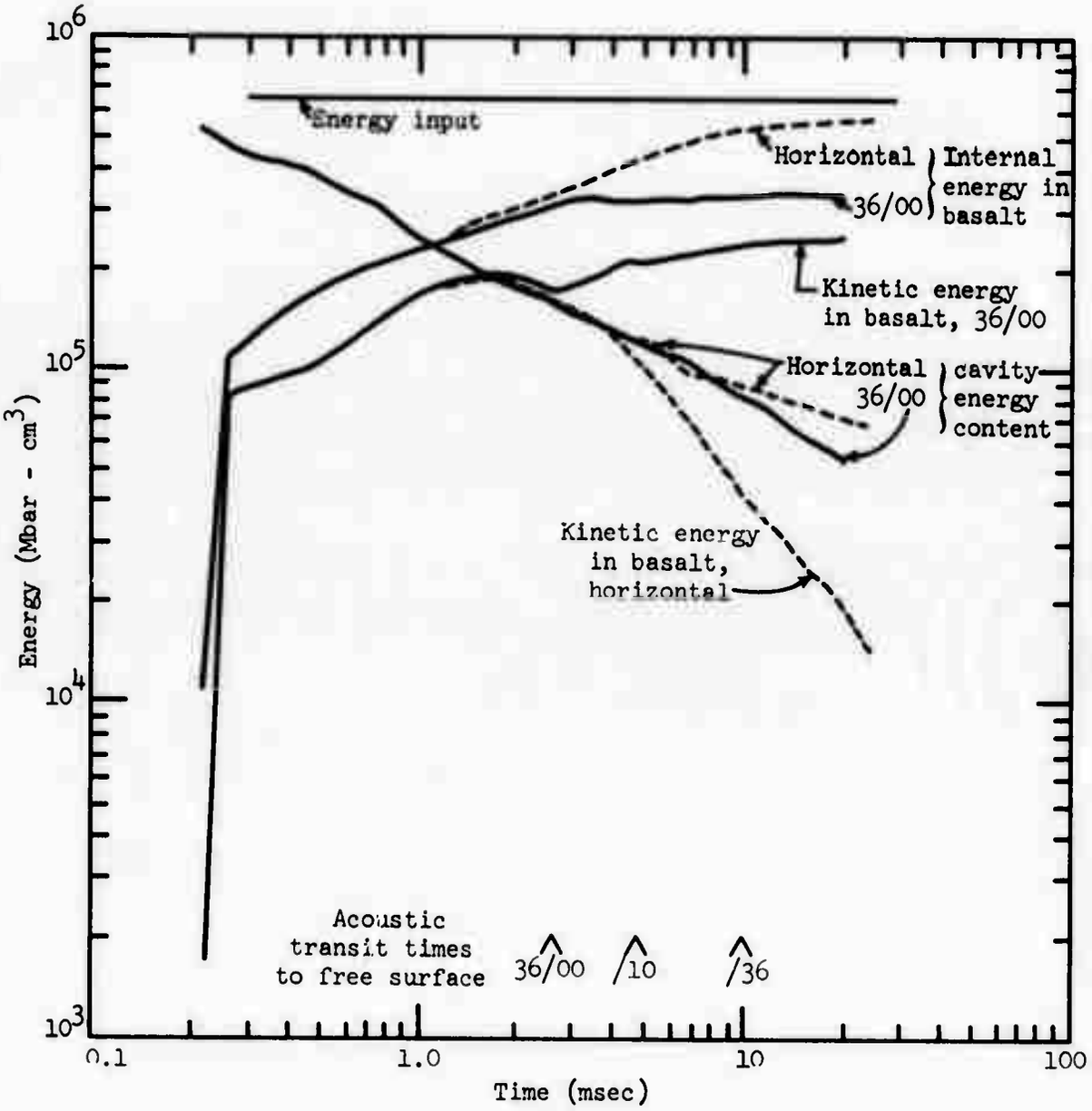

Figure 69a. Kinetic, internal, and cavity energy, basalt configurations (36/00 and horizontal).

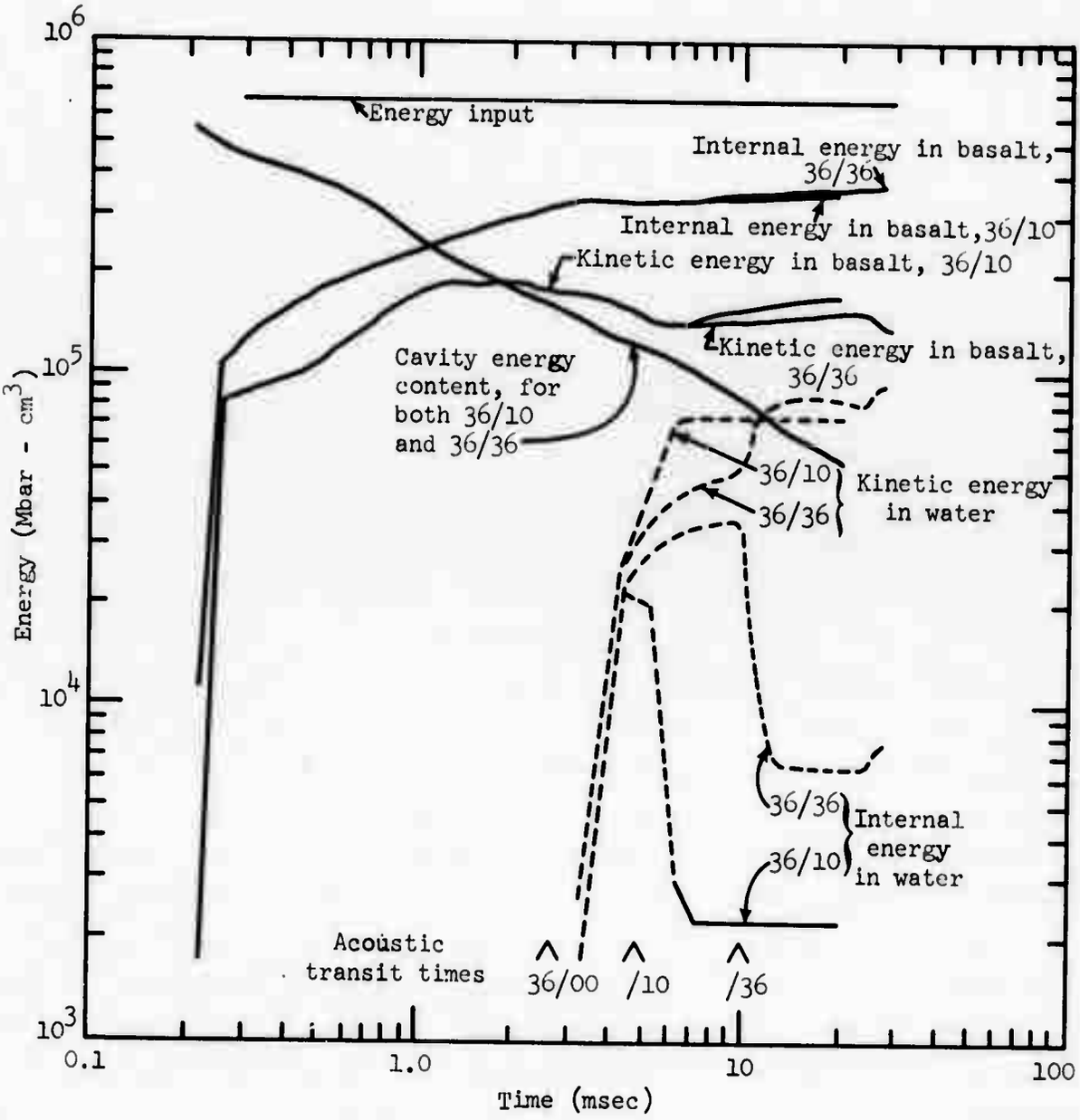

Figure 69b. Kinetic, internal, and cavity energy for basalt configurations (36/10 and 36/36)

All of the kinetic energy figures show trends consistent with previous discussions, although the water layer damping effects are somewhat exaggerated due to the extreme velocity sensitivity. Primary features of the kinetic energy behavior are summarized as follows:

(1) Kinetic energy curves for all problems in a given medium are identical until reflection occurs at the rock surface or rock-water interface. The kinetic energy for rock free-surface problems (30/00 and 36/00) then rises steeply throughout the spall phase and tends to level off at later times. The rock kinetic energy for underwater problems continues to decline after rock-water interface reflection due to water layer damping at the interface. However, the kinetic energies then begin to increase as spallation spreads through the rock mound and as the water surface reflection returns to relieve damping near the rock-water interface. The kinetic energies finally become almost constant, with slight variations at late times. Horizontal problem kinetic energies decline steeply at late times, as expected. (2) The kinetic energy in water rises steeply after the shock wave reaches the rock-water interface. This increase continues as spall reflection occurs at the rock-water interface. Ballistic spallation then spreads throughout the water layer and the kinetic energy curves level off (water layer in freefall). Water dynamics are most clearly displayed in the "deep" 30/36 or 36/36 problems. Kinetic energy in water rises steeply as the shock enters the water (time 30/00Λ, or 36/00Λ), increases more slowly as the shock moves through the water layer, jumps suddenly as the shock is reflected at the free surface (time 30/36Λ or 36/36Λ), increases rapidly as spallation spreads through the water layer, then levels off during ballistic freefall. Further small increases may occur at very late times if the rock layer again catches up with and recompacts the bottom part of the water spall (gas acceleration pulse reaches water layer). (3) Kinetic energy content in rock is decreased significantly by the presence of an overlying water layer, with most of the decrease occurring even for the shallowest water depths (D_w = 5 or 10 ft). Additional water layer depth has little influence on the rock kinetic energy, and likewise does not increase the water layer kinetic energies dramatically. (4) The rock kinetic energy curves are slowly varying functions beyond 10-15 msec (after initial spall phase is complete) and are not extremely

sensitive to late-time interactions. This trend clearly shows that overall mound dynamics are not crucially dependent on late-time effects, and the use of one-dimensional vertical calculations and kinetic energies to analyze mound dynamics is quite appropriate. (5) The late-time effects which do appear consist primarily of a slight continuing increase in rock energy due to gas acceleration. This phase is followed by a very late-time decrease in the rock kinetic energy for coral 30/36 (Figure 66), coral 36/36 (Figure 67), basalt 36/36 (Figure 69b), and granite 36/36 (Figure 68). The water kinetic energy then increases for these same problems at still later times. This interaction is explained as recompaction of the mound following the gas acceleration phase (see previous discussion). The gas acceleration and subsequent recompaction effects spread slowly upward through the rock mound, eventually transferring kinetic energy to the upper regions of the problem (water layer). Note that the granite kinetic energy curve actually shows two gradual increases followed by two deceleration phases (Figure 68); these correspond with the two separate gas acceleration pulses and subsequent recompaction phases noted earlier (cf., Figure 50b and others). Only the first gas acceleration pulse reaches the water surface layer for granite 36/36 (single late-time increase in water kinetic energy).

The shallow water layer problems were not carried late enough to show these mound recompaction effects or late-time interactions with the water layer. Recompaction would occur at very late times for these configurations, but the dispersion of the rapidly-moving spalled rock and water layers obviously decreases the intensity and speed of propagation of late-time effects.

The internal and cavity energies are also shown for the basalt events (Figures 69a-b). The cavity energy content at late times is highest for the horizontal calculation, and is lower for the vertical configurations (energy is transferred from the cavity to basalt during the gas acceleration phase). The cavity energy curves are similar for vertical problems 36/00, 36/10, and 36/36 (as were the cavity radii and pressures discussed earlier). Again, this behavior supports the conclusion that the water layers have little influence on gas acceleration and late-time close-range effects for basalt. The internal energy curve for basalt (horizontal problem) shows a

steady increase at late times, corresponding with the decrease in kinetic energy. Internal energy approaches total problem energy after 20 msec. The basalt vertical problems reveal almost-constant internal energies at late times; event 36/00 has the lowest internal energies, while the underwater problems 36/10 and 36/36 are successively a little higher. However, the difference in internal energy between these three problems is extremely small, much smaller than the loss of kinetic energy for the underwater problems. The relationships between kinetic and internal energy are more clearly shown in Figure 70, which plots the ratio of kinetic energy to internal energy (KE/IE) for both basalt and water layers. The ratio in basalt is highest for 36/00, increasing dramatically during the spall phase. The ratios for 36/10 and 36/36 decline due to water damping in the same time period, converging on lower levels at late time. It is evident that the presence of a water layer causes only a slight increase of internal energy but a large decrease of kinetic energy and KE/IE ratio in the underlying basalt. Almost all of the kinetic energy lost from basalt goes into the water layer (rather than into internal energy of basalt). This situation is expected to occur for all shallowly-buried spall-dominated problems. The internal energy curves for the water layers (Figure 69b) reveal interesting trends not visible in the kinetic energy curves alone. Internal energy increases until spall reflection at the water surface occurs, then decreases rapidly as spallation spreads throughout the water layer, finally reaching a constant value when the entire water layer enters freefall. These relationships are also illustrated in Figure 70 (KE/IE ratio in water layer). The ratio of kinetic to internal energy actually remains constant or declines slightly as the shock propagates through the water layer (times from 36/00$_\Lambda$ to 36/10$_\Lambda$ or 36/00$_\Lambda$ to 36/36$_\Lambda$). However, after reflection at the water surface (see times after 36/10$_\Lambda$ or 36/36$_\Lambda$), the internal energy decreases and the ratio of KE/IE increases rapidly, again approaching a constant value at late time. The late-time internal energy content in the rapidly-moving water spall layer is quite small and the ratio of KE/IE is very large as expected. The water internal energy curve for basalt 36/36 shows a slight increase near the end of the problem, corresponding with the water kinetic energy increase at the same time (gas acceleration pulse and recompaction effects reach bottom of the water layer).

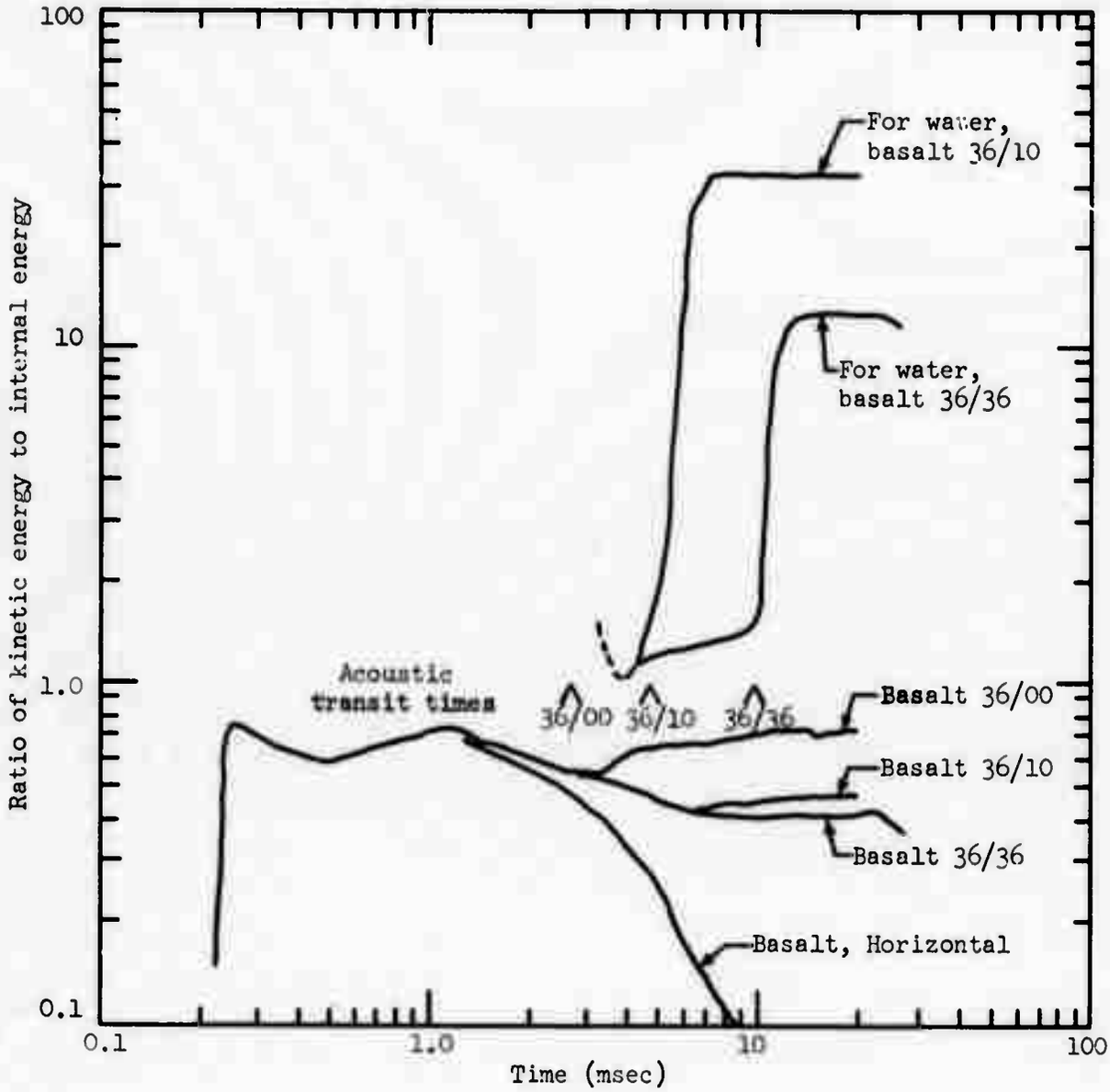

Figure 70. Ratio of kinetic energy to internal energy (KE/IE) as a function of time, basalt calculations.

Some of the representative late-time energy data have been abstracted from Figures 66-69, and are summarized in Tables 8 and 9. The tables also list corresponding data for three subsidiary sample problems (lower three entries of each table). These results will be discussed in Chapter X. All energies are selected at times later than two shock transit times throughout the problem, after spallation is complete and the energy curves have"leveled off." In most cases, a two-value range is listed for each quantity, representing the approximate variability at late times. Table 8 lists the ratios of kinetic energy (KE) to total input energy for each problem; this ratio is given for the rock layer (KE (rock)/total energy), water layer (KE (water)/total energy), and both layers combined (total KE/total energy). Also, the relative partition of kinetic energy between rock and water is listed. Table 9 presents the ratios of kinetic energy to internal energy; the ratio is compiled for the rock layer [KE (rock)/IE (rock)] and for the water layer [KE (water)/IE (water)]. Rock values list an approximate range of variability at late times. The water layer ratios tend to converge on a constant value at late times, since most or all of the water layer is in ballistic freefall.

The ratios of kinetic energy in rock to total problem energy (Table 8) are highest for coral 30/00 (about 0.45, or 45% of total energy is converted into kinetic energy) and for coral 36/00 (about 0.4 or 40%), becoming progressively lower for basalt 36/00 (38%) and granite 36/00 (15%). These ratios decline somewhat as water layers of increasing thickness are added to the problems, and the ratio (kinetic energy in water)/(total energy) increases correspondingly. It is quite interesting to note that the ratio (total kinetic energy)/(total energy) for each set of problems declines by only about 0.02 to 0.06 (2 to 6%) as thicker water layers are added (up to D_W = 36 ft). Thus, the addition of water does not greatly decrease the total available kinetic energy, in spite of the increase in overburden. The addition of 6 ft of coral (30/00 to 36/00) modified the total available kinetic energy about as much as 36 ft of water overburden for similar problems. Since total kinetic energy does not change dramatically with water depth, we may conveniently deduce water layer effects by comparing

Table 8 Ratio of Kinetic Energy to Total Problem Input Energy (late times, after rock layer spallation is complete).**

Configuration	KE(rock) / Total Energy	KE(water) / Total Energy	Total KE *** / Total Energy	KE Partition Rock	KE Partition Water
Coral 30/00	0.434 0.452	-- --	0.434 0.452	1.0 1.0	0 0
Coral 30/05	0.261 0.279	0.165 0.165	.426 .444	.613 .628	.387 .372
Coral 30/10	.225 .228	.189 .189	.414 .417	.543 .547	.457 .453
Coral 30/36	.194 .150	.197 .227	.391 .377	.496 .398	.504 .602
Coral 36/00	.389 .404	-- --	.389 .404	1.0 1.0	0 0
Coral 36/05	.234 .251	.148 .147	.382 .398	.613 .631	.387 .369
Coral 36/10	.200 .216	.174 .173	.374 .389	.535 .555	.465 .445
Coral 36/36	.176 .147	.189 .203	.365 .350	.482 .420	.518 .580
Basalt 35/00	.374 .389	-- --	.374 .389	1.0 1.0	0 0
Basalt 36/10	.246 .260	.112 .112	.358 .372	.687 .699	.313 .301
Basalt 36/36	.222 .209	.125 .141	.347 .350	.640 .597	.360 .403
Granite 36/00	.143 .149	-- --	.143 .149	1.0 1.0	0 0
Granite 36/10	.116 .120	.018 .018	.134 .138	.866 .870	.134 .130
Granite 36/36	.112 .084	.021 .026	.133 .11	.842 .764	.158 .236
	(Lower Layer)	(Upper Layer)	Total KE/Total	(lower)	upper)
Coral 41.31*	.185 .199	.167 .167	.352 .366	.526 .544	.474 .456
Coral 55.11*	.083 .101	.197 .194	.280 .295	.296 .342	.704 .658
Basalt 39.83*	.246 .260	.103 .102	.349 .363	.705 .719	.295 .281

* Equivalent overburden comparison calculations (no water layer) - see text, Chap X.
** Two values are listed in each case, corresponding to the approximate range of variability at late times.
*** Total KE = Rock KE + Water KE

TABLE 9. Kinetic Energy/Internal Energy Ratios at Late Times ($t \geq$ 2 transit times).

CONFIGURATION	KE/IE RATIO,** ROCK	LATE-TIME KE/IE RATIO IN WATER
Coral 30/00	0.86 - 0.95	--
30/05	.49 - .58	37.9
30/10	.46 - .48	22
30/36	.46 - .3	8.5
36/00	0.73 - 0.78	--
36/05	.46 - .43 - .48	54.3
36/10	.45 - .38 - .41	32
36/36	.45 - .33	12
Basalt 36/00	0.66 - 0.74	--
36/10	.44 - .43 - .48	33
36/36	.44 - .42	12.8
Granite 36/00	0.17 - 0.20	--
36/10	.13 - .16	11
36/36	.13 - .15 - 0.1	$\approx$ 7
	RATIO, LOWER LAYER	RATIO, UPPER LAYER
Coral 41.31*	.331 - .376	(8.95)
Coral 55.11*	.151 - .168	(3.27)
Basalt 39.83*	.396 - .480	(19.5)

* Equivalent overburden comparison calculations (no water layer) - see text, Chapter X.

** A range of values is listed, corresponding to the approximate variation at late times, after two transit times.

the kinetic energy partition for each set of problems. Using average values, the fraction of kinetic energy partitioned into the rock declines from 1.0 to 0.44 for the series coral 30/00 to coral 30/36 (the kinetic energy partition in water correspondingly increases from 0 to 0.56). The partition in rock decreases from 1.0 to 0.45 for coral 36/00 to 36/36, from 1.0 to 0.62 for basalt 36/00 to 36/36, and from 1.0 to 0.80 for granite 36/00 to 36/36. In all cases, the greatest decrease of rock kinetic energy occurs for the shallow water layer (D_w = 5 or 10 ft), with small additional decreases at greater water depths. The water layer causes the largest kinetic energy decrease in rock for the coral events (slight impedance mismatch at the rock-water interface); the decrease is much less severe for basalt and for granite (gross impedance mismatch, efficient tensile reflection at the interface). This situation has a very significant effect on the KE (rock)/total energy ratio: The "rock" kinetic energy for coral 36/00 is greater than kinetic energy for basalt 36/00, but the basalt kinetic energy in rock becomes greater for events 36/10 and 36/36. The implications for underwater cratering in high and low impedance rock are obvious. Kinetic energy partitioning into the rock is even more efficient for the granite 36/10 and 36/36 events (≈ 0.86 to 0.80). Note, however, that the kinetic energy (rock)/total energy ratios for all granite problems are extremely small (≈ 0.15 to 0.1). The rock kinetic energy for granite 36/00 is less than the rock kinetic energies for coral 36/36 and basalt 36/36, with deep water layers. This result once more verifies that the high-strength granite configurations are at deeper-than-optimum burial and do not model realistic cratering events. Nonetheless, the fundamental result obtained here, high kinetic energy partition into the rock layer for high impedance rock, is expected to hold at all burial depths.

The KE/IE ratios (Table 9) show trends similar to the above. The ratios are highest for coral 30/00 and 36/00, declining for the other media. The KE/IE ratios for high-strength granite are quite low, again revealing inefficient material ejection and excessively deep burial. Most of the explosive energy is effectively lost as internal energy of the medium, and does not contribute to material ejection.

General conclusions of the kinetic energy analysis may be stated as follows: (1) Presence of a water layer is more important than water depth in determining overall mound dynamics (even for relatively deep water layers, $D_w/D_r \approx 1.0$); (2) The kinetic energy partitioned into rock depends primarily on the acoustic mismatch at the rock-water interface, and only secondarily on water depth; (3) Increasing water layer depth does not rapidly modify the total kinetic energy available to eject material; by contrast, the available kinetic energy decreases precipitously with increasing burial depth in a single-layer rock medium; and (4) Following conclusions (1) - (3), the water layer should never be treated as an "equivalent weight" of rock overburden in cratering problems.

VIII. SPALL VELOCITIES-ACOUSTIC ANALYSIS

This chapter compares SOC-calculated shock propagation and spall velocities in the water layer with the results of a simple acoustic transmission analysis. It is assumed that the shock front is transmitted and reflected as a low-amplitude (acoustic) wave at the rock-water interface. Angle of refraction and radius of curvature are described by geometric laws. Further, the front is assumed to propagate at sonic velocity (linear elastic medium) and with a constant peak attenuation rate in the water layer. These assumptions are reasonable because the peak amplitudes near the interface are moderate ($P \simeq 1$ kbar) and peak waveforms are relatively well-resolved.

For acoustic waves, the angle of reflection at an interface is equal to the angle of incidence. The angle of the refraction into the overlying layer is given by,

$$\cos \theta_w = \frac{C_w}{C_r} \cos \theta_r$$

where "θ" is measured between the direction of shock propagation and the interface; $\theta = 90°$ for normal incidence.

θ_w = angle of refraction into upper (water) layer

θ_r = angle of incidence in lower (rock) layer

C_w = front velocity of propagation in upper layer

C_r = front velocity of propagation in lower layer.

Continuity of pressure and particle velocity across the interface may be applied to derive transmission and reflection factors. The reflected peak pressure at the interface is determined to be,

$$P\ (\text{reflected}) = P_r \frac{\rho C_w \sin\theta_r - \rho C_r \sin\theta_w}{\rho C_w \sin\theta_r + \rho C_r \sin\theta_w}$$

P_r = incident peak pressure in lower (rock) layer
ρC_r = acoustic impedance of lower layer
ρC_w = acoustic impedance of upper layer

Similarly, the peak particle velocity after reflection at the interface is,

$$V\ (\text{reflected}) = V_r \frac{\rho C_w \sin\theta_r - \rho C_r \sin\theta_w}{\rho C_w \sin\theta_r + \rho C_r \sin\theta_w}$$

V_r = incident peak particle velocity in the lower (rock) layer.

The quantity"sin θ" is of course equal to 1.0 for normal incidence. Note that the velocity or pressure reflection factor is negative at a high-to-low impedance interface ($\rho C_r > \rho C_w$, $C_r > C_w$, $\theta_w > \theta_r$). Thus, an incident compression wave is reflected as a downward-travelling tensile wave (upward velocity component). The spall velocity at the interface is obtained by summing the vertical velocity components:

$$V_{spall}\ (\text{rock}) = [V_r + V\ (\text{reflected})] \sin\theta_r \leq 2V_r$$

Note that this rock interface spall velocity is a peak value; velocity near the interface may be damped by the water layer at later times, as the transmitted shock propagates away from the interface and velocities in the water layer decrease.

The peak pressure transmitted into the upper layer at the interface is,

$$P_w = P_r \left[\frac{2\rho C_w \sin\theta_r}{\rho C_w \sin\theta_r + \rho C_r \sin\theta_w}\right]$$

P_w = transmitted peak pressure in the upper (water) layer

The term in brackets will be denoted as the pressure transmission factor into the water layer. The transmission factor decreases for increasing impedance mismatch between rock and water and for increasing incident angle "θ_r"; Figure 71 presents a plot of the rock-water pressure transmission factor as a function of angle for the coral, basalt, and granite media used in this study.

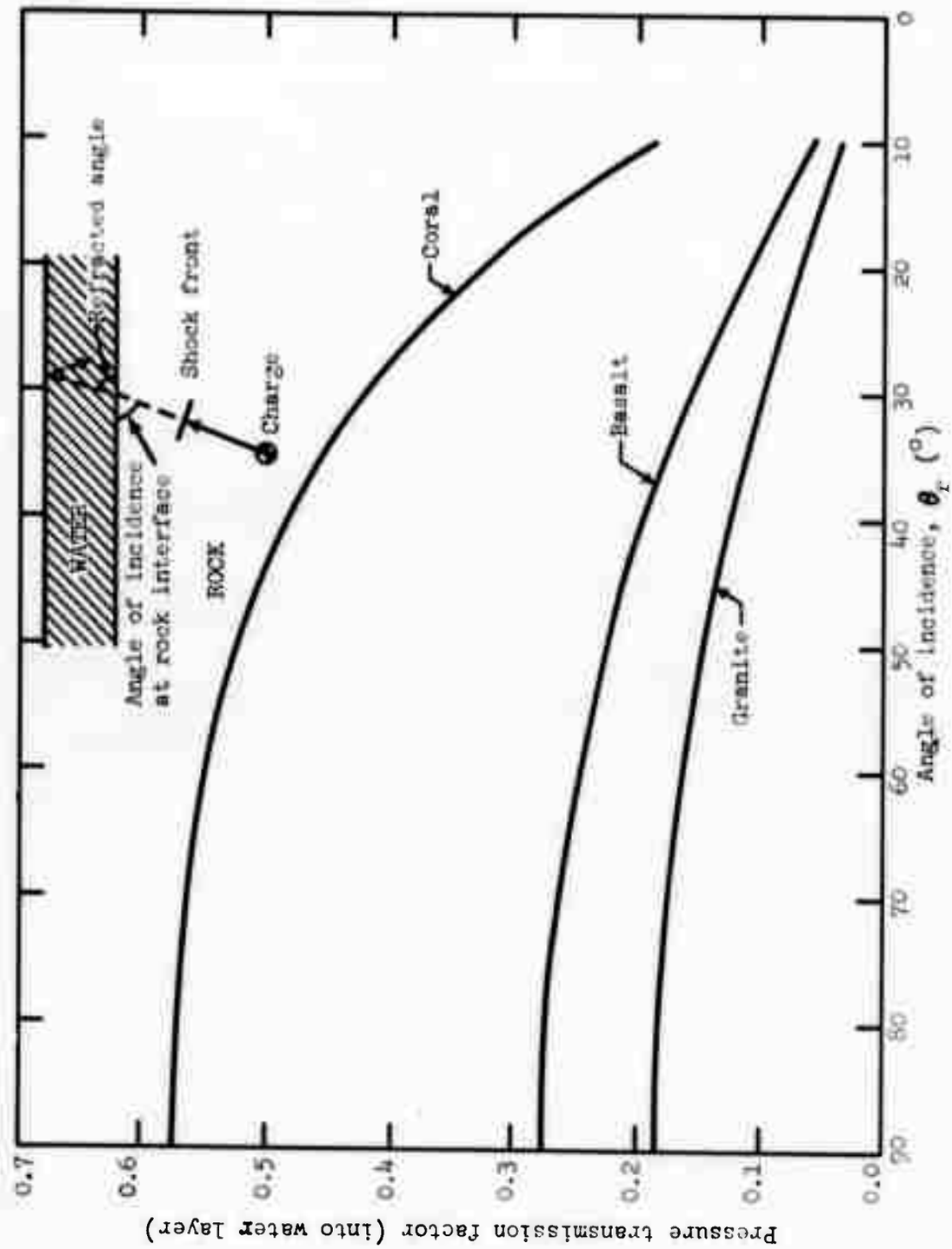

Figure 71. Acoustic pressure transmission factor as a function of angle of incidence, θ_r.

The impedances of rock and water differ, so the velocity transmission factor into the water layer is not the same as the pressure transmission factor. Peak particle velocity and peak pressure at the shock front in the water layer are related by the acoustic equation,

$$P_w = \rho C_w V_w$$

V_w = peak particle velocity at the front.

Thus, the transmission equation may be expressed in terms of velocity as,

$$V_w = V_r \frac{\rho C_r}{\rho C_w} \frac{2\rho C_w \sin\theta_r}{\rho C_w \sin\theta_r + \rho C_r \sin\theta_w}$$

Note also that either peak velocity or peak pressure at the shock front may be determined if the other quantity is known. For the properties of water assumed in these problems,

$$\rho C_w \cong 66.3 \frac{\text{psi-sec}}{\text{ft}} = 217.5 \frac{\text{psi-sec}}{\text{m}}$$

and the peak pressure is given by,

$$P_w = \rho C_w V_w = 217.5 V_w \quad (V_w \text{ in m/sec, } P_w \text{ in psi})$$

This relationship applies at the shock front (peak values), but not to spall velocities in the surface cutoff layer adjacent to an interface, where the tensile reflection truncates the peak pressure of the incident wave.

For water, it has been shown[28] that peak attenuation of weak pulses and even of relatively strong shock fronts occurs at the rate of "$R^{-1.13}$", where R is the range from center for a spherically divergent front, or, more generally, the radius of curvature of the front. Hence, attenuation of the transmitted shock in the water layer may be adequately modeled by a power law dependence. Spall launch velocities of the water surface may likewise be calculated, since perfect tensile reflection occurs at a free surface and the vertical component of particle velocity is doubled:

$$V_{spall}(\text{water}) = 2V_w(\text{at surface})\sin\theta_w = \frac{2P(\text{water, at surface})}{\rho C_w} \sin\theta_w$$

The peak pressures and velocities at or above the rock-water interface and the peak surface spall velocities may thus be acoustically simulated if the following parameters are available: Peak pressure or particle velocity of

the shock front incident at the interface, angle of incidence, impedances and sonic velocities of the two layers, and attenuation rate in the upper layer. All of these quantities are known except the peak pressure (particle velocity) at the interface, which must be derived from SOC calculations for a given medium. Preston and Wheeler[55] have demonstrated that peak shock front parameters in rock may be accurately fitted over a broad range interval by power law equations. However, separate equations are needed for the "high pressure" regime (range < a fixed transition range) and the "low pressure" or acoustic regime (range > transition range). Approximate relations have been derived for the coral, basalt, and granite calculations. It was convenient in this case to fit peak particle velocities at the shock front. The horizontal calculations were first used, but results proved slightly inaccurate (≈ 10% low) due to the coarse zoning. Small corrections were applied to better match the finely-zoned vertical calculations. Fitted equations take the form,

$V_1 = a_1 R^{b1}$ (for Range R < transition range R_{tr})

$V_2 = a_2 R^{b2}$ (for R > R_{tr})

$V_1 = V_2$ at R_{tr}

a and b are constants

Peak velocity relations for the three media are presented in Table 10. Note that attenuation rates "b_1" and "b_2" in each medium are always more rapid for the close-in region ("b_1") than at long ranges ("b_2"). Comparing materials, the attenuation rates in both regions are most rapid for granite. Power law fits proved slightly inaccurate at very close ranges (R < 10 ft) for these SOC calculations; all of the events discussed here were buried more deeply than 10 ft so the close-range inaccuracies have no effect at the interface.

Given a suitable model of the rock-layer peak particle velocities, the velocity or stress at any interface location may be determined and acoustic calculations for the ray transmitted at that location may be performed. Note that these calculations are applicable for any intercept angle (as well as for the vertical direction), thus giving a two-dimensional picture of shock transmission into the upper layer. Figure 72 schematically depicts the

TABLE 10. Empirical Equations Used to Approximate Free-Field Peak Particle Velocity at the Shock Front.*

$V_1(ft/sec) = a_1 R^{b1}$ Close-in Region, $R<R_{TR}$; "R" in ft

$V_2(ft/sec) = a_2 R^{b2}$ Longer Ranges, $R>R_{TR}$; "R" in ft

For Acoustic Waves: Peak radial stress $\sigma_r=\rho CV$ ρC= impedance of local medium

Medium*	a_1	b_1	R_{TR}(ft)	a_2	b_2
Coral (smoothed EOS)	8.0369×10^4	-1.8395	13.124	2.9138×10^4	-1.4454
Basalt	9.1272×10^4	-2.0873	13.124	1.9069×10^4	-1.4791
Granite	9.3539×10^4	-2.1481	16.405	4.3924×10^4	-1.8779

*The fitted equations are generally valid within the range interval from 4 to 70 ft; the close-range equations are somewhat inaccurate due to changes in the slopes of the SOC - calculated peak velocity curves, which cause velocities to deviate slightly below straight line fits at ranges ≈ 5 to 10 ft. These close-range deviations have no effect on the water-layer transmission calculations in this report ($D_{rock} \geq 30$ ft).

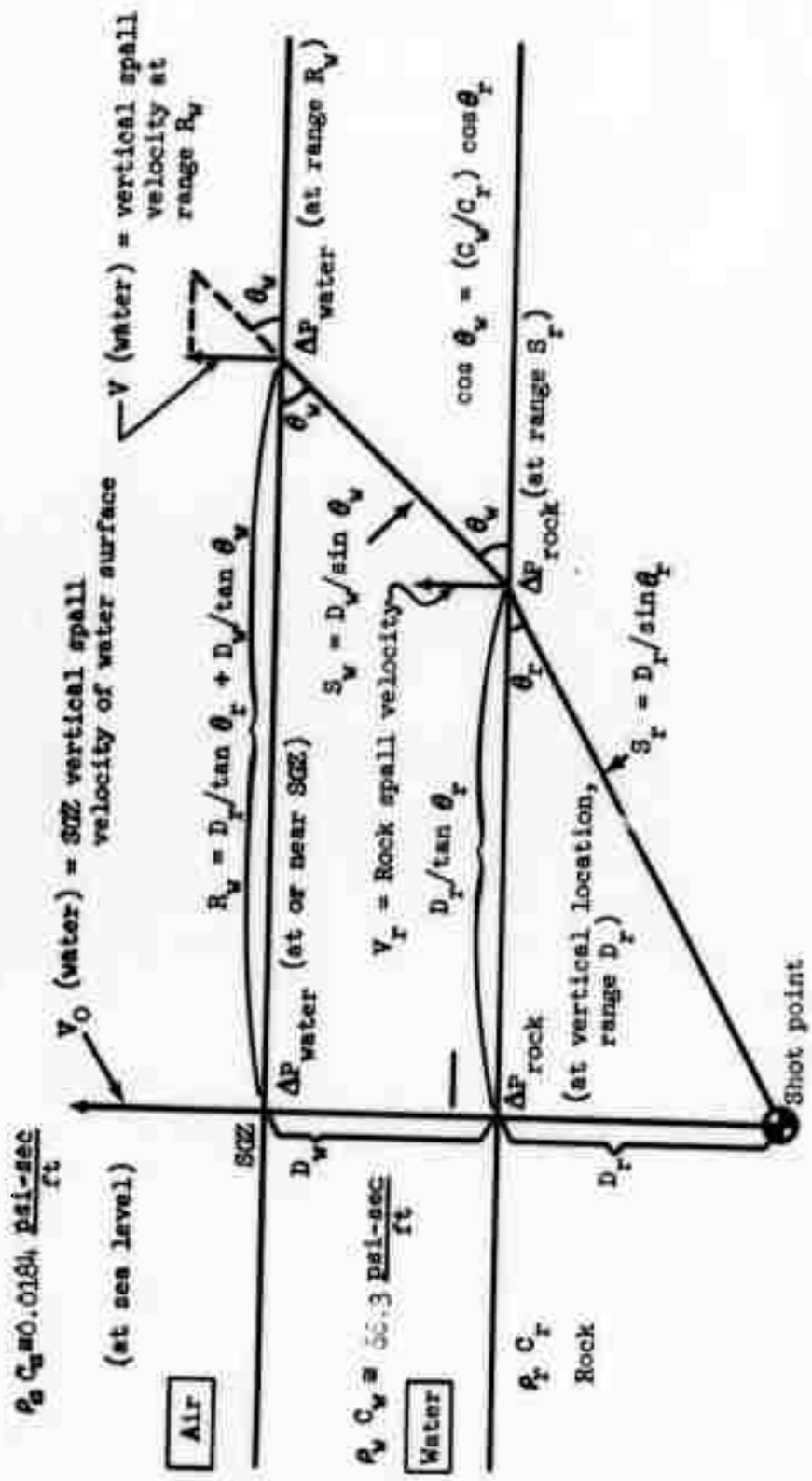

Figure 72. Shock wave transmission for cratering medium overlain by water layer of small-to-moderate thickness ($D_w \approx D_r$).

transmission of a vertical ray and an oblique ray in a two-layer configuration. (The figure shows a third overlying layer of air as well; we will treat the water surface as a free surface for present purposes.)

Acoustic calculations have been performed for events at a variety of rock and water layer depths, in coral, basalt, and granite. Velocity fits from Table 10 provided the input rock velocities "V_r". Results of these calculations may be conveniently compared with the "SOC" interface and surface spall velocities (vertical direction only). However, it should be remembered that the SOC one-dimensional calculations necessarily impose the condition of a spherically-divergent geometry. No corrections are included for refraction effects and change in wavefront curvature at an interface. The error thus introduced will be negligible very close to the interface (thin water layer), and will become progressively larger as the transmitted shock propagates away from the interface. In order to compare "SOC" and "acoustic" velocities, it was necessary to make two sets of acoustic calculations. The first set assumes spherical divergence of the transmitted shock in the water layer,* and will be denoted as the "linear" or "uncorrected" set. The second set of calculations includes the correct treatment of refraction and change in divergence at the interface for all rays.[27,26] These calculations will be known as the "corrected" set. The two sets are identical at the rock interface, but the water surface spall velocities deviate progressively for increasing water layer depths.

Spall velocities above shot point. Table 11 compares the spall velocities at the rock-water interface and at the water surface for the SOC calculations and acoustic calculations. All of these velocities are in the vertical direction, directly above shot point. In addition to peak values, the SOC tabulations list a range of spall velocities for the near-surface high-velocity

* For example, the vertical (normal) ray transmitted into the water layer attenuates as $[D_r/(D_r+D_w)]^{1.13}$ beyond the rock-water interface. No change in the radius of curvature of the wavefront occurs at the interface. Corresponding equations may be written for other angles of incidence in the case of "two-dimensional" calculations (oblique incidence).

TABLE 11. SOC - Calculated Surface Layer Spall Velocities, and Acoustic Calculation Peak Spall Velocities.

		SOC CALCULATIONS			ACOUSTIC VALUES		
		VELOCITIES (m/sec)					
Medium, D_{rock}/D_{water} (in ft)		Rock Surface Layer Spall Velocity	Water Surface Layer Spall Velocity	Water Layer, Top 1.5 m Depth Interval	Acoustic Calculation, Straight Line Fit		
					Rock Spall Velocity	Water Spall Vel.(Linear)	Water Spall Vel.(corrected)
Coral	30/00	82-128 *	-----	-----	130	-----	-----
	30/05	79-90(91.2)	88-156	54-156 (@ 6.3 msec)	92.7	155.8	162.1
	30/10	79-90(91.2)	76-133	56-133 (@ 7.3 msec)	92.7	134	143.7
	30/36	79-90(91.2)	39-71	29-71 (@12.3 msec)	92.7	76.2	89.3
	36/00	64-100 *	-----	-----	100	-----	-----
	36/05	60-70(71.25)	69-123	43-123 (@ 7.3 msec)	71.25	123.0	127.2
	36/10	60-70(71.25)	60-107	48-107 (@ 8.3 msec)	71.25	108.0	114.8
	36/36	60-70(71.25)	34-62.1	28-62.1 (@13.3 msec)	71.25	65.1	75.3
Basalt	36/00	44-62-58	-----	-----	58	-----	-----
	36/10	43-52(53.4-50) *	44-74	42-74 (@ 6.3 msec)	50	75.8	88.3
	36/36	43-52(53.4-50)	25-43.3	24-43.3 (@ 12.3 msec)	50	45.7	67.4
Granite	36/00	25-32.6-32.2	-----	-----	32	-----	-----
Coarse Water Zones	36/10	21-32(29.6-29.2) *	20-31.2	17-31.2 (@ 5.3 msec)	29	44.0	53.4
	36/36	21-32(29.6-29.2)	9.5-16.1	9.7-16.1 (@ 10.3 msec)	29	26.5	44
Fine Water Zones	36/10	21-32(29.6-29.2)	21-35.2	18-35.2 (@ 5.3 msec)	29	44.0	53.4
	36/36	21-32(29.6-29.2)	10-18.0	10.6-18.0 (@ 10.3 msec)	29	26.5	44

*Values in parentheses represent the rock-water interface velocity calculated from the rock free-surface velocity for the same rock depth "D_r."

spall region (see Appendix A). The first column of SOC results gives the rock interface spall velocities for each configuration. The next two columns list the water surface spall velocities (in the high-velocity spall region, and over an arbitrary 1.5 m depth interval below the surface). Two sets of velocities are listed in the case of granite, for the coarse and fine water zone SOC calculations. The acoustic section of the table gives the rock interface spall velocity (identical for both uncorrected and corrected calculations), the water surface spall velocity for linear or uncorrected calculations, and the water surface spall velocity for corrected calculations. The rock interface velocities agree quite closely between SOC and acoustic results, as would be expected (SOC calculations were used to model peak shock front parameters in the rock layer). However, the SOC interface velocity for granite (36/10 and 36/36) is somewhat higher than the acoustically-calculated value for reflection at a rock-water interface. Comparing the water surface peak spall velocities for coral and basalt events, we find that the acoustic linear (uncorrected) values are in excellent agreement with the corresponding SOC results. The corrected acoustic water surface velocities are much higher than the uncorrected and SOC results (refraction at a high- to low-velocity interface decreases divergence of the shock front, thus increasing water layer pressures and spall velocities). Largest errors occur for the deep water layer configurations. The errors for D_W = 36 ft are approximately 21-26% (coral) or 36% (basalt, strong impedance mismatch). The acoustically-calculated water surface velocities for granite configurations are all significantly higher than the SOC values; agreement improves somewhat for the "fine" water zone calculations. In summary, the uncorrected acoustic calculations match the SOC results for basalt and coral configurations, but not for granite. The corrected acoustic velocities are higher, showing that the assumption of spherical divergence causes errors in the SOC water layer calculations. Errors are greatest for deep water layers (far from the interface) and for a large acoustic mismatch at the interface.

The disagreement between acoustic and SOC calculations for granite is closely related to the attenuation effect mentioned previously (Chapter VI, peak velocities and pressures). It was noted that peak velocities beyond the granite-water interface suffered a sudden drop, then continued to attenuate

rapidly throughout the water layer. The use of "fine" (half-size) water zones reduced the sudden drop but rapid attenuation remained. It is not surprising that the constant "$R^{-1.13}$" attenuation rate of the acoustic calculations generates higher water spall velocities than the SOC calculations. The water layer attenuation rates for "SOC" results are examined in Table 12. Table 12a presents the approximate attenuation rate of peak particle velocity at the shock front (excluding the narrow surface spall layer where peaks are reinforced by the tensile reflection). The water attenuation above coral and basalt varies approximately as $R^{-1.15}$ to $R^{-1.2}$, rates which are slightly greater than the "acoustic" assumption. The rate above granite is $R^{-1.55}$. The attenuation rates of water surface spall velocity between the various calculations (i.e., coral 36/05-36/10-36/36, etc.), show a similar trend (Table 12b).* The granite-water calculations once more show an attenuation rate on the order of $R^{-1.5}$. This question will be further examined in Chapter X.

More detailed results of the acoustic calculations for the vertical direction are presented in Figures 73-79:

Figure 73 shows the rock interface peak spall velocities as a function of burial depth in rock, "D_r". Acoustically-calculated velocities are shown for the case of no water layer (free surface) and for the case of an overlying water layer (partial reflection at interface, spall velocities are lower, decrease does not depend on water layer depth). SOC-calculated velocities (with and without water layers) are included for comparison. Some additional SOC velocities (from Chapter X) have also been added to demonstrate agreement at other burial depths.

Figures 74-77 depict the corrected water surface spall velocities as a function of water layer depth. The water surface velocities for all three media are given. Figure 74 is for a rock burial depth D_r = 24 ft, Figure 75 for a depth D_r = 30 ft, Figure 76 for D_r = 36 ft, and Figure 77 for D_r = 42 ft. This encompasses the range of burial depths commonly used with 10-ton excavation charges. Note that the water spall velocities are generally highest for coral, lower for basalt, and lower still for granite. However, coral calculation velocities decrease most rapidly with increasing water layer depth. This

*Free-surface spall velocity is approximately twice the local peak particle velocity at the shock front; therefore, the attenuation rate of surface spall velocity between the various water-layer depth calculations should match the attenuation rate of peak particle velocity in the water layer.

Table 12a. Approximate Attenuation Rates of SOC - Calculated Peak Particle Velocities In The Water Layer (Not Including The Surface Spall Layer, Where The Peak Of the Wave Is Truncated).

C A L C U L A T I O N S	Attenuation Rate, Linear (uncorrected) Geometry
Coral (D_r = 30 ft.)	$\sim R^{-1.20}$
Coral (D_r = 36 ft.)	$\sim R^{-1.16}$
Basalt (D_r = 36 ft.)	$\sim R^{-1.15}$
Granite (D_r = 36 ft.)	$\sim R^{-1.55}$

Table 12b. Approximate Attenuation Rates of SOC - Calculated Water Surface Peak Spall Velocities; Determined Between The Spall Velocities For The Various Water Layer Depth Calculations.

C A L C U L A T I O N S Medium; D_{rock}/D_{water}	Attenuation Rate, Linear (uncorrected) Geometry
Coral; 30/05,30/10, and 30/36	$\sim R^{-1.24}$
Coral; 36/05,36/10, and 36/36	$\sim R^{-1.21}$
Basalt; 36/10 and 36/36	$\sim R^{-1.20}$
Granite; 36/10 and 36/36	$\sim R^{-1.5}$

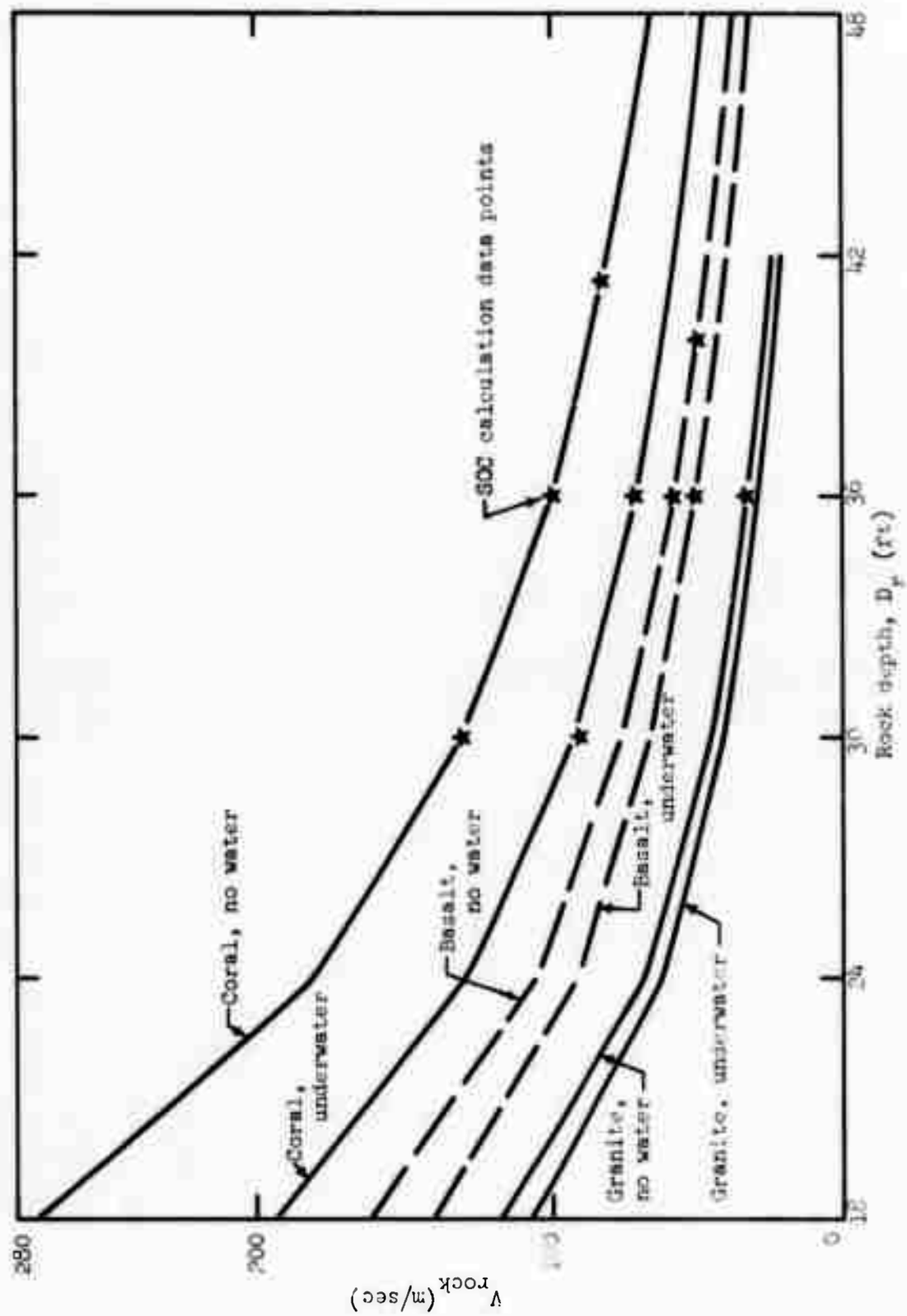

Figure 73. Acoustic peak spall velocities of rock surface, V_{rock}, as a function of rock depth, D_r.

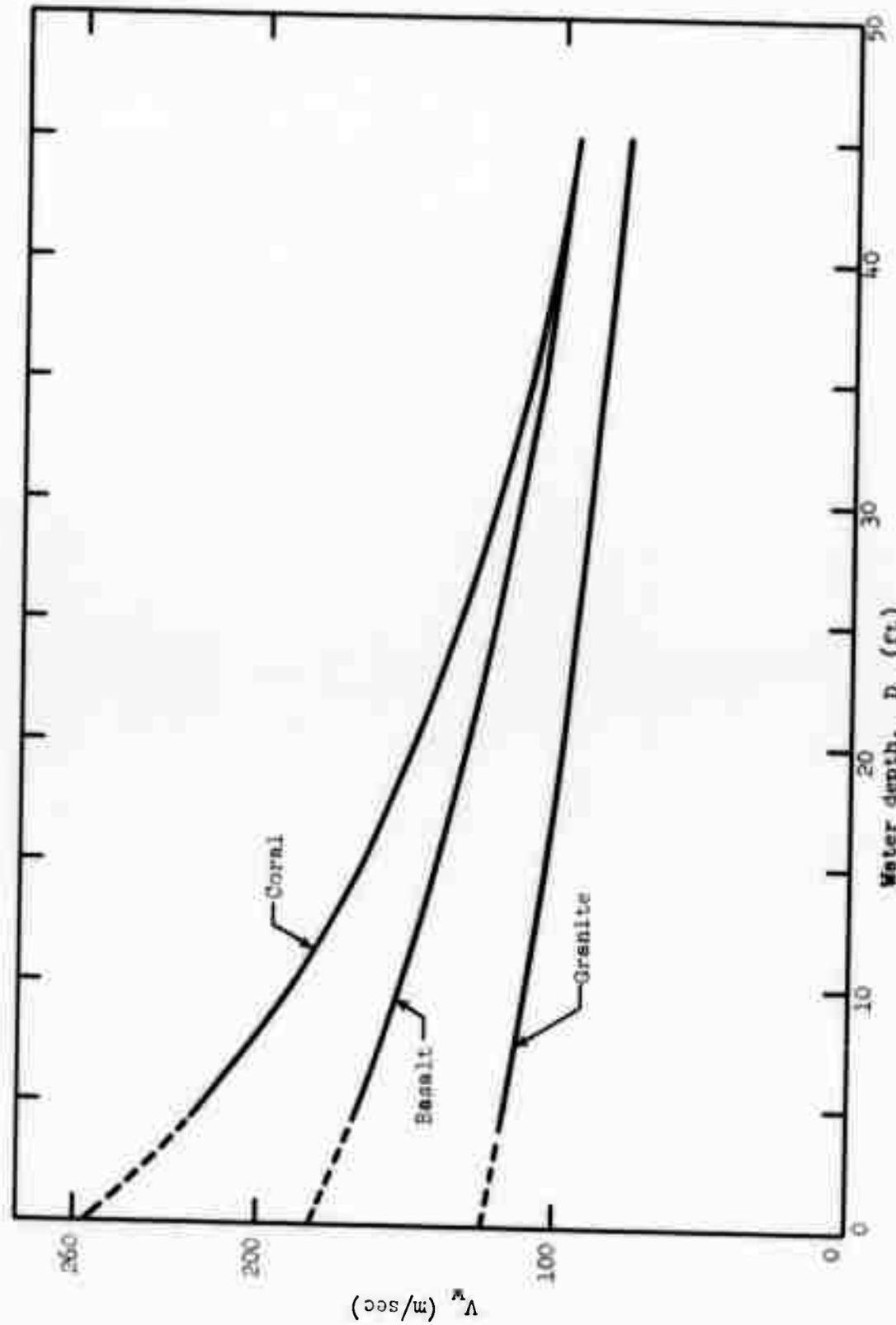

Figure 74. Water surface spall velocities as a function of water depth for D_r = 24 ft.

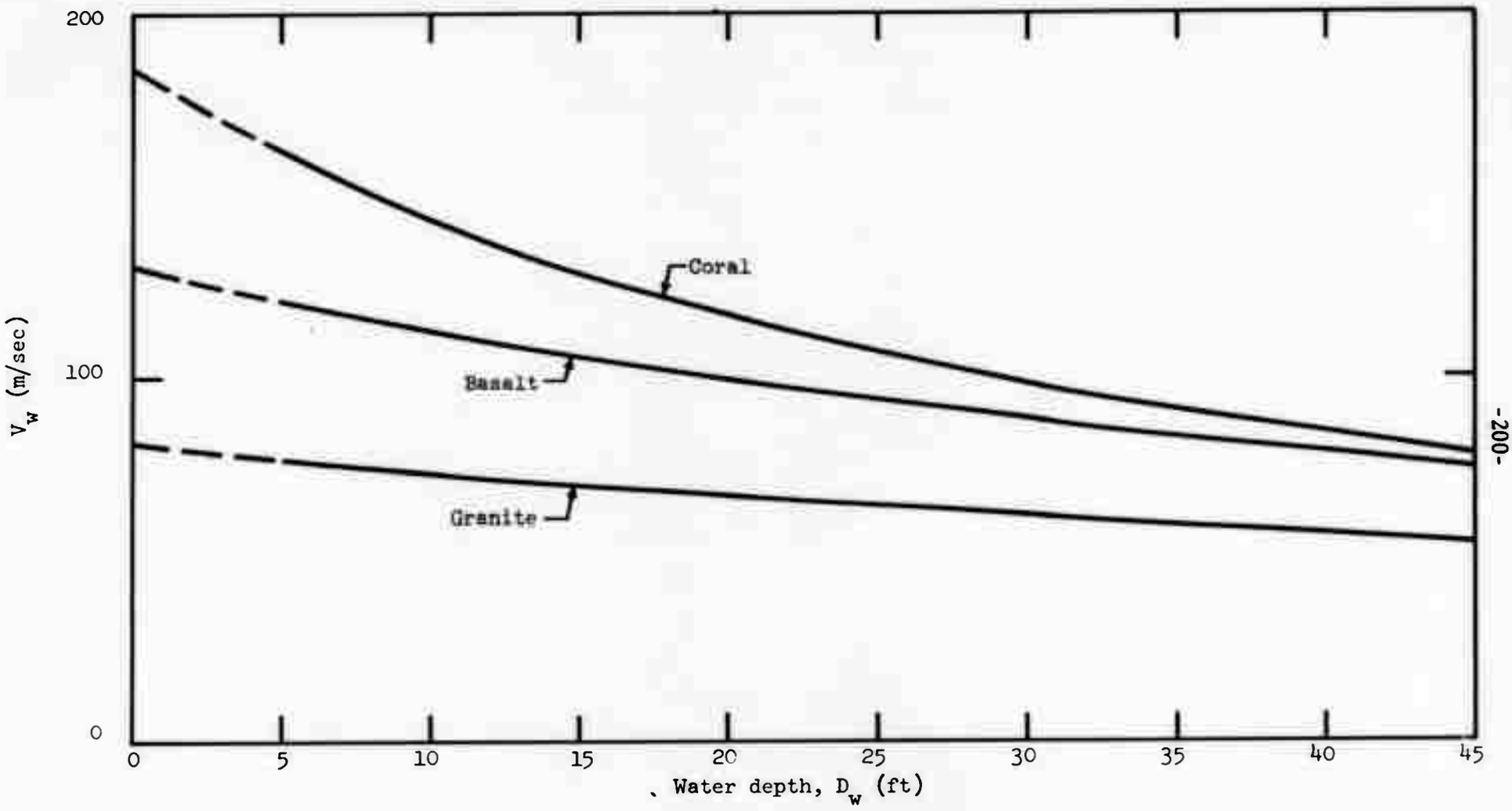

Figure 75. Water surface spall velocities as a function of water depth, for D_r = 30 ft.

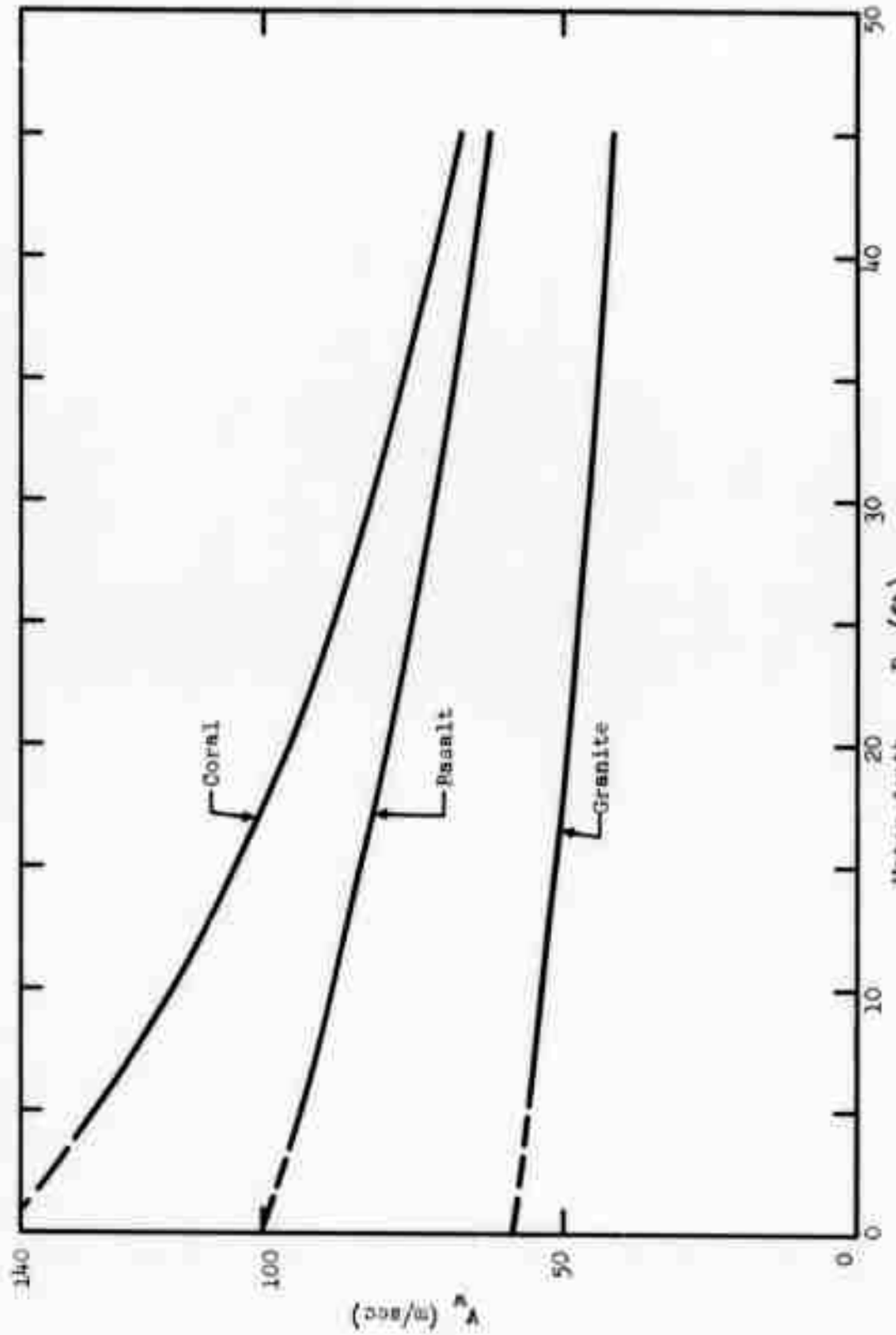

Figure 76. Water surface spall velocities as a function of water depth for D_r = 36 ft.

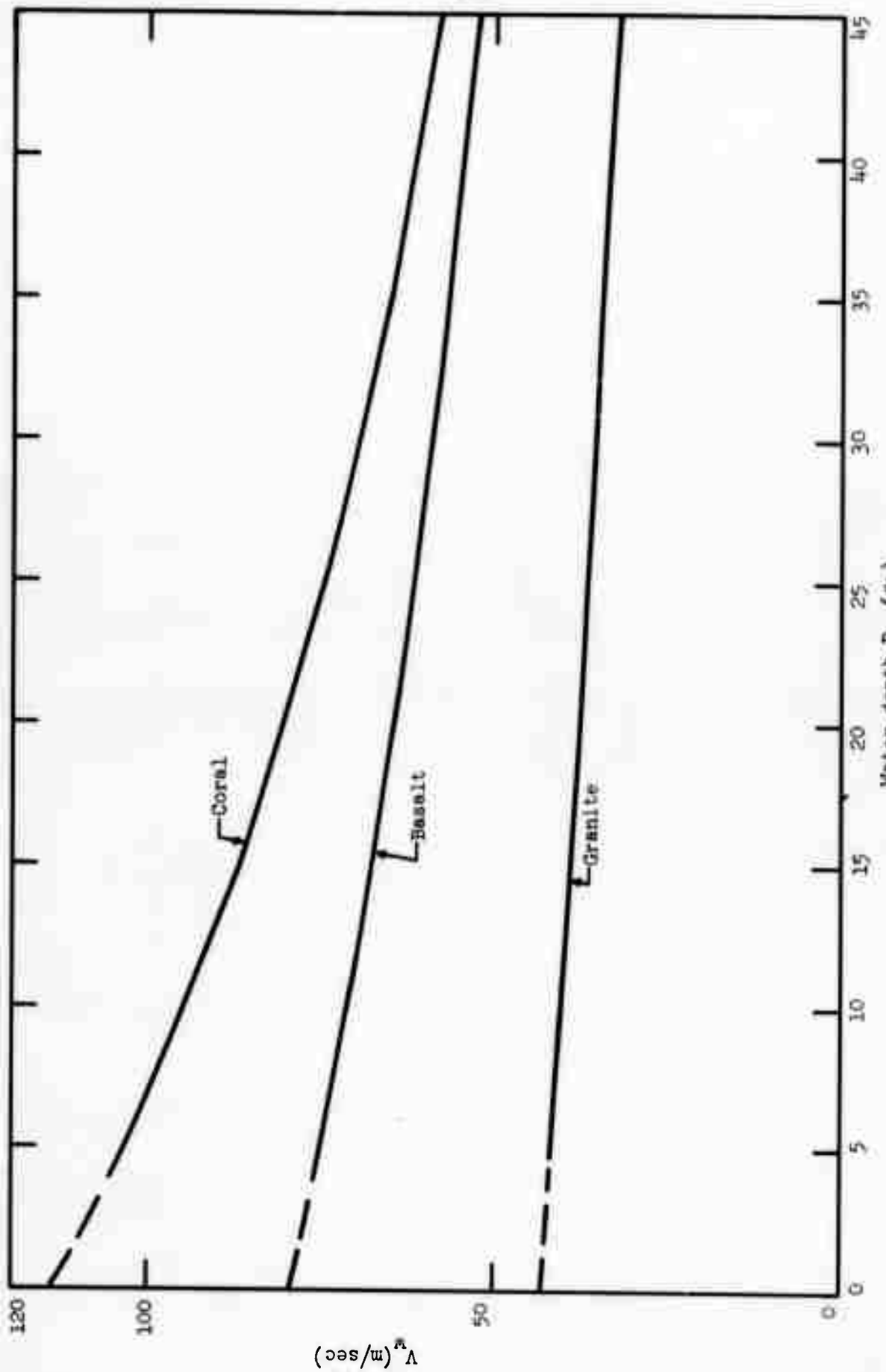

Figure 77. Water surface spall velocities as a function of water depth, for D_r = 42 ft.

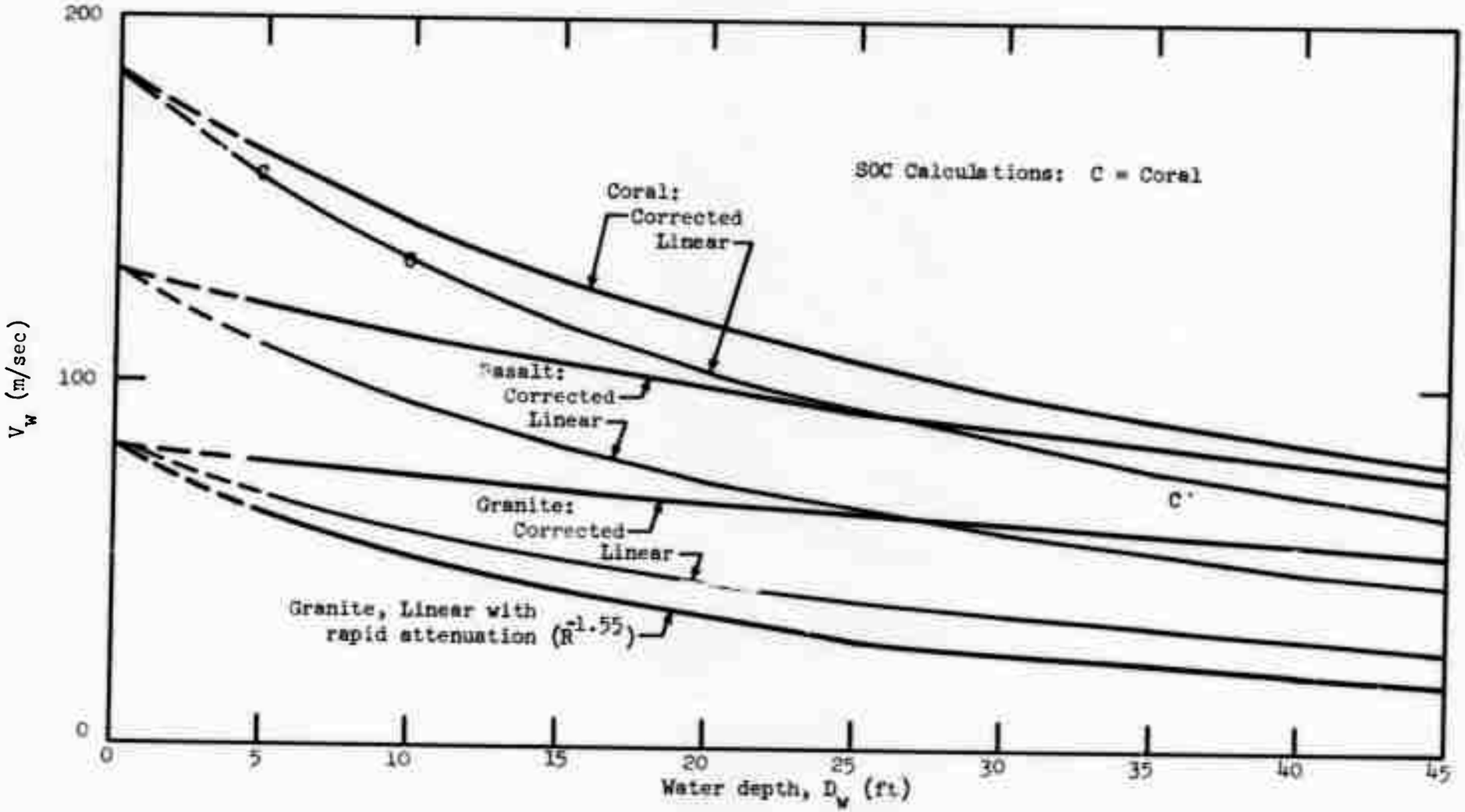

Figure 78. Water surface spall velocities, comparison of corrected and linear or uncorrected acoustic calculations, for a rock depth of D_r = 30 ft.

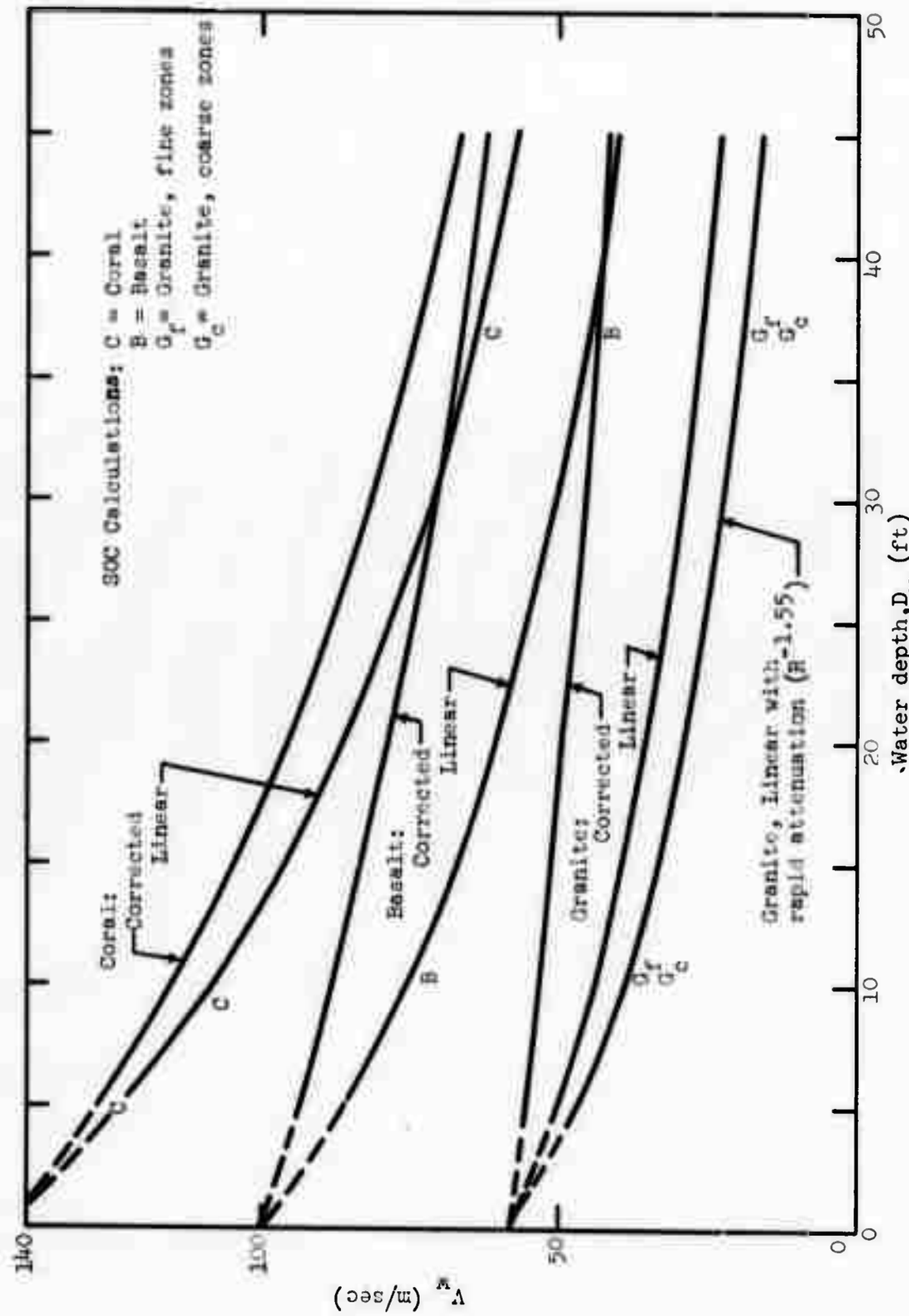

Figure 79. Water surface spall velocities, comparison of corrected and linear acoustic calculations, for a rock depth of D_r = 36 ft.

trend again illustrates the importance of interface refraction effects: Strong refraction at the basalt or granite interface causes the shock front to diverge more slowly. Spall velocities far from the interface correspondingly decrease less rapidly. This difference between coral and basalt behavior would not be apparent for uncorrected calculations (spherical divergence).

Figures 78 and 79 show both the corrected and linear (uncorrected) water surface spall velocities for coral, basalt, and granite. The SOC-calculated peak spall velocity data points are plotted for comparison. The coral (C) and basalt (B) points agree with the linear acoustic calculations, as discussed above. The granite points (G_f = fine zone, G_c = coarse zone) are low. In order to examine attenuation effects, the linear (uncorrected) acoustic calculations for granite were redone with a water-layer attenuation rate of $R^{-1.55}$. The resultant curve is shown in Figure 79. Agreement with the "fine-zone" granite calculations is greatly improved, with SOC data points slightly below the revised acoustic calculations.

Empirical data. Water surface velocities have been measured for the Tugboat Phase I underwater events in coral.[42] Data are listed in Table 13. Four of these events were of one-ton yield; the rock burial depths "D_r" and water layer depths "D_w" have been cube-root scaled to 10 tons, in order to render the results comparable with calculations. All velocity measurements were made using late-time low-resolution photographic techniques (time > 90 msec, mound height ≈ 10 to 100 ft). For this reason, the data cannot be directly compared with early-time peak surface spall velocities. The water medium has very low tensile strength and spalls upward in thin layers when a shock wave is reflected at the surface. These thin layers, unlike massive rock spall, suffer enormous air drag deceleration at early times. Indeed, the initial surface deceleration may be on the order of hundreds of g's, even for greater ranges and lower velocities than those encountered here.[56] The rapid deceleration ceases and a stable freefall configuration is achieved only after an appreciable thickness of water is accreted to the bottom of the spall. Thus, velocities measured over distance scales on the order of many feet and time scales much greater than the initial spall launch time

Table 13. Tugboat Phase I Events, Measured Ground Zero Water Surface Vertical Velocities At Late Time ($t \geq 90$ msec, Mound Height >10 to 20 ft).

Event	Yield (charge weight, tons)	D_r (scaled to 10 tons charge weight)	D_w (scaled to 10 tons charge weight)	Mean Velocity	
				(ft/sec)	(m/sec)
IA	1.0	24 ft.	13.6	286	88
IB	1.0	30.8	7.7	261	80
IC	1.0	37.9	8.9	184	56
ID	1.0	44.4	11.3	148	45
IE	10.0	35.7	7.2	287	88

will be representative of the "average" accreted velocity throughout several feet of the water mound (rather than the instantaneous peak very near the free surface).

The SOC-calculated range of water peak spall velocities in the high-velocity near-surface region and in the top 1.5 m of the water layer are plotted against water layer depth in Figures 80 (coral, D_r = 30 ft), 81 (coral D_r = 36 ft), 82 (basalt), and 83 (granite). The corrected acoustic peak spall velocity curves are also shown. Data points for the Tugboat coral events at the closest comparable rock depths "D_r" are presented in Figures 80 ($D_r \approx$ 30 ft) and 81 ($D_r \approx$ 36 ft). It is evident that the measurements fall below the "SOC" and "acoustic" peak surface velocities, and are more nearly comparable with the velocities about 1 to 1.5 m below the surface. Note that event "ID" in Figure 81 may not be legitimately compared with the other data and calculations, since it was at a very great scaled depth of D_r = 44.4 ft.

The differences between Tugboat data and the corrected acoustic calculations are more accurately compared in Figure 84. Acoustic calculations were performed for the precise (scaled) rock and water depths of each Tugboat configuration. Figure 84 plots the apparent error "V(acoustic)/V(measured)." The "acoustic" peak velocities are about 1.9 times as high as the measurements for the one-ton events (IA-ID), about 1.37 times as high for the 10-ton event (IE). This fact in itself indicates a photographic time-scale and resolution problem, since accretion occurs over the smallest distance and shortest time interval for the "small scale" one-ton events. However, Figure 84 again indicates that measured velocities are representative of the top layers of water spall rather than the peak surface velocity.

A final comparison between calculation and experiment is presented in Figures 85-87. These Figures show the SOC-calculated spall velocity (or residual velocity) profiles throughout the water mound after spallation is complete. The corrected acoustic surface velocities are also shown as crosses (somewhat higher than the SOC surface velocities). The SOC calculations reveal the characteristic features of slowly changing velocities deep within the mound, followed by a sharp increase in spall velocity within about 2 m of the free surface. The measured velocity for Tugboat IB is

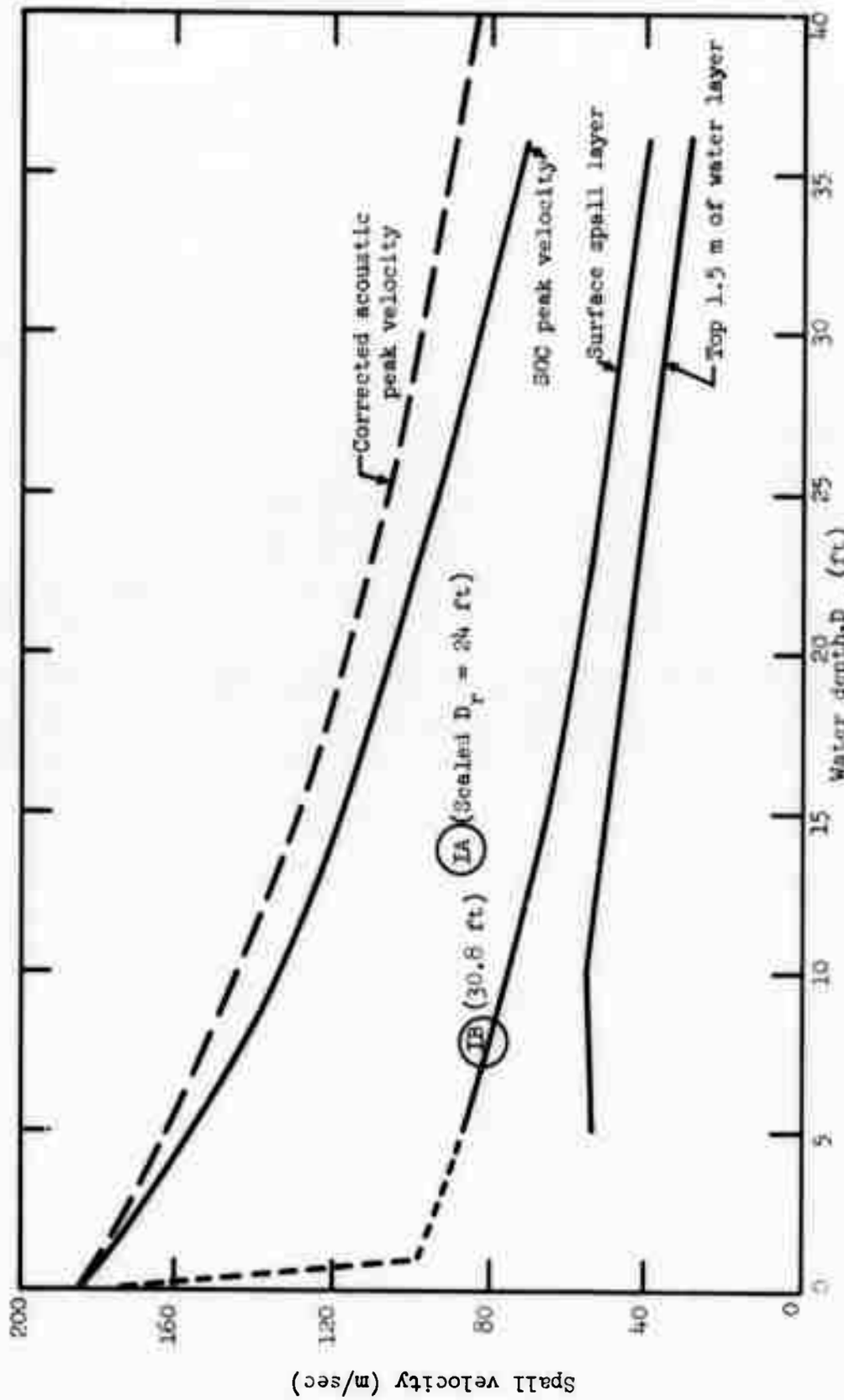

Figure 80. SOC-calculated water surface layer spall velocities for coral, D_r = 30 ft - comparison with photographic data (assumed "D_r" is listed in parentheses after each photographic data point).

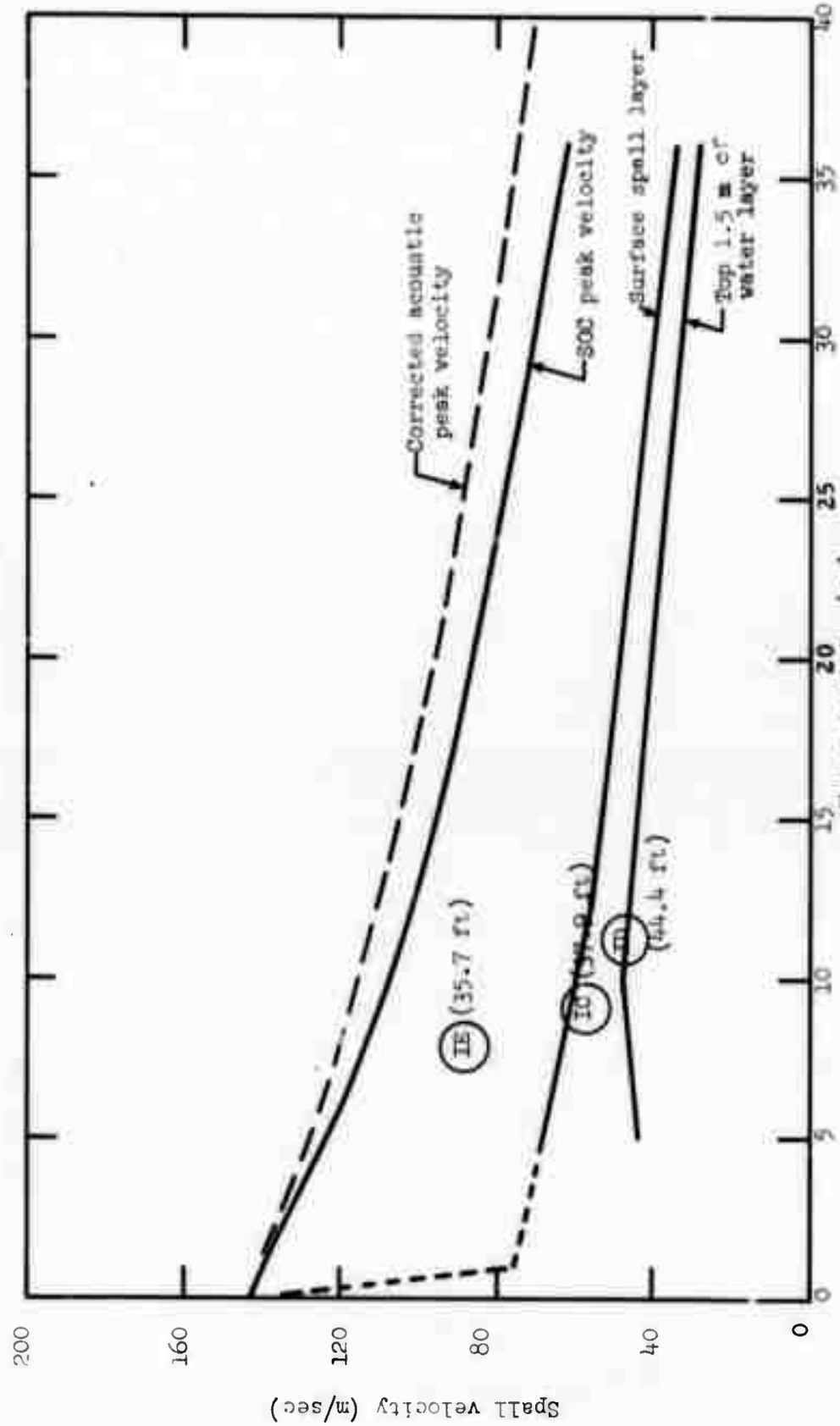

Figure 81. SOC-calculated water surface layer spall velocities for coral, f_t = 36 ft - comparison with photographic data (assumed "D_r" is listed in parentheses after each photographic data point).

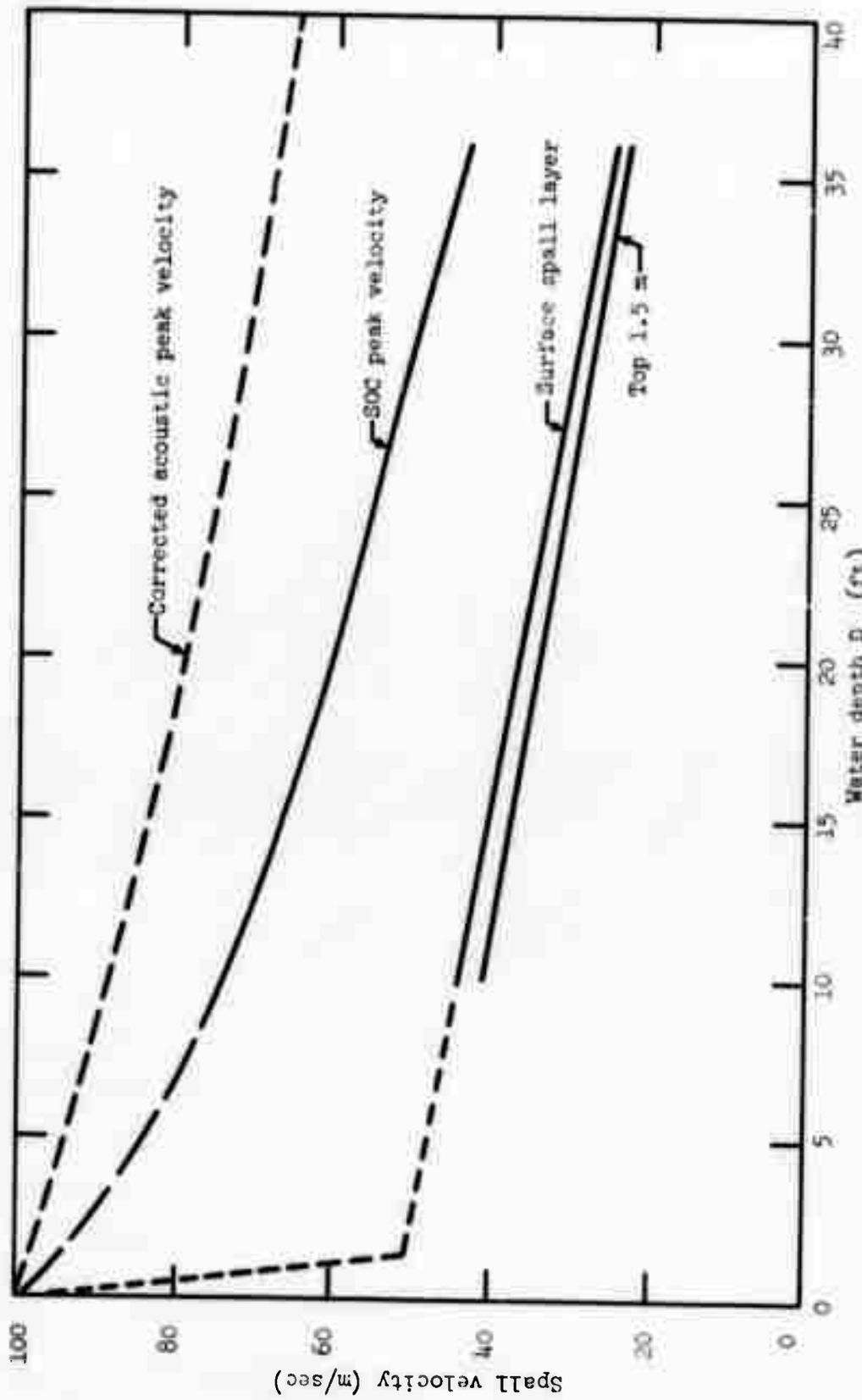

Figure 82. SOC-calculated water surface layer spall velocities for basalt, D_r = 36 ft.

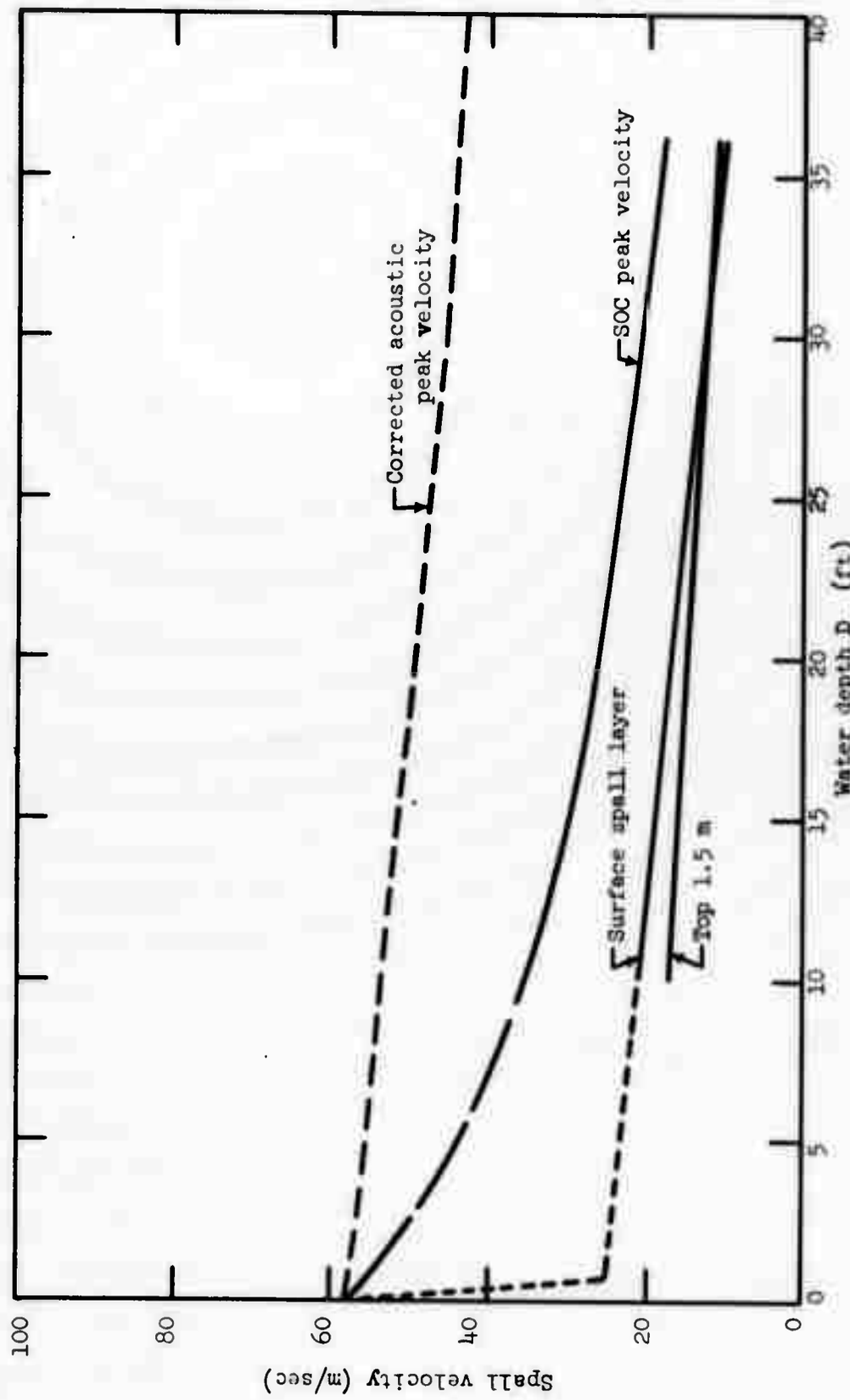

Figure 83. SOC-calculated water surface layer spall velocities for granite (fine water zoning), D_r = 36 ft.

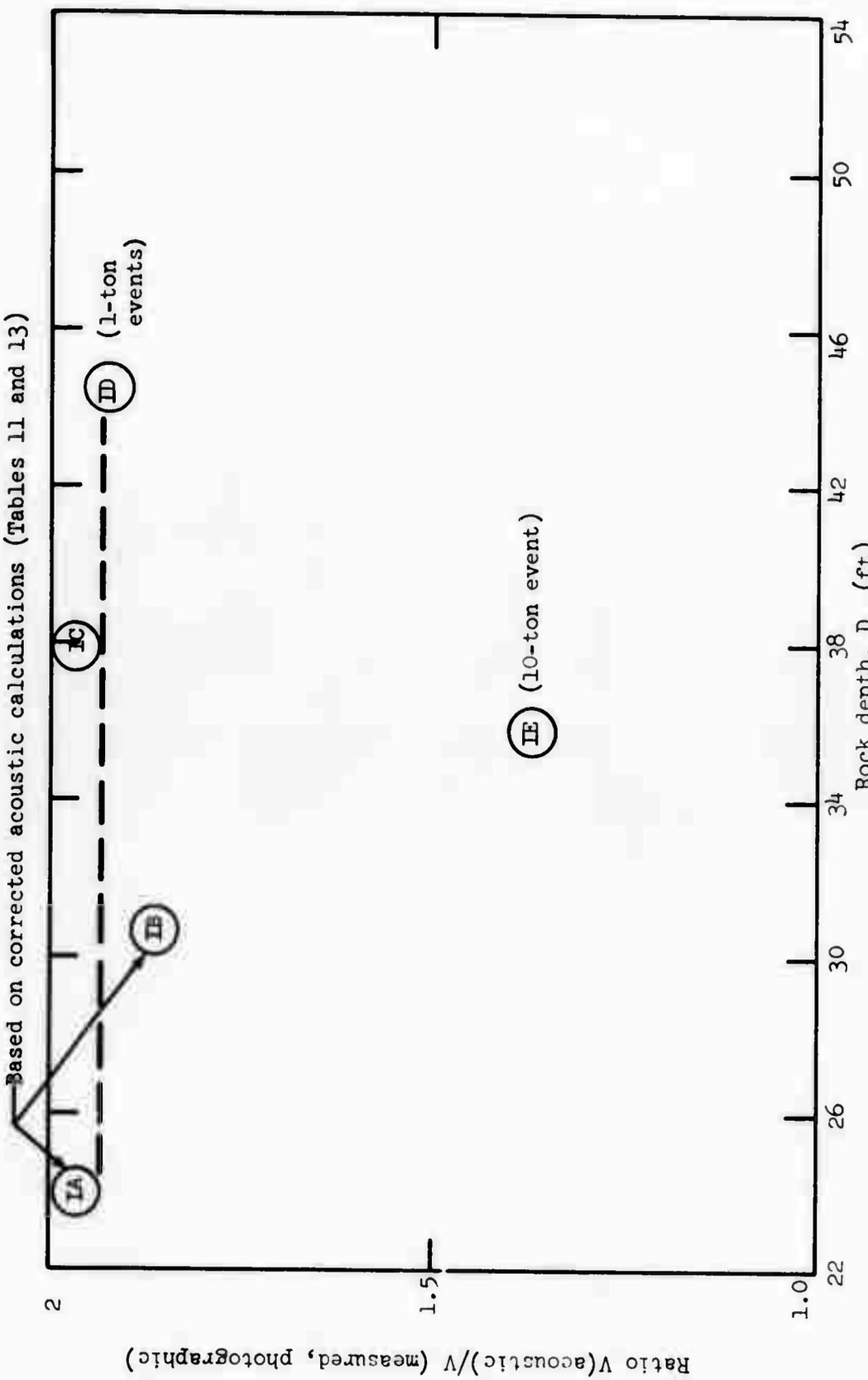

Figure 84. Water surface spall velocity, apparent errors: V (acoustic)/V (measured) vs rock depth, D_r (scaled to 10 tons).

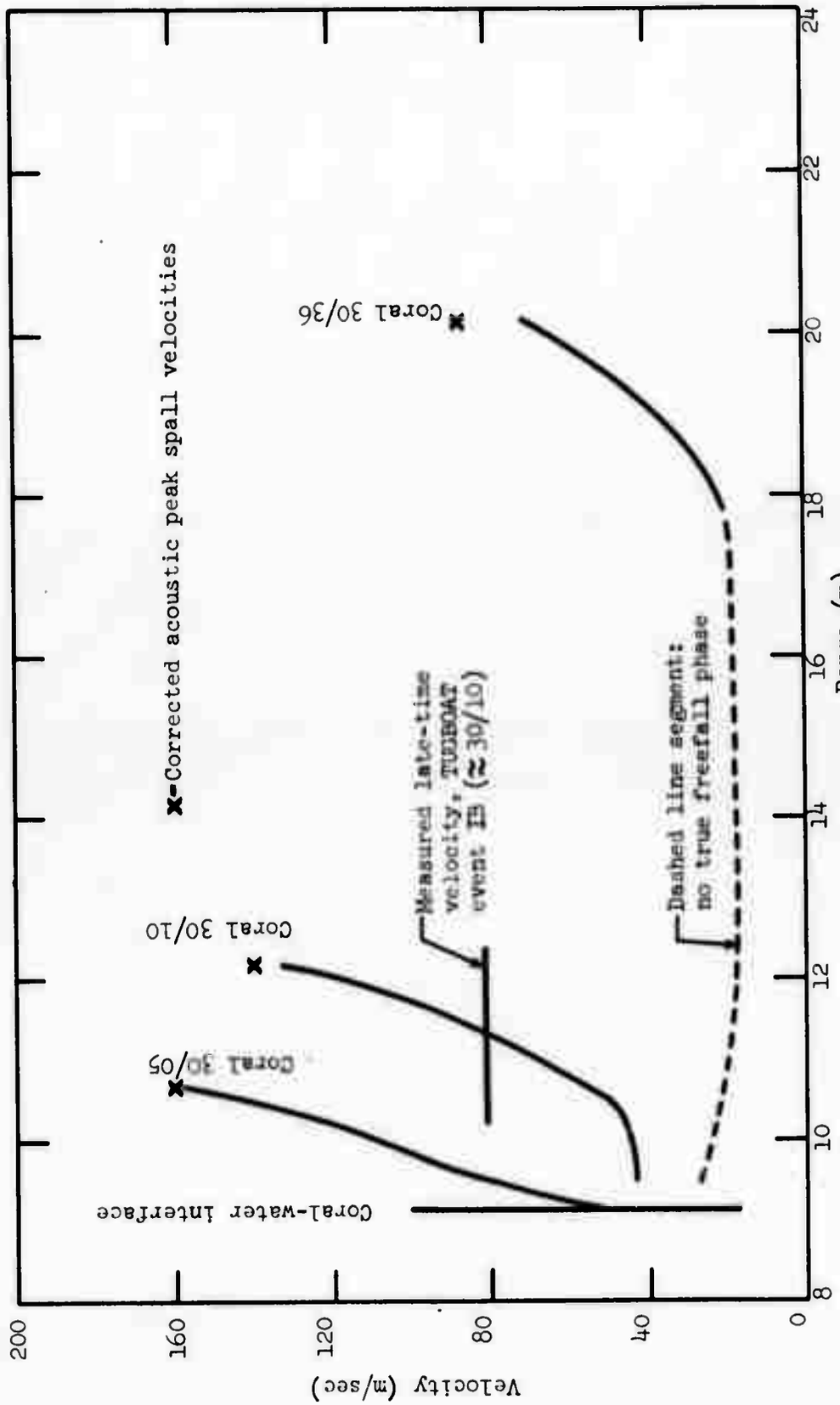

Figure 85. Spall velocities or residual velocities in the water layer for coral, D_f = 30 ft.

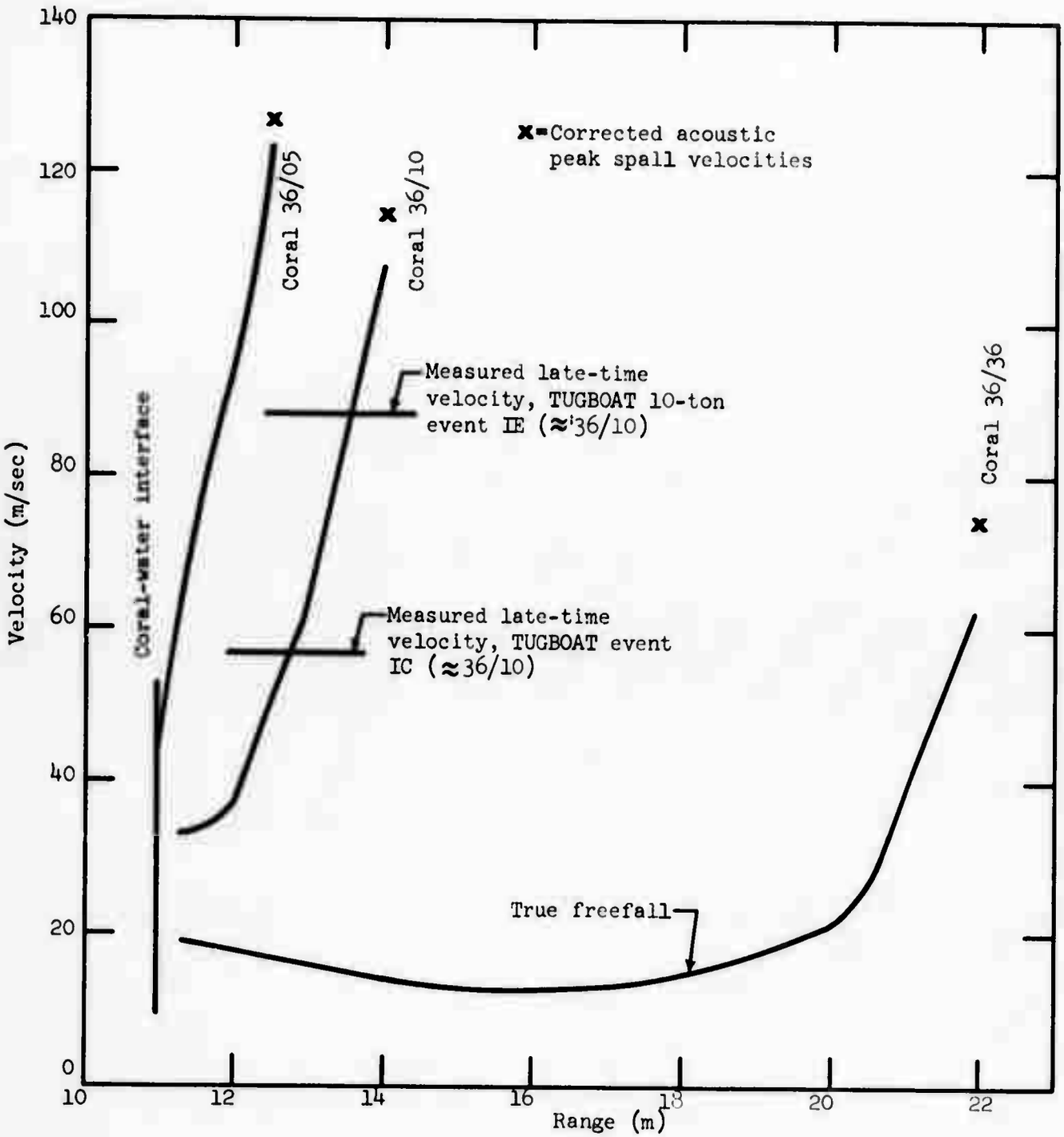

Figure 86. Spall velocities or residual velocities in the water layer for coral, D_r = 36 ft.

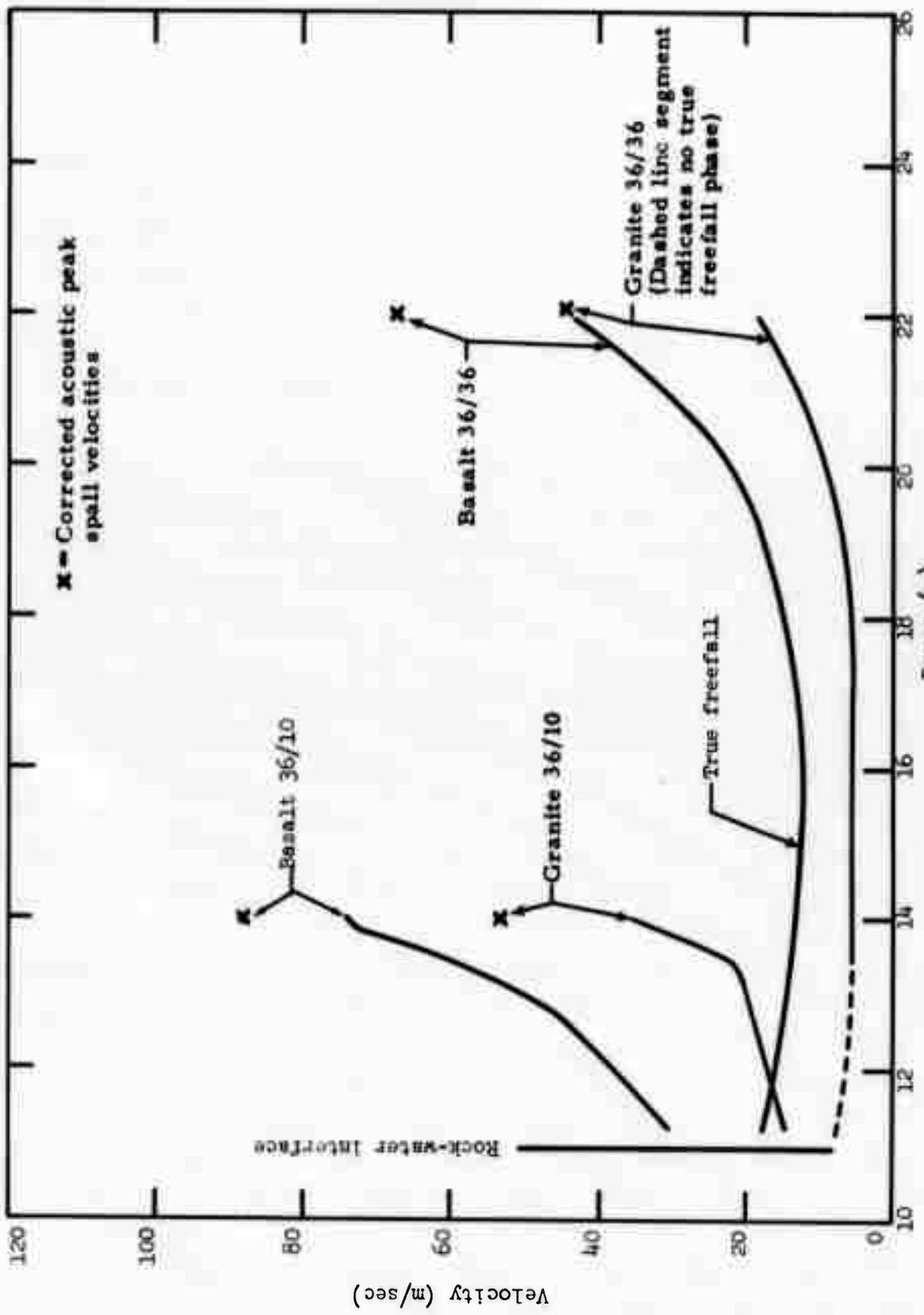

Figure 87. Spall velocities or residual velocities in the water layer for basalt and granite, D_r = 36 ft.

indicated in Figure 85 (compare with coral 30/10). Measurements for Tugboat IC and IE are marked in Figure 86 (compare with coral 36/10). The late-time measured velocities indeed appear consistent with the interpretation of "averaged" velocities throughout the accreted water spall mound. Water velocity profiles for basalt and granite calculations are shown in Figure 87 (no measurements available). These data are slightly less accurate than coral due to the larger refraction errors (high-impedance media) and the resolution difficulties for the granite-water calculations.

"Two-dimensional" calculations. As noted previously, the acoustic transmission equations may be used to simulate shock transmission for intercept angles other than the normal (vertical) direction. Thus, transmitted pressure and velocity may be determined anywhere within the water layer; peak vertical spall velocities may likewise be calculated for any location along the rock interface and water surface, giving an approximate "two-dimensional"picture of mound growth. Corrected acoustic calculations have been performed for a variety of configurations; sample results are shown in Figures 88 (coral, D_r = 30 ft), 89 (coral, D_r = 36 ft), 90 (basalt, D_r' = 36 ft), and 91 (granite, D_r = 36 ft). Each diagram plots the peak vertical spall velocity profiles of the rock free surface (no water), rock interface (overlying water layer, imperfect reflection at the interface), water surface (for D_w = 10 ft), and water surface (for D_w = 36 ft). Note that the water surface spall velocities frequently exceed the underlying rock spall velocities at the same surface range, even for the 36 ft water layers (Figures 89-91). This situation is a result of the low impedance of water and of the interface refraction effects which decrease divergence in the water layer. These acoustic calculations give only peak particle velocities at the shock front and spall velocities at an interface; thus, they are not equivalent to true two-dimensional dynamic calculations used to simulate the entire history of the mound and predict crater dimensions. Currently, there are no available mound growth data or two-dimensional dynamic calculations with which Figures 88-91 may be compared.

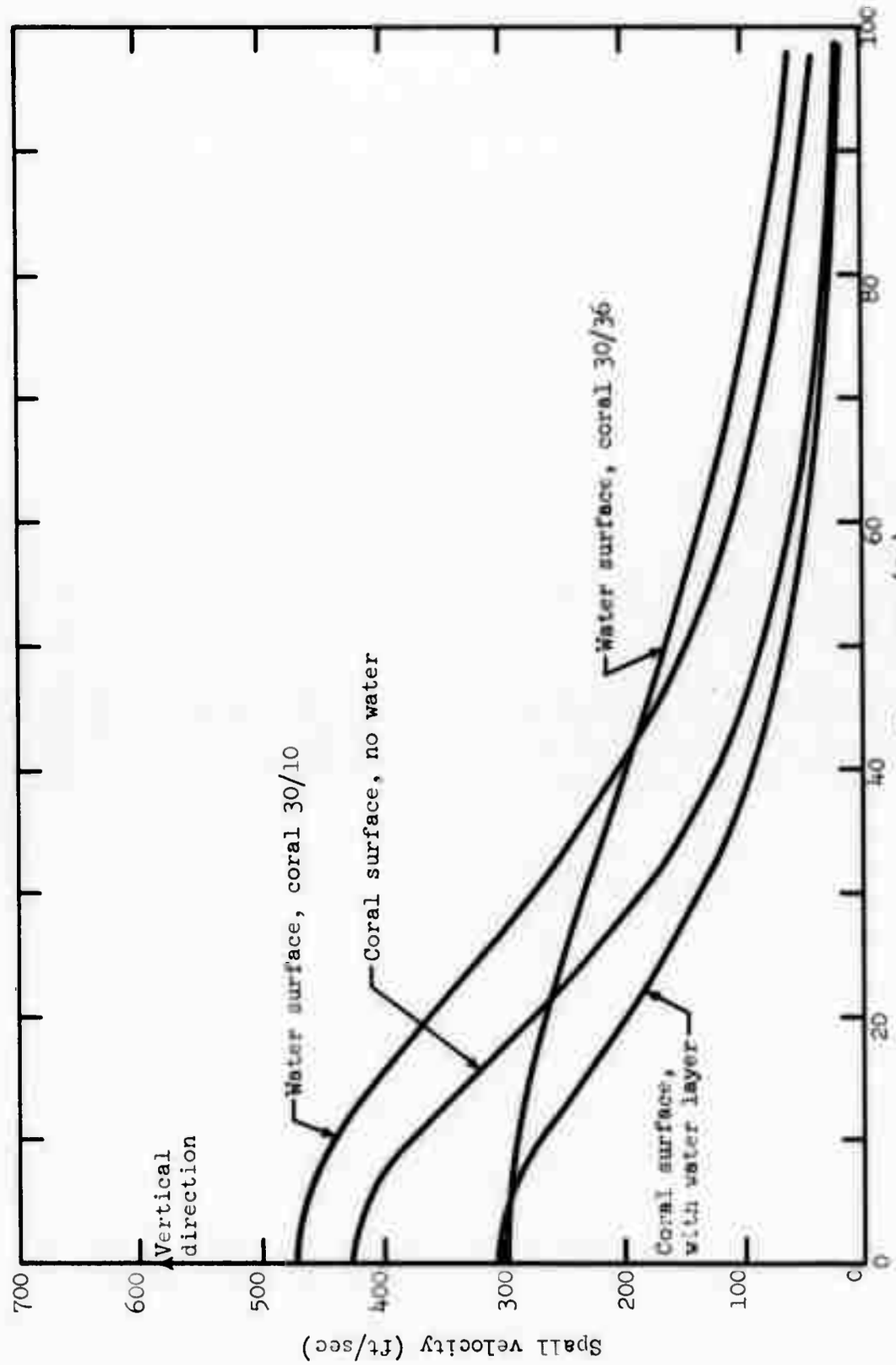

Figure 88. Peak surface spall velocity profiles for coral, D_r = 30 ft.

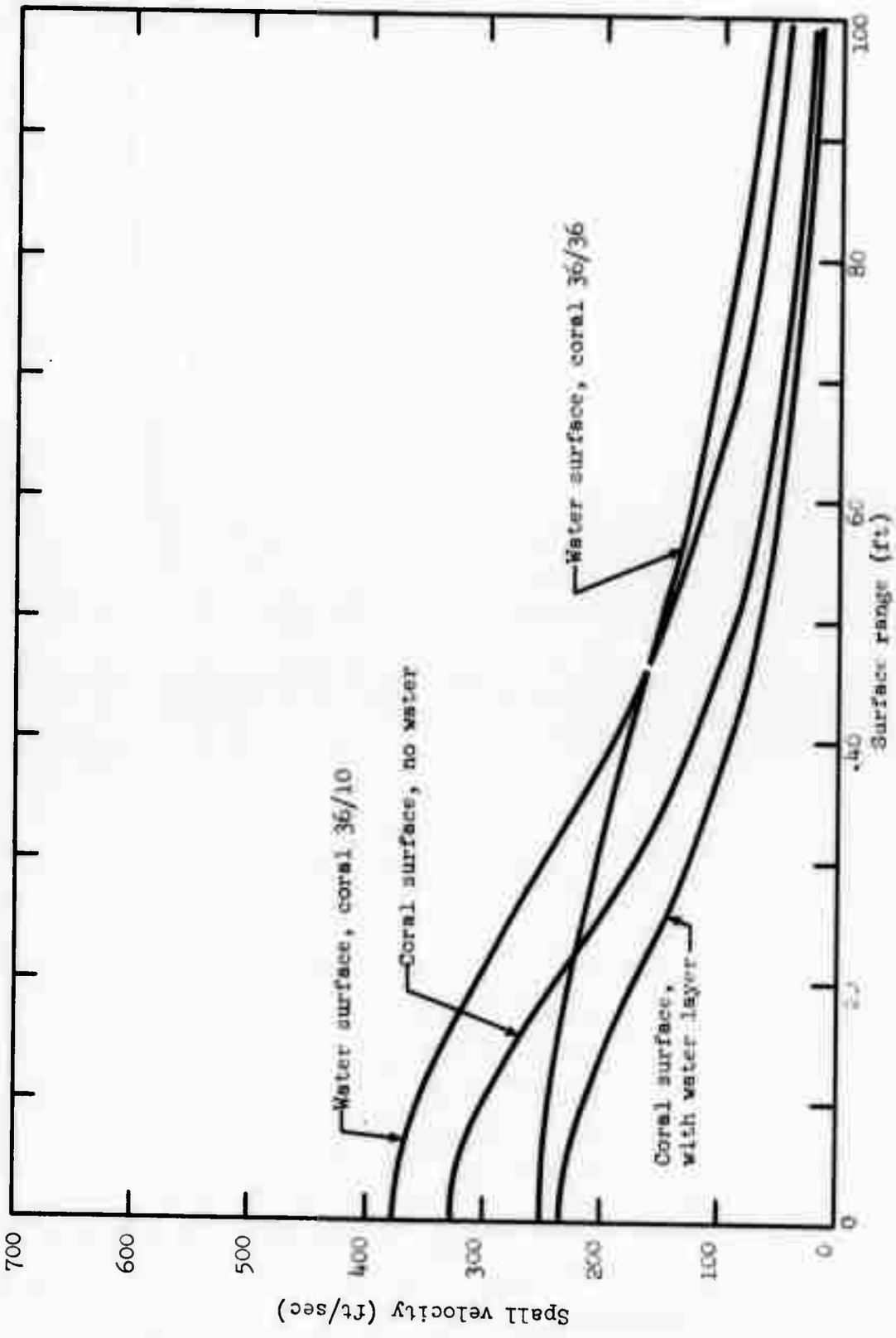

Figure 89. Peak surface spall velocity profiles for coral, D_r = 36 ft.

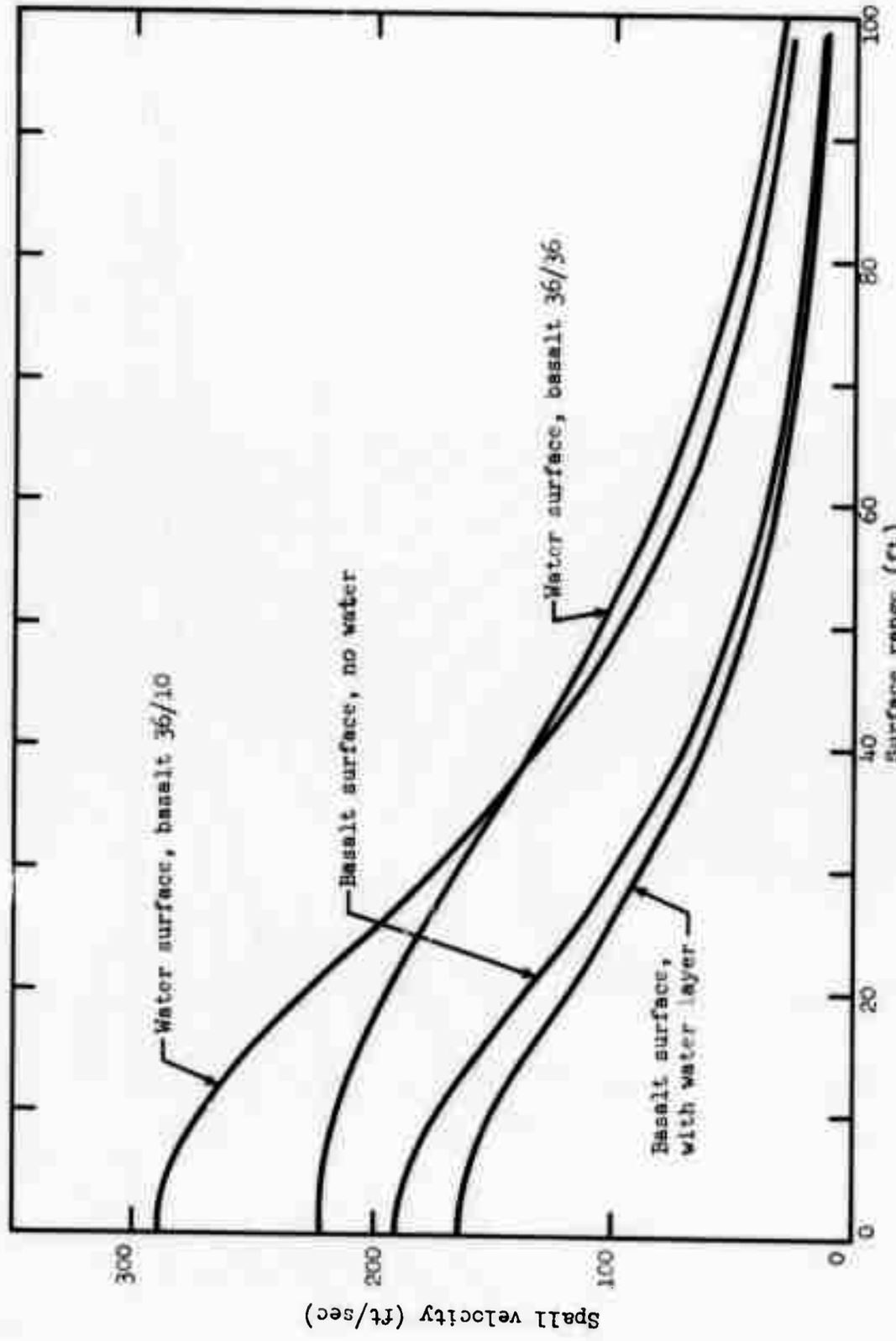

Figure 90. Peak surface spall velocity profiles for basalt, D_r = 36 ft.

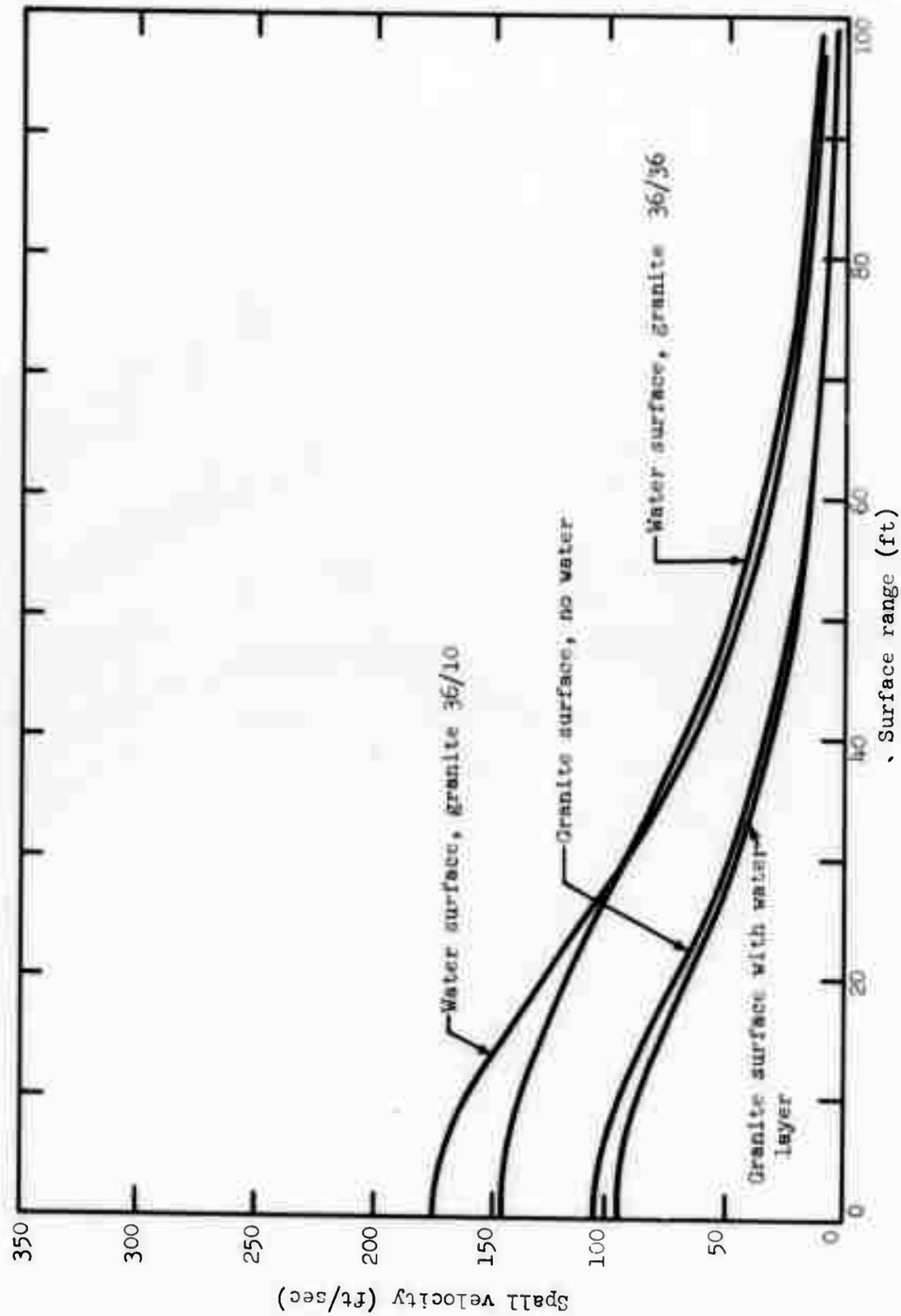

Figure 91. Peak surface spall velocity profiles for granite, D_r = 36 ft.

IX. AIRBLAST

In the foregoing discussion, the water surface above a submerged cratering event has been treated as a free surface. This approximation is a reasonable one to make when studying the instantaneous peak spall velocities or overall dynamics of the water layer at early times, since water has a much greater density and impedance than air. However, the airblast shock transmitted into the overlying air is also of interest for safety predictions. Window breakage and undesirable noise effects are often limiting factors in designing underwater excavation shots. This section discusses airblast prediction for underwater events and provides a comparison with empirical data.

Explosive cratering events usually generate two airblast pulses. The first of these is the spall-induced shock, coupled into the air by the piston effect of the spalled rock (or water) surface. The intensity of the spall-induced airblast is closely related to the peak surface spall velocity, and may be accurately predicted if the surface velocity profile is known.[57,26] The second or gas-vent-induced pulse originates when the material mound begins to disintegrate and cavity gases vent to the surrounding atmosphere. The intensity of gas vent airblast is related to the pressure and volume of cavity gases at vent time; this pulse may be weak or absent if cavity pressure is near or below atmospheric pressure when venting occurs (i.e., late vent time or deeply buried event). It has been observed that vent times are relatively late and gas vent airblast is negligible for events near or below optimum burial depth in saturated and saturated submerged media. This trend is presumably attributable to the coherency of the saturated material mound, which efficiently contains the cavity gas bubble until late time. Since gas-vent airblast is negligible for typical cratering events in saturated media, this discussion will be concerned with the predominant spall-induced pulse.

Due to the very long duration or wavelength of the airblast signal from a large excavation event, window breakage and other distant damage effects are related primarily to the peak amplitude (rather than impulse or duration). Thus, safety criteria may be established on the basis of the peak overpressure "ΔP" (greatest increase above the local ambient air pressure). Surface spall velocities may be used to predict the peak airblast overpressure, both in the immediate vicinity of the spall mound ("near field"), and at ranges beyond this

vicinity ("far field").[57] Specifically, the peak spall-induced overpressure "ΔP_o" directly above the center of the mound (surface ground zero) is determined from the acoustic equation:

$$\Delta P_o \cong \rho C_a V_{spall} \text{ (at SGZ)} \qquad \text{Eqn. I.}$$

ρC_a = acoustic impedance of air

$\cong 0.0184 \frac{\text{psi-sec}}{\text{ft}}$ at sea level

$V_{spall}(SGZ)$ = peak spall velocity of the mound at surface ground zero.

The far field peak airblast overpressure "ΔP" as a function of horizontal range "R" is given by,

$$\Delta P = \Delta P_o \alpha \frac{DOB}{R}$$ where DOB = total depth of burial of detonation

or, for a two-layer configuration,

$$\Delta P = \Delta P_o \alpha \frac{D_r + D_w}{R} \qquad \text{Eqn. II}$$

ΔP_o = peak local airblast overpressure at surface ground zero (near field).

α = dimensionless "source strength" parameter which is related to the overall or integrated mound velocity profile.

R = horizontal range from surface ground zero (measured along the rock or water surface).

Note the different use of the symbol "R" in this connection. The above equation applies only in the horizontal direction (i.e., close to surface level), and only at far field ranges beyond the rapidly-rising spall mound [$R >> (D_r + D_w)$].

As might be expected, the source strength parameter "α" is dependent on the width of the surface velocity field and the integral of the spall velocity profile throughout the field. For the cases under consideration here, "α" may be satisfactorily approximated by a cross-sectional integral of the (symmetric) surface spall velocity profile:

$$\alpha = \frac{1}{2\pi V_{spall}(\text{at SGZ})(D_r+D_w)} \int_{-\infty}^{\infty} V_{spall}(R)dR \qquad \text{Eqn. III}$$

$V_{spall}(R)$ = Peak surface spall velocity as a function of range "R" from SGZ.

This relationship has been found to be accurate for explosive cratering events in a wide variety of media. In practice, the profile integral is carried only over the "high velocity" inner portion of the velocity field, which is entirely responsible for creating the airblast pulse. The surface velocity declines rapidly away from SGZ, and the outer "wings" of the velocity profile do not contribute significantly to the integral.

Since the impedance of air is much lower than that of water, tensile reflection of an incident compressional shock at the water surface (water-air interface) is almost perfect. Therefore, the vertical component of particle velocity is very nearly doubled at the interface, and water surface velocities calculated on the basis of the "free surface" assumption may be used to predict airblast. Water surface spall velocities for the underwater cratering media included in this study are obtainable from either "SOC" or acoustic calculations. The acoustic calculations are corrected for refraction effects, and can easily be performed for a variety of different water depths (only ten "SOC" underwater calculations are available). Also, acoustic calculations may be used to generate the entire surface spall velocity profile (as well as the velocity in the vertical direction, at SGZ). Accordingly, the corrected acoustic results have been adopted for airblast predictions.

Water surface spall velocities as a function of water layer depth were presented in Figures 74 through 77. These velocities have been used to calculate "ΔP_o" (Eqn. I). Likewise, the acoustic water surface spall velocity profiles were integrated to obtain "α" (Eqn. III). (Typical examples of the velocity profiles were shown in Figures 88-91.) The results of these calculations are displayed in Figures 92-94:

Figure 92 shows "ΔP_o" (psi) and "α" (dimensionless) as functions of overlying water layer depth for events buried in coral (D_r = 30,36, and 42 ft). The "ΔP_o" scale is calibrated along the left vertical axis, the "α" scale along the right axis.

Figure 93 presents "ΔP_o" and "α" as functions of water depth for events in basalt (D_r = 30,36, and 42 ft).

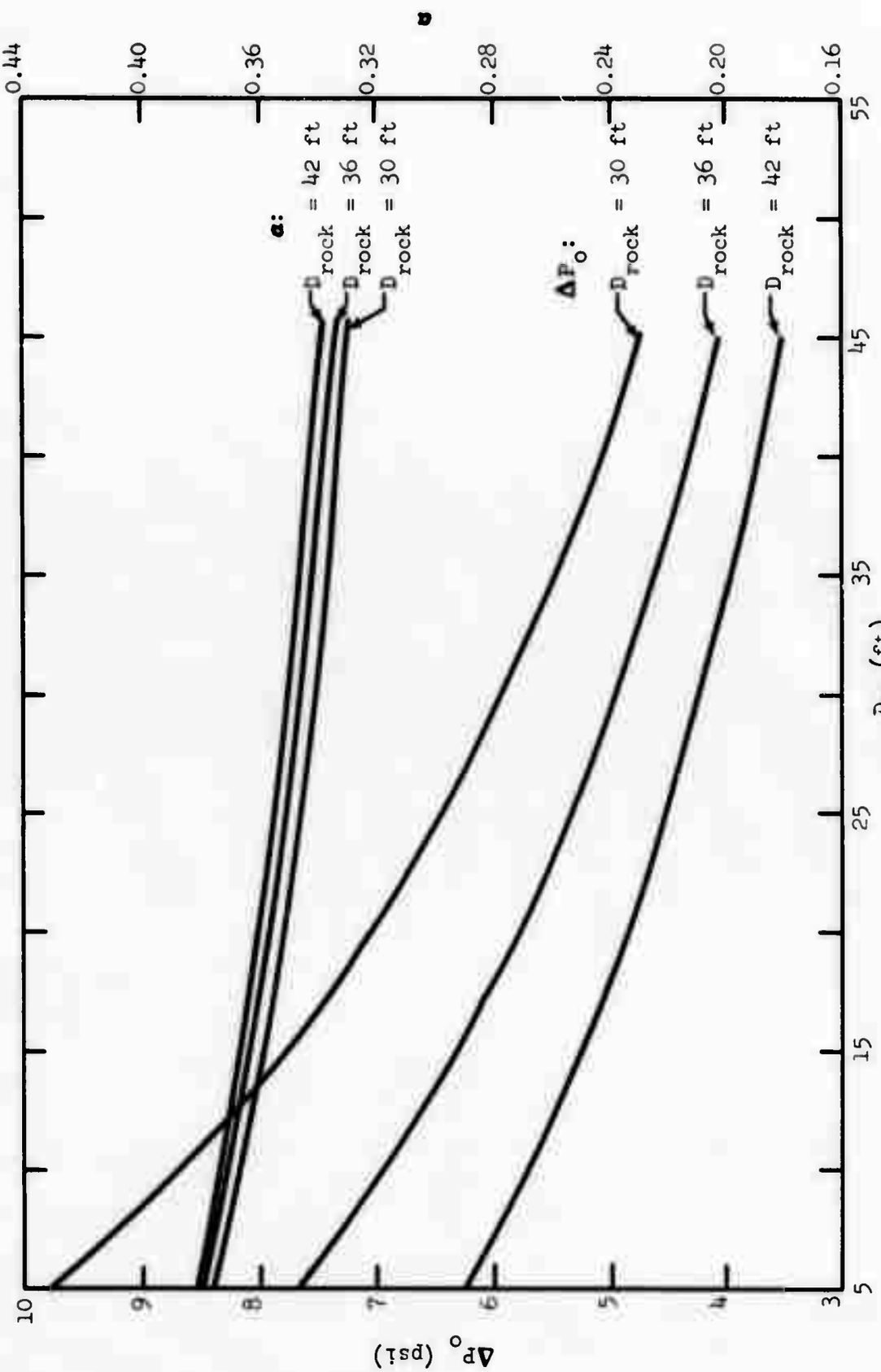

Figure 92. Corrected acoustic calculation - airblast parameters ΔP_o and α for coral.

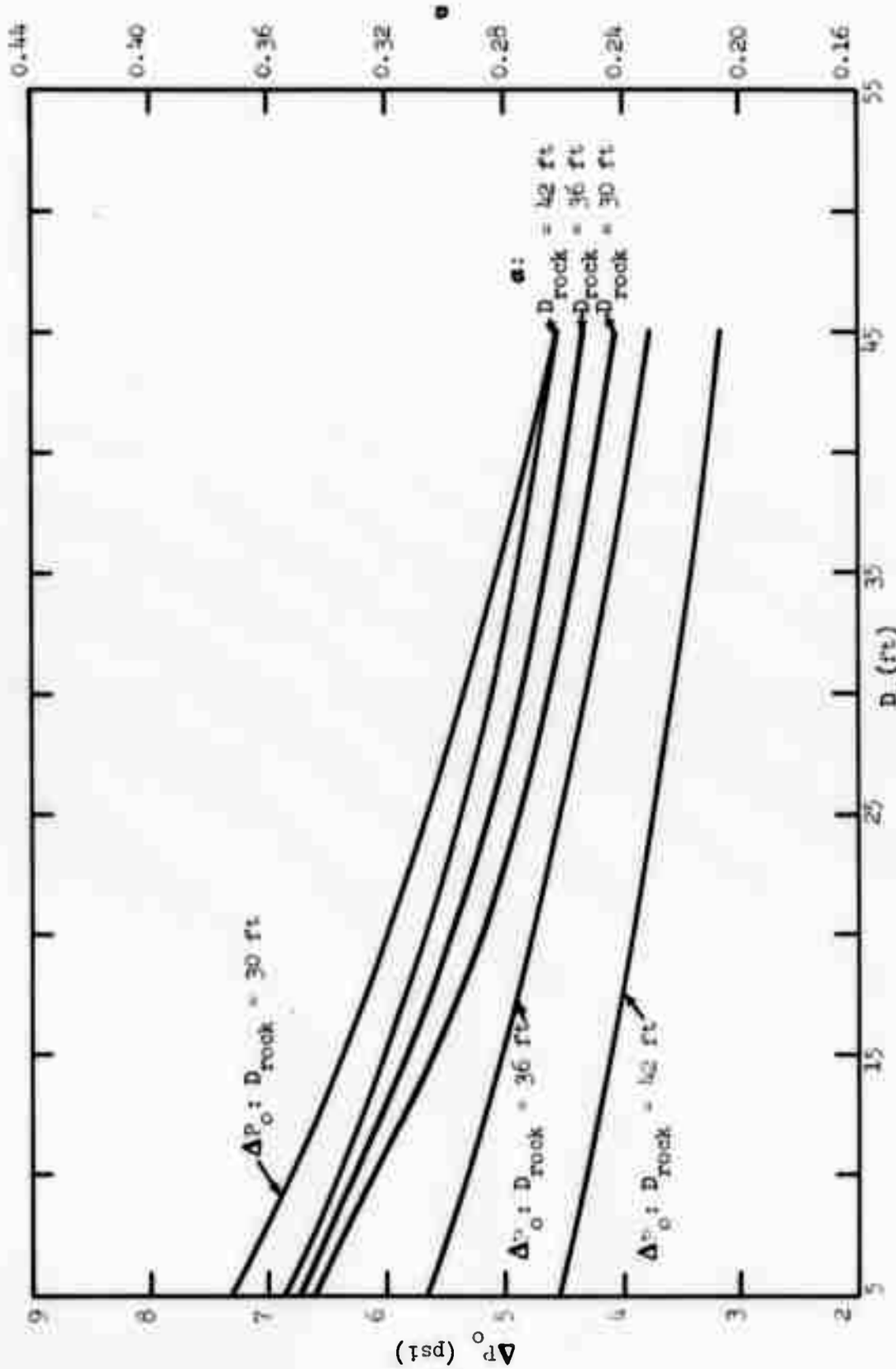

Figure 93. Corrected acoustic calculation - airblast parameters, ΔP_o and α for basalt.

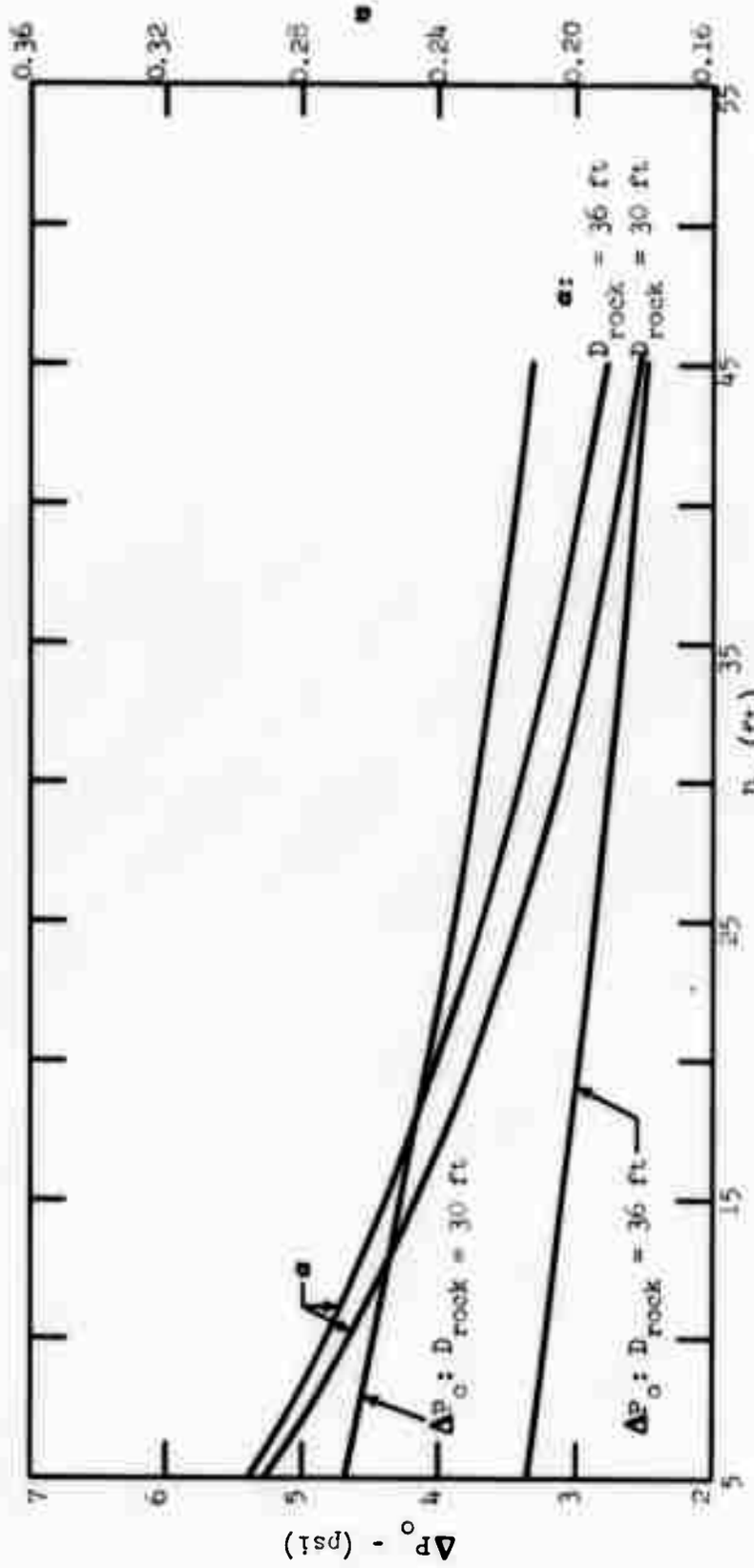

Figure 94. Corrected acoustic calculation - airblast parameters ΔP_o and α for granite.

Figure 94 gives "ΔP_o" and "α" as functions of water depth for events in granite (D_r = 30 and 36 ft).

Note that the water depths "D_w" and rock depths "D_r" in Figures 92-94 are for a 10-ton AANS charge yield (15.9 tons energy). These depths may be cube-root scaled to other yields of interest. The water depth range and sample rock depths used here were chosen to represent typical cratering events near optimum burial depth. Acoustic calculations and airblast predictions may also be performed for other burial depth combinations of interest.

Tugboat airblast data. Airblast measurements were obtained for the five Tugboat Phase I single-charge experiments in submerged coral.[41] Data show certain deviations from acoustic behavior (Eqn. II): The peak overpressure attenuation rates far from surface ground zero are typically on the order of $R^{-1.2}$, instead of R^{-1}. Rapid attenuation is observed when air temperature decreases with increasing altitude (sound rays are refracted away from surface level, progressively decreasing the surface overpressures at long ranges). Such conditions often exist at seashore locations. Reverse refraction may also occur at higher altitudes or at an inversion layer, bending the rays back toward ground level and creating a "focus" (area of increased overpressure) several thousand feet from ground zero. Tugboat measurements show indications of both effects: rapid attenuation at intermediate ranges, with one "high" data point at long range (in three cases). These deviations must be taken into account when comparing measurements with acoustic predictions.

Corrected acoustic calculations have been performed and airblast predictions have been obtained for each of the five Tugboat Phase I configurations (coral + water layer). The acoustic results and measured data are summarized in Table 14. This tabulation lists the approximate charge weight and true depth of burial for each event. Since four of the events were one-ton charges, the length dimensions (D_r,D_w, and R) have been cube-root scaled to a charge weight of 10 tons. Next, the acoustic calculations for the given rock and water depth are presented: Water spall velocity "V_{spall}" at SGZ, "ΔP_o" in psi, and "α". Finally, the measured airblast data have been least-squares fitted by an equation of the form,

$$\frac{\Delta P}{\Delta P_o} = \alpha \left(\frac{D_r+D_w}{R}\right)^n \qquad \text{Eqn. IV.}$$

Table 14. Tugboat Phase I Events - Corrected Acoustic Calculations; Measured Airblast and Airblast Parameters Derived From Acoustic Calculations.

Event	Approx. Charge Weight (tons)	Total DOB (in ft, not scaled)	Total DOB= D_r+D_w (Scaled)*	D_R (Scaled)*	D_W (Scaled)*	Acoustic Calculations			Least Squares Fit to Data	
						$V_{spall(water)}$ (ft/sec)	ΔP_o (psi)	α	$\frac{\Delta P}{\Delta P_o}=\alpha\left(\frac{D_r+D_w}{R}\right)^n$	α (=intercept at $(D_r+D_w)/R=1$)
IA	1.0	17.4	37.6	24	13.6	562.5	10.35	0.3549	$\frac{\Delta P}{\Delta P_o}=0.454\left(\frac{D_r+D_w}{R}\right)^{1.251}$	0.454
IB	1.0	17.86	38.5	30.8	7.7	485.5	8.93	.3725	$\frac{\Delta P}{\Delta P_o}=.282\left(\frac{D_r+D_w}{R}\right)^{1.1092}$	0.282
IC	1.0	21.72	46.8	37.9	8.9	363.7	6.69	.3742	$\frac{\Delta P}{\Delta P_o}=.288\left(\frac{D_r+D_w}{R}\right)^{1.1434}$	0.288
ID	1.0	25.84	55.7	44.4	11.3	284.7	5.23	.3734	$\frac{\Delta P}{\Delta P_o}=.355\left(\frac{D_r+D_w}{R}\right)^{1.2549}$	0.355
IE	10.0	42.9	42.9	35.7	7.2	399.5	7.35	.3761	$\frac{\Delta P}{\Delta P_o}=.299\left(\frac{D_r+D_w}{R}\right)^{1.1155}$	0.299

*These length dimensions have been cube-root scaled to an equivalent charge weight of 10 tons.

where "ΔP_o" is obtained from the acoustic predictions; "α" and "n" are the least-squares constants. The complete fitted equations and the "α" constant are listed in the last two columns of Table 14. The longest-range "high" data point(which shows evidence of a focus)has been omitted from the fit in three cases.

The acoustic airblast predictions listed in Table 14 may be expressed as,

$$\frac{\Delta P}{\Delta P_o} = \alpha \frac{D_r+D_w}{R} \qquad \text{Eqn. V.}$$

ΔP_o and α = acoustic prediction parameters.

This form is directly comparable with the least squares fit given above (Eqn. IV). Substituting the acoustically-predicted "ΔP_o" and "α" values and the layer depths ("D_r" and "D_w") for each event into Eqn. V, we obtain a predicted airblast function "$\Delta P/\Delta P_o$" vs "$(D_r+D_w)/R$" (straight line of slope "R^{-1}"). The acoustic prediction R^{-1} lines and the least squares fits (dashed lines) for each of the five Tugboat events are presented in Figures 95-99. The measured data points are also shown. In this case, it has been convenient to plot "$\Delta P/\Delta P_o$" against "$R/(D_r+D_w)$" [rather than "$(D_r+D_w)/R$"]; this convention is followed because airblast overpressures are normally plotted as decreasing overpressure vs. increasing range "R". It is evident in all figures that the data and the least squares fits are lower and show a faster attenuation rate than the acoustic "R^{-1}" predictions. The average attenuation rate for the least squares lines is about "$R^{-1.175}$" (constant n = +1.175 in fitted equation). Rapid attenuation is attributed to refraction of the airblast pulse away from ground level.

Due to the differing attenuation rates, Tugboat measurements and acoustic predictions cannot be directly compared at long ranges. No data points are available at very close ranges, near the high-velocity spall mound. However, an approximate comparison may be based on close-range predictions and the expected behavior of the spall-induced airblast signal. The airblast pulse from a buried cratering event originates within the range interval $R/(D_r+D_w) \lesssim 1$ to 3 [i.e., $(D_r+D_w)/R \gtrsim 1$ to 0.33]. Beyond this interval,

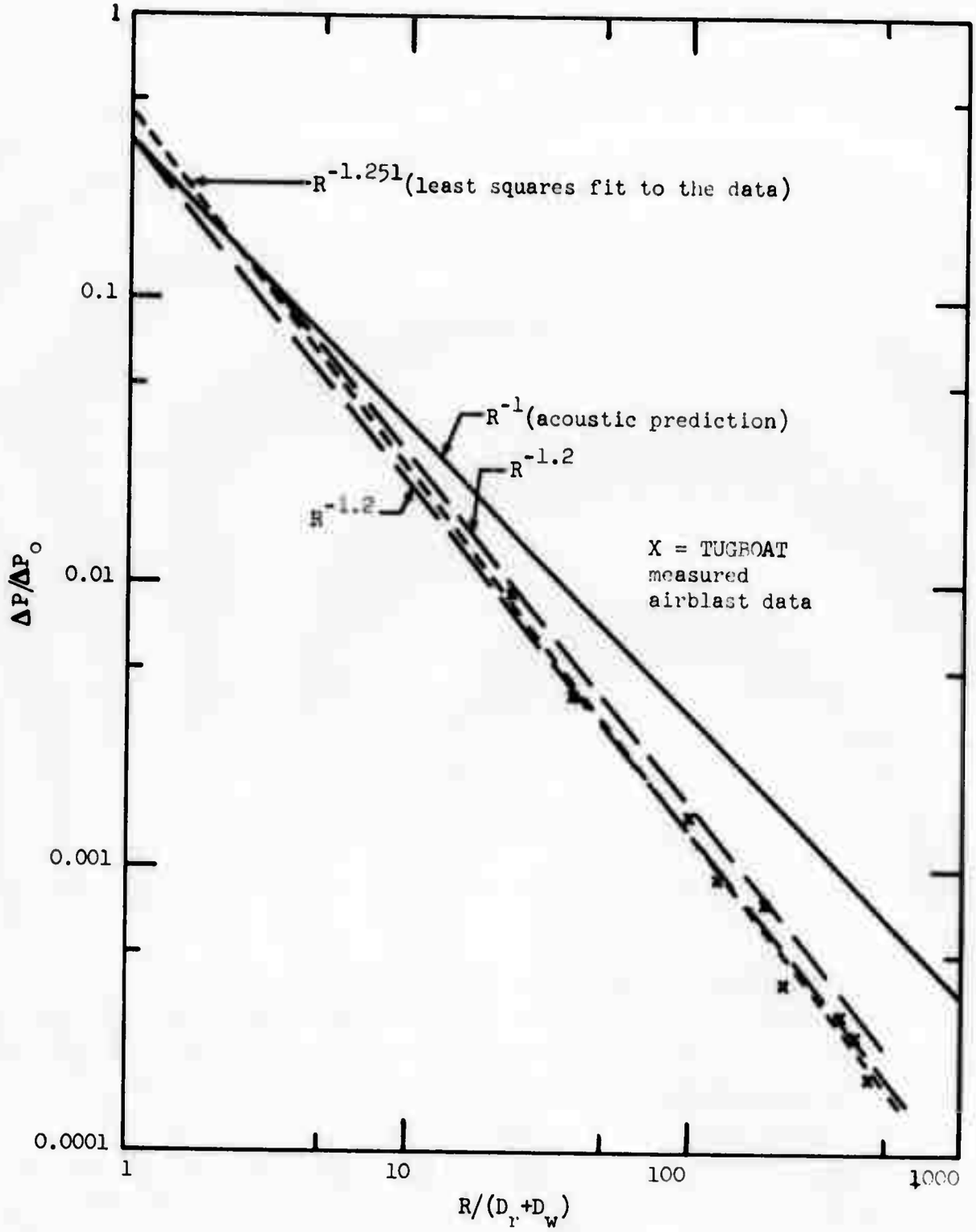

Figure 95. Airblast overpressures, TUGBOAT IA event (in saturated coral overlain by seawater).

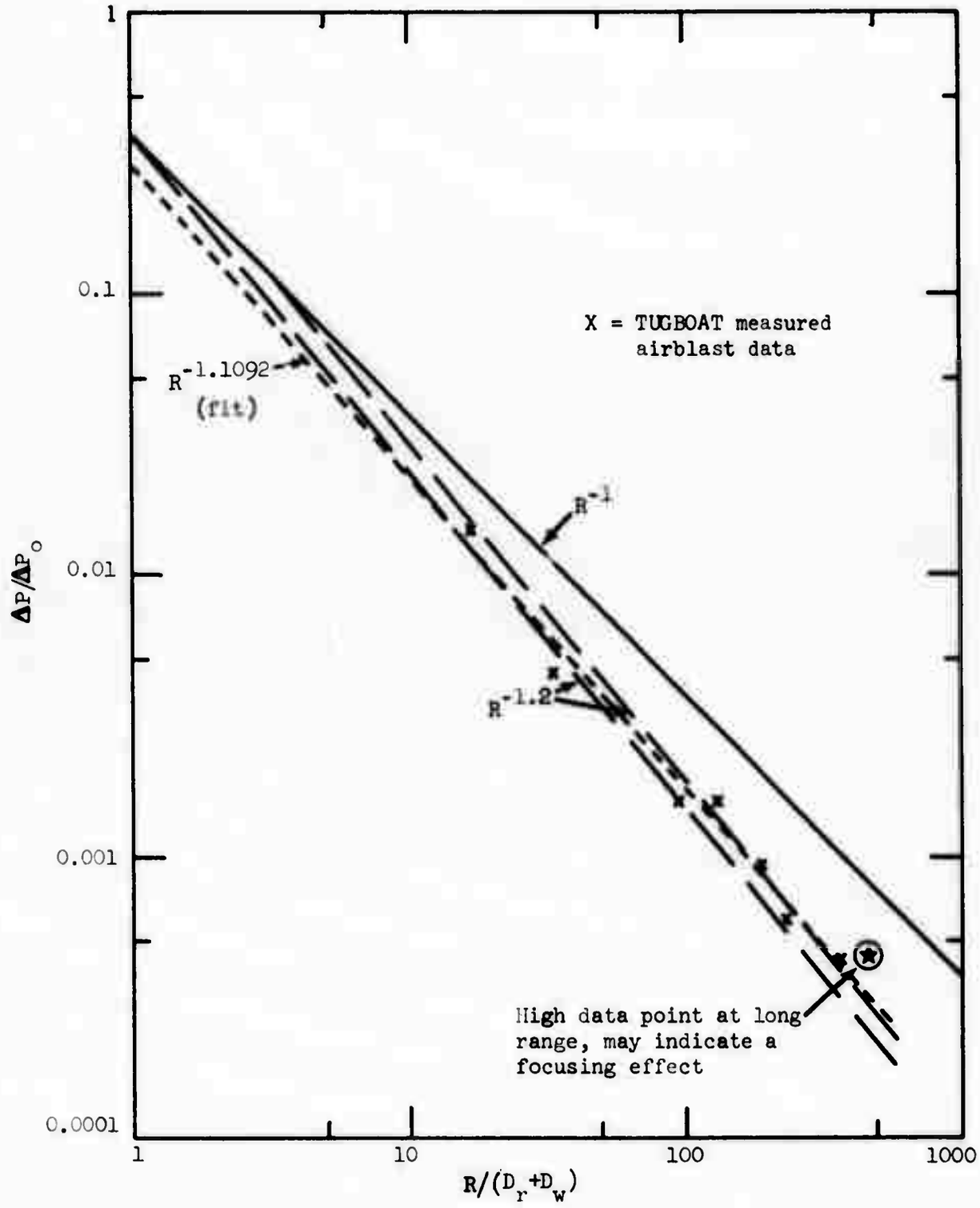

Figure 96. Airblast overpressures, TUGBOAT IB event.

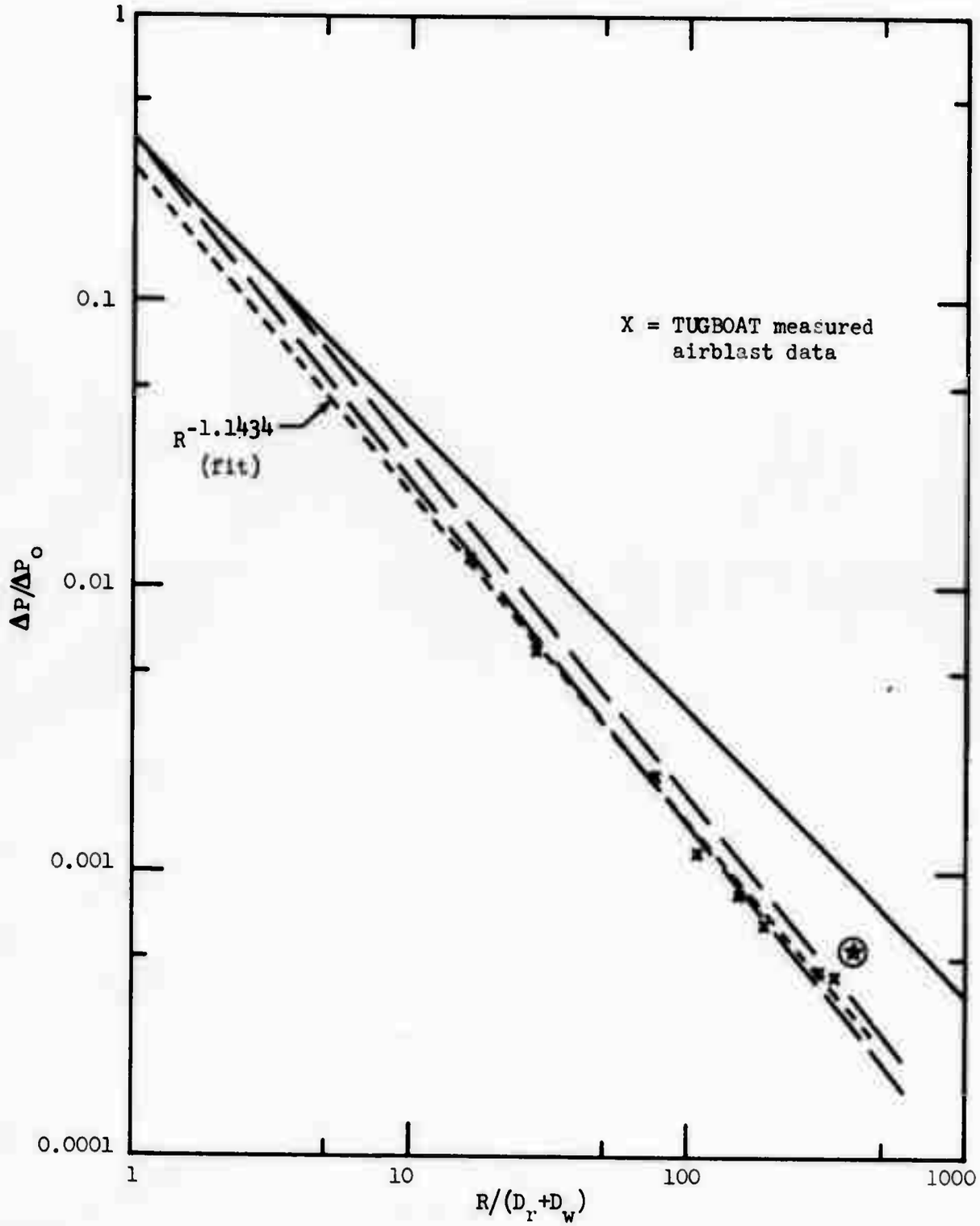

Figure 97. Airblast overpressures, TUGBOAT IC event.

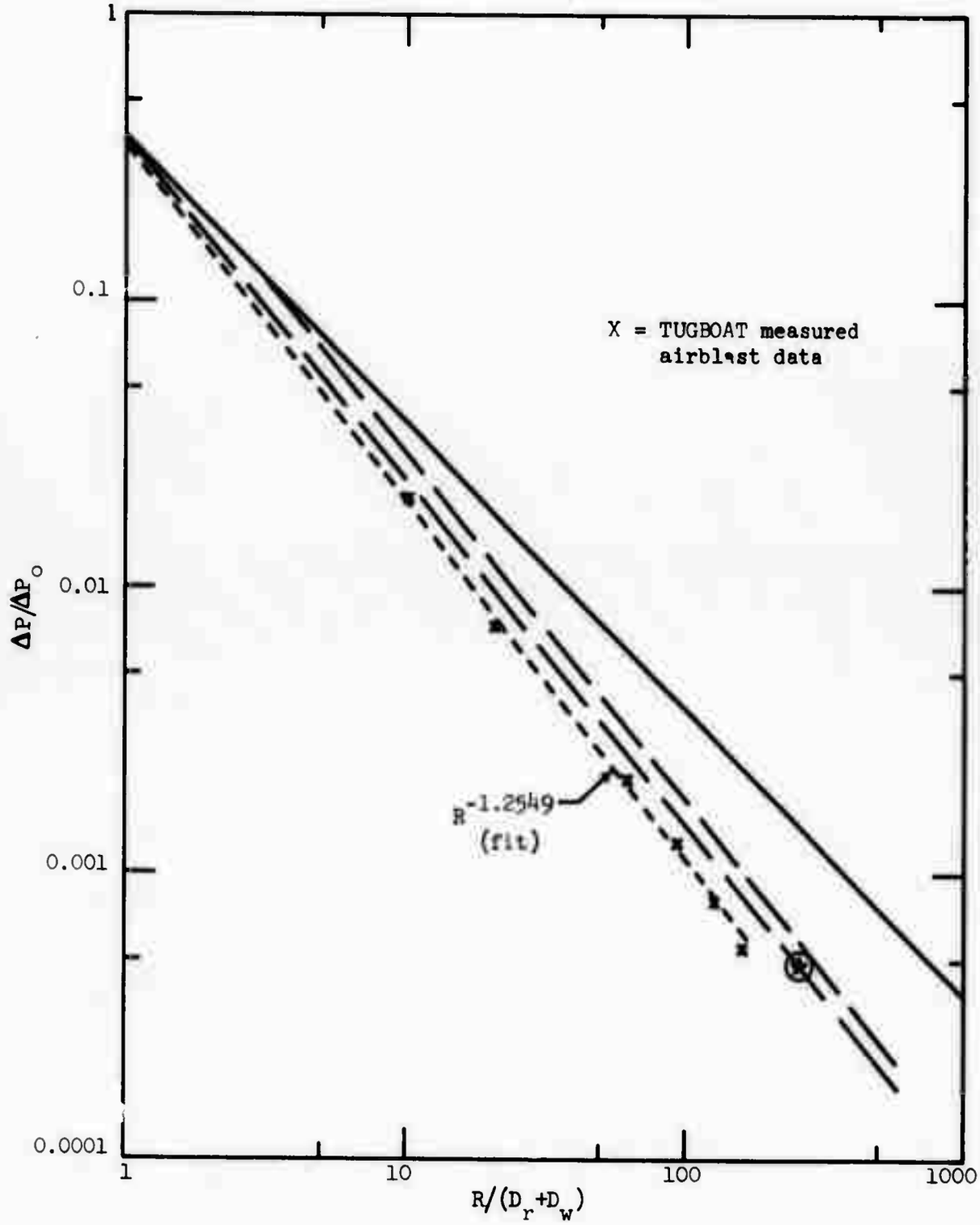

Figure 98. Airblast overpressures, TUGBOAT ID event.

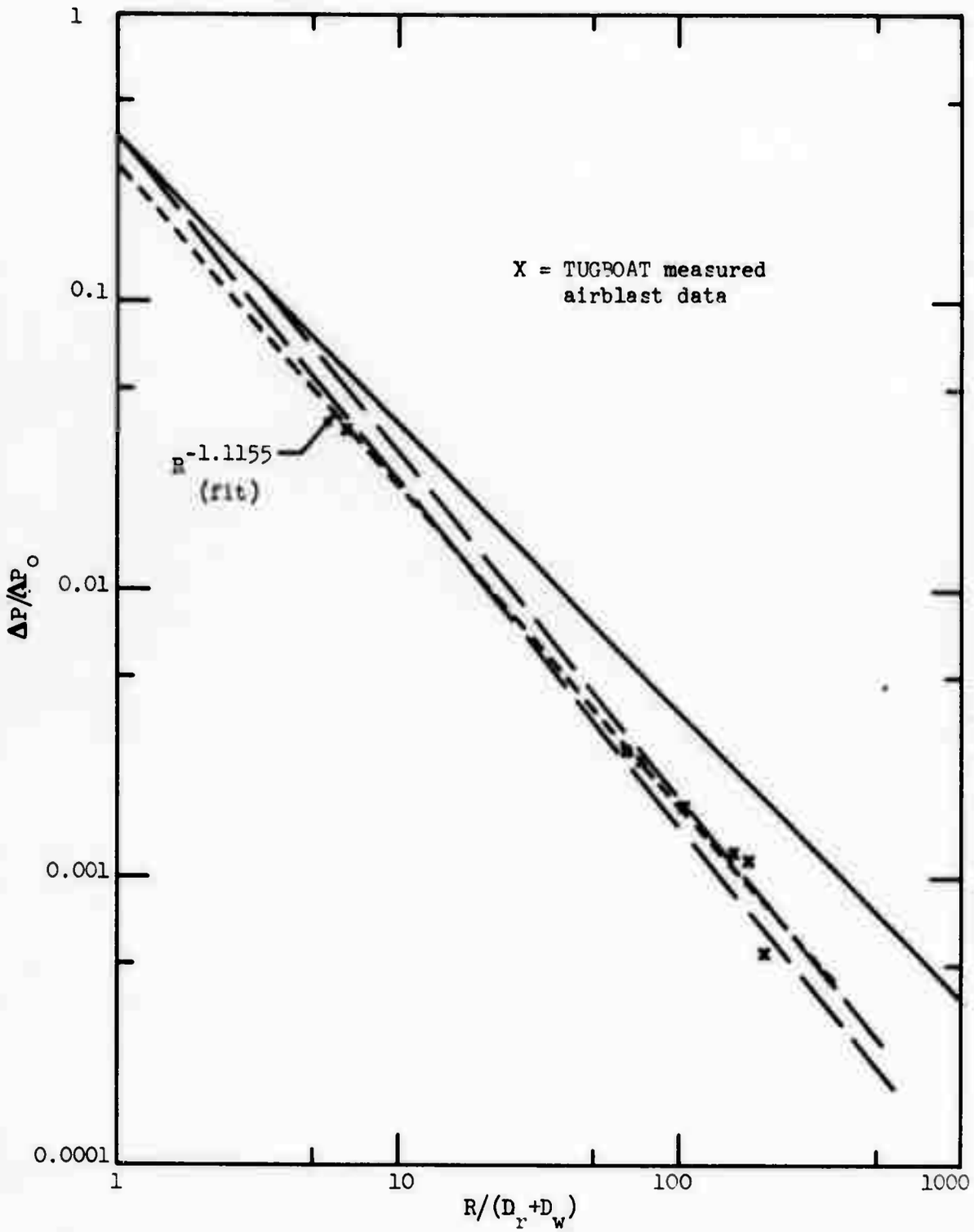

Figure 99. Airblast overpressures, TUGBOAT IE event.

surface spall velocities are usually much less than 1/2 to 1/10 of the SGZ velocity, and most of the airblast pulse energy may be expected to have decoupled from the ground (or water) surface. Thus, it is legitimate to expect that refraction effects and faster attenuation will become apparent at ranges $R/(D_r+D_w) \gtrsim 1$ to 3. Accordingly, straight lines of slope "$R^{-1.2}$" have been extrapolated from the acoustic "R^{-1}" predictions at $R/(D_r+D_w) = 1$ and at $R/(D_r+D_w) = 3$. These lines encompass most of the data points and the least-squares fits within the region of the data for four of the five events (Figures 95-99). Event ID (Figure 98) still lies below the prediction. Note that ID also shows the fastest apparent attenuation rate ($R^{-1.2549}$).

The measurements and acoustic predictions may also be compared by extrapolating the least squares fits inward, toward the high-velocity spall region. The intercept of the fitted line at $R/(D_r+D_w) = 1$ is equal to the constant "α" in Eqn. IV. This intercept may be compared with the acoustic prediction of "α" for each event. The predicted α-values are listed in column 9 of Table 14, while the least-squares intercepts are given in the last column. Four of the predicted values appear slightly higher than the extrapolated fits (Fig. 96-99), although the event IA prediction is somewhat lower (Fig. 95). These results may indicate that either the acoustically predicted "ΔP_o's" (and spall velocities) or the α-values are slightly too high.

As noted in the previous section, photographically-measured late-time velocities for the Tugboat events are somewhat lower than the corrected acoustic predictions (peak spall velocity). The measured velocities and "ΔP_o" values calculated from these velocities are listed in Table 15. The Tugboat airblast data have been reanalyzed, using the new ΔP_o values to determine "$\Delta P/\Delta P_o$". Least-squares fits to the revised data give the α-intercept values listed in the last column of Table 15. The theoretical maximum value of acoustic "α" (for spall launch by a spherical non-dissipative shock wave) is equal to 0.5.[57] Four of the five α's in Table 15 exceed 0.5 (measured surface velocity for the fifth event, Tugboat IE, was in much closer agreement with the corrected acoustic predictions). The systematic deviation indicates that measured velocities and corresponding ΔP_o-values are too low. The corrected acoustic predictions are apparently more consistent with measured

Table 15. Tugboat Phase I Events, Calculated Airblast Parameters For Measured (Photographic) Surface Velocities

Event	Velocity (ft/sec)	ΔP_o Calculated (psi)	Least Squares Fit α - Intercept (for measured velocities)
IA	286	5.26	0.893
IB	261	4.80	0.525
IC	184	3.39	0.569
ID	148	2.72	0.683
IE	287	5.28	0.416

airblast data. This result supports the earlier conclusion that measured velocities do not represent the true early-time peak spall velocity at the water surface.

It is concluded that the acoustic technique can be used to predict airblast from submerged cratering events; however, allowance must be made for the variations in long-range airblast pulse attenuation rate which occur under some circumstances.

X. SUBSIDIARY CALCULATIONS

In an effort to resolve some of the uncertainties and pursue interesting results revealed by the first suite of SOC problems, several additional SOC calculations were run. These include: (a) Modified coral and granite underwater configurations, intended to examine methods for better modeling shock propagation in the water layer; and (b) coral and basalt "equivalent overburden" calculations (no water layer), undertaken to compare the dynamic effects of a water layer with those of an equivalent mass of rock. This section reviews the subsidiary calculations and compares results with the previous set of problems.

Shock resolution in the water layer. Significant difficulties involving excessive shock damping, rapid attenuation, and disagreement with the spherical acoustic calculations in the water layer were encountered only for the granite underwater events. It therefore seems probable that these difficulties are related to unusual granite medium properties (stiff, high strength), errors in the acoustic analysis, or errors in the water layer SOC modeling. Shock resolution in the water layer presents an immediate candidate as a causative mechanism. Waveforms have been examined for the 36/36 ft (deep water layer) vertical calculations in coral, basalt, and granite. The velocity waveforms at the rock interface ($R = 10.93$ m), in water just beyond the rock interface ($R \approx 11.3$ m), and at long range in the water layer ($R \approx 19.9$ m) are presented in Figures 100 (coral 36/36), 101 (basalt 36/36), 102 (granite 36/36 - coarse water zones), and 103 (granite 36/36 - fine water zones). The vertical (velocity) scales in these figures are arbitrary; all peaks have been plotted about the same height to permit comparison of rise times. The horizontal scale consists of an arbitrary 10 msec time interval, and the waveforms for each medium have been moved close

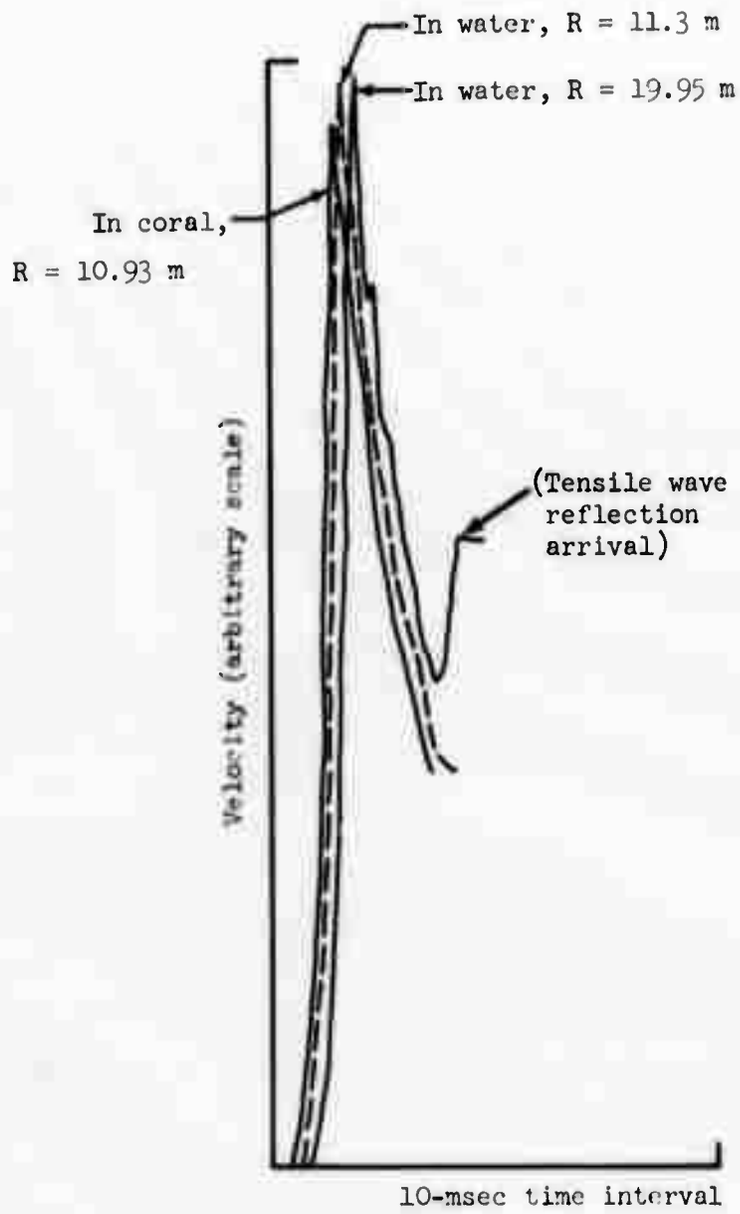

Figure 100. Velocity waveforms: coral 36/36 (arbitrary scales).

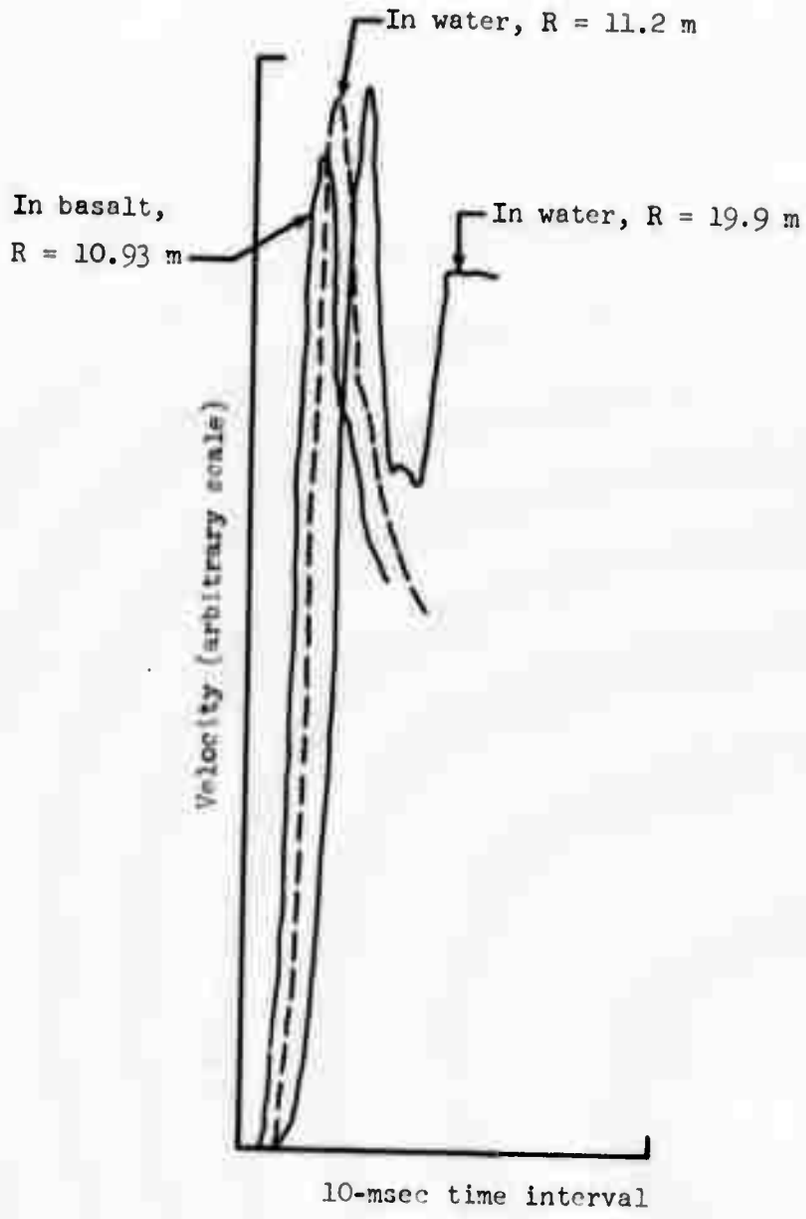

Figure 101. Velocity waveforms: basalt 36/36 (arbitrary scales).

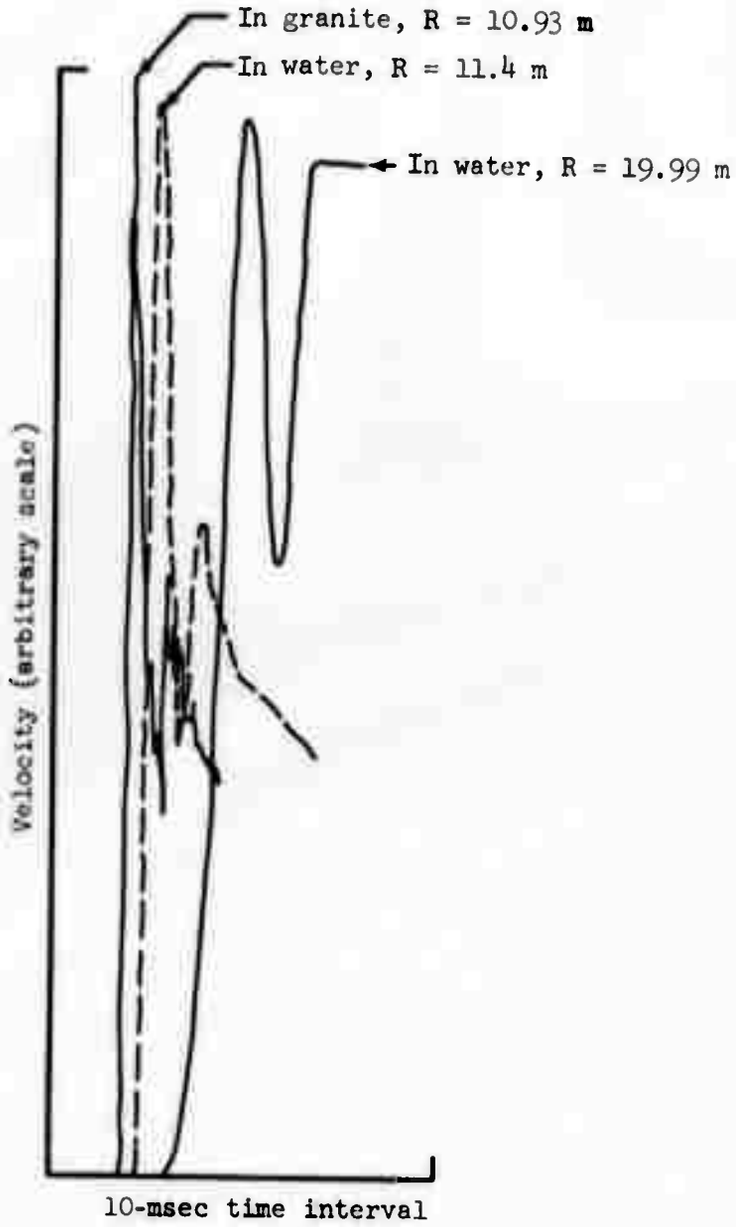

Figure 102. Velocity waveforms: granite 36/36, coarse water zones (arbitrary scales).

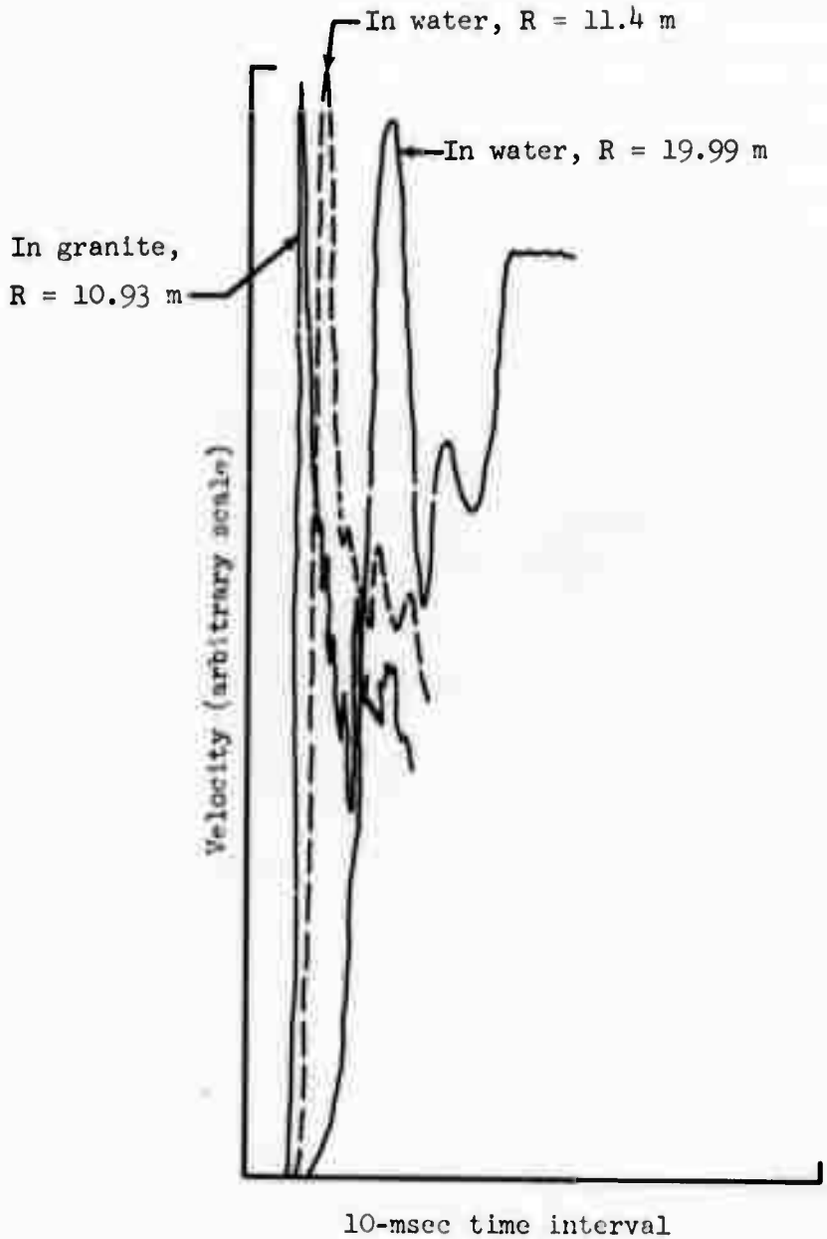

Figure 103. Velocity waveforms: granite 36/36, fine water zones (arbitrary scales).

together. It is evident that the moderately sharp velocity peaks for coral (Figure 100) and the somewhat rounded waveforms of basalt (Figure 101) undergo no dramatic modification upon transmission at the interface,or in travelling about 9 m through the water layer. A quite different situation occurs for the sharp, short-duration and rather noisy pulses in granite (Figures 102, 103). An abrupt increase in rise time and an even more noticeable broadening of the peak is apparent just beyond the water interface. More gradual changes continue throughout the water layer. Waveforms near the surface (R = 19.99 m) resemble the broad, smooth peaks for coral and basalt calculations (note the slight differences in time scales between figures). Smearing of the front and rise time increase are more noticeable for the "coarse water zone" granite calculation, but occur even in the "fine zone" case. The "fine zone" waveforms (half-size water zones) show evidence of noise transmission and "ringing" on the declining edge of the water-layer waveforms (Figure 103). This effect is also visible in the waveforms shown in Appendix F (Figures F7-F8).

A more quantitative comparison of rock and water layer waveforms for the 36/36 ft calculations is given in Table 16; this tabulation presents the approximate velocity peak rise times in the top part of the rock layer and in the water layer, and the pressure or velocity peak half-widths* near the rock interface and in the water layer. The quantities are listed for coral 36/36, basalt 36/36, and granite 36/36 (coarse and fine zone) calculations, and also for additional calculations "coral 36/36" with very low damping in the water layer,and "modified granite 36/36" with <u>equal size</u> rock and water zones of width = 0.099 m (discussed in greater detail below). The half-widths of the rapidly-declining pressure peaks were measured for coral and basalt; however, the "granite" pressure peaks were so rapidly damped and noisy that velocity peak half-widths were used instead. It is most useful to compare

* Pulse width in msec at one-half of peak amplitude.

Table 16. Velocity Waveform Rise Times And Velocity Or Pressure Pulse Peak Half-Widths In The Rock Layer (Near Interface) And In The Water Layer, For The 36 ft/ 36 ft Calculations. (A Water Damping Factor Of $\nu = 0.1$ Was Used Unless Otherwise Noted.)

CALCULATION	Approximate Velocity Peak Rise Time (in msec)		Pressure Or Velocity Peak Half-Width † (in msec)	
	Top part of Rock Layer	Water Layer (Ranges ≈11.3-19.9m)	Rock (at interface)	Water Layer (Ranges ≈11.3-19.9m)
Coral 36/36	0.7 - 1.0	1.0 - 1.1	1.03 (Pres.)	1.16 - 1.44 (Pres.)
Coral 36/36 ($\nu \simeq 0.05$, low damping)	0.7 - 1.0	1.0 - 1.05	1.03 (Pres.)	1.12 (Pres.)
Basalt 36/36	0.8 - 1.2	1.2 - 1.8	1.45 (Pres.)	1.64 - 1.75 (Pres.)
Granite 36/36 Coarse Water Zones	0.2 - 0.3	≈0.6 - 2.0**	0.63 (Vel. Pulse)	0.79 - 1.5 (Vel.)
Granite 36/36 Fine Water Zones	0.2 - 0.3	0.45 - 1.3**	0.58 (Vel.)	0.61 - 1.0 (Vel.)
Modified Granite 36/36*	0.3 - 0.4	0.4 - 1.0	0.64 (Vel.)	0.72 - 1.0 (Vel.)

* Equal zones of approximately 0.099m width.

** Very rapid pressure and velocity decreases corresponding to rapid smearing of the wave occur close to the interface. Space resolution in the problem edits is not sufficient to define the rapid resolution loss across only a few zones.

† Pressure peak half-widths in granite are not accurately definable due to calculation noise; therefore, the half-widths of the rapidly declining velocity peaks in this medium have been measured instead to provide an idea of the shock width.

the relative trends in rise time and peak half-width for the three media. The rise times undergo no significant modification very close to the rock-water interface for coral (1.0 msec) and basalt (1.2 msec), and only a gradual change while traversing the thick water layer. Indeed, the waveform parameters remain almost constant for the sample "coral 36/36" low-damping calculation. The pressure pulse half-widths likewise show only moderate changes near the interface and in the water layer. It is interesting to note that the factor by which the pressure pulse half-width increases in the water layer is roughly comparable for basalt and coral, in spite of the enormous water zone size used in the "basalt" calculations. This fact is attributed to the relatively smooth and well-resolved waveforms entering the water layer. It indicates that excellent resolution was achieved in the water layer for these events and explains the close agreement with acoustic calculations.

The granite "coarse" and "fine" zone calculations (Table 16) reveal a dramatic increase in rise time close to the rock-water interface. This change occurs over a very few calculational zones (the exact distance cannot be defined due to inadequate resolution in the data edits) and is most severe for the coarse-zoned calculation. Its immediate effect is to smear the shock front and severely decrease the peak. The consequent sudden decline of particle velocities near the interface was discussed in Chapter VI (Figures A38, A39, A46, A47), and obviously results from an abrupt loss of resolution. In order to reduce this effect, a modified granite 36/36 calculation was performed with somewhat coarser rock zones and with equal-size water zones. This calculation eliminated the sudden increase in rise time near the interface, and the peak velocities likewise ceased to decrease abruptly at the interface. However, the general trend of increasing rise time and rapid attenuation throughout the entire water layer persisted. Rise time within the water layer increased by a factor of 2.5, in spite of the elimination of the discontinuous behavior near the interface. The attenuation rate of peak velocity also remained close to $R^{-1.5}$ in the water layer, comparable with the $R^{-1.55}$ factor for the other granite events (beyond

the immediate vicinity of the interface). In summary, rise times for all three of the granite calculations tend to increase from a few tenths of a millisecond to about 1 or 2 msec within the water layer, and correspondingly rapid attenuation of the peaks is observed. This trend is not noticed for the coral and basalt calculations, which fall in close agreement with predictions for compressional acoustic wave transmission. Possible reasons for the differing behavior are examined below.

Modified coral 36/36 calculation, low damping in the water layer. Good shock resolution and near-acoustic behavior in the water layer were achieved for the coral and basalt underwater events. In order to more precisely define the factors which influence the best multilayer calculations, further SOC runs were undertaken for the coral 36/36 configuration. The problem format and the impedance-matched rock and water zoning were identical, but very low water viscosity factors $\nu \approx 0.05$ to 0.07 were used. Viscosity factors lower than ≈ 0.1 normally cause peak overshoot and severe ringing behind the shock front. In this case, it was noted that noise from the coral layer was transmitted undamped into the water, but remarkably little evidence of overshoot or ringing was apparent (relative to the "normal" coral 36/36 calculation). Noticeable ringing began to develop several meters beyond the rock-water interface when the viscosity factor was reduced to 0.05. The success of these calculations is attributed to the gradual rise times and smooth shock contours near the coral-water interface. At $\nu = 0.05$, at water layer velocity attenuation rate of about $R^{-1.03}$ was achieved (compared with spherical nondissipative attenuation rate of $R^{-1.0}$, and with the measured rate for water and earlier SOC-calculated rates $\sim R^{-1.13}$ to $R^{-1.2}$). For problems of this type, shock attenuation in the water layer may be adjusted and nondissipative acoustic behavior may be simulated with no serious adverse effect on the solution. Modifying the water layer viscosity did not significantly influence the initial reflection at the rock-water interface, nor did

it change the calculated dynamic behavior of the rock layer. Spall velocities near the rock interface were 60-70 m/sec, similar to the previous SOC calculation and to the acoustically-calculated interface peak spall velocity of 71.25 m/sec. However, shock attenuation in the water layer was decreased, and the water surface spall velocity increased correspondingly. Water surface layer spall velocities were 38-70 m/sec, compared with 34-62 m/sec for the earlier coral 36/36 calculation and with a peak water surface spall velocity of 65.1 m/sec for the spherical (uncorrected) $R^{-1.13}$ acoustic calculation (Table 11). A revised acoustic calculation (uncorrected) was performed with a "water" attenuation rate of $R^{-1.03}$, to match the lower rate attained in this problem. The acoustic peak water surface spall velocity was found to be 69.8 m/sec, in excellent agreement with the 70 m/sec SOC result.

Additional calculations were attempted with still lower water viscosity factors, but ringing and overshoot were encountered at ranges close to the interface. The use of lower viscosity factors is not justified, since essentially acoustic attenuation can be achieved in this case. It is concluded that, for smoothly-rising "resolvable" shock waveforms typical of coral and basalt, the viscosity factor controls attenuation in the water layer. Loss of resolution due to impedance matching and water zone size is not a significant effect. No serious discontinuity in shock behavior occurs at the interface. These conclusions are consistent with the earlier discussion of rise times and peak widths. The viscosity factor may be used to control the water layer calculation and achieve any desired attenuation rate for underwater calculations in coral- and basalt-type media.

"Standard" and modified granite underwater calculations - zone size effects. Granite underwater events present the opposite situation of very sharply-rising, noisy waveforms at the interface and resolution-limited propagation within the water. Attenuation rates greatly exceed the acoustic level throughout the water layer. Low water viscosity factors cannot be used to reduce attenuation because of the sharply rising and noisy shock input from the rock layer. Likewise, the use of very fine water zones

creates a severe acoustic mismatch at the interface, which also causes ringing for sharp-fronted shock waves. The succeeding paragraphs discuss in more detail some of the results of granite underwater calculations.

The initial granite 36/10 and 36/36 calculations were conducted with the standard rock zone size of 0.04 m and impedance-matched water zones of about 0.39 m (Chap.III, Table 2). These coarse water zone configurations produced a sudden drop in particle velocity and a lack of pressure restoral beyond the rock-water interface (just above the "low-pressure" rock zones in the spall cutoff region below the interface). A corresponding loss of shock resolution and sudden peak-smearing were noted near the interface. At slightly longer ranges, the particle velocities approached a constant but rapid attenuation rate of about $R^{-1.55}$, and gradual smearing of the wavefront continued throughout the 10 ft and 36 ft water layers. The two granite calculations were repeated using halved water zone size (= 0.196 m), with the result that the sudden velocity dropoff and the degree of smearing of the front near the interface were reduced significantly. However, these fine-zone calculations continued to show gradual loss of resolution and a rapid attenuation rate in the water layer. The fine-zoned calculations also began to reveal impedance-mismatch effects in the water layer. Impedance mismatch may be easily distinguished from artificial viscosity effects, since mismatch tends to cause erratic ringing on the declining edge of the waveform close to the interface, while inadequate damping gives rise to gradually-developing overshoot and oscillations at longer ranges (for a low-amplitude wave). Water waveforms near the interface (R = 11.4 m) for granite 36/36 are shown in Figures 104 (coarse zones) and 105 (fine zones). Artificial viscosity factor for the water layer was $\nu = 0.1$ in both cases. The fine-zoned calculation gives a higher pressure and better peak resolution, but some erratic ringing is apparent in the late-time waveform (impedance mismatch = factor of 2).

A closer examination of the coarse and fine zone calculations demonstrated that the major differences were primarily confined to the water layer and had little influence on the underlying rock. Waveforms in the rock layer were almost identical except for slight changes in tensile reflection arrival time and duration

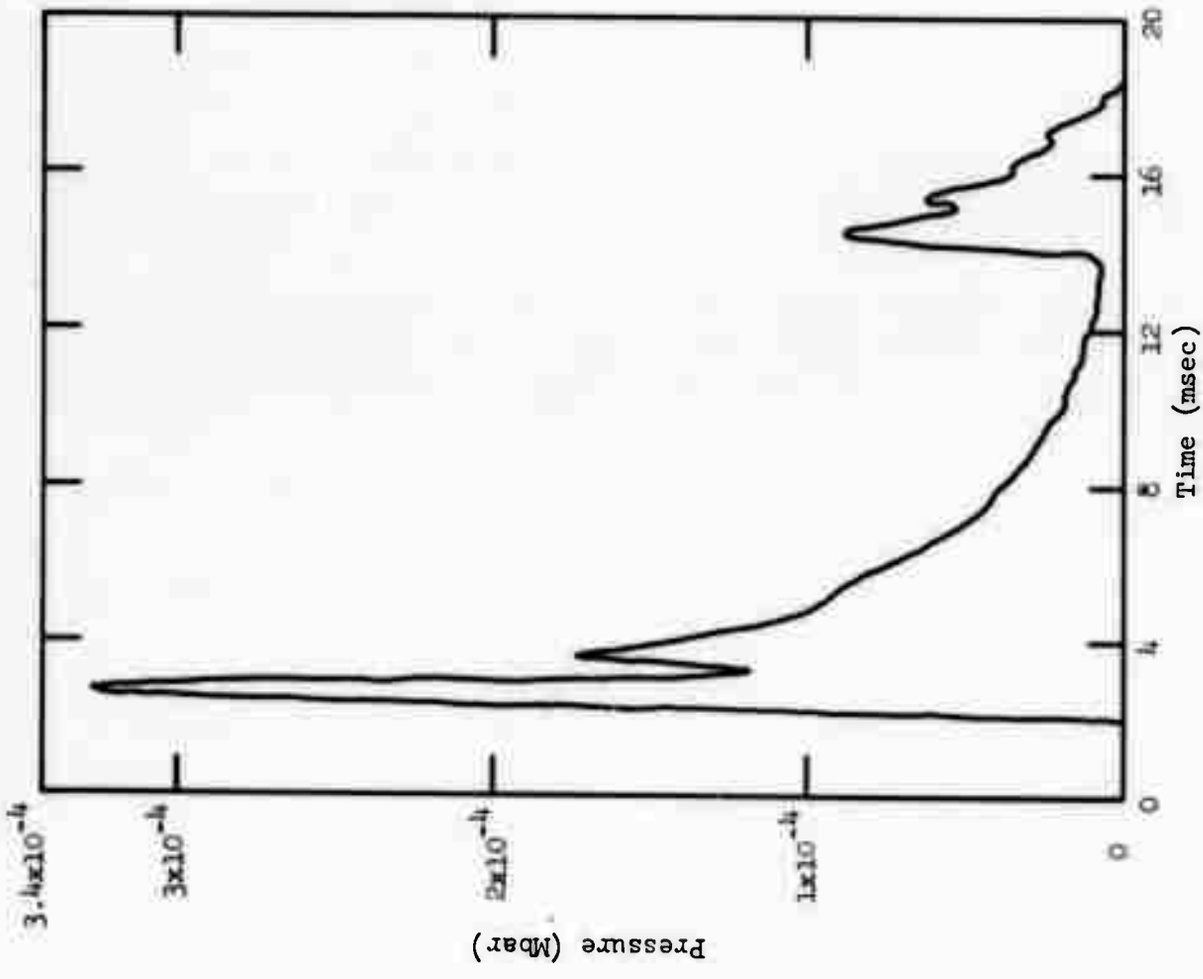

Figure 104. Granite 36/36, pressure waveform in water layer at R = 11.4 m; ν = 0.1, coarse zones.

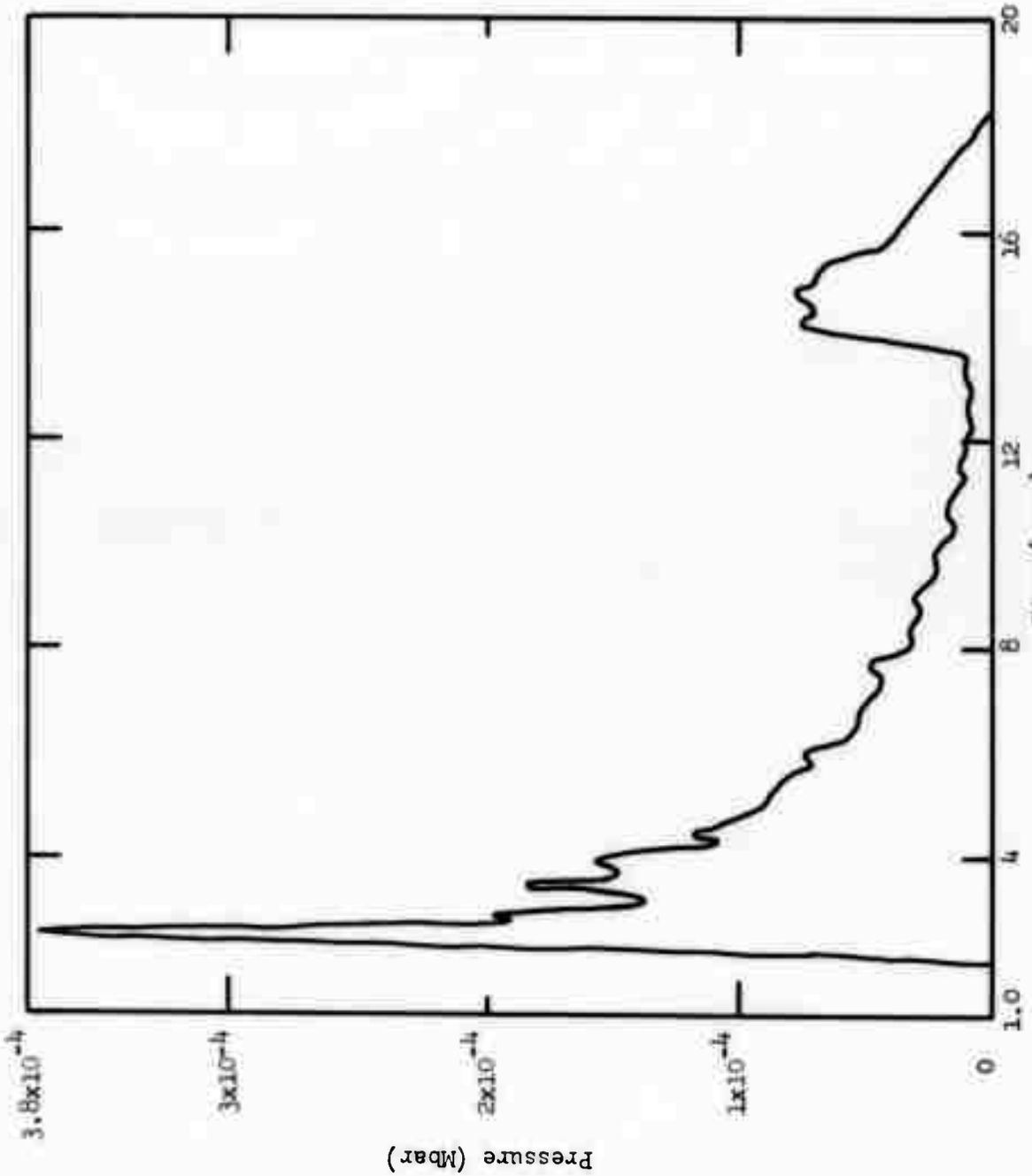

Figure 105. Granite 36/36, pressure waveform in water layer at R = 11.4 m; ν = 0.1, fine zones.

of the freefall phase, and in the late-time residual velocities. The beginning of the "water overburden" deceleration (recompaction) phase well below the rock-water interface and the subsequent arrival of the upward-moving gas acceleration pulse were slightly earlier for the "fine" zone calculations. The overall kinetic and internal energies in the rock layer were modified by less than 3%, and did not diverge at late times. However, the water layer velocities and energies began to differ noticeably as the water surface spall reflection moved downward through the water layer. Kinetic energies increased by about 4% and internal energies decreased by up to 10% at late times for the fine-zoned calculations, due to better shock resolution and higher spall velocities in the water.

The granite 36/36 calculation was repeated in modified form with equal rock and water zone sizes of 0.099 m. Shock rise time in the rock layer was slightly increased due to the coarser rock zones, but the peak values and shock width near $R \approx 10$ m (close to the rock-water interface) were only negligibly changed. This fact indicates that somewhat coarser rock zoning could have been used with no deleterious effect in the vertical calculations.

The equal zone sizes and finer water zones exerted a considerable influence on the water layer calculations, as discussed previously. The abrupt loss of peak resolution at the rock-water interface and the corresponding sudden decline of velocity in the water layer just beyond the interface both disappeared. However, the slowly-increasing rise time (to about 1 msec) and rapid overall attenuation in the water layer persisted. The use of equal water zones also caused almost undamped transmission of "granite" noise throughout the thick water layer, with the addition of severe ringing near the interface due to the gross impedance mismatch.

The elimination of discontinuous behavior near the interface and improvement of water-layer resolution slightly affected other aspects of the calculations. The previous granite underwater events (Table 11) gave a rock interface peak spall velocity of about 32 m/sec, approximately equal to the peak spall velocity with no water overburden (granite 36/00). The peak velocity was thus not reduced as expected for imperfect reflection at the

granite-water interface. The early-time effects of the water layer were not properly calculated due to the large water zone size (zone width greater than the effective wavelength of the incoming shock). The modified granite 36/36 calculation with equal zoning produced a velocity range of 18 to 30 m/sec in the rock surface spall layer. The peak velocity of 30 m/sec lies close to the acoustic value of 29-29.6 m/sec for reflection at a granite-water interface (Table 11). Hence, the modified SOC calculation is seen to be more consistent with expected spall velocity. The difference in spall velocities between the SOC calculations declines at locations further below the interface; even at the interface, differences in peak velocity disappear soon after shock arrival, as the peak is damped by water-layer deceleration of the rock material.

The modified water layer calculation also influences water spall velocities. The surface spall layer is somewhat thinner and more clearly defined due to improved resolution of the shock front. Surface layer spall velocities for the modified granite 36/36 configuration are 11.5 to 20 m/sec, significantly higher than the previous coarse-zoned (9.7-16.1 m/sec) and fine-zoned(10.6-18 m/sec) calculations. However, the peak spall velocity remains lower than the spherical (uncorrected) acoustic value of 26.5 m/sec (Table 11, Figure 79; assuming $R^{-1.13}$ attenuation). Substituting a water-layer attenuation rate of $R^{-1.55}$ into the spherical acoustic analysis gives a spall velocity of 20.0 m/sec (Figure 79), in precise agreement with the modified SOC result.

We see that the apparent disagreements between "SOC" and "acoustic" calculations for granite are attributable to discontinuous behavior near the interface (eliminated in the modified calculation) and rapid attenuation through the water layer (not eliminated). Rapid attenuation is not solely attributable to water zone sizes, since near-acoustic behavior was attained in coral calculations (water zones ≈0.1 m) and even in the basalt calculations with coarse water zoning (≈0.254 m). Granite events consistently show rapid attenuation well beyond the rock-water interface, even when equal-size rock and water zones are used. This may represent a physical inconsistency in the results or a real trend dependent on material properties. The underlying

granite is a stiff high-velocity rock which transmits sharp waveforms. It possesses a high shear strength and a low Poisson's ratio. Thus, the material supports large shear stresses which build up even at close ranges, and shows a high shear-wave velocity. The radial and tangential stress components differ considerably at ranges ≈10m, near the interface range (see, for example, peak stresses plotted in Figure A15, Appendix A). This situation differs from the coral and basalt media, for which the low ultimate strength severely limits shear stress and behavior is more nearly fluid. The acoustic analysis used here takes account only of peak compressional wave transmission and refraction at an interface. Shear wave effects and shear wave reflection at the interface are not considered. The errors thus incurred may influence peak attenuation beyond the interface for the stiff, shear-supporting granite material. The situation is further complicated in this case because of the failure behavior and spallation taking place near the interface. The granite rapidly undergoes shear failure at a pressure and stress level below its ultimate strength, fails in tension, spalls, and then is reloaded in shear by water layer recompaction. The behavior at and immediately after shock arrival may thus be quite complex. Rapid attenuation encountered in other multilayer one-dimensional calculations[58] has been attributed to unloading and energy feedback into the low-pressure reflected rarefaction region beneath the interface. This effect could become important for granite, a strong material with a very narrow high-velocity spall zone at the interface and rapid velocity damping beneath the interface. Two-dimensional calculations may be required to solve the general layer transmission problem for granite and similar stiff, high-strength materials. Part of the apparent inconsistency in attenuation is undoubtedly due to the shear reflection effects, which can be studied by a more comprehensive acoustic treatment. Part may be due to failure and other nonlinear material behavior which can be properly analyzed only by complete calculations.

To summarize, a judicious choice of problem format and zone size produced valid two-layer calculations for the coral and basalt submerged cratering configurations examined here. Peak pressures and velocities for the water layer and other safety-related parameters such as airblast can be predicted by a simple acoustic analysis. The granite medium imposes rather more severe calculational restrictions due to the large density and sonic

velocity mismatch at the interface, and due to the shear supporting characteristics and other properties of the material. Fortunately, the precise behavior in the water layer exerts very little influence on the underlying rock. Lagrangian codes with coarse water zoning may be confidently used to predict shock transmission, long-term dynamics, and cratering for the rock layer.

Equivalent overburden calculations. Attempts have been made to treat the multilayer cratering problem with simple "overburden" models. Possible approaches include the use of a single layer of the same total depth and average density (weighted by layer thickness) as the series of layers in the actual configuration. The two-layer underwater case has been analyzed by assuming that the water layer acts as a depth of rock equivalent to the overburden weight (lithostatic head) of the water layer [12]; [Equivalent "rock" depth of water layer = D_w (ρ_w/ρ_r); total equivalent burial depth of shot = $D_r + D_w$ (ρ_w/ρ_r)]. Dimensional arguments may be cited in support of this approach. The complexity of multilayer shock interactions provides certain counter-arguments. Consider the cases of an underwater cratering event and of its "equivalent overburden" analog in rock alone.* The underwater event experiences an initial rock layer spall phase caused by partial tensile reflection at the rock-water interface. This is followed by a delayed spall pulse from the water surface, transmitted through the water layer. The gas acceleration phase begins at relatively early time, when the interface spall reflection reaches the cavity. In the"equivalent overburden"case, the initial shock wave is perfectly reflected as a single tensile wave at the rock free surface. Due to the added rock overburden, this pulse arrives at a given "rock" location relatively later than the corresponding rock-water interface reflection, but much earlier than the corresponding water surface reflection (which must travel through the thicker, low-velocity water layer). The gas acceleration phase also begins somewhat later because of the increased rock depth. Comparison is further complicated by the fact that the underwater event experiences early-time spall rarefaction

* The "equivalent overburden" event has additional rock overburden thinner than the water layer but of equal overburden weight; added rock overburden thickness = D_w (ρ_w/ρ_r).

of the rock layer, followed successively by recompaction due to water overburden and relief from the water surface reflection. These depth dependent interactions begin immediately after interface spall reflection, and affect the later dynamic history and transmission of all subsequent pulses in the rock layer. The interactions are not identical to the delayed single spall pulse and the more continuous damping which occur for the equivalent overburden event in rock alone. Finally, the water layer and rock overburden problems differ with regard to strength effects, shock attenuation, and spall velocities in the upper (water or rock) region. Even ignoring these inherently different aspects of solid medium behavior, such as ability to support shear and the material strength, it seems improbable that the complex double pulse spall and recompaction phenomena for the underwater event would produce exactly the same dynamic results as the single-reflection overburden case. One might expect the greatest discrepancies to occur for thick water layers (i.e., largest difference between water layer and rock overburden thicknesses, greatest difference between reflection arrival times, severe recompaction effects near the rock-water interface for the underwater event), and for large impedance mismatch at the rock-water interface (largest differences between depths and sonic velocities of the water and rock overburden layers, greatest difference between pulse arrival times, longest relative delay between first and second spall pulses for the underwater event).

A set of three "equivalent overburden" SOC calculations has been implemented to examine the dynamic effects of rock and water overburden. These include coral 41.31 (rock depth D_r = 41.31 ft, simulates coral 36/10), coral 55.11 (D_r = 55.11 ft, simulates coral 36/36), and basalt 39.83 (D_r = 39.83 ft, simulates basalt 36/10). In all cases, the added rock depth was chosen to match the overburden depth of the corresponding water layer. The "equivalent overburden" rock calculations used constant rock zoning throughout (homogeneous rock material, no impedance mismatch); however, the rock was arbitrarily divided into two sections for purposes of analysis. These sections encompass the "lower" 36 ft and the "upper" overburden region, corresponding with the "rock" and "water" layers of the underwater calculations.

In comparing spall and late-time residual velocities of the various calculations, the following trends are noted:

For the "shallow" (36/10 and equivalent) configurations, the water layer spall velocities are generally higher than the "upper" region rock spall velocities of the equivalent overburden events. This effect is expected from the lower impedance of the water medium. More important to cratering dynamics, the residual velocities near R=36 ft (near the interface) are relatively lower for the underwater events (due to water-layer damping of the initial peak spall velocity near the interface, and due to the nearness of the rock free surface for the equivalent overburden events); the residual velocities then become relatively higher for the underwater events further below the interface. Velocity waveforms are illustrated in Figure 106a (basalt 36/10, and equivalent overburden calculation basalt 39.83). The residual velocity after water recompaction near the interface (R = 10.6 m) for basalt 36/10 is dramatically lower than the spall velocity at the same location for basalt 39.83. The water layer damping effects are quite evident. At R = 9.06 m, well below the rock-water interface, this trend is reversed; the basalt 36/10 late-time residual velocity (after slight water damping) is higher than the "equivalent"overburden" spall velocity for basalt 39.83. This relationship persists throughout the lower regions of the rock layer.

Somewhat different behavior is noted in the "deep" calculations (coral 36/36 and coral 55.11). In this case, the lower portion of the rock layer for coral 55.11 is far removed from the free surface. Initial peak velocities within the lower 36 ft of the rock are strongly damped before the much-delayed free-surface spall reflection arrives. The spall velocities are accordingly very low. The earlier-arriving interface spall reflection for coral 36/36 proves more efficient in ejecting material, despite water layer damping effects. Velocity waveforms near the interface (R = 10.6 m and 9.01 m) are presented in Figure 106b. In both cases, the late-time residual velocities for coral 36/36 ($t \approx 10$ to 20 msec) are seen to be significantly higher than the corresponding single-layer rock spall velocities. Evidently, the underwater

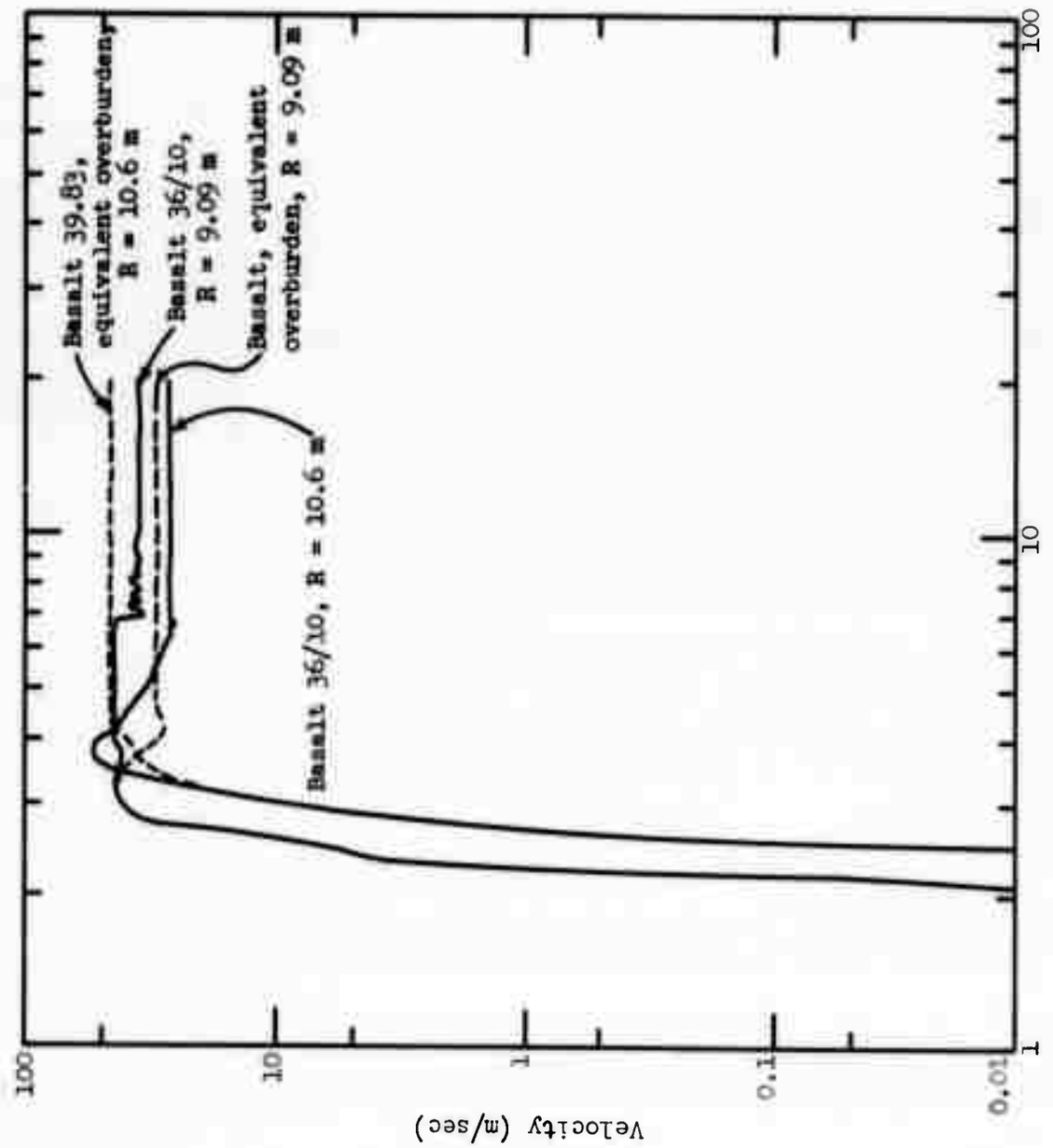

Figure 106a. Basalt 36/10 and equivalent overburden calculation (basalt 39.83 ft); velocity waveforms at R = 10.6 m and R = 9.09 m.

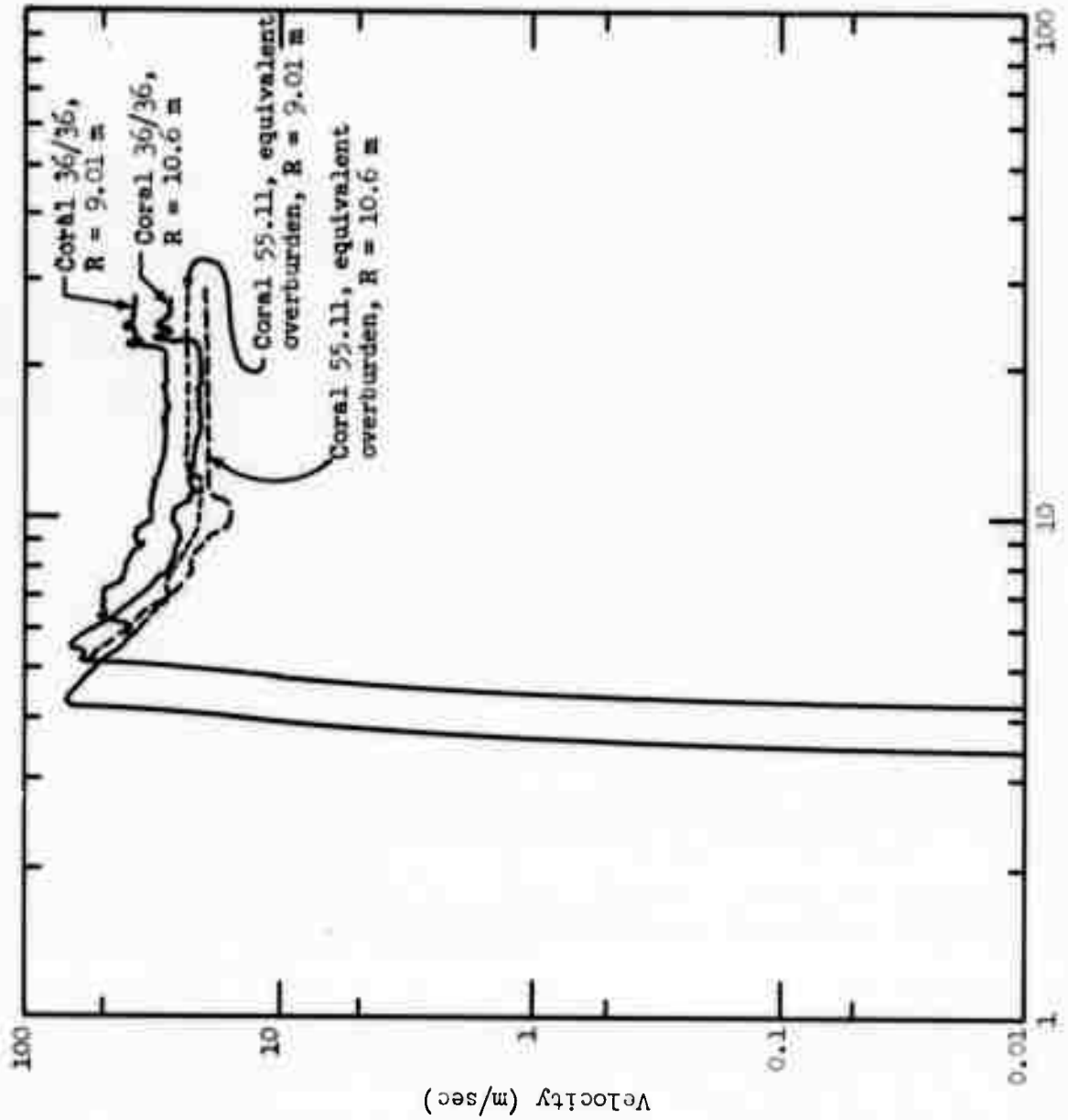

Figure 106b. Coral 36/36 and equivalent overburden calculation (coral 55.11 ft); velocity waveforms at R = 10.6 m and R = 9.01 m.

36/36 event produces more efficient material ejection within the critical rock region (R < 36 ft or 10.97 m) than the deeply-buried 55.11 ft "equivalent overburden" event. The difference with regard to cratering effectiveness will be still greater, since there is no additional rock overburden above 36 ft to be ejected for coral 36/36. After 20 msec, another modification becomes apparent: The early-arriving gas acceleration pulse for coral 36/36 reaches the upper regions of the rock layer, increasing the velocities still further above "coral 55.11". Due to the short distance between the cavity and the interface, gas acceleration occurs sooner and is expected to be a more effective ejection mechanism for coral 36/36. To summarize, the underwater configuration has less rock material to eject and the velocities within the critical region are higher than for the "equivalent overburden" event. The discrepancy is greatest for "deep" overburden layers (i.e., 36/36 ft comparison). The coral 36/36 ft configuration thus simulates a more shallowly buried "rock" event, and is effectively closer to optimum depth of burial than its 55.11 ft analog. The "equivalent overburden" analogy is conservative, tending to underestimate cratering efficiency and crater dimensions for submerged events relative to their dryland counterparts.

The overall mound dynamic parameters have also been examined for the equivalent overburden calculations. Residual velocities at late time are plotted in igures 107 (coral) and 108 (basalt). Other events in the respective media are shown for comparison. The coral 41.31 velocities are much less than coral 36/10 in the lower parts of the mound, becoming greater within 2 m of the 36 ft (10.97 m) location of the coral 36/10 interface. The coral 55.11 velocities are lower than coral 36/36 throughout the "36 foot" region, and are significantly less than 50 m/sec for most of the mound (even within the deeper "high-velocity" regions). These velocities were determined after the initial spallation phase was complete. Coral 55.11 is obviously below optimum cratering depth. The basalt 39.83 spall velocities (Figure 108) are somewhat less than basalt 36/10 in the lower mound, but rise

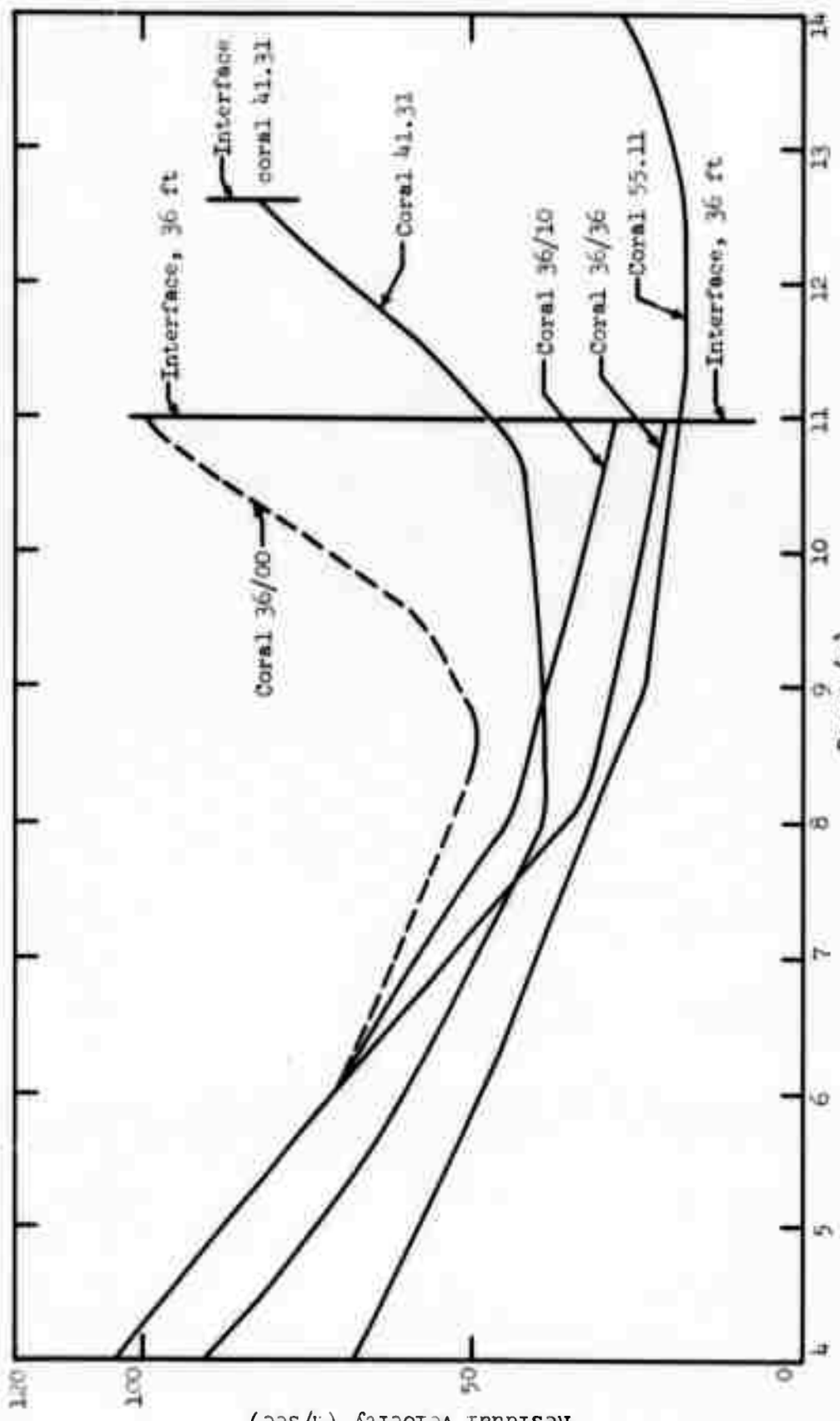

Figure 107. Residual velocities for coral 36/00, coral 36/10, coral 36/36, and equivalent overburden calculations coral 41.31 (simulates 36/10) and coral 55.11 (simulates 36/36).

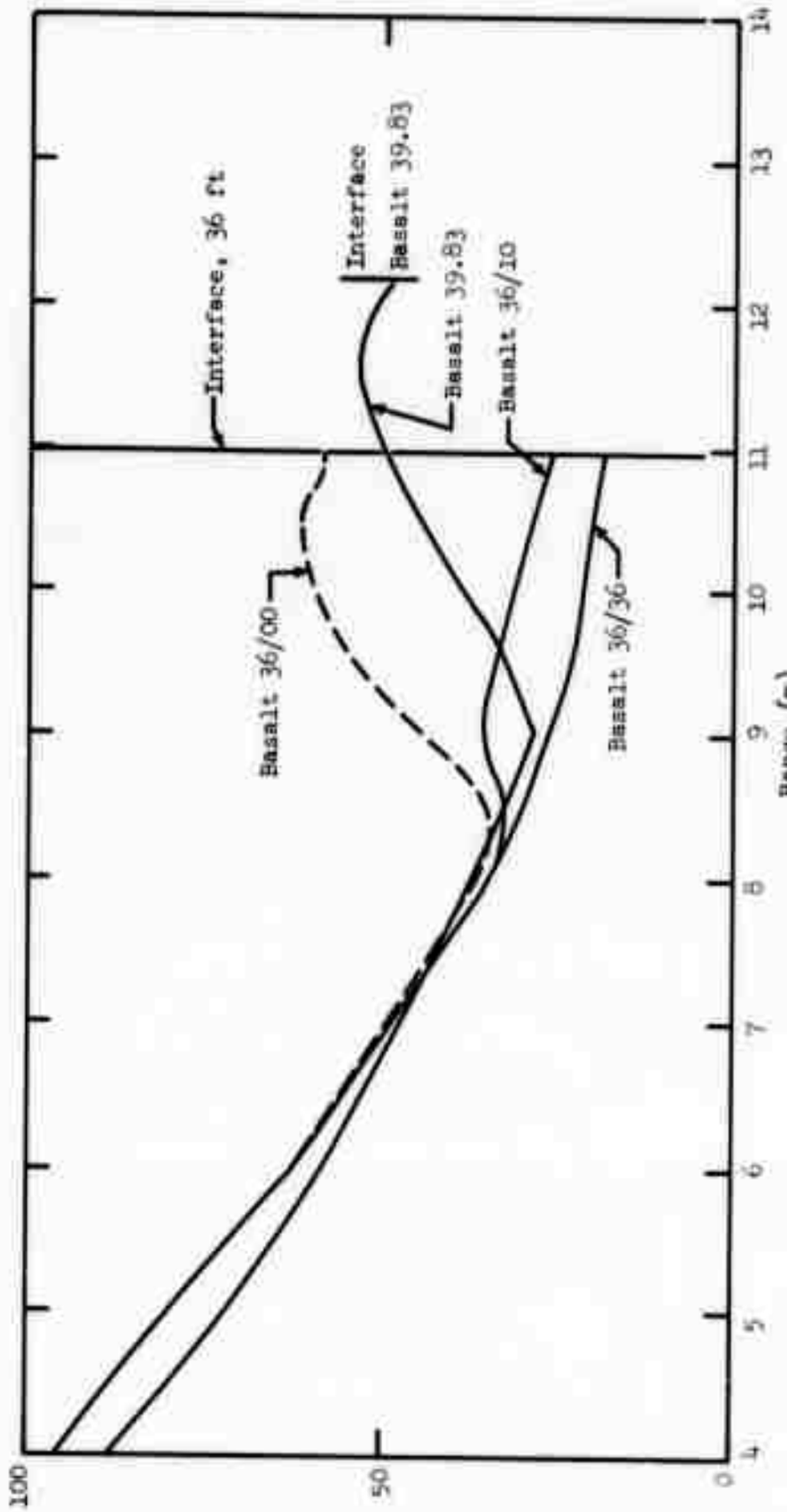

Figure 108. Residual velocities for basalt 36/00, basalt 36/10, basalt 36/36, and equivalent overburden calculation basalt 39.83 (simulates 36/10).

rapidly within 1.5 m of the 36 ft location. This behavior is attributable to the free surface at 39.83 ft (located only slightly beyond the 36 ft range). The overall velocity profiles within the 36 ft layer for basalt 36/10 and 39.83 are much more similar than the corresponding profiles for the coral events. Thus, the basalt "equivalent overburden" calculation (with large impedance mismatch) did a better job of modeling the underwater event than the coral calculation (smaller impedance mismatch). The conclusion applies only for these two specific media. A much larger discrepancy would be expected between basalt 36/36 (deep) event and its equivalent overburden calculation. A "deep" overburden calculation for basalt would provide useful information, but has not yet been performed due to the long calculation time required.

Cavity radii and cavity pressures for all of the equivalent overburden calculations are shown in Figures 109 and 110, respectively. These parameters give a good idea of the relative gas acceleration effects for the "overburden" and"underwater" events. In all cases, the underwater calculations reveal progressively greater cavity radii and lower cavity pressures than the equivalent overburden events at late time. Energy transfer by gas acceleration is considerably more effective for the underwater calculations, and the closer location of the rock-water interface obviously has a significant influence on this phase of cratering dynamics. Note that the radii and pressures are virtually identical for coral 36/10 and 36/36; the interface reflection completely controls cavity growth for these events. The discrepancy between underwater and overburden calculations is rather large for coral 36/36-coral 55.11, somewhat less for coral 36/10-coral 41.31, and least for basalt 36/10-basalt 39.83 (time > 10-15 msec). Once more, the basalt overburden calculation fell closest to the underwater event, and the basalt curves do not diverge dramatically at late times.

The calculated energies as a function of time for equivalent overburden and underwater calculations are depicted in Figures 111a-b (coral) and 112 (basalt). To permit meaningful comparison, the problems have been divided into a "lower" region (below 36 ft), and an "upper" water or overburden region

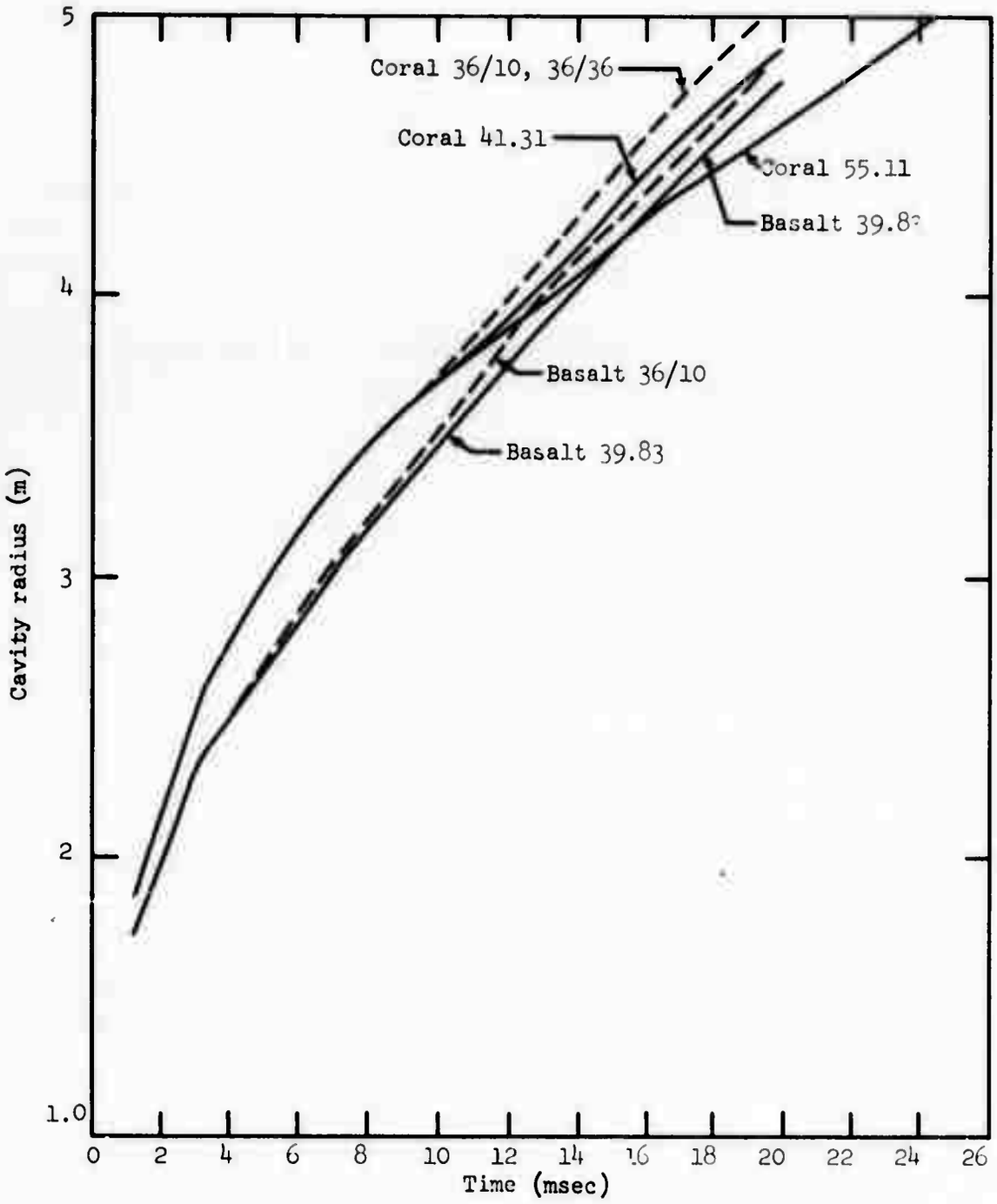

Figure 109. Cavity radii for basalt and coral underwater calculations, and comparable calculations with the same amount of basalt and coral overburden (no water).

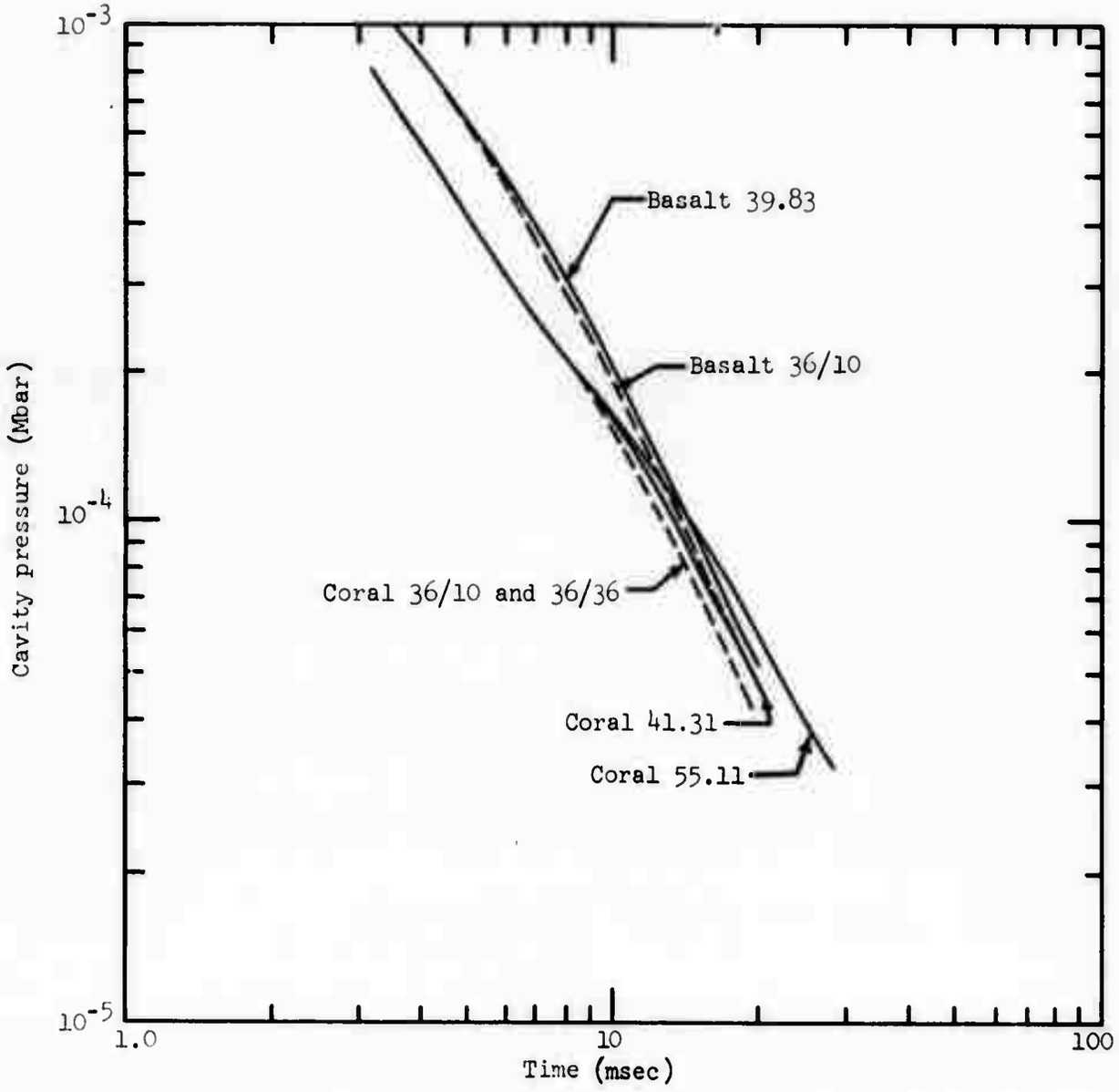

Figure 110. Late-time cavity pressures for basalt and coral underwater calculations, and comparable calculations with the same amount of basalt and coral overburden (no water).

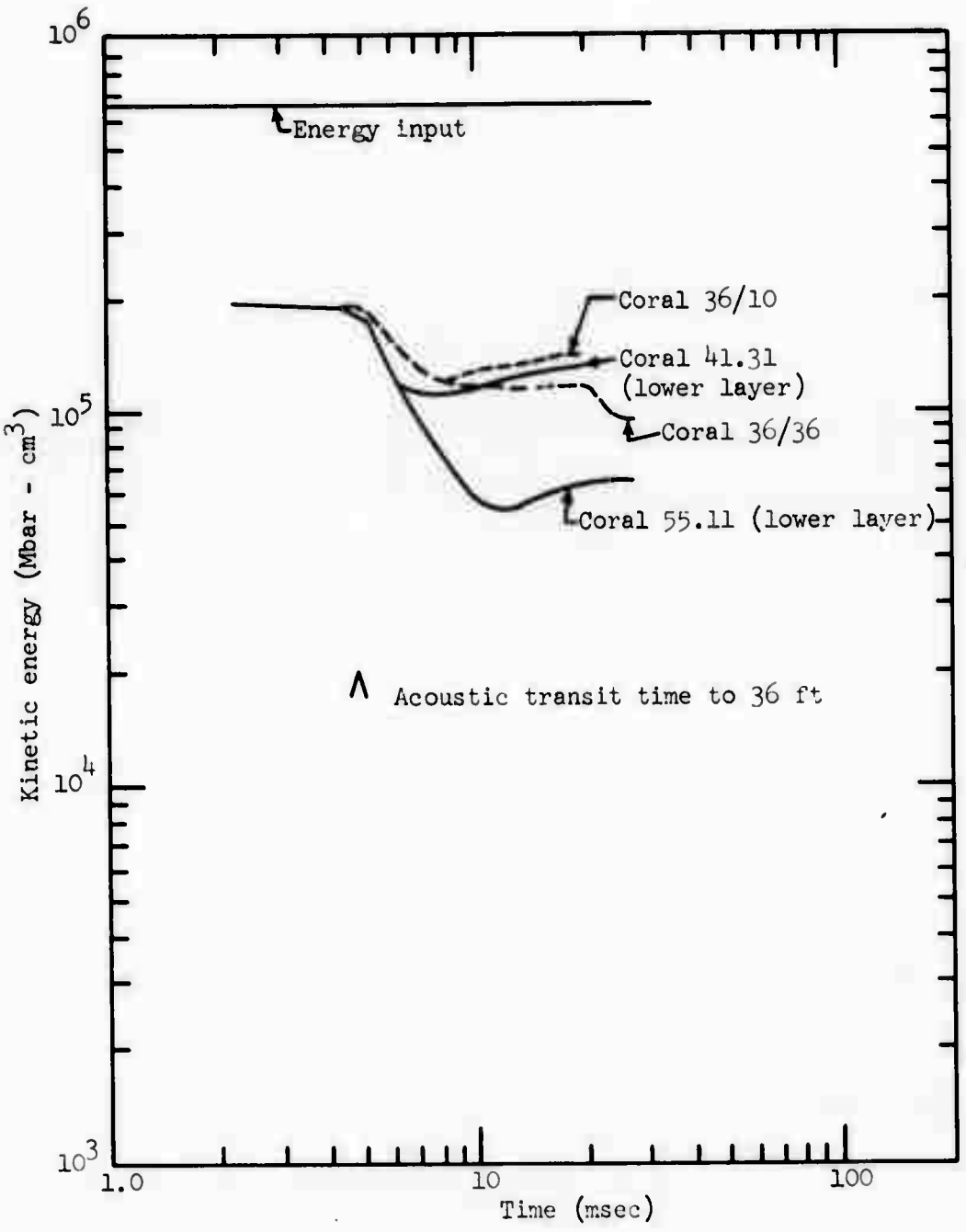

Figure 111a. Kinetic energy in the lower layer, coral underwater calculations (coral 36/10 and 36/36), and comparable coral calculations with the same amount of overburden (no water).

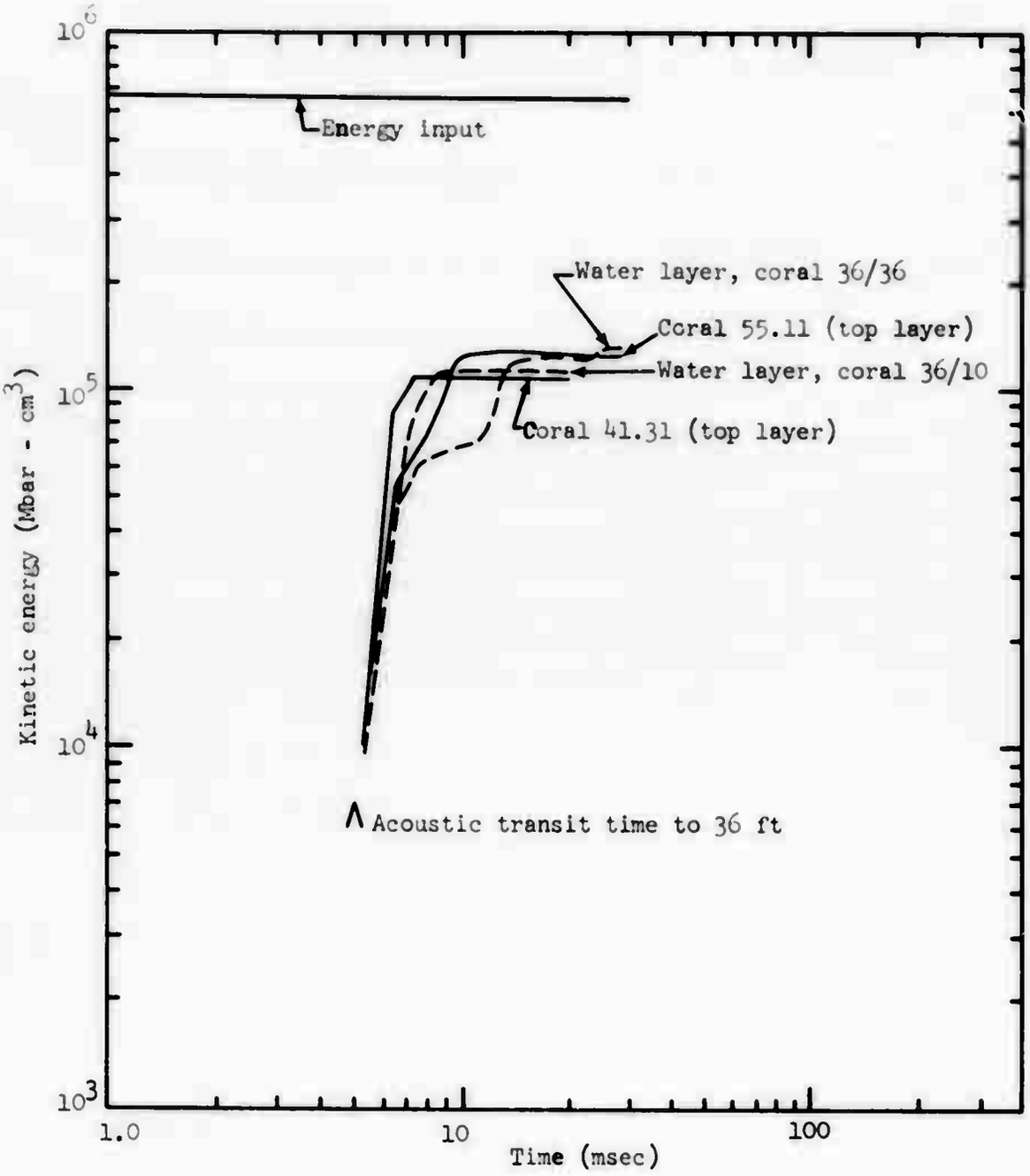

Figure 111b. Kinetic energy in water layer or top layer, coral underwater calculations (coral 36/10 and 36/36), and comparable coral calculations with the same amount of overburden (no water).

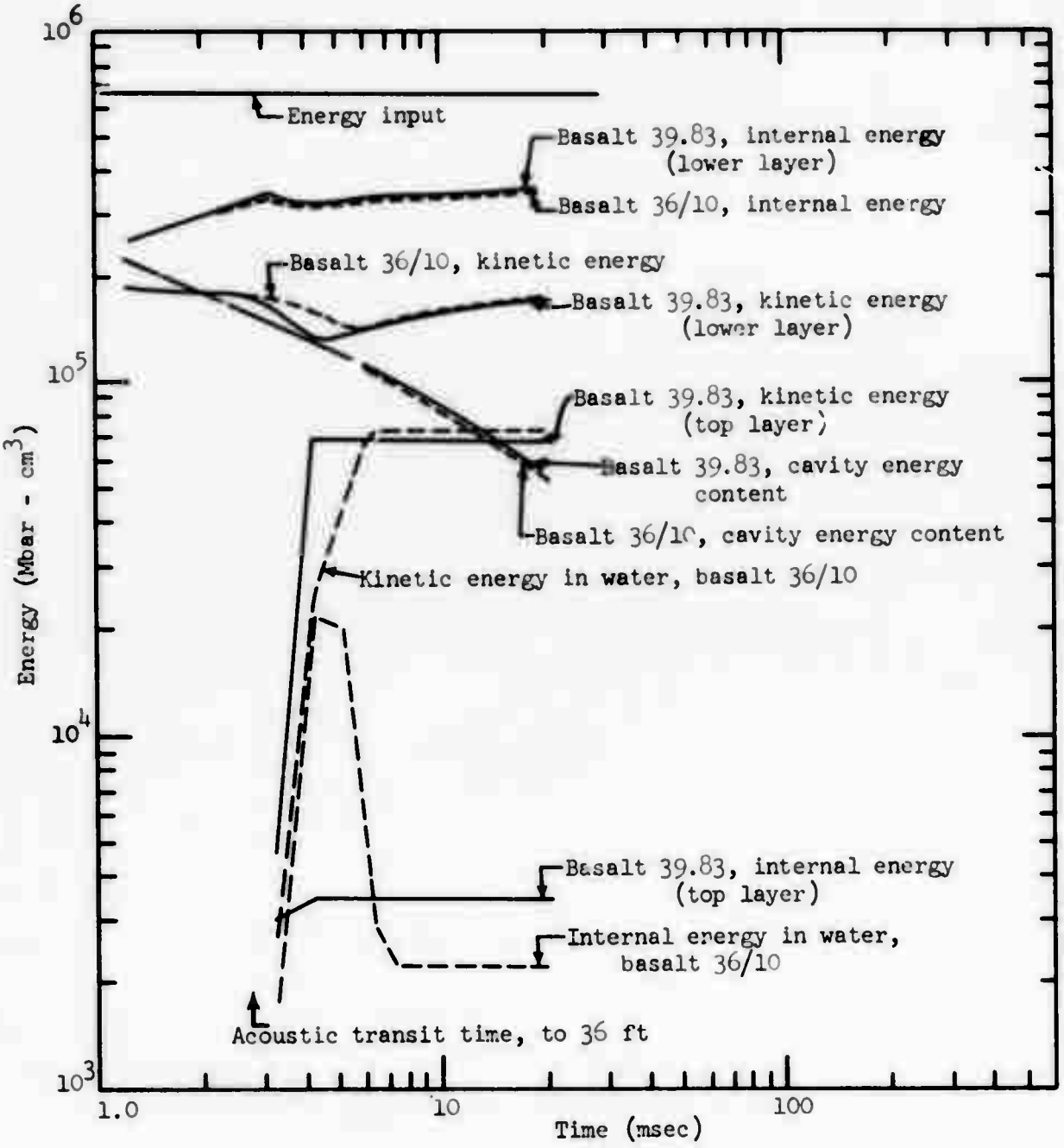

Figure 112. Kinetic, internal, and cavity energy; basalt underwater (basalt 36/10), and comparable basalt calculation with the same amount of overburden (no water).

(underwater or equivalent overburden events). Coral kinetic energies in the lower region or rock layer are shown in Figure 111a. This kinetic energy plot clearly reveals the overall differences in relative mound velocities for the various events. Kinetic energies for the underwater events immediately deviate above the equivalent overburden calculations when reflection occurs at the rock-water interface, and remain appreciably higher at late times. The discrepancy is greatest for the "deep" layer events. The coral 36/10 curve lies somewhat above and almost parallel to coral 41.31, while coral 36/36 lies far above coral 55.11. The relative loss of kinetic energy to the lower 36 ft region is very much less between coral 36/10 and coral 36/36 than between coral 41.31 and coral 55.11. The addition of a thick water overburden layer therefore has less effect on the lower problem region than the addition of an equivalent depth of rock overburden. It is significant to note that the coral 36/36 rock mound kinetic energy is actually much closer to the near-optimum coral 41.31 and 36/10 events than to the "deep" equivalent overburden analog (coral 55.11). The great importance of the interface spall reflection and lower layer spall velocities is quite evident here, particularly for the "deep" water layer event.

Kinetic energies in the upper region or water layer for the "coral" calculations are displayed in Figure 111b. The upper section may be thought of as a high-velocity spallation layer, most of which enters freefall upon return of the free surface reflection. In this case, the discrepancies between underwater and equivalent overburden events are less evident than in Figure 111a. The "water layer" kinetic energies rise more gradually and achieve the "free-fall" (constant) value later than the equivalent overburden events because of the greater thickness and lower transmission velocity of the water layer. The final kinetic energies are slightly higher for the underwater events, a fact which may be partly attributed to the zero strength, low internal energy content, and efficient shock transmission of the fluid material.

Energy curves for basalt 36/10 and basalt 39.83 are plotted in Figure 112. In this case, the kinetic, internal, and cavity energies are all shown. Kinetic energy in the lower layer is slightly greater for the underwater event "36/10"

than for "39.83", although the discrepancy is much less than for coral. The internal energy in the lower layer is slightly smaller for basalt 36/10, again indicating more efficient conversion to kinetic energy and better material ejection in the lower region for the underwater case. The basalt 36/10 water layer achieves freefall spallation later than the upper layer of basalt 39.83; its final kinetic energy is higher and the internal energy is lower, as expected for a fluid. The cavity energy content for basalt 36/10 drops below basalt 39.83 after the interface reflection impinges on the cavity, and remains lower at late times. Thus, transfer of cavity energy to rock is more efficient and the gas acceleration phase is stronger for basalt 36/10, as noted previously.

Late-time energy data abstracted from the equivalent overburden calculations are summarized in Tables 8 and 9 (see Chapter VII, with accompanying discussion). Comparing the appropriate pairs of calculations, we see that coral 41.31 places less kinetic energy in both "lower" and "upper" regions than coral 36/10 does in the corresponding rock and water layers (Table 8). Hence, the ratio of total KE/total energy is also less for coral 41.31. The kinetic energy partition fractions between lower and upper regions show that relatively more of the available kinetic energy goes into the upper region and less into the lower region for coral 41.31. Comparing coral 55.11 with coral 36/36, we find that the discrepancy between "lower layer" kinetic energies is still greater; the coral 55.11 "lower layer" energy is less than half of the coral 36/36 energy in the same region. However, the upper region or water layer kinetic energies in the two cases are about the same. The ratio of total KE/total energy is obviously smaller for coral 55.11 than for "36/36", and the partition fraction shows that much less of the available energy goes into the lower region and more into the upper region for coral 55.11. These observations verify and extend previously noted trends: The "equivalent overburden" coral calculations give less kinetic energy in the lower region (equivalent to the rock layer) and less total mound kinetic

energy than the corresponding underwater events. Relatively more of the available energy is partitioned into the upper region. Discrepancies are worst for "deep" layer events (i.e., a thick water or overburden layer comprising a significant portion of the entire problem). The "equivalent overburden" events thus simulate detonations at a relatively deeper scaled burial depth; the inefficiency of kinetic material ejection from these events will be further accentuated by additional rock fallback material from the "upper" rock region.

Kinetic energies for the basalt 36/10 and 39.83 calculations (Table 8) show the same similarity of behavior mentioned earlier. The late-time kinetic energies in the rock layer or lower layer are approximately equal, while the water (upper) layer energies and total energies are slightly greater for the underwater event. This similarity would probably break down for deeper overburden layers, and the underwater event would again be expected to attain relatively greater kinetic energies in the lower region.

The ratios of kinetic energy to internal energy (KE/IE) in the lower and upper regions are listed in Table 9. The KE/IE ratio of the lower or rock layer is less for coral 41.31 than for coral 36/10, and much less for coral 55.11 than for coral 36/36, again indicating inefficient material ejection in the "equivalent overburden" cases. Note that the ratio for coral 55.11 is less than half that for coral 36/36 or any of the other coral events, and is actually comparable with the "rock layer" ratio for the granite 36/36 event (low spall velocities, below optimum burial depth). This ratio is quite useful for defining the overall dynamic behavior of the mound, and particularly in determining the transition from efficient kinetic ejection (high KE/IE ratio), to predominant crushing and mounding of material (low KE/IE ratio). The lower layer KE/IE ratios for basalt 39.83 and basalt 36/10 are closely comparable. In the upper or water layer, KE/IE ratios are always smaller for the equivalent overburden events, although the discrepancy is least for the basalt calculations. The ratio is less meaningful in the freely-launched spall region, since all material has high ejection velocities and very low internal energy content.

In summary, significant dynamic differences do occur between two-layer underwater events and the equivalent overburden calculations. The differences are greatest for thick overburden layers. In most instances, the underwater event may be expected to be relatively more efficient for cratering. The discrepancies between two-layer and equivalent overburden configurations are not directly correlated with the degree of impedance mismatch at the interface, and material properties play an important role in defining multilayer interactions. Calculations are required to accurately assess overburden effects for each specific combination of media and layer depths. The easily-accomplished "SOC" vertical calculations are very useful for determining relative layer-depth effects and particularly for establishing "optimal" or "non-optimal" configurations in a medium of known properties.

XI. CONCLUSIONS

Hydrodynamic code calculations provide a viable and informative approach to the problems of shock propagation and material dynamics in underwater cratering. The effects of water overburden and layer depth on the overall mound motion may be defined by one-dimensional vertical calculations. Indeed, such calculations very accurately depict the entire time-dependent dynamics of the underlying rock layer throughout the period of interest for crater formation. High-velocity spall launch is the predominant material ejection mechanism near optimum burial depth in saturated media. The tensile waves reflected from the interface and free surface control material dynamics. Multiple reflection effects and detailed dynamics of the water layer have little influence on the rock. Thus, one-dimensional calculations are particularly appropriate for cratering events in an underwater environment. Likewise, peak shock parameters and safety-related effects in the water layer may be predicted on the basis of selected one-dimensional results in combination with an acoustic analysis. Two-dimensional code calculations are required to determine final crater dimensions, detailed particle dynamics within the water layer, and very late-time interactions for deeply-buried multilayer configurations.

In view of the progress achieved during this study, it is suggested that two-dimensional comparison calculations for one of the media and burial depth combinations used here might prove worthwhile. Understanding of the multilayer cratering process has been advanced, and the ability to perform underwater cratering design calculations for cohesive rock media is within reach.

REFERENCES

1. T. R. Butkovich, "Aids for Estimating Effects of Underground Nuclear Explosions," UCRL 50929, Revision 1, Lawrence Livermore Laboratory, Livermore, California, February 1973.

2. Sydney P. Clark, Jr., (ed), Handbook of Physical Constants, Revised Edition, Section 16 (G. C. Kennedy and W. T. Holser), pp. 371 ff; Geological Society of America Memoir 97, 1966.

3. B. K. Crowley, D. E. Burton, and J. B. Bryan, "Bearpaw Shale: Material Properties Derived from Experiment and One-Dimensional Studies," UCID 15915, Lawrence Livermore Laboratory, Livermore, Calif., September 1971.

4. E. Teller, W. Talley, G. Higgins, and G. Johnson, The Constructive Uses of Nuclear Explosives, McGraw-Hill Book Co., New York, 1968; pp. 227 ff.

5. R. L. LaFrenz, "Explosive Excavation for Water Environment and Road Cut Applications," MP-E-72-1, U. S. Army Engineer Waterways Experiment Station Explosive Excavation Research Laboratory, Livermore, Calif., June 1972.

6. S. M. Johnson, "Explosive Excavation Technology," Technical Report NCG-TR-21, U.S. Army Engineer Waterways Experiment Station Explosive Excavation Research Laboratory (formerly the Nuclear Cratering Group), Livermore, Calif., June 1971.

7. R. H. Gillespie and K. E. Sprague, "Cratering in an Underwater Environment," U.S. Army Engineer Waterways Experiment Station Explosive Excavation Research Laboratory, Livermore, Calif., 1972.

8. C. M. Snell and R. H. Gillespie, "Project Drum Inlet: Explosive Excavation in Saturated Sand," Technical Report E-73-5, U.S. Army Engineer Waterways Experiment Station Explosive Excavation Research Laboratory, Livermore, Calif., October 1973.

9. W. C. Day, et al., "Project Tugboat: Explosive Excavation of a Harbor in Coral," Technical Report E-72-23, U.S. Army Engineer Waterways Experiment Station Explosive Excavation Research Laboratory, Livermore, Calif., February 1972.

10. L. K. Davis and A. D. Rooke, "High-Explosive Cratering Experiments in Shallow Water," M P No. 1-946, U.S. Army Engineer Waterways Experiment Station, Vicksburg, Mississippi, December 1968.

11. J. N. Strange, "Effects of Explosions in Shallow Water," Final Report, Technical Memorandum No. 2-406, U.S. Army Engineer Waterways Experiment Station, Vicksburg, Mississippi, April 1955.

12. K. T. Sakai and R. F. Bourque, "Summary of Underwater Cratering Tests Conducted at Site 300 During 1970," Technical Memorandum EERO-TM-70-11, U.S. Army Engineer Waterways Experiment Station Explosive Excavation Research Laboratory, Livermore, Calif., August 1971.

13. E. H. Kleist and M. R. Florey, "Underwater Explosive Excavation Modeling Tests," Technical Memorandum EERO-TM-71-9, U.S. Army Engineer Waterways Experiment Station Explosive Excavation Research Laboratory, Livermore, Calif., January 1972.

14. J. T. Cherry and F. L. Petersen, "Numerical Simulation of Stress Wave Propagation from Underground Nuclear Explosions," American Nuclear Society, Symposium on Engineering with Nuclear Explosives, CONF 700101 (Vol. 1), Las Vegas, Nevada, 1970.

15. J. T. Cherry and F. L. Petersen, "SOC User's Manual," UCID 30012, Lawrence Livermore Laboratory, Livermore, Calif., May 1971.

16. J. T. Cherry, S. Sack, G. Maenchen, and V. J. Kransky, "Two-Dimensional Stress-Induced Adiabatic Flow," UCRL 50987, Lawrence Livermore Laboratory, Livermore, Calif., December 1970.

17. R. W. Terhune, T. F. Stubbs, and J. T. Cherry, "Nuclear Cratering on a Digital Computer," UCRL 50898, Lawrence Livermore Laboratory, Livermore, Calif., July 1970.

18. D. E. Burton and J. B. Bryan, "Applications of Numerical Modeling Techniques to Problems in Explosive Excavation Engineering," UCID 16148, Lawrence Livermore Laboratory, Livermore, Calif., November 1972.

19. D. E. Burton, C. M. Snell, and J. B. Bryan, "Computer Design of High-Explosive Experiments to Simulate Subsurface Nuclear Detonations," UCRL 75190, Lawrence Livermore Laboratory, Livermore, Calif., 1973.

20. D. E. Burton and C. M. Snell, "User's Guide to TENPLT (Tensor Graphics Code)," MP-E-74-1, U.S. Army Engineer Waterways Experiment Station Explosive Excavation Research Laboratory, Livermore, Calif., March 1974.

21. W. E. Baker, P. S. Westine, and F. T. Dodge, Similarity Methods in Engineering Dynamics, Hayden Book Co., Inc., Rochelle Park, New Jersey, 1973.

22. J. W. White, "Some Observations Related to Modeling Explosive Cratering Phenomena," UCRL 51358, Lawrence Livermore Laboratory, Livermore, Calif., March 1973.

23. J. Chabai, "On Scaling Dimensions of Craters Produced by Buried Explosives," Journal of Geophysical Research, 70, p. 5075, 1965.

24. D. Burton, Lawrence Livermore Laboratory, Livermore, Calif.; private communication, September, 1973.

25. B. K. Crowley, "Effects of Porosity and Saturation on Shock-Wave Response in Tuffs," UCRL 74207 (preprint), Lawrence Livermore Laboratory, Livermore, Calif., September 1972; Prepared for Submission to Int. J. Rock Mech. Min. Sci..

26. C. M. Snell, "Estimating Water-Shock-Induced Airblast from Detonations in a Medium Overlain with Water," Technical Report E-7?-16, U.S. Army Engineer Waterways Experiment Station Explosive Excavation Research Laboratory, Livermore, California, April 1972.

27. H. F. Cooper, Jr., and J. B. Seamon, "A Geometric Technique for Studying Surface Motions from Underground Nuclear Explosions in Real Geologic Layered Media," AFWL-TR-66-123, Air Force Weapons Laboratory, Kirtland Air Force Base, New Mexico, January 1967.

28. R. H. Cole, Underwater Explosions, Dover Publications, Inc., New York, 1965 (reprint; 1948), pp. 47 ff.

29. E. L. Lee, H. C. Hornig, and J. W. Kury, "Adiabatic Expansion of High Explosive Detonation Products," UCRL 50422, Lawrence Livermore Laboratory, Livermore, Calif., May 1968.

30. J. B. Bryan, Lawrence Livermore Laboratory, Livermore, Calif.; private communication, October 1973.

31. Sydney P. Clark, Jr., (ed), Handbook of Physical Constants, Revised Edition, Geological Society of America Memoir 97, 1966.

32. W. E. Sharp, "The Thermodynamic Functions for Water in the Range -10 to 1000°C and 1 to 250,000 Bars," UCRL 7118, Lawrence Livermore Laboratory, Livermore, Calif., October 1962.

33. M. H. Rice and J. M. Walsh, J. Chem. Phys., 26, 824, 1957.

34. R. A. Papetti and M. Fujisaki, J. App. Phys., 39, 5412, 1968.

35. C. W. F. T. Pistorius and W. E. Sharp, Am. J. Sci., 258, 757, 1960.

36. D. R. Stephens, "Thermodynamic Data for Water," Lawrence Livermore Laboratory, Livermore, Calif., June 1969.

37. R. C. Schroeder and W. H. McMaster, "Shock-Compression Freezing and Melting of Water and Ice," UCRL 74253, Lawrence Livermore Laboratory, Livermore, Calif., October 1972.

38. C. E. Chapin, "Estimates of the Thermodynamic Properties of Water for Temperatures from 1000 to 6000°C and Pressures from 10 to 250,000 Bars," Lawrence Livermore Laboratory, Livermore, Calif., August 1969.

39. T. R. Butkovich, "A Technique for Generating Pressure-Volume Relationships and Failure Envelopes for Rocks," UCRL 51441, Lawrence Livermore Laboratory, Livermore, Calif., November 1973.

40. D. R. Stephens and H. C. Heard, "High-Pressure Mechanical Properties of Tugboat Coral," CDTN 71-39, Chemistry Department, Lawrence Livermore Laboratory, Livermore, Calif., May 1971.

41. L. J. Vortman, "Airblast from Project Tugboat Detonations," SC-RR-70-541, Sandia Laboratories, Albuquerque, New Mexico, 1970.

42. J. Lattery, Explosive Excavation Research Laboratory, Livermore, Calif.; private communication, September 1973.

43. C. F. Petersen, "Hugoniot Shock Testing of Rock Samples from Proposed Route 17, Atlantic-Pacific Interoceanic Canal Studies," Technical Report #1, U.S. Army Engineer District, Jacksonville, Florida, February 1969.

44. E. Chamberlain and G. Dante, "Solid-Cell P-V Tests; Interoceanic Canal Studies, Routes 17 and 25," U.S. Army Engineer District, Jacksonville, Florida, 1969.

45. D. R. Stephens, "P-V Curves for Cracked and Consolidated Pre-Gondola Mudstone and Greeley Tuff," Memorandum PMD-226, Lawrence Livermore Laboratory, Livermore, Calif., September 1966.

46. P. Turner, Lawrence Livermore Laboratory, Livermore, Calif.; private communication, September 1973.

47. D. R. Stephens and E. M. Lilley, "Loading-Unloading Pressure-Volume Curves for Rocks," American Nuclear Society, Symposium on Engineering with Nuclear Explosives, CONF-700101 (Vol. 1), Las Vegas, Nevada, 1970.

48. H. C. Heard, "The Influence of Environment on the Inelastic Behavior of Rocks," ANS Symposium, CONF 700101 (Vol. 1), 1970.

49. T. R. Butkovich, J. Geophys. Res., 70, p. 885, 1965

50. Atlantic-Pacific Interoceanic Canal Study Commission, "Summary of Geology and Rock Physical Properties, Route 25," IOCS Memorandum NCG-33, NCG-203-25, U.S. Army Engineer Nuclear Cratering Group, Livermore, Calif., October 1969.

51. Atlantic-Pacific Interoceanic Canal Study Commission, "Summary of Geology and Rock Physical Properties, Route 17," IOCS Memorandum NCG-31, NCG-203-17, U.S. Army Engineer Nuclear Cratering Group, Livermore, Calif., September 1969.

52. O. Brovont, Lawrence Livermore Laboratory, Livermore, Calif.; private communication, August 1973.

53. T. R. Butkovich, Lawrence Livermore Laboratory, Livermore, Calif.; private communication, August 1973.

54. R. N. Schock and H. C. Heard, "Static Mechanical Properties and Shock-Loading Response in Granite," UCRL 74708, Lawrence Livermore Laboratory, Livermore, Calif., April 1973.

55. V. E. Wheeler and R. G. Preston, "Scaled Free-field Particle Motions from Underground Nuclear Explosions," UCRL 50563, Lawrence Livermore Laboratory, Livermore, Calif., August 1968.

56. V. J. Cushing, "On the Theory of Bulk Cavitation," Contract Nonr-3709(00), Office of Naval Research; Engineering Physics Company, 12721 Twinbrook Parkway, Rockville, Maryland, December 1969.

57. C. M. Snell and D. L. Oltmans, "Prediction of Ground-Shock-Induced Airblast Overpressures for Subsurface Explosions from Peak Vertical Spall Velocity," EERO-TR-40, U.S. Army Engineer Waterways Experiment Station, Explosive Excavation Research Laboratory, Livermore, Calif., November 1971.

58. T. R. Butkovich, "Studies on the Propagation of Stress Waves Through Layered Media," UCON 73-9, K-Division Memorandum, Lawrence Livermore Laboratory, Livermore, Calif., February 1973.

Appendix A

Peak Velocities, Pressures, and Stresses

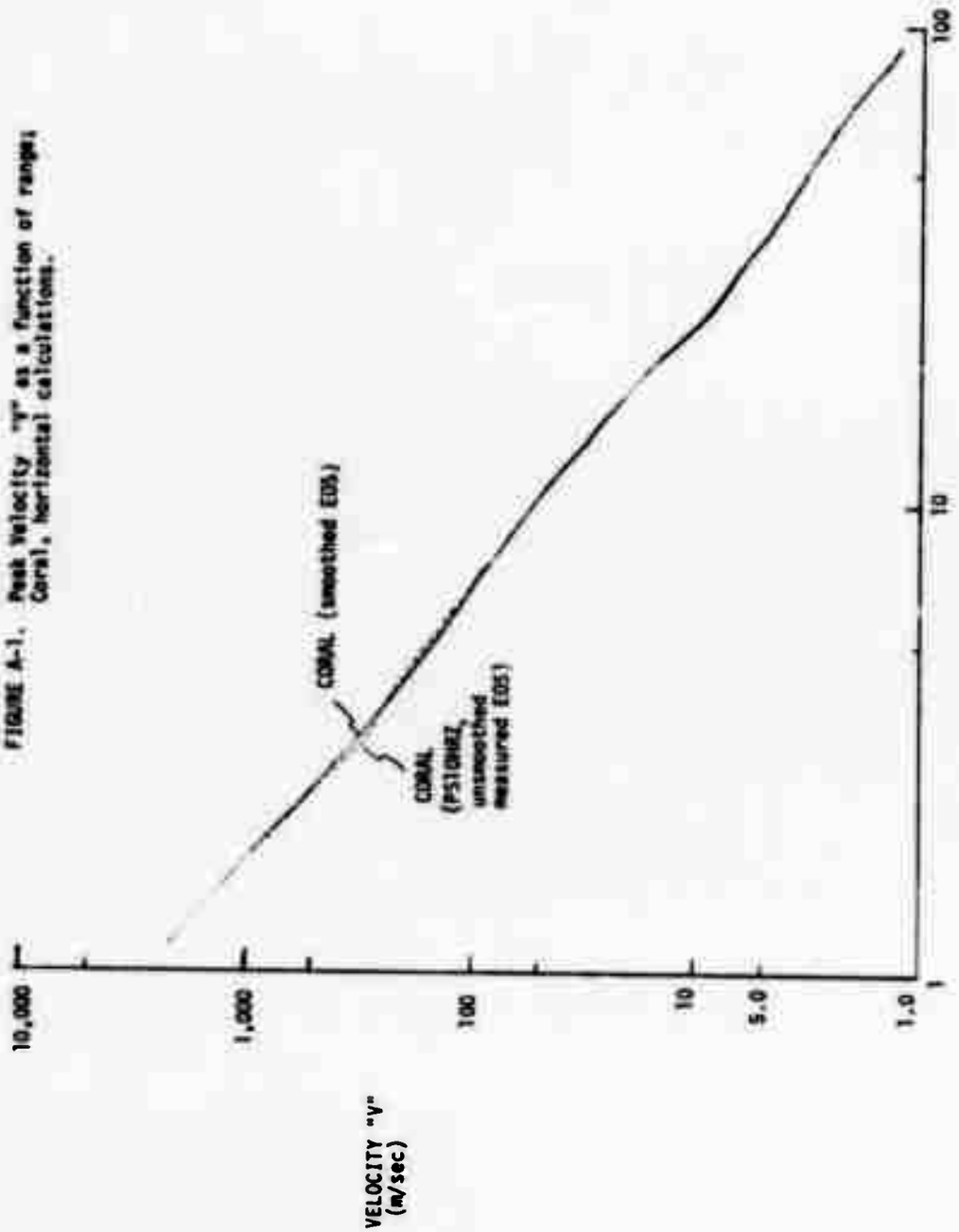

FIGURE A-1. Peak Velocity "v" as a function of range; Coral, horizontal calculations.

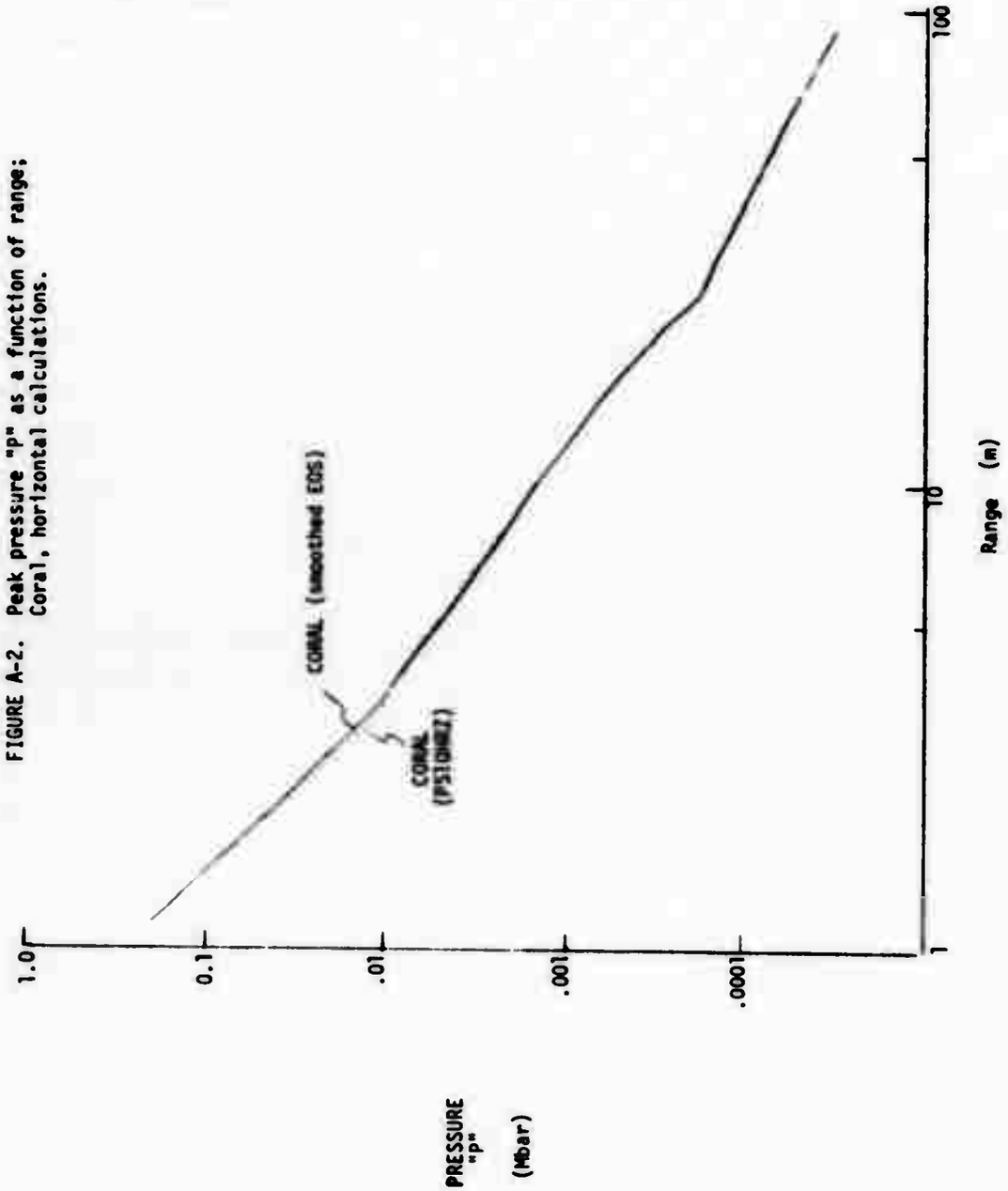

FIGURE A-2. Peak pressure "p" as a function of range: Coral, horizontal calculations.

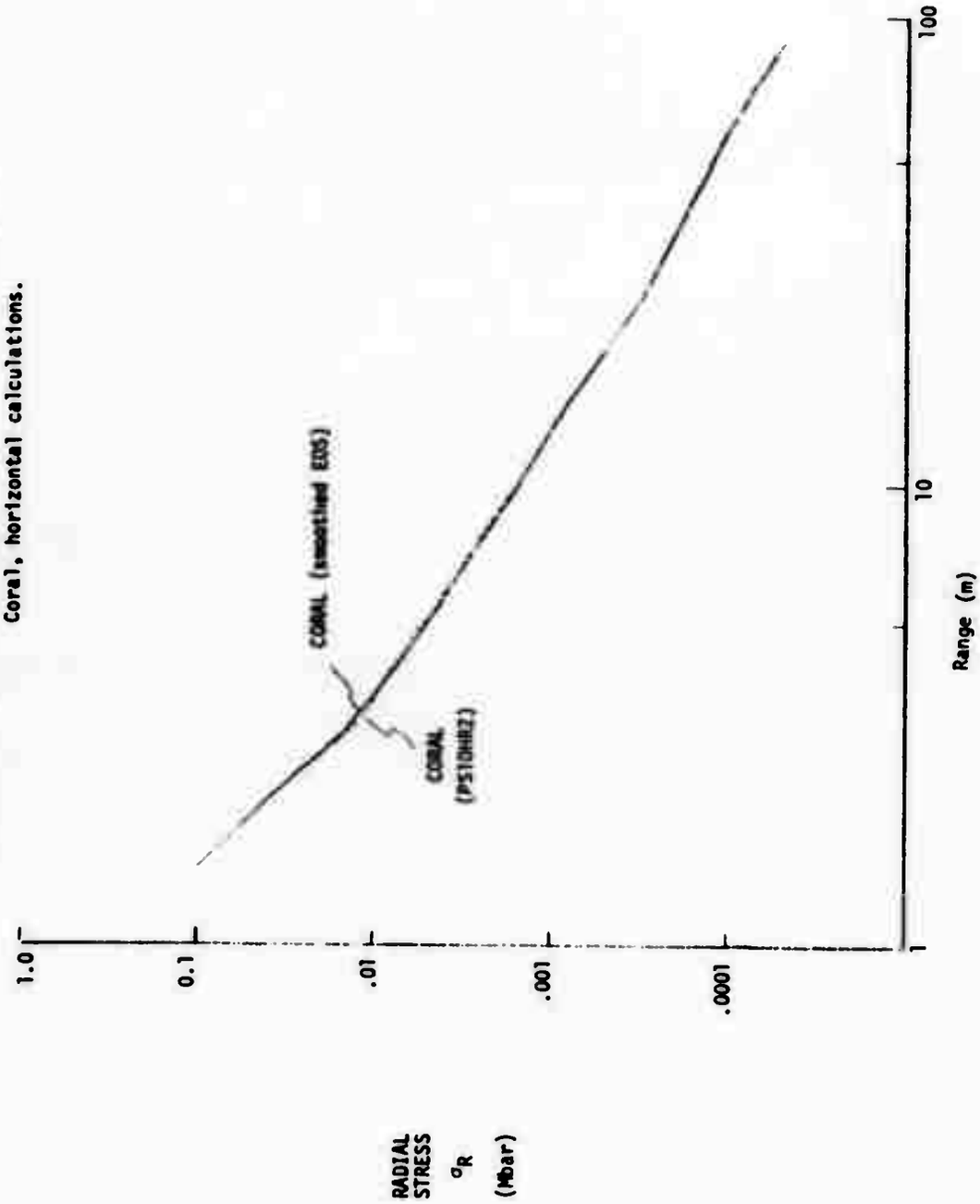

FIGURE A-3. Peak radial stress "σ_R" as a function of range: Coral, horizontal calculations.

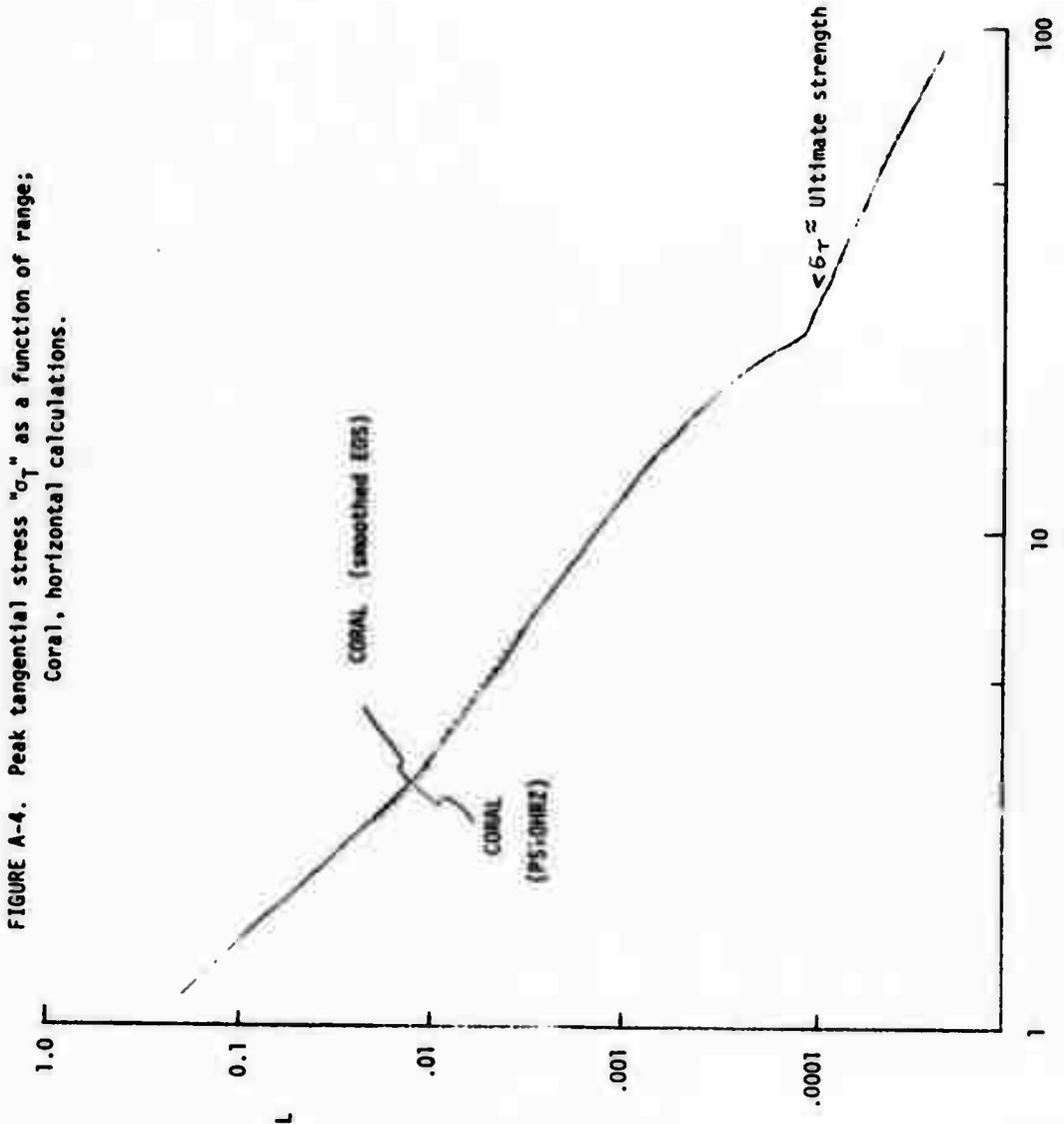

FIGURE A-4. Peak tangential stress "σ_T" as a function of range; Coral, horizontal calculations.

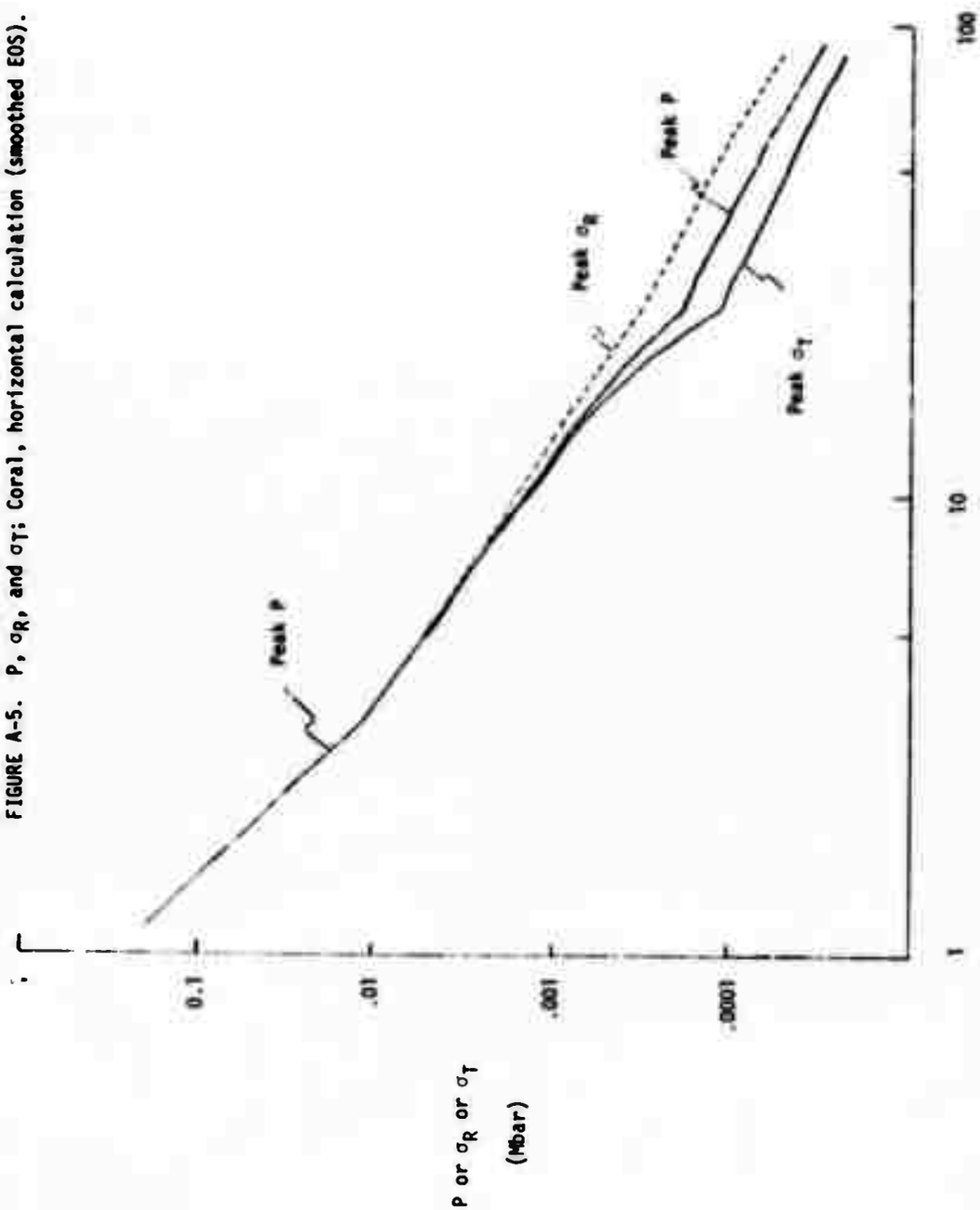

FIGURE A-5. P, σ_R, and σ_T; Coral, horizontal calculation (smoothed EOS).

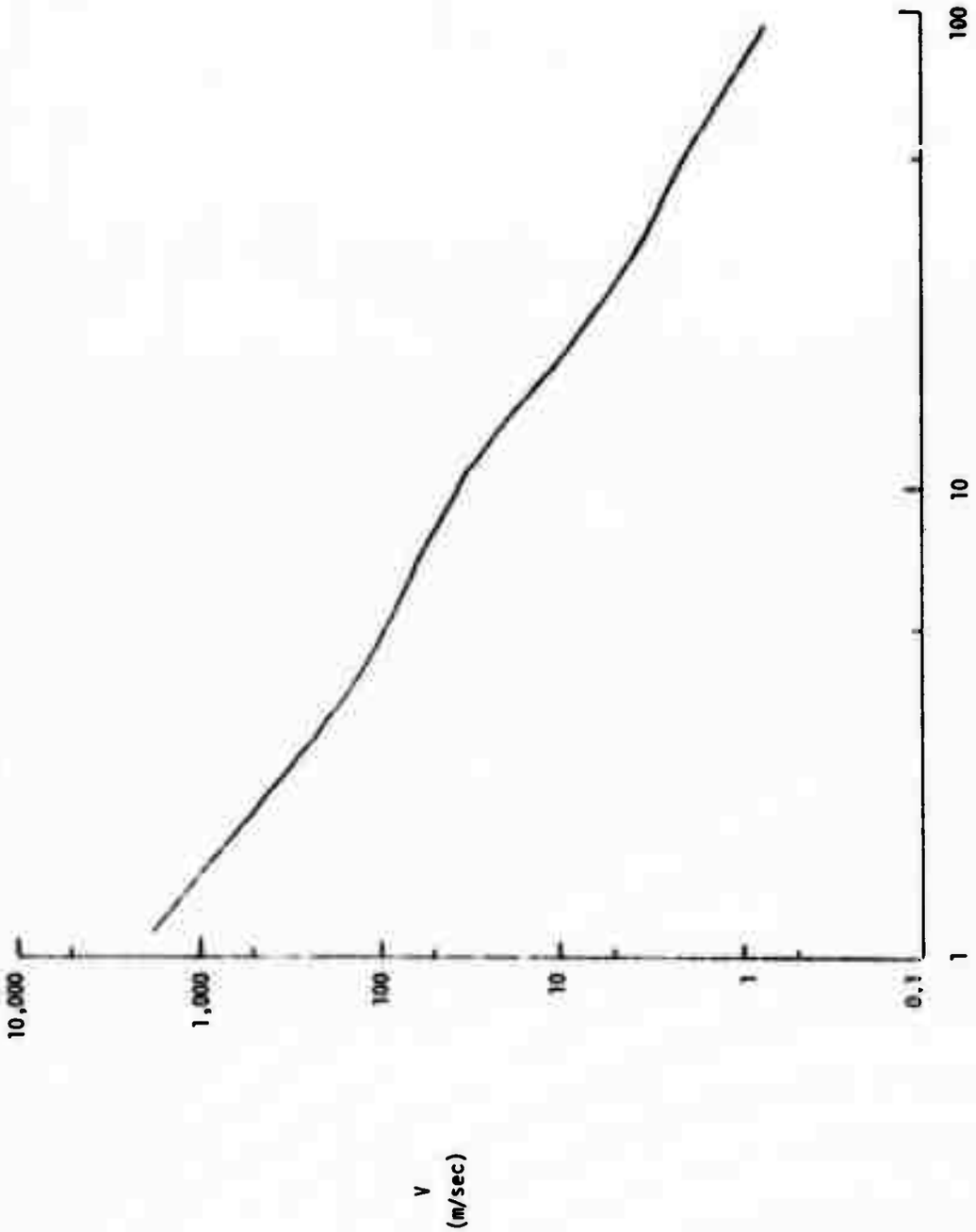

FIGURE A-6. V; basalt, horizontal calculation.

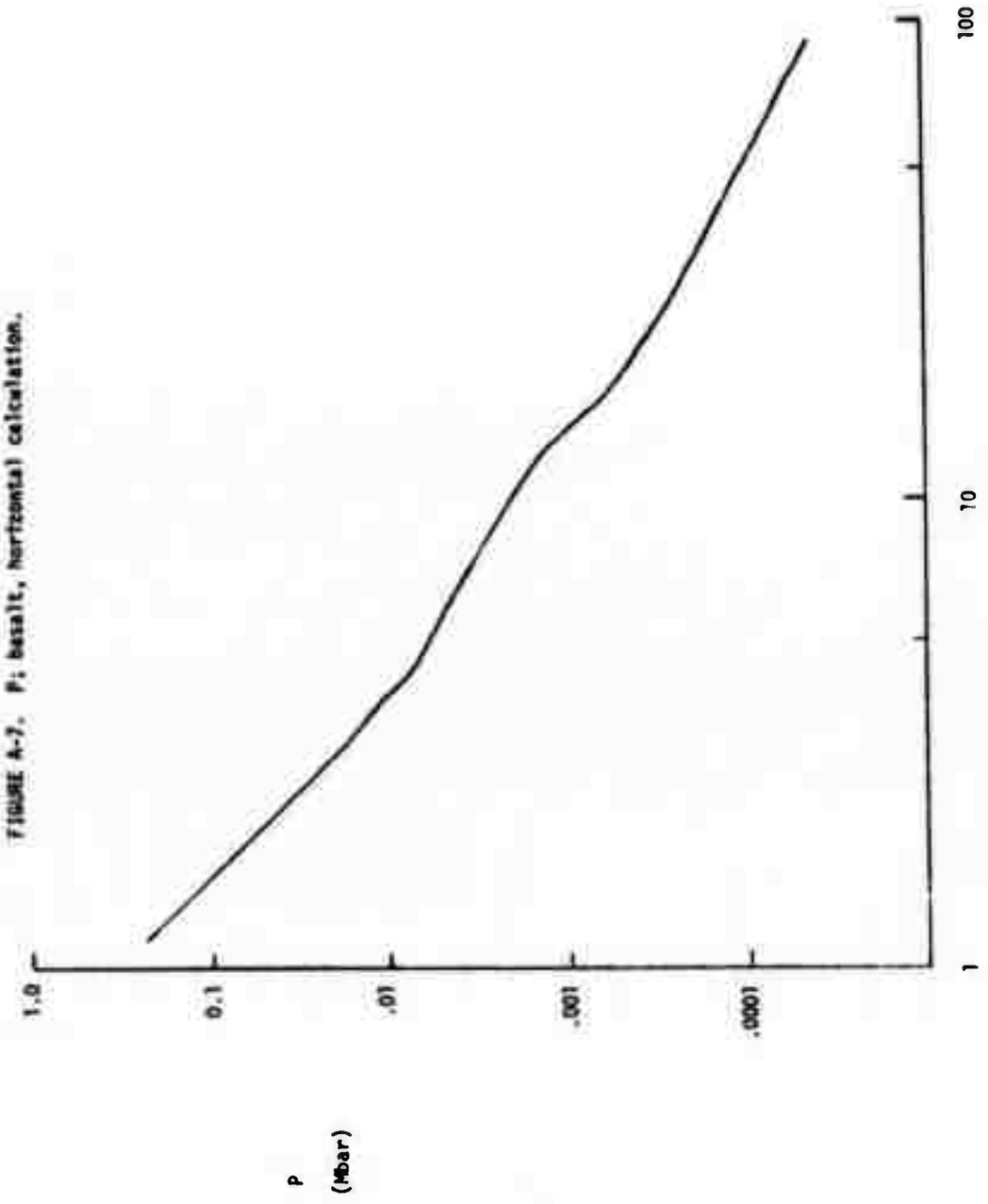

FIGURE A-7. P; basalt, horizontal calculation.

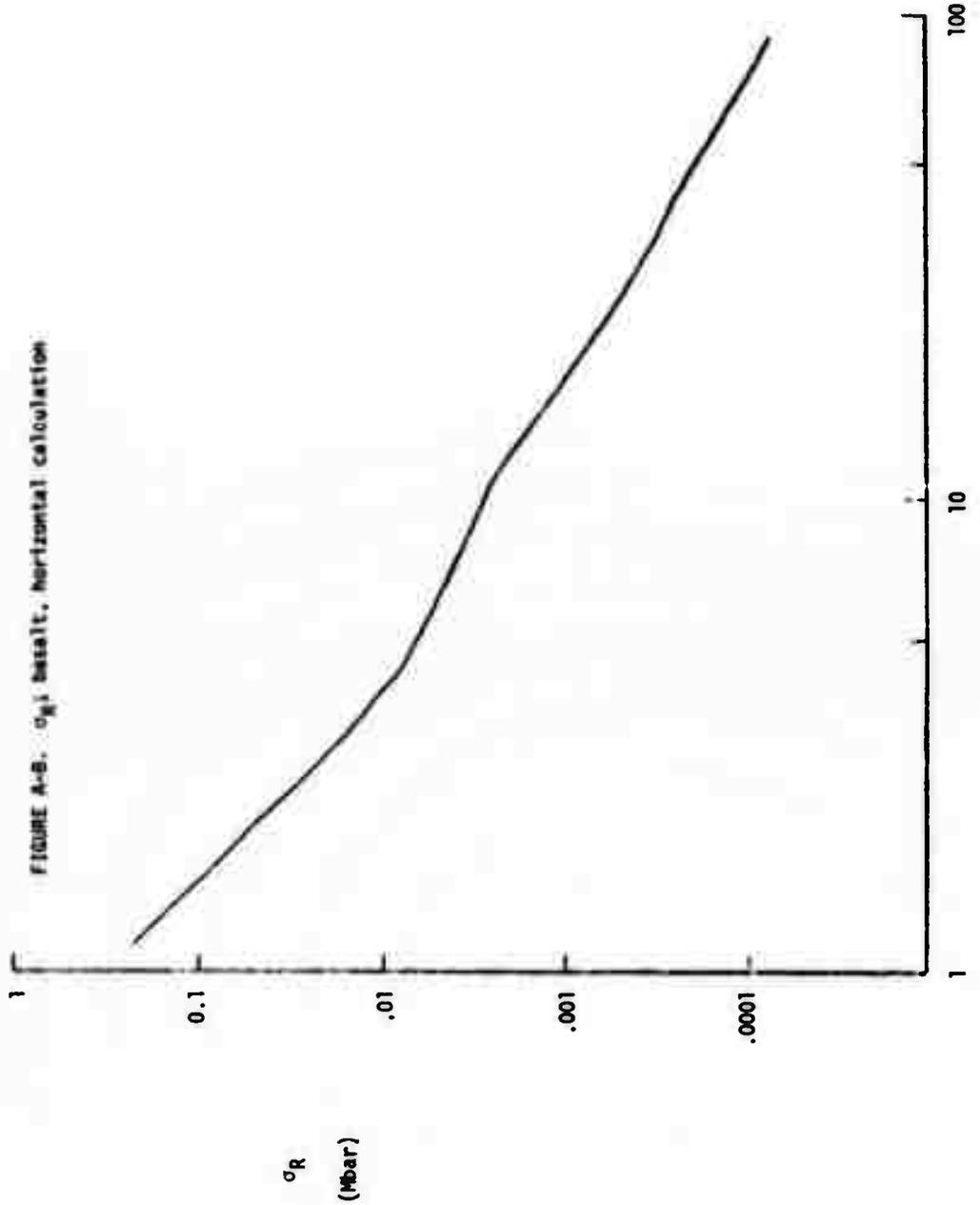

FIGURE A-8. σ_R, Basalt, Horizontal calculation

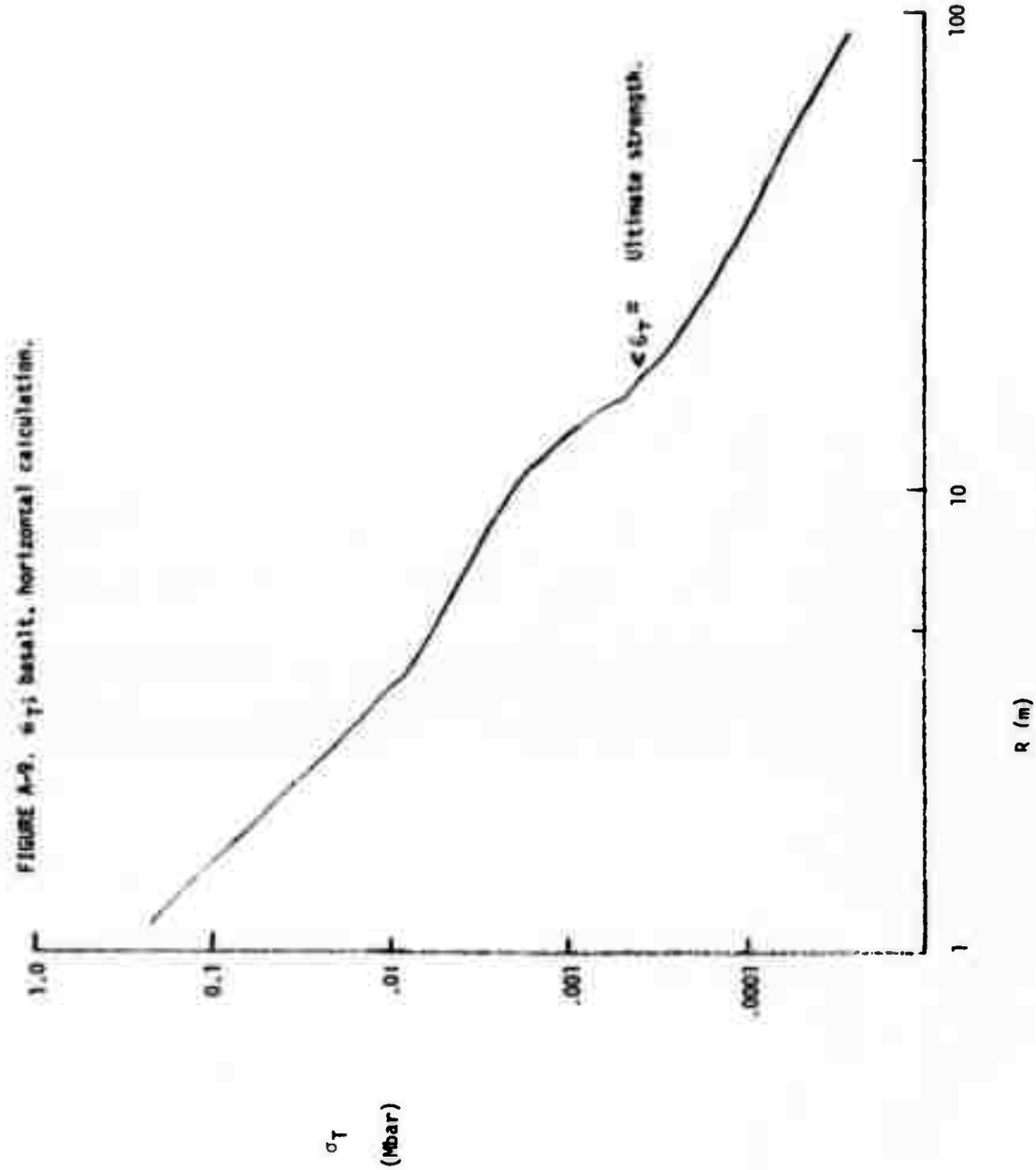

FIGURE A-9. σ_T; basalt, horizontal calculation.

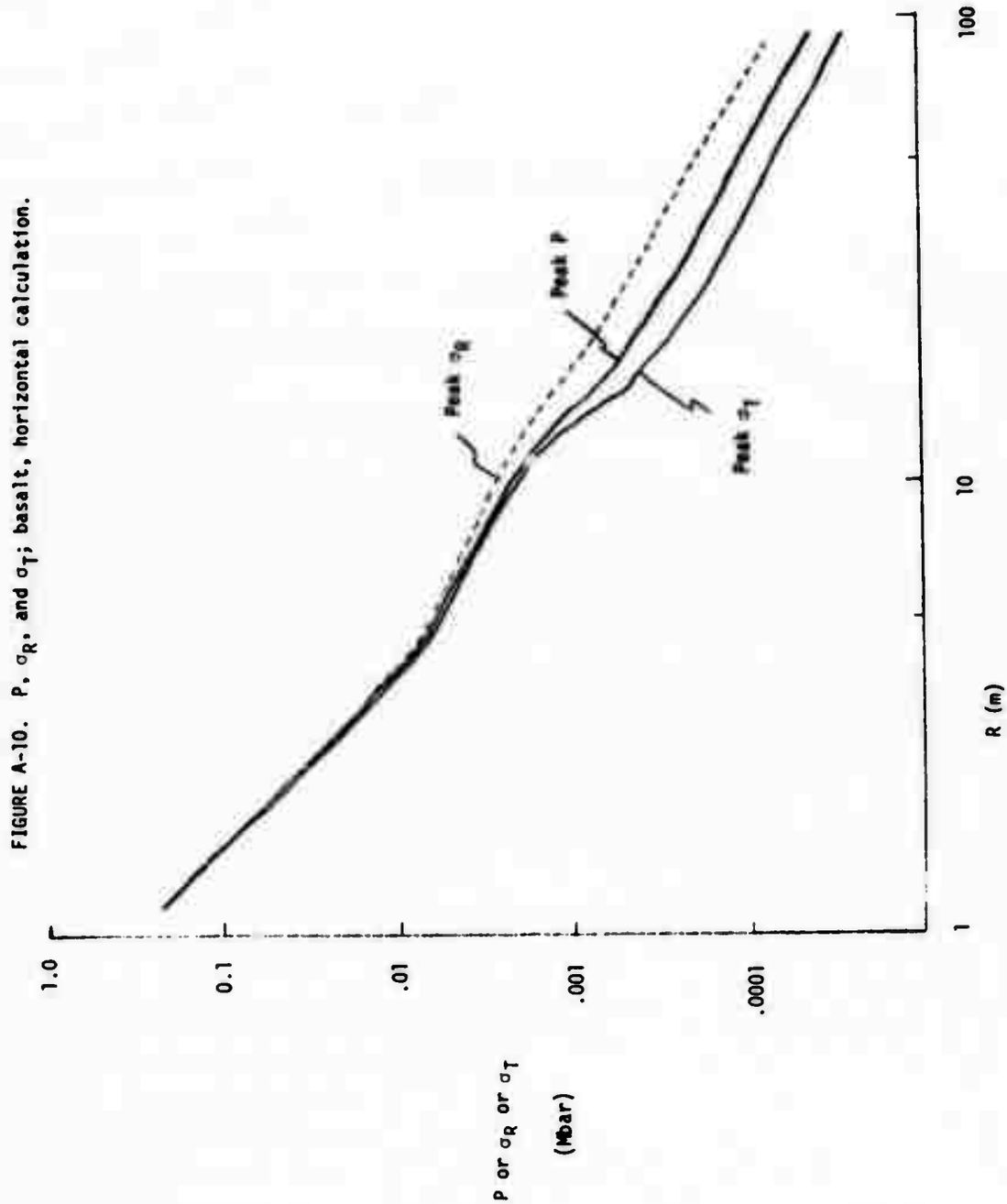

FIGURE A-10. P, σ_R, and σ_T; basalt, horizontal calculation.

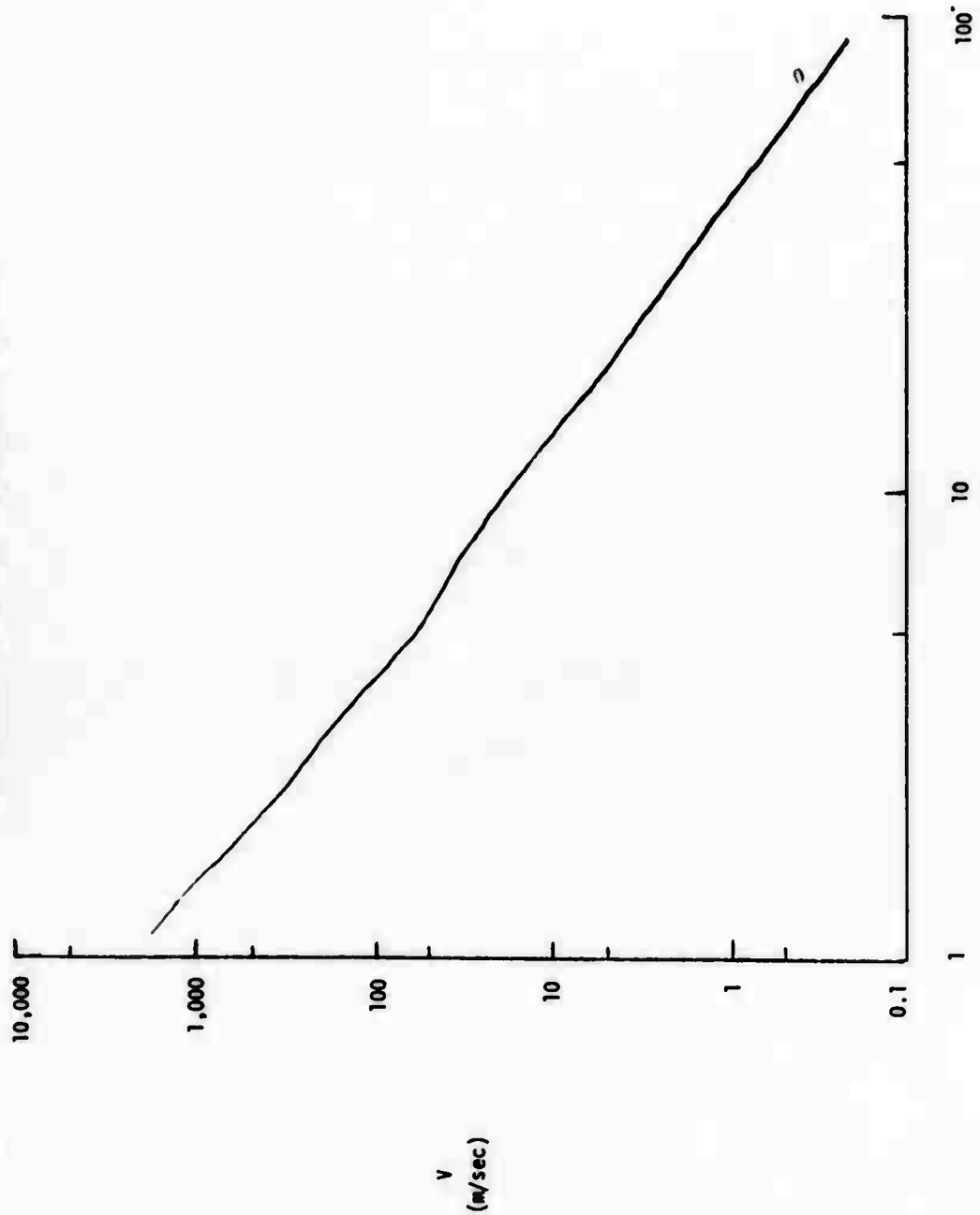

FIGURE A-11. V; granite, horizontal calculation.

FIGURE A-12. P; granite, horizontal calculation.

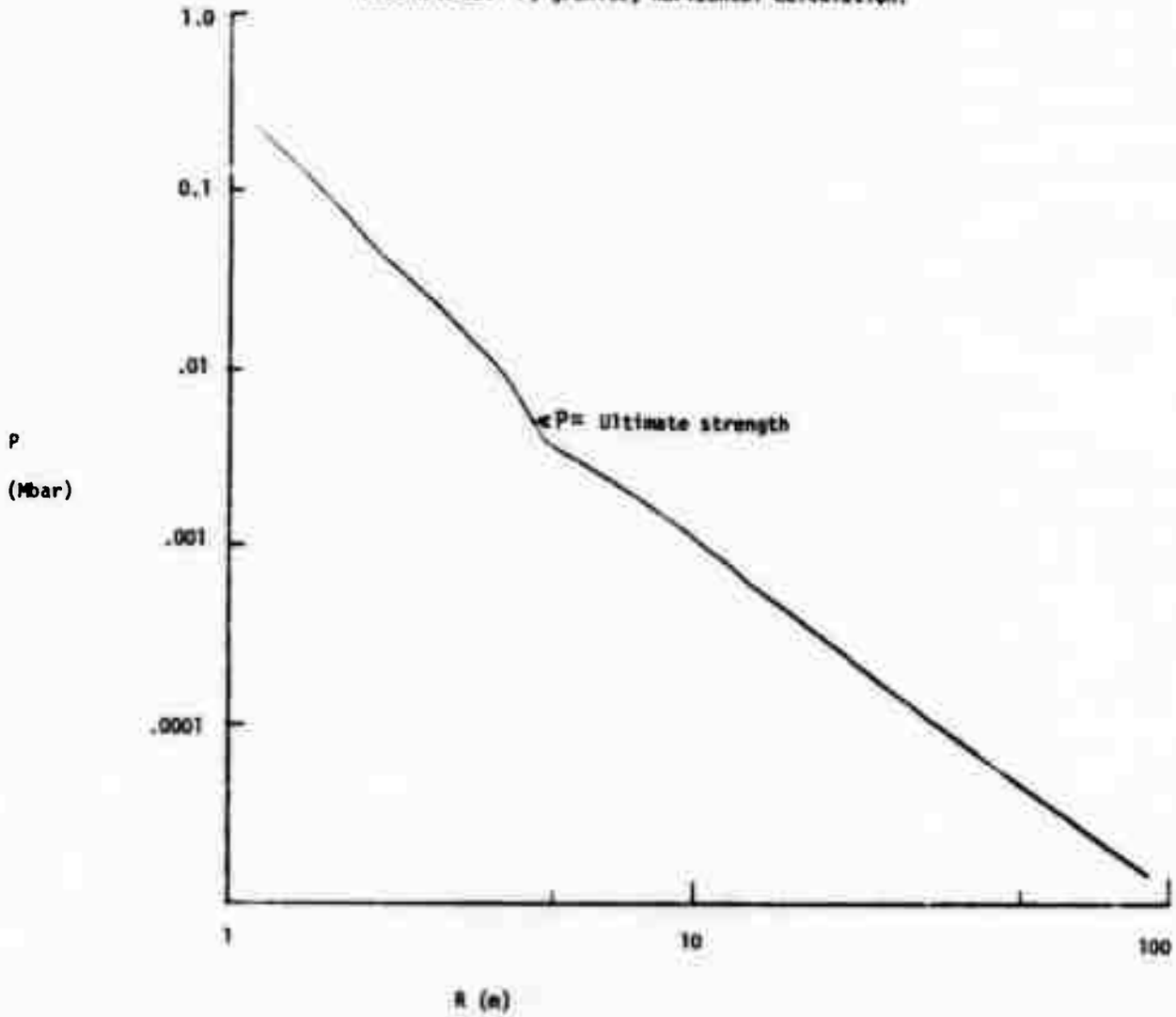

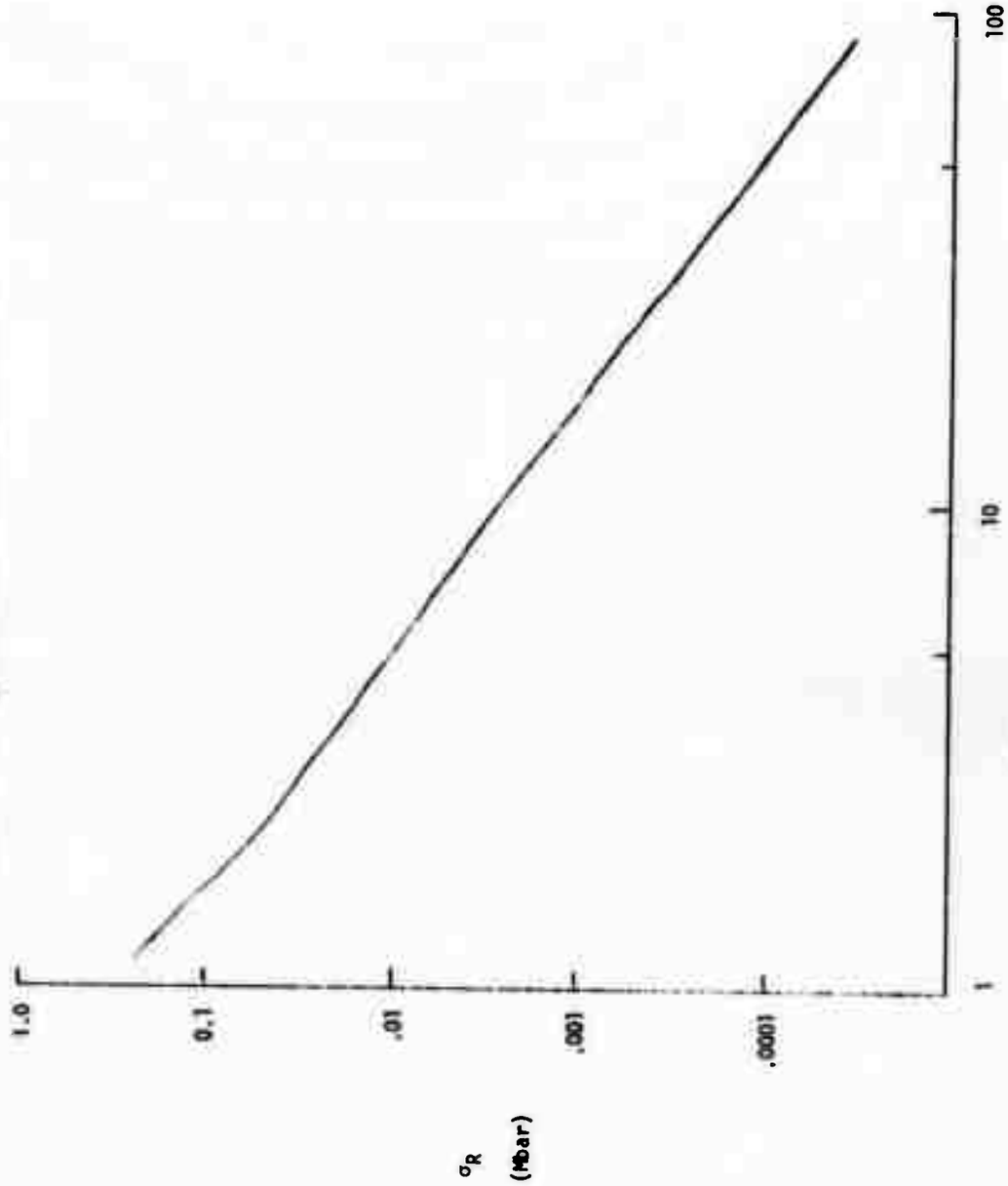

FIGURE A-13. σ_R; granite, horizontal calculation.

FIGURE A-14. σ_T; granite, horizontal calculation.

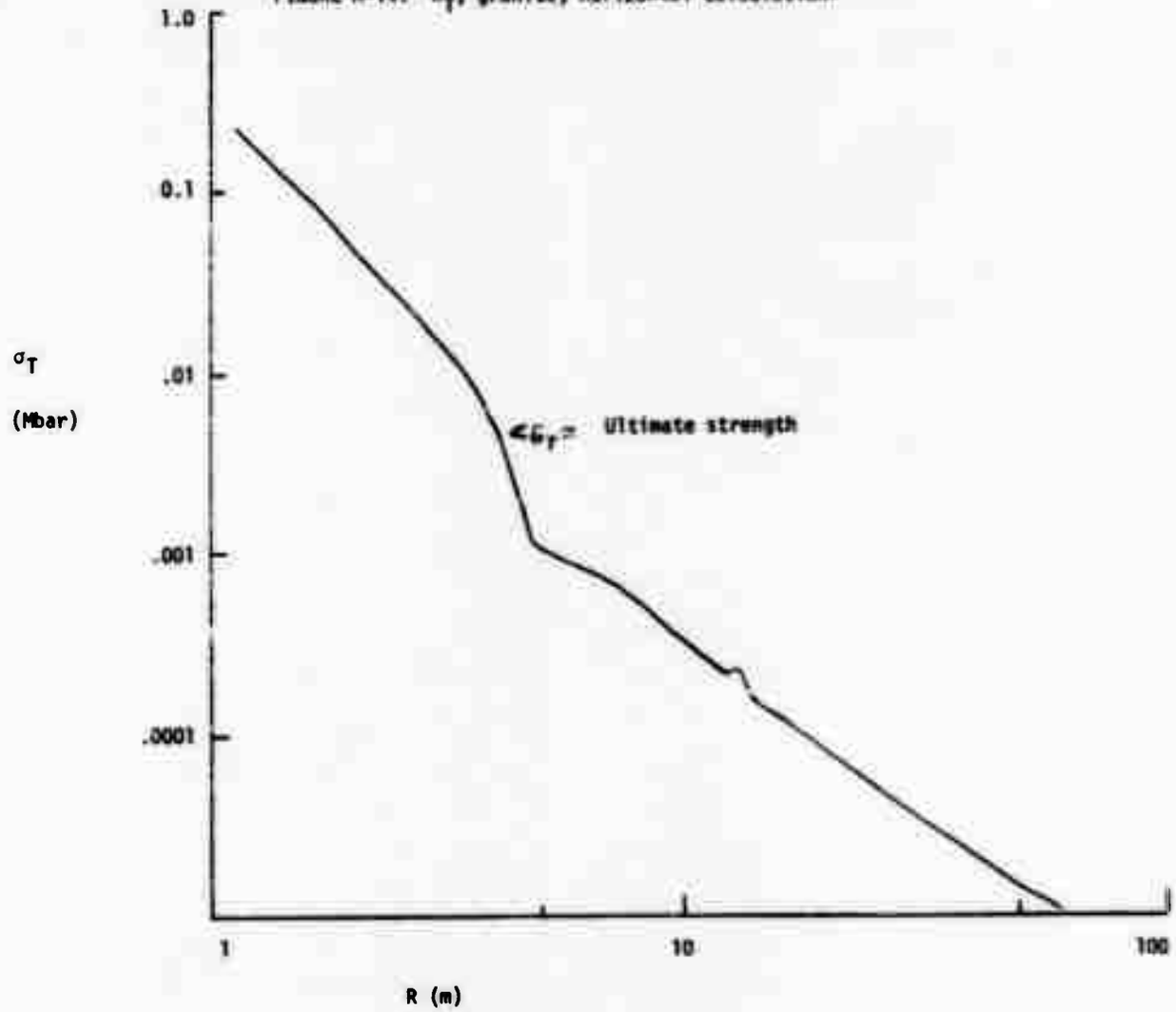

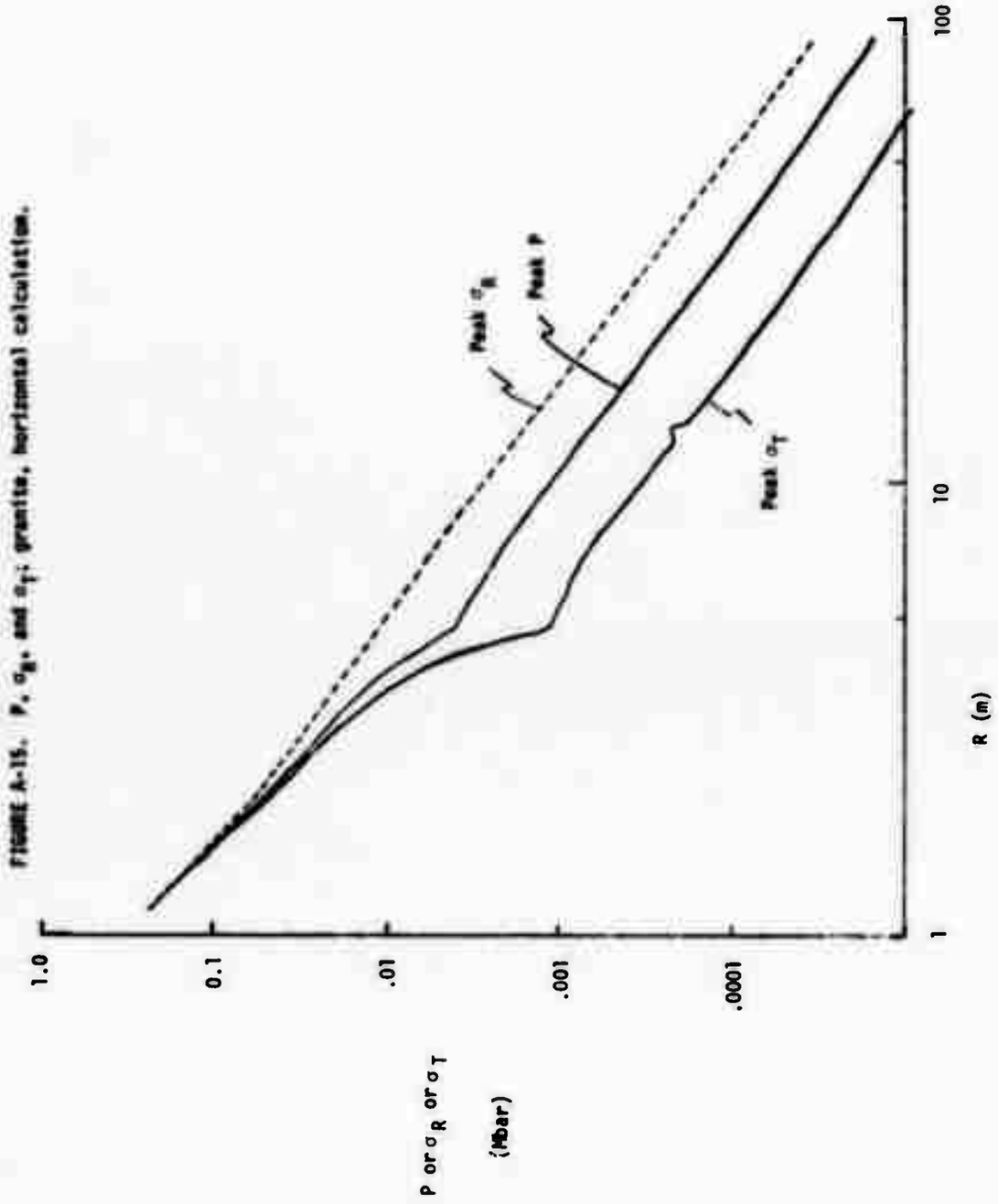

FIGURE A-15. P, σ_R, and σ_T; granite, horizontal calculation.

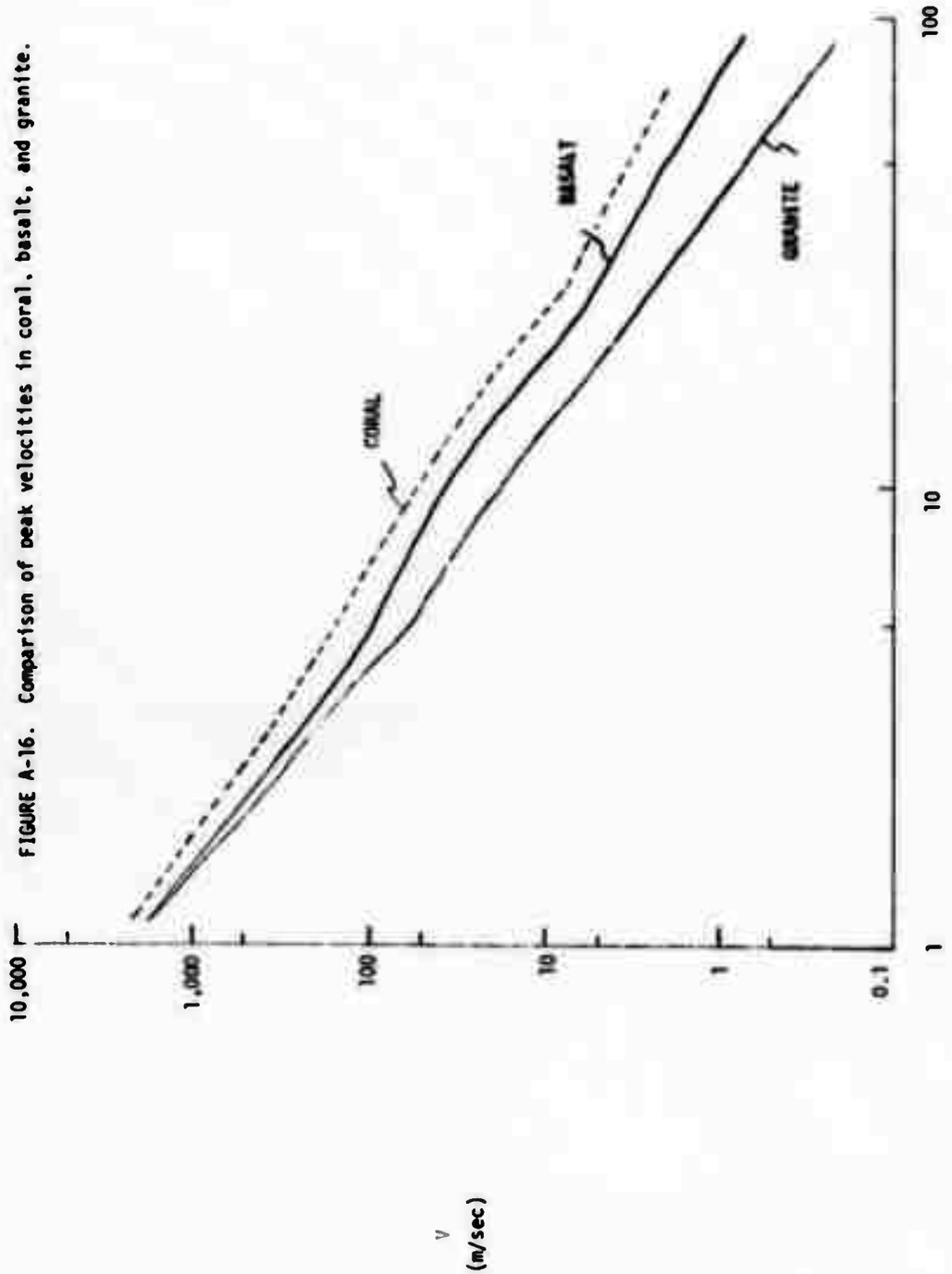

FIGURE A-16. Comparison of peak velocities in coral, basalt, and granite.

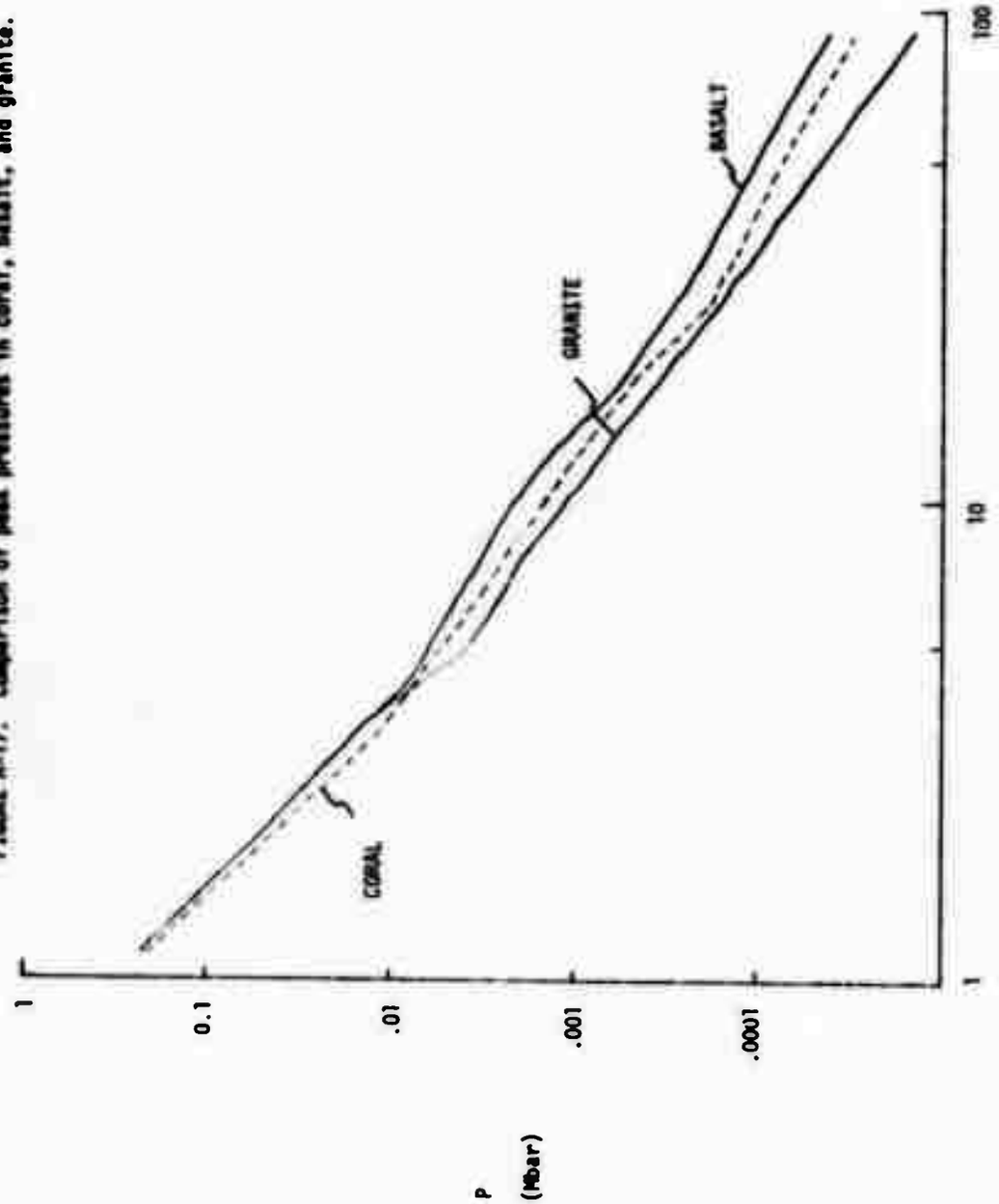

FIGURE A-17. Comparison of peak pressures in coral, basalt, and granite.

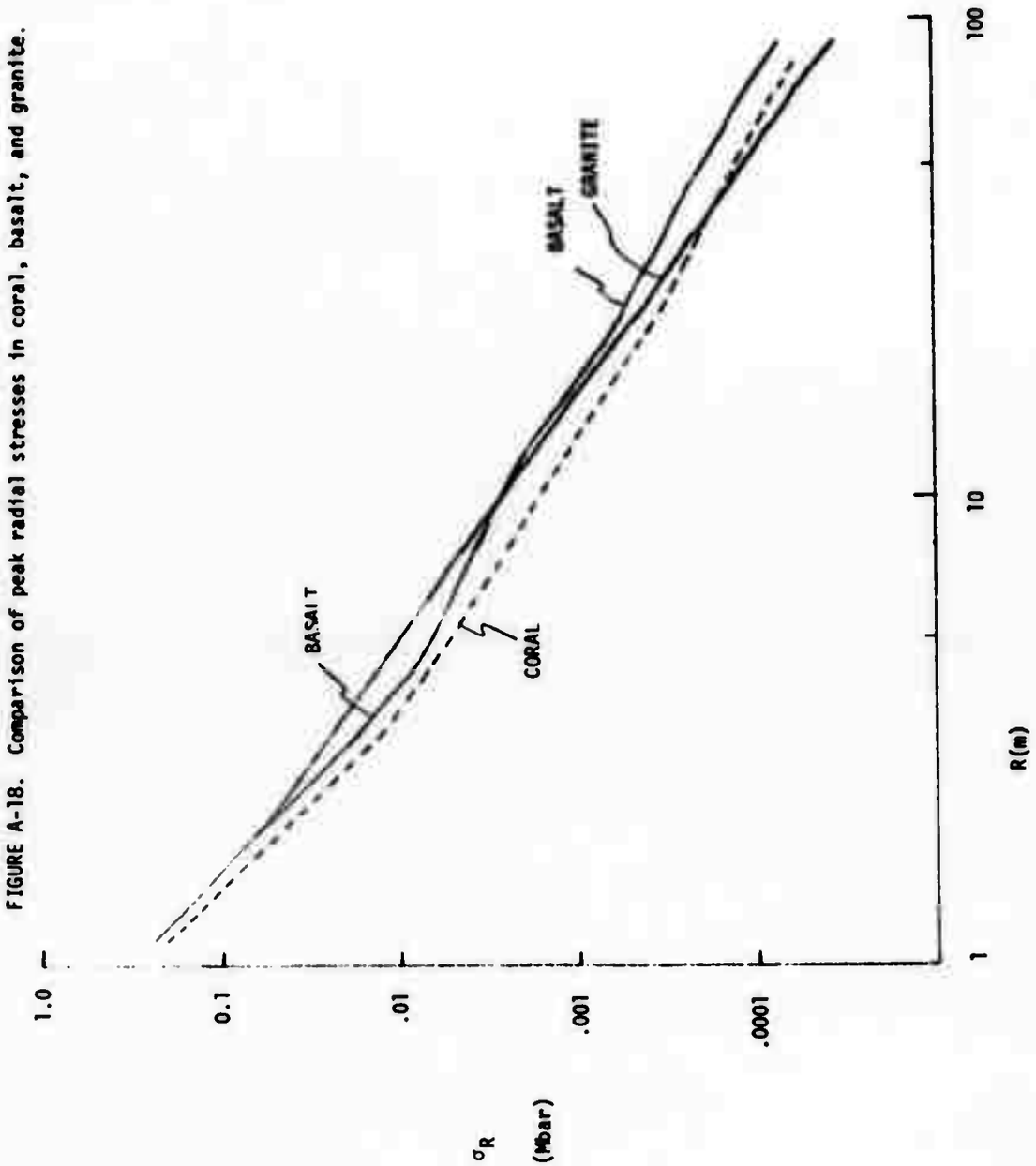

FIGURE A-18. Comparison of peak radial stresses in coral, basalt, and granite.

FIGURE A-19. Comparison of peak tangential stresses in coral, basalt, and granite.

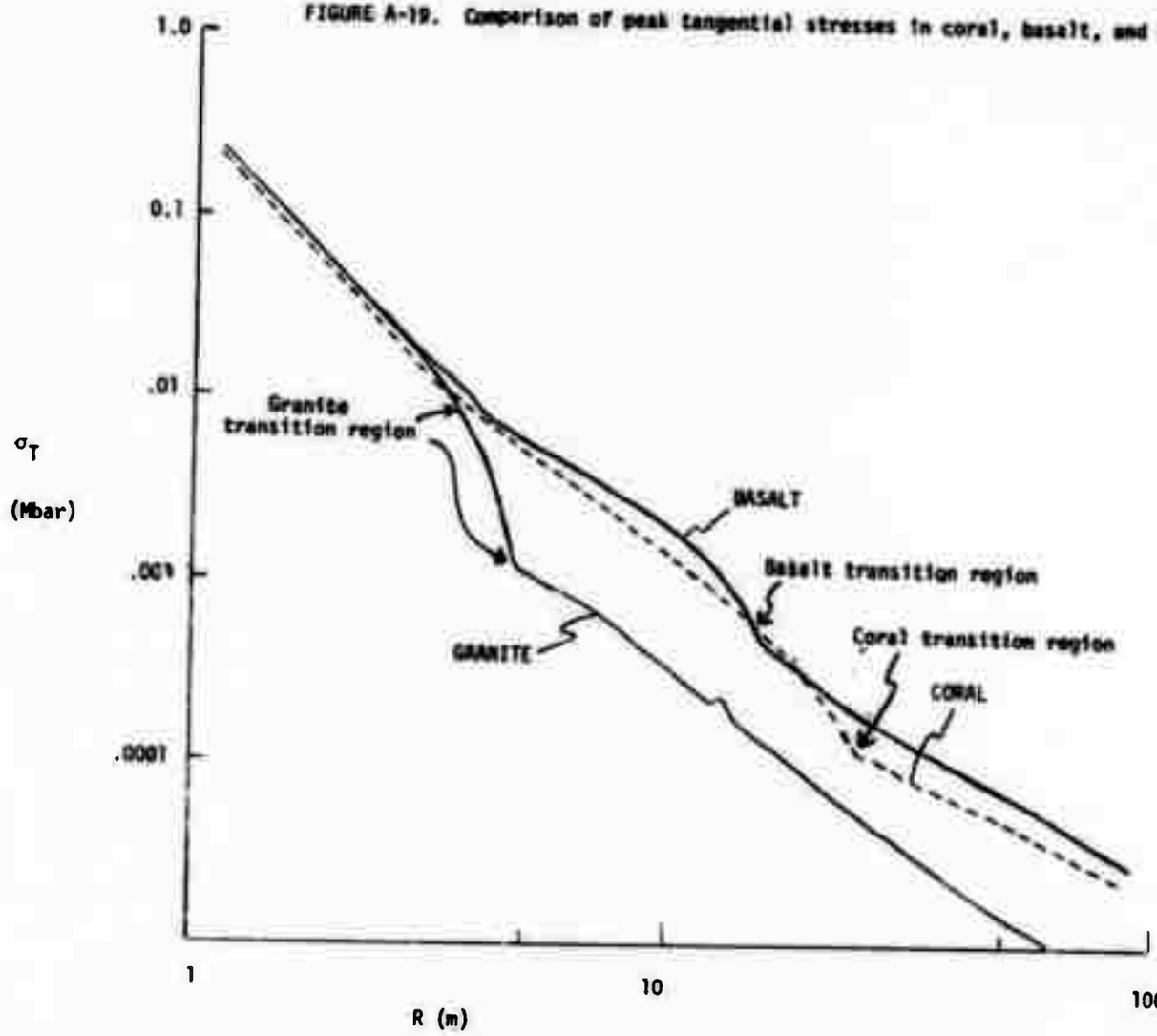

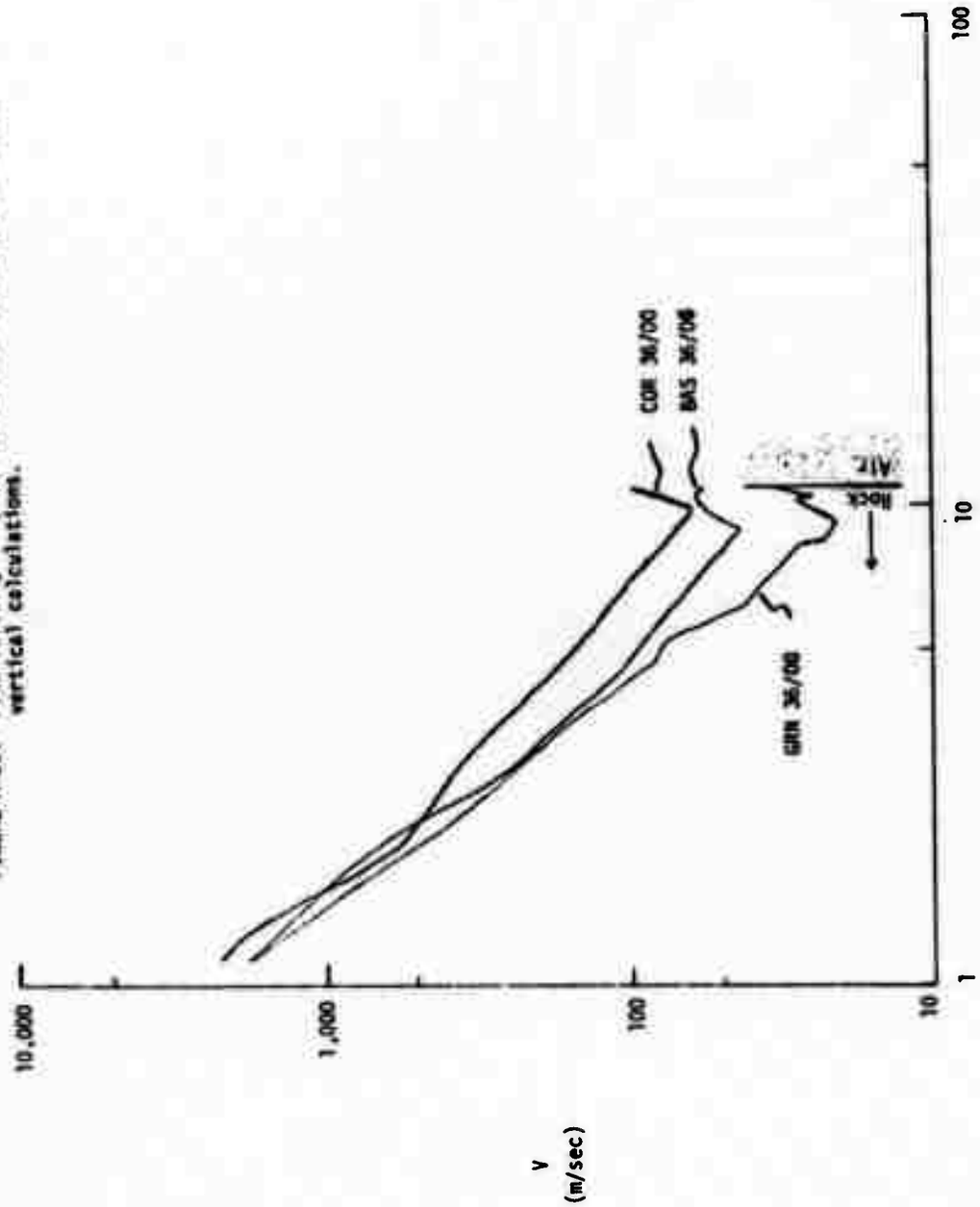

FIGURE A-20. Peak velocity "V"; for COR 36/00, BAS 36/00, GRN 36/00 vertical calculations.

FIGURE A-21. Peak pressure "P"; for COR 36/00, BA5 36/00, GRN 36/00.

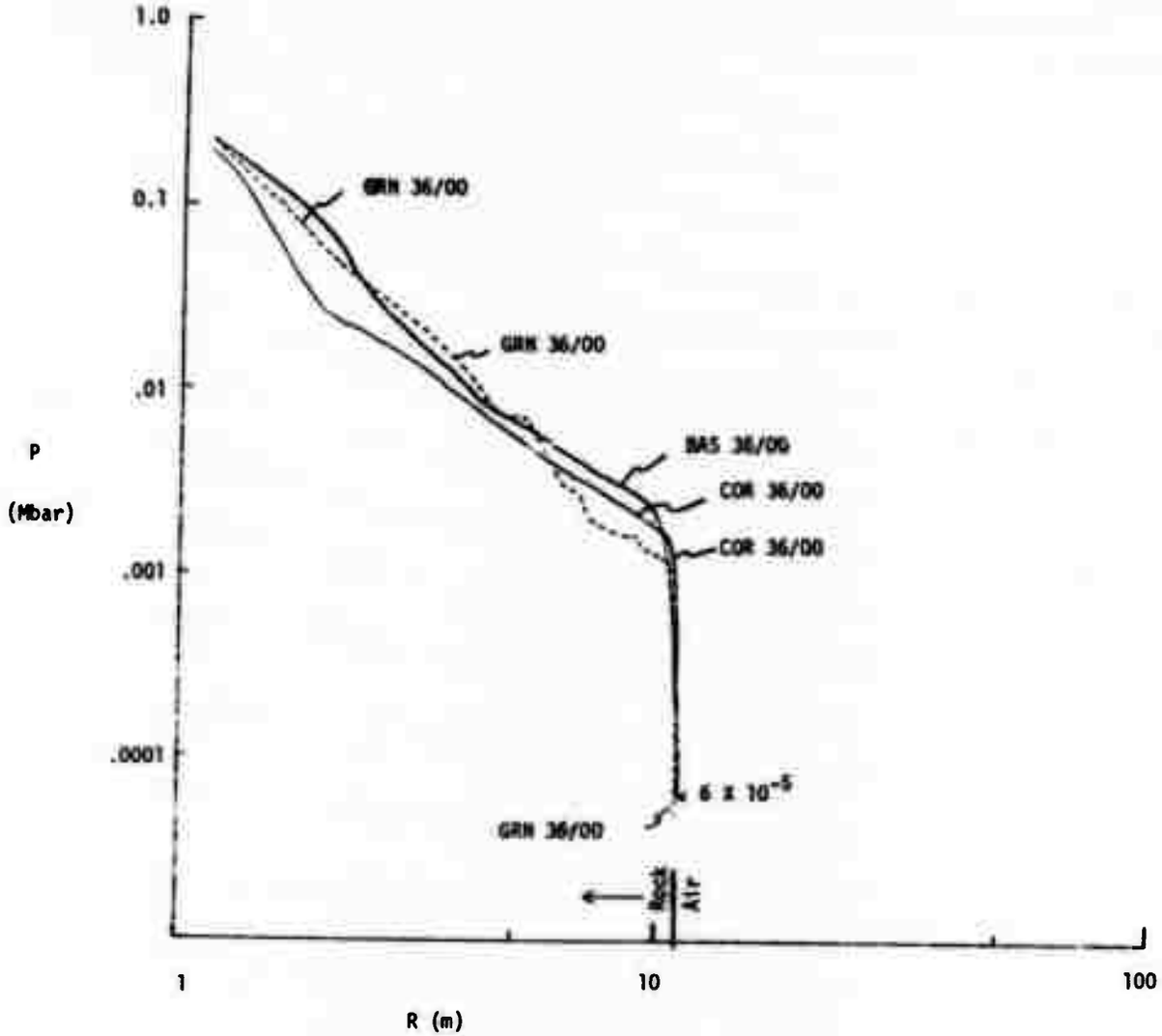

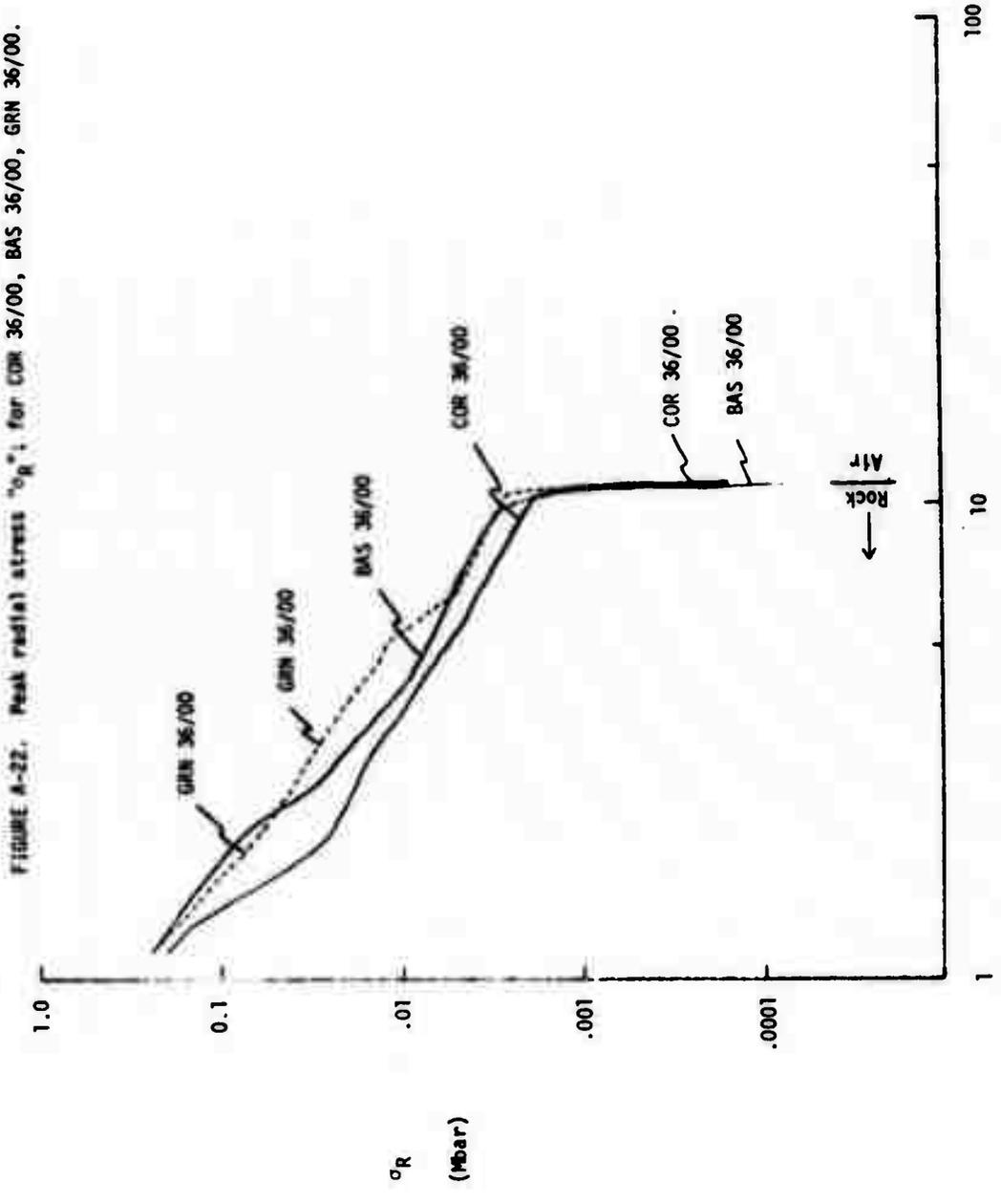

FIGURE A-22. Peak radial stress "σ_R"; for COR 36/00, BAS 36/00, GRN 36/00.

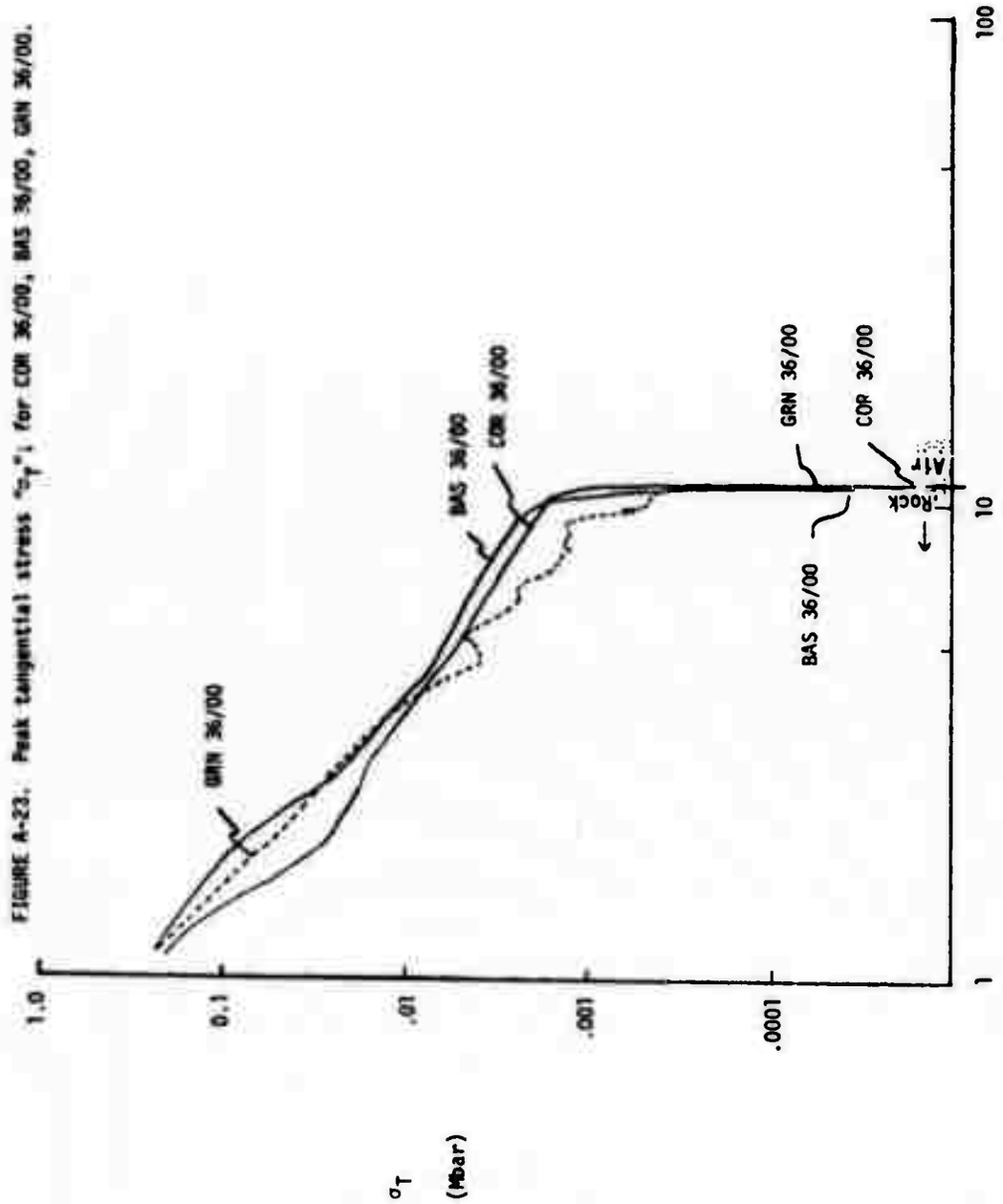

FIGURE A-23. Peak tangential stress "σ_T" for COR 36/00, BAS 36/00, GRN 36/00.

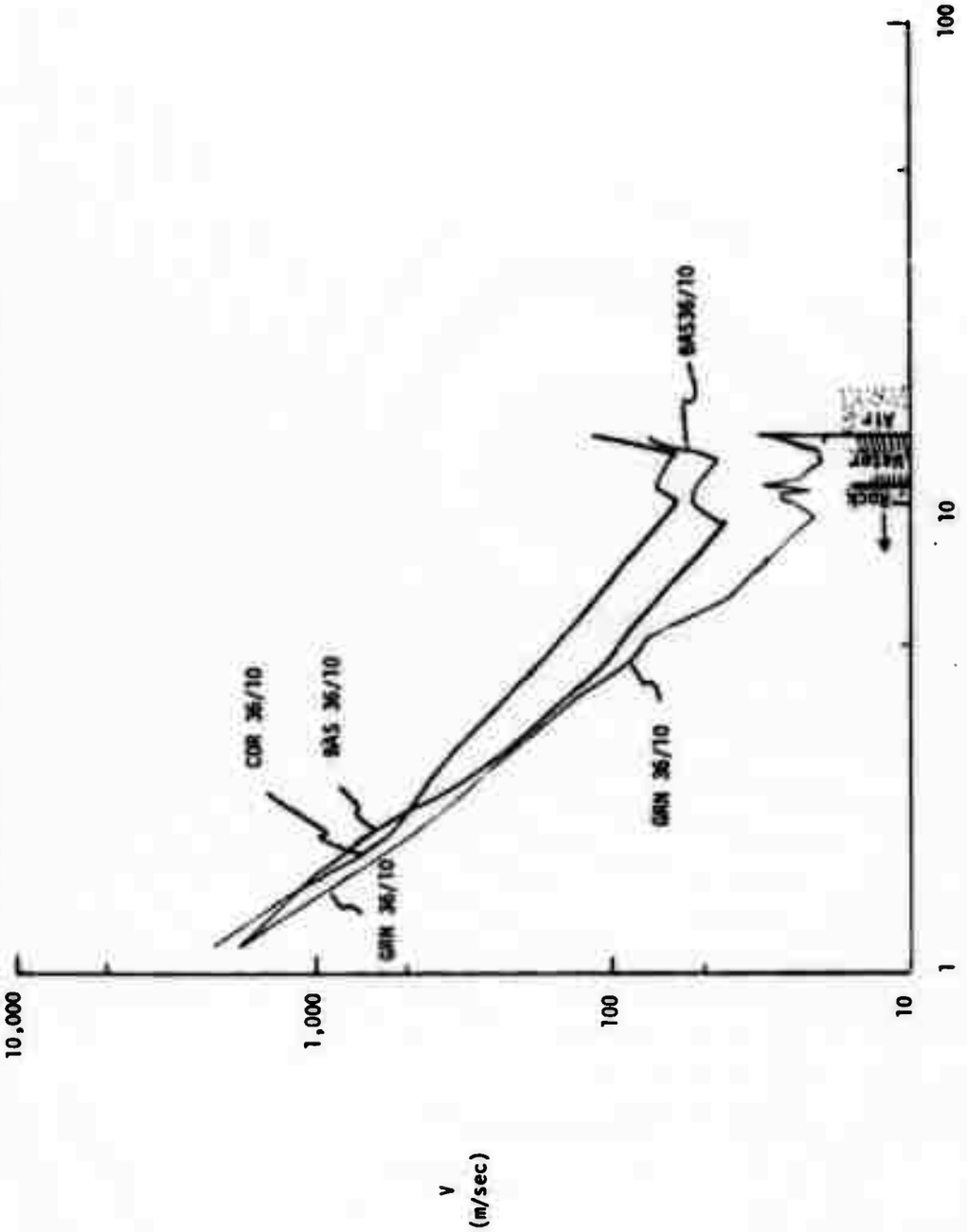

FIGURE A-24. "V"; for COR 36/10, BAS 36/10, GRN 36/10.

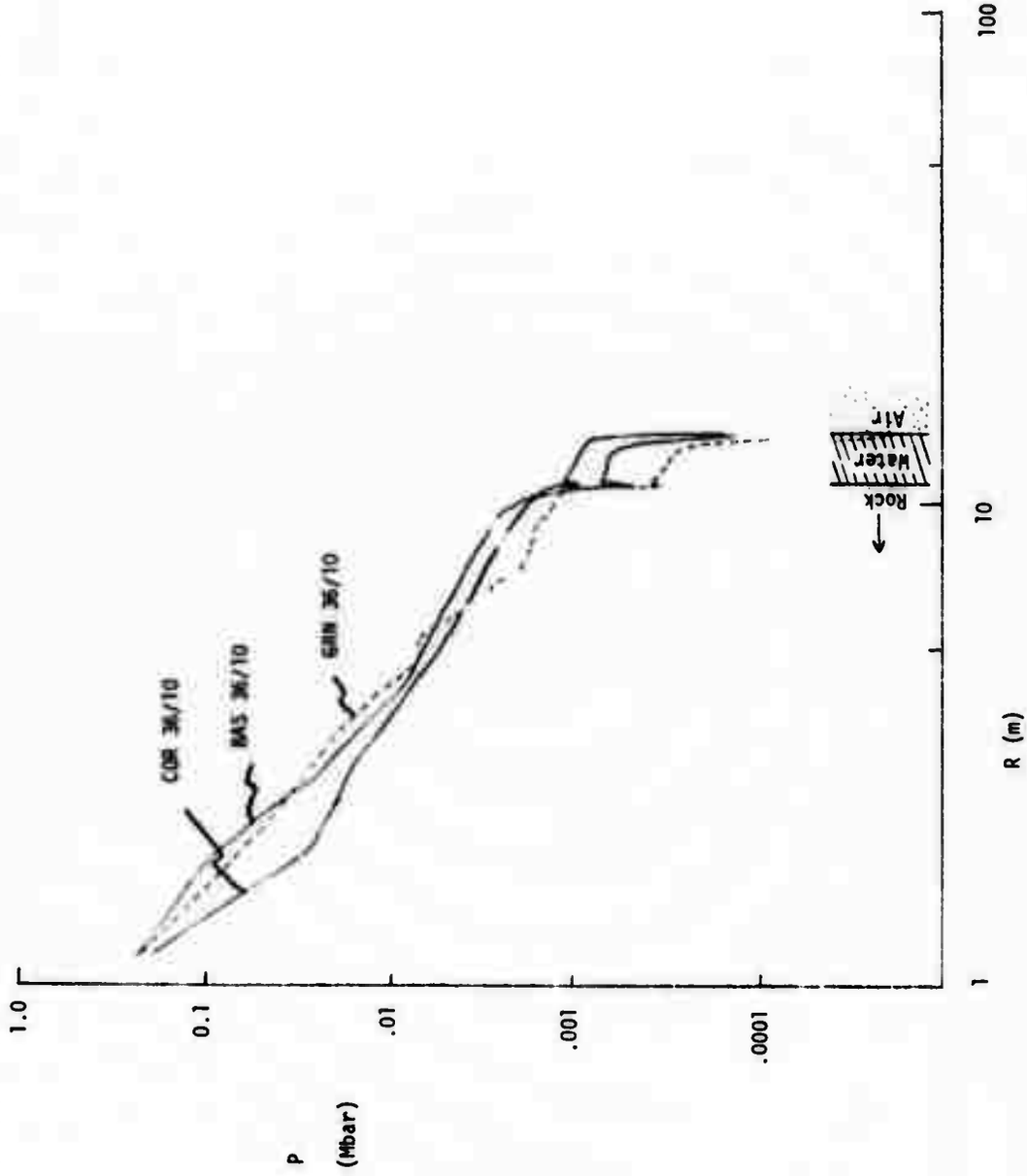

FIGURE A-25. "P"; for COR 36/10, BAS 36/10, GRN 36/10.

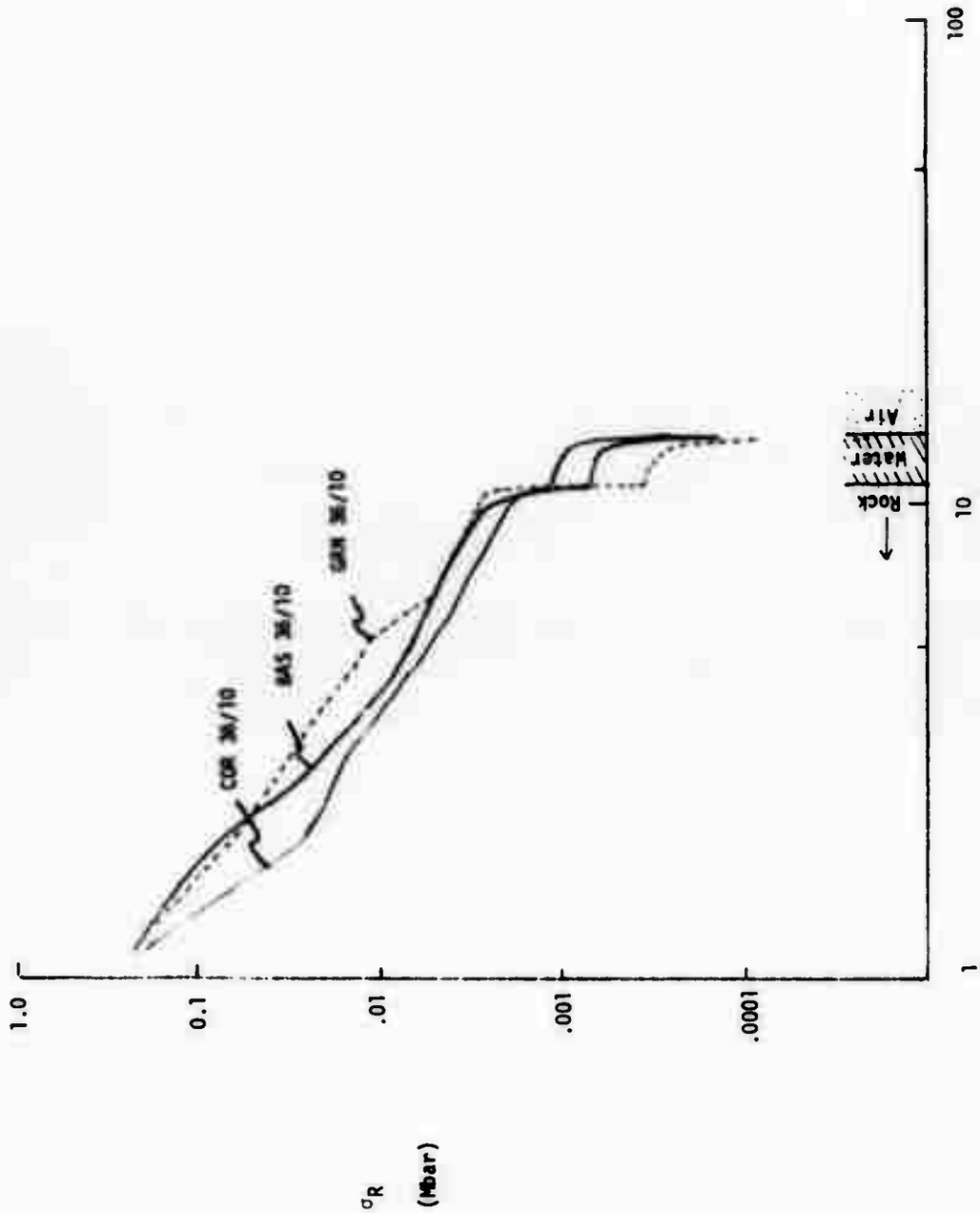

FIGURE A-26. "σ_R"; for COR 36/10, BAS 36/10, GRN 36/10.

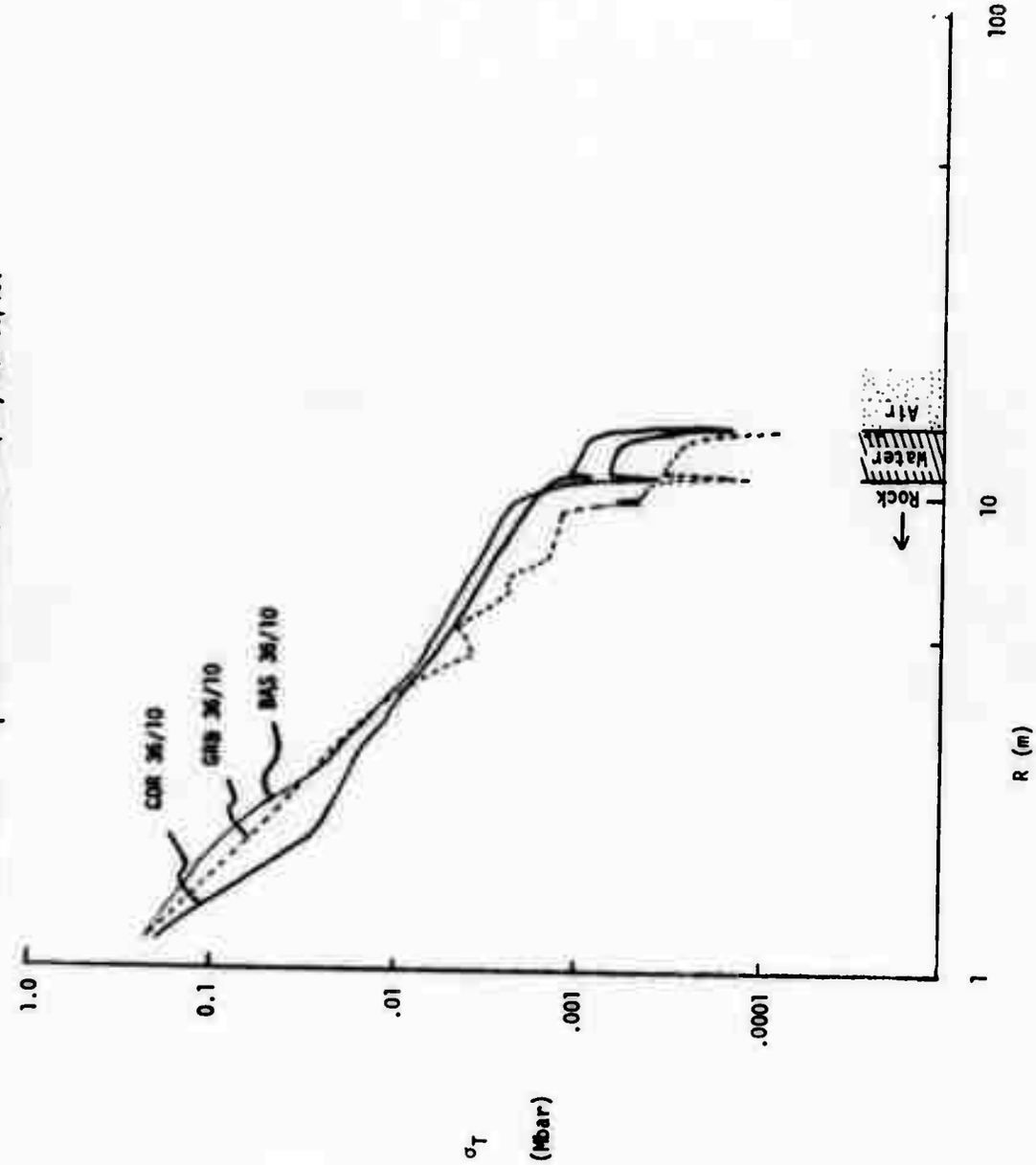

FIGURE A-27. "σ_T": for COR 36/10, BAS 36/10, GRN 36/10.

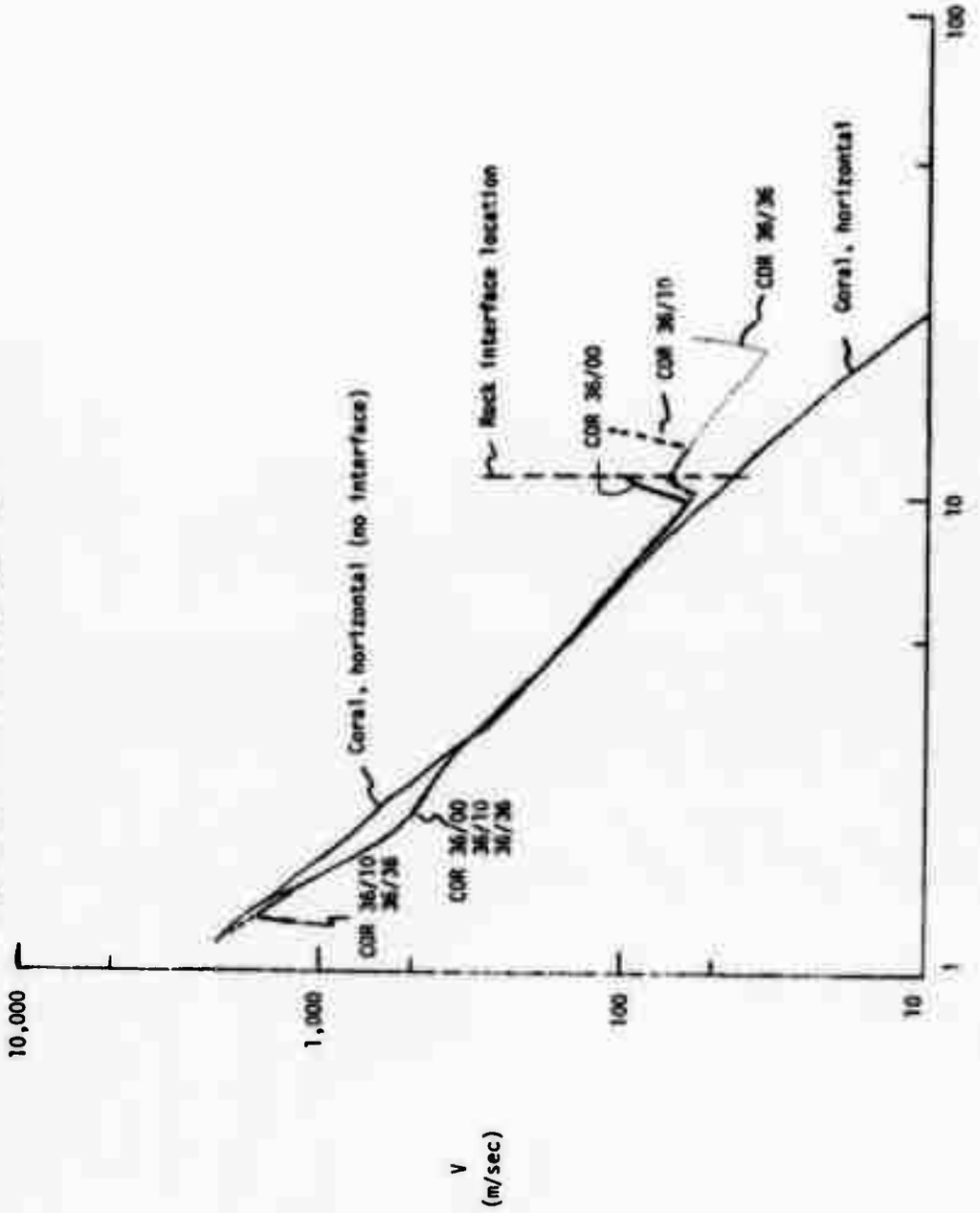

FIGURE A-28. "V"; for coral, DOB = 36 ft

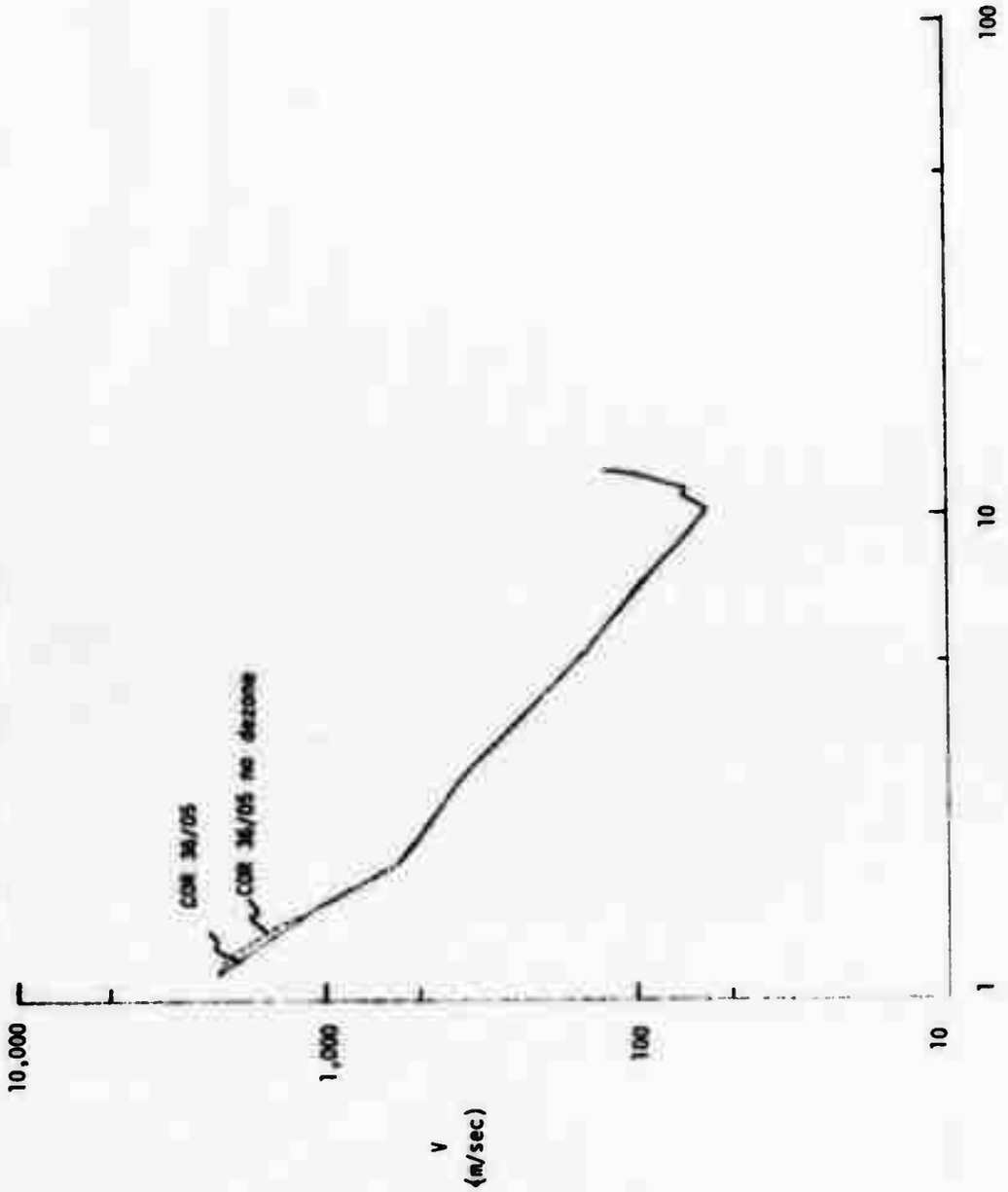

FIGURE A-29. "V"; for COR 36/05

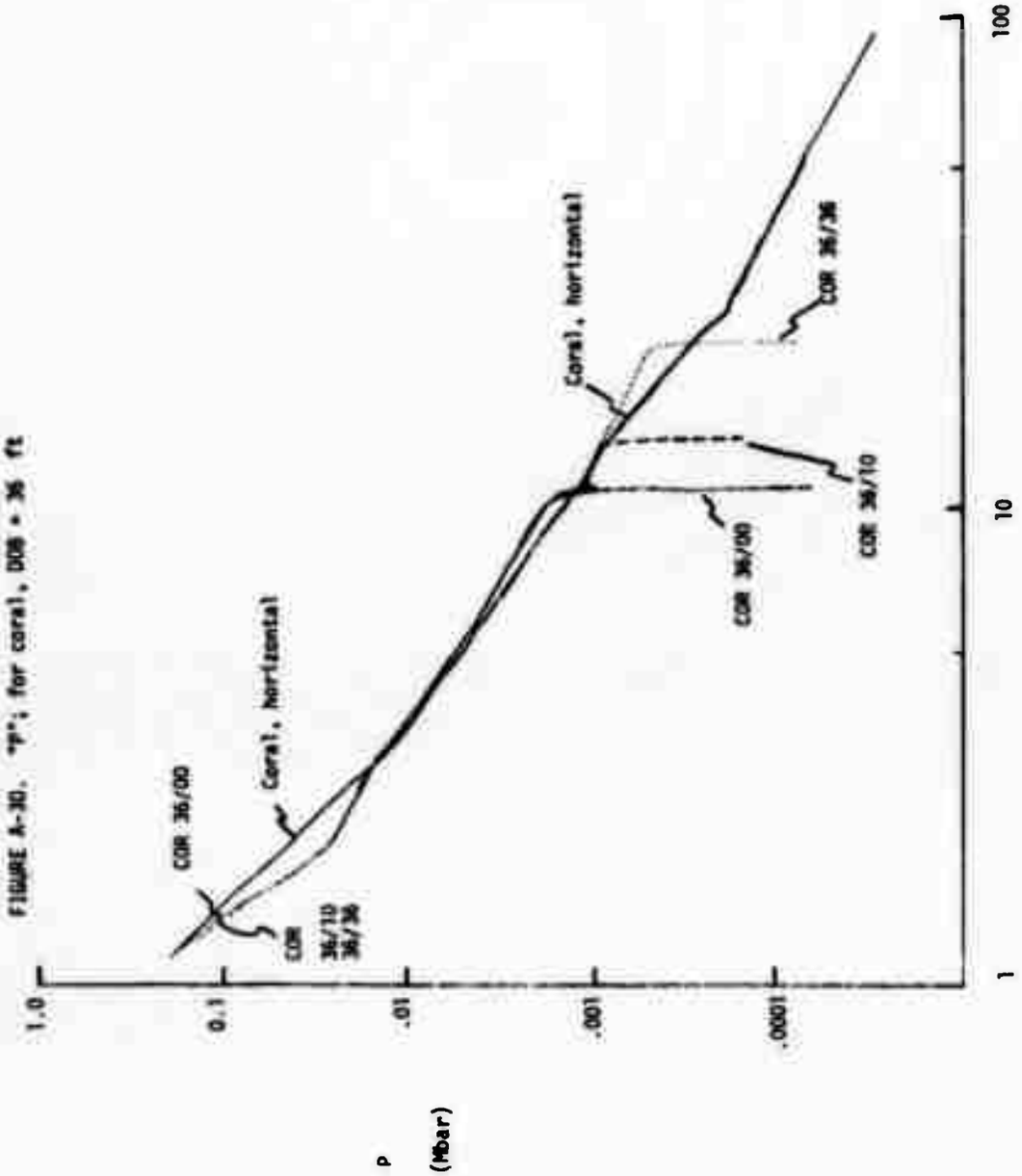

FIGURE A-30. "P"; for coral, DOB = 36 ft

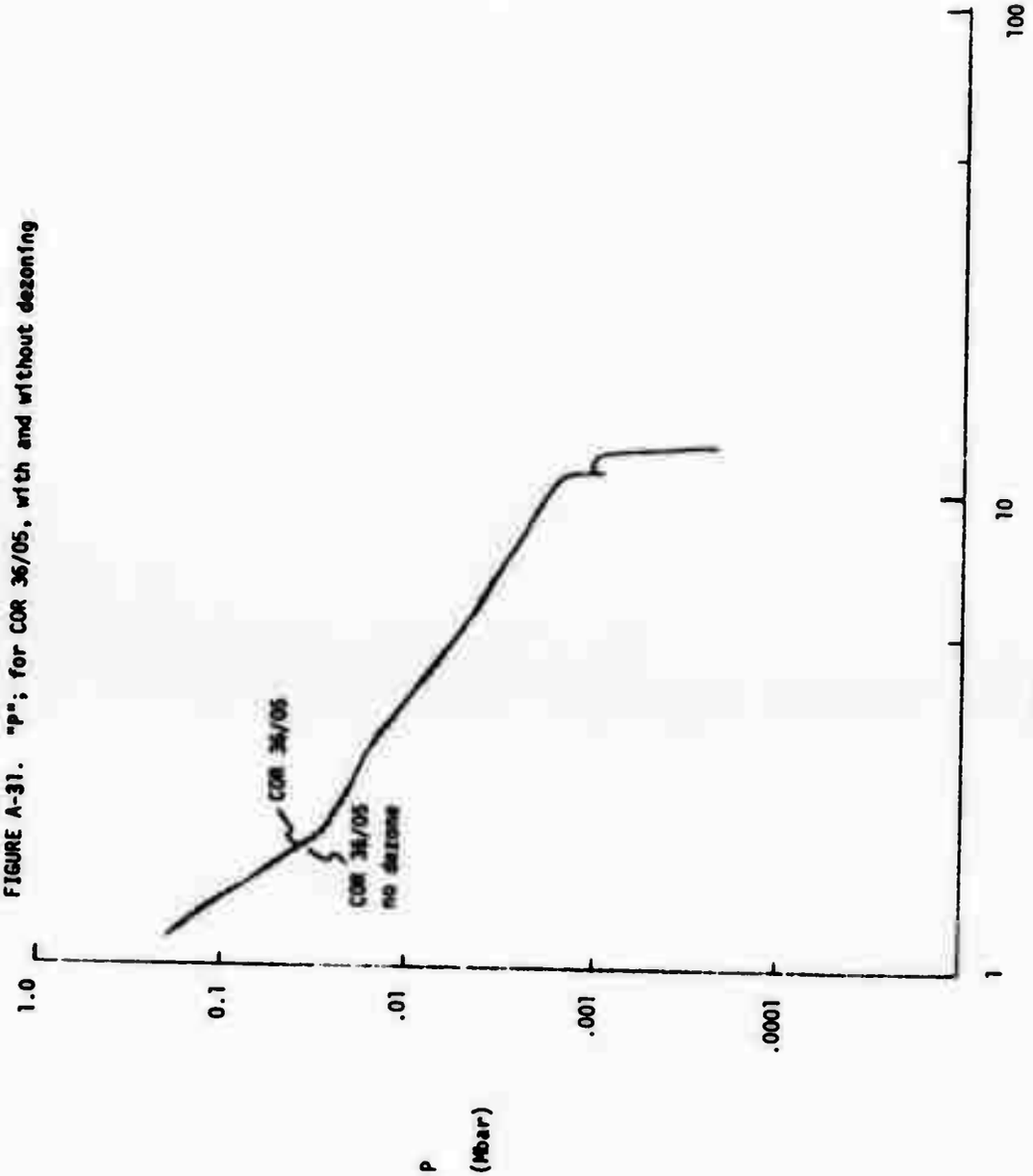

FIGURE A-31. "P"; for COR 36/05, with and without dezoning

FIGURE A-32. "V", for coral, DOB = 30 ft

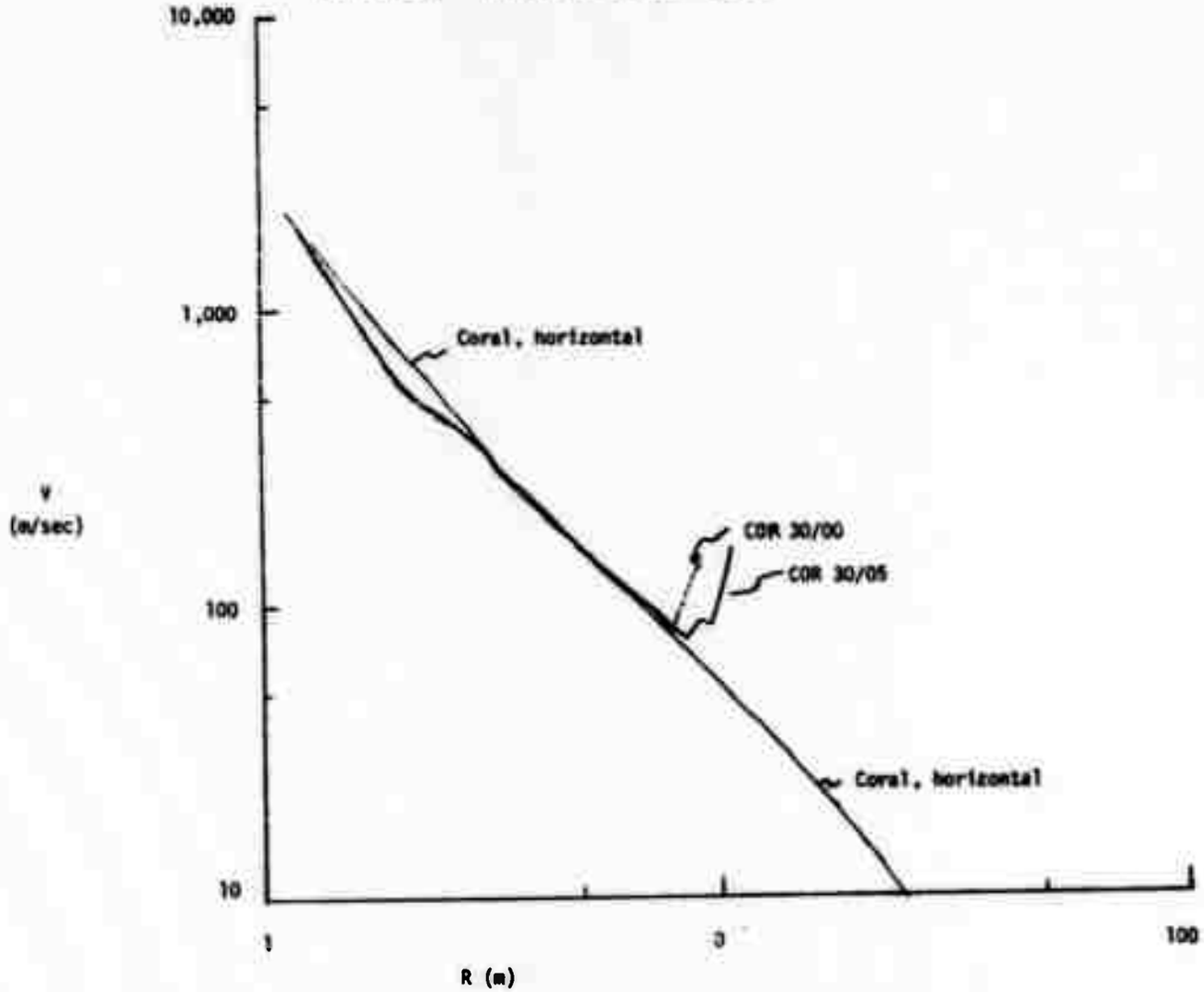

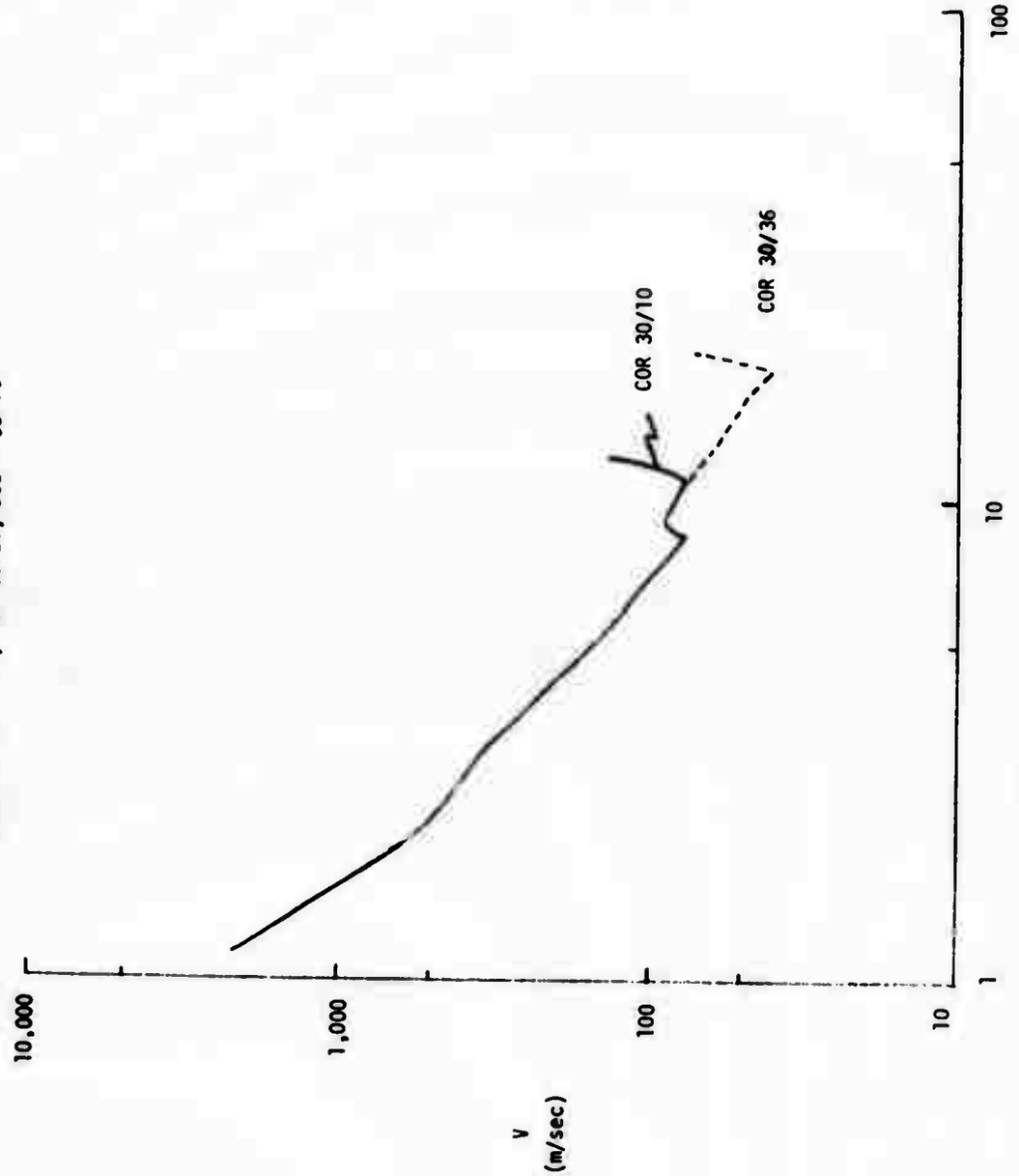

FIGURE A-38. "V"; for coral, DOB = 30 ft

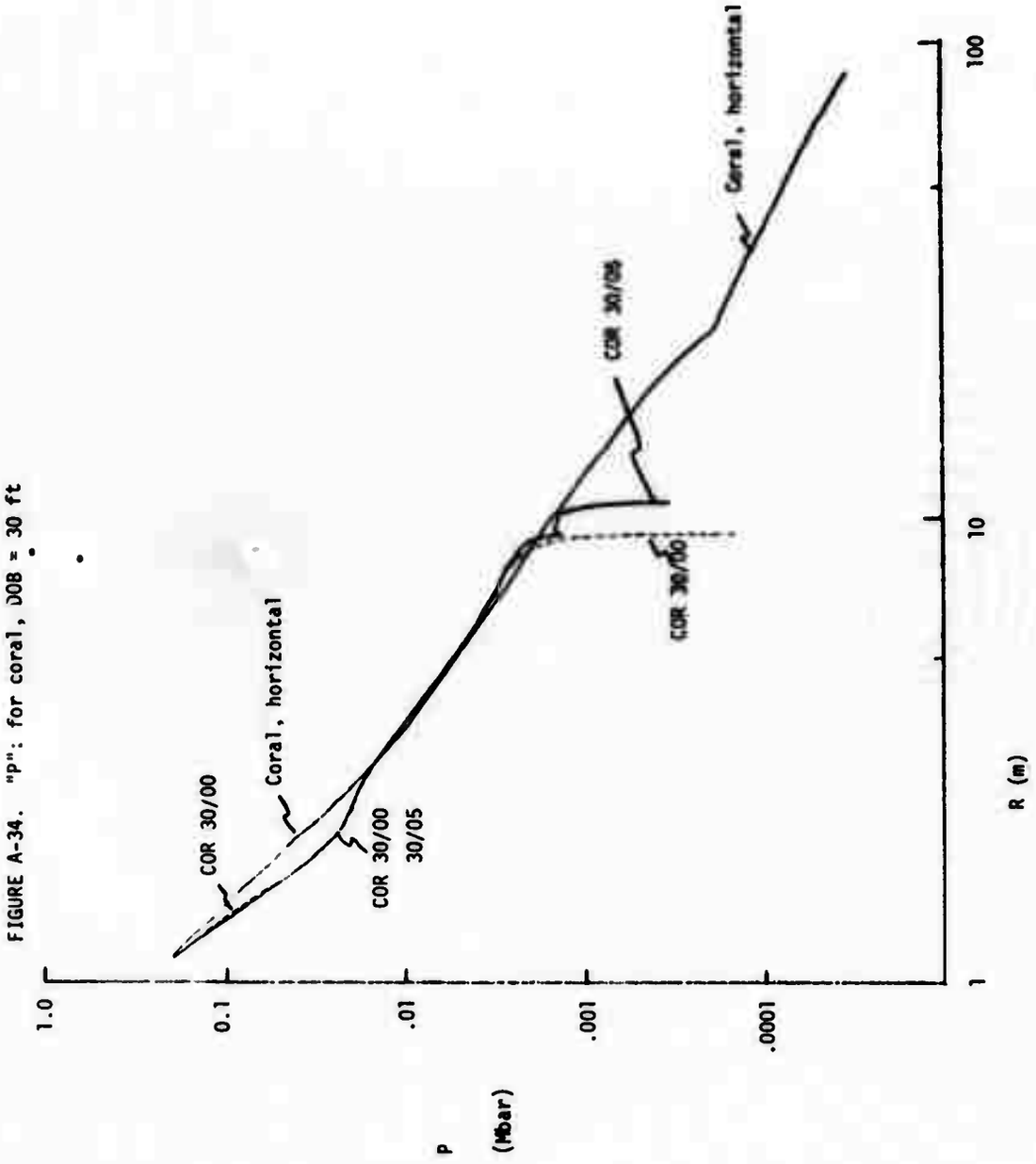

FIGURE A-34. "P": for coral, DOB = 30 ft

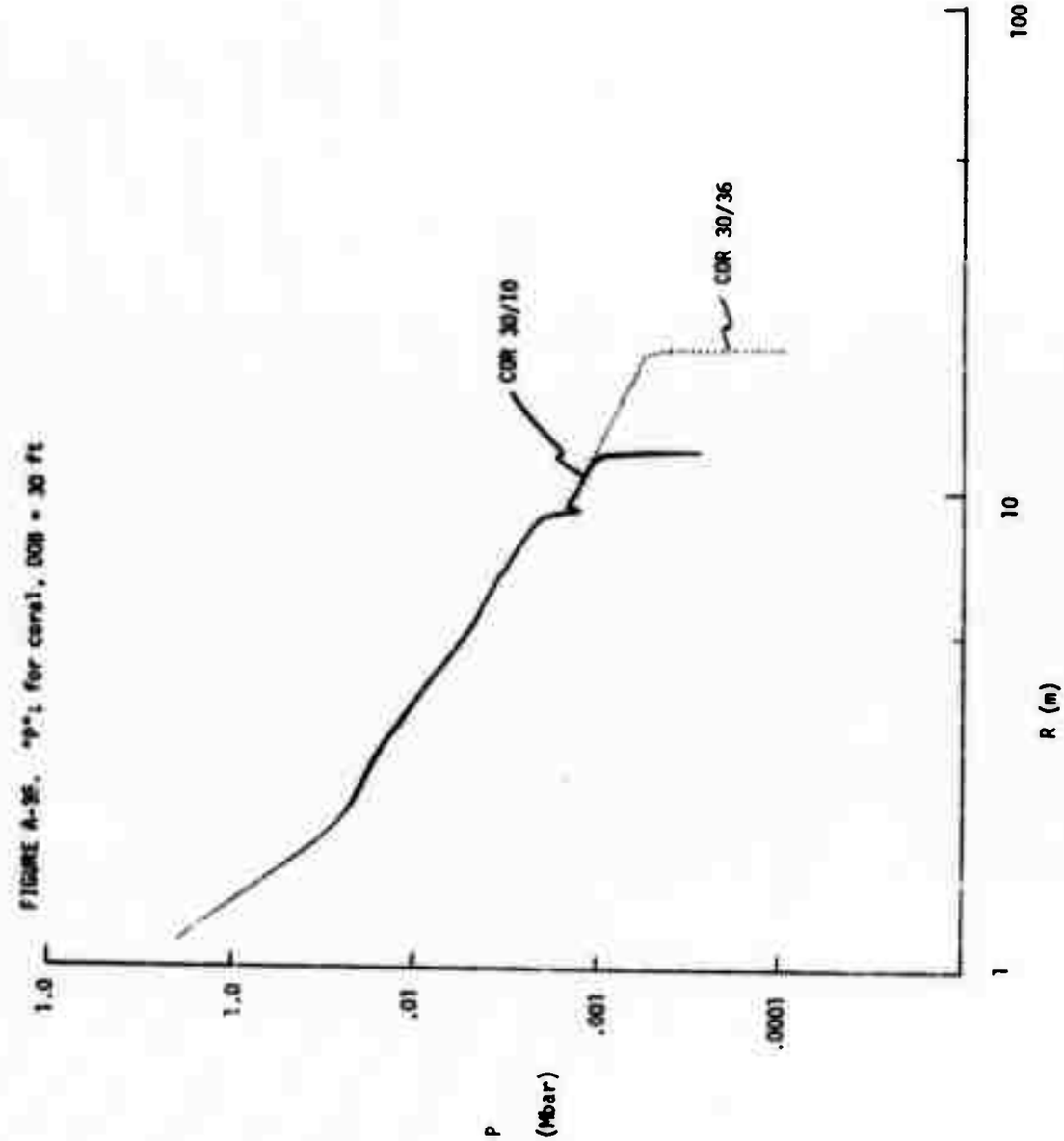

FIGURE A-35. "P"; for coral, DOB = 30 ft

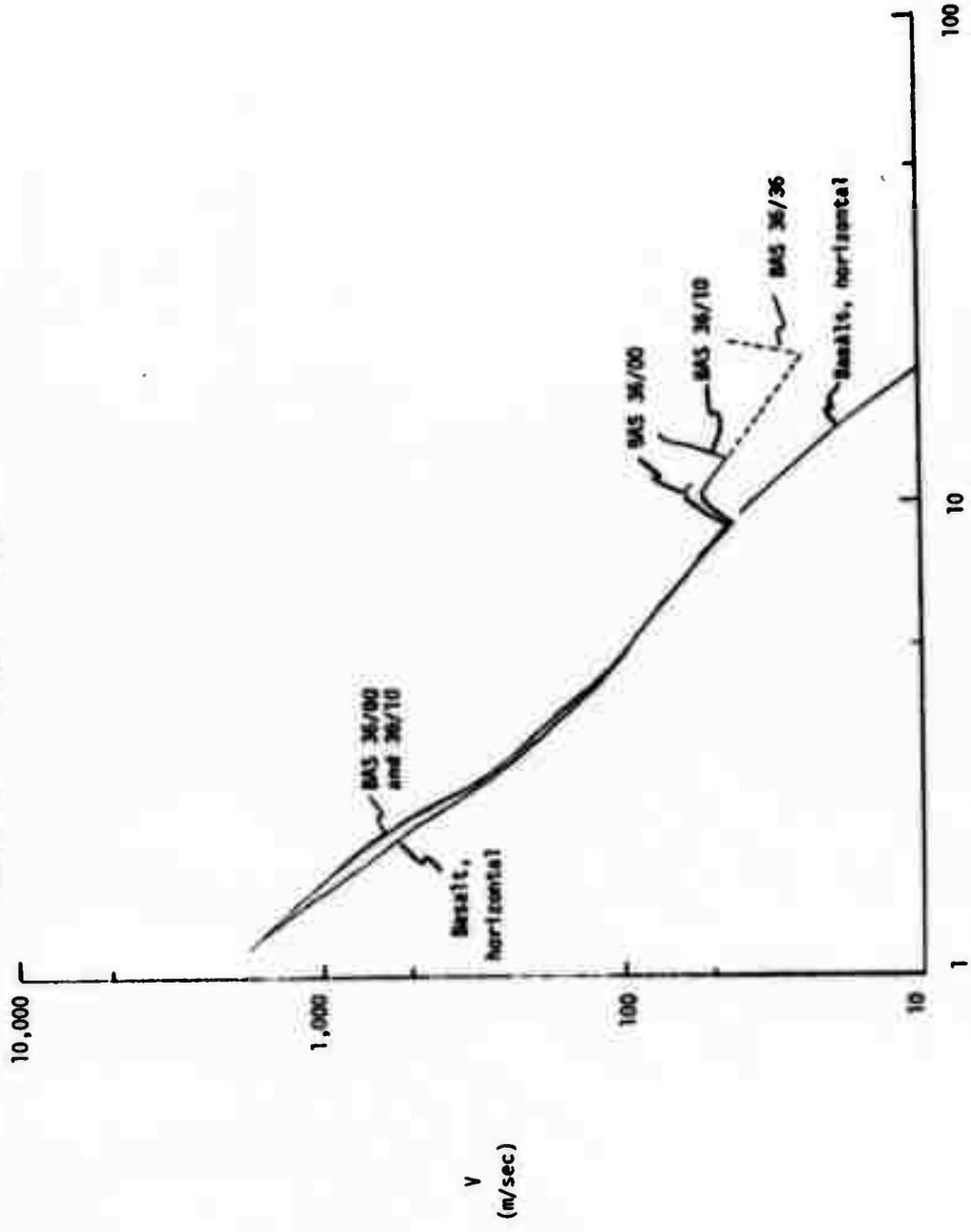

FIGURE A-36. "V"; basalt, DOB = 36 ft

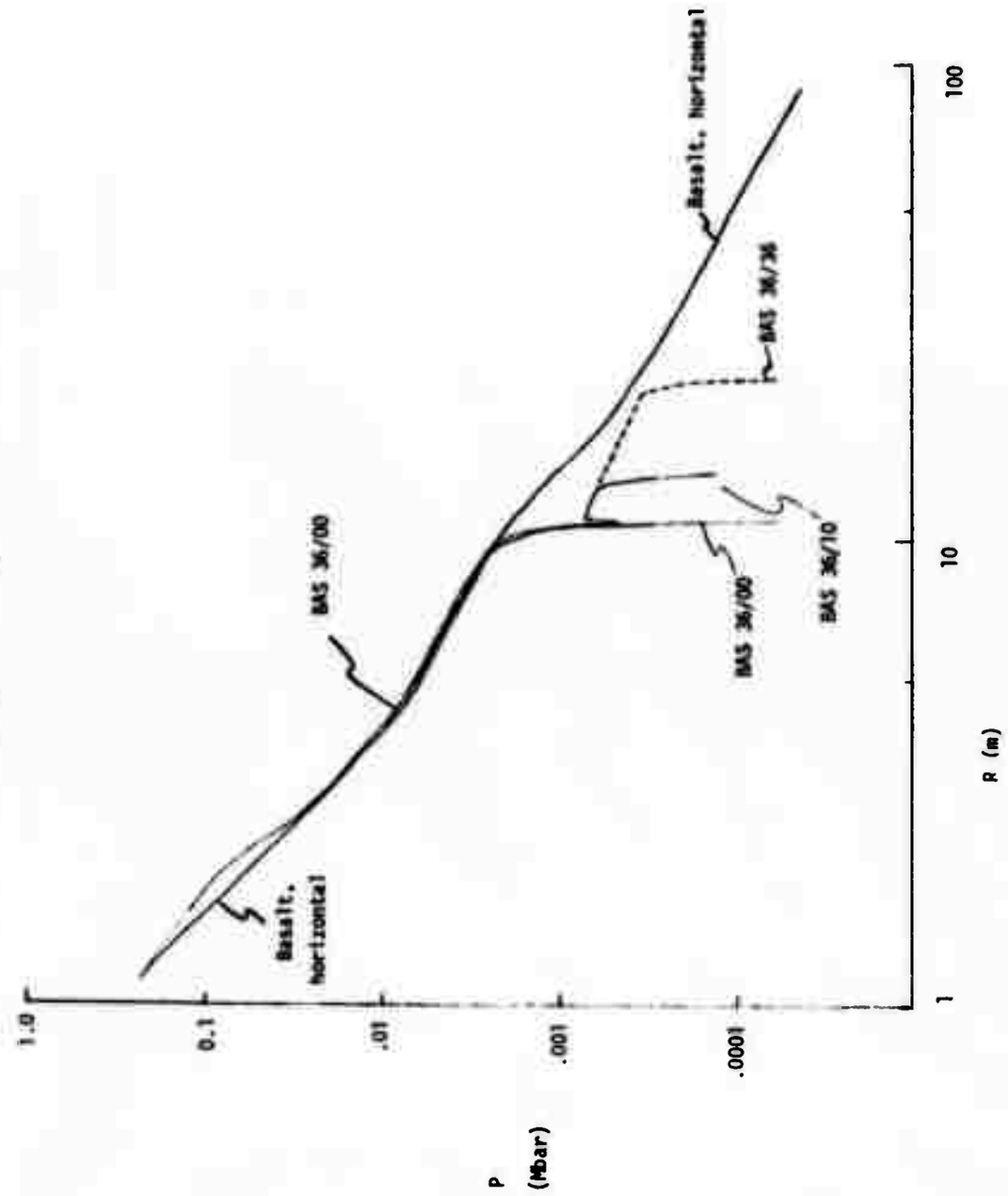

FIGURE A-37. "P"; basalt, DOB = 36 ft

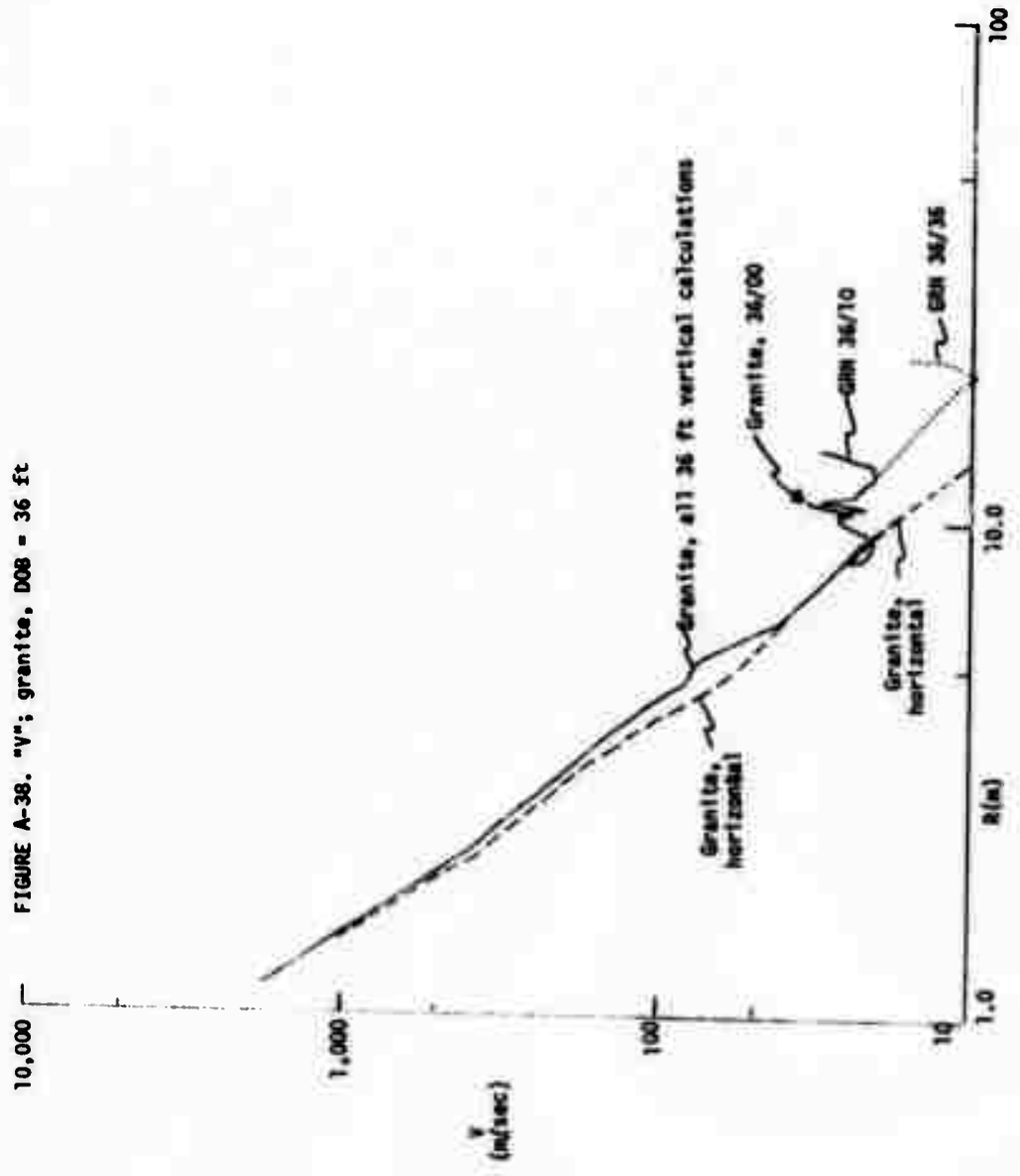

FIGURE A-38. "V"; granite, DOB = 36 ft

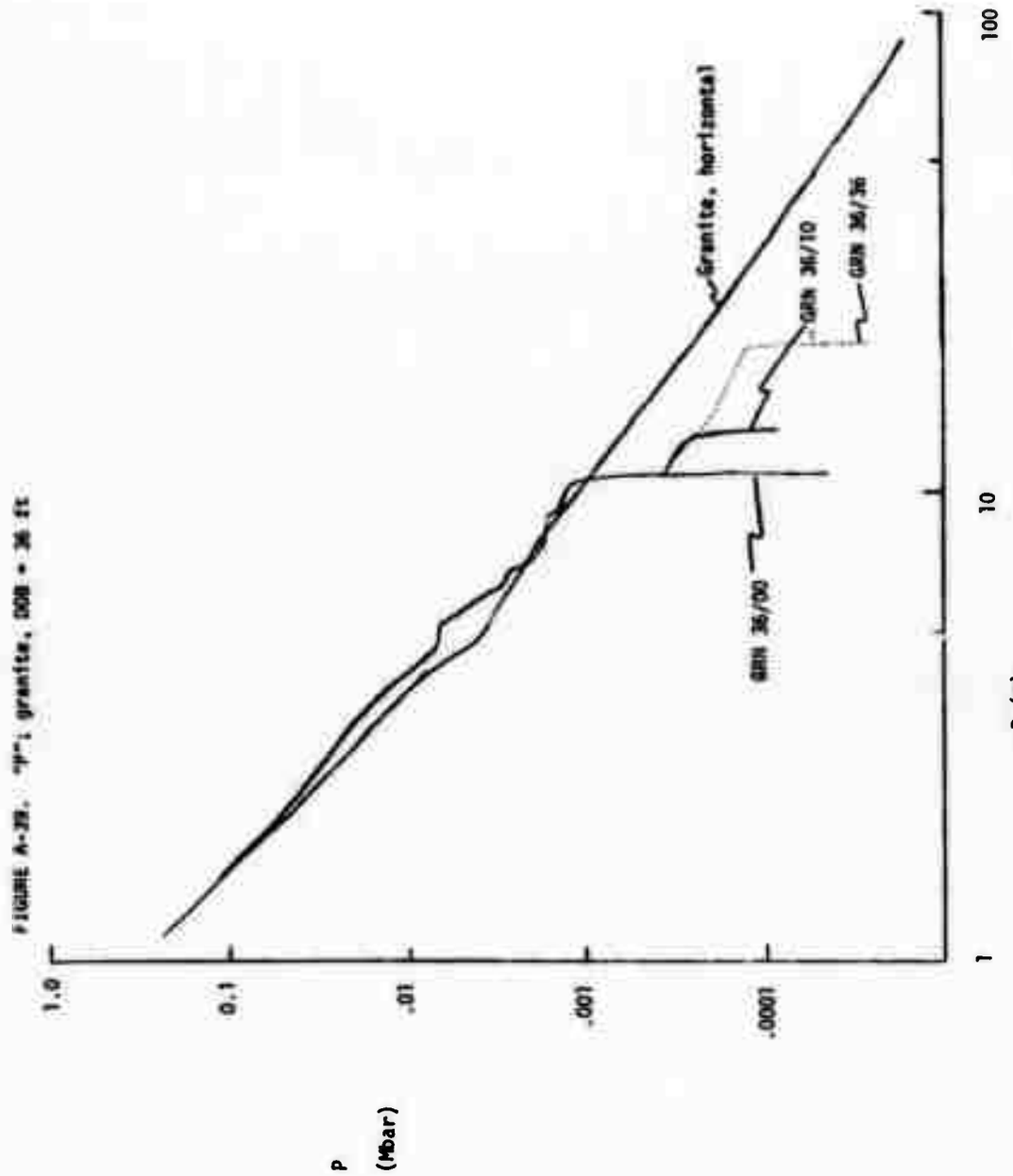

FIGURE A-39. "P"; granite, DOB = 36 ft

FIGURE A-40. "V"; for coral, horizontal calculations, artificial viscosity factors of $\nu = 0.1$ and $\nu = 0.2$.

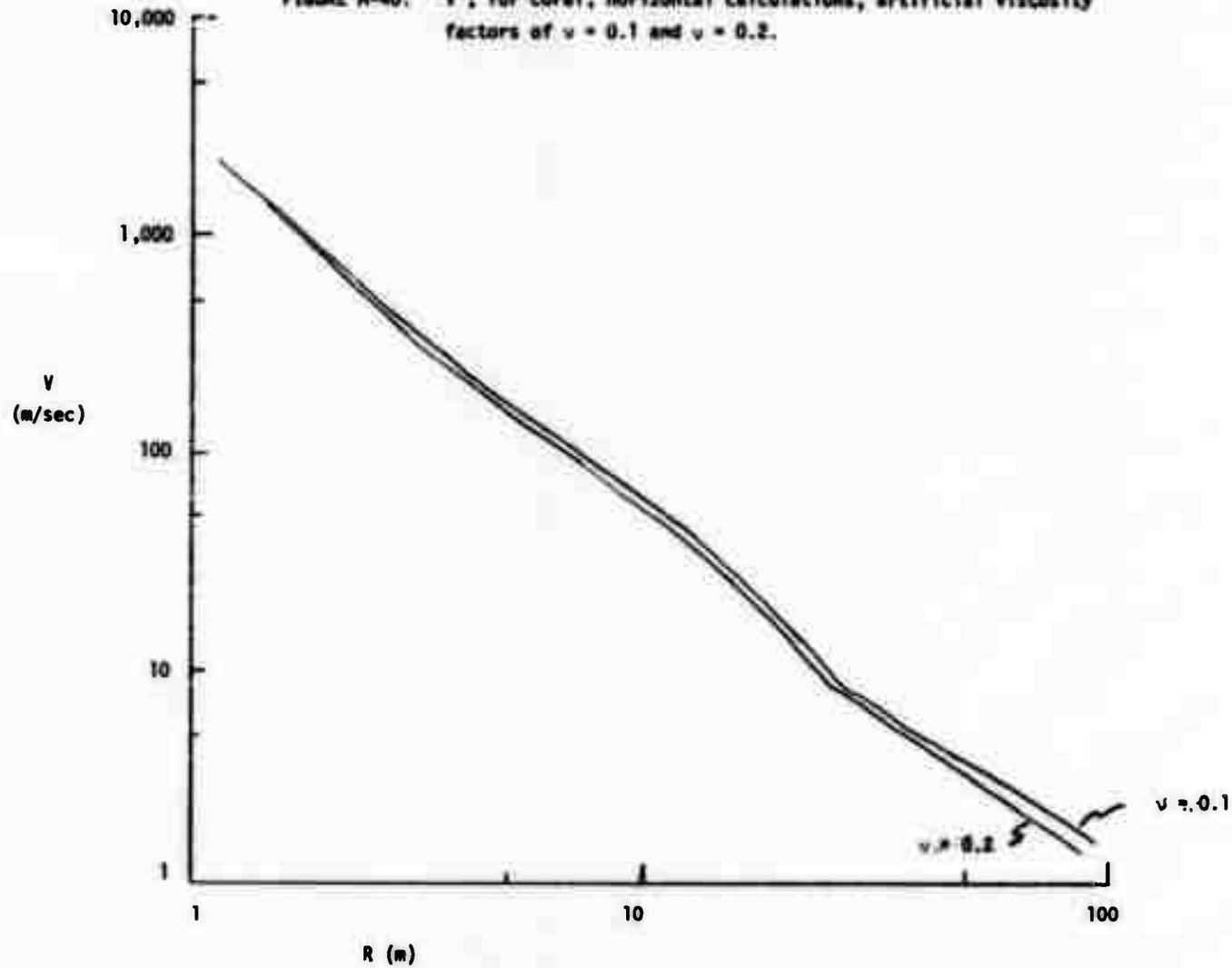

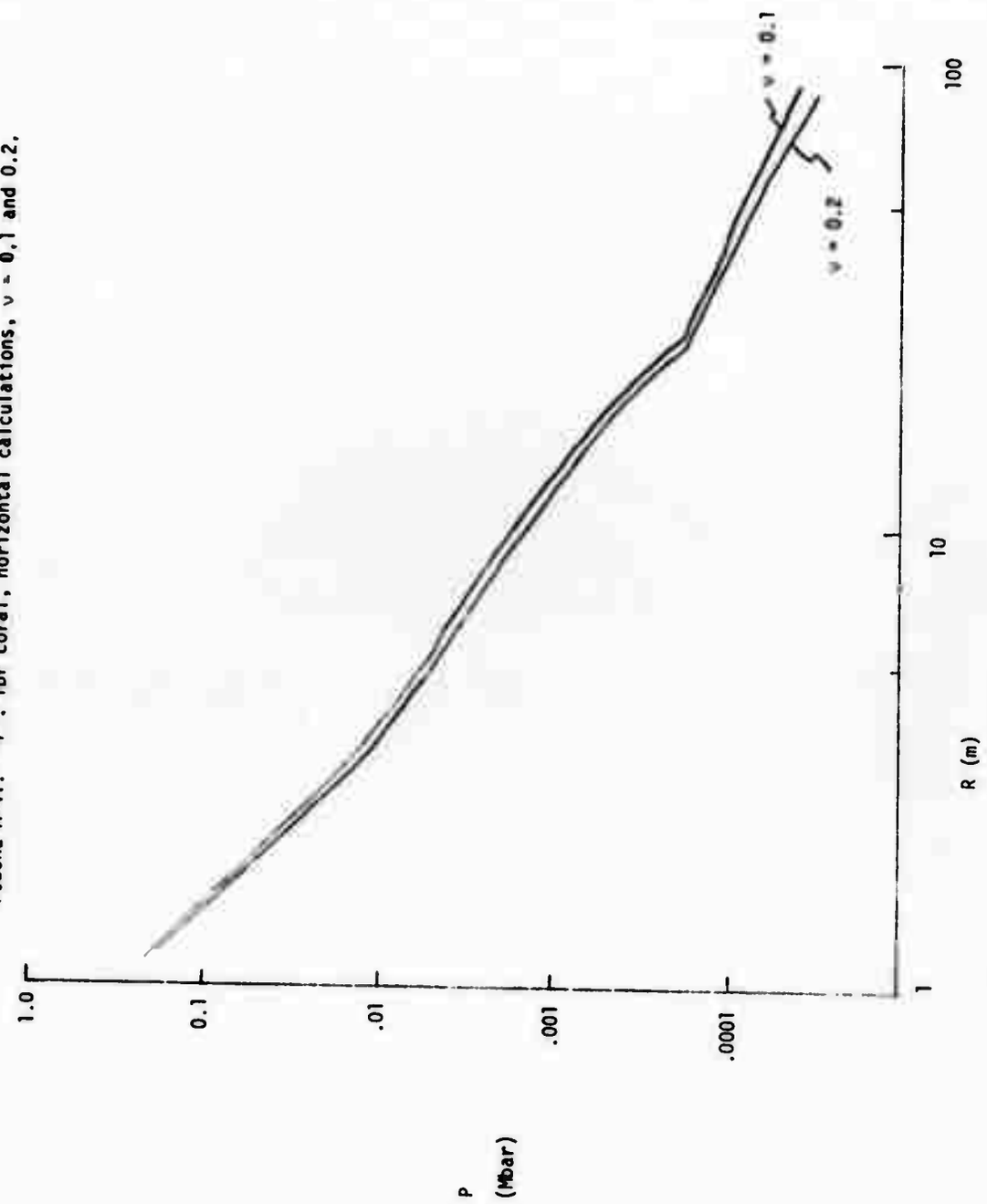

FIGURE A-41. "p": for coral, horizontal calculations, ν = 0,1 and 0.2.

FIGURE A-42. "σ_R" and "σ_T"; for coral, horizontal calculations, ν = 0.1 and 0.2.

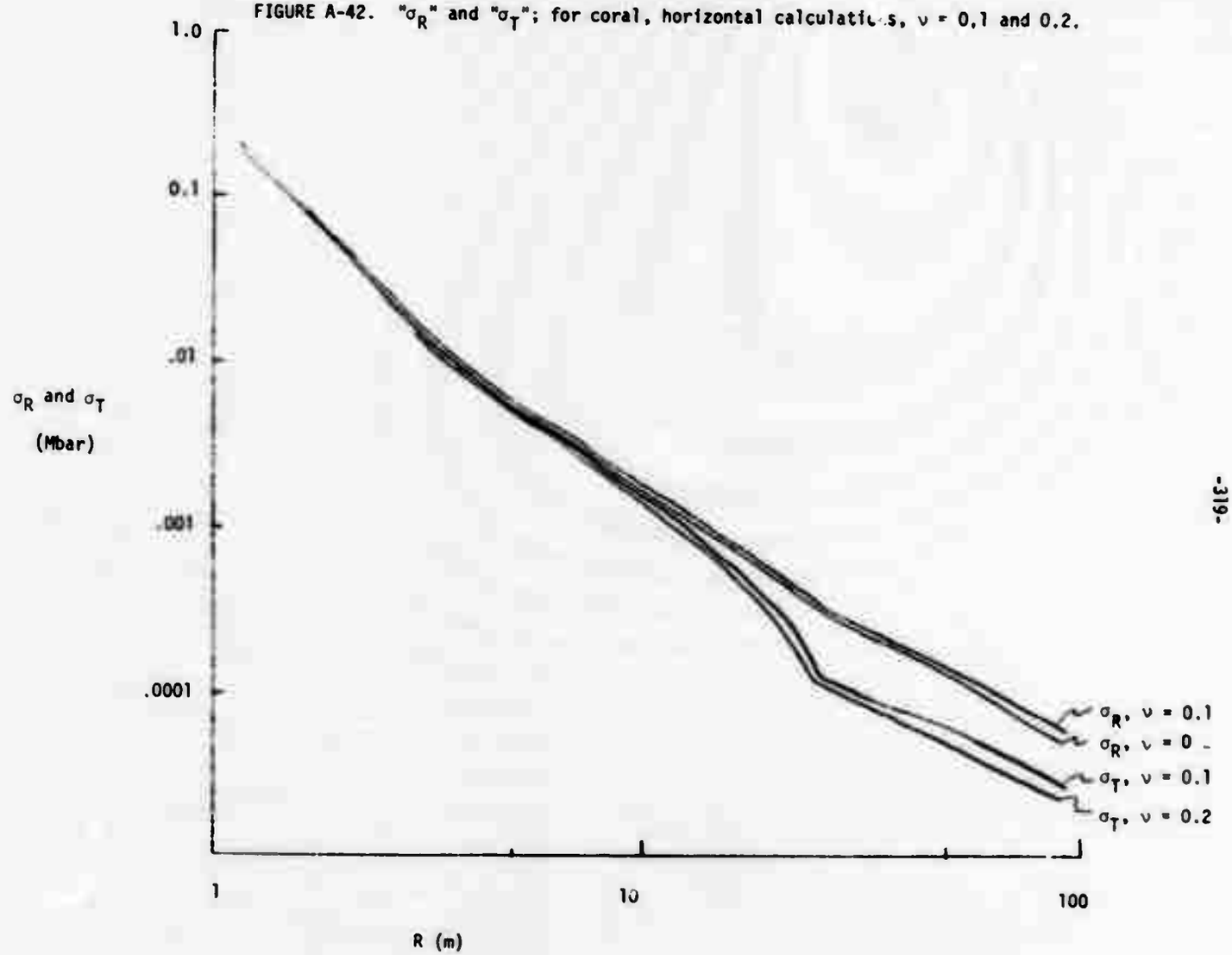

FIGURE A-43. "V"; for basalt, horizontal calculations, ν = 0.1 and 0.2.

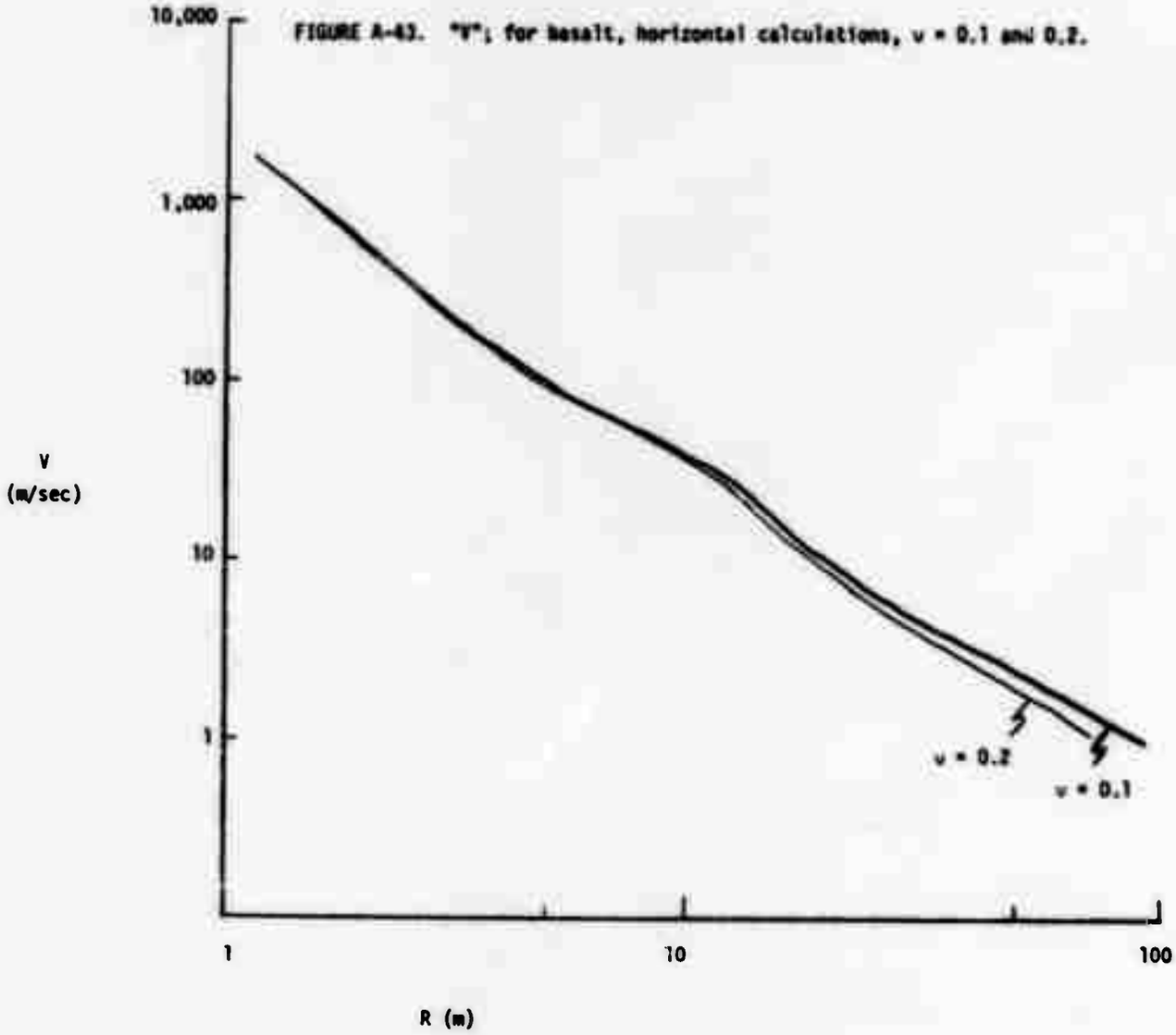

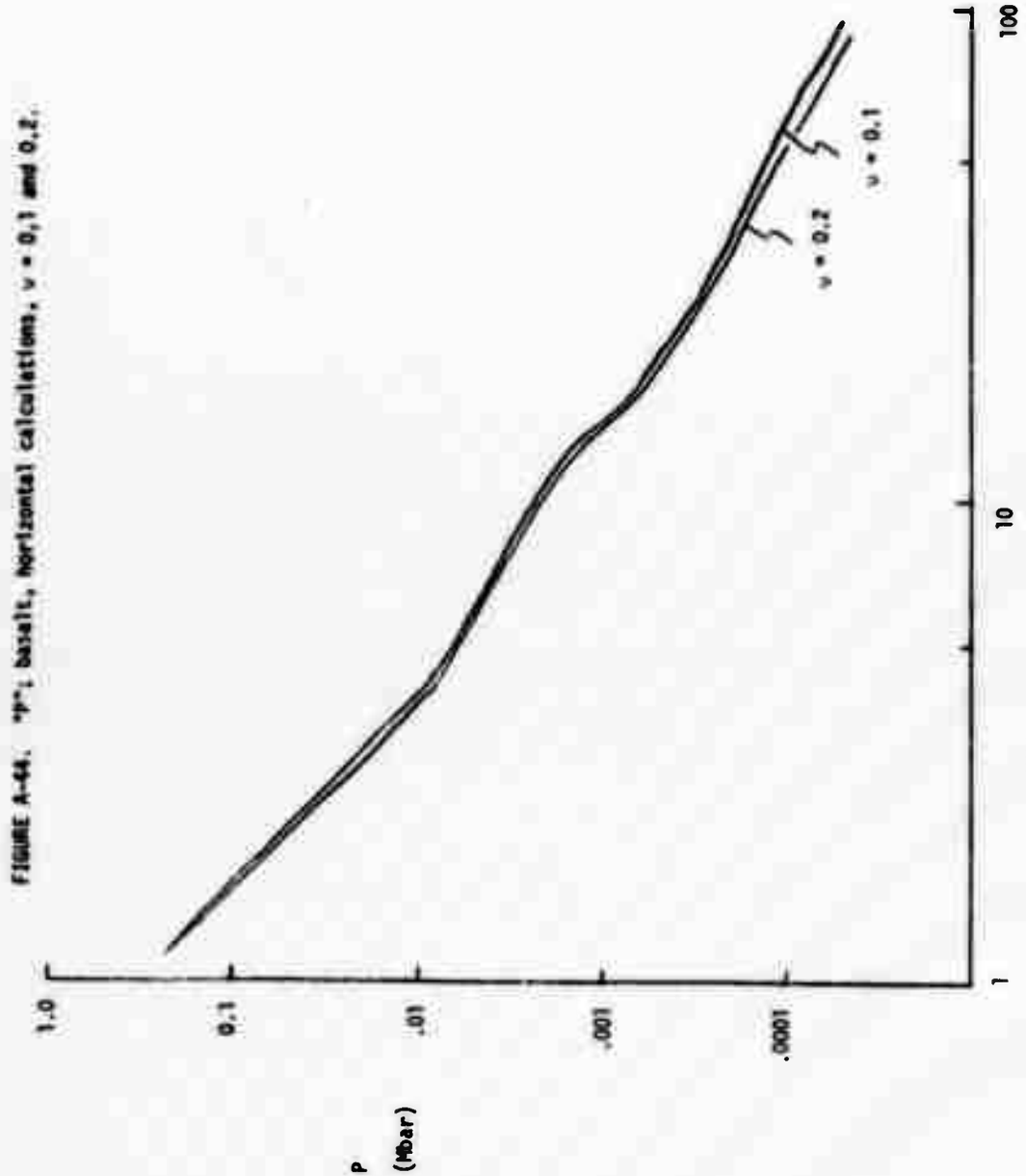

FIGURE A-44. "P"; basalt, horizontal calculations, ν = 0.1 and 0.2.

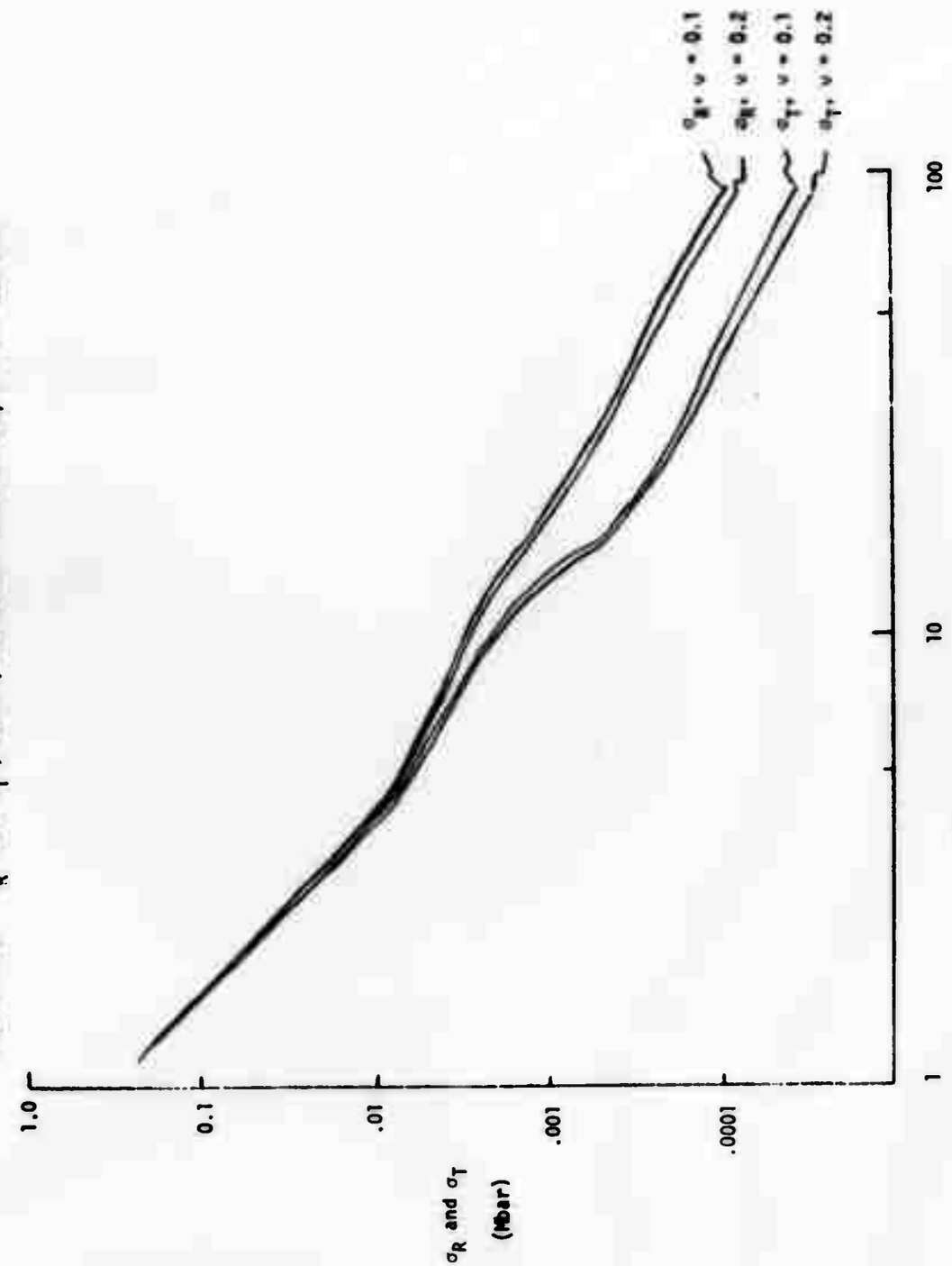

FIGURE A-45. "σ_R" and "σ_T"; basalt, horizontal calculations, ν = 0.1 and 0.2.

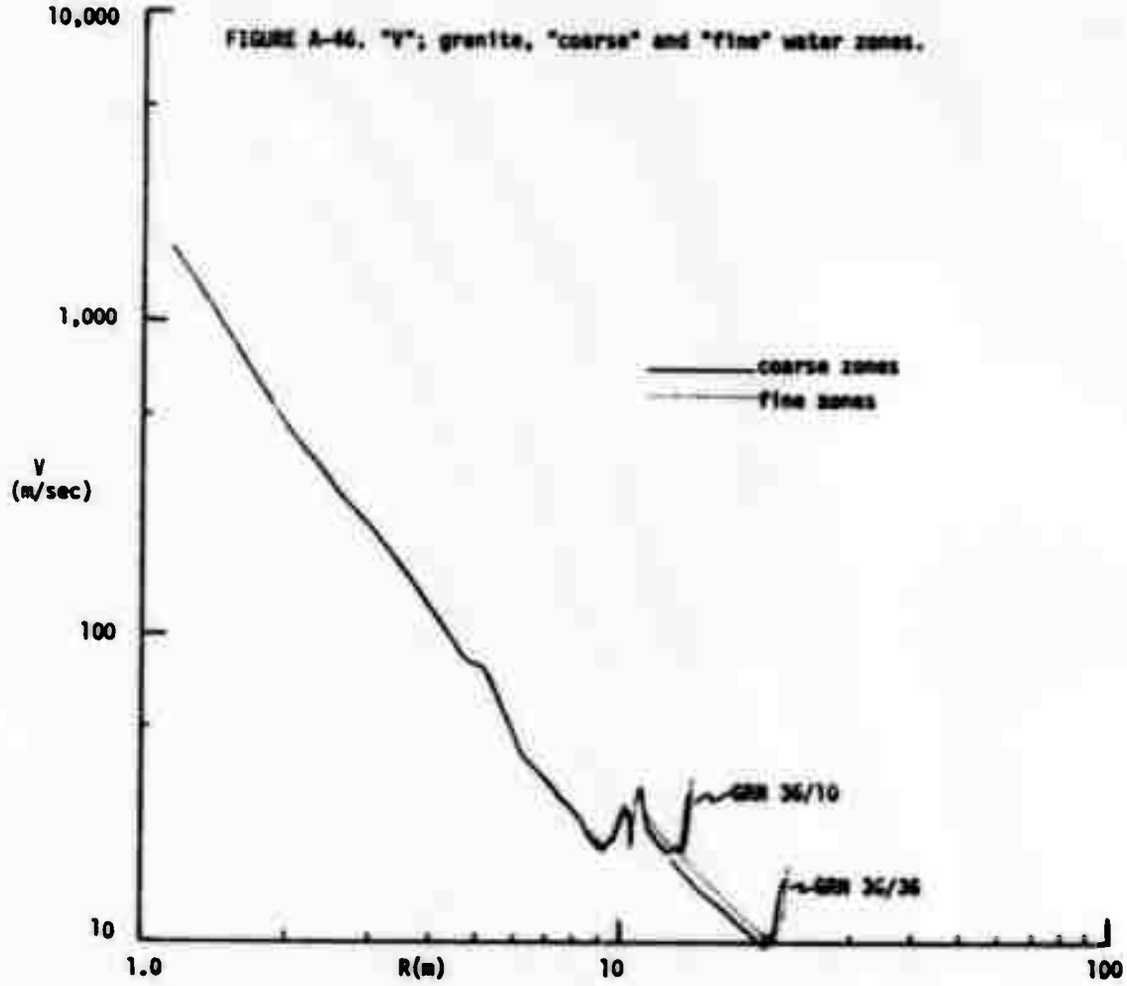

FIGURE A-46. "V"; granite, "coarse" and "fine" water zones.

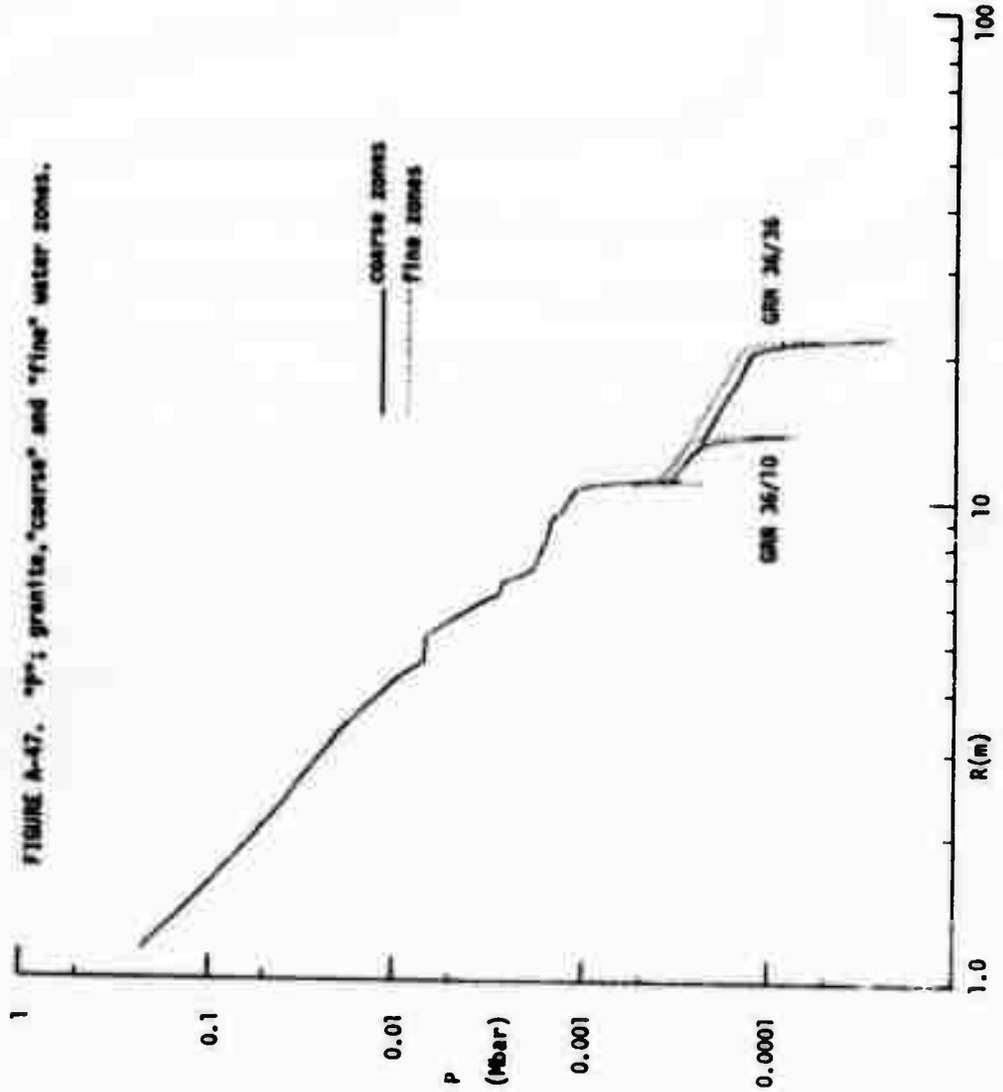

FIGURE A-47. "P"; granite, "coarse" and "fine" water zones.

KEY TO WAVEFORM DIAGRAMS

Key to Waveform Diagrams

Velocity (m/sec)

or

Pressure (Mbar)

(One Megabar ≡ 14.5×10^6 psi)

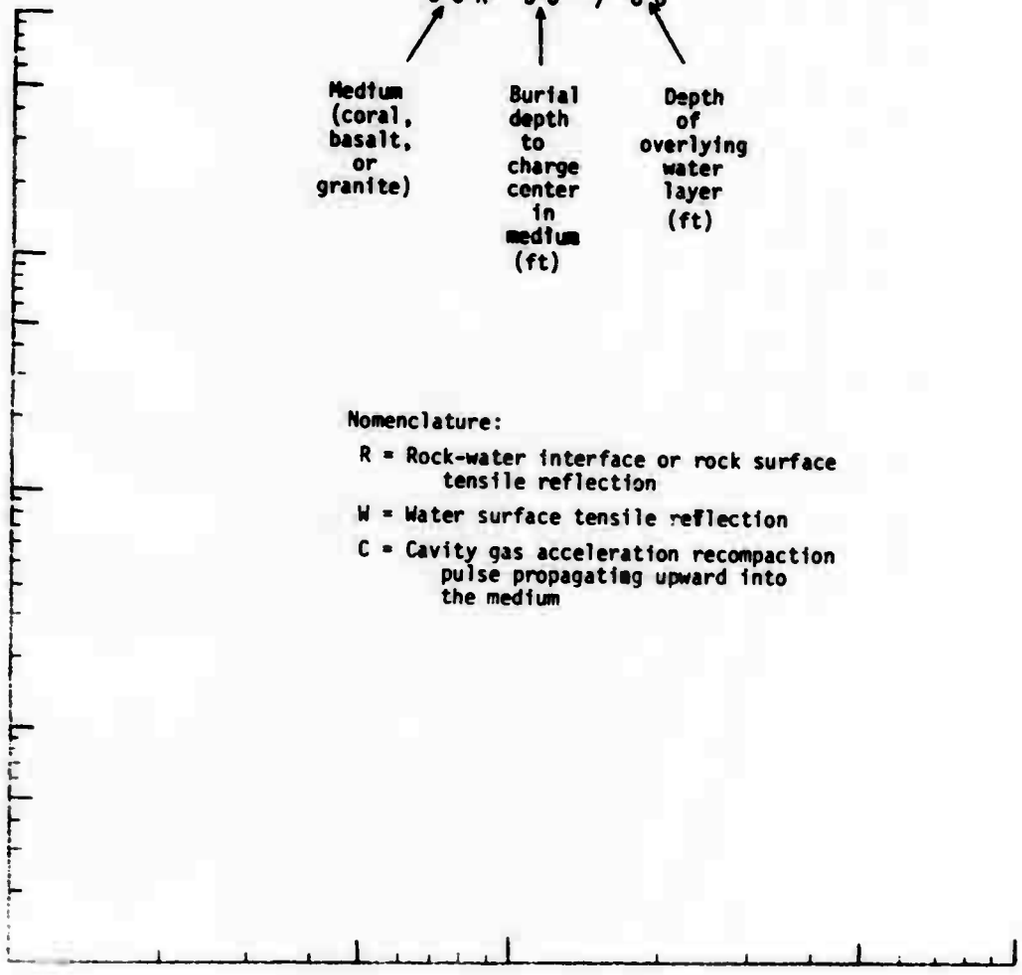

Time (msec) ⟶

Nomenclature:

R = Rock-water interface or rock surface tensile reflection

W = Water surface tensile reflection

C = Cavity gas acceleration recompaction pulse propagating upward into the medium

Appendix B

Waveforms for the Horizontal Calculations in all Media

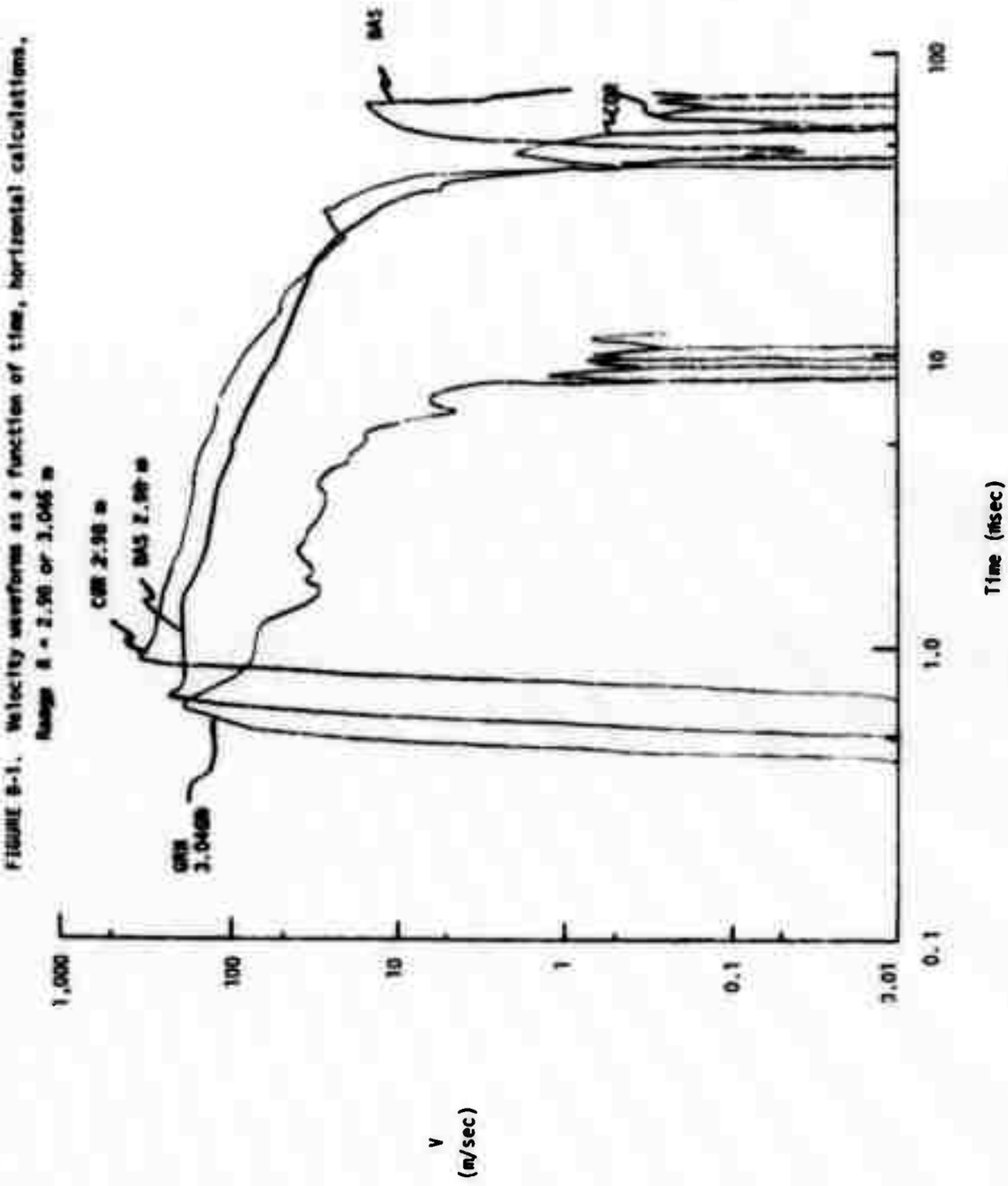

FIGURE B-1. Velocity waveforms as a function of time, horizontal calculations.

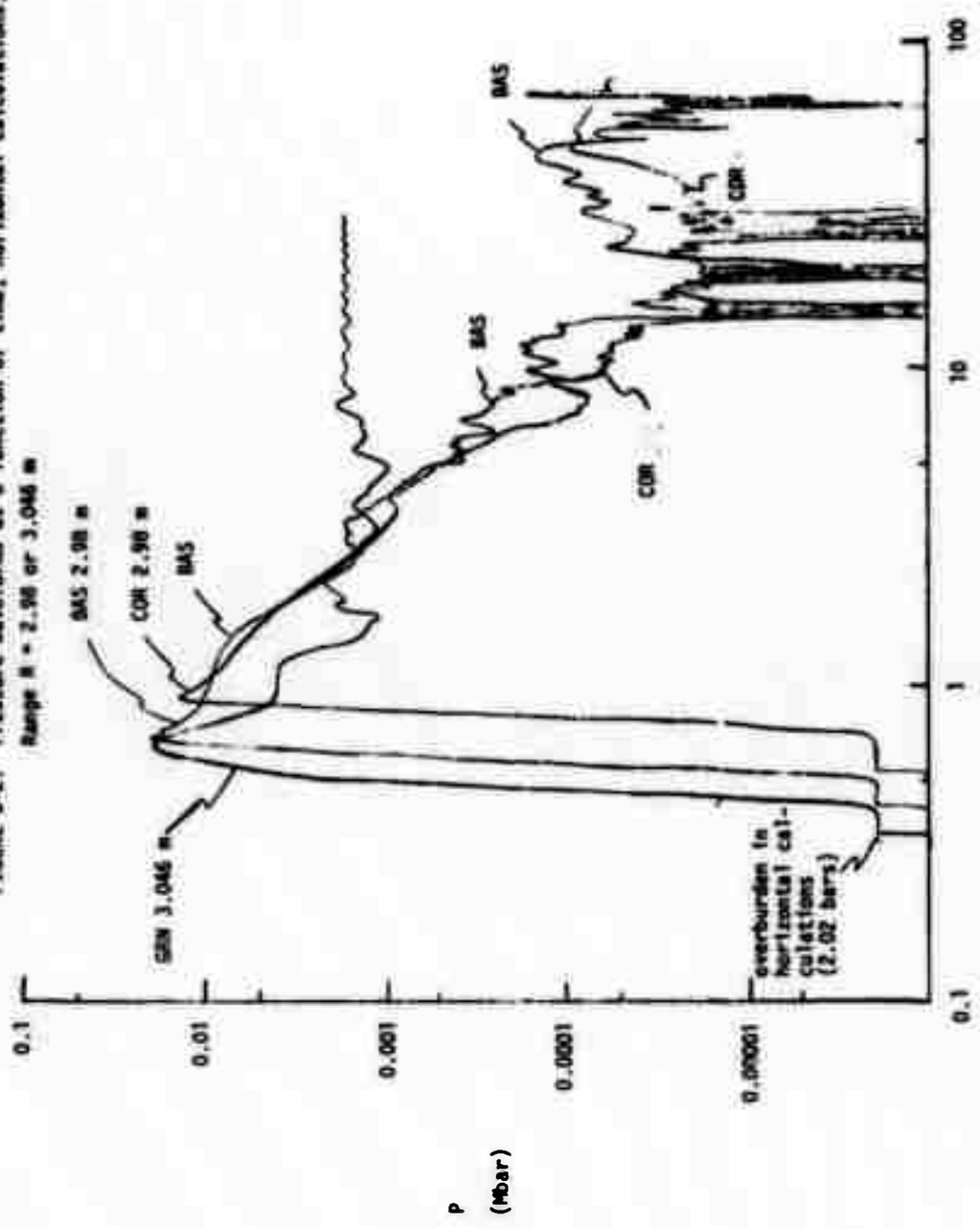

FIGURE B-2. Pressure waveforms as a function of time, horizontal calculations, Range R = 2.98 or 3.046 m

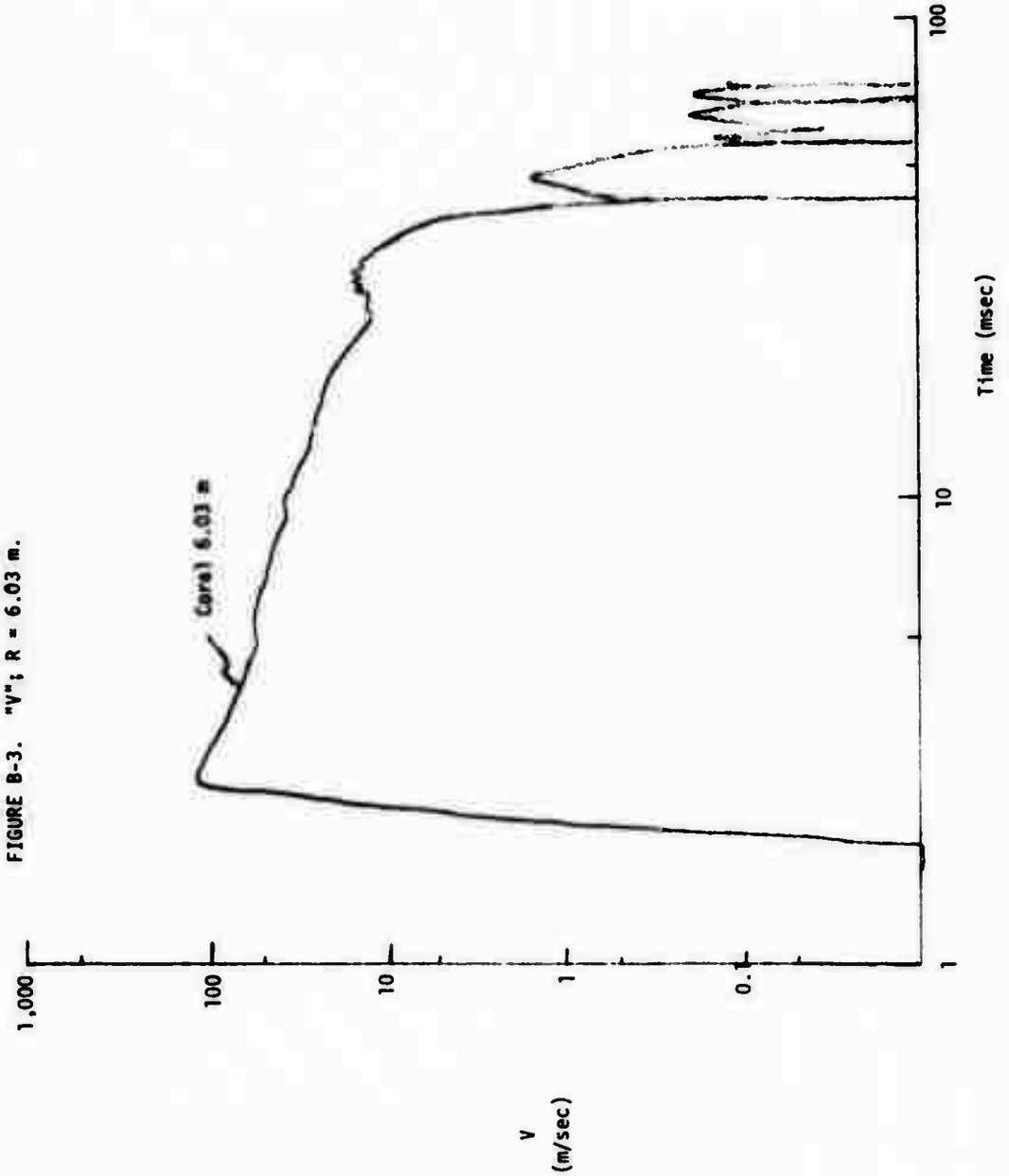

FIGURE B-3. "V"; R = 6.03 m.

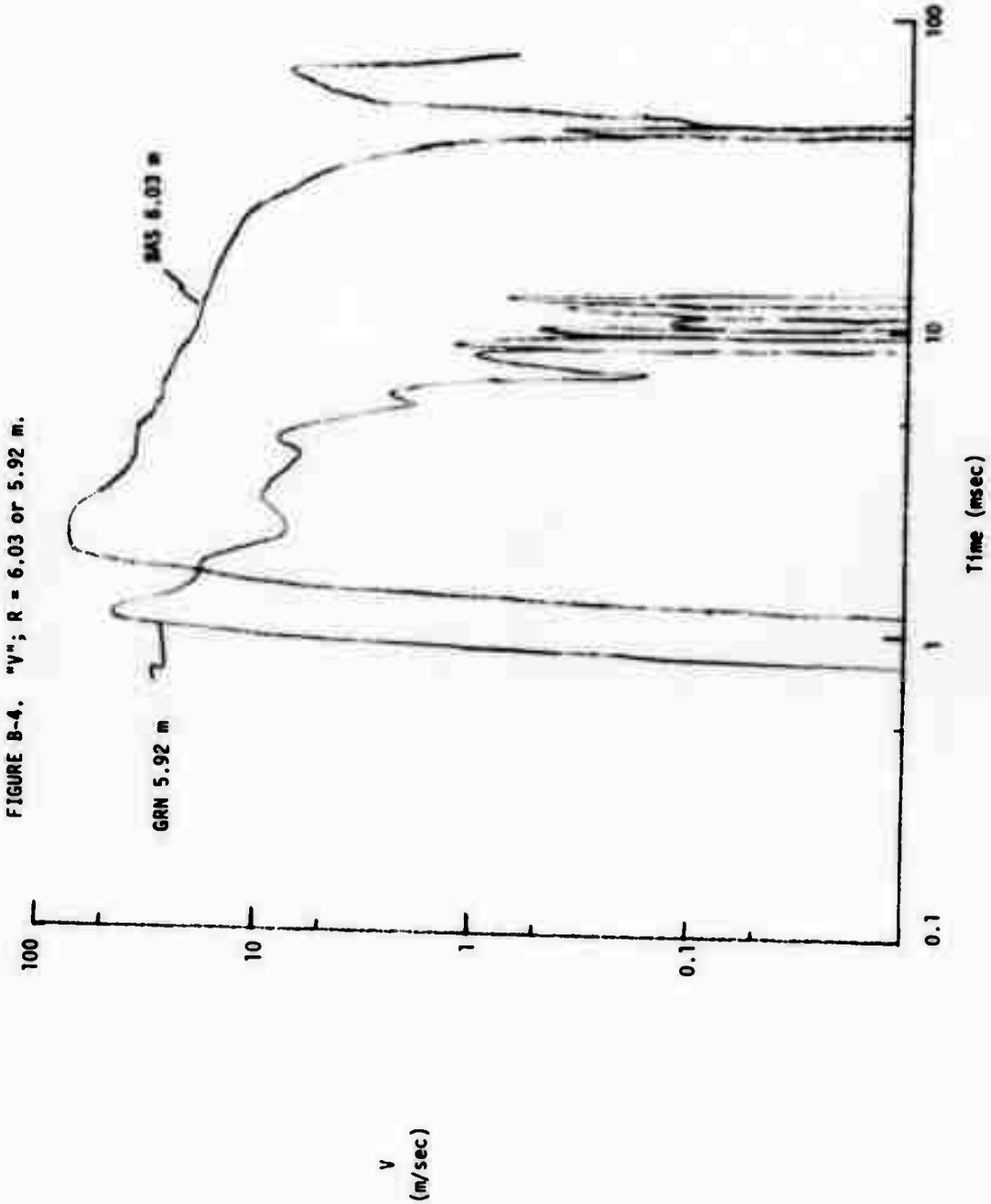

FIGURE B-4. "V"; R = 6.03 or 5.92 m.

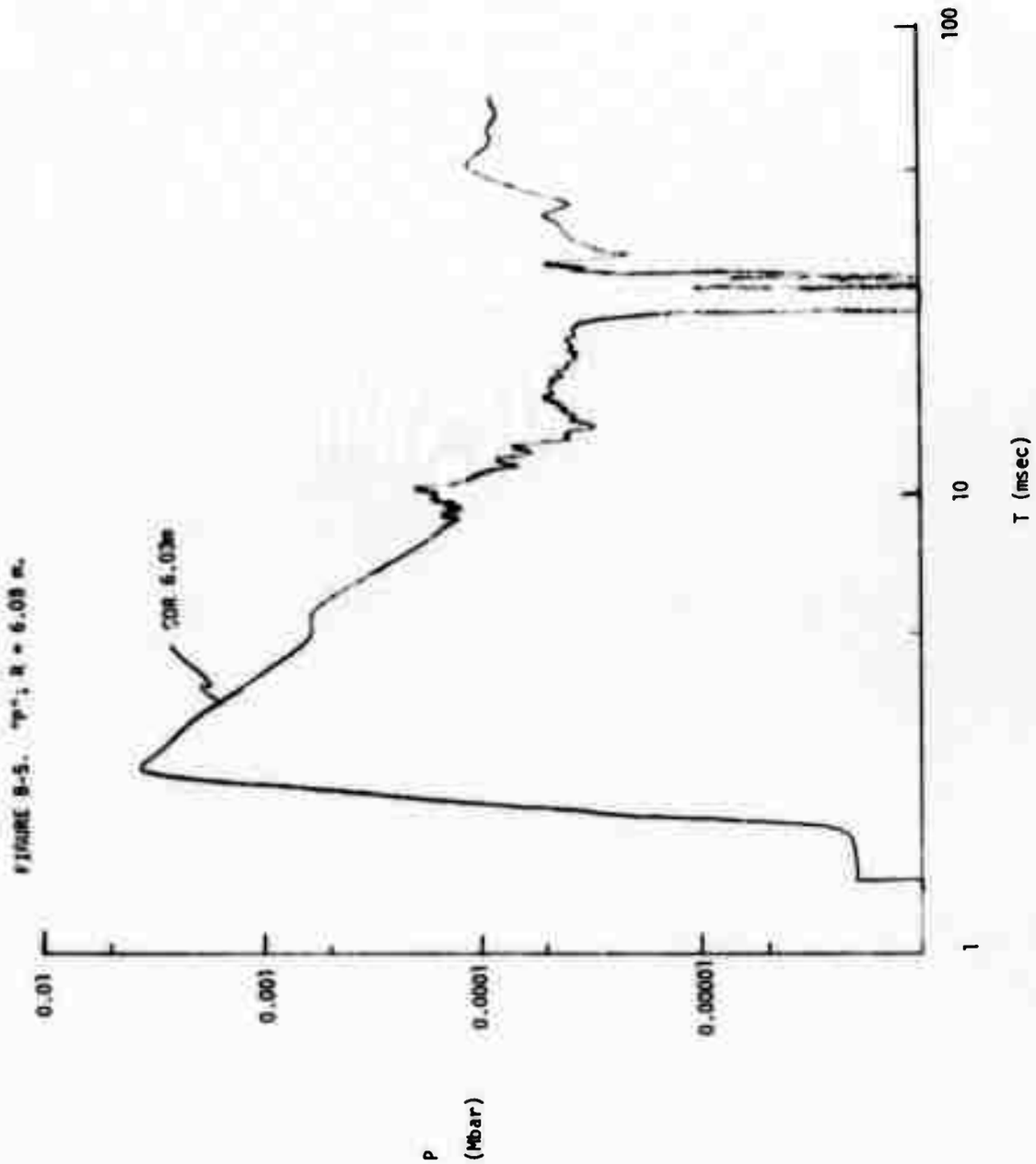
FIGURE B-5. "P"; R = 6.03 m.
CDR 6.03m
0.01
0.001
0.0001
0.00001
P
(Mbar)
1
10
100
T (msec)

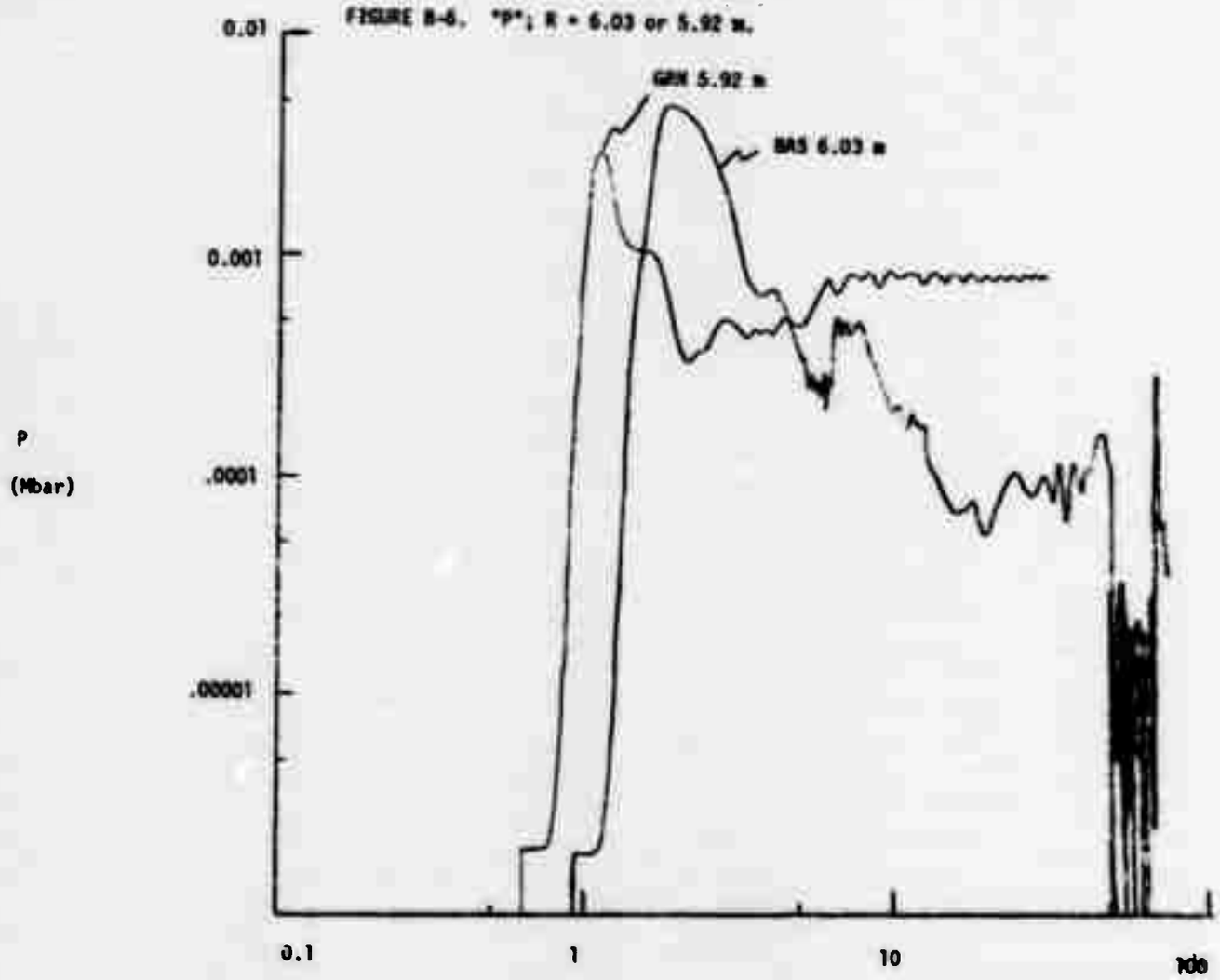
FIGURE B-6. "P"; R = 6.03 or 5.92 m.
GRN 5.92 m
BAS 6.03 m
0.01
0.001
.0001
.00001
P
(Mbar)
0.1
1
10
100
I (msec)

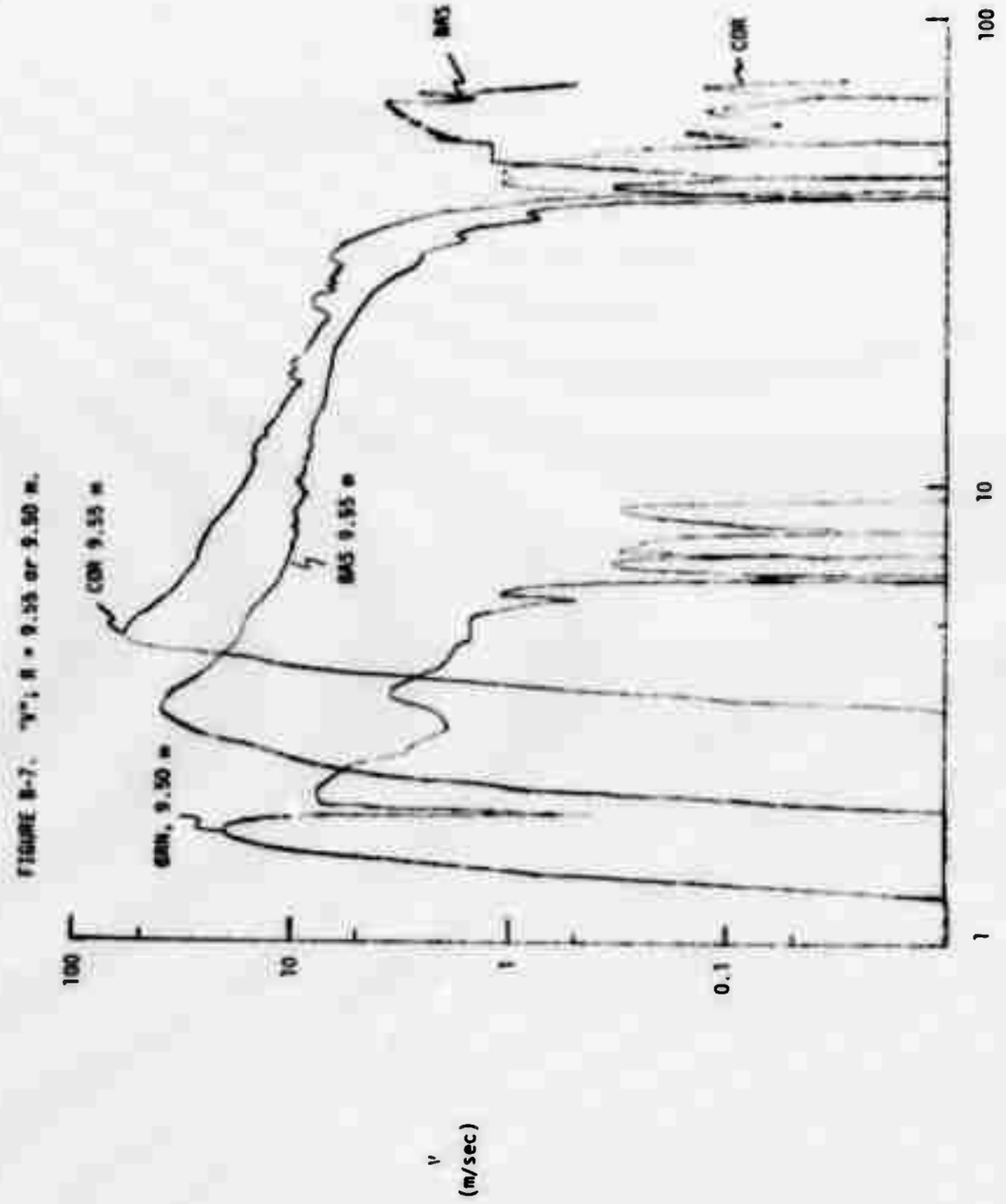

FIGURE B-7. "v"; R = 9.55 or 9.50 m.

FIGURE B-8. "F"; R = 9.55 or 9.50 m.

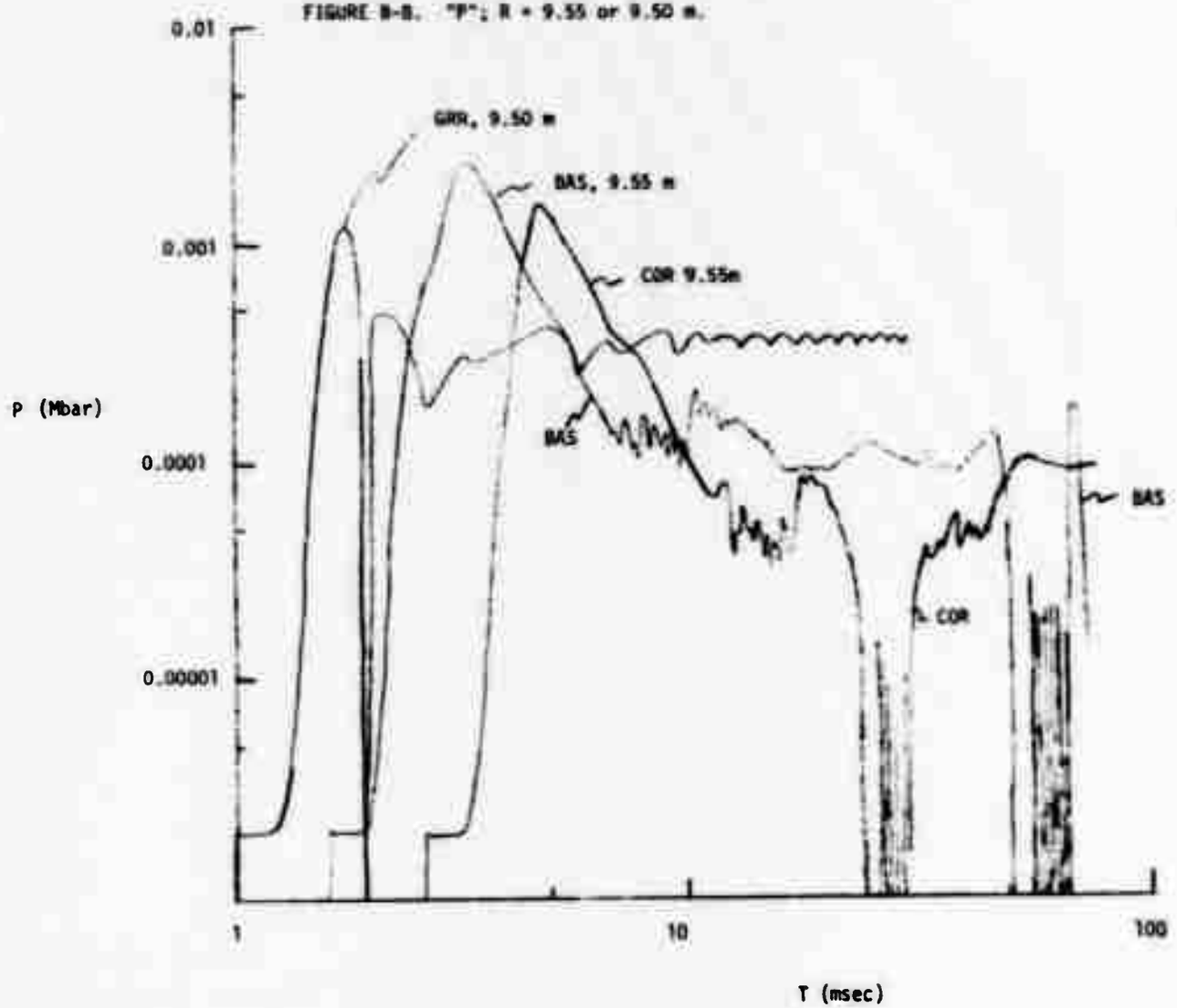

FIGURE 8-9. "V"; R = 12.07 or 12.02 m.

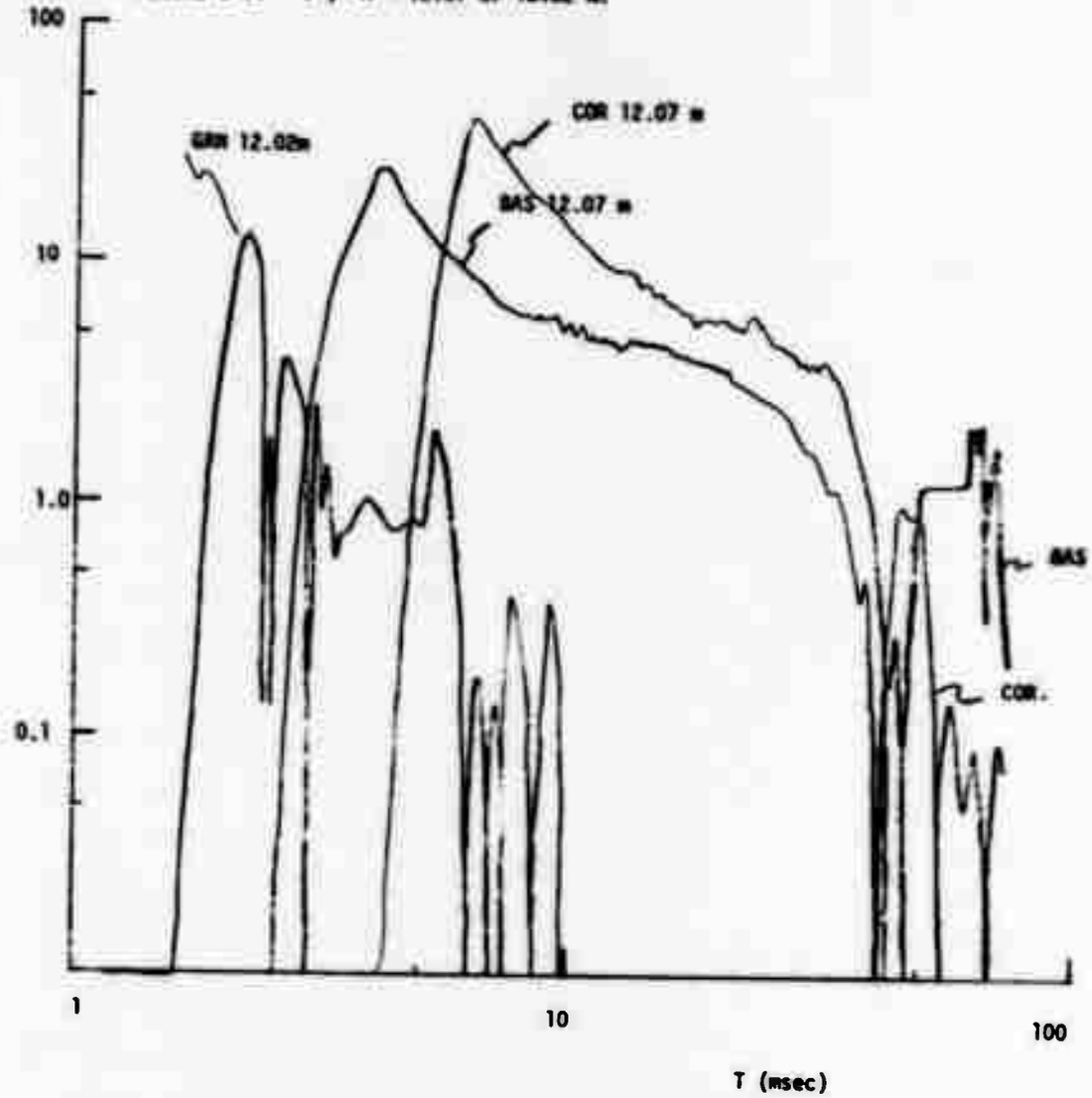

V

(m/sec)

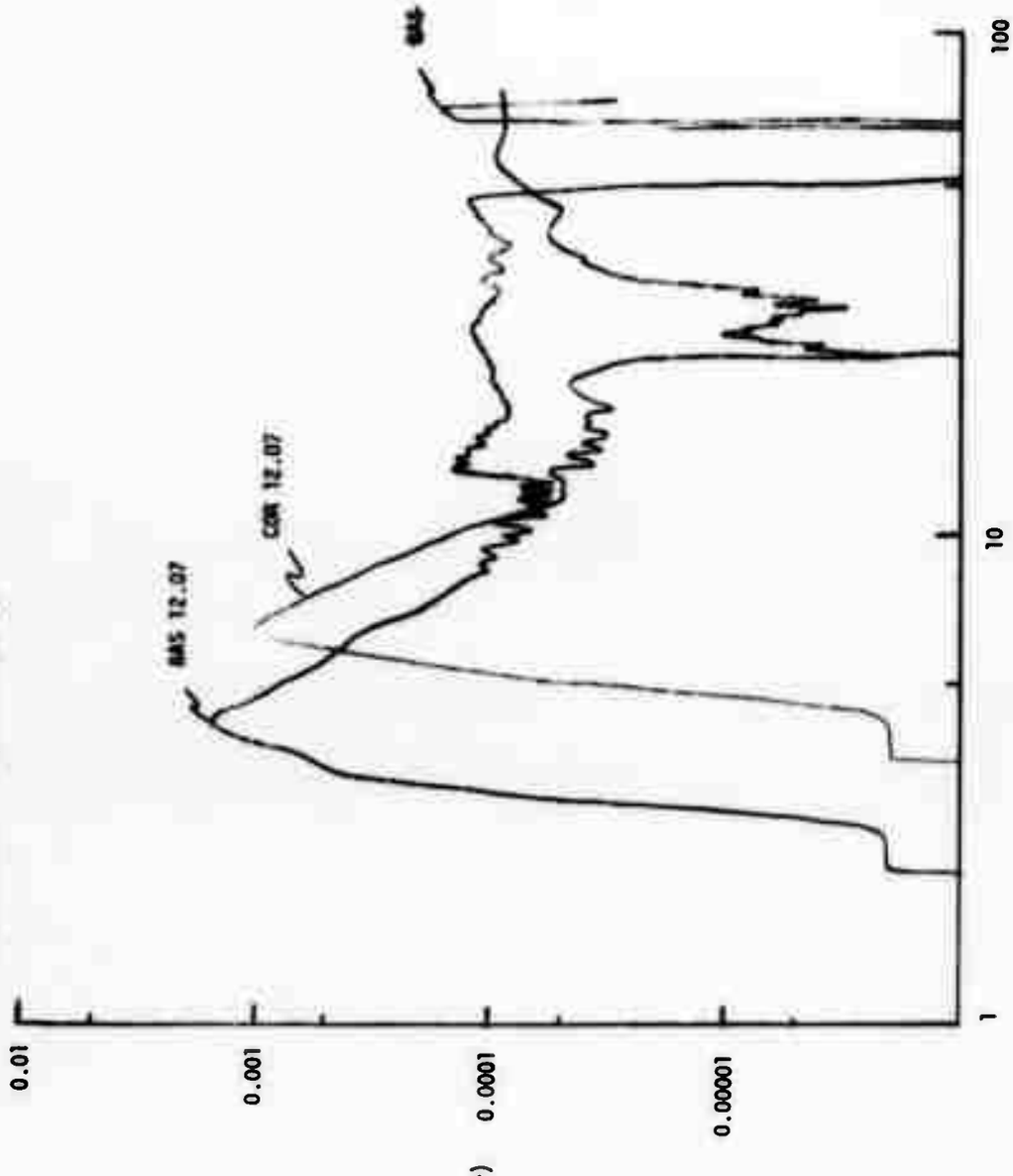

FIGURE B-10. "P"; R = 12.07 m.

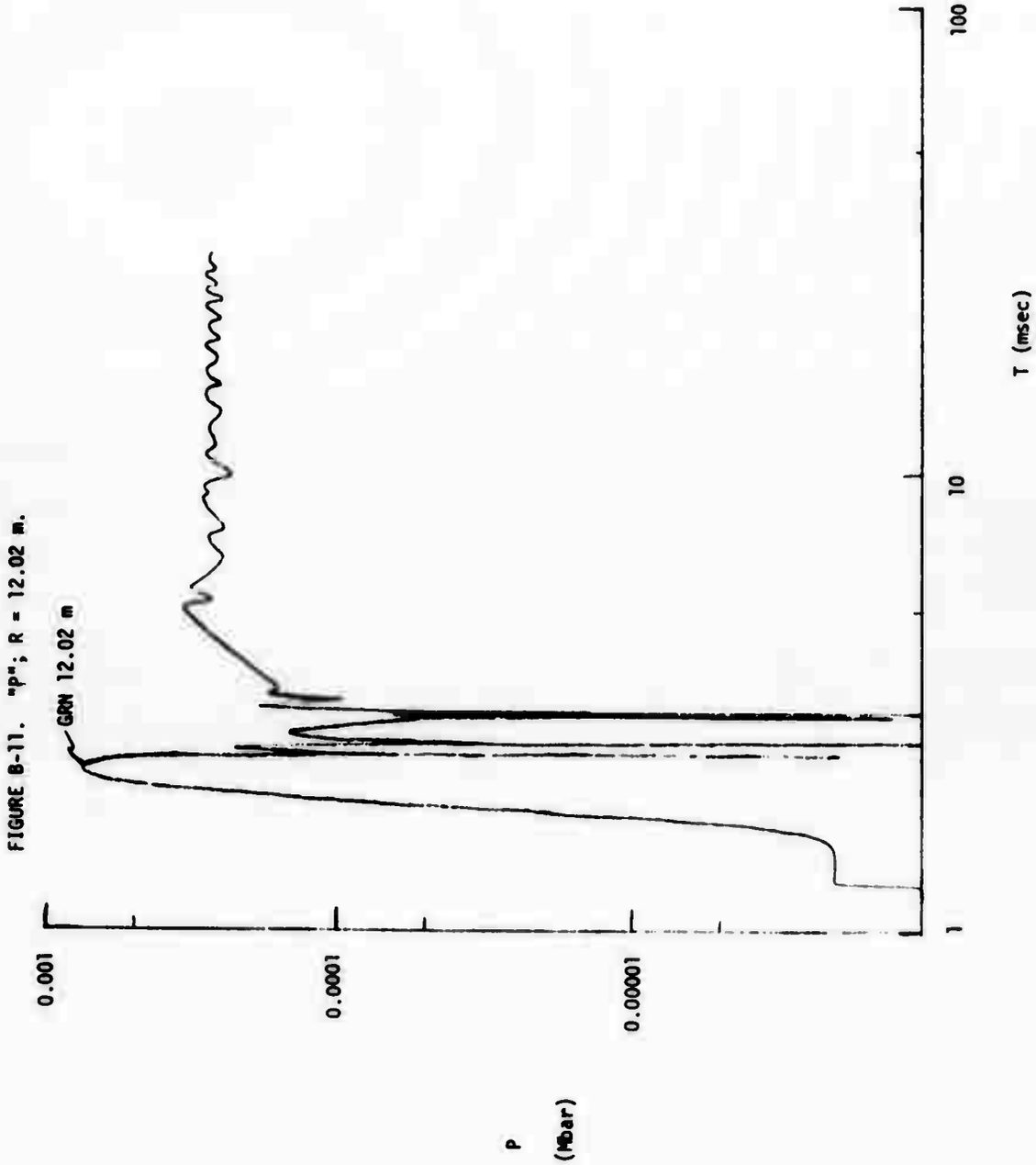

FIGURE B-11. "P"; R = 12.02 m.

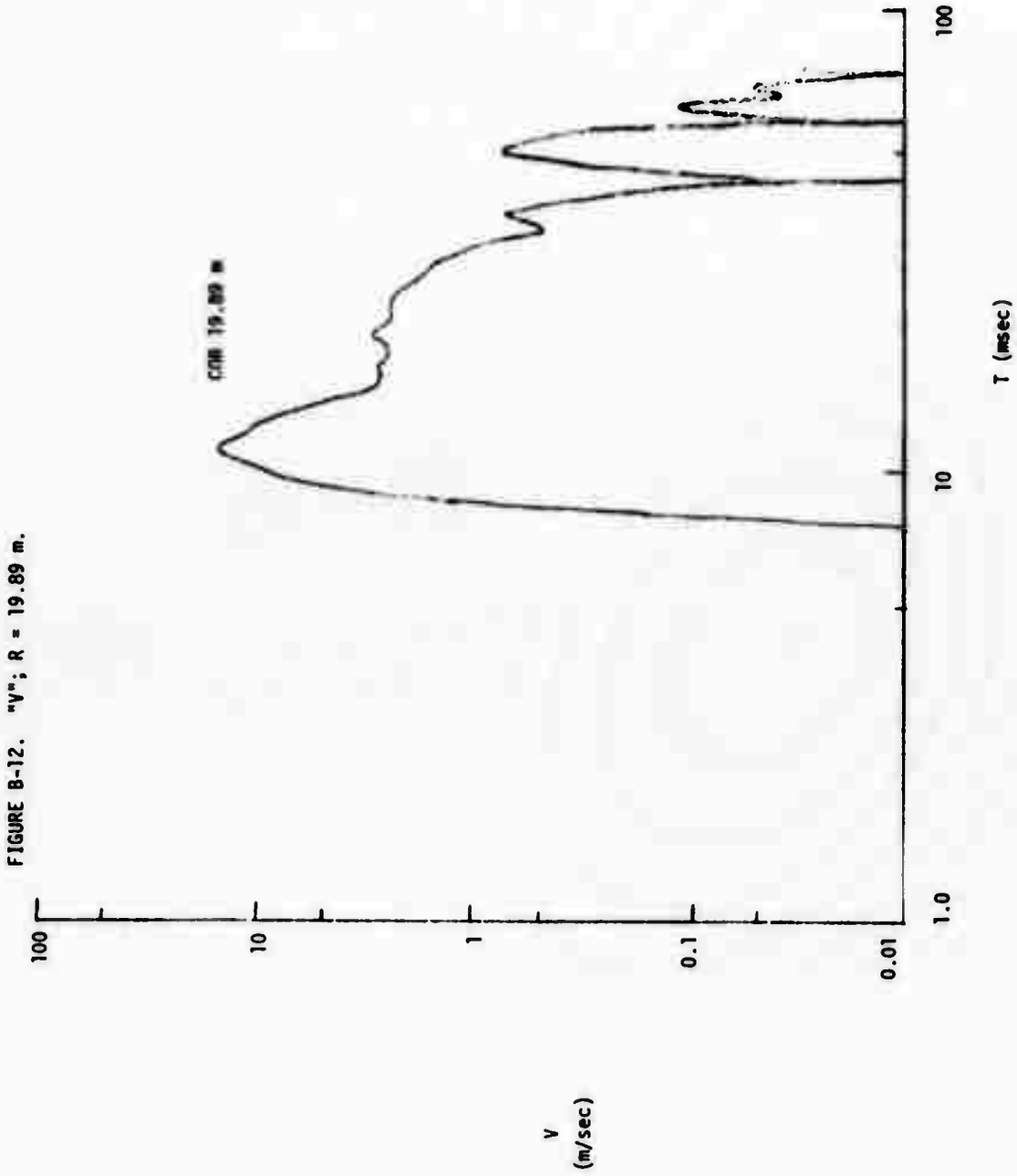

FIGURE B-12. "V"; R = 19.89 m.

FIGURE 8-13. "V"; R = 19.88 or 19.74 m.

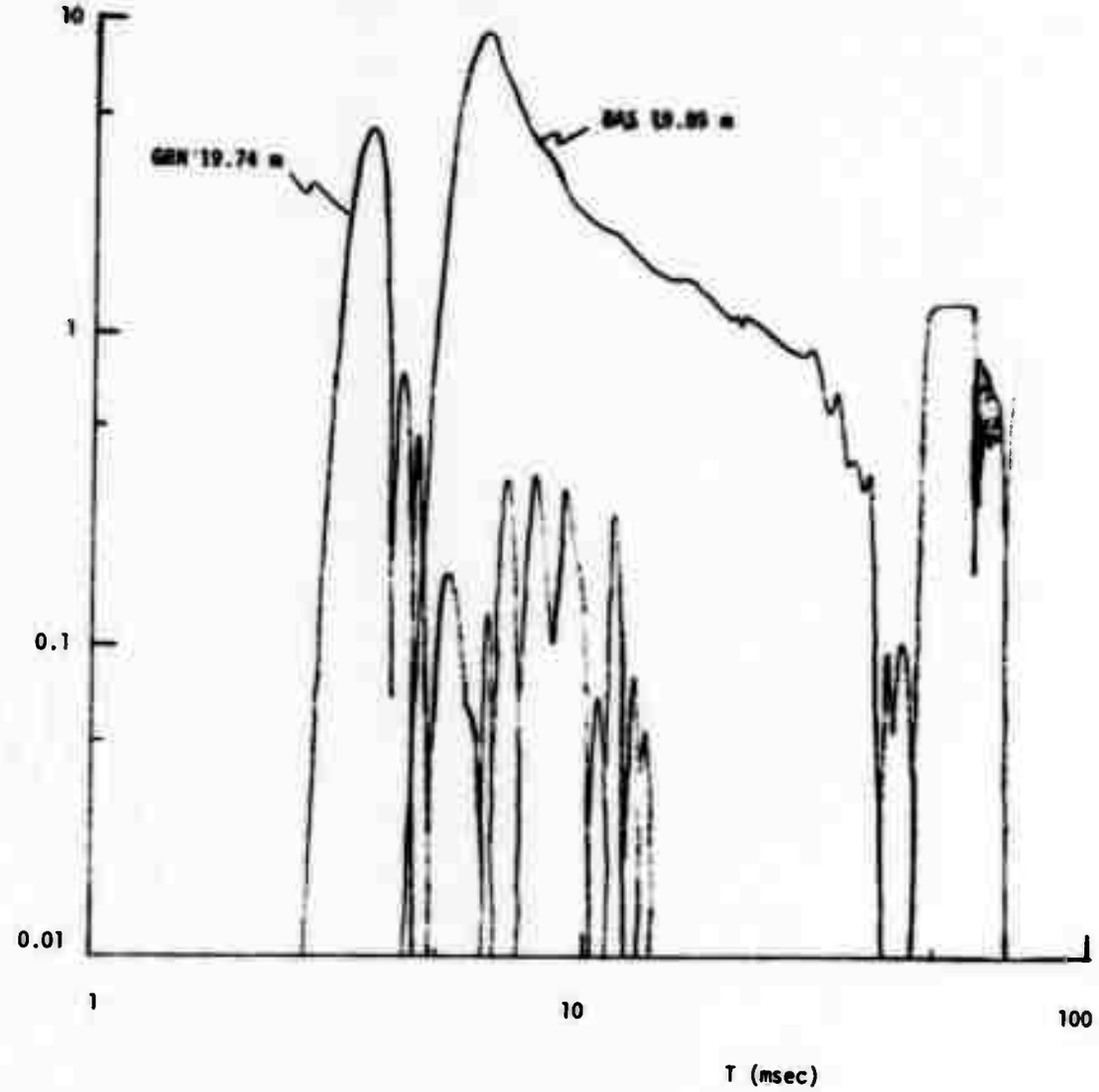

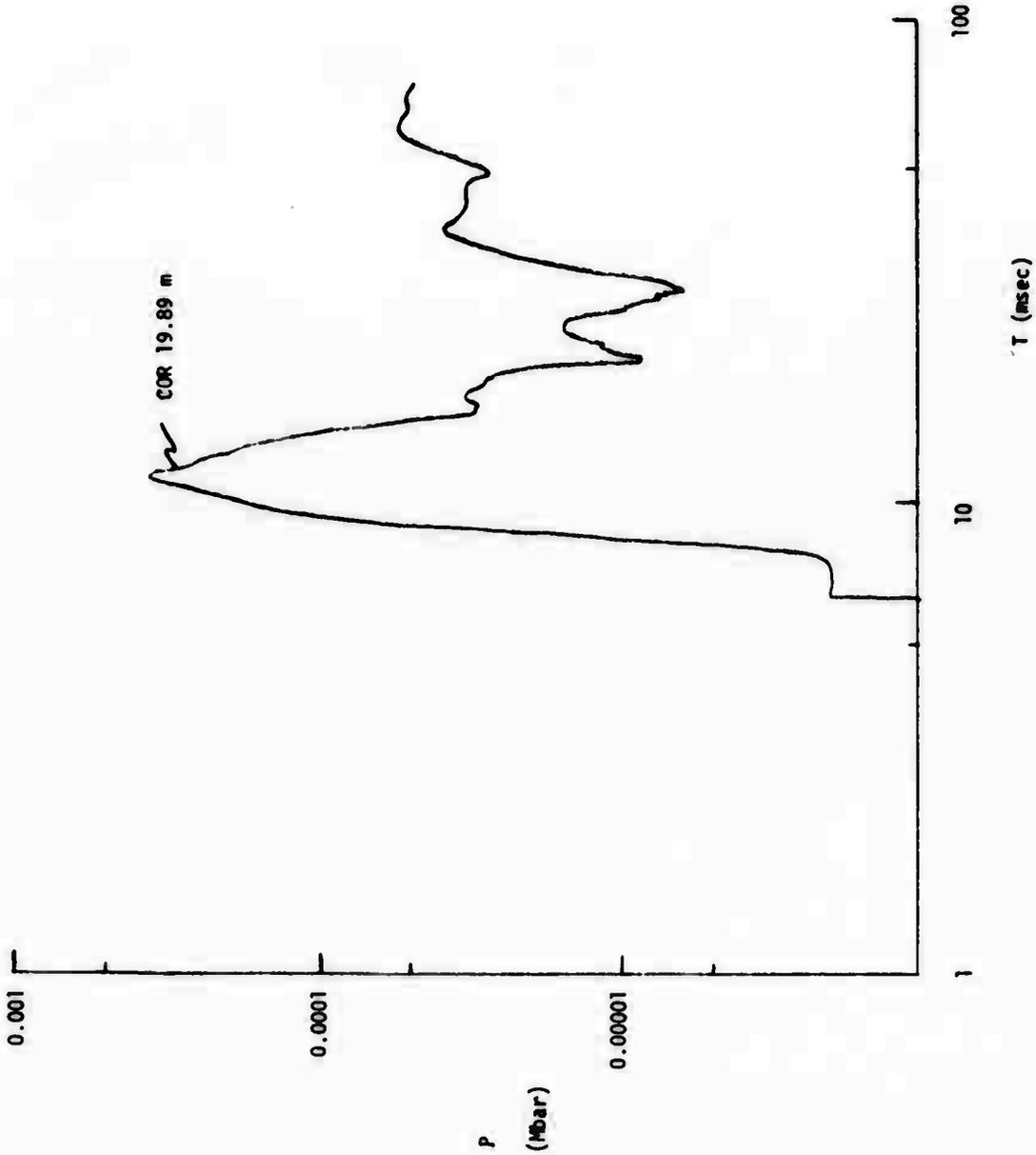

FIGURE B-14. "P"; R = 19.89 m.

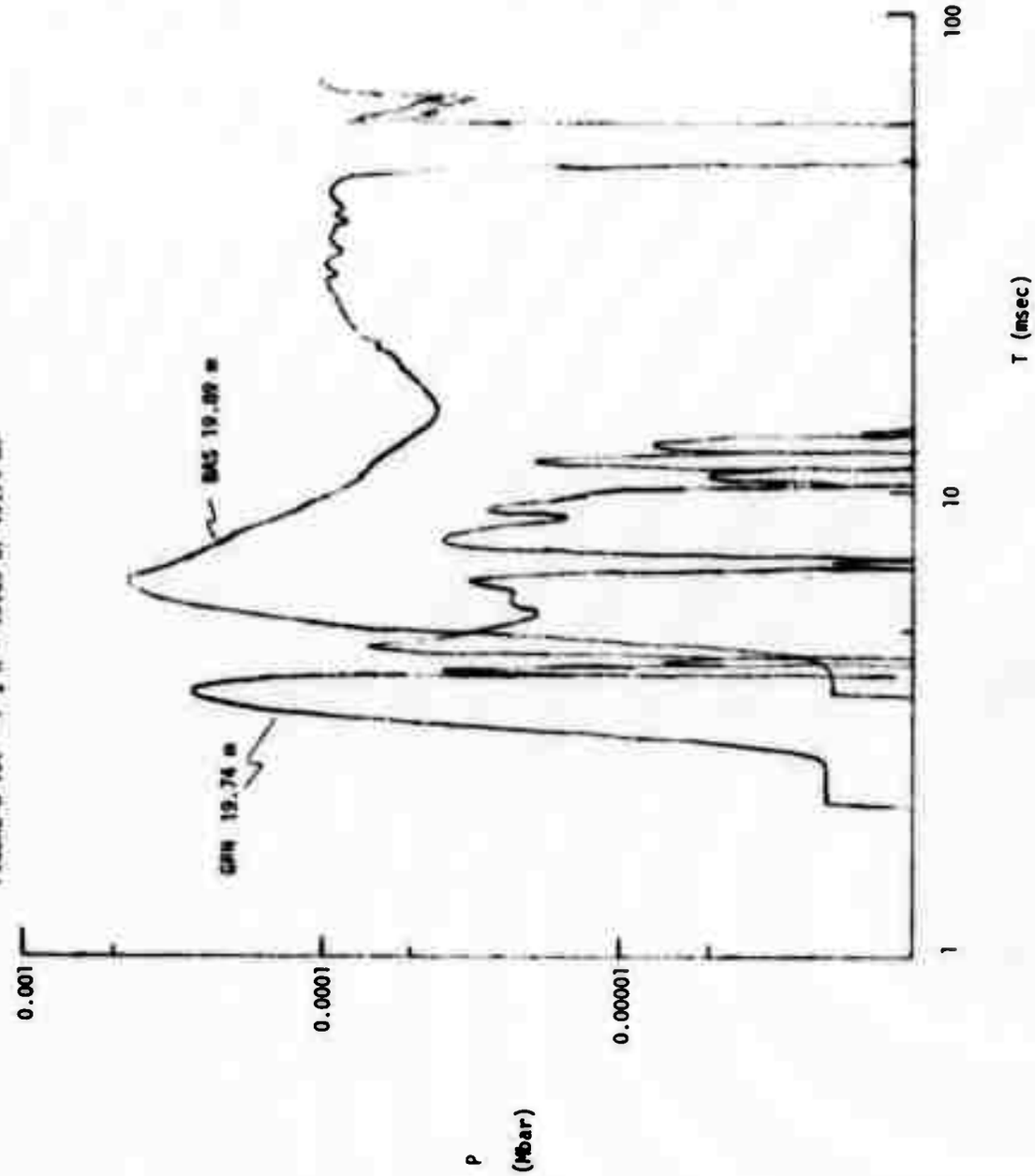

FIGURE B-15. "P"; R = 19.89 or 19.74 m.

Figure [illegible]. "P"; R = 17.0 m (granite).

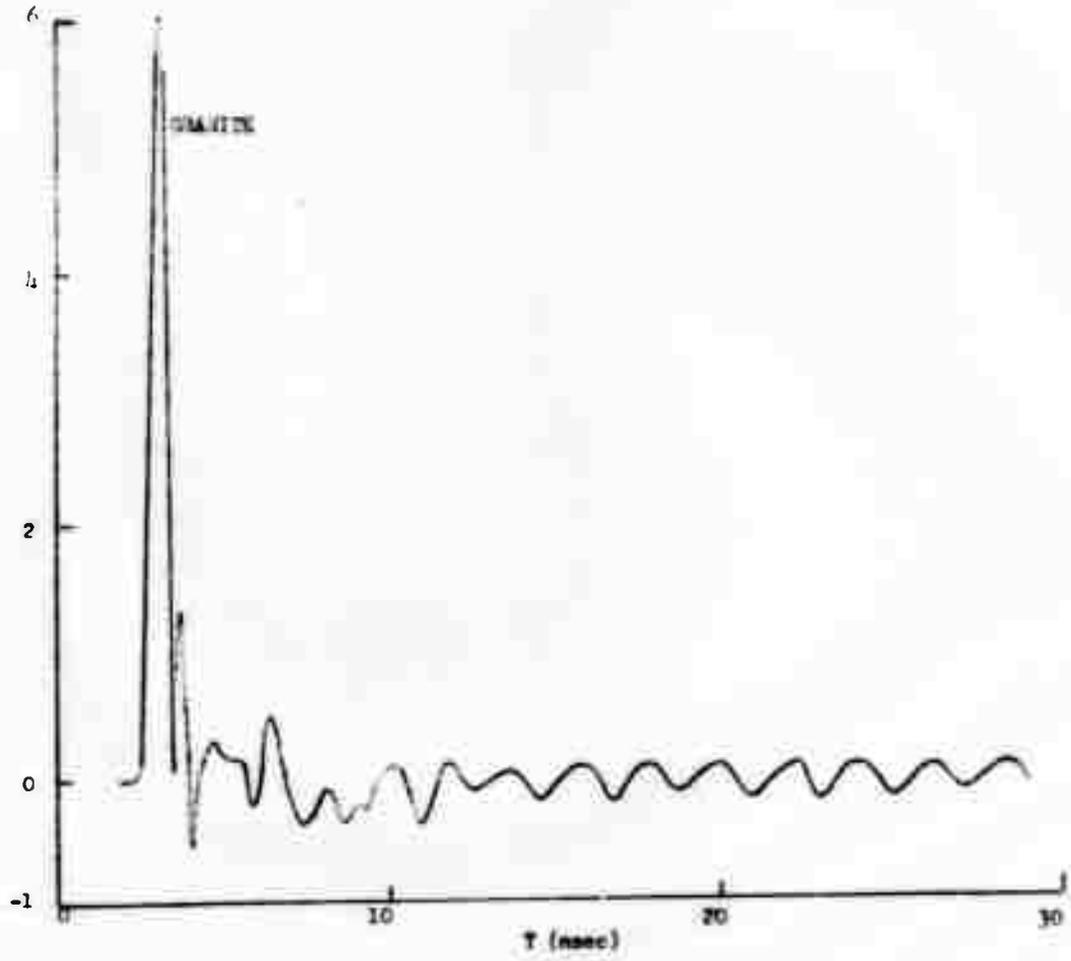

Figure B-17. "P"; R = 17.06 m (granite).

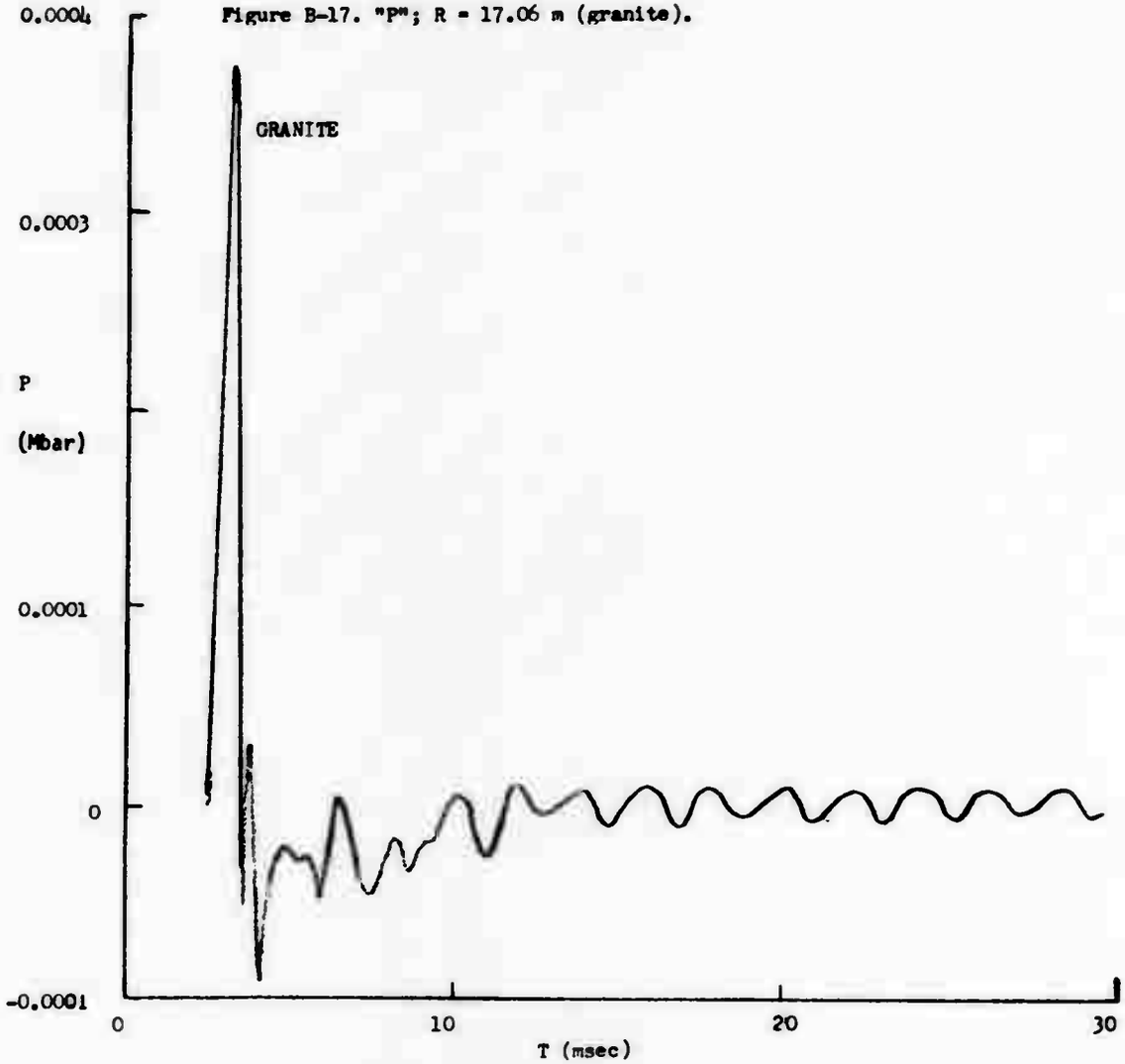

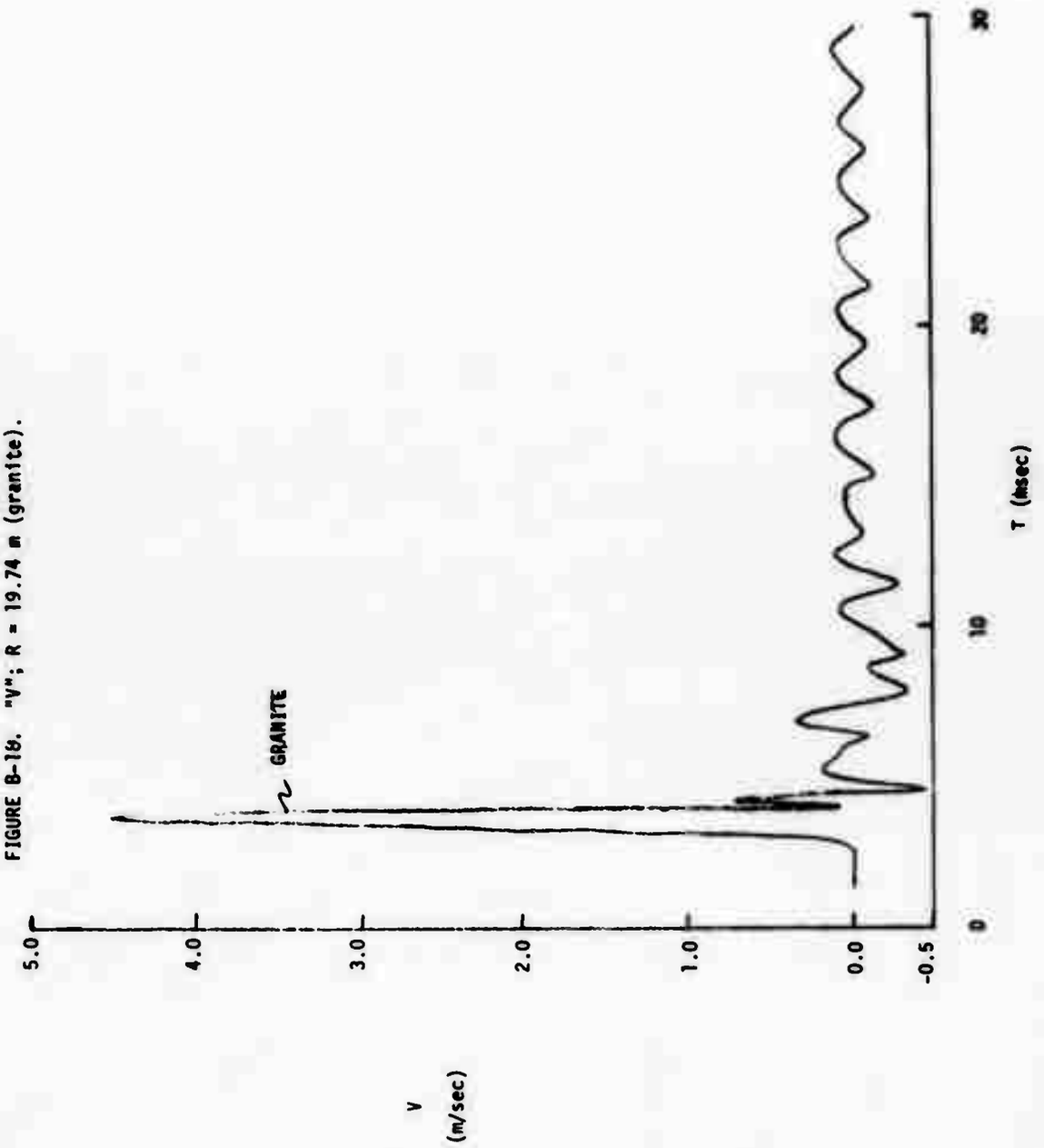

FIGURE B-18. "V"; R = 19.74 m (granite).

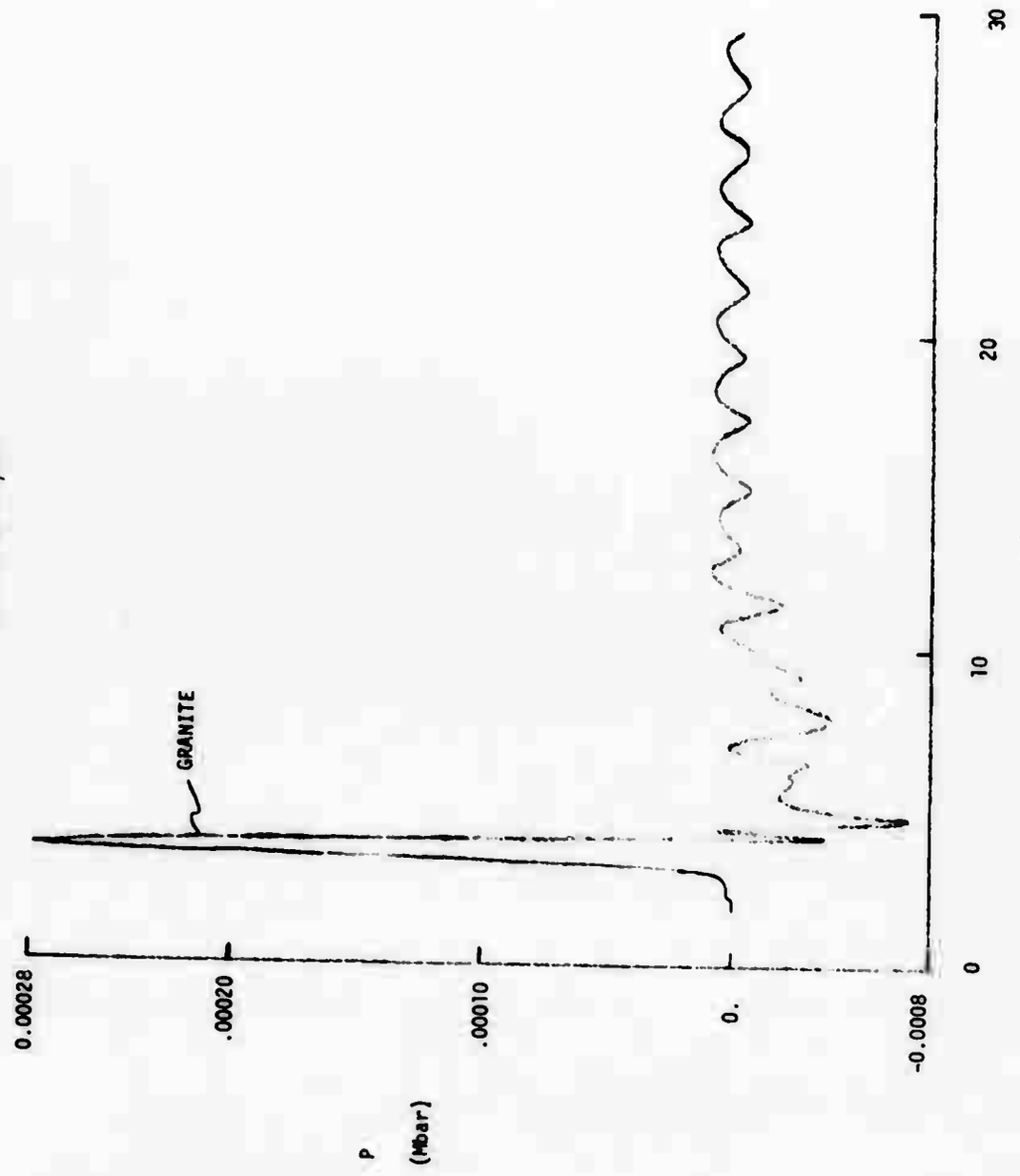

FIGURE B-19. "p"; R = 19.74 m (granite).

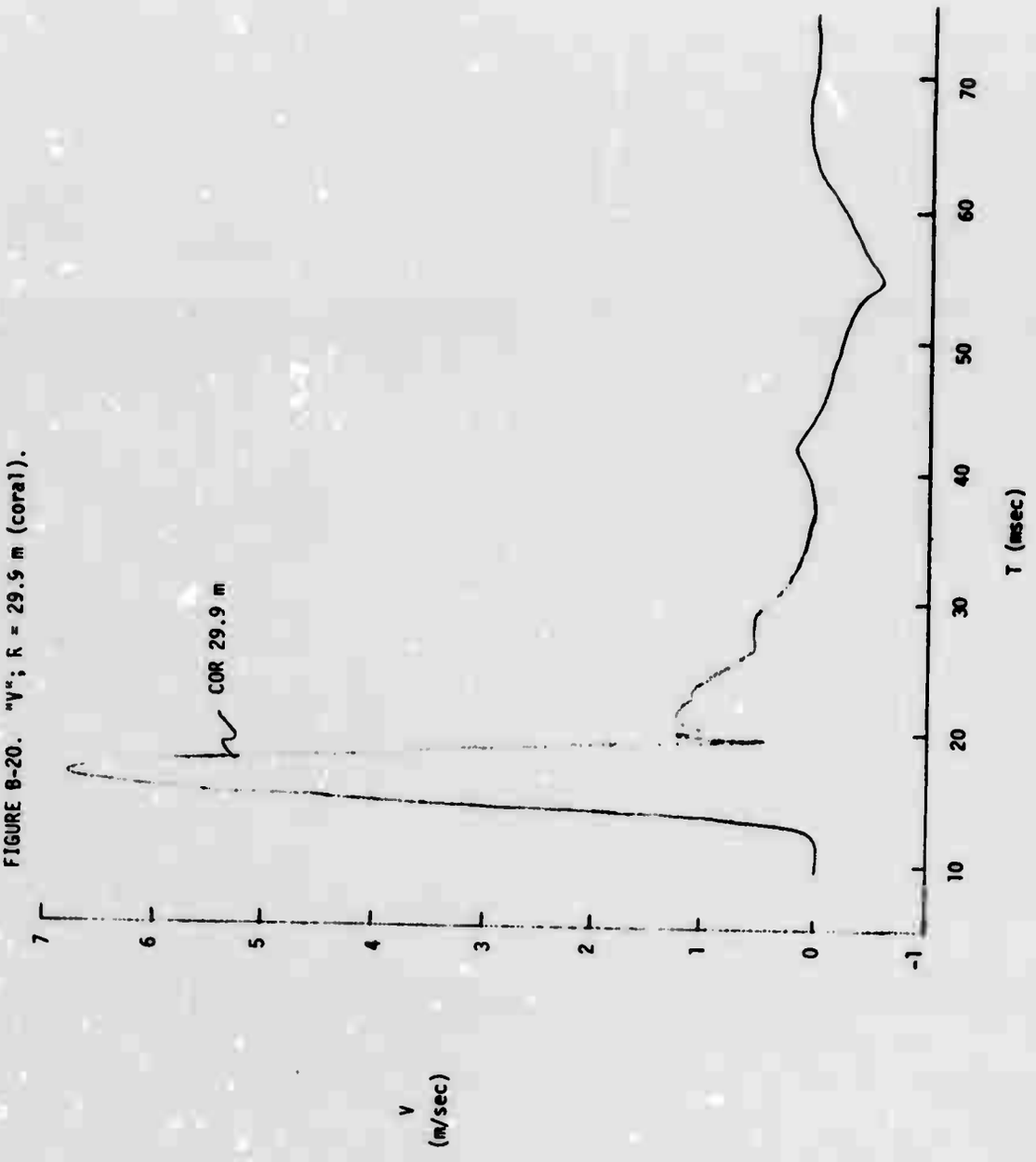

FIGURE B-20. "V"; R = 29.9 m (coral).

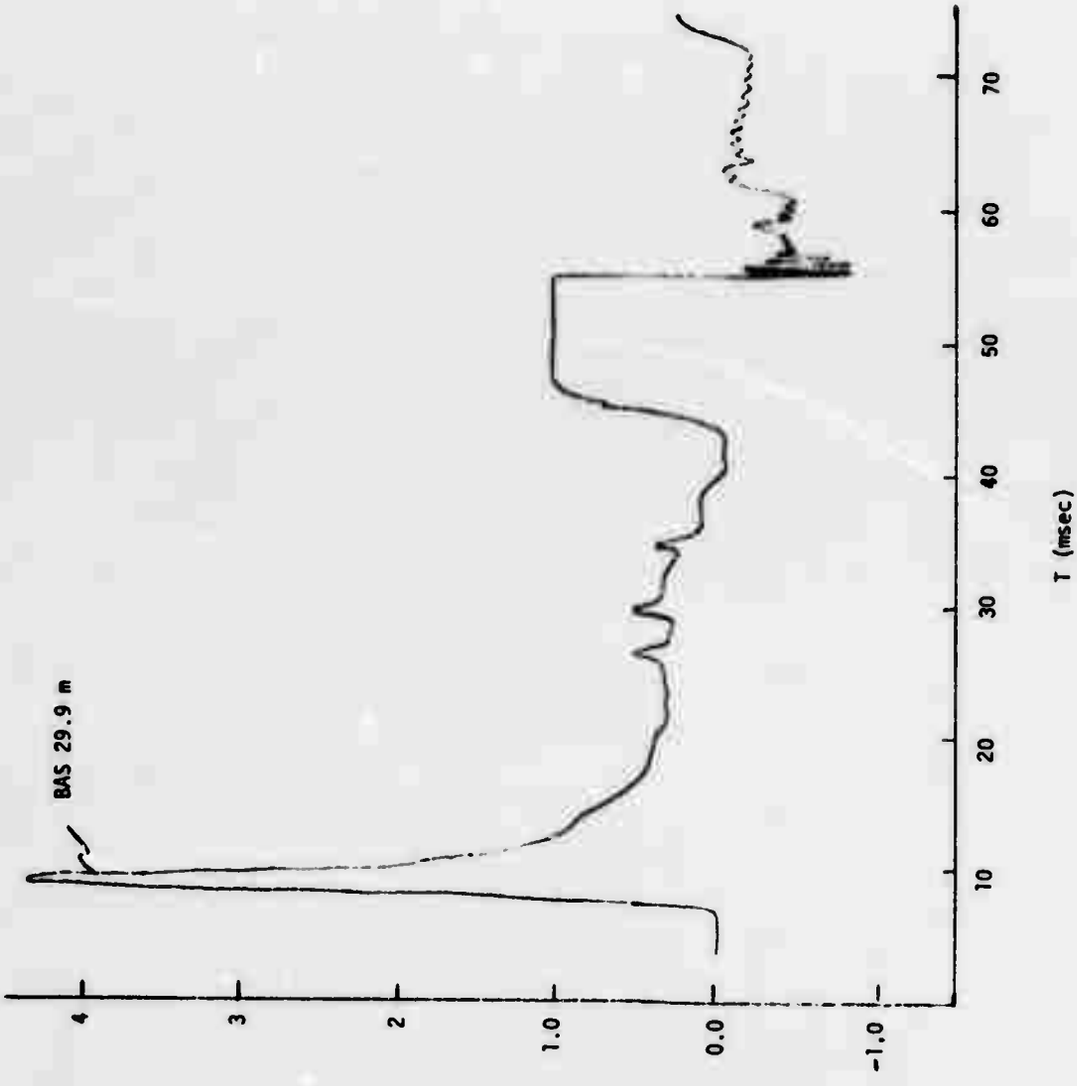

FIGURE B-21. "V"; R = 29.9 m (basalt)

FIGURE B-22. "P"; R = 29.9 m (core).

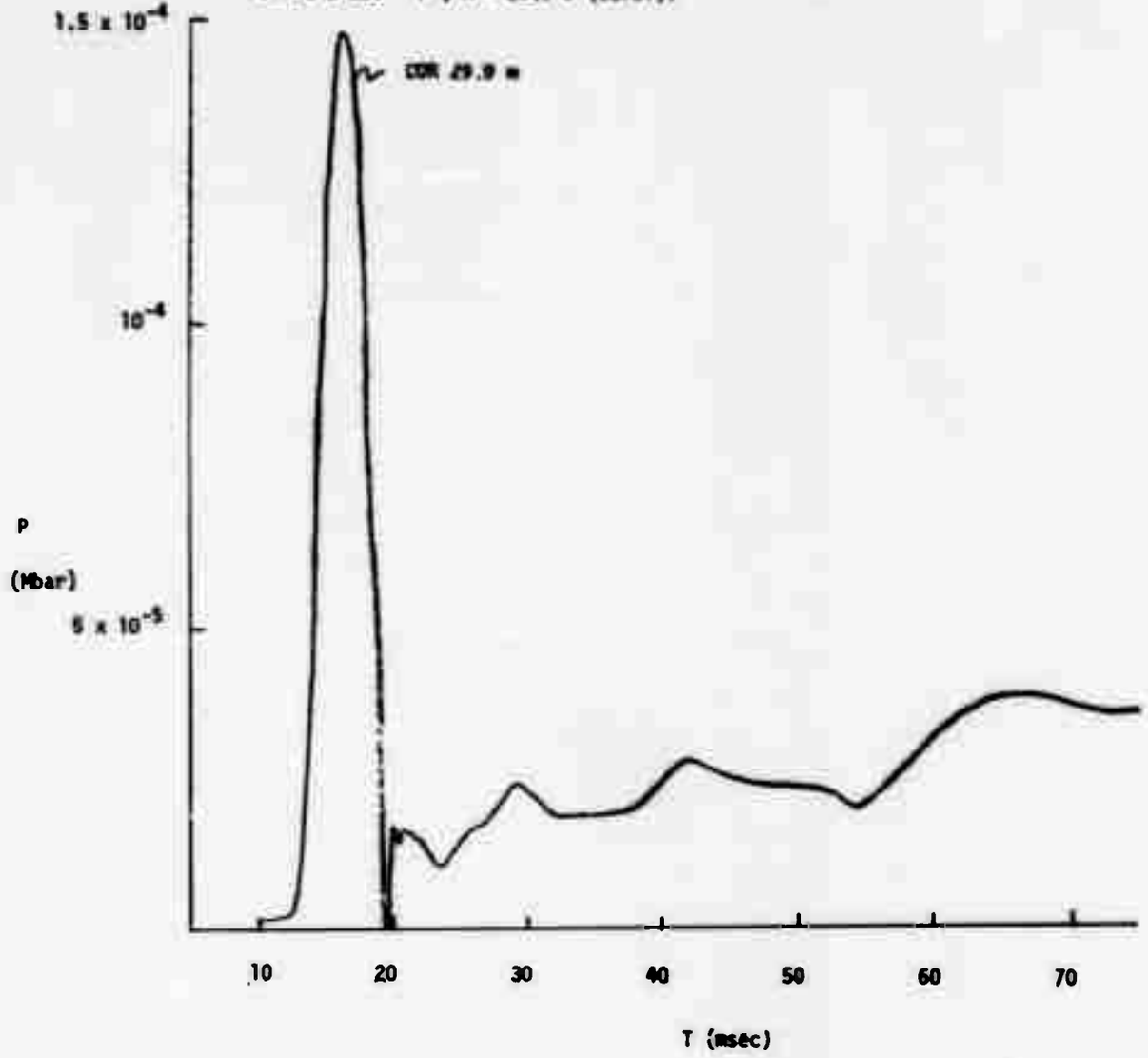

FIGURE B-23. "P"; R = 29.9 m (basalt).

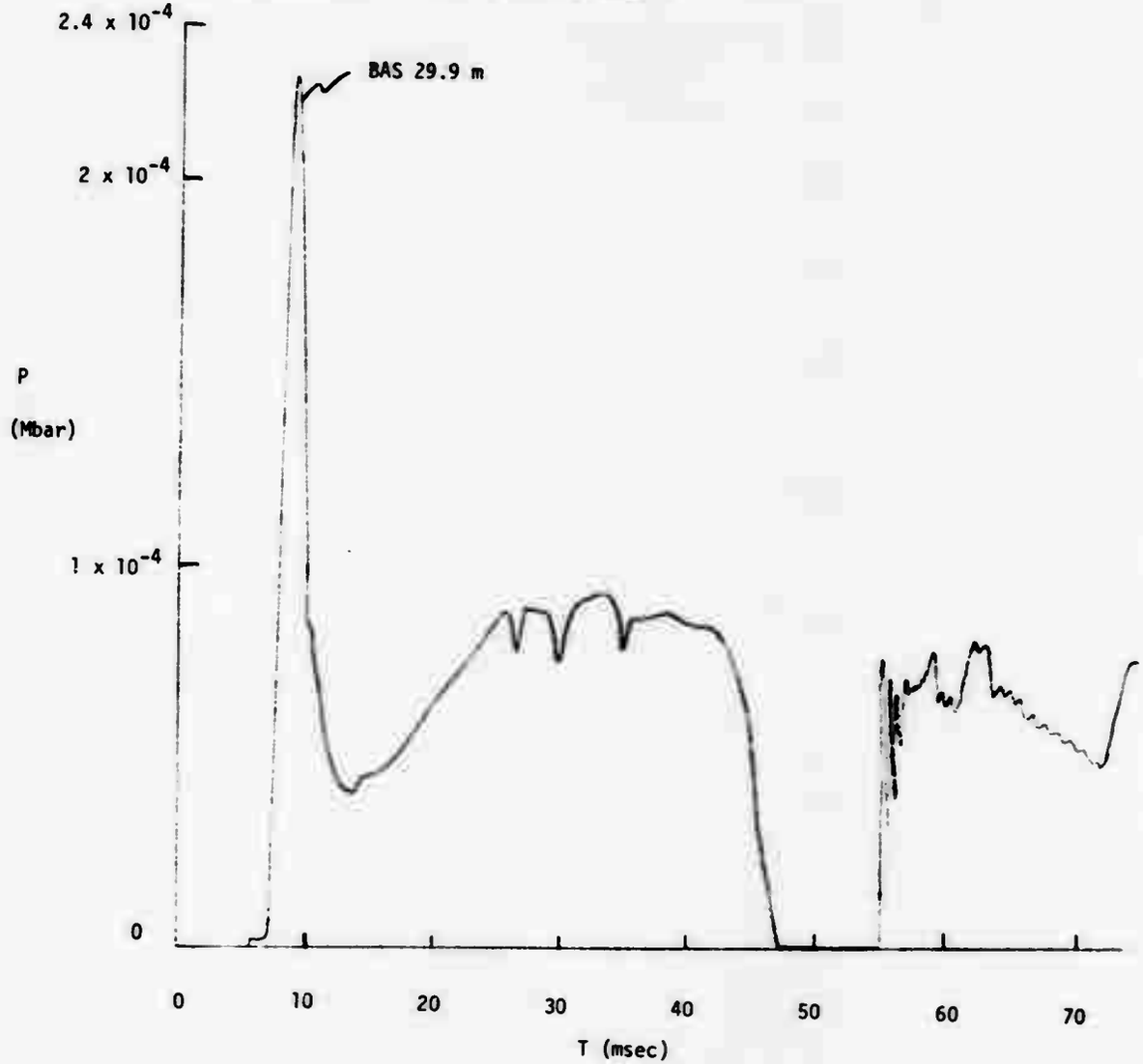

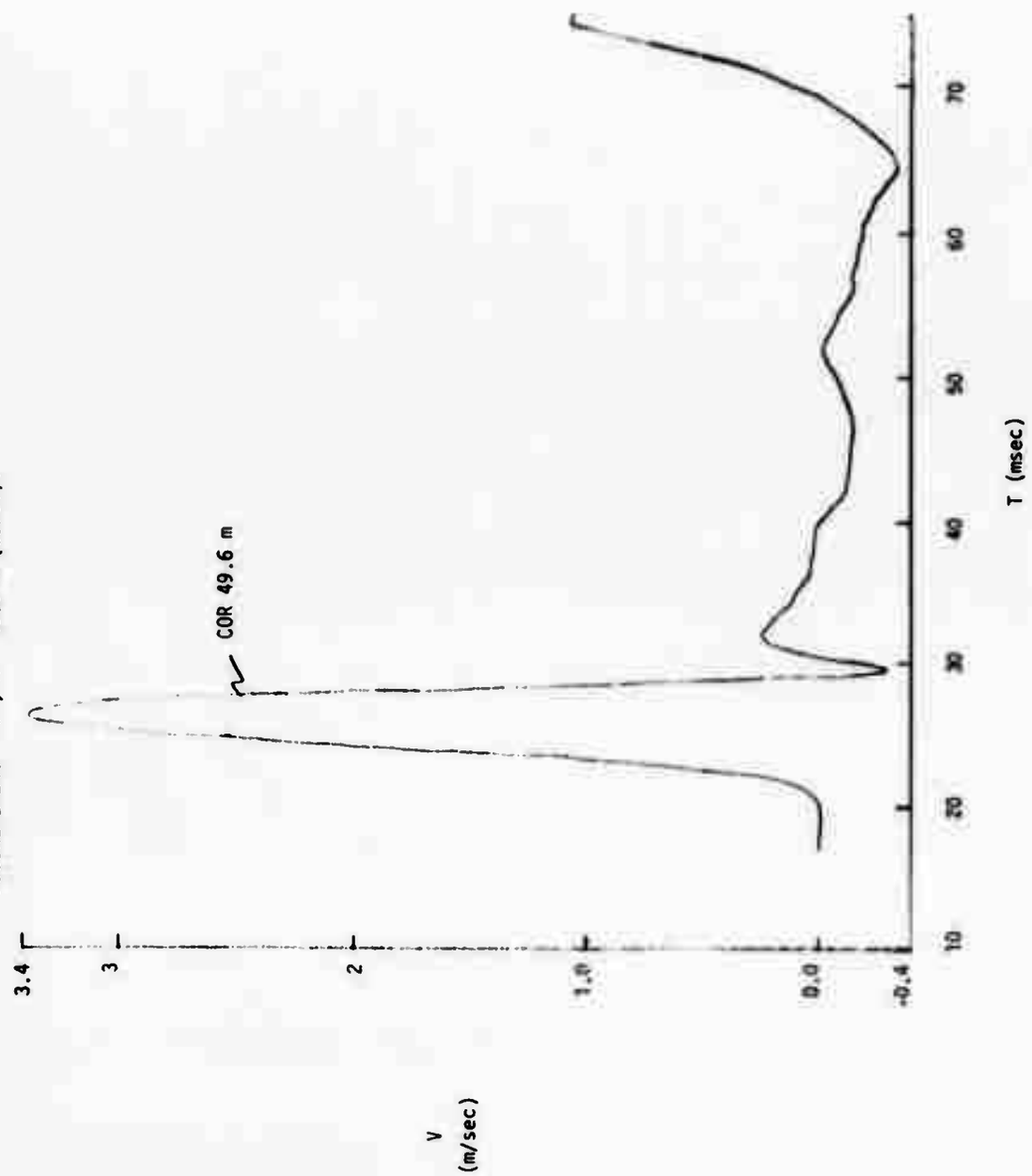

FIGURE B-24. "V"; R = 49.6 m (coral).

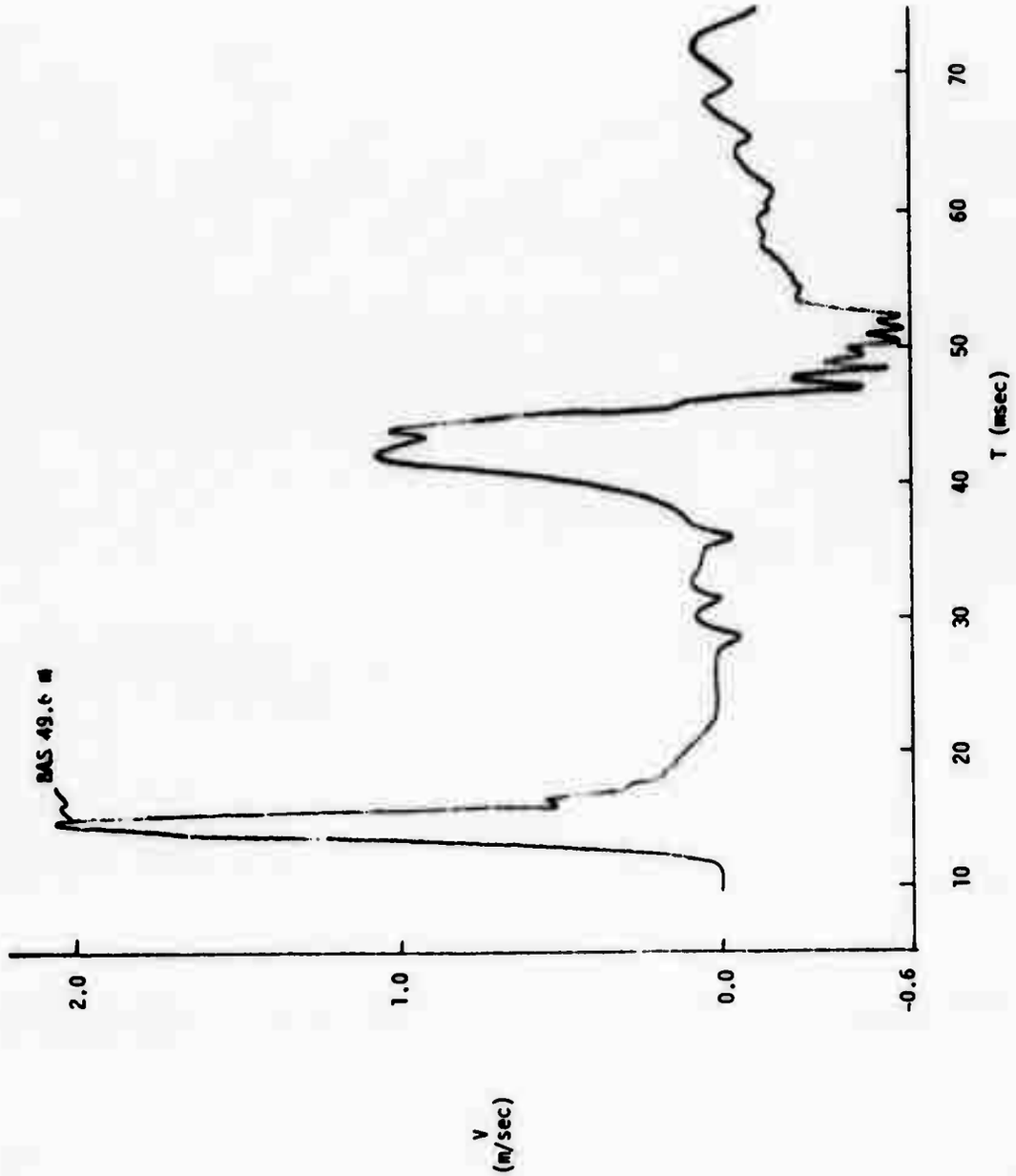

FIGURE B-25. "V"; R = 49.6 m (basalt).

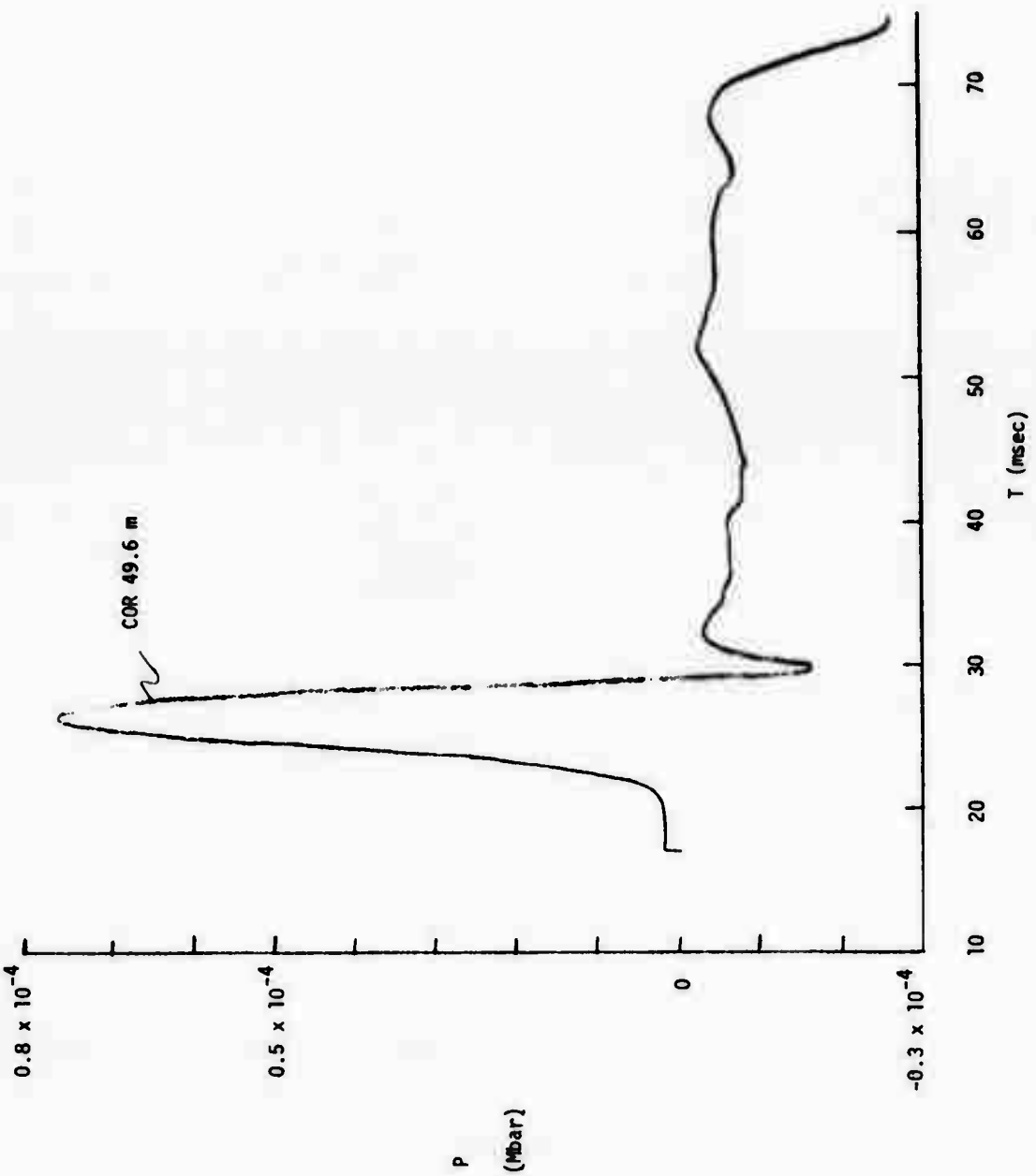

FIGURE B-26. "P"; R = 49.6 m (coral).

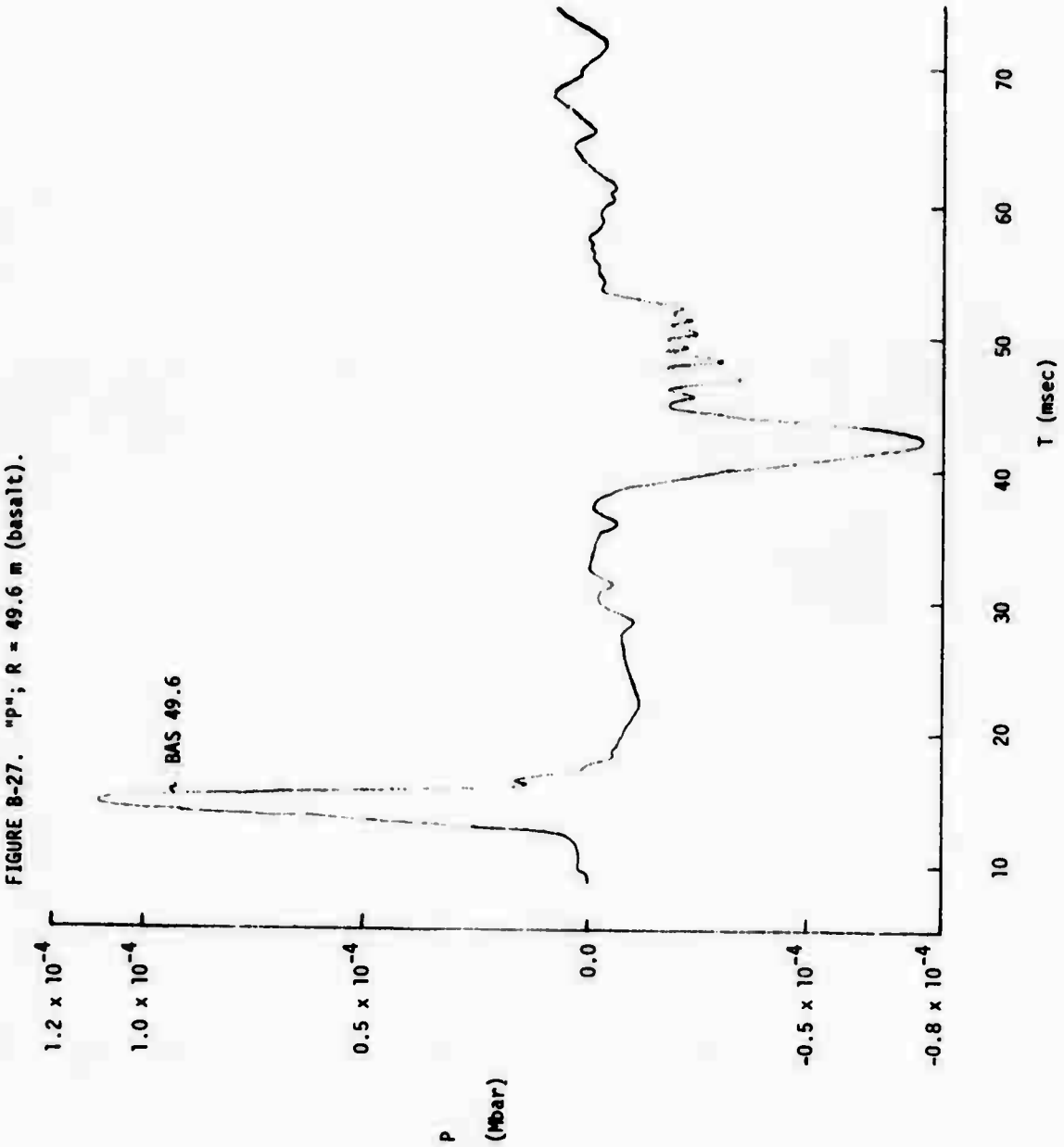

FIGURE B-27. "P"; R = 49.6 m (basalt).

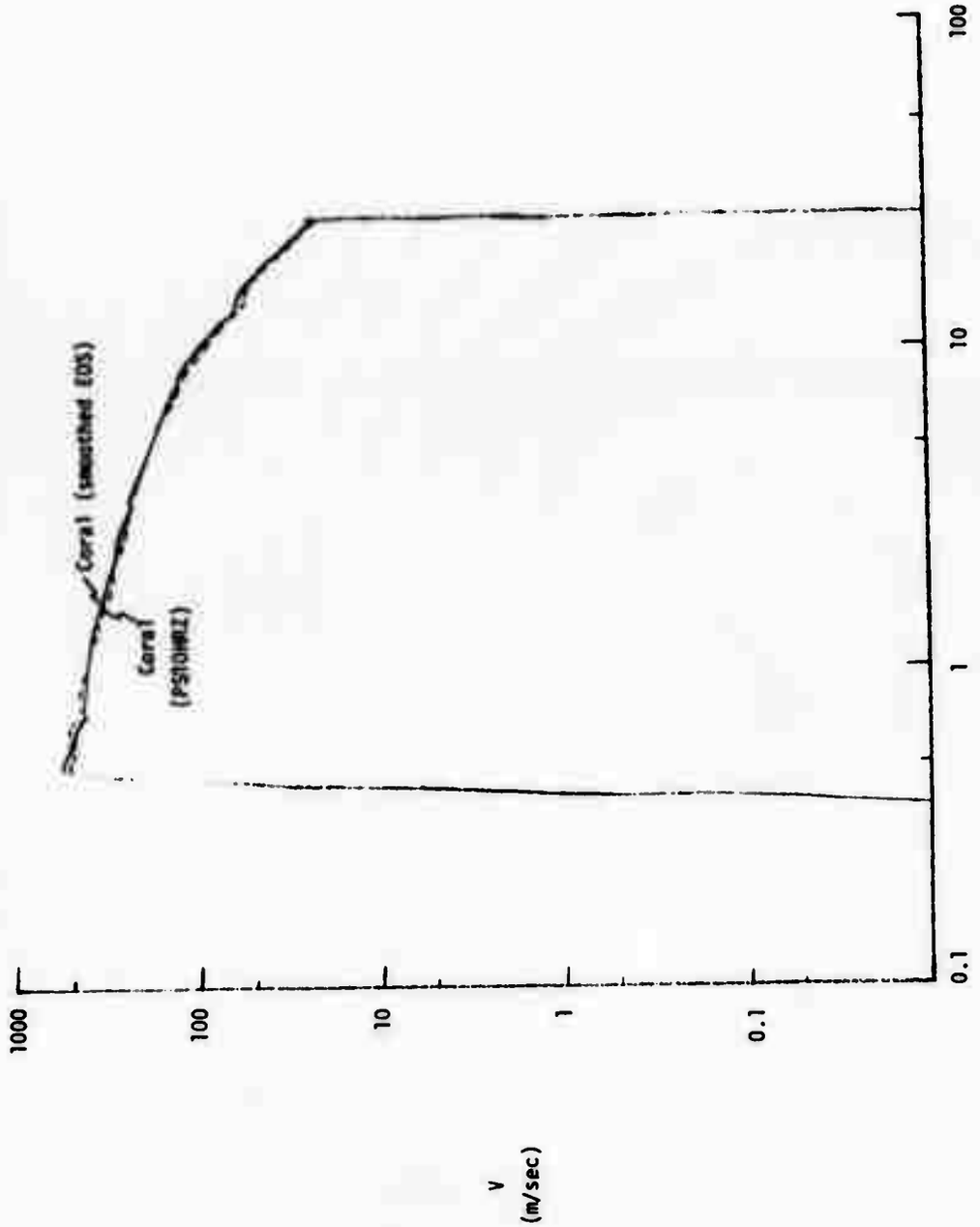

FIGURE B-28. "V"; R = 2.008 m (coral-PS1OHRZ and smoothed EOS).

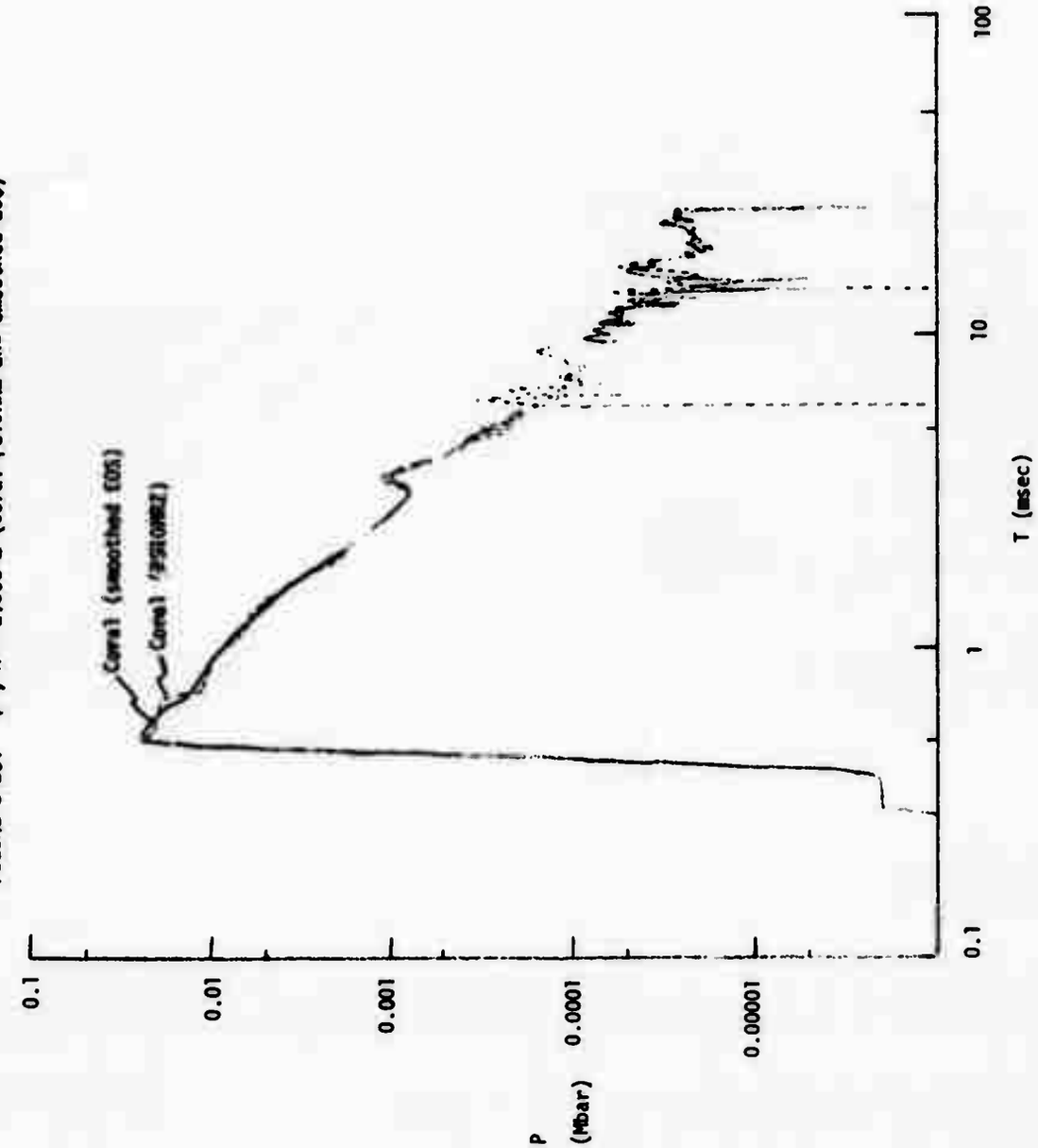

FIGURE B-29. "P"; R ~ 2.008 ■ (Coral-PSIOHRZ and smoothed EOS)

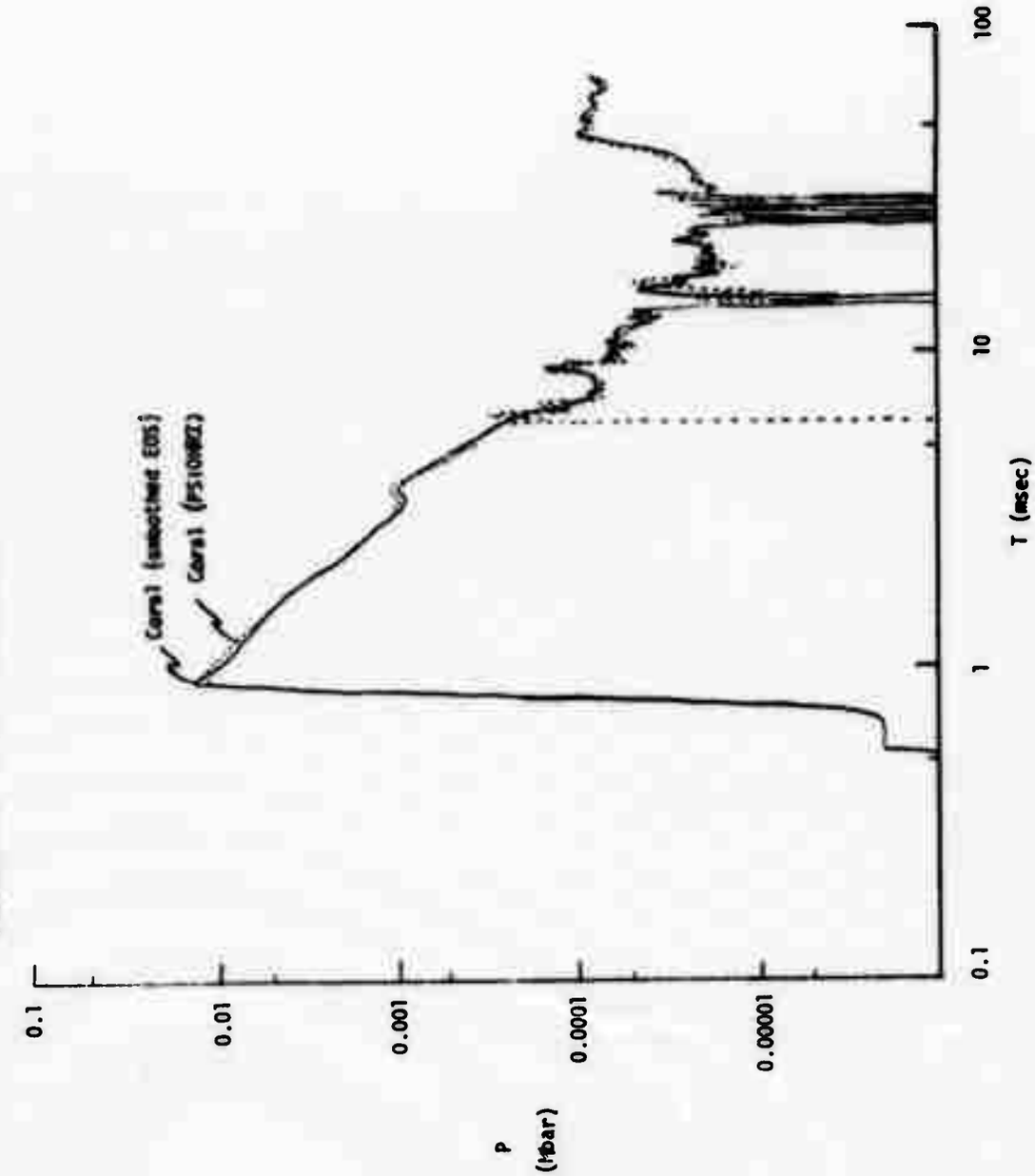

FIGURE B-30. "P"; R = 2.98 m (Coral-PS10HRZ and smoothed EOS).

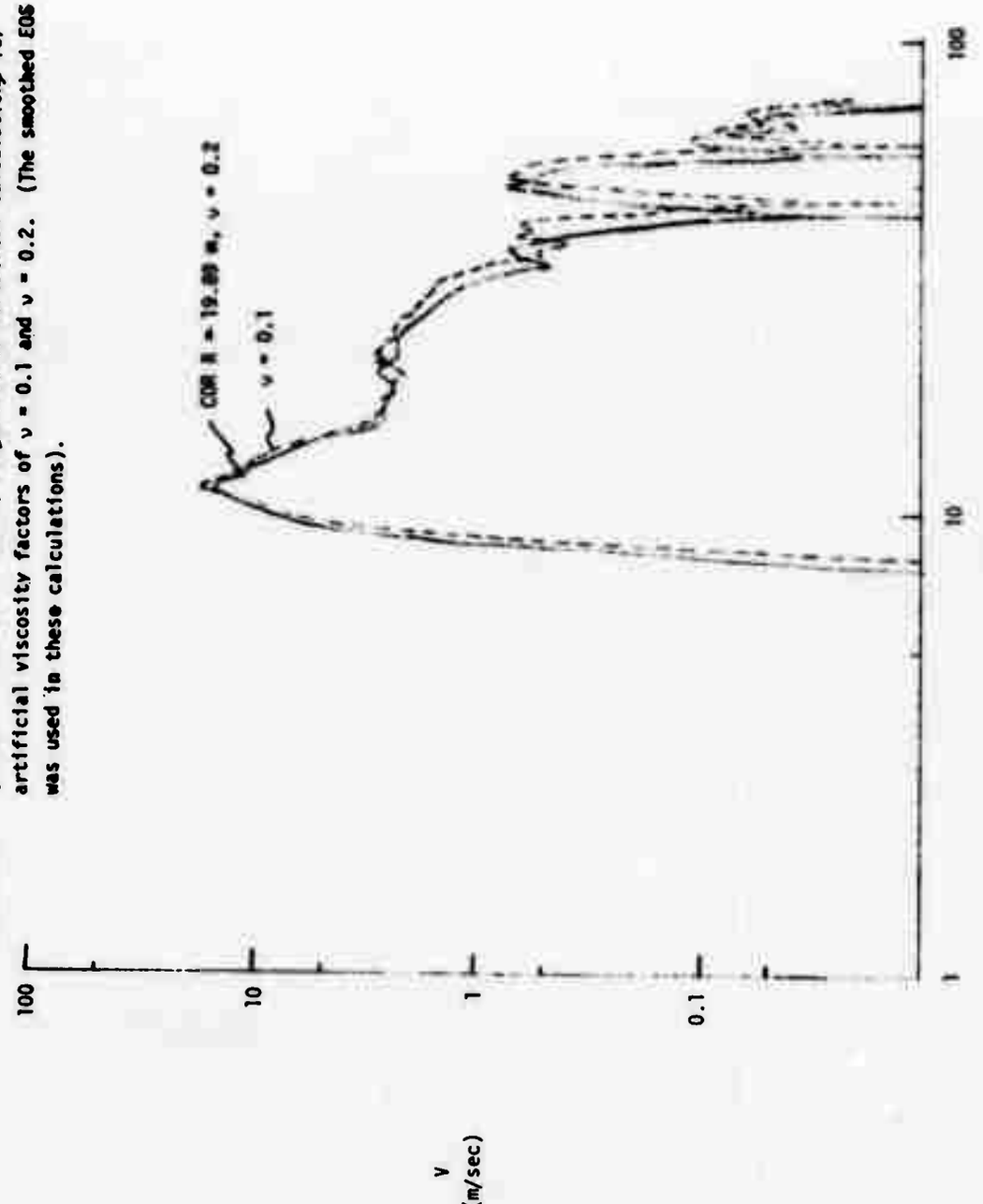

FIGURE B-31 "V" at R = 19.89 m - Coral; comparison of horizontal calculations for artificial viscosity factors of ν = 0.1 and ν = 0.2. (The smoothed EOS was used in these calculations).

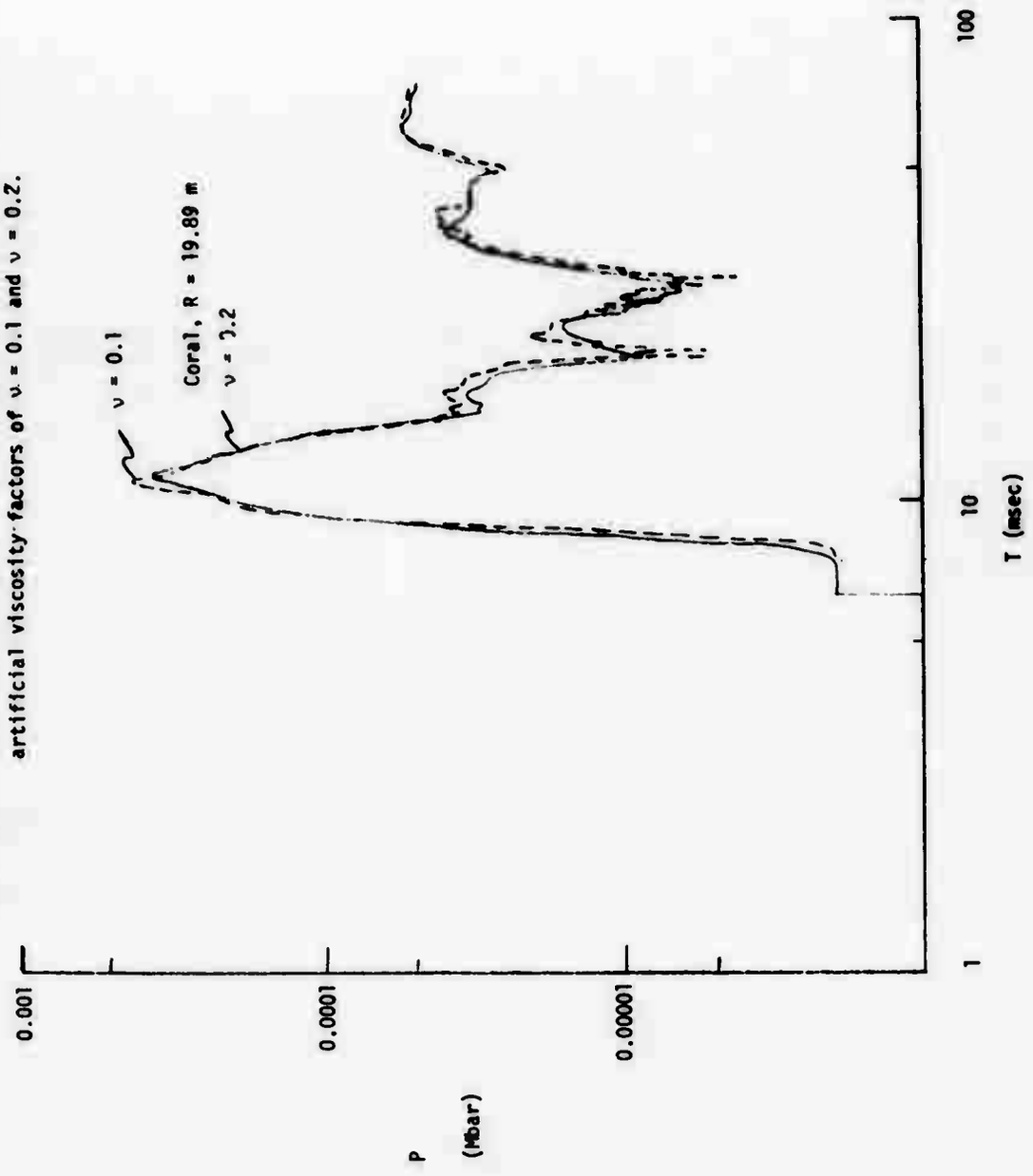

FIGURE B-32. "P"; at R = 19.89 m - Coral, comparison of horizontal calculations for artificial viscosity factors of ν = 0.1 and ν = 0.2.

FIGURE B-33. "V"; at R = 19.89 m - basalt, comparison of horizontal calculations for artificial viscosity factors of ν = 0.1 and ν = 0.2.

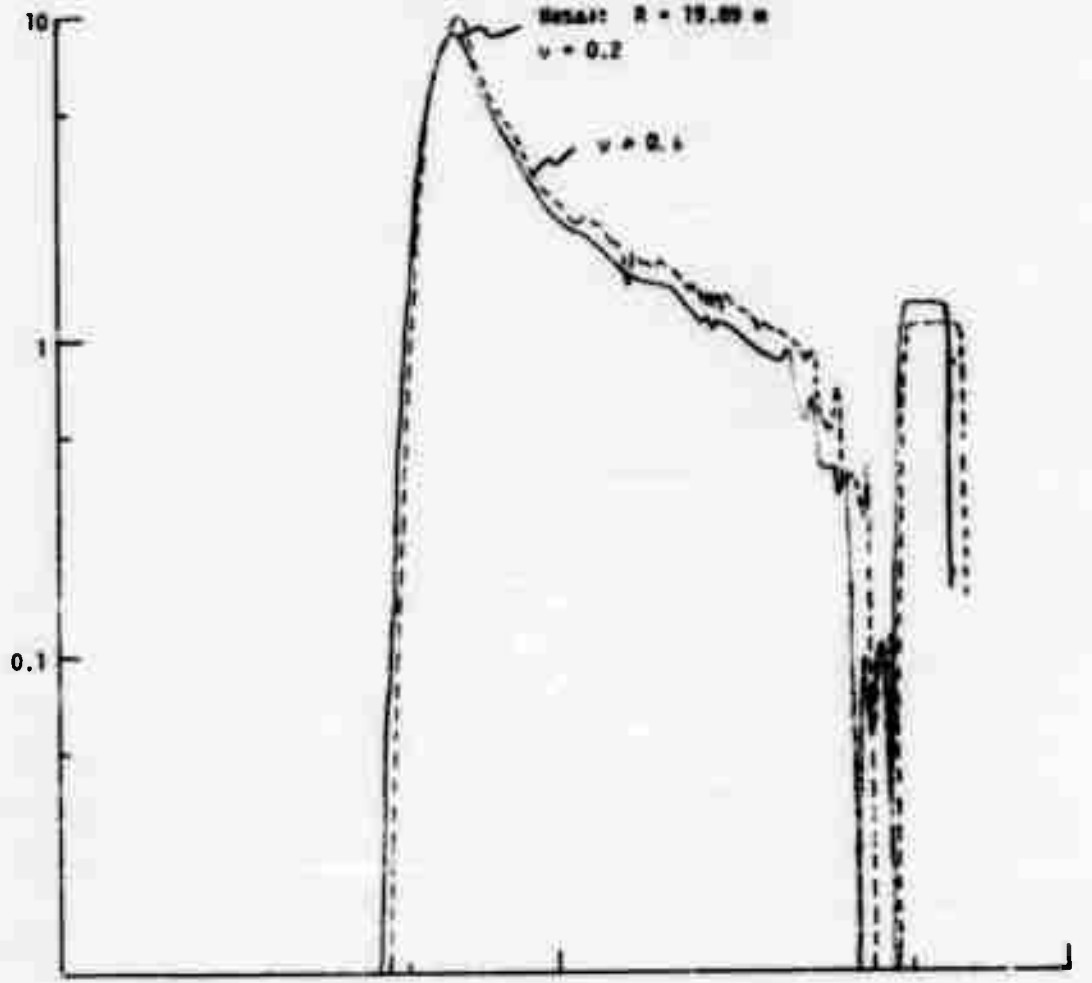

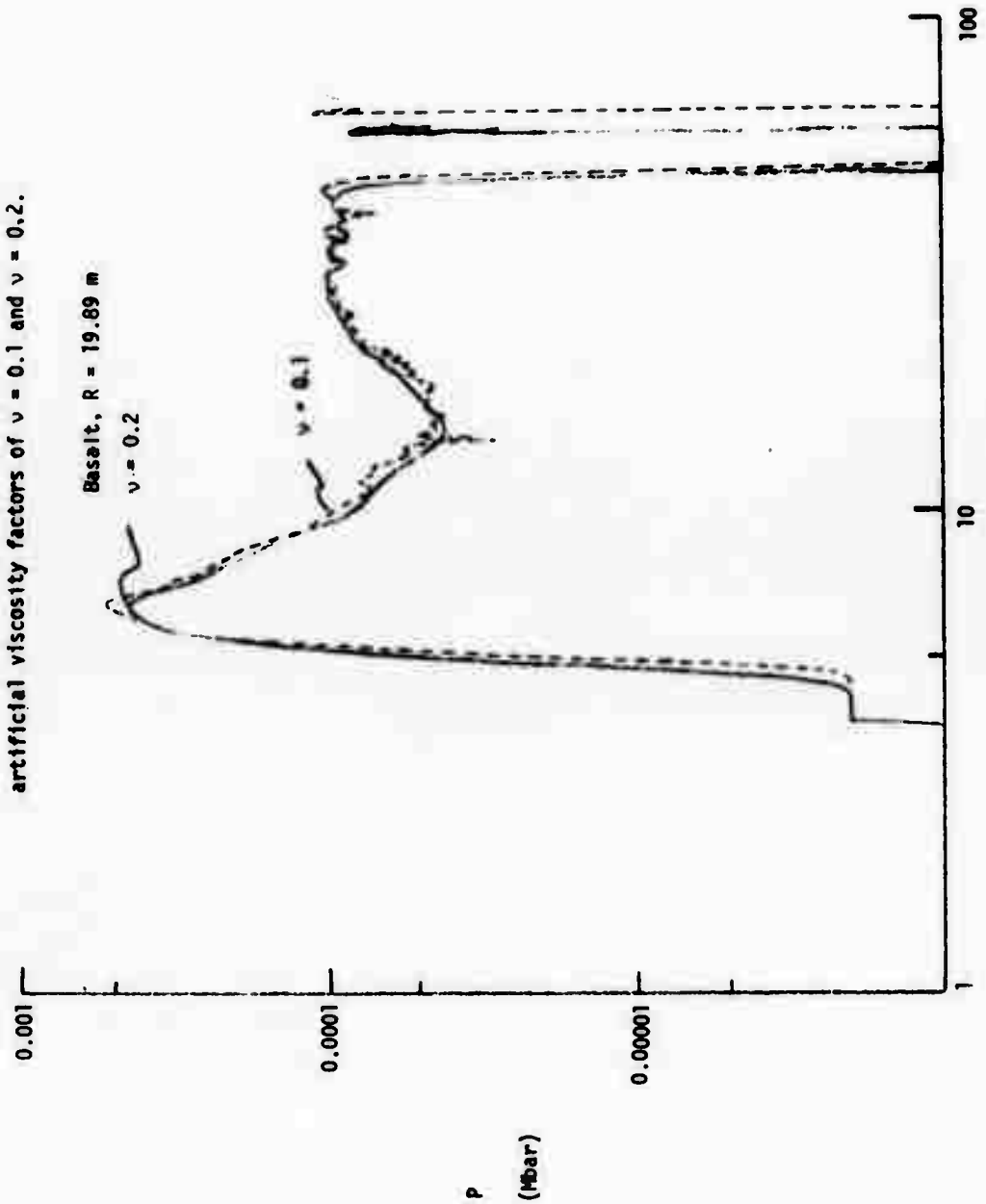

FIGURE B-34. "P"; at R = 19.89 m - basalt, comparison of horizontal calculations for artificial viscosity factors of ν = 0.1 and ν = 0.2.

Appendix C

Waveforms for the Vertical and Vertical Underwater Calculations in Coral

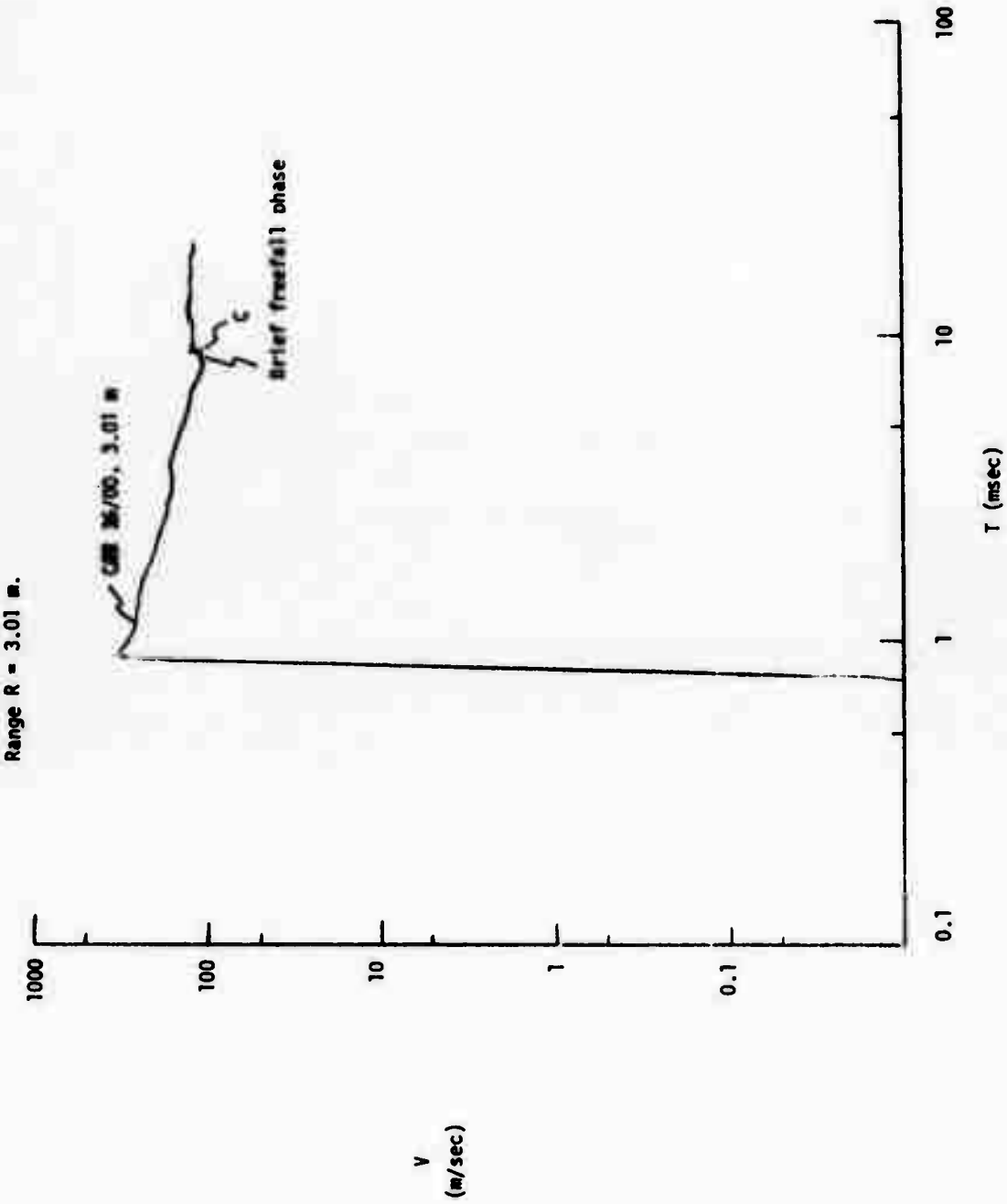

FIGURE C-1. Velocity-waveform as a function of time for coral calculation CDR 36/00, Range R = 3.01 m.

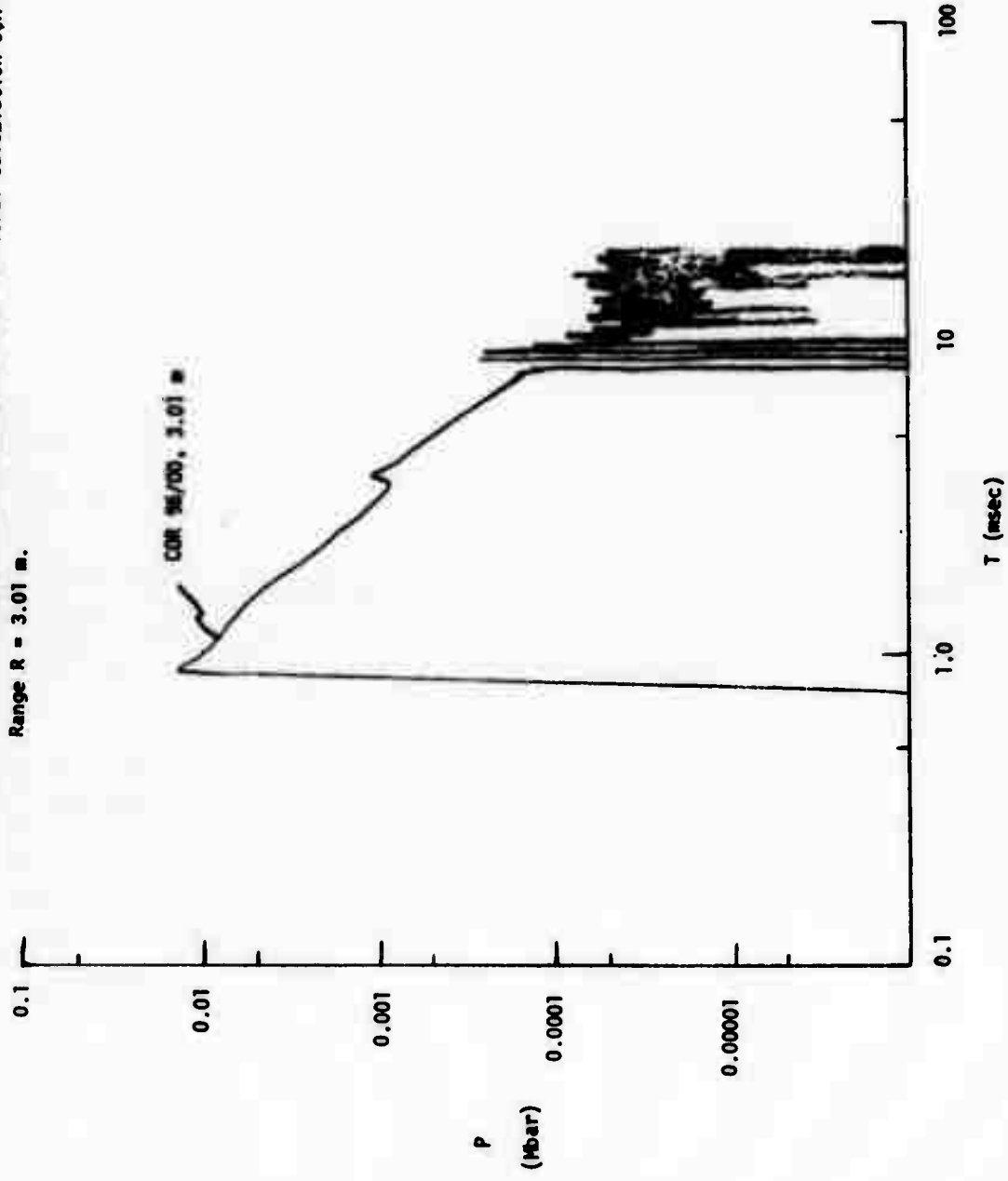

FIGURE C-2. Pressure waveform as a function of time for coral calculation COR 36/00, Range R = 3.01 m.

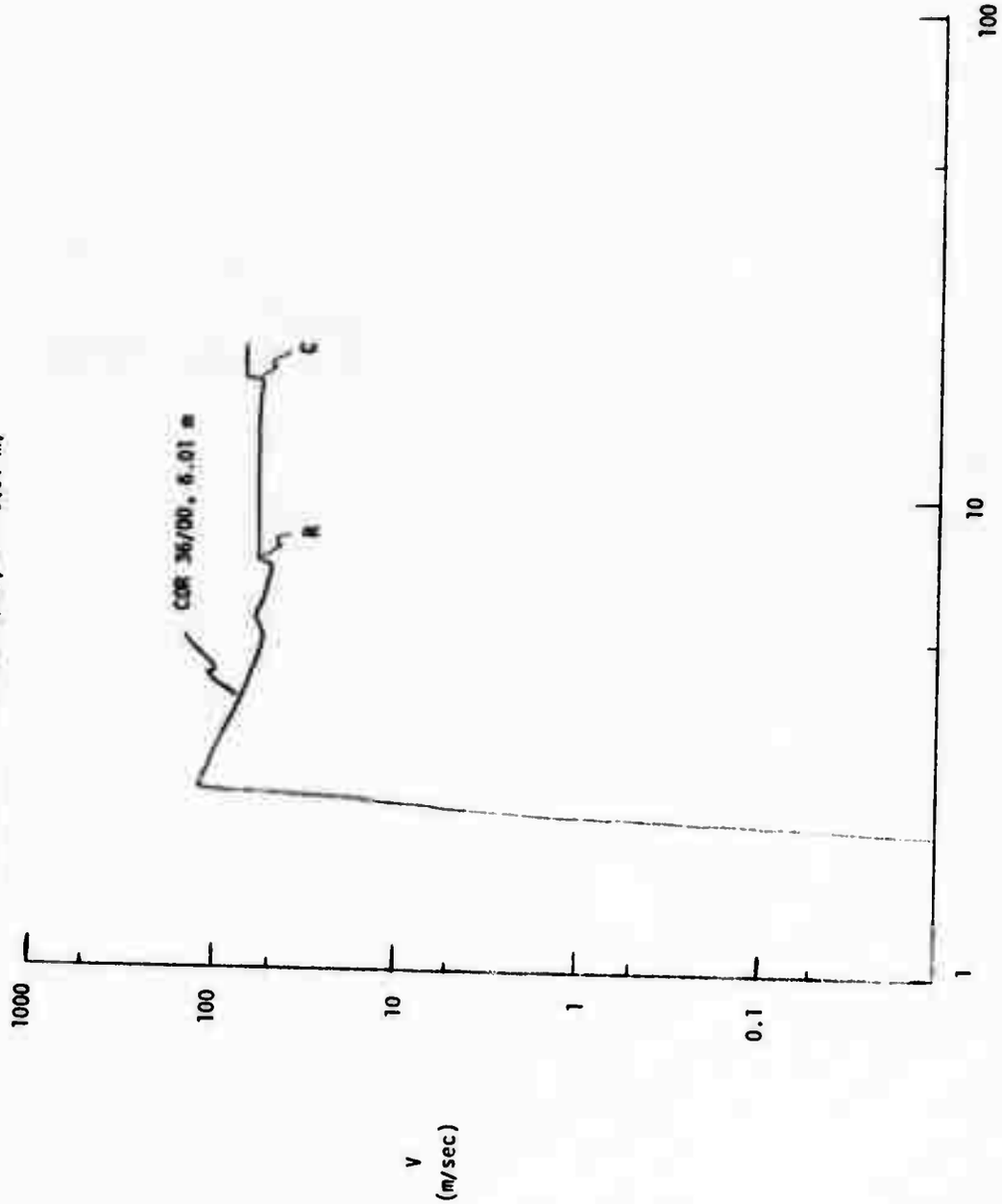

FIGURE C-3. "V"; COR 36/00, R = 6.01 m.

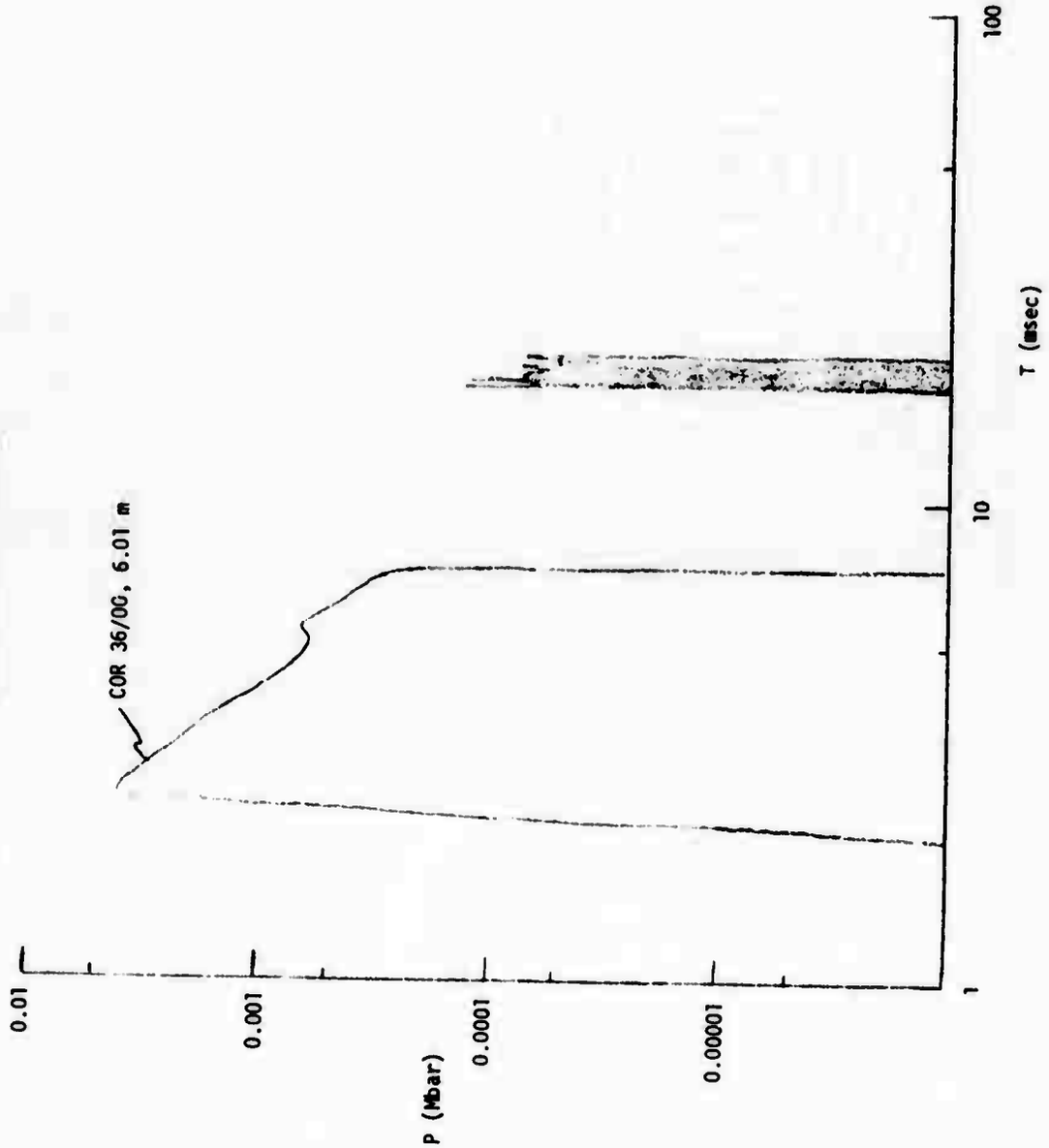

FIGURE C-4. "P"; COR 36/00, R = 6.01 m.

FIGURE C-6. "V"; COR 36/00, R = 0.01 m.

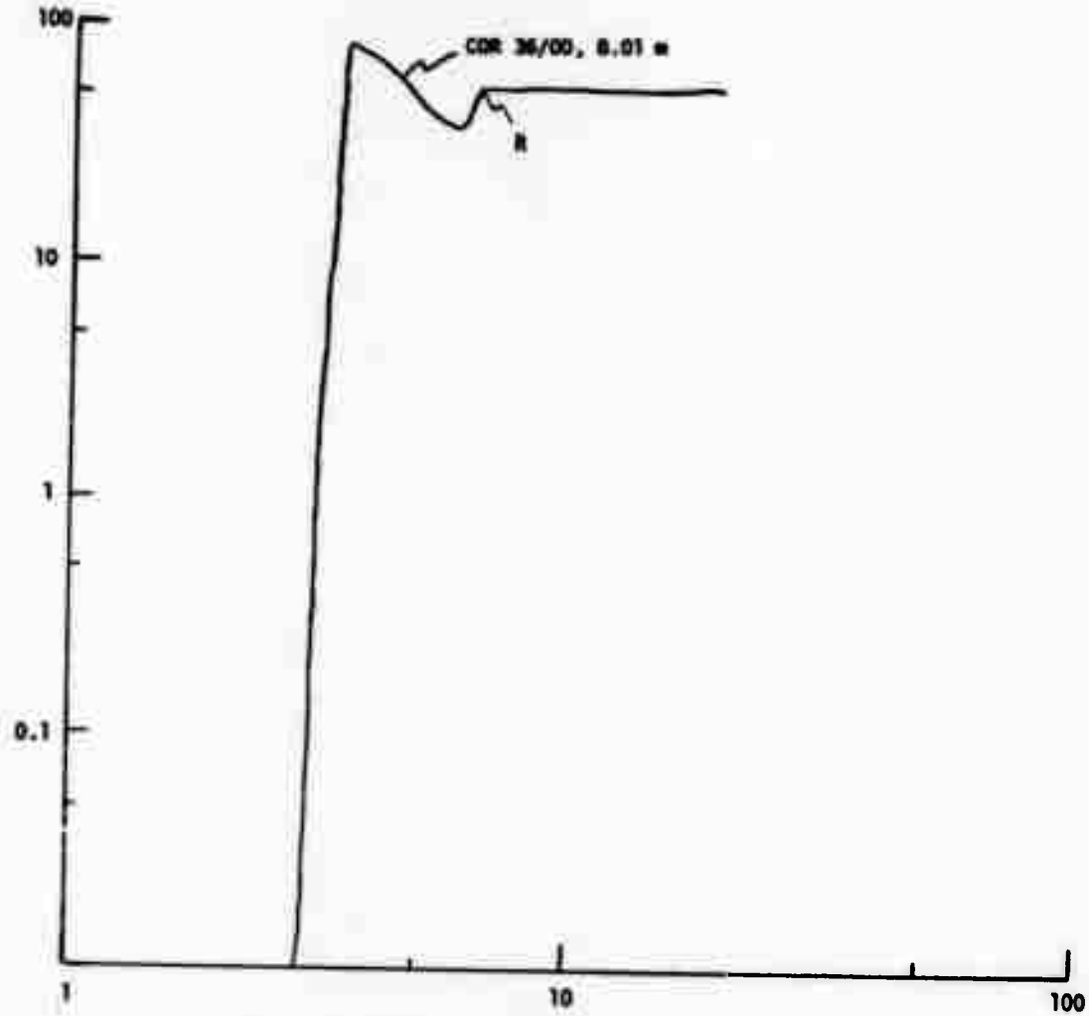

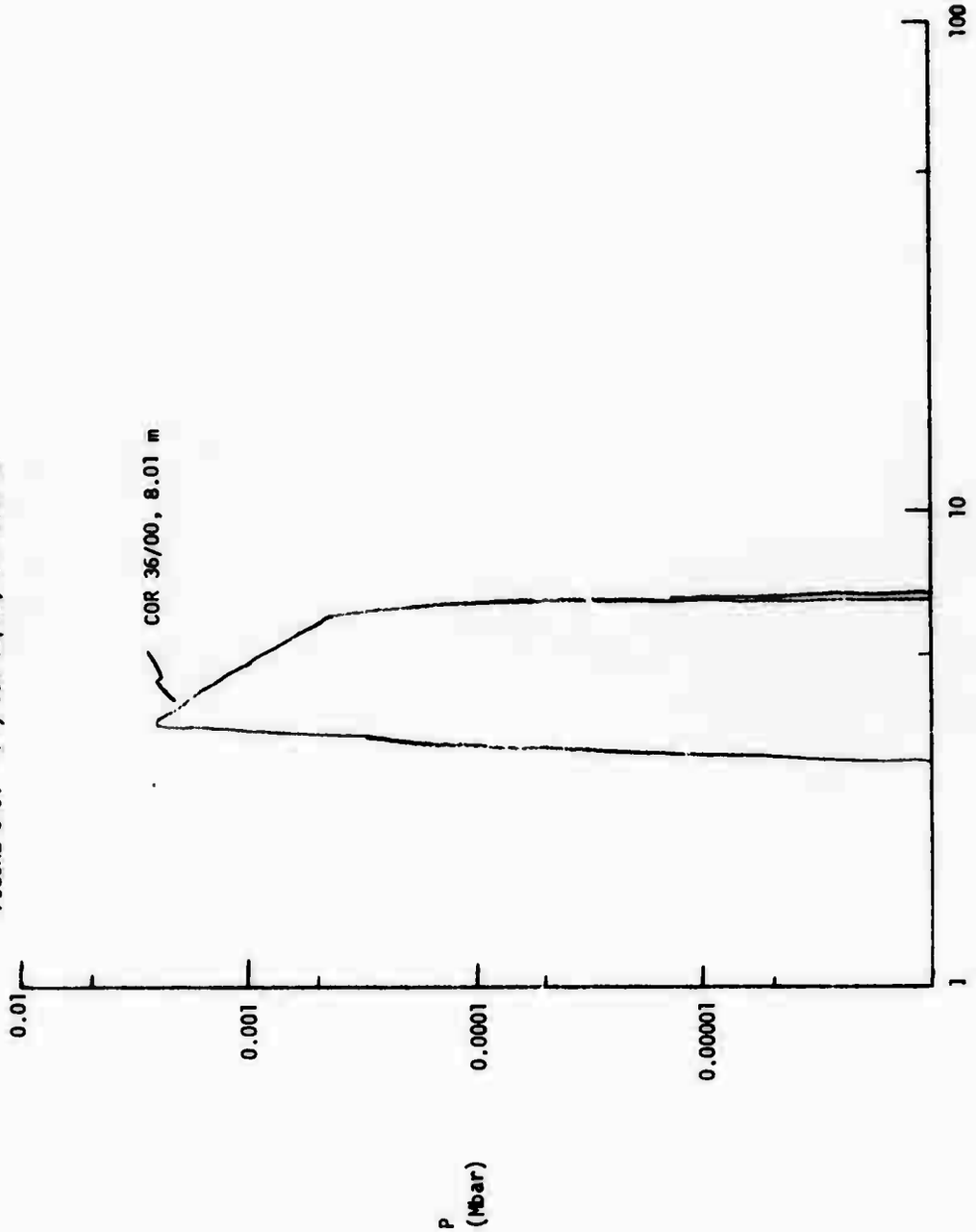

FIGURE C-6. "P"; COR 36/00, R = 8.01 m.

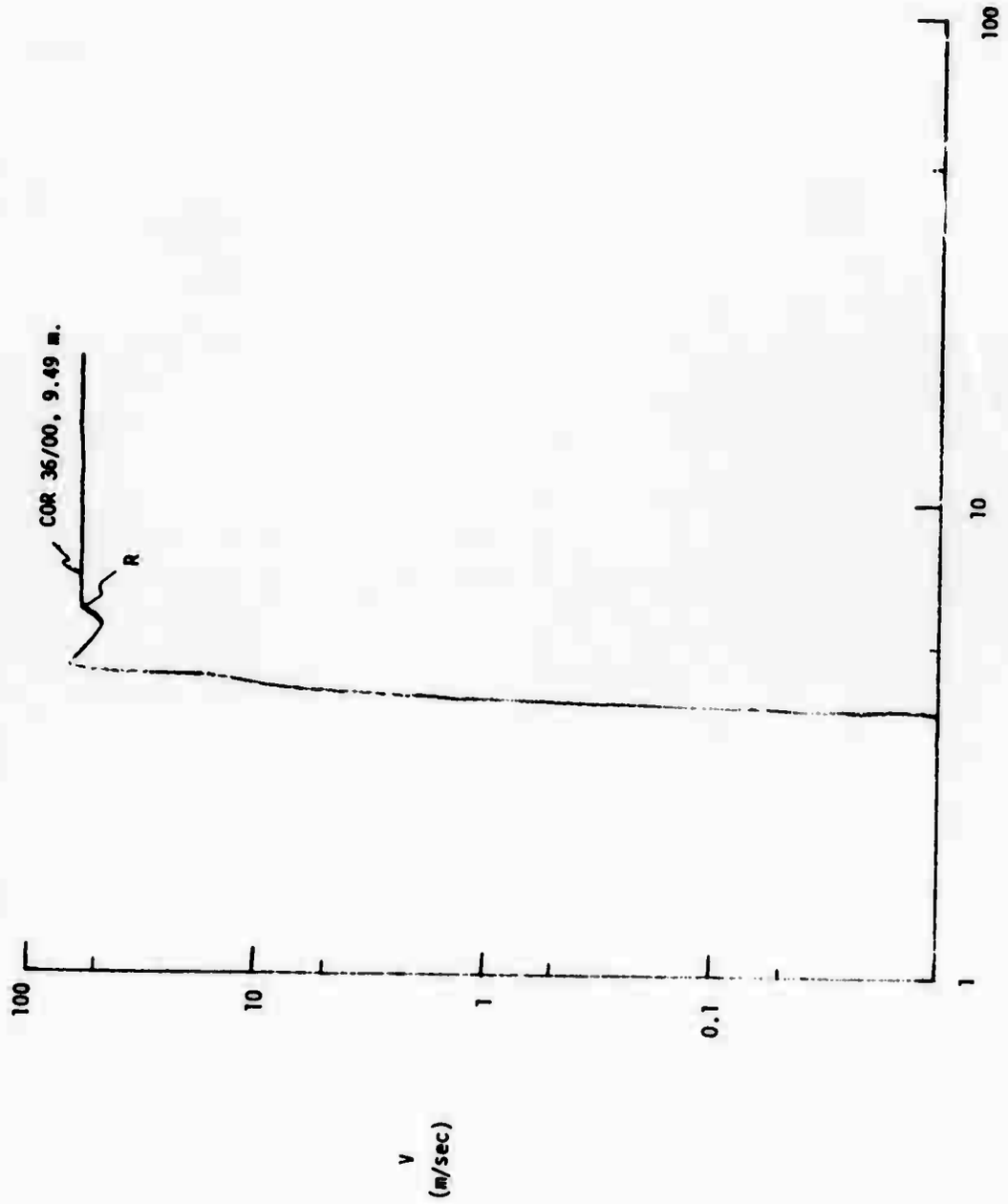

FIGURE C-7. "V"; COR 36/00, R = 9.49 m.

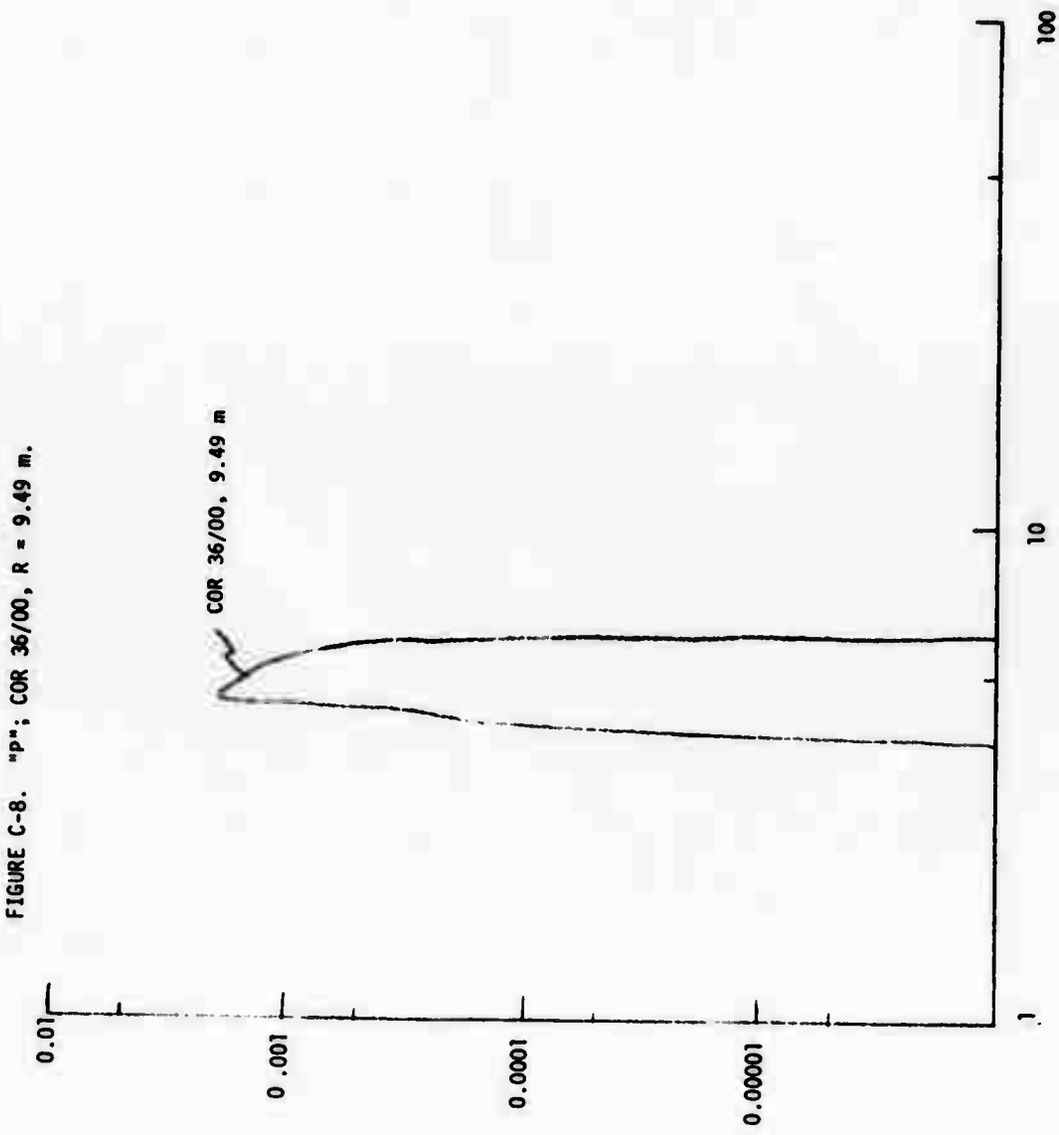

FIGURE C-8. "P"; COR 36/00, R = 9.49 m.

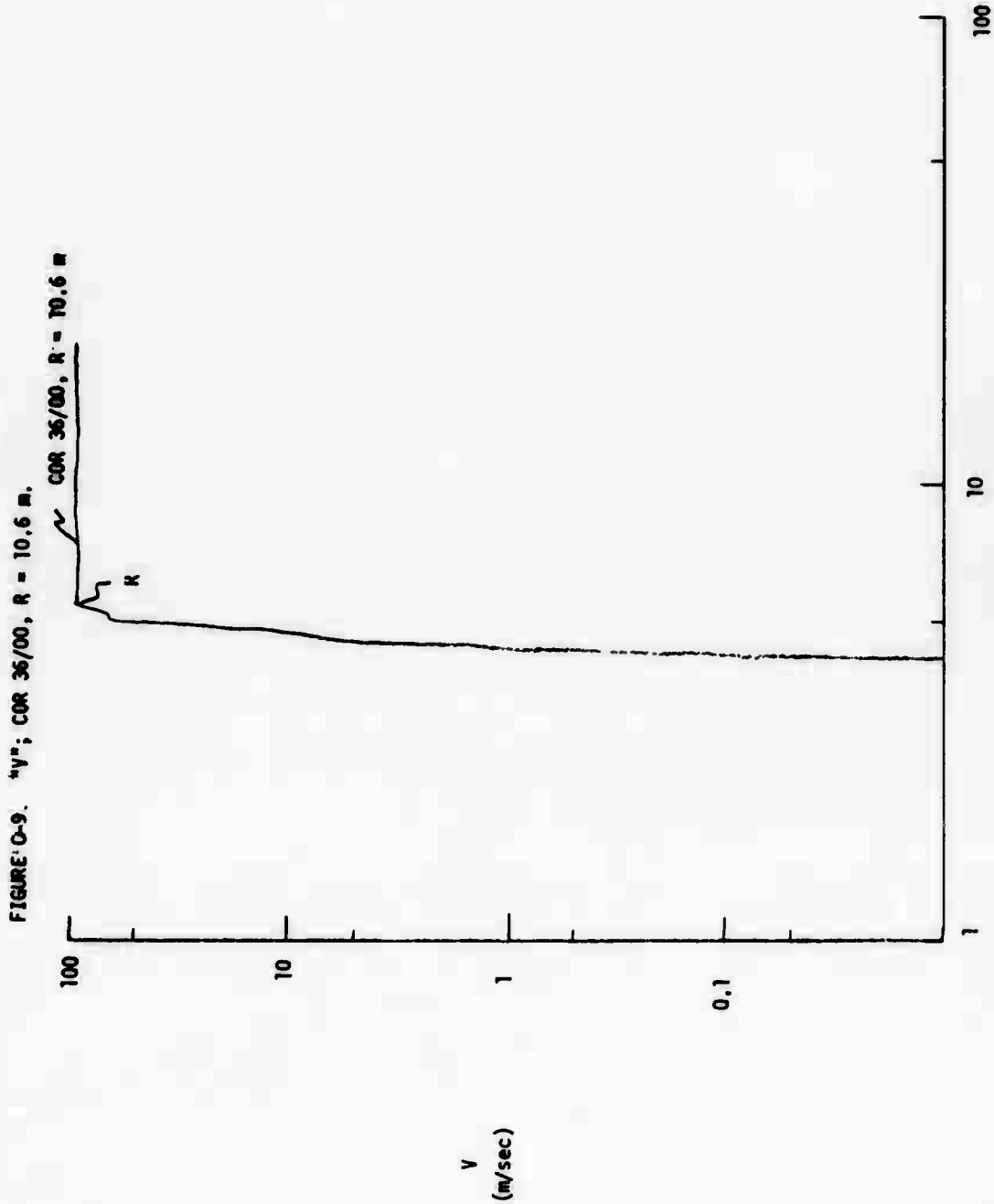

FIGURE C-9. "V"; COR 36/00, R = 10.6 m.

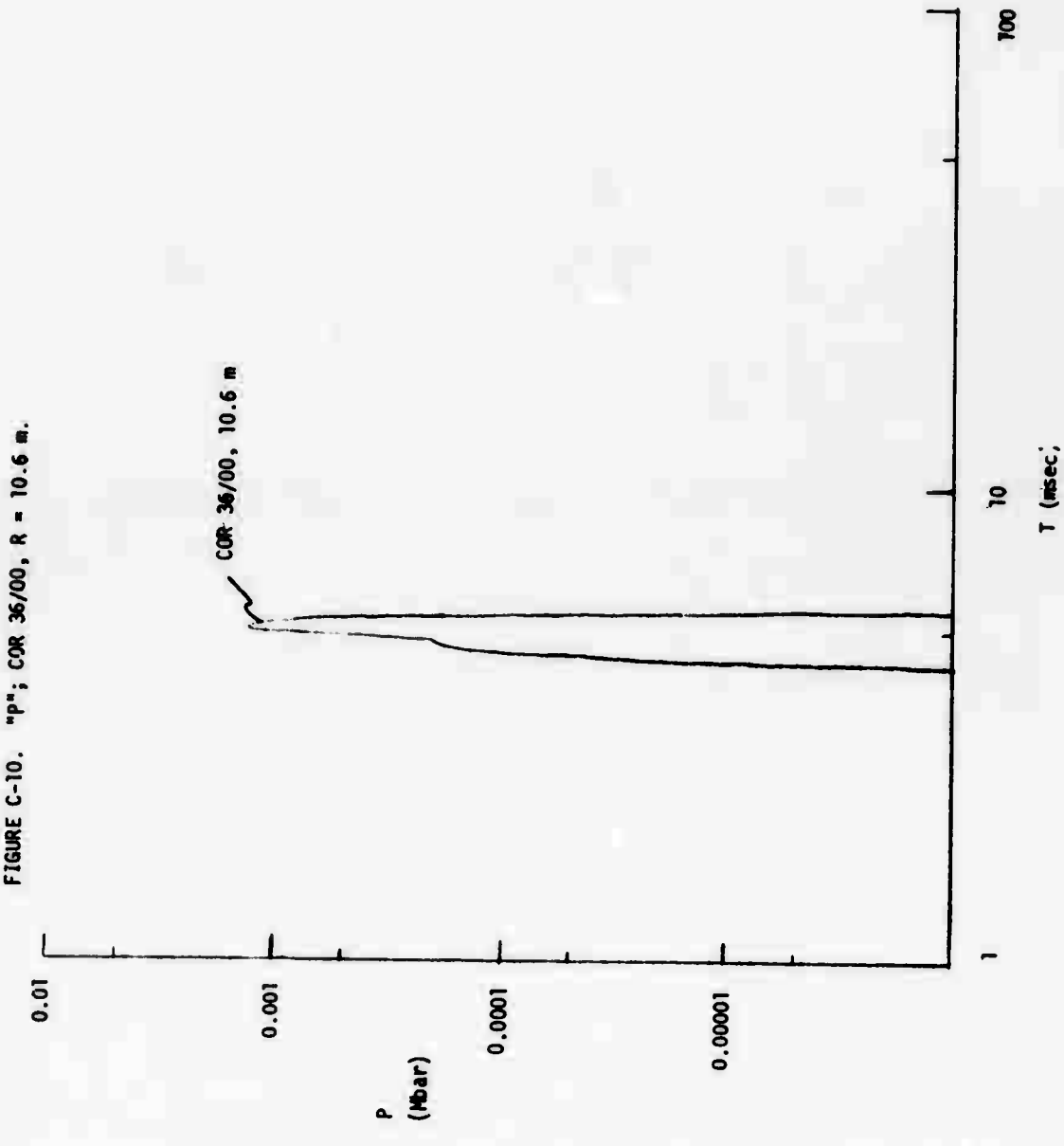

FIGURE C-10. "p"; COR 36/00, R = 10.6 m.

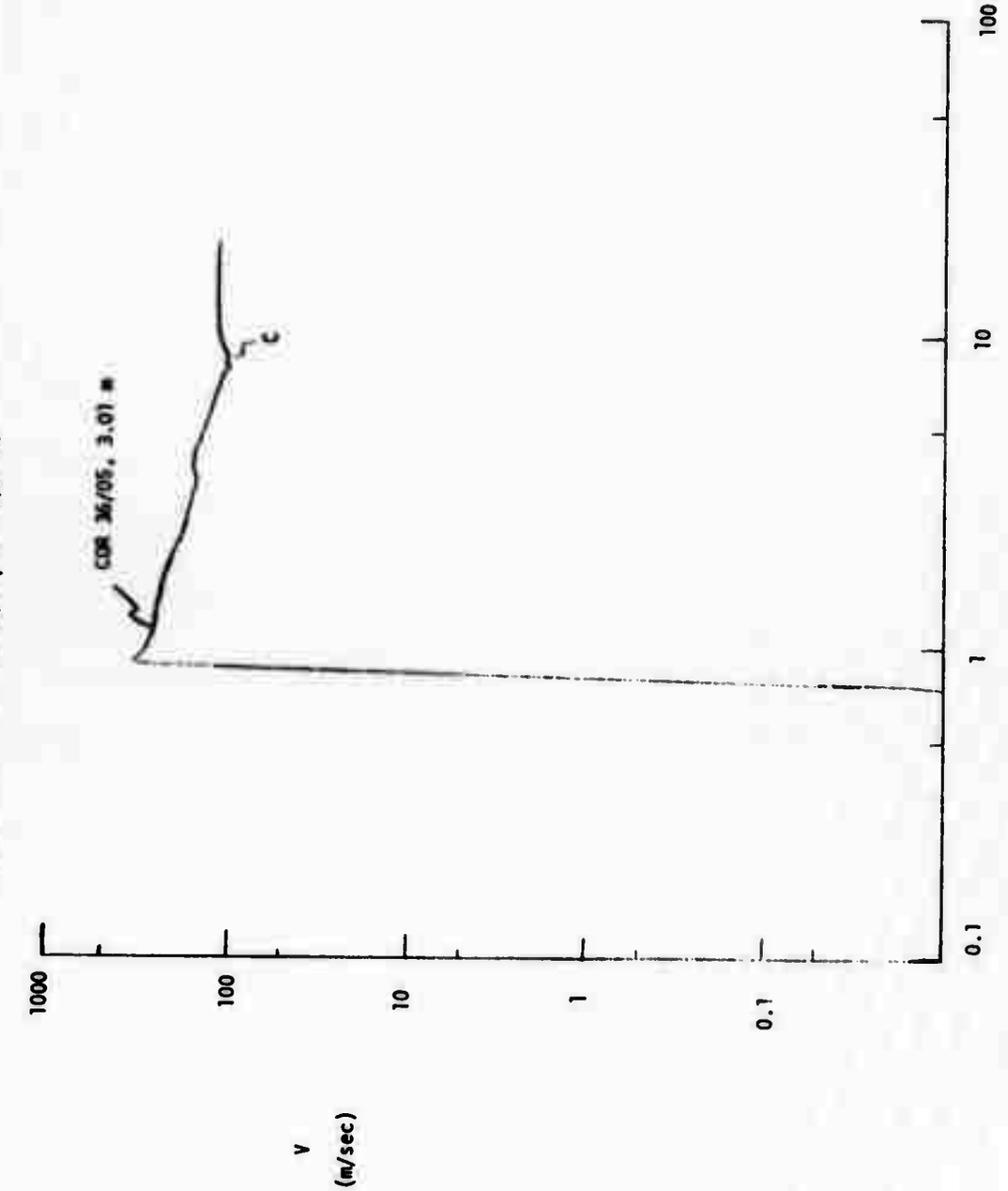

FIGURE C-11. "V"; COR 36/05, R = 3.01 m.

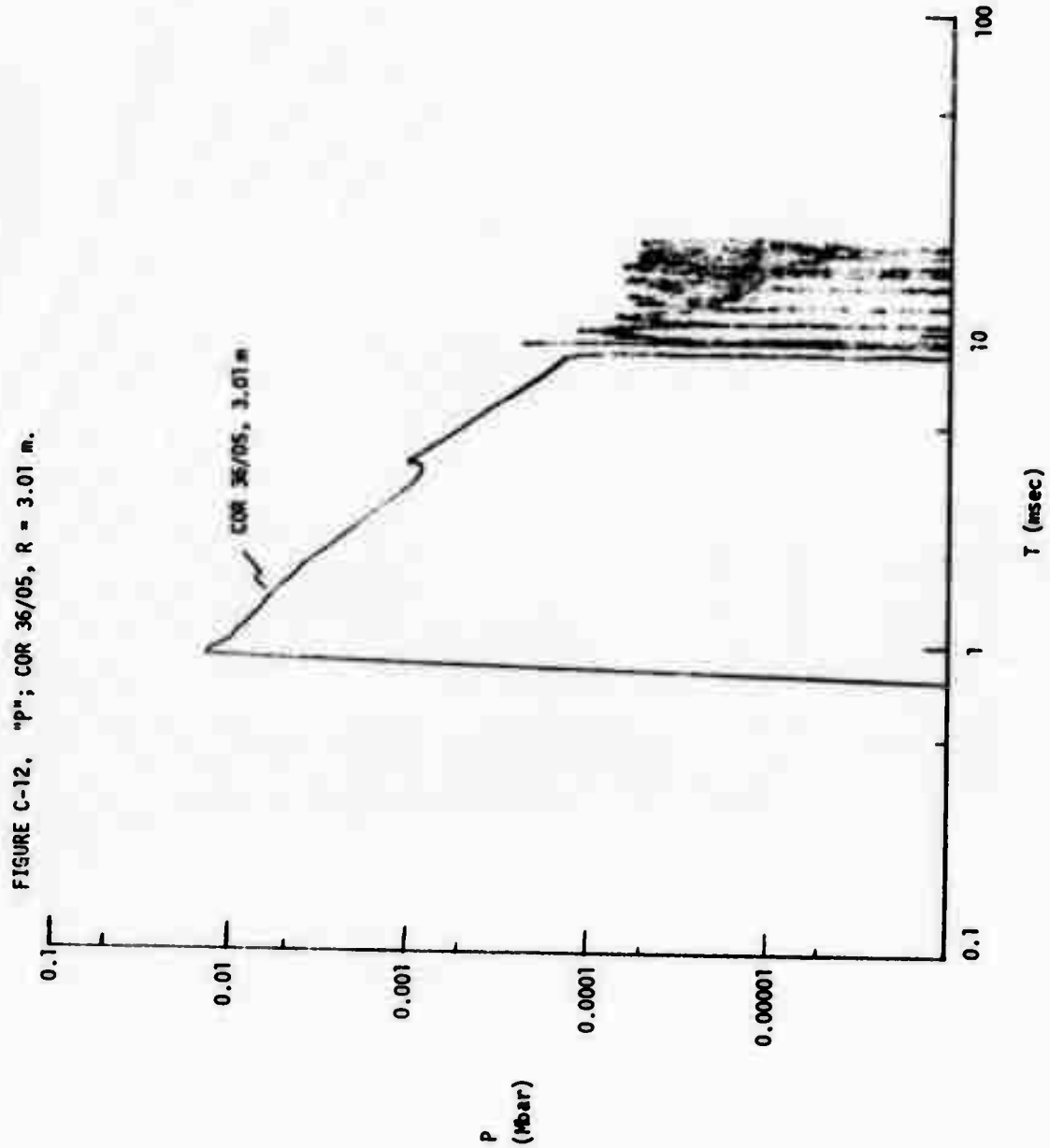

FIGURE C-12, "P"; COR 36/05, R = 3.01 m.

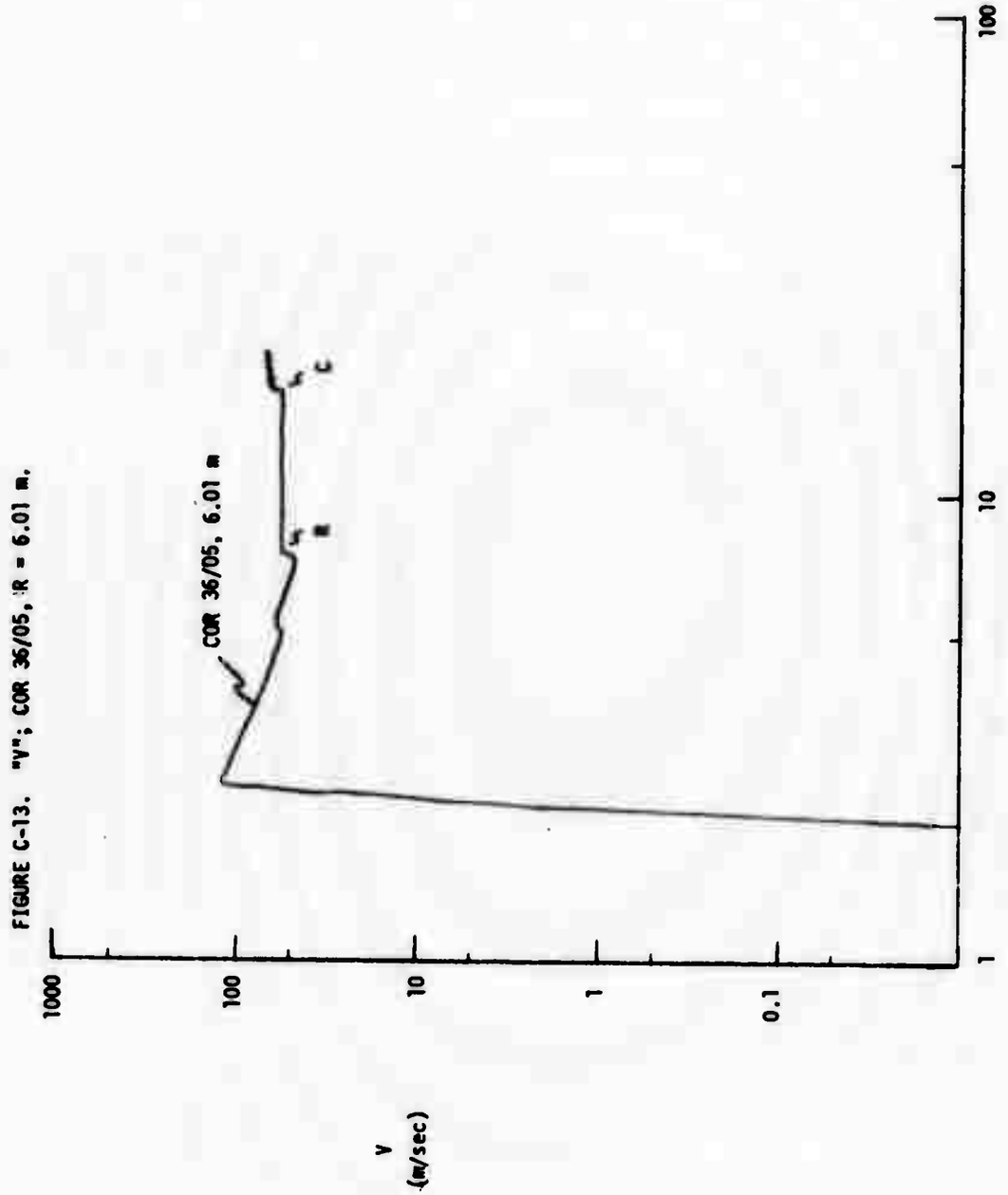

FIGURE C-13. "V"; COR 36/05, R = 6.01 m.

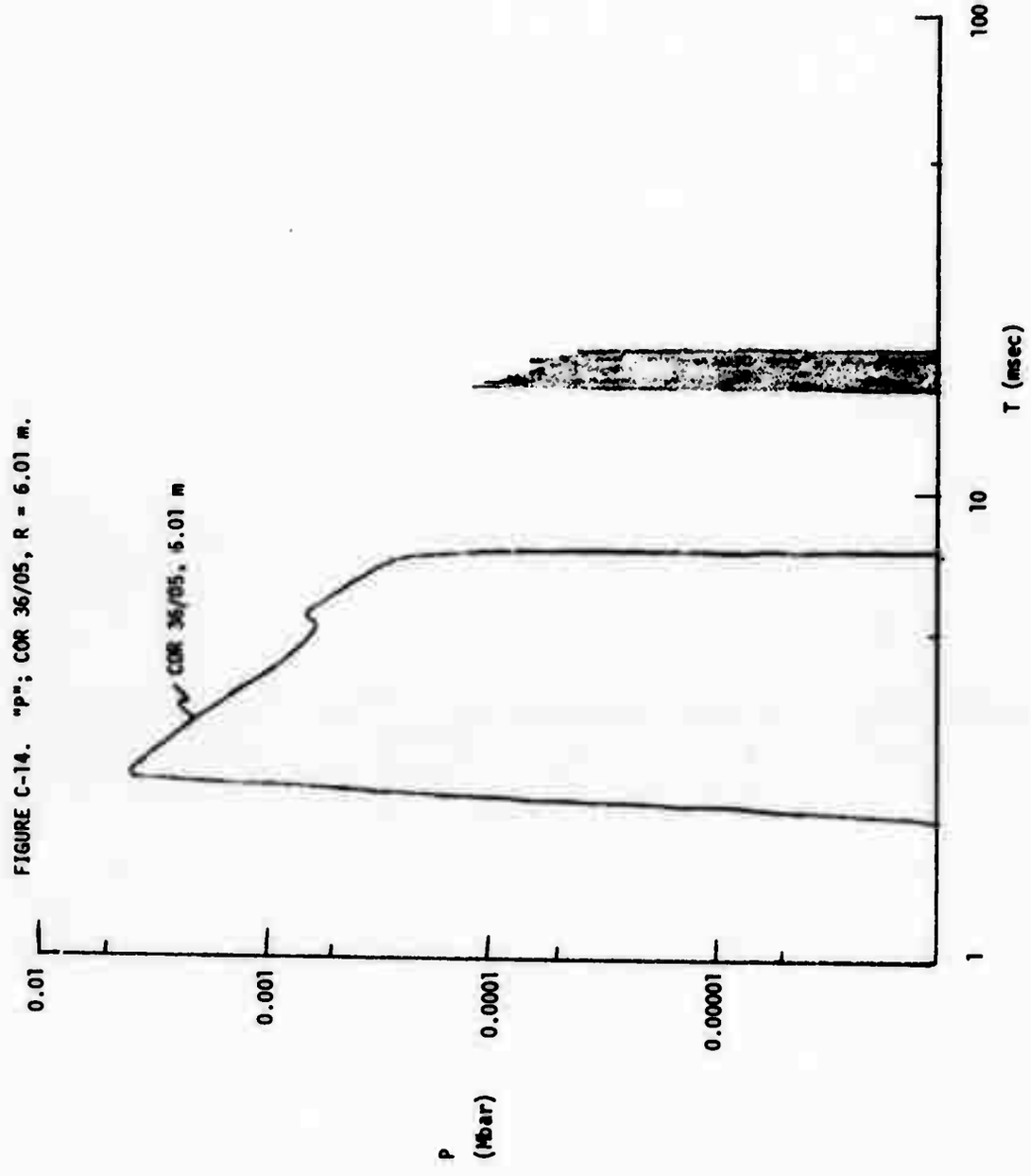

FIGURE C-14. "p"; COR 36/05, R = 6.01 m.

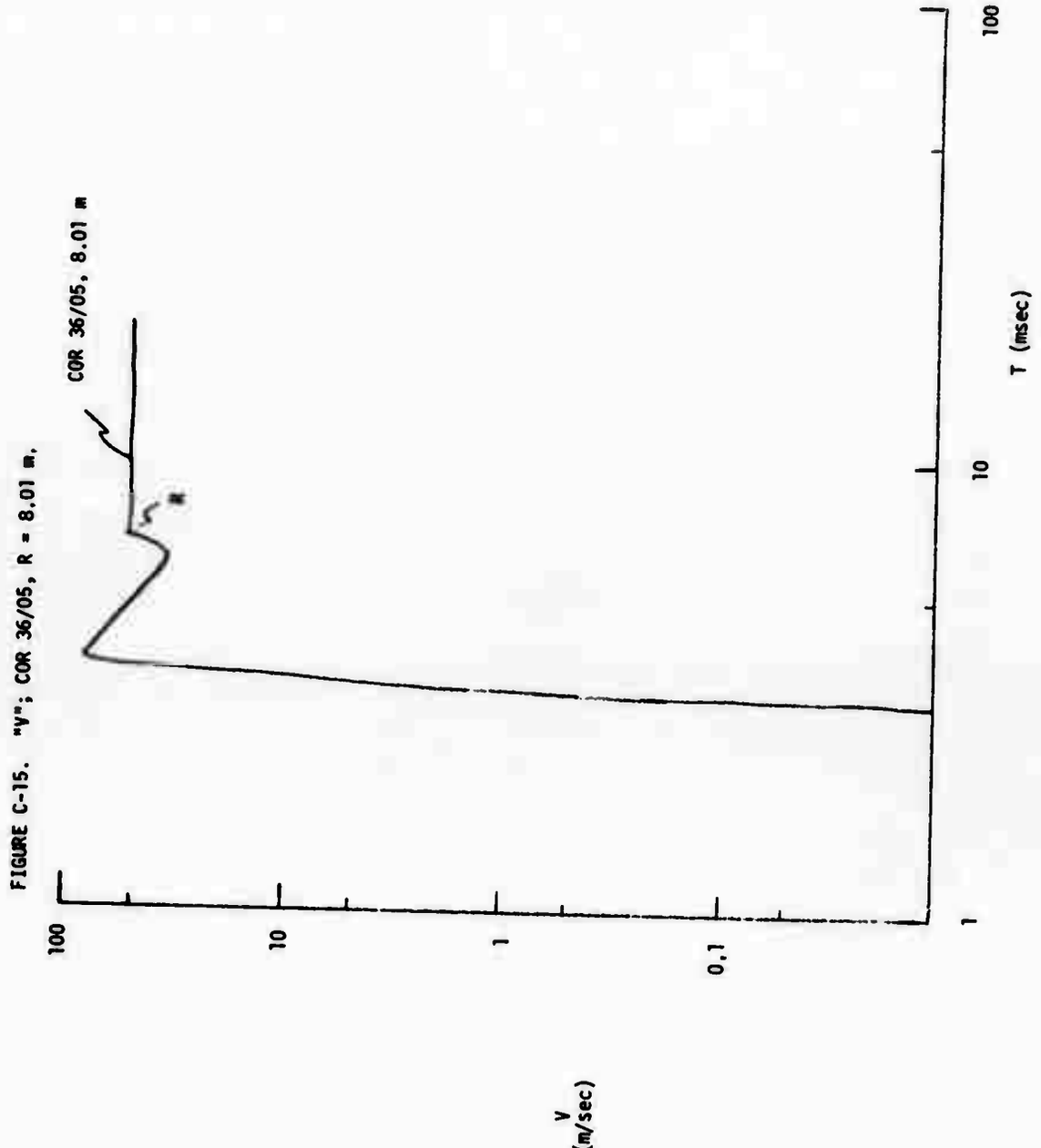

FIGURE C-15. "V"; COR 36/05, R = 8.01 m.

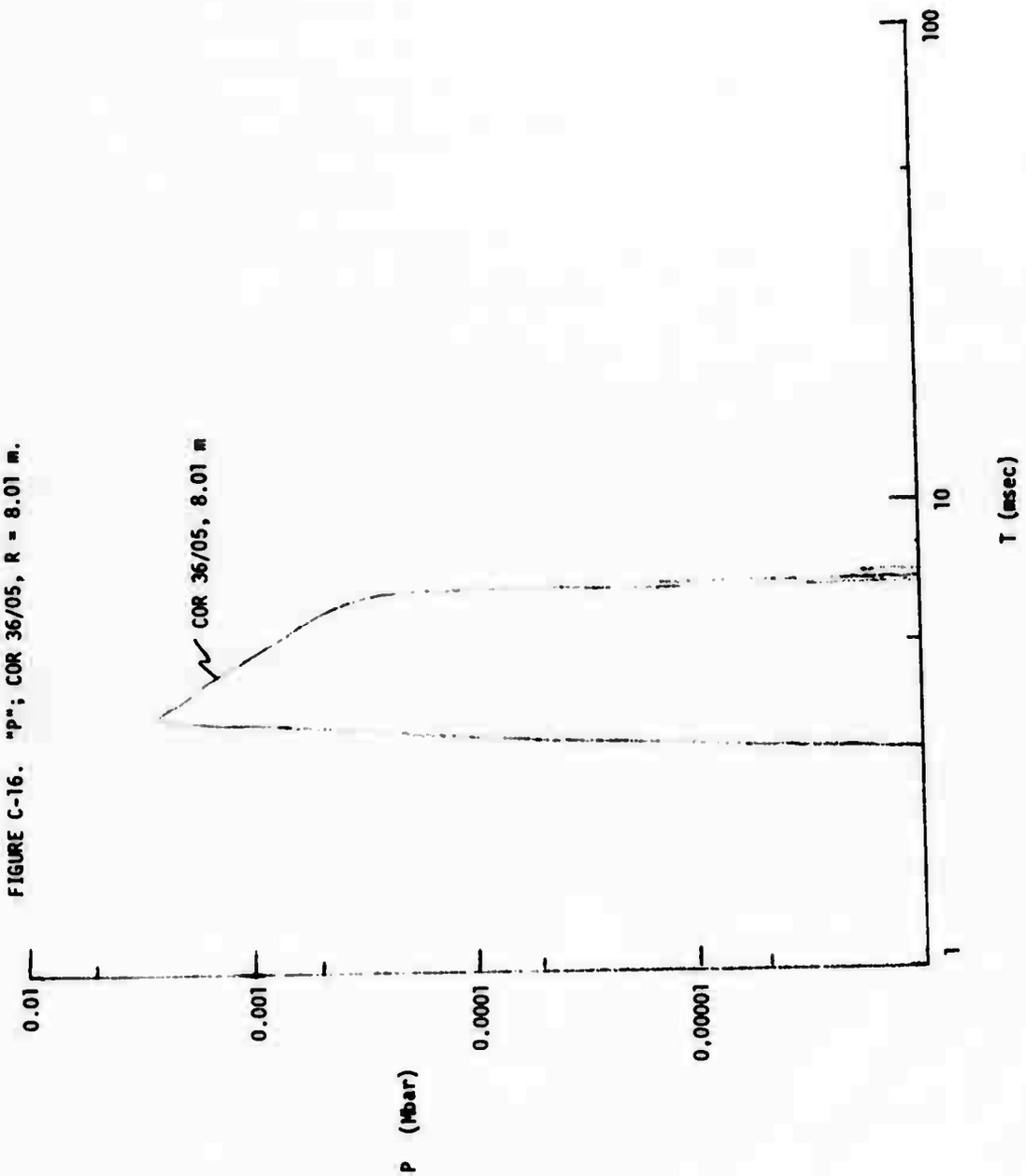

FIGURE C-16. "P"; COR 36/05, R = 8.01 m.

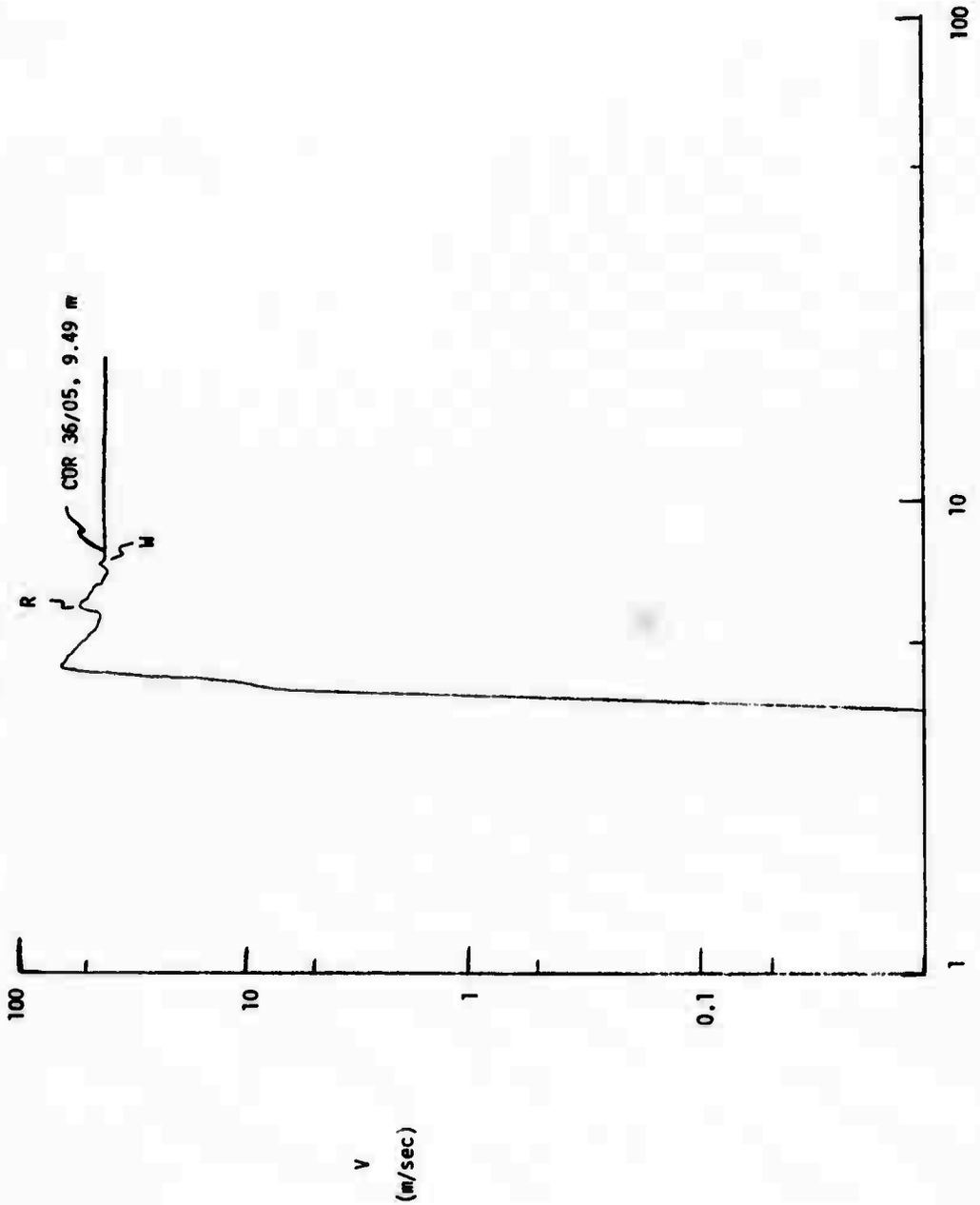

FIGURE C-17. "V"; COR 36/05, R = 9.49 m.

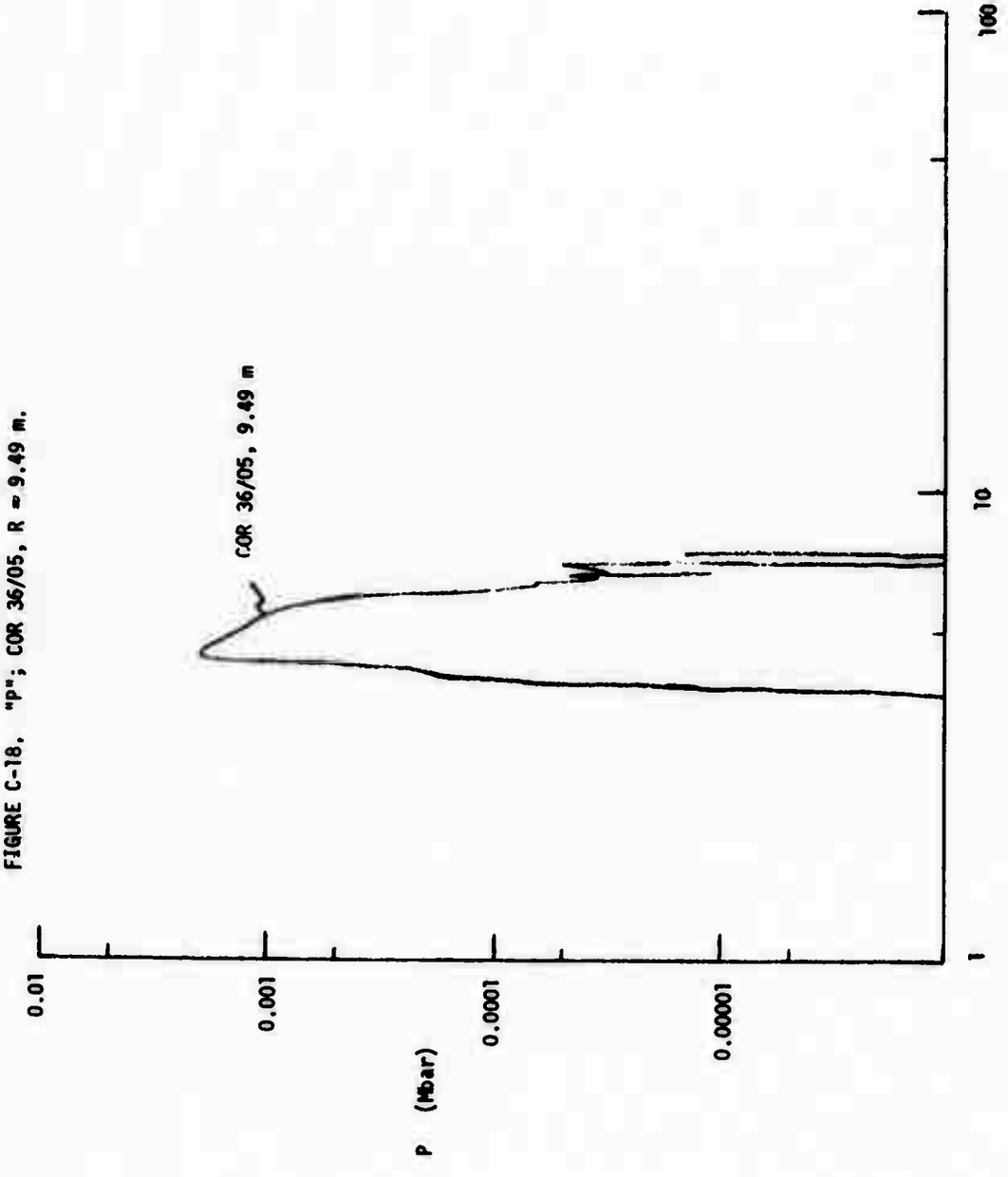

FIGURE C-18, "P"; COR 36/05, R = 9.49 m.

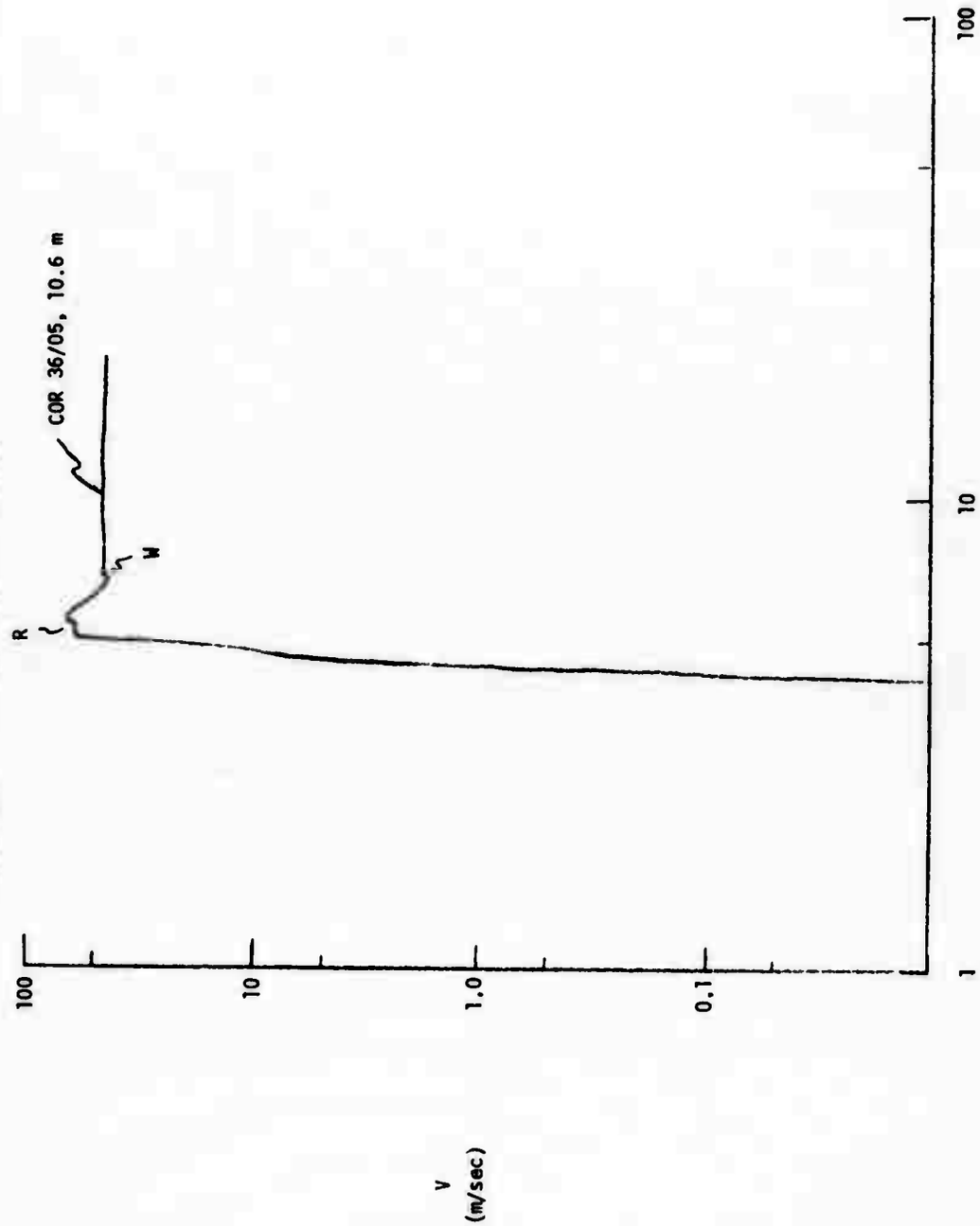

FIGURE C-19. "V"; COR 36/05, R = 10.6 m.

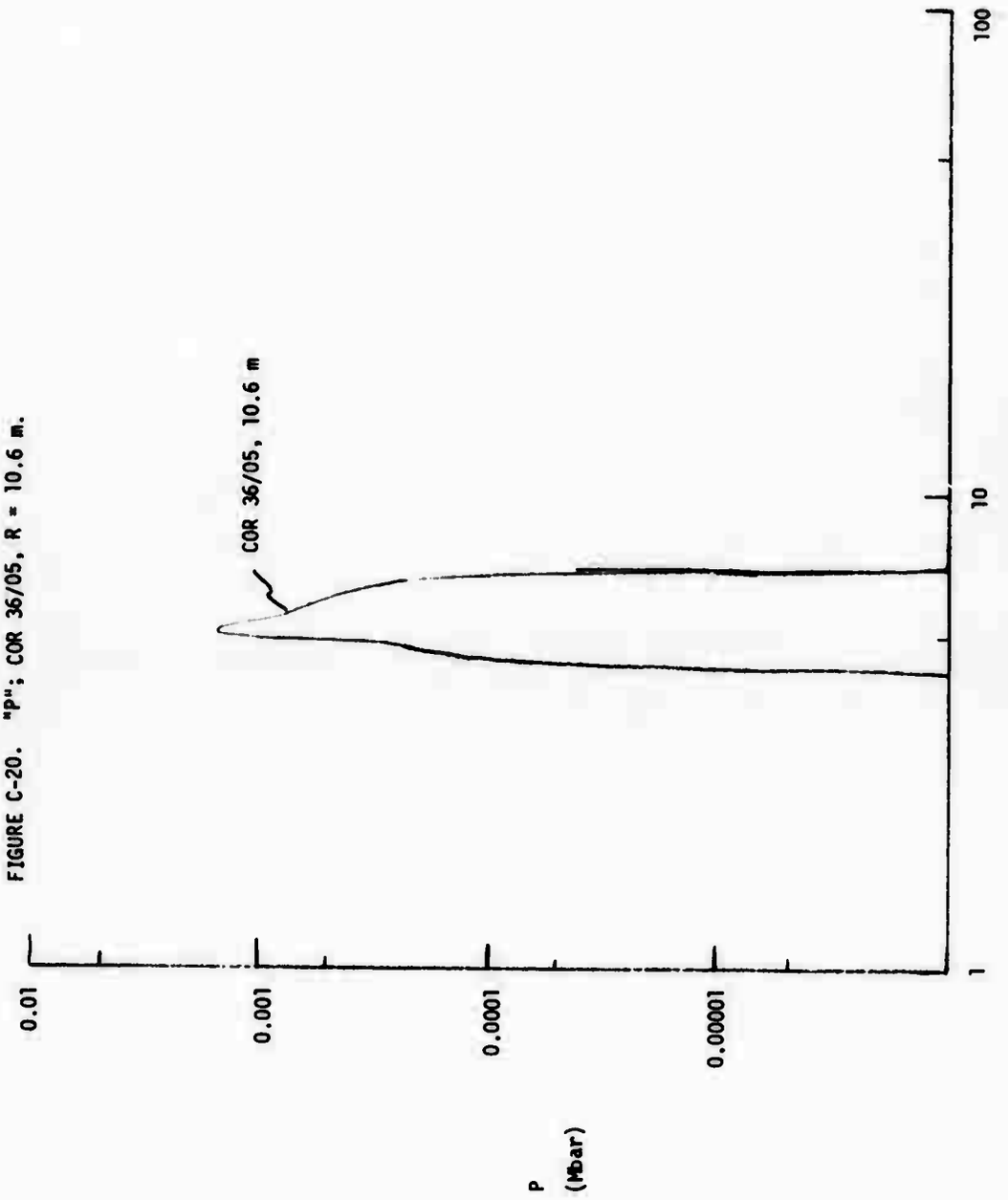

FIGURE C-20. "P"; COR 36/05, R = 10.6 m.

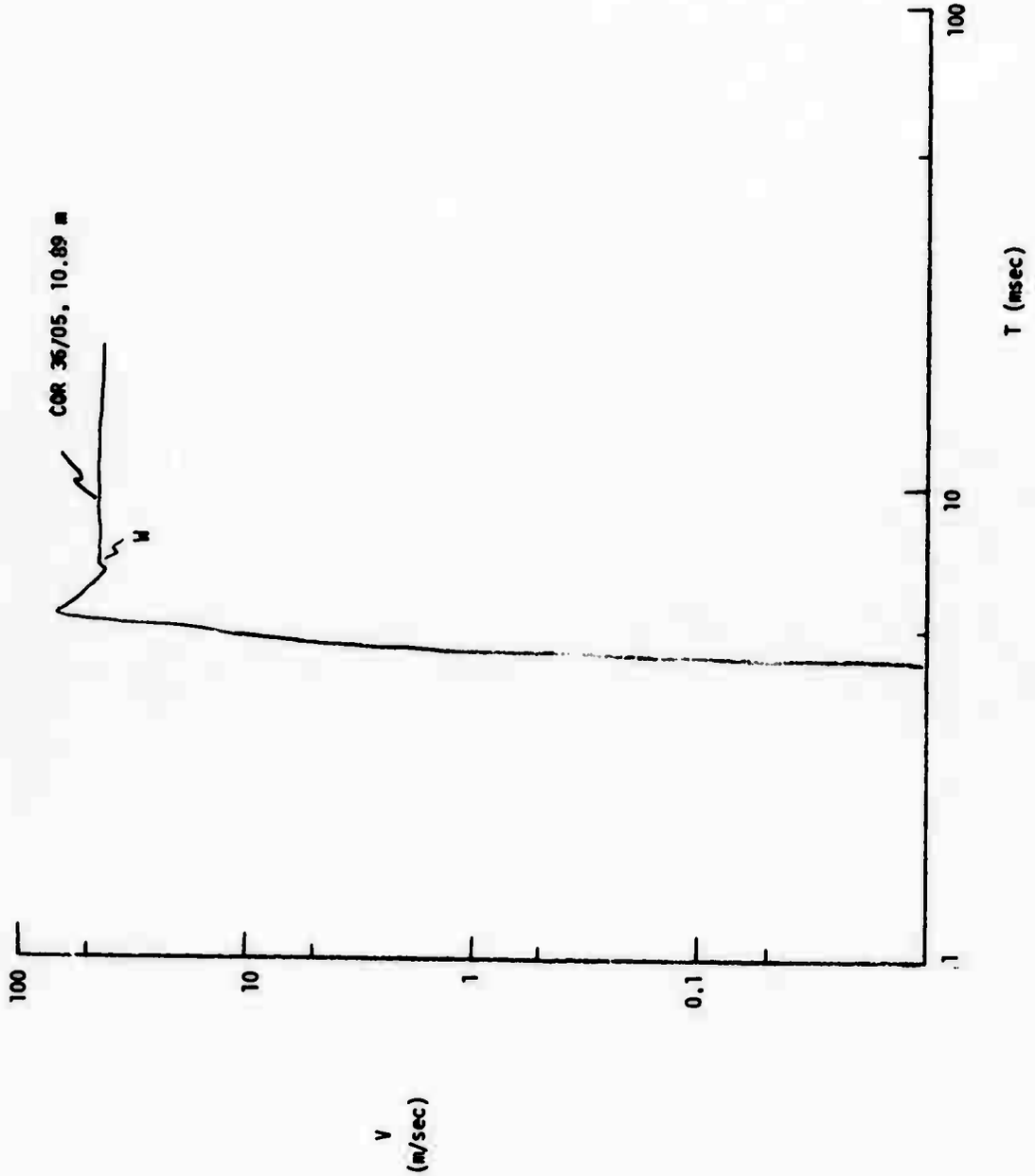

FIGURE C-21. "Y"; COR 36/05, R = 10.99 m.

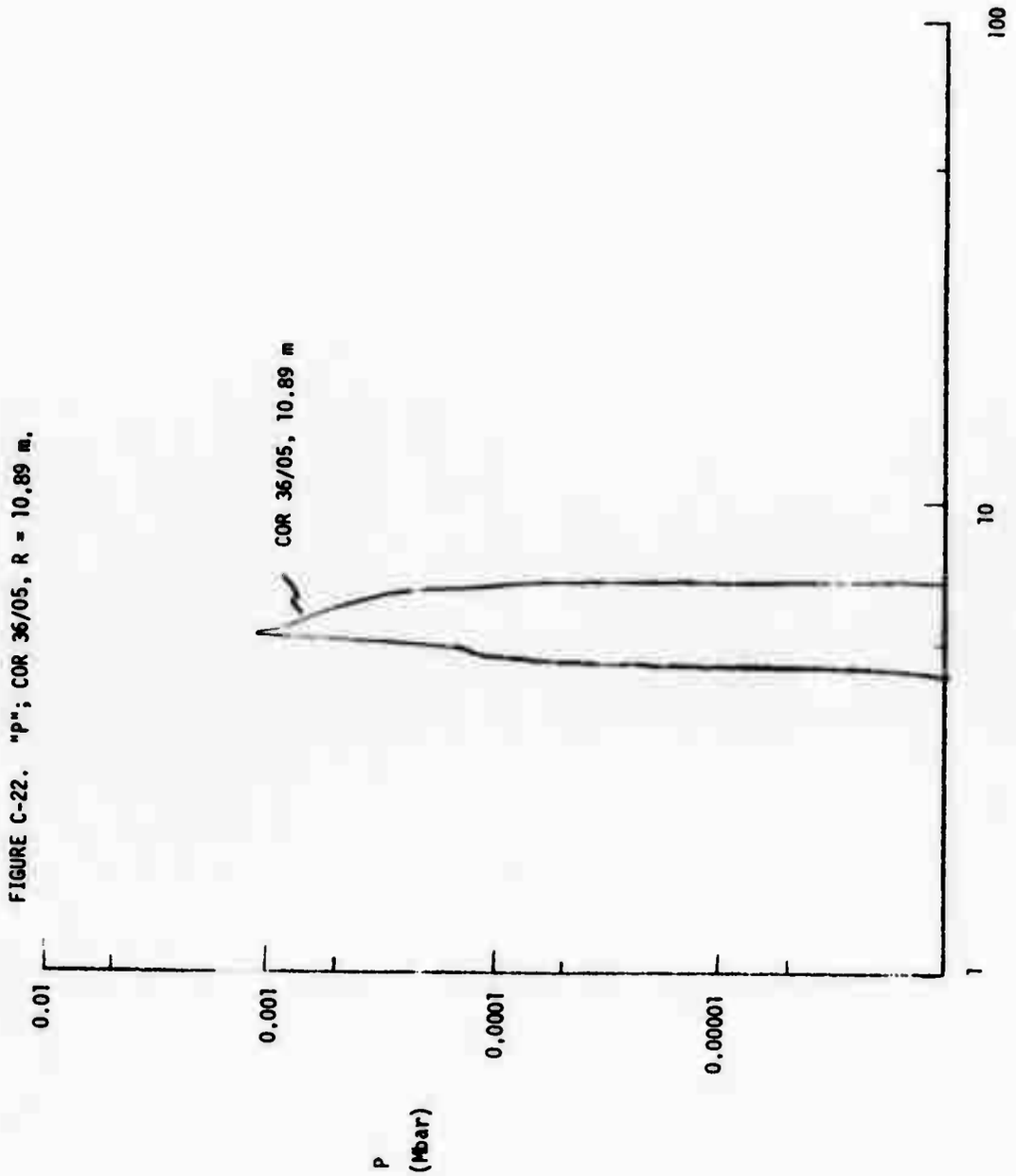

FIGURE C-22. "P"; COR 36/05, R = 10.89 m.

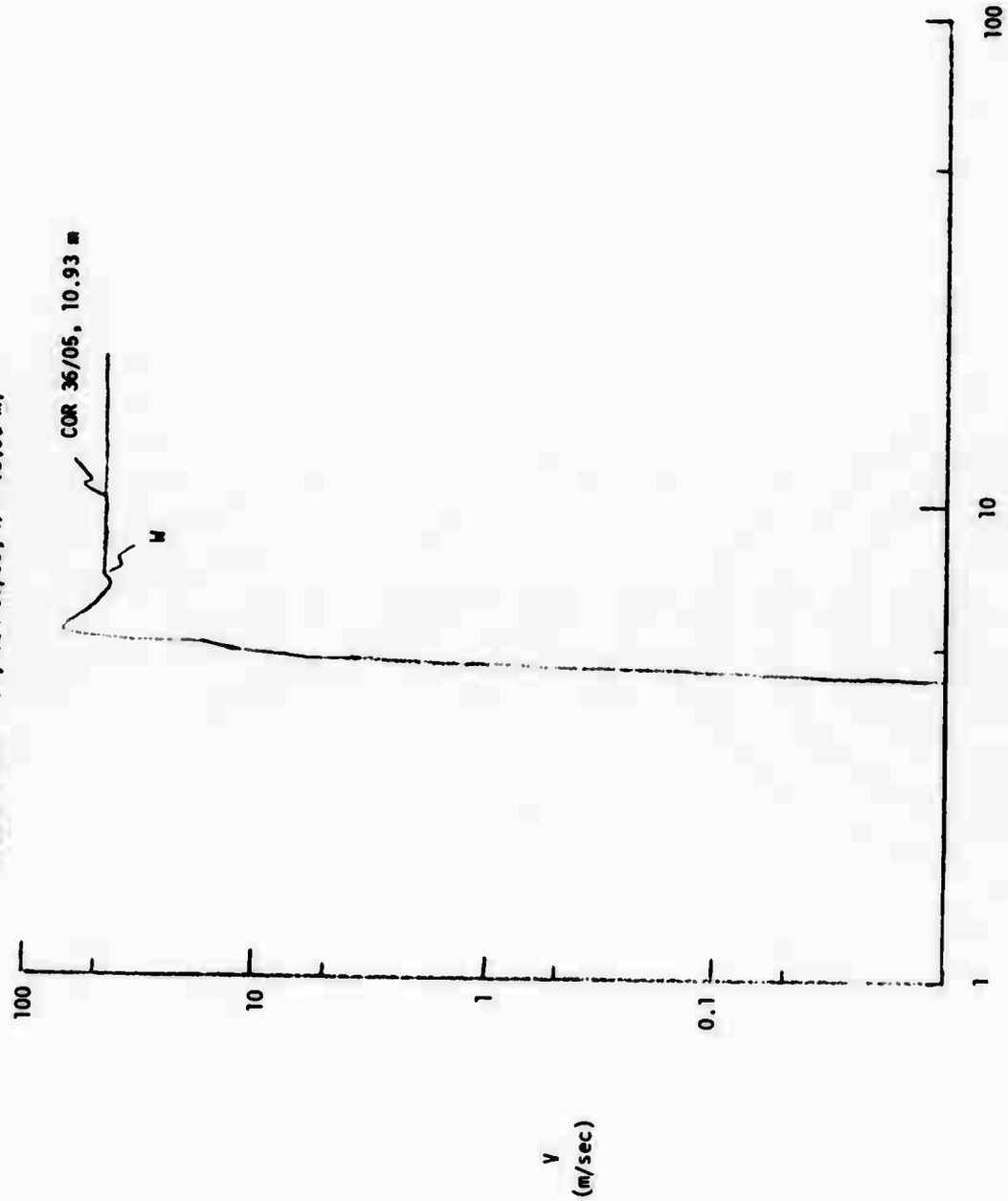

FIGURE C-23. "V"; COR 36/05, R = 10.93 m.

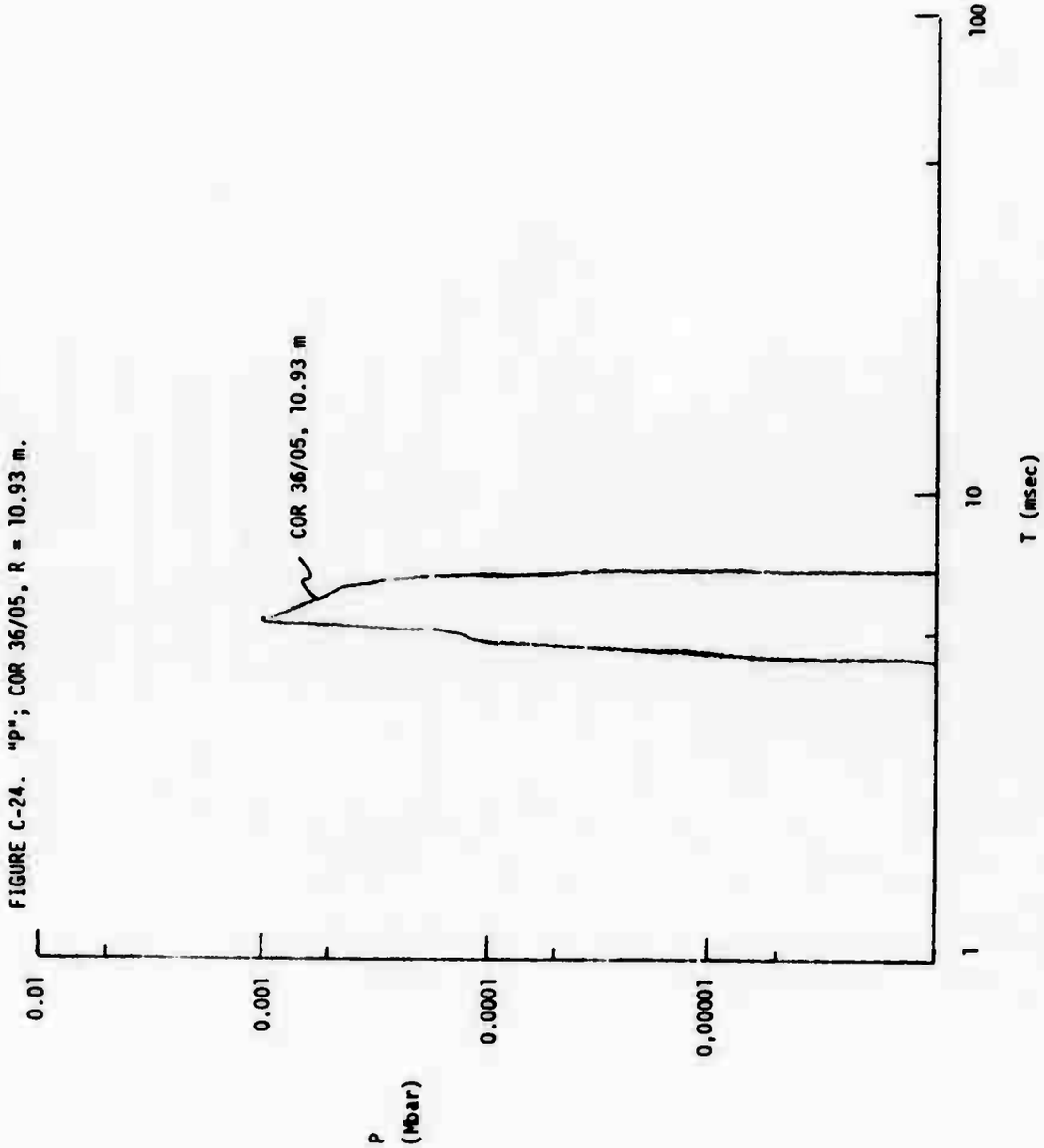

FIGURE C-24. "P"; COR 36/05, R = 10.93 m.

EIGURE C-25. "V"; COR 36/05, R = 6.01 m, with rezoning after shock crosses interface (linear plot).

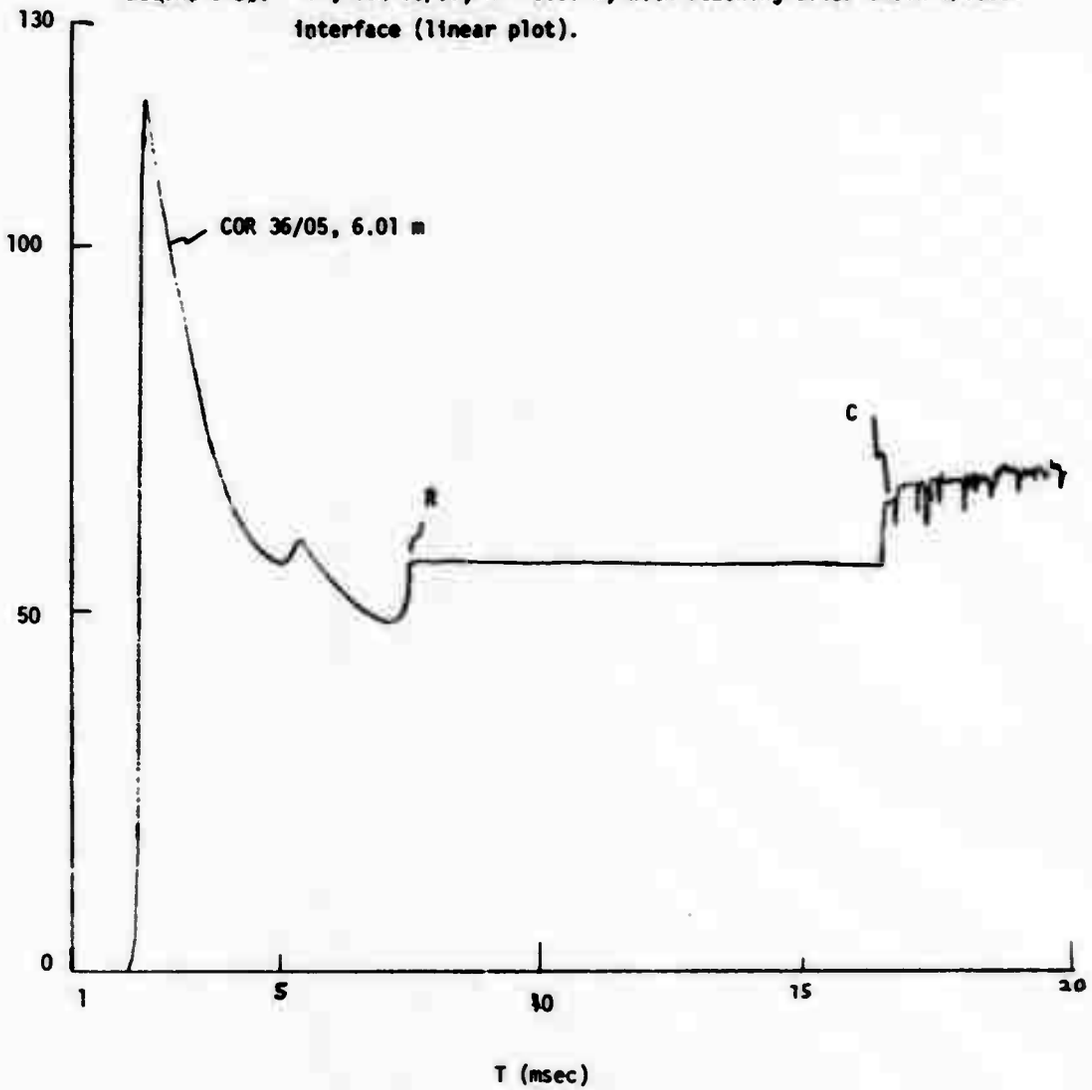

FIGURE C-26. "V"; COR 36/05, R=6.01 m, without dezoning, constant zone size; (linear plot).

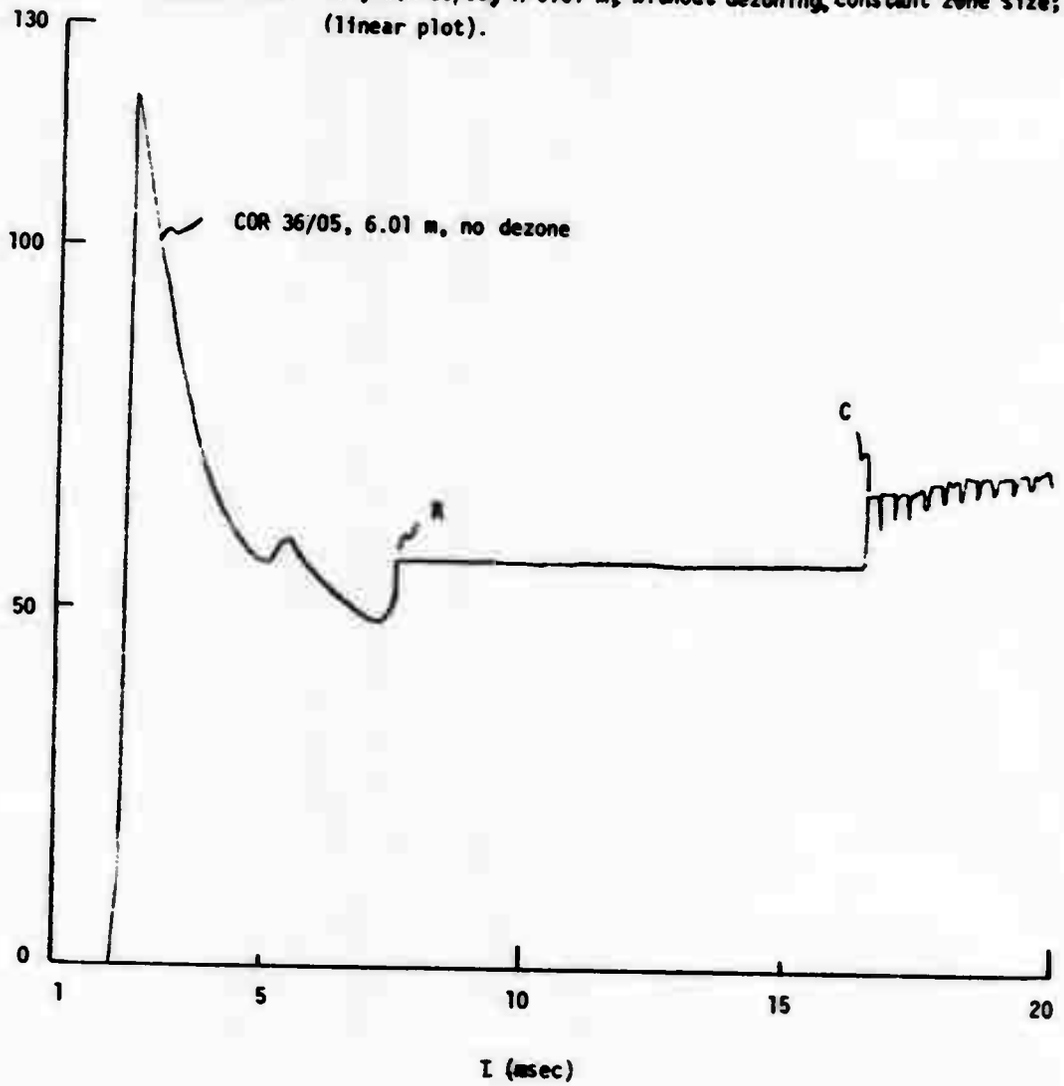

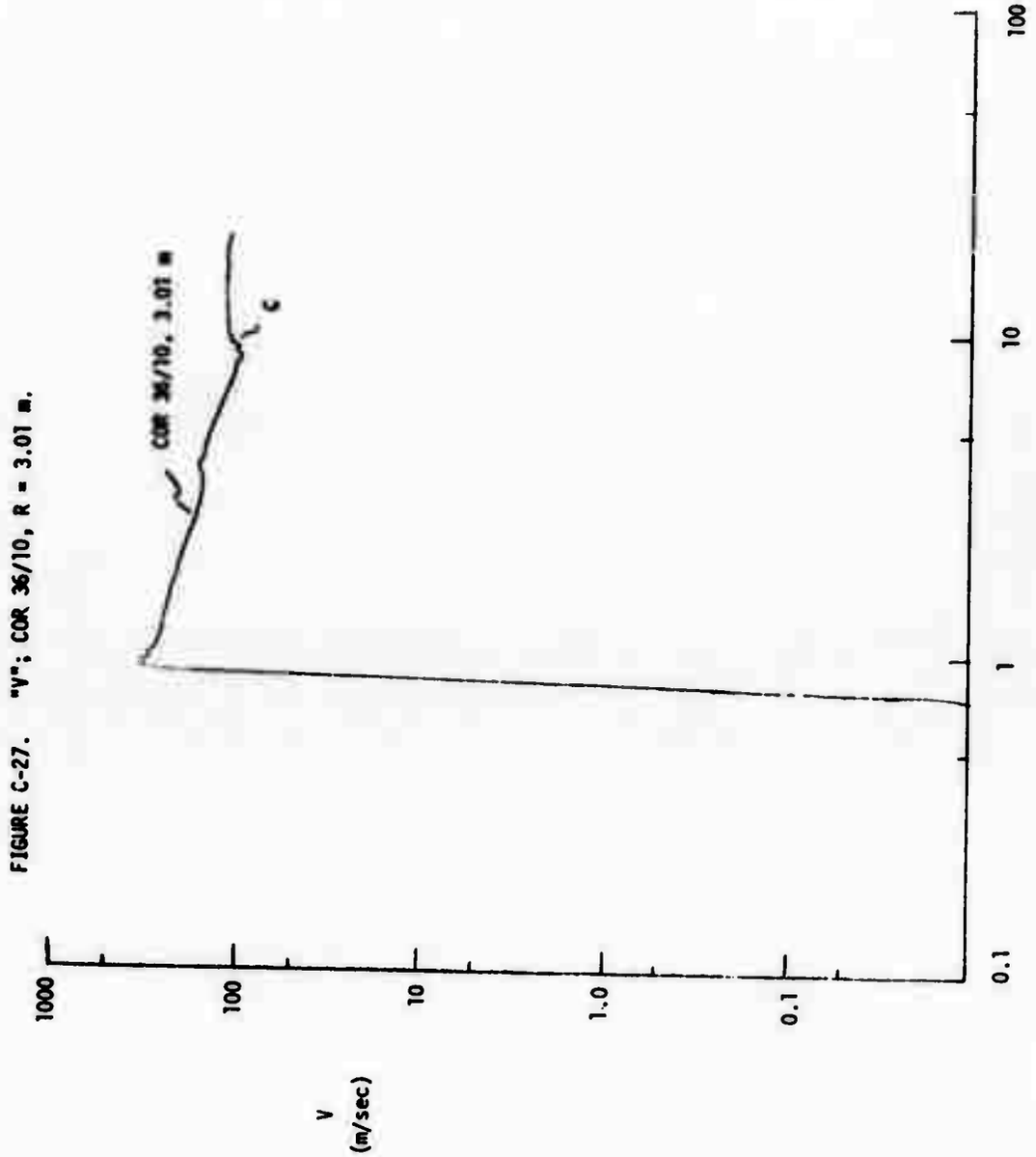

FIGURE C-27. "V"; COR 36/10, R = 3.01 m.

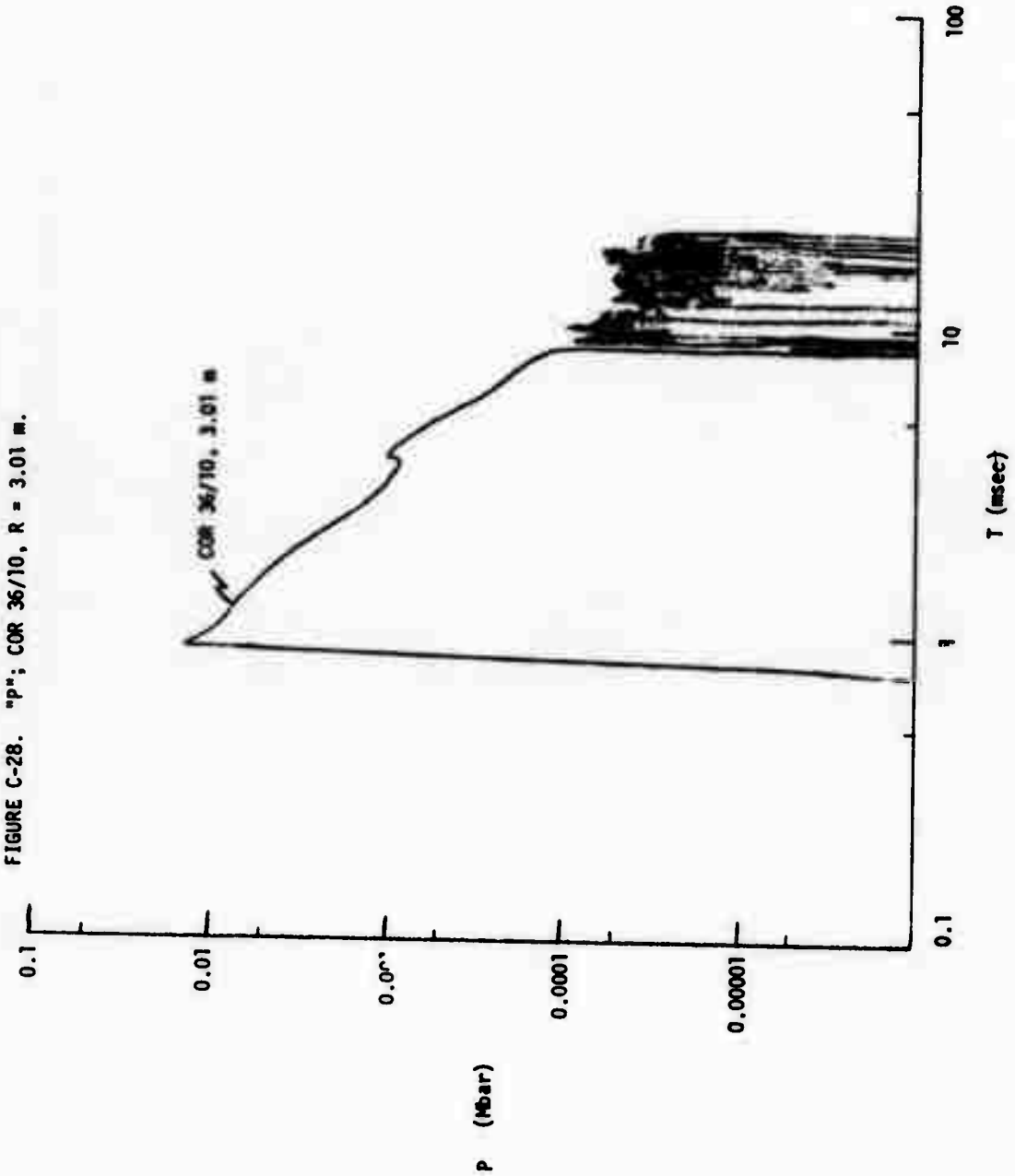

FIGURE C-28. "P"; COR 36/10, R = 3.01 m.

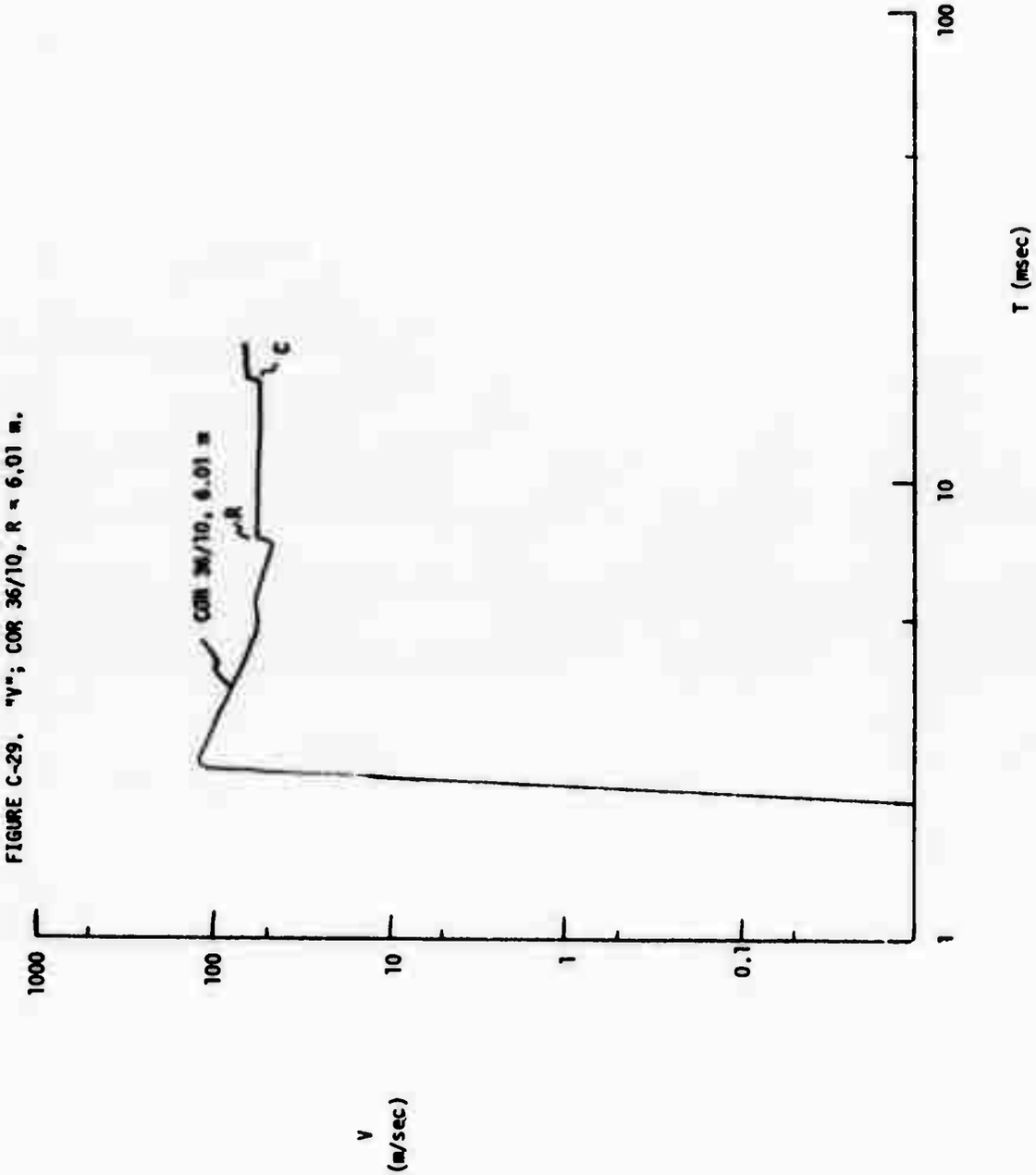

FIGURE C-29. "V"; COR 36/10, R = 6.01 m.

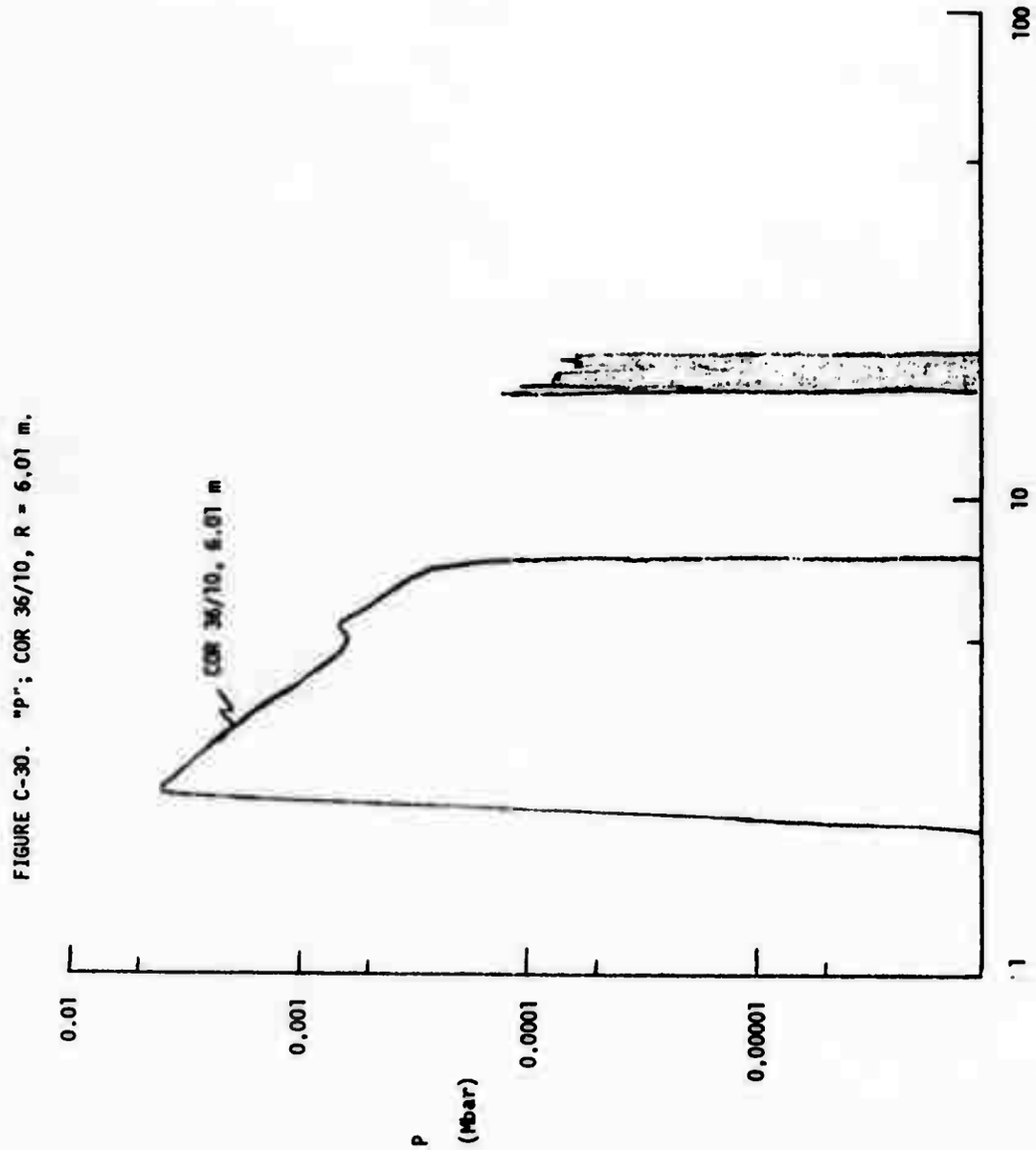

FIGURE C-30. "p"; COR 36/10, R = 6.01 m.

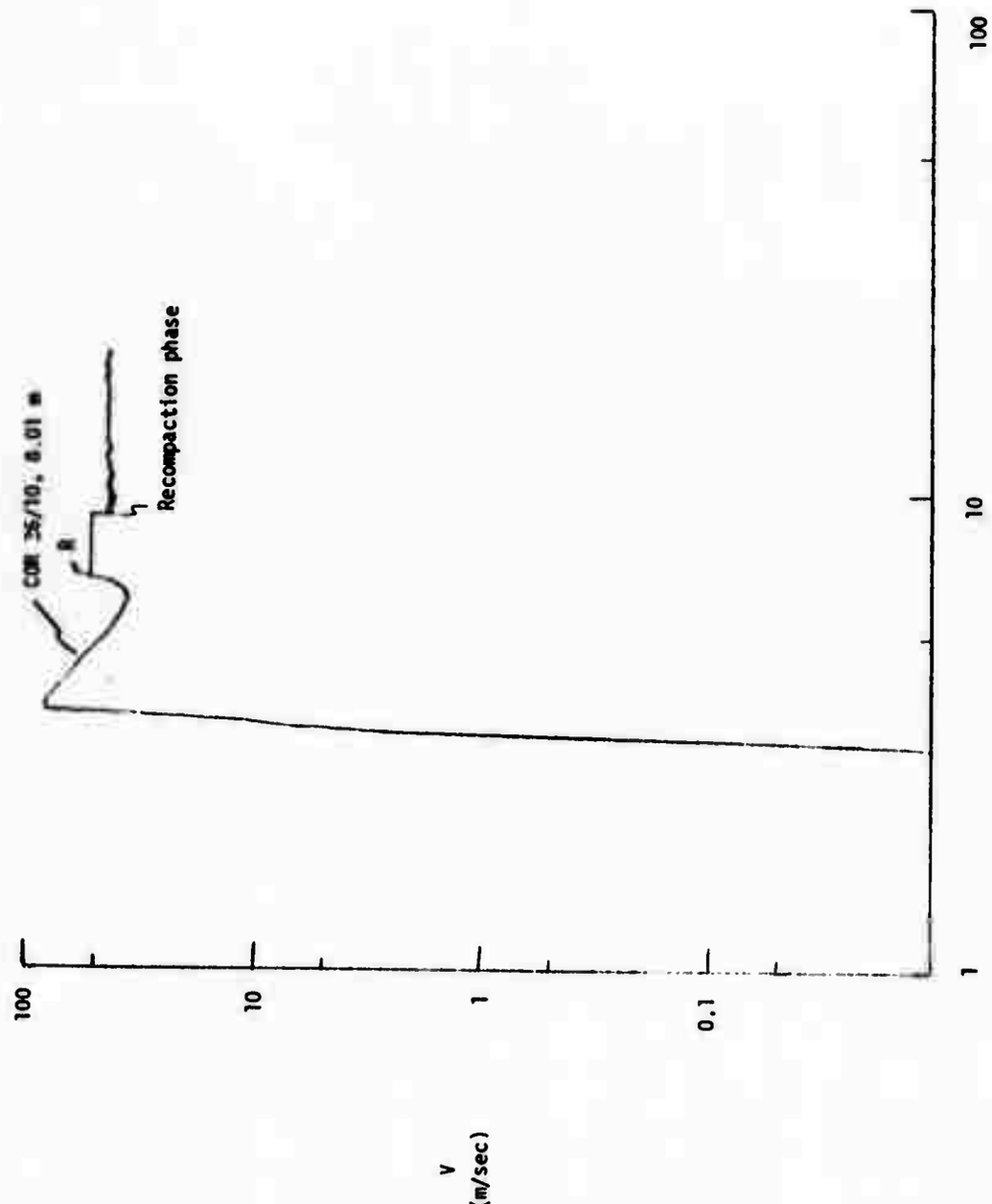

FIGURE C-31. "V"; COR 36/10, R = 8.01 m.

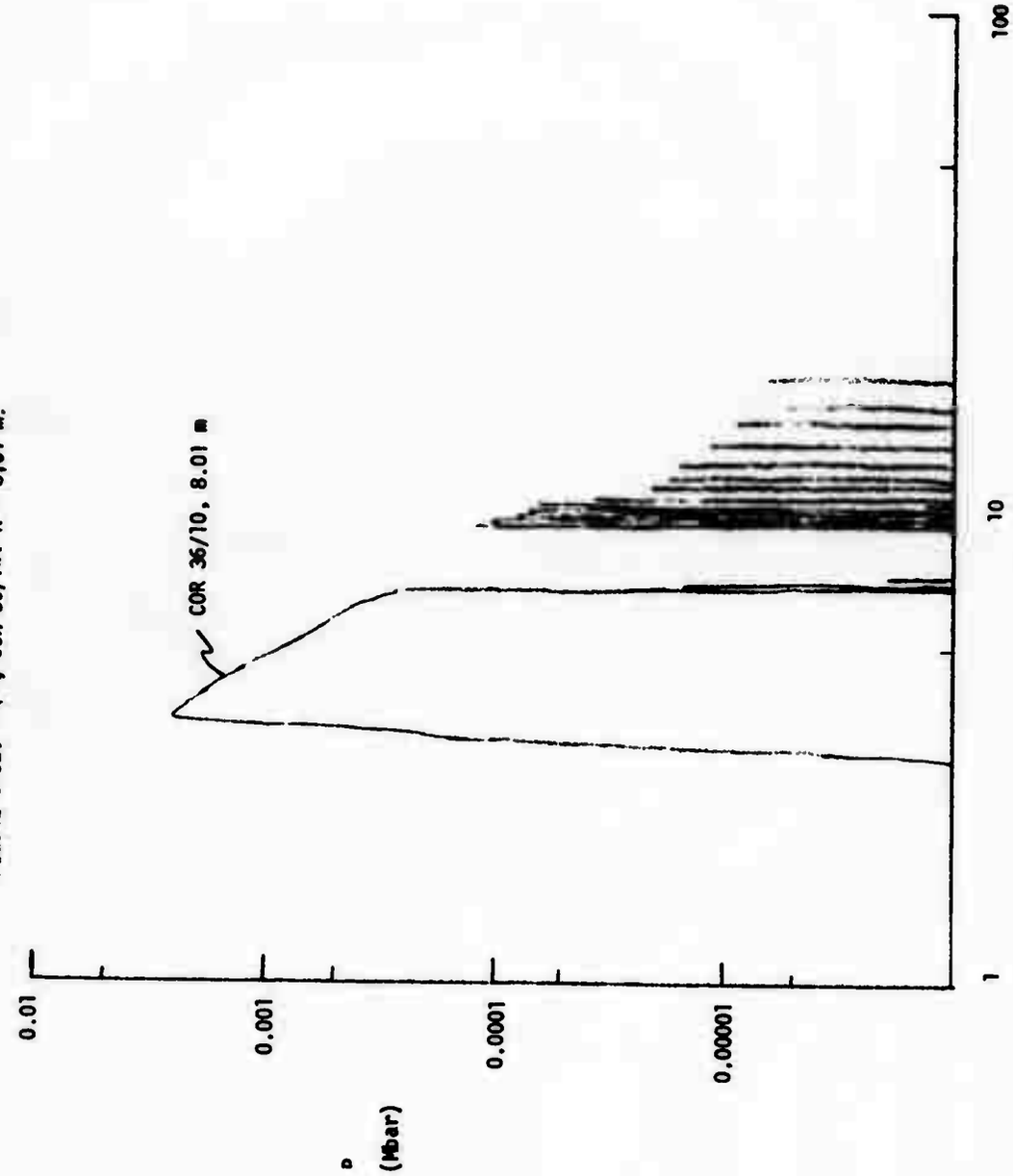

FIGURE C-32. "P"; COR 36/10. R = 8,01 m.

FIGURE C-33. "V"; COR 36/10, R = 9.49 m.

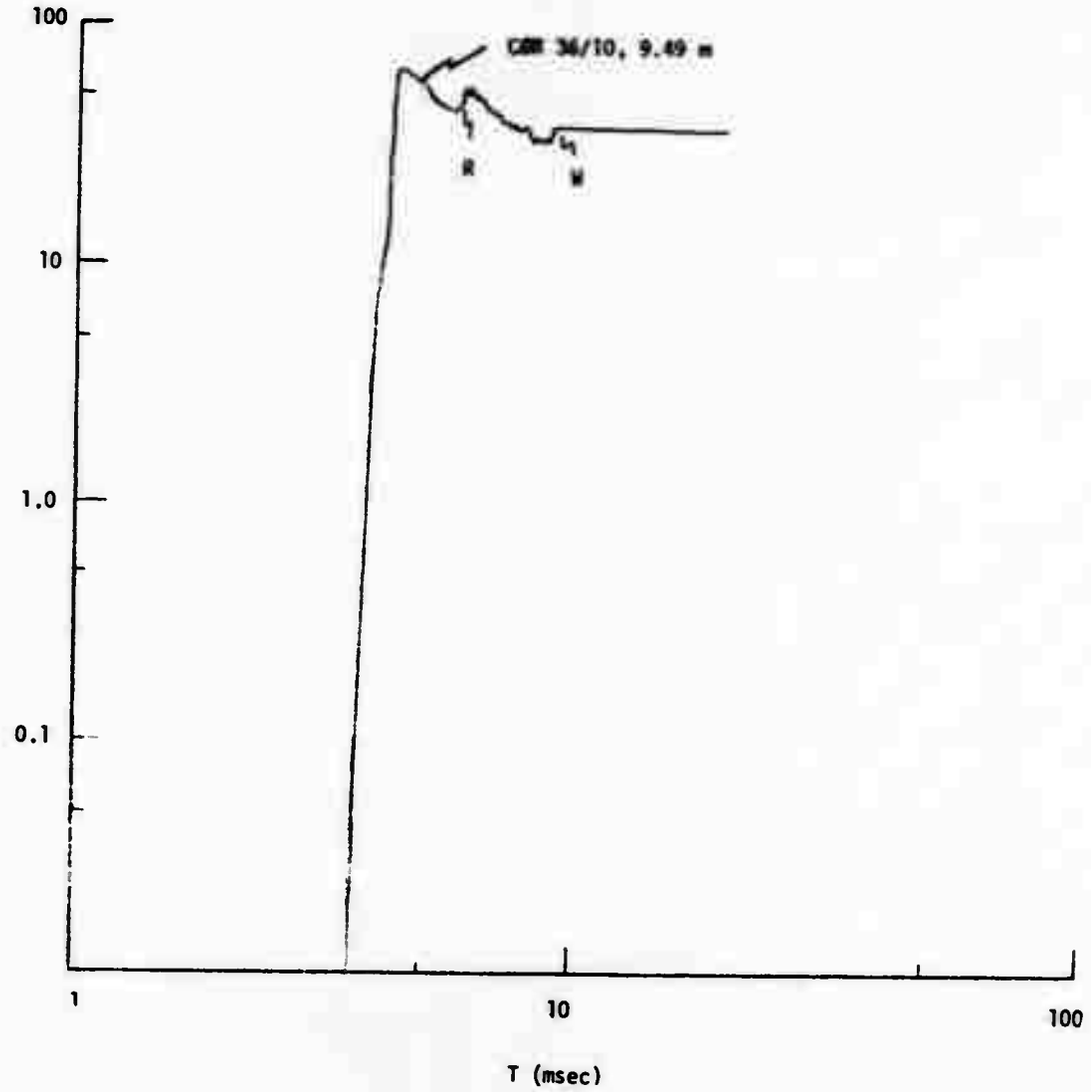

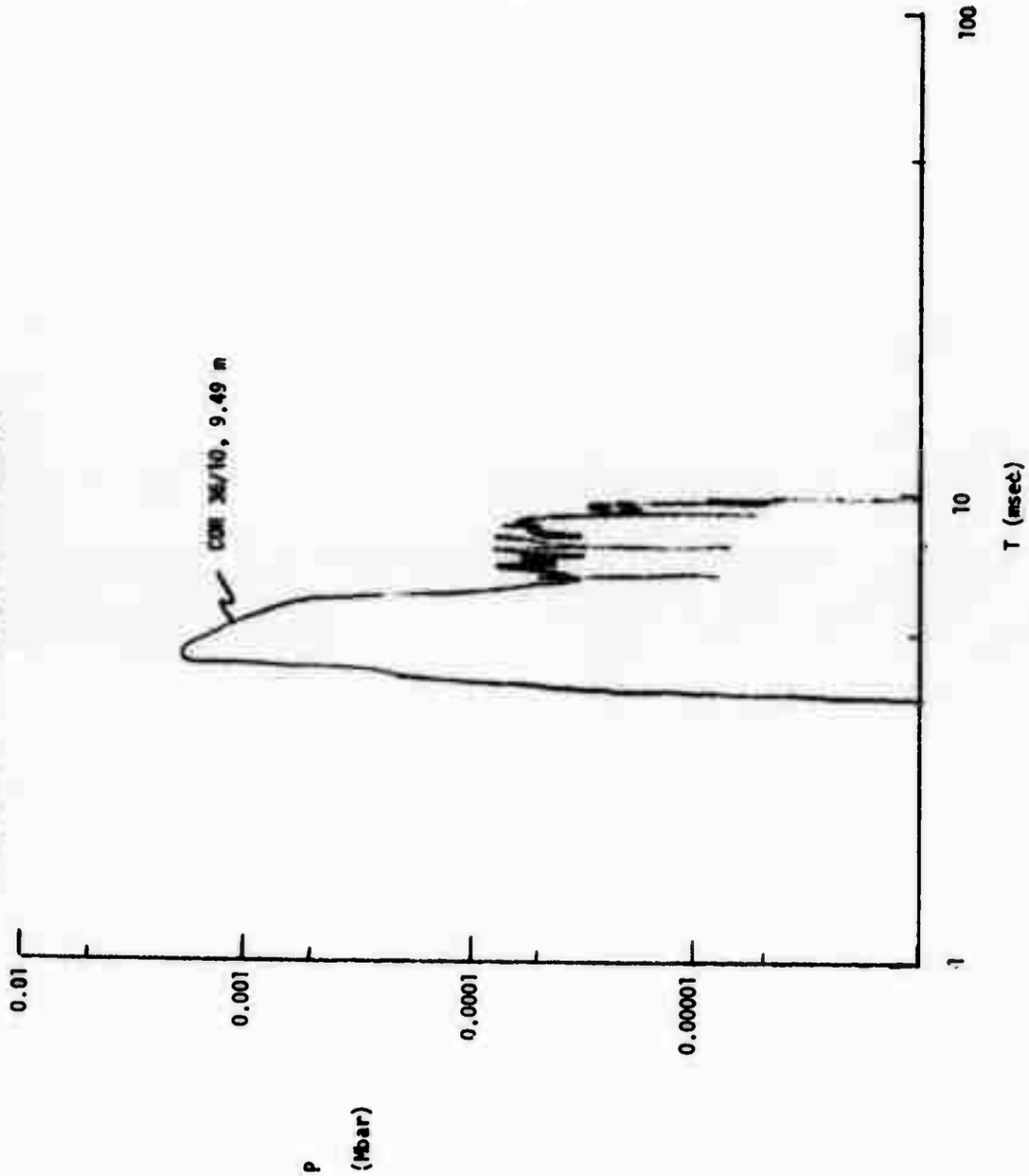

FIGURE C-34. "P"; COR 36/10, R = 9.49 m.

FIGURE C-35. "V"; COR 36/10, R = 10.6 m.

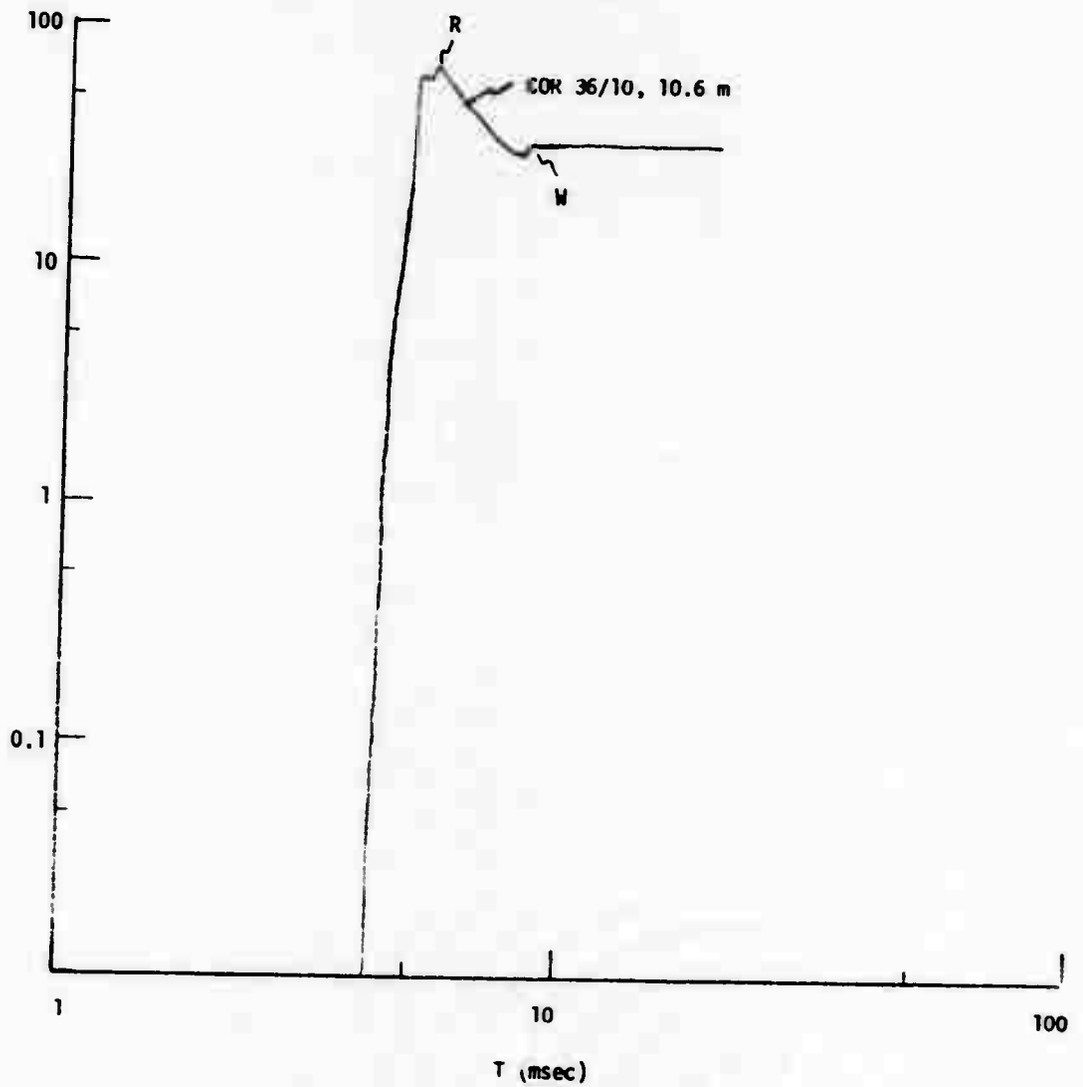

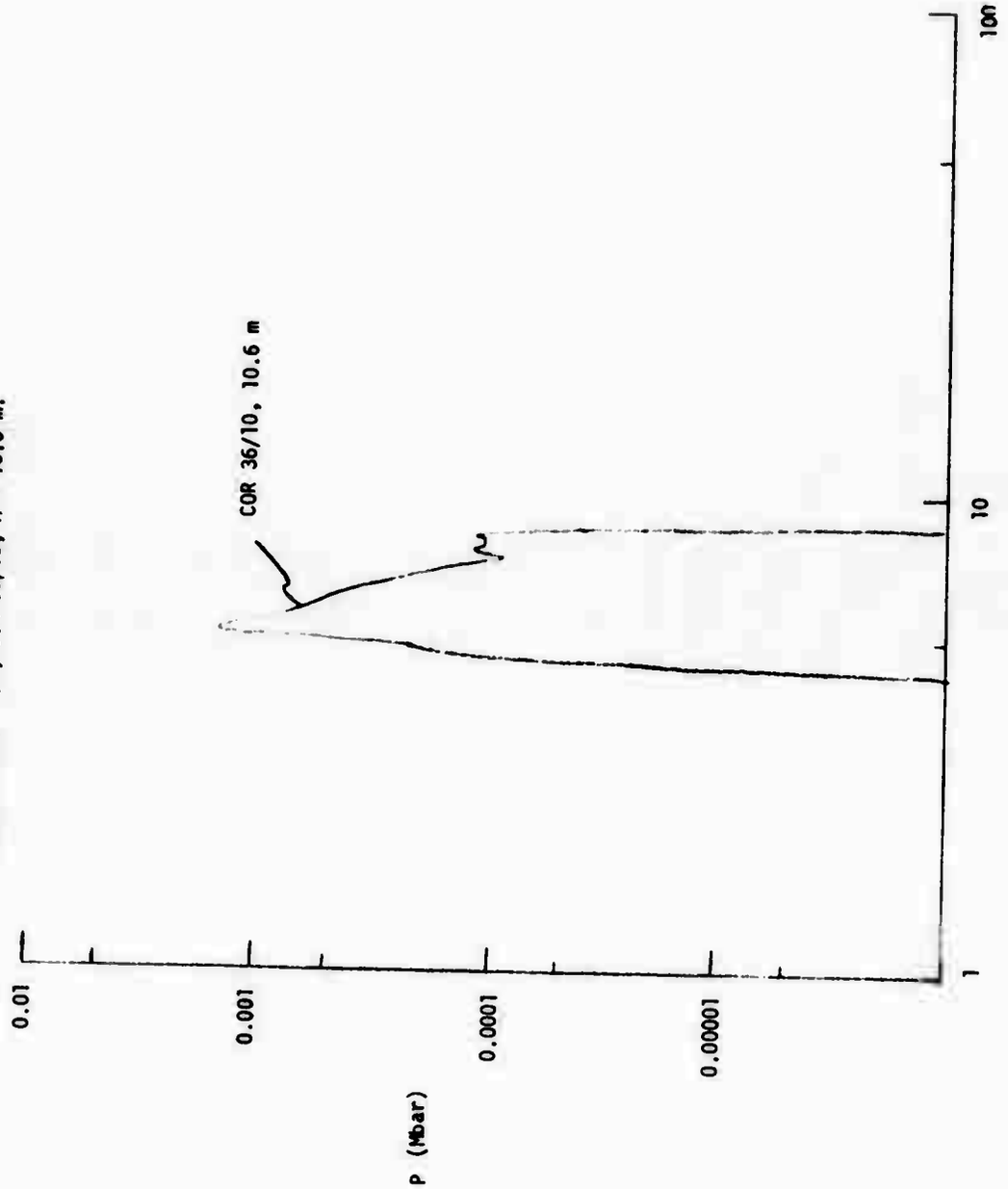

FIGURE C-36. "P"; COR 36/10, R = 10.6 m.

FIGURE C-37. "V"; COR 36/10, R = 10.89 m.

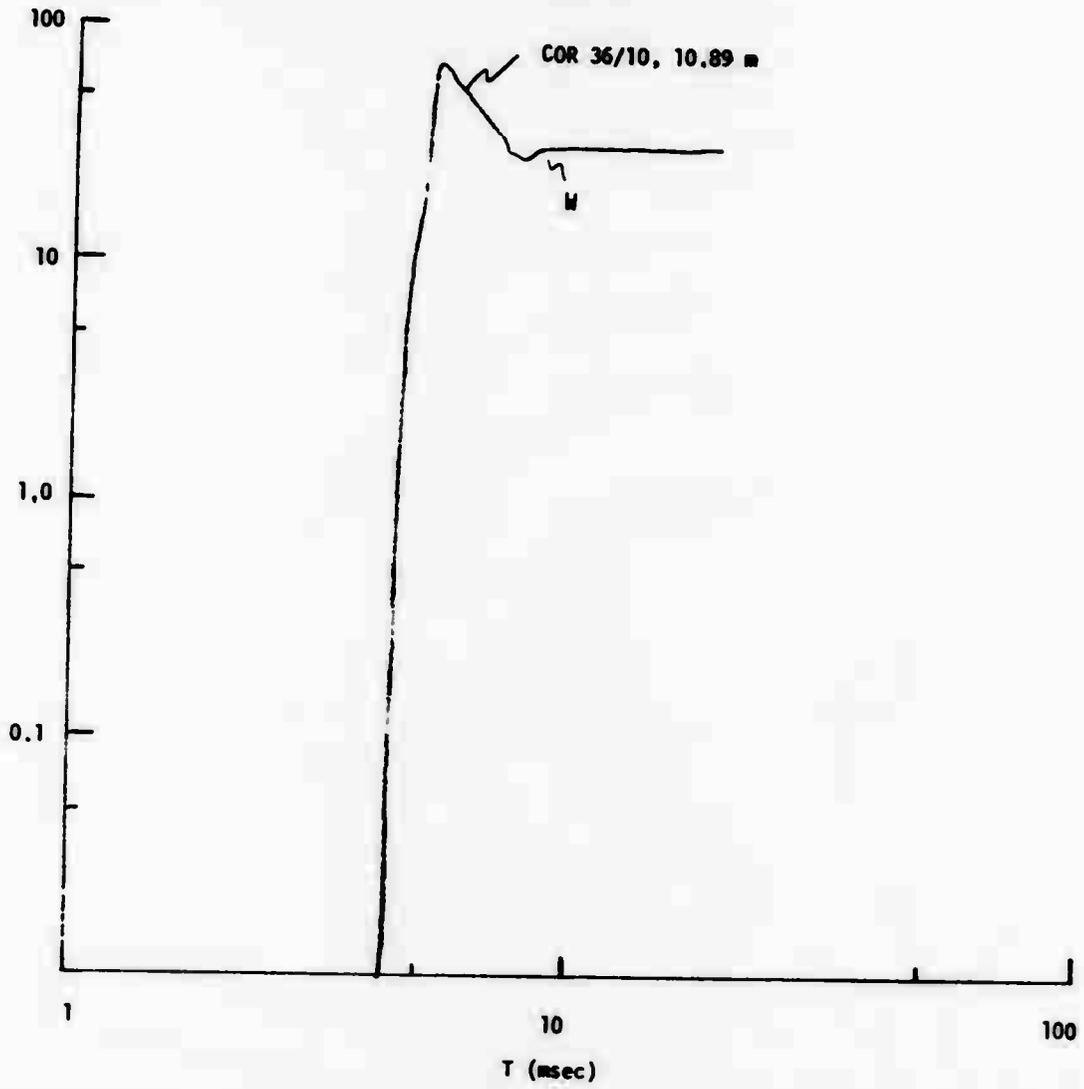

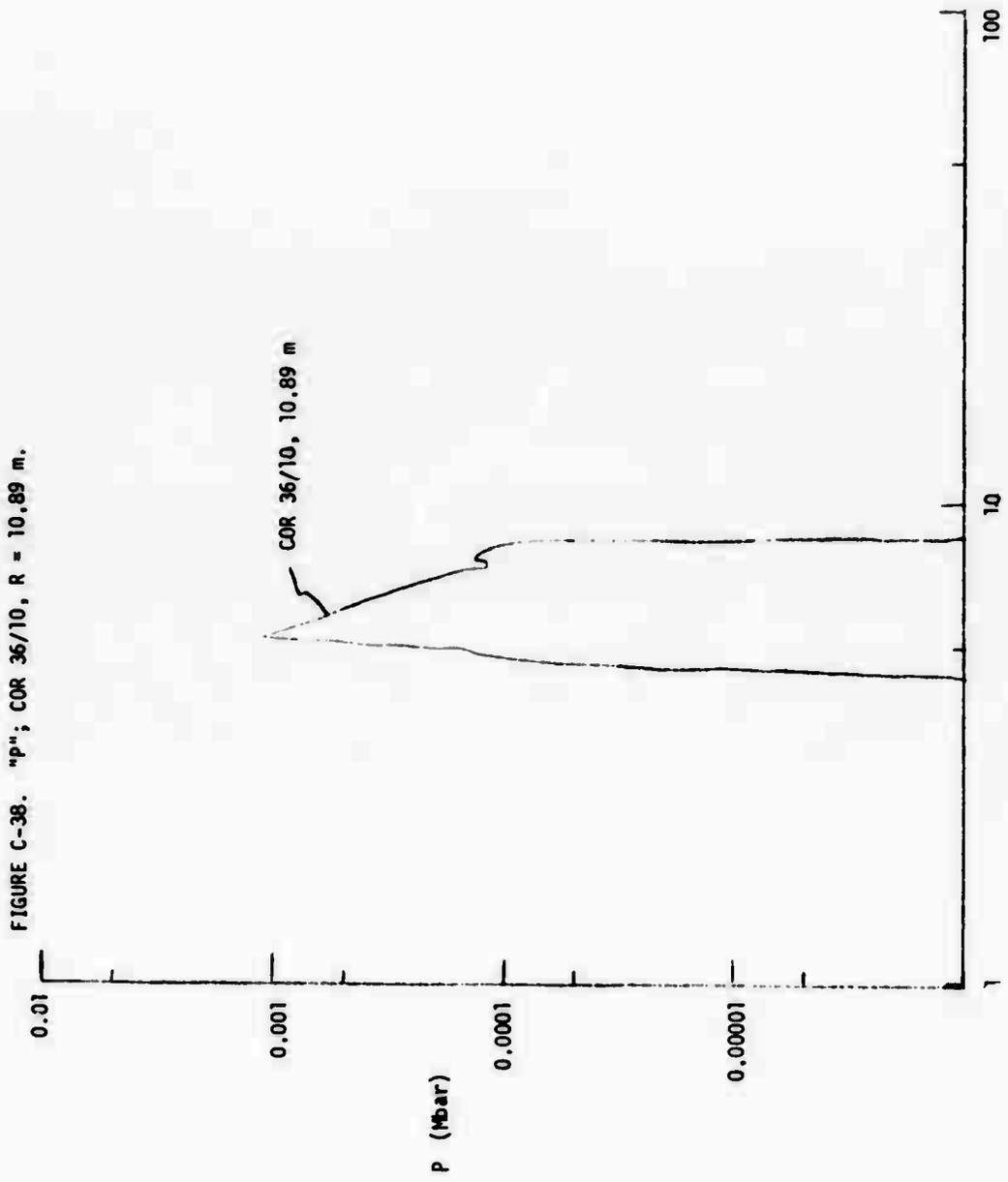

FIGURE C-38. "P"; COR 36/10, R = 10.89 m.

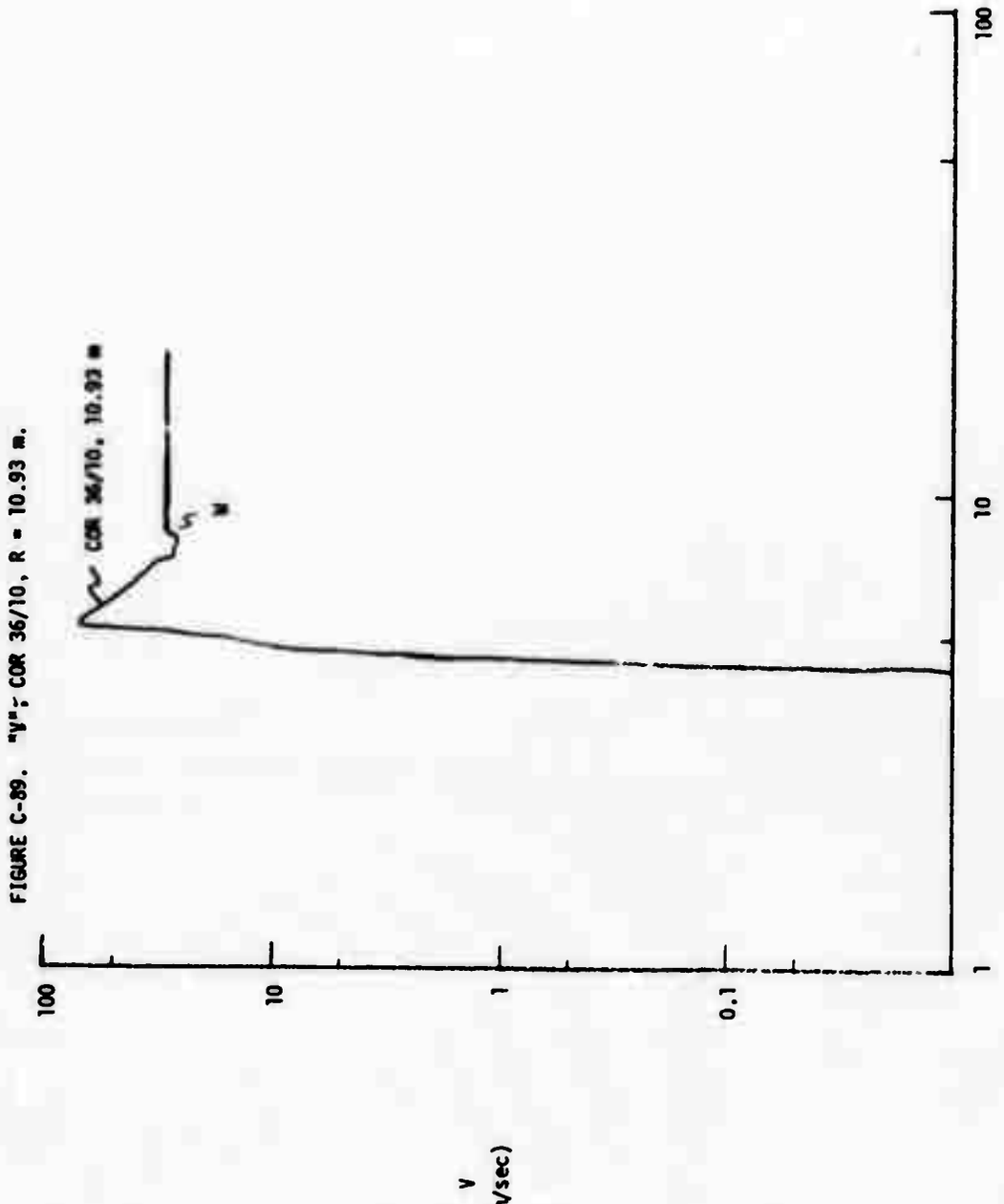

FIGURE C-89. "V"; COR 36/10, R = 10.93 m.

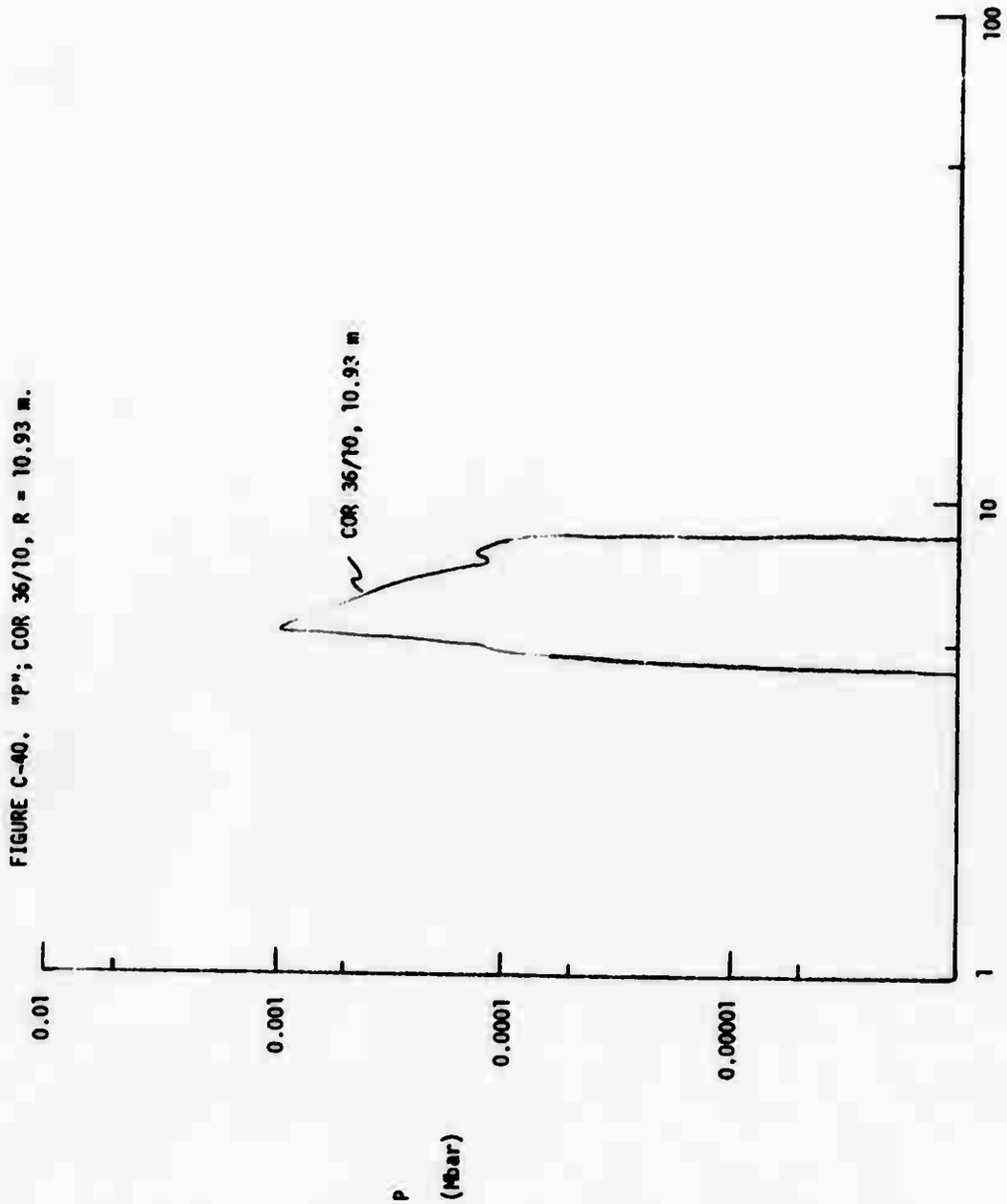

FIGURE C-40. "P"; COR 36/10, R = 10.93 m.

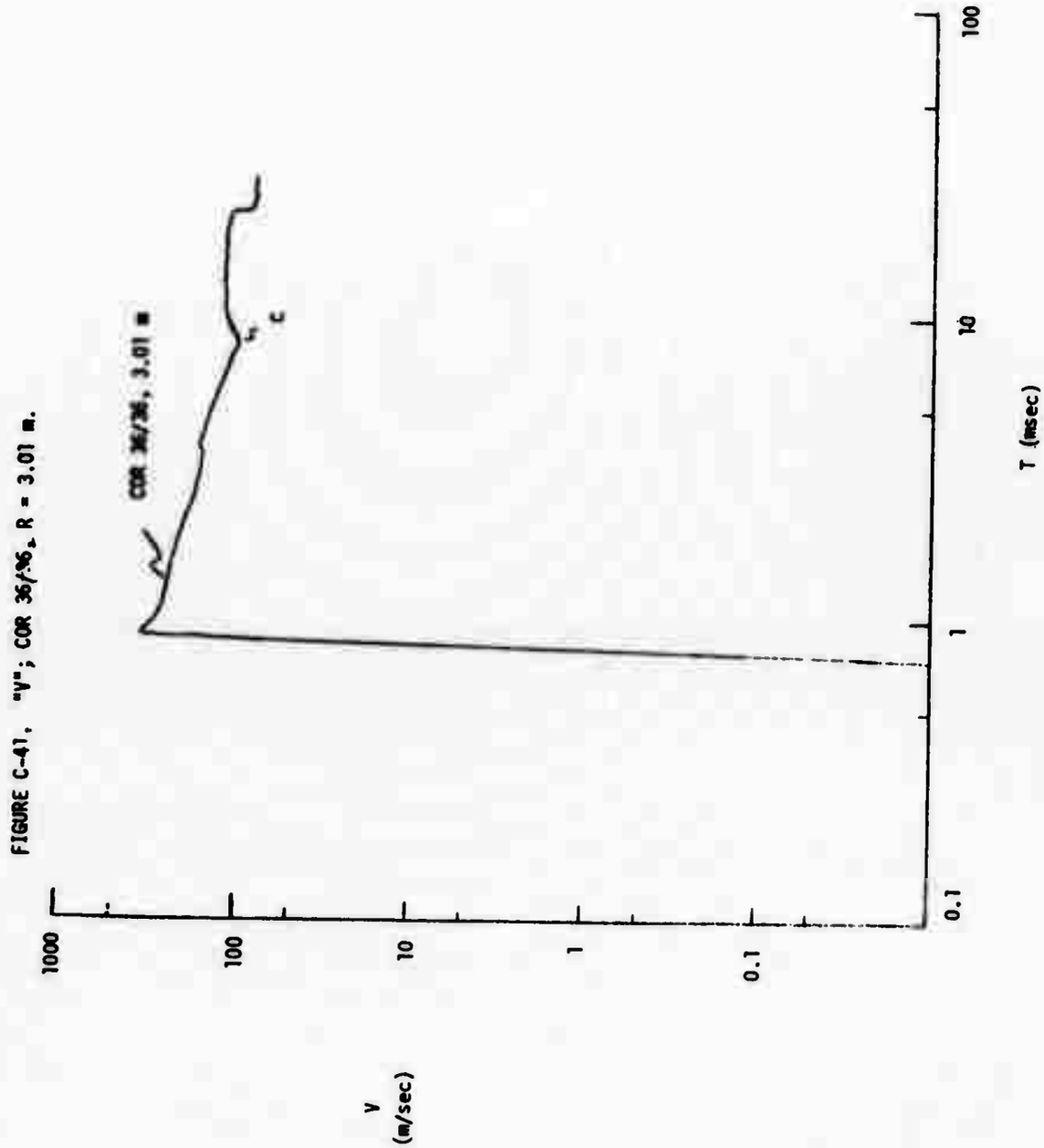

FIGURE C-41, "V"; COR 36/36, R = 3.01 m.

FIGURE C-42. "P"; COR 36/36, R = 3,01 m.

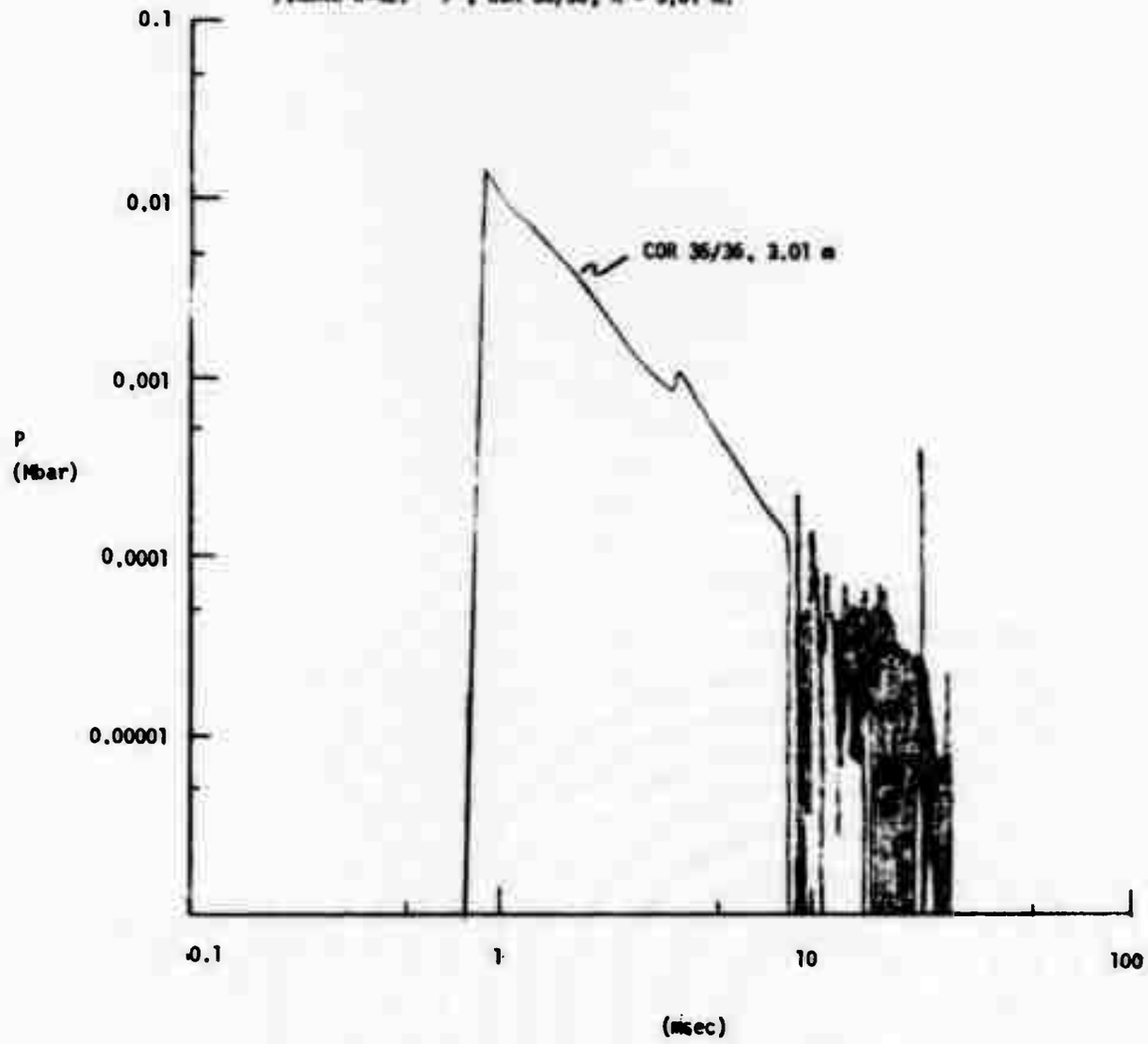

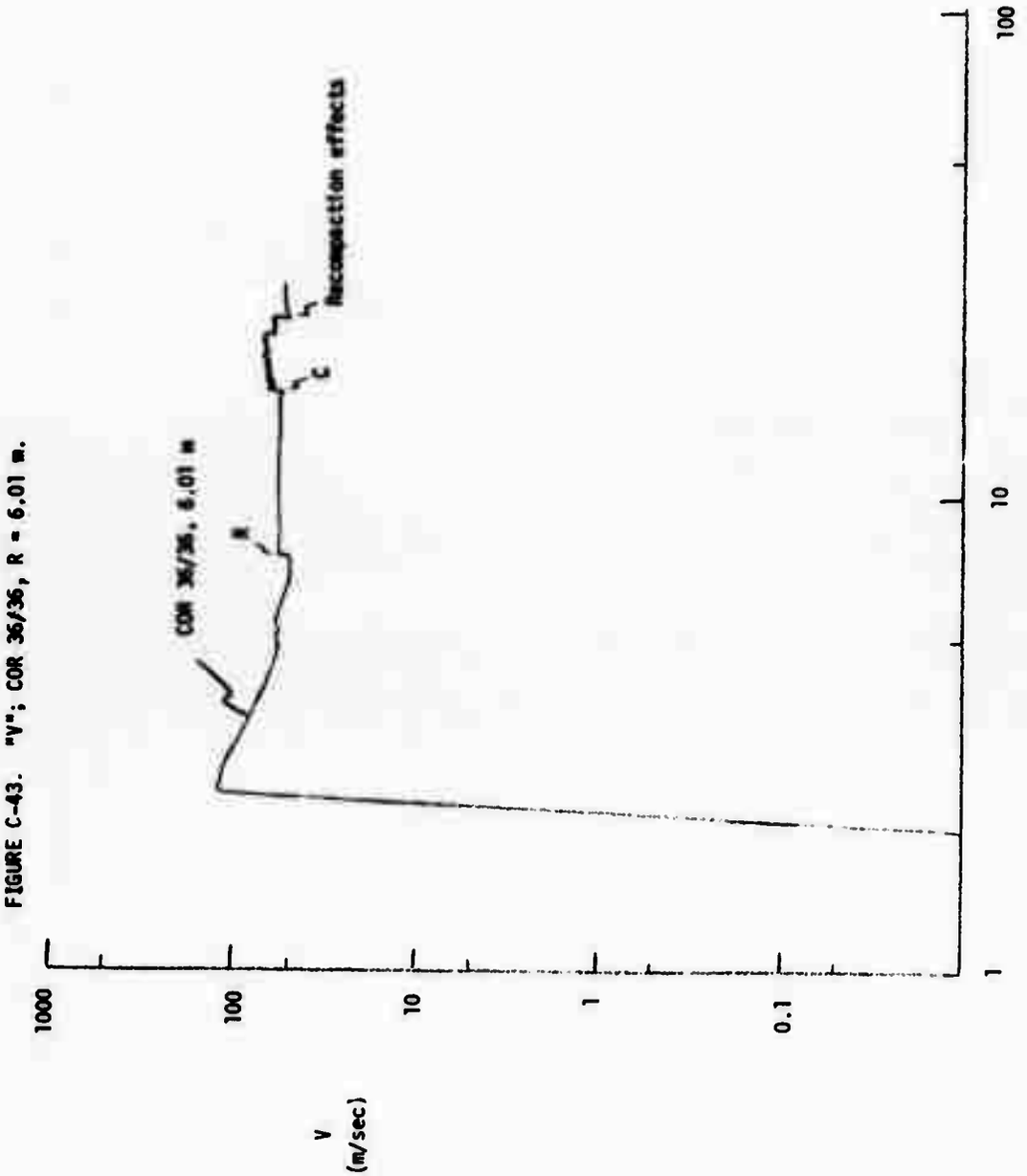

FIGURE C-43. "V"; COR 36/36, R = 6.01 m.

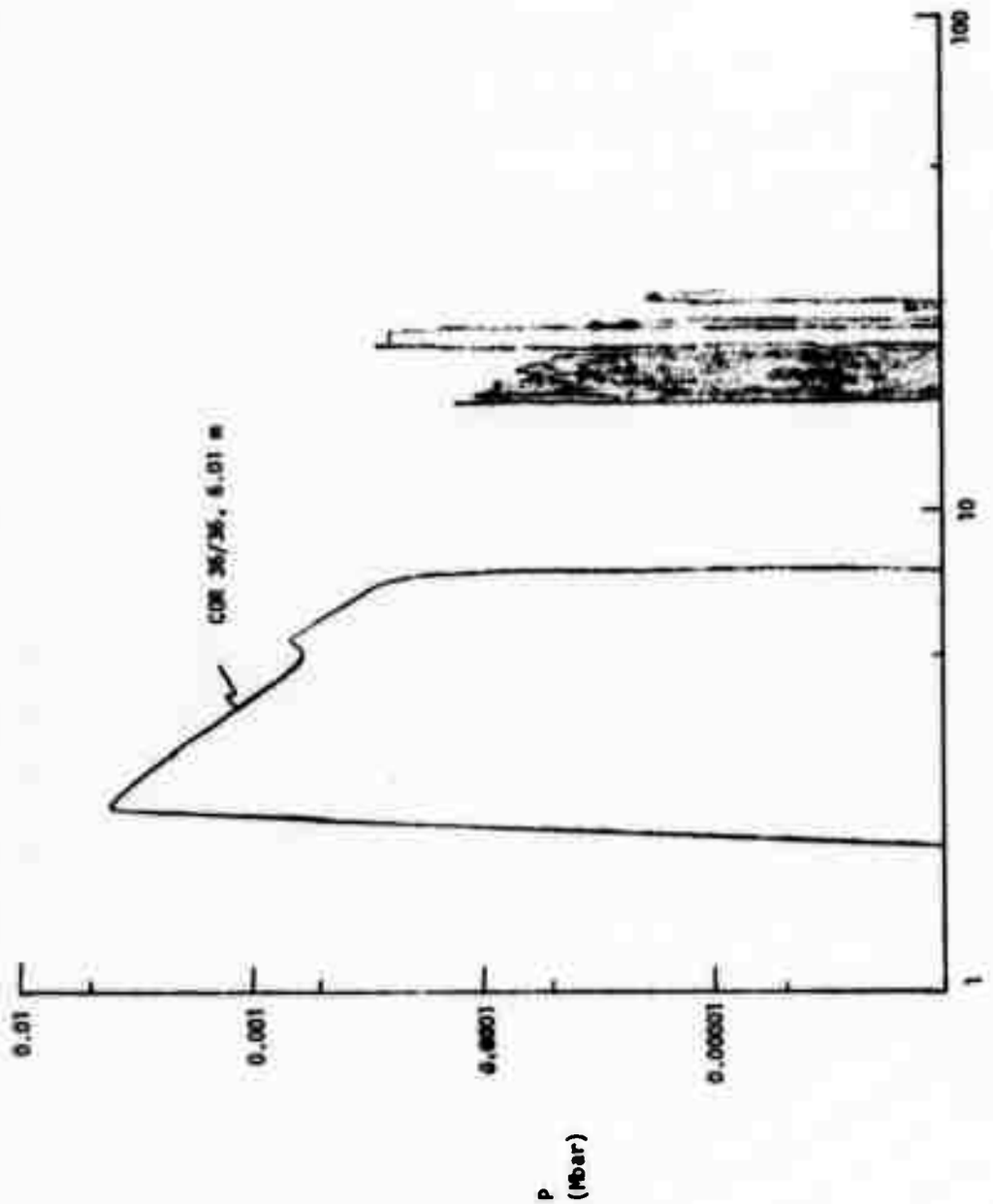

FIGURE C-44. "p"; COR 36/36, R = 6.01 m.

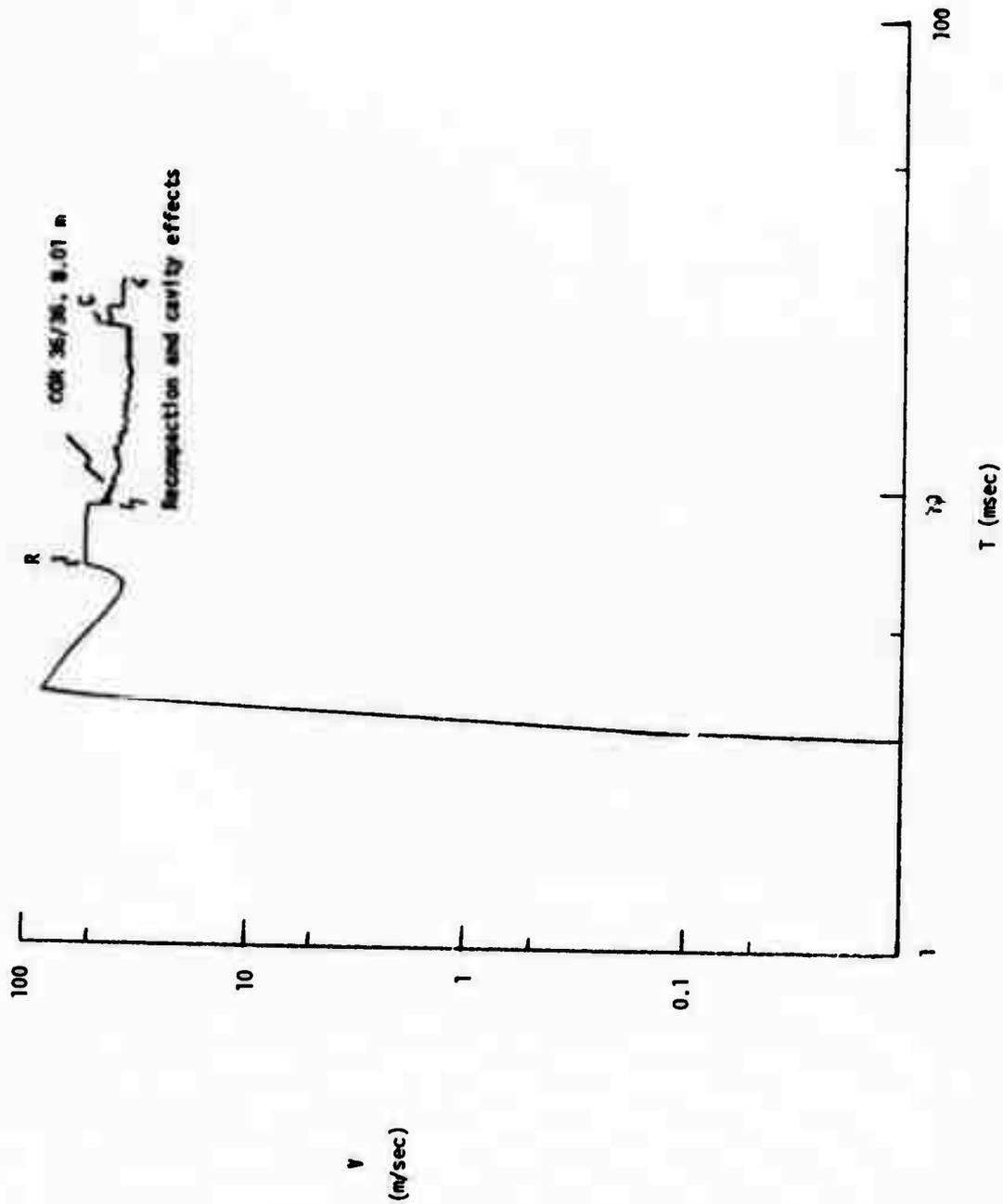

FIGURE C-45. "y"; COR 36/36, R = 8.01 m.

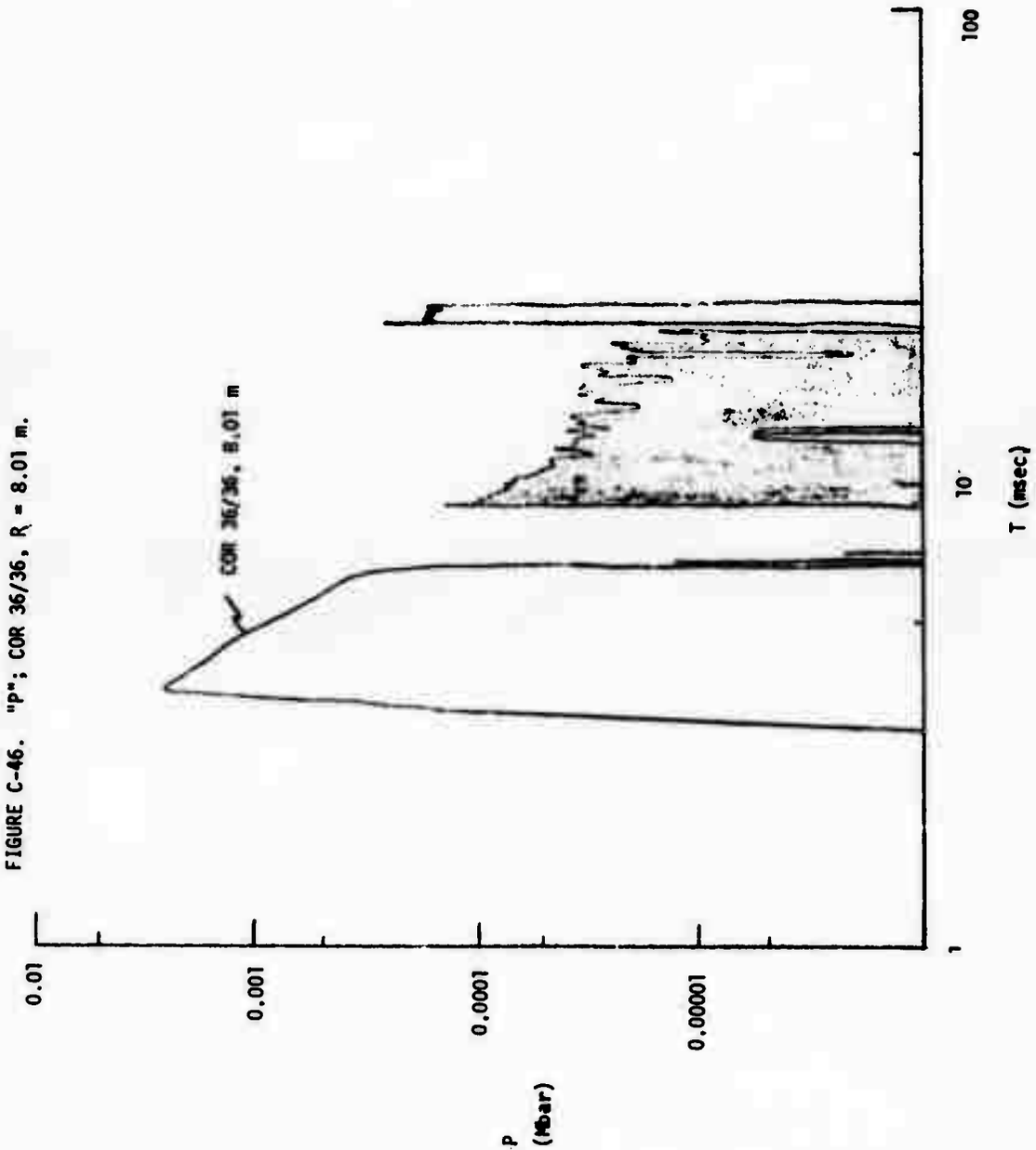

FIGURE C-46. "P"; COR 36/36, R = 8.01 m.

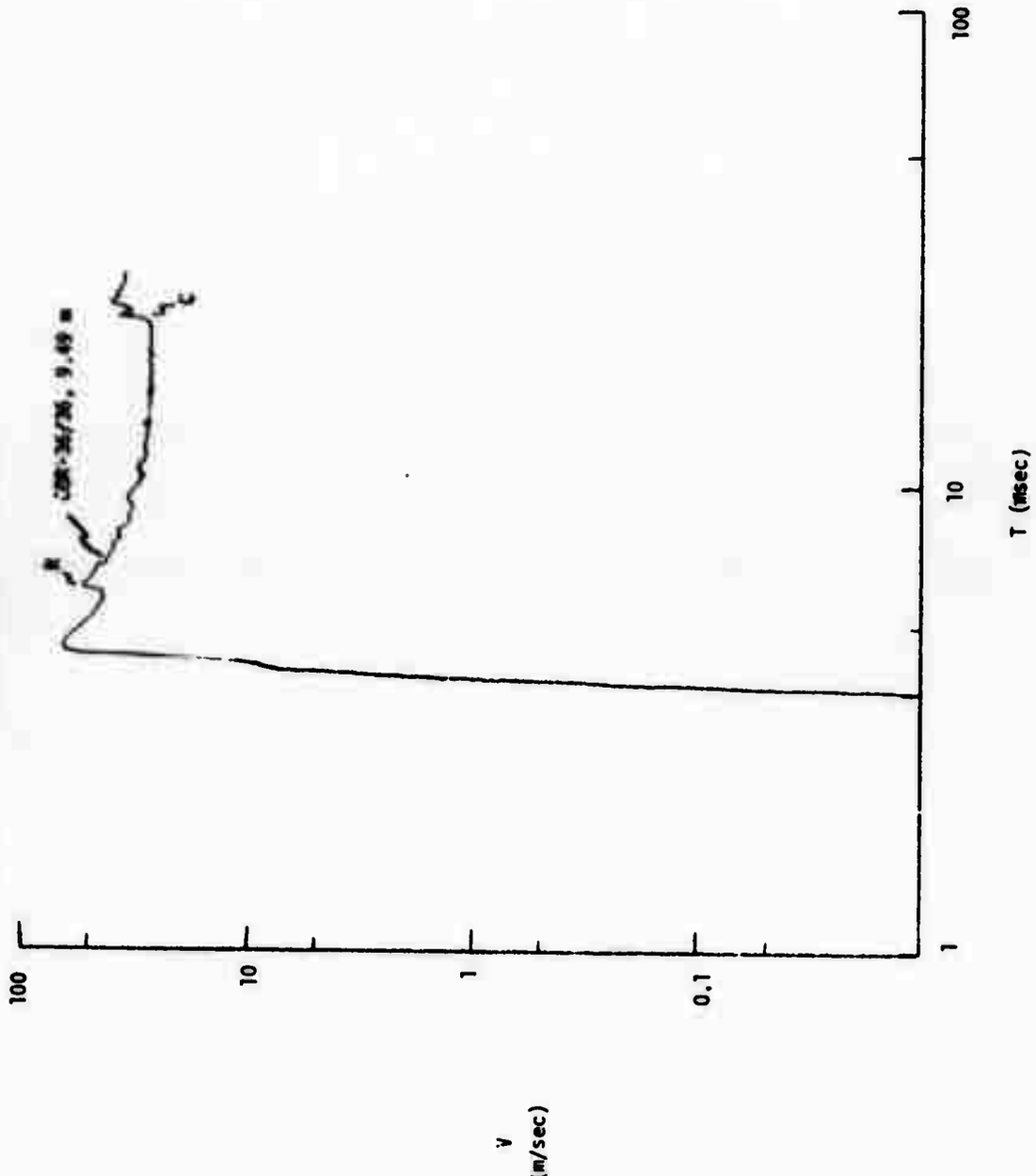

FIGURE C-47 "V"; COR 36/36, R = 9.49 m.

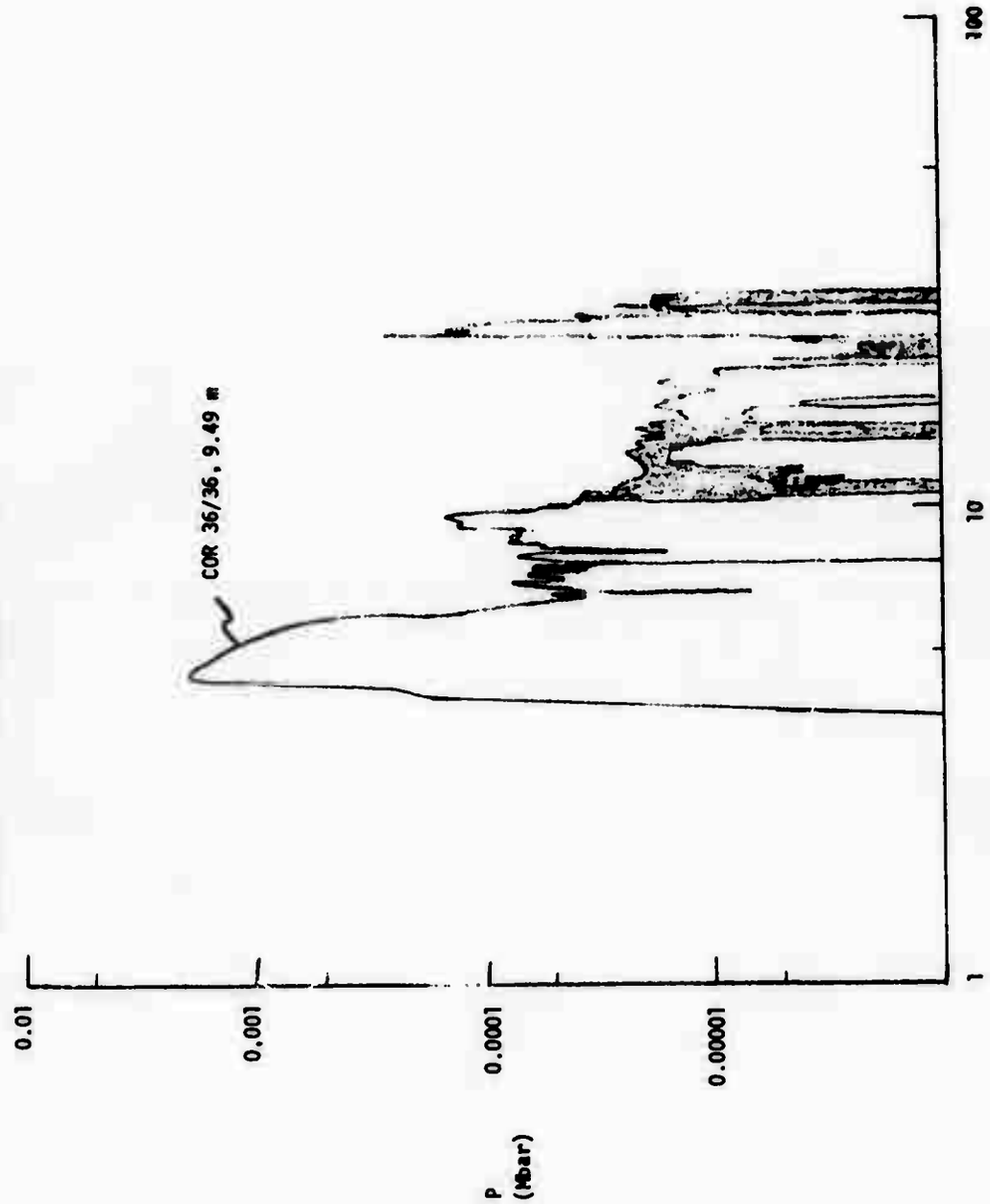

FIGURE C-48. "P"; COR 36/36, R = 9.49 m.

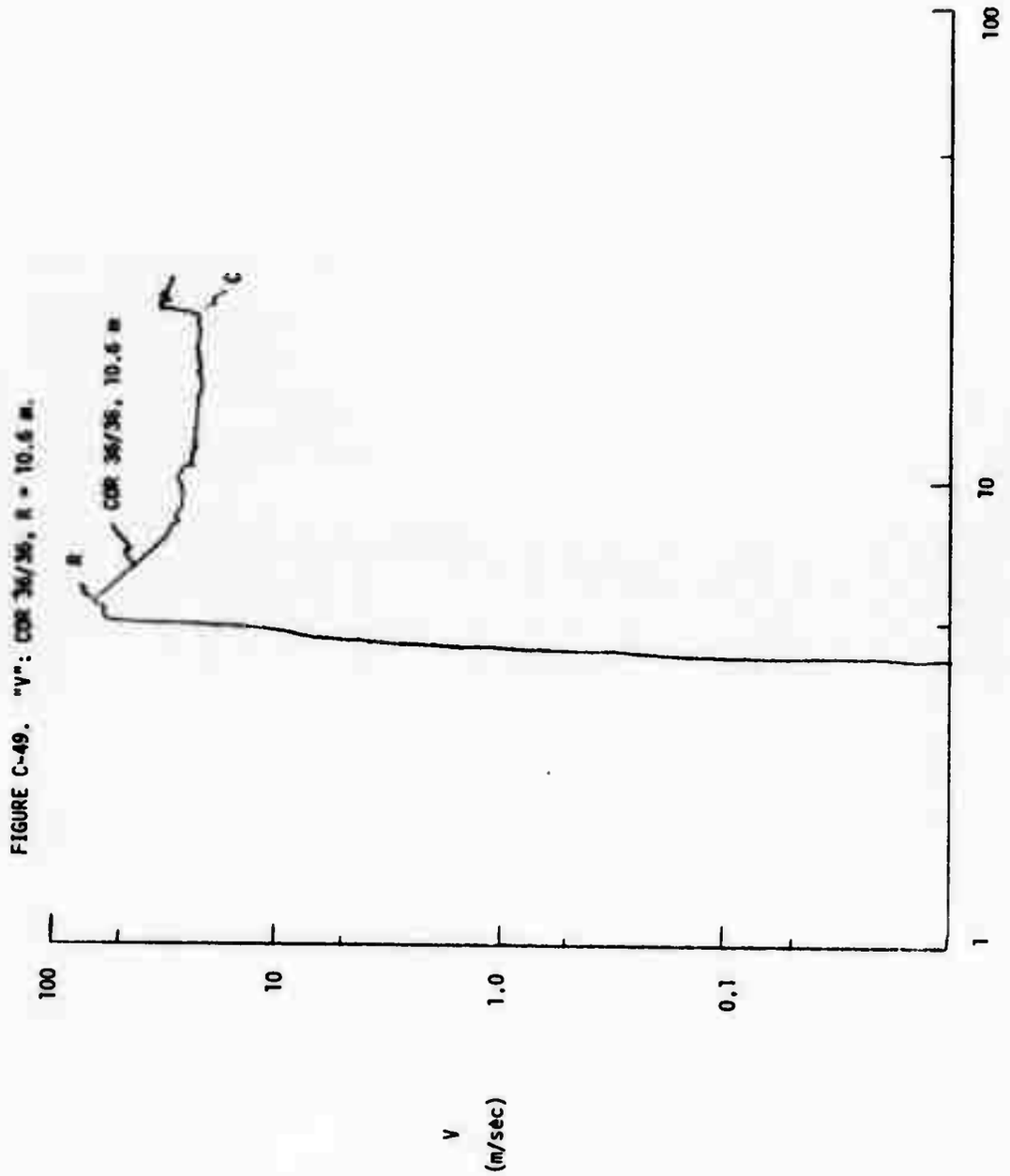

FIGURE C-49. "V": CDR 36/36, R = 10.6 n.

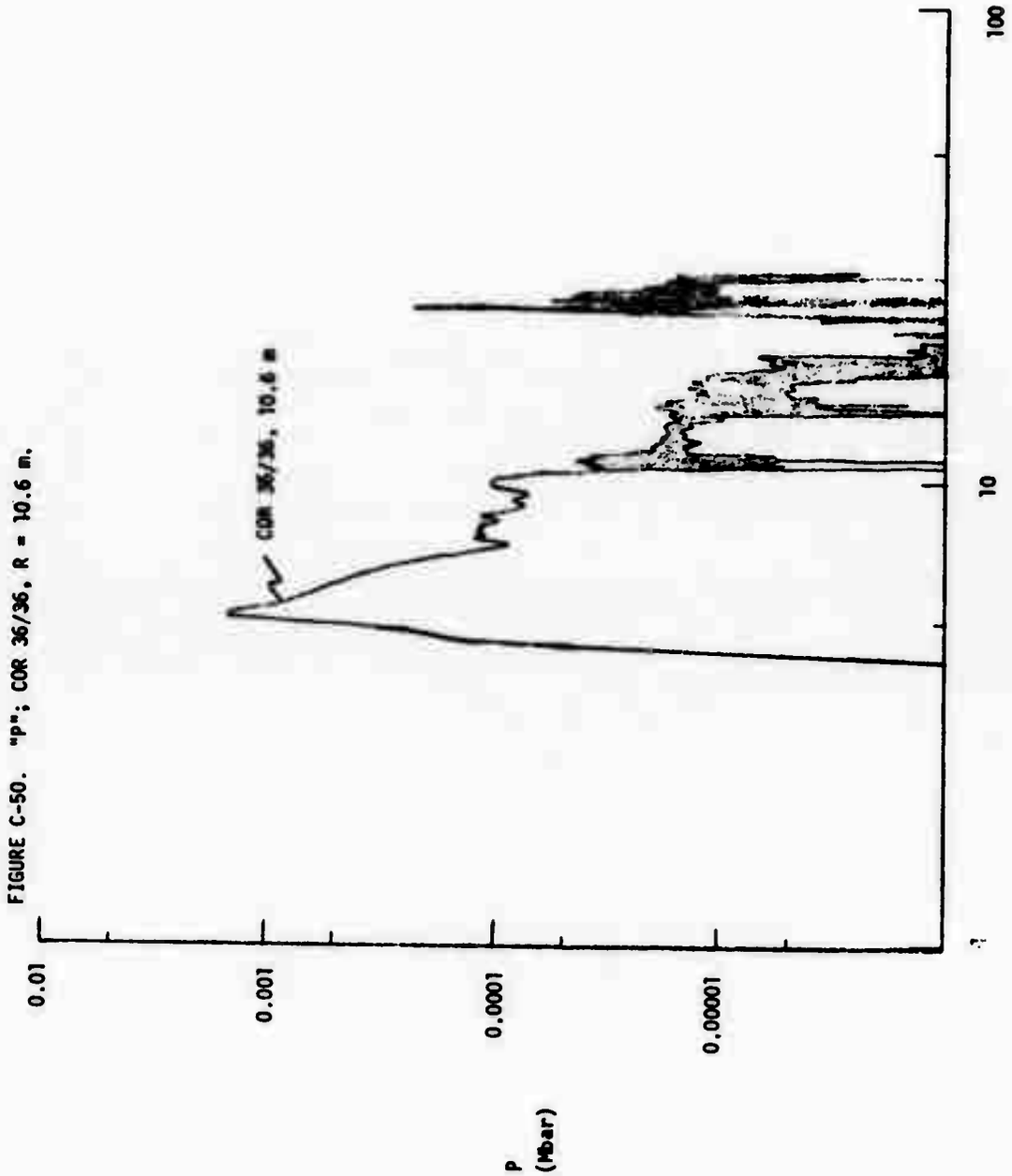

FIGURE C-50. "p"; COR 36/36, R = 10.6 m.

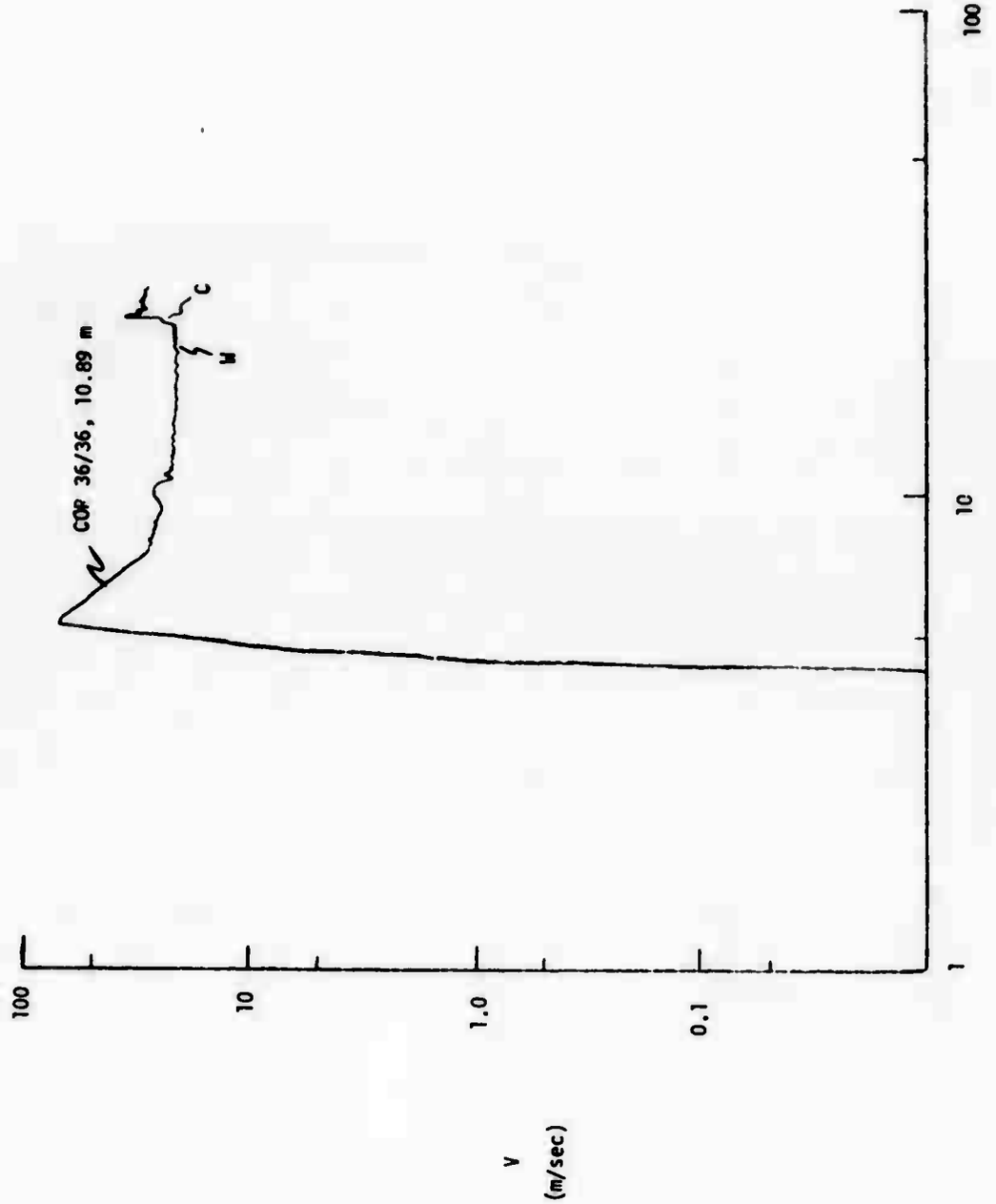

FIGURE C-51. "V"; COR 36/36, R = 10.89 m.

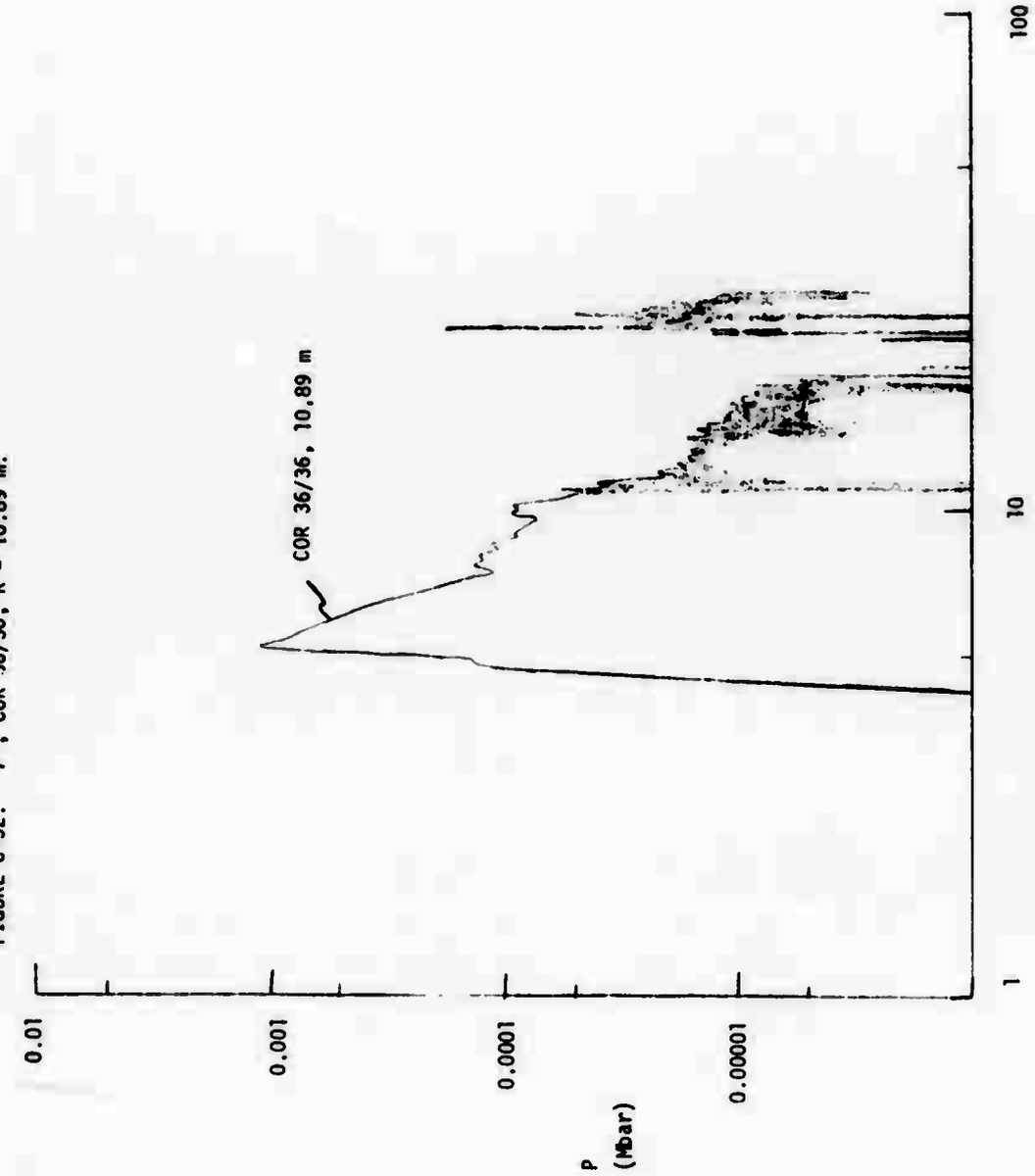

FIGURE C-52. "p"; COR 36/36, R = 10.89 m.

FIGURE C-53, "V"; COR 36/36, R = 10.93 m.

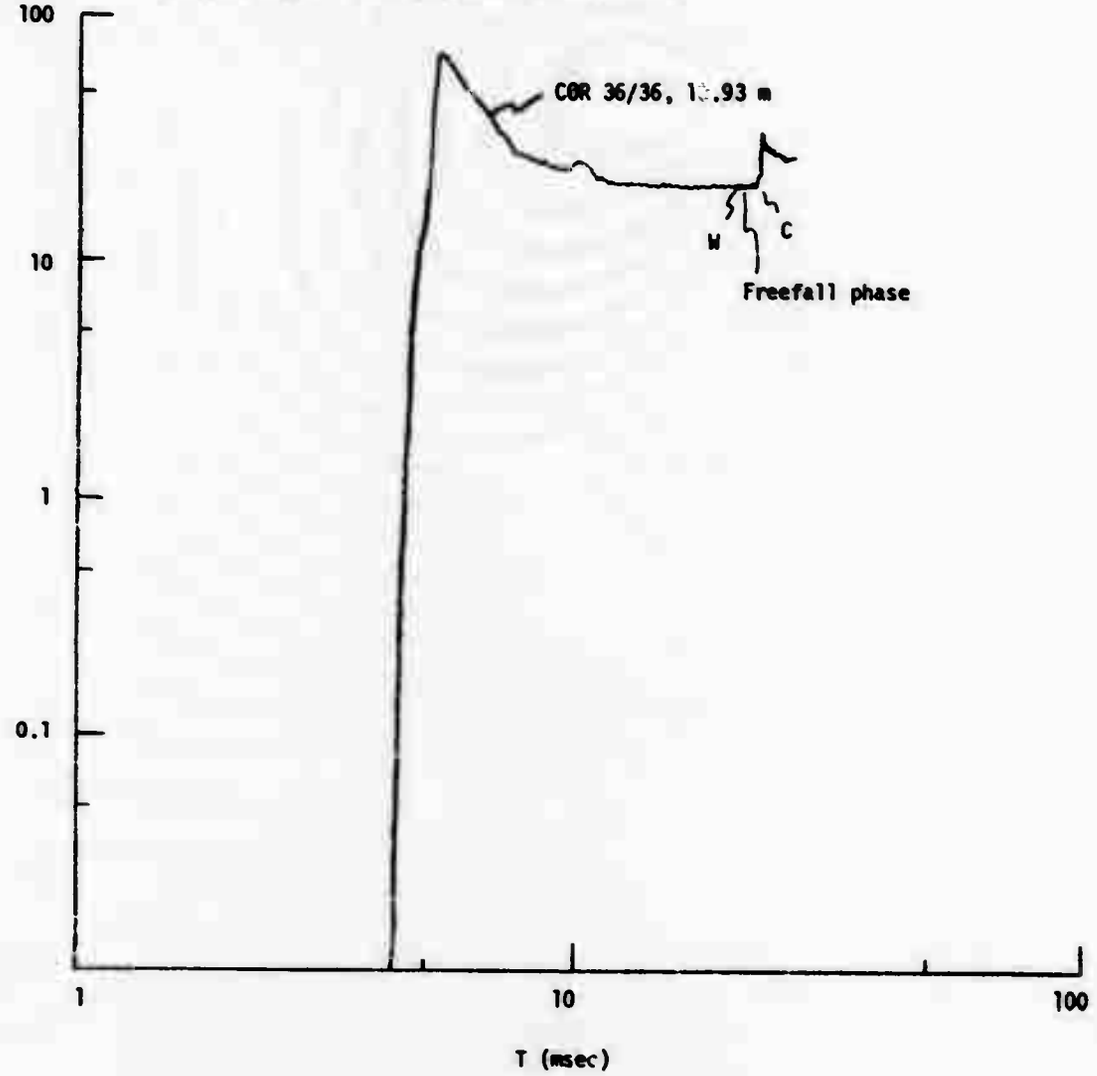

FIGURE C-54. "P"; COR 36/36, R = 10.93 m.

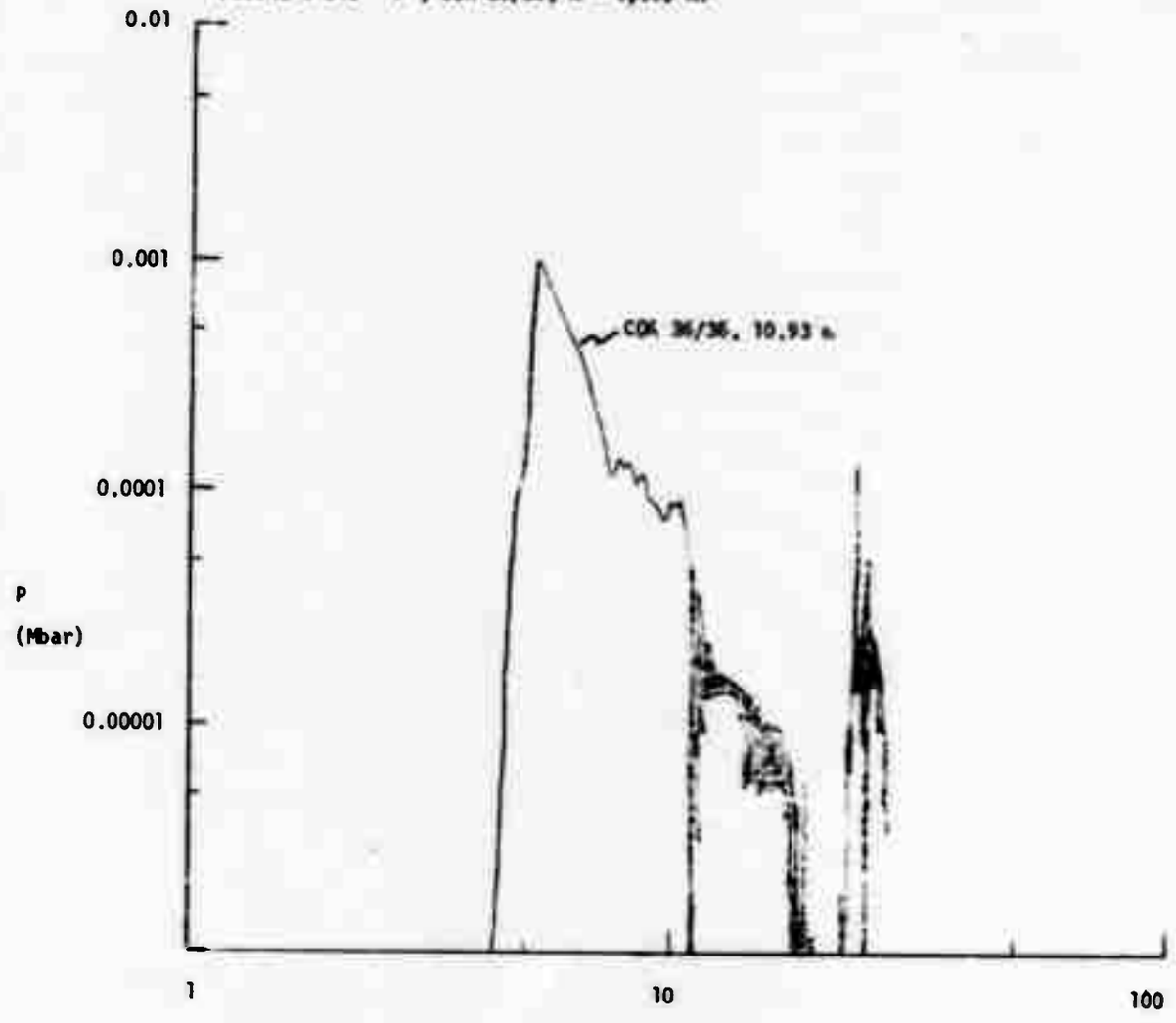

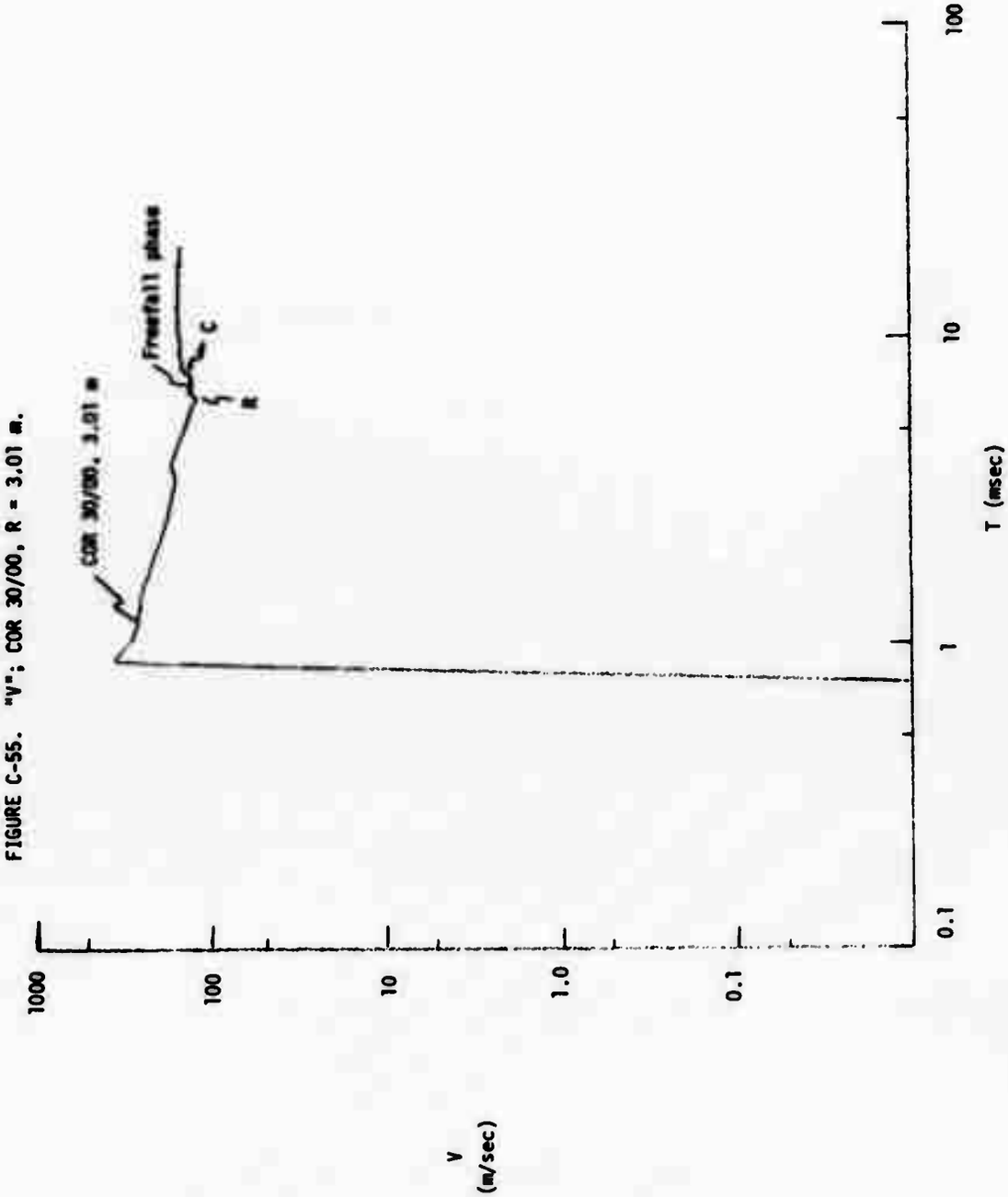

FIGURE C-55. "V"; COR 30/00, R = 3.01 m.

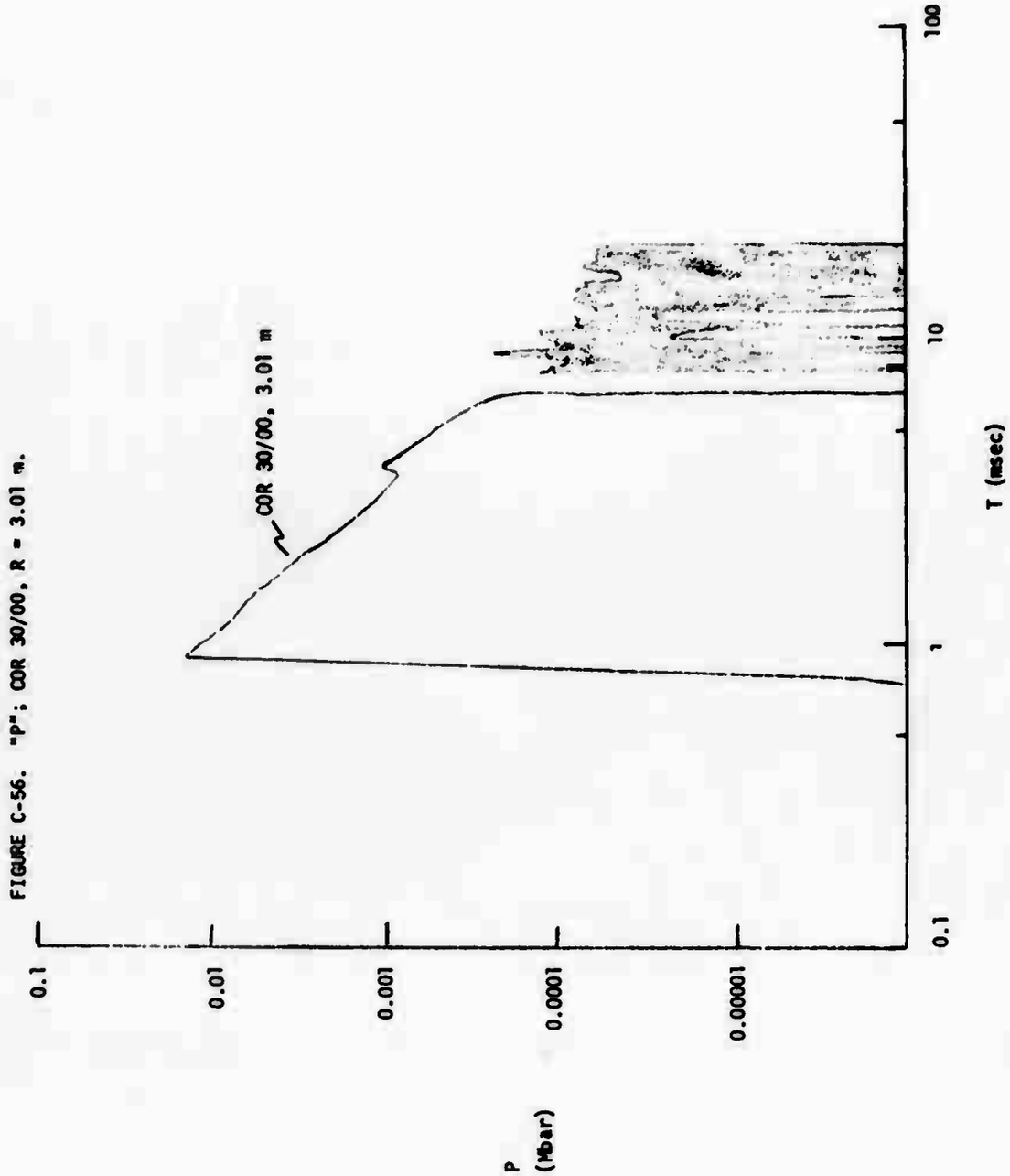

FIGURE C-56. "P"; COR 30/00, R = 3.01 m.

FIGURE C-57. "V"; COR 30/00, R = 5.01 m.

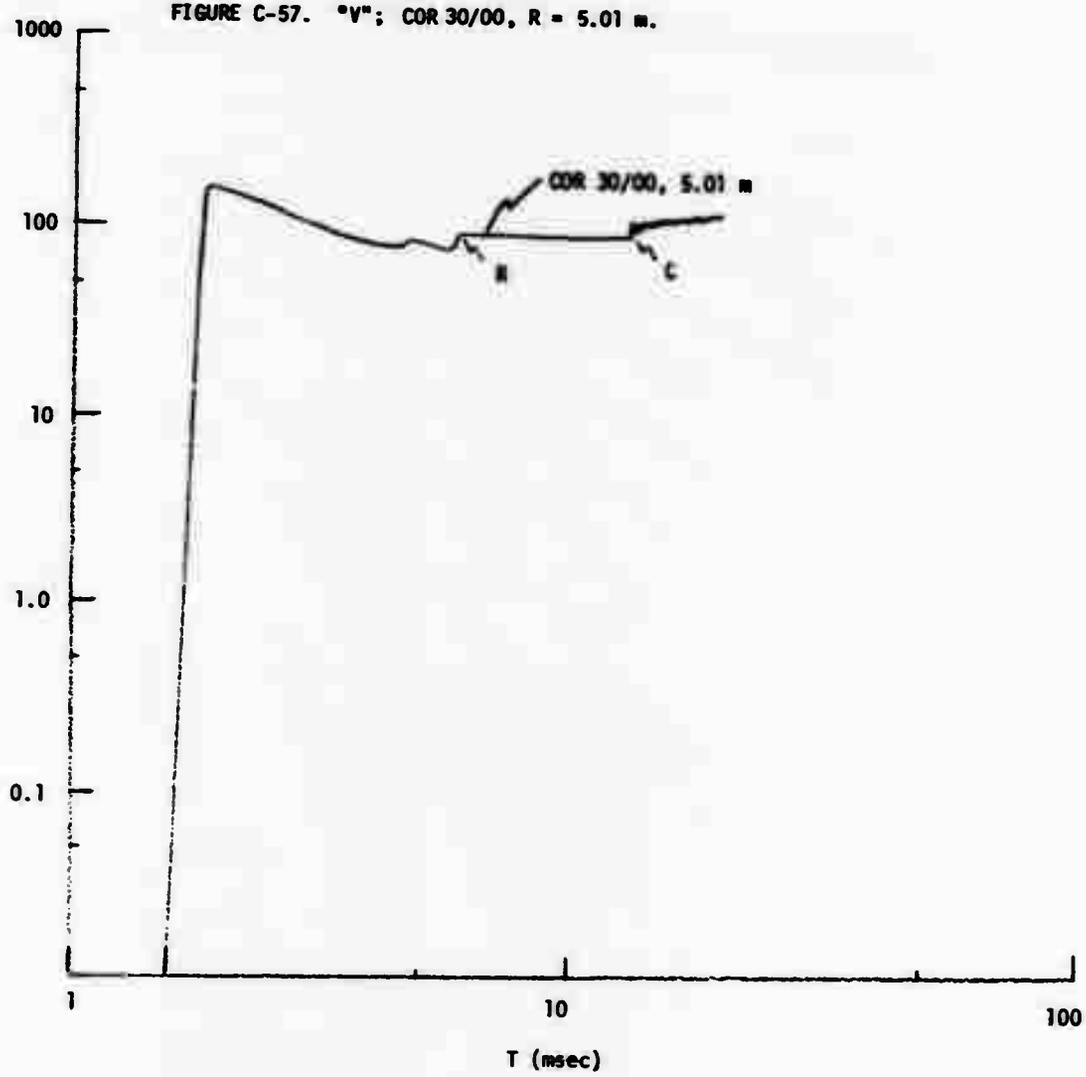

FIGURE C-58. "P"; COR 30/00, R = 5.01 m.

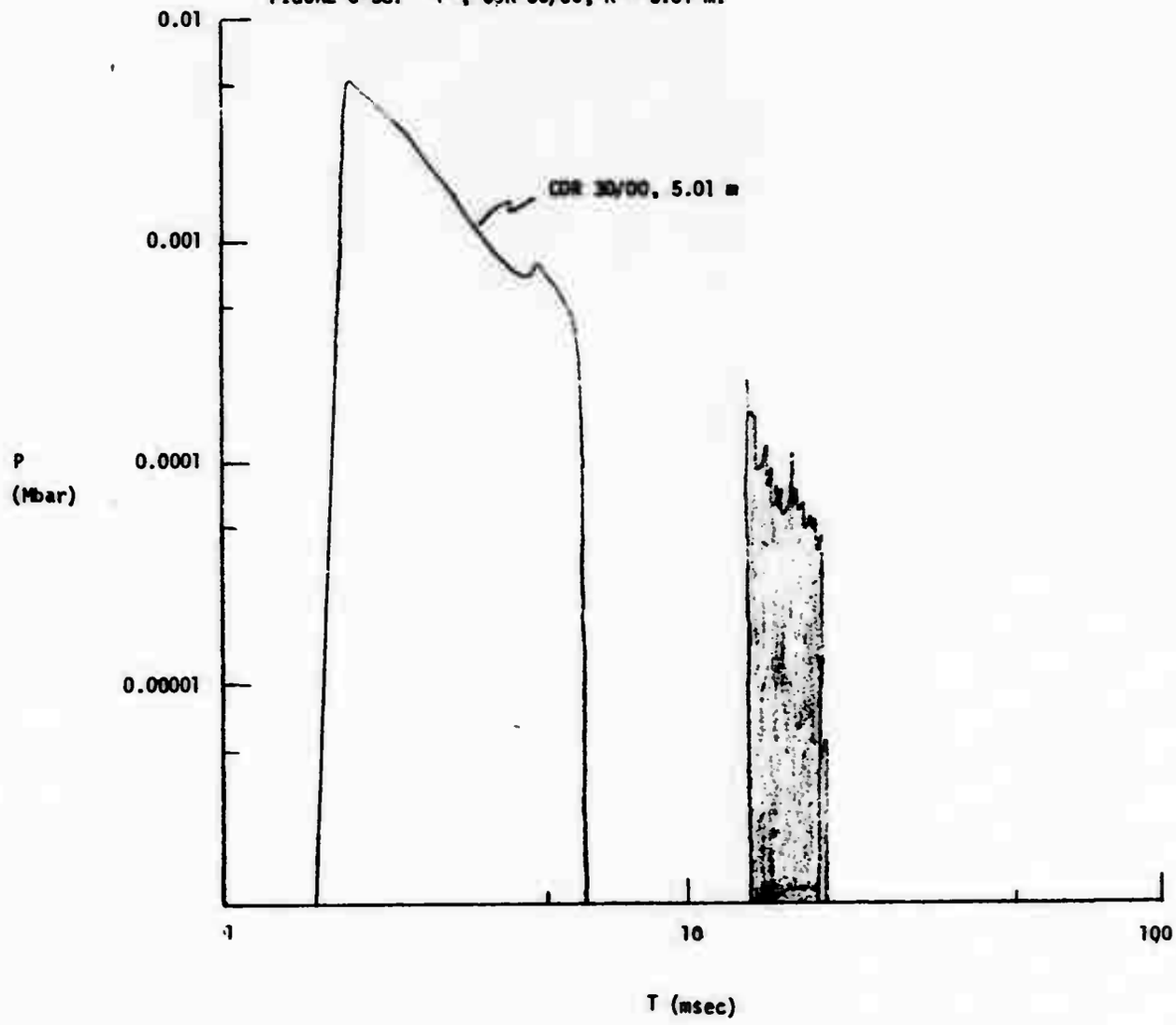

FIGURE C-59. "V"; COR 30/00, R = 5.98 m.

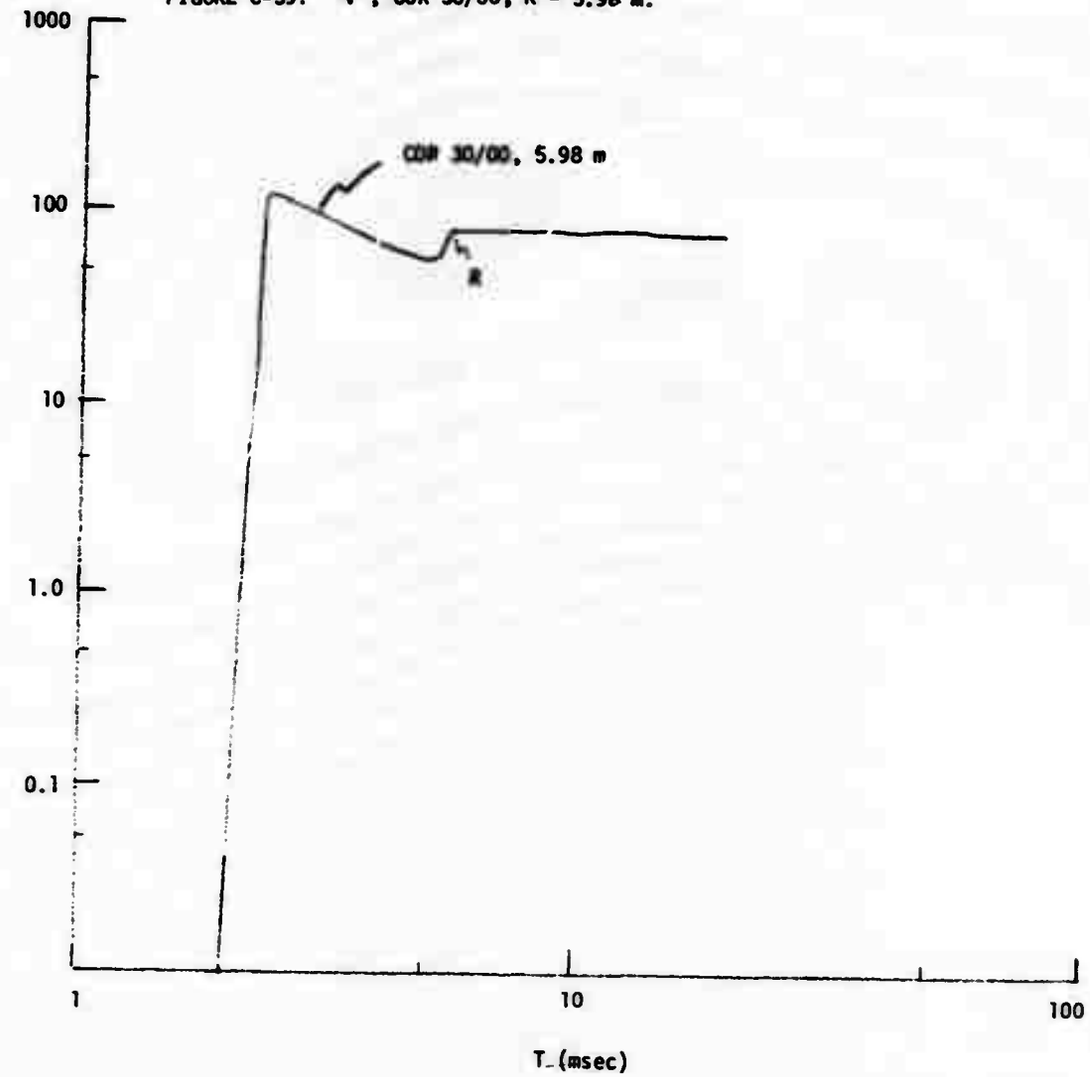

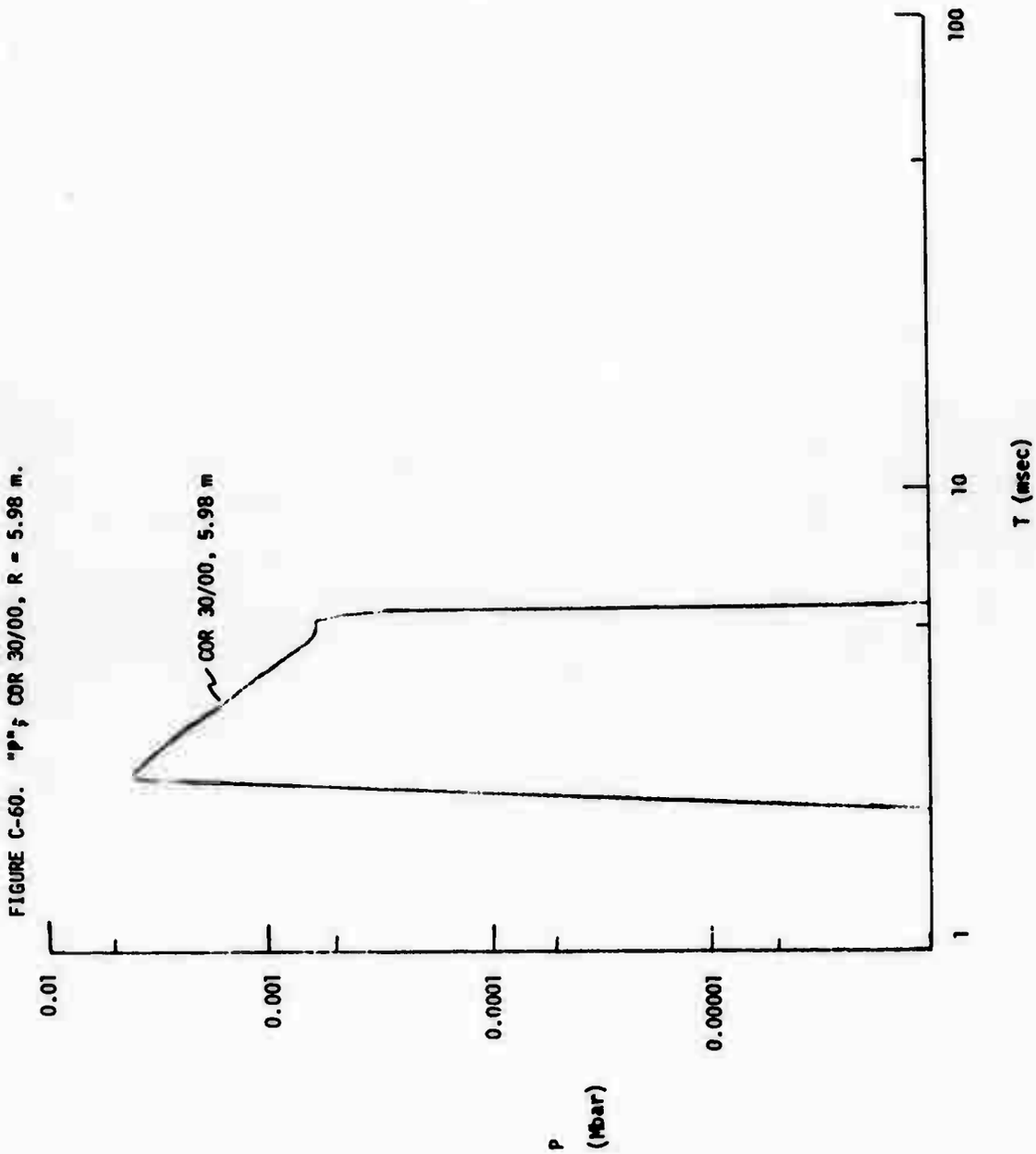

FIGURE C-60. "P"; COR 30/00, R = 5.98 m.

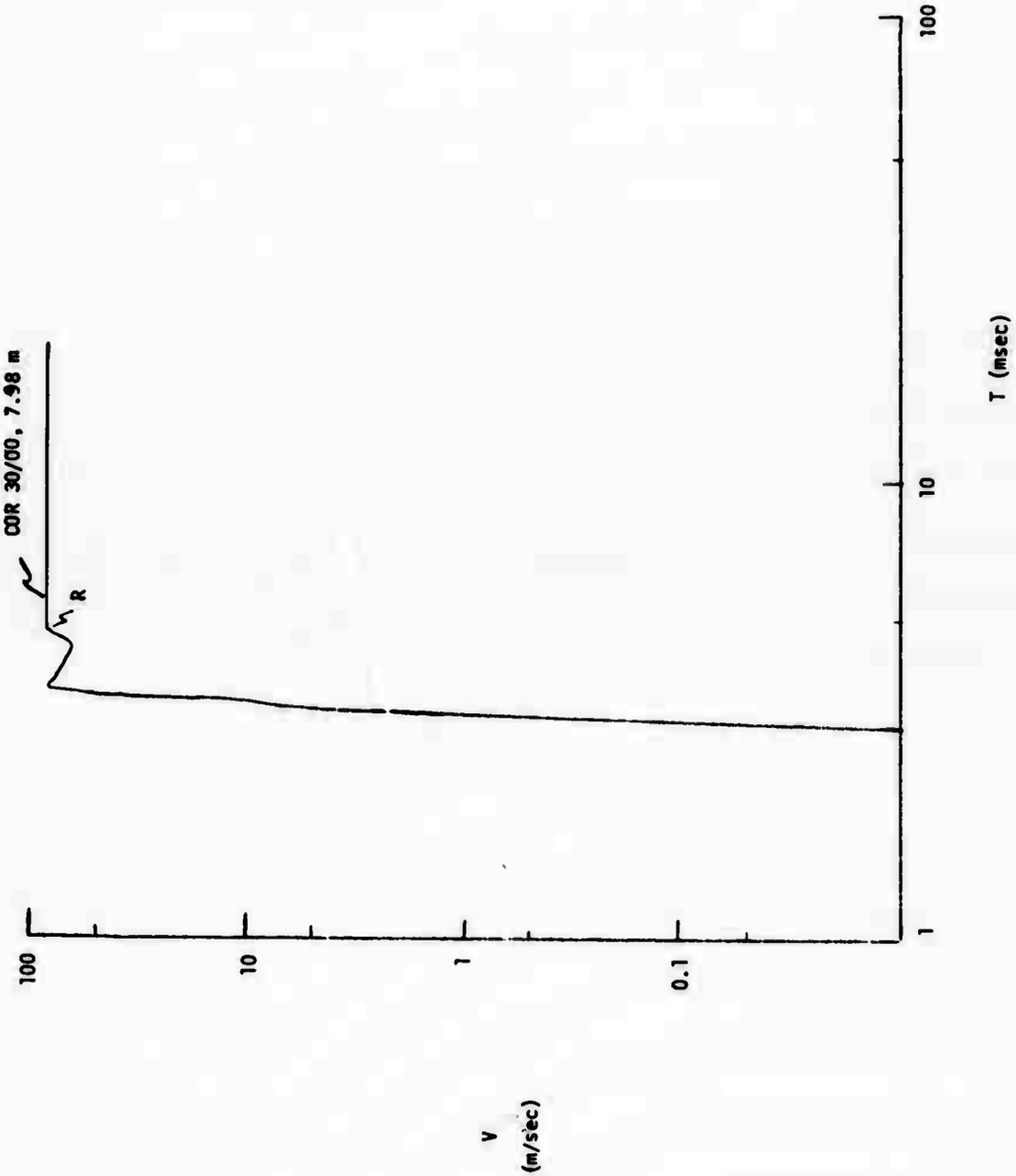

FIGURE C-61. "V"; COR 30/00, R = 7.98 m.

FIGURE C-62. "P"; COR 30/00, R = 7.98 m.

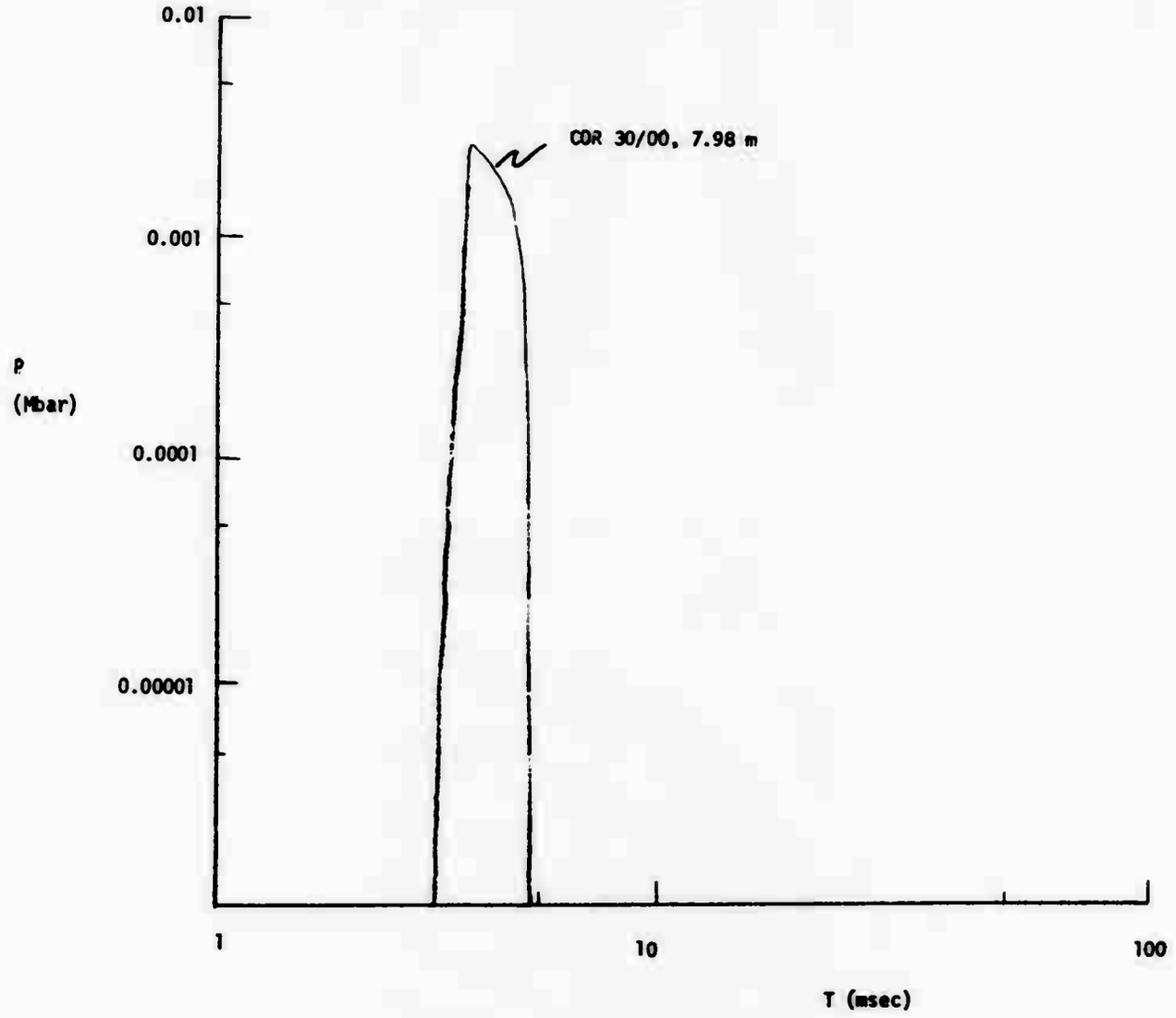

FIGURE C-63. "V"; COR 30/00, R = 8.98 m.

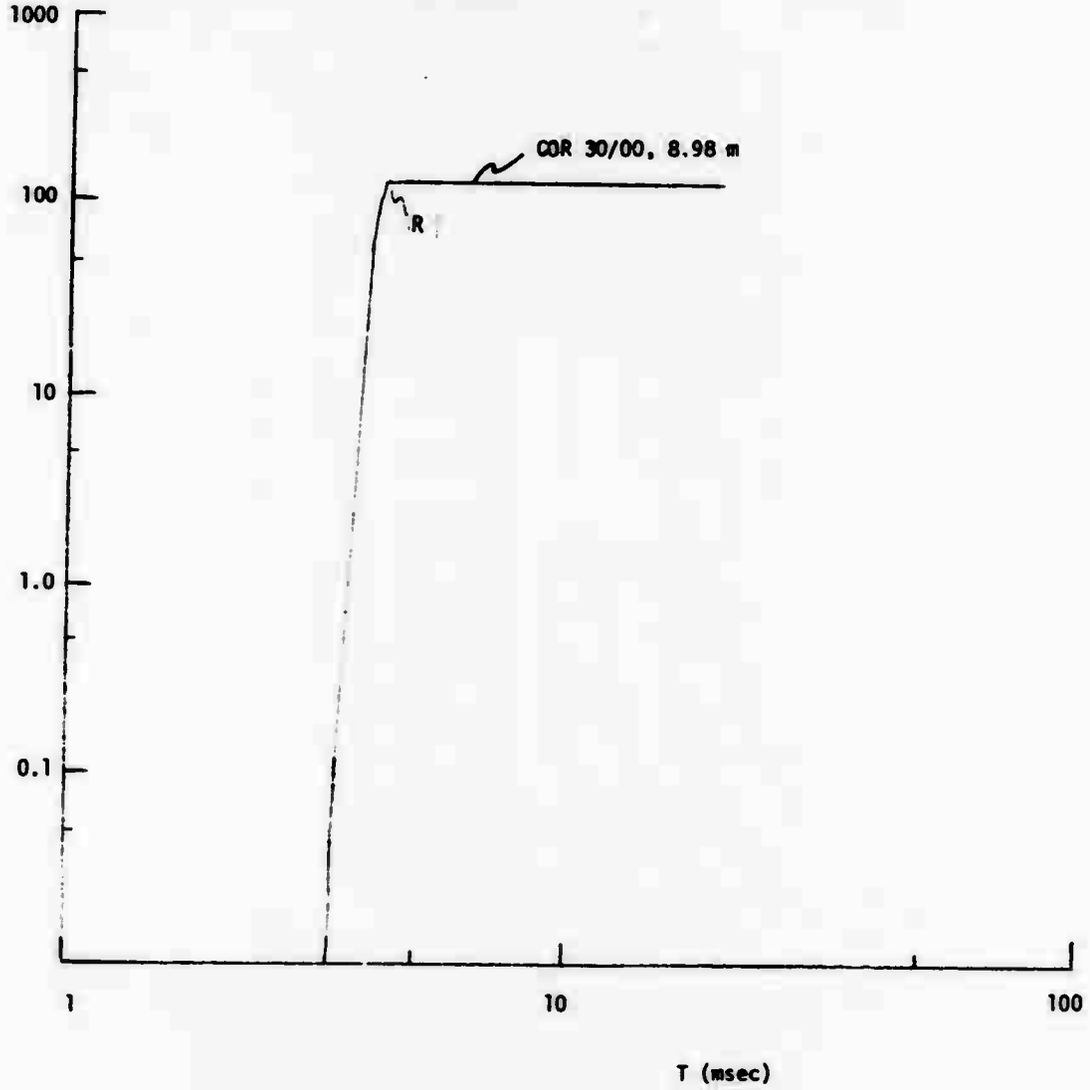

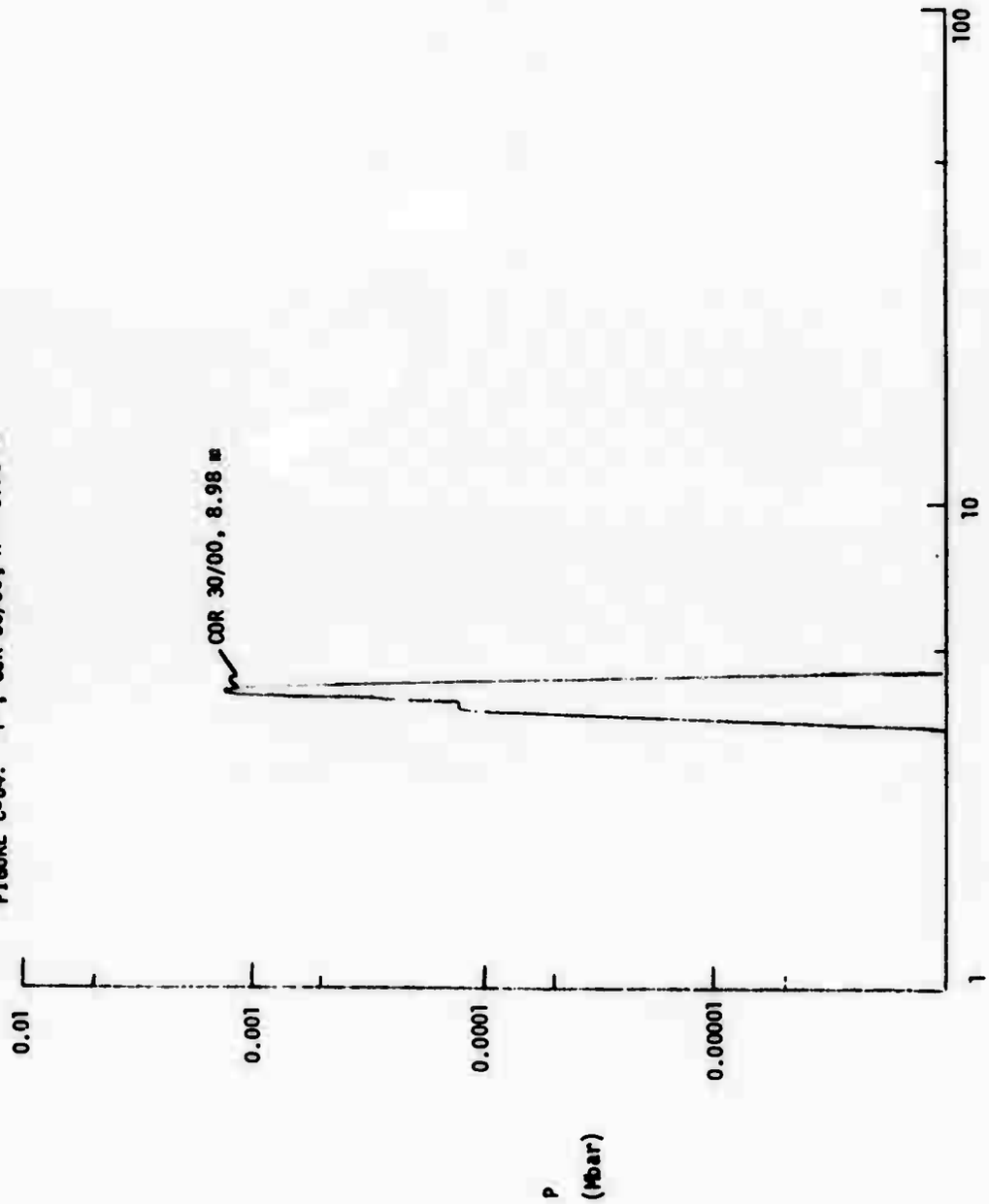

FIGURE C-64. "P"; COR 30/00, R = 8.98 m.

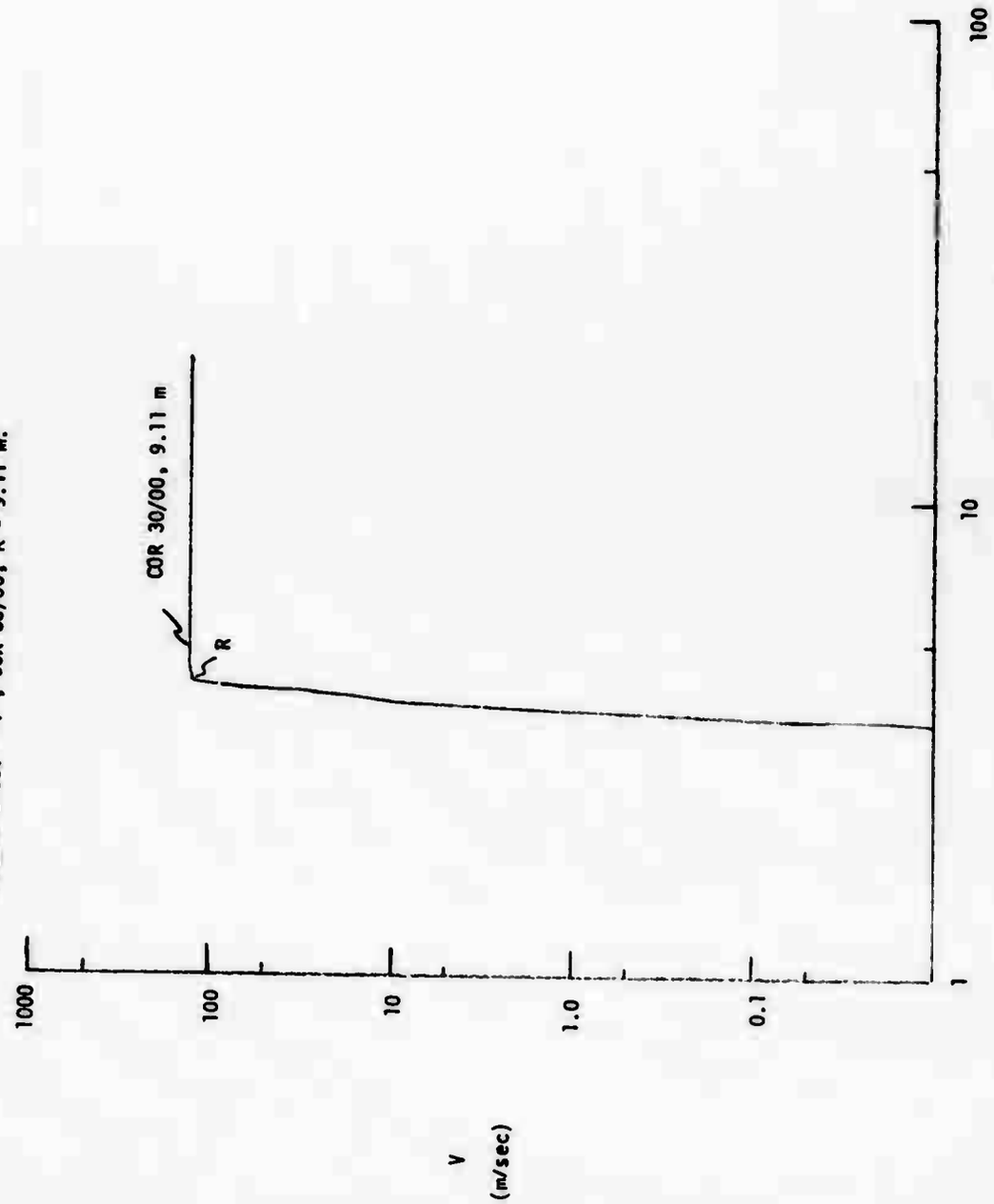

FIGURE C-65. "V"; COR 30/00, R = 9.11 m.

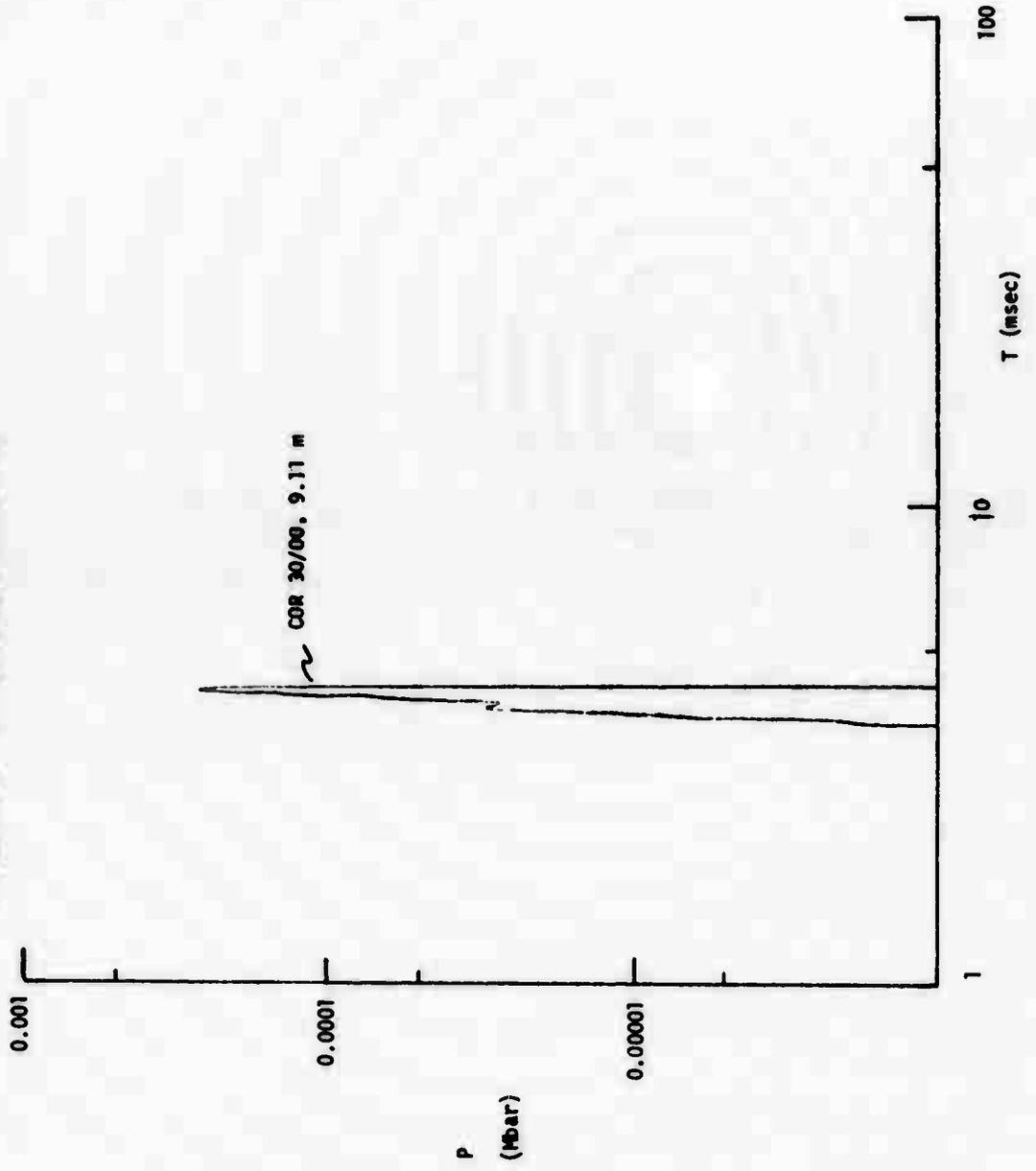

FIGURE C-66. "P"; COR 30/00, R = 9.11 m.

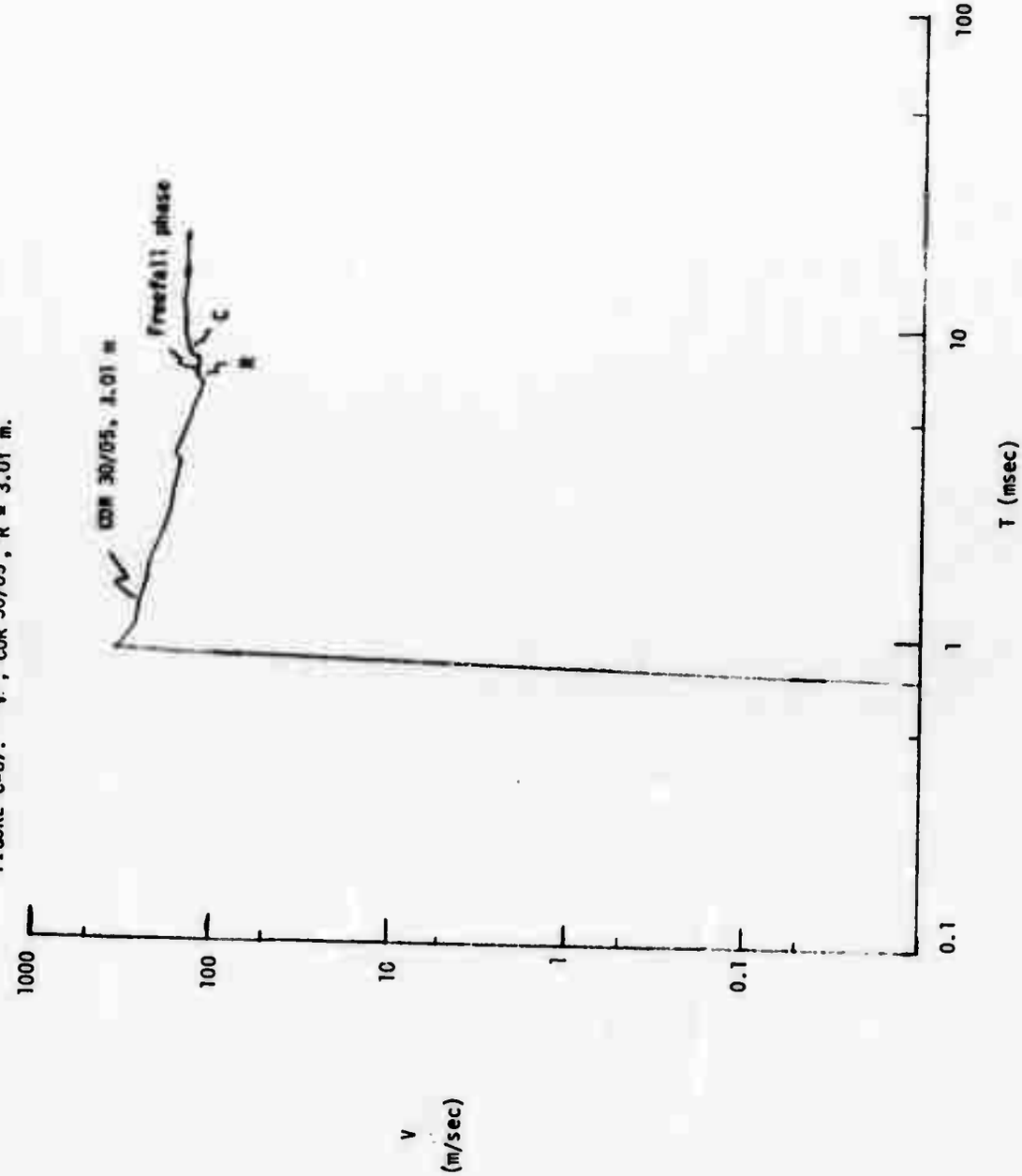

FIGURE C-67. "V"; COR 30/05, R = 3.01 m.

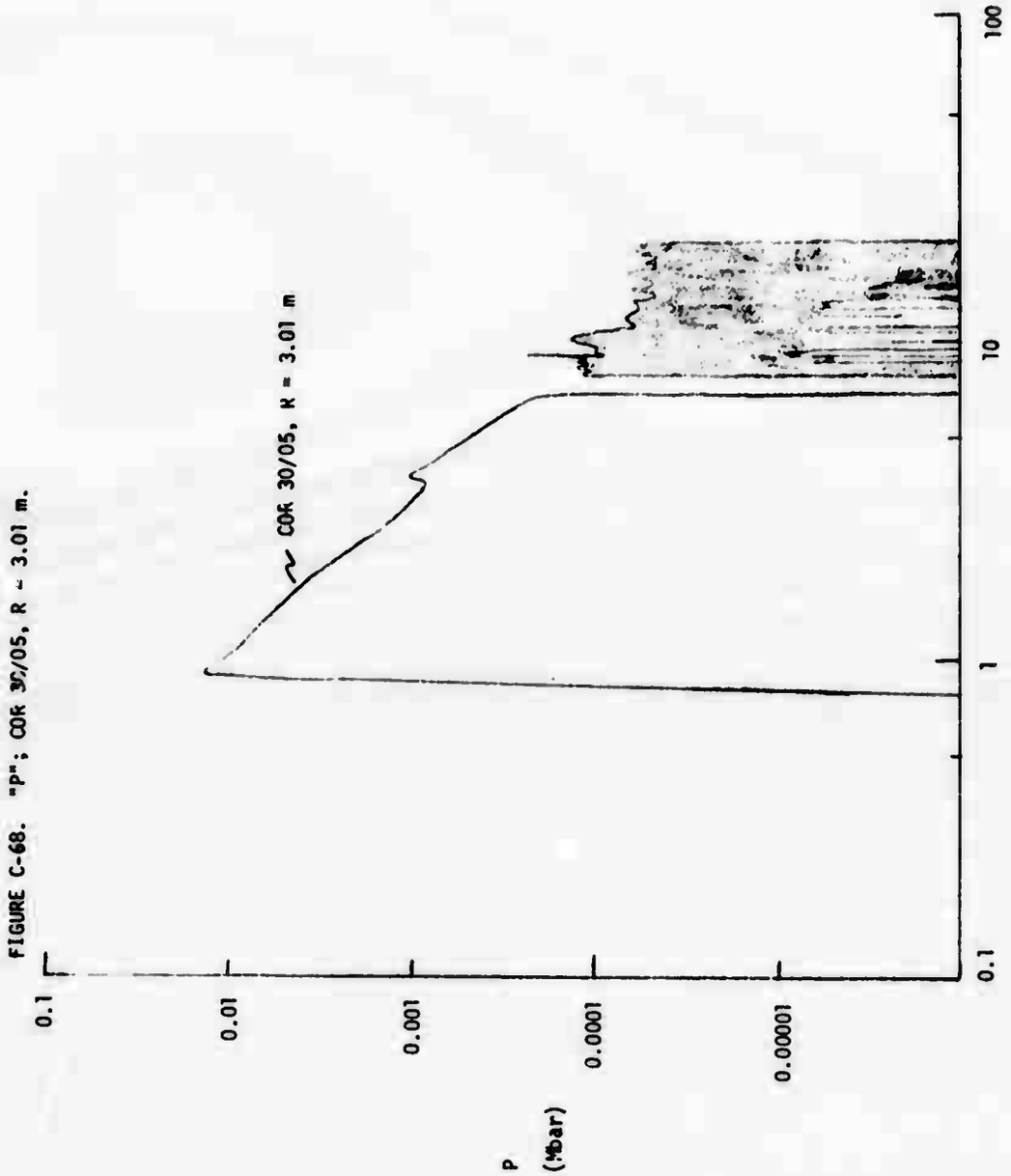

FIGURE C-68. "P"; COR 30/05, R ~ 3.01 m.

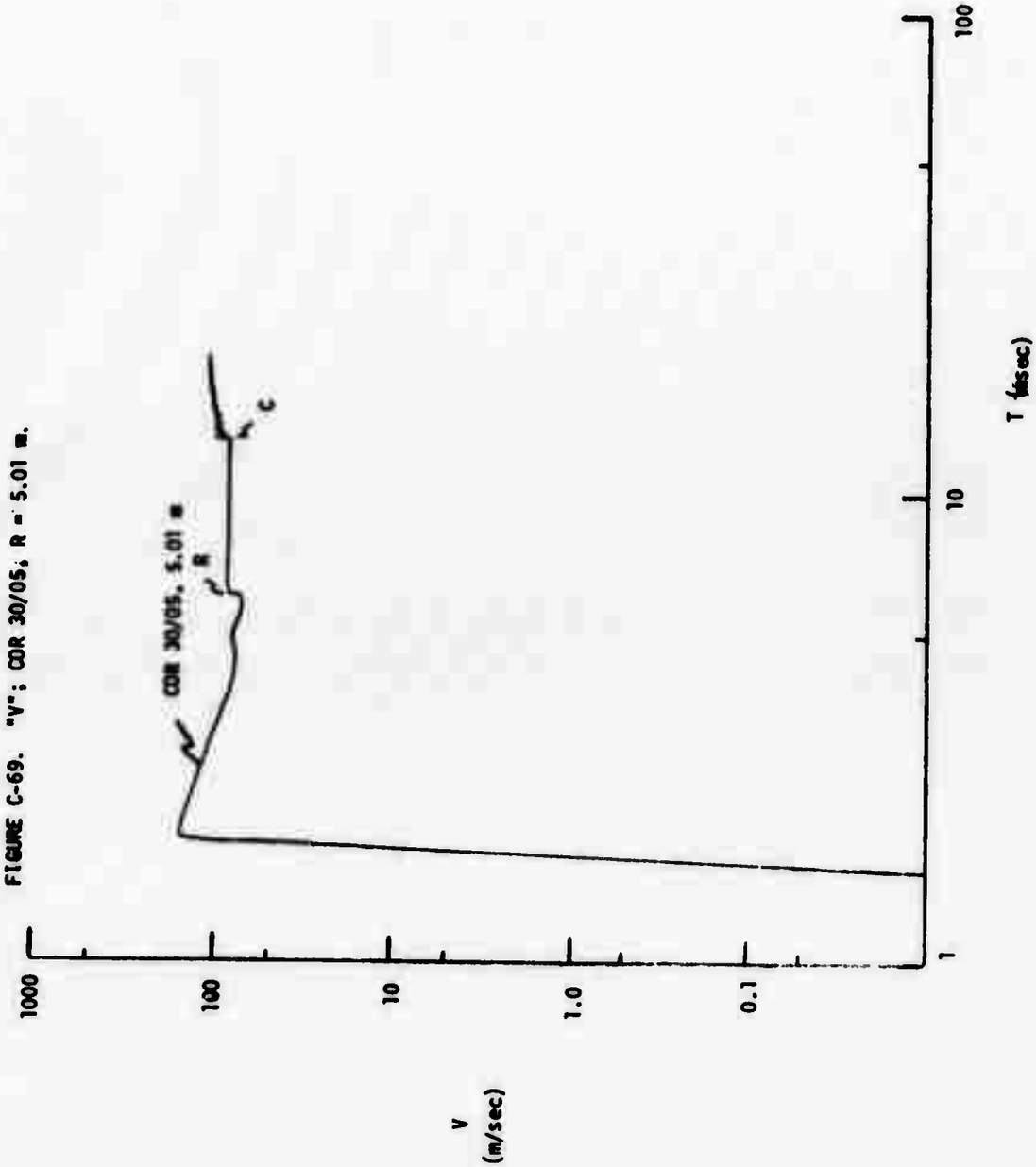

FIGURE C-69. "V"; COR 30/05; R = 5.01 m.

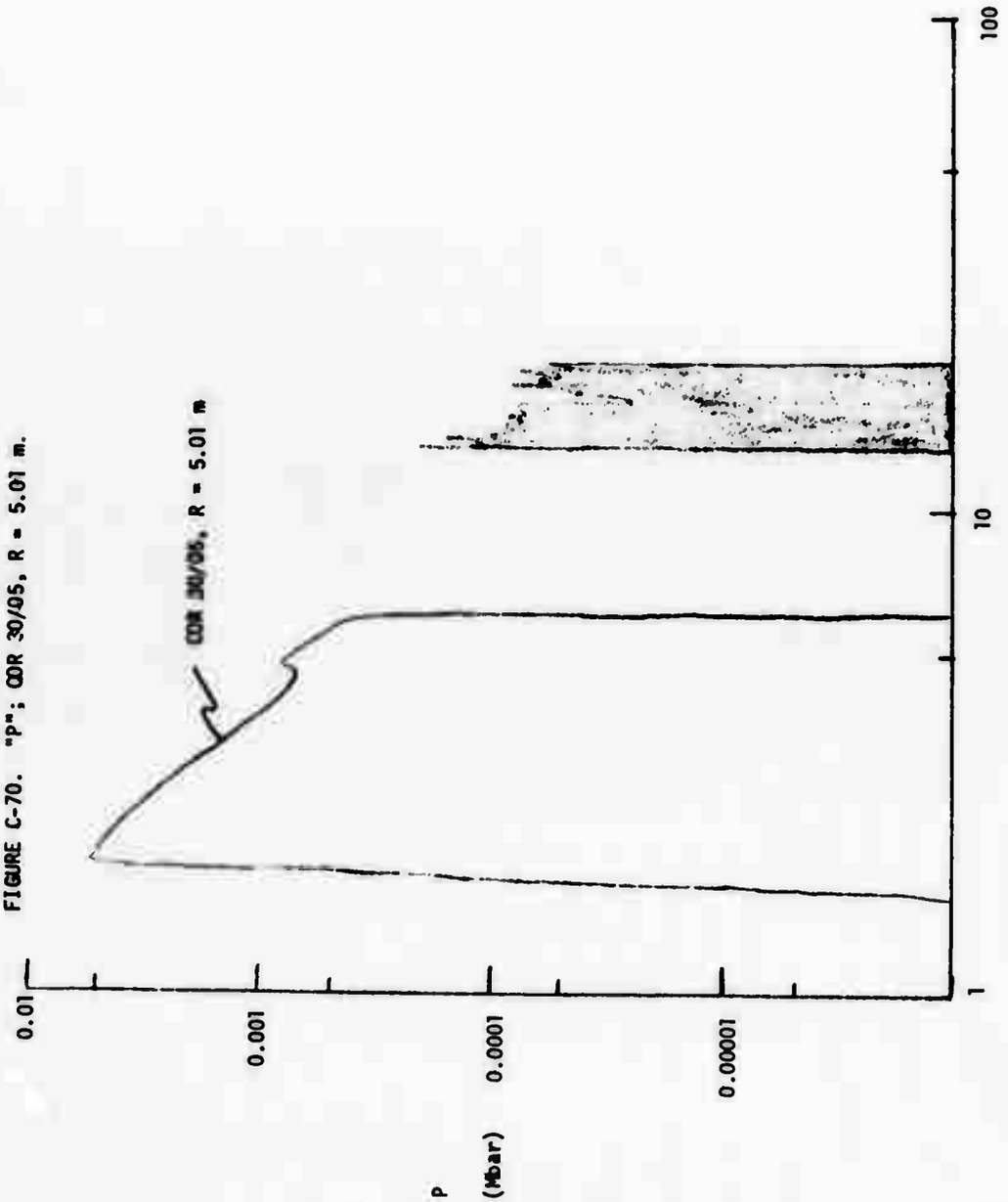

FIGURE C-70. "P"; COR 30/05, R = 5.01 m.

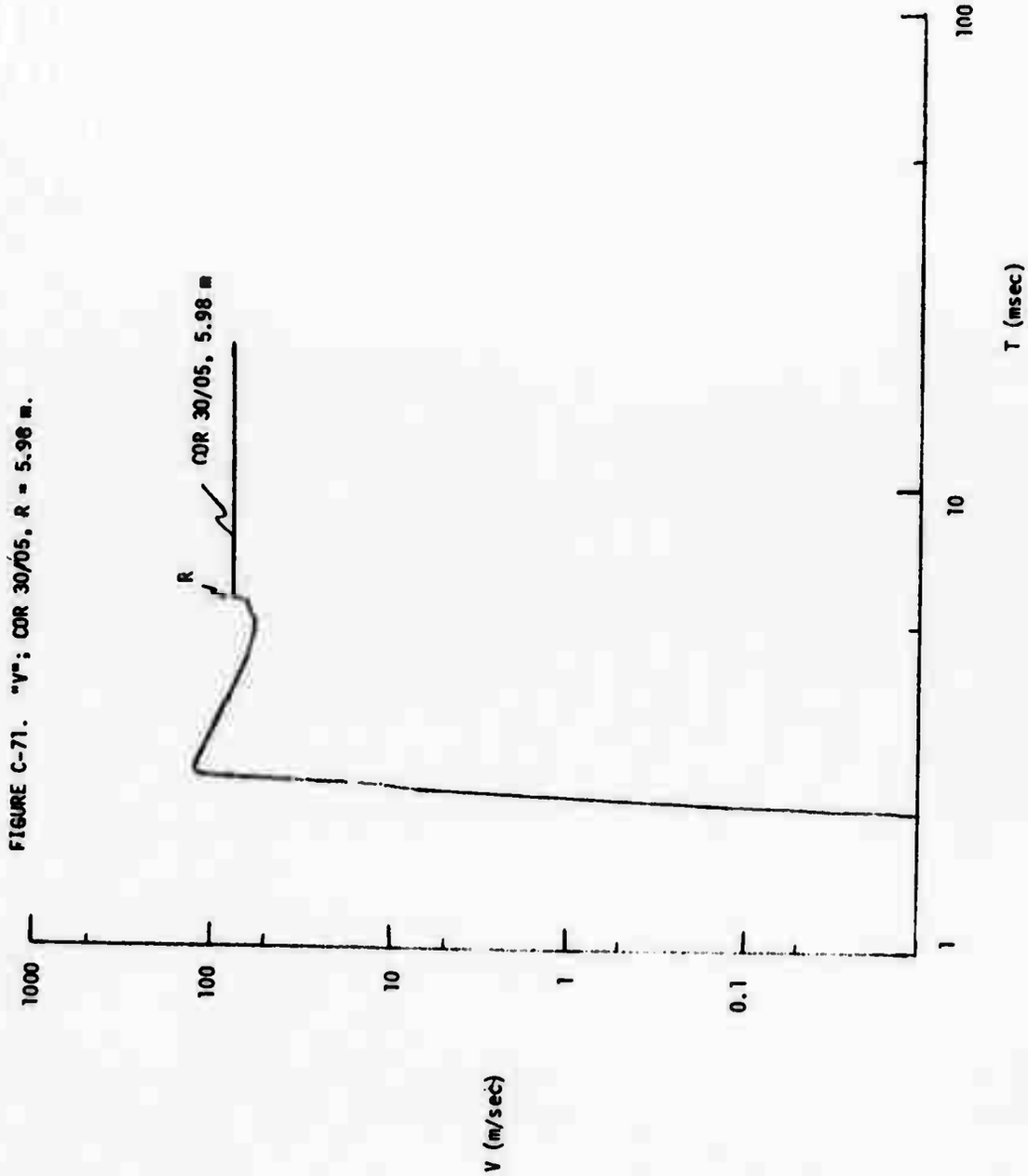

FIGURE C-71. "V"; COR 30/05, R = 5.98 m.

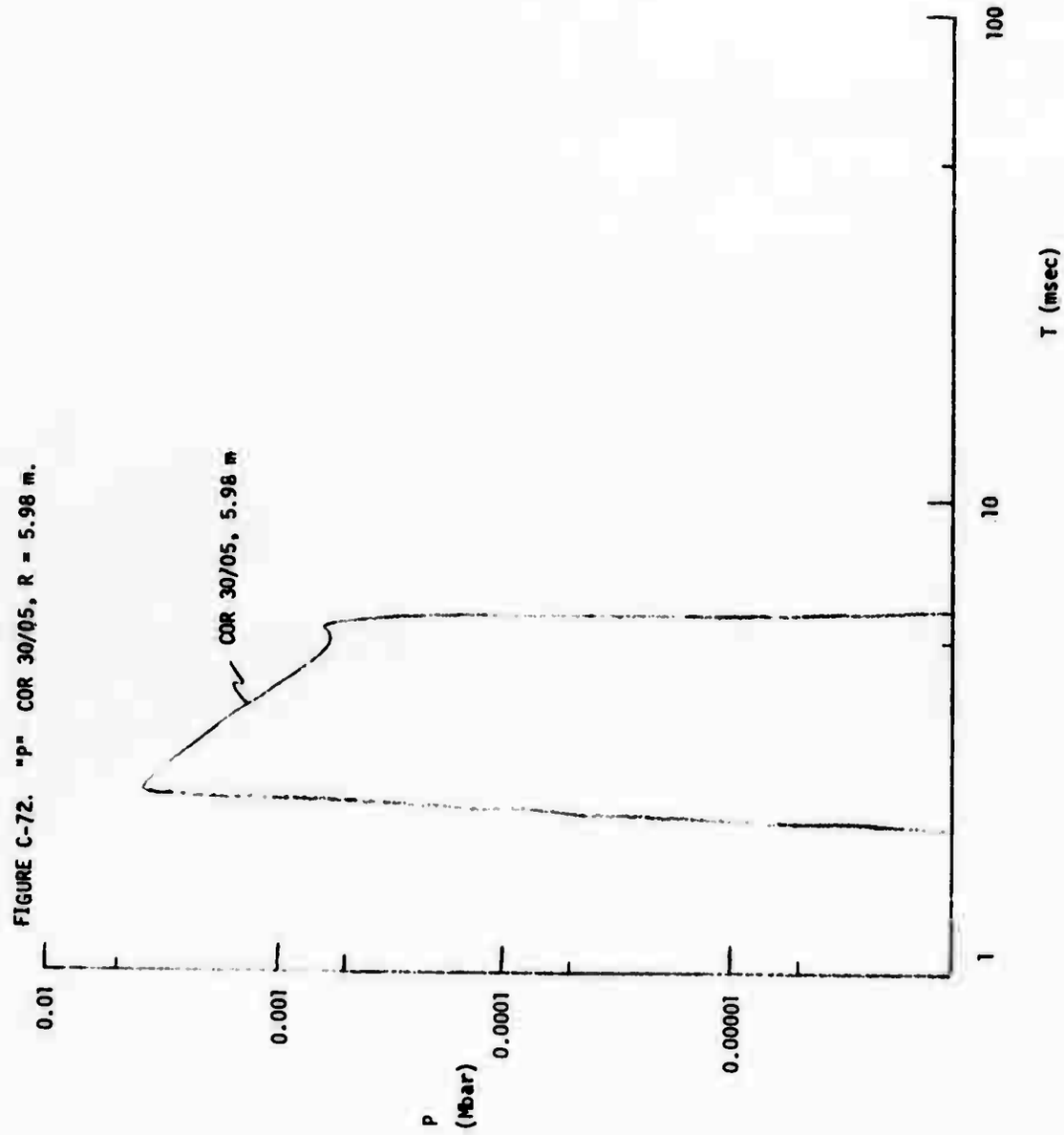

FIGURE C-72. "P" COR 30/05, R = 5.98 m.

FIGURE C-73. "V"; COR 30/05, R = 7.98 m.

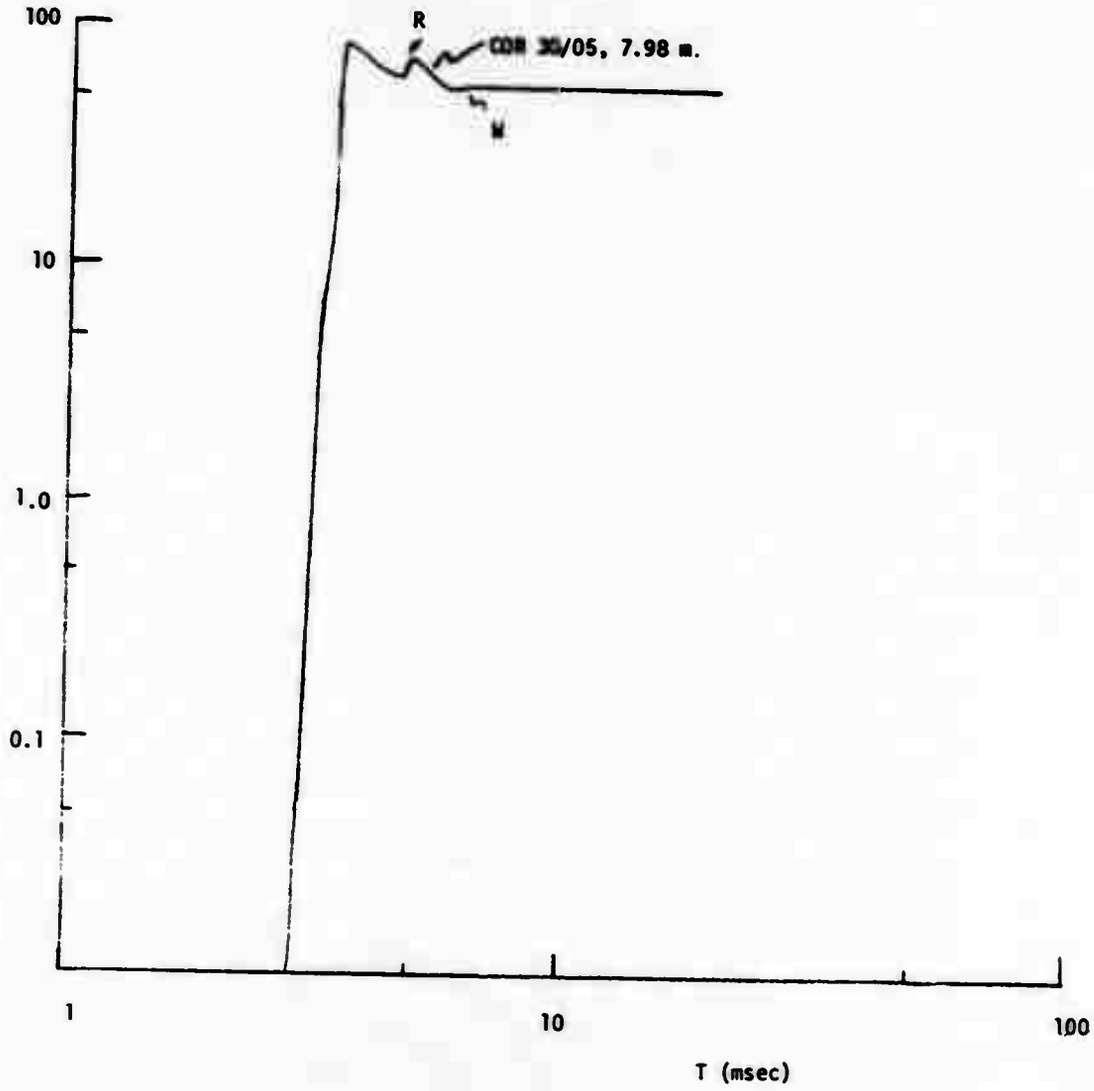

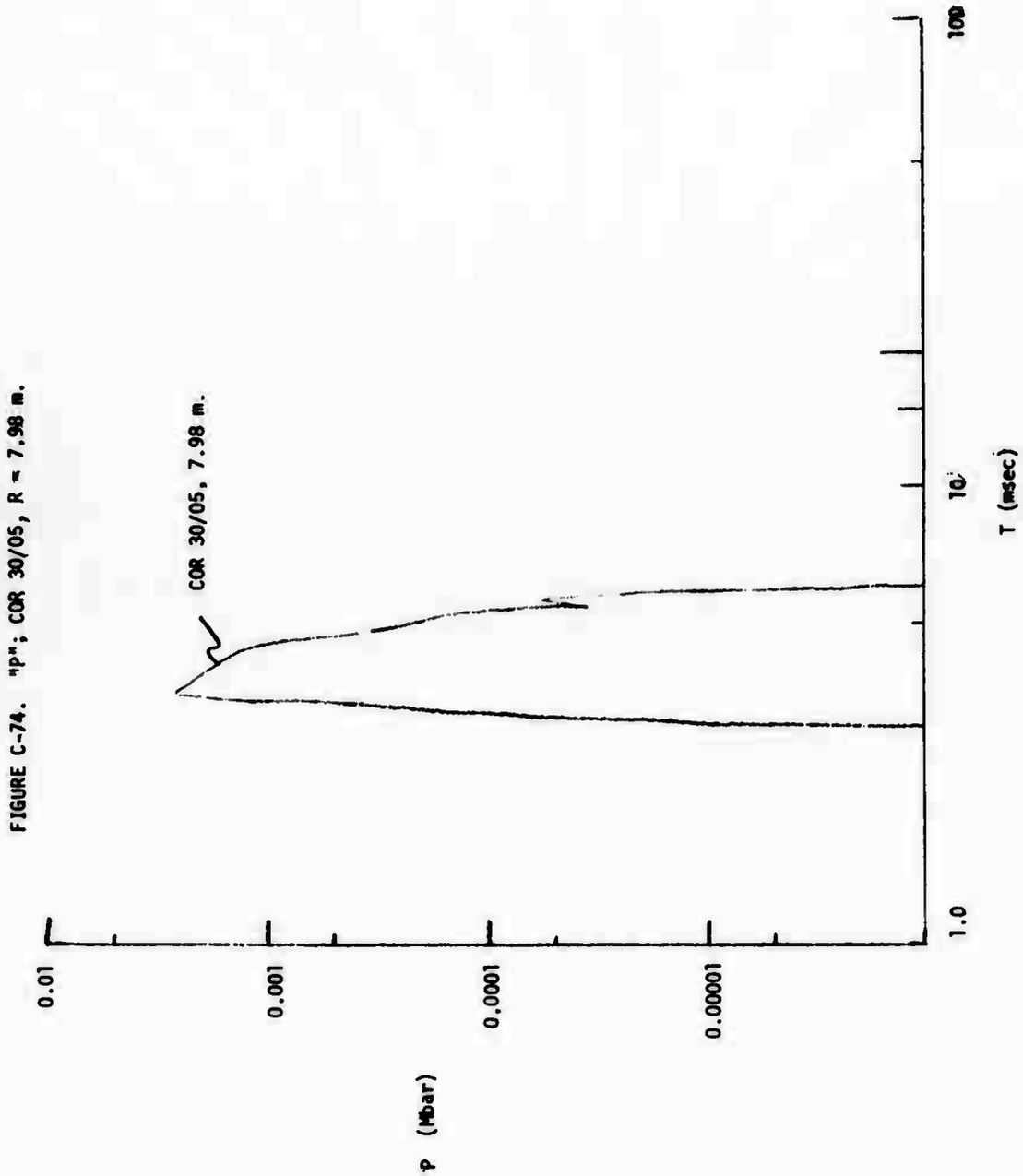

FIGURE C-74. "p"; COR 30/05, R = 7.98 m.

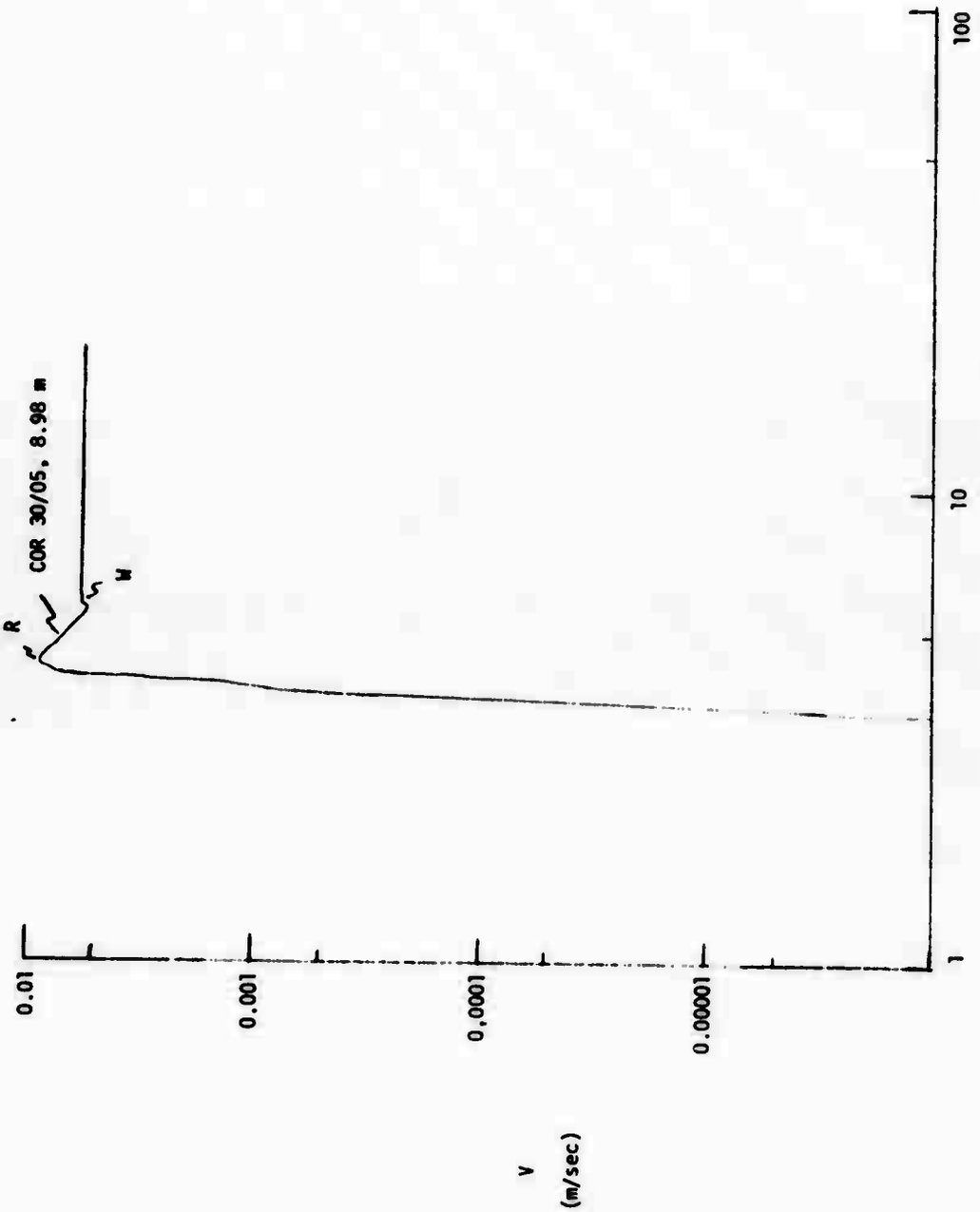

FIGURE C-75. "V"; COR 30/05, R = 8.98 m.

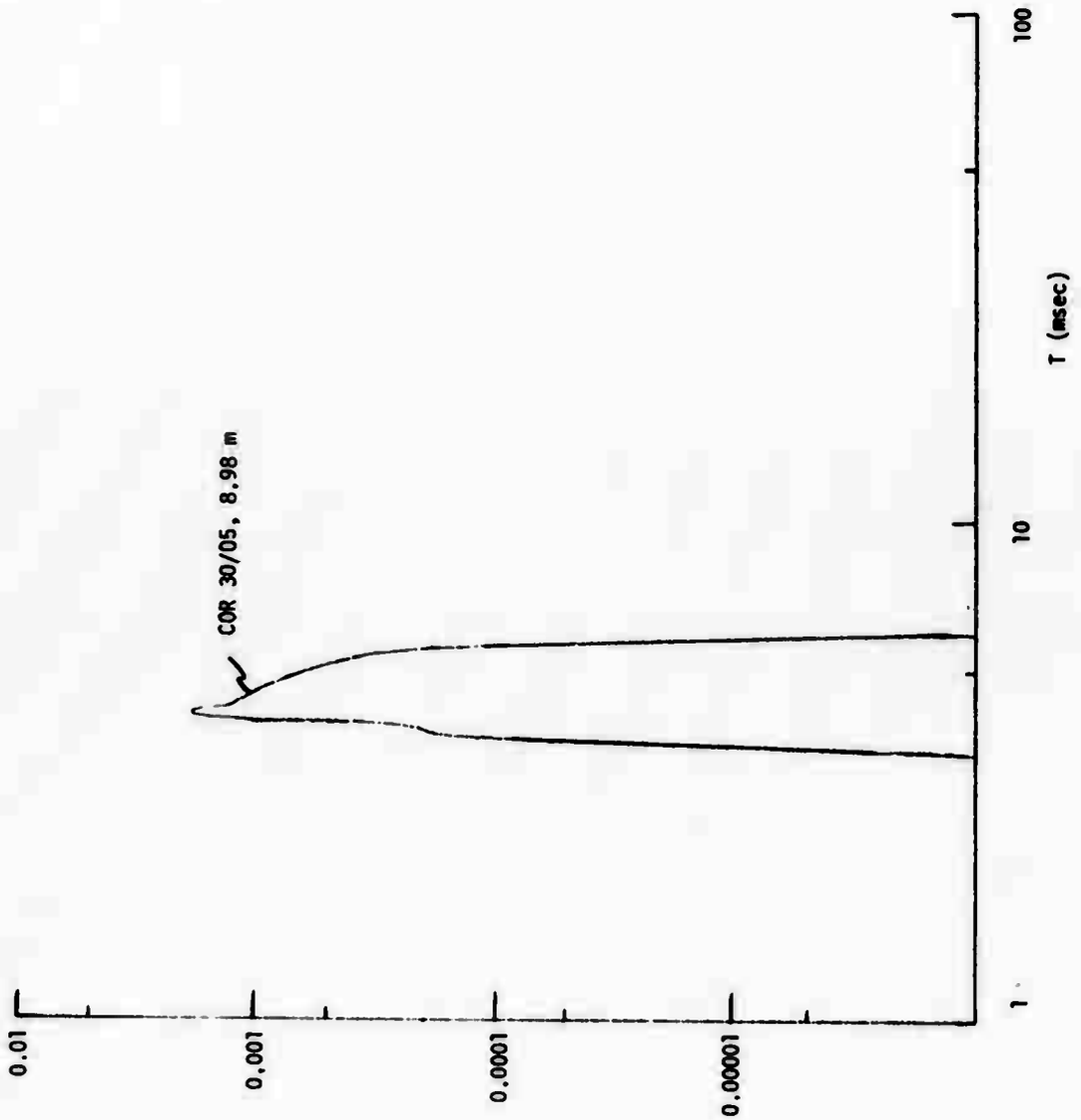

FIGURE C-76. "P"; COR 30/05, R = 8.98 m.

FIGURE C-77. "V"; COR 30/05, R = 9.11 m.

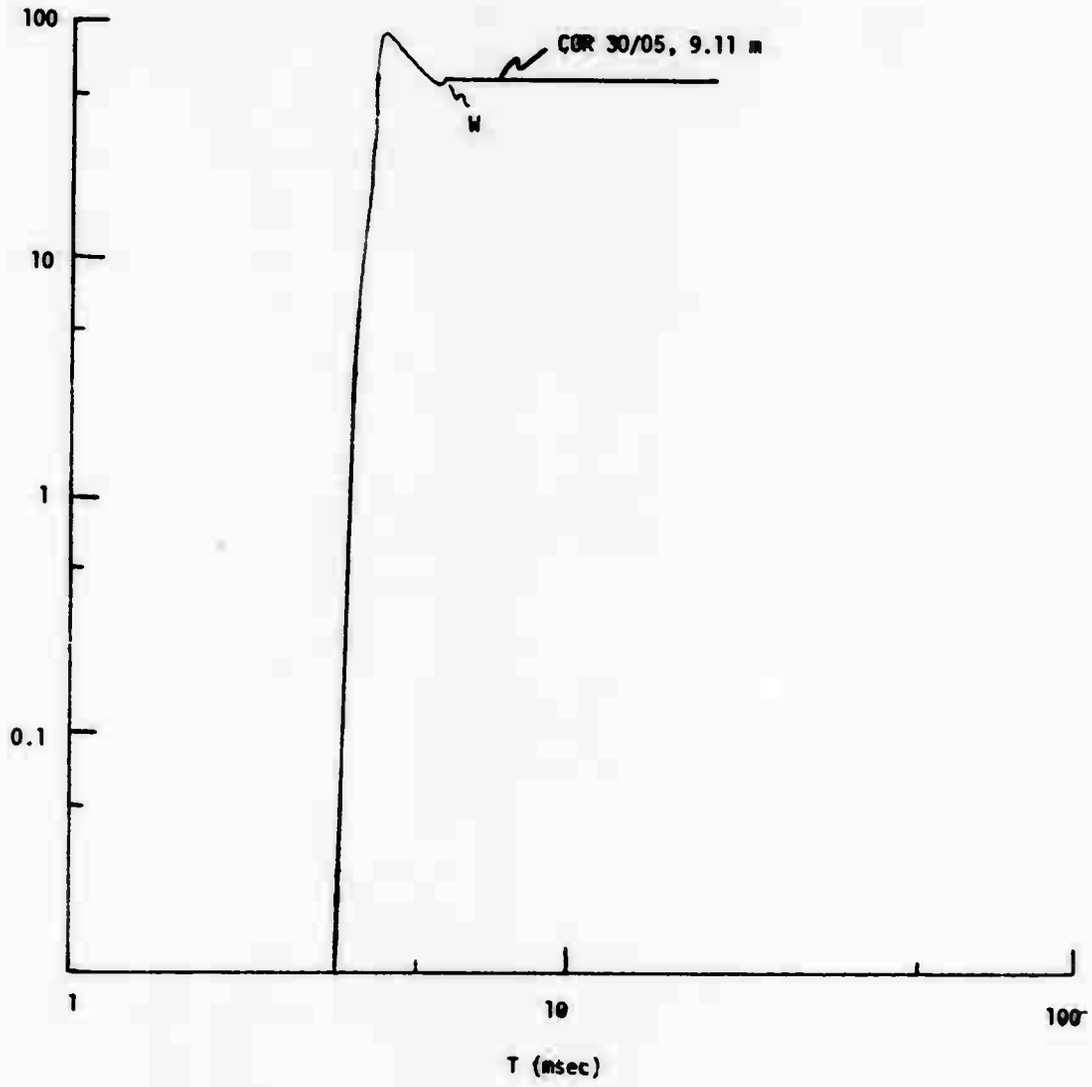

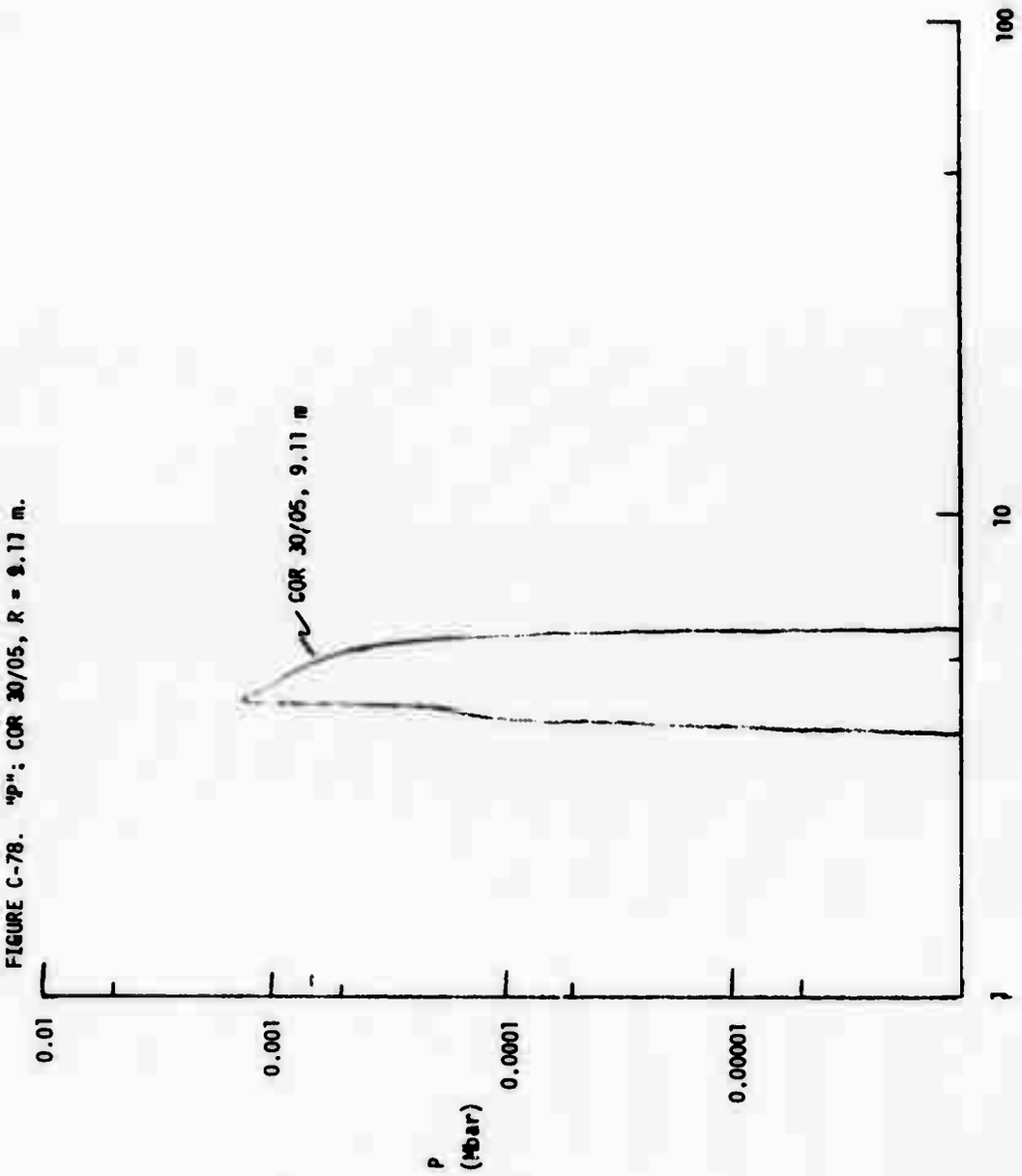

FIGURE C-78. "P"; COR 30/05, R = 9.11 m.

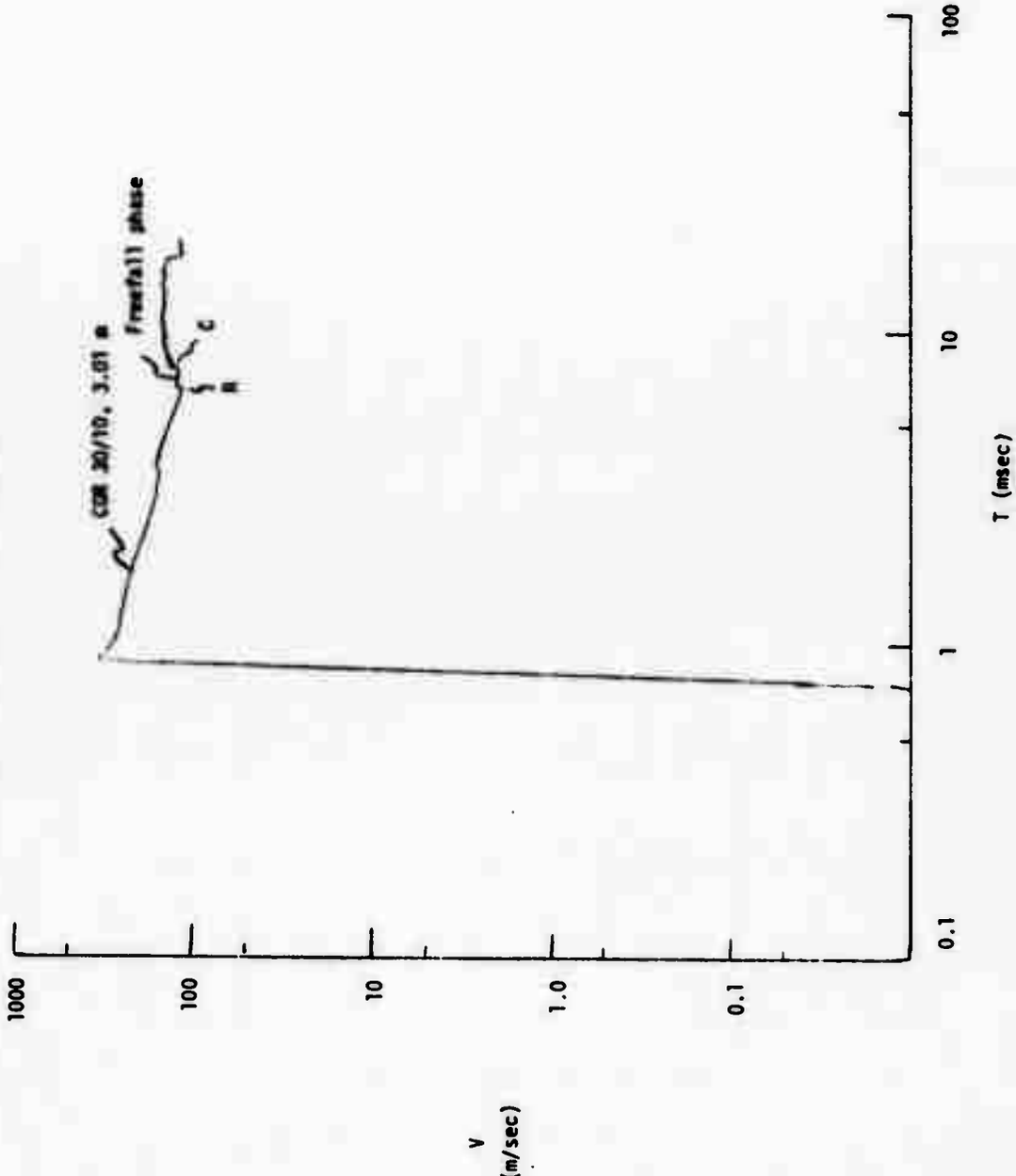

FIGURE C-79. "V"; COR 30/10, R = 3.01 m.

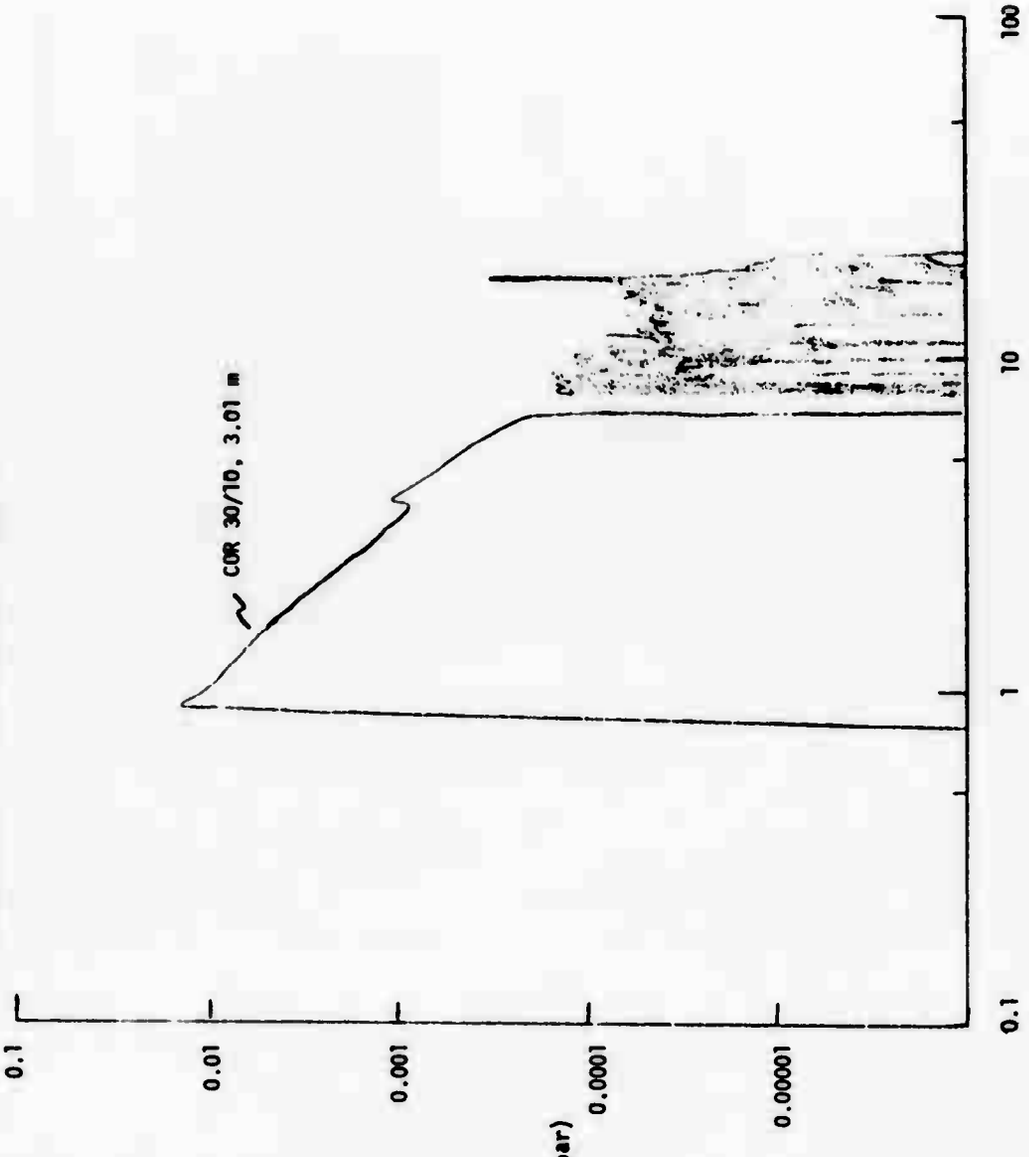

FIGURE C-80. "P"; COR 30/10, R = 3.01 m.

FIGURE C-81. "V"; COR 30/10, R = 5.01 m.

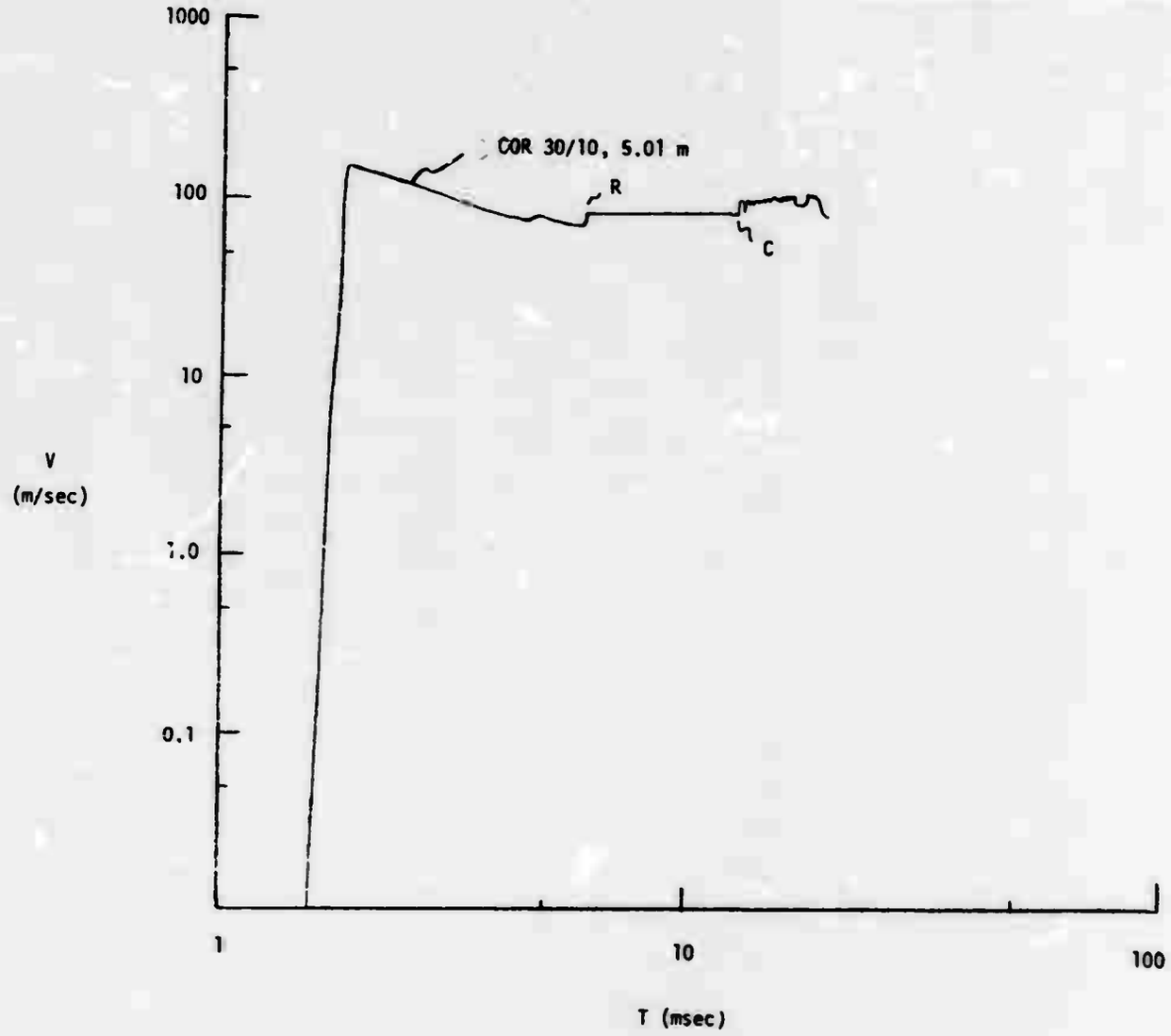

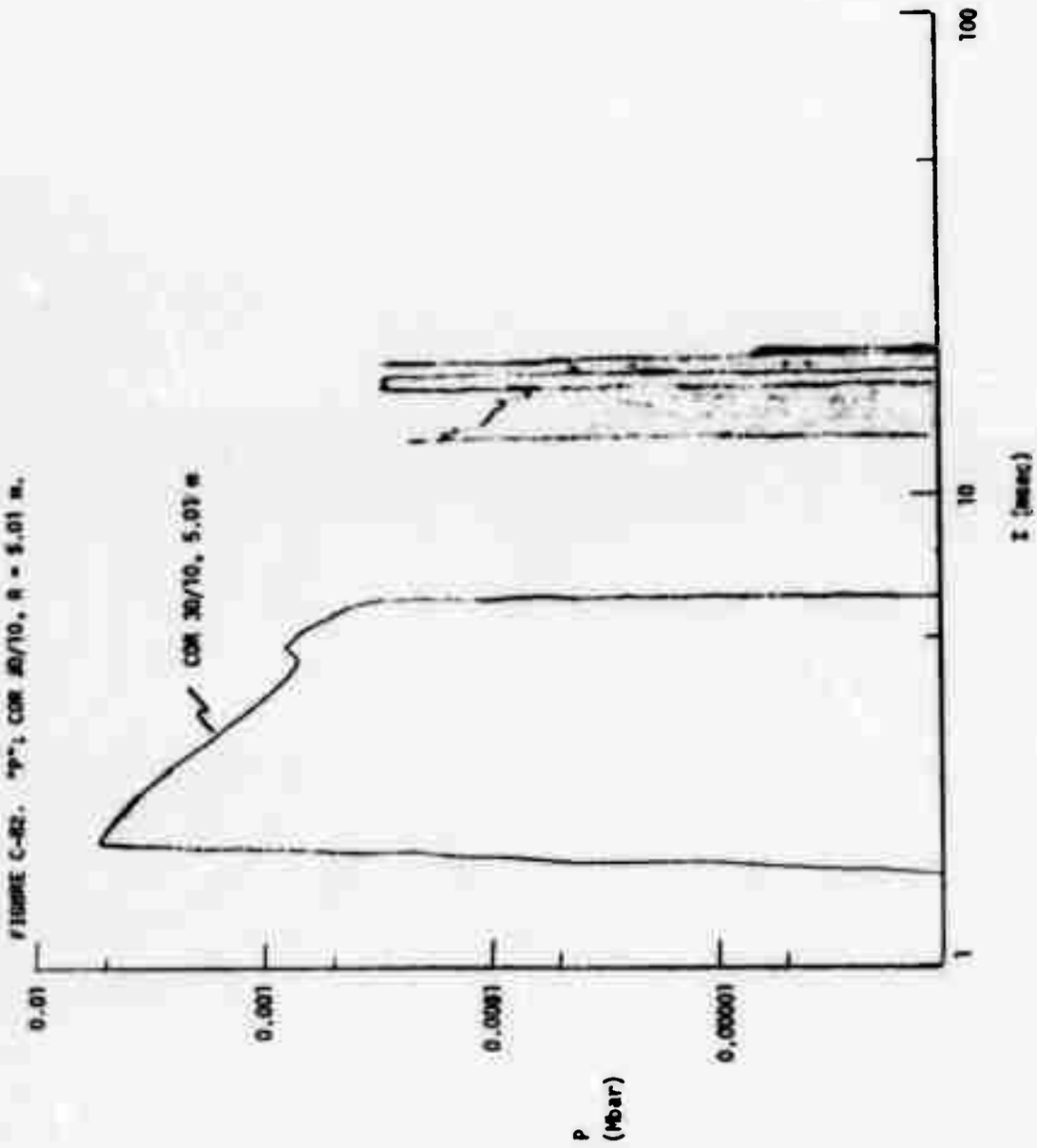

FIGURE C-82. "P"; COR 30/10, m = 5.01 m.

FIGURE C-83. "V"; COR 30/10, R = 5.98 m.

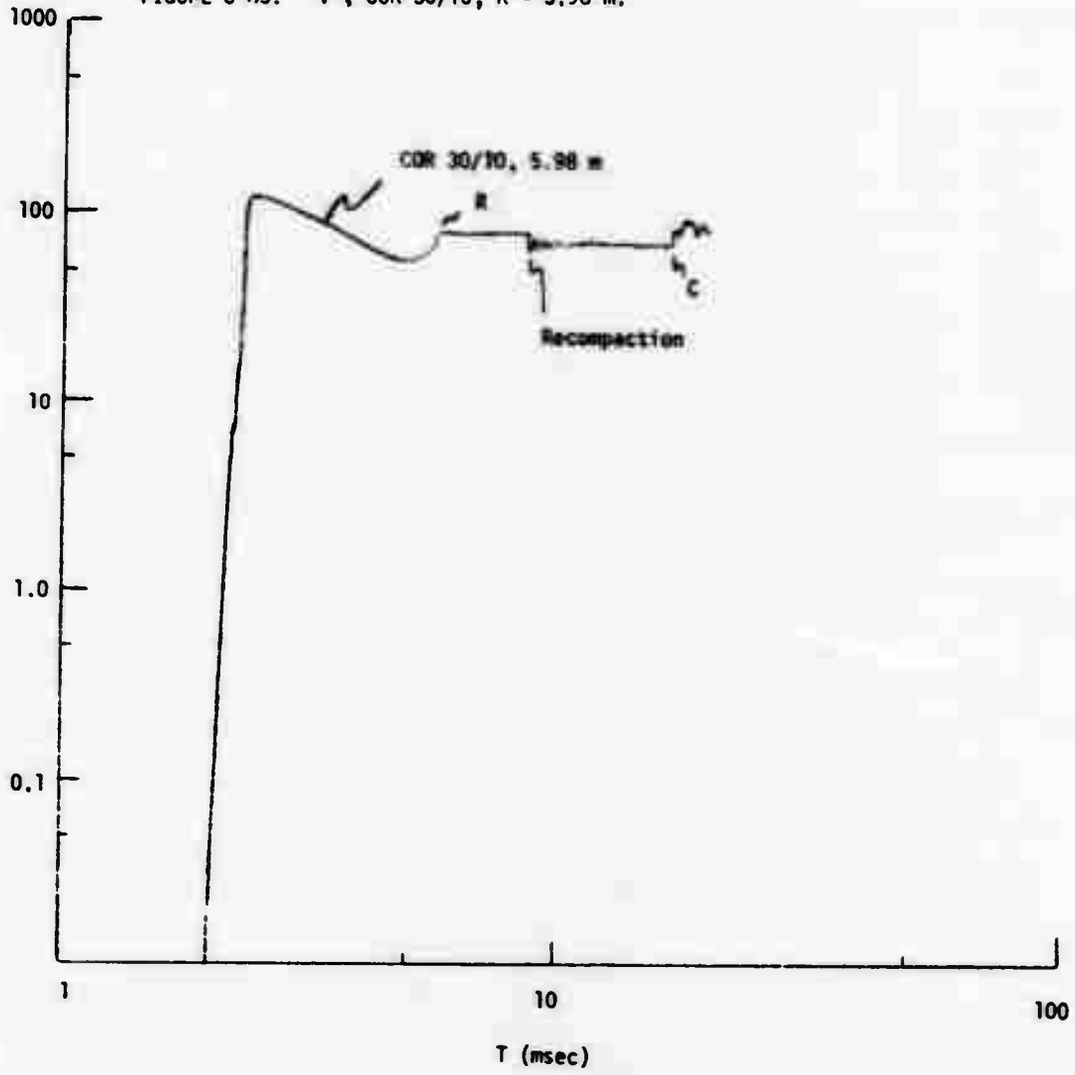

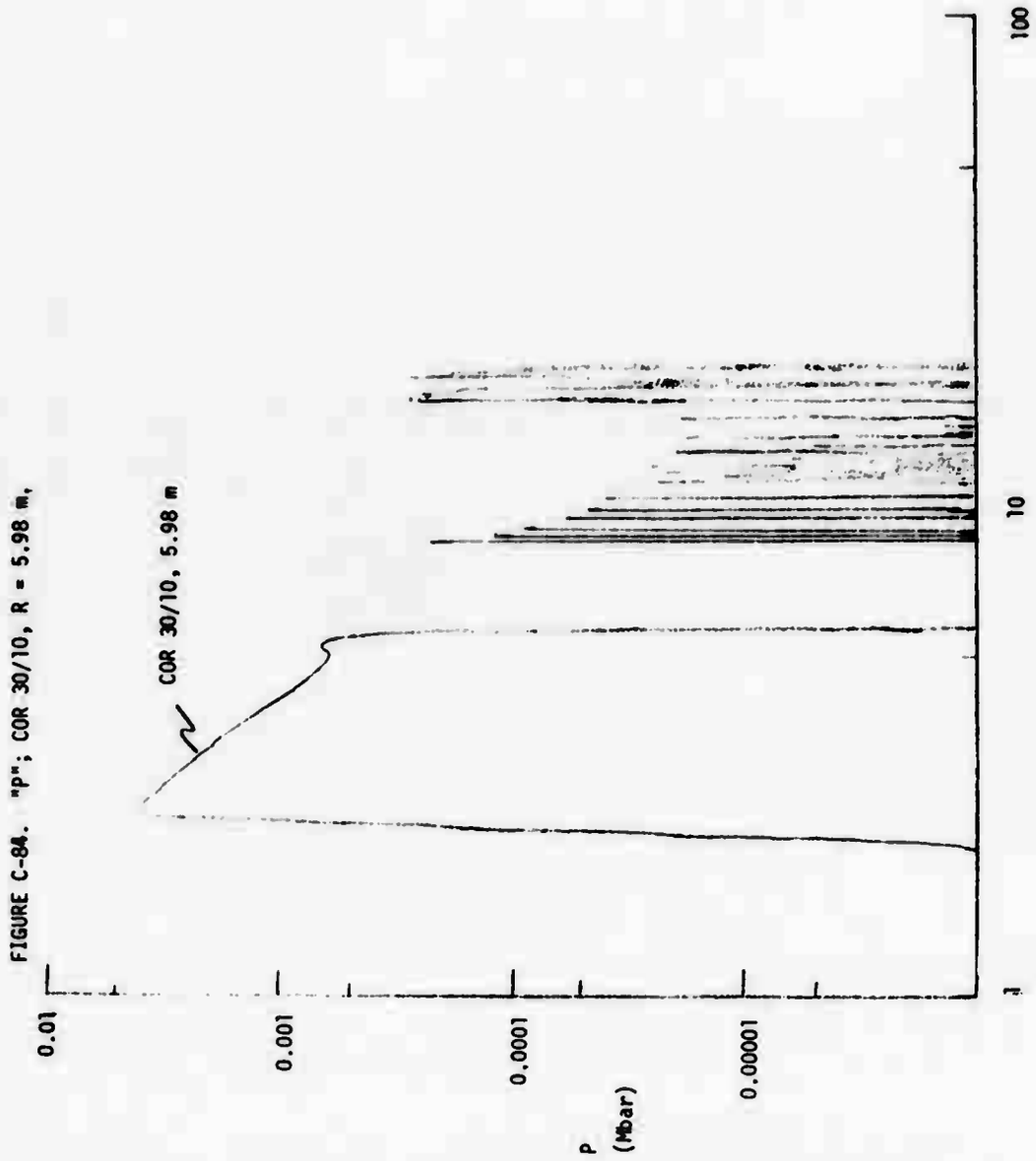

FIGURE C-84. "P"; COR 30/10, R = 5.98 m,

FIGURE C-85. "V"; COR 30/10, R = 7.98 m.

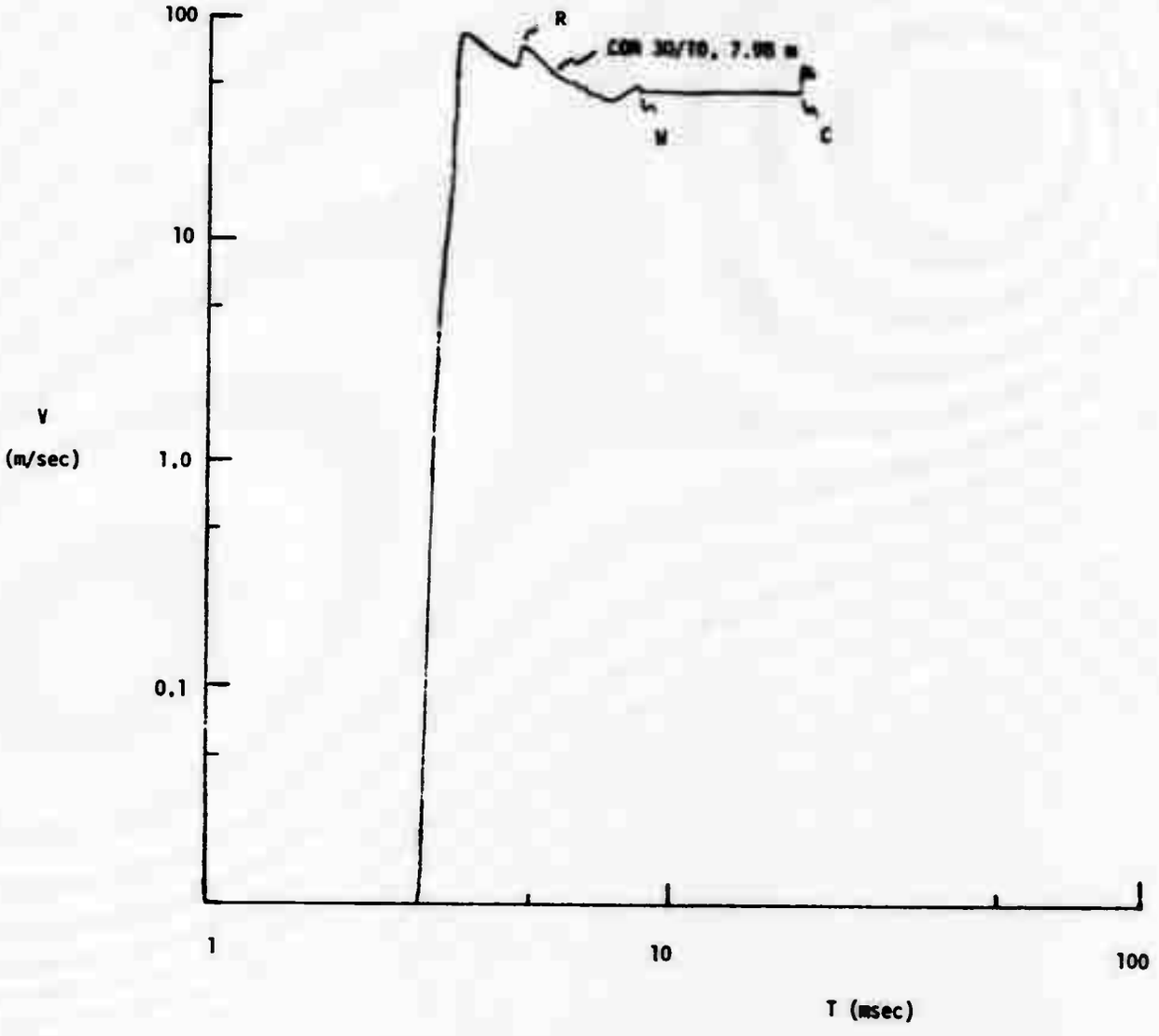

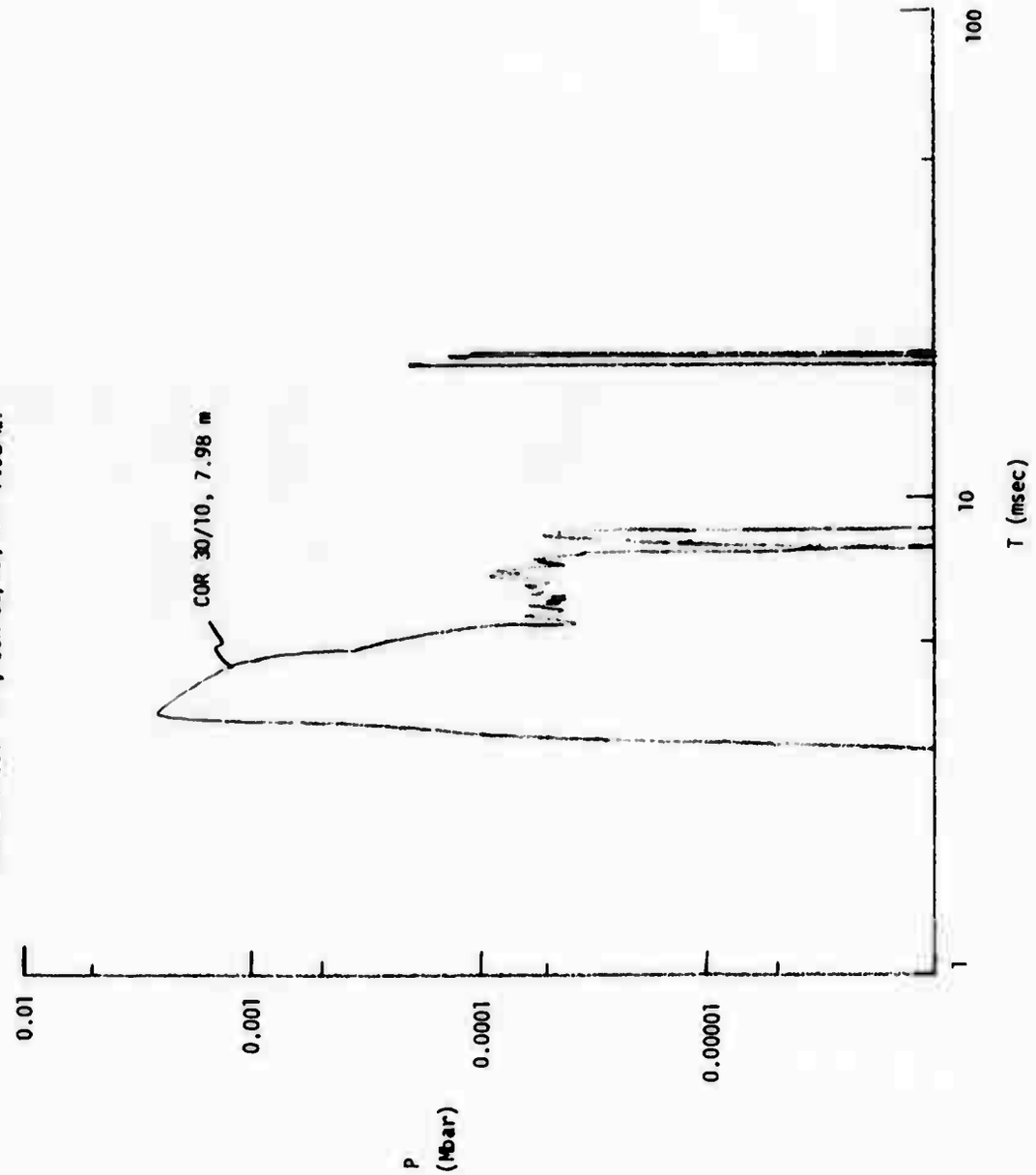

FIGURE C-86. "P"; COR 30/10, R = 7.98 m.

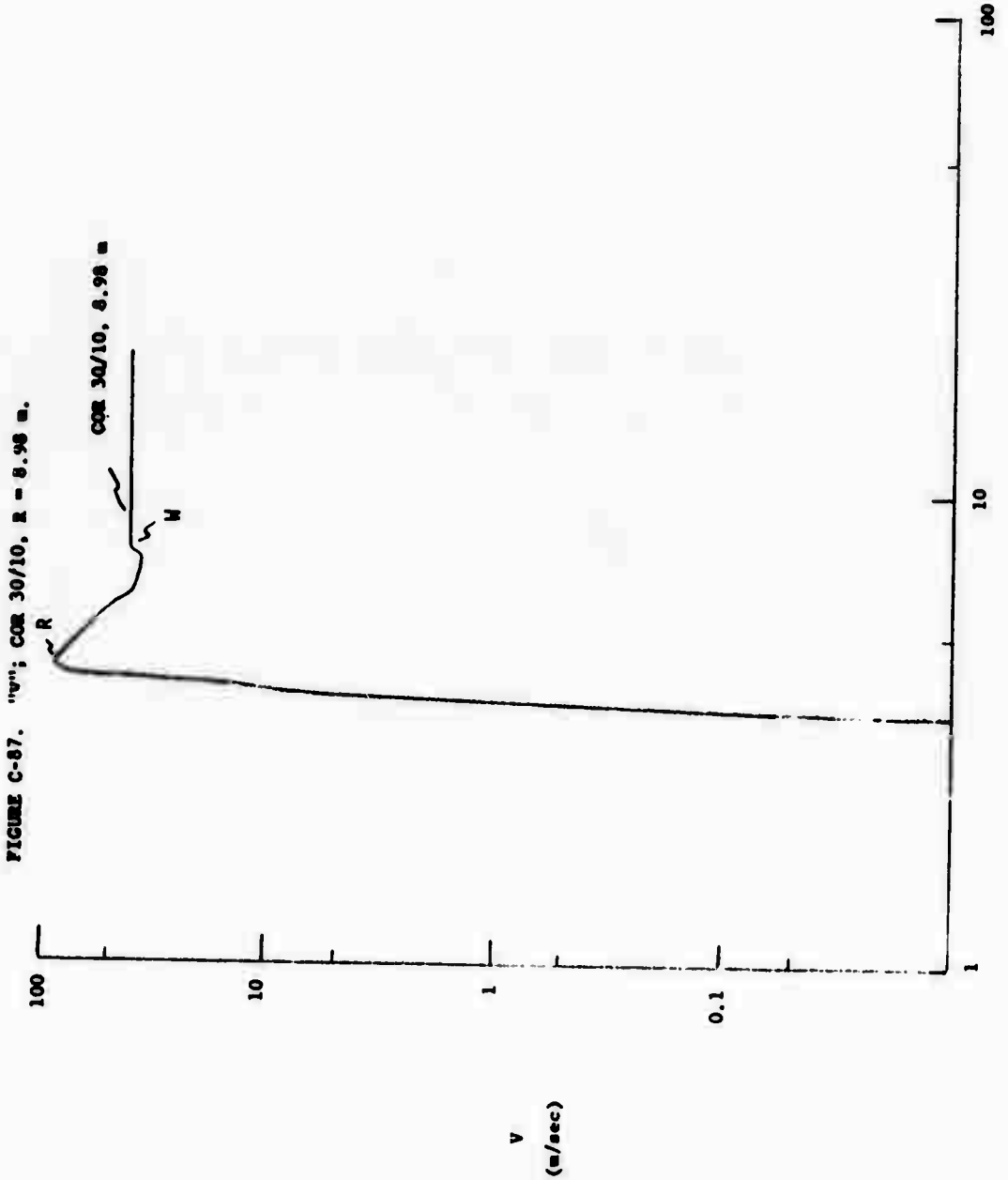

FIGURE C-87. "ψ"; COR 30/10, R = 8.98 m.

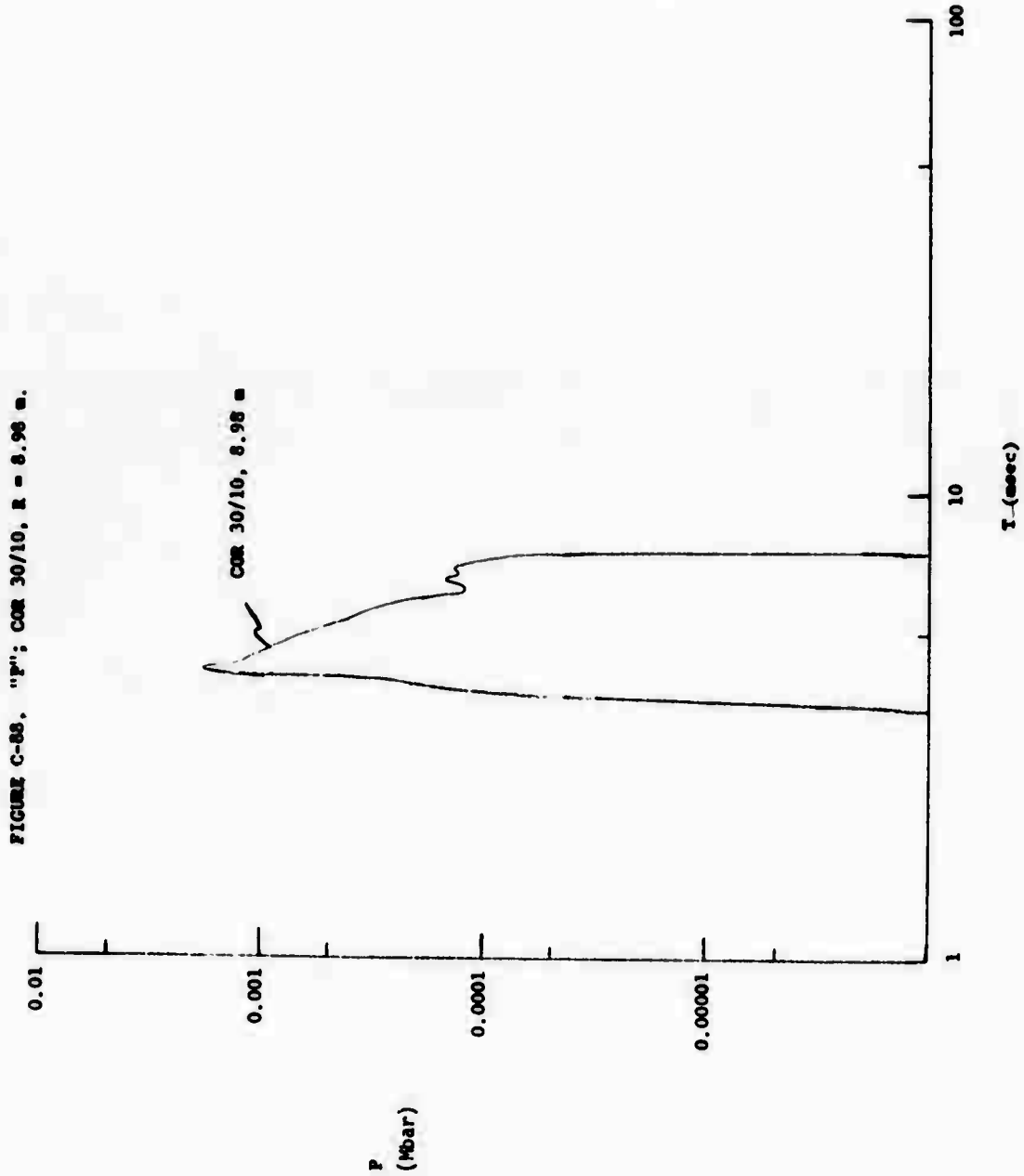

FIGURE C-88. "P"; COR 30/10, R = 8.98 m.

FIGURE C-89. "V"; CON 30/10, R = 9.11 m.

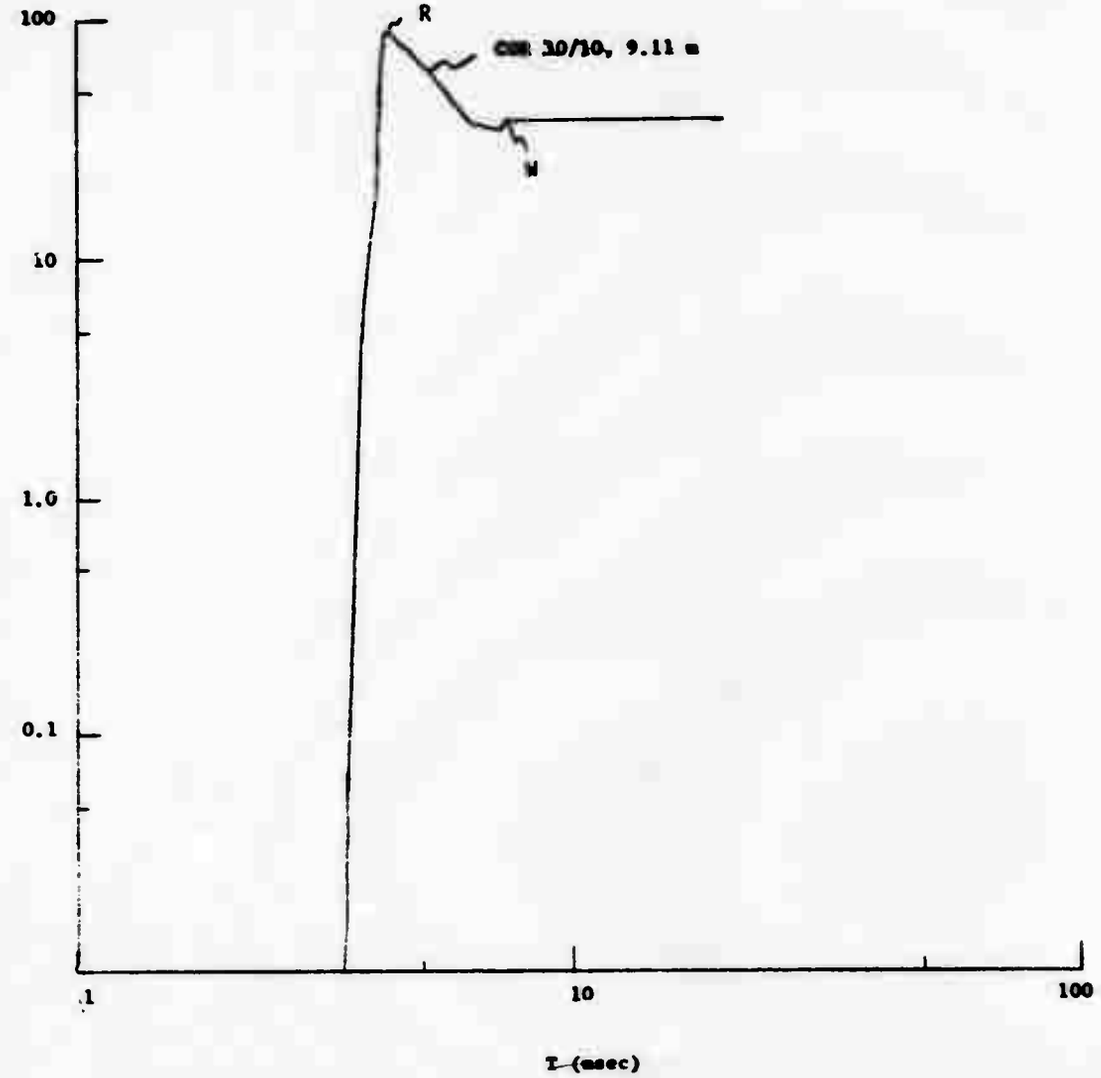

FIGURE C-90. "P"; COR 30/10, R = 9.11 m.

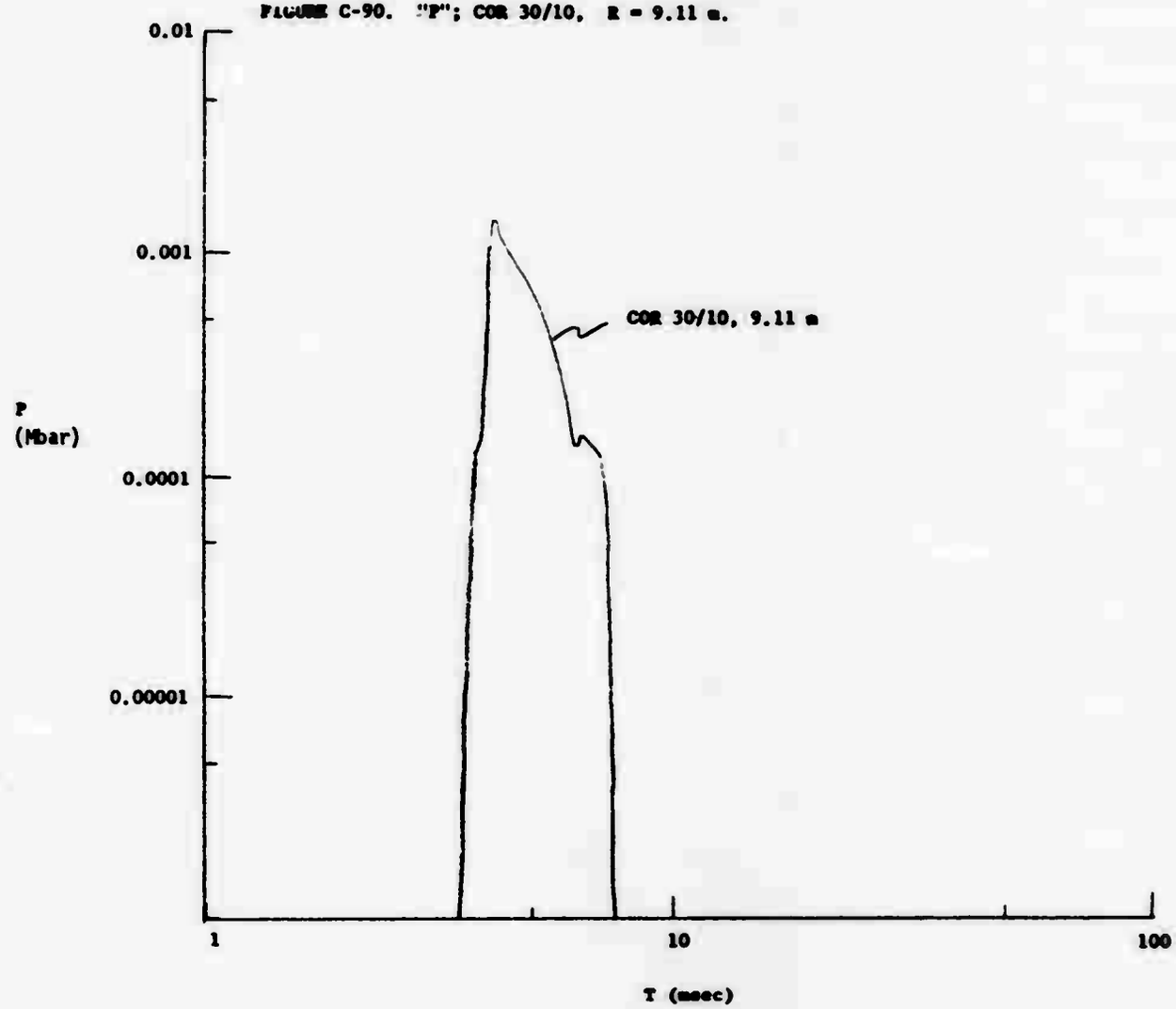

FIGURE C-91. "V": COE 30/36, R = 3.01 m.

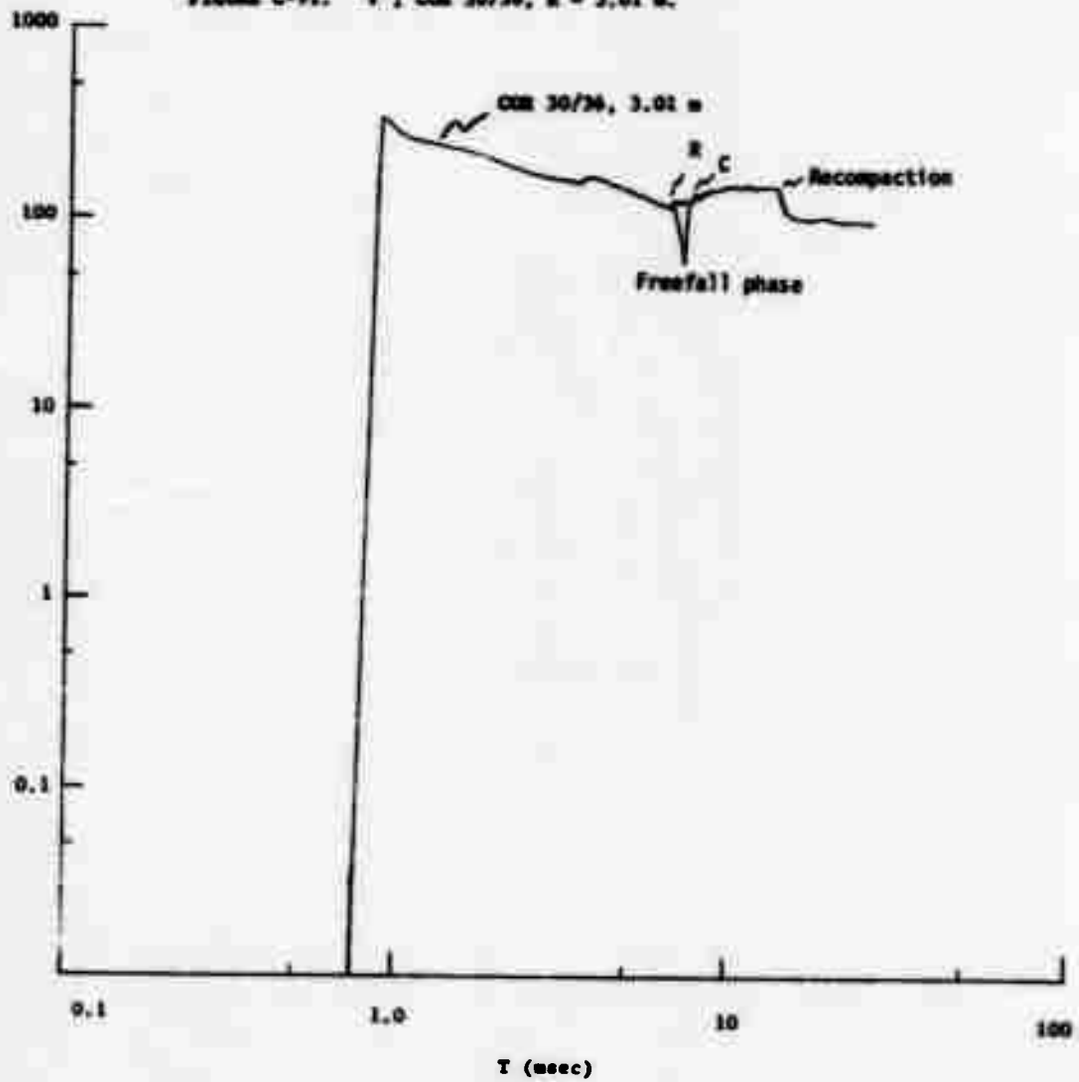

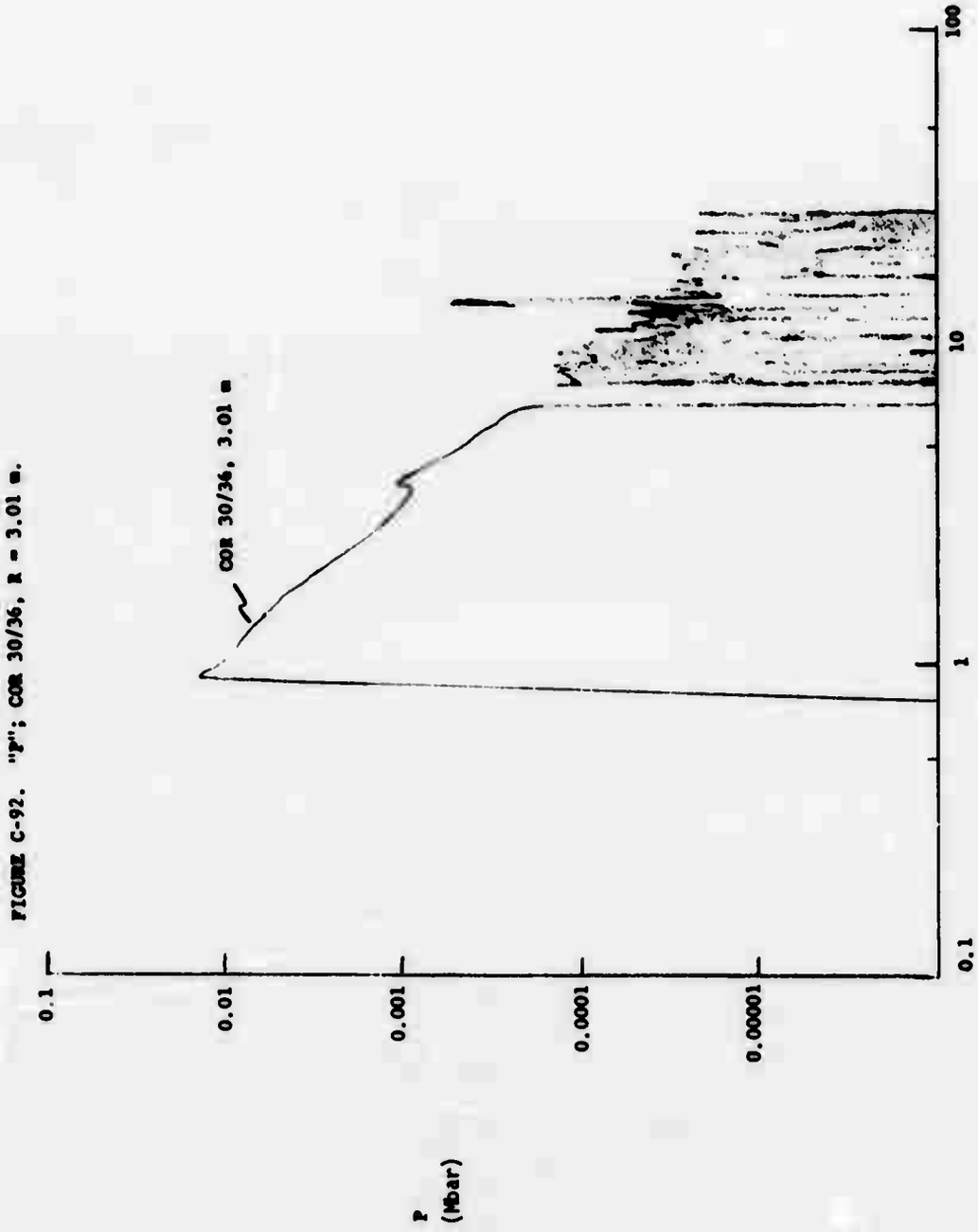

FIGURE C-92. "P"; COR 30/36, R = 3.01 m.

FIGURE C-43. "F": CDP 50/30, Z = 3,01 m.

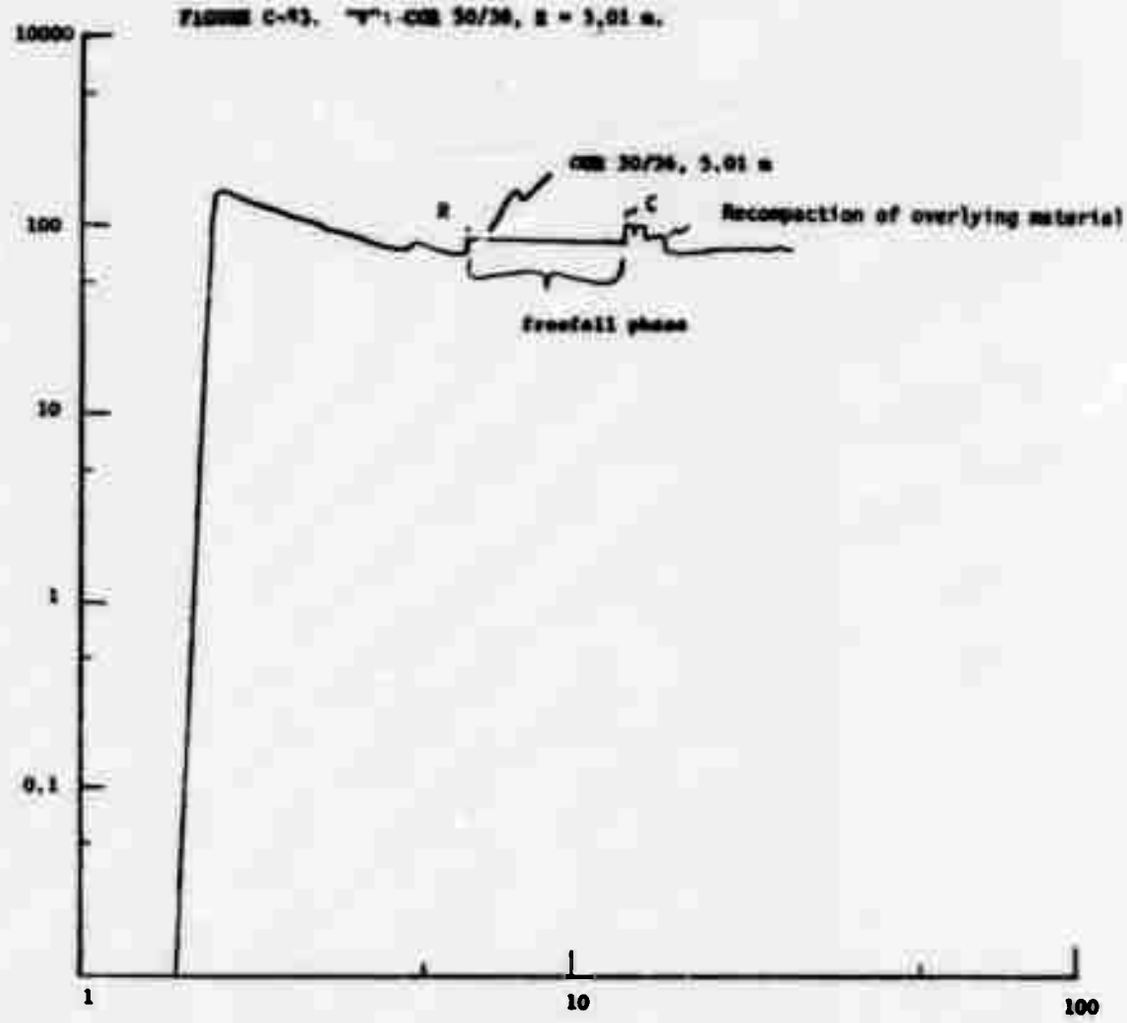

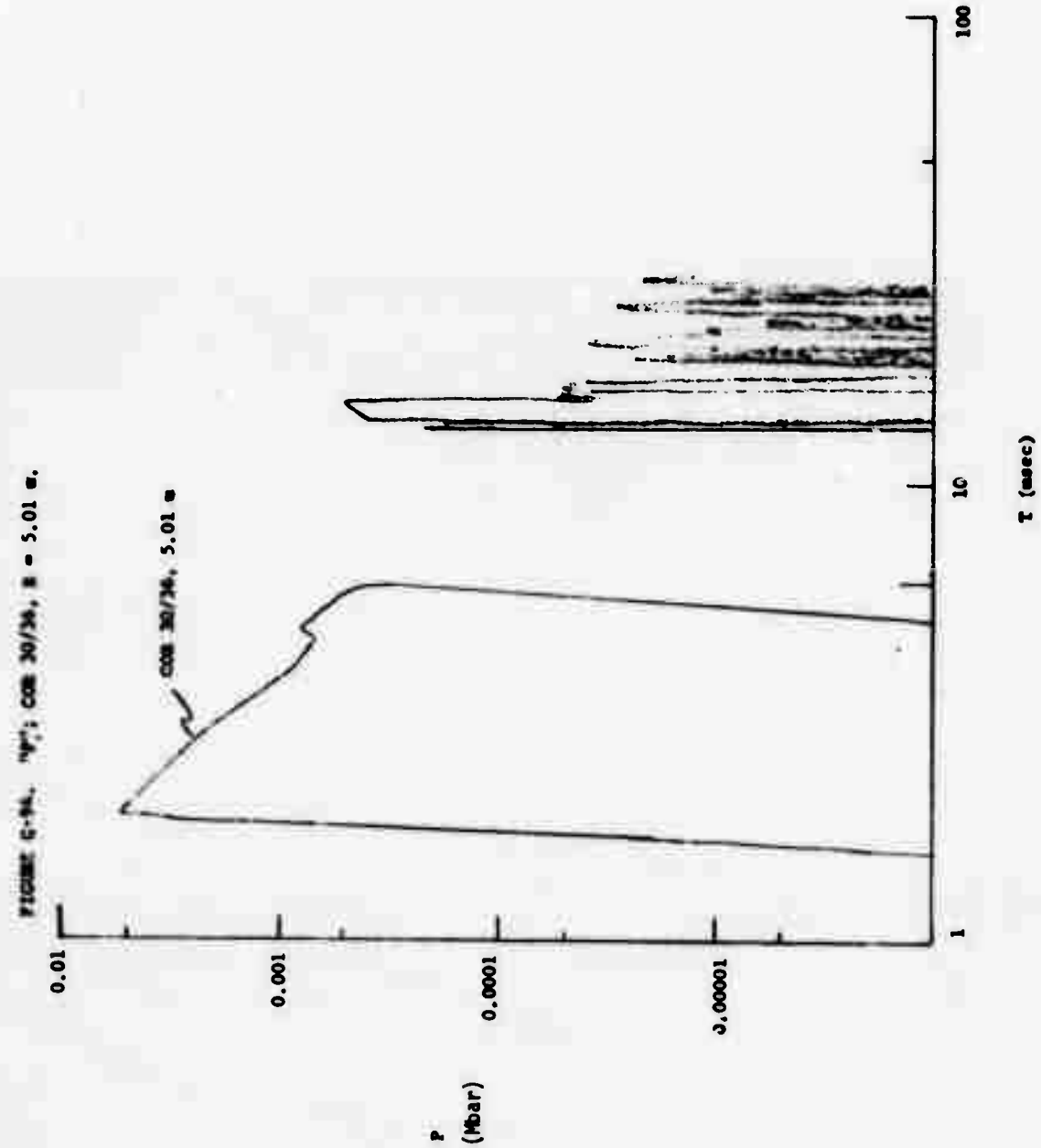
COR 30/36, 5.01 m
0.01
0.001
0.0001
0.00001
P
(Mbar)
1
10
100
T (msec)

FIGURE C-95. "V"; COR 30/36, R = 5.98 m.

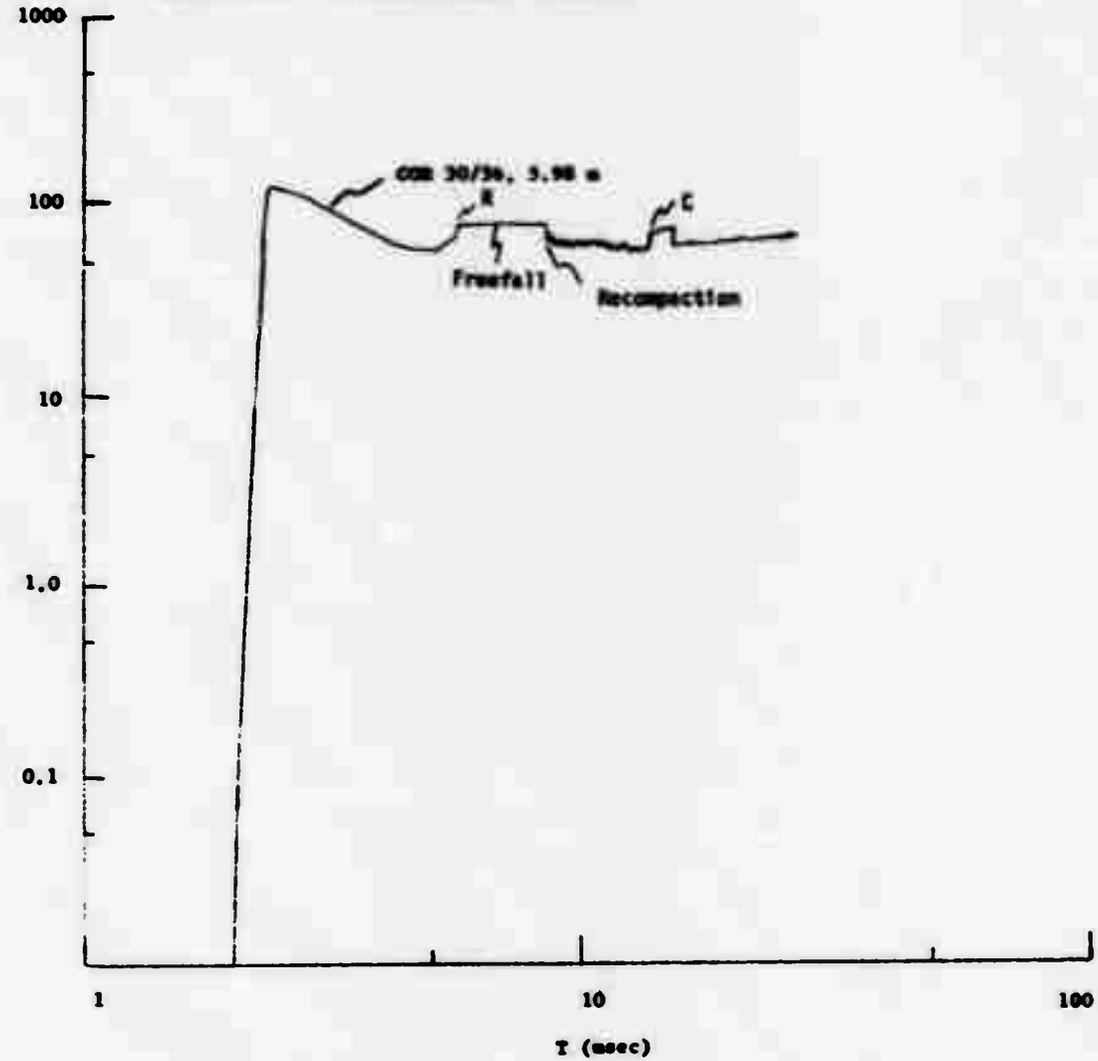

FIGURE C-96. "P"; COR 30/36, R = 5.98 m.

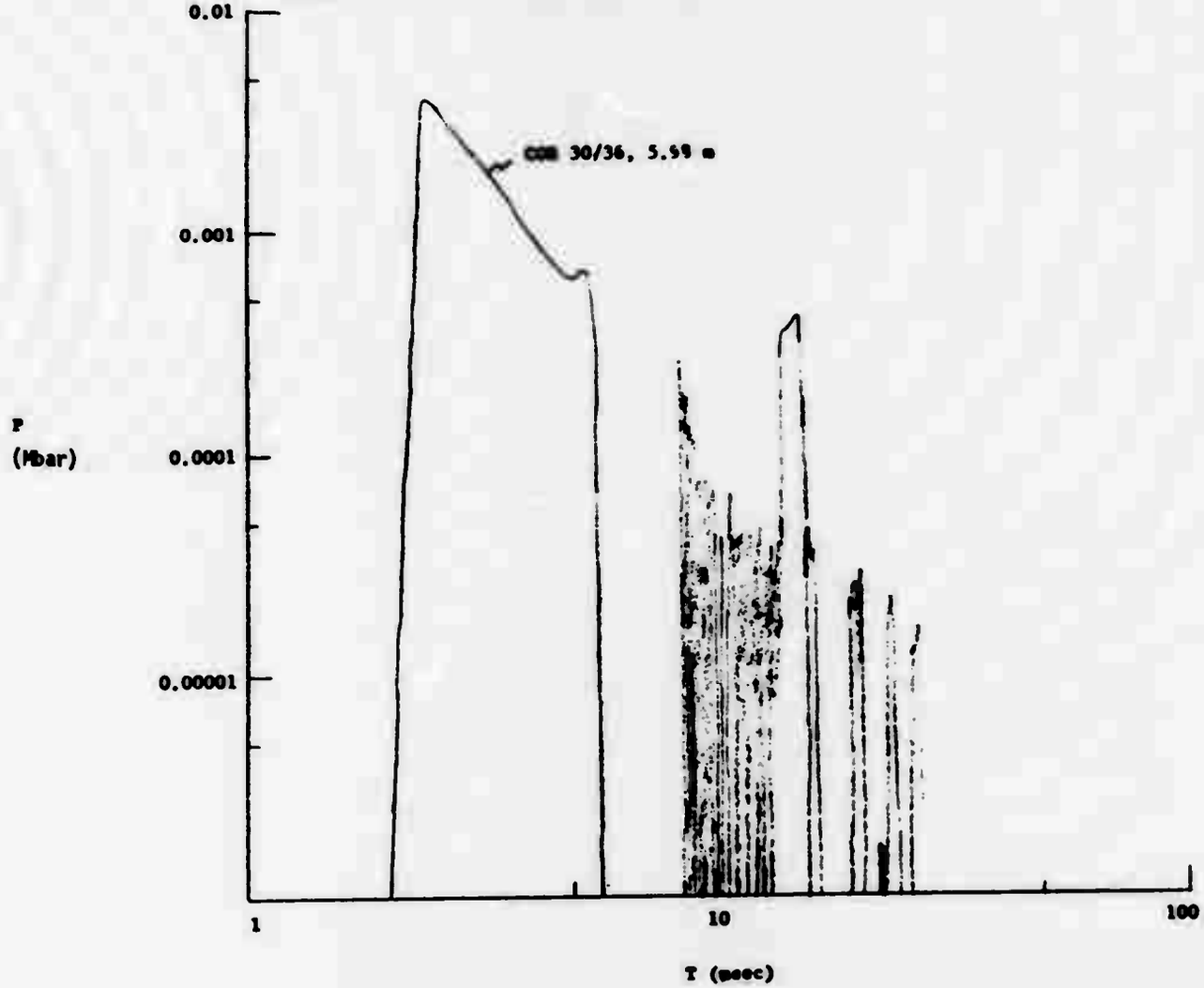

FIGURE C-97. "V"; COM 30/36, R = 7.98 m.

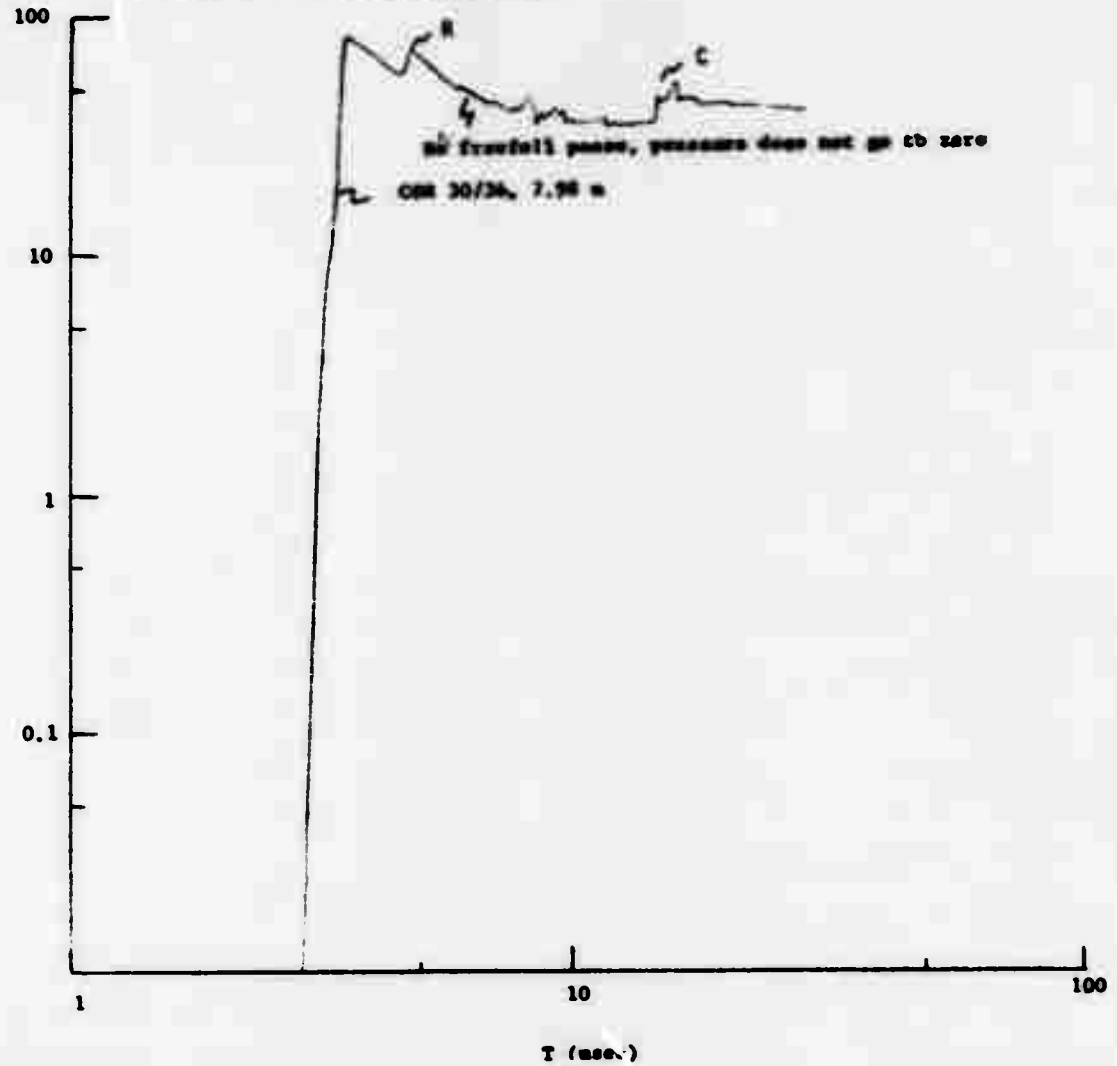

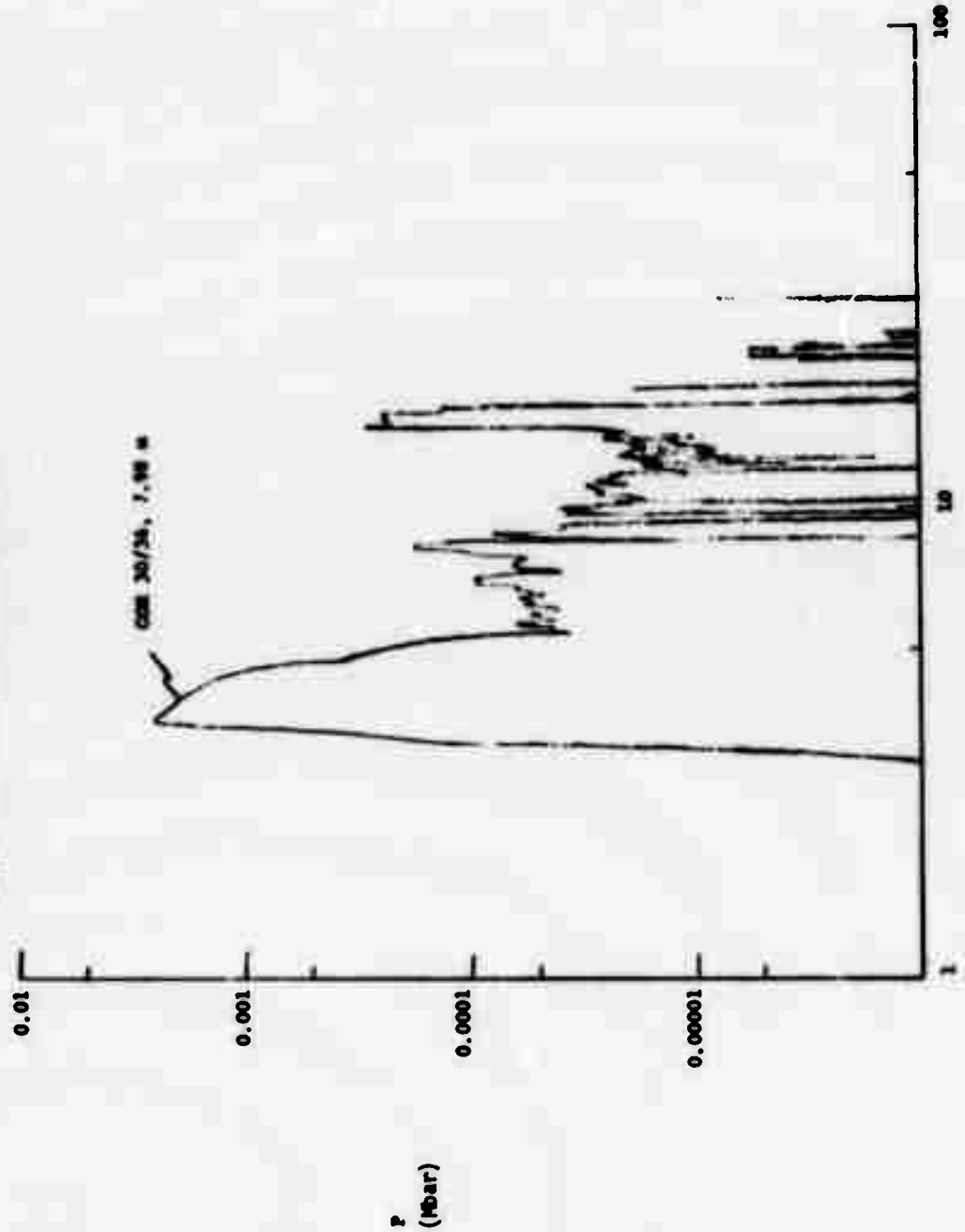

FIGURE C-98. "P"; CCR 30/36, R = 7.56 m.

FIGURE C-99. "V"; COR 30/36, R = 8.98 m.

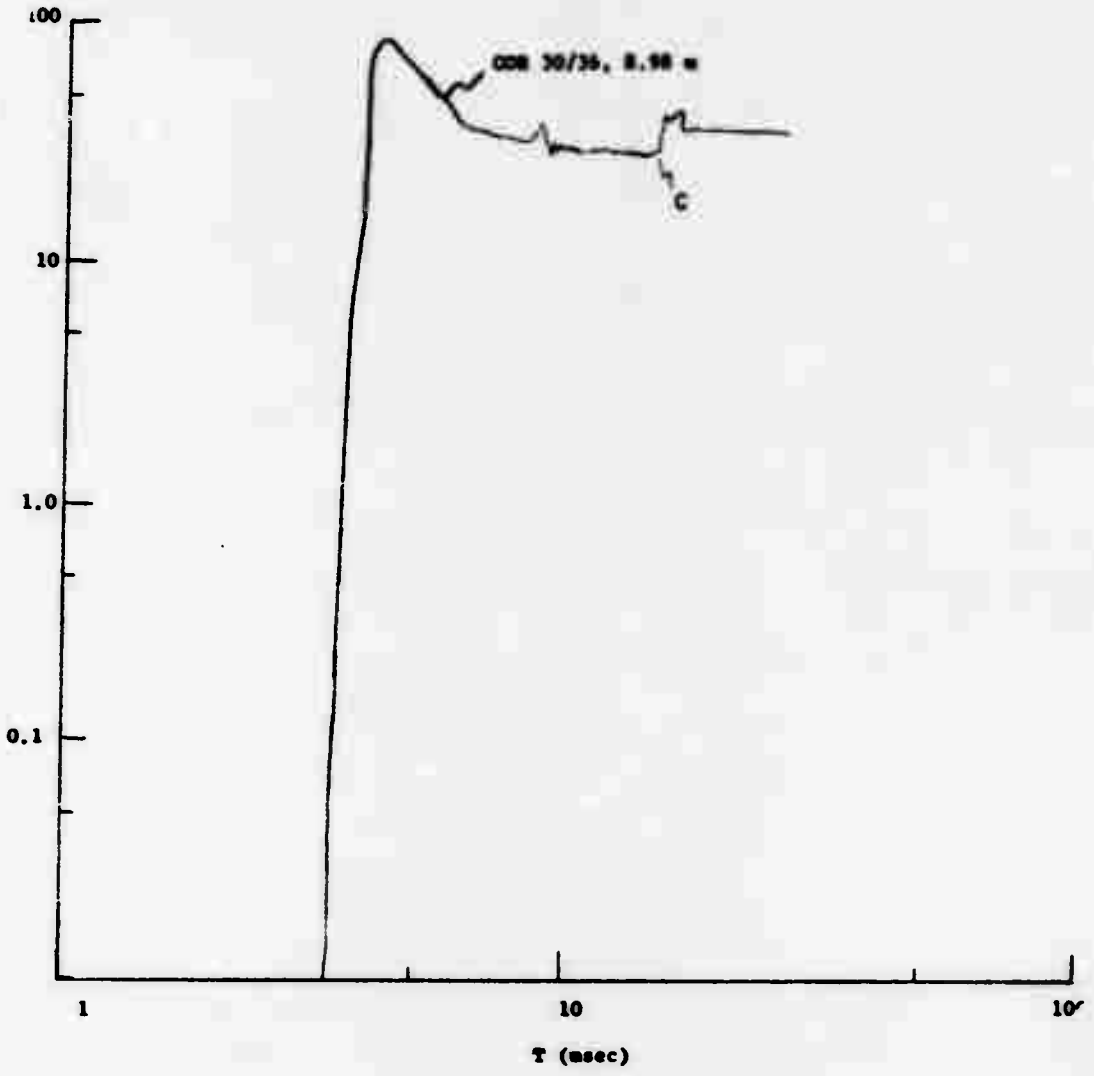

FIGURE C-100. "P"; COE 30/36, R = 8.98 m.

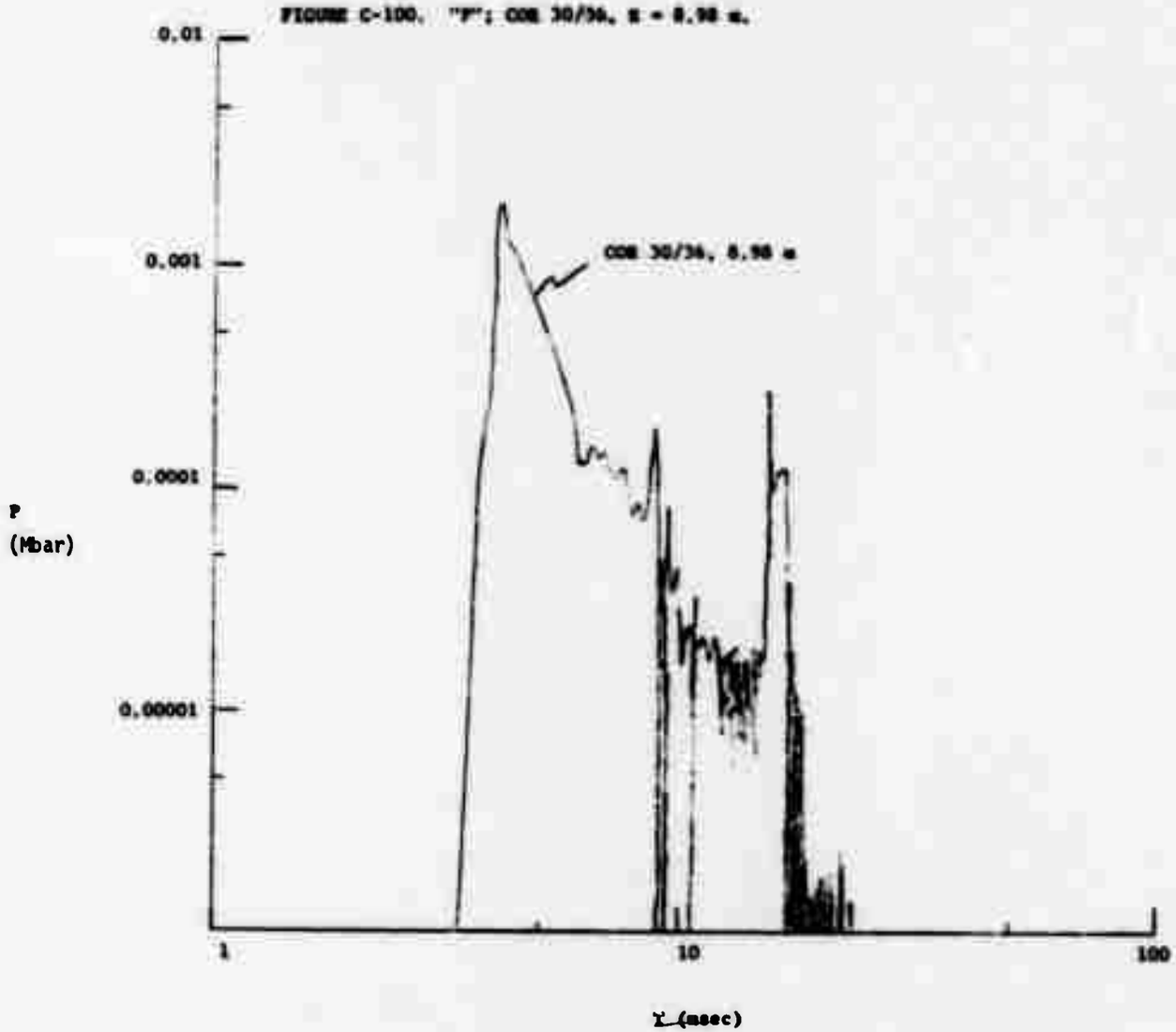

FIGURE C-101. "V"; COR 30/36, R = 9.11 m.

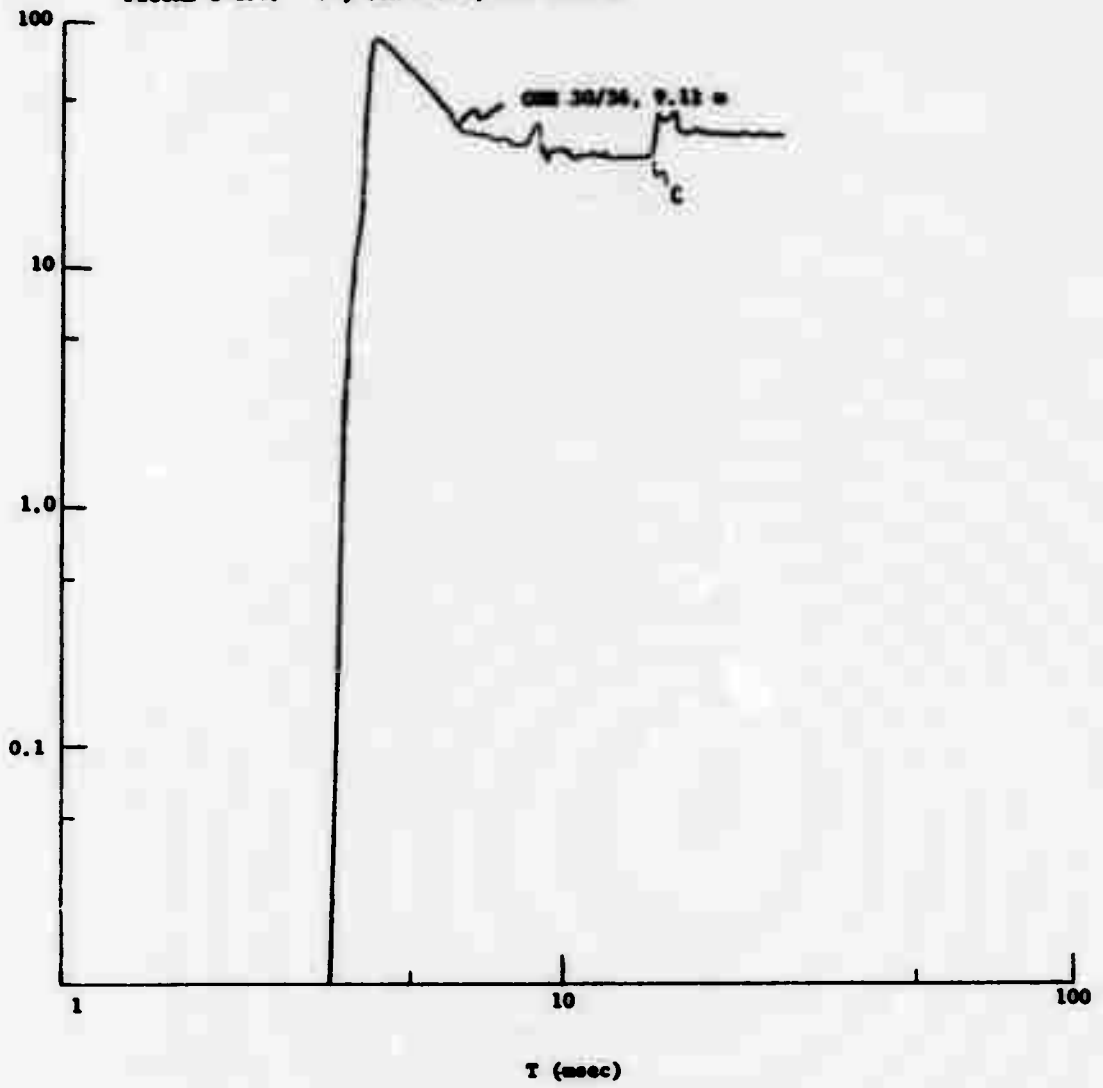

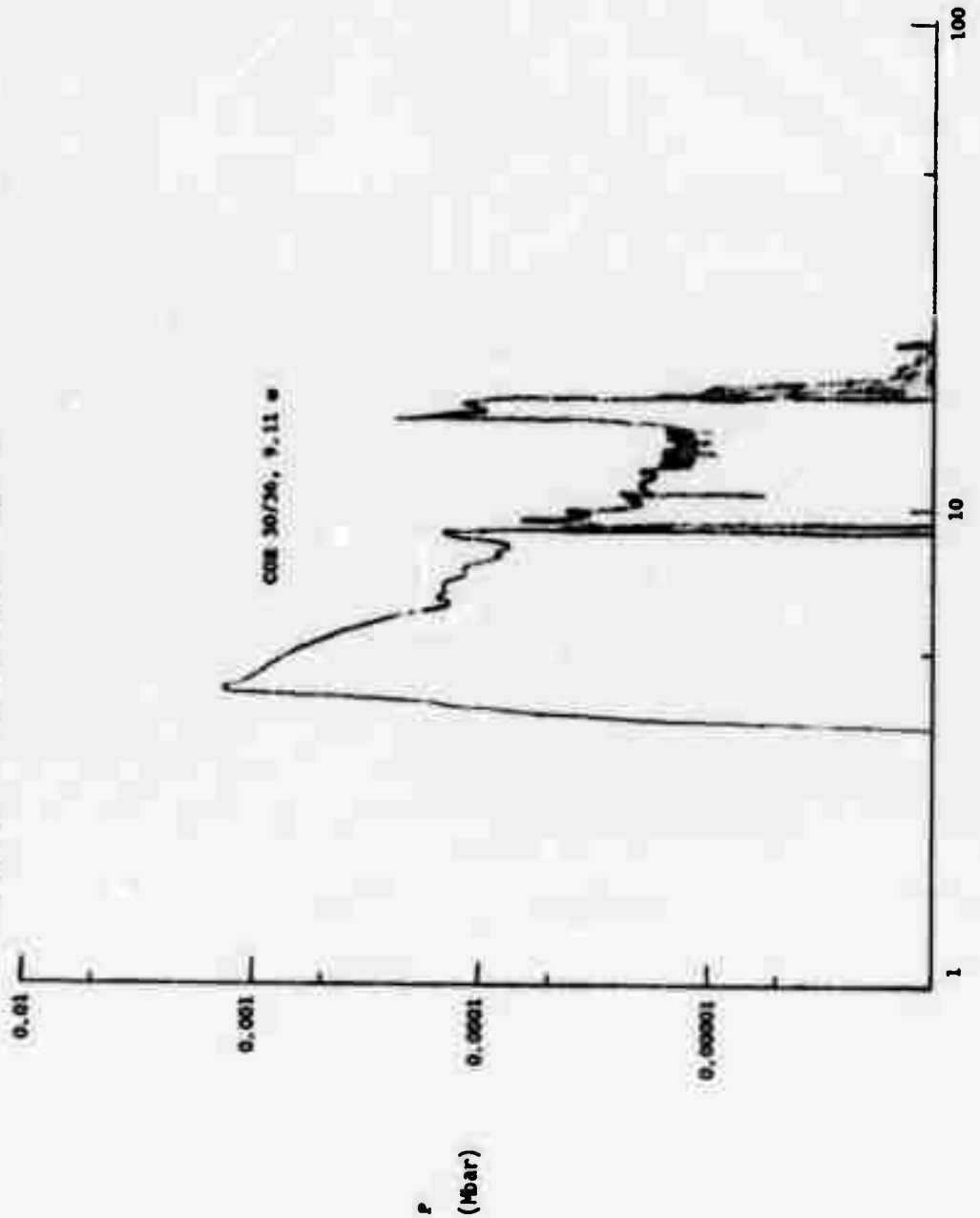

FIGURE C-102. "P"; COR 30/36, R = 9.11 m.

Appendix D

Waveforms for the Vertical and Vertical Underwater Calculations in Basalt

FIGURE D-1. "V"; Basalt, BAS 36/00, R = 3.01 m

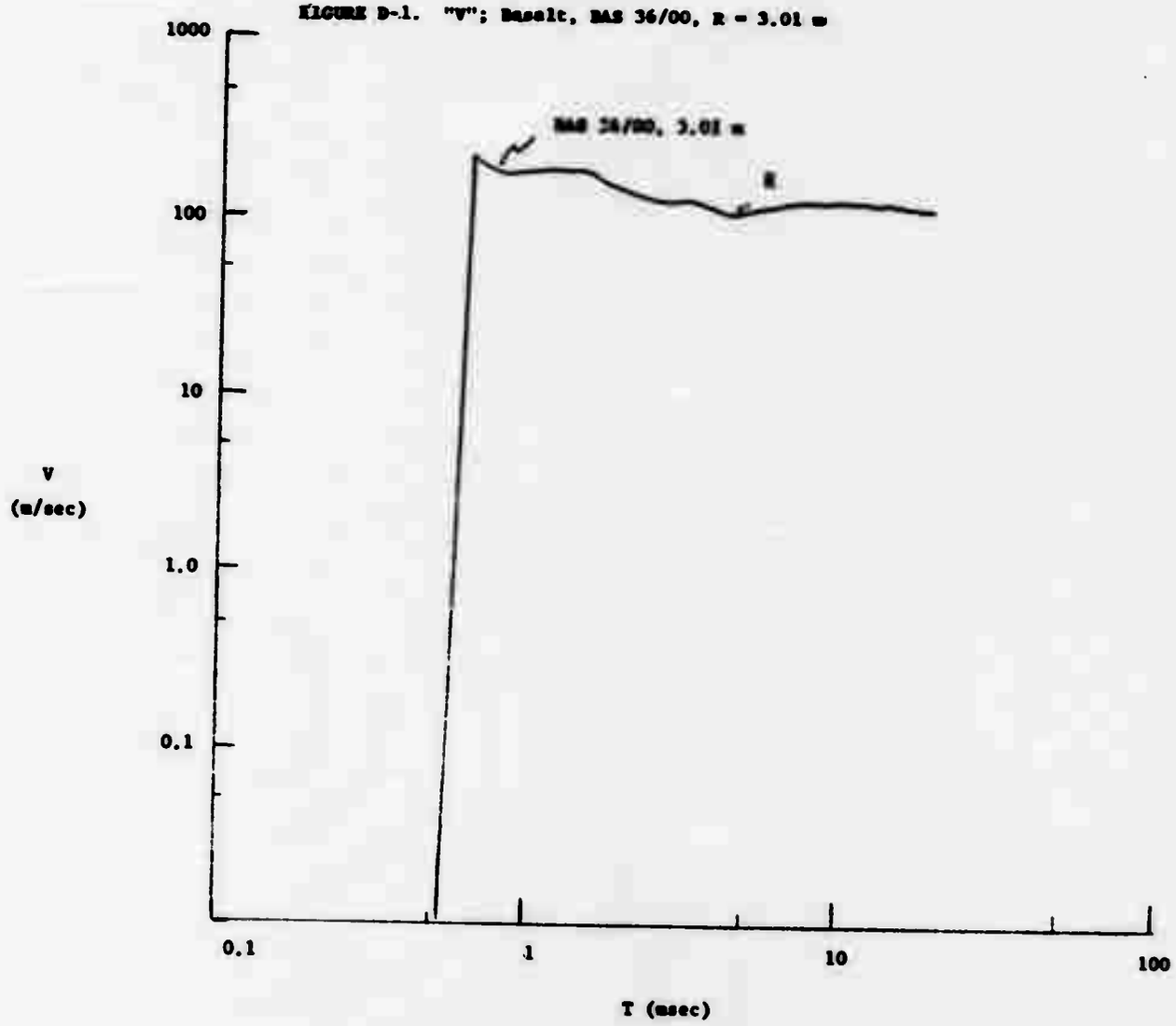

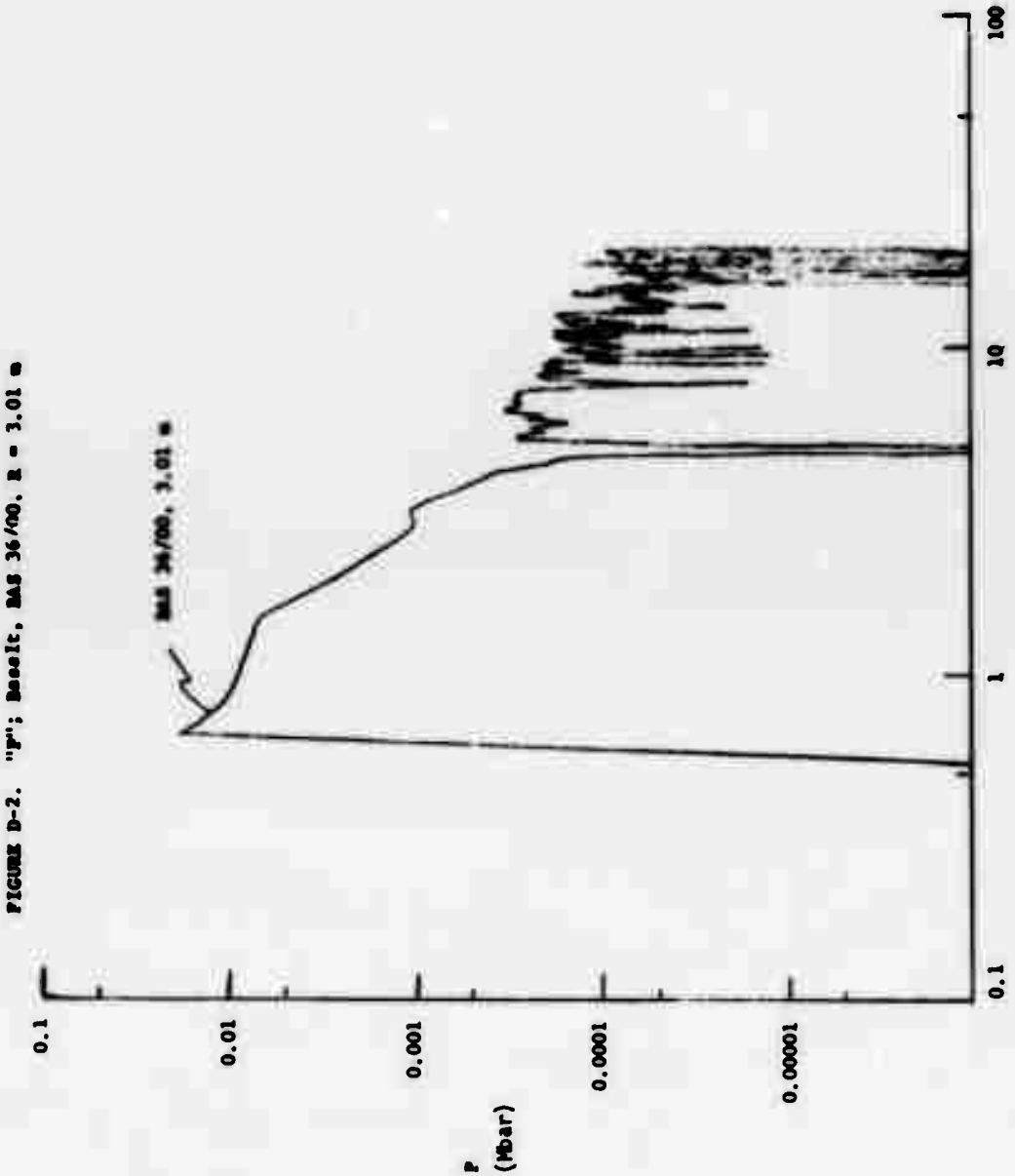

FIGURE D-2. "P"; Basalt, BAS 36/00, R = 3.01 m

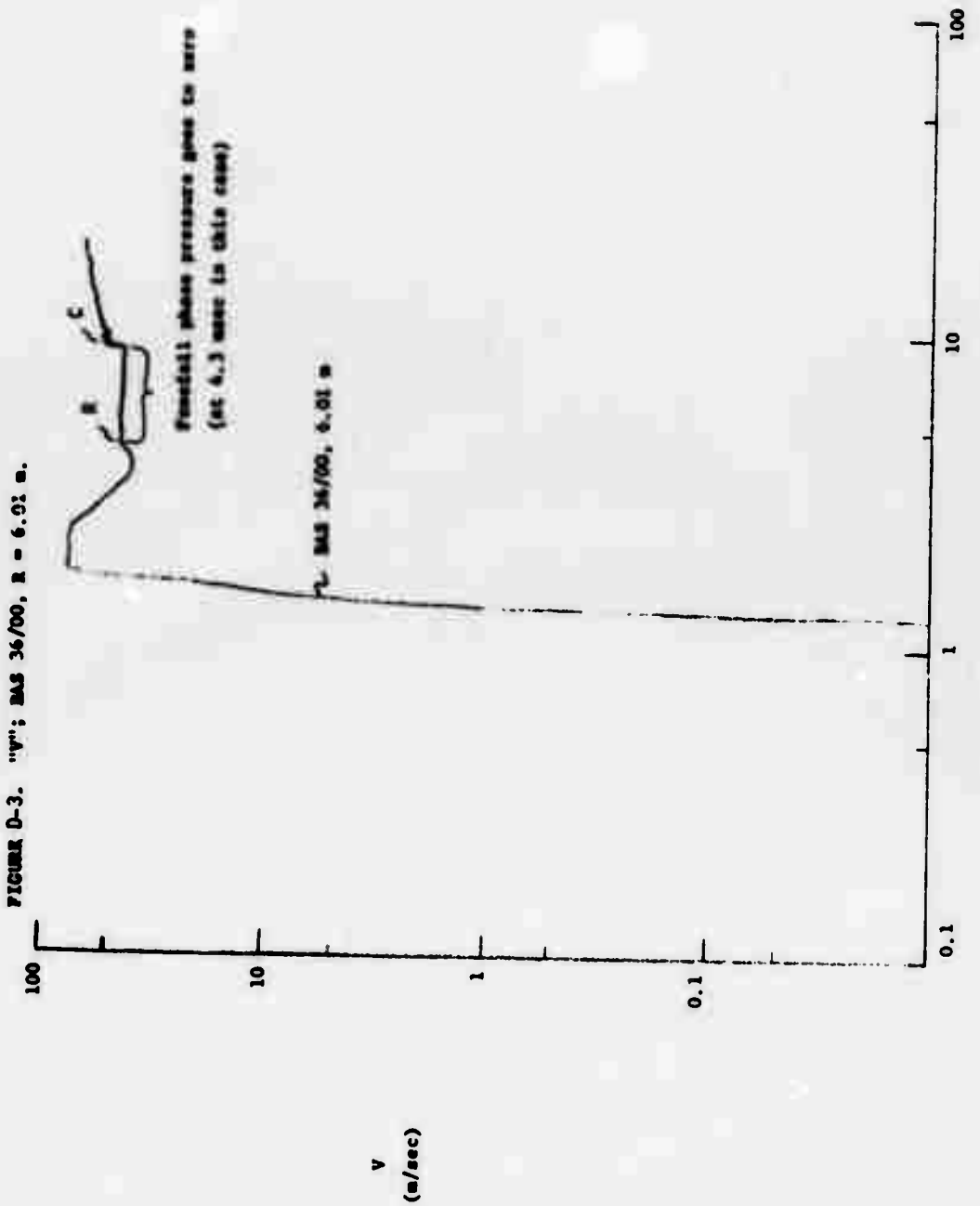

FIGURE D-3. "V"; BAS 36/00, R = 6.01 m.

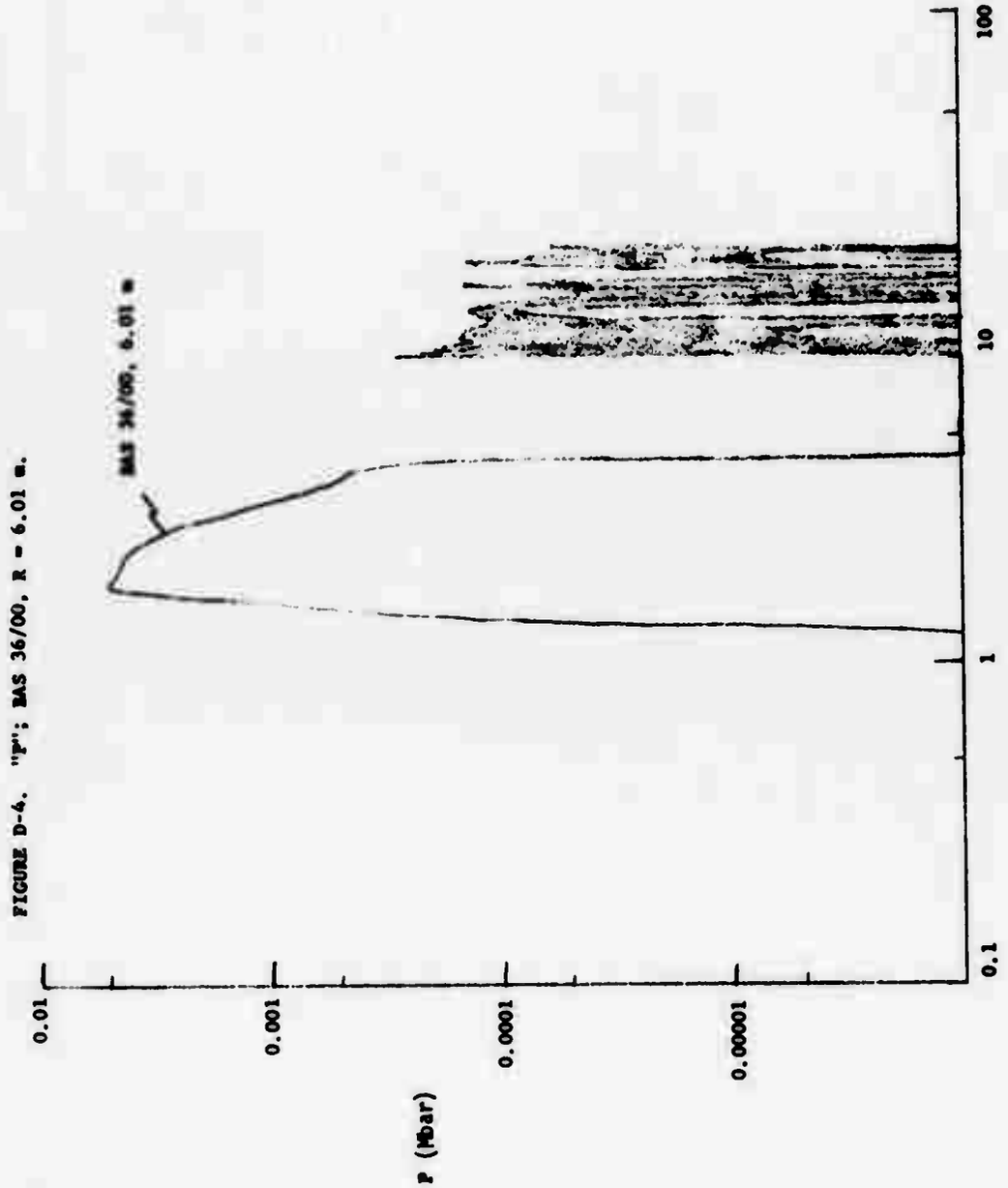

FIGURE D-4. "P"; BAS 36/00, R = 6.01 m.

FIGURE D-5. "V"; BAS 36/00, R = 8.01 m.

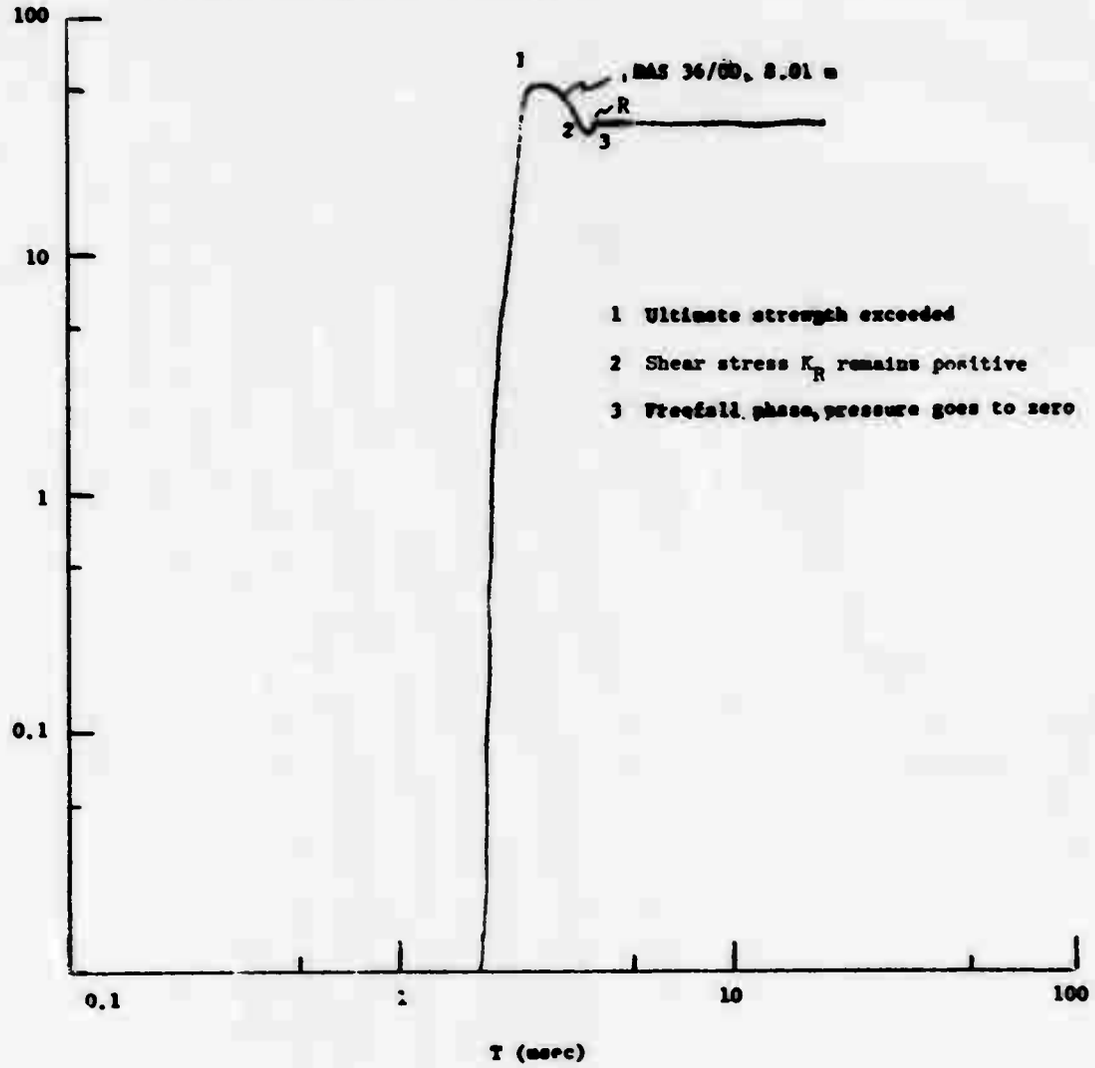

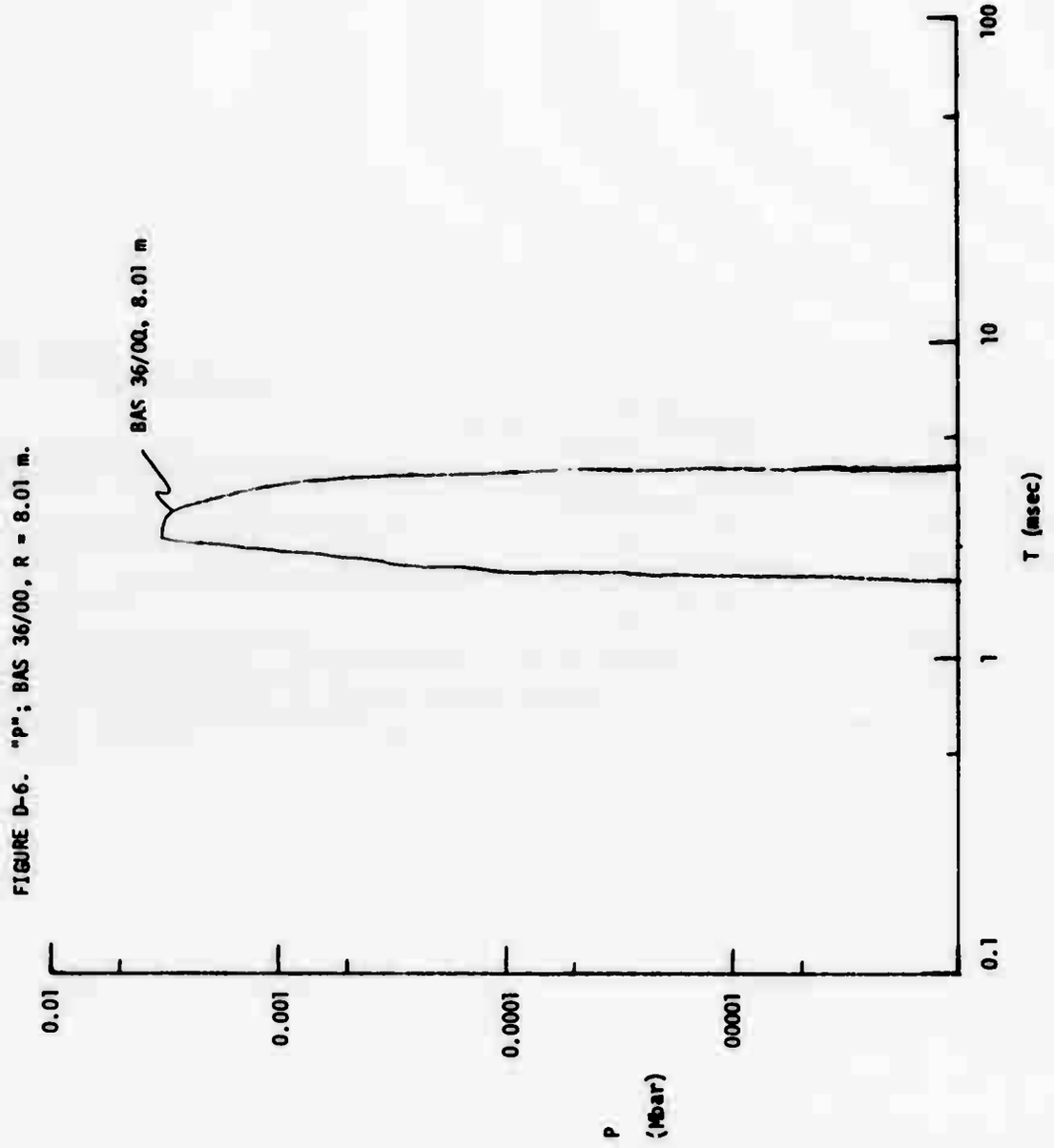

FIGURE D-6. "P"; BAS 36/00, R = 8.01 m.

FIGURE D-7. "V"; BAS 36/00, R = 9.49 m.

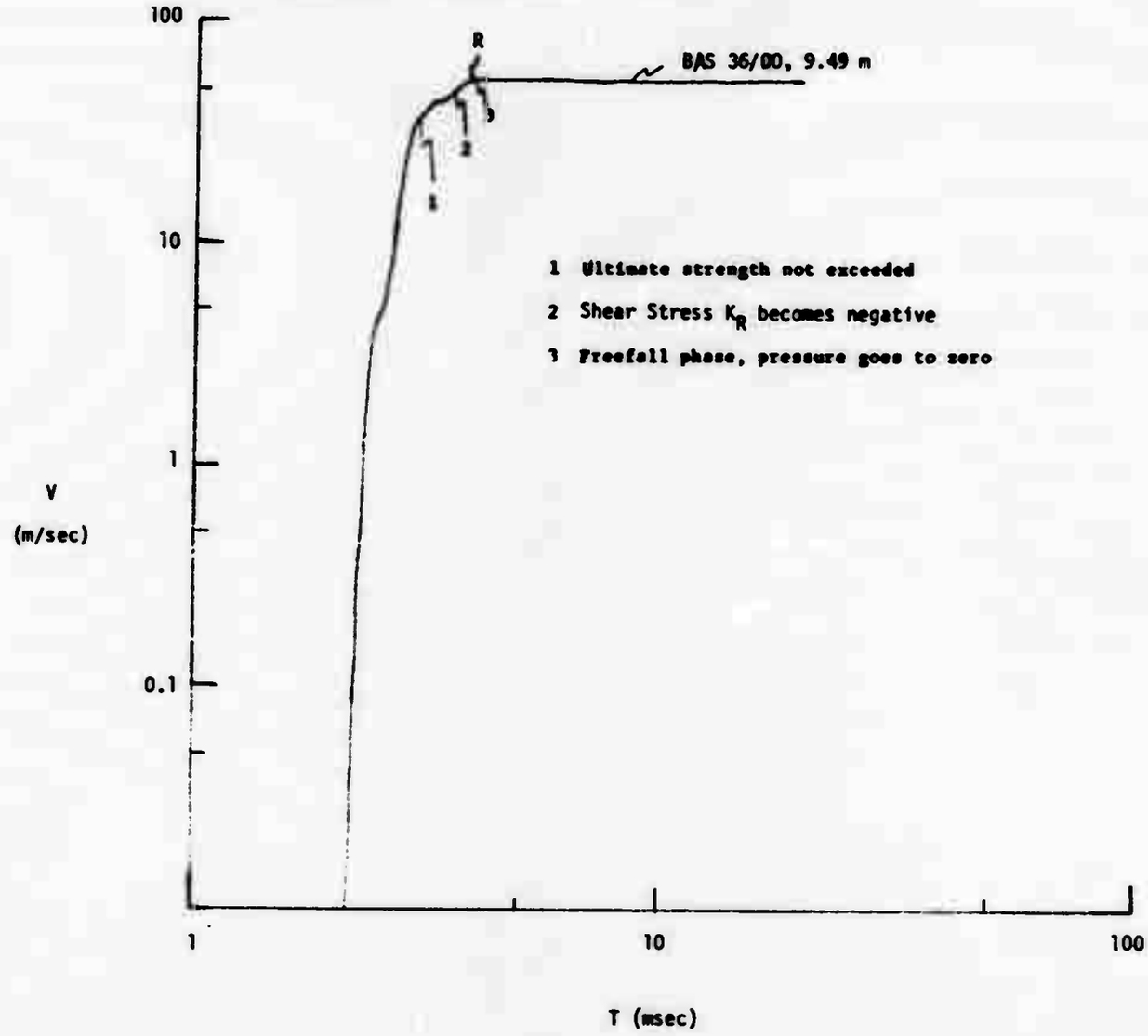

FIGURE D-8. "P"; BAS 36/00, R = 9.49 m.

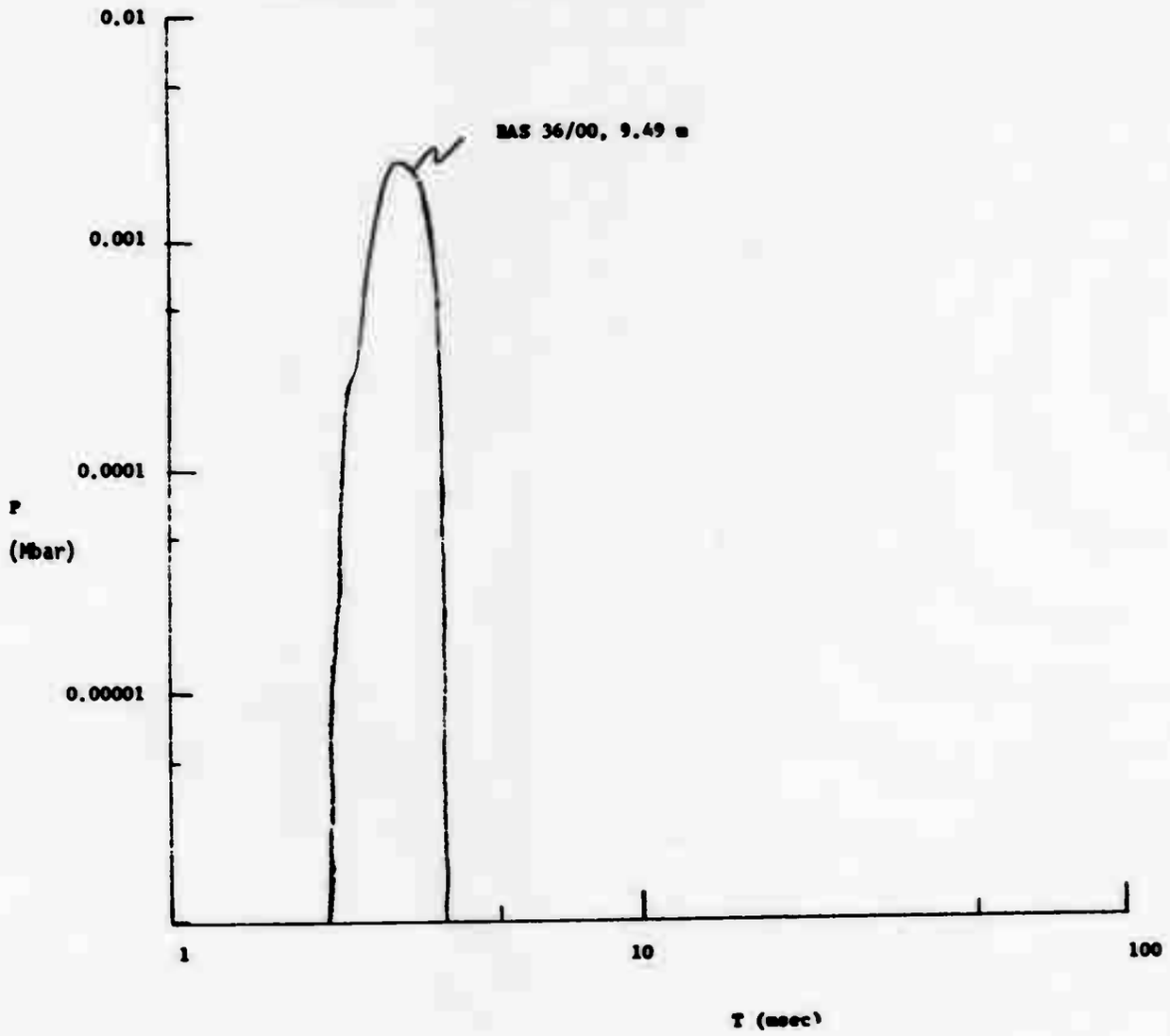

FIGURE D-9. "V": BAS 36/00, R = 10.6 m.

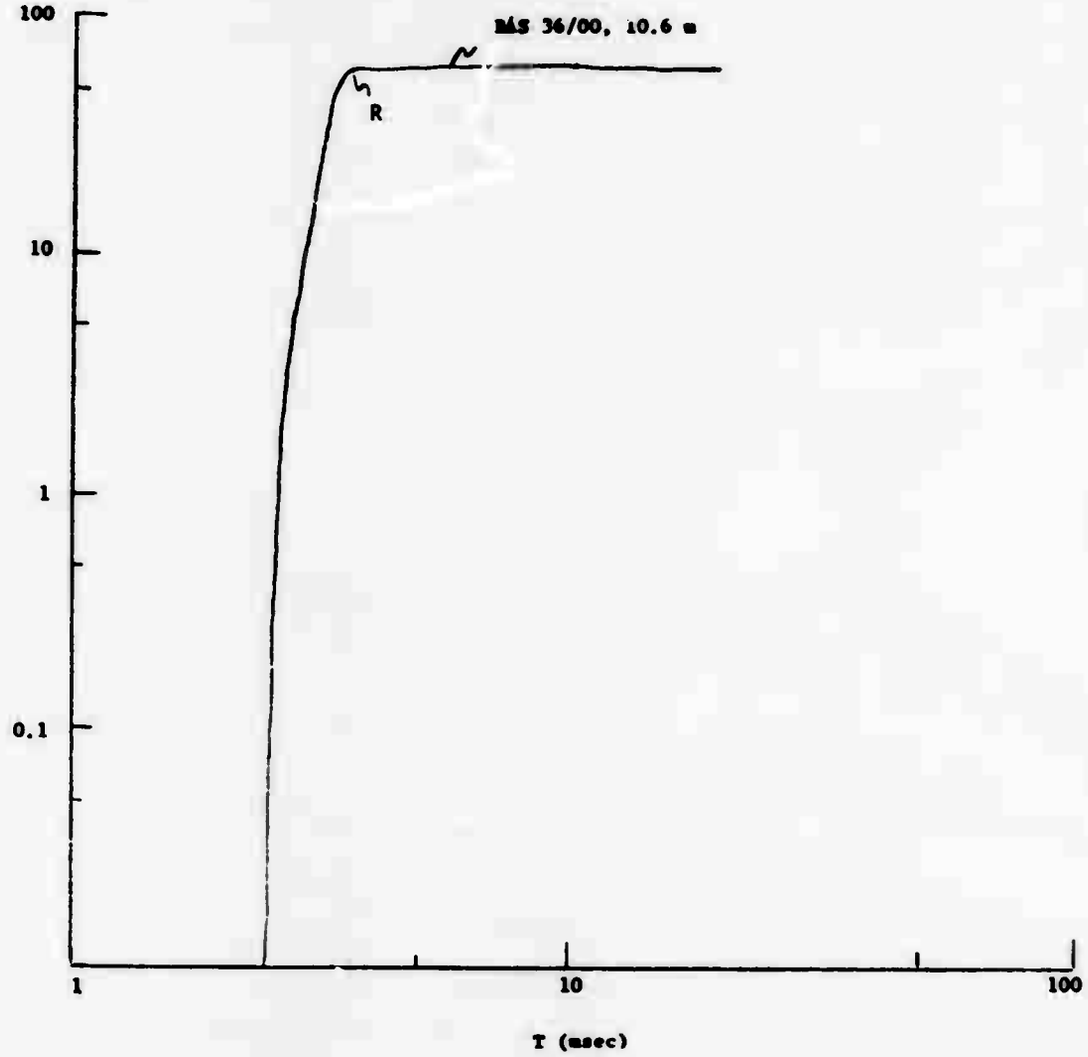

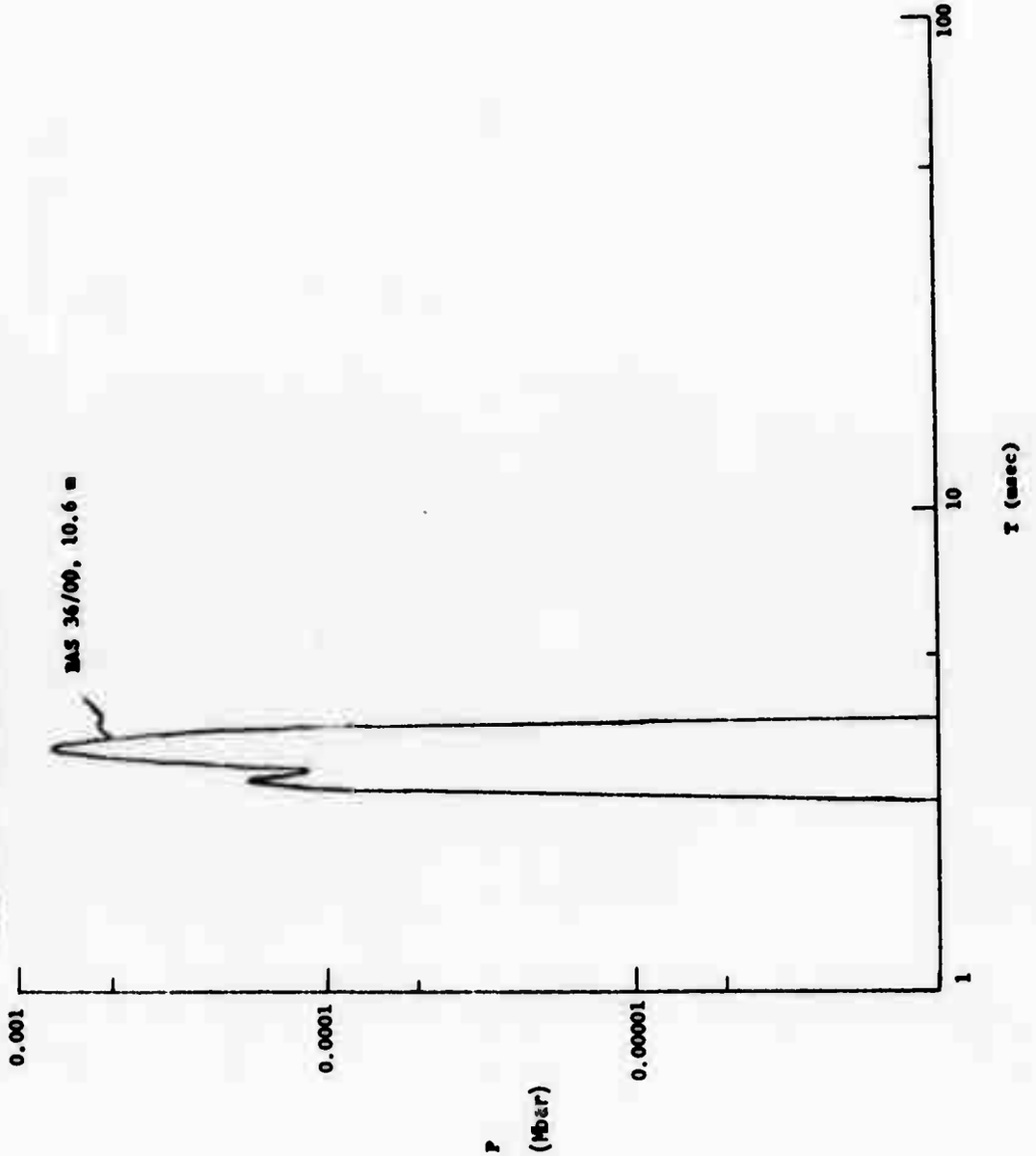

FIGURE D-10. "p": BAS 36/00, R = 10.6 m.

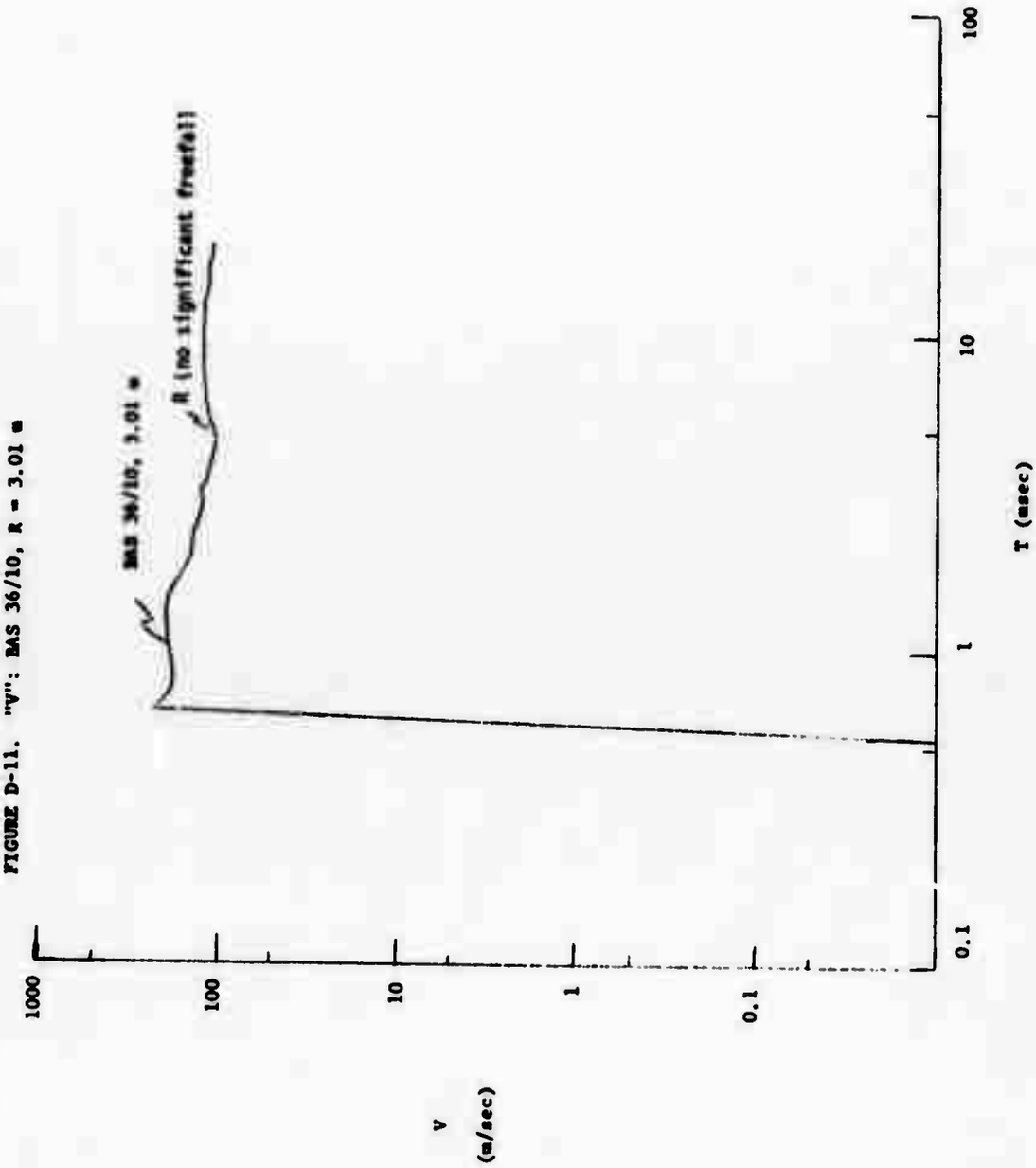

FIGURE D-11. "v": BAS 36/10, R = 3.01 m

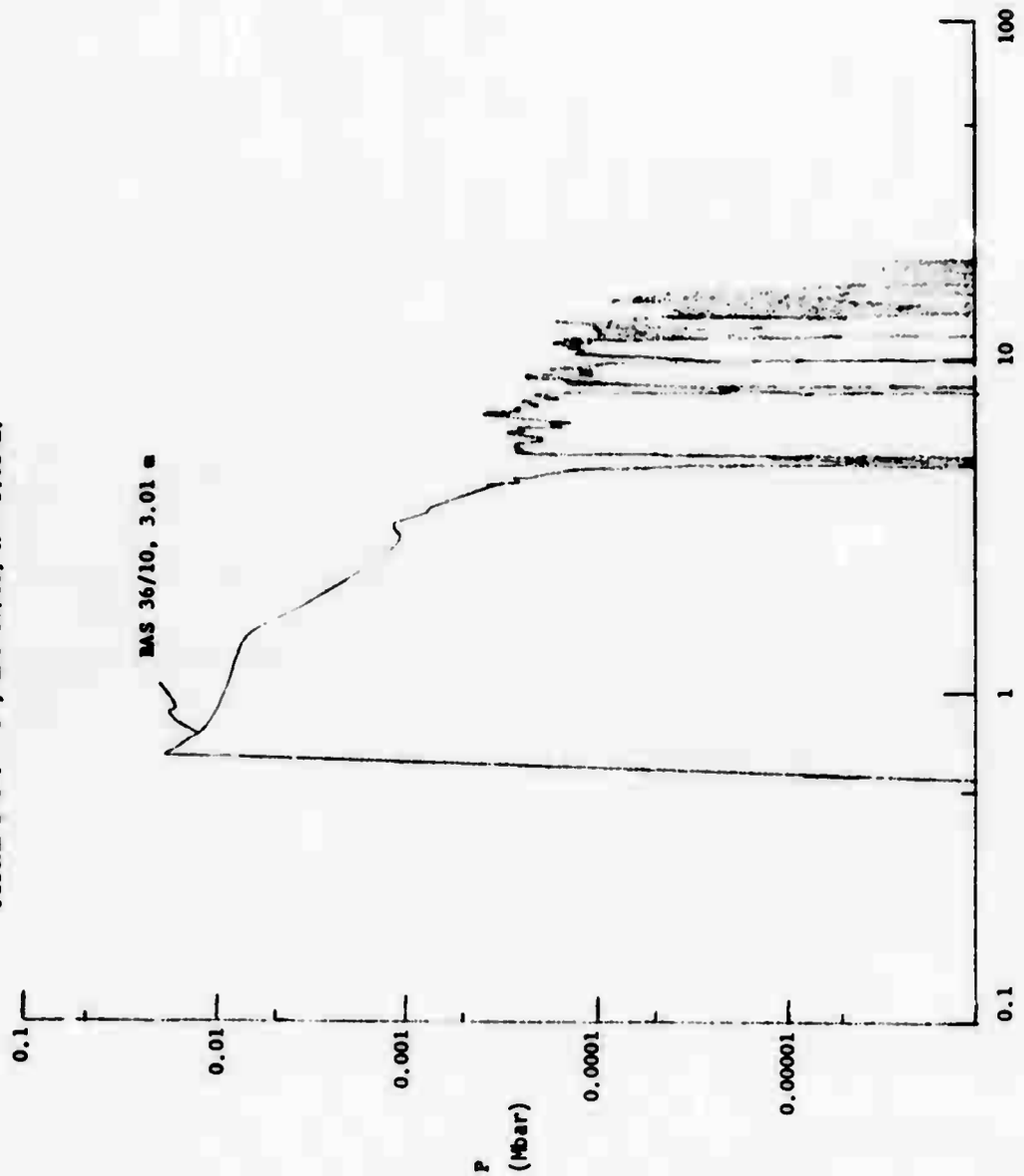

FIGURE D-12. "P"; BAS 36/10, R = 3.01 m.

FIGURE D-13. "V"; BAS 36/10, R = 6.01 m.

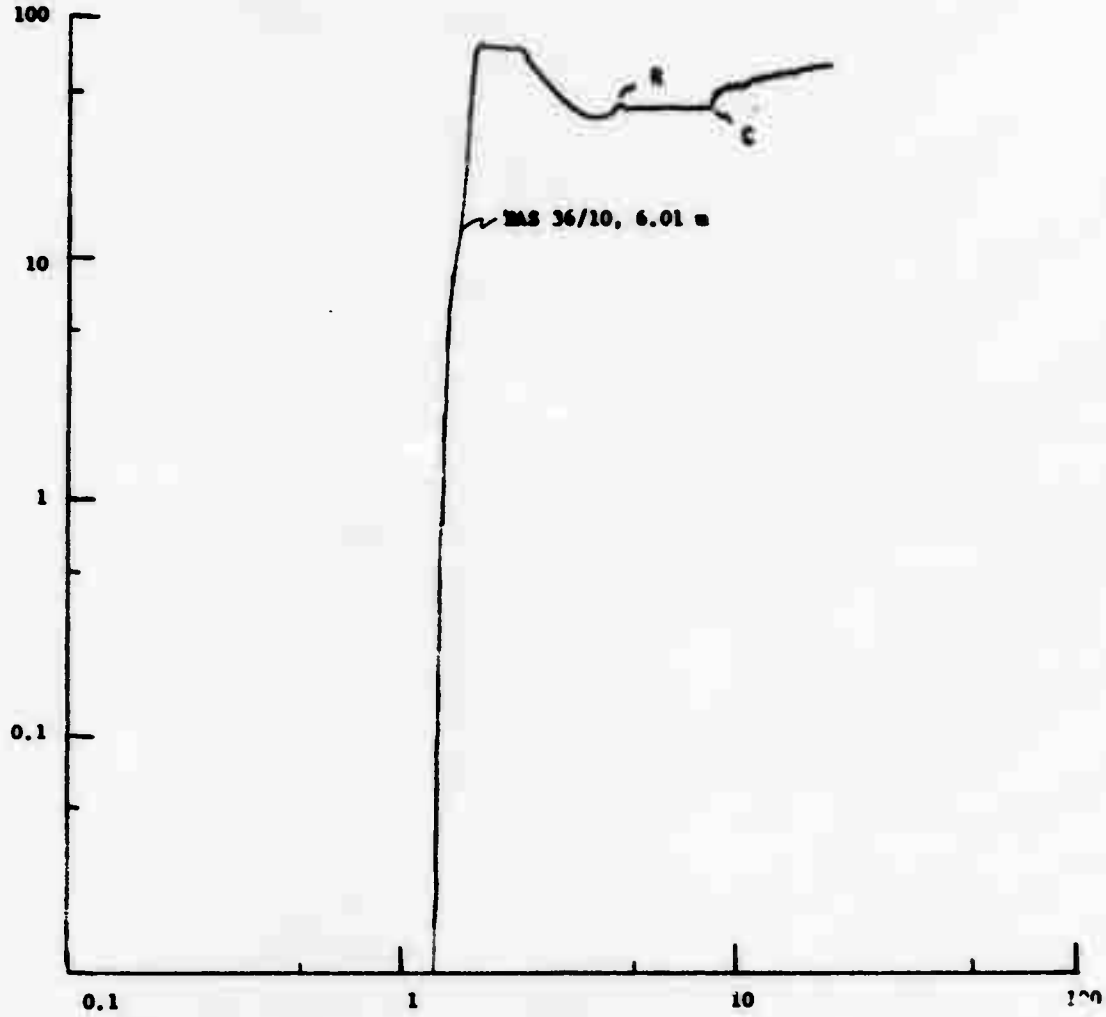

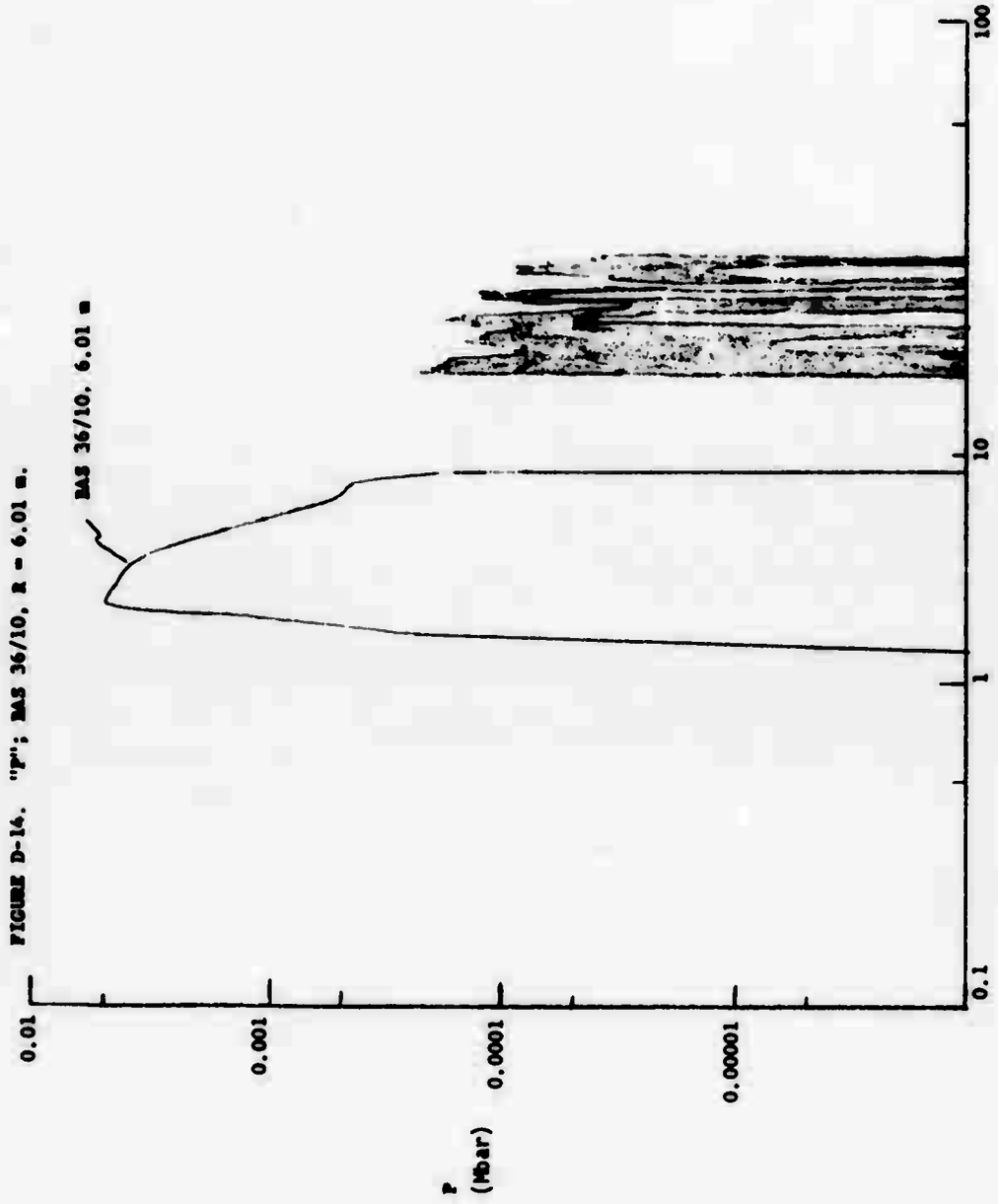

FIGURE D-14. "P"; BAS 36/10, R = 6.01 m.

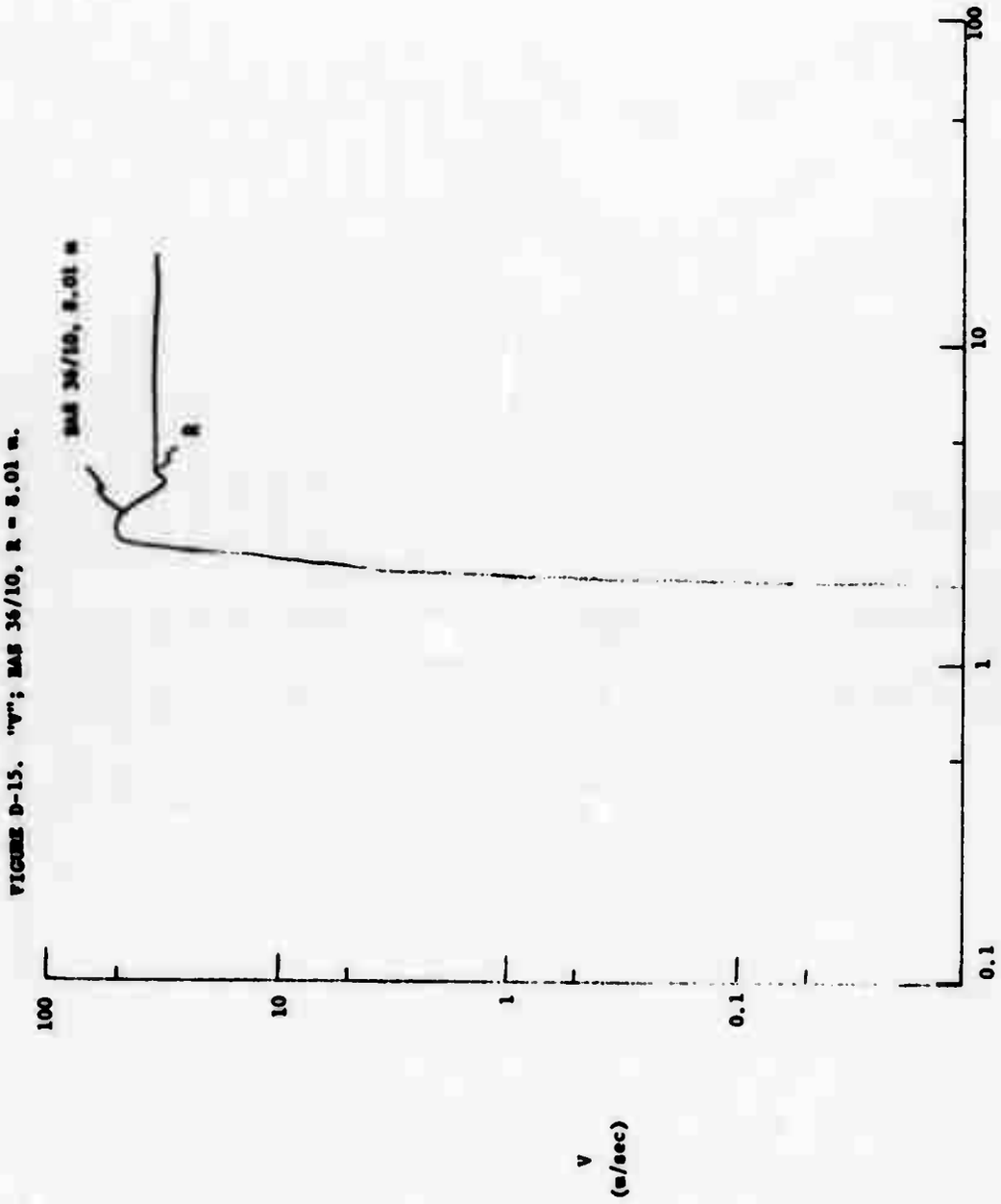

FIGURE D-15. "V"; BAS 36/10, R = 0.01 m.

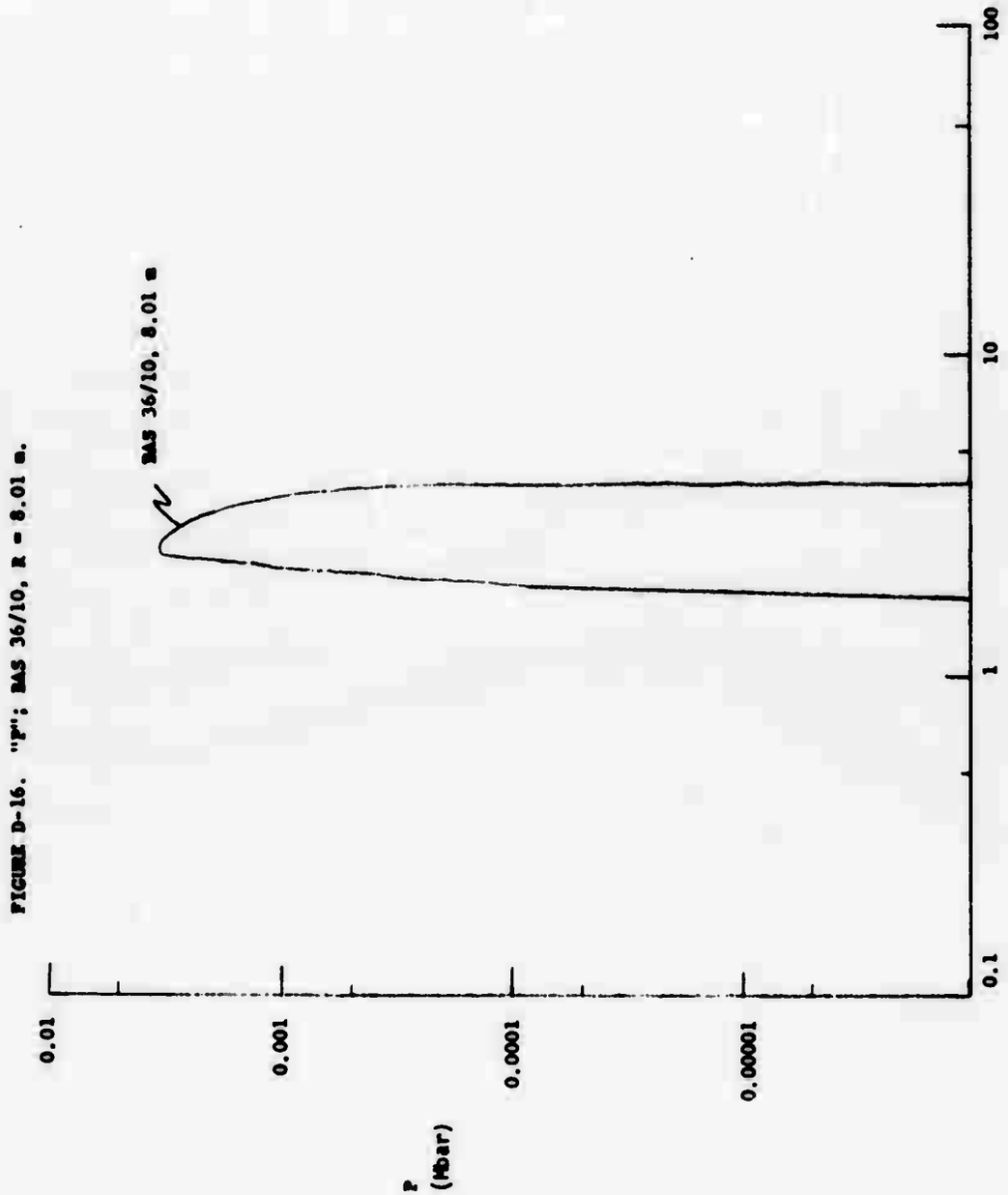

FIGURE D-16. "P"; BAS 36/10, R = 8.01 m.

FIGURE D-17. "V"; BAS 36/10, R = 9.49 m.

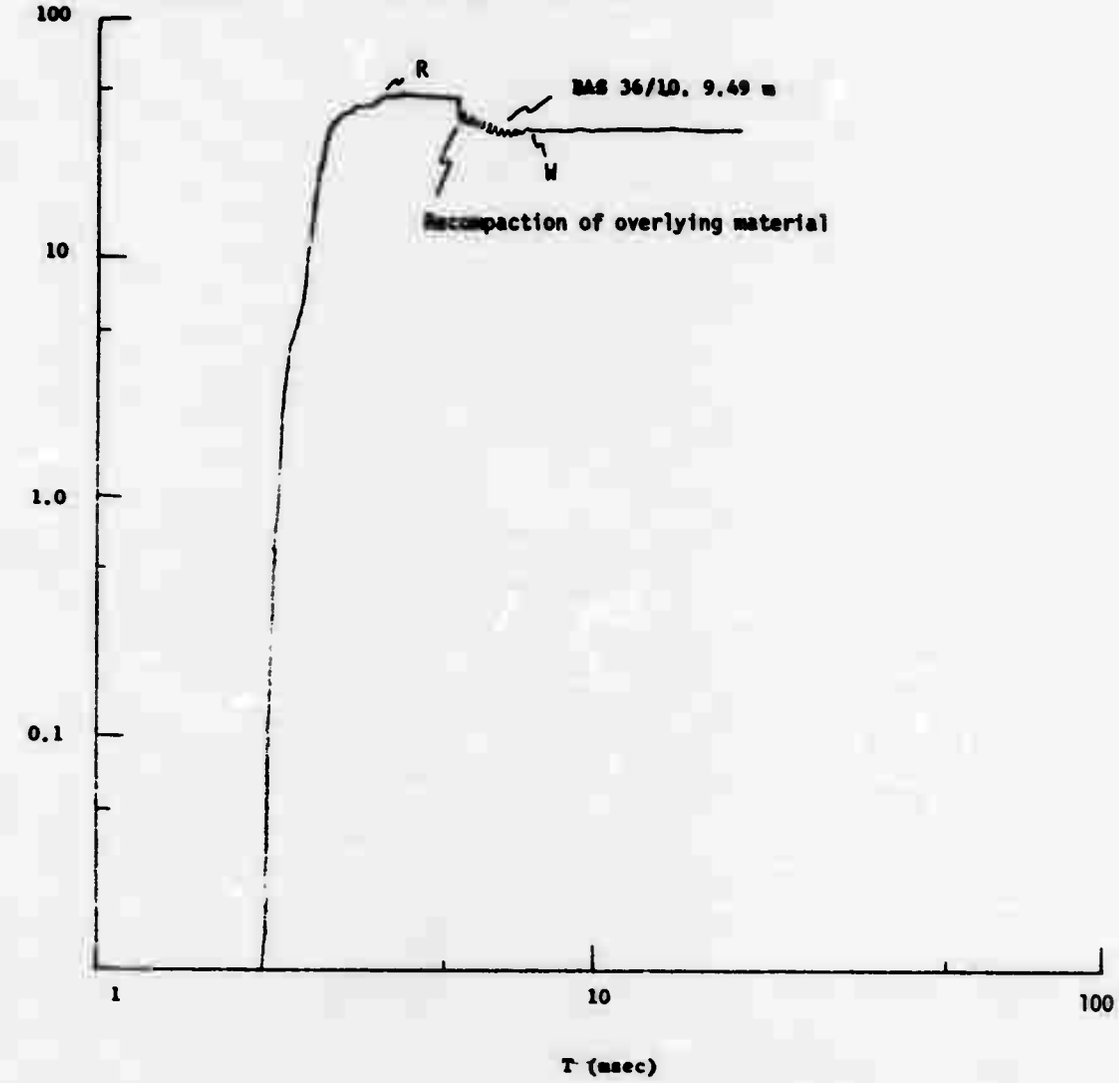

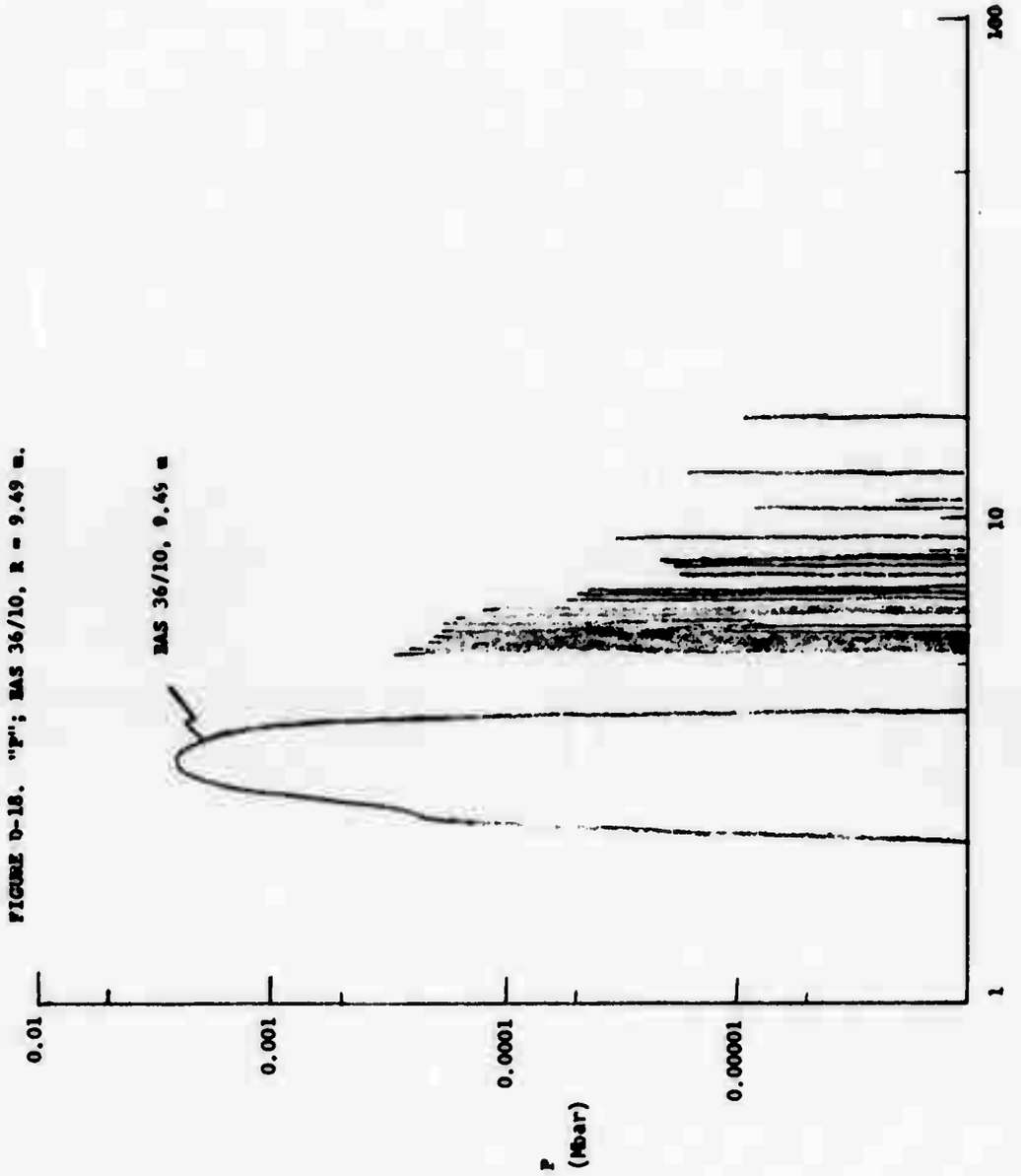

FIGURE D-18. "P"; BAS 36/10, R = 9.49 m.

FIGURE D-19. "V"; BAS 36/10, R = 10.6 m.

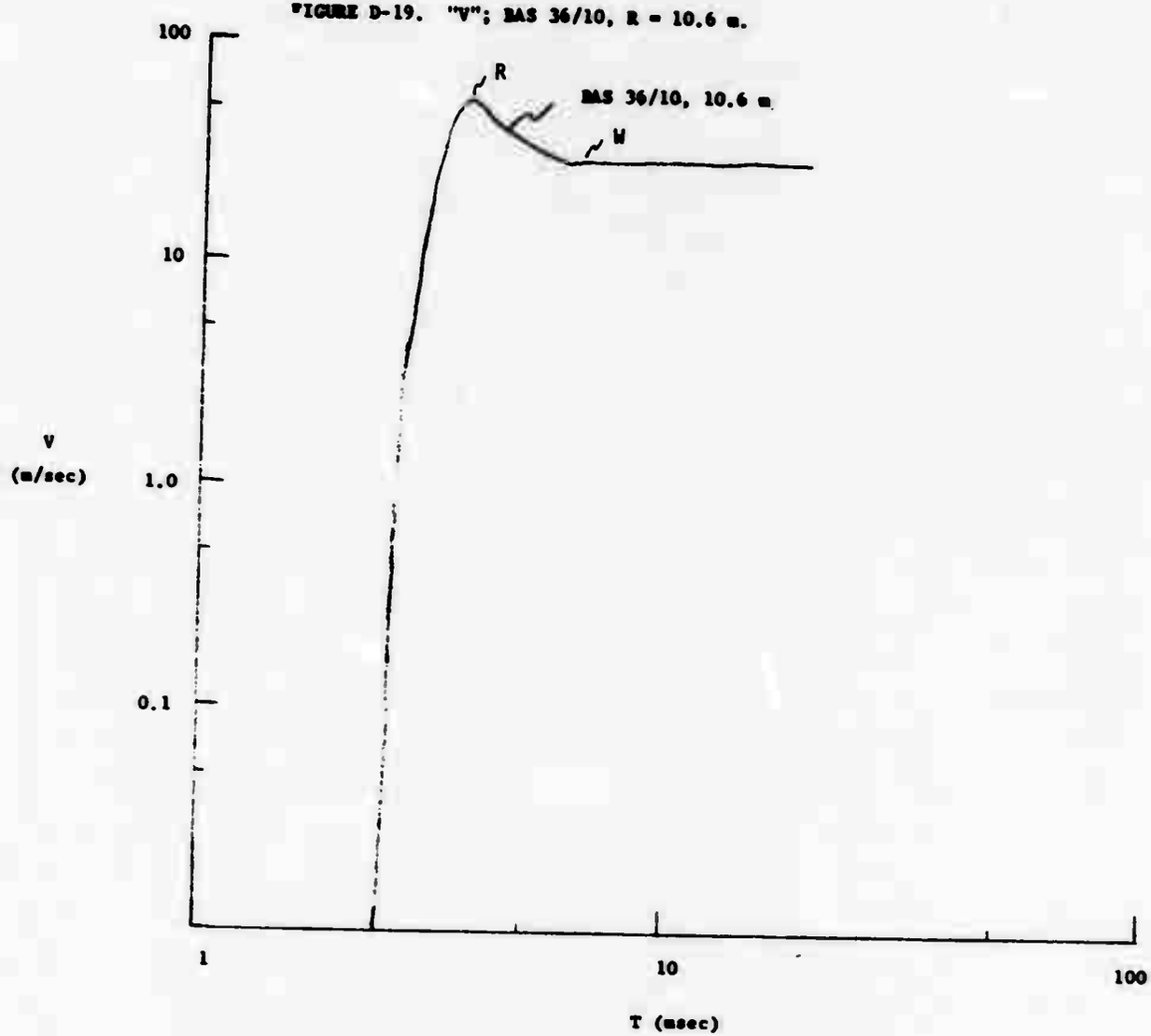

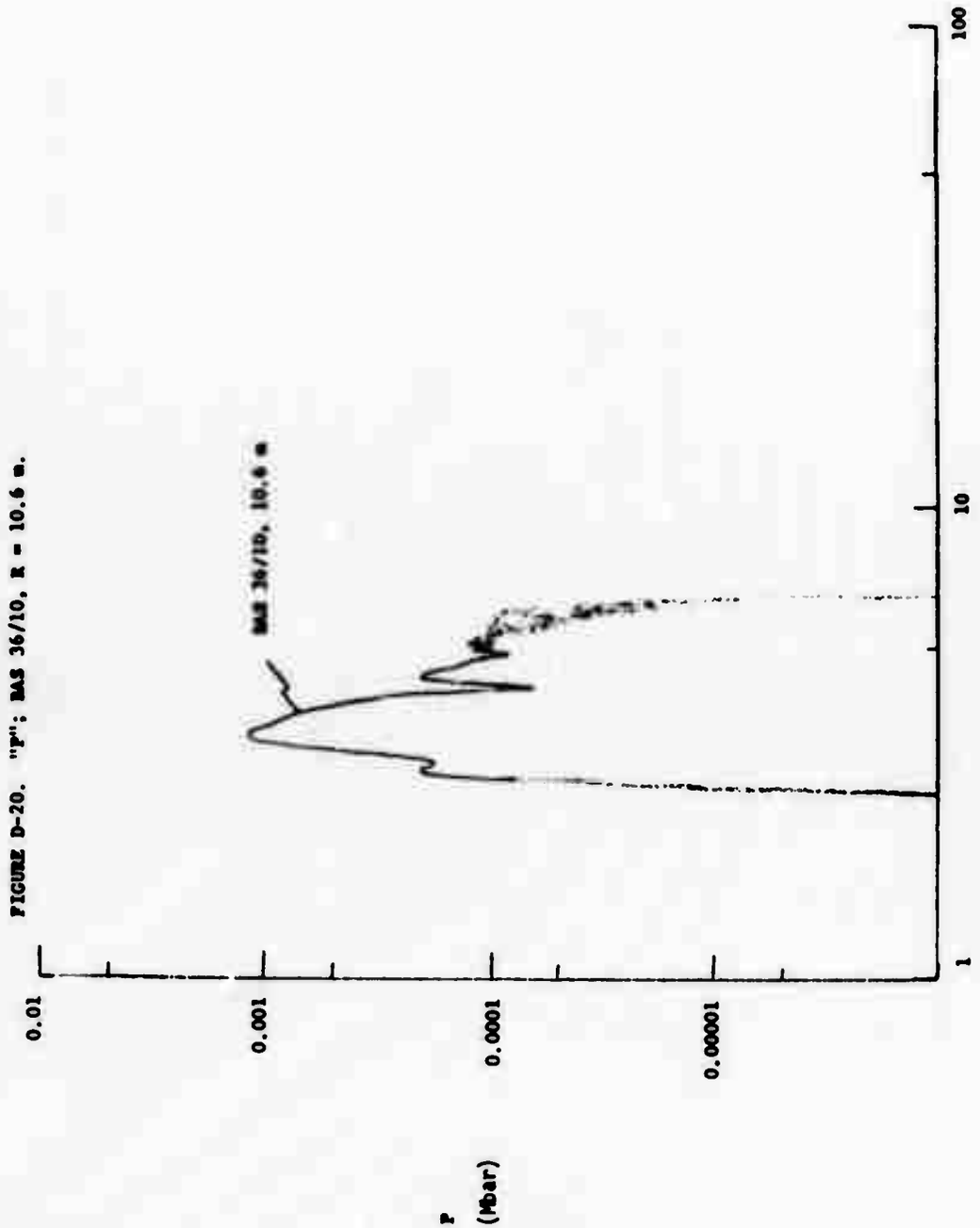

FIGURE D-20. "P"; BAS 36/10, R = 10.6 m.

FIGURE D-21. "V"; BAS 36/10, R = 10.89 m.

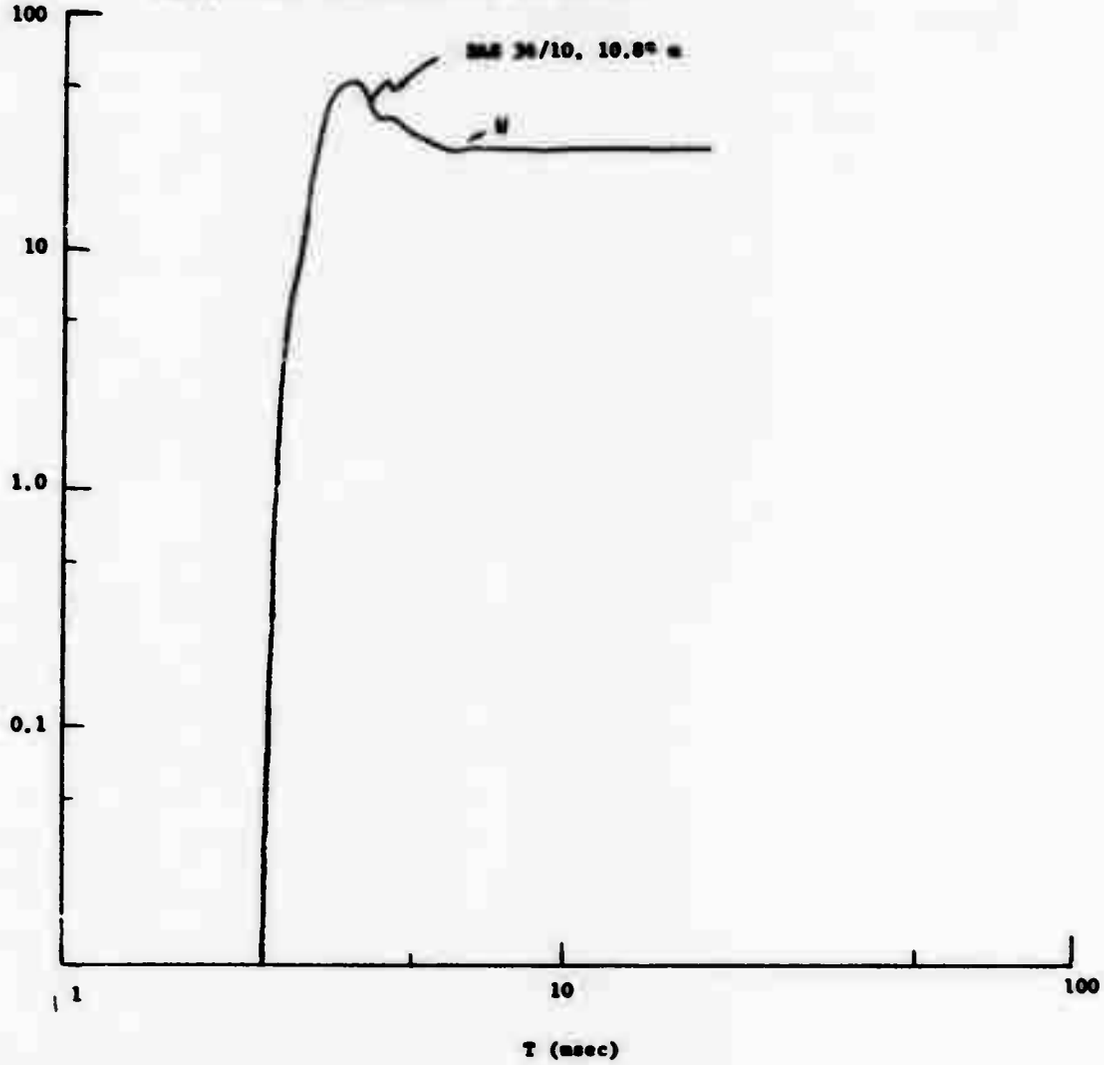

FIGURE D-22. "V"; BAS 36/10, R = 10.93 m.

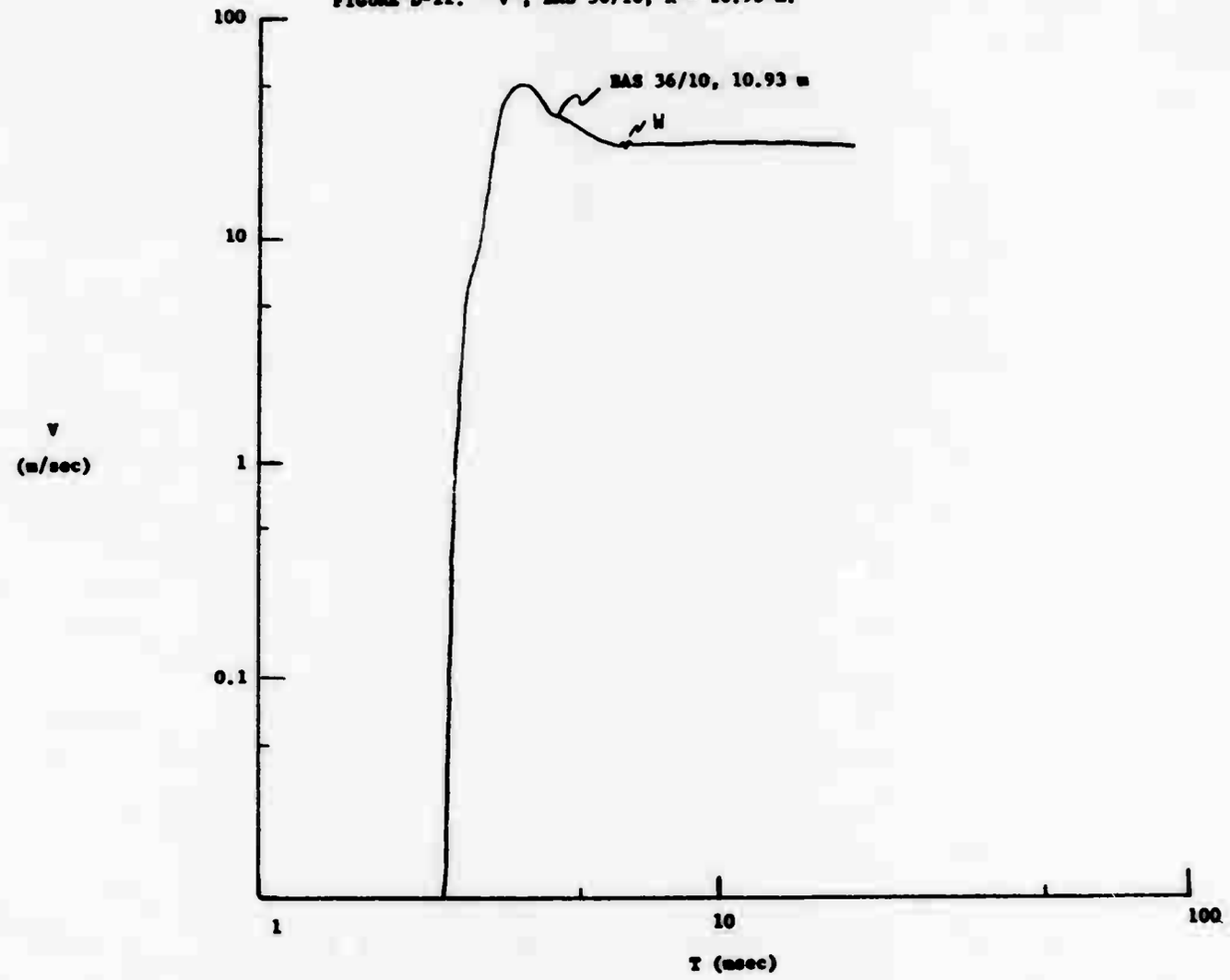

FIGURE D-23. "V"; BAS 36/36, R = 3.01 m.

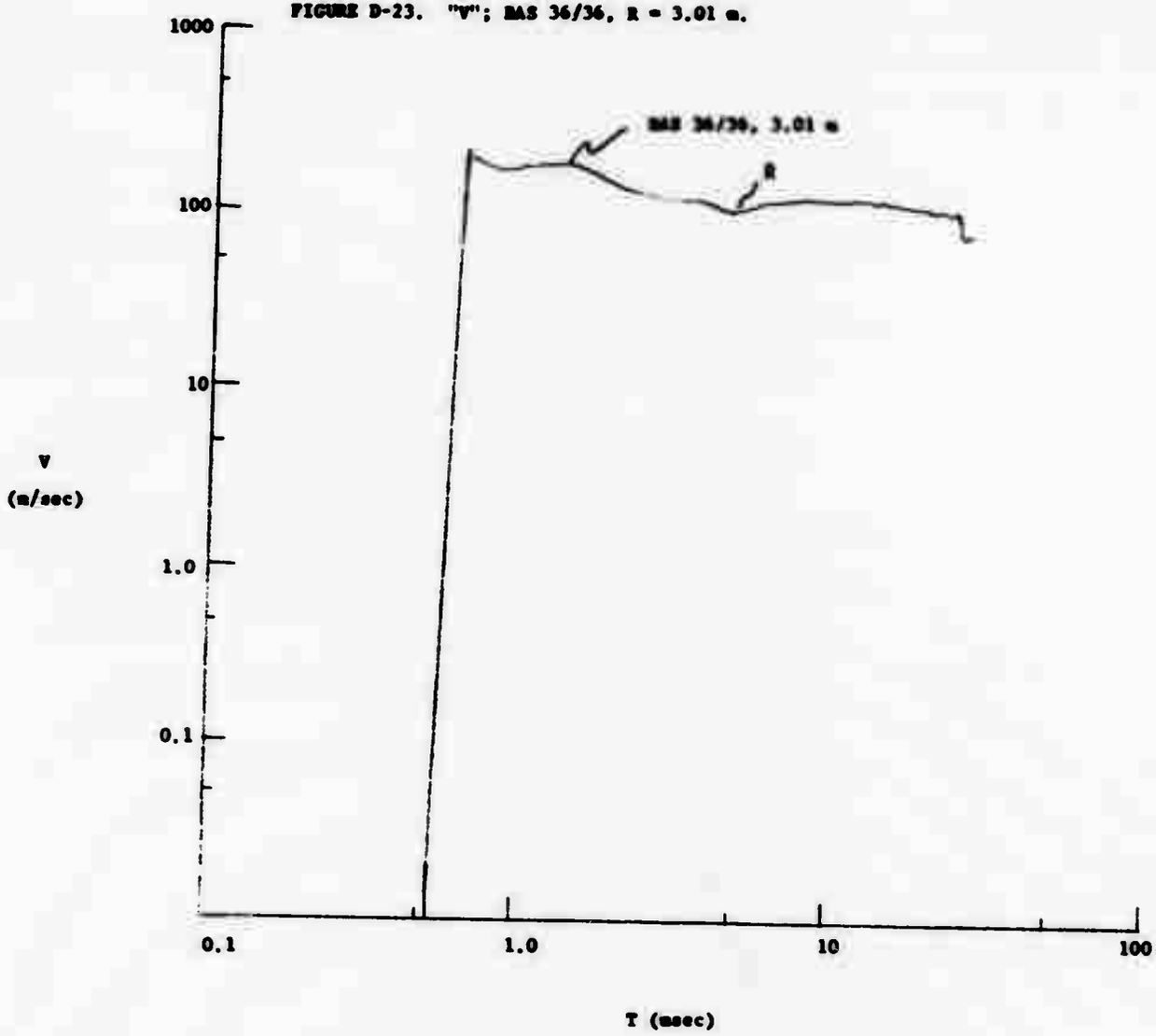

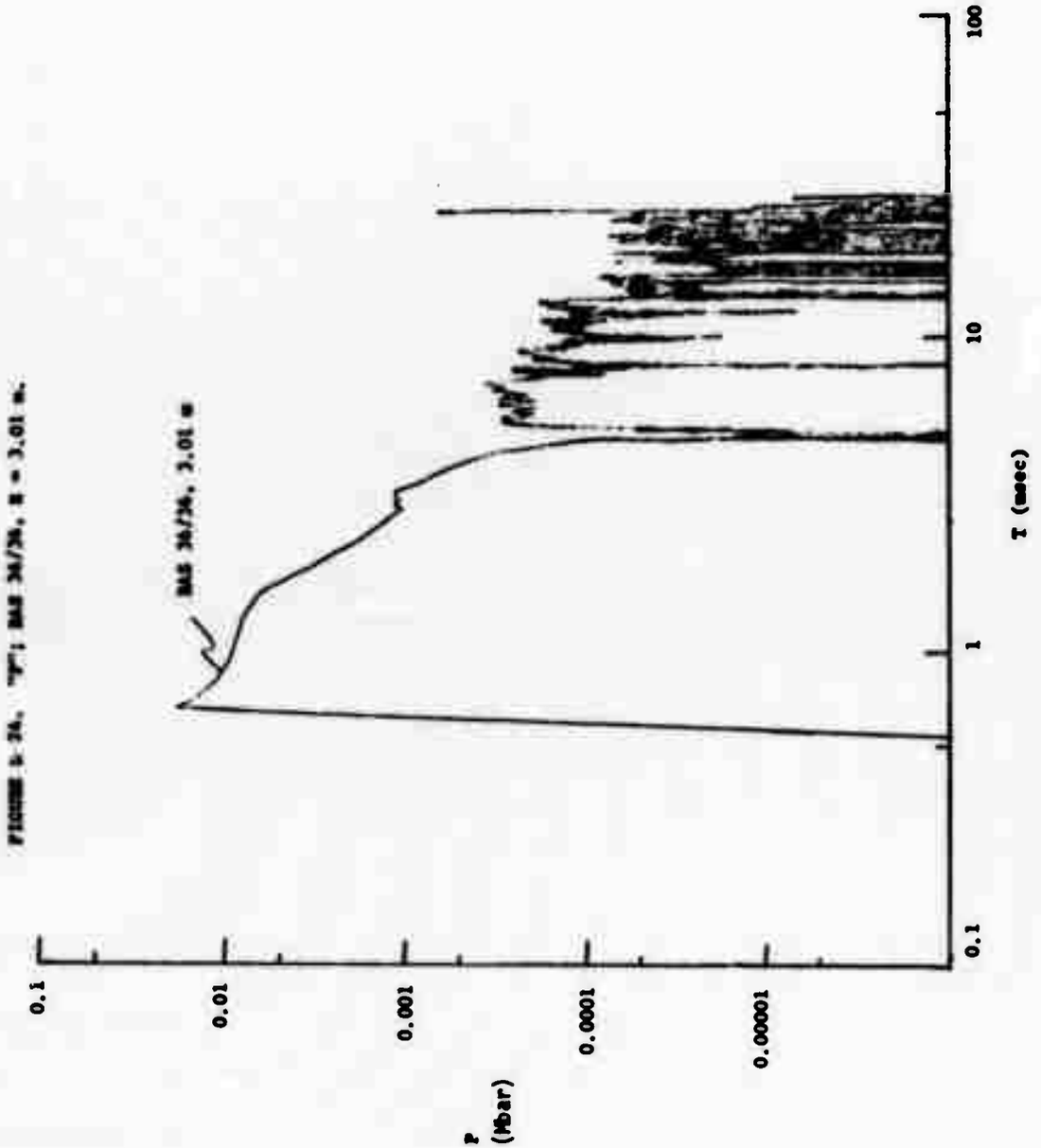
0.1
0.01
0.001
0.0001
0.00001
P
(Mbar)
0.1
1
10
100
τ (msec)

FIGURE D-25. "V"; BAS 36/36, R = 6.01 m.

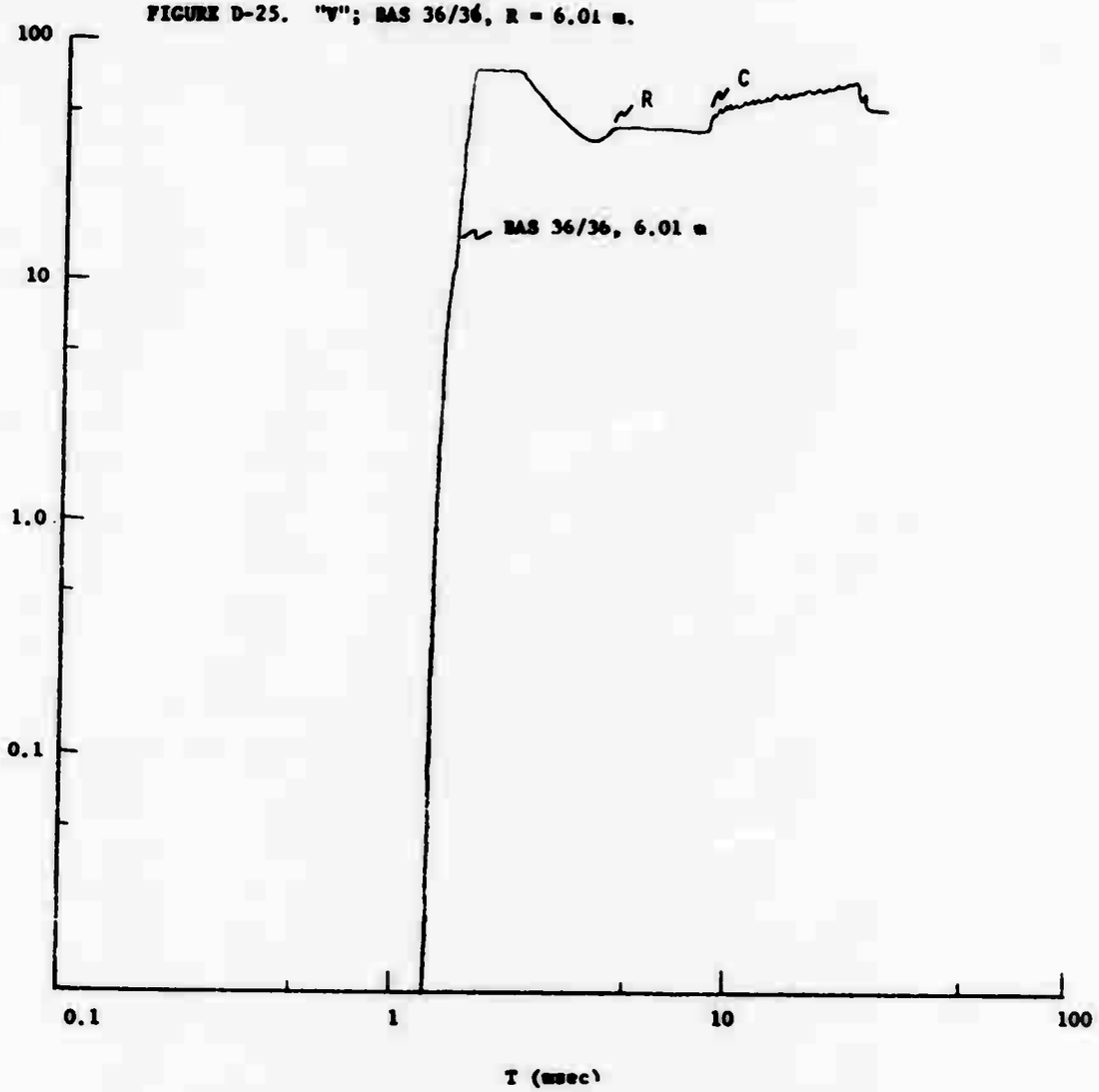

FIGURE D-26. "P"; BAS 36/36, R = 6.01 m.

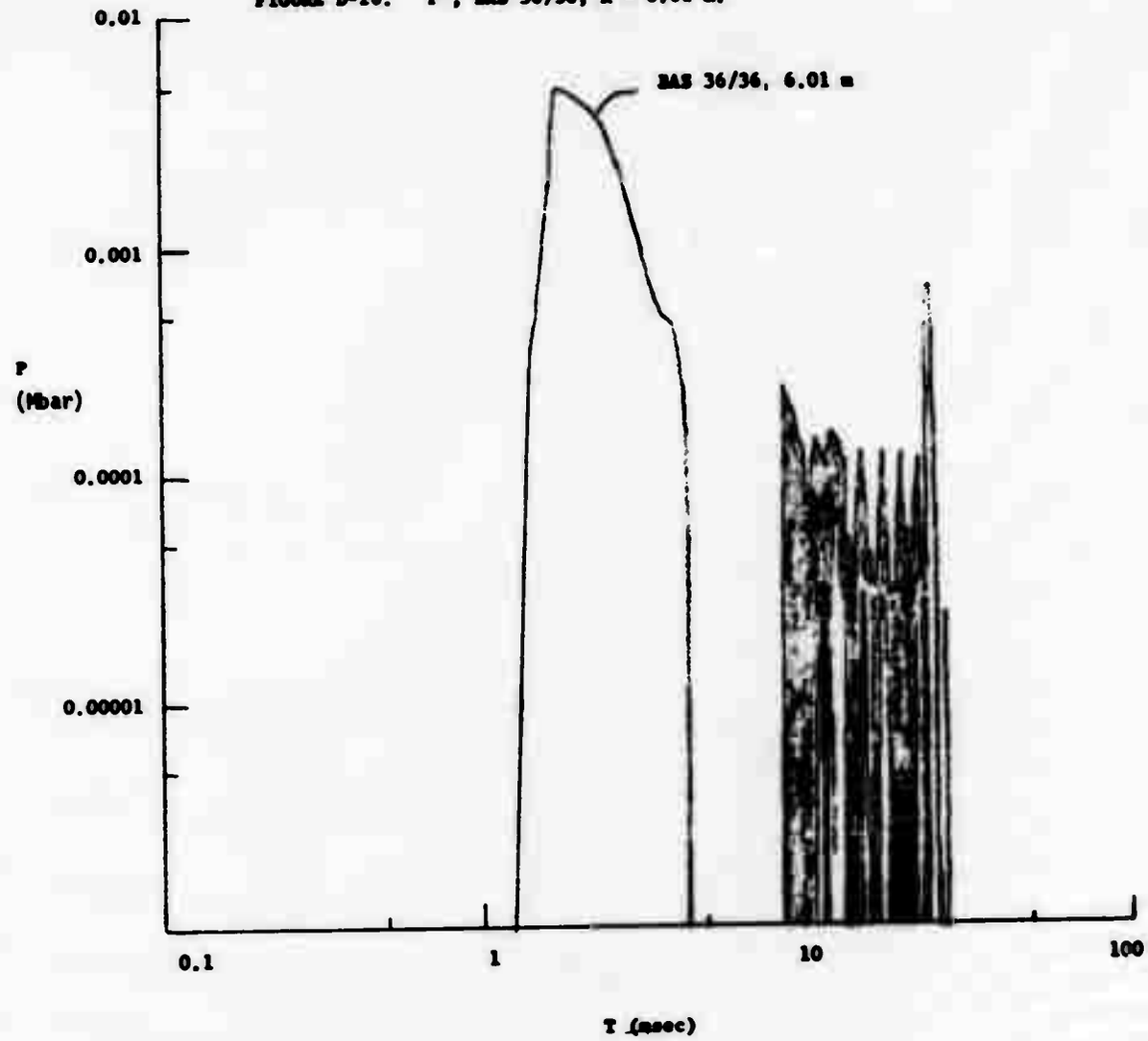

FIGURE D-27. "V"; BAS 36/36, R = 8.01 m.

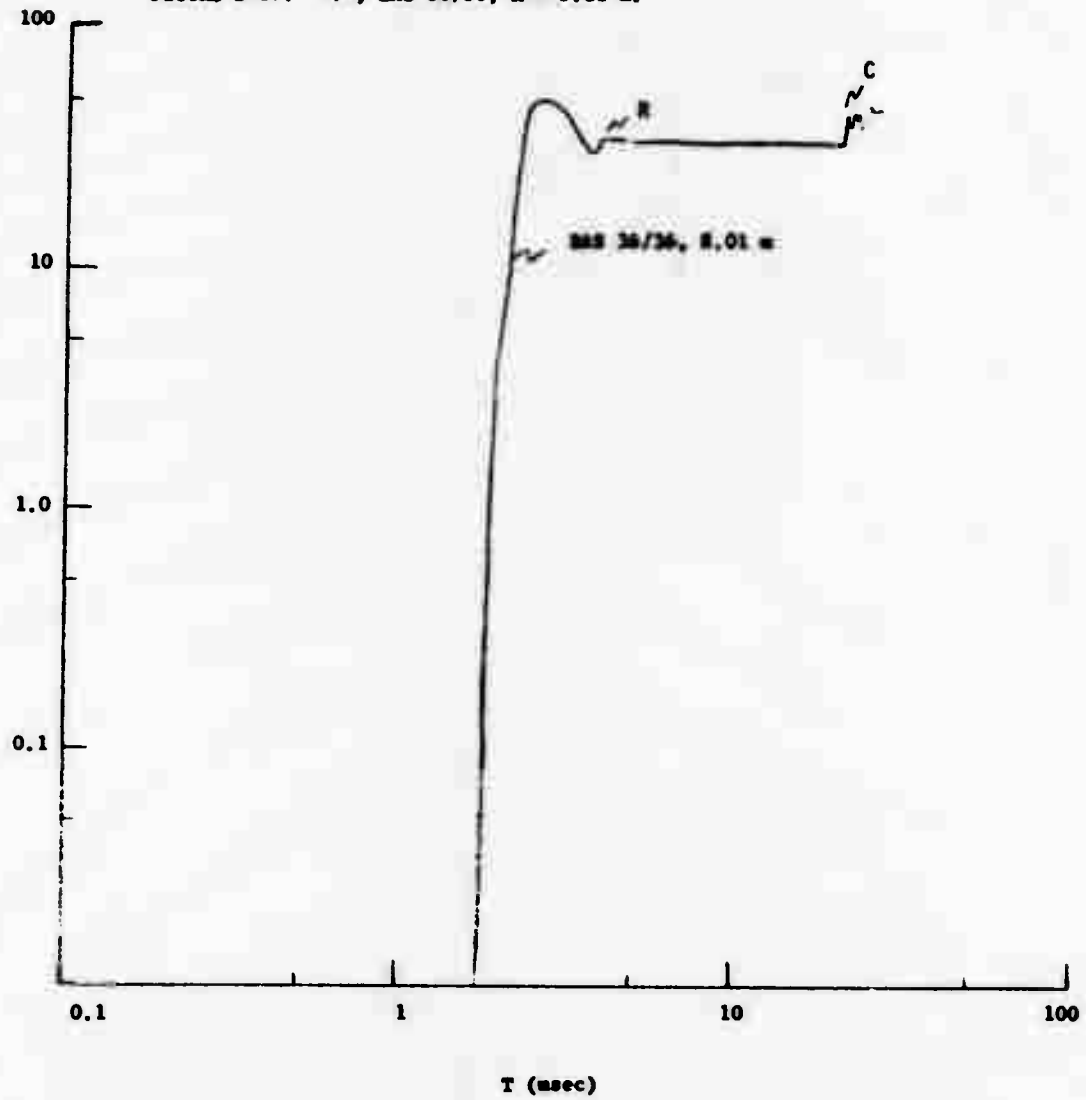

FIGURE D-28. "F"; BAS 36/36, R = 8.01 m.

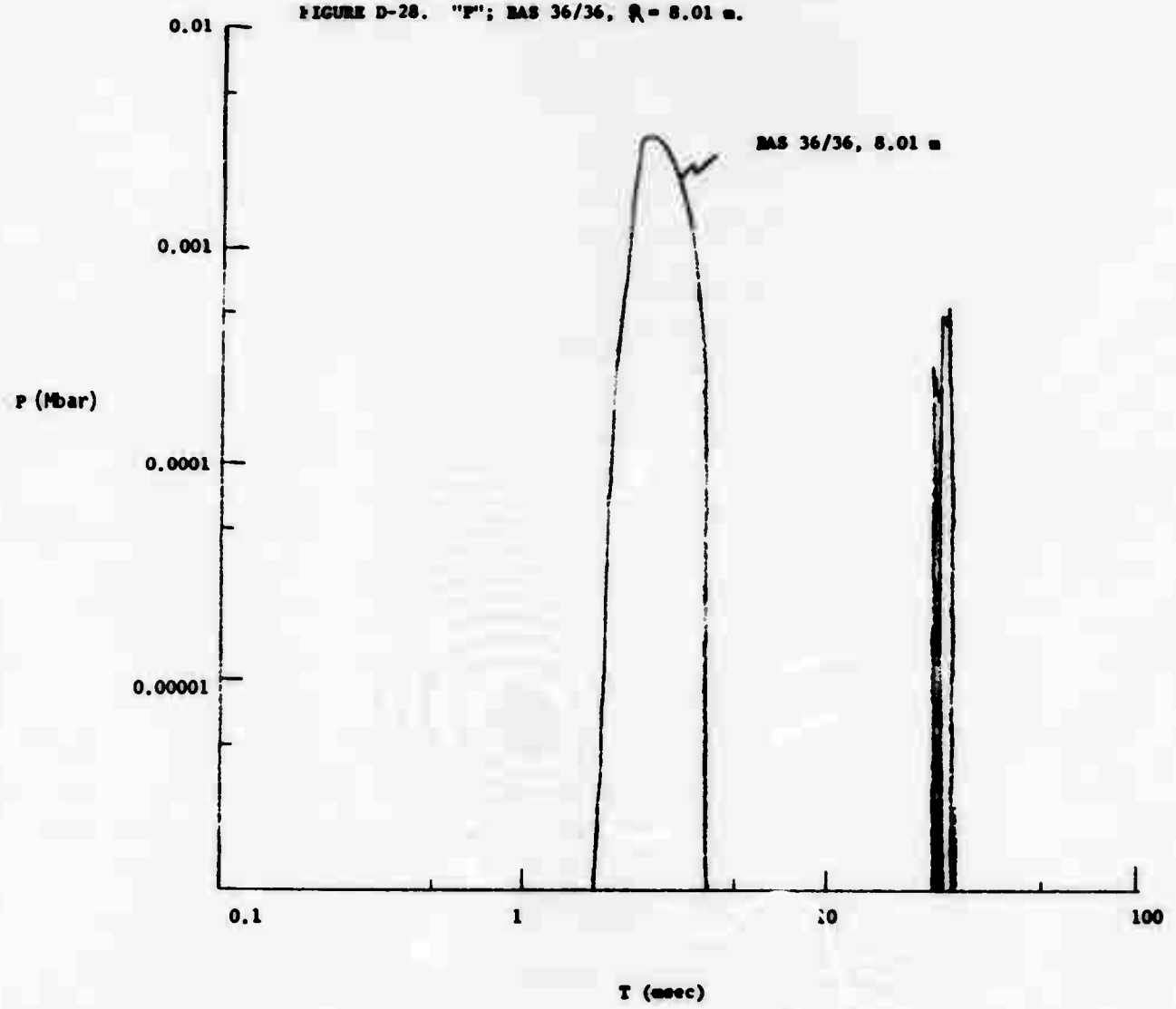

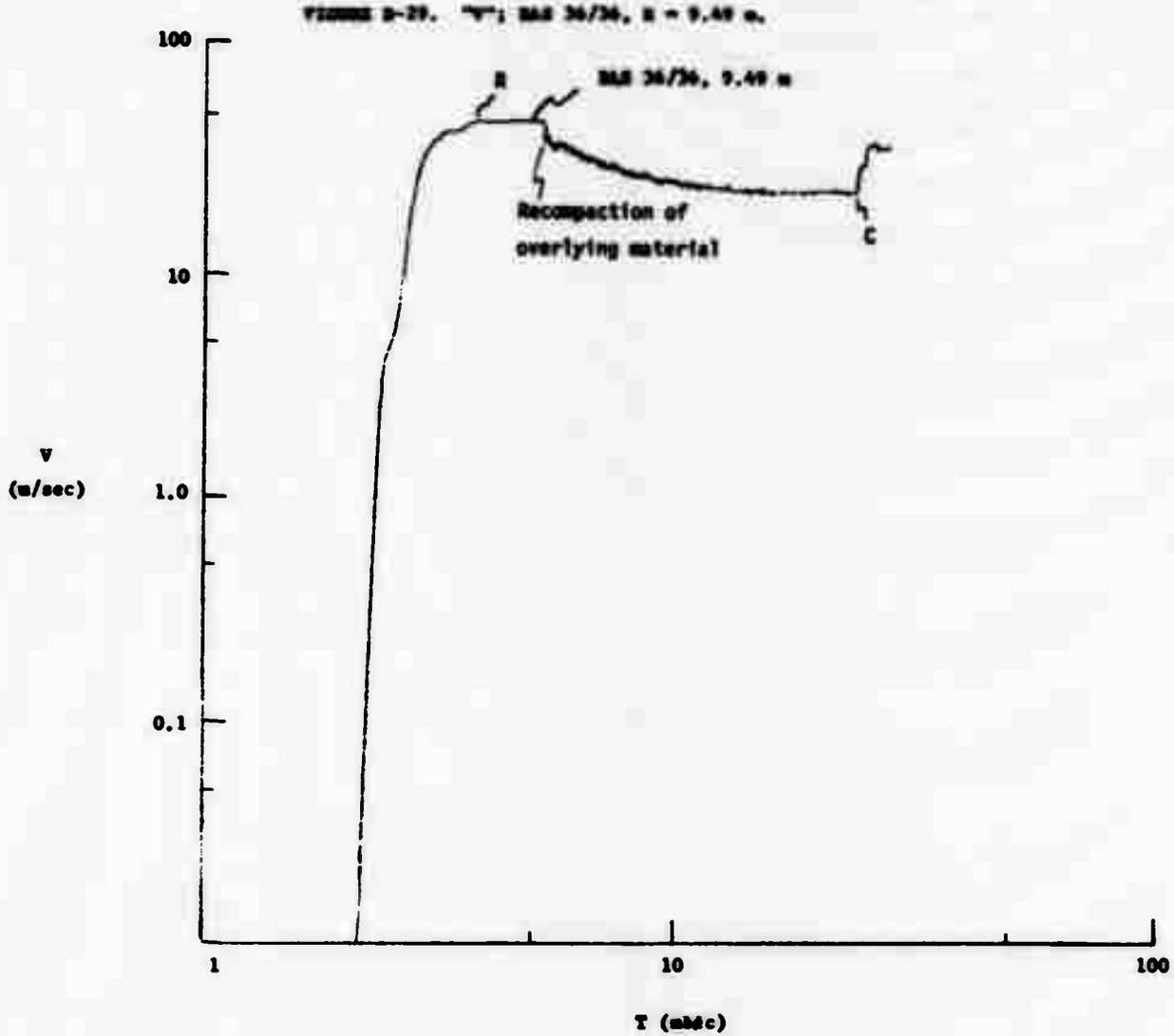
100
10
1.0
0.1
V
(m/sec)
B
B&B 36/36, 9.49 m
Recompaction of
overlying material
C
1
10
100
T (msec)

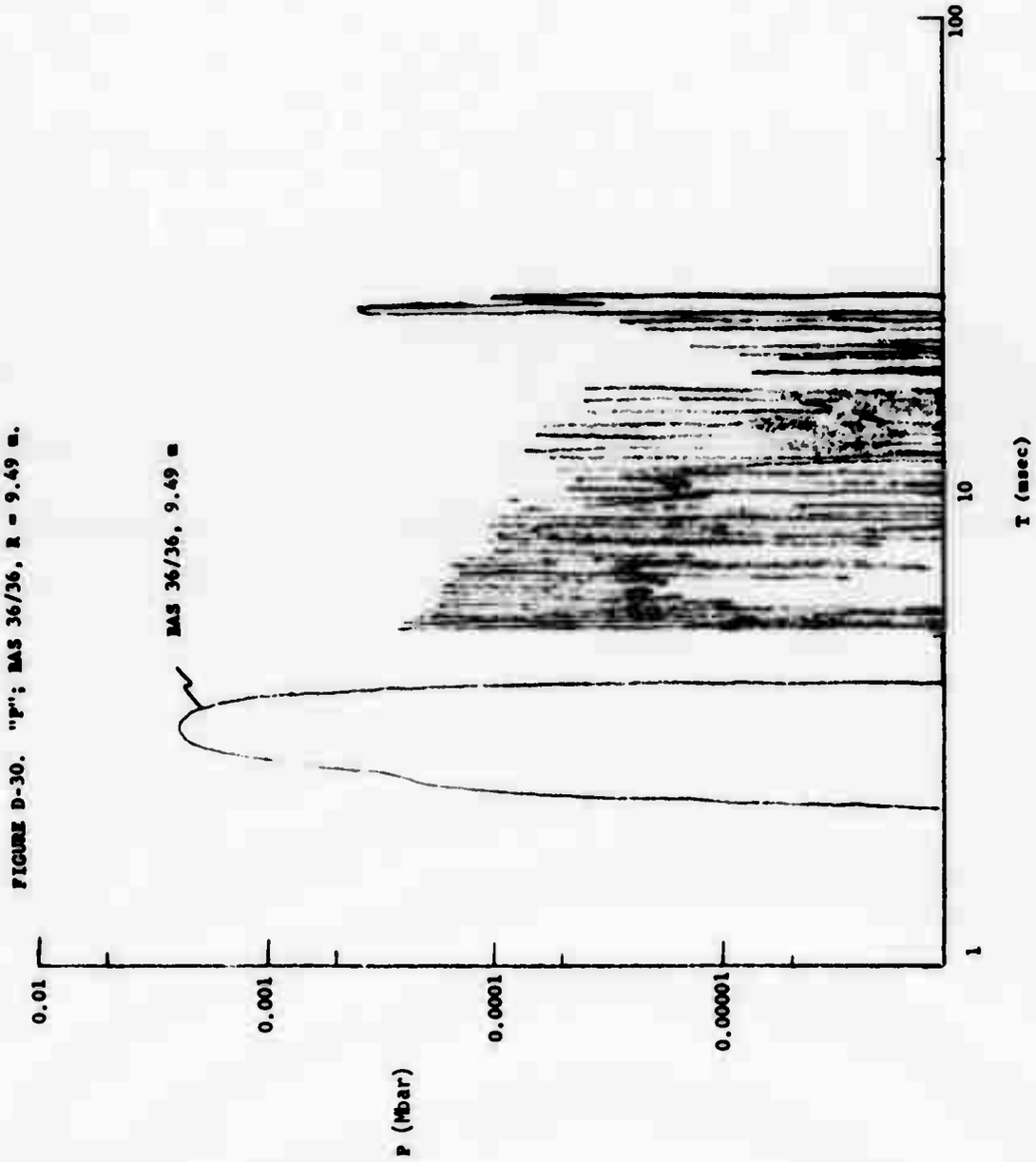

FIGURE D-30. "p"; BAS 36/36, R = 9.49 m.

FIGURE D-31. "V"; BAS 36/36, R = 10.6 m.

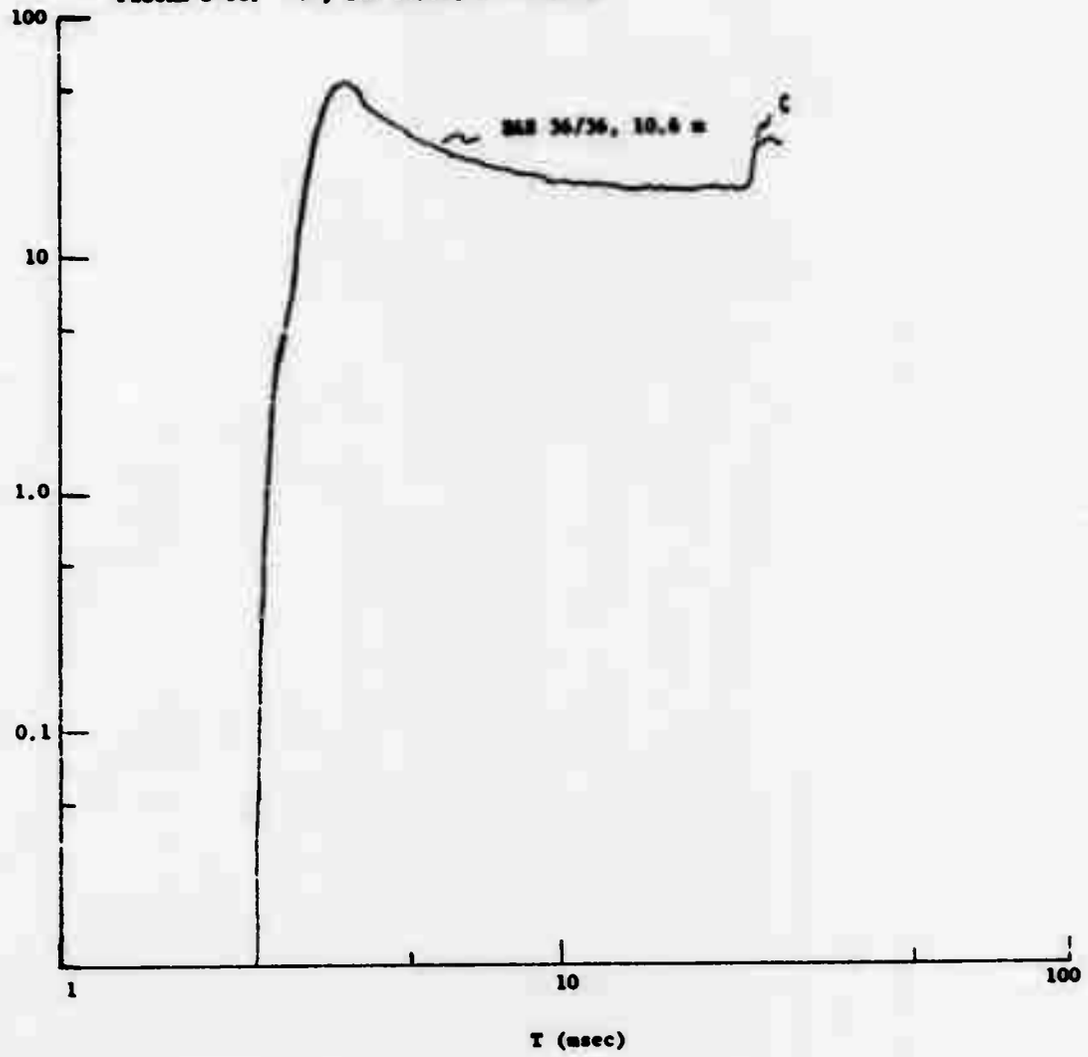

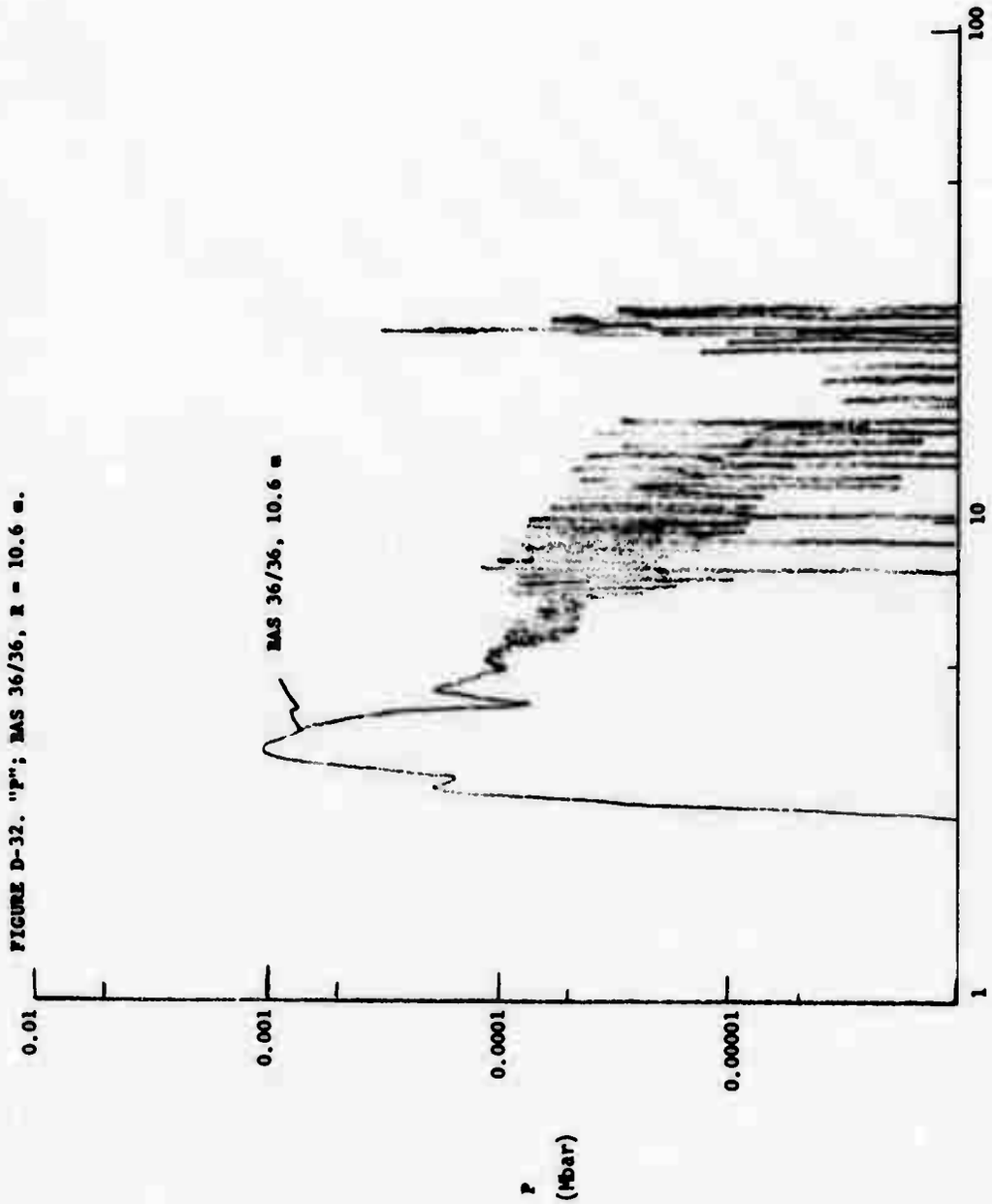

FIGURE D-32. "P"; RAS 36/36, R = 10.6 m.

FIGURE D-33. "V"; BAS 36/36, R = 10.89 m.

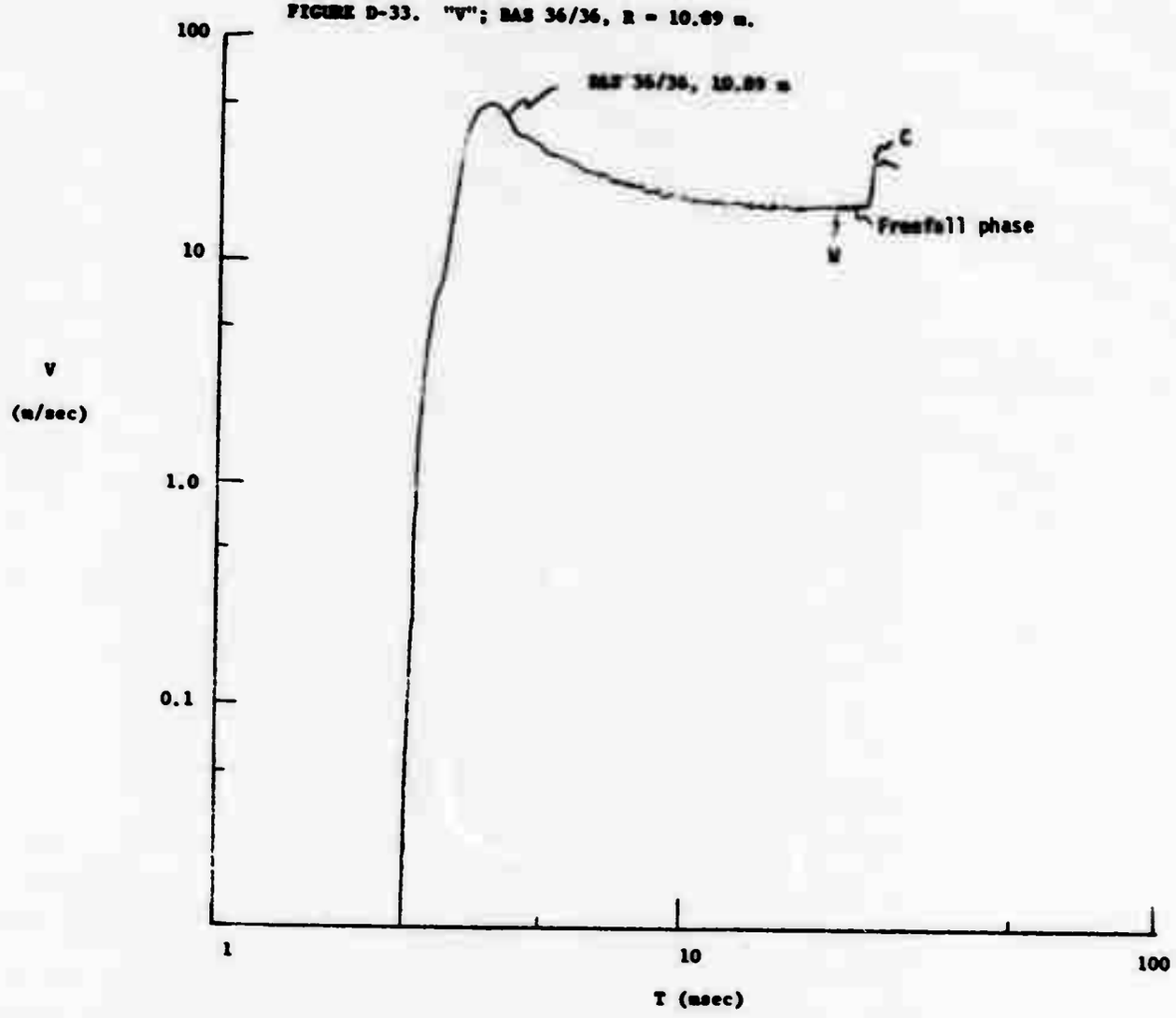

FIGURE D-34. "F"; BAS 36/36, R = 10.93 m.

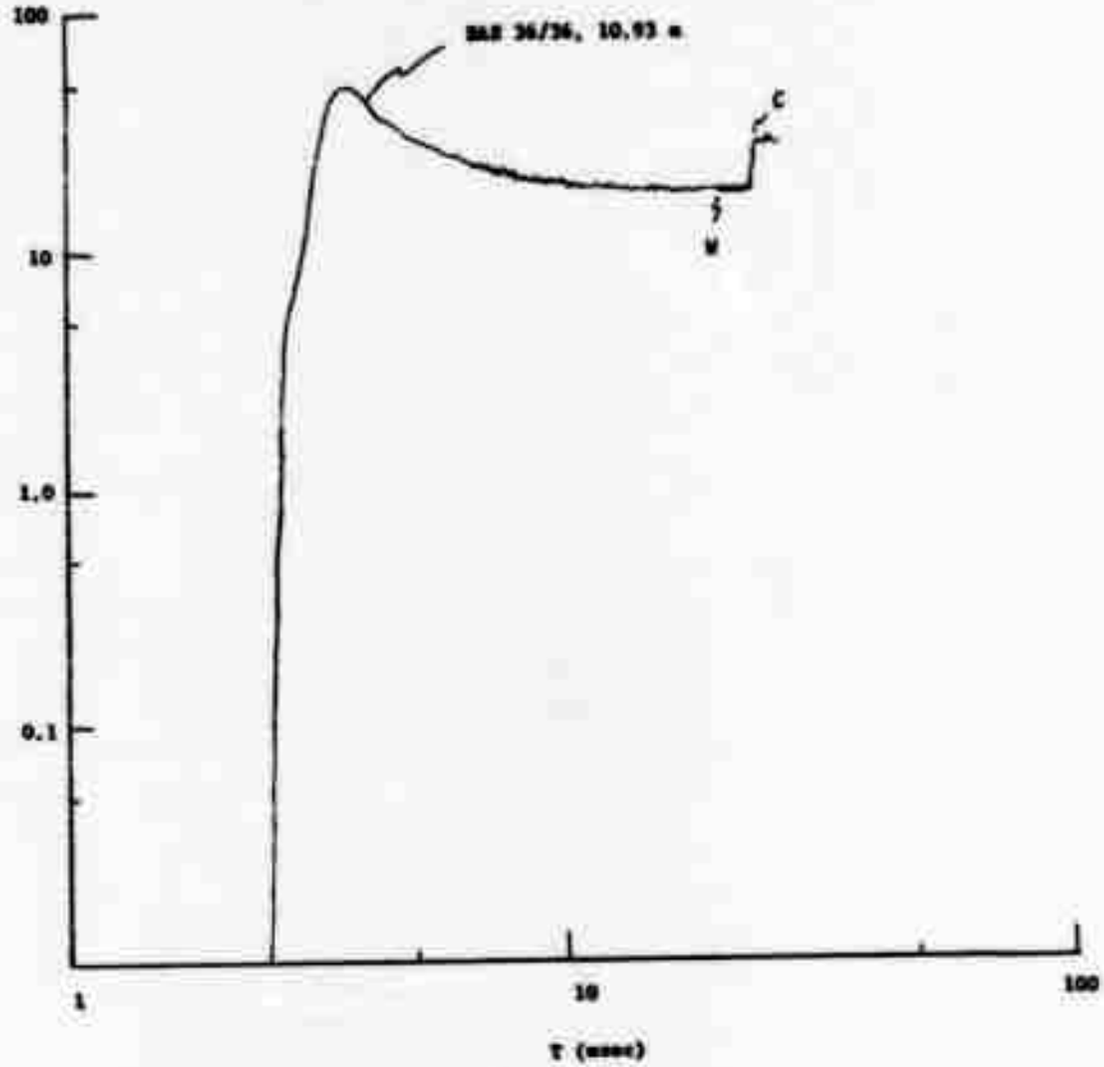

Appendix E

Waveforms for the Vertical and Vertical Underwater Calculations in Granite

FIGURE E-1. "V"; Granite, GRN 36/00, R = 3.01 m

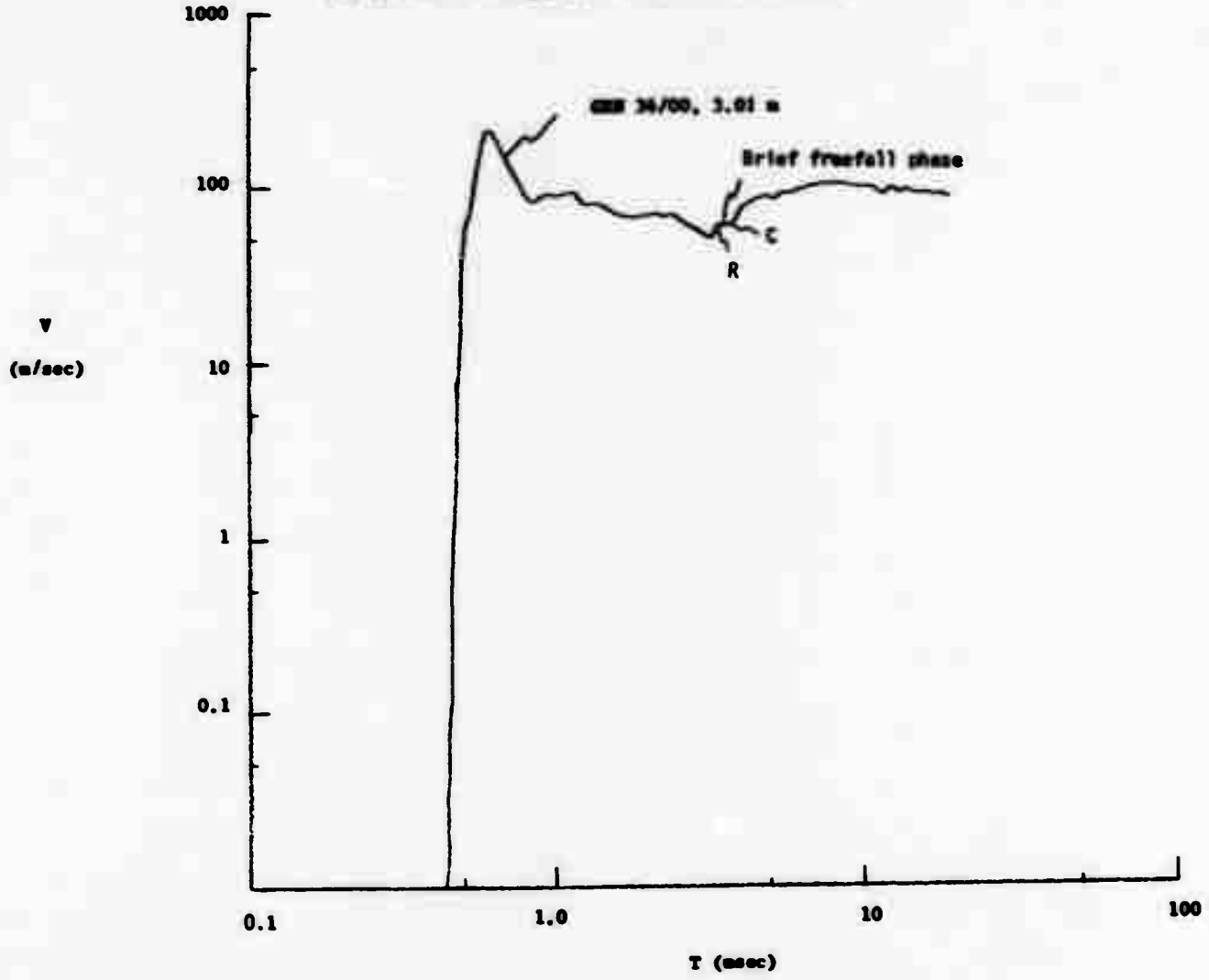

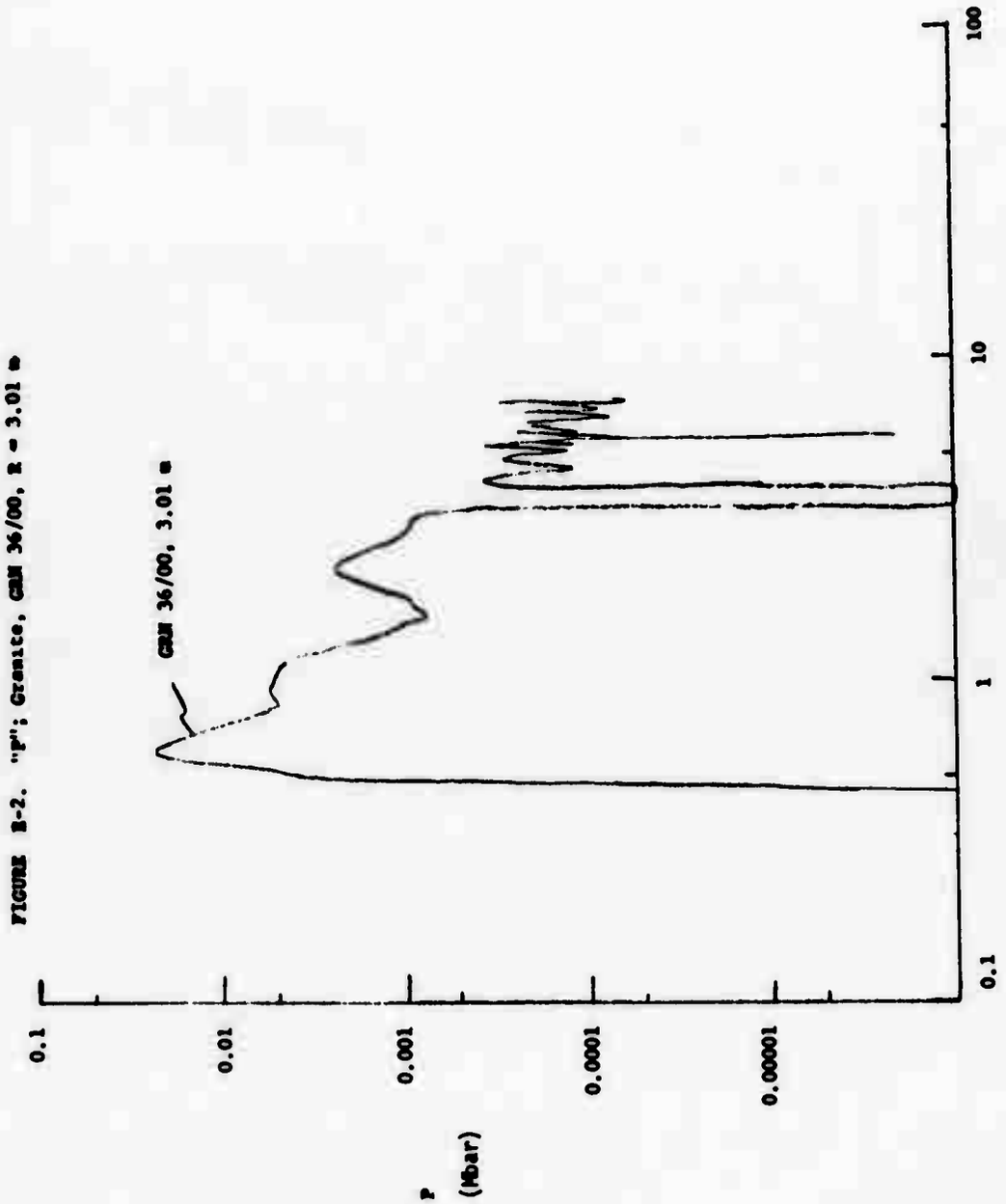

FIGURE B-2. "P"; Granite, CRM 36/00, R = 3.01 m

FIGURE E-3. "V"; GMR 36/00, R = 6.01 m.

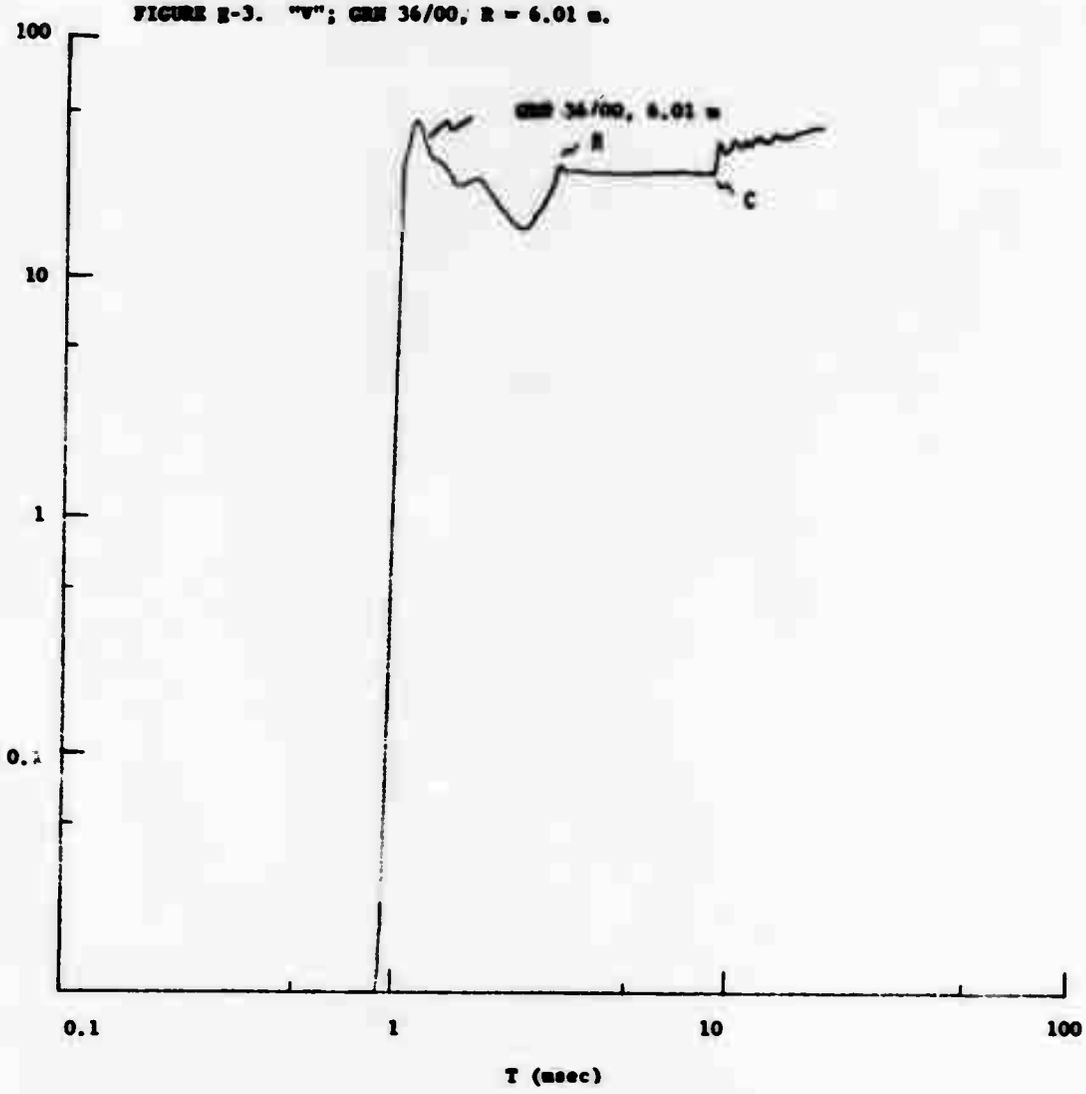

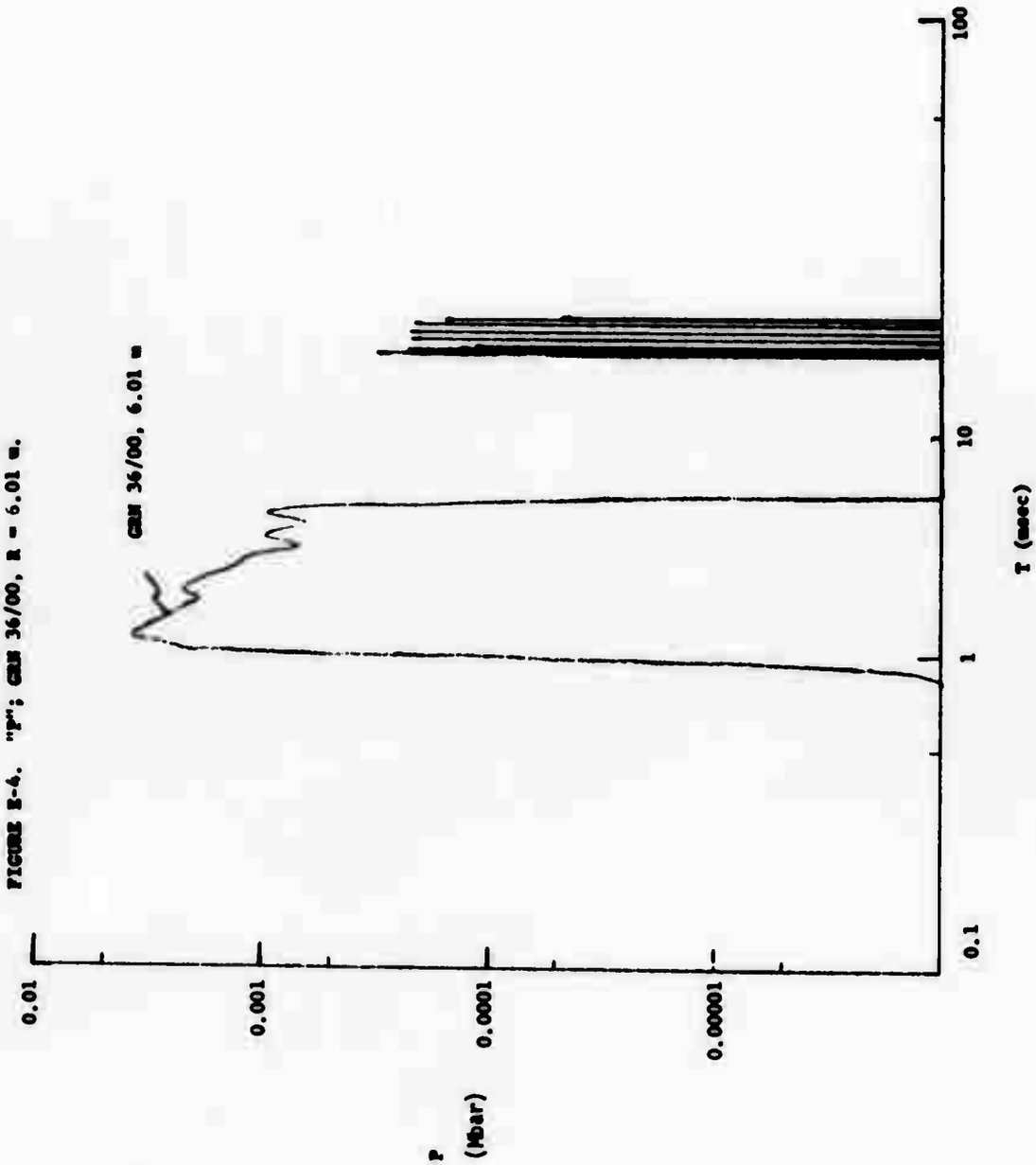

FIGURE E-4. "P"; GEM 36/00, R = 6.01 m.

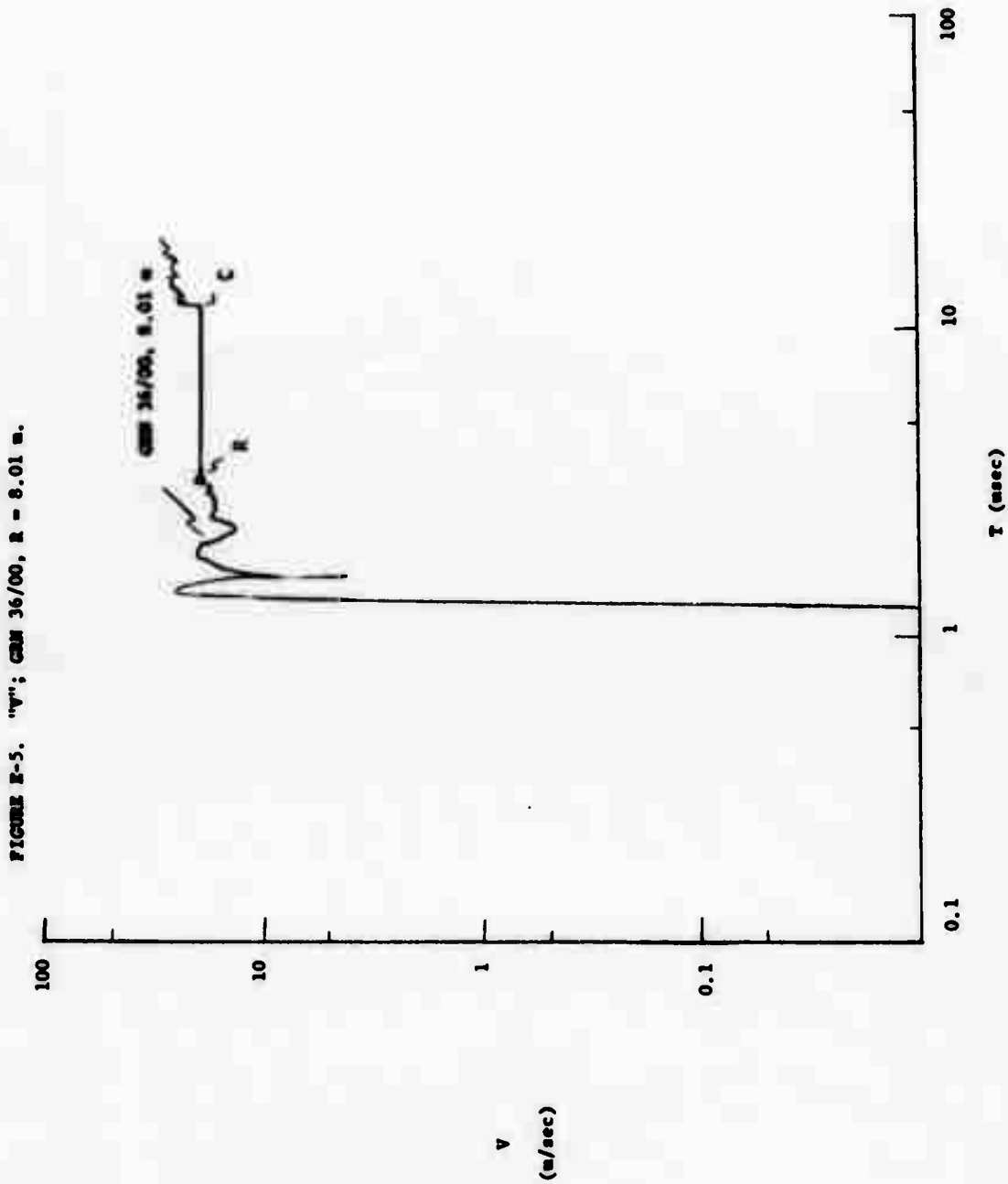

FIGURE E-5. "V"; CRM 36/00, R = 0.01 m.

FIGURE E-6. "P"; GRN 36/00, R = 8.01 m.

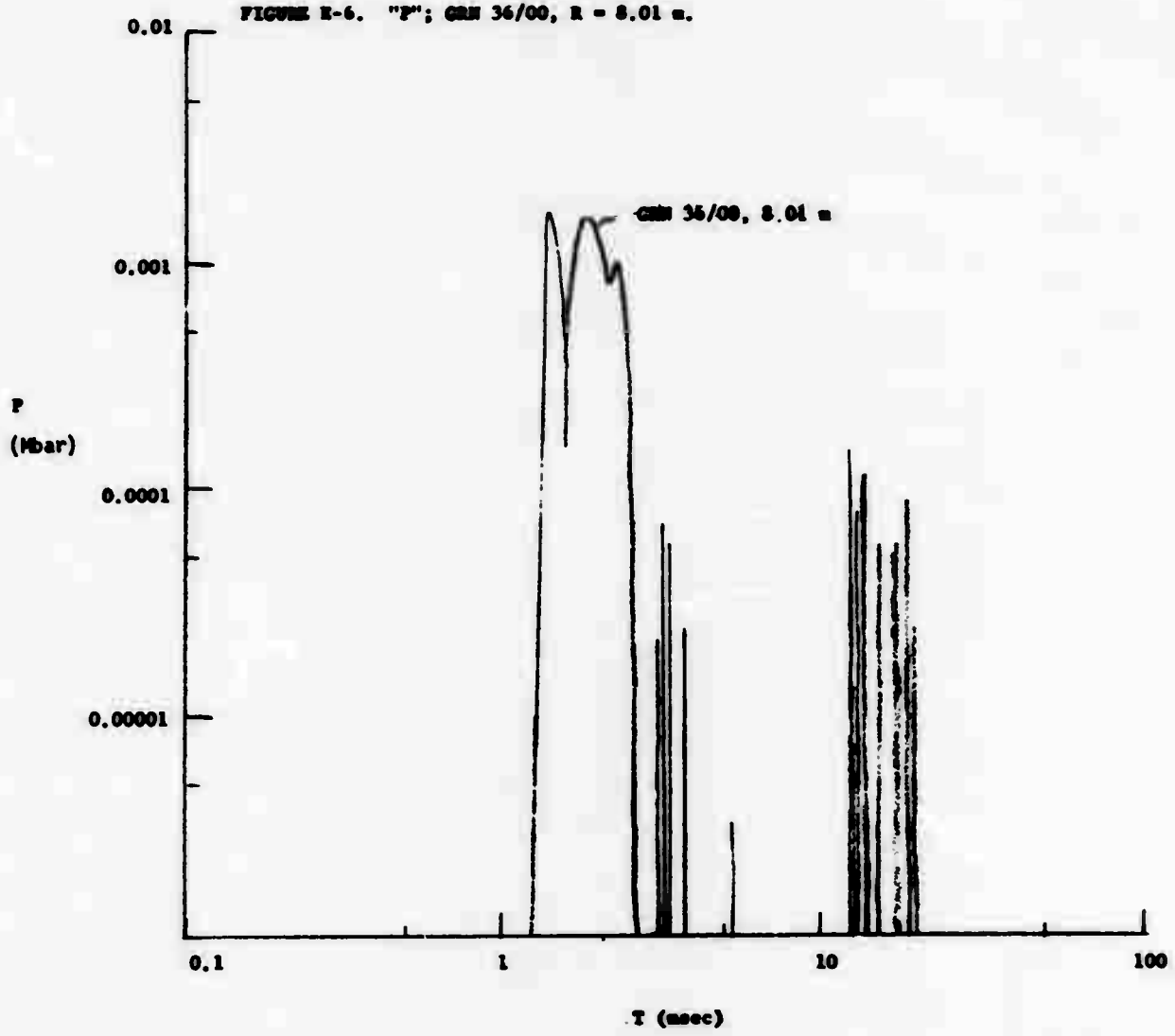

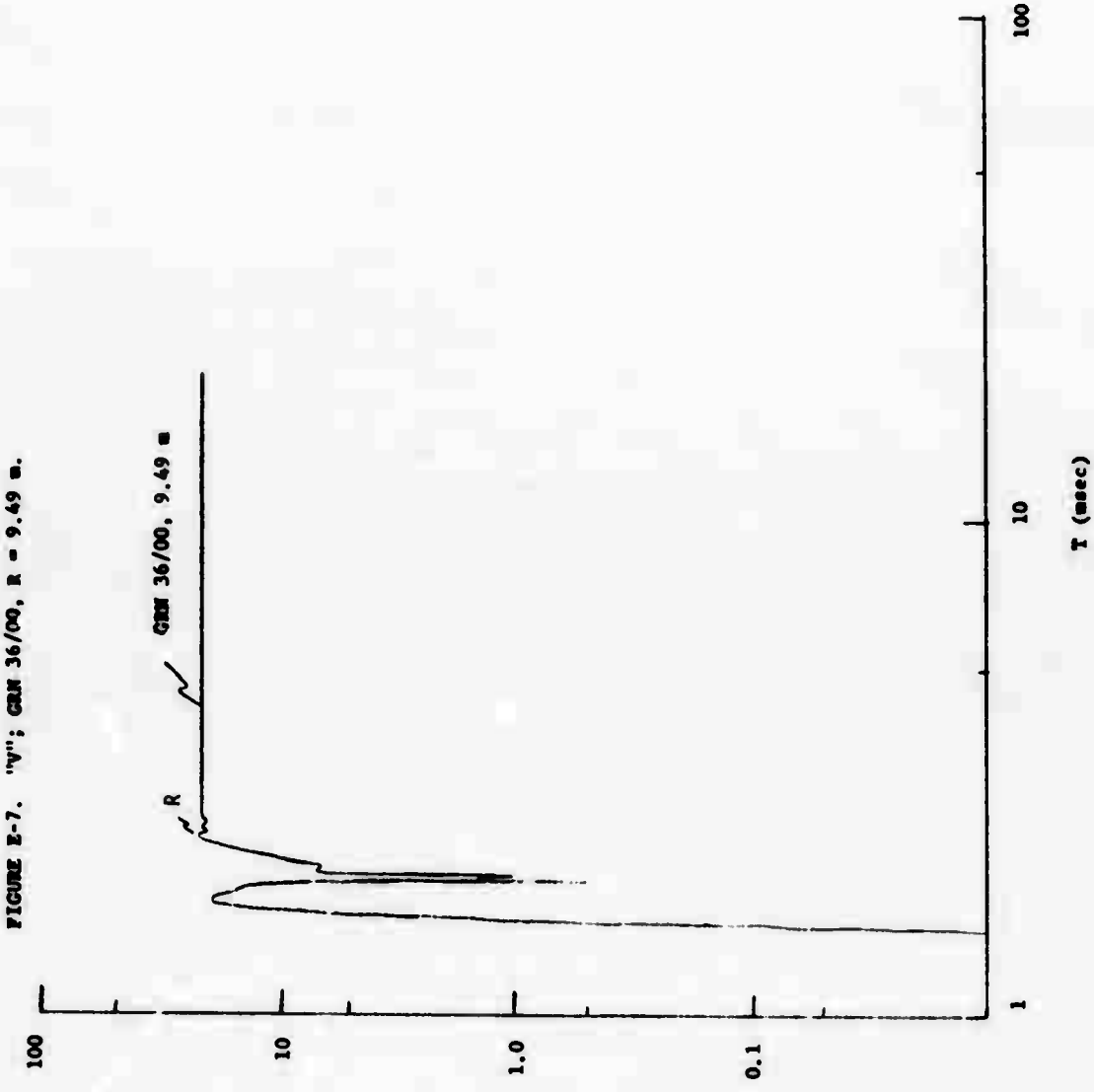

FIGURE E-7. "y"; GEM 36/00, R = 9.49 m.

FIGURE E-6. "P"; GRH 36/00, R = 9.49 m.

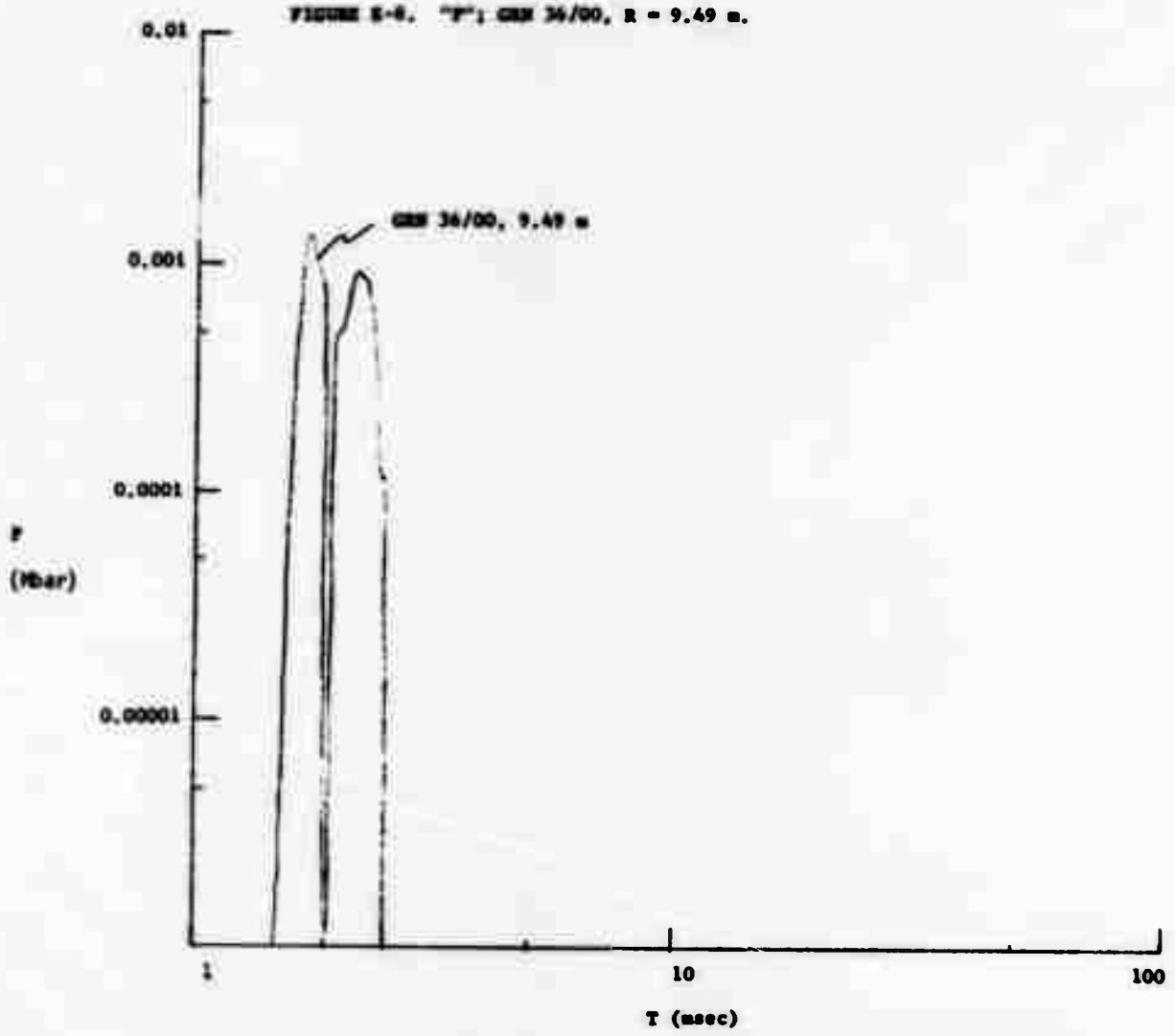

FIGURE E-9. "V"; GRN 36/00, R = 10.6 m.

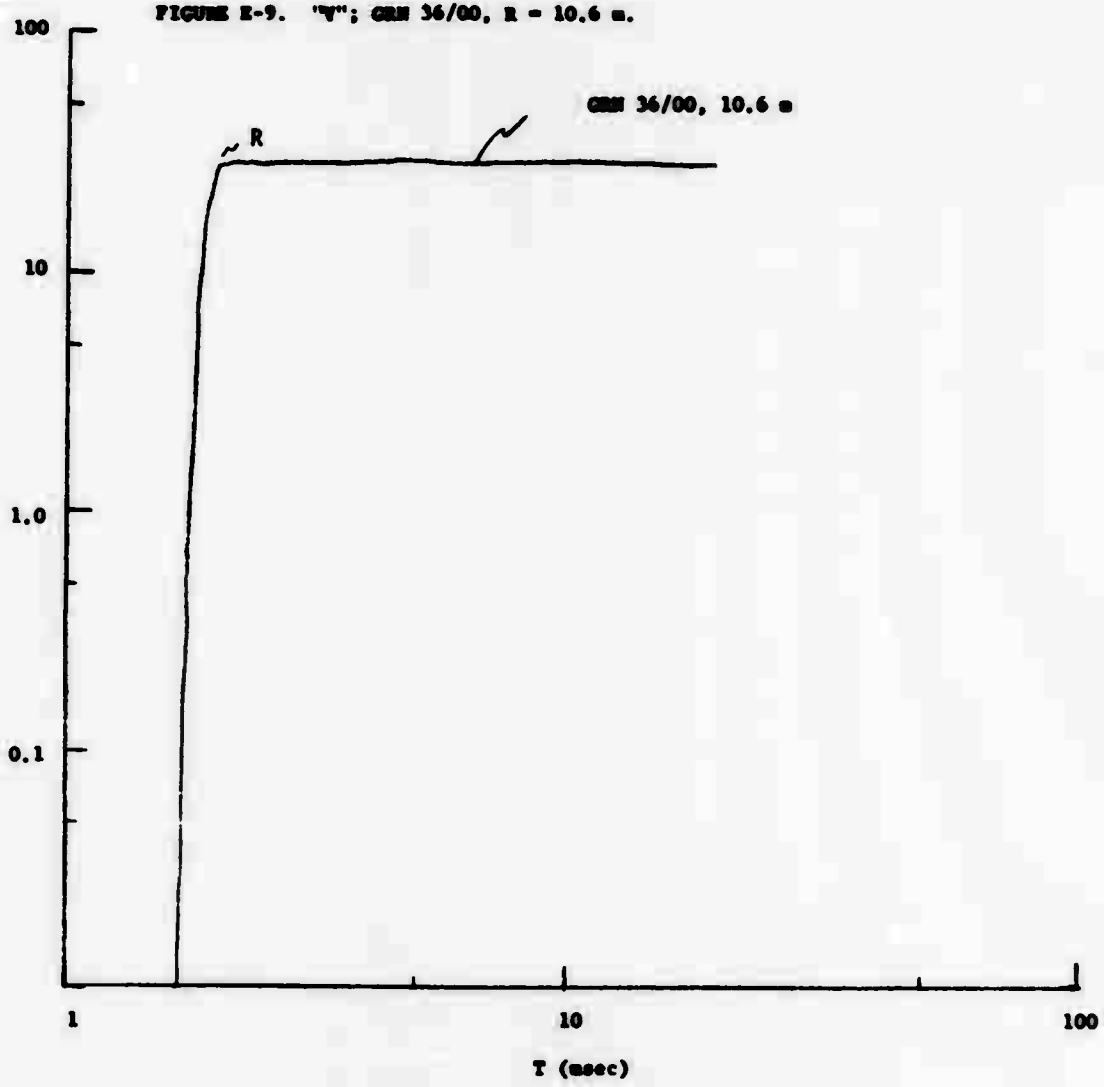

FIGURE E-10. "P"; GRN 36/00, R = 10.6 m.

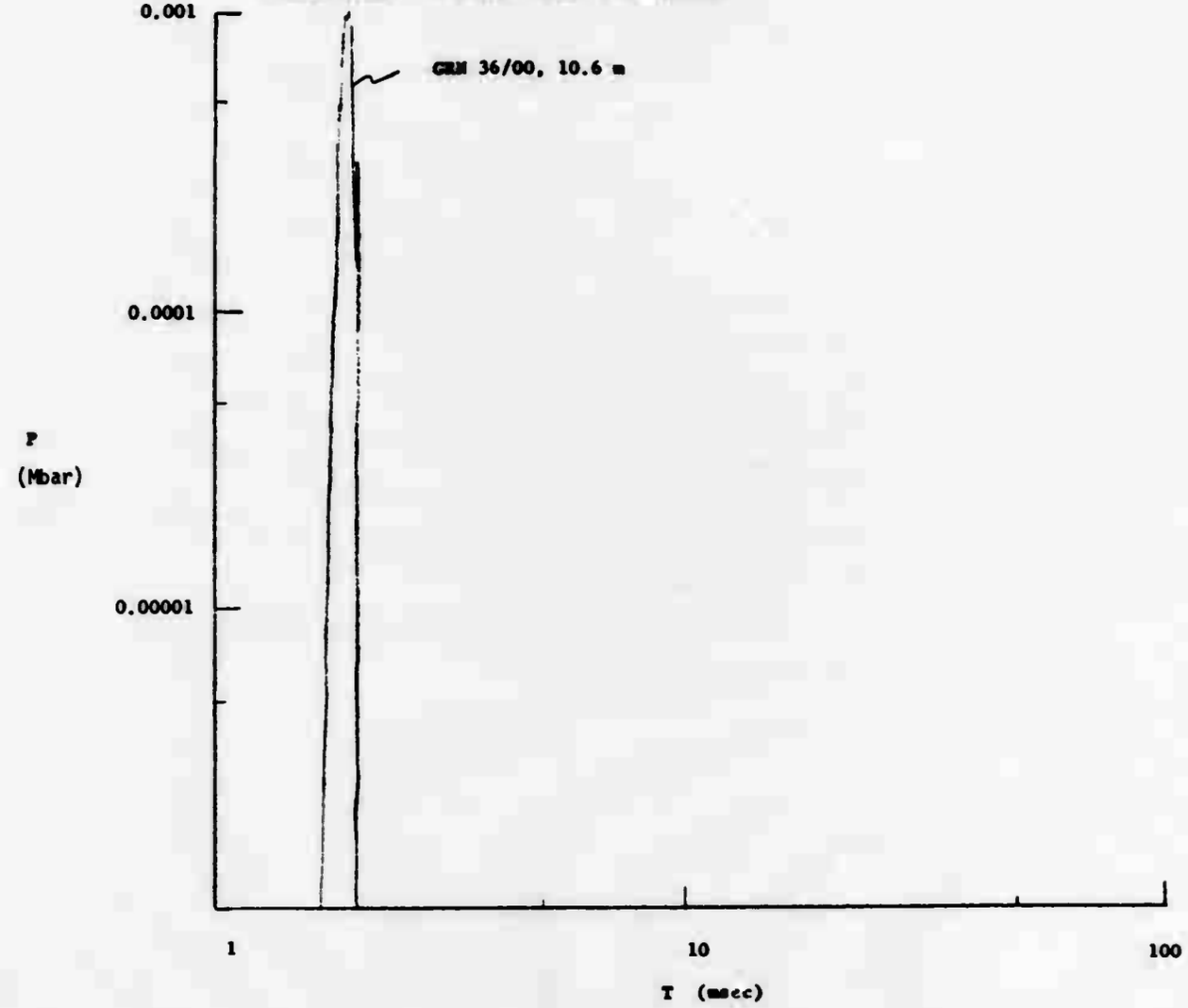

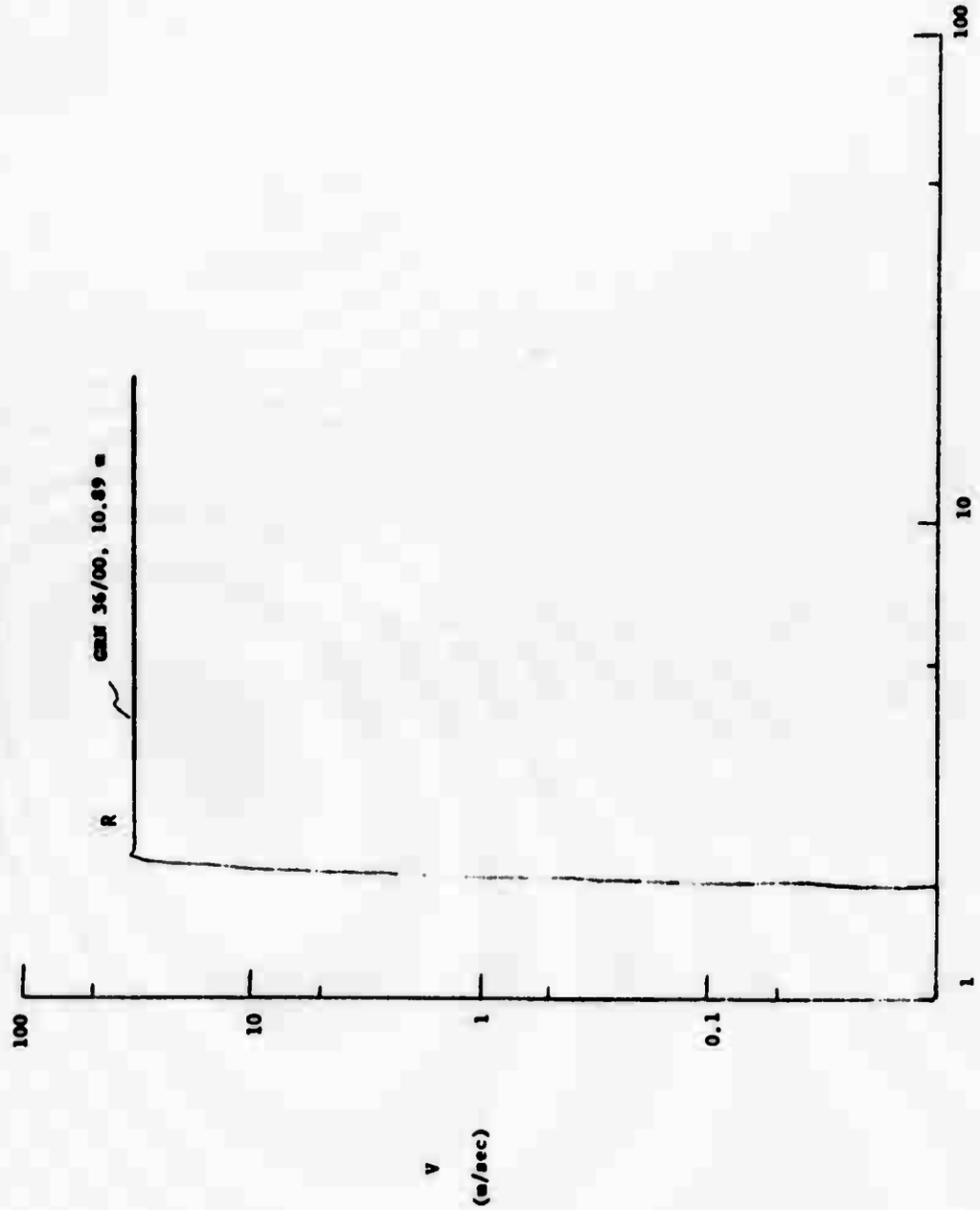

FIGURE E-11. "v"; CEM 36/00, R = 10.89 m.

FIGURE 8-12. "P"; GRN 36/00, R = 10.89 m.

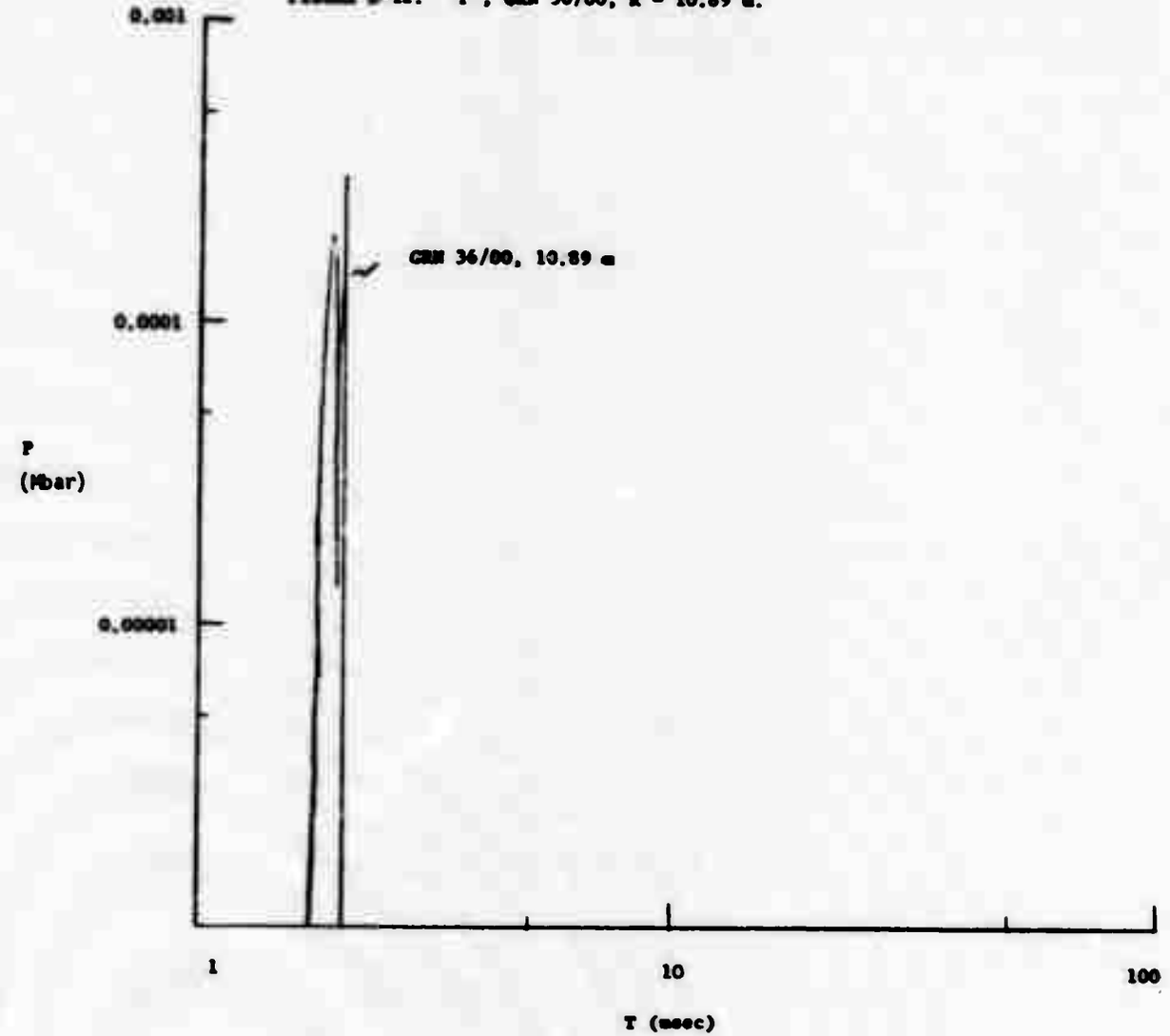

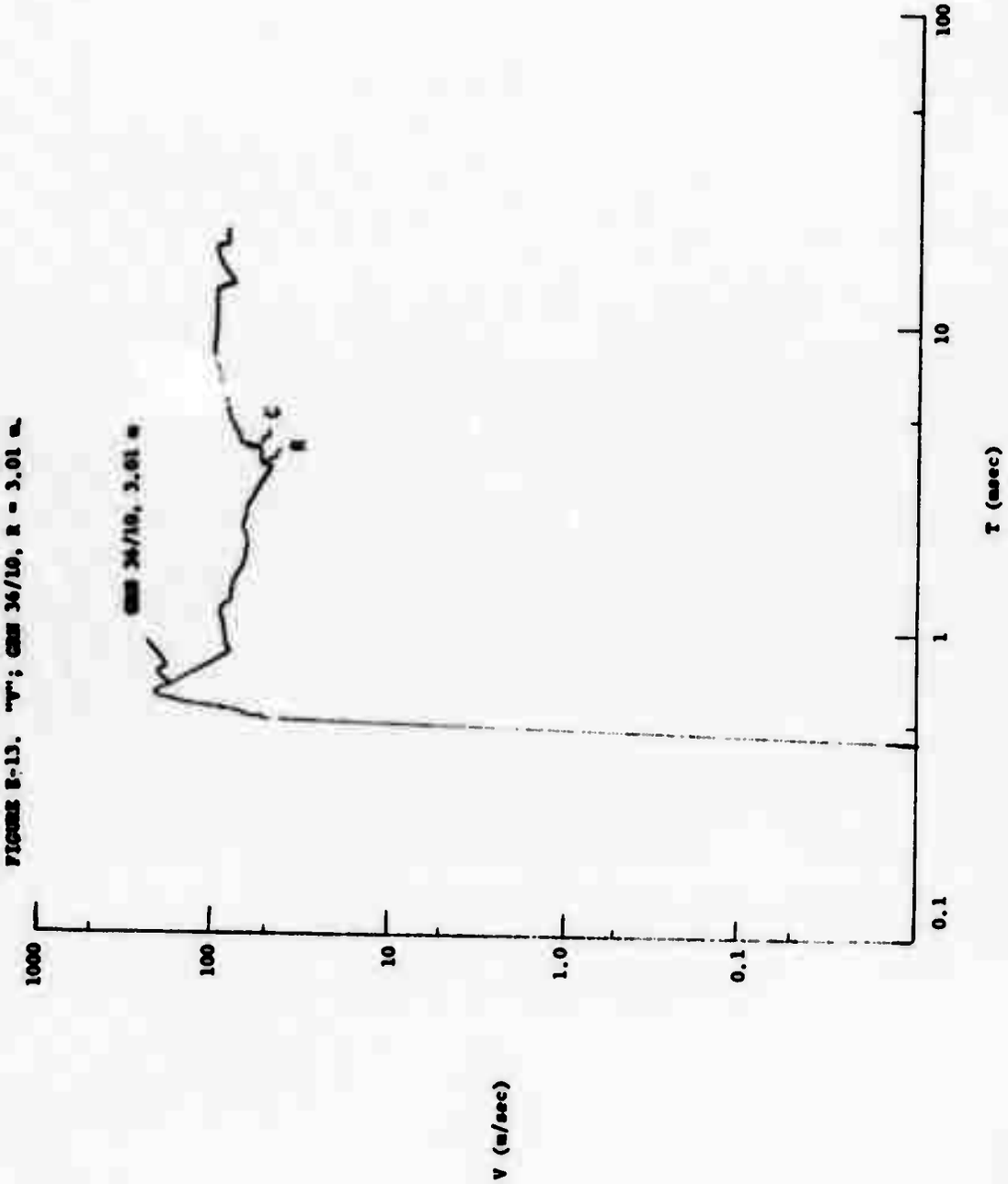

FIGURE E-13. "P"; GEM 36/10, R = 3.01 m.

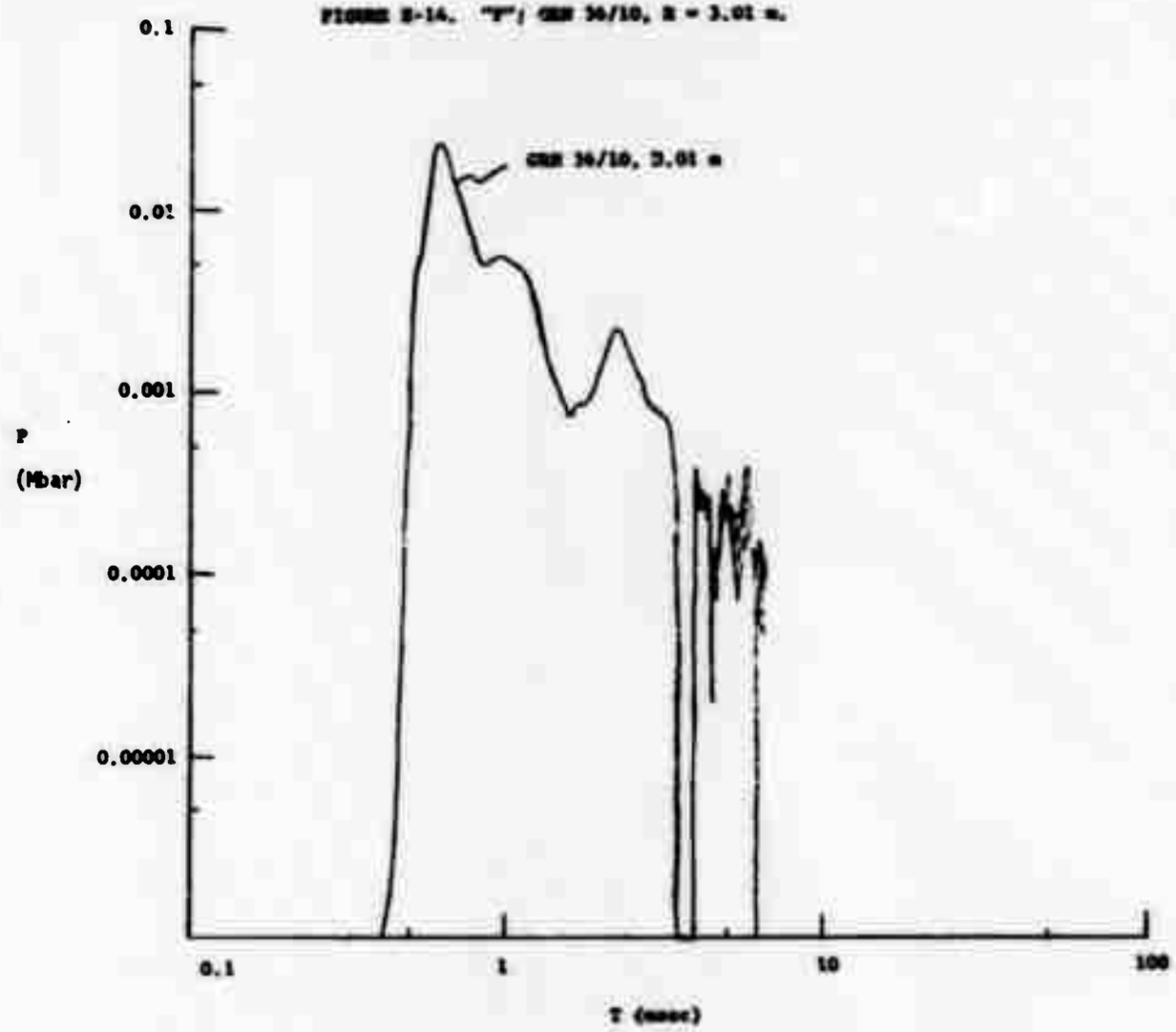
0.1
0.01
0.001
P
(Mbar)
0.0001
0.00001
0.1
1
10
100
T (msec)

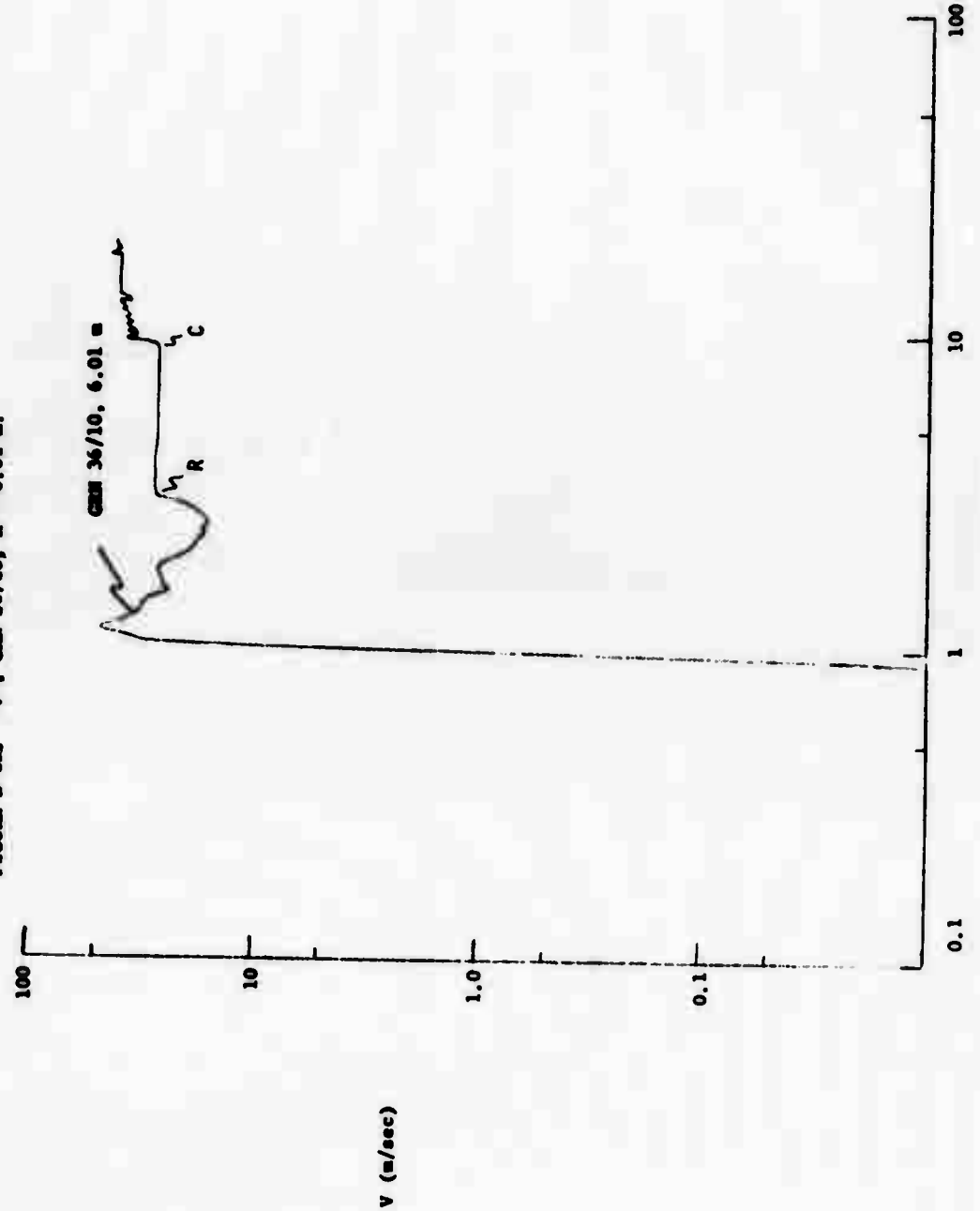

FIGURE E-15. "V": CEM 36/10, R = 6.01 m.

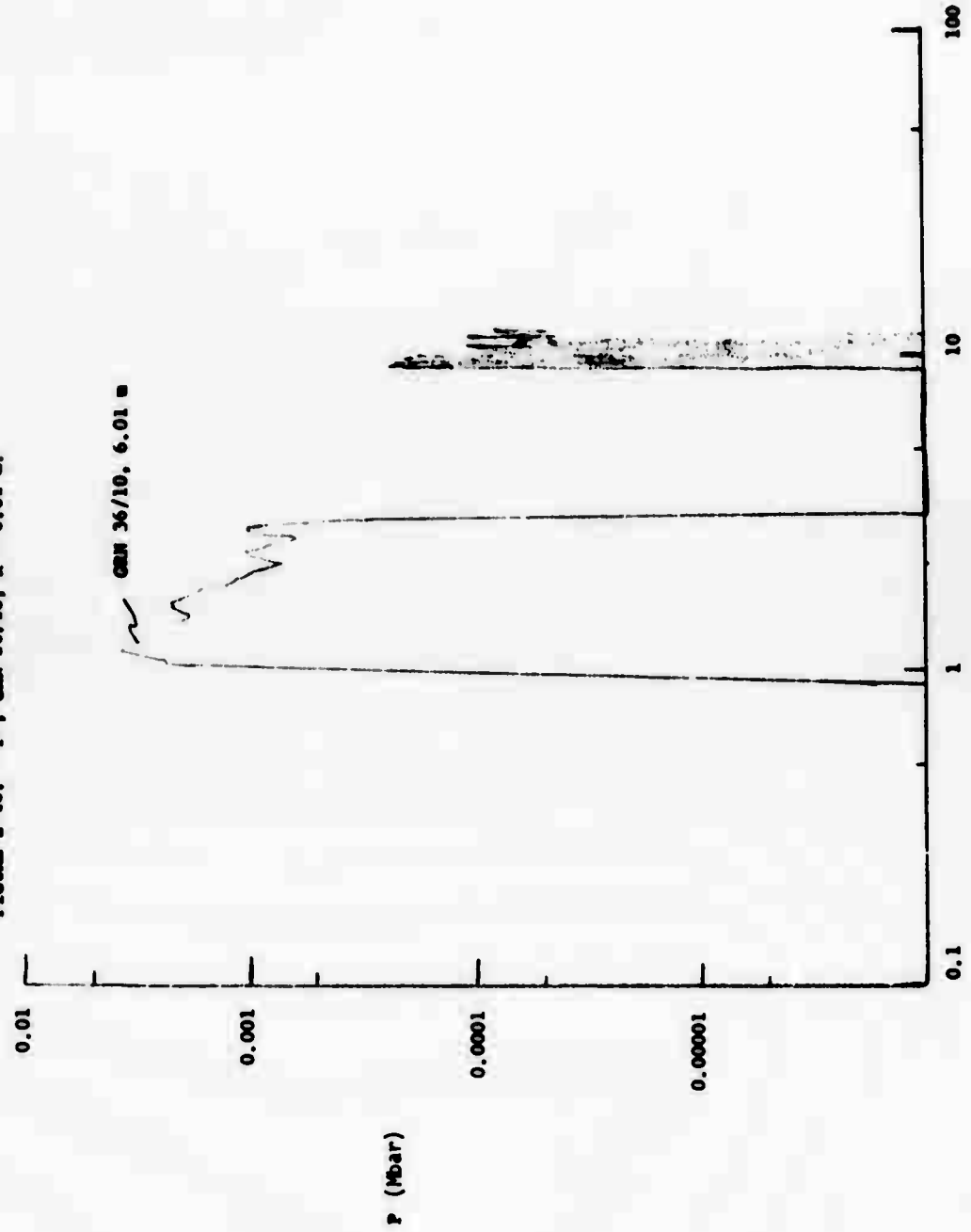

FIGURE E-16. "P"; CRN 36/10, R = 6.01 m.

FIGURE E-17. "V*: GRF 36/10, R = 8.01 m.

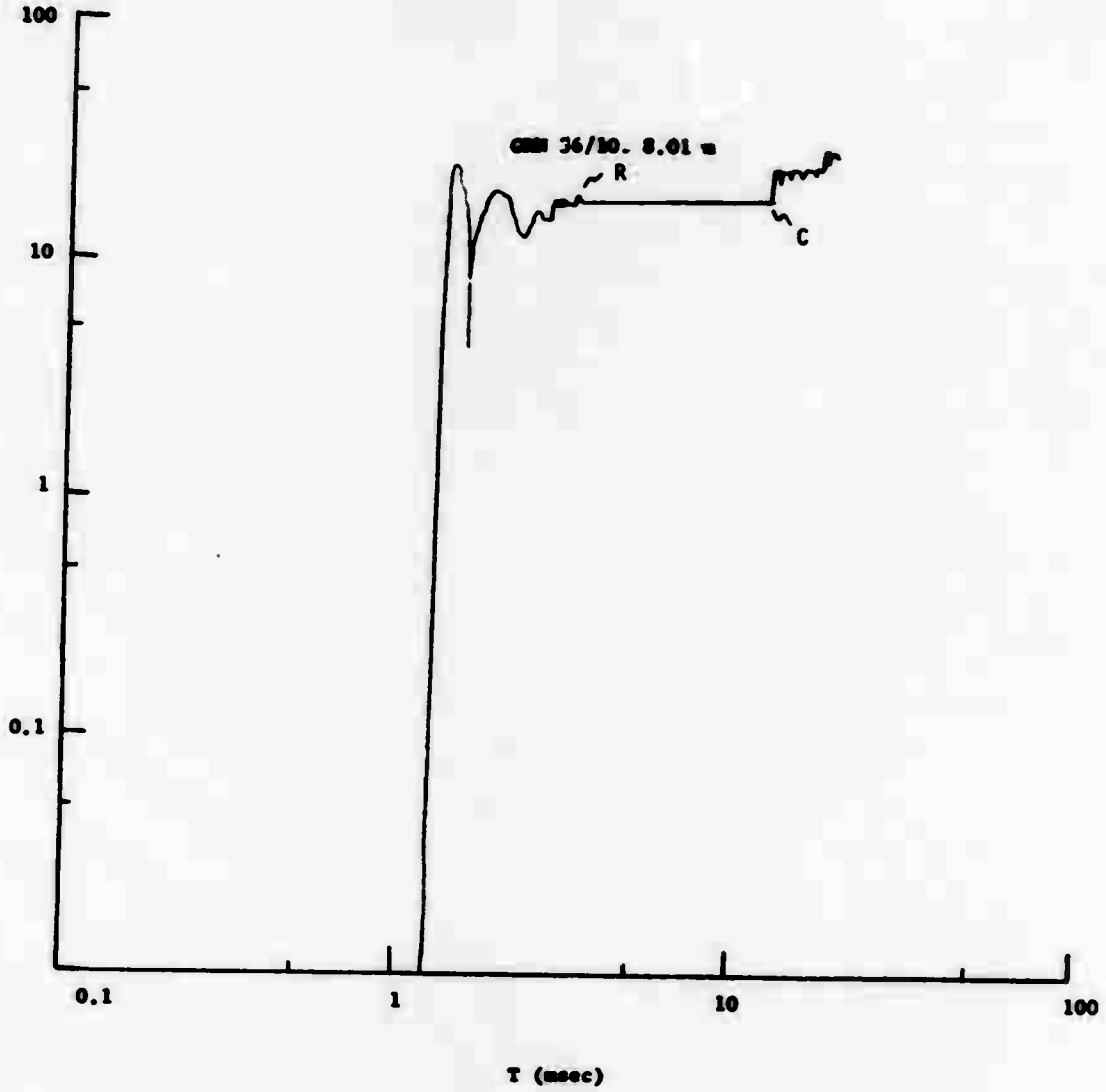

FIGURE E-18. "F"; GEM 36/10, S = 0.01 m.

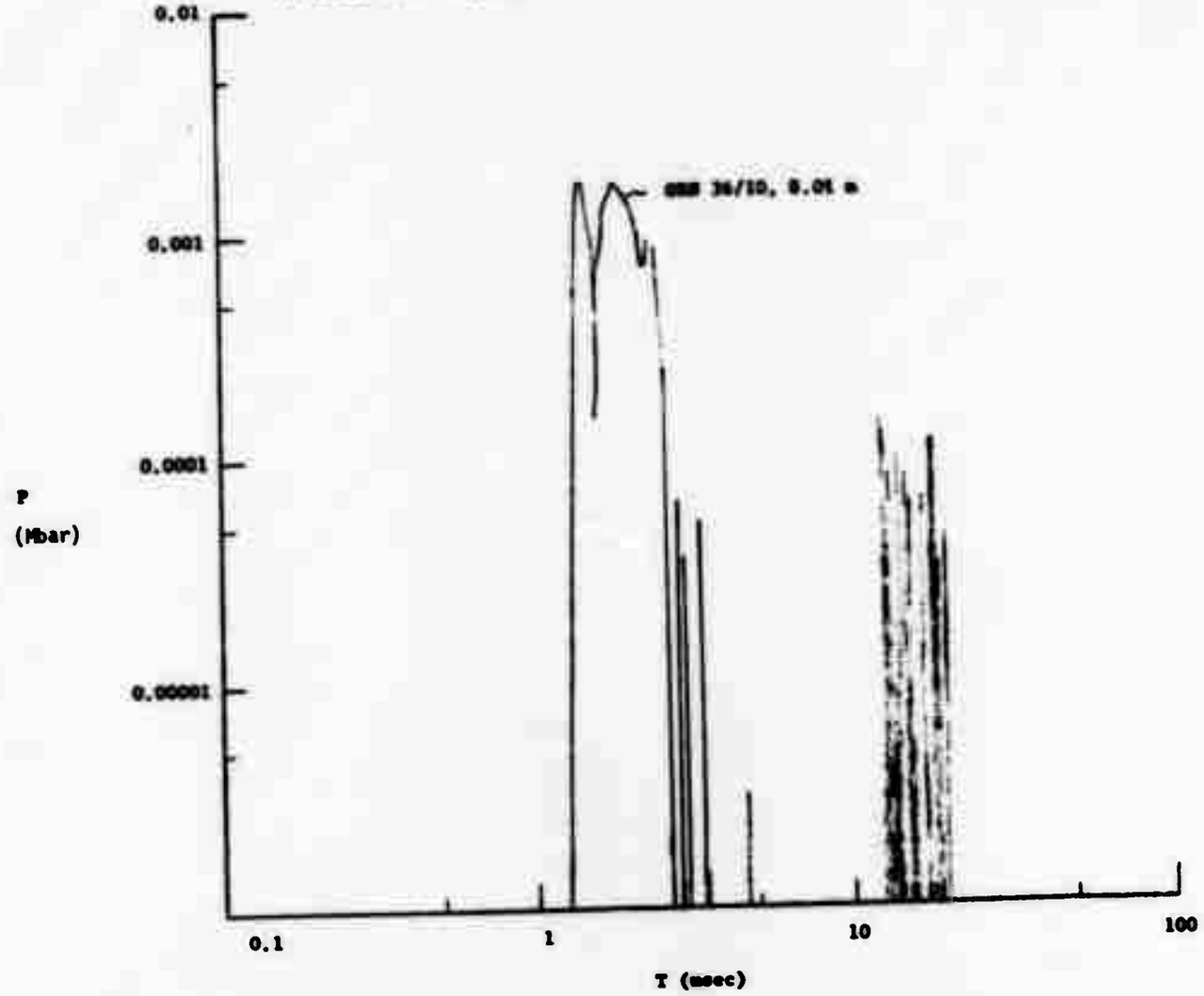

FIGURE E-19. "V"; GRB-36/10, R = 9.49 m.

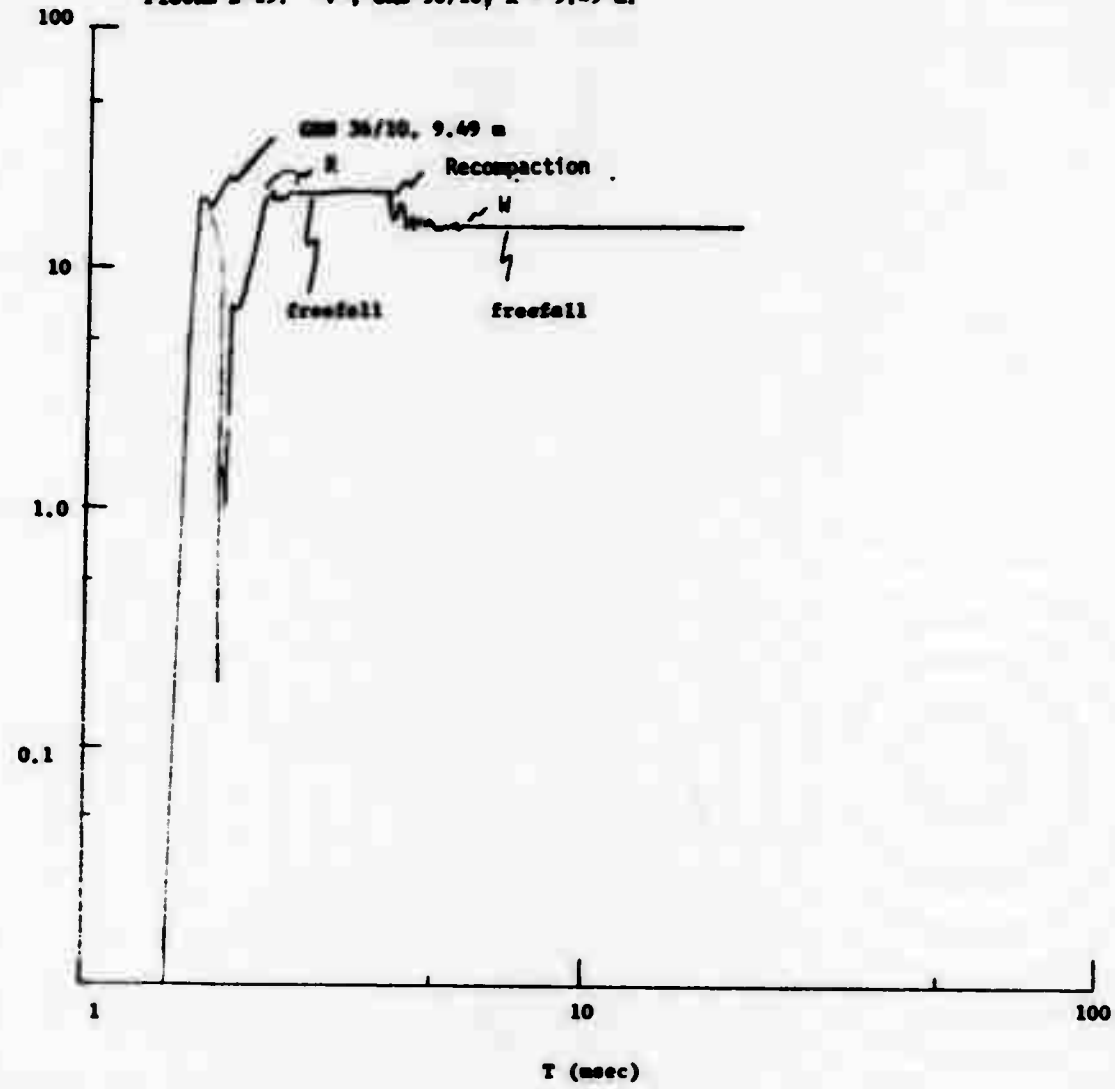

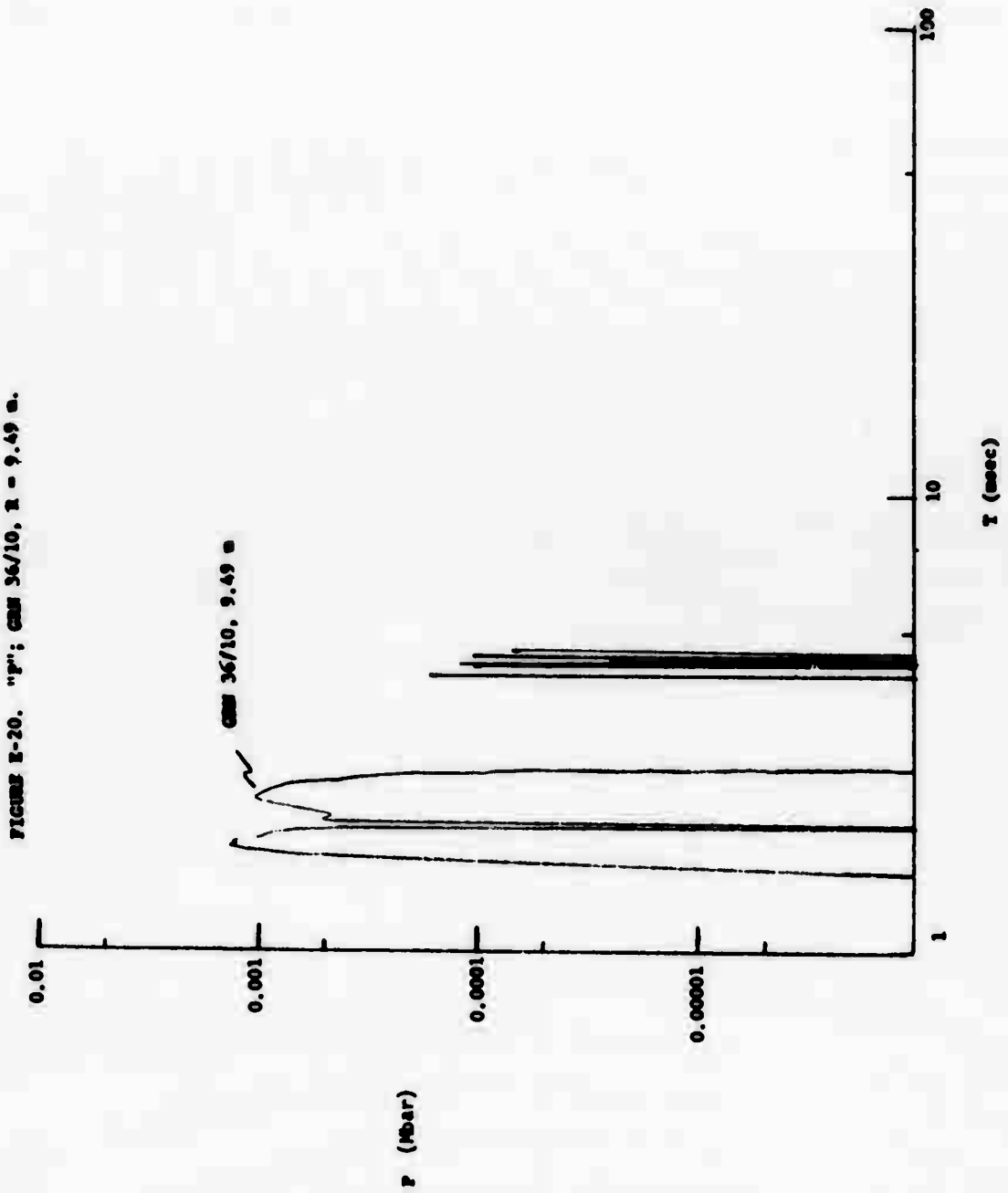

FIGURE E-20. "P"; GRM 36/10, R = 9.49 m.

FIGURE E-21. "V"; GRN 36/10, R = 10.6 m.

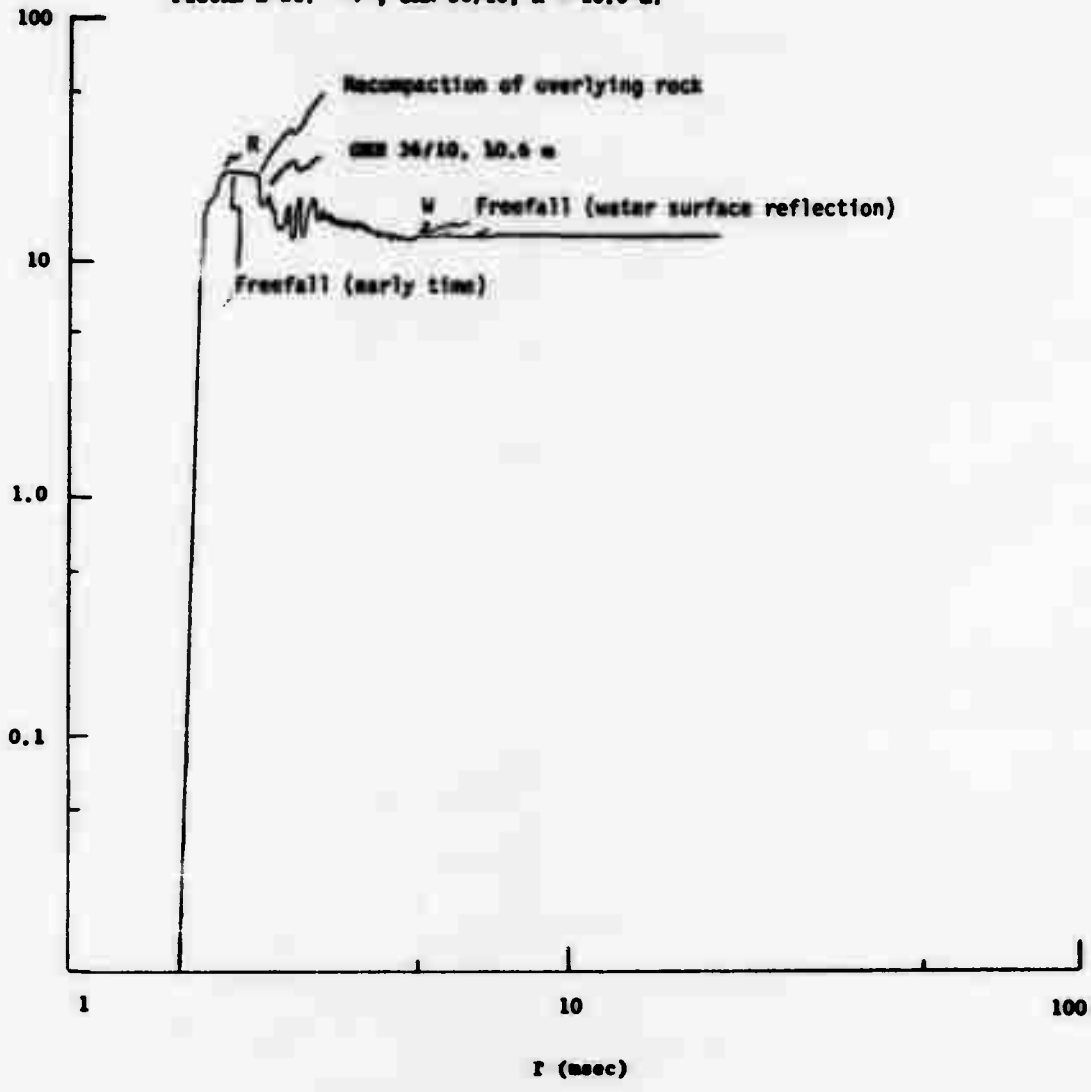

FIGURE E-22. "V"; GRN 36/10, R = 10.89 m.

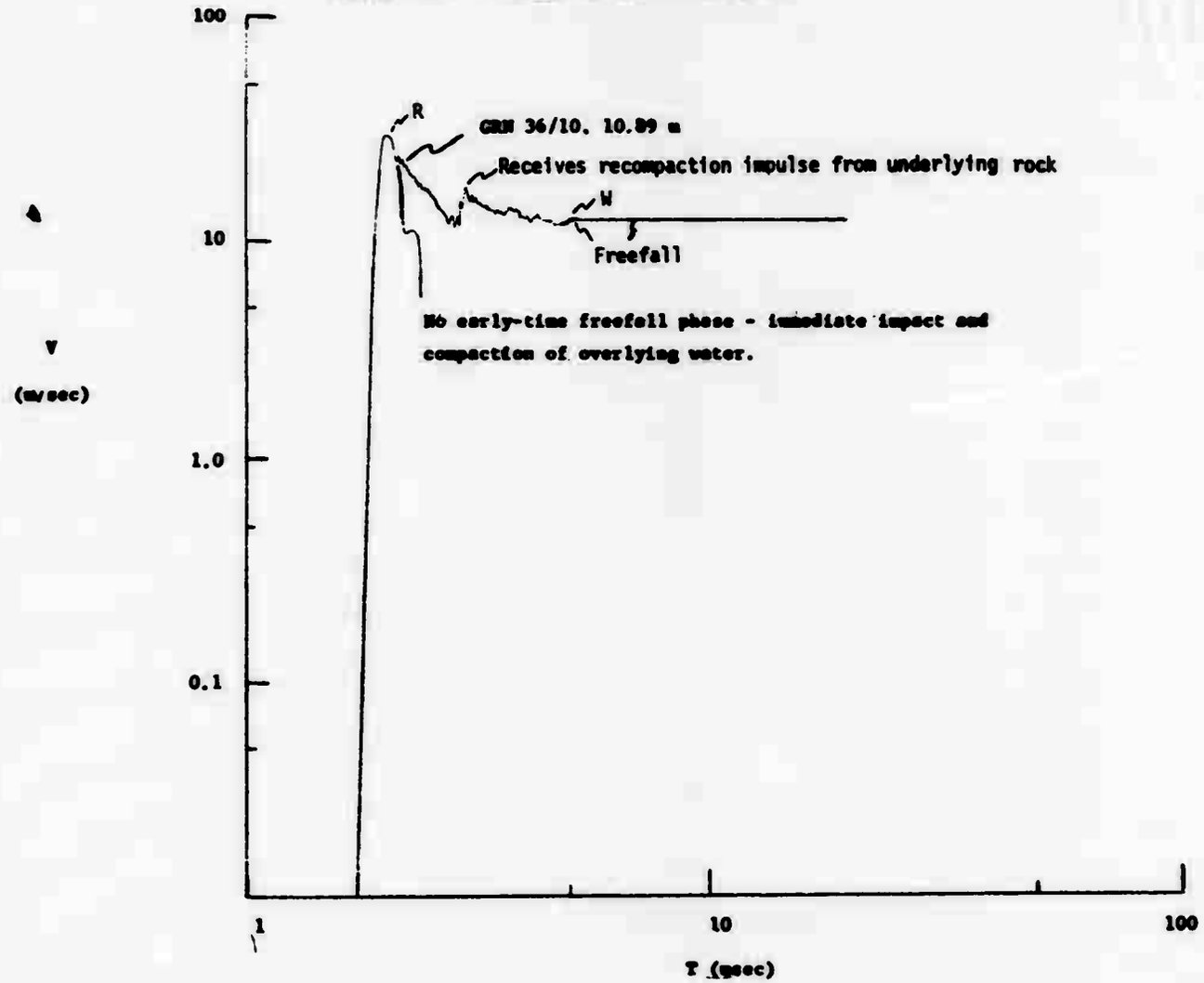

FIGURE E-23. "V"; GRN 36/10, R = 10.93 m.

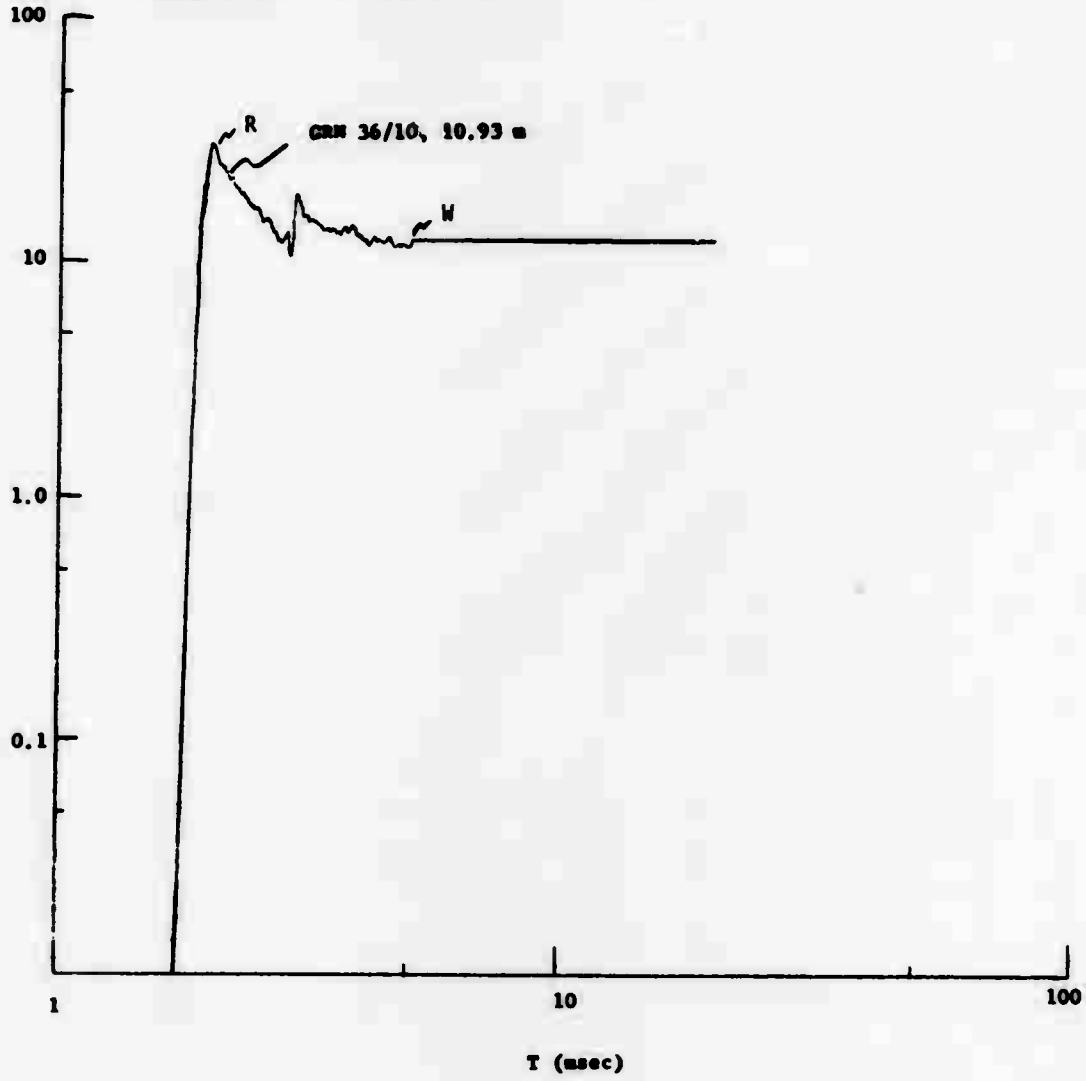

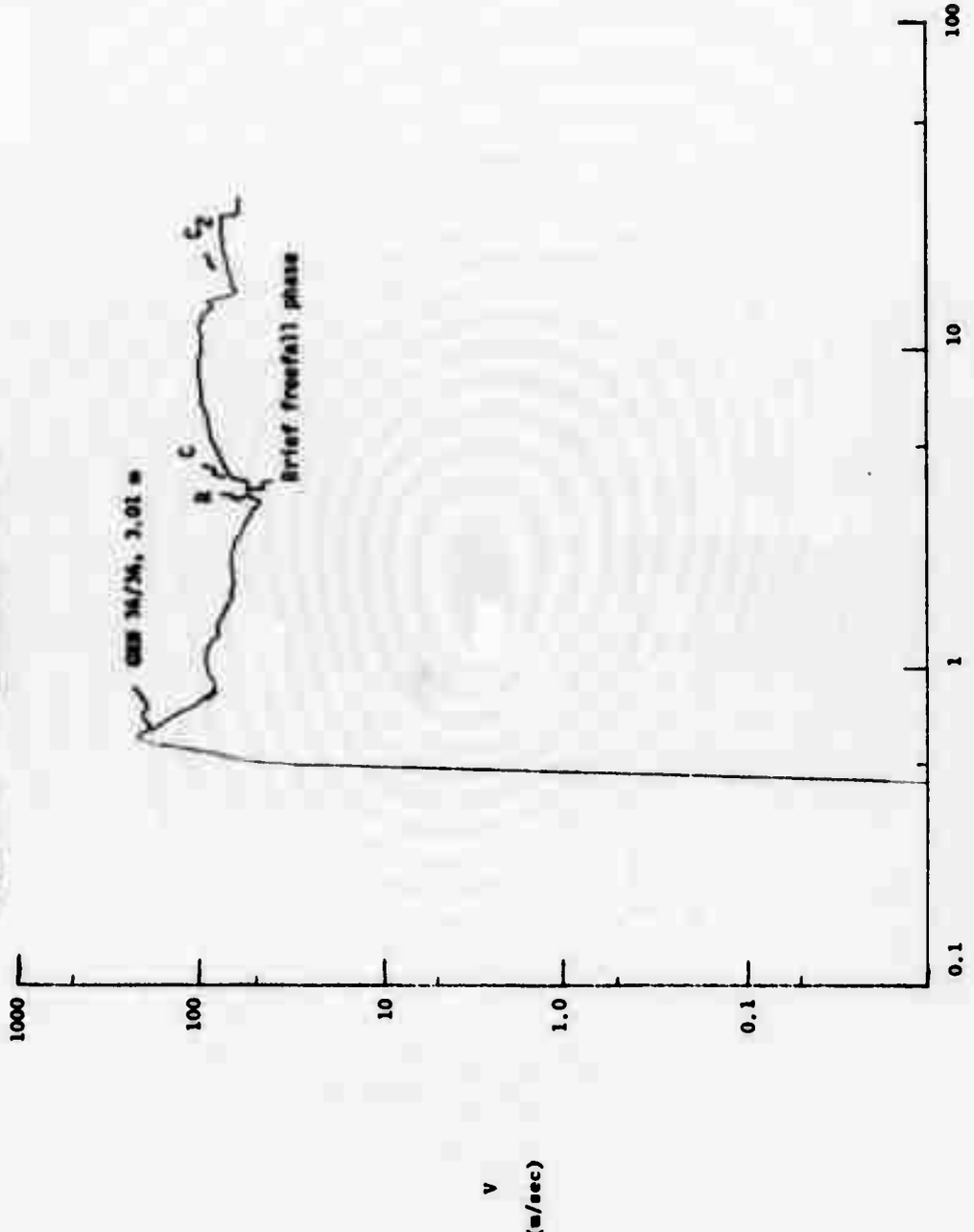

FIGURE E-24. "V": CRM 36/36, R = 3.01 m.

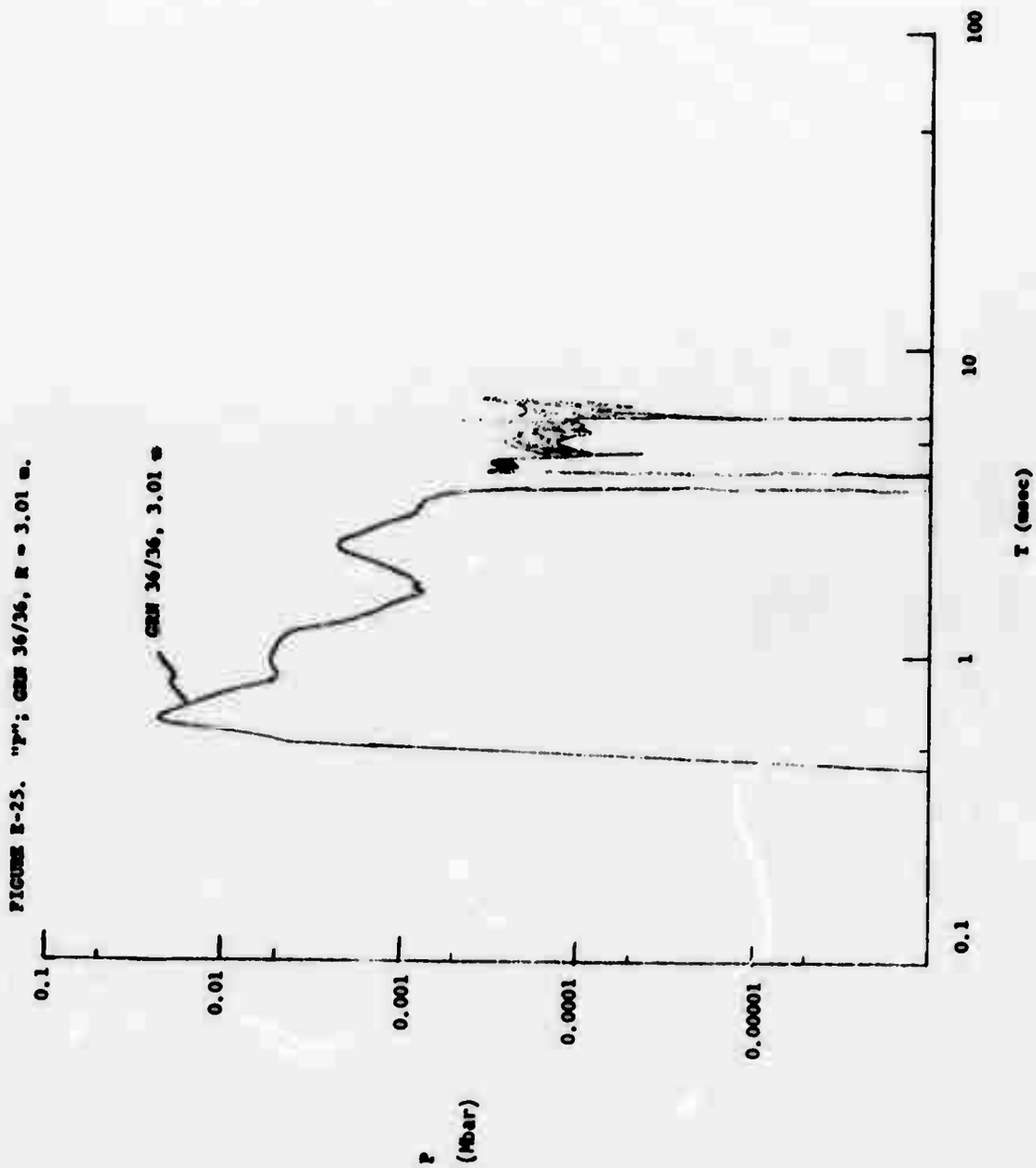

FIGURE E-25. "p"; CSM 36/36, R = 3.01 n.

FIGURE E-26. "V": GRH 36/36, R = 6.01 m.

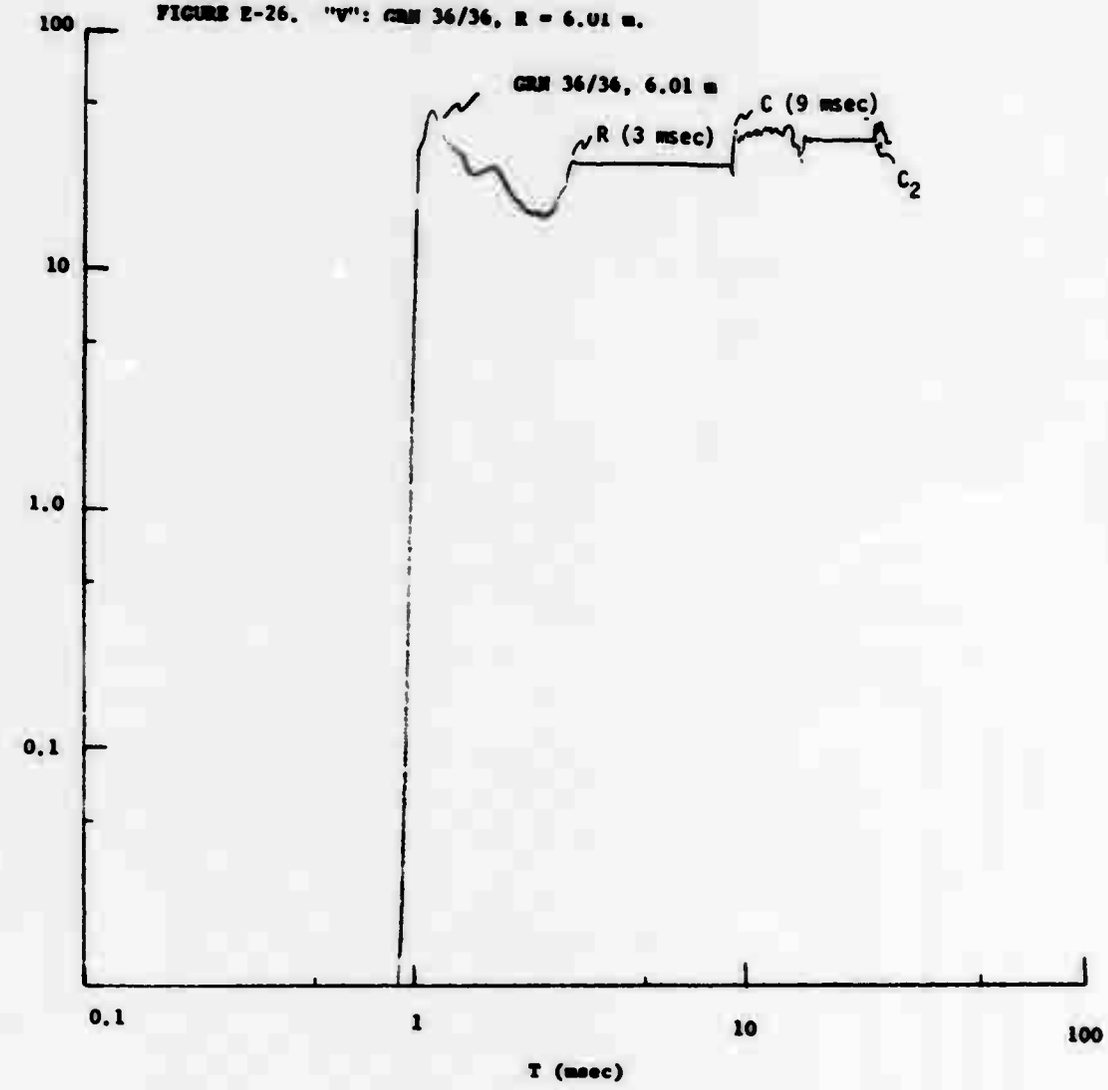

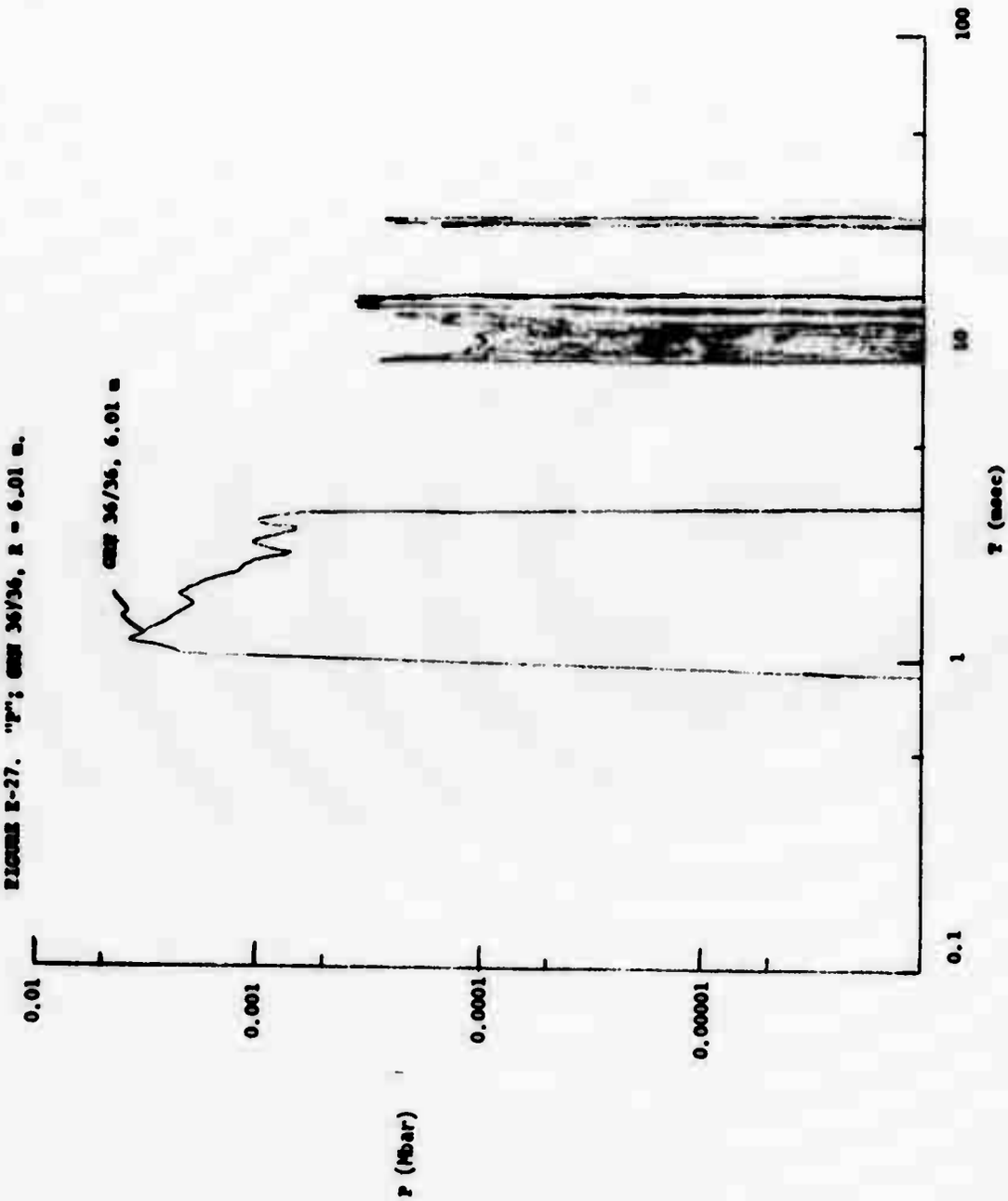

FIGURE E-27. "P"; GMX 36/36, R = 6.01 m.

FIGURE E-28. "V"; GRH 36/36, R = 8.01 m.

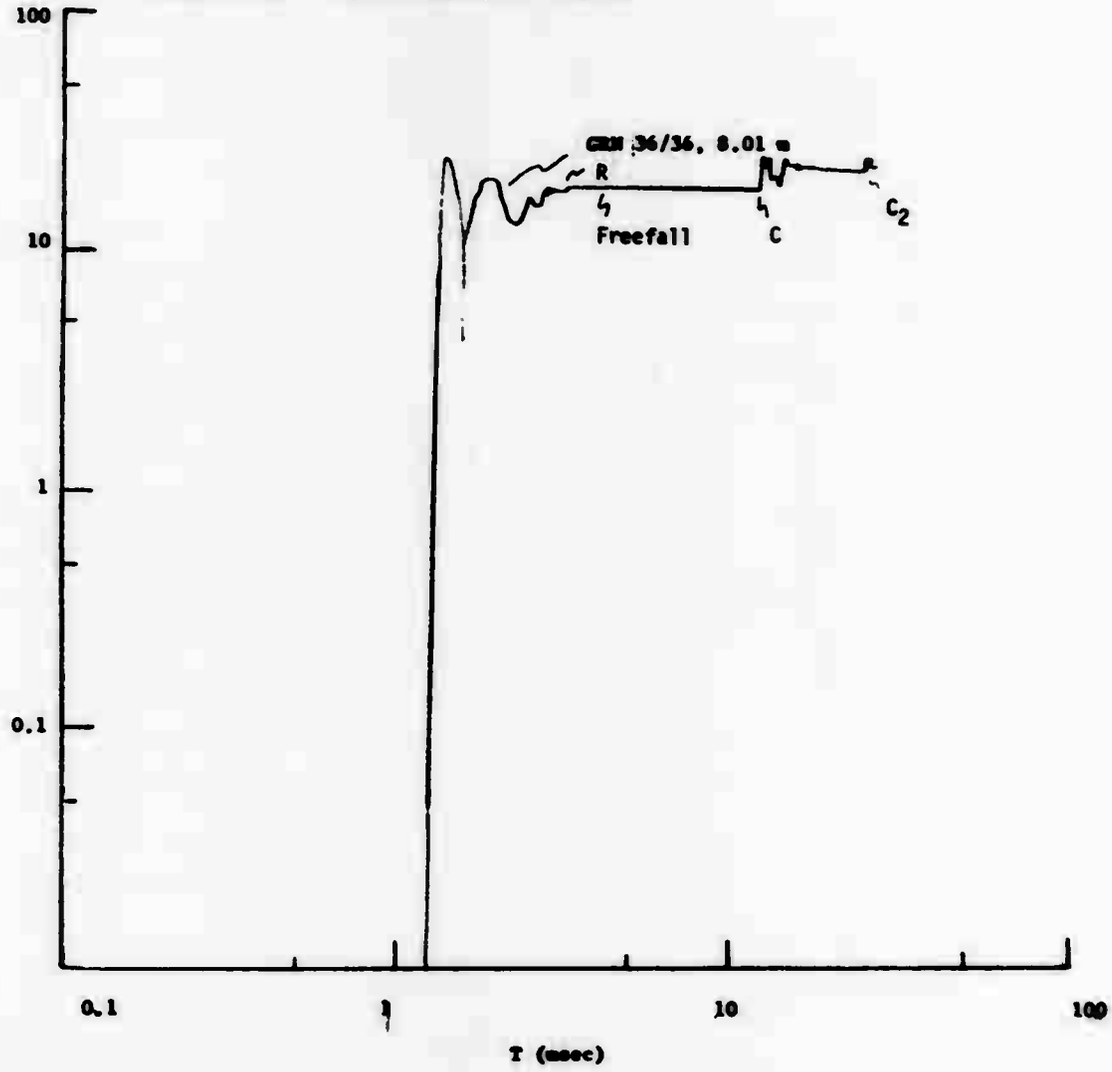

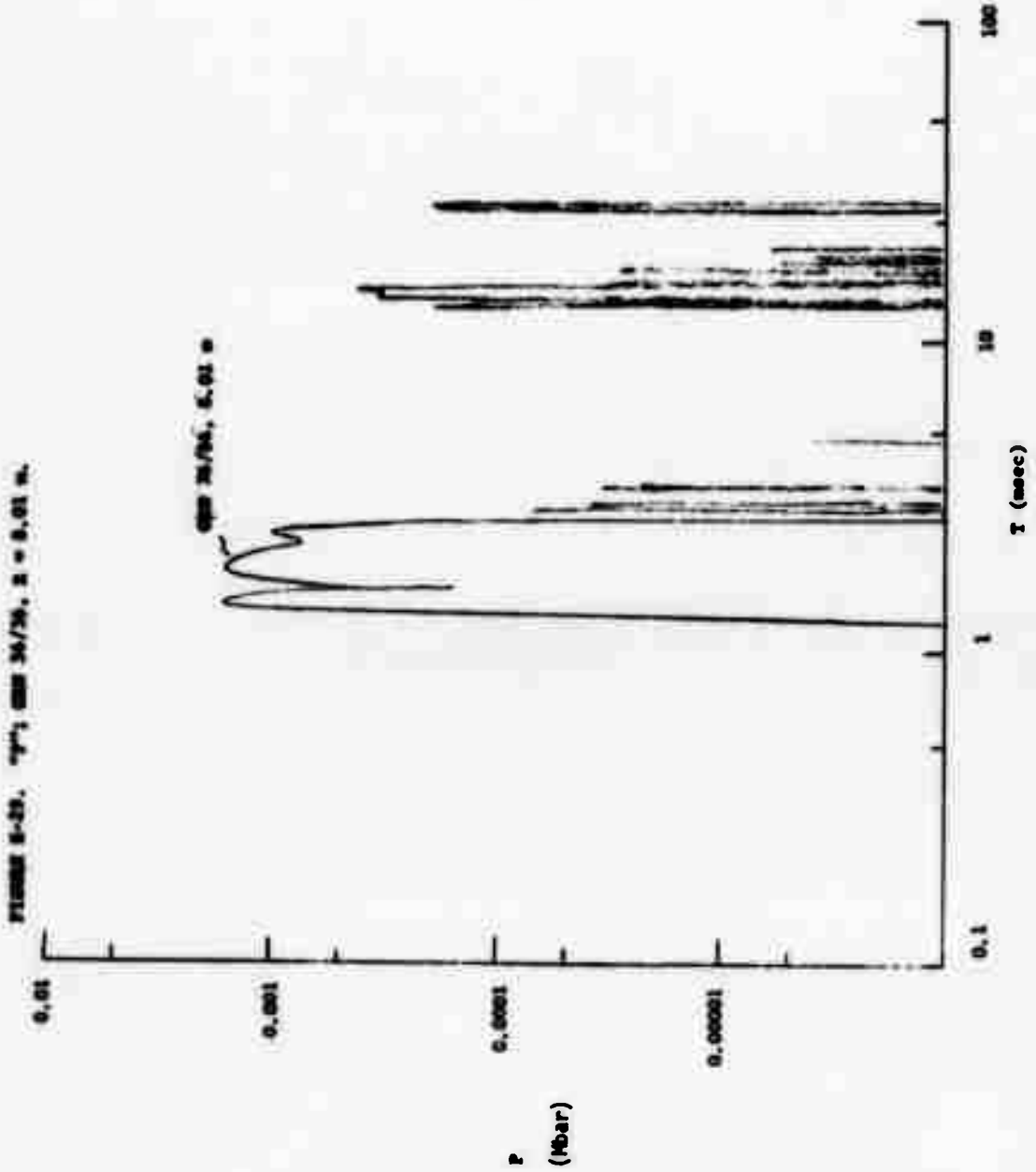
0.01
0.001
0.0001
0.00001
P (Kbar)
0.1
1
10
100
T (msec)

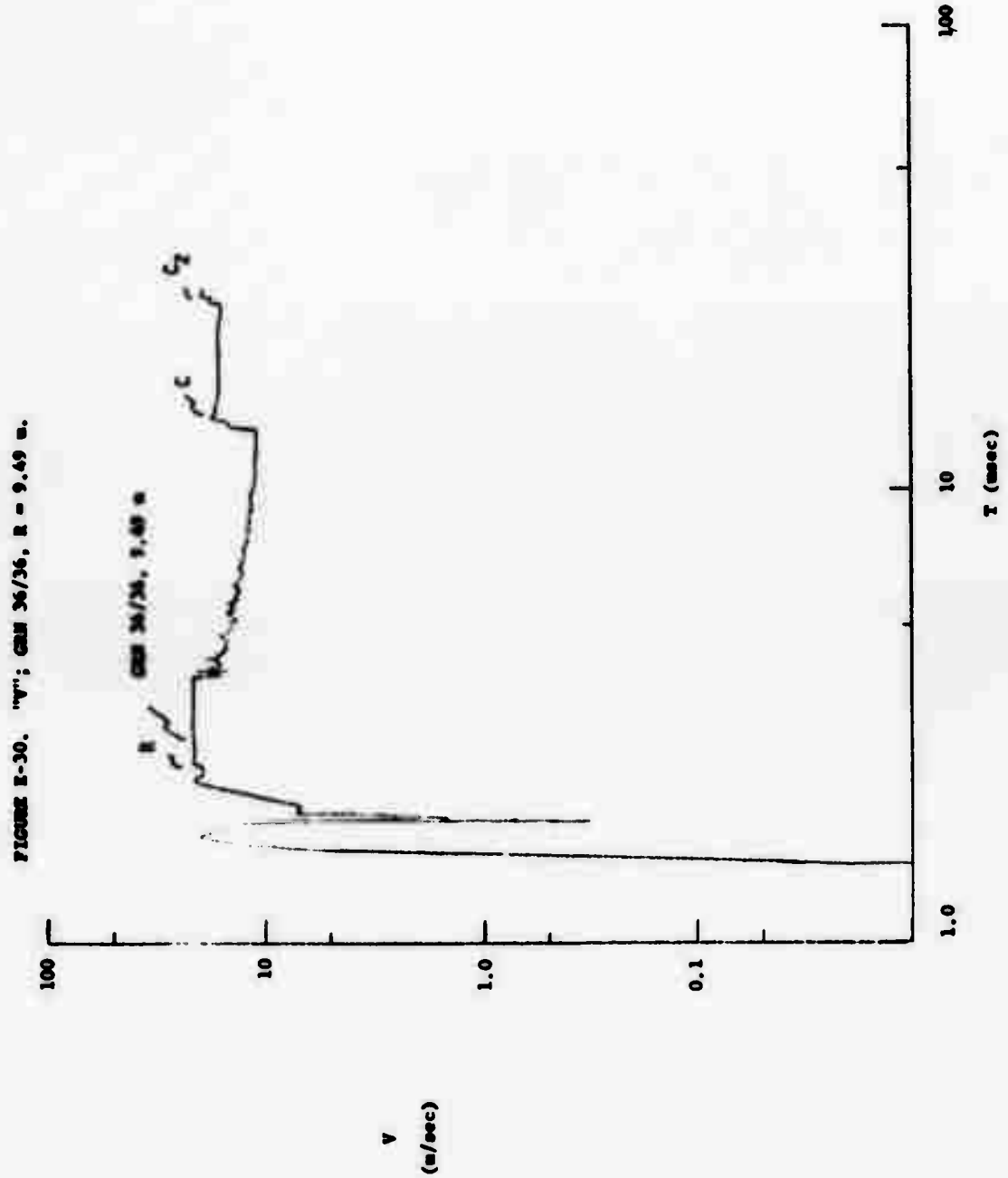

FIGURE E-30. "P"; CRH 36/36, R = 9.49 m.

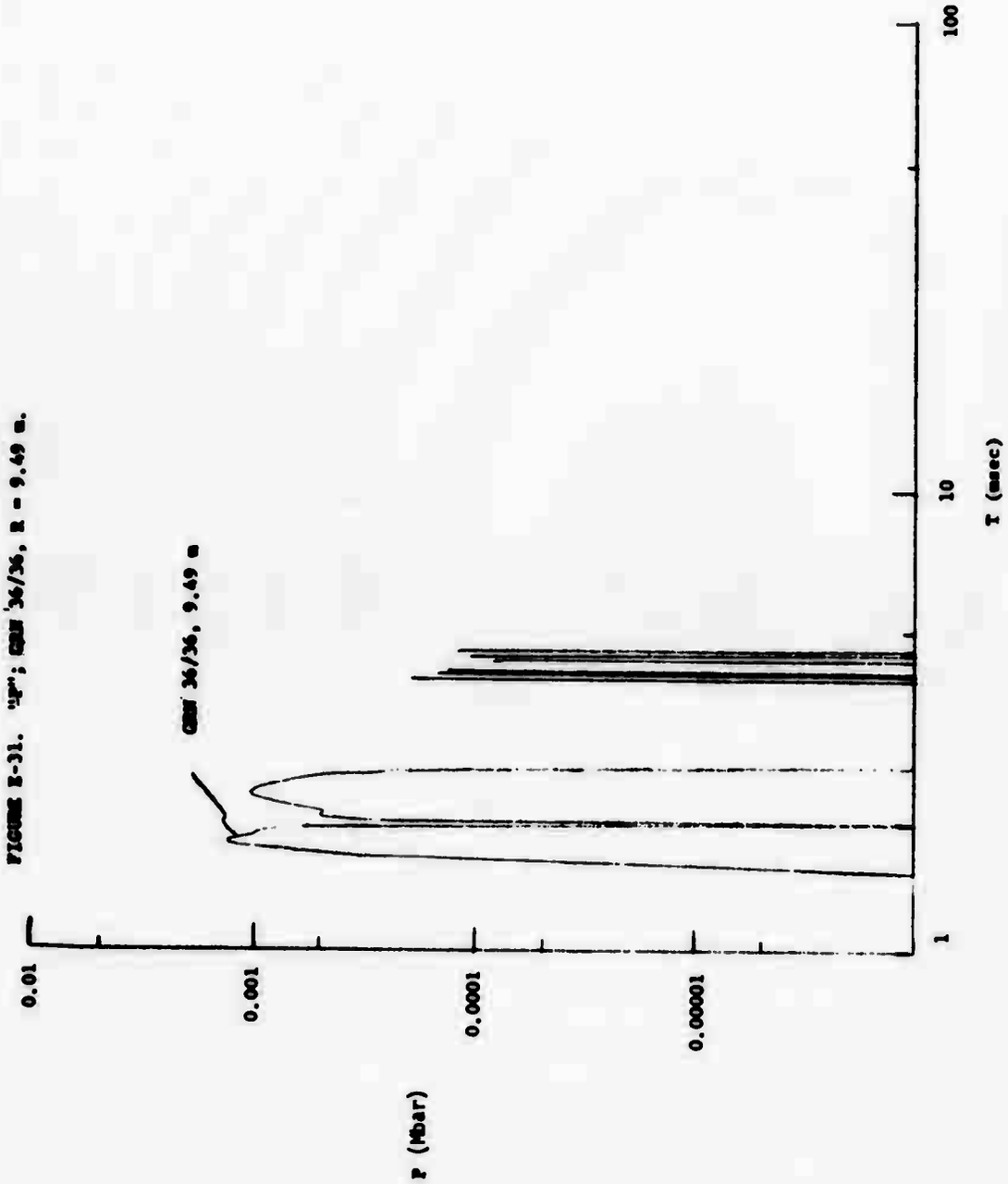

FIGURE E-31. "P"; CHR 36/36, R = 9.49 m.

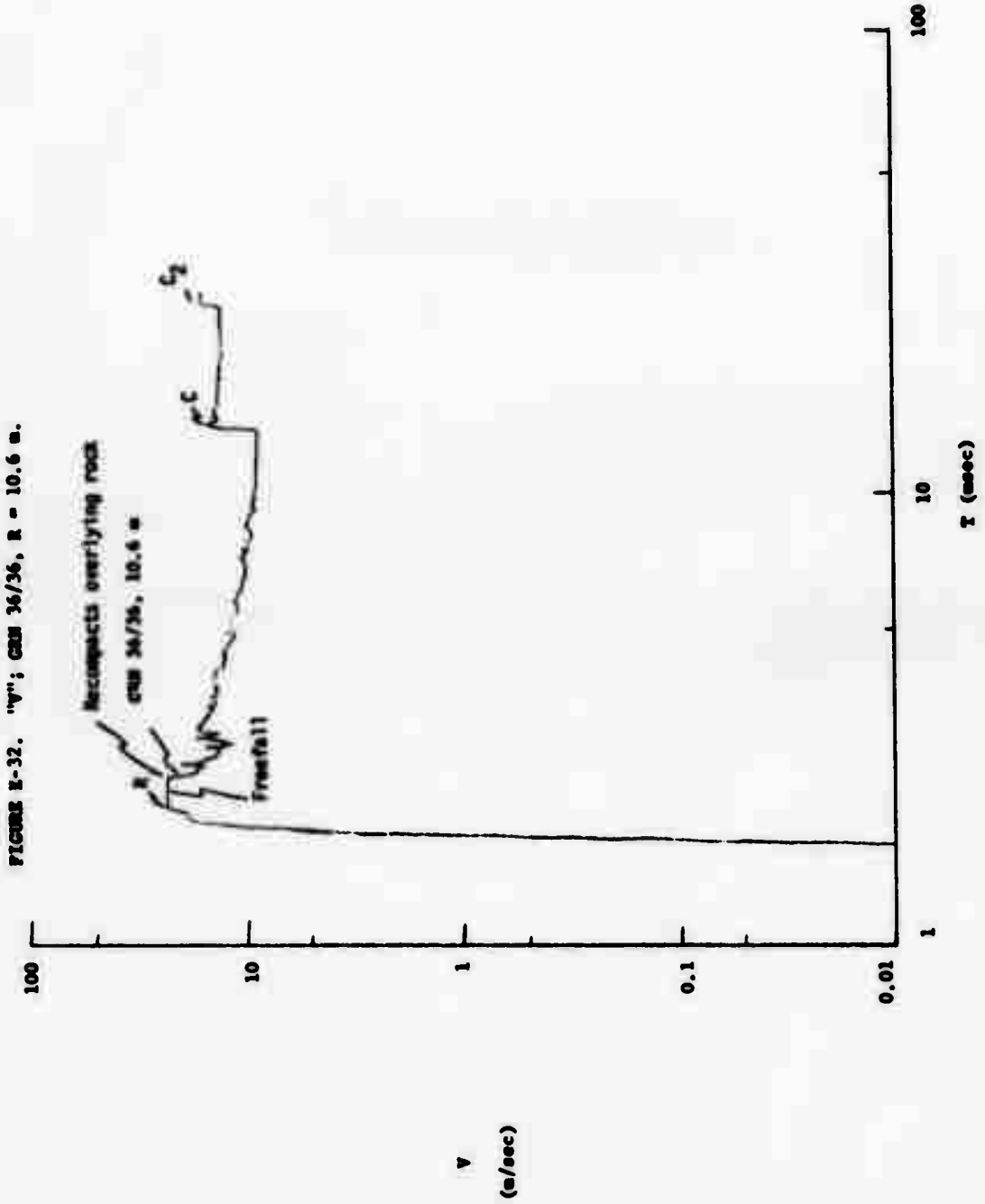

FIGURE E-32. "v"; GEH 36/36, R = 10.6 m.

FIGURE E-33. "V"; GRN 30/36, R = 10.89 m.

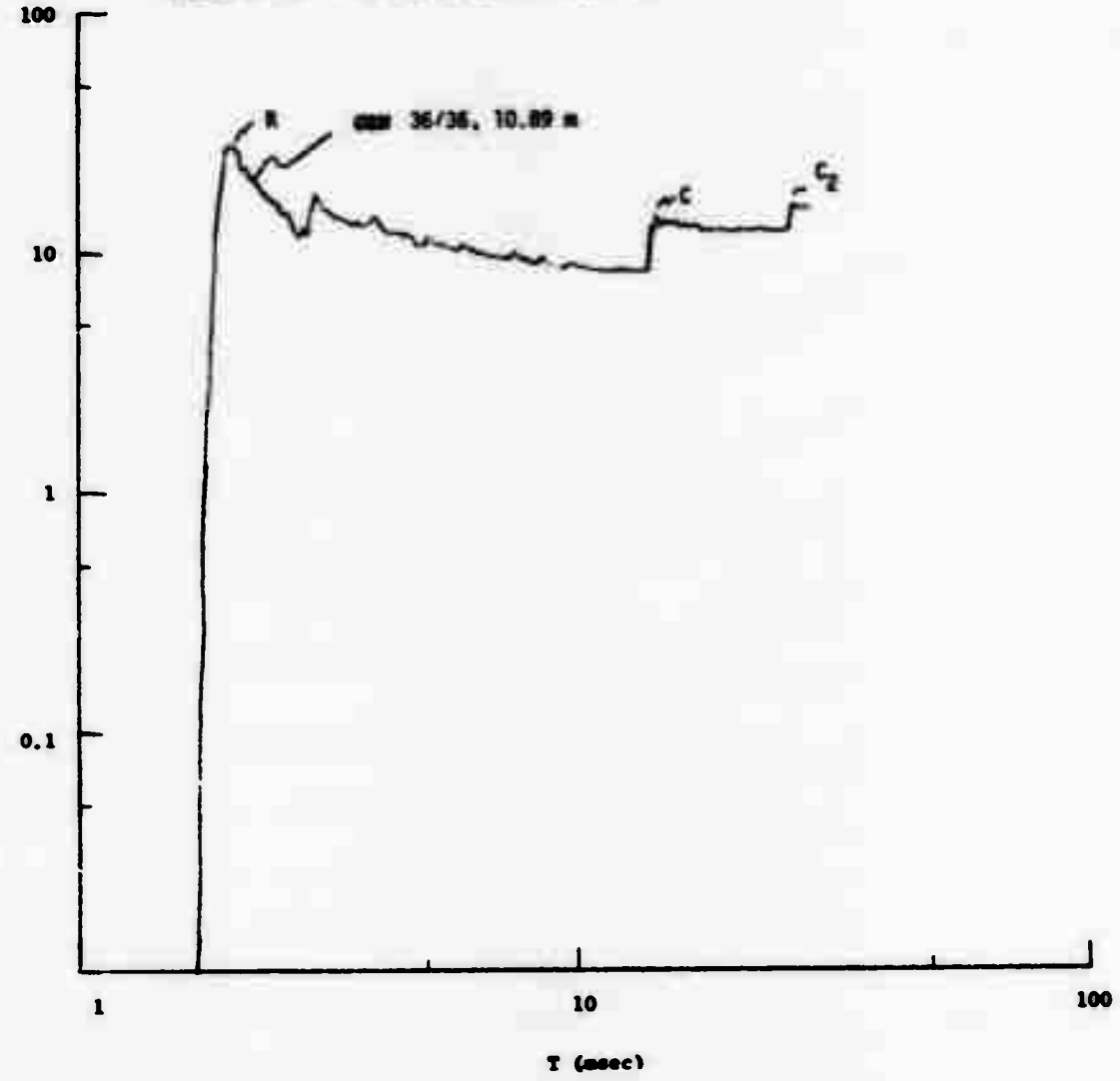

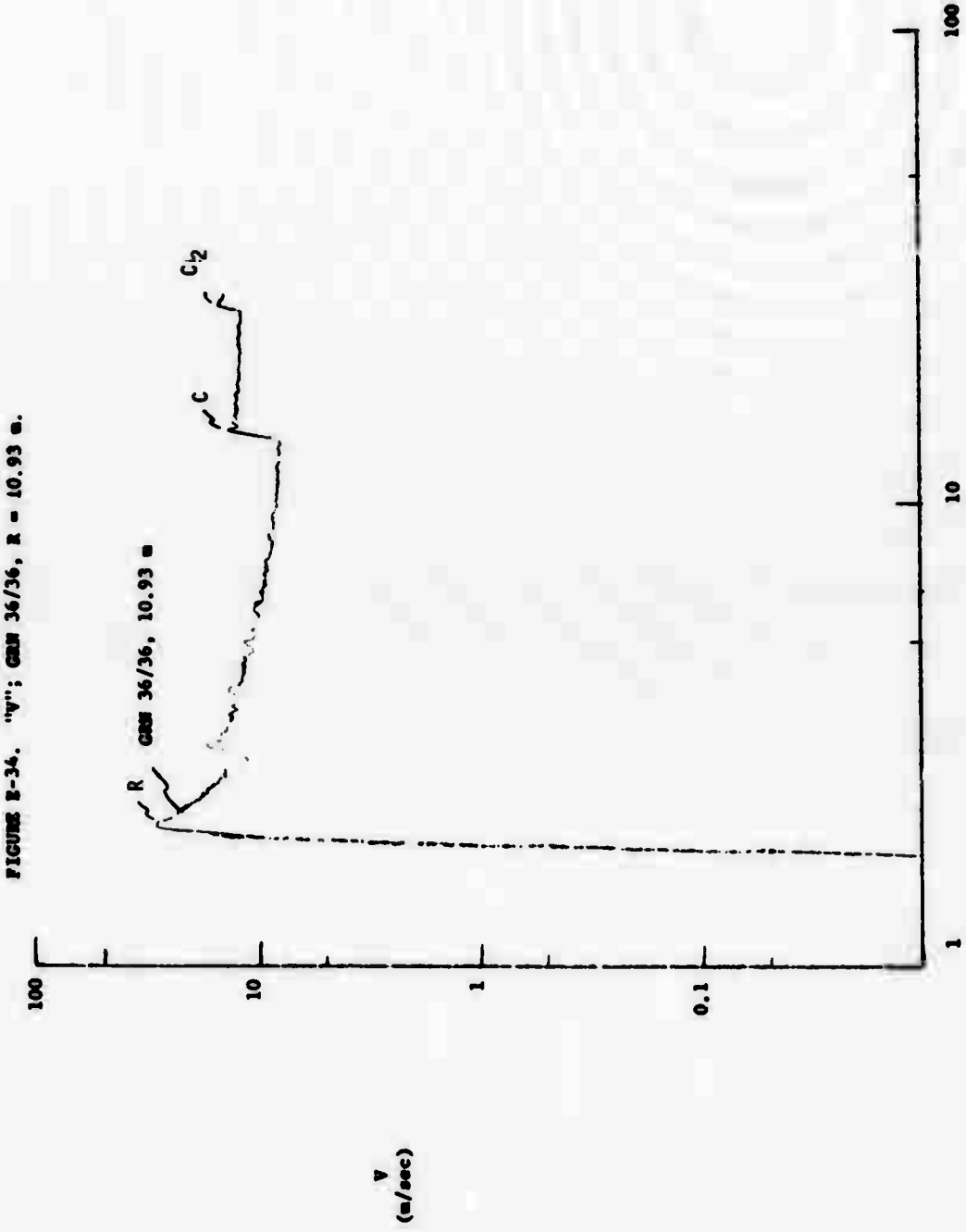

FIGURE E-34. "V"; GEM 36/36, R = 10.93 m.

Appendix F

Water Layer Waveforms
for Vertical Underwater Calculations

(Selected Examples)

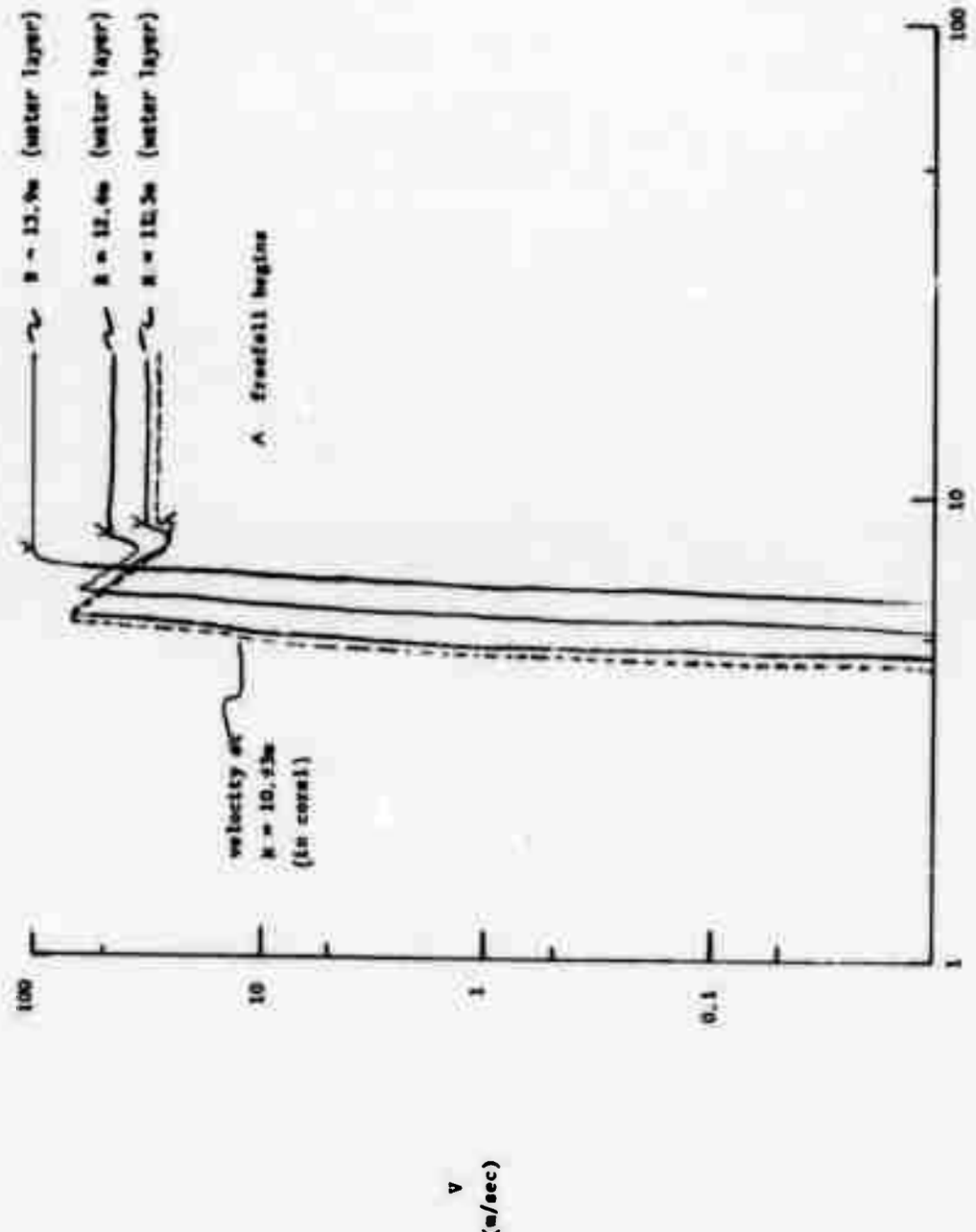

Figure F1. Coral 36/10, Velocity waveforms in water layer.

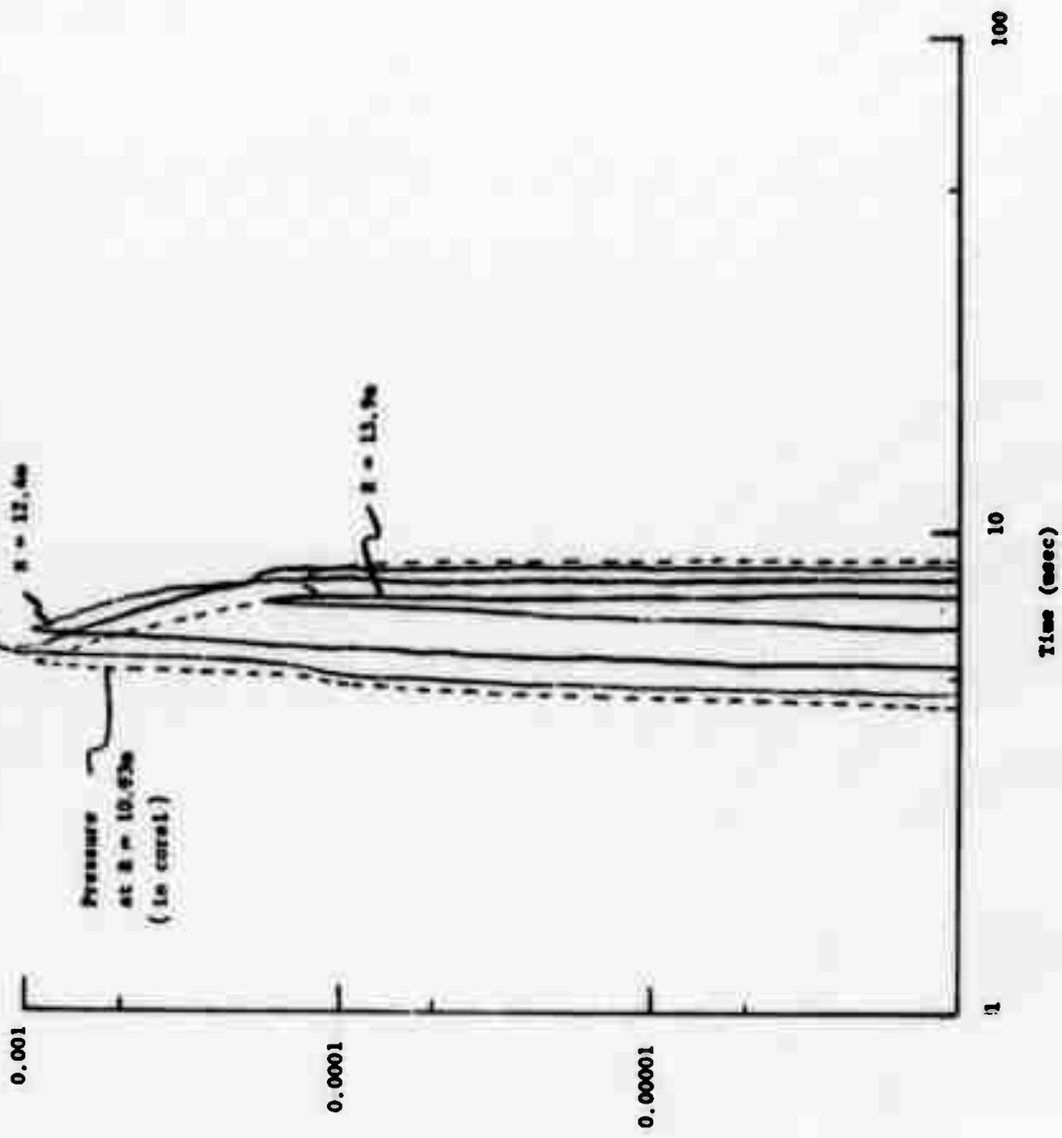

Figure F2. Coral, 35/10, Pressure waveforms in water layer.

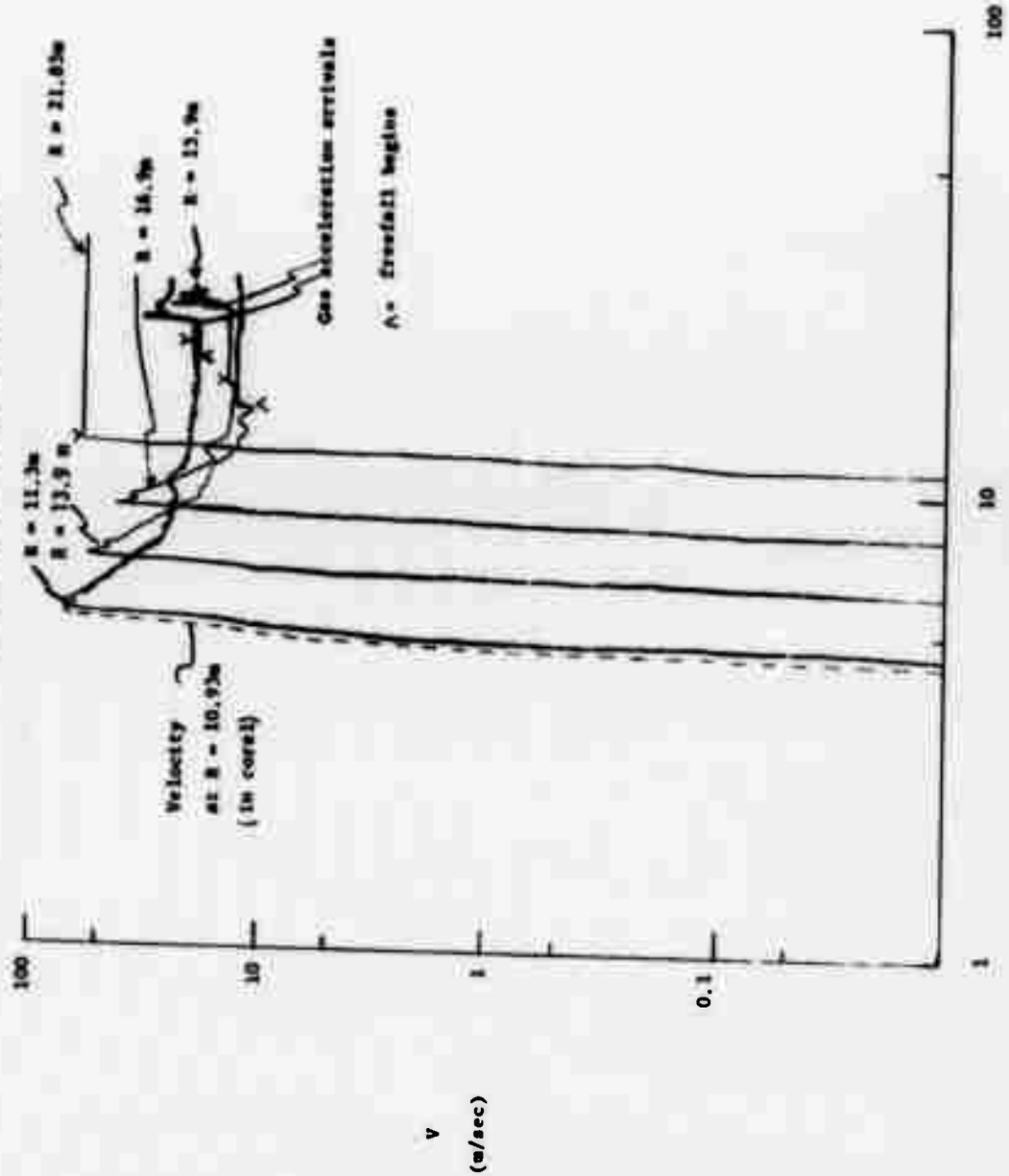

Figure 23. Cast 36/38, velocity waveforms in the water layer.

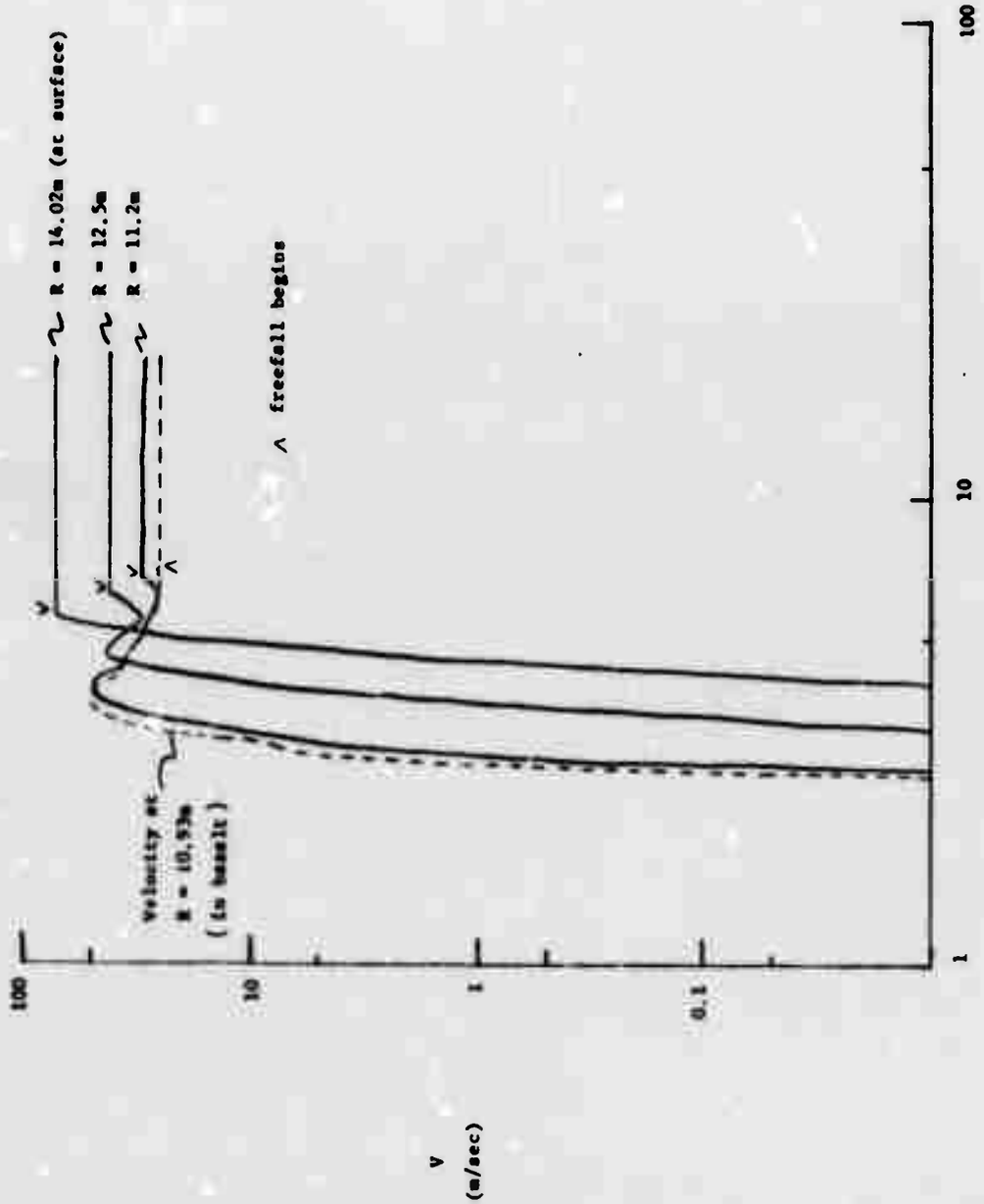

Figure F4. Basalt 36/10, velocity waveforms in water layer.

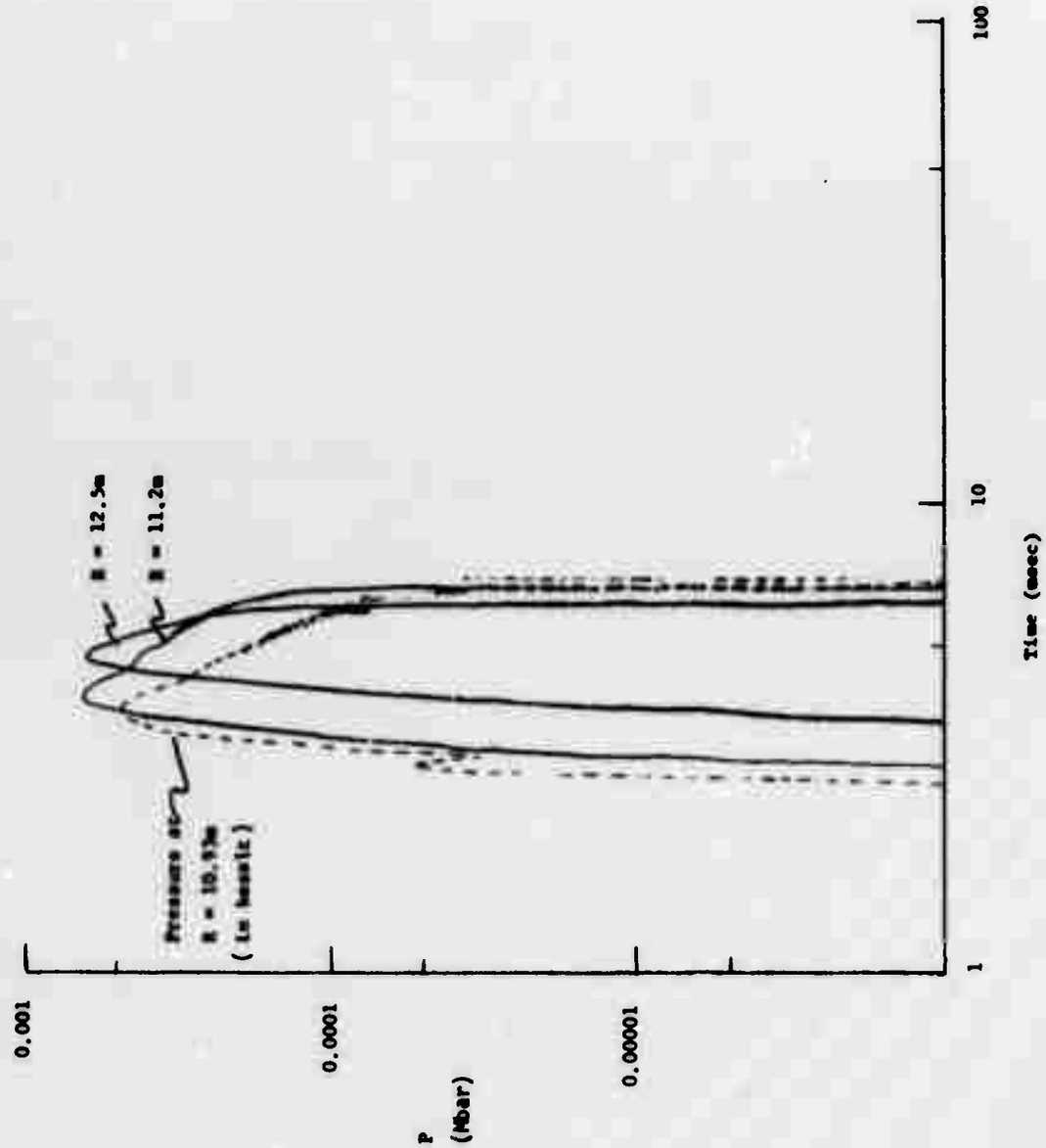

Figure F5. Basalt 36/10, pressure waveforms in water layer.

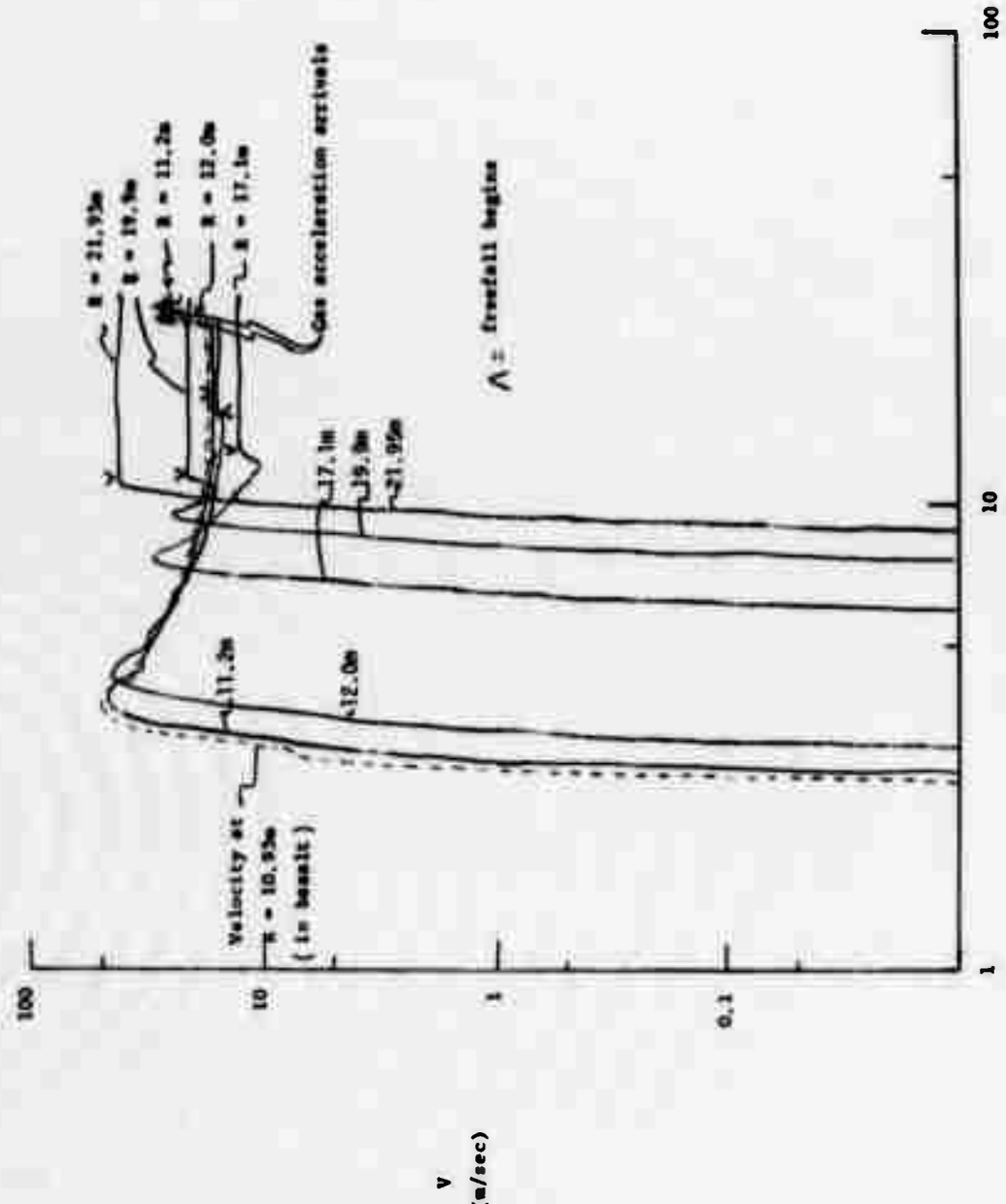

Figure F6. Basalt 30/36, velocity waveforms in the water layer.

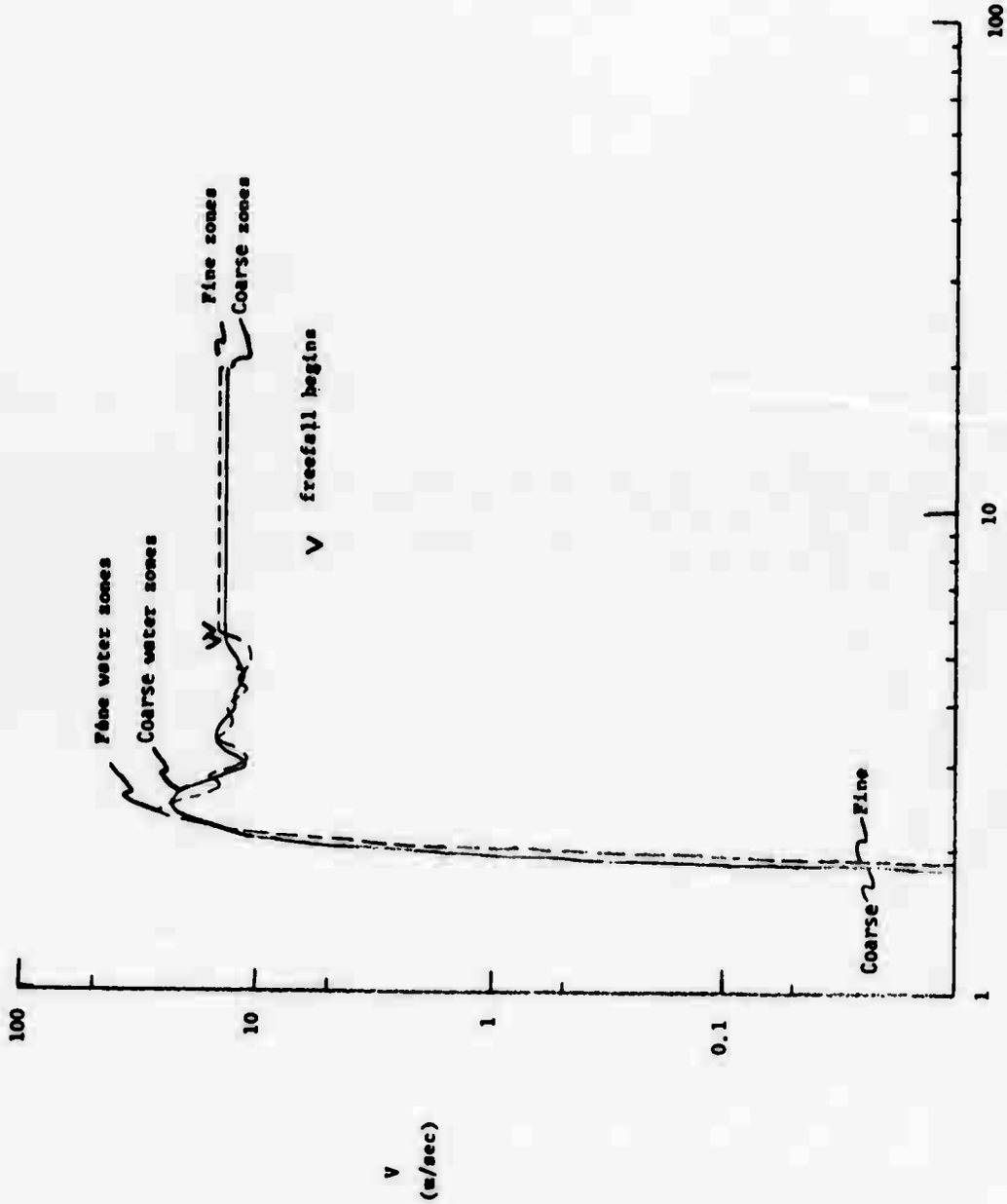

Figure F8. Granite,36/10, velocity waveforms in the water layer at R = 11.4m.

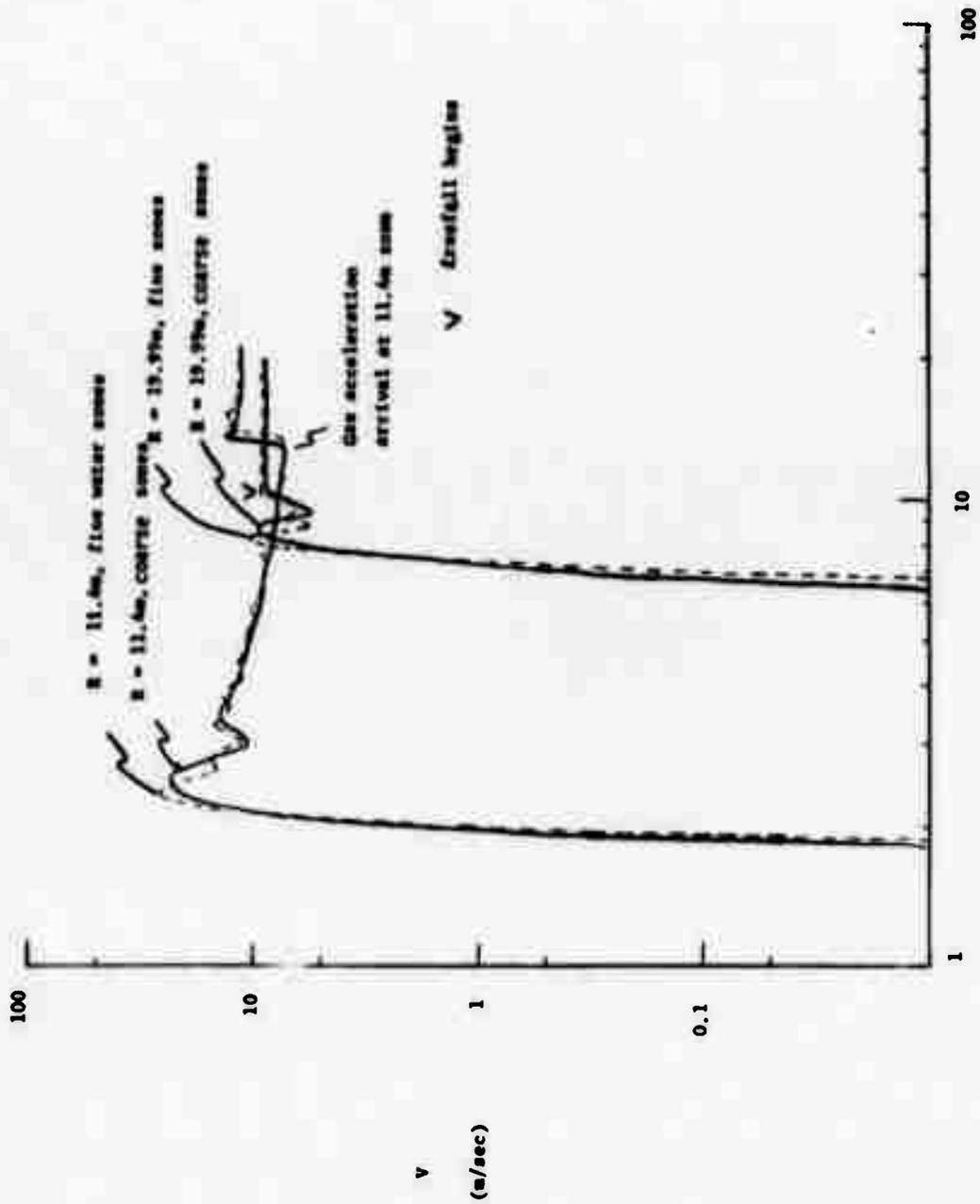

Figure F8. Granite 36/36, velocity waveforms in the water layer.